

Olena Fesenko
Leonid Yatsenko *Editors*

Nanomaterials and Nanocomposites, Nanostructure Surfaces, and Their Applications

Selected Proceedings of the IX
International Conference
Nanotechnology and Nanomaterials
(NANO2021), 25–28 August 2021, Lviv,
Ukraine

Springer Proceedings in Physics

Volume 279

Indexed by Scopus

The series Springer Proceedings in Physics, founded in 1984, is devoted to timely reports of state-of-the-art developments in physics and related sciences. Typically based on material presented at conferences, workshops and similar scientific meetings, volumes published in this series will constitute a comprehensive up-to-date source of reference on a field or subfield of relevance in contemporary physics. Proposals must include the following:

- Name, place and date of the scientific meeting
- A link to the committees (local organization, international advisors etc.)
- Scientific description of the meeting
- List of invited/plenary speakers
- An estimate of the planned proceedings book parameters (number of pages/articles, requested number of bulk copies, submission deadline).

Please contact:

For Americas and Europe: Dr. Zachary Evenson; zachary.evenson@springer.com

For Asia, Australia and New Zealand: Dr. Loyola DSilva; loyola.dsilva@springer.com

Olena Fesenko · Leonid Yatsenko
Editors

Nanomaterials and Nanocomposites, Nanostructure Surfaces, and Their Applications

Selected Proceedings of the IX International
Conference Nanotechnology
and Nanomaterials (NANO2021),
25–28 August 2021, Lviv, Ukraine

 Springer

Editors

Olena Fesenko
Institute of Physics
National Academy of Sciences of Ukraine
Kyiv, Ukraine

Leonid Yatsenko
Institute of Physics
National Academy of Sciences of Ukraine
Kyiv, Ukraine

ISSN 0930-8989

ISSN 1867-4941 (electronic)

Springer Proceedings in Physics

ISBN 978-3-031-18095-8

ISBN 978-3-031-18096-5 (eBook)

<https://doi.org/10.1007/978-3-031-18096-5>

© The Editor(s) (if applicable) and The Author(s), under exclusive license to Springer Nature Switzerland AG 2023

This work is subject to copyright. All rights are solely and exclusively licensed by the Publisher, whether the whole or part of the material is concerned, specifically the rights of translation, reprinting, reuse of illustrations, recitation, broadcasting, reproduction on microfilms or in any other physical way, and transmission or information storage and retrieval, electronic adaptation, computer software, or by similar or dissimilar methodology now known or hereafter developed.

The use of general descriptive names, registered names, trademarks, service marks, etc. in this publication does not imply, even in the absence of a specific statement, that such names are exempt from the relevant protective laws and regulations and therefore free for general use.

The publisher, the authors, and the editors are safe to assume that the advice and information in this book are believed to be true and accurate at the date of publication. Neither the publisher nor the authors or the editors give a warranty, expressed or implied, with respect to the material contained herein or for any errors or omissions that may have been made. The publisher remains neutral with regard to jurisdictional claims in published maps and institutional affiliations.

This Springer imprint is published by the registered company Springer Nature Switzerland AG
The registered company address is: Gewerbestrasse 11, 6330 Cham, Switzerland

Preface

This book highlights the most recent advances in nanoscience from leading researchers in Ukraine, Europe, and beyond. It features contributions from participants of the 10th International Research and Practice Conference “Nanotechnology and Nanomaterials” (NANO-2021), held in Lviv, Ukraine, on August 25–27, 2021. This event was organized jointly by the Institute of Physics of the National Academy of Sciences of Ukraine, Taras Shevchenko National University of Kyiv (Ukraine), University of Tartu (Estonia), University of Turin (Italy), and Pierre and Marie Curie University (France). Internationally recognized experts from a wide range of universities and research institutes shared their knowledge and key results in the areas of nanocomposites and nanomaterials, nanostructured surfaces, microscopy of nanoobjects, nanooptics and nanophotonics, nanoplasmonics, nanochemistry, nanobiotechnology, and surface-enhanced spectroscopy.

Today, nanotechnology is becoming one of the most actively developing and promising fields of science. Numerous nanotechnology investigations are already producing practical results that can be applied in various areas of human life from science and technology to medicine and pharmacology. The aim of these books is to highlight the latest investigations from different areas of nanoscience and to stimulate new interest in this field. Volume II of this two-volume work covers such important topics as nanocomposites, nanostructured surfaces, and their applications.

This book is divided into two parts: Part One—*Nanomaterials and Nanocomposites*; Part Two—*Nanostructured Surfaces*. Parts covering nanooptics photonics and nanobiotechnology can be found in Volume I: *Nanooptics and Photonics, Nanochemistry and Nanobiotechnology and Their Applications*.

The papers published in these four parts fall under the broad categories of nanomaterial preparation and characterization, nanobiotechnology, nanodevices and quantum structures, and spectroscopy and nanooptics. We hope that both volumes will be equally useful and interesting for young scientists or Ph.D. students and mature scientists alike.

Kyiv, Ukraine

Olena Fesenko
Leonid Yatsenko

Contents

Nanomaterials and Nanocomposites

Properties of Liquid Systems Within Nanostructure in the Vicinity of a Critical Point	3
D. Gavryshenko, N. Atamas, G. Taranyik, and G. Verbinska	
Electron Tunneling in Heterostructures with Germanium Quantum Dots	13
Sergey I. Pokytnyi and Volodymyr Ya. Gayvoronsky	
Thermodynamic Analysis of the Process Obtaining Promoted Iron in Various Gaseous Media	23
L. Frolova and B. Blyuss	
Formation of Carbon Nanotubes from Products of Methane Air Conversion on Ni/Cr and Fe Catalysts	31
A. I. Khovavko, A. A. Nebesnyi, D. S. Filonenko, M. Yu. Barabash, A. A. Kolesnichenko, A. M. Sviatenko, S. Ya. Brichka, and Guochao Nie	
Generalized Constitutive Equations and Coupled Phenomena at the Nanoscale: Applications to Nanofluidics	43
Natalya Kizilova	
Investigation of Long-Term Oxidation Resistance of Titanium Alloys with a Coating Based on Ti–Al–C System Nanocomposites	59
Viktoryia Podhurska, Tetiana Prikhna, Orest Ostash, Bogdan Vasyliv, Yuriy Holovatyuk, Volodymyr Sverdun, Tetiana Serbeniuk, Oleksandr Kuprin, and Margarita Bortnitskaya	

Analytical Solutions for N-Electron Interacting System Confined in Graph of Coupled Electrostatic Semiconductor and Superconducting Quantum Dots in Tight-Binding Model with Focus on Quantum Information Processing	67
Krzysztof Pomorski	
Morphology and Physico-mechanical Properties of Antifriction Epoxy Nanocomposites	167
V. Havrylova, S. Zhyltsova, Ye. Mamunya, N. Babkina, and V. Tkach	
Advanced Carbon Nanomaterials and Their Composites for Removal of U(VI) Compounds from Aqueous Solutions (Review)	177
Yuliya Dzyazko, Olga Perlova, and Ivan Martovyi	
The Effect of Ultra-fine Alloying Elements on High-Temperature Strength and Fracture Toughness of Ti-Si-X and Ti-Cr-X Composites	195
Bogdan Vasylyv, Z. A. Duriagina, V. V. Kulyk, V. I. Vavrukh, P. Ya. Lyutyy, T. M. Kovbasiuk, I. A. Lemishka, V. V. Vira, and M. Ya. Holovchuk	
The Study of Properties of Mechanochemical and Ultrasonic Treated BaO/ZrO₂ Composites	217
Olena Sachuk, Valery Zazhigalov, Piotr Dulian, Dorota Rutkowska-Zbik, Olena Kiziun, Michael Kurmach, Ludmyla Kotynska, Volodymyr Starchevskyy, and Sergey Shcherbakov	
State of the Art of Microplastic and Nanoplastic Pollution: Origin and Removal Methods	229
Svitlana Kyrii, Tetiana Dontsova, Olga Karaschuk, and Olena Yanushevska	
Nanostructured Iron-Based Sorption Materials for Drinking Water and Wastewater Treatment	243
Marta Litynska, Tetiana Dontsova, and Anna Gusak	
Tunneling of the Dirac Quasiparticles Through the Fermi Velocity Barriers Based on the Gapped Graphene	257
A. M. Korol, N. V. Medvid, A. I. Sokolenko, and O. Shevchenko	
Electron Interaction-Driven Peculiarities of Strongly Correlated System Thermopower	269
Oleksandr Kramar, Yuriy Dovhopyatyy, and Yuriy Skorenkyy	
Ultrasonic Synthesis and Characterization of Zinc Pyrovanadate Nanostructures	289
O. A. Diyuk, Valery Zazhigalov, N. D. Shcherban, N. V. Diyuk, V. V. Permyakov, S. M. Shcherbakov, L. S. Kuznetsova, and M. M. Tsyba	

Electrical Characteristics of Nanosized ZnO Films, Obtained Using Polyvinyl Alcohol, in Different Atmospheres	301
A. P. Chebanenko, L. M. Filevska, V. S. Grinevych, and V. A. Smytyna	
Estimation of the Role of Nanosized Stabilizing Powders in Gaining High-Level Crack Growth Resistance of Partially Stabilized Zirconia	311
V. V. Kulyk, Bogdan Vasylyv, Z. A. Duriagina, V. I. Vavruk, P. Ya. Lyutyy, T. M. Kovbasiuk, T. L. Tepla, and M. Ya. Holovchuk	
The Effect of Sintering Temperature on Crack Growth Resistance Characteristics of Fine-Grained Partially Stabilized Zirconia Determined by Various Test Methods	331
V. V. Kulyk, Z. A. Duriagina, Bogdan Vasylyv, V. I. Vavruk, T. M. Kovbasiuk, P. Ya. Lyutyy, and T. L. Tepla	
Conductivity of Polymer Composites with Nanocarbon Filler	347
Iryna V. Ovsienko, Lyudmila L. Vovchenko, Lyudmila Yu. Matzui, Tatiana L. Tsaregradskaya, Tetiana A. Len, Galyna V. Saenko, and Vladyslav M. Heraskevych	
Properties of Spectral Parameters of Multicascade Nanostructure Being a Model of Quantum Cascade Detector	361
J. Seti, E. Vereshko, O. Voitsekhivska, and M. Tkach	
Theory of Double Injection in Core-shell Nanowire Radial <i>p-i-n</i> Diodes	377
Vitalii L. Borblik	
Selection of Optimal Technological Parameters for Obtaining Encapsulated Organic-Mineral Fertilizers with Nanoporous Structure	385
S. V. Vakal, V. S. Vakal, A. E. Artyukhov, V. Y. Shkola, and A. O. Yanovska	
Nanostructure Surfaces	
Dispersion Kinetics of Thin Double Hafnium-Copper Films Deposited onto Oxide Materials and Annealed in Vacuum	399
T. V. Stetsyuk, I. I. Gab, O. M. Fesenko, and D. B. Shakhnin	
Structure-Properties Relationships of Nanocomposites Based on Polyethylene Oxide and Anisometric Nanoparticles	409
E. A. Lysenkov, Valeriy Klepko, and M. M. Lazarenko	
Gas-Phase and Plasma-Chemical Bromination: Key Techniques to Prepare Heteroatom-Functionalized Carbon Surfaces	439
V. E. Diyuk, L. M. Grishchenko, A. V. Vakaliuk, G. G. Tsapyuk, O. V. Mischanchuk, O. Yu. Boldyrieva, R. Mariychuk, and V. V. Lisnyak	

Theoretical Analysis of the Heating Process of the Material Surface by a Laser Pulse with Allow for the Accompanying Factors	481
L. V. Shmeleva, A. D. Suprun, and S. M. Naumenko	
Dielectric Behavior of Solid Polymer Electrolyte Films Formed by Double Hydrophilic Block Copolymers	493
L. Kunitskaya, T. Zheltonozhskaya, S. Nesin, Valeriy Klepko, and N. Minenko	
Hybrid Magnetic Particles Based on Laponite RD®: Structure, Stability, and Electrosurface Properties	505
Maryna Manilo, Tetiana Borodinova, Valeriy Klepko, Serhii Cherepov, and Nikolai Lebovka	
Technological Calculation of Granulation Equipment for the Production of Ammonium Nitrate with a Nanoporous Structure: Algorithm and Software Implementation	519
A. E. Artyukhov, I. I. Volk, J. Krmela, O. B. Shandyba, A. S. Chernenko, and D. Ospanov	
Glass Binding for Nanocomposite Materials for Thick-Film Hybrid Integrated Circuits	531
Ya. I. Lepikh, V. A. Borshchak, N. N. Sadova, and N. P. Zatovskaya	
Influence of Titanium Nitride Thin Films on the Electrical Properties of Isotype n-TiN/n-Si Heterostructures	537
I. G. Orletskyi, M. I. Ilashchuk, I. P. Koziarskyi, M. M. Solovan, D. P. Koziarskyi, E. V. Mastruk, and O. A. Parfenyuk	
Water-Soluble Polymers as Substances Modifying the Stability of Colloidal Systems, the Nanostructure of Adsorption Layers	551
Małgorzata Wiśniewska	
Kinetic Regularities of the Interphase Diffusion-Controlled Processes Within Thin Film Formation	569
Yu. P. Vyshnevskaya and I. V. Brazhnyk	
Ionic Conductivity in Single Crystals, Amorphous and Nanocrystalline $\text{Li}_2\text{Ge}_7\text{O}_{15}$ Doped with Cr, Mn, Cu, Al, Gd	585
M. Trubitsyn, M. Koptiev, and M. Volnianskii	
Granulation Unit for Modification and Obtaining of Ammonium Nitrate with Nanoporous Structure: Basics of Calculation and Design	599
N. O. Artyukhova, J. Krmela, A. E. Artyukhov, O. V. Savastru, I. I. Volk, N. S. Borozenets, and D. Ospanov	

Features Forming and Studying Quantum-Dimensional Structures on Surface Electrons Over Helium	613
V. A. Nikolaenko	
Porous Surface Structure and Physico-Chemical Properties of the Urea–Formaldehyde Polyfoam	623
S. Kurta, A. Nemish, S. Fedorchenko, O. Khatsevich, and V. Riy	

Contributors

A. E. Artyukhov Sumy State University, Sumy, Ukraine

N. O. Artyukhova Sumy State University, Sumy, Ukraine

N. Atamas Taras Shevchenko National University of Kyiv, Kyiv, Ukraine

N. Babkina Institute of Macromolecular Chemistry of National Academy of Sciences of Ukraine, Kyiv, Ukraine

M. Yu. Barabash Technical Center of the National Academy of Sciences of Ukraine, Kyiv, Ukraine

B. Blyuss Ukrainian State University of Chemical Technology, Dnipro, Ukraine

O. Yu. Boldyrieva Taras Shevchenko National University of Kyiv, Kyiv, Ukraine

Vitalii L. Borblik V. Lashkarev Institute of Semiconductor Physics, Kyiv, Ukraine

Tetiana Borodinova IBCC: F. D. Ovcharenko Institute of Biocolloidal Chemistry, National Academy of Sciences of Ukraine, Kyiv, Ukraine

N. S. Borozenets Sumy National Agrarian University, Sumy, Ukraine

V. A. Borshchak Odesa I.I. Mechnikov National University, Odesa, Ukraine

Margarita Bortnitskaya Laboratory of Ion-Plasma Processing of Materials, National Science Center Kharkiv Institute of Physics and Technology, Kharkiv, Ukraine

I. V. Brazhnyk Gimasi SA, Mendrisio, Switzerland

S. Ya. Brichka The Gas Institute of the National Academy of Sciences of Ukraine, Kyiv, Ukraine

A. P. Chebanenko Odesa I.I. Mechnikov National University, Odesa, Ukraine

Serhii Cherepov Institute of Magnetism NAS of Ukraine, NAS of Ukraine, Kyiv, Ukraine

- A. S. Chernenko** Odesa I.I. Mechnikov National University, Odessa, Ukraine
- N. V. Diyuk** Taras Shevchenko National University of Kyiv, Kyiv, Ukraine
- O. A. Diyuk** Institute for Sorption and Problems of Endoecology, National Academy of Sciences of Ukraine, Kyiv, Ukraine
- V. E. Diyuk** Taras Shevchenko National University of Kyiv, Kyiv, Ukraine
- Tetiana Dontsova** National Technical University of Ukraine “Igor Sikorsky Kyiv Polytechnic Institute”, Kyiv, Ukraine
- Yuriy Dovhopyatyy** Ternopil Ivan Puluji National Technical University, Ternopil, Ukraine
- Piotr Dulian** Faculty of Chemical Engineering and Technology, Cracow University of Technology, Cracow, Poland
- Z. A. Duriagina** Department of Materials Science and Engineering, Lviv Polytechnic National University, Lviv, Ukraine;
Department of Materials Engineering, The John Paul II Catholic University of Lublin, Lublin, Poland
- Yuliya Dzyazko** VI Vernadskii Institute of General and Inorganic Chemistry of the National Academy of Science of Ukraine, Kyiv, Ukraine
- S. Fedorchenko** Department of Chemistry, Vasyl Stefanyk Precarpathian National University, Ivano-Frankivsk, Ukraine
- O. M. Fesenko** Institute of Physics of National Academy Sciences of Ukraine, Kyiv, Ukraine
- L. M. Filevska** Odesa I.I. Mechnikov National University, Odessa, Ukraine
- D. S. Filonenko** The Gas Institute of the National Academy of Sciences of Ukraine, Kyiv, Ukraine
- L. Frolova** Ukrainian State University of Chemical Technology, Dnipro, Ukraine
- I. I. Gab** Frantsevich Institute for Problems of Materials Science of National Academy Sciences of Ukraine, Kyiv, Ukraine
- D. Gavryshchenko** Taras Shevchenko National University of Kyiv, Kyiv, Ukraine
- Volodymyr Ya. Gayvoronsky** Institute of Physics, National Academy of Sciences of Ukraine, Kyiv, Ukraine
- V. S. Grinevych** Odesa I.I. Mechnikov National University, Odessa, Ukraine
- L. M. Grishchenko** Taras Shevchenko National University of Kyiv, Kyiv, Ukraine
- Anna Gusak** Igor Sikorsky Kyiv Polytechnic Institute, Kyiv, Ukraine
- V. Havrylova** V. Bakul Institute for Superhard Materials, National Academy of Sciences of Ukraine, Kyiv, Ukraine

Vladyslav M. Heraskevych Department of Physics, Taras Shevchenko National University of Kyiv, Kyiv, Ukraine

Yuriy Holovatyuk Department of Hydrogen Technologies and Alternative Energy Materials, Karpenko Physico-Mechanical Institute of the NAS of Ukraine, Lviv, Ukraine

M. Ya. Holovchuk Department of Corrosion and Corrosion Protection, Karpenko Physico-Mechanical Institute of the NAS of Ukraine, Lviv, Ukraine

M. I. Ilashchuk Department of Electronics and Power Engineering, Yuriy Fedkovych Chernivtsi National University, Chernivtsi, Ukraine

Olga Karaschuk National Technical University of Ukraine “Igor Sikorsky Kyiv Polytechnic Institute”, Kyiv, Ukraine

O. Khatsevich Department of Chemistry, Vasyl Stefanyk Precarpathian National University, Ivano-Frankivsk, Ukraine

A. I. Khovavko The Gas Institute of the National Academy of Sciences of Ukraine, Kyiv, Ukraine

Natalya Kizilova Institute of Aeronautics and Applied Mechanics, Warsaw University of Technology, Warsaw, Poland;
V.N. Karazin, Kharkov National University, Kharkov, Ukraine

Olena Kiziun Institute for Sorption and Problems of Endoecology, National Academy of Sciences of Ukraine, Kyiv, Ukraine

Valeriy Klepko Institute of Macromolecular Chemistry, NAS of Ukraine, Kyiv, Ukraine

A. A. Kolesnichenko Technical Center of the National Academy of Sciences of Ukraine, Kyiv, Ukraine

M. Koptiev Experimental Physics Department, Oles Honchar Dnipro National University, Dnipro, Ukraine

A. M. Korol National University for Food Technologies, Kyiv, Ukraine;
Laboratory On Quantum Theory in Linkoping, International Society for Independent Research (ISIR), Linkoping, Sweden

Ludmyla Kotynska Institute for Sorption and Problems of Endoecology, National Academy of Sciences of Ukraine, Kyiv, Ukraine

T. M. Kovbasiuk Department of Materials Science and Engineering, Lviv Polytechnic National University, Lviv, Ukraine

D. P. Koziarskyi Department of Electronics and Power Engineering, Yuriy Fedkovych Chernivtsi National University, Chernivtsi, Ukraine

I. P. Koziarskyi Department of Electronics and Power Engineering, Yuriy Fedkovych Chernivtsi National University, Chernivtsi, Ukraine

Oleksandr Kramar Ternopil Ivan Puluj National Technical University, Ternopil, Ukraine

J. Krmela Alexander Dubcek University of Trencin, I. Krasku, Puchov, Slovak Republic

V. V. Kulyk Department of Materials Science and Engineering, Lviv Polytechnic National University, Lviv, Ukraine

L. Kunitskaya Institute of Macromolecular Chemistry of the NAS of Ukraine, Kyiv, Ukraine

Oleksandr Kuprin Laboratory of Ion-Plasma Processing of Materials, National Science Center Kharkiv Institute of Physics and Technology, Kharkiv, Ukraine

Michael Kurmach L. V. Pisarzhevskii Institute of Physical Chemistry, National Academy of Sciences of Ukraine, Kyiv, Ukraine

S. Kurta Department of Chemistry, Vasyl Stefanyk Precarpathian National University, Ivano-Frankivsk, Ukraine

L. S. Kuznetsova Institute for Sorption and Problems of Endoecology, National Academy of Sciences of Ukraine, Kyiv, Ukraine

Svitlana Kyrii National Technical University of Ukraine “Igor Sikorsky Kyiv Polytechnic Institute”, Kyiv, Ukraine

M. M. Lazarenko Taras Shevchenko National University of Kyiv, Kyiv, Ukraine

Nikolai Lebovka IBCC: F. D. Ovcharenko Institute of Biocolloidal Chemistry, National Academy of Sciences of Ukraine, Kyiv, Ukraine

I. A. Lemishka Department of Materials Science and Engineering, Lviv Polytechnic National University, Lviv, Ukraine

Tetiana A. Len Department of Physics, Taras Shevchenko National University of Kyiv, Kyiv, Ukraine

Ya. I. Lepikh Odesa I.I. Mechnikov National University, Odesa, Ukraine

V. V. Lisnyak Taras Shevchenko National University of Kyiv, Kyiv, Ukraine

Marta Litynska Igor Sikorsky Kyiv Polytechnic Institute, Kyiv, Ukraine

E. A. Lysenkov Petro Mohyla Black Sea National University, Mykolaiv, Ukraine

P. Ya. Lyutyi Department of Materials Science and Engineering, Lviv Polytechnic National University, Lviv, Ukraine

E. V. Maistruk Department of Electronics and Power Engineering, Yuriy Fedkovych Chernivtsi National University, Chernivtsi, Ukraine

Ye. Mamunya Institute of Macromolecular Chemistry of National Academy of Sciences of Ukraine, Kyiv, Ukraine

Maryna Manilo IBCC: F. D. Ovcharenko Institute of Biocolloidal Chemistry, National Academy of Sciences of Ukraine, Kyiv, Ukraine

R. Mariychuk Faculty of Humanities and Natural Sciences, University of Prešov, Prešov, Slovakia

Ivan Martovyi Odessa II Mechnikov National University, Odesa, Ukraine

Lyudmila Yu. Matzui Department of Physics, Taras Shevchenko National University of Kyiv, Kyiv, Ukraine

N. V. Medvid National University for Food Technologies, Kyiv, Ukraine

N. Minenko Institute of Macromolecular Chemistry of the NAS of Ukraine, Kyiv, Ukraine

O. V. Mischanchuk Chuiko Institute of Surface Chemistry of the NAS of Ukraine, Kyiv, Ukraine

S. M. Naumenko Faculty of Physics, Taras Shevchenko National University of Kyiv, Kyiv, Ukraine

A. A. Nebesnyi The Gas Institute of the National Academy of Sciences of Ukraine, Kyiv, Ukraine

A. Nemish Department of Chemistry, Vasyl Stefanyk Precarpathian National University, Ivano-Frankivsk, Ukraine

S. Nesin Institute of Macromolecular Chemistry of the NAS of Ukraine, Kyiv, Ukraine

Guochao Nie School of Physics and Telecommunication Engineering, Yulin Normal University, Yulin, China

V. A. Nikolaenko B. Verkin Institute for Low Temperature Physics and Engineering of NAS of Ukraine, Kharkov, Ukraine

I. G. Orletskiy Department of Electronics and Power Engineering, Yuriy Fedkovych Chernivtsi National University, Chernivtsi, Ukraine

D. Ospanov Saken Seifullin Kazakh Agrotechnical University, Nur-Sultan, Republic of Kazakhstan

Orest Ostash Department of Hydrogen Technologies and Alternative Energy Materials, Karpenko Physico-Mechanical Institute of the NAS of Ukraine, Lviv, Ukraine

Iryna V. Oviienko Department of Physics, Taras Shevchenko National University of Kyiv, Kyiv, Ukraine

O. A. Parfenyuk Department of Electronics and Power Engineering, Yuriy Fedkovych Chernivtsi National University, Chernivtsi, Ukraine

Olga Perlova Odessa II Mechnikov National University, Odesa, Ukraine

V. V. Permyakov Institute of Geological Sciences, National Academy of Sciences of Ukraine, Kyiv, Ukraine

Viktoriya Podhurska Department of Hydrogen Technologies and Alternative Energy Materials, Karpenko Physico-Mechanical Institute of the NAS of Ukraine, Lviv, Ukraine

Sergey I. Pokytnyi Chuiko Institute of Surface Chemistry, National Academy of Sciences of Ukraine, Kyiv, Ukraine;
Institute of Physics, National Academy of Sciences of Ukraine, Kyiv, Ukraine

Krzysztof Pomorski Faculty of Computer Science and Telecommunications, Cracow University of Technology, Cracow, Poland;
School Of Electrical And Electronic Engineering, University College Dublin, Dublin, Ireland;
Quantum Hardware Systems, Lodz, Poland

Tetiana Prikhna Department of Sintering Technologies of Ceramics, Institute for Superhard Materials of the NAS of Ukraine, Kyiv, Ukraine

V. Riy Department of Chemistry, Vasyl Stefanyk Precarpathian National University, Ivano-Frankivsk, Ukraine

Dorota Rutkowska-Zbik Jerzy Haber Institute of Catalysis & Surface Chemistry, Polish Academy of Sciences, Cracow, Poland

Olena Sachuk Institute for Sorption and Problems of Endoecology, National Academy of Sciences of Ukraine, Kyiv, Ukraine

N. N. Sadova Odesa I.I. Mechnikov National University, Odesa, Ukraine

Galyna V. Saenko Department of Physics, Taras Shevchenko National University of Kyiv, Kyiv, Ukraine

O. V. Savastru Odesa I.I. Mechnikov National University, Odessa, Ukraine

Tetiana Serbeniuk Department of Sintering Technologies of Ceramics, Institute for Superhard Materials of the NAS of Ukraine, Kyiv, Ukraine

J. Seti Department of Theoretical Physics and Computer Simulation, Yuriy Fedkovych Chernivtsi National University, Chernivtsi, Ukraine

D. B. Shakhnin University “Ukraine”, Kyiv, Ukraine

O. B. Shandyba Sumy National Agrarian University, Sumy, Ukraine

S. M. Shcherbakov M.G. Kholodny Institute of Botany, National Academy of Sciences of Ukraine, Kyiv, Ukraine

Sergey Shcherbakov M.G. Kholodny Institute of Botany, National Academy of Science of Ukraine, Kyiv, Ukraine

N. D. Shcherban L.V. Pisarzhevsky Institute of Physical Chemistry, National Academy of Sciences of Ukraine, Kyiv, Ukraine

O. Shevchenko National University for Food Technologies, Kyiv, Ukraine

V. Y. Shkola Sumy State University, Sumy, Ukraine

L. V. Shmeleva Faculty of Physics, Taras Shevchenko National University of Kyiv, Kyiv, Ukraine

Yuriy Skorenkyy Ternopil Ivan Puluj National Technical University, Ternopil, Ukraine

V. A. Smyntyna Odesa I.I. Mechnikov National University, Odesa, Ukraine

A. I. Sokolenko National University for Food Technologies, Kyiv, Ukraine

M. M. Solovan Department of Electronics and Power Engineering, Yuriy Fedkovych Chernivtsi National University, Chernivtsi, Ukraine

Volodymyr Starchevskyy National University «Lviv Polytechnic». 12, Lviv, Ukraine

T. V. Stetsyuk Frantsevich Institute for Problems of Materials Science of National Academy Sciences of Ukraine, Kyiv, Ukraine

A. D. Suprun Faculty of Physics, Taras Shevchenko National University of Kyiv, Kyiv, Ukraine

Volodymyr Sverdun Department of Sintering Technologies of Ceramics, Institute for Superhard Materials of the NAS of Ukraine, Kyiv, Ukraine

A. M. Sviatenko The Gas Institute of the National Academy of Sciences of Ukraine, Kyiv, Ukraine

G. Taranyik International European University, Kyiv, Ukraine

T. L. Tepla Department of Materials Science and Engineering, Lviv Polytechnic National University, Lviv, Ukraine

M. Tkach Department of Theoretical Physics and Computer Simulation, Yuriy Fedkovych Chernivtsi National University, Chernivtsi, Ukraine

V. Tkach V. Bakul Institute for Superhard Materials, National Academy of Sciences of Ukraine, Kyiv, Ukraine

M. Trubitsyn Experimental Physics Department, Oles Honchar Dnipro National University, Dnipro, Ukraine

G. G. Tsapyuk Taras Shevchenko National University of Kyiv, Kyiv, Ukraine

Tatiana L. Tsaregradskaya Department of Physics, Taras Shevchenko National University of Kyiv, Kyiv, Ukraine

M. M. Tsyba Institute for Sorption and Problems of Endoecology, National Academy of Sciences of Ukraine, Kyiv, Ukraine

S. V. Vakal Scientific-Research Institute of Mineral Fertilizers and Pigments of the Sumy State University, Sumy, Ukraine

V. S. Vakal Scientific-Research Institute of Mineral Fertilizers and Pigments of the Sumy State University, Sumy, Ukraine

A. V. Vakaliuk Taras Shevchenko National University of Kyiv, Kyiv, Ukraine

Bogdan Vasyliiv Department of Hydrogen Technologies and Alternative Energy Materials, Karpenko Physico-Mechanical Institute of the NAS of Ukraine, Lviv, Ukraine

V. I. Vavrukh Department of Materials Science and Engineering, Lviv Polytechnic National University, Lviv, Ukraine

G. Verbinska Taras Shevchenko National University of Kyiv, Kyiv, Ukraine

E. Vereshko Department of Theoretical Physics and Computer Simulation, Yuriy Fedkovych Chernivtsi National University, Chernivtsi, Ukraine

V. V. Vira Department of Strength of Materials and Structural Mechanics, Lviv Polytechnic National University, Lviv, Ukraine

O. Voitsekhivska Department of Theoretical Physics and Computer Simulation, Yuriy Fedkovych Chernivtsi National University, Chernivtsi, Ukraine

I. I. Volk Sumy State University, Sumy, Ukraine

M. Volnianskii Experimental Physics Department, Oles Honchar Dnipro National University, Dnipro, Ukraine

Lyudmila L. Vovchenko Department of Physics, Taras Shevchenko National University of Kyiv, Kyiv, Ukraine

Yu. P. Vyshnevska National Technical University of Ukraine, Igor Sikorsky Kyiv Polytechnic Institute, Kyiv, Ukraine

Małgorzata Wiśniewska Faculty of Chemistry, Department of Radiochemistry and Environmental Chemistry, Institute of Chemical Sciences, Maria Curie- Skłodowska University in Lublin, Lublin, Poland

A. O. Yanovska Sumy State University, Sumy, Ukraine

Olena Yanushevska National Technical University of Ukraine “Igor Sikorsky Kyiv Polytechnic Institute”, Kyiv, Ukraine

N. P. Zatovskaya Odesa I.I. Mechnikov National University, Odesa, Ukraine

Valery Zazhigalov Institute for Sorption and Problems of Endoecology, National Academy of Sciences of Ukraine, Kyiv, Ukraine

T. Zheltonozhkaya Institute of Macromolecular Chemistry of the NAS of Ukraine,
Kyiv, Ukraine

S. Zhyltsova Vasyl' Stus Donetsk National University, Vinnytsia, Ukraine

Nanomaterials and Nanocomposites

Properties of Liquid Systems Within Nanostructure in the Vicinity of a Critical Point



D. Gavryshenko, N. Atamas, G. Taranyik, and G. Verbinska

Abstract The influence of a spatial nanoconfinement on a thermodynamic behavior of equilibrium properties of fluid systems has been investigated. The correlation effects generalization of a confined non-uniform fluid theory has been built in the case of a binary solution for nanostructures. The obtained results let us calculate the concentration spatial distribution of a binary fluid system within a wide range of variations of the thermodynamic parameters for nanosystems of a different form. A second-order differential equations for a local density and concentration were obtained on the base of solution of isoparametric problem minimization of system's free energy as a functional of density and concentration under the condition of a constant number of particles. Density profiles of a binary solution were calculated along the critical isochor within the nanostructure. Obtained results show that in this case, density and concentrations become a nonlinear function of the coordinate. The density profiles of fluid were calculated within a single-wall carbon nanotube. It is shown that bulk density essentially inclines from the average value.

Keywords Binary solution in confined geometry · Nanovolumes · Density spatial distribution · Concentration spatial distribution

D. Gavryshenko · N. Atamas (✉) · G. Verbinska
Taras Shevchenko National University of Kyiv, Kyiv, Ukraine
e-mail: atamasphys@mail.univ.kiev.ua

D. Gavryshenko
e-mail: dg@univ.kiev.ua

G. Verbinska
e-mail: verbin@univ.kiev.ua

G. Taranyik
International European University, Kyiv, Ukraine

1 Introduction

The study of the density profile, as well as the spatial distribution of concentrations, and chemical potentials of solution components in the external field (gravitational effect [1]) in a limited system near a critical point liquid vapor, and critical stratification points of important amplitudes of the corresponding scale laws, and also widely applied in research of processes of adsorption in the limited systems [2, 3], and thermodynamic behavior of liquid systems in nanovolumes [4]. Both theoretical methods [5, 6] and computer modeling methods [7] are used to study this problem. It is also important to construct a solution of this problem for supercritical states [8].

In classical thermodynamics, this problem is solved in the local approximation on the basis of a known algebraic relationship between the chemical potential of the system $\mu(\vec{r})$ and an potential of the external field $u(\vec{r})$:

$$\mu_0 - \mu(\vec{r}) = u(\vec{r}),$$

where μ_0 is the chemical potential of the system in the absence of an external field [9]. However, with large gradients of the external field, or in the vicinity of critical points of different nature, non-local effects become significant. Therefore, in the general case, to calculate the local density $\rho(\vec{r})$ and concentration $x(\vec{r})$ for nanosystems and for the systems under the external field, it is necessary to solve the problem of minimizing the free energy functional of the system.

The calculation of the liquid density profile $n = n(\vec{r}, T)$ for individual liquid substances in a gravitational field $u(\vec{r})$ was first proposed by Van der Waals on the basis of a local expression. Later, the refined form of this classical result was taken as a basis for a number of studies by different authors [10, 11]. In [12, 13], paired correlation functions are found within the framework of Ornstein–Zernike theory and in the approximation of anomalous dimension, and also situations when paired correlations become long-range [14] are analyzed. This approach allowed to obtain refinement of expressions for calculating the density of an inhomogeneous system.

The presence of limiting surfaces leads, firstly, to the need to consider the thermodynamics of matter and critical phenomena in a limited volume on the phase boundary [15] (in particular, there is no boundary thermodynamic transition), and secondly, to the need to take into account the interaction potential fluid with a wall [16].

In spatially bounded fluids in the critical region, which are essentially anisotropic systems, there must be effects due to the density distribution both in the surface layers in the direction perpendicular to the bounding surface, and the height density distribution resulting from the gravitational effect [17].

The state of such a system can be fully determined by a set of intensive parameters, none of which describes the size of the system or the shape of the surface that limits it, and the total number of particles $N = N_A + N_B$, where N_A and N_B are the number of particles of the variety “A” and “B”, accordingly.

To build a consistent thermodynamic theory to describe the behavior of a one-component inhomogeneous system, a fundamental approach was previously proposed based on calculating the contribution from each layer between equipotential surfaces not to the corresponding thermodynamic potentials, but to the Hamiltonian of the system. In this case, one can write:

$$u(\vec{r}) = \mu_0 - \mu(\vec{r}) + \Delta\mu_{cor}(\vec{r}), \quad (1)$$

where $\Delta\mu_{cor}$ is the contribution due to correlation effects for which the expression in the form of an infinite series was obtained [18].

The aim of this work is to generalize the formalism proposed in [19] in the case of a two-component solution under the action of an external field in nanosystems in a wide range of changes of thermodynamic parameters, including around the critical stratification point. This paper also considers the problem of obtaining density and concentration profiles of a binary solution in a plane-parallel layer with exponential near-wall potential.

2 Results and Discussion

2.1 Chemical Potential of an Inhomogeneous Binary System

To describe the thermodynamic behavior of an inhomogeneous binary fluid in a bounded system, we use a lattice model of a fluid in which an external field $u(z)$ acts along the axis Oz ; in addition, the system is bounded in this direction: z it can vary within $[-L, L]$. Having constructed the decomposition of the potential of the external field $u_{BA}(\vec{r}) = u_B(\vec{r}) - u_A(\vec{r})$ into the Taylor functional series $\Delta x(\vec{r}) = x(\vec{r}) - x^0$ according to the deviations of the concentration from its value x^0 under the absence of an external field, we obtain an expression $u_{BA}(\vec{r})$ similar to the expression (1):

$$\beta u_{BA}(z) = \beta(\mu_0 - \mu(z)) + a \frac{d^2}{dz^2} \Delta x(z), \quad (2)$$

where a is spatial moment of direct correlations function, $\beta = 1/kT$.

The construction of the solution of the obtained equation for nanosystems has certain features. In particular, the solution of this equation must be subjected to the conditions of transversality, which in this case have the following obvious form:

$$\left. \frac{d}{dz} \Delta x(z) \right|_{\pm L} = 0, \quad (3)$$

and isoparametry (in this case—the condition of the number of particles constancy in the system):

$$\int_{-L}^L dz \Delta x(z) = 0. \quad (4)$$

Note, that the imposition of the additional condition (4) in the solution of Eq. (2) is related to the need of specificity of the chemical potential of a homogeneous system. The obtained results indicate that the formula for a local approximation can be used only to describe the concentration distribution of inhomogeneous binary systems in the presence of external fields of a small spatial gradients that are far from a critical point. But as we approach the critical point, the role of correlation terms increases, and therefore it is necessary to use the obtained expression.

2.2 Distribution of Concentration in a Non-Ideal Pore in the Gravitational Field Near the Critical Point of Stratification

Consider the case when the system along the axis of the gravitational field $0z$, the potential of which is given by the obvious expressions:

$$\begin{aligned} u_A(z) &= -m_{0A}gz, \\ u_B(z) &= -m_{0B}gz, \end{aligned} \quad (5)$$

where g —is free fall acceleration, and there are forces of attraction or repulsion near the walls (so-called non-ideal time), the potential of which is modeled by the following expressions [18]:

$$\begin{aligned} u_A(z) &= B_{A1}e^{-k(L+z)} + B_{A2}e^{-k(L-z)} \\ &= (B_{A1} + B_{A2})e^{-kL}ch\kappa z + (B_{A1} - B_{A2})e^{-kL}sh\kappa z, \\ u_B(z) &= B_{B1}e^{-k(L+z)} + B_{B2}e^{-k(L-z)} \\ &= (B_{B1} + B_{B2})e^{-kL}ch\kappa z + (B_{B1} - B_{B2})e^{-kL}sh\kappa z, \end{aligned} \quad (6)$$

where B_{A1} (B_{B1}) and B_{A2} (B_{B2}) are the amplitudes of the wall potentials on the left and right pore boundaries for substances, respectively. Then, in the approximation of smooth inhomogeneity, the solution of Eq. (2) under the conditions (3) and (4) has the following form:

$$\begin{aligned} \Delta x(z) &= -A m_{0BA}gL \left\{ \left(\frac{1}{\kappa L ch\kappa L} - \frac{z}{L} \right) \right. \\ &\quad \left. - C_1 e^{-kL} \frac{k}{\kappa} \frac{1}{k^2 - \kappa^2} \frac{sh\kappa L}{sh\kappa L} ch\kappa z \right\} \end{aligned}$$

$$\begin{aligned}
 & - C_2 e^{-kL} \frac{k}{\kappa} \frac{1}{k^2 - \kappa^2} \frac{ch\kappa L}{ch\kappa L} sh\kappa z \\
 & + C_1 e^{-kL} \frac{1}{k^2 - \kappa^2} ch\kappa z + C_2 e^{-kL} \frac{1}{k^2 - \kappa^2} sh\kappa z \\
 & + C_2 (B_{BA1} + B_{BA2}) e^{-kL} \frac{1}{k\kappa^2 L} sh\kappa L \}. \quad (7)
 \end{aligned}$$

where $C_1 = \frac{B_{BA1} + B_{BA2}}{m_{0BA} g L}$ and $C_2 = \frac{B_{BA1} - B_{BA2}}{m_{0BA} g L}$ are dimensionless parameters that characterize the ratio of the characteristic energy of near-wall potentials to the change in the energy of the gravitational field at altitude L .

Figures 1, 2, 3 and 4 show the spatial distribution of the concentration of the model binary solution $\Delta x(z)$ at different values of the correlation radius ξ for systems with $L = 10^{-7}$ m with different values of constants B_{BA1} and B_{BA2} at a fixed value m_{0BA} .

The analysis of the given concentration profiles shows that when the system is relatively far from the critical point, the concentration profiles are determined exclusively by the external gravitational field at any of the considered values of constants B_{BA1} and B_{BA2} .

The local approximation in this case also leads to the emergence of concentration profiles, which coincide with the concentration profiles in a system with ideal walls, i.e., are determined only by the existence of a gravitational field.

Fig. 1 Spatial distribution of the concentration $\Delta x(z)$ of binary solution in a flat non-ideal pore in the gravitational field for the system $k^{-1} = 3 \cdot 10^{-10}$ m, $B_{BA1} = 10^{-24}$ J, $B_{BA2} = 10^{-24}$ J, $C_1 = 2 \cdot 10^5$, $C_2 = 0$ at different values ξ : 1 – $5 \cdot 10^{-9}$, 2 – 10^{-8} , 3 – $5 \cdot 10^{-8}$, 4 – 10^{-7} m, 5 – at local approximation

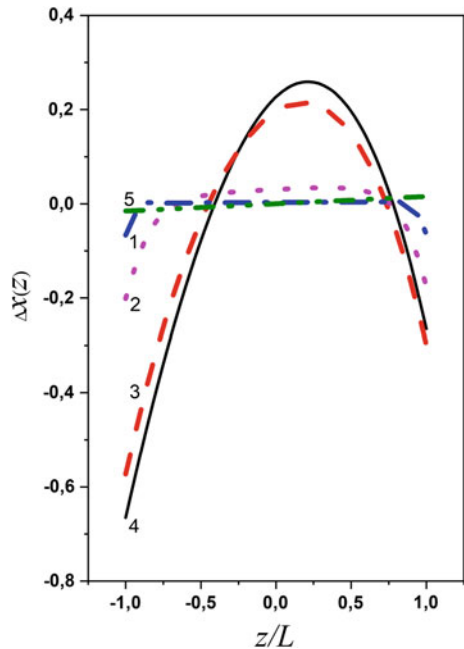


Fig. 2 Spatial distribution of the concentration $\Delta x(z)$ of binary solution in a flat non-ideal pore in the gravitational field for the system $k^{-1} = 3 \cdot 10^{-10}$ m, $B_{BA1} = 10^{-24}$ J, $B_{BA2} = 0.1 \cdot 10^{-24}$ J, $C_1 = 1.1 \cdot 10^5$, $C_2 = 0.5 \cdot 10^5$ at different values ξ : 1 – $5 \cdot 10^{-9}$, 2 – 10^{-8} , 3 – $5 \cdot 10^{-8}$, 4 – 10^{-7} m, 5—at local approximation

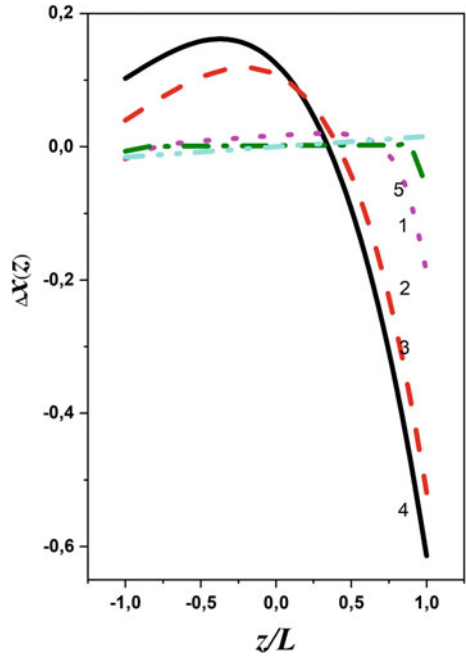


Fig. 3 Spatial distribution of the concentration $\Delta x(z)$ of binary solution in a flat non-ideal pore in the gravitational field for the system $k^{-1} = 3 \cdot 10^{-10}$ m, $B_{BA1} = 0.5 \cdot 10^{-24}$ J, $B_{BA2} = -0.25 \cdot 10^{-24}$ J, $C_1 = 2.5 \cdot 10^5$, $C_2 = 7.5 \cdot 10^5$ at different values ξ : 1 – $5 \cdot 10^{-9}$, 2 – 10^{-8} , 3 – $5 \cdot 10^{-8}$, 4 – 10^{-7} m, 5—at local approximation

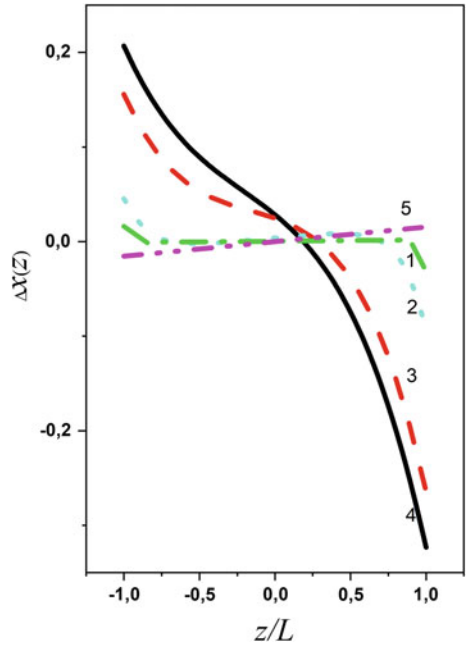
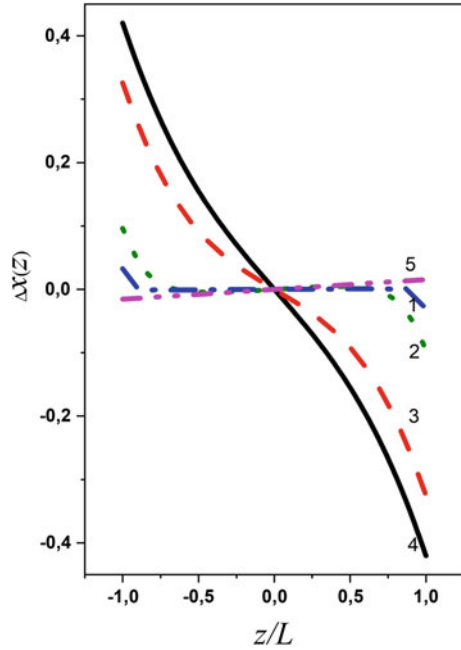


Fig. 4 Spatial distribution of the concentration $\Delta x(z)$ of binary solution in a flat non-ideal pore in the gravitational field for the system $k^{-1} = 3 \cdot 10^{-10}$ m, $B_{BA1} = 0.5 \cdot 10^{-24}$ J, $B_{BA2} = -0.5 \cdot 10^{-24}$ J, $C_1 = 0$, $C_2 = 1 \cdot 10^5$ at different values ξ : 1 – $5 \cdot 10^{-9}$, 2 – 10^{-8} , 3 – $5 \cdot 10^{-8}$, 4 – 10^{-7} m, 5 – at local approximation



The existence of walls in this case leads to a certain deformation of the profiles at the boundaries of the system at distances of the order of the effective radius of the wall forces, i.e., experimentally, these effects cannot be observed.

As the correlation radius increases, the contribution of non-local terms increases, which leads to a significant dependence of concentration profiles on the coordinate throughout the system, C_1 and C_2 as the selected “asymmetry” of the wall potential at fixed parameter values (see Figs. 3 and 4).

In Figs. 5 and 6, it is shown the spatial distribution of the concentration of the model binary solution $\Delta x(z)$ for different values of the correlation radius ξ for systems with $L = 10^{-7}$ m with different and fixed values of constants B_{BA1} and B_{BA2} .

It is easy to see the change in value m_{0BA} , and hence the change in the values of the parameters C_1 and C_2 , then a significant qualitative change in the concentration profiles binary solution is observed, i.e., the presence of imperfect walls can be significant way to distort the picture observed in the classical gravitational effect.

The absolute value of the deviation at fixed values C_1 and C_2 is determined by the value of m_{0BA} .

If the concentration of the solution is large enough, C_1 and C_2 should be observed, it practically coincides with the distribution in the absence of an external field. As these parameters decrease, the contribution of the gravitational term increases, C_1 and C_2 at sufficiently small values, a practically constant distribution of the solution

Fig. 5 Spatial distribution of the concentration $\Delta x(z)$ of binary solution in a flat non-ideal pore in the gravitational field for the system $k^{-1} = 3 \cdot 10^{-10}$ m, $B_{BA1} = 0.5 \cdot 10^{-24}$ J, $B_{BA2} = -0.5 \cdot 10^{-24}$ J, $C_1 = 0$, $C_2 = 0.47 \cdot 10^5$ at different values ξ : 1 – $5 \cdot 10^{-9}$, 2 – 10^{-8} , 3 – $5 \cdot 10^{-8}$, 4 – 10^{-7} m, 5—at local approximation

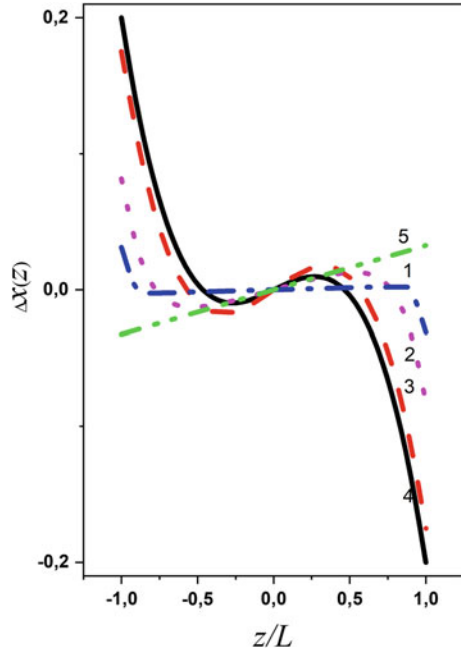
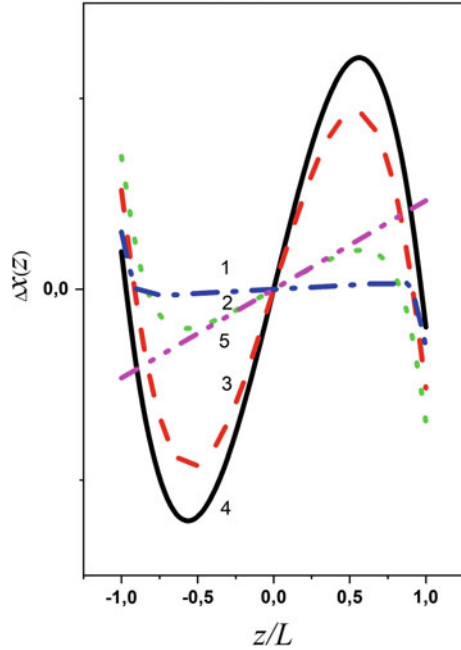


Fig. 6 Spatial distribution of the concentration $\Delta x(z)$ of binary solution in a flat non-ideal pore in the gravitational field for the system $k^{-1} = 3 \cdot 10^{-10}$ m, $B_{BA1} = 0.5 \cdot 10^{-24}$ J, $B_{BA2} = -0.5 \cdot 10^{-24}$ J, $C_1 = 0$, $C_2 = 0.25 \cdot 10^5$ at different values ξ : 1 – $5 \cdot 10^{-9}$, 2 – 10^{-8} , 3 – $5 \cdot 10^{-8}$, 4 – 10^{-7} m, 5—at local approximation



concentration for a system with ideal walls must be observed—a pure gravitational effect.

The data given in Fig. 5 show that in the middle of the system (in the layer bounded by planes with coordinates $z \approx \pm 0.3L$), the gravitational field leads to insignificant ($\approx 2\%$) deviations of the concentration that coincide in sign with those that calculated in the local approximation, and a more significant deviation occurs near the system walls, and the value of this deviation is determined only by the magnitude of the near-wall potential.

Thus, the analysis of the data presented in Figs. 1, 2, 3, 4, 5 and 6 indicates that for this model system under the condition $C_1 \geq 10^5$ or $C_2 \geq 10^5$, the concentration profile is determined exclusively by the near-wall potential, and under the conditions $C_1 \leq 10^4$ or $C_2 \leq 10^4$ the gravitational field. At constant C_1 and C_2 intermittent values $\sim 10^4 - 10^5$, the spatial distribution of the solution concentration is determined by both the near-wall potential, and the presence of an external gravitational field.

In general case, the presence of non-ideal walls leads to the fact that the concentration profiles lose the properties of the odd coordinate function, which must be taken into account in the experimental study of the critical properties of the fluid and in calculating the corresponding critical amplitudes. In addition, the spatial distribution of the concentration gradient changes significantly, which could affect the results of experiments on the scattering of light, and neutrons in the vicinity of the critical point of stratification.

3 Conclusions

1. It is shown that in the vicinity of the critical point of stratification, the presence of non-ideal walls leads to the change in the concentration profile of a mixture in the volume determined by the correlation radius of the corresponding homogeneous system.
2. It is shown that in the systems bounded by non-ideal walls, the correlation contribution leads to decrease in gravitational effect, and its increase depending to the symmetry of the near-wall potential, and the orientation of the system relatively to the gravitational field.
3. It is established that the presence of walls of different nature causes significant deviations in the concentration from that which is found in the local approximation, which affects the values of the critical amplitudes calculated on the results of experimental studies.

References

1. Moldover MR, Sengers JV, Gammon RW (1979) Gravity effects in fluids near the critical point. *Rev Mod Phys* 51:79
2. Monson PA (2012) Understanding adsorption/desorption hysteresis for fluids in mesoporous materials using simple molecular models and classical density functional theory. *Microporous Mesoporous Mater* 160:47
3. Puibasset J, Kierlik E, Tarjus G (2014) Influence of system size on the properties of a fluid adsorbed in a nanopore: physical manifestations and methodological consequences. *J Chem Phys* 141:044716
4. Chen M, Yang C, Guo Z-Y (2000) Monte-Carlo simulation of argon in nano-space. *Chin Phys Let* 17:313
5. Chen YY, Jiang YZ, Guan XW, Qi Z (2014) Critical behaviours of contact near phase transitions. *Nat Commun* 5:5140
6. Pellicane G, Vink RLC, Russo B (2013) Giaquinta PV fluids in porous media: the case of neutral walls. *Phys Rev E* 88:042131
7. Sharma D (2018) Numerical modeling of highly compressible near-critical fluids. Université de Bordeaux, 2018. English. NNT:2018BORD0003
8. Khmelinskii I, Woodcock LV (2020) Supercritical fluid gaseous and liquid states: a review of experimental results. *Entropy* 22:437
9. Munster A (1969) *Chemische thermodynamik*. Chemie, Wein heim
10. Ebner C, Krishnamurthy HR, Pandit R (1991) Density-functional theory for classical fluids and solids. *Phys Rev* 73:1179
11. Kozlovskii MP, Patsahan OV, Melnyk RS (2004) Thermodynamic characteristics of binary symmetric mixture in the vicinity of the vapor-liquid critical point. *Ukr J Phys* 49:55
12. Yasutomi M, Ginoza M (2000) Analytical solution of the Ornstein-Zernike equation for a multicomponent fluid. *J Phys Condens Matter* 12:L605
13. Yasutomi M (2002) Analytical structure factor for a multicomponent fluid with a screened Coulomb plus power series interaction. *J Phys: Condens Matter* 14:L435
14. Atamas N, Gavryushenko D, Taranyk G, Kashchenko V (2021) Clustering in water-propanol solutions. In: 2021 IEEE 11th international conference nanomaterials: applications and properties (NAP), p. 1
15. Dietrich S (1990) Critical phenomena at interfaces. *Phys A* 168:160
16. Brovchenko I, Oleinikova A (2008) *Interfacial and confined water*. Amsterdam, Elsevier p 320
17. Lipa JA, Coleman M, Stricker DA (2001) Specific heat of helium confined to cylinders near the lambda point. *J Low Temp Phys* 124:443
18. Gavryushenko DA, Starovoitov OO (2005) Nonlocal fluid density distribution in the vicinity of the critical point. *J Mol Liq* 120:123
19. Bulavin LA, Gavryushenko DA (2016) Influence of radiation on the phase transition temperature in liquids. *Ukrainian J Phy* 61, 9:819

Electron Tunneling in Heterostructures with Germanium Quantum Dots



Sergey I. Pokytnyi and Volodymyr Ya. Gayvoronsky

Abstract It is shown that electron tunneling through a potential barrier that separates two quantum dots of germanium leads to the splitting of electron states localized over spherical interfaces (a quantum dot–a silicon matrix). The dependence of the splitting values of the electron levels on the parameters of the nanosystem (the radius a quantum dot germanium, as well as the distance D between the surfaces of the quantum dots) is obtained. It is shown that the splitting of electron levels in the QD chain of germanium causes the appearance of a zone of localized electron states, which is located in the bandgap of silicon matrix. It was found that the motion of a charge-transport exciton along a chain of quantum dots of germanium causes an increase in photoconductivity in the nanosystems.

Keywords Splitting of electronic states · Charge-transfer exciton · Spherical interfaces · Potential barrier · Coulomb interaction · Quantum dots

1 Introduction

In germanium/silicon, heterostructures with germanium quantum dots (QDs) are of the second type, the main electron level was in the silicon matrix, and the main level of holes was in the germanium QD [1–11]. A significant shift of the shift of the valence band ($\Delta E_{v(Ge)} = 610$ meV) of germanium QDs (relative to the ceiling of the valence band of the silicon matrix) caused hole localization in the QDs. A substantial shift of the bottom of the conduction band ($\Delta E_{c(Si)} = 340$ meV) of the silicon matrix (relative to the bottom of the conduction band of germanium QDs) in the heterostructure was a potential barrier for electrons (electrons moved in the matrix

S. I. Pokytnyi (✉)

Chuiko Institute of Surface Chemistry, National Academy of Sciences of Ukraine, 17 General Naumov Str., Kyiv 03164, Ukraine
e-mail: pokutnyi.serg@gmail.com

S. I. Pokytnyi · V. Ya. Gayvoronsky

Institute of Physics, National Academy of Sciences of Ukraine, 46 Nauky Ave., Kyiv 03028, Ukraine

and did not penetrate into the QD) [1–11]. When studying the optical properties of Ge/Si nanoheterostructures with germanium QDs, experimental work [1] was the first to reveal the spatial separation of electrons and holes, as a result of which electrons were localized above the QD surface, and holes moved into QDs. The transition between such states was indirect in space [1, 2, 9–12]. In experimental studies [1, 2], it was established that in nanosystems consisting of germanium QDs located in silicon matrices, the excitation of spatially indirect excitons (SIE) is possible [3–16].

The effect of significant increase in the SIE binding energy (by almost two orders of magnitude) is found in nanosystems containing semiconductor (cadmium sulfide, zinc selenide, germanium) QDs, compared with the exciton binding energy in the corresponding single crystals [12–17]. Such an effect of significant increase in the SIE binding energy opens the possibility for the use of nanosystems as an active field of nanolasers operating on exciton transitions at room temperatures.

In [3, 7], heterostructures, which are linear germanium QD chains on silicon substrates, were obtained using the method of electron-beam lithography. The average radii of QD of germanium did not exceed 30 nm. In Ge/Si heterostructures with germanium QDs, it was established in experimental works [1, 2] that low-temperature optical absorption and photoluminescence spectra were caused by interband electron transitions from the valence band of germanium QD to the conduction band of the silicon matrix. The photoluminescence signal of nanostructures in the infrared spectral region (0.20–1.14) eV was observed up to room temperature [1–8].

At low concentrations N QDs of germanium, when in linear chains the average distance ($\sim N^{-1/3}$) between the surfaces of the QD significantly exceeds the Bohr radius of the electron ($a_e = 0.63$ nm) in the silicon matrix, that is,

$$a_e N^{1/3} \ll 1, \quad (1)$$

the interaction between QDs can be neglected. The optical properties of such nanosystems were mainly determined by the energy spectra of electrons and holes localized near the surface of single germanium QDs grown in a silicon matrix [1–5, 7, 8, 15, 16].

With the increase of the concentration N of germanium QD in linear chains, the average distance between the surfaces of the QD decreased. In nanostructures with large concentrations N of QDs at distances between the QD surfaces (about a_e), it is necessary to take into account the interaction between the QD surfaces. In this case, the condition should be satisfied

$$a_e N^{1/3} \sim 1 \quad (2)$$

As the spacing between the QDs surfaces is decreased, the overlapping integral $S(a, D)$ of the exciton wave functions and the energy of the exchange interaction of the electrons with the holes substantially increase. Therefore, a coupled state of two excitons is formed in the nanosystem, i.e., an exciton quasimolecule consisting of two QDs appeared in the nanosystem [17–19]. In such exciton quasimolecule,

electrons and holes were separated in space (the holes moved in germanium QDs, and the electrons were localized over a spherical interface (QD—silicon matrix)). In [17], it was shown that the appearance of a quasimolecule had a threshold nature and was possible in the nanosystem, in which the distance D between the surfaces of the QDs was determined by the condition $D_c^{(1)} \leq D \leq D_c^{(2)}$. The existence of such a distance $D_c^{(1)}$ was due to quantum size effects, in which the decrease in the energies of interaction of the electrons and holes entering into the Hamiltonian of the exciton quasimolecule with decrease of the distance D between the QD surfaces could not compensate for the increase in the kinetic energy of electrons and holes. At larger distance D between the surfaces of QDs, such that $D \geq D_c^{(2)}$, the exciton quasimolecule splits into two excitons (from spatially separated electrons and holes) [17].

The interband and intraband radiation from the n-InGaAs/GaAs heterostructures with the double and triple tunnel coupled and selectively doped quantum wells has been investigated [20–22]. A steep increase of the interband radiation intensity was found which appeared under the lateral electric field. This effect was due to the long lifetime of the injected charge carriers, which is three orders of magnitude longer than the lifetime in a similar bulk direct-gap semiconductor. It is shown that the long lifetimes of the injected charge carriers were caused by the spatial separation of the injected holes and electrons between the bound wells.

At present, the optical properties of Ge/Si heterostructures with germanium QDs have not been adequately studied. In particular, there are no works that investigate electron tunneling between the surfaces of germanium QDs in the linear chains of germanium QDs on silicon substrates. Therefore, in this paper, in contrast to [18, 19], the splitting of electron states localized over a spherical interface (germanium QD—silicon matrix) due to electron tunneling through a potential barrier separating two QDs is investigated.

2 The Splitting of Electron States in Germanium/Silicon Heterostructure with Germanium Quantum Dots

In [18, 19], a model of nanosystems consisting of two spherical QD(A) and QD(B) with radii a , containing germanium with a dielectric constant ($\epsilon_2 = 16.3$) grown in a silicon matrix with a dielectric constant ($\epsilon_1 = 11.7$). It was assumed that the holes $h(A)$ и $h(B)$ with effective masses ($(m_h/m_0) = 0.39$) were located at the centers of QD(A) and QD(B). In the nanosystem, electrons $e(1)$ and $e(2)$ with effective masses ($(m_e^{(1)}/m_0) = 0.98$) were localized over the spherical surfaces of QD(A) and QD(B) in potential wells caused by the Coulomb attraction $V_{eh}(x)$ electron and hole in a silicon matrix. The energy of the Coulomb interaction of an electron with a hole was described by the formula [12, 13]

$$V_{eh}(x) = -\frac{e^2}{\epsilon x} \quad (3)$$

where $\tilde{\varepsilon} = 2 \varepsilon_1 \varepsilon_2 / (\varepsilon_1 + \varepsilon_2)$ —dielectric constant of the nanosystem and x — electron distance from the surface of the QD). If in the nanosystem with a high concentration of QDs N (condition (2) is satisfied), the distance D between the surfaces of the germanium QDs exceeded the value $D_c^{(2)}$, then the exciton quasimolecule would have been decayed into two excitons in which electrons were located above the spherical interface (QD–matrix), and the holes were in the valence band of germanium QDs [17].

If the distances D between the surfaces of QD of germanium in the nanosystem exceeded the value of $D_c^{(2)}$, then the exciton quasimolecule decayed into two excitons, in which electrons were localized above the spherical interface (QD–matrix), and the holes were in the valence band of germanium QD [17]. Such excitons appeared when the photon with the energy smaller than the width of the band gap $E_{g(Si)}$ of the silicon matrix was absorbed by the nanosystem [17]. The ground state $E_0(a)$ of the exciton with the increase of the radius QD a (so that $a \geq 22.2$ nm) passed into the ground state of a two-dimensional exciton (from a spatially separated electron and hole) localized above the flat interface (germanium–silicon) with the energy [15, 16]

$$E_0(a) = -E_{ex}^{2D}, E_{ex}^{2D} = 2\hbar^2/\mu_{ex}^{2D} (a_{ex}^{2D})^2, \quad (4)$$

where $E_{ex}^{2D} = 82$ meV is the binding energy of the two-dimensional SIE. The Bohr radii of such SIE is

$$a_{ex}^{2D} = \tilde{\varepsilon} (m_0/\mu_{ex}^{2D}) (\hbar^2/m_0 e^2), \quad (5)$$

where $\mu_{ex}^{2D} = m_e^{(1)} m_h / (m_e^{(1)} + m_h)$ —the reduced mass of the SIE, wherein $a_{ex}^{2D} = 2.6$ nm.

In [15] and [16], the energy of the SIE state $E_0(a)$ was measured from the bottom of the conduction band of the silicon matrix ($E_{c(Si)} = E_{g(Si)} = 1.17$ eV). Between the electronic states localized over the spherical surfaces of QD(A) and QD(B), tunneling is possible through the potential barrier that separates these QDs. Such a potential barrier is caused by the Coulomb attraction $V_{eh}(x)$ (3) of electrons $e(1)$ and $e(2)$ to their holes located in the centers of QD(A) and QD(B). We can write the expression describing the potential barrier $U(x)$ in this form [18, 19]:

$$U(x) = -\frac{e^2}{\tilde{\varepsilon}((D/2) - x)}, \quad 0 \leq x \leq (D/2) \quad (6)$$

$$U(x) = -\frac{e^2}{\tilde{\varepsilon}((D/2) + x)}, \quad (-D/2) \leq x \leq 0 \quad (7)$$

The potential energy $U(x)$ consists of two symmetric potential wells (6) and (7), separated by a potential barrier of height

$$U_0(D) = U(x=0) - \frac{2e^2}{\varepsilon D} \quad (8)$$

Electron tunneling through the potential barrier $U(x)$ (6)–(8), separating two QDs, causes the splitting of the exciton energy level $E_{ex}(a)$, which is located in the potential wells $U(x)$ (6, 7) in the silicon matrix at two close exciton levels $E_{ex}^{(1)}(a)$ and $E_{ex}^{(2)}(a)$. Such close exciton levels $E_{ex}^{(1)}(a)$ and $E_{ex}^{(2)}(a)$ correspond to states in which the electron moves simultaneously in both potential wells $U(x)$ (6, 7). We will assume that the potential barrier $U(x)$ (6, 7) is described by a semiclassical field. Using approach [13], we obtain the expression that determines the splitting $\Delta E_{ex}(a, D) = (E_{ex}^{(1)}(a) - E_{ex}^{(2)}(a))$ of the exciton level ($E_{ex}(a) = -E_0(a) = E_0$).

$$\Delta E_{ex}(a, D) = (\hbar\omega_0(a, D)/\pi) \exp\left[-(2/\hbar) \int_0^b p(x) dx\right] \quad (9)$$

In formula (9), the quantity

$$\omega_0(a, D) = (\pi/\mu_{ex}^{2D}) \left[\int_0^b dx/p(x) \right]^{-1}, \quad (10)$$

describes the frequency of the classical periodic electron motion in the field $U(x)$ (6, 7), and $p(x)$ determines the momentum of an electron moving in the field $U(x)$ (6, 7), wherein

$$p(x) = [-2\mu_{ex}^{2D}(U(x) + E_0)]^{1/2}, \quad (11)$$

b —turning point whose value is determined from the expression $U(x=b) = E_0(a)$.

After integrating formula (9), taking into account (6)–(8), we obtain an expression that describes the splitting $\Delta E_{ex}(a, D)$ of the exciton level ($E_{ex}(a) = -E_0$) [18, 19]:

$$\begin{aligned} \Delta E_{ex}(a, D) &= 2^{-3/2} \left\{ \left[1 - (\tilde{E}_0 \tilde{D})^{1/2} (\tilde{E}_0 \tilde{D} - 1)^{1/2} \right] (2\tilde{E}_0)^{-3/2} \right. \\ &\quad \left. + \ln \left[(\tilde{E}_0 \tilde{D})^{1/2} + (\tilde{E}_0 \tilde{D} - 1)^{1/2} \right] \right\}^{-1} \\ &\quad \times \left[(\tilde{E}_0 \tilde{D})^{1/2} + (\tilde{E}_0 \tilde{D} - 1)^{1/2} \right]^{-2\sqrt{2}} \exp\left[-2\tilde{D}^{1/2} (\tilde{E}_0 \tilde{D} - 1)^{1/2}\right] E_{ex}^{2D} \end{aligned} \quad (12)$$

where $(\tilde{E}_0 = (E_0/E_{ex}^{2D}))$ and $\tilde{D} = (D/a_{ex}^{2D})$. Formula (12) is valid only for the weak splitting $\Delta E_{ex}(a, D)$ of the exciton level $E_{ex}(a)$. In this case, the following condition should be satisfied

$$(\Delta E_{ex}(a, D)/E_0) \ll 1 \quad (13)$$

Expression (12) is obtained in the semiclassical approximation, in which it is assumed that the potential field $U(x)$ (6), (7) is a semiclassical field. In this case, the condition [18, 19] should be satisfied

$$\hbar \frac{d}{dx} (p(x))^{-1} \ll 1, \quad (14)$$

which is performed at

$$\left(\tilde{E}_0 \cdot \tilde{D} \right) > 1 \quad (15)$$

Magnitude splitting (12) is $\Delta E_{ex}(a, D) > 0$, if

$$\left(\tilde{E}_0 \tilde{D} \right)^{1/2} \left(\tilde{E}_0 \tilde{D} - 1 \right)^{1/2} < 1 \quad (16)$$

Conditions (15) and (16) are satisfied when

$$\left(\tilde{E}_0 \cdot \tilde{D} \right) > 2^{-1} (1 + 5^{1/2}) \quad (17)$$

Thus, the fulfillment of the requirement (17) allows us to obtain an expression that describes the splitting $\Delta E_{ex}(a, D)$ (12) of the exciton level $E_{ex}(a)$, in the semiclassical approximation. From formula (12), it is followed that with the increase of the distance D between the surfaces of the QD (so that $\tilde{D} \gg 1$), the splitting $\Delta E_{ex}(a, D)$ decreases ($\Delta E_{ex}(a, D) \tilde{D}^{-\sqrt{2}}$). Therefore, in a nanosystem with a small concentration of QDs N (so that condition (1) is satisfied), the probability of electron tunneling through the potential barrier $U(x)$ (6)–(8) separating two QDs takes a small value. In this case, the splitting values $\Delta E_{ex}(a, D)$ (12) of the exciton levels $E_{ex}(a)$ will be negligible compared with the energies of the excitonic levels $E_{ex}(a)$.

The exciton levels $E_0(a)$, as well as the potential barrier $U(x)$ (6)–(8), are in the forbidden zone of the silicon matrix. Therefore, in order for the potential barrier $U(x)$ (6)–(8) to be located in the forbidden zone of the silicon matrix, the condition [18, 19]:

$$|U_0(D)| < E_{g(Si)} \quad (18)$$

Requirement (18), taking into account (8), (4), and (5), is satisfied for nanosystems in which the distance D between the surfaces of the QDs exceeds the value

$$D > \left(E_{ex}^{2D} / E_{g(Si)} \right) a_{ex}^{2D} \quad (19)$$

Inequality (19) holds for nanosystems in which the distances D between the surfaces of the QDs exceed the values ($D > 0.18$ nm).

The positions of the exciton levels $E_0(a)$, which are located in the band gap of the silicon matrix, do not depend on the temperature T , if the distances of these

levels from the bottom of the conduction band $E_{c(Si)}$ of the silicon matrix significantly exceed the thermal energy ($k_B T$) of the electron (where k_B is a constant Boltzmann), i.e., the following condition must be met [18, 19]:

$$(E_{c(Si)} + E_0(a)) \gg k_B T \quad (20)$$

3 Calculation Results and Discussion

We will estimate the splitting $\Delta E_{ex}(a, D)$ (12) of the exciton levels ($E_{ex}(\bar{a}_1) = -E_0(\bar{a}_1) = -64$ meV) and ($E_{ex}(\bar{a}_2) = -E_0(\bar{a}_2) = -72$ meV) in the nanosystem consisting of a chain of germanium QDs with average radii $\bar{a}_1 = 12.8$ nm and $\bar{a}_2 = 15$ nm [15, 16], grown in a silicon matrix, and studied under experimental conditions [1–11] (see Tables 1 and 2). For average distances D between the surfaces of QDs, which continuously vary in the range from $D_1 = 7.8$ nm to $D_2 = 8.4$ nm, using the formula (12), we obtain for the exciton level $E_{ex}(\bar{a}_1)$ the splitting values $\Delta E_{ex}(a, D)$ monotonically varying in the interval from $\Delta E_{ex}(\bar{a}_1, D_1) = 8$ meV to $\Delta E_{ex}(\bar{a}_1, D_2) = 0.16$ meV (see Table 1) [18, 19]. In this case, for the exciton level $E_{ex}(\bar{a}_2)$, the splitting $\Delta E_{ex}(a, D)$ takes a monotonically varying value in the range from $\Delta E_{ex}(\bar{a}_2, D_1) = 8.8$ meV to $\Delta E_{ex}(\bar{a}_2, D_2) = 0.2$ meV (see Table 2) [18, 19]. Such splittings $\Delta E_{ex}(\bar{a}_1, D_1)$ and $\Delta E_{ex}(\bar{a}_1, D_2)$ correspond to the temperatures $T_1^{(1)} = 92$ K and $T_2^{(1)} = 1.85$ K. Splittings $\Delta E_{ex}(\bar{a}_2, D_1)$ and $\Delta E_{ex}(\bar{a}_2, D_2)$ correspond to the temperatures $T_1^{(2)} = 102$ K and $T_2^{(2)} = 2.3$ K. Requirements (13) for the smallness of splittings $\Delta E_{ex}(\bar{a}_1, D)$ and $\Delta E_{ex}(\bar{a}_2, D)$ in comparison with the value of the energy of the exciton levels $E_0(\bar{a}_1)$ and $E_0(\bar{a}_2)$ are satisfied [18, 19].

The splitting values $\Delta E_{ex}(\bar{a}_1, D)$ and $\Delta E_{ex}(\bar{a}_2, D)$, according to (12), have a strong exponential dependence on the distance D between the surfaces QD. With a slight increase in the distance D from $D_1 = 7.8$ nm to $D_2 = 8.4$ nm, the splitting values $\Delta E_{ex}(a, D)$ (12) substantially decrease from $\Delta E_{ex}(\bar{a}_1, D_1) = 8$ meV to $\Delta E_{ex}(\bar{a}_1, D_2) = 0.16$ meV, as well as from $\Delta E_{ex}(\bar{a}_2, D_1) = 8.8$ meV to $\Delta E_{ex}(\bar{a}_2, D_2) = 0.2$ meV (see Table 1 and Table 2) [18, 19]. With an increase in the average radius of the QD a (from $\bar{a}_1 = 12.8$ nm to $\bar{a}_2 = 15$ nm), the exciton-level energy values $E_0(a)$ increase (from $E_0(\bar{a}_1) = 64$ meV to $E_0(\bar{a}_2) = 72$ meV) [15, 16].

Table 1 Dependence of the splitting $\Delta E_{ex}(\bar{a}_1, D)$ (12) of the exciton level ($E_0(\bar{a}_1) = -64$ meV) in a nanosystem that consists of two germanium QDs with average radii $\bar{a}_1 = 12.8$ nm, on the distance D between the surfaces of the QD

\bar{a}_1 nm	$E_0(\bar{a}_1)$ meV	D nm	$\Delta E_{ex}(\bar{a}_1, D)$ meV
12.8	64	7.8	8
12.8	64	8	2.4
12.8	64	8.2	0.64
12.8	64	8.4	0.16

Table 2 Dependence of the splitting $\Delta E_{ex}(\bar{a}_2, D)$ (12) of the exciton level ($E_0(\bar{a}_2) = -72$ meV) in a nanosystem that consists of two germanium QDs with average radii $\bar{a}_2 = 15$ nm, on the distance D between the surfaces of the QD

\bar{a}_2 nm	$E_0(\bar{a}_2)$ meV	D nm	$\Delta E_{ex}(\bar{a}_2, D)$ meV
15	72	7.8	8.8
15	72	8	2.8
15	72	8.2	0.78
15	72	8.4	0.2

It should be noted that the estimates of the splitting values $\Delta E_{ex}(a, D)$ (12) of the exciton levels $E_{ex}(a)$ are obtained here within the framework of the theory we have developed, and the conditions (13), (14) and (18)–(20) are satisfied.

It was shown in [15, 16] that in a Ge/Si nanosystem with germanium QDs in the integral of average QD radii ($6.4 \text{ nm} \leq a \leq 22.2 \text{ nm}$) upon absorption of a quantum of light with energy

$$\hbar\omega_{ex}(a) = E_{g(Ge)} - \Delta E_{c(Si)} - E_{ex}(a), \quad (21)$$

in the band gap of the silicon matrix, an SIE state with energy $E_{ex}(a)$ appeared. In formula (21), $E_{ex}(a)$ is the SIE binding energy, and the value $(E_{g(Ge)} - \Delta E_{c(Si)}) = 330$ meV. For the appearance in the nanosystem with germanium QDs with radii $\bar{a}_1 = 12.8$ nm and $\bar{a}_2 = 15$ nm of exciton levels ($E_{ex}(\bar{a}_1) = -64$ meV) and ($E_{ex}(\bar{a}_2) = -72$ meV), according to (21), light quanta with following energies $\hbar\omega_{ex}(\bar{a}_1) = 266$ meV and $\hbar\omega_{ex}(\bar{a}_2) = 258$ meV are required [15, 16]. Such energies $\hbar\omega_{ex}(\bar{a}_1) = 266$ meV and $\hbar\omega_{ex}(\bar{a}_2) = 258$ meV were contained in the infrared spectral region (0.20–1.14) eV, which was observed under experimental conditions up to room temperature [1, 2].

Let us assume that the distances D between the surfaces of the QDs will be the same in the entire linear chain of germanium QDs on the substrate of the silicon matrix [3, 7]. As a result, of electron tunneling through the potential barrier $U(x)$ (6)–(8), which separates QDs, the exciton states $E_{ex}(a)$ are split, forming a zone of localized electron states in a linear germanium QD chain. The qualitative estimate of the width of the zone of localized electronic states gives a value that is determined by the magnitude of the order of splitting $\Delta E_{ex}(a, D)$ (12) of the exciton levels $E_{ex}(a)$. Such a zone of localized electronic states is located in the band gap of the silicon matrix. The position of the zone of localized electron states in the nanosystem is determined by the position of the exciton level $E_0(a)$. With an increase in the average radius of QD a (for $a \geq 22.2$ nm), the exciton level $E_0(a)$ approached the ground level of the two-dimensional exciton $E_{ex}^{2D} = 82$ meV (4) [15, 16]. The position of the zone of localized electron states also approaches the main level of the two-dimensional SIE E_{ex}^{2D} (4). Thus, the position of the zone of localized electronic states depends on the average radius a of the QD, and the width of the zone of localized electronic states depends on the distance D between the surfaces of the QD. Comparing the splitting dependence $\Delta E_{ex}(a, D)$ (12) of the exciton level $E_{ex}(a)$ at a certain QD's radius

a with the experimental value of the width of the zone of localized electron states arising in the QD chain of germanium, one can obtain the distances D between the QD surfaces [18, 19].

In the linear chain of germanium QDs [3, 7], due to the presence of translational symmetry, the electronic excitation moves in the zone of localized electron states. In this case, the electron excitation in the nanosystem is a charge-transfer exciton [23], in which the hole is in the valence band of a germanium QD, and the electron, tunneling between the quantum dots, moves in the zone of localized electron states. As the QD radius a increased, the binding energy $|E_{ex}(a)|$ of the ground state of the exciton in the nanosystem increased [15, 16]. Therefore, the distance D , for which the square of the overlapping integral $S(D, a)$ of the exciton wave functions took the maximum value, decreased with increasing radius QD a [17]. The spatial separation of electrons and holes in a Ge/Si heterostructure with germanium QDs resulted in a small overlap integral of electron and hole wave functions that described the motion of electrons and holes in a nanoheterostructure not exceeding the value ($\cong 0.08$) [17]. Therefore, the lifetimes of excitons from spatially separated electrons and holes are substantially longer (by two orders of magnitude) to the lifetimes of excitons in a single crystal of silicon [1, 2, 11]. The motion of such a “long-lived” electron in the zone of localized electronic states located in the band gap of the silicon matrix leads to an increase in photoconductivity in the nanosystem.

Using approach [18, 19], we obtain an expression that qualitatively describes the current density $j(a, D)$, caused by the movement of electrons in the zone of localized electron states:

$$j(a, D) \approx K(a, D) \approx \exp\left[-2\tilde{D}^{1/2}(\tilde{E}_0\tilde{D}-1)^{1/2}\right] \quad (22)$$

In formula (22), $K(a, D)$ determines the coefficient of transparency of the potential barrier $U(x)$ (6)–(8). With the increase of the distance D between the QD surfaces (so that $\tilde{D} \gg 1$), the current density $j(a, D)$ (22) decreases $\left(j(a, D) \exp(-\tilde{D})\right)$.

4 Conclusion

It is shown that in the QD chain of germanium, a zone of localized electron states arises, which is located in the bandgap of the silicon matrix. Such a zone of local electron states is caused by the splitting of electron levels in the QD chain of germanium. Moreover, the motion of an electron in the zone of localized electron states causes an increase in photoconductivity in the nanosystem. The effect of increasing photoconductivity can make a significant contribution in the process of converting the energy of the optical range in photosynthesizing nanosystems [24–28].

It has been established that comparison of the splitting dependence $\Delta E_{ex}(a, D)$ (12) of the exciton level $E_{ex}(a)$ at a certain radius a QD with the experimental

value of the width of the zone of localized electron states arising in the QD chain of germanium allows us to obtain the distances D between the QD surfaces.

It has been shown that by changing the parameters of Ge/Si heterostructures with germanium QDs (radii a QD germanium, as well as the distance D between the surfaces of the QDs), it is possible to vary the positions and widths of the zones of localized electronic states. The latter circumstance opens up new possibilities in the use of such nanoheterostructures as new structural materials for the creation of new nanooptoelectronics and nanophotosynthesizing devices of the infrared range [24–28].

References

1. Yakimov AI, Dvurechensky AV, Nikiforov AI (2001) JETP Lett 73:529
2. Yakimov AI, Dvurechensky AV, Nikiforov AI (2001) JETP 119:574
3. Smagina JV, Dvurechensky AV, Selesnev VA (2015) Semiconductors 49:749
4. Yakimov AI, Kirienko VV, Bloskhin AA (2015) Appl Phys Lett 106:32104
5. Yakimov AI, Kirienko VV, Bloskhin AA, Armbrister VA, Dvurechensky AV (2015) JETP Lett 101:750
6. Yakimov AI, Kirienko VV, Bloskhin AA, Armbrister VA, Dvurechensky AV (2015) JETP Lett 102:594
7. Zinovieva AF, Smagina JV, Nenashev AV, Dvurechensky AV (2015) JETP Lett 102:108
8. Zinovieva AF, Zinovyev VA, Nikiforov AI, Timofeev VA, Mudryi AV, Nenashev AV, Dvurechenskii AV (2016) JETP Lett 104:823
9. Yakimov AI, Bloskhin AA, Dvurechensky AV (2009) JETP Lett 90:569
10. Grydlik M, Hackl F, Groiss H, Glaser M, Halilovic A, Fromherz T, Jantsch W, Schäffler F, Brehm M (2016) ACS Photonics 3:298
11. Brehm M, Grydlik M (2017) Nanotechnology 28:392001
12. Pokutnyi SI (2013) Semiconductors 47:791
13. Pokutnyi SI (2013) Tech Phys Lett 39:233
14. Pokutnyi SI (2015) Tech Phys 60:1615
15. Pokutnyi SI (2016) Low Temp Phys 42:1151
16. Pokutnyi SI (2018) Low Temp Phys 44:819
17. Pokutnyi SI (2017) Opt Eng 56:067104
18. Pokutnyi SI (2020) Phys Status Solidi B 257:2000221
19. Pokutnyi SI (2020) Phys. B: Phys. Condens. Matter 601:412583
20. Tulupenko V, Duque CA, Demediuk R, Belykh V, Tiutiunnyk A, Morales AL, Akimov V, Restrepo RL, Moraramos ME, Poroshin V, Fomina O (2015) Phys E 66:162
21. Tulupenko V, Duque CA, Demediuk R, Belykh V, Belichenko Y, Duque CM, Akimov V, Poroshin V, Fomina O: Philos. Mag. Lett. **93**, 42 (2013)
22. Tulupenko V, Duque CA, Demediuk R, Fomina O, Akimov V, Belykh V, Dmitrichenko T, Poroshin V (2014) Bull Mater Sci 37:1347
23. Antonyuk BP, Antonyuk VB, Frolov AA (2000) Optic. Commun. 174:427
24. van Loo, A.F., Fedorov, A., Lalumiere, K., Sanders, B.C., Blais, A., Wallraff, A.: Science **342**, 1494 (2013)
25. Calman EV, Fogler MM, Butov LV, Hu S, Mishenko A, Geim AK (2018) Nat Commun. 9:1895
26. Diaz AS, Aragones GV, Buckhout-White S (2017) J Phys Chem Lett 18:218
27. Yakunin S, Chaaban J, Benin B, Cherniukh I et al (2021) Nat Commun. 12:981
28. Pokutnyi SI (1997) Phys Solid Stat 39:634

Thermodynamic Analysis of the Process Obtaining Promoted Iron in Various Gaseous Media



L. Frolova and B. Blyuss

Abstract A thermodynamic analysis of the reduction process of iron-based oxide systems with nickel and cobalt additives in various gaseous media (coke oven gas, carbon monoxide(II), and hydrogen) has been carried out. The method of minimizing the total thermodynamic potentials was used to calculate the equilibrium compositions of the products of the process under study. The expediency of using hydrogen for the reduction of iron oxide is shown. Its optimal concentration and process temperature are established.

Keywords Iron oxide · Reduction · Gas media · Thermodynamics

1 Introduction

Currently, the areas of use of nanodispersed metals and alloys are expanding, including in environmental technologies [1–5]. One of these materials is nanocomposites based on nanoiron, which have high catalytic and adsorption characteristics in the purification of aqueous media from organic and inorganic contaminants and high magnetic characteristics [6]. The efficiency of using such materials is associated with the high dispersion of iron nanoparticles and, accordingly, their large specific surface area and chemical activity. Despite many advantages, such systems have a number of disadvantages, the main of which is significant pyrophoricity, the tendency of particles to aggregate. One way to slow down these processes is doping nanoiron particles with transition metal cations and synthesizing composites [7–9]. Therefore, the presence of cobalt and nickel stabilizes nanosized iron. Thus, the relevance of the work is pre-determined by the need to improve modern highly efficient photocatalysts, catalysts, and adsorbents. There are various technologies for obtaining dispersed iron. For example, the decomposition of $\text{Fe}(\text{CO})_5$ in organic solvents or in argon. But the most common method is the reduction of Fe^{2+} or Fe^{3+} ions from solutions of their salts with alkali metal borohydrides [10, 11]. The iron obtained

L. Frolova (✉) · B. Blyuss
Ukrainian State University of Chemical Technology, Dnipro, Ukraine
e-mail: 19kozak83@gmail.com

© The Author(s), under exclusive license to Springer Nature Switzerland AG 2023
O. Fesenko and L. Yatsenko (eds.), *Nanomaterials and Nanocomposites, Nanostructure Surfaces, and Their Applications*, Springer Proceedings in Physics 279,
https://doi.org/10.1007/978-3-031-18096-5_3

in this way has a typical so-called “core–shell” structure in which the central part consists of iron, and the surface is covered with a thin layer of Fe(II) and Fe(III) oxides, which are formed as a result of oxidative processes. These materials have a large specific surface area and high reactivity. However, a significant disadvantage is that nanoiron has a tendency to aggregate and is easily oxidized with the formation of an oxide layer on the particle surface. These factors reduce the activity and efficiency of nanoiron [12].

The most common variant of the technology for producing iron powder is the reduction of iron oxides and hydroxides (Fe_2O_3 , Fe_3O_4 , $\text{Fe}(\text{OH})_3$, and $\alpha\text{-FeOOH}$) with hydrogen [13–15]. In this case, the metal particles mainly retain the shape and particle size distribution of the original powder during the reduction process under certain conditions.

The same group of methods includes obtaining oxides through carbonate, oxalate, oxyhydroxides (goethite, lepidocrocite), or other insoluble but easily decomposing compounds. The main advantage of these methods is the possibility of obtaining a pure product even when raw materials of low purity are used.

By calcining powders of coagulated Ni- and Fe-tartrates at 250–400 °C (2 h), ultra-fine Ni(II) ferrite powders with a particle size of 10 nm were obtained. In powders, mixtures of Ni- and Fe-tartrates have the chemical properties of individual salts. The homogeneity of their mixing strongly affects the course of the thermal reaction and the properties of the resulting powders. The reservoir temperature and particle size increase with the deterioration of mixing, which initiates an increase in the size of intermediate phases ($\alpha\text{-Fe}_2\text{O}_3$, NiO, or Ni) [16].

The general scheme for obtaining highly dispersed iron powder can be represented as follows:

- production of hydroxides
- dehydration of hydroxides to oxides
- reduction of oxides to metallic iron.

In this case, the size and shape of powder particles are mainly determined by the structure of hydroxides.

The reduction process is the final stage and largely determines the important parameters such as the granulometric composition of products, the content of metallic iron in them, and the structure of particles [17–19]. These parameters can be significantly affected by the choice of reducing gas, since it determines the temperature regime of the process, the composition of the gaseous medium, and, consequently, the state of the surface of the final product [20].

It is known that the reduction and regeneration of iron oxides can be carried out not only with hydrogen, carbon monoxide, and ammonia, but also with technically available gas mixtures: coke, generator, water, etc.

2 Methodology

For reasonable choice of the optimal gas medium, a thermodynamic analysis of the reduction process was carried out.

Thermodynamic calculations were carried out according to the method, which is based on the first variational principle of chemical thermodynamics, using the ASTRA program.

On the basis of thermodynamic calculations, the equilibrium compositions of the products of chemical reactions were determined at various initial compositions, temperatures, and pressures.

The powder with the optimal weight content of the components was taken as the feedstock. In terms of oxides in wt %: Fe_2O_3 –95, NiO–4, and CoO–1.

Coke oven gas based on, (composition: 57% CH_4 , 34% H_2 , 3% CO, 4.4% ($\text{CO}_2 + \text{N}_2$), 0.4 O_2 , 1.2% heavy hydrocarbons), CO and hydrogen. The amounts of gases were taken in excess of the stoichiometric amount.

The calculation was carried out in the temperature range 300–1100 K at a pressure of 0.1 MPa. During the calculation, the influence of the composition of the reducing gaseous medium on the course of the process was studied. The calculation was carried out taking into account the possibility of formation of the following products: Fe_2O_3 , Fe_3O_4 , FeO, CoO, NiO, Fe, C, Fe_3C , Co, and Ni in the condensed phase and H, H_2 , H_2O , NH_3 , CO, CO_2 , CH_4 , CH_3 , C_2H_2 , C_6H_6 , CH_2O , N_2C , and HCN in the gas phase. The concentrations of substances were expressed in mol/kg of the system under study.

3 Results and Its Discussion

The temperature dependence of the equilibrium composition of the Fe_2O_3 –CoO–NiO oxide system during reduction with coconut gas is shown in Fig. 1.

From the analysis of the dependence, it follows that the complete reduction of iron oxides to metal occurs at 700 K, and with a further increase in temperature, its amount decreases due to the formation of iron carbide. Nickel oxides are completely reduced at 400 K and cobalt at 900 K.

Figure 2 shows the temperature dependence of the equilibrium compositions of the same system during the reduction of carbon monoxide(II).

As can be seen from Fig. 2, the reduction of oxides begins at 500 K; however, the degree of reduction strongly depends on temperature and is maximum at 1000 K.

Nickel oxide is reduced at 400 K and cobalt oxide at 800 K. At 900 K, the existence of iron carbide is thermodynamically possible. The reducing properties of the released carbon appear at a temperature of 1000 K.

Figure 3 shows the results of thermodynamic calculations of the chemisorbent reduction process in a hydrogen medium. Nickel oxide is completely reduced to metal at 400 K, at 600 K oxides of iron and cobalt.

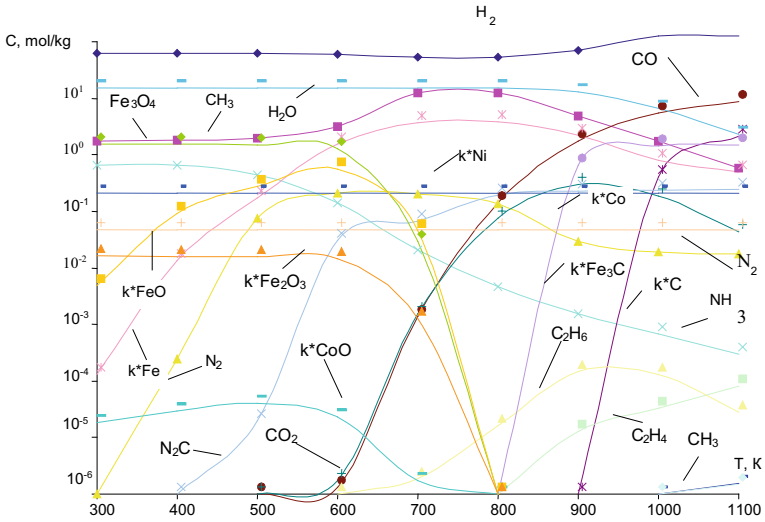


Fig. 1 Dependence of the equilibrium composition of the Fe–Co–Ni–C–N–O–H system on temperature during reduction with coke oven gas, pressure 0.1 MPa

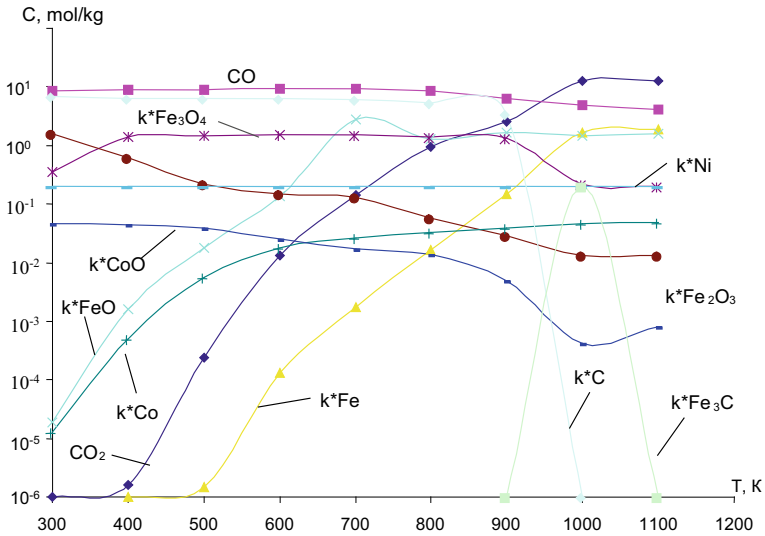


Fig. 2 Dependence of the equilibrium composition of the Fe–Co–Ni–C–N–O–H system on temperature during CO reduction, pressure 0.1 MPa

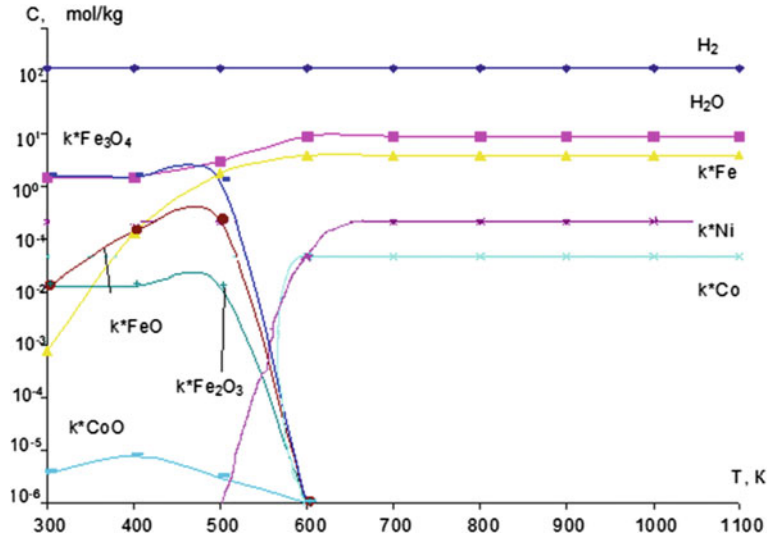
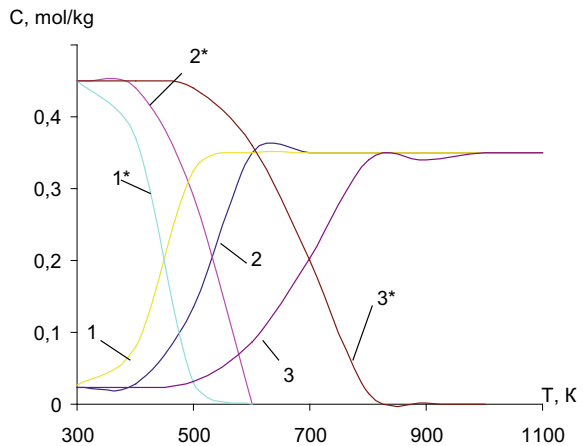


Fig. 3 Dependence of the equilibrium composition of the Fe–Co–Ni–O–H system on temperature during hydrogen reduction, pressure 0.1 MPa

To clarify the optimal hydrogen concentrations, which allow the reduction of the complex Fe–Co–Ni oxide system at lower temperatures, the influence of the hydrogen content in the gas mixture on the temperature of the complete reduction of oxides was studied.

Figure 4 shows the generalized temperature dependence of the total concentrations of two solid phases. The first contains metal oxides, and the second contains metals at different hydrogen concentrations.

Fig. 4 Dependence of the total concentrations of the solid phase of the Fe–Co–Ni–C–N–O–H system on temperature at $P = 0.1$ MPa, the gaseous medium is hydrogen; 1–3—total concentration of metals; 1*–3*—total concentration of metal oxides; 1–1*—90% H_2 , 2–2*—60% H_2 , and 3–3*—20% H_2



Comparing the presented results, we can conclude that with an increase in the hydrogen content in the gas mixture, the temperature region of the existence of a solid solution of iron, cobalt, and nickel increases, and the temperature of the complete reduction of oxides shifts to lower temperatures.

According to the results obtained from thermodynamic calculations, hydrogen is the optimal gas medium, since it provides complete reduction of iron, cobalt, and nickel oxides to metals at 600 K (hydrogen concentration 60% wt.), while the product is not cracked by carbon and iron carbide. Thus, the highly developed porous surface of the catalyst, the structure of the particles, and, as a result, the good adsorption capacity of the metal powder are preserved.

References

1. Tanwar R, Kumar S, Mandal UK (2017) Photocatalytic activity of PANI/Fe⁰ doped BiOCl under visible light-degradation of Congo red dye. *J Photochem Photobiol A: Chem* 333:105–116
2. Zhou M et al (2005) Preparation and photocatalytic activity of Fe-doped mesoporous titanium dioxide nanocrystalline photocatalysts. *Mater Chem Phys* 93(1):159–163
3. Hu B et al (2018) Co/Fe-bimetallic organic framework-derived carbon-incorporated cobalt–ferric mixed metal phosphide as a highly efficient photocatalyst under visible light. *J Colloid Interface Sci* 531:148–159
4. Till BA, Weathers LJ, Alvarez PJJ (1998) Fe(0)-supported autotrophic denitrification. *Environ Sci Technol* 32(5):634–639
5. Cheng R, Wang J, Zhang W (2007) Comparison of reductive dechlorination of p-chlorophenol using Fe⁰ and nanosized Fe⁰. *J Hazard Mater* 144(1–2):334–339
6. Son HS, Im JK, Zoh KD (2009) A Fenton-like degradation mechanism for 1, 4-dioxane using zero-valent iron (Fe⁰) and UV light. *Water Res* 43(5):1457–1463
7. Scorzelli RB (1997) A study of phase stability in invar Fe–Ni alloys obtained by non-conventional methods. *Hyperfine Interact* 110(1):143–150
8. Yao LH et al (2010) Core–shell structured nanoparticles (M@ SiO₂, Al₂O₃, MgO; M= Fe, Co, Ni, Ru) and their application in CO_x-free H₂ production via NH₃ decomposition. *Catal Today* 158(3–4):401–408
9. Frolova L, Kharytonov M (2019) Synthesis of magnetic biochar for efficient removal of Cr(III) cations from the aqueous medium. *Adv Mater Sci Eng* 2019
10. Nguyen TH et al (2021) Impact of iron on the Fe–Co–Ni ternary nanocomposites structural and magnetic features obtained via chemical precipitation followed by reduction process for various magnetically coupled devices applications. *Nanomaterials* 11(2):341
11. Bilgiliyoy E et al (2021) Low energy electron-and ion-induced surface reactions of Fe(CO)₅ thin films. *J Phys Chem C* 125(32):17749–17760
12. Kwak YJ, Park HR, Song MY (2017) Analysis of the metal hydride decomposition temperatures of Zn(BH₄)₂–MgH₂–Tm (Tm = Ni, Ti or Fe) using a sievert’s type volumetric apparatus. *Mater Sci* 23(1):21–26
13. Toneguzzo P et al (2000) CoNi and FeCoNi fine particles prepared by the polyol process: physico-chemical characterization and dynamic magnetic properties. *J Mater Sci* 35(15):3767–3784
14. Frolova LA, Hrydnieva TV (2020) Influence of various factors on the ferric oxyhydroxide synthesis. *J Chem Technol* 28(1):61–67
15. Frolova LA, Khmelenko OV (2021) The study of Co–Ni–Mn ferrites for the catalytic decomposition of 4-nitrophenol. *Catal Lett* 151(5):1522–1533

16. Wang D et al (2017) Innovative evaluation of CO–H₂ interaction during gaseous wustite reduction controlled by external gas diffusion. *Int J Hydrogen Energy* 42(20):14047–14057
17. Yang JM, Tsuo WJ, Yen FS (1999) Preparation of ultrafine nickel ferrite powders using mixed Ni and Fe tartrates. *J Solid State Chem* 145(1):50–57
18. Orth WS, Gillham RW (1995) Dechlorination of trichloroethene in aqueous solution using Fe⁰. *Environ Sci Technol* 30(1):66–71
19. Geng B et al (2009) Kinetics of hexavalent chromium removal from water by chitosan-Fe⁰ nanoparticles. *Chemosphere* 75(6):825–830
20. Mikhailichenko AI, Nefedova NV, Karateeva EY (1998) Hydrogen reduction of ultrafine α-Fe₂O₃ powders. *Russ J Inorg Chem* 43(2):138–141

Formation of Carbon Nanotubes from Products of Methane Air Conversion on Ni/Cr and Fe Catalysts



A. I. Khovavko, A. A. Nebesnyi, D. S. Filonenko, M. Yu. Barabash, A. A. Kolesnichenko, A. M. Sviatenko, S. Ya. Brichka, and Guochao Nie

Abstract The aim of this work is to determine the mechanisms of formation of carbon nanotubes on substrates with Fe and Ni/Cr nanostructures. The promoters of nanotube growth were deposited by thermal evaporation in a vacuum universal post as thin polydisperse layers of metals. The surface layers of iron and chromel were deposited on sital (glass–ceramic) substrates. X-ray phase analysis of as-deposited catalysts showed the formation of growth centers of nanotubes. Carbon nanomaterials with different morphology were synthesized from methane air conversion products by chemical vapor deposition. The Raman spectra showed the defective nature of the deposited materials.

Keywords Carbon nanotubes · Spectroscopy · Electron microscopy · X-ray phase analysis

1 Introduction

Today, nanocarbon materials of different types attract the attention of researchers and developers of new devices in various fields of science and technology due to a unique combination of electrical, mechanical, thermal, optical, and other properties. In particular, they are considered as the materials for building blocks for the development of new nanostructured materials for the functional elements of electronic and photonic devices. These materials improve mechanical, thermal, and interfacial

A. I. Khovavko · A. A. Nebesnyi · D. S. Filonenko (✉) · A. M. Sviatenko · S. Ya. Brichka
The Gas Institute of the National Academy of Sciences of Ukraine, 39, Dehtyarivska St.,
Kyiv 03113, Ukraine
e-mail: ingaskiev@gmail.com

M. Yu. Barabash · A. A. Kolesnichenko
Technical Center of the National Academy of Sciences of Ukraine, 13, Pokrovska St.,
Kyiv 04070, Ukraine

G. Nie
School of Physics and Telecommunication Engineering, Yulin Normal University, Yulin 537000,
China

properties of multiphase polymeric composites graphene/carbon nanotubes (CNTs) [1].

The optimal functional characteristics of nanocarbon materials are directly related to their internal structure which can vary significantly depending on the conditions of their production and additional treatment. Therefore, the information about their structure and its dependence on different methods of impact is important for targeted development of materials with specified physical and mechanical properties. Data on the effect of the structure of nanocarbon materials on their optical characteristics is key in determining the conditions for producing samples with improved functional parameters for photonic elements.

Acetylene, methane, ethylene, propylene, and benzene are most often used for the synthesis of CNTs from hydrocarbons. It is known that effective catalysts for the formation of CNTs are metals of the iron subgroup—Fe, Co, and Ni, and their mixtures. SiO_2 and Al_2O_3 are usually used as catalyst carriers. As a carbon source, we chose a conversion gas with a significant content of carbon monoxide (CO). One carbon atom per molecule provides significant control over the technological parameters of carbon materials, namely the precursor concentration, flow rate, partial pressure, temperature, the type of catalyst, and so on. Researchers have described in detail the Co–Mo/ SiO_2 catalysts that were used for the synthesis of single-walled CNTs using the CO disproportionation reaction at 700–850 °C. It is believed [2] that the use of carbon monoxide made it possible to produce single-layer nanotubes. The thermal decomposition of pure CO on a Ni–CO catalyst deposited on Al_2O_3 was performed at a pressure slightly above atmospheric pressure and at 1200 °C. Single-layer CNTs were also produced.

A great achievement was the synthesis of molybdenum catalyst used for the synthesis of CNTs from CO. The catalyst was produced by impregnation of alumina with a solution of molybdenum derivatives in methanol, followed by heating to 200 °C. The diameter of CNTs formed on this catalyst was 1–5 nm. At the ends of many of them, catalyst particles several nanometers in size were found, which allowed the researchers to suggest the “yarmulke” mechanism for coating growth. The film of chemisorbed carbon atoms on the surface of a catalyst particle is called a “yarmulke”. According to this mechanism, the catalyst particles promote the dehydrogenation of hydrocarbon molecules deposited on them from the gas phase. Carbon diffuses to the open end of a CNT (where the catalyst particle is located) along the surface or in the volume of the catalyst, and fits into the CNT structure. The systems Ni–MgO, CO–MgO, and Ni– AlPO_4 were also successfully tested as catalysts for the decomposition of CO [3].

This paper presents the results of producing nanocarbon materials. This topic belongs to the priority fields of scientific research, development, and technology in Ukraine.

2 Materials and Methods

Iron [4] and standard chromel K alloy (89–91 Ni, 8.5–10 wt.% Cr) [5] catalysts were deposited on sitall substrates [6] in a modernized vacuum universal post VUP-5 M (Fig. 1) by vacuum thermal evaporation of iron and chromel at a residual gas pressure of 10^{-2} – 10^{-3} Pa, field strength $E = 60$ – 80 V/cm², and substrate temperature 300 °C. The layers were formed on the surfaces of polished sitall substrates pre-cleaned by a standard chemical method [7]. The substrates were positioned in a separate zone of the vacuum post. The samples were located at a distance of $h = 8 \cdot 10^{-2}$ m above the evaporator, which promoted a uniform deposition of iron and chromel. The advantage of this technique is the ability to use two evaporators in one cycle and to apply annealing without need to depressurize the chamber. A system of automatic control of the film growth was developed to control the reproducibility of a given distribution of components through the thickness of the films [8]. The control of evaporated material was performed by monitoring the shift of the resonant frequency of quartz sensors (8 MHz), the parameters of electric arc evaporation, and the substrate temperature. The signals of the quartz resonant sensors that registered the mass of each film component were used to control the molecular fluxes in real time. The sensitivity of quartz sensors was $6 \cdot 10^{-8}$ kg/m², and the software-controlled frequency drift did not exceed 10 Hz/h.

The synthesis of carbon nanotubes was carried out using as raw material—one of the most affordable and cheap hydrocarbon gas—natural gas. The main component of natural gas is methane; its content can reach 90% or more. The bond in the CH₄ molecule between carbon and hydrogen atoms is relatively strong, so the decomposition of methane, even with a catalyst, requires elevated temperatures which provide the pre-conditions for the formation of soot carbon together with the nanotubes. In order to convert the carbon contained in CH₄ molecules into a less stable compound, natural gas is pre-converted by transforming methane into unstable carbon monoxide (CO) at low temperatures. The use of natural gas conversion products made it possible to reduce both the synthesis temperature of carbon nanotubes to 600–650 °C and the content of amorphous carbon in these nanotubes.

The conversion of natural gas was performed at the converter developed and constructed at the Gas Institute of the National Academy of Sciences of Ukraine (Fig. 2).

The converter 1 was heated by an electric furnace, and the temperature in the catalyst film was about 950 °C. The conversion of natural gas was carried out with air heated in the air heater 2 to 550 °C; the air flow rate was about 0.3. The converted gas was first cooled in the cooler 3, and then dried in the desiccant 4 filled with silica gel. As a result, the converted gas contained up to 18% CO and 35% H₂, 1.5–2% oxidants, and 0.5–1.5% CH₄, N₂ balance. The gas composition was measured using a Gazochrom gas analyzer.

The dried converted gas was fed into the unit for CNT production, where the carbon material was grown on sitall substrates with deposited catalyst layer in the quartz reactor. It was determined in [9] that the highest rate of carbon yield occurs at

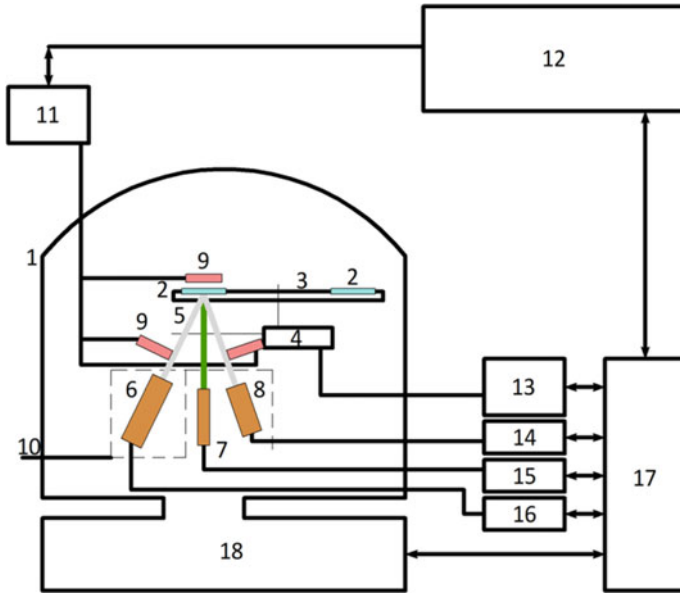
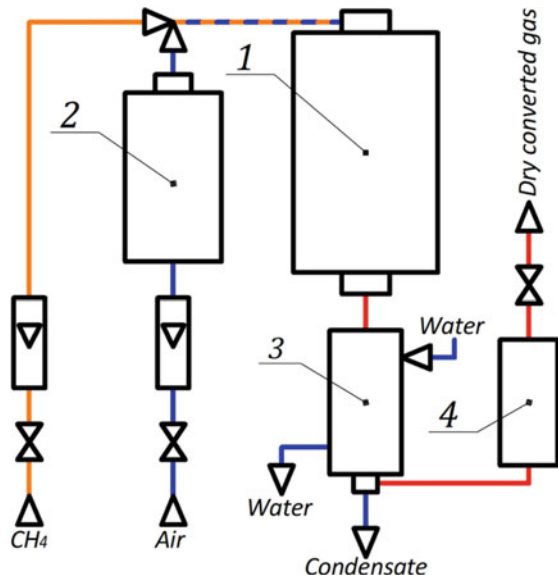


Fig. 1 Scheme of technological unit for producing thin nanocomposite films by vacuum co-deposition: 1—vacuum chamber; 2—samples; 3—substrate transport system; 4—transportation system engine; 5—shutter; 6, 7, 8—metal evaporators; 9—quartz sensors for controlling molecular beams and film mass; 10—light guides; 11—quartz resonator controller; 12—ADC, DAC, coupling board; 13—pressure sensor with controller; 14, 15, 16—power supply; 17—converters and manipulators; 18—vacuum unit VUP-5 M [8]

Fig. 2 Scheme of laboratory gas converter: 1—converter; 2—air heater; 3—cooler; 4—drying unit



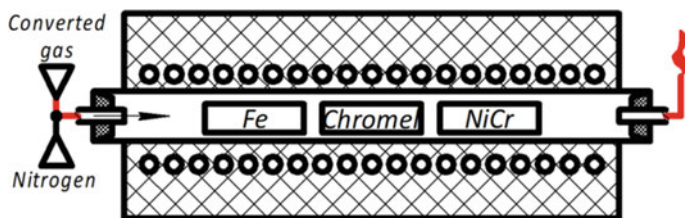


Fig. 3 Scheme of experimental unit for producing carbon nanomaterials

about 650 °C, so the reactor was pre-heated to this temperature in our experiments. The consumption of converted gas was about 6 l/h.

The carbon nanotubes were grown in a horizontal quartz reactor with external electric heating (Fig. 3).

As the catalyst carriers, sitalt plates were used; nanosized films of iron, chromel, and nichrome were deposited on the surfaces of these plates. The plates were sequentially placed in the center of the reactor. The substrate coated with Fe was oxidized at $T = 600$ °C in air atmosphere for 30 min. After oxidation, the reactor was blown down with nitrogen. Oxidized plates were reduced in a hydrogen atmosphere for one hour with a gradual temperature increase from 400 °C to 650 °C. Reductive treatment of iron oxides (on iron plates) with hydrogen at relatively low temperatures enables to get a surface of freshly reduced iron with high catalytic activity. After hydrogen treatment, the gas atmosphere in the reactor was replaced by the products of natural gas air conversion. The converted gas was continuously fed into the reactor heated up to 650 °C for 2.5 h.

After the deposition of the carbon nanomaterial, the reactor with the plates in it was blown down with nitrogen and cooled to 80 °C. The sequence of heat treatment of the material in different gas atmosphere is shown in Fig. 4.

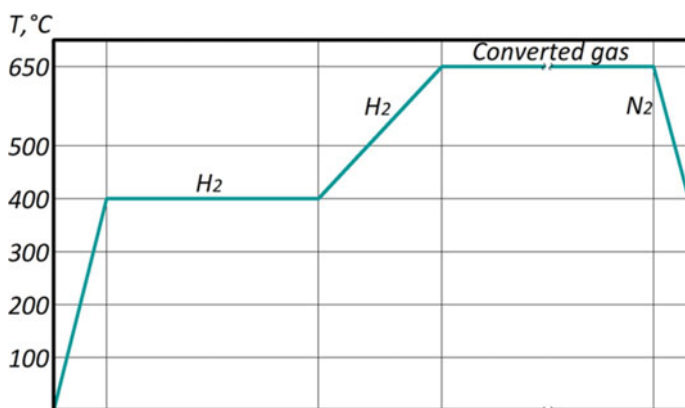


Fig. 4 Thermogram of treatment of substrate with deposited catalyst in atmospheres of H_2 , converted gas, N_2

X-ray phase analysis was carried out with an X-ray diffractometer Ultima-IV, Rigaku, Japan (National Technical University of Ukraine “Igor Sikorsky Kyiv Polytechnic Institute”) in $\text{CuK}\alpha$ radiation. The peaks in diffraction patterns were identified using the databases ICDD PDF-2 and PDF-4. The carbon nanomaterials were investigated with scanning electron microscopy (JSM-6490LV microscope) with a resolution of up to 1 nm (Fig. 6). The Raman spectra of the samples were investigated using a Raman spectrometer mini-Raman Pro (Lightnovo, Denmark). A laser with wavelength $\lambda = 785$ nm was used for the spectrum range $600\text{--}2000$ cm^{-1} . The accuracy of determining the wave number was in the range $0.5\text{--}2$ cm^{-1} . The registration parameters were the following: exposure 100 ms, 50 spectra were averaged. The laser power was 5.88–47.38 mW.

3 Results and Discussion

The catalyst layers of chromel and iron were deposited under the conditions described above. The deposition process was provided by the possibility to deposit several materials without depressurizing the chamber, with little thermal impact on the treated structure. To control the reproducibility of films with a given distribution of components through the thickness, a system of automatic control of the process of film growth was developed. The synthesis and growth of the films were controlled with two computerized control systems. These measures provided the production of films with reproducible technical parameters. The mass scatter of the samples in the experiments of the same type of did not exceed 15%.

Diffraction maxima of nickel and chromium were observed in diffractograms from chromel film (Fig. 5). Apparently, during the deposition of chromel, it decomposed with the formation of metals and chromium oxide (Cr_2O_3). X-ray spectrum analysis also revealed the signals that correspond to the structure of nickel chromate NiCr_2O_4 . According to [10], nickel chromate can be the center of growth of carbon nanotubes and is a promising catalytic material along with pure metals. Oxides of silicon and aluminum are considered as the contribution from the substrate. The most intense diffraction maxima of chromium oxide Cr_2O_3 are observed in the ranges $2\theta = 10\text{--}18^\circ$ and $28\text{--}30^\circ$.

From the viewpoint of thermodynamics, the reaction of thermal decomposition of CO (with CO_2 and carbon as products) crucially differs from the processes of pyrolysis of hydrocarbons: the equilibrium yield of carbon at atmospheric pressure approaches noticeable values in the region of low temperatures 300–750 K, and it reduces as temperature increases and pressure decreases. On the contrary, the carbon yield in the pyrolysis of C_2H_2 and CH_4 increases with increasing temperature and decreasing pressure, approaching noticeable values at 1250–1500 K. Therefore, it would seem that carbon monoxide is a less convenient starting reagent for the synthesis of CNTs. However, it is more difficult to heat hydrocarbons above 800–900 °C before contact with the catalyst as compared to CO for kinetic reasons. In this regard, CO has an advantage over hydrocarbons.

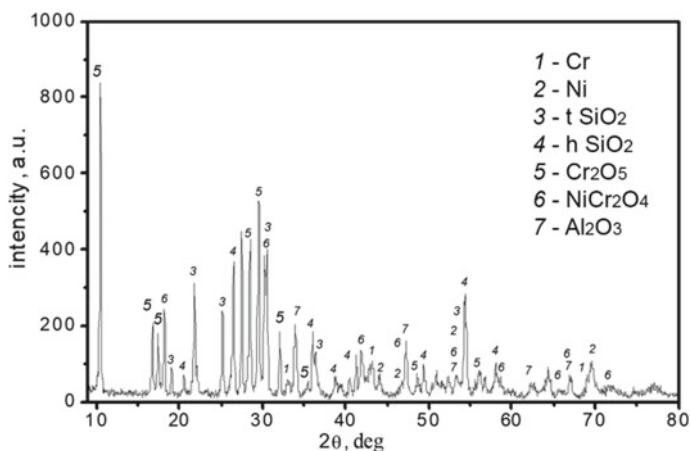


Fig. 5 Diffractogram of thin chromel layer on sital substrate

Carbon formed on metals of the subgroup of iron and their alloys with other metals appears in the form of deposits with different morphological and crystallographic characteristics that depend on the properties of the catalysts and experimental conditions. These dependencies make it possible to purposefully control the technology of obtaining carbon deposits with different morphology. Carbon can be deposited as threads of various configurations, nanotubes, plates, and so on [11]. The mechanisms of catalytic formation of CNTs are divided into root growth and tip growth [12]. In the first, CNTs grow from the surface of the metal particles that remain in contact with the substrate. In the second, a metal particle detaches from the substrate and is held on a growing nanotube. The synthesis of CNTs from arc discharge or by laser dispersion in most cases occurs by root growth [13].

Raman spectroscopy is a technique for rapid and non-destructive monitoring of electron and phonon parameters of carbon materials, which correlate with their chemical composition and structure at the level of chemical interactions. The Raman spectra (Fig. 7) of the produced materials are characterized by the position, half-width, and relative intensity of the spectral bands, which are determined by the structural state of carbon. Typically, the Raman spectra of chemically synthesized multilayer carbon nanotubes have two bands, in the region of 1590 cm^{-1} (G band, tangential mode E_{2g} of symmetric valent vibrations of sp^2 hybridized carbon bonds), and about 1340 cm^{-1} (D band caused by totally symmetric vibrations of A_{1g} aromatic sp^2 hybridized carbon rings). The classical spectrum of carbon nanotubes contains two characteristic peaks at 1298 and 1586 cm^{-1} , which correspond to the D and G mode, respectively (Fig. 7a). The first mode D characterizes the defect structure of graphene layers of nanotubes. The second mode G corresponds to the tangential valent carbon-carbon vibrations and characterizes the ordering of the carbon phase. The ratio of these two modes shows the amount of defects in nanotubes.

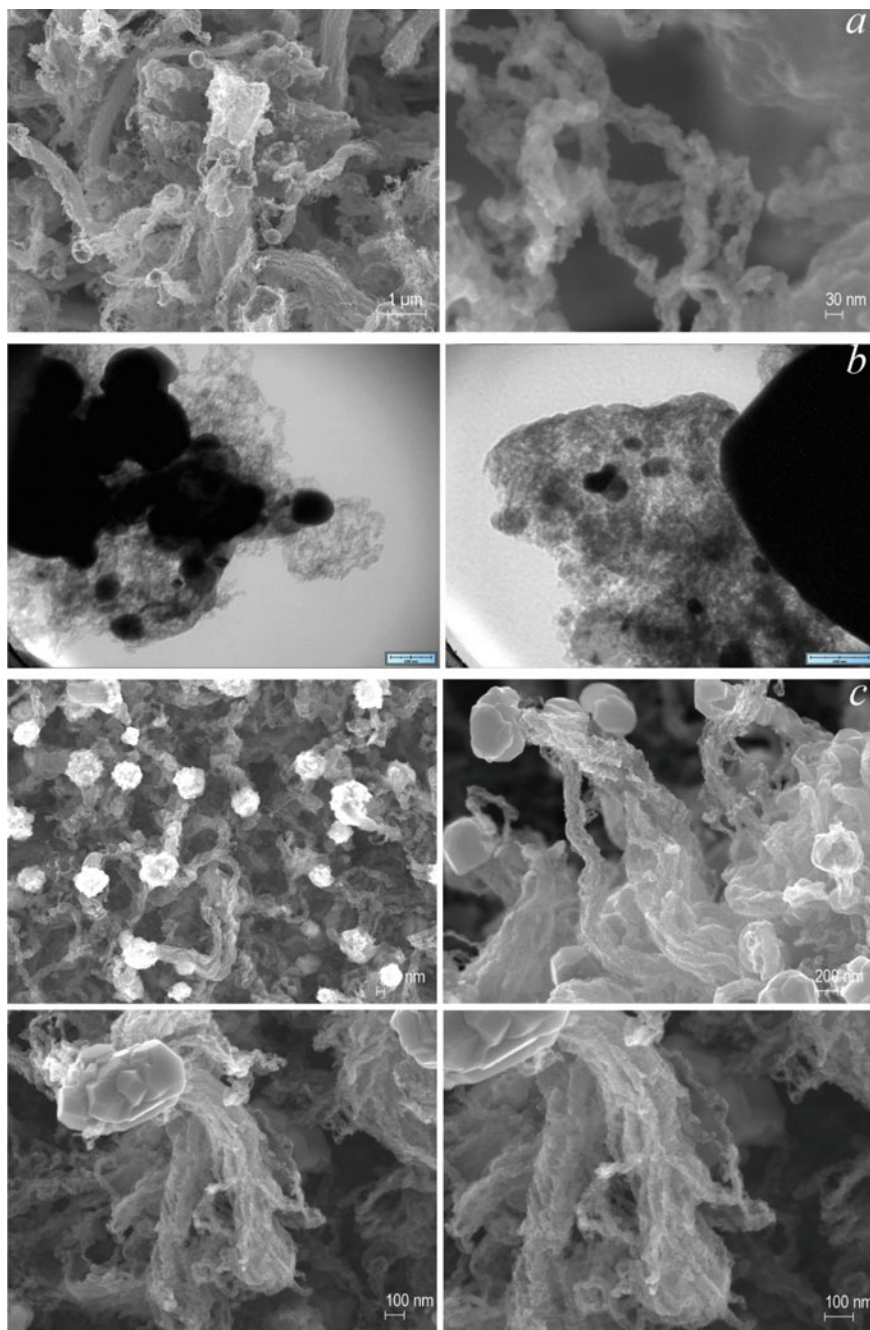


Fig. 6 Micrographs of carbon nanomaterials: **a, b**—iron catalyst (SEM and TEM); **c**—chromel catalyst (SEM)

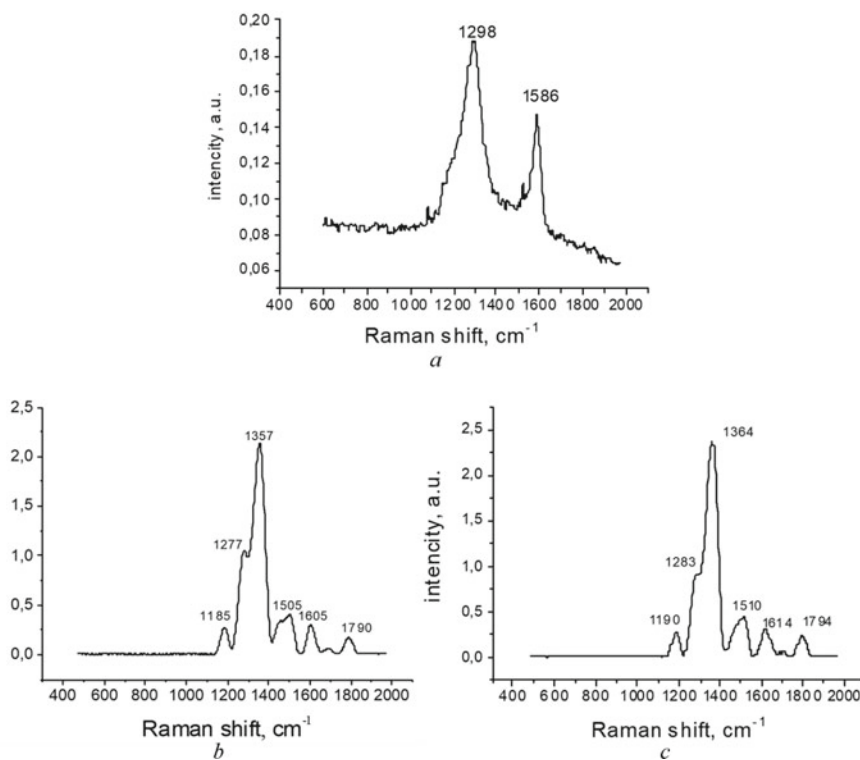


Fig. 7 Raman spectra of carbon materials with: **a**— iron catalyst; **b**—chromel catalyst; **c**—multi-layer nanotubes

Known lines in the Raman spectra of insufficiently ordered graphite are within $1585\text{--}1570\text{ cm}^{-1}$ and $1350 \div 1300\text{ cm}^{-1}$ [14].

The Raman spectra in Figs. 7b and c are almost identical. These spectra show strong luminescence in the range $1100\text{--}2000\text{ cm}^{-1}$, which is not typical for the samples of purified nanotubes (Fig. 7c). Additional signals are observed, probably from different types of carbon and/or catalysts. This luminescence can be caused by the transparency of the sample and the contribution from the substrate (the beam hit the area where the number of nanotubes was very small); however, this hypothesis requires further study. Characteristic *D* and *G* modes at frequencies 1364 and 1510 cm^{-1} are found out. These modes can be caused by multilayer nanotubes which were observed in electron microscopy images. It was found that the *D* line is more intense and wider than the *G* line (Fig. 7), which indicates a large number of defects ($D/G < 1$). This ratio also characterizes the curvature (bending) of the layer. Besides, the *G* mode disintegrates into *G* + and *G* - (peak splitting), which indicates the presence of single-layer CNTs.

4 Conclusions

Thin layers of iron and chromel catalysts were produced in the developed unit. CNTs were synthesized from the products of methane air conversion by chemical vapor deposition in a flow reactor. It is shown that the synthesis of CNTs at $T > 650\text{ }^{\circ}\text{C}$ increases the mobility of catalytic particles in the carrier, which leads to their agglomeration, and therefore, affects the growth of CNTs.

The electron microscopy (SEM and TEM) studies of the structure of carbon nanomaterials showed that the developed synthesis technology makes it possible to form CNTs of different morphology and thickness. The Raman spectra confirmed the presence of carbon nanotubes with two characteristic peaks at 1364 and 1510 cm^{-1} , which correspond to *D* and *G* modes, respectively. The ratio of these two modes indicated a significant number of defects in carbon nanotubes.

Acknowledgements Research was financed by budget program 6541230 of the National Academy of Sciences of Ukraine "Supporting the development of priority areas of research". Also this research was supported by a funding from a Nation China Natural Science, No. 81660508 and grants from the Guangxi Science and Technology Plan Project, Guike AB16380153, Guike AB17195076.

Authors' Contribution AN and DF development laboratory equipment for methane air conversion, data processing, and preparation and approval of the final manuscript. AN theoretical calculations. AS experiment on carbon nanomaterials synthesis. AK contributed to the statement of the problem and the way to solve it. SB analysis of Raman spectra. NG discussed the results and helped in preparing and approving the final manuscript. GN contributed to the statement of the problem and discussion of the results. MB and AK took part in the formulation of problems and ways to solve it and participated in the task and designed according to the requirements of article publication. All authors read and approved the final manuscript. All authors read and approved the final manuscript.

Competing Interest

The authors declare that they have no competing interests.

References

1. Kumar A, Sharma K, Dixit AR (2020) Carbon nanotube- and graphene-reinforced multiphase polymeric composites: review on their properties and applications. *J Mater Sci* 55(3):2682–2724
2. Herrera JE, Balzano L, Borgna A, Alvarez WE, Resasco DE (2001) Relationship between the structure/composition of Co–Mo catalysts and their ability to produce single-walled carbon nanotubes by CO disproportionation. *J Catal* 204(1):129–145
3. Rakov EG (2007) Preparation of thin carbon nanotubes by catalytic pyrolysis on a support. *Russ Chem Rev* 76(1):3–26. <https://doi.org/10.1070/RC2007v076n01ABEH003641> (Russia)
4. Shanov V, Yun Y-H, Schulz MJ (2006) Synthesis and characterization of carbon nanotube materials (Review). *J Univ Chem Technol Metall* 41(4):377–390
5. Kenneth BK, Teo (2003) Catalytic synthesis of carbon nanotubes and nanofibers. *Encycl Nanosci Nanotechnol* 10:1–22

6. Maskaeva LN, Fedorova EA, Markova VF (2019) Thin films and coatings technology. Study guide. Ministry of science and higher education R.F., Ural. federal university. Yekaterinburg, Publishing house of the Ural university, 236 p. ISBN 978-5-7996-2560-3 (Russia)
7. Luchkin AG, Luchkin GS (2012) Surface cleaning of substrates for coating by vacuum-plasma methods. Kazan: Bulletin of Kazan Technological University, pp 208–210 (Russia)
8. Barabash MY, Grinko DO, Sperskach SO (2015) Formation of nanostructure on templates by radiation from a visible shade. Kiyv, IMFNASU, 202 p. (Ukrainica)
9. Bondarenko BI, Sviatenko OM, Khovavko AI, Kotov VG, Nebesnyi AA, Filonenko DS. Big multi-walled carbon nanotubes synthesis using a reduced iron as a catalyst. In: Proceedings of the 2018 IEEE 8th international conference on nanomaterials: applications and properties (NAP-2018) 9–14 Sept 2018. Zatoka, Odessa Region, Ukraine pp 50–53. <https://doi.org/10.1109/NAP.2018.8914865>
10. Słoczyński J, Janas J, Machej T, Rynkowski J, Stoch J (2000) Catalytic activity of chromium spinels in SCR of NO with NH₃. Appl Catal B: Environ 24:45–60
11. Chesnokov VV, Buyanov RA (2000) The formation of carbon filaments upon decomposition of hydrocarbons catalysed by iron subgroup metals and their alloys. Russ Chem Rev 69(7):623–638. <https://doi.org/10.1070/RC2000v069n07ABEH000540>
12. Mishchenko SV, Tkachev AG (2008) [Carbon nanomaterials. Production, properties and applications]. Moscow, Mashinostroenie, 320 p. (Russia)
13. Harris PJF (2007) Solid state growth mechanisms for carbon nanotubes. Carbon 45:229–239
14. Yanchuk IB, Koval's'ka EO, Brichka AV, Brichka SY (2009) Raman scattering studies of the influence of thermal treatment of multi-walled carbon nanotubes on their structural characteristics. Ukr J Phys 54(4):407

Generalized Constitutive Equations and Coupled Phenomena at the Nanoscale: Applications to Nanofluidics



Natalya Kizilova

Abstract Physical phenomena at the micro and nanoscales have specific features that must be accounted for in the governing equations. Wall roughness at such scales has the same order of magnitude as the size of micro/nanoparticles in the fluids moving through solid geometries. Diffusive scattering of the particles at the roughness leads to the tangential momentum transfer along the flow direction that is considered as velocity slip conditions. Heat transfer in the boundary fluid layer is amplified by the scattering that is observed as temperature jump boundary conditions. Besides, in the basic physical laws, the terms with space gradients are more important than those at the macroscales that leads in the high-order governing equations instead of the Navier–Stokes and turbulent flow equations. Those conclusions are supported by experimental measurements that reveal discrepancy between the pressure–flow relationships computed from the classical equations and real flows in the same geometry. In this paper, a systematic review of generalized constitutive equations and coupled phenomena based on the wave propagation in the fluids and viscoelastic solids at the micro and nanoscales is given.

1 Introduction

Fluid flows and related physical processes at micro and nanoscales are determined by general balance laws for mass, momentum, moment of force, energy, charge, and entropy, but the corresponding constitutive equations must be generalized to account for the small-scale and fast phenomena [1]. Besides, the boundary conditions (BC) at the fluid–solid interfaces must be modified [2–4]. Numerous experimental data revealed a noticeable discrepancy between the measured pressure–flow dependences and the theoretical ones computed on the Poiseuille flow through a channel/tube with

N. Kizilova (✉)

Institute of Aeronautics and Applied Mechanics, Warsaw University of Technology, Ul. Nowowiejska 24, 00-665 Warsaw, Poland
e-mail: n.kizilova@gmail.com

V.N. Karazin, Kharkov National University, Svobody Sq., 4, 61022 Kharkov, Ukraine

© The Author(s), under exclusive license to Springer Nature Switzerland AG 2023
O. Fesenko and L. Yatsenko (eds.), *Nanomaterials and Nanocomposites, Nanostructure Surfaces, and Their Applications*, Springer Proceedings in Physics 279,
https://doi.org/10.1007/978-3-031-18096-5_5

circular/rectangular/triangular/trapezoidal or other geometries [5–11]. The experimental studies confirmed that the flow resistances were ~10–90% higher than the theoretical values computed with velocity no-slip BC for the corresponding geometry, and some of them are by ~350% over the theoretical predictions. The explanation of the micro/nanoscale phenomena is based on the diffusive scattering of the fluid particles at the wall roughness that is compatible to the particle size, and the high surface-to-volume ratios (S/V) in the micro/nanoscales. First theory of velocity slip BC had been developed for rarefied gas [12, 13] including the heat transfer processes [14]. Later, its applicability had been shown for fluids at the small scales [1, 3, 4, 15]. Importance of the generalized heat transfer law instead of the Fourier law for the heat balance equation has always been shown in numerous theoretical and experimental studies [16–19]. In this study, the effects of the both generalized physical laws and BC on the fluid flows at different conditions are studied. The corresponding analytical/semianalytical solutions are important for validation of the numerical code and finite element modeling (FEM) for the internal and external flows of micro/nanofluids in complex geometries [20–22] including the soft viscoelastic solids [23] and biological fluids and tissues [24, 25].

2 Diffusive Scattering and Velocity Slip Boundary Conditions (BC)

Recent development of microelectro-mechanical systems (MEMS) based on microfluidic technologies revealed importance of more general BC at the fluid–solid boundaries. The gas microflows are used as small-scale heat exchangers for cooling integrated circuits, and miniature gas chromatography systems for the detection of pollutants, small chemical, and bioreactors for medical and biological purposes have revised the applicability of conventional physical laws and BC at the micro and nanoscales [1, 3, 4, 15]. The flow parameters are gas flow-based MEMS depend on the Knudsen number ($Kn = \lambda/h$) which is defined as the ratio of the molecular mean-free path (λ) to a characteristic dimension (h) of the flow. When $Kn \ll 1$, the gas can be considered as a continuous medium that is governed by hydrodynamic equations, while at $Kn \sim 1$, the gas molecules can be modeled based on the kinetic theory. In the hydrodynamic regime, the flow properties are assumed to be in the local thermodynamic equilibrium with their surroundings, and the linear dependencies between the thermodynamic forces and fluxes are valid, namely.

1. Fourier heat flux

$$\vec{J}_T = -k\nabla T, \quad (1)$$

2. Fick's diffusion law

$$\vec{J}_D = -D\nabla C, \quad (2)$$

3. Darcy's percolation law

$$\vec{J}_m \equiv \rho_f \vec{v} = -\frac{K\rho_f}{\mu_f} \nabla p, \quad (3)$$

4. Ohm's law

$$\vec{J}_e = -\rho_e \nabla \varphi_e, \quad (4)$$

where T is the temperature, k is the thermal conductivity, D is the diffusion coefficient, C is the mass concentration, ρ_f , μ_f are the fluid density and viscosity, p is the hydrostatic pressure, K is the permeability of the porous medium, ρ_e is the electric charge density, and φ_e is the electric field potential.

Thermodynamic equilibrium also confirms the no-velocity-slip and no-temperature-jump BC in the hydrodynamic regime. The linear dependence between the shear stress tensor (τ_{ik}) and strain rate tensor ($\dot{\varepsilon}_{ik}$) (Newton's law of viscosity) corresponds to the so-called Newtonian fluids while more general no-linear dependencies $F(\tau_{ik}, \dot{\tau}_{ik}, \varepsilon_{ik}, \dot{\varepsilon}_{ik}) = 0$ correspond to different types of the non-Newtonian macroscopic fluids. In the kinetic regimes, the assumption of thermodynamic equilibrium could be invalid due to the compatibility of the free path and the length scale ($\lambda \sim h$) when the gas molecules could slide over the solid surface and a discontinuity in the velocity at the wall occurs. In dilute gases, the mean-free pass is determined by the diameters d_p of particles and their numerical concentration N (number per unit volume) as $\lambda = (\sqrt{2}N\pi d_p^2)^{-1}$ [1-3].

Based on the experimental studies and theoretical considerations, the following Kn -based flow regimes have been distinguished [3]

- (1) Continuum flow (ordinary fluid) for $Kn < 0.001$,
- (2) Slip-flow regime (slightly rarefied) for $0.001 < Kn < 0.1$,
- (3) Transition regime (moderately rarefied) for $0.1 < Kn < 10$,
- (4) Free-molecule flow (highly rarefied) for $10 < Kn$.

Such discrepancy had been observed in the rarefied gas flows, and Navier in 1873 proposed the first formulation of the velocity slip BC

$$\partial\Omega : \left(\hat{T}\vec{n} \right)_\tau + \kappa v_\tau = 0, \quad (5)$$

where $\partial\Omega$ is the boundary of the flow domain Ω , \vec{v} , and \hat{T} are the fluid velocity and stress tensor, \vec{n} and $\vec{\tau}$ are normal and tangential unit vectors to $\partial\Omega$, κ is the "friction" coefficient.

In 1879, J.C. Maxwell proposed another formulation for the velocity slip at the rough isothermal wall [26]

$$\left(v_\tau - v_w \pm \frac{2 - \sigma}{\sigma} Kn \frac{\partial v_\tau}{\partial n} \right) \Big|_{\partial\Omega} = 0, \quad (6)$$

where v_w is the wall velocity and σ is the tangential momentum accommodation factor ($\sigma = 1$ for purely diffuse reflection and $\sigma \rightarrow 0$ for pure no-slip).

In the case of non-isothermal wall, the condition (6) was generalized by Maxwell as [26] in the form

$$\left(v_\tau - v_w - \frac{2 - \sigma}{\sigma} Kn \frac{\partial v_\tau}{\partial n} - \frac{3}{4} \frac{\mu_f}{\rho_f T} \frac{\partial T}{\partial \tau} \right) \Big|_{\partial\Omega} = 0. \quad (7)$$

The BC (7) well describes slip flow over a non-isothermal plane wall, while for the flows along the curved walls, the better correspondence can be obtained by application the BC in the form [26]

$$\left(v_\tau - v_w - \frac{2 - \sigma}{\sigma} \frac{\lambda}{\mu_f} \Upsilon - \frac{3}{4} \frac{1 - \gamma}{\gamma} \frac{\text{Pr}}{p} \Theta \right) \Big|_{\partial\Omega} = 0, \quad (8)$$

where Υ and Θ are the tangential shear stress and heat flux at the wall, p is the hydrostatic pressure, $\text{Pr} = c_p \mu_f / k$ is the Prandtl number, c_p is the specific heat capacity, and $\gamma = c_p / c_v$ is the ratio of specific heats.

For the fluid flows over the isothermal microparticles, the BC (6) can be generalized as

$$\left(v_\tau - v_w - \frac{2 - \sigma}{\sigma} \frac{Kn}{1 - Kn \cdot G(Kn)} \frac{\partial v_\tau}{\partial n} \right) \Big|_{\partial\Omega} = 0, \quad (9)$$

where the function $|G(Kn)| < 1$ can be determined from experiments.

The BC (6)–(9) describe well the slightly rarefied gases and microfluids (fluids with particles of $d_p \sim 5\text{--}500 \mu\text{m}$) while for the moderately rarefied gases and nanofluids (fluids with particles of $d_p \sim 5\text{--}500 \text{nm}$), the second-order derivatives cannot be neglected, and instead of (6), the isothermal BC must be rewritten as [26]

$$\left(v_\tau - v_w - \frac{2 - \sigma}{\sigma} Kn \left(\frac{\partial v_\tau}{\partial n} + \frac{Kn}{2} \frac{\partial^2 v_\tau}{\partial n^2} \right) \right) \Big|_{\partial\Omega} = 0. \quad (10)$$

In 1898, M. Smoluchowski derived similar velocity slip BC with the temperature jump in the form [27]

$$\left(T - T_w - \frac{2 - \sigma_T}{\sigma_T} \frac{2\gamma}{1 + \gamma} \frac{\lambda}{\text{Pr}} \frac{\partial T}{\partial n} \right) \Big|_{\partial\Omega} = 0, \quad (11)$$

where T_w is the wall temperature, σ_T is the thermal accommodation at the wall which represents the fraction of reflected molecules possessing the mean energy

of gas molecules at the temperature T_w [28], and $\sigma_T = 1$ when the energy of the reflected (scattered) particles corresponds to T_w .

The modified Maxwell-Smolochowski's BCs at the isothermal wall were formulated in [29] as

$$\begin{aligned} \left(v - v_w - \frac{2-\sigma}{\sigma} Kn \frac{\partial v}{\partial n} - \frac{3(\gamma-1)}{2\pi\gamma} \frac{Kn^2 Re}{Ec} \frac{\partial T}{\partial \tau} \right) \Big|_{\partial\Omega} &= 0, \\ \left(T - T_w - \frac{2\gamma(2-\sigma_T)}{(\gamma+1)\sigma_T} \frac{Kn}{Pr} \frac{\partial T}{\partial n} \right) \Big|_{\partial\Omega} &= 0, \end{aligned} \quad (12)$$

where $Re = \rho_f v h / \mu_f$ is the Reynolds number, $Ec = v^2 / c_p \Delta T$ is the Eckert number, and ΔT is the characteristic temperature difference in Ω .

According to numerous measurements, the tangential (σ) and thermal (σ_T) accommodation coefficients strongly depend on the physical properties of fluid and solid materials [1–4, 15, 29]. In practical applications, the simplified expressions for (12) can be used in the form [3, 30, 31]

$$\begin{aligned} \left(v - v_w - \alpha Kn \frac{\partial v}{\partial n} + \beta Kn^2 \frac{\partial^2 v}{\partial n^2} \right) \Big|_{\partial\Omega} &= 0, \\ \left(T - \xi T_w - \zeta \frac{\partial T}{\partial n} \right) \Big|_{\partial\Omega} &= 0, \end{aligned} \quad (13)$$

where $\alpha \in [1; 1.15]$, $\beta \in [0.5; 1.31]$ represent the first and second-order slip effects, $\{\xi, \zeta\} \in [0, 1][0, 1]$ represent the interfacial conditions and adsorption properties of the materials that can be measured from experiments in known flow conditions, fluid and solid materials.

Better correspondence of the velocity slip BC have been confirmed in the experiments with Newtonian fluid flows [32], porous walls [33], walls with slide coating [34], biological fluids [35], flows of polymer melts [36], and in turbulent flows [37]. Recently, more generalized formulations of the BCs (5)–(13) based on the slip length concept [38] and superexponential models [39] have been proposed.

- (1) **Rectangular channels.** Experimental studies of the gas flow through the rectangular glass channels with hydraulic diameters $D_h = 45.5\text{--}83.1 \mu\text{m}$ and silicon channels with $D_h = 55.8\text{--}72.4 \mu\text{m}$ and the friction coefficient $\sim 10\text{--}30\%$ higher in silica channels and in 3–5 times high in glass channels compared to the Poiseuille formula [12]. When the temperature varies from $T = 0$ to $T = 85^\circ\text{C}$, the friction coefficient of the fluid flows in the silicon channels with $D_h = 5; 12; 25 \mu\text{m}$ increased by 5–30% [40]. In the metallic microchannels with heights $H = 22.7\text{--}26.3 \mu\text{m}$ and widths $W = 150\text{--}600 \mu\text{m}$, an increase of $\sim 20\%$ over the no-slip BC was measured [5]. Laminar and turbulent flows in the stainless steel channels with $D_h = 133\text{--}367 \mu\text{m}$ also demonstrated deviations from the classic no-slip BC [8]. The laminar-to-turbulent transition has been detected at the critical Reynolds numbers $Re^* = 200\text{--}700$ depending on D_h , and the value Re^* decreases with D_h .
- (2) **Trapezoidal channels.** Laminar flows of water ($Re < 1500$) in the silicon microchannels with $D_h = 51.3\text{--}168.9 \mu\text{m}$ and wall roughness $\varepsilon = (0.0176\text{--}0.0285)D$ demonstrated the friction factor by 8–38% higher than those predicted

by the no-slip BC [9]. Gaseous flows (nitrogen, helium, and argon) in the microchannels exhibited good correspondence to theoretical computations with first-order slip BC [41].

- (3) **Circular tubes.** In the stainless steel and silica tubes with diameters $D = 50\text{--}254 \mu\text{m}$ and $\varepsilon = (0.007\text{--}0.035)D$ at $\text{Re} = 100\text{--}2000$, the deviation between the no-slip flow increased with increasing Re and decreasing D . The laminar-to-turbulence transition in the circular tubes was detected at $\text{Re}^* = 300\text{--}900$ depending on the diameter [8].

Generalizations of the analytical solutions for classical Poiseuille and Couette flows in the channels with different cross sections with velocity slip BC at the isothermal walls was computed in [2] for the case of different roughness of the upper and bottom walls. It was shown, by a proper choice of the channel geometry, wall roughness, and flow regime, the hydraulic resistance of the channel could be decreased. The corresponding expressions for the mass flow rate $Q(\text{m}^3/\text{s})$ and wall shear stress $\tau(\text{N}/\text{m}^2)$ are summarized in Table 1.

Similar correspondence has been obtained in the experiments with non-isothermal walls [29, 42]. Analytical expressions for the velocity and temperature have been computed for the Poiseuille flow between the parallel plates and constant heat flux ($J_w = \text{const}$) at the walls [29]:

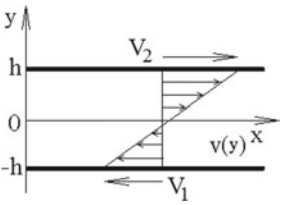
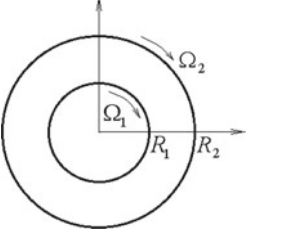
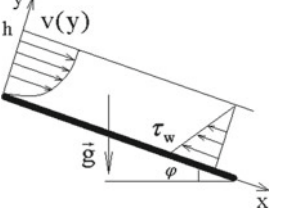
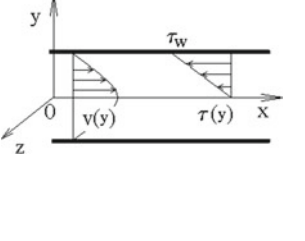
$$\begin{aligned}
 v(y) &= \frac{\Delta p \text{Re}}{2L} \left(1 - \left(\frac{y}{h} \right)^2 + 2 \frac{2 - \sigma}{\sigma} \frac{2Kn}{2 + Kn} + \frac{3(\gamma - 1) Kn^2 \text{Re}}{2\pi\gamma} \frac{T_s}{Ec} \right), \\
 Q &= \frac{4}{3} + 4 \frac{2 - \sigma}{\sigma} \frac{2Kn}{2 + Kn} + \frac{3(\gamma - 1) Kn^2 \text{Re}}{\pi\gamma} \frac{T_s}{Ec}, \\
 \frac{\Delta p}{L} &= \frac{3\sigma(\gamma - 1)Kn^2(2 + Kn)}{2\pi\gamma Ec(2\sigma - 5\sigma Kn) + 12Kn}, \\
 T(x, y) &= T_s x + \text{Re Pr } T_s \left(\frac{C_1 y^2}{2} - \frac{y^4}{12} \right) - Ec \text{Pr} \frac{y^4}{3} + C_2 y + C_3, \\
 T_s &= \frac{1}{\text{Re Pr } Q} \left(J_w + \frac{8}{3} Ec \text{Pr} \right), \tag{14}
 \end{aligned}$$

where the constants $C_{1,2,3}$ are not presented here due to their complexity, h is the distance between the plates.

Similar solution for the Couette flow between the parallel plates [29]:

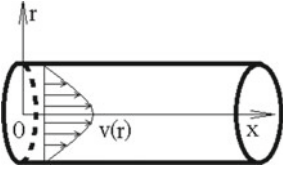
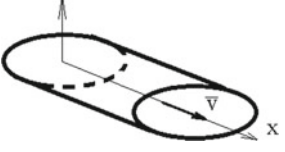
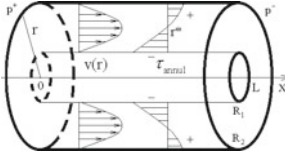
$$\begin{aligned}
 v(y) &= v_w \left(\frac{y/h + (2 - \sigma)Kn/\sigma}{1 + 2(2 - \sigma)Kn/\sigma} + \frac{3(\gamma - 1) Kn^2 \text{Re}}{2\pi\gamma} \frac{T_s}{Ec} \right), \\
 Q &= \frac{1}{2} + \frac{3(\gamma - 1) Kn^2 \text{Re}}{2\pi\gamma} \frac{T_s}{Ec}, \\
 T(x, y) &= T_s x + \frac{C_1 y^3}{6} + \frac{C_2 y^2}{2} - \left(\frac{C_1}{2} + C_2 \right) y + C_3,
 \end{aligned}$$

Table 1 Expressions for the mass flow rate $Q(\text{m}^3/\text{s})$ and wall shear stress $\tau(\text{N}/\text{m}^2)$ Poiseuille and Couette flows in the channels with different cross sections with velocity slip BC; α_1, α_2 are roughness coefficients for the corresponding walls

N	Expressions	Schemes
1	<p>Couette flow between parallel plates</p> $Q = \frac{(V_1 + V_2)h^2 + 2h(\alpha_2 V_1 + \alpha_1 V_2)}{2(h + \alpha_2 + \alpha_1)},$ $\tau = \mu \frac{V_2 - V_1}{h + \alpha_2 + \alpha_1}.$	
2	<p>Couette flow between coaxial rotating cylinders</p> $Q = A_3 \frac{R_2^3 - R_1^3}{3} - A_4(R_2 - R_1), \tau(r) = A_3 + \frac{A_4}{r^2},$ $A_3 = \frac{\Omega_2 R_2^4 A_1 - \Omega_1 R_1^4 A_2}{R_2^3(R_2 - \alpha_2)A_1 - R_1^3(R_1 + \alpha_1)A_2}$ $A_4 = \frac{\Omega_2 R_1^3 R_2^4 (R_1 + \alpha_1) - \Omega_1 R_1^4 R_2^3 (R_2 - \alpha_2)}{R_2^3(R_2 - \alpha_2)A_1 - R_1^3(R_1 + \alpha_1)A_2}$ $A_{1,2} = R_{1,2}^2 + \alpha_{1,2} R_{1,2} - \beta_{1,2}$	
3	<p>Laminar flow in an inclined duct</p> $Q = \frac{\rho g \sin \alpha}{\mu} h \left(\alpha h + \beta + \frac{h^2}{3} \right),$ $\tau(y) = \rho g h \sin \alpha \left(1 - \frac{y}{h} \right),$	
4	<p>Poiseuille flow between parallel plates</p> $Q = \frac{2}{3} \frac{\Delta p h}{\mu L h_{12}} \begin{pmatrix} 2h^3 + 2h^2(\alpha_1 + \alpha_2) \\ +3h(\beta_1 + \beta_2 - 2\alpha_1 \alpha_2) \\ +3(\beta_1 \alpha_2 - \beta_2 \alpha_1) \end{pmatrix}$ $\tau(y) = \frac{\Delta p}{L h_{12}} (\beta_1 - \beta_2 - h(\alpha_1 + \alpha_2) - y h_{12}).$ $h_{12} = 2h - (\alpha_1 - \alpha_2)$	

(continued)

Table 1 (continued)

N	Expressions	Schemes
5	<p>Poiseuille flow in the circular tubes</p> $Q = \frac{\Delta p}{8\mu L} \pi R^2 (R^2 + 4(\beta - \alpha R)),$ $\tau(r) = \frac{\Delta p}{2L} r$	
6	<p>Poiseuille flow in the tubes of elliptic cross section</p> $Q = \frac{\pi a^3 b^3 \Delta p}{4\mu L (a^2 + b^2)} \left(1 + \frac{\beta - \alpha a}{a^2} + \frac{\beta - \alpha b}{b^2} \right),$ $\tau_{zx}(x) = \frac{\Delta p}{2\mu L} \frac{b^2}{a^2 + b^2} x, \quad \tau_{zy}(y) = \frac{\Delta p}{2\mu L} \frac{a^2}{a^2 + b^2} y$	
7	<p>Poiseuille flow in the annulus between two coaxial circular tubes</p> $Q = \frac{\pi \Delta p}{8\mu L} \left(2 \frac{(A_1 - A_2)(R_2^2 - R_1^2)}{R_1 R_2 \ln(R_2/R_1) + \alpha_1 R_2 + \alpha_2 R_1} + \frac{R_1 R_2}{2} A_3 (2R_2^2 \ln R_2 - 2R_1^2 \ln R_1 - R_2^2 + R_1^2) - (R_2^4 - R_1^4) \right),$ $\tau(r) = \frac{\Delta P}{4L} \left(A_5 \frac{R_1 R_2}{r} - 2r \right),$ $A_1 = R_1 (R_1^2 + 2\alpha_1 R_1 + 2\beta_1) (R_2 \ln R_2 - \alpha_2),$ $A_2 = R_2 (R_2^2 - 2\alpha_2 R_2 + 2\beta_2) (R_1 \ln R_1 + \alpha_1),$ $A_3 = \frac{R_2^2 - R_1^2 - 2(\alpha_1 R_1 + \alpha_2 R_2 + \beta_2 + \beta_1)}{R_1 R_2 \ln(R_2/R_1) + \alpha_1 R_2 + \alpha_2 R_1}.$	

$$T_s = \frac{2}{\text{Re Pr } Q} \left(J_w + \frac{Ec \text{ Pr}}{(1 + 2Kn)^2} \right). \quad (15)$$

Solution for the Poiseuille flow with different constant heat fluxes at the walls has been found by asymptotic methods [43]. An atomistic theory for the velocity slip and temperature jump BCs has been recently developed in [44].

3 Generalization of the Heat Transfer Law

It is well known, substitution of the Fourier heat Eq. (1) into the energy balance law gives the parabolic equation for the temperature [45]

$$\rho c_p \frac{dT}{dt} = -\text{div} \vec{J}_T + \sigma_T = \text{div}(k \nabla T) + \sigma_T, \quad (16)$$

where $\sigma_T(t, \vec{r})$ is the distributed heat sources.

The parabolic Eq. (16) predicts that thermal signals propagate with infinite speed that is not valid for thermal waves as it was had first been noted by Nernst (1917). Based on the kinetic theory developed in the works by J. C. Maxwell, the Maxwell–Cattaneo equation had been derived [46] to introduce the finite speed of the thermal waves

$$\left[I + \tau_{rel} \frac{\partial}{\partial t} \right] \vec{J} = -k \nabla T, \quad (17)$$

where τ_{rel} is the relaxation time and I is the unit operator.

Substitution of (17) into the energy balance law instead of (1) gives the hyperbolic equation for temperature in the form

$$\tau_{rel} \frac{\partial^2 T}{\partial t^2} + \frac{\partial T}{\partial t} = \vartheta \Delta T + \frac{1}{\rho c_p} \left(\sigma_T + \tau_{rel} \frac{\partial \sigma_T}{\partial t} \right), \quad (18)$$

where $\vartheta = k/\rho c_p$ is the thermal diffusivity.

Hyperbolic Eq. (18) describes the heat waves propagated at the speed $c = \sqrt{\vartheta/\tau_{rel}}$. The generalized Guyer–Krumhansl law formulation includes not only the relaxation time but also space derivatives of the hear flux in the form [47]

$$\tau_{rel} \frac{\partial \vec{J}_T}{\partial t} + \vec{J}_T = -k \nabla T + \kappa \nabla^2 \vec{J}_T, \quad (19)$$

where $\kappa = l^2$, l is the characteristic length scale.

Then the temperature balance Eq. (18) can be re-written as

$$\tau_{rel} \frac{\partial^2 T}{\partial t^2} + \frac{\partial T}{\partial t} - \kappa \frac{\partial}{\partial t} \Delta T = \vartheta \Delta T + \frac{1}{\rho c_p} \left(\sigma_T + \tau_{rel} \frac{\partial \sigma_T}{\partial t} - \kappa \Delta \sigma_T \right). \quad (20)$$

When the heat propagation at the nanoscale is considered ($\kappa \ll |\vec{J}_T|/|\nabla^2 \vec{J}_T|$) (19) can be reduced to the Poiseuille-type law of phonon hydrodynamics [48]

$$\Delta \vec{J}_T = \frac{k}{\kappa} \nabla T, \quad (21)$$

where \vec{J}_T , T , and κ/k are equivalent to the \vec{v} , p , μ_f in the Poiseuille flow.

The generalized Eq. (20) describes the heat waves propagated at different speeds exhibiting wave dispersion (e.g., frequency-dependent properties). In the case of 1D heat transfer problem along axis $0x$, the solution of (20) can be found in the form of the heat waves [45, 48]

$$T(t, x) = T * e^{i\omega(t-x/c)}, \quad (22)$$

where $T*$ is the wave amplitude and $m = \omega/c$ is the wave number. In the absence of the heat sources substitution of (22) into (20) gives for the wave speed c , phase speed v_p , and the wave attenuation length L_a the following expressions

$$c^2 = \frac{\vartheta + i\kappa\omega}{\tau\omega - i}\omega, v_p = \frac{\omega}{\text{Re}(m)} = \sqrt{\frac{(\vartheta^2 + \kappa^2\omega^2)\omega}{\tau^2\kappa^2\omega^4 + (\tau^2\vartheta^2 + \kappa^2)\omega^2 + \vartheta^2}} \cos^{-1}(\psi/2),$$

$$L_a = (\text{Im}(m))^{-1} = \sqrt{\frac{\vartheta^2 + \kappa^2\omega^2}{(\tau^2\kappa^2\omega^4 + (\tau^2\vartheta^2 + \kappa^2)\omega^2 + \vartheta^2)\omega}} \sin^{-1}(\psi/2), \quad (23)$$

where $\psi = a \tan\left(\frac{\vartheta + \tau\kappa\omega^2}{\kappa - \tau\vartheta}\right)$.

At $\kappa = 0$ and small frequency approximation $\omega\tau_{rel} \ll 1$, (23) gives the expressions $v_p = \sqrt{2k\omega}$, $L_a = \sqrt{2k/\omega}$ predicted by classical Fourier heat transfer law. When the internal heat sources $\sigma_T \neq 0$, solution of the non-uniform Eq. (20) must be added in (20) (forced heat transfer). This term is very important in biological systems [43] and at the heat (infrared) exposition, chemical reactions with heat effect, and radiate heat transfer.

4 Generalization of the Rheological Law

Laminar and turbulent flows of Newtonian fluids can be modeled based on the Navier–Stokes equations for compressible and incompressible fluids and their modifications, Reynolds-averaged equations, etc. The generalized velocity slip and temperature jump BCs allow more accurate estimations of the viscous and thermal effects at slow (steady and low Re number) flows and relatively large scales ($\kappa \sim 0$). Correct estimations of the coupled thermomechanical phenomena at the micro/nanoscales can be carried out when the more general physical laws are accounted for. The nonlinear relationships between the shear stress ($\hat{\tau}$) and strain rate (\hat{v}) tensors with fast phenomena at small scales can be described by the momentum balance law

$$\rho \frac{d\vec{v}}{dt} = -\nabla p + \text{div}(\hat{\tau}) \quad (24)$$

and the generalized rheological law

$$\tau' \frac{\partial \hat{\tau}}{\partial t} + \hat{\tau} = 2\mu \left(\hat{v} + \tau'' \frac{\partial \hat{v}}{\partial t} \right) + \tilde{\mu} \hat{v}^2, \quad (25)$$

where τ' , τ'' are the stress relaxation and retardation times, $\tilde{\mu}$ is the transverse viscosity.

Substitution (25) into (24) gives the momentum equation for the non-Newtonian fluid with transverse viscosity

$$\begin{aligned} \rho \left[I + \tau' \frac{\partial}{\partial t} \right] \frac{\partial \vec{v}}{\partial t} + \rho \left[I + \tau' \frac{\partial}{\partial t} \right] (\vec{v} \cdot \nabla) \vec{v} \\ = - \left[I + \tau' \frac{\partial}{\partial t} \right] \nabla p + \mu \left[I + \tau'' \frac{\partial}{\partial t} \right] \Delta \vec{v} + \tilde{\mu} \text{div}(\hat{v}^2). \end{aligned} \quad (26)$$

Equation (26) and the incompressibility condition

$$\frac{\partial \rho}{\partial t} + \text{div}(\rho \vec{v}) = 0 \quad (27)$$

where $\rho = \rho(p)$ present the system of two partial differential equations (PDE) for $\{\vec{v}(t, \vec{r}), p(t, \vec{r})\}$.

The systems (26), (27) has also solution in the form of the pressure and flow waves (small excitations). For instance, in the 1D case

$$v(t, x) = v^* e^{i\omega(t-x/c)}, \quad p(t, x) = p^* e^{i\omega(t-x/c)}, \quad (28)$$

where v^* , p^* are the velocity and pressure amplitudes.

Substitution of (28) into the system (26), (27) linearized around the steady point $(p, v) = (p_0, 0)$, $p_0 = \text{const}$, gives the following algebraic system for the amplitudes

$$\begin{vmatrix} \rho(i\omega - \omega^2\tau') + \mu(1 + i\omega\tau'')\frac{\omega^2}{c^2} - \frac{i\omega}{c}(1 + i\omega\tau') & \\ -\rho\frac{\omega}{c} & \frac{\Theta}{p_0}\omega \end{vmatrix} \begin{pmatrix} v^* \\ p^* \end{pmatrix} = \begin{pmatrix} 0 \\ 0 \end{pmatrix}. \quad (29)$$

where $\Theta = p_0 \partial \rho / \partial p|_{p=p_0}$ is the compressibility of the medium.

The compatibility condition for the matrix (29) gives the dispersion relationship for the wave speed

$$c^2 = \frac{(1 + i\omega\tau'')\Theta\mu\omega - i\rho p_0(1 + i\omega\tau')}{\rho(\omega\tau' - i)\Theta}. \quad (30)$$

The phase speed v_p and the wave attenuation length L_a in this case are

$$v_a = \Xi^{-1} \cos^{-1}(\psi/2), \quad L_a = \Xi^{-1} \omega^{-1} \sin^{-1}(\psi/2), \quad (31)$$

where $\Xi = \sqrt{\frac{(\rho\Theta\omega\tau' B_1 + B_2)^2 + \rho^2\Theta^2(B_1 + \omega\tau' B_2)^2}{B_1^2 + B_2^2}}$, $\psi = -a \tan\left(\frac{B_1 + \omega\tau' B_2}{\rho\Theta\omega\tau' B_1 + B_2} \rho\Theta\right)$, $B_1 = \mu\Theta\omega + \rho p_0\omega\tau'$, $B_2 = \omega^2\tau''\Theta - \rho p_0$.

The coupled heat and mass transfer problems in the micro/nanosystems must be considered based on the systems (20), (26), (27) with BC (12), (13), or (7)–(10) and (11). The flow stability problems can be studied based on the steady flow solutions (14) or (15) in the non-isothermal case or based on the solutions listed in Table 1 for the isothermal case. Then the corresponding PDE system (20), (26), (27) must be linearized around the corresponding steady solution (Table 1 or (14), (15)) with the small excitations (22), (28).

5 Generalization of the Diffusion Law

In the same way, the Fick's diffusion law (2) can be generalized to the case of the fast transfer at the micro/nanoscale in the form of the unsteady Fick's law

$$\tau_{rel} \frac{\partial \vec{J}_D}{\partial t} + \vec{J}_D = -D\nabla C + \kappa\nabla^2 \vec{J}_D \quad (32)$$

Since substitution of (2) into the mass balance equation gives the second Fick's law presented by the parabolic equation

$$\frac{\partial C}{\partial t} = D\Delta C \quad (33)$$

that cannot describe the concentration waves presented in the chemical reactions and long-range signaling in plants [49]. Substitution (32) instead (2) gives the generalized diffusion equation

$$\tau_{rel} \frac{\partial^2 C}{\partial t^2} + \frac{\partial C}{\partial t} - \kappa \frac{\partial}{\partial t} \Delta C = D\Delta C \quad (34)$$

that describes the concentration waves with speed $c = \sqrt{D/\tau_{rel}}$.

Solution of (34) can also be found as running waves. For instance, in the 1D case substitution $C(t, x) = C * e^{i\omega(t-x/c)}$ into (34) gives the dispersion relationship for the wave speed, the phase speed v_p , and the wave attenuation length L_a in the form

$$c = \omega \sqrt{\frac{(D\tau_{rel} - \kappa)^2 \omega^2 + (D + \tau_{rel}\kappa\omega^2)^2}{(\tau_{rel}^2 \omega^2 + 1)}},$$

$$v_p = \sqrt{P\omega} \cos^{-1}(\psi/2), \quad L_a = \sqrt{\frac{P}{\omega}} \sin^{-1}(\psi/2), \quad (35)$$

where $\psi = a \tan\left(\frac{D+\omega^2\kappa\tau_{rel}}{\omega(\kappa-\tau_{rel}D)}\right)$ and $P = \frac{D^2+\omega^2\kappa^2}{(\omega^4\kappa^2\tau_{rel}^2+\omega^2(\tau_{rel}^2D^2-\kappa^2)+D^2)}$.

6 Further Generalizations

The fluid and gas flow through a porous medium composed by micro/nanoparticles, tubes, fibers, crystals, fullerenes, and other small-scale elements must be described by a generalized unsteady Darcy law with Brinkman term for fluid percolation in porous materials

$$\tau_{rel} \frac{\partial \vec{J}_m}{\partial t} + \vec{J}_m = -\frac{K\rho_f}{\mu_f} \nabla p + \kappa \nabla^2 \vec{J}_m. \tag{36}$$

instead the classical Darcy law (3) [] that produces more detailed relationship between the flow velocity and hydrostatic pressure.

Substitution of (3) into the continuity condition (27) gives the elliptic equation for

$$\tau \frac{\partial \vec{v}}{\partial t} + \vec{v} - \kappa \frac{\partial}{\partial t} \Delta \vec{v} = -\frac{K}{\mu} (\nabla p - \gamma), \tag{37}$$

where γ is the threshold pressure gradient.

Electric phenomena in the micro/nanowires, ribbons, and tubes can be described by the generalized unsteady Ohm’s law for electric charge \vec{J}_e

$$\tau \frac{\partial \vec{J}_e}{\partial t} + \vec{J}_e = -\rho_e \nabla \varphi_e + \kappa \nabla^2 \vec{J}_e. \tag{38}$$

Substitution of (38) instead of (4) into the electric charge balance law

$$\frac{\partial \rho_e}{\partial t} + \text{div} \vec{J}_e = 0$$

gives the resulting electric charge balance equation at the micro/nanoscale

$$\tau_{rel} \frac{\partial^2 \rho_e}{\partial t^2} + \frac{\partial \rho_e}{\partial t} - \kappa \Delta \frac{\partial \rho_e}{\partial t} + \rho_e \Delta \varphi_e + \nabla \rho_e \nabla \varphi_e = 0 \tag{39}$$

That must be solved together with Maxwell equations.

The modified Eq. (37) and (39) have solutions in the form of running waves. The coupled problems of heat transfer in the convective, diffusive, percolation flows with electromagnetic phenomena can be solved based on the corresponding generalized equations with modified BC accounted for the diffusive scatter of the micro/nanoparticles at the wall roughness.

7 Conclusions

Classical physical laws at the macroscale at the thermodynamic equilibrium conditions are presented by linear dependencies between the corresponding fluxes and thermodynamic forces. At the micro/nanoscale, the high gradient space derivatives and time derivatives of the fluxes become prevalent and must be accounted for in the general mass, momentum, energy, and electric charge balance laws. That changes the type of the corresponding PDE from parabolic to hyperbolic and, therefore, allows propagation of the heat, concentration, charge and hydrodynamic waves, and their interconnections in the coupled thermomechano-electric processes. A brief review of the generalized Fourier, Fick, Darcy, Ohm, and rheological law is presented. The corresponding modified systems of PDE are derived. Solutions of the obtained system in the form of the running waves (small excitations) are presented for the 1D case. The generalized BCs at the micro/nanoscales include the first/second-order velocity slip and temperature jump due to diffusive scatter of the particles at the wall roughness. This conclusion is confirmed by numerous experiments with micro/nanofluid flows in the miniature ducts/tubes or over the micro/nanoparticles.

Analytical solutions for the Poiseuille flows of Newtonian fluids through circular, elliptic, rectangle, and open channels with velocity slip BC for both isothermal and non-isothermal walls are presented. Those solutions can be used as steady case state for further investigation of the stability of coupled heat and mass transfer in the convective, diffusive, and percolation flows with/without electric phenomena as well as fluid–structure interaction at the micro/nanoscales.

References

1. Petersen NO (2017) Foundations for nanoscience and nanotechnology. CRC Press
2. Cherevko V, Kizilova N (2017) Complex flows of micro/nanofluids with velocity slip boundary conditions, In: Fesenko O, Yatsenko L (eds) Nanophysics, nanomaterials, interface studies, and applications, vol 183. Springer Proceedings in Physics, pp 207–230
3. Karniadakis GE, Beskok A, Aluru N (2005) Microflows and nanoflows: fundamentals and simulation. *Interdisc Appl Math Ser* 29:51–77
4. Islam N (ed) (2012) MEMS microfluidics for lab-on-a-chip applications, microelectromechanical systems and devices. InTech
5. Mala GM, Li DQ (1999) Flow characteristics of water in microchannels. *Int J Heat Fluid Flow* 20:142–148
6. Tang GH, Li Z, He YL, Tao WQ (2007) Experimental study of compressibility, roughness and rarefaction influences on microchannel flow. *Intern, J Heat Mass Transfer* 50:2282–2295
7. Peng XF, Peterson GP, Wang BX (1994) Frictional flow characteristics of water flowing through rectangular channels. *Exp Heat Transfer* 7:249–264
8. Papautsky I, Gale BK, Mohanty S, Ameal TA, Frazier AB (1999) Effects of rectangular microchannel aspect ratio on laminar friction constant. In: Proceedings of the society of photo-optical instrumentation engineers (SPIE), vol 3877, pp 147–158
9. Qu WL, Mala GM, Li DQ (2000) Pressure-driven water flows in trapezoidal silicon microchannels. *Int J Heat Mass Transfer* 43:353–364

10. Wang H, Wang Y (2007) Influence of three-dimensional wall roughness on the laminar flow in microtube. *Intern J Heat Fluid Flow* 28:220–228
11. Kleinstreuer C, Koo L (2004) Computational analysis of wall roughness effects for liquid flow in micro-conduits. *J Fluids Eng* 126:1–9
12. Wu PY, Little WA (1983) Measurement of the friction factors for the flow of gases in very fine channels used for microminiature Joule-Thomson refrigerators. *Cryogenics* 23:273–277
13. Zhang W-M, Meng G, Wei X (2012) A review on slip models for gas microflows. *Microfluid Nanofluid* 13:845–882
14. Urbanek W, Zemel JN, Bau H (1993) An investigation of the temperature dependence of Poiseuille numbers in microchannel flow. *J Micromech Microeng* 3:206–208
15. Gad-el-Hak M (2006) MEMS Introduction and fundamentals. *The MEMS Handbook* (2nd ed). Taylor & Francis Group, LLC
16. Cattaneo C (1948) Sulla conduzione del calore, *Atti del Seminario Matematico e Fisico dell'Universita di Modena* 3:83–101
17. Vernotte P (1958), Les paradoxes de la théorie continue de l'équation de la chaleur, *Comptes rendus hebdomadaires des séances de l'Académie des Sci* 46:3154–3155
18. Tzou DY (1995) A unified field approach for heat conduction from macro- to microscales. *J Heat Transfer* 117:8–16
19. Tzou DY (1997) *Macro- to microscale heat transfer: the lagging behavior*. Taylor and Francis, New York
20. Pushenko V, Klepikov V, Brjukhovetski V, Kizilova N, Litvinenko V (2017) A multiscale rheological model of superelastic metal alloys: from nano to macro scale, 59th Ilmenay scientific colloquium engineering for a changing world. Technische University, Ilmenau Germany, pp 100–110
21. Baranets V, Kizilova N (2019) On hyperbolicity and solution properties of the continual models of micro/nanoparticle aggregation and sedimentation in concentrated suspensions. *Visnyk of Kyiv National Univ, Ser Phys Math* 4:60–64
22. Batyuk L, Kizilova N (2019) Magnetohydrodynamic flows of micro/nano fluids through thin capillaries. *Visnyk of Kyiv National Univ, Ser Phys Math* 3:32–36
23. Hamadiche M, Kizilova N (2013) Pulsatile flows in distensible tubes: a membrane model with fluid-structure interaction. In: *Shell and membrane theories in mechanics and biology: from macro- to nanoscale structures*. Belarusian State University, Minsk, pp 139–142
24. Batyuk LV, Kizilova NN, Berest VP (2017) Investigation of antiradiation and anticancer efficiency of nanodiamonds on rat erythrocytes. In: *IEEE 7th International conference nanomaterials: application and properties*. Odessa, 04NB23
25. Batyuk L, Kizilova N (2020) Protective action of nanodiamonds against influence of ionizing radiation in rats. *Acta Sci Cancer Biol* 4:01–05
26. Maxwell JC (1879) On stresses in rarefied gases arising from inequalities of temperature. *Phil Trans R Soc London* 170:231–256
27. Smoluchowski MS (1898) Ueber waermeleitung in verduennten gasen. *Ann Phys* 300:101–130
28. Kennard EH (1954) *Kinetic theory of gases*. McGraw-Hill
29. Karniadakis GE, Beskok A (2002) *Microflows: fundamentals and simulation*
30. Shu J-J, Teo JBM, Chan WK (2016) A new model for fluid velocity slip on a solid surface. *Soft Matter* 12:8388–8397
31. Shu J-J, Teo JBM, Chan WK (2016) A new model for temperature jump at a fluid-solid interface. *PLoS ONE* 11:e0165175
32. Neto C, Evans DR, Bonaccorso E, Butt H-J, Craig VJS (2005) Boundary slip in Newtonian liquids: a review of experimental studies. *Rep Prog Phys* 68:2859–2897
33. Beavers GS, Joseph DD (1967) Boundary conditions at a naturally permeable wall. *J Fluid Mech* 30:197–207
34. Christodoulou KN, Scriven LE (1992) The fluid mechanics of slide coating. *J Fluid Mech* 99:39–55
35. Bechert DW, Bruse M, Hage W, Meyer R (2004) Fluid mechanics of biological surfaces and their technological application. *Naturwissenschaften* 87:157–171

36. Denn MM (1990) Issues in viscoelastic fluid mechanics. *Annu Rev Fluid Mech* 22:13–34
37. Mohammadi B, Pironneau O (1974) Analysis of the k - ϵ turbulence model. Wiley
38. Crowdy DG (2021) Slip length formulas for longitudinal shear flow over a superhydrophobic grating with partially filled cavities. *J Fluid Mech* 925:R2
39. Aminpour M, Torres SAG, Scheuermann A, Li L (2021) Slip-flow regimes in nanofluidics: a universal superexponential model. *Phys Rev Appl* 15:054051
40. Urbanek W, Zemel JN, Bau H (1993) An investigation of the temperature dependence of Poiseuille numbers in microchannel flow. *J Micromech Micro-Eng* 3:206–208
41. Aydın O, Avcı M (2007) Analysis of laminar heat transfer in micro-Poiseuille flow. *Intern J Thermal Sci* 46:30–37
42. Rostami AA, Mujumdar AS, Saniei N (2002) Flow and heat transfer for gas flowing in microchannels: a review. *Heat Mass Transf* 38:359–367
43. Kizilova N, Korobov A (2019) Bioheat equation with fourier and non-fourier heat transport laws: applicability to heat transfer in human tissues. *J Thermal Eng* 5:149–161
44. Hadjiconstantinou NG (2021) An atomistic model for the Navier slip condition. *J Fluid Mech* 912:A26
45. Joseph DD, Preziosi L (1989) Heat waves. *Rev Mod Phys* 61:41
46. Cattaneo C (1948) Sulla conduzione de calore, *Atti del Semin. Mat e Fis Univ Modena* 3:3
47. Yang CC, Mai Y-W (2014) Thermodynamics at the nanoscale. *Mat Sci Engin* 79:1–40
48. Jou D, Casas-Vázquez J, Lebon G (2001) Extended irreversible thermodynamics. Springer
49. Kizilova N (2007) Long-distance liquid transport in plants. *Proc Estonian Acad Sci Ser Phys Math* 57:179–203

Investigation of Long-Term Oxidation Resistance of Titanium Alloys with a Coating Based on Ti–Al–C System Nanocomposites



Viktoriya Podhurska, Tetiana Prikhna, Orest Ostash, Bogdan Vasylyv, Yuriy Holovatyuk, Volodymyr Sverdun, Tetiana Serbeniuk, Oleksandr Kuprin, and Margarita Bortnitskaya

Abstract Physical and mechanical properties of thin sheets (0.5 mm) of titanium grades VT1-0 and OT4-1 in the operating conditions of intermedium-temperature fuel cell were compared. It is established that the heat and oxidation resistance of the OT4-1 alloy was dominated by titanium VT1-0, which allows it to be considered as a promising substrate material for the manufacture of thin interconnects of solid oxide fuel cell. The oxidation resistance of Ti–Al–C coatings obtained by magnetron deposition under different modes has been studied. The 2.5 μm thick coating obtained by the method of magnetron deposition having the Young's modulus close to the OT4-1 alloy substrate can be considered promising for this purpose.

1 Introduction

Nowadays, solid oxide fuel cell (SOFC) interconnects are traditionally made of sheets (0.3...0.5 mm thick) of Crofer steels, which contain 20...24% Cr [1]. However, it is known that due to the diffusion of chromium from the interconnect to the cathode, functional properties of the interconnect deteriorate. Due to oxidation, the surface electrical conductivity of such interconnects is lost. This requires the creation of special coatings on their surface [2]. In addition, the high density of Crofer steels ($\gamma \sim 8 \text{ g/cm}^3$) causes a significant weight of a SOFC.

V. Podhurska (✉) · O. Ostash · B. Vasylyv · Y. Holovatyuk
Department of Hydrogen Technologies and Alternative Energy Materials, Karpenko
Physico-Mechanical Institute of the NAS of Ukraine, 5 Naukova Str., Lviv 79060, Ukraine
e-mail: podhurskavika@gmail.com

T. Prikhna · V. Sverdun · T. Serbeniuk
Department of Sintering Technologies of Ceramics, Institute for Superhard Materials of the NAS
of Ukraine, 2 Avtozavodska Str., Kyiv 04074, Ukraine

O. Kuprin · M. Bortnitskaya
Laboratory of Ion-Plasma Processing of Materials, National Science Center Kharkiv Institute of
Physics and Technology, 1 Akademicheskaya Str., Kharkiv 61108, Ukraine

An alternative to Crofer steels is composites based on the titanium MAX phases ($\gamma \sim 4.1 \dots 4.3 \text{ g/cm}^3$) [3–5], especially in the case of intermediate temperature (550–650 °C) SOFC. Here, the MAX phase of Ti_2AlC is preferred over the MAX phase of Ti_3AlC_2 . Oxidation resistance of Ti_3AlC_2 at 600 °C in contrast to Ti_2AlC is abnormally lowered due to the formation of TiO_2 oxide of the anatase type [6–8]. Higher oxidation resistance of Ti_2AlC is probably due to the ability of oxygen to penetrate the crystal lattice of Ti_2AlC , forming a solid solution of $\text{Ti}_2\text{Al}(\text{C}_{1-x}\text{O}_x)$ and inhibiting the formation of titanium and aluminum oxides in the near-surface layers [5, 9, 10]. However, like Crofer steels, during long-term exposure to air at 600 °C, the MAX samples of the Ti_3AlC_2 and Ti_2AlC phases lose their electrical conductivity [11–13].

Interconnects made of thin (0.2...0.5 mm) titanium sheets with coatings based on MAX phases of the Ti–Al–C system can be more efficient [14]. Behavior of coatings obtained by vacuum-arc deposition under conditions of long-term exposure to oxidizing media at 600 °C was studied in [15]. Here, a thin sheet of titanium grade VT1-0 was used as a substrate. It is known [16] that this material is not oxidation-resistant, so for the interconnects of fuel cells with an operating temperature of 550... 650 °C, it is necessary to change the substrate material. In this paper, the influence of technological parameters of coatings on their long-term oxidation resistance depending on the substrate material was investigated.

2 Materials and Methods

Mechanical characteristics σ_B (ultimate tensile strength) and $\sigma_{0.2}$ (yield strength) were determined on standard fivefold flat specimens 0.5 mm thick and 2 mm wide of the working part, in air at 20 °C and after heating to 600 °C.

Oxidation resistance tests of the material were performed during 4 stages. Each stage involved heating of a polished sample to 600 °C in air, holding for 250 h and cooling to room temperature. The weight gain of the sample Δm was measured on analytical scales of the brand Radwag-AS after each stage of the test with an accuracy of $\pm 0.1 \text{ mg}$. Oxidation resistance of the material was evaluated by the ratio $\Delta m/S$, where S is the initial surface area of the sample.

The Nano Indenter G200 system (Agilent Technologies, USA) equipped with a Berkovich diamond tip was used to determine the nanohardness H (10 mN) and the elastic modulus E of the coatings [17]. Ten indentations were made on each sample. The maximum load was 10 mN, for which the depth of indentation was approximately 200...300 nm.

Planar rectangle target based on Ti_2AlC MAX phase of $180 \times 90 \text{ mm}$ and 6 mm thick was used for the coatings deposition by DC magnetron sputtering. Preliminary evacuation of the setup was carried out until the vacuum in the chamber was at least 10^{-3} Pa . Ar was used as a working gas at a pressure of 2 Pa. The distance between the target and rotating substrates was 120 mm. A negative bias potential of 50 V was applied to the substrate. The deposition of coatings was carried out at different

power of the magnetron discharge. The discharge power was controlled by varying the discharge voltage 320 to 430 V.

Zeis EVO-40XVP scanning electron microscope was used for microstructural studies, where SEM EDX analysis of local content of alloying elements was also performed using INCA Energy 350 system.

3 Results and Discussion

In order to improve the oxidation resistance of SOFC interconnects, titanium alloy grade OT4-1, the properties of which were compared to those of titanium grade VT1-0, was chosen as a substrate material. The chemical composition of these materials is given in Table 1.

It is found that tensile strength and yield strength of OT4-1 alloy in the temperature range of 20...600 °C significantly exceed those of VT1-0 titanium. At the operating temperature of the fuel cell (600 °C), it meets the requirements for interconnect materials ($\sigma_{0.2} > 100$ MPa), in contrast to titanium grade VT1-0 (Fig. 1, Table 2).

In the previous stage of the work, the efficiency of vacuum-arc coating was substantiated. However, this method is technologically complex and of high-energy

Table 1 Chemical composition (wt.%) of the studied titanium alloys

Titanium grade	Ti	Al	Mn	C	Fe	Si	Zr
VT1-0	Balance	–	–	0.03	0.20	0.10	–
OT4-1	Balance	1.83	1.54	0.04	0.09	0.14	0.11

Fig. 1 Temperature dependence of strength characteristics of titanium grades VT1-0 and OT4-1

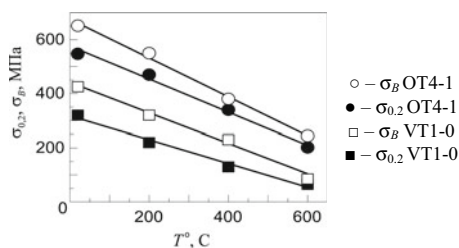


Table 2 Strength characteristics of titanium grades VT1-0 and OT4-1 at different temperatures

Titanium grade	$\sigma_{0.2}$, MPa		σ_B , MPa	
	20 °C	600 °C	20 °C	600 °C
OT4-1	547	202	652	244
VT1-0	320	65	425	85

consumption [14, 15]. To simplify the technology of coating the interconnects, the method of magnetron deposition in different modes was chosen (Table 3).

It was also found that the OT4-1 alloy is twice superior to titanium grade VT1-0 in long-term (based on 1000 h) oxidation resistance (Fig. 2), which for both alloys vary in parabolic dependence. Thus, according to the obtained results, a OT4-1 titanium alloy substrate with a coating resistant to high temperature oxidation can be used for the manufacture of thin-walled (0.5 mm) interconnects for intermediate temperature (550...650 °C) SOFC.

The study of oxidation resistance of coatings on OT4-1 titanium alloy substrate at 600 C on the basis of 1000 h has showed that the ones based on Ti–Al–C composite, formed by high-energy deposition (MAX-1) has the best oxidation resistance ($\Delta m/S = 0.22 \text{ mg/cm}^2$). Coatings formed by medium-energy magnetron deposition (MAX-2 and MAX-3) had oxidation resistance at the level of OT4-1 alloy, and oxidation resistance of the coating obtained by low-energy deposition (MAX-4) was intermediate (Fig. 2).

Table 3 Technological modes of coatings deposition

Sample No	Mode	P, W	t, min	δ , μm
MAX-1	HP+Mo	2800	90	9
MAX-2	MP	960	180	9.5
MAX-3	MP	930	120	4.8
MAX-4	LP	612	120	2.5

Comment HP+Mo: high power mode; LP: low power mode; MP: medium power mode; P is the power applied; t is the deposition time; δ is the thickness of the coating

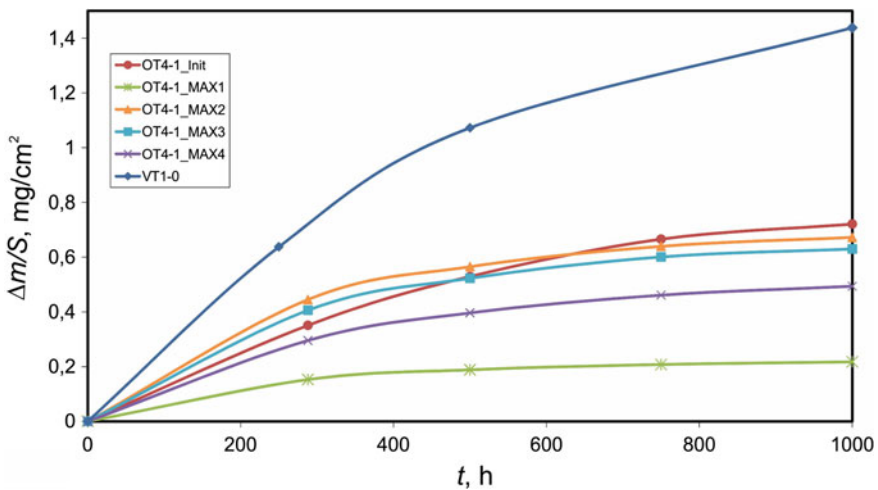


Fig. 2 Oxidation resistance of titanium grades VT1-0 and OT4-1 and coatings based on Ti–Al–C composite at 600 °C on the basis of 1000 h

Microstructural analysis showed that all coatings have a columnar structure with high adhesion to the substrate (Fig. 3).

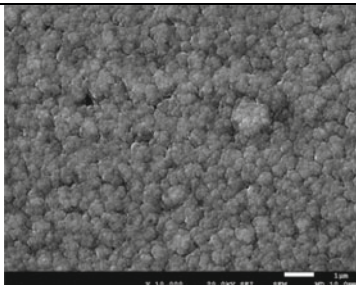
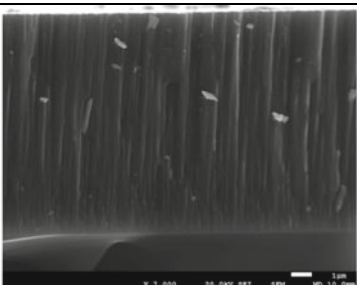
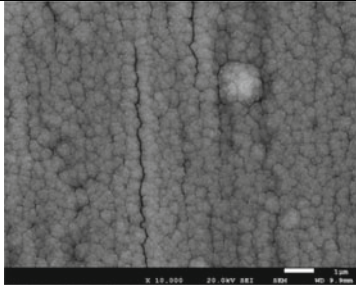
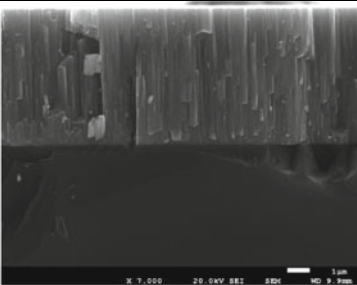
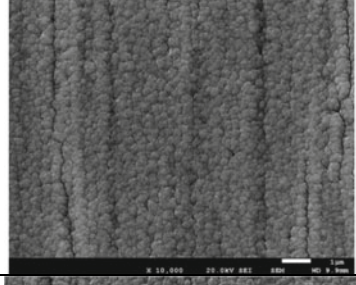
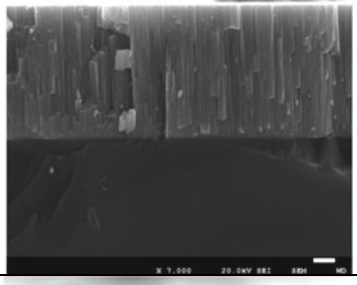
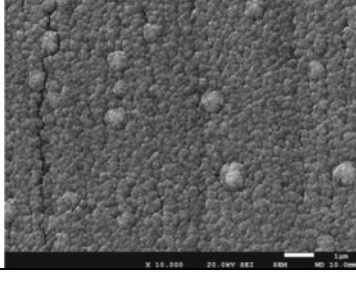
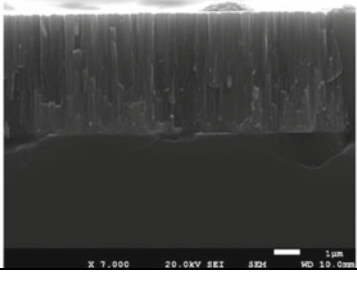
Sample No.	SEM microstructure	
	Surface	Cross section
MAX-1		
MAX-2		
MAX-3		
MAX-4		

Fig. 3 SEM microstructure on the surface and in the cross section of the coatings

Table 4 Influence of substrate material on chemical composition and mechanical properties of coatings based on MAX phases of titanium

Substrate material	Sample No	Chemical composition, at %			δ , μm	H, GPa	E, GPa
		Ti	Al	C			
OT4-1	MAX-1	45	22.7	32.3	9	15 ± 1	240 ± 10
OT4-1	MAX-2	46	22.1	31.9	9.5	11 ± 1	200 ± 10
OT4-1	MAX-3	53	20.1	26.9	4.8	10 ± 1	170 ± 10
OT4-1	MAX-4	57.6	22.2	20.2	2.5	9 ± 1	150 ± 10
VT1-0	MAX-5 [15]	51.7	21.8	26.5	6	$5, 5 \pm 1$	132 ± 10

In high-energy and long-term medium-energy deposition modes (MAX-1 and MAX-2), a coating thickness of $\sim 9 \mu\text{m}$ with high hardness and Young's modulus was obtained, but local microcracking zones were detected on the coating surface (Fig. 3, Table 4). With decreasing both power and deposition durations (MAX-3), the coating thickness decreased by half with some decrease in hardness, Young's modulus, and surface microcracking. With further reduction in power (MAX-4), the coating thickness became $2.5 \mu\text{m}$, nanohardness $H = 9 \text{ GPa}$, and Young's modulus $E = 150 \text{ GPa}$, which is closest to the characteristics determined for the titanium alloy OT4-1 substrate material ($H = 4.2 \text{ GPa}$; $E = 145 \text{ GPa}$). In this case, the proximity of the physical and mechanical characteristics of the coating material and the substrate determines the minimum surface microcracking of the sample MAX-4 (Fig. 3).

Local chemical analysis of the surfaces of coatings obtained in different technological modes (MAX-1... MAX-4) showed (Table 4) that their phase compositions present MAX phases of different structural type, obviously Ti_2AlC and Ti_3AlC_2 , which provide high conductivity of the coatings ($3 \dots 4 \cdot 10^5 \text{ Sm/m}$).

In addition, it should be noted that the characteristics of the material of the sample MAX-4 are close to those of a coating obtained earlier [15] by vacuum-arc deposition on a titanium substrate grade VT1-0 (Table 4), according to which a fuel cell interconnect material with high functional properties was obtained [15].

Thus, according to the obtained results, the $2.5 \mu\text{m}$ thick coating obtained by the method of magnetron deposition having Young's modulus close to that of the OT4-1 alloy substrate can be considered promising for fuel cell interconnects.

4 Conclusions

According to the obtained results, a OT4-1 titanium alloy substrate with a coating resistant to high temperature oxidation can be used for the manufacture of thin-walled (0.5 mm) interconnects for intermediate temperature fuel cells ($550 \dots 650 \text{ }^\circ\text{C}$). The $2.5 \mu\text{m}$ thick coating obtained by the method of magnetron deposition having

Young's modulus close to the OT4-1 alloy substrate can be considered promising for this purpose.

Acknowledgements The work was supported by the National Research Foundation of Ukraine under the grant №2020.02/0301 "Development of new functional materials for the needs of hydrogen energy".

References

1. Magdefrau, N.J.: Evaluation of solid oxide fuel cell interconnect coatings: reaction layer microstructure, chemistry and formation mechanisms. Doctoral dissertation. University of Connecticut, Mansfield, USA. 106 (2013)
2. Chu, C.L., Wand, J.Y., Lee, J., et al.: Evaluation on some metallic alloys for SOFC interconnect. *Mater. Sci. Forum.* 989–992 (2007)
3. Radovic M, Barsoum MW (2013) MAX phases: bridging the gap between metals and ceramics. *Am Ceram Soc Bull* 92(3):20–27
4. Zhao X, Sokol M, Barsoum MW et al (2021) Effect of grain orientation on the compressive response of highly oriented MAX phase Ti_3SiC_2 . *Mater Sci Eng A* 809:140869. <https://doi.org/10.1016/j.msea.2021.140869>
5. Zhang Z, Duan X, Jia D et al (2021) On the formation mechanisms and properties of MAX phases: a review. *J Eur Ceram Soc* 41(7):3851–3878. <https://doi.org/10.1016/j.jeurceramsoc.2021.02.002>
6. Prikhna, T., Ostash, O., Sverdun, V., Karpets, M., Zimych, T., Ivasyshyn, A., Cabioć'h, T., Chartier, P., Dub, S., Javorska, L., Podgurska, V., Figel, P., Cyboron, J., Moshchil, V., Kovylaev, V., Ponomaryov, S., Romaka, V., Serbenyuk, T., Starostina, A.: Presence of oxygen in Ti–Al–C MAX phases-based materials and their stability in oxidizing environment at elevated temperatures. *Acta. Physica. Polon. A.* **133**(4), 789–793 (2018)
7. Hanaor, D.A.H., Sorrel, C.S.: Review of the anatase to rutile phase transformation. *J. Mater. Sci.* **46**, 855–874 (2011)
8. Ivasyshyn, A., Ostash, O., Prikhna, T. et al.: Oxidation resistance of materials based on Ti_3AlC_2 nanolaminate at 600 °C in air. *Nanoscale Res. Lett.* **11**, 358 (2016). <https://doi.org/10.1186/s11671-016-1571-x>
9. Zhao H, Hu L, Li C et al (2021) Influence of metallic Cr addition on the phase structure and mechanical properties of plasma-sprayed Ti–Si–C coatings. *Ceram Int* 47(12):17570–17579. <https://doi.org/10.1016/j.ceramint.2021.03.075>
10. Tan Y, Xia Y, Teng Z et al (2021) Synthesis and enhanced mechanical properties of compositionally complex MAX phases. *J Eur Ceram Soc* 41(8):4658–4665. <https://doi.org/10.1016/j.jeurceramsoc.2021.03.027>
11. Yu D, Tan Y (2021) Oxidation behaviors of compositionally complex MAX phases in air. *Ceram Int* 47(21):30188–30193. <https://doi.org/10.1016/j.ceramint.2021.07.198>
12. Serbenyuk TB, Prikhna TO, Sverdun VB et al (2018) Effect of the additive of Y_2O_3 on the structure formation and properties of composite materials based on AlN–SiC. *J Superhard Mater.* 40(1):8–15. <https://doi.org/10.3103/S1063457618010021>
13. Kashkarov EB, Pushilina NS, Syrtanov MS et al (2021) Preceramic paper-derived $SiC_f/Ti_3Al(Si)C_2$ and SiC_f/Ti_3SiC_2 MAX-phase based laminates fabricated using spark plasma sintering. *Scr Mater* 194:113696. <https://doi.org/10.1016/j.scriptamat.2020.113696>
14. Ostash, O.P., Prikhna, T.O., Kuprin, O.S., Podhurska, V.Y., Sverdun, V.B., Vasylyv, B.D.: A production method of the thin interconnects for solid oxide fuel cells. UA patent 121831, (27 July 2020)

15. Prikhna T, Ostash O, Kuprin O, Podhurska V et al (2021) A new MAX phases-based electro-conductive coating for high-temperature oxidizing environment. *Compos Struct* 277:114649. <https://doi.org/10.1016/j.compstruct.2021.114649>
16. Trush, V., Luk'yanenko, A.: Kinetics of high-temperature interaction of titanium alloys with a carbon-containing gaseous medium. *Ukr. J. Mech. Eng. Mat. Sci.* **4**(1), 29–39 (2018)
17. Oliver W, Pharr G (2004) Measurement of hardness and elastic modulus by instrumented indentation: advances in understanding and refinements to methodology. *J Mater Res* 19(1):3–20

Analytical Solutions for N -Electron Interacting System Confined in Graph of Coupled Electrostatic Semiconductor and Superconducting Quantum Dots in Tight-Binding Model with Focus on Quantum Information Processing



Krzysztof Pomorski

Abstract Analytical solutions for a tight-binding model are presented for a position-based qubit and N interacting qubits realized by quasi-one-dimensional network of coupled quantum dots expressed by connected or disconnected graphs of any topology in 2 and 3 dimensions where one electron is presented at each separated graphs. Electron(s) quantum dynamic state is described under various electromagnetic circumstances with an omission spin degree-of-freedom. The action of Hadamard and phase rotating gate is given by analytical formulas derived and formulated for any case of physical field evolution preserving the occupancy of two-energy level system. The procedure for heating up and cooling down of the quantum state placed in position based qubit is described. The interaction of position-based qubit with electromagnetic cavity is described. In particular non-local communication between position based qubits is given. It opens the perspective of implementation of quantum internet among electrostatic CMOS quantum computers (quantum chips). The interface between superconducting Josephson junction and semiconductor position-based qubit implemented in coupled semiconductor q-dots is described such that it can be the base for electrostatic interface between superconducting and semiconductor quantum computer. Modification of Andreev Bound State in Josephson junction by the presence of semiconductor qubit in its proximity and electrostatic interaction with superconducting qubit is spotted by the minimalistic tight-binding model. The obtained results allow in creating interface between semiconductor quantum computer and superconducting quantum computer. They open the perspective

K. Pomorski (✉)

Faculty of Computer Science and Telecommunications, Cracow University of Technology,
Cracow, Poland

School Of Electrical And Electronic Engineering, University College Dublin, Dublin, Ireland

Quantum Hardware Systems, Lodz, Poland

e-mail: kdvpomorski@gmail.com

URL: <http://www.quantumhardwaresystems.com>

© The Author(s), under exclusive license to Springer Nature Switzerland AG 2023
O. Fesenko and L. Yatsenko (eds.), *Nanomaterials and Nanocomposites, Nanostructure Surfaces, and Their Applications*, Springer Proceedings in Physics 279,
https://doi.org/10.1007/978-3-031-18096-5_7

of construction of QISKIT like software that will describe both types of quantum computers as well as **their interface**.

Keywords N-body problem · Tight-binding · Semiconductor electrostatic position-based qubit · Wannier qubit · Semiconductor Wannier qubit interface with Josephson junction · Quantum gates · Quantum non-local communication · Electrostatic entanglement · Entanglement between matter and radiation

1 Introduction to Recent Trends in Q-Technologies

Quantum technology opens the gate for quantum computation and quantum sensing as well as quantum communication. Also in the nearest perspective one shall consider quantum Artificial Intelligence as extension of classical Artificial Intelligence. Because of high technical cost of implementation of quantum technologies one shall think about usage of both classical and quantum technologies at one chip what is possible in FD SOI CMOS technology that currently manufactures transistors with 3nm of channel length. The quantum mechanics offers the superposition of states and massive parallelism as well as non-local correlations that are non-present in classical world perceived by us. However these phenomena occurs only in special time scale and under specific thermodynamic conditions in the case of special geometries and confining potentials. Basically the quantum system needs to be maximally decoupled from the world to keep its unique quantum features. On the other hand we need to be able to interact with quantum system relatively quickly what brings the need for not so small interaction of qubit with classical or semiclassical interface via specific channels. At the same time we would expect the quantum technology to be highly reproducible in large scale, compact and having an easy interface with already existing technologies mostly working at room temperature. Basically ideal candidate for qubit does not exist and we have to make trade-off between certain technical parameters. The first option is to chose the system that is maximally decoupled from external world so we arrive to the idea of ion traps. We are placing atomic ions in almost ideal vacuum and we trap them by strong magnetic and electric fields. Maxwells equations does not allow for complicated topologies of EM confinement field affecting ion positions and thus we are limited to the case of ions on one line as it is indicated by many experimentalist. However every time we are about to use quantum ionic processor we need to cool down and set the ions in certain positions what makes structure to be practically not adjustable for large scales. However the decoherence times are more than promising since T_1 and T_2 time is in range of seconds what makes it bigger by 4 orders magnitude than any other quantum technology available so far. This makes ion trap to be excellent quantum sensors.

On the other hand we can think about use of electron or electron spin to represent the state of qubit. So far the electron is most successful carrier of classical information. Thus we need to use it on the level of qubit implementation in semiconductor or in superconductor. In the natural way we arrive to the electrostatic qubit in semicon-

ductor, where presence of single electron corresponds to logical $|1\rangle$ and its lack to $|0\rangle$ (Fujisawa [1], Petta [2]) or to superconducting Cooper pair box. However electron-electron interaction is quite strong as in comparison with spin to spin interaction. The strength of the interaction preimposes the decoherence time since the stronger is the interaction the smaller is the decoherence time. At the same time big quantum information density is usually leading to higher decoherence times since qubit-qubit interaction is more prominent.

Every qubit assemblies can be described by the following Hamiltonian operator:

$$\begin{aligned}
\hat{H}_I = & H_{|Q_0\rangle} + ((H_Q - H_{Q_0})_{|Q\setminus Q_0\rangle} + H_{|Q-Env\rangle} + H_{|Q-Q\rangle} + H_{|Env\rangle} = \\
& \sum_{l=1}^{N_{qbits}} (E_{e,l}(t)|e_l(t)\rangle\langle e_l(t)| + E_{g,l}(t)|g_l(t)\rangle\langle g_l(t)| + \\
& + T_{g\rightarrow e,l}(t)|e_l(t)\rangle\langle g_l(t)| + T_{e\rightarrow g,l}(t)|g_l(t)\rangle\langle e_l(t)|)_{|Q_0\rangle} \\
& + \sum_{l=1}^{N_{qbits}} \left(\sum_{s_{1l}=3}^{+\infty} (E_{s_{1l},l}(t)|s_{1l}(t)\rangle\langle s_{1l}(t)| + \sum_{s_{2l}=3, s_{2l}\neq s_{1l}}^{+\infty} T_{s_{1l}\rightarrow s_{2l},l}(t)|s_{1l}(t)\rangle\langle s_{2l}(t)|) + \right. \\
& + T_{e_{s_l}\rightarrow s_{3l},l}(t)|e_{s_l}(t)\rangle\langle s_{3l}(t)| + T_{s_{3l}\rightarrow e_{s_l},l}(t)|s_{3l}(t)\rangle\langle e(t)_{s_l}| + T_{g_{s_l}\rightarrow s_{3l},l}(t)|g_{s_l}(t)\rangle\langle s_{3l}(t)| + \\
& \left. + T_{s_{3l}\rightarrow g_{s_l},l}(t)|s_{3l}(t)\rangle\langle g(t)_{s_l}| \right)_{|Q\setminus Q_0\rangle} + \\
& + \left(\sum_{i=1}^{+\infty} \sum_{l=1}^{N_{qbits}} \sum_{s_{1l}=(g,e,\dots)}^{+\infty} \sum_{s_{2l}=(g,e,\dots)}^{+\infty} U_3(s_{1l}, s_{2l}, i, t) |s_{1l}(t), i(t)\rangle\langle s_{2l}(t), i(t)| \right)_{|Q-Env\rangle} + \\
& + \left(\sum_{l=1}^{N_{qbits}} \sum_{k=1, k\neq l}^{N_{qbits}} \sum_{s_{1k}=(g,e,\dots)}^{+\infty} \sum_{s_{2l}=(g,e,\dots)}^{+\infty} U_4(s_{1k}, s_{2l}, t) |s_{1k}(t), s_{2l}(t)\rangle\langle s_{1k}(t), s_{2l}(t)| \right)_{|Q-Q\rangle} + \\
& + \left(\sum_{i=1}^{+\infty} E_i(t) |i(t)\rangle\langle i(t)| \right)_{|Env\rangle}.
\end{aligned}$$

The given Hamiltonian is describing quantum system embedded in external environment (external world) and it has terms H_{Q_0} , $H_{Q\setminus Q_0}$, H_{Q-Env} , H_{Q-Q} , H_{Env} . In particular we have idealistic mathematical model of qubit that is isolated from external world and denoted by H_{Q_0} (blue color). Next Hamiltonian term $H_{Q\setminus Q_0}$ (green color) describes Hamiltonian setting qubit state and Hamiltonian term capable of qubit readout. However it is not surprising that Hamiltonian term responsible for qubit setting and reading can also contribute to its decoherence. The Hamiltonian terms describing the decoherence are due to qubit-qubit interaction and due to qubit-environment interaction (red and orange color). Usually we drop the last H_{env} term since we assume that environment has infinite size and has well-defined thermodynamical state that cannot be changed by the small size and finite quantum system Q that implements qubits. The value of E_e and E_g is determined by the qubit confinement potential, while functions $f_1(t)$ and $f_2(t)$ give us the ways to implement qubit setting mechanism and qubit reading mechanism by means of time-dependent Hamiltonians that are driven by external biasing circuit [qubit controlling circuit]. Formally we recognize that qubit assembly is the many body system with certain desired degrees of freedom (in general the available number of degrees of freedom

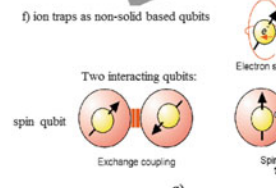
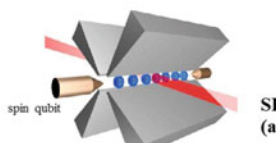
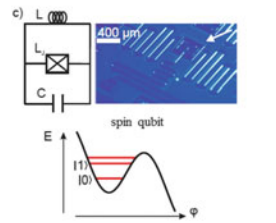
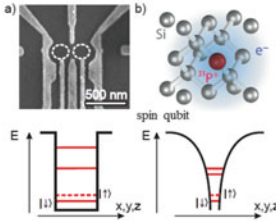
is much bigger than desired and it is a function of given quantum technology) that are controlled by given quantum technology placed in special thermodynamic conditions and given qubit implementation scheme. Study of the quantum system Q being assemble of interacting qubits embedded in external world denoted as environment is fundamental study and as much important for fundamental science as for technology.

Basically the thermodynamics is against preservation of information stored in qubit since entropy is increasing with time. The difference between energy levels of ground state (g) and excited state (e) is tiny and can be directly evaluated from Schrodinger equation. Once the excited level is occupied to certain extent it is in metastable state and tends to decay into ground state g . This decay time in case lack of external perturbations is shorter for the case of systems with bigger difference between excited and ground state. Because of this decay quantum state needs to be refreshed all the times to maintain its content (IBM Q-Experience provides superconducting Josephson junction qubits of $100 \mu s$ coherence time). The biggest danger to qubit coherence is energy of surrounding environment that is expressed especially by H_{env} last Hamiltonian term and by H_{env-Q} . Moderate decoherence to qubit state is by qubit-qubit interaction H_{Q-Q} that is potential factor limiting the maximum density of quantum logic.

Zoo of existing quantum technologies is growing. However still there exists two fundamental representation of q -information in spin of electron or Cooper pair and in electric charge as it is depicted in Fig. 1.

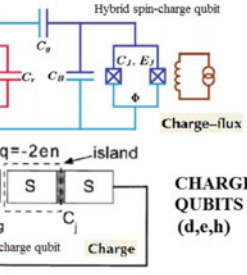
Currently there exist various paradigms for quantum computation. The most common is by the use of quasiparticle that is trapped in effective field that builds up the quantization of the energetic levels.

Paradigms existing currently assume that the quantum system shall be controlled either by electric or magnetic field factor or by combined magnetic and electric field that is generated by the controlling circuit. The good example are superconducting Cooper pair box (JJ-Josephson junction controlled by external capacitor), flux-qubit JJ (JJ controlled by external solenoid), phase JJ qubit (controlled by biasing electric current) and transmon qubit (controlled both by solenoid and capacitor). Indeed very recent progress was done very much up to electrical control of various types of technologies. The experiments conducted in 2003 by Fujisawa [1] have revealed significant charge noise problem and contributed to the change of the dominant paradigm in development of quantum circuits that was about shift from electric to magnetic field control and later electromagnetic control what is greatly expressed in superconducting technologies by common use of transmon superconducting qubit (and transmon like qubits: Xmon, etc.). The details are specified in the attached Table 1.

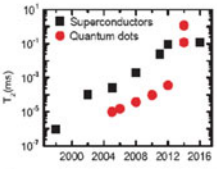
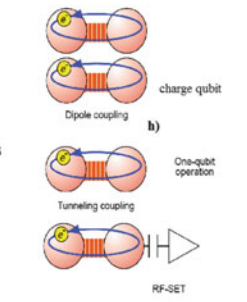


Universal picture on emerging quantum technologies in various solid state systems as basing on spin & charge qubits and hybrid

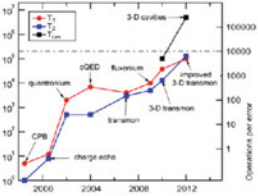
SPIN QUBITS (a, b, c, f, g)



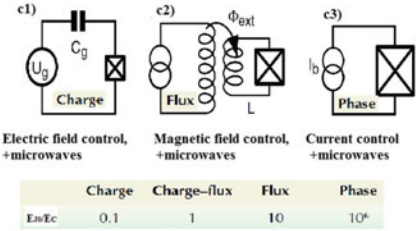
CHARGE QUBITS (d,e,h)



Phase decoherence time T_2



Two coherence times T_1 and T_2 in Josephson junction systems



Charging energy of one Cooper pair ($2e$): $E_C = (2e)^2/2C$

Inductive energy: $E_L = \hbar^2/(4e^2L)$

Josephson energy: $E_J = \hbar^2/(4e^2I_{J0})$

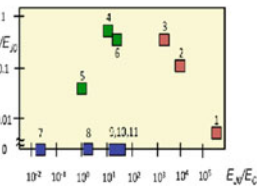
Resistance 'quantum': $R_Q = h/(2e)^2 \approx 1.027\ 059\ \text{k}\Omega$

Impedance: $Z \sim \sqrt{L_{J0}/C} = R_Q\sqrt{2}/\sqrt{E_{J0}/E_C}$

- Semiconductor qubits:**
1. Charge qubit
 2. Spin qubit
 3. Singlet-triplet qubit
 4. Exchange only qubit
 5. Resonant exchange qubit
- +superconductor-semiconductor qubit system and electrostatic interaction between charge-charge and sc-flux vs semiconductor charge or spin based qubits?????**

Superconducting qubits:

1. Phase qubit
2. Flux qubit
3. SQUID
4. Flux qubit
5. Fluxonium
6. C-shunt
7. Charge qubit
8. Quasitritium
9. Transmon
10. Xmon
11. Gatemon



◀**Fig. 1** Summary of quantum information technologies [Arxiv: 1801.06722] as in case of one- and two-qubit operations and single-shot measurement, for (a) and semiconductor spin qubit in a single quantum dot (b) [T. Fujisawa, NTT Technical Review, Vol. 1 No. 3, 2003], for a phase controlled Josephson junction qubit (c) polarized by external electric current, for a chargeflux or transmon superconducting qubit (d) polarized by both external magnetic and electric field, for a Cooper pair box Josephson junction qubit (e) as polarized by external electric field, for charged ions Pauli trap qubit as in (f) as with interactions given by (g) and a semiconductor charge qubit in a double quantum dot with interactions given in (h). One can encounter 3 main architectures of superconducting qubits as given in (c1), (c2), (c3) as corresponding to charge, flux and phase qubit.

Table 1 Quick overview on quantum technologies

Comparison of dominant quantum technologies			
Quantum technology [S-spin or C-charge like] qbits	Scalability	Coherence time T_1	Coherence time T_2
Ion traps [S]	Relatively low	$> 10^{10} \mu\text{s}$!	$> 10^6 \mu\text{s}$!
Semiconductor qubits	High	$\sim 1-10 \text{ ns}$	$\sim 1-10 \text{ ns}$
→ Charge qubit [C]	High	7 ns	250 ps
→ Spin qubit [S]	High	59 ns	59 ns
→ Spin singlet-triplet qubit [S]			
→ Spin exchange qubit [S]	High		19
→ Spin resonant exchange qbit [S]	High	0	19 μs
→ Spin-charge qbit [S-C qbit]	High		80 ns
Josephson junction qubits	Moderate	0.1–100 μs	0.1–100 μs
→ Cooper pair box [C]	Moderate	2 μs	2 μs
→ Flux qubit [S]	Moderate	4.6 μs	1.2 μs
→ Phase qubit	Moderate	0.5 μs	0.3 μs
→ 3D Transmon [S-C]	High	$> 100 \mu\text{s}$	$> 140 \mu\text{s}$
→ 2 D Transmon [S-C]	Moderate	50 μs	20 μs
→ Fluxm [S-C]	Moderate	1000 μs	$> 10 \mu\text{s}$
→ C-shunt [S-C]	Moderate	55 μs	40 μs
→ Xmon [S-C]	Moderate	50 μs	20 μs
→ Gatemon [S-C]	Moderate	5.3 μs	3.7 μs

2 Description of Position Based-Qubit in Tight-Binding Model

We refer to the physical situation from Fig. 2 and we consider position based-qubit in tight-binding model [3] and its the Hamiltonian of this system is given as

$$\begin{aligned}\hat{H}(t) &= \begin{pmatrix} E_{p1}(t) & t_{s12}(t) \\ t_{s12}^*(t) & E_{p2}(t) \end{pmatrix}_{[x=(x_1, x_2)]} \\ &= (E_1(t) |E_1\rangle_t \langle E_1|_t + E_2(t) |E_2\rangle \langle E_2|)_{[E=(E_1, E_2)]}.\end{aligned}\quad (1)$$

The Hamiltonian $\hat{H}(t)$ eigenenergies $E_1(t)$ and $E_2(t)$ with $E_2(t) > E_1(t)$ are given as

$$\begin{aligned}E_1(t) &= \left(-\sqrt{\frac{(E_{p1}(t) - E_{p2}(t))^2}{4} + |t_{s12}(t)|^2} + \frac{E_{p1}(t) + E_{p2}(t)}{2} \right), \\ E_2(t) &= \left(+\sqrt{\frac{(E_{p1}(t) - E_{p2}(t))^2}{4} + |t_{s12}(t)|^2} + \frac{E_{p1}(t) + E_{p2}(t)}{2} \right),\end{aligned}\quad (2)$$

and energy eigenstates $|E_1(t)\rangle$ and $|E_2(t)\rangle$ have the following form

$$\begin{aligned}|E_1, t\rangle &= \begin{pmatrix} \frac{(E_{p2}(t) - E_{p1}(t)) + \sqrt{\frac{(E_{p2}(t) - E_{p1}(t))^2}{4} + |t_{s12}(t)|^2}}{-it_{sr}(t) + t_{si}(t)} - 1 \end{pmatrix}, \\ |E_2, t\rangle &= \begin{pmatrix} \frac{-(E_{p2}(t) - E_{p1}(t)) + \sqrt{\frac{(E_{p2}(t) - E_{p1}(t))^2}{4} + |t_{s12}(t)|^2}}{t_{sr}(t) - it_{si}(t)} + 1 \end{pmatrix}.\end{aligned}\quad (3)$$

This Hamiltonian gives a description of two coupled quantum wells as depicted in Fig. 2. In such situation we have real-valued functions $E_{p1}(t)$, $E_{p2}(t)$ and complex-valued functions $t_{s12}(t) = t_s(t) = t_{sr}(t) + it_{si}(t)$ and $t_{s21}(t) = t_{s12}^*(t)$, what is equivalent to the knowledge of four real valued time-dependent continuous or discontinues functions $E_{p1}(t)$, $E_{p1}(2)$, $t_{sr}(t)$ and $t_{si}(t)$. The quantum state is a superposition of state localized at node 1 and 2 and therefore is given as

$$|\psi\rangle_{[x]} = \alpha(t) |1, 0\rangle_x + \beta(t) |0, 1\rangle_x = \alpha(t) \begin{pmatrix} 1 \\ 0 \end{pmatrix} + \beta(t) \begin{pmatrix} 0 \\ 1 \end{pmatrix}, \quad (4)$$

where $|\alpha(t)|^2$ ($|\beta(t)|^2$) is probability of finding particle at node 1(2) respectively, which brings $|\alpha(t)|^2 + |\beta(t)|^2 = 1$ and obviously $\langle 1, 0|_x || 1, 0\rangle_x = 1 = \langle 0, 1|_x || 0, 1\rangle_x$ and $\langle 1, 0|_x || 0, 1\rangle_x = 0 = \langle 0, 1|_x || 1, 0\rangle_x$. In Schrödinger formalism, states $|1, 0\rangle_x$ and $|0, 1\rangle_x$ are Wannier functions that are parameterized by position x . We work in tight-binding approximation and quantum state evolution with time as given by

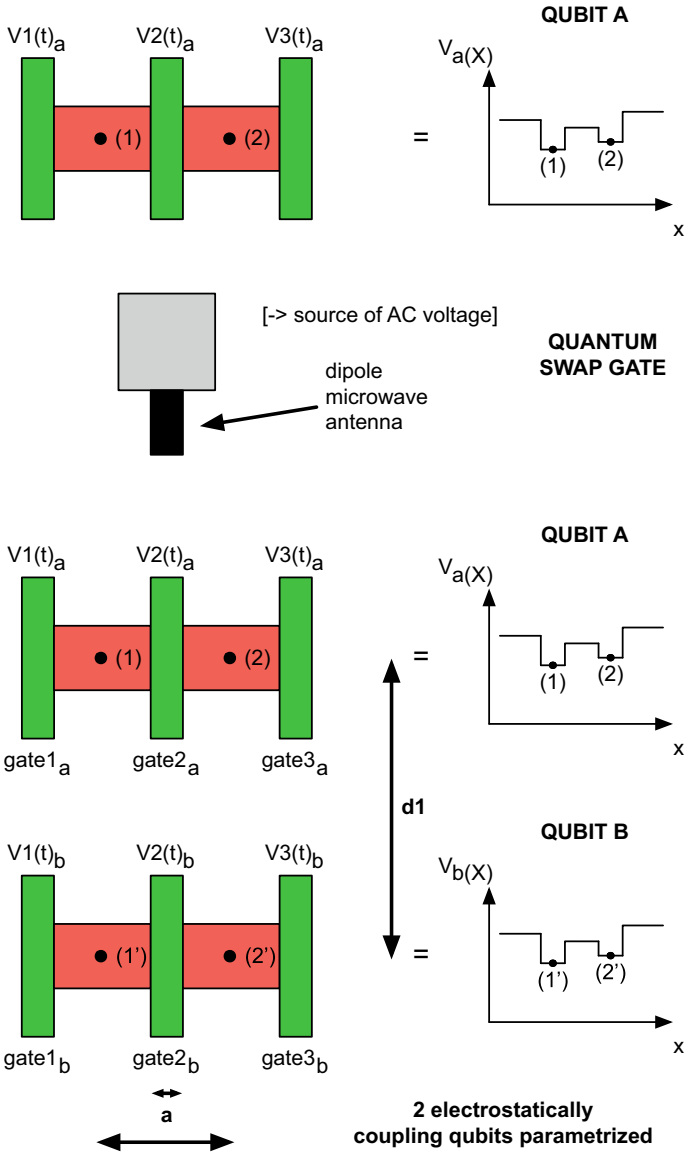


Fig. 2 [Left]: Electrostatic position-based qubit implemented in CMOS technology [4]. [Upper Left]: Simplistic representation by particle localized in two regions of space denoted by nodes (1) and (2); [Lower Left]: case of two electrostatically interacting qubits implementing quantum swap gate. Quantum dynamics are parameterized by presence of electrons at nodes 1, 2, 1' and 2'

$$i\hbar \frac{d}{dt} |\psi(t)\rangle = \hat{H}(t) |\psi(t)\rangle = E(t) |\psi(t)\rangle. \quad (5)$$

The last equation has an analytic solution

$$|\psi(t)\rangle = e^{\frac{1}{i\hbar} \int_0^t \hat{H}(t_1) dt_1} |\psi(t_0)\rangle = e^{\frac{1}{i\hbar} \int_0^t \hat{H}(t_1) dt_1} \begin{pmatrix} \alpha(0) \\ \beta(0) \end{pmatrix} \quad (6)$$

and in quantum density matrix theory we obtain

$$\begin{aligned} \hat{\rho}(t) &= \hat{\rho}^\dagger(t) = |\psi(t)\rangle \langle \psi(t)| = \\ &= \hat{U}(t, t_0) \hat{\rho}(t_0) \hat{U}^\dagger(t, t_0) = \\ &= e^{\frac{1}{i\hbar} \int_0^t \hat{H}(t_1) dt_1} (|\psi(t_0)\rangle \langle \psi(t_0)|) e^{-\frac{1}{i\hbar} \int_0^t \hat{H}(t_1) dt_1} = \\ &= e^{\frac{1}{i\hbar} \int_0^t \hat{H}(t_1) dt_1} \begin{pmatrix} \alpha(0) \\ \beta(0) \end{pmatrix} \begin{pmatrix} \alpha^*(0) & \beta^*(0) \end{pmatrix} e^{-\frac{1}{i\hbar} \int_0^t \hat{H}(t_1) dt_1} = \\ &= \hat{U}(t, t_0) \begin{pmatrix} |\alpha(0)|^2 & \alpha(0)\beta^*(0) \\ \beta(0)\alpha^*(0) & |\beta(0)|^2 \end{pmatrix} \hat{U}^\dagger(t, t_0)^\dagger. \end{aligned} \quad (7)$$

Having Hermitian matrix \hat{A} with real-valued coefficients $a_{11}(t)$, $a_{22}(t)$, $a_{12r}(t)$, $a_{12i}(t)$ and Pauli matrices $\sigma_1, \sigma_2, \sigma_3, \sigma_0 = \hat{I}_{2b \times 2}$ we observe that

$$\begin{aligned} \hat{A}_{2 \times 2} &= \begin{pmatrix} a_{11} & a_{12r} + ia_{12i} \\ a_{12r} - ia_{12i} & a_{22} \end{pmatrix}, = \\ &= a_{12r} \sigma_1 - a_{12i} \sigma_2 + \frac{1}{2}(a_{11} - a_{22}) \sigma_3 + \frac{1}{2}(a_{11} + a_{22}) \sigma_0. \end{aligned} \quad (8)$$

and for $\hat{A}_{2N \times 2N} = \sum_{k_1, k_2, \dots, k_N} b_{k_1, k_2, \dots, k_N} (\sigma_{k_1} \times \sigma_{k_2} \times \dots \times \sigma_{k_N})$ we obtain the unique matrix decomposition in terms of Pauli matrix tensor products, where $k_i = 0, \dots, 3$. Using the above property for matrix of size 2×2 we obtain $e^{\frac{1}{i\hbar} \int_0^t \hat{H}(t_1) dt_1} = \hat{U}(t, t_0)$, and assuming $E_{p1}(t) = E_{p2}(t) = E_p(t)$ and we are given matrix $e^{\frac{1}{i\hbar} \int_0^t \hat{H}(t_1) dt_1} =$

$$\begin{pmatrix} e^{-\frac{i \int_0^t E_p(t') dt'}{\hbar}} ch \left(\frac{\sqrt{-\int_0^t (|t_s(t')|^2) dt'}}{\hbar} \right) & \frac{e^{-\frac{i \int_0^t E_p(t') dt'}{\hbar}} \left(\int_0^t (t_s^*(t')) dt' \right) sh \left(\frac{\sqrt{-\int_0^t |t_s(t')|^2} dt'}{\hbar} \right)}{\sqrt{-\int_0^t ((t_{si}(t')^2 + t_{sr}(t')^2) dt')}}} \\ \frac{e^{-\frac{i \int_0^t E_p(t') dt'}{\hbar}} \left(\int_0^t (-t_s(t')) dt' \right) sh \left(\frac{\sqrt{-\int_0^t |t_s(t')|^2} dt'}{\hbar} \right)}{\sqrt{-\int_0^t ((t_{si}(t')^2 + t_{sr}(t')^2) dt')}}} & e^{-\frac{i \int_0^t E_p(t') dt'}{\hbar}} ch \left(\frac{\sqrt{-\int_0^t (|t_s(t')|^2) dt'}}{\hbar} \right) \end{pmatrix}, \quad (9)$$

where $sh(\cdot)$ and $ch(\cdot)$ are sinh and cosh hyperbolic functions, where $|t_s(t)|^2 = |t_{sr}(t)|^2 + |t_{si}(t)|^2$. This matrix is unitary so $\hat{U}^\dagger(t, t_0) = \hat{U}^{-1}(t, t_0)$. At the very end we will also consider more general case when $E_{p1}(t) \neq E_{p2}(t)$. At first let us con-

sider the case of two localized states in the left and right quantum well so there is no hopping which implies $t_s = 0$. In such case the evolution matrix $\hat{U}(t, t_0)$ is unitarian and has the following form

$$\hat{U}(t, t_0) = e^{\frac{1}{i\hbar} \int_{t_0}^t \hat{H}(t_1) dt_1} = \begin{pmatrix} e^{-i \int_{t_0}^t \frac{E_{p1}(t') dt'}{\hbar}} & 0 \\ 0 & e^{-i \int_{t_0}^t \frac{E_{p2}(t') dt'}{\hbar}} \end{pmatrix}, \quad (10)$$

what implies that left and right quantum dot are two disconnected physical systems subjected to its own evolution with time. However since one electron is distributed between those physical systems the measurement conducted on the left quantum dot will have its immediate effect on the right quantum dot. Another extreme example is the situation when hopping energy is considerably bigger than localization energy. In such case we set $E_{p1} = E_{p2} = 0$ and in case of non-zero hopping terms we obtain

$$\begin{aligned} \hat{U}(t, t_0) &= e^{\frac{1}{i\hbar} \int_{t_0}^t \hat{H}(t_1) dt_1} \\ &= \begin{pmatrix} ch \left(\frac{\sqrt{-\int_{t_0}^t (|t_s(t')|^2) dt'}{\hbar}} \right) & \frac{(\int_{t_0}^t (t_s^*(t')) dt') sh \left(\frac{\sqrt{-\int_{t_0}^t |t_s(t')|^2 dt'}}{\hbar}} \right)}{\sqrt{-\int_{t_0}^t ((t_{si}(t')^2 + t_{sr}(t')^2) dt')}} \\ \frac{(\int_{t_0}^t (-t_s(t')) dt') sh \left(\frac{\sqrt{-\int_{t_0}^t |t_s(t')|^2 dt'}}{\hbar}} \right)}{\sqrt{-\int_{t_0}^t ((t_{si}(t')^2 + t_{sr}(t')^2) dt')}} & ch \left(\frac{\sqrt{-\int_{t_0}^t (|t_s(t')|^2) dt'}{\hbar}} \right) \end{pmatrix}, \quad (11) \end{aligned}$$

Now it is time to move to most general situation of $E_{p1} \neq E_{p2}$, t_{sr} , $t_{si} \neq 0$. We have 4 elements of evolution matrix given as $\hat{U}(t, t_0) = e^{\frac{1}{i\hbar} \int_{t_0}^t \hat{H}(t_1) dt_1} = \begin{pmatrix} U(t, t_0)_{1,1} & U(t, t_0)_{1,2} \\ U(t, t_0)_{2,1} = U(t, t_0)_{1,2}^* & U(t, t_0)_{2,2} \end{pmatrix}$.

$$\begin{aligned} U(t, t_0)_{1,1} &= \frac{\exp \left[\frac{-\hbar^2 \left(\left| \int_{t_0}^t dt' (E_{p1}(t') - E_{p2}(t')) \right|^2 + 4 \left(\left| \int_{t_0}^t dt' t_{si}(t') \right|^2 + \left| \int_{t_0}^t dt' t_{sr}(t') \right|^2 \right) \right)}{2\hbar^2} + i\hbar \int_{t_0}^t dt' (E_{p1}(t') + E_{p2}(t')) \right]}{2\hbar \left(\left(\int_{t_0}^t dt' (E_{p1}(t') - E_{p2}(t')) \right)^2 + 4 \left(\left| \int_{t_0}^t dt' t_{si}(t') \right|^2 + \left| \int_{t_0}^t dt' t_{sr}(t') \right|^2 \right) \right)} \times \\ &\times \left[-i \int_{t_0}^t dt' E_{p1}(t') \right. \\ &\left. \sqrt{-\hbar^2 \left(\left| \int_{t_0}^t dt' (E_{p1}(t') - E_{p2}(t')) \right|^2 + 4 \left(\left| \int_{t_0}^t dt' t_{si}(t') \right|^2 + \left| \int_{t_0}^t dt' t_{sr}(t') \right|^2 \right) \right)} + \right. \\ &\left. + \hbar \left(\left| \int_{t_0}^t dt' (E_{p1}(t') - E_{p2}(t')) \right|^2 + 4 \left(\left| \int_{t_0}^t dt' t_{si}(t') \right|^2 + \left| \int_{t_0}^t dt' t_{sr}(t') \right|^2 \right) \right) \right] \times \end{aligned}$$

$$\sqrt{-\hbar^2 \left(\left| \int_{t_0}^t dt' (E_{p1}(t') - E_{p2}(t')) \right|^2 + 4 \left(\left| \int_{t_0}^t dt' t_{si}(t') \right|^2 + \left| \int_{t_0}^t dt' t_{sr}(t') \right|^2 \right) \right)} + \\ -i \left(\int_{t_0}^t dt' E_{p2}(t') \right) \sqrt{-\hbar^2 \left(\left| \int_{t_0}^t dt' (E_{p1}(t') - E_{p2}(t')) \right|^2 + 4 \left(\left| \int_{t_0}^t dt' t_{si}(t') \right|^2 + \left| \int_{t_0}^t dt' t_{sr}(t') \right|^2 \right) \right)}. \quad (14)$$

We recognize that more efficient mathematical representation of qubit evolution with time is by introducing 4 quantities that are real valued functions of the form:

$$EP_1(t) = EP[E_{p1}]_t = \int_{t_0}^t dt' E_{p1}(t'), \quad EP_2(t) = EP[E_{p2}]_t = \int_{t_0}^t dt' E_{p2}(t'), \\ TR(t) = TR[t_{sr}]_t = \int_{t_0}^t dt' t_{sr}(t'), \quad TI(t) = TI[t_{si}]_t = \int_{t_0}^t dt' t_{si}(t').$$

It shall be underlined that $E_{p1}(t')$, $E_{p2}(t')$, $t_{sr}(t')$ and $t_{si}(t')$ can be continuous or discontinuous real valued functions of finite value of any dependence and that $EP[.]$, $TR[.]$ and $TI[.]$ are functionals of Hamiltonian parameters. Usually in case of nanocircuit their range of values and time-dependence is limited but can be extended with more advanced engineering and circuit topology. It can be carefully examined if one moves from Schroedinger to tight-binding formalism so value E_{p1} is associated with energy of particle localized at node 1 and E_{p2} is associated with energy of particle localized at node 2, while t_s is measure of energy that can be transported between node 1 and 2 that takes places during particle movement. t_s can also be measured by the delocalized energy between 2 nodes. Therefore highly energetic particle moving across nanostructure of q-wells shall have high value of t_s and low value of E_{p1} and E_{p2} so ballistic transport takes place. On another hand slowly moving particle participating in diffusive transport between one q-well and neighbouring q-well is strongly localized so $E_{p1}, E_{p2} \gg |t_s|$.

3 Action of Phase Rotating Gate Described Analytically

Let us consider the situation of single qubit from Fig. 2 when we assume the following dependencies: $E_{p1}(t) = E_{p2}(t) = E_p = \text{constant}$ and $t_{s12}(t) = t_{s21}(t) = t_s(t) = \text{constant}_1$. In such we have two time-independent eigenenergies $E_1 = E_p - t_s$ and $E_p + t_s$. For simplicity we assume $(\alpha(0) \in R)$, $(\beta(0) \in R)$. The probability of finding electron at node 1 is given by angle Θ at Bloch sphere expressed as

$$\begin{aligned}
P_1(t) &= |\alpha(t)|^2 = \frac{1}{2} (|\alpha(0)|^2 + |\beta(0)|^2) \\
&\quad + \frac{1}{2} (|\alpha(0)|^2 - |\beta(0)|^2) \cos\left(\frac{E_2 - E_1}{\hbar} t\right) = \cos(\Theta(t))^2, \\
P_2(t) &= |\alpha(t)|^2 = \frac{1}{2} (|\alpha(0)|^2 + |\beta(0)|^2) \\
&\quad - \frac{1}{2} (|\alpha(0)|^2 - |\beta(0)|^2) \cos\left(\frac{E_2 - E_1}{\hbar} t\right) = \sin(\Theta(t))^2, \quad (15)
\end{aligned}$$

and it oscillates periodically with frequency proportional to distance between energetic levels E_2 and E_1 and is given as $\omega_0 = \frac{E_2 - E_1}{\hbar}$. Therefore the same occupancy at node is repeating with periodic time $t_d = n \frac{2\pi\hbar}{E_2 - E_1}$ for integer n . Obviously probability of finding of particle at node 2 is $P_2 = 1 - P_1$. The phase difference between wavefunctions at node 1 and 2 is denoted as $\phi(t)$ and can be expressed analytically by formula

$$\begin{aligned}
-\phi(t) &= ASin \left[\frac{\sin\left(\frac{E_1 t}{\hbar}\right)(|\alpha(0)|^2 - |\beta(0)|^2) + \sin\left(\frac{E_2 t}{\hbar}\right)(|\alpha(0)|^2 + |\beta(0)|^2)}{\cos\left(\frac{E_1 t}{\hbar}\right)(|\alpha(0)|^2 - |\beta(0)|^2) + \cos\left(\frac{E_2 t}{\hbar}\right)(|\alpha(0)|^2 + |\beta(0)|^2)} \right] \\
&= ASin \left[\frac{\frac{1}{2i} (\exp(i\frac{E_1 t}{\hbar}) - \exp(-i\frac{E_1 t}{\hbar})) (|\alpha(0)|^2 - |\beta(0)|^2) + \frac{1}{2i} (\exp(i\frac{E_2 t}{\hbar}) - \exp(-i\frac{E_2 t}{\hbar})) (|\alpha(0)|^2 + |\beta(0)|^2)}{\frac{1}{2} (\exp(i\frac{E_1 t}{\hbar}) + \exp(-i\frac{E_1 t}{\hbar})) (|\alpha(0)|^2 - |\beta(0)|^2) + \frac{1}{2} (\exp(i\frac{E_2 t}{\hbar}) + \exp(-i\frac{E_2 t}{\hbar})) (|\alpha(0)|^2 + |\beta(0)|^2)} \right] \\
&= ASin \left[\frac{\frac{1}{2i} (1 - \exp(-i\frac{2E_1 t}{\hbar})) (|\alpha(0)|^2 - |\beta(0)|^2) + \frac{1}{2i} (\exp(i\frac{E_2 - E_1 t}{\hbar}) - \exp(-i\frac{E_2 + E_1 t}{\hbar}))}{\frac{1}{2} (1 + \exp(-i\frac{2E_1 t}{\hbar})) (|\alpha(0)|^2 - |\beta(0)|^2) + \frac{1}{2} (\exp(i\frac{E_2 - E_1 t}{\hbar}) + \exp(-i\frac{E_1 + E_2 t}{\hbar}))} \right] = \\
&= ASin \left[\frac{\frac{1}{2i} (1 - \exp(-i\frac{2E_1 t}{\hbar})) (|\alpha(0)|^2 - |\beta(0)|^2) + \frac{1}{2i} (\cos(\frac{E_2 - E_1 t}{\hbar}) + i \sin(\frac{E_2 - E_1 t}{\hbar})) - \exp(-i\frac{E_2 + E_1 t}{\hbar})}{\frac{1}{2} (1 + \exp(-i\frac{2E_1 t}{\hbar})) (|\alpha(0)|^2 - |\beta(0)|^2) + \frac{1}{2} (\cos(\frac{E_2 - E_1 t}{\hbar}) + i \sin(\frac{E_2 - E_1 t}{\hbar})) + \exp(-i\frac{E_1 + E_2 t}{\hbar})} \right] \\
&= ASin \left[\frac{\left((1 - e^{-i\frac{2E_1 t}{\hbar}}) (|\alpha(0)|^2 - |\beta(0)|^2) \right) + \left(\frac{\cos(\Theta(t))^2 - \frac{1}{2}}{\frac{1}{2} (|\alpha(0)|^2 - |\beta(0)|^2)} + i \sqrt{1 - \left(\frac{\cos(\Theta(t))^2 - \frac{1}{2}}{\frac{1}{2} (|\alpha(0)|^2 - |\beta(0)|^2)}\right)^2} \right) \sin\left(\frac{E_2 - E_1}{\hbar} t\right) - e^{-i\frac{E_2 + E_1}{\hbar} t}}{i(1 + e^{-i\frac{2E_1 t}{\hbar}}) (|\alpha(0)|^2 - |\beta(0)|^2)} + \left(\frac{\cos(\Theta(t))^2 - \frac{1}{2}}{\frac{1}{2} (|\alpha(0)|^2 - |\beta(0)|^2)} + i \sqrt{1 - \left(\frac{\cos(\Theta(t))^2 - \frac{1}{2}}{\frac{1}{2} (|\alpha(0)|^2 - |\beta(0)|^2)}\right)^2} \right) \sin\left(\frac{E_2 - E_1}{\hbar} t\right) + e^{-i\frac{E_1 + E_2}{\hbar} t}} \right] \quad (16)
\end{aligned}$$

We recognize that three frequencies are involved $\omega_1 = \frac{E_1}{\hbar}$, $\omega_{21m} = \frac{E_2 - E_1}{\hbar}$, $\omega_{21p} = \frac{E_2 + E_1}{\hbar}$ in the dynamics of phase difference of quantum state between nodes 2 and 1. We are using sign function as $\text{Sign}(\sin(\frac{E_2 - E_1}{\hbar} t)) = s_{\sin(\frac{E_2 - E_1}{\hbar} t)}$ so it has 1 and -1 values for positive and negative values of $\sin(\frac{E_2 - E_1}{\hbar} t)$ and 0 otherwise. More phase difference across position based qubit between nodes 1 and 2 is codependent on the occupancy of the left and right node as given by last equation in the case of time-

independent Hamiltonian. Such situation is not taking place in most conventional qubits using energy eigenbases to encode information but takes place in position based semiconductor qubit. The ideal phase rotating gate implemented in position based qubit brings desired phase difference between wavefunctions at nodes 2 and 1 is not changing the occupancy of node 1 and 2. If we want to keep the occupancy from time $t = 0$ we need to consider times $t_d = n \frac{2\pi\hbar}{E_2 - E_1}$. At time $t=0$ phase difference was assumed to be 0.

4 Action of Hadamard Gate in Position Qubit

The Hadamard gate is able to conduct the following unitary transformation on quantum state $|\psi(t)\rangle$ and is given as

$$U_{\text{Hadamard}} = \begin{pmatrix} 1 & 1 \\ 1 & -1 \end{pmatrix}. \quad (17)$$

It has property $U_{\text{Hadamard}}^\dagger = U_{\text{Hadamard}}$ and $U_{\text{Hadamard}} U_{\text{Hadamard}}^\dagger = 1$ so double action of Hadamard gate gives $U_{\text{Hadamard}} U_{\text{Hadamard}}^{-1} = 1$.

Let us concentrate on the position dependent qubit with time-independent parameters $E_{p1}, E_{p2} = E_{p1} = E_p, t_s \in R$. In such case we obtain following eigenenergies $E_1 = E_p - t_s$ and $E_2 = E_p + t_s$. From simple calculations we can notice that two eigenenergies $E_1 = E_p - t_s$ and $E_1 = E_p + t_s$ have corresponding eigenstates

$$|E_1\rangle = \frac{1}{\sqrt{2}}(|1, 0\rangle_x - |0, 1\rangle_x), |E_2\rangle = \frac{1}{\sqrt{2}}(|1, 0\rangle_x + |0, 1\rangle_x), \quad (18)$$

that are orthonormal so $\langle 1, 0|1, 0\rangle = \langle 0, 1|0, 1\rangle = 1$ and $\langle 1, 0|0, 1\rangle = \langle 0, 1|1, 0\rangle = 0$. At the same time $\langle E_1|E_1\rangle = \langle E_2|E_2\rangle = 1$ and $\langle E_1|E_2\rangle = \langle E_2|E_1\rangle = 0$. We recognize that Formula 18 can be written in the compact form as

$$\begin{pmatrix} |E_2\rangle \\ |E_1\rangle \end{pmatrix} = \frac{1}{\sqrt{2}} \begin{pmatrix} 1 & 1 \\ 1 & -1 \end{pmatrix} \begin{pmatrix} |1, 0\rangle_x \\ |0, 1\rangle_x \end{pmatrix} = \hat{U}_{\text{Hadamard}} \begin{pmatrix} |1, 0\rangle_x \\ |0, 1\rangle_x \end{pmatrix}, \\ \begin{pmatrix} |1, 0\rangle_x \\ |0, 1\rangle_x \end{pmatrix} = \frac{1}{\sqrt{2}} \begin{pmatrix} 1 & 1 \\ 1 & -1 \end{pmatrix} \begin{pmatrix} |E_2\rangle \\ |E_1\rangle \end{pmatrix} = \hat{U}_{\text{Hadamard}} \begin{pmatrix} |E_2\rangle \\ |E_1\rangle \end{pmatrix}. \quad (19)$$

We recognize that quantum transformation is naturally encoded in transformation from position quantum system eigenbases into energy eigenbases. Quantum logical 0 can be spanned (represented) by state $|1, 0\rangle_x = |0\rangle_L$ (presence of electron in qubit on the left side in Fig. 2) and quantum logical 1 can be spanned (represented) by the state $|0, 1\rangle_x = |1\rangle_R$ (presence of electron in qubit on the right side). Therefore qubit state shall be defined by

$$\begin{aligned}
|\psi_t\rangle &= \alpha(t) |1, 0\rangle_x + \beta |0, 1\rangle_x = e^{iPh(\alpha(t))=i\xi(t)} (\alpha(t) |1, 0\rangle_x \\
&+ e^{Ph(\beta(t))-Ph(\alpha(t))} \beta(t) |0, 1\rangle_x) = \\
&= e^{i\xi(t)} (\alpha(t) |1, 0\rangle_x + e^{i\phi(t)} \beta |0, 1\rangle_x).
\end{aligned} \tag{20}$$

Action of Hadamard gate requires

$$\begin{aligned}
|0\rangle_L &= |1, 0\rangle_x \rightarrow \frac{1}{\sqrt{2}} (|1, 0\rangle_x + |0, 1\rangle_x) \\
&= \frac{1}{\sqrt{2}} (|1\rangle_L + |2\rangle_L), \\
|0\rangle_R &= |0, 1\rangle_x \rightarrow \frac{1}{\sqrt{2}} (|1, 0\rangle_x - |0, 1\rangle_x) \\
&= \frac{1}{\sqrt{2}} (|1\rangle_L - |2\rangle_L).
\end{aligned} \tag{21}$$

that is heating up (left transition from occupancy of two energetic levels expressed by quantum state $|1, 0\rangle_x$ to occupancy of E_2 level given by quantum state $\frac{1}{\sqrt{2}} (|1, 0\rangle_x + |0, 1\rangle_x)$) or cooling down (right transition from occupancy of 2 energetic levels expressed by quantum state $|0, 1\rangle_x$ to the occupancy of ground state E_1 given by quantum state $\frac{1}{\sqrt{2}} (|1\rangle_L - |2\rangle_L)$) of quantum state in 2 energy level system. We recognize that quantum logical 0 or presence of state (electron) in left well is achieved when there is equal occupancy (given by c_{E1}) of energetic level E_1 and E_2 so $|c_{E1}(t)|^2 = |c_{E2}(t)|^2$. The scheme how to change the complete occupancy of energetic level E_1 into full occupancy of energetic level E_2 is given by Formula 37 that is associated with time-dependent Hamiltonian applied to position based qubit. The quantum state is given as

$$\begin{aligned}
|\psi(t)\rangle &= \frac{1}{\sqrt{2}} [(c_{E1}(t)(|1, 0\rangle_x - |0, 1\rangle_x) + (c_{E2}(t)(|1, 0\rangle_x + |0, 1\rangle_x))] = \\
&\frac{1}{\sqrt{2}} [e^{\frac{i}{\hbar}} (e^{\frac{i}{\hbar}(t-t_0)E_1} c_{E1}(t_0)(|1, 0\rangle_x - |0, 1\rangle_x)) \\
&+ (e^{\frac{i}{\hbar}(t-t_0)E_2(t-t_0)} c_{E2}(t_0)(|1, 0\rangle_x + |0, 1\rangle_x))] = \\
&\frac{1}{\sqrt{2}} [(+e^{\frac{i}{\hbar}(t-t_0)E_1} c_{E1}(t_0) + (e^{\frac{i}{\hbar}(t-t_0)E_2(t-t_0)} c_{E2}(t_0)) |1, 0\rangle_x + \\
&((-e^{\frac{i}{\hbar}(t-t_0)E_1} c_{E1}(t_0) + (e^{\frac{i}{\hbar}(t-t_0)E_2(t-t_0)} c_{E2}(t_0)) |0, 1\rangle_x].
\end{aligned}$$

Such state will evolve after characteristic time from logical state $|0\rangle_L$ into quantum logical $|1\rangle_L$ and later into $|0\rangle_L$ and so on. We can also set logical quantum state in position space parameterized by x and we can read the results of Hadamard operation action in energy space or reversely. Engineers have the choice of setting qubit state in a position space (what is more intuitive if one aims to obtain high integration

circuits) or in energy space. By setting the quantum state in position space (as by injecting electron from left side into left well of qubit) one needs to read it by energy space or reversely. Reading the quantum state after Hadamard operation (or any other quantum operation) in energy space requires either spectroscopy of occupation of energy levels which basically means that we need to use microwaves in order to populate or depopulate given energy level(s). Alternative method for reading the qubit state after Hadamard operation (or any other quantum operation) is determination the state of neighbouring qubit that interacts with measured qubit in electrostatic way as it is depicted in the right side of Fig. 2. The determination of occupancy of energy level E_1 and E_2 will give us the information on the qubit state after Hadamard operation (so presence of at least 2 energy levels in physical system is the requirement) and formally we have

$$\begin{aligned} |\psi\rangle_{\text{output}} &= c_{E_1} |E_1\rangle + c_{E_2} |E_2\rangle = c_{E_1} |0\rangle_{L\text{-output}} + c_{E_2} |1\rangle_{L\text{-output}} \\ &= \hat{U}_{\text{Hadamard}} (\alpha |0\rangle_{L\text{-input}} + \beta |1\rangle_{L\text{-input}}). \end{aligned} \quad (22)$$

5 Rabi Oscillations in General Case for 2 Energy Level System

In general case during heating up of q-state or during cooling down of q-state we need to consider the Hamiltonian as $H = E_1 |E_1\rangle \langle E_1| + E_2 |E_2\rangle \langle E_2| + f_1(t) |E_2\rangle \langle E_1| + f_2(t) |E_1\rangle \langle E_2|$. If we want to have time-dependent only $E_1(t)$ and only $E_2(t)$ states we need to consider $H = E_1 |E_1(t)\rangle \langle E_1(t)| + E_2 |E_2(t)\rangle \langle E_2(t)| + f_1(t) |E_2(t)\rangle \langle E_1(t)| + f_2(t) |E_1(t)\rangle \langle E_2(t)|$. Let us see the dynamics of quantum states with time so we have $f_1(t), f_2(t) = 0$ for $t \leq 0$ and constant non-zero otherwise ($f_1(t) = f_1 = \text{const}_1, f_2(t) = f_2 = \text{const}_2$) so one obtains the equation

$$\begin{aligned} + \hbar i \frac{d}{dt} c_{E_1}(t) &= (c_{E_1}(t) E_1 + f_2(t) c_{E_2}(t)), \\ + \hbar i \frac{d}{dt} c_{E_2}(t) &= (c_{E_2}(t) E_2 + f_1(t) c_{E_1}(t)). \end{aligned} \quad (23)$$

From first equation we have $\frac{1}{f_2(t)} (+\hbar i \frac{d}{dt} c_{E_1}(t) - E_1 c_{E_1}(t)) = c_{E_2}(t)$ and we obtain the second equation

$$\begin{aligned} + \hbar i \frac{d}{dt} \left(\frac{1}{f_2(t)} (+\hbar i \frac{d}{dt} c_{E_1}(t) - E_1 c_{E_1}(t)) \right) \\ = \left(\frac{1}{f_2(t)} (+\hbar i \frac{d}{dt} c_{E_1}(t) - E_1 c_{E_1}(t)) \right) E_2 + f_1(t) c_{E_1}(t). \end{aligned} \quad (24)$$

which gives,

$$\begin{aligned}
& \frac{d}{dt} \left(\frac{1}{f_2(t)} (+\hbar i \frac{d}{dt} c_{E_1}(t) - E_1 c_{E_1}(t)(t)) \right) \\
&= -\frac{df_2}{dt} \frac{1}{f_2^2(t)} (+\hbar i \frac{d}{dt} c_{E_1}(t) - E_1 c_{E_1}(t)(t)) \\
&+ \left(\frac{1}{f_2(t)} (+\hbar i \frac{d^2}{dt^2} c_{E_1}(t)(t) - E_1 \frac{d}{dt} c_{E_1}(t)) \right) \\
&= \frac{1}{i\hbar} \left(\frac{1}{f_2(t)} (+\hbar i \frac{d}{dt} c_{E_1}(t) - E_1 c_{E_1}(t)(t)) \right) \\
&E_2 + \frac{1}{i\hbar} f_1(t) c_{E_1}(t)(t). \tag{25}
\end{aligned}$$

and it implies

$$\begin{aligned}
& \frac{d^2}{dt^2} c_{E_2}(t) \frac{\hbar i}{f_2(t)} + \frac{d}{dt} c_{E_2}(t) \left[-\frac{df_2}{dt} \frac{\hbar i}{f_2^2(t)} - \frac{(E_1 + E_2)}{f_2(t)} \right] \\
&+ c_{E_2}(t) \left[\frac{E_1}{i\hbar} \frac{E_2}{f_2(t)} + \frac{df_2}{dt} \frac{E_1}{f_2(t)^2} - \frac{1}{\hbar i} f_1(t) \right] = 0. \tag{26}
\end{aligned}$$

After multiplication by $\frac{f_2(t)}{\hbar i}$ the last equation gives

$$\begin{aligned}
& \frac{d^2}{dt^2} c_{E_1}(t) + \frac{d}{dt} c_{E_1}(t) \left[-\frac{df_2}{dt} \frac{1}{f_2(t)} + i \frac{(E_1 + E_2)}{\hbar} \right] \\
&+ \beta(t) \left[-\frac{E_1 E_2}{\hbar^2} - \frac{i}{\hbar} \frac{df_2}{dt} \frac{E_1}{f_2(t)} + \frac{1}{\hbar^2} f_1(t) f_2(t) \right] = 0. \tag{27}
\end{aligned}$$

In analogical way we obtain

$$\begin{aligned}
& \frac{d^2}{dt^2} c_{E_2}(t) + \frac{d}{dt} c_{E_2}(t) \left[-\frac{df_1}{dt} \frac{1}{f_1(t)} + i \frac{(E_1 + E_2)}{\hbar} \right] \\
&+ \beta(t) \left[-\frac{E_1 E_2}{\hbar^2} - \frac{i}{\hbar} \frac{df_1}{dt} \frac{E_2}{f_1(t)} + \frac{1}{\hbar^2} f_1(t) f_2(t) \right] = 0. \tag{28}
\end{aligned}$$

Boundary conditions are given as

$$\begin{aligned}
& i\hbar \frac{d}{dt} c_{E_1}(t_0^+) = E_1 c_{E_2}(t_0^+) + f_2(t_0^+) c_{E_1}(t_0), \\
& i\hbar \frac{d}{dt} c_{E_2}(t_0^+) = E_2 c_{E_1}(t_0^+) + f_1(t_0^+) c_{E_2}(t_0), \\
& c_{E_2}(t_0^+) = c_{E_2}(t_0), c_{E_1}(t_0^+) = c_{E_1}(t_0). \tag{29}
\end{aligned}$$

From later considerations it turns out that $f_1(t)^* = f_2(t)$ so $f_1(t) = f_a(t) + i f_b(t)$ and $f_2(t) = f_a(t) - i f_b(t)$, where $f_a(t)$ and $f_b(t)$ are real valued functions. Therefore we can write the equations of motion as

$$\begin{aligned} & \frac{d^2}{dt^2} c_{E1}(t) + \frac{d}{dt} c_{E1}(t) \left[-\frac{df_2}{dt} \frac{1}{f_2(t)} + i \frac{(E_1 + E_2)}{\hbar} \right] \\ & + c_{E1}(t) \left[-\frac{E_1 E_2}{\hbar^2} - \frac{i}{\hbar} \frac{df_2}{dt} \frac{E_1}{f_2(t)} + \frac{1}{\hbar^2} f_a(t) f_b(t) \right] = 0. \end{aligned} \quad (30)$$

In analogical way we obtain

$$\begin{aligned} & \frac{d^2}{dt^2} c_{E2}(t_0)(t) + \frac{d}{dt} c_{E2}(t_0) \left[-\frac{df_1}{dt} \frac{1}{f_1(t)} + i \frac{(E_1 + E_2)}{\hbar} \right] \\ & + c_{E1}(t) \left[-\frac{E_1 E_2}{\hbar^2} - \frac{i}{\hbar} \frac{df_1}{dt} \frac{E_2}{f_1(t)} \right. \\ & \left. + \frac{1}{\hbar^2} (f_a(t)^2 + f_b(t)^2) \right] = 0. \end{aligned} \quad (31)$$

Boundary conditions are given as

$$\begin{aligned} i\hbar \frac{d}{dt} c_{E2}(t_0^+) &= E_1 c_{E2}(t_0^+) + (f_a(t_0) - i f_b(t_0)) c_{E1}(t_0), \\ i\hbar \frac{d}{dt} c_{E1}(t_0)(t_0^+) &= E_2 c_{E1}(t_0)(t_0^+) + (f_a(t_0) + i f_b(t_0)) c_{E2}(t_0), \\ c_{E2}(t_0^+) &= c_{E2}(t_0), c_{E1}(t_0^+) = c_{E1}(t_0). \end{aligned} \quad (32)$$

Very special case is when $f_1(t) = a \exp(ct) + ib \exp(ct)$, $f_2(t) = a \exp(ct) - ib \exp(ct)$, where c , a and b are real valued. In such cases we obtain the equations for the occupancy of energy state E_1 and E_2 expressed as

$$\begin{aligned} & \frac{d^2}{dt^2} c_{E2}(t) + \frac{d}{dt} c_{E2}(t) \left[-c + i \frac{(E_1 + E_2)}{\hbar} \right] \\ & + c_{E2}(t) \left[-\frac{E_1 E_2}{\hbar^2} - \frac{i}{\hbar} E_1 c + \frac{1}{\hbar^2} (a^2 + b^2) \exp(2ct) \right] = 0. \end{aligned} \quad (33)$$

First case is $c = 0$, $\hbar = 1$ and solution is

$$\begin{aligned} c_{E1}(t) &= e^{-\frac{1}{2}i(E_1+E_2-i\sqrt{-4a^2-4b^2-E_1^2+2E_1E_2-E_2^2})t} g_1 \\ &+ e^{\frac{1}{2}(-i(E_1+E_2)+\sqrt{-4a^2-4b^2-E_1^2+2E_1E_2-E_2^2})t} g_2, \end{aligned} \quad (34)$$

where g_1 and g_2 are complex values. Having non-zero c we obtain solutions

$$\begin{aligned} c_{E1}(t) &= c_1 \exp\left(\frac{1}{2}t \left(-\sqrt{-4a^2e^{2ct} - 4b^2e^{2ct} + c^2 - 2icE_1 + 2icE_2 - E_1^2 + 2E_1E_2 - E_2^2} + c - iE_1 - iE_2 \right)\right) + \\ &c_2 \exp\left(\frac{1}{2}t \left(\sqrt{-4a^2e^{2ct} - 4b^2e^{2ct} + c^2 - 2icE_1 + 2icE_2 - E_1^2 + 2E_1E_2 - E_2^2} + c - iE_1 - iE_2 \right)\right), \end{aligned} \quad (35)$$

$$\begin{aligned}
 c_{E2}(t) = & c_1 \exp\left(\frac{1}{2}t \left(-\sqrt{-4a^2e^{2ct} - 4b^2e^{2ct} + c^2 + 2icE_1 - 2icE_2 - E_1^2 + 2E_1E_2 - E_2^2} + c - iE_1 - iE_2\right)\right) + \\
 & c_2 \exp\left(\frac{1}{2}t \left(\sqrt{-4a^2e^{2ct} - 4b^2e^{2ct} + c^2 + 2icE_1 - 2icE_2 - E_1^2 + 2E_1E_2 - E_2^2} + c - iE_1 - iE_2\right)\right). \quad (36)
 \end{aligned}$$

The simplified case of last formula can be given as

$$\begin{aligned}
 c_{E2}(t) = & -g_4 \exp\left(-\frac{1}{2}it \left(-i\sqrt{-E_1^2 + 2E_1E_2 - E_2^2 - 4 + E_1 + E_2}\right)\right) \\
 & \left(-1 + \exp\left(\frac{1}{2}it \left(-i\sqrt{-E_1^2 + 2E_1E_2 - E_2^2 - 4 + E_1 + E_2}\right)\right)\right) \\
 & + \frac{1}{2}t \left(\sqrt{-E_1^2 + 2E_1E_2 - E_2^2 - 4} - i(E_1 + E_2)\right) \Bigg) \quad (37)
 \end{aligned}$$

and the numerical example of its dependence on time is depicted in Fig. 6, where initially energy level E_1 was completely populated and with time the full population of energy level E_2 was achieved while energy level E_1 was completely depopulated. Such dependence can be used for example in the action of Hadamard gate implemented in electrostatic position dependent qubit. If $f_1(t)$ and $f_2(t)$ functions have small values one can assume $|E_1\rangle = \frac{1}{\sqrt{2}}(|1, 0\rangle_x - |0, 1\rangle_x)$ and $|E_2\rangle = \frac{1}{\sqrt{2}}(|1, 0\rangle_x + |0, 1\rangle_x)$ and

$$\hat{H}(t)_x = \begin{pmatrix} E_p & t_s \\ t_s^* & E_p \end{pmatrix} + \frac{1}{2} \begin{pmatrix} +f_1(t) + f_2(t) & -f_1(t) + f_2(t) \\ +f_1(t) - f_2(t) & -(f_1(t) + f_2(t)) \end{pmatrix}. \quad (38)$$

Hermicity of last Hamiltonian requires that $f_1(t) = f_2(t)^*$ (Figs. 3, 4 and 5).

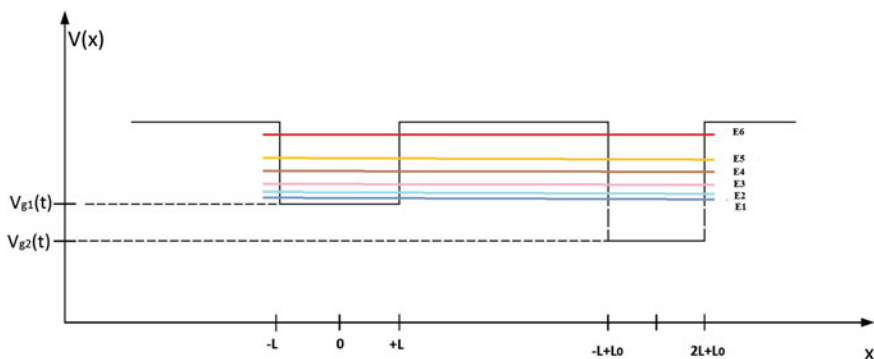


Fig. 3 Case of position based qubit with $N = 6$ energetic levels and unoccupied ground state

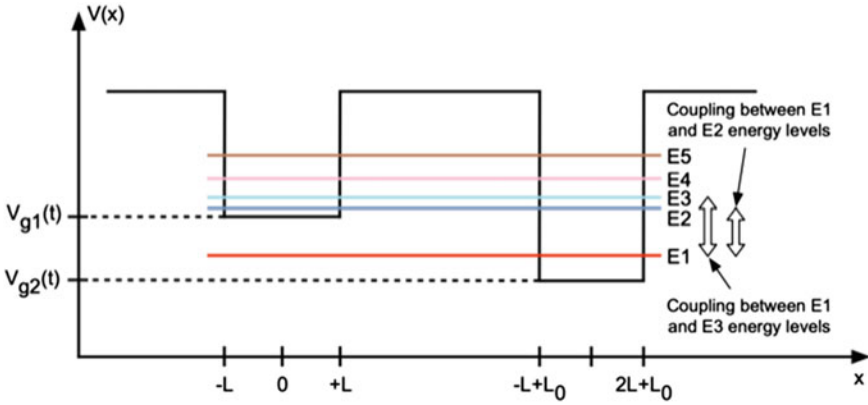


Fig. 4 Position based qubit with 5 energetic levels, two-different potential minima and one occupied localized state

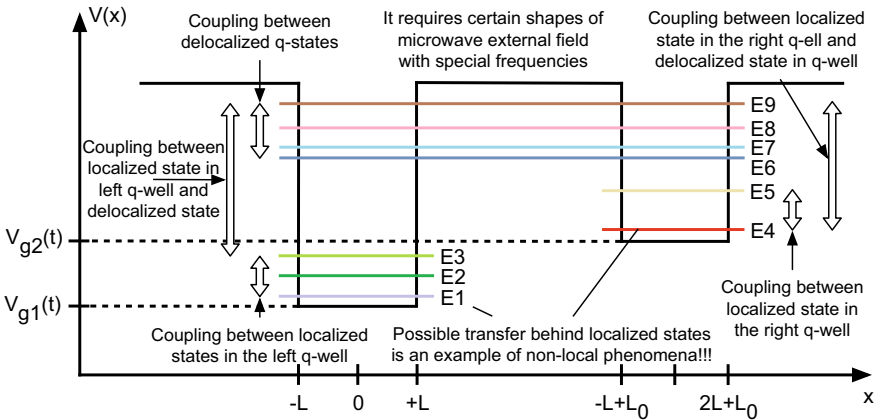


Fig. 5 All possible quantum processes in the system of 2 coupled q-dots in the case of various microwave fields: transitions between delocalized eigen energetic levels (P1), transitions between left localized eigen energies (P2), transitions between right localized eigen energy states (P3), transitions between left and right delocalized eigen energy states (P4), transitions between left localized q-states and delocalized q-states (P5), transitions between right localized q-states and delocalized q-states (P6). One can also distinguish process on injection of electron from outside to 2-qwell system (P7) and process of ejection of electron from 2-qwell system to the outside (P8). Six processes P1–P6 are described by the Hamiltonian (48) and its precursor Hamiltonian (48)

6 Extension of 2-Energy Tight Binding Model into N Energetic Levels for Position Based Qubit in Arbitrary Electromagnetic Environment

Pictures presented before as in Eq. 1 with $N=2$ energetic levels can be easily extended for arbitrary number of energy levels $E_1 < E_2 < \dots < E_{2N_1=N}$ what is valid in time-independent case. It is worth mentioning that very last chain of inequalities between time dependent eigenenergies does not need to be always valid in the general case of time-dependent Hamiltonian. In most general case we have $N = 2N_1$ energetic levels among 2 coupled quantum wells controlled electrostatically. Quite obviously we are omitting continuum spectrum of eigenenergies and we only concentrate on the system with electrons confinement by some effective potential. It requires introduction of $2N_1$ orthogonal Wannier functional bases such that $|x_1\rangle_1, \dots, |x_1\rangle_{N_1}, |x_2\rangle_1, \dots, |x_2\rangle_{N_1} = (|1, 0\rangle_{E_1-E_2}, \dots, |1, 0\rangle_{E_{N_1-1}-E_{N_1}}, |0, 1\rangle_{E_1-E_2}, \dots, |0, 1\rangle_{E_{N_1-1}, E_{N_1}})$ and such that $\langle x_1|_k (|x_2\rangle_m) = 0$ for any m different than k . In such case the quantum state for $N_1 = 3$ ($N = 2N_1$) is described as

$$\begin{aligned}
 |\psi\rangle(t) &= \gamma_{E_1-E_2, p1}(t) |x_1\rangle_{E_1, E_2} + \gamma_{E_3-E_4, p1}(t) |x_1\rangle_{E_3, E_4} \\
 &+ \gamma_{E_5-E_6, p1}(t) |x_1\rangle_{E_5, E_6} + \gamma_{E_5-E_6, p2}(t) |x_2\rangle_{E_5-E_6} \\
 &+ \gamma_{E_3-E_4, p2}(t) |x_2\rangle_{E_3-E_4} + \gamma_{E_1, p2}(t) |x_2\rangle_{E_1-E_2} = \\
 &= \frac{1}{\sqrt{N}} \left[\gamma_{E_1-E_2, p1}(t) \begin{pmatrix} 1 \\ 0 \\ 0 \\ 0 \\ 0 \\ 0 \end{pmatrix} + \gamma_{E_3-E_4, p1}(t) \begin{pmatrix} 0 \\ 1 \\ 0 \\ 0 \\ 0 \\ 0 \end{pmatrix} + \dots + \gamma_{E_1-E_2, p2}(t) \begin{pmatrix} 0 \\ 0 \\ 0 \\ 0 \\ 0 \\ 1 \end{pmatrix} \right] \\
 &= \begin{pmatrix} \gamma_{E_1-E_2, p1}(t) \\ \gamma_{E_3-E_4, p1}(t) \\ \gamma_{E_5-E_6, p1}(t) \\ \gamma_{E_5-E_6, p2}(t) \\ \gamma_{E_3-E_4, p2}(t) \\ \gamma_{E_1-E_2, p2}(t) \end{pmatrix}. \tag{39}
 \end{aligned}$$

The probability of presence of electron at node 1 is $P_1(t) = |\gamma_{E_1-E_2, p1}(t) + \gamma_{E_3-E_4, p1}(t) + \gamma_{E_5-E_6, p1}(t)|^2$ and the probability of presence of electron at node 2 is $P_2(t) = |\gamma_{E_1-E_2, p2}(t) + \gamma_{E_3-E_4, p2}(t) + \gamma_{E_5-E_6, p2}(t)|^2$. The act of measurement on position based qubit is represented by the operator

$$P_{Left} = |1, 0\rangle_{E_1, E_2} \langle 1, 0|_{E_1, E_2} + |1, 0\rangle_{E_3, E_4} \langle 1, 0|_{E_3, E_4} + |1, 0\rangle_{E_5, E_6} \langle 1, 0|_{E_5, E_6}, \tag{40}$$

$$P_{Right} = |0, 1\rangle_{E_1, E_2} \langle 0, 1|_{E_1, E_2} + |0, 1\rangle_{E_3, E_4} \langle 0, 1|_{E_3, E_4} + |0, 1\rangle_{E_5, E_6} \langle 0, 1|_{E_5, E_6}. \quad (41)$$

Let us review the Hamiltonian describing system with $N = 2N_1$ energy levels. Essentially we have $2N_1$ coefficients describing energy localized at 2 nodes $E_{p1,1}, E_{p1,2}, \dots, E_{p1,N_1}, E_{p2,1}, E_{p2,2}, \dots, E_{p2,N_1}$, so we are dealing with $E_{pu,m}$ coefficients, where $m=1 \dots N_1$, pu is 1 or 2 and we have taken into account existence of all $N = 2N_1$ energetic levels. Let us set $N_1 = 3$ and in such case the quantum state Hamiltonia in the case of lack of transition between energetic levels corresponding to Fig. 4. can be written as

$$\begin{aligned} \hat{H} &= \begin{pmatrix} E_{1,p1} & 0 & 0 & 0 & 0 & t_{1,p1 \rightarrow p2} \\ 0 & E_{2,p1} & 0 & 0 & t_{2,p1 \rightarrow p2} & 0 \\ 0 & 0 & E_{3,p1} & t_{3,p1 \rightarrow p2} & 0 & 0 \\ 0 & 0 & t_{3,p2 \rightarrow p1} & E_{3,p2} & 0 & 0 \\ 0 & t_{2,p2 \rightarrow p1} & 0 & 0 & E_{2,p2} & 0 \\ t_{1,p2 \rightarrow p1} & 0 & 0 & 0 & 0 & E_{1,p2} \end{pmatrix}_x = \\ &= E_{1,t} |E_{1,t}\rangle \langle E_{1,t}| + E_{2,t} |E_{2,t}\rangle \langle E_{2,t}| + E_{3,t} |E_{3,t}\rangle \langle E_{3,t}| \\ &+ E_{4,t} |E_{4,t}\rangle \langle E_{4,t}| + E_{5,t} |E_{5,t}\rangle \langle E_{5,t}| \\ &+ E_{6,t} |E_{6,t}\rangle \langle E_{6,t}|. \end{aligned} \quad (42)$$

It is important to mention that in the case of lack of time-dependent Hamiltonian having any among frequency components $\frac{E_k - E_l}{\hbar}$ for $k \neq l$ such that $(k, l) = 1 \dots 6$ there is no possibility for the occurrence of resonant state and change of probability of occupancy among different energetic levels. In such case $\langle 1, 0|_{E_1, E_2} \langle 1, 0|_{E_1, E_2} \langle 1, 0|_{E_3, E_4} \langle 1, 0|_{E_3, E_4} = 0$. However it is not true if there exists resonant state and if for example Hamiltonian consists following non-zero components with frequencies $(\frac{E_1 - E_3}{\hbar}, \frac{E_1 - E_4}{\hbar}, \frac{E_2 - E_3}{\hbar}, \frac{E_2 - E_4}{\hbar})$.

Now we are moving towards the situation of system with position based qubit with 5 energetic levels, two-different potential minima and one occupied localized state on the right side as depicted in Fig. 5. We have Hamiltonian of the form

$$\begin{aligned} \hat{H} &= \begin{pmatrix} E_{2,p1} & 0 & 0 & t_{2,p1 \rightarrow p2} & 0 \\ 0 & E_{3,p1} & t_{3,p1 \rightarrow p2} & 0 & 0 \\ 0 & t_{3,p2 \rightarrow p1} & E_{3,p2} & 0 & 0 \\ t_{2,p2 \rightarrow p1} & 0 & 0 & E_{2,p2} & 0 \\ 0 & 0 & 0 & 0 & E_{1,p1} \end{pmatrix} \\ &= E_1(t) |E_1(t)\rangle \langle E_1(t)| + \dots + E_5(t) |E_5(t)\rangle \langle E_5(t)| \end{aligned} \quad (43)$$

with corresponding quantum state given as

$$\begin{aligned} |\psi, t\rangle_x &= \gamma_{E5, E4, p1}(t) |1, 0\rangle_{E5, E4} + \gamma_{E3, E2, p1}(t) |1, 0\rangle_{E3, E2} \\ &+ \gamma_{E5, E4, p2}(t) |0, 1\rangle_{E5, E4} + \gamma_{E3, E2, p2}(t) |1, 0\rangle_{E3, E2} + \end{aligned}$$

$$+ \gamma_{E_1, p_2}(t) |0, 1\rangle_{E_1} = \begin{pmatrix} \gamma_{E_5, E_4, p_1}(t) \\ \gamma_{E_3, E_2, p_1}(t) \\ \gamma_{E_3, E_2, p_2}(t) \\ \gamma_{E_5, E_4, p_2}(t) \\ \gamma_{E_1, p_2}(t) \end{pmatrix}_x. \quad (44)$$

The energetic states parametrized by E_5, E_4 or E_3, E_2 can move freely between node 1 and 2 so they are delocalized while the state numerated by E_1 is the particular localized ground state. Specified Hamiltonian structure implies that the ground state cannot be moved to excited states and reversely excited states cannot be moved into ground state .

The coupling between ground state and first excited state at node 2 occurs in the case of modified Hamiltonian of the following form as

$$\begin{aligned} \hat{H} &= \begin{pmatrix} E_{2, p_1} & 0 & 0 & t_{2, p_1 \rightarrow p_2} & 0 \\ 0 & E_{3, p_1} & t_{3, p_1 \rightarrow p_2} & 0 & 0 \\ 0 & t_{3, p_2 \rightarrow p_1} & E_{3, p_2} & 0 & 0 \\ t_{2, p_2 \rightarrow p_1} & 0 & 0 & E_{2, p_2} & t_{1 \rightarrow 2, p_2 \rightarrow p_2} \\ 0 & 0 & 0 & t_{2 \rightarrow 1, p_2 \rightarrow p_2} & E_{1, p_1} \end{pmatrix} \\ &= E_1(t) |E_1(t)\rangle \langle E_1(t)| + E_2(t) |E_2(t)\rangle \langle E_2(t)| + \dots \\ &+ E_5(t) |E_5(t)\rangle \langle E_6(t)| + f_1(t) |E_2\rangle \langle E_1| \\ &+ f_2(t) |E_1\rangle \langle E_2| + f_3(t) |E_3\rangle \langle E_1| + f_4(t) |E_1\rangle \langle E_3|. \end{aligned} \quad (45)$$

In a particular state it is allowed for the wave-packet in the right-well to undergo transition from energetic state E_1 to E_2 and E_3 and reversely. A better picture can be obtained from Schroedinger equation. Last Hamiltonian implies presence of time-dependent component in matrix that has $\omega_{21} = \frac{E_2 - E_1}{\hbar}$ and $\omega_{31} = \frac{E_3 - E_1}{\hbar}$ frequency components.

In such case the projectors $(|0, 1\rangle_{E_1, E_2} \langle 0, 1|_{E_1, E_2})$ $(|0, 1\rangle_{E_1, E_3} \langle 0, 1|_{E_3, E_1})$ are different from zero because of existence of resonant states characterized by frequencies ω_{21} and ω_{31} . Now we are moving from position based Hamiltonian representation into energy based that is by identity transformation

$$\hat{H}(t) = \begin{pmatrix} E_5 & 0 & 0 & 0 & 0 \\ 0 & E_4 & 0 & 0 & 0 \\ 0 & 0 & E_3 & 0 & 0 \\ 0 & 0 & 0 & E_2 & 0 \\ 0 & 0 & 0 & 0 & E_1 \end{pmatrix} \begin{pmatrix} \frac{1}{E_5} & 0 & 0 & 0 & 0 \\ 0 & \frac{1}{E_4} & 0 & 0 & 0 \\ 0 & 0 & \frac{1}{E_3} & 0 & 0 \\ 0 & 0 & 0 & \frac{1}{E_2} & 0 \\ 0 & 0 & 0 & 0 & \frac{1}{E_1} \end{pmatrix}$$

$$\begin{pmatrix} E_{2,p1} & 0 & 0 & t_{2,p1 \rightarrow p2} & 0 \\ 0 & E_{3,p1} & t_{3,p1 \rightarrow p2} & 0 & 0 \\ 0 & t_{3,p2 \rightarrow p1} & E_{3,p2} & 0 & 0 \\ t_{2,p2 \rightarrow p1} & 0 & 0 & E_{2,p2} & t_{1 \rightarrow 2,p2 \rightarrow p2} \\ 0 & 0 & 0 & t_{2 \rightarrow 1,p2 \rightarrow p2} & E_{1,p1} \end{pmatrix} = \begin{pmatrix} E_5 & 0 & 0 & 0 & 0 \\ 0 & E_4 & 0 & 0 & 0 \\ 0 & 0 & E_3 & 0 & 0 \\ 0 & 0 & 0 & E_2 & 0 \\ 0 & 0 & 0 & 0 & E_1 \end{pmatrix} \begin{pmatrix} \frac{E_{2,p1}}{E_5} & 0 & 0 & \frac{t_{2,p1 \rightarrow p2}}{E_5} & 0 \\ 0 & \frac{E_{3,p1}}{E_4} & \frac{t_{3,p1 \rightarrow p2}}{E_4} & 0 & 0 \\ 0 & \frac{t_{3,p2 \rightarrow p1}}{E_3} & \frac{E_{3,p2}}{E_3} & 0 & 0 \\ \frac{t_{2,p2 \rightarrow p1}}{E_2} & 0 & 0 & \frac{E_{2,p2}}{E_2} & \frac{t_{1 \rightarrow 2,p2 \rightarrow p2}}{E_2} \\ 0 & 0 & 0 & \frac{t_{2 \rightarrow 1,p2 \rightarrow p2}}{E_1} & \frac{E_{1,p1}}{E_1} \end{pmatrix}$$

Now we need to specify the energy eigenstates introducing $\hat{E} = \text{diag}(E_5, E_4, E_3, E_2, E_1)$ and we obtain \hat{E} acting on

$$\begin{pmatrix} \frac{E_{2,p1}}{E_5} & 0 & 0 & \frac{t_{2,p1 \rightarrow p2}}{E_5} & 0 \\ 0 & \frac{E_{3,p1}}{E_4} & \frac{t_{3,p1 \rightarrow p2}}{E_4} & 0 & 0 \\ 0 & \frac{t_{3,p2 \rightarrow p1}}{E_3} & \frac{E_{3,p2}}{E_3} & 0 & 0 \\ \frac{t_{2,p2 \rightarrow p1}}{E_2} & 0 & 0 & \frac{E_{2,p2}}{E_2} & \frac{t_{1 \rightarrow 2,p2 \rightarrow p2}}{E_2} \\ 0 & 0 & 0 & \frac{t_{2 \rightarrow 1,p2 \rightarrow p2}}{E_1} & \frac{E_{1,p1}}{E_1} \end{pmatrix} \begin{pmatrix} \gamma_{E_3, E_2, p1} \\ \gamma_{E_4, E_5, p1} \\ \gamma_{E_4, E_5, p2} \\ \gamma_{E_3, E_2, p2} \\ \gamma_{E_1, p2} \end{pmatrix}_x \\ = \hat{E} \begin{pmatrix} \gamma_{E_3, E_2, p1}(t) \frac{E_{2,p1}}{E_5} + \frac{t_{2,p1 \rightarrow p2}}{E_5} \gamma_{E_3, E_2, p2}(t) \\ \gamma_{E_4, E_5, p1}(t) \frac{E_{3,p1}}{E_4} + \frac{t_{3,p1 \rightarrow p2}}{E_4} \gamma_{E_4, E_5, p2}(t) \\ \gamma_{E_4, E_5, p2}(t) \frac{E_{3,p2}}{E_3} + \gamma_{E_4, E_5, p1}(t) \frac{t_{3,p2 \rightarrow p1}}{E_3} \\ \frac{E_{2,p2} \gamma_{E_3, E_2, p2} + \gamma_{E_1, p2} t_{1 \rightarrow 2, p2 \rightarrow p2}}{E_2} + \frac{\gamma_{E_3, E_2, p1} t_{2, p2 \rightarrow p1}}{E_2} \\ \frac{t_{2 \rightarrow 1, p2 \rightarrow p2}}{E_1} \gamma_{E_2, E_3, p2}(t) + \gamma_{E_1, p2}(t) \frac{E_{1,p1}}{E_1} \end{pmatrix}_x \\ = \begin{pmatrix} \gamma_{E_2, E_3, p1}(t) E_{2,p1} + t_{2,p1 \rightarrow p2} \gamma_{E_2, E_3, p2}(t) \\ 0 \\ 0 \\ 0 \\ 0 \end{pmatrix}_{E_5} + \begin{pmatrix} 0 \\ \gamma_{E_4, E_5, p1}(t) E_{3,p1} + t_{3,p1 \rightarrow p2} \gamma_{E_4, E_5, p2}(t) \\ 0 \\ 0 \\ 0 \end{pmatrix}_{E_4} \\ + \begin{pmatrix} 0 \\ 0 \\ \gamma_{E_4, E_5, p2}(t) E_{3,p2} + \gamma_{E_4, E_5, p1}(t) t_{3,p2 \rightarrow p1} \\ 0 \\ 0 \end{pmatrix}_{E_3} \\ + \begin{pmatrix} 0 \\ 0 \\ 0 \\ E_{2,p2} \gamma_{E_2, E_3, p2} + \gamma_{E_1, p2} t_{1 \rightarrow 2, p2 \rightarrow p2} + \gamma_{E_2, E_3, p1} t_{2, p2 \rightarrow p1} \\ 0 \end{pmatrix}_{E_2} \\ + \begin{pmatrix} 0 \\ 0 \\ 0 \\ 0 \\ t_{2 \rightarrow 1, p2 \rightarrow p2} \gamma_{E_2, E_3, p2}(t) + \gamma_{E_1, p2}(t) E_{1,p1} \end{pmatrix}_{E_1} \quad (46)$$

It is noticeable to recognize that the ground state eigenvector from localized state was converted into delocalized state by the presence of non-zero $\gamma_{E_1,p_2}(t)E_{1,p_1}$ term in the Hamiltonian .

$$\begin{pmatrix} 0 \\ 0 \\ 0 \\ 0 \\ \gamma_{E_1,p_2}(t)E_{1,p_1} \end{pmatrix}_{E_1} \rightarrow \begin{pmatrix} 0 \\ 0 \\ 0 \\ 0 \\ t_{2 \rightarrow 1,p_2 \rightarrow p_2} \gamma_{E_5,E_4,p_2}(t) + \gamma_{E_1,p_2}(t)E_{1,p_1} \end{pmatrix}_{E_1} .$$

Also second energy level eigenvector was changed.

$$\begin{pmatrix} 0 \\ 0 \\ 0 \\ E_{2,p_2} \gamma_{E_5,E_4,p_2} + \gamma_{E_5,E_4,p_1} t_{2,p_2 \rightarrow p_1} \\ 0 \end{pmatrix}_{E_2} \rightarrow \begin{pmatrix} 0 \\ 0 \\ 0 \\ (E_{2,p_2} \gamma_{E_5,E_4,p_2} + \gamma_{E_5,E_4,p_1} t_{2,p_2 \rightarrow p_1}) + \gamma_{E_1,p_2} t_{1 \rightarrow 2,p_2 \rightarrow p_2} \\ 0 \end{pmatrix}_{E_2} . \quad (47)$$

The element $t_{2 \rightarrow 1,p_2 \rightarrow p_2}$ is responsible for heating up or cooling down of the localized state. We notice that all other eigenenergy vectors were not changed by the presence of non-zero elements $t_{2 \rightarrow 1,p_2 \rightarrow p_2} = t_{1 \rightarrow 2,p_2 \rightarrow p_2}^*$ in the Hamiltonian 45.

It may occur that potential minima (bottom) in position based qubit can have arbitrary depth so more than one eigenenergy state can be localized. The number of localized states can be arbitrary big both on the left and the right side. In considered example we have only localized on the right state. Localized states can be heated up or cool down so one localized state is transferring into another localized state in the same quantum well. In general k states (as $k = 2$ in reference to the matrix 48) can be localized on the right side among $k + m$ all energetic states (where $m = 4$ is number of delocalized eigenenergy states) so total number of Hamiltonian eigenenergy state $k + m$ is $4 + 2 = 6$.

$$\hat{H} = \begin{pmatrix} E_{2,p_1} & 0 & 0 & t_{2,p_1 \rightarrow p_2} & 0 & 0 \\ 0 & E_{3,p_1} & t_{3,p_1 \rightarrow p_2} & 0 & 0 & 0 \\ 0 & t_{3,p_2 \rightarrow p_1} & E_{3,p_2} & 0 & 0 & 0 \\ t_{2,p_2 \rightarrow p_1} & 0 & 0 & E_{2,p_2} & t_{1 \rightarrow 2,p_2 \rightarrow p_2} & t_{0 \rightarrow 2,p_2 \rightarrow p_2} \\ 0 & 0 & 0 & t_{2 \rightarrow 1,p_2 \rightarrow p_2} & E_{1,p_2} & t_{0 \rightarrow 1,p_2 \rightarrow p_2} \\ 0 & 0 & 0 & t_{2 \rightarrow 0,p_2 \rightarrow p_2} & t_{1 \rightarrow 0,p_2 \rightarrow p_2} & E_{0,p_2} \end{pmatrix} \quad (48)$$

We recognize that term the $t_{1 \rightarrow 0, p2 \rightarrow p2}$ is able to heat up and cool down the localized q-state between 0 and 1 energetic level in q-well p2 and term $t_{2 \rightarrow 0, p2 \rightarrow p2}$ is describing interaction between 0 and 2 energy level in q-well p2, while term $t_{2 \rightarrow 1, p2 \rightarrow p2}$ describes the interaction between 1st and 2nd energetic level in second quantum well p2.

Now to describe the situation of 3 localized states in the left well (associated with matrix coefficients in green) and 2 localized states in the right wells (associated with matrix coefficients in red) and 4 states that are delocalized so we are dealing with matrix of 9 states.

$$\hat{H} = \begin{pmatrix} E_{-1,p1} & t_{0 \rightarrow -1, p1 \rightarrow p1} & t_{1 \rightarrow -1, p1 \rightarrow p1} & 0 & 0 & 0 & 0 & 0 & 0 & t_{0 \rightarrow -1, p1 \rightarrow p2} \\ t_{-1 \rightarrow 0, p1 \rightarrow p1} & E_{0,p1} & t_{1 \rightarrow 0, p1 \rightarrow p1} & 0 & 0 & 0 & 0 & 0 & 0 & 0 \\ t_{-1 \rightarrow 1, p1 \rightarrow p1} & t_{0 \rightarrow 1, p1 \rightarrow p1} & E_{1,p1} & t_{2 \rightarrow 1, p1 \rightarrow p1} & 0 & 0 & 0 & 0 & 0 & 0 \\ 0 & 0 & t_{1 \rightarrow 2, p1 \rightarrow p1} & E_{2,p1} & 0 & 0 & t_{2, p1 \rightarrow p2} & 0 & 0 & 0 \\ 0 & 0 & 0 & 0 & E_{3,p1} & t_{3, p1 \rightarrow p2} & 0 & 0 & 0 & 0 \\ 0 & 0 & 0 & 0 & t_{3, p2 \rightarrow p1} & E_{3,p2} & 0 & 0 & 0 & 0 \\ 0 & 0 & 0 & t_{2, p2 \rightarrow p1} & 0 & 0 & E_{2,p2} & t_{1 \rightarrow 2, p2 \rightarrow p2} & t_{0 \rightarrow 2, p2 \rightarrow p2} & 0 \\ 0 & 0 & 0 & 0 & 0 & 0 & t_{2 \rightarrow 1, p2 \rightarrow p2} & E_{1,p2} & t_{0 \rightarrow 1, p2 \rightarrow p2} & 0 \\ t_{-1 \rightarrow 0, p2 \rightarrow p1} & 0 & 0 & 0 & 0 & 0 & t_{2 \rightarrow 0, p2 \rightarrow p2} & t_{1 \rightarrow 0, p2 \rightarrow p2} & E_{0,p2} & 0 \end{pmatrix}$$

Heating up and cooling down of the localized quantum state in the left q-well is controlled by Hamiltonian coefficients $t_{0 \rightarrow -1, p1 \rightarrow p1}$, $t_{1 \rightarrow 0, p1 \rightarrow p1}$, $t_{1 \rightarrow -1, p1 \rightarrow p1}$ and its conjugate counterparts $t_{-1 \rightarrow 0, p1 \rightarrow p1}$, $t_{0 \rightarrow 1, p1 \rightarrow p1}$, $t_{-1 \rightarrow 1, p1 \rightarrow p1}$. Moving delocalized q-state in the left q-well p1 into delocalized q-state in the left p2 well is by non-zero $t_{1 \rightarrow 2, p1 \rightarrow p1}$ and its conjugate $t_{2 \rightarrow 1, p1 \rightarrow p1}$ in orange color. From the point of view of q-mechanics it is also possible to transfer one q-state localized in the left q-well into the q-state localized in the right q-well. It is achieved by the non-zero coefficient $t_{0 \rightarrow -1, p1 \rightarrow p2}$ and its conjugate $t_{-1 \rightarrow 0, p2 \rightarrow p1}$ in brown color. All these transfer between states of different energies requires microwave field or AC voltage components. In case of matrix 9 by 9 we can spot $(9^2 - 9)/2$ processes of transfer from one energetic state into another energetic state in the same q-well or into opposite q-well. In general for a N by N matrix one has $(N^2 - N)/2$ such processes. More detailed knowledge about this processes might be only extracted from Schrodinger formalism in 1, 2 or 3 dimensions. In most general case in the case of system with 9 energetic levels are depicted in Fig. 6.

Now we are describing the most general situation for the system preserving 6 energy levels where position of potential minima and maxima can change in time so localized states can change into delocalized or reversely. It is thus describing the system is placed in outside time-dependent electromagnetic field of any dependence so the matrix of position-based qubit $\hat{H}(t)$ can be written as

$$\hat{H}(t) = \begin{pmatrix} E_{1,p1} & t_{2 \rightarrow 1,p1 \rightarrow p1} & t_{3 \rightarrow 1,p1 \rightarrow p1} & t_{3 \rightarrow 1,p2 \rightarrow p1} & t_{2 \rightarrow 1,p2 \rightarrow p1} & t_{1,p2 \rightarrow p1} \\ t_{1 \rightarrow 2,p1 \rightarrow p1} & E_{2,p1} & t_{3 \rightarrow 2,p1 \rightarrow p1} & t_{3 \rightarrow 2,p2 \rightarrow p1} & t_{2,p2 \rightarrow p1} & t_{1 \rightarrow 2,p2 \rightarrow p1} \\ t_{1 \rightarrow 3,p1 \rightarrow p1} & t_{2 \rightarrow 3,p1 \rightarrow p1} & E_{3,p1} & t_{3,p2 \rightarrow p1} & t_{2 \rightarrow 3,p2 \rightarrow p1} & t_{1 \rightarrow 3,p2 \rightarrow p1} \\ t_{1 \rightarrow 3,p1 \rightarrow p2} & t_{2 \rightarrow 3,p1 \rightarrow p2} & t_{3,p1 \rightarrow p2} & E_{3,p2} & t_{2 \rightarrow 3,p2 \rightarrow p2} & t_{1 \rightarrow 3,p2 \rightarrow p2} \\ t_{1 \rightarrow 2,p1 \rightarrow p2} & t_{2,p1 \rightarrow p2} & t_{3 \rightarrow 2,p1 \rightarrow p2} & t_{3 \rightarrow 2,p2 \rightarrow p2} & E_{2,p2} & t_{1 \rightarrow 2,p2 \rightarrow p2} \\ t_{1,p1 \rightarrow p2} & t_{2 \rightarrow 1,p1 \rightarrow p2} & t_{3 \rightarrow 1,p1 \rightarrow p2} & t_{3 \rightarrow 1,p2 \rightarrow p2} & t_{2 \rightarrow 1,p2 \rightarrow p2} & E_{1,p2} \end{pmatrix}_x \quad (49)$$

Such matrix is Hermitian so $t_{k \rightarrow s,pk \rightarrow pl}^* = t_{k \rightarrow s,pk \rightarrow pl}$ for k and s among 1, 2 and 3 and p_k and p_l having value p_1 (presence of electron in left quantum well) or p_2 (presence of electron in right quantum well) and having real-valued diagonal elements. The meaning of non-diagonal coefficients is non-trivial.

In the general case the eigenvalues of described matrix cannot be determined analytically unless there are some preimposed symmetries as for example $E_{k,p1} = E_{k,p2}$ for $k = 1, 2$ and 3 and in such case eigenvalues are determined by the roots of polynomial of 3rd order in an analytical way. Final reasoning can be conducted also for the system with 8 energetic levels when one deals with roots of polynomial of 4th order. By proper electromagnetic engineering the system with 6 energetic levels can be controlled by $((36 - 6)/2) + 6 = 15 + 6 = 21$ time dependent parameters. In most general case the system of position based qubit having 2 coupled quantum dots with 6 energy levels can be parametrized by 36 real valued functions that are time-dependent. Quite obviously the same system with $2N$ energetic levels can be parametrized by $(2N)^2$ real valued functions under the assumption that occupancy of electron is distributed among $2N$ energetic levels. We introduce the notation $\gamma_{1,p1} = \gamma_{E1-E2,p1}$, $\gamma_{2,p1} = \gamma_{E3-E4,p1}$, $\gamma_{3,p1} = \gamma_{E5-E6,p1}$, $\gamma_{3,p2} = \gamma_{E5-E6,p2}$, $\gamma_{2,p2} = \gamma_{E3-E4,p2}$, $\gamma_{1,p2} = \gamma_{E1-E2,p2}$. The last matrix can be written in energy bases by using the last matrix of Hamiltonian with identity $\hat{H}(t) |\psi\rangle(t) =$

$$\begin{pmatrix} E_1 & 0 & 0 & 0 & 0 & 0 \\ 0 & E_2 & 0 & 0 & 0 & 0 \\ 0 & 0 & E_3 & 0 & 0 & 0 \\ 0 & 0 & 0 & E_4 & 0 & 0 \\ 0 & 0 & 0 & 0 & E_5 & 0 \\ 0 & 0 & 0 & 0 & 0 & E_6 \end{pmatrix} \begin{pmatrix} \frac{1}{E_1} & 0 & 0 & 0 & 0 & 0 \\ 0 & \frac{1}{E_2} & 0 & 0 & 0 & 0 \\ 0 & 0 & \frac{1}{E_3} & 0 & 0 & 0 \\ 0 & 0 & 0 & \frac{1}{E_4} & 0 & 0 \\ 0 & 0 & 0 & 0 & \frac{1}{E_5} & 0 \\ 0 & 0 & 0 & 0 & 0 & \frac{1}{E_6} \end{pmatrix} \begin{pmatrix} E_{1,p1} & t_{2 \rightarrow 1,p1 \rightarrow p1} & t_{3 \rightarrow 1,p1 \rightarrow p1} & t_{3 \rightarrow 1,p2 \rightarrow p1} & t_{2 \rightarrow 1,p2 \rightarrow p1} & t_{1,p2 \rightarrow p1} \\ t_{1 \rightarrow 2,p1 \rightarrow p1} & E_{2,p1} & t_{3 \rightarrow 2,p1 \rightarrow p1} & t_{3 \rightarrow 2,p2 \rightarrow p1} & t_{2,p2 \rightarrow p1} & t_{1 \rightarrow 2,p2 \rightarrow p1} \\ t_{1 \rightarrow 3,p1 \rightarrow p1} & t_{2 \rightarrow 3,p1 \rightarrow p1} & E_{3,p1} & t_{3,p2 \rightarrow p1} & t_{2 \rightarrow 3,p2 \rightarrow p1} & t_{1 \rightarrow 3,p2 \rightarrow p1} \\ t_{1 \rightarrow 3,p1 \rightarrow p2} & t_{2 \rightarrow 3,p1 \rightarrow p2} & t_{3,p1 \rightarrow p2} & E_{3,p2} & t_{2 \rightarrow 3,p2 \rightarrow p2} & t_{1 \rightarrow 3,p2 \rightarrow p2} \\ t_{1 \rightarrow 2,p1 \rightarrow p2} & t_{2,p1 \rightarrow p2} & t_{3 \rightarrow 2,p1 \rightarrow p2} & t_{3 \rightarrow 2,p2 \rightarrow p2} & E_{2,p2} & t_{1 \rightarrow 2,p2 \rightarrow p2} \\ t_{1,p1 \rightarrow p2} & t_{2 \rightarrow 1,p1 \rightarrow p2} & t_{3 \rightarrow 1,p1 \rightarrow p2} & t_{3 \rightarrow 1,p2 \rightarrow p2} & t_{2 \rightarrow 1,p2 \rightarrow p2} & E_{1,p2} \end{pmatrix}_x$$

$$\begin{aligned}
 & + E_6 \left(\begin{array}{c} 0 \\ 0 \\ 0 \\ 0 \\ 0 \\ \frac{t_1 \rho_1 - \rho_2}{E_6} \gamma_{1,\rho_1}(t) + \frac{t_2 - 1, \rho_1 - \rho_2}{E_6} \gamma_{2,\rho_1}(t) + \frac{t_3 - 1, \rho_1 - \rho_2}{E_6} \gamma_{3,\rho_1}(t) + \frac{t_3 - 1, \rho_2 - \rho_2}{E_6} \gamma_{3,\rho_2}(t) + \frac{t_2 - 1, \rho_2 - \rho_2}{E_6} \gamma_{2,\rho_2}(t) + \frac{E_1 \rho_2}{E_6} \gamma_{1,\rho_2}(t) \end{array} \right)_E = \\
 & = E_1(t) c_{E_1,t} |E_1, t\rangle + E_2(t) c_{E_2,t} |E_2, t\rangle + E_3(t) c_{E_3,t} |E_3, t\rangle \\
 & + E_4(t) c_{E_4,t} |E_4, t\rangle \\
 & + E_5(t) c_{E_5,t} |E_5, t\rangle + E_6(t) c_{E_6,t} |E_6, t\rangle = \\
 & = \langle E_1(t) |E_1, t\rangle \langle E_1, t| + E_2(t) |E_2, t\rangle \langle E_2, t| \\
 & + E_3(t) |E_3, t\rangle \langle E_3, t| \\
 & + E_4(t) |E_4, t\rangle \langle E_4, t| + E_5(t) |E_5, t\rangle \langle E_5, t| + \\
 & E_6(t) |E_6, t\rangle \langle E_6, t| \rangle |\psi, t\rangle. \tag{50}
 \end{aligned}$$

where $|E_k, t\rangle \langle E_k, t|$ is projector on energy eigenstate E_k and $\langle E_k, t| |E_l, t\rangle = \delta_{k,l}$ and

$$\begin{aligned}
 \hat{E} & = \begin{pmatrix} E_1 & 0 & 0 & 0 & 0 & 0 \\ 0 & E_2 & 0 & 0 & 0 & 0 \\ 0 & 0 & E_3 & 0 & 0 & 0 \\ 0 & 0 & 0 & E_4 & 0 & 0 \\ 0 & 0 & 0 & 0 & E_5 & 0 \\ 0 & 0 & 0 & 0 & 0 & E_6 \end{pmatrix}, |E_1, t\rangle = \begin{pmatrix} 1 \\ 0 \\ 0 \\ 0 \\ 0 \\ 0 \end{pmatrix}, \\
 |E_1, t\rangle \langle E_1, t| & = \begin{pmatrix} 1 & 0 & 0 & 0 & 0 & 0 \\ 0 & 0 & 0 & 0 & 0 & 0 \\ 0 & 0 & 0 & 0 & 0 & 0 \\ 0 & 0 & 0 & 0 & 0 & 0 \\ 0 & 0 & 0 & 0 & 0 & 0 \\ 0 & 0 & 0 & 0 & 0 & 0 \end{pmatrix}, \\
 |E_2, t\rangle & = \begin{pmatrix} 0 \\ 1 \\ 0 \\ 0 \\ 0 \\ 0 \end{pmatrix}, |E_2, t\rangle \langle E_2, t| = \begin{pmatrix} 0 & 0 & 0 & 0 & 0 & 0 \\ 0 & 1 & 0 & 0 & 0 & 0 \\ 0 & 0 & 0 & 0 & 0 & 0 \\ 0 & 0 & 0 & 0 & 0 & 0 \\ 0 & 0 & 0 & 0 & 0 & 0 \\ 0 & 0 & 0 & 0 & 0 & 0 \end{pmatrix}, \dots,
 \end{aligned}$$

$$|E_6, t\rangle = \begin{pmatrix} 0 \\ 0 \\ 0 \\ 0 \\ 0 \\ 1 \end{pmatrix}, \quad |E_6, t\rangle \langle E_6, t| = \begin{pmatrix} 0 & 0 & 0 & 0 & 0 & 0 \\ 0 & 0 & 0 & 0 & 0 & 0 \\ 0 & 0 & 0 & 0 & 0 & 0 \\ 0 & 0 & 0 & 0 & 0 & 0 \\ 0 & 0 & 0 & 0 & 0 & 0 \\ 0 & 0 & 0 & 0 & 0 & 1 \end{pmatrix}. \quad (51)$$

It is worth noticing that having knowledge on all eigenvalues $E_1(t), \dots, E_N(t)$ with time we can determine the eigenenergy occupancy with time from position occupancy in unique way. From the above considerations the following relations takes place

$$\begin{pmatrix} \frac{E_{1,p1}}{E_1} & \frac{t_{2 \rightarrow 1,p1 \rightarrow p1}}{E_1} & \frac{t_{3 \rightarrow 1,p1 \rightarrow p1}}{E_1} & \frac{t_{3 \rightarrow 1,p2 \rightarrow p1}}{E_1} & \frac{t_{2 \rightarrow 1,p2 \rightarrow p1}}{E_1} & \frac{t_{1,p2 \rightarrow p1}}{E_1} \\ \frac{t_{1 \rightarrow 2,p1 \rightarrow p1}}{E_2} & \frac{E_{2,p1}}{E_2} & \frac{t_{3 \rightarrow 2,p1 \rightarrow p1}}{E_2} & \frac{t_{3 \rightarrow 2,p2 \rightarrow p1}}{E_2} & \frac{t_{2,p2 \rightarrow p1}}{E_2} & \frac{t_{1 \rightarrow 2,p2 \rightarrow p1}}{E_2} \\ \frac{t_{1 \rightarrow 3,p1 \rightarrow p1}}{E_3} & \frac{t_{2 \rightarrow 3,p1 \rightarrow p1}}{E_3} & \frac{E_{3,p1}}{E_3} & \frac{t_{3,p2 \rightarrow p1}}{E_3} & \frac{t_{2 \rightarrow 3,p2 \rightarrow p1}}{E_3} & \frac{t_{1 \rightarrow 3,p2 \rightarrow p1}}{E_3} \\ \frac{t_{1 \rightarrow 3,p1 \rightarrow p2}}{E_4} & \frac{t_{2 \rightarrow 3,p1 \rightarrow p2}}{E_4} & \frac{t_{3,p1 \rightarrow p2}}{E_4} & \frac{E_{3,p2}}{E_4} & \frac{t_{2 \rightarrow 3,p2 \rightarrow p2}}{E_4} & \frac{t_{1 \rightarrow 3,p2 \rightarrow p2}}{E_4} \\ \frac{t_{1 \rightarrow 2,p1 \rightarrow p2}}{E_5} & \frac{t_{2,p1 \rightarrow p2}}{E_5} & \frac{t_{3 \rightarrow 2,p1 \rightarrow p2}}{E_5} & \frac{t_{3 \rightarrow 2,p2 \rightarrow p2}}{E_5} & \frac{E_{2,p2}}{E_5} & \frac{t_{1 \rightarrow 2,p2 \rightarrow p2}}{E_5} \\ \frac{t_{1,p1 \rightarrow p2}}{E_6} & \frac{t_{2 \rightarrow 1,p1 \rightarrow p2}}{E_6} & \frac{t_{3 \rightarrow 1,p1 \rightarrow p2}}{E_6} & \frac{t_{3 \rightarrow 1,p2 \rightarrow p2}}{E_6} & \frac{t_{2 \rightarrow 1,p2 \rightarrow p2}}{E_6} & \frac{E_{1,p2}}{E_6} \end{pmatrix}_{E/x} \begin{pmatrix} \gamma_{E1-E2,p1}(t) \\ \gamma_{E3-E4,p1}(t) \\ \gamma_{E5-E6,p1}(t) \\ \gamma_{E5-E6,p2}(t) \\ \gamma_{E3-E4,p2}(t) \\ \gamma_{E1-E2,p2}(t) \end{pmatrix}_x \\ = \begin{pmatrix} c_{E1,p1}(t) \\ c_{E2,p1}(t) \\ c_{E3,p1}(t) \\ c_{E3,p2}(t) \\ c_{E2,p2}(t) \\ c_{E1,p2}(t) \end{pmatrix}_E = \hat{A}(t) \hat{\gamma}.$$

By proper controlling matrix in position representation we can achieved desired occupancy of energetic levels with time expressed by $c_{E1,p1}(t), \dots, c_{E1,p2}(t)$ coefficients. On another hand preimposing dependence of occupancy of energetic levels by quantum state expressed in $c_{E1,p1}(t), \dots, c_{E1,p2}(t)$ with time one can achieve desired dependence of electrons positions $\gamma_{E1,p1}(t), \dots, \gamma_{E1,p2}(t)$ by using relation $|\psi, t\rangle_x = \hat{\gamma}(t) = \hat{A}(t)^{-1} \hat{c}_E(t) = \hat{A}(t)^{-1} |\psi, t\rangle_E$.

7 Case of Electrostatic Qubit Interaction

We consider most minimalist model of electrostatically interacting two position-based qubits that are double quantum dots A (with nodes 1 and 2 and named as U-upper qubit) and B (with nodes 1' and 2' and named as L-lower qubit) with local confinement potentials as given in the right side of Fig. 2. By introducing notation $|1, 0\rangle_x = |1\rangle$, $|0, 1\rangle_x = |2\rangle$, $|1', 0'\rangle_x = |1'\rangle$, $|0', 1'\rangle_x = |2'\rangle$ the minimalistic Hamiltonian of the system of electrostatically interacting position based qubits can be written as

$$\hat{H} = (t_{s21}(t) |2\rangle \langle 1| + t_{s12}(t) |1\rangle \langle 2|) \hat{I}_b + (\hat{I}_a (t_{s2'1'}(t) |2'\rangle \langle 1'| + t_{s1'2'}(t) |2'\rangle \langle 1'|) +$$

$$\begin{aligned}
& + (E_{p1}(t) |1\rangle \langle 1| + E_{p2}(t) |2\rangle \langle 2|) \hat{I}_b + \hat{I}_a (E_{p1'}(t) |1'\rangle \langle 1'| + E_{p2'}(t) |2'\rangle \langle 2'|) + \\
& + \frac{q^2}{d_{11'}} |1, 1'\rangle \langle 1, 1'| + \frac{q^2}{d_{22'}} |2, 2'\rangle \langle 2, 2'| + \frac{q^2}{d_{12'}} |1, 2'\rangle \langle 1, 2'| + \frac{q^2}{d_{21'}} |2, 1'\rangle \langle 2, 1'| = \\
& H_{\text{kinetic1}} + H_{\text{pot1}} + H_{\text{kinetic2}} + H_{\text{pot2}} + H_{A-B}
\end{aligned} \tag{52}$$

described by parameters $E_{p1}(t)$, $E_{p2}(t)$, $E_{p1'}(t)$, $E_{p2'}(t)$, $t_{s12}(t)$, $t_{s1'2'}(t)$ and distances between nodes k and l' : $d_{11'}, d_{22'}, d_{21'}, d_{12}'$. In such case q-state of the system is given as

$$\begin{aligned}
|\psi, t\rangle = & \gamma_1(t) |1, 0\rangle_U |1, 0\rangle_L + \gamma_2(t) |1, 0\rangle_U |0, 1\rangle_L \\
& + \gamma_3(t) |0, 1\rangle_U |1, 0\rangle_L + \gamma_4(t) |0, 1\rangle_U |0, 1\rangle_L,
\end{aligned} \tag{53}$$

where normalization condition gives $|\gamma_1(t)|^2 + \dots + |\gamma_4(t)|^2$. Probability of finding electron in upper system at node 1 is by action of projector $\hat{P}_{1U} = |1, 0\rangle_U \langle 1, 0|_U + |1, 0\rangle_U \langle 0, 1|_U$ on q-state $\hat{P}_{1U} |\psi\rangle$ so it gives probability amplitude $|\gamma_1(t) + \gamma_3(t)|^2$. On the other hand probability of finding electron from qubit A (U) at node 2 and electron from qubit B(L) at node 1 is obtained by projection $\hat{P}_{2U,1L} = |0, 1\rangle_U \langle 1, 0|_L$ acting on q-state giving $\langle 0, 1|_U \langle 1, 0|_L |\psi\rangle$ that gives probability amplitude $|\gamma_3(t)|^2$. Referring to picture from Fig. 2 we set distances between nodes as $d_{11'} = d_{22'} = d_1$, $d_{12}' = d_{21'} = \sqrt{(a+b)^2 + d_1^2}$ and assume Coulomb electrostatic energy to be of the form $E_c(k, l) = \frac{q^2}{d_{kl}}$ and hence we obtain the matrix Hamiltonian given as $\hat{H}(t) =$

$$\begin{pmatrix}
E_{p1}(t) + E_{p1'}(t) + \frac{q^2}{d_1^2} & t_{s1'2'}(t) & t_{s12}(t) & 0 \\
t_{s1'2'}(t)^* & E_{p1}(t) + E_{p2'}(t) + \frac{q^2}{\sqrt{(d_1)^2 + (b+a)^2}} & 0 & t_{s12}(t) \\
t_{s12}^*(t) & 0 & E_{p2}(t) + E_{p1'}(t) + \frac{q^2}{\sqrt{(d_1)^2 + (b+a)^2}} & t_{s1'2'}(t) \\
0 & t_{s12}^*(t) & t_{s1'2'}(t)^* & E_{p2}(t) + E_{p2'}(t) + \frac{q^2}{d_1^2}
\end{pmatrix} \tag{54}$$

We can introduce notation $E_{c1} = \frac{q^2}{d_1^2}$ and $E_{c2} = \frac{q^2}{\sqrt{d_1^2 + (b+a)^2}}$. In most general case of 2 qubit electrostatic interaction one of which has 4 different Coulomb terms on matrix diagonal $E_{c1} = \frac{q^2}{d_{11'}}$, $E_{c2} = \frac{q^2}{d_{12}'}$, $E_{c3} = \frac{q^2}{d_{21'}}$, $E_{c4} = \frac{q^2}{d_{22'}}$ and $|\psi, t\rangle = \hat{U}(t, t_0) |\psi, t_0\rangle$. We introduce $q_1 = E_{p1}(t) + E_{p1'}(t) + E_{c11'}$, $q_2 = E_{p1}(t) + E_{p2'}(t) + E_{c12'}$, $q_3 = E_{p2}(t) + E_{p1'}(t) + E_{c21'}$, $q_4 = E_{p2}(t) + E_{p2'}(t) + E_{c22'}$ and in such case by using Formula (8) one can decompose 2 particle Hamiltonian 54 as

$$\begin{aligned}
\hat{H} = & \left[\frac{(q_1 + q_2 + q_3 + q_4)}{4} \sigma_0 \times \sigma_0 + \frac{(q_1 - q_2 + q_3 - q_4)}{4} \sigma_0 \right. \\
& \times \sigma_3 + \frac{(q_1 + q_2 - q_3 - q_4)}{4} \sigma_3 \times \sigma_0 + \\
& \left. \frac{(q_1 - q_2 - q_3 + q_4)}{4} \sigma_3 \times \sigma_3 + t_{sr1}(t) \sigma_0 \times \sigma_1 - t_{s11}(t) \sigma_0 \right]
\end{aligned}$$

$$\times \sigma_2 + t_{sr2}(t)\sigma_1 \times \sigma_0 - t_{si2}(t)\sigma_2 \times \sigma_0 \quad (55)$$

A very similar procedure is for the case of 3 or N interacting particles so one deals with tensor product of 3 or N Pauli matrices. In order to simplify representation of unitary matrix describing physical system of 2 particles evolution with time it is helpful to define $Q_1(t) = \int_{t_0}^t (E_{p1}(t') + E_{p1'}(t') + E_{c11'})dt'$, $Q_2(t) = \int_{t_0}^t (E_{p1}(t') + E_{p2'}(t') + E_{c12'})dt'$, $Q_3(t) = \int_{t_0}^t (E_{p2}(t') + E_{p1'}(t') + E_{c21'})dt'$, $Q_4(t) = \int_{t_0}^t (E_{p2}(t') + E_{p2'}(t') + E_{c22'})dt'$ and $TR1(t) = \int_{t_0}^t dt' t_{s1r}(t')$, $TI1(t) = \int_{t_0}^t dt' t_{s1i}(t')$. We consider the situation when there is no hopping between q-wells $t_{s2} = 0$ so, the second particle is localized among two quantum wells and first particle can move freely among 2 q-wells. We obtain the following unitary matrix evolution with time with following $\hat{U}(t, t_0)_{1,2} = \hat{U}(t, t_0)_{1,4} = 0 = \hat{U}(t, t_0)_{2,3} = \hat{U}_{3,4}$ and

$$\begin{aligned} \hat{U}(t, t_0)_{1,1} = & \frac{1}{2\sqrt{(Q_1(t) - Q_3(t))^2 + 4(TR_1(t)^2 + TI_1(t)^2)}} \\ & \left[Q_1(t) \left(-e^{i\hbar\sqrt{(Q_1(t)-Q_3(t))^2+4(TR_1(t)^2+TI_1(t)^2)}} \right) \right. \\ & + \left(\sqrt{|Q_1(t) - Q_3(t)|^2 + 4(TR_1(t)^2 + TI_1(t)^2)} + Q_3(t) \right) \\ & \times \left(-e^{i\hbar\sqrt{(Q_1(t)-Q_3(t))^2+4(TR_1(t)^2+TI_1(t)^2)}} \right) + \\ & \left. \sqrt{(Q_1(t) - Q_3(t))^2 + 4(TR_1(t)^2 + TI_1(t)^2)} \right. \\ & \left. + (Q_1(t) - Q_3(t)) e^{-\frac{1}{2}i\hbar\left(\sqrt{|\int_{t_0}^t dt'(q_1(t')-q_3(t'))|^2+4(t_{s1r}^2+t_{s1i}^2)}+(Q_1(t)+Q_3(t))\right)} \right] \quad (56) \end{aligned}$$

$$\hat{U}(t, t_0)_{1,3} = \frac{2(TI_1(t) - iTR_1(t))e^{-\frac{1}{2}(Q_1(t)+Q_3(t))i\hbar} \sin\left(\frac{1}{2}\hbar\sqrt{|Q_1(t) - Q_3(t)|^2 + 4(TR_1(t)^2 + TI_1(t)^2)}\right)}{\sqrt{|Q_1(t) - Q_3(t)|^2 + 4(TR_1(t)^2 + TI_1(t)^2)}}. \quad (57)$$

$$\begin{aligned} \hat{U}(t, t_0)_{2,2} = & \left[e^{\left(\frac{1}{2}i\hbar\left(\sqrt{(Q_2(t)-Q_4(t))^2+4(TR_1(t)^2+TI_1(t)^2)}-(Q_2(t)+Q_4(t))\right)\right)} \times \right. \\ & \times \frac{\left(\sqrt{(Q_2(t) - Q_4(t))^2 + 4(TR_1(t)^2 + TI_1(t)^2)} - Q_2(t) + Q_4(t)\right)}{2\sqrt{(Q_2 - Q_4)^2 + 4(TR_1(t)^2 + TI_1(t)^2)}} \\ & \left. - e^{\left(\frac{1}{2}i\hbar\left(-\sqrt{(Q_2(t)-Q_4(t))^2+4(TR_1(t)^2+TI_1(t)^2)}-(Q_2(t)+Q_4(t))\right)\right)} \times \right. \end{aligned}$$

$$\times \frac{\left(-\sqrt{(\mathcal{Q}_2(t) - \mathcal{Q}_4(t))^2 + 4(TR_1(t)^2 + TI_1(t)^2)} - \mathcal{Q}_2(t) + \mathcal{Q}_4(t)\right)}{2\sqrt{(\mathcal{Q}_2 - \mathcal{Q}_4)^2 + 4(TR_1(t)^2 + TI_1(t)^2)}} \quad (58)$$

$$\begin{aligned} \hat{U}(t, t_0)_{3,3} = & \frac{\exp\left(-\frac{1}{2}i\hbar\left(\sqrt{(\mathcal{Q}_1(t) - \mathcal{Q}_3(t))^2 + 4(TR_1(t)^2 + TI_1(t)^2)} + \mathcal{Q}_1(t) + \mathcal{Q}_3(t)\right)\right)}{2\sqrt{(\mathcal{Q}_1(t) - \mathcal{Q}_3(t))^2 + 4(TR_1(t)^2 + TI_1(t)^2)}} \times \\ & \left[\mathcal{Q}_1(t) \left(-1 + e^{i\hbar\sqrt{(\mathcal{Q}_1(t) - \mathcal{Q}_3(t))^2 + 4(TR_1(t)^2 + TI_1(t)^2)}}\right) + \right. \\ & \left. \left(\sqrt{(\mathcal{Q}_1(t) - \mathcal{Q}_3(t))^2 + 4(TR_1(t)^2 + TI_1(t)^2)} - \mathcal{Q}_3\right) \right. \\ & \left. e^{i\hbar\sqrt{(\mathcal{Q}_1(t) - \mathcal{Q}_3(t))^2 + 4(TR_1(t)^2 + TI_1(t)^2)}} + \right. \\ & \left. + \sqrt{(\mathcal{Q}_1(t) - \mathcal{Q}_3(t))^2 + 4(TR_1(t)^2 + TI_1(t)^2)} + \mathcal{Q}_3(t) \right] \quad (59) \end{aligned}$$

$$\begin{aligned} \hat{U}(t, t_0)_{4,4} = & \frac{\exp\left(-\frac{1}{2}i\hbar\left(\sqrt{(\mathcal{Q}_2(t) - \mathcal{Q}_4(t))^2 + 4(TR_1(t)^2 + TI_1(t)^2)} + \mathcal{Q}_2(t) + \mathcal{Q}_4(t)\right)\right)}{2\sqrt{(\mathcal{Q}_2(t) - \mathcal{Q}_4(t))^2 + 4(TR_1(t)^2 + TI_1(t)^2)}} \times \\ & \times \left[\mathcal{Q}_2(t) \left(-1 + e^{i\hbar\sqrt{(\mathcal{Q}_2(t) - \mathcal{Q}_4(t))^2 + 4(TR_1(t)^2 + TI_1(t)^2)}}\right) + \right. \\ & + \left(\sqrt{(\mathcal{Q}_2(t) - \mathcal{Q}_4(t))^2 + 4(TR_1(t)^2 + TI_1(t)^2)} - \mathcal{Q}_4(t)\right) \\ & e^{i\hbar\sqrt{(\mathcal{Q}_2(t) - \mathcal{Q}_4(t))^2 + 4(TR_1(t)^2 + TI_1(t)^2)}} + \\ & \left. \sqrt{(\mathcal{Q}_2(t) - \mathcal{Q}_4(t))^2 + 4(TR_1(t)^2 + TI_1(t)^2)} + \mathcal{Q}_4(t) \right] \end{aligned}$$

$$\hat{U}(t, t_0)_{2,4} = \frac{2(TI_1(t) - iTR_1(t))e^{-\frac{1}{2}i\hbar(\mathcal{Q}_2(t) + \mathcal{Q}_4(t))} \sin\left(\frac{1}{2}\hbar\sqrt{(\mathcal{Q}_2(t) - \mathcal{Q}_4(t))^2 + 4(TR_1(t)^2 + TI_1(t)^2)}\right)}{\sqrt{(\mathcal{Q}_2(t) - \mathcal{Q}_4(t))^2 + 4(TR_1(t)^2 + TI_1(t)^2)}} \quad (60)$$

The example of function dependence of eigenenergy spectra of 2 electrostatically interacting qubits on distance is given by Fig. 6.

An important observation is that any element of matrix $\hat{H}(t')$ for $t' \in (t_0, t)$ denoted as $H_{k,l}(t')$ is transferred to element $\hat{U}_{k,l}(t, t_0) = e^{\frac{1}{\hbar} \int_{t_0}^t dt' (H_{k,l}(t'))}$ of matrix $\hat{U}(t, t_0)$. We can easily generalize the presented reasoning for the system of N electrostatically coupled electrons confined by some local potentials. However we need to know the position dependent Hamiltonian eigenstate at the initial time t_0 . In case $N > 2$ finding such eigenstate is the numerical problem since analytical solutions for roots of polynomials of one variable for higher order than 4 does not exist. Using numerical eigenstate at time instance t_0 we can compute the system quantum

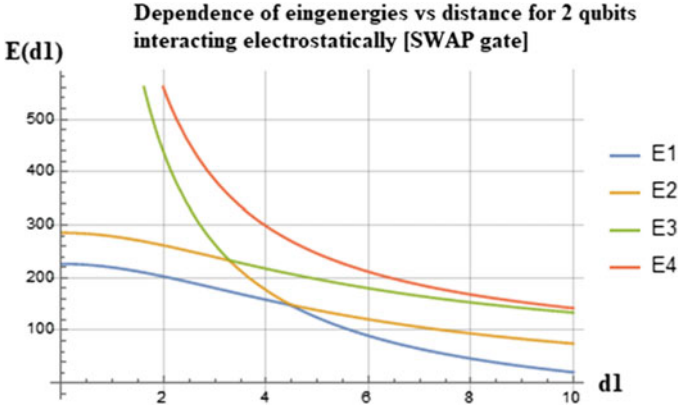


Fig. 6 Case of dependence of energy spectra on the distance d_1 for the case of 2 electrostatically interacting qubits from Fig. 2

dynamics in analytical way. This give us a strong and relatively simple mathematical tool giving full determination of quantum dynamical state at the any instance of time. The act of measurement on position based qubit is represented by the operator $P_{Left} = |1, 0\rangle_{E_1, E_2} \langle 1, 0|_{E_1, E_2}$ and $P_{Right} = |0, 1\rangle_{E_1, E_2} \langle 0, 1|_{E_1, E_2}$.

7.1 Simplified Picture of Symmetric Q-Swap Gate

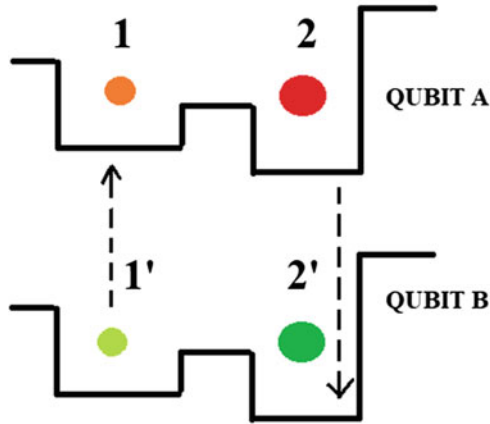
Now we need to find a system 4 eigenvalues and eigenstates (4 orthogonal 4-dimensional vectors) so we are dealing with a matrix eigenvalue problem) what is the subject of classical algebra. Let us assume that 2 double quantum dot systems are symmetric and biased by the same voltages generating potential bottoms V_s so we have $E_{p1} = E_{p2} = E_{p1'} = E_{p2'} = E_p = V_s$ and that $t_{s12} = t_{s1'2'} = t_s$. Denoting $E_c(1, 1') = E_c(2, 2') = E_{c1}$ and $E_c(1, 2') = E_c(2, 1') = E_{c2}$ we are obtaining 4 orthogonal Hamiltonian eigenvectors

$$\begin{aligned}
 |E_1\rangle &= \begin{pmatrix} -1 \\ 0 \\ 0 \\ +1 \end{pmatrix} = -|1, 0\rangle_U |1, 0\rangle_L + |0, 1\rangle_U |0, 1\rangle_L \\
 &\neq (a_1 |1, 0\rangle_U + a_2 |0, 1\rangle_U)(a_3 |1, 0\rangle_U + a_4 |0, 1\rangle_U), \quad (61)
 \end{aligned}$$

$$|E_2\rangle = \begin{pmatrix} 1 \\ 0 \\ 0 \\ -1 \end{pmatrix} = |1, 0\rangle_U |0, 1\rangle_L - |0, 1\rangle_U |1, 0\rangle_L$$

Fig. 7 Scheme of renormalization in the system of coupled qubits

Oscillating charge in qubit A brings phase imprint on qubit B and reversely.



Qubit B deforms effective potential affecting qubit A and reversely !!! (->renormalization of hopping term and localization energy in self-consistent treatment).

$$\neq (a_1 |1, 0\rangle_U + a_2 |0, 1\rangle_U)(a_3 |1, 0\rangle_U + a_4 |0, 1\rangle_U). \tag{62}$$

We observe that two first energetic states are degenerated so the same quantum state corresponds to 2 different eigenenergies E_1 and E_2 . This degeneracy is non-present if we come back to Schrodinger picture and observe that localized energy and hopping terms for one particle are depending on another particle presence that will bring renormalization of wavevectors. Situation is depicted in Fig.7. Degeneracy of eigenstates is lifted if we set $E_{p1}(|\psi(1')|^2, |\psi(2')|^2)$, $E_{p2}(|\psi(1')|^2, |\psi(1)|^2)$, $E_{p1'}(|\psi(1)|^2, |\psi(2)|^2)$, $E_{p2'}(|\psi(1)|^2, |\psi(1)|^2)$ and $t_{1\rightarrow 2}(|\psi(1')|^2, |\psi(2')|^2)$, $t_{1'\rightarrow 2'}(|\psi(1')|^2, |\psi(2')|^2)$.

The same argument is for another wavevectors as given below.

$$\begin{aligned} |E_{3(4)}\rangle &= \begin{pmatrix} 1 \\ \mp \frac{4t_s}{\pm(-E_{c1}+E_{c2})+\sqrt{(E_{c1}-E_{c2})^2+16t_s^2}} \\ \mp \frac{4t_s}{\pm(-E_{c1}+E_{c2})+\sqrt{(E_{c1}-E_{c2})^2+16t_s^2}} \\ 1 \end{pmatrix} \\ &= |1, 0\rangle_U |1, 0\rangle_L + |0, 1\rangle_U |0, 1\rangle_L \\ &+ c(|1, 0\rangle_U |0, 1\rangle_L + |0, 1\rangle_U |1, 0\rangle_L) = \\ &= (|1, 0\rangle_U + |0, 1\rangle_U)(|1, 0\rangle_L + |0, 1\rangle_L) \end{aligned}$$

$$\begin{aligned}
& + (c - 1)(|1, 0\rangle_U |0, 1\rangle_L + |0, 1\rangle_U |1, 0\rangle_L) \\
& \neq (a_1 |1, 0\rangle_U + a_2 |0, 1\rangle_U)(a_3 |1, 0\rangle_U + a_4 |0, 1\rangle_U), \tag{63}
\end{aligned}$$

where $c = \mp \frac{4t_s}{\pm(-E_{c1}+E_{c2})+\sqrt{(E_{c1}-E_{c2})^2+16t_s^2}}$ First two $|E_1\rangle$ and $|E_2\rangle$ energy eigenstates are always entangled, while $|E_3\rangle$ and $|E_4\rangle$ eigenenergies are only partially entangled if $\mp \frac{4t_s}{\pm(-E_{c1}+E_{c2})+\sqrt{(E_{c1}-E_{c2})^2+16t_s^2}} \neq 1$. If $c = 1 = \mp \frac{4t_s}{\pm(-E_{c1}+E_{c2})+\sqrt{(E_{c1}-E_{c2})^2+16t_s^2}}$ last two energy eigenstates are not entangled. The situation of $c = 1$ takes place when $E_{c1} = E_{c2}$ so when two qubits are infinitely far away so when they are electrostatically decoupled. Situation of $c=0$ is interesting because it means that $|E_3\rangle$ and $|E_4\rangle$ are maximally entangled and it occurs when $t_s = 0$ so when two electrons are maximally localized in each of the qubit so there is no hopping between left and right well.

The obtained eigenenergy states correspond to 4 eigenenergies

$$\begin{aligned}
E_1 &= E_{c1} + 2V_s, E_2 = E_{c2} + 2V_s, E_1 > E_2 \\
E_3 &= \frac{1}{2}((E_{c1} + E_{c2}) - \sqrt{(E_{c1} - E_{c2})^2 + 16t_s^2} + 4V_s) = \\
&= \frac{1}{2}((q^2(\frac{1}{d_1} + \frac{1}{\sqrt{d_1^2 + (a+b)^2}})) \\
&\quad - \sqrt{(q^2(\frac{1}{d_1} - \frac{1}{\sqrt{d_1^2 + (a+b)^2}}))^2 + 16t_s^2 + 4V_s}), \\
E_4 &= \frac{1}{2}((E_{c1} + E_{c2}) + \sqrt{(E_{c1} - E_{c2})^2 + 16t_s^2} + 4V_s) = \\
&= \frac{1}{2}((q^2(\frac{1}{d_1} + \frac{1}{\sqrt{d_1^2 + (a+b)^2}}) \\
&\quad + \sqrt{(q^2(\frac{1}{d_1} - \frac{1}{\sqrt{d_1^2 + (a+b)^2}}))^2 + 16t_s^2 + 4V_s}), E_4 > E_3. \tag{64}
\end{aligned}$$

We also notice that the eigenenergy states $|E_1\rangle, |E_2\rangle, |E_3\rangle, |E_4\rangle$ do not have its classical counterpart since upper electron exists at both positions 1 and 2 and lower electron exists at both positions at the same time. We observe that when distance between two systems of double quantum dots goes into infinity the energy difference between quantum state corresponding to $|E_3\rangle$ and $|E_4\rangle$ goes to zero. This makes those two entangled states degenerated.

Normalized 4 eigenvectors of 2 interacting qubits in SWAP Q-Gate configuration are of the following form

$$\begin{aligned}
 |E_1\rangle_n &= \frac{1}{\sqrt{\left(8\left(\frac{t_{sr1}-t_{sr2}}{\sqrt{(E_{c1}-E_{c2})^2+4(t_{sr1}-t_{sr2})^2-E_{c1}+E_{c2}}}\right)\right)^2+2}} \\
 &\quad \left(\begin{array}{c} -1, \\ \frac{2(t_{sr1}-t_{sr2})}{\sqrt{(E_{c1}-E_{c2})^2+4(t_{sr1}-t_{sr2})^2-E_{c1}+E_{c2}}}, \\ \frac{2(t_{sr1}-t_{sr2})}{\sqrt{(E_{c1}-E_{c2})^2+4(t_{sr1}-t_{sr2})^2-E_{c1}+E_{c2}}} \\ 1 \end{array} \right) \\
 &= \frac{1}{\sqrt{\left(8\left(\frac{t_{sr1}-t_{sr2}}{\sqrt{(E_{c1}-E_{c2})^2+4(t_{sr1}-t_{sr2})^2-E_{c1}+E_{c2}}}\right)\right)^2+2}} |E_1\rangle
 \end{aligned}$$

$$\begin{aligned}
 |E_2\rangle_n &= -\frac{1}{\sqrt{\left(8\left(\frac{t_{sr1}-t_{sr2}}{\sqrt{(E_{c1}-E_{c2})^2+4(t_{sr1}-t_{sr2})^2+E_{c1}-E_{c2}}}\right)\right)^2+2}} \\
 &\quad \left(\begin{array}{c} -1 \\ \frac{2(t_{sr1}-t_{sr2})}{\sqrt{(E_{c1}-E_{c2})^2+4(t_{sr1}-t_{sr2})^2+E_{c1}-E_{c2}}} \\ -\frac{2(t_{sr1}-t_{sr2})}{\sqrt{(E_{c1}-E_{c2})^2+4(t_{sr1}-t_{sr2})^2+E_{c1}-E_{c2}}} \\ 1 \end{array} \right) \\
 &= -\frac{1}{\sqrt{\left(8\left(\frac{t_{sr1}-t_{sr2}}{\sqrt{(E_{c1}-E_{c2})^2+4(t_{sr1}-t_{sr2})^2+E_{c1}-E_{c2}}}\right)\right)^2+2}} |E_2\rangle
 \end{aligned}$$

$$\begin{aligned}
 |E_3\rangle_n &= \frac{1}{\sqrt{\left(8\left(\frac{t_{sr1}+t_{sr2}}{\sqrt{(E_{c1}-E_{c2})^2+4(t_{sr1}+t_{sr2})^2-E_{c1}+E_{c2}}}\right)\right)^2+2}} \\
 &\quad \left(\begin{array}{c} 1, \\ \frac{2(t_{sr1}+t_{sr2})}{\sqrt{(E_{c1}-E_{c2})^2+4(t_{sr1}+t_{sr2})^2-E_{c1}+E_{c2}}}, \\ -\frac{2(t_{sr1}+t_{sr2})}{\sqrt{(E_{c1}-E_{c2})^2+4(t_{sr1}+t_{sr2})^2-E_{c1}+E_{c2}}}, \\ 1 \end{array} \right) \\
 &= \frac{1}{\sqrt{\left(8\left(\frac{t_{sr1}+t_{sr2}}{\sqrt{(E_{c1}-E_{c2})^2+4(t_{sr1}+t_{sr2})^2-E_{c1}+E_{c2}}}\right)\right)^2+2}} |E_3\rangle
 \end{aligned}$$

$$\begin{aligned}
|E_4\rangle_n &= \frac{1}{\sqrt{\left(8\left(\frac{t_{sr1}+t_{sr2}}{\sqrt{(E_{c1}-E_{c2})^2+4(t_{sr1}+t_{sr2})^2-E_{c2}+E_{c1}}}\right)\right)^2+2}} \\
&\quad \left(\begin{array}{c} 1, \\ \frac{2(t_{sr1}+t_{sr2})}{\sqrt{(E_{c1}-E_{c2})^2+4(t_{sr1}+t_{sr2})^2-E_{c1}-E_{c2}}}, \\ \frac{2(t_{sr1}+t_{sr2})}{\sqrt{(E_{c1}-E_{c2})^2+4(t_{sr1}+t_{sr2})^2-E_{c1}-E_{c2}}}, \\ 1 \end{array}\right) \\
&= \frac{1}{\sqrt{\left(8\left(\frac{t_{sr1}+t_{sr2}}{\sqrt{(E_{c1}-E_{c2})^2+4(t_{sr1}+t_{sr2})^2-E_{c2}+E_{c1}}}\right)\right)^2+2}} |E_4\rangle.
\end{aligned}$$

We are obtaining simplifications after assuming $t_{sr1}(t) = t_{sr2}(t)$ so we obtain

$$|E_1\rangle_n = \frac{1}{\sqrt{2}} \begin{pmatrix} -1 \\ 0 \\ 0 \\ 1 \end{pmatrix}, |E_2\rangle_n = \frac{1}{\sqrt{2}} \begin{pmatrix} 1 \\ 0 \\ 0 \\ -1 \end{pmatrix}, \quad (65)$$

$$|E_3\rangle_n = \frac{1}{\sqrt{\left(\frac{4t_s}{(E_{c2}-E_{c1})+8t_s-\sqrt{(E_{c1}-E_{c2})^2+16t_s^2}}\right)^2+2}} \begin{pmatrix} \frac{1}{4t_s} \\ \frac{(-E_{c1}+E_{c2})+\sqrt{(E_{c1}-E_{c2})^2+16t_s^2}}{4t_s} \\ \frac{(-E_{c1}+E_{c2})+\sqrt{(E_{c1}-E_{c2})^2+16t_s^2}}{4t_s} \\ 1 \end{pmatrix}, \quad (66)$$

$$|E_4\rangle_n = \frac{1}{\sqrt{\left(\frac{4t_s}{(E_{c1}-E_{c2})+8t_s-\sqrt{(E_{c1}-E_{c2})^2+16t_s^2}}\right)^2+2}} \begin{pmatrix} \frac{1}{4t_s} \\ \frac{(E_{c1}-E_{c2})+\sqrt{(E_{c1}-E_{c2})^2+16t_s^2}}{4t_s} \\ \frac{(E_{c1}-E_{c2})+\sqrt{(E_{c1}-E_{c2})^2+16t_s^2}}{4t_s} \\ 1 \end{pmatrix}. \quad (67)$$

It is worth mentioning that if we want to bring two electrostatic qubits to the entangled state we need to cool down (or heat-up) the system of interacting qubits to the energy E_1 (or to energy E_2). Otherwise we might also wish to disentangle two electrostatically interacting qubits. In such way one of the scenario is to bring the quantum system either to energy E_3 or E_4 so only partial entanglement will be achieved. Other scenario would be by bringing the occupancy of different energetic levels so net entanglement is reduced. One can use the entanglement witness in quantifying the existence of entanglement. One of the simplest q-state entanglement measurement is von Neumann entanglement entropy as it is expressed by Formula 185 that requires the knowledge of q-system density matrix with time. Such matrices can be obtained analytically for the case of 2 electrostatically interacting qubits.

It is interesting to spot the dependence of eigenenergies on distance between interacting qubits in the general case as it is depicted in Fig. 6. Now we are moving towards description the procedure of cooling down or heating up in Q-Swap gate. The procedure was discussed previously in the case of single qubit. Now it is exercised in the case of 2-qubit electrostatic interaction. For the sake of simplicity we will change the occupancy of the energy level E_1 and energy level level E_2 and keep the occupancy of other energy levels unchanged. We can write the $|E_2\rangle_n \langle E_1|_n$ as

$$\begin{aligned} |E_2\rangle_n \langle E_1|_n &= \frac{1}{2} \begin{pmatrix} 1 \\ 0 \\ 0 \\ -1 \end{pmatrix} (-1 \ 0 \ 0 \ 1) = \begin{pmatrix} -1 \ 0 \ 0 \ +1 \\ 0 \ 0 \ 0 \ 0 \\ 0 \ 0 \ 0 \ 0 \\ +1 \ 0 \ 0 \ -1 \end{pmatrix}, \\ |E_1\rangle_n \langle E_2|_n &= \frac{1}{2} \begin{pmatrix} -1 \\ 0 \\ 0 \\ 1 \end{pmatrix} (1 \ 0 \ 0 \ -1) = \begin{pmatrix} -1 \ 0 \ 0 \ +1 \\ 0 \ 0 \ 0 \ 0 \\ 0 \ 0 \ 0 \ 0 \\ +1 \ 0 \ 0 \ -1 \end{pmatrix}. \end{aligned} \quad (68)$$

We are introducing f_1 and f_2 real valued functions of small magnitude $f(t) = f_1(t) = f_2(t)$, ($|f_1|, |f_2| \ll (E_1, E_2)$) and we are considering the following Hamiltonian having H_0 that is time-independent and other part dependent part as

$$\begin{aligned} \hat{H} &= \hat{H}_0 + f_1(t) |E_2\rangle_n \langle E_1|_n + f_2(t) |E_1\rangle_n \langle E_2|_n = E_1 |E_1\rangle \langle E_1| + E_2 |E_2\rangle \langle E_2| \\ &\quad + f_1(t) |E_2\rangle_n \langle E_1|_n + f_2(t) |E_1\rangle_n \langle E_2|_n = \\ &= \begin{pmatrix} 2E_p + \frac{q^2}{d_1} & t_s & t_s & 0 \\ t_s^* & 2E_p + \frac{q^2}{\sqrt{(d_1)^2 + (b+a)^2}} & 0 & t_s \\ t_s^* & 0 & 2E_p + \frac{q^2}{\sqrt{(d_1)^2 + (b+a)^2}} & t_s \\ 0 & t_s^* & t_s^* & 2E_p + \frac{q^2}{d_1} \end{pmatrix} \\ &+ \frac{1}{2} \left(f_1 \begin{pmatrix} -1 & 0 & 0 & 1 \\ 0 & 0 & 0 & 0 \\ 0 & 0 & 0 & 0 \\ 1 & 0 & 0 & -1 \end{pmatrix} + f_2 \begin{pmatrix} -1 & 0 & 0 & 1 \\ 0 & 0 & 0 & 0 \\ 0 & 0 & 0 & 0 \\ 1 & 0 & 0 & -1 \end{pmatrix} \right) = \\ &= \begin{pmatrix} 2E_p + \frac{q^2}{d_1} - f(t) & t_s & t_s & f(t) \\ t_s^* & 2E_p + \frac{q^2}{\sqrt{(d_1)^2 + (b+a)^2}} & 0 & t_s \\ t_s^* & 0 & 2E_p + \frac{q^2}{\sqrt{(d_1)^2 + (b+a)^2}} & t_s \\ f(t) & t_s^* & t_s^* & 2E_p + \frac{q^2}{d_1} - f(t) \end{pmatrix} \\ &= \hat{H}(t)_{E_1 \leftrightarrow E_2, Q\text{-Swap}}. \end{aligned} \quad (69)$$

Initially we have established the following parameters of tight-binding model as $t_{s12} = t_{s1'2'}$. Changing t_{s12} into $t_{s12} - \frac{f(t)}{2}$ and $t_{s1'2'}$ into $t_{s1'2'} + \frac{f(t)}{2}$ while keeping other parameters of tight-binding model unchanged will result in the heating up (cooling down) of q-state of SWAP gate so population of energy level E_1 and E_2 are time-dependent, while populations of energy levels E_3 and E_4 are unchanged. Practically our results mean that we need to keep all our confinement potential bottoms constant, while changing barrier height between neighbouring q-dots in each of position based qubits. In such way we have established the procedure of perturbative cooling (heating up) of q-state. Non-perturbative approach is absolutely possible but it requires full knowledge of time dependent eigenstates and eigenenergies (solutions of eigenenergies of 4th order polynomial are very lengthy in general case) and therefore corresponding expression are very lengthy. In similar fashion we can heat up or cool down two coupled Single Electron Lines [3] as in Fig. 1 or any other q-system having N interacting q-bodies that can be represented by the system of N-interacting position based qubits.

7.2 Case of Density Matrix in Case of 2 Interacting Particles in Symmetric Case

We consider the simplifying matrix and highly symmetric matrix of the form

$$\begin{aligned} \hat{H}(t) &= \begin{pmatrix} 2E_p(t) + \frac{q^2}{d_1} = q_{11} + q_{22} & t_{sr2}(t) & t_{sr1}(t) & 0 \\ t_{sr2}(t) & 2E_p(t) + \frac{q^2}{\sqrt{(d_1)^2 + (b+a)^2}} = q_{11} - q_{22} & 0 & t_{sr1}(t) \\ t_{sr1}(t) & 0 & 2E_p(t) + \frac{q^2}{\sqrt{(d_1)^2 + (b+a)^2}} = q_{11} - q_{22} & t_{sr2}(t) \\ 0 & t_{sr1}(t) & t_{sr2}(t) & 2E_p(t) + \frac{q^2}{d_1} = q_{11} + q_{22} \end{pmatrix} = \\ &= \hat{\sigma}_0 \times \hat{\sigma}_0 q_{11} + \hat{\sigma}_3 \times \hat{\sigma}_3 q_{22} + t_{sr2}(t) \hat{\sigma}_0 \times \hat{\sigma}_3 + t_{sr1}(t) \hat{\sigma}_3 \times \hat{\sigma}_0 \end{aligned} \quad (70)$$

that has only real value components $H_{k,l}$ with $q_{11} = E_p(t) + \frac{E_{c1} + E_{c2}}{2} = E_p(t) + \frac{1}{2} \left(\frac{q^2}{d_1} + \frac{q^2}{\sqrt{(d_1)^2 + (b+a)^2}} \right)$, $q_{22} = \frac{E_{c1} - E_{c2}}{2} = \frac{1}{2} \left(\frac{q^2}{d_1} - \frac{q^2}{\sqrt{(d_1)^2 + (b+a)^2}} \right)$ and $Q_{11}(t) = \int_{t_0}^t dt' q_{11}(t')$, $Q_{22}(t) = \int_{t_0}^t dt' q_{22}(t')$, $TR1(t) = \int_{t_0}^t dt' t_{sr1}(t')$, $TR2(t) = \int_{t_0}^t dt' t_{sr2}(t')$. We obtain the density matrix

$$\hat{U}(t) = \begin{pmatrix} U_{1,1}(t) & U_{1,2}(t) & U_{1,3}(t) & U_{1,4}(t) \\ U_{2,1}(t) & U_{2,2}(t) & U_{2,3}(t) & U_{2,4}(t) \\ U_{3,1}(t) & U_{3,2}(t) & U_{3,3}(t) & U_{3,4}(t) \\ U_{4,1}(t) & U_{4,2}(t) & U_{4,3}(t) & U_{4,4}(t) \end{pmatrix},$$

$$\hat{\rho}(t) = \hat{U}(t, t_0) \begin{pmatrix} \rho_{1,1}(t_0) & \rho_{1,2}(t_0) & \rho_{1,3}(t_0) & \rho_{1,4}(t_0) \\ \rho_{2,1}(t_0) & \rho_{2,2}(t_0) & \rho_{2,3}(t_0) & \rho_{2,4}(t_0) \\ \rho_{3,1}(t_0) & \rho_{3,2}(t_0) & \rho_{3,3}(t_0) & \rho_{3,4}(t_0) \\ \rho_{4,1}(t_0) & \rho_{4,2}(t_0) & \rho_{4,3}(t_0) & \rho_{4,4}(t_0) \end{pmatrix} \hat{U}^{-1}(t, t_0) \quad (71)$$

with the following components of unitary matrix

$$U_{1,1}(t) = \frac{e^{-i\hbar Q_{11}(t)}}{2} \left[-i Q_{22}(t) \times \left(\frac{\sin\left(\hbar\sqrt{|Q_{22}(t)|^2 + (TR1(t) - TR2(t))^2}\right)}{\sqrt{|Q_{22}(t)|^2 + (TR1(t) - TR2(t))^2}} \right) + \frac{\sin\left(\hbar\sqrt{|Q_{22}(t)|^2 + (TR1(t) + TR2(t))^2}\right)}{\sqrt{|Q_{22}(t)|^2 + (TR1(t) + TR2(t))^2}} \right) + \cos\left(\hbar\sqrt{|Q_{22}(t)|^2 + (TR1(t) - TR2(t))^2}\right) + \cos\left(\hbar\sqrt{|Q_{22}(t)|^2 + (TR1(t) + TR2(t))^2}\right) \right]. \quad (72)$$

$$U_{1,2}(t) = \frac{ie^{-i\hbar Q_{11}(t)} \left((TR1(t) - TR2(t)) \sin\left(\hbar\sqrt{|Q_{22}(t)|^2 + (TR1(t) - TR2(t))^2}\right) \right)}{2\sqrt{|Q_{22}(t)|^2 + (TR1(t) - TR2(t))^2}} - \frac{(TR1(t) + TR2(t)) \sin\left(\hbar\sqrt{|Q_{22}(t)|^2 + (TR1(t) + TR2(t))^2}\right)}{2\sqrt{|Q_{22}(t)|^2 + (TR1(t) + TR2(t))^2}}, \quad (73)$$

$$U_{1,3}(t) = -ie^{-i\hbar Q_{11}(t)} \left[\frac{(TR1(t) - TR2(t)) \sin\left(\hbar\sqrt{|Q_{22}(t)|^2 + (TR1(t) - TR2(t))^2}\right)}{2\sqrt{|Q_{22}(t)|^2 + (TR1(t) - TR2(t))^2}} + \frac{(TR1(t) + TR2(t)) \sin\left(\hbar\sqrt{|Q_{22}(t)|^2 + (TR1(t) + TR2(t))^2}\right)}{2\sqrt{|Q_{22}(t)|^2 + (TR1(t) + TR2(t))^2}} \right]. \quad (74)$$

$$U_{1,4}(t) = \frac{1}{2} e^{-i\hbar Q_{11}(t)} \left[i Q_{22}(t) \left[\frac{\sin\left(\hbar\sqrt{|Q_{22}(t)|^2 + (TR1(t) - TR2(t))^2}\right)}{\sqrt{|Q_{22}(t)|^2 + (TR1(t) - TR2(t))^2}} \right) - \frac{\sin\left(\hbar\sqrt{|Q_{22}(t)|^2 + (TR1(t) + TR2(t))^2}\right)}{\sqrt{|Q_{22}(t)|^2 + (TR1(t) + TR2(t))^2}} \right] - \cos\left(\hbar\sqrt{|Q_{22}(t)|^2 + (TR1(t) - TR2(t))^2}\right)$$

$$+ \cos \left(\hbar \sqrt{|Q_{22}(t)|^2 + (TR1(t) + TR2(t))^2} \right) \Big] \quad (75)$$

$$U_{2,1}(t) = -\frac{i}{2} e^{-i\hbar Q_{11}(t)} \left[\frac{(TR1(t) - TR2(t)) \sin \left(\hbar \sqrt{|Q_{22}(t)|^2 + (TR1(t) - TR2(t))^2} \right)}{\sqrt{|Q_{22}(t)|^2 + (TR1(t) - TR2(t))^2}} \right. \\ \left. - \frac{(TR1(t) + TR2(t)) \sin \left(\hbar \sqrt{|Q_{22}(t)|^2 + (TR1(t) + TR2(t))^2} \right)}{\sqrt{|Q_{22}(t)|^2 + (TR1(t) + TR2(t))^2}} \right] \quad (76)$$

$$U_{2,2}(t) = \frac{1}{2} e^{-i\hbar Q_{11}(t)} \left[i Q_{22}(t) \left[\frac{\sin \left(\hbar \sqrt{|Q_{22}(t)|^2 + (TR1(t) - TR2(t))^2} \right)}{\sqrt{|Q_{22}(t)|^2 + (TR1(t) - TR2(t))^2}} + \right. \right. \\ \left. \frac{\sin \left(\hbar \sqrt{|Q_{22}(t)|^2 + (TR1(t) + TR2(t))^2} \right)}{\sqrt{|Q_{22}(t)|^2 + (TR1(t) + TR2(t))^2}} \right] + \\ + \cos \left(\hbar \sqrt{|Q_{22}(t)|^2 + (TR1(t) - TR2(t))^2} \right) \\ + \cos \left(\hbar \sqrt{|Q_{22}(t)|^2 + (TR1(t) + TR2(t))^2} \right) \Big] \quad (77)$$

$$U_{2,3}(t) = e^{-i\hbar Q_{11}(t)} \left[\frac{-Q_{22}(t) \sin \left(\hbar \sqrt{|Q_{22}(t)|^2 + (TR1(t) - TR2(t))^2} \right)}{2\sqrt{|Q_{22}(t)|^2 + (TR1(t) - TR2(t))^2}} + \right. \\ + \frac{Q_{22}(t) \sin \left(\hbar \sqrt{|Q_{22}(t)|^2 + (TR1(t) + TR2(t))^2} \right)}{2\sqrt{|Q_{22}(t)|^2 + (TR1(t) + TR2(t))^2}} + \\ \left. + \frac{i \cos \left(\hbar \sqrt{|Q_{22}(t)|^2 + (TR1(t) - TR2(t))^2} \right) - i \cos \left(\hbar \sqrt{|Q_{22}(t)|^2 + (TR1(t) + TR2(t))^2} \right)}{2} \right] \quad (78)$$

$$U_{2,4}(t) = -\frac{i e^{-i\hbar Q_{11}(t)} \left[(TR1(t) - TR2(t)) \sin \left(\hbar \sqrt{|Q_{22}(t)|^2 + (TR1(t) - TR2(t))^2} \right) \right]}{2\sqrt{|Q_{22}(t)|^2 + (TR1(t) - TR2(t))^2}} + \\ + \frac{(TR1(t) + TR2(t)) \sin \left(\hbar \sqrt{|Q_{22}(t)|^2 + (TR1(t) - TR2(t))^2} \right)}{2\sqrt{|Q_{22}(t)|^2 + (TR1(t) + TR2(t))^2}} \Big] \quad (79)$$

$$U_{3,1}(t) = -i e^{-i\hbar Q_{11}(t)} \left[\frac{(TR1(t) - TR2(t)) \sin \left(\hbar \sqrt{|Q_{22}(t)|^2 + (TR1(t) - TR2(t))^2} \right)}{2\sqrt{|Q_{22}(t)|^2 + (TR1(t) - TR2(t))^2}} + \right. \\ \left. + \frac{(TR1(t) + TR2(t)) \sin \left(\hbar \sqrt{|Q_{22}(t)|^2 + (TR1(t) + TR2(t))^2} \right)}{2\sqrt{|Q_{22}(t)|^2 + (TR1(t) + TR2(t))^2}} \right] \quad (80)$$

$$\begin{aligned}
U_{3,2}(t) = e^{-i\hbar Q_{11}(t)} & \left[\frac{-Q_{22}(t) \sin\left(\hbar\sqrt{|Q_{22}(t)|^2 + (TR1(t) - TR2(t))^2}\right)}{2\sqrt{|Q_{22}(t)|^2 + (TR1(t) - TR2(t))^2}} + \right. \\
& \frac{Q_{22}(t) \sin\left(\hbar\sqrt{|Q_{22}(t)|^2 + (TR1(t) + TR2(t))^2}\right)}{2\sqrt{|Q_{22}(t)|^2 + (TR1(t) + TR2(t))^2}} + \\
& \left. \frac{i \cos\left(\hbar\sqrt{|Q_{22}(t)|^2 + (TR1(t) - TR2(t))^2}\right) - i \cos\left(\hbar\sqrt{|Q_{22}(t)|^2 + (TR1(t) + TR2(t))^2}\right)}{2} \right] \quad (81)
\end{aligned}$$

$$\begin{aligned}
U_{3,3}(t) = \frac{1}{2} e^{-i\hbar Q_{11}(t)} & \left[i Q_{22}(t) \left[\frac{\sin\left(\hbar\sqrt{|Q_{22}(t)|^2 + (TR1(t) - TR2(t))^2}\right)}{\sqrt{|Q_{22}(t)|^2 + (TR1(t) - TR2(t))^2}} \right. \right. \\
& \left. \left. + \frac{\sin\left(\hbar\sqrt{|Q_{22}(t)|^2 + (TR1(t) + TR2(t))^2}\right)}{\sqrt{|Q_{22}(t)|^2 + (TR1(t) + TR2(t))^2}} \right] + \right. \\
& \left. + \cos\left(\hbar\sqrt{|Q_{22}(t)|^2 + (TR1(t) - TR2(t))^2}\right) \right. \\
& \left. + \cos\left(\hbar\sqrt{|Q_{22}(t)|^2 + (TR1(t) + TR2(t))^2}\right) \right] \quad (82)
\end{aligned}$$

$$\begin{aligned}
U_{3,4}(t) = (\sin(\hbar Q_{11}(t))) & \left[\frac{(TR1(t) - TR2(t)) \sin\left(\hbar\sqrt{|Q_{22}(t)|^2 + (TR1(t) - TR2(t))^2}\right)}{2\sqrt{|Q_{22}(t)|^2 + (TR1(t) - TR2(t))^2}} + \right. \\
& \left. + i \cos(\hbar Q_{11}(t)) \frac{(TR1(t) + TR2(t)) \sin\left(\hbar\sqrt{|Q_{22}(t)|^2 + (TR1(t) + TR2(t))^2}\right)}{2\sqrt{|Q_{22}(t)|^2 + (TR1(t) + TR2(t))^2}} \right] \quad (83)
\end{aligned}$$

$$\begin{aligned}
U_{4,1}(t) = \frac{1}{2} e^{-i\hbar Q_{11}(t)} & \left[i Q_{22}(t) \left[\frac{\sin\left(\hbar\sqrt{|Q_{22}(t)|^2 + (TR1(t) - TR2(t))^2}\right)}{\sqrt{|Q_{22}(t)|^2 + (TR1(t) - TR2(t))^2}} \right. \right. \\
& \left. \left. - \frac{\sin\left(\hbar\sqrt{|Q_{22}(t)|^2 + (TR1(t) + TR2(t))^2}\right)}{\sqrt{|Q_{22}(t)|^2 + (TR1(t) + TR2(t))^2}} \right] + \right. \\
& \left. - \cos\left(\hbar\sqrt{|Q_{22}(t)|^2 + (TR1(t) - TR2(t))^2}\right) \right. \\
& \left. + \cos\left(\hbar\sqrt{|Q_{22}(t)|^2 + (TR1(t) + TR2(t))^2}\right) \right] \quad (84)
\end{aligned}$$

$$\begin{aligned}
U_{4,2}(t) = - \frac{ie^{-i\hbar Q_{11}(t)} & \left[(TR1(t) - TR2(t)) \sin\left(\hbar\sqrt{|Q_{22}(t)|^2 + (TR1(t) - TR2(t))^2}\right) \right]}{2\sqrt{|Q_{22}(t)|^2 + (TR1(t) - TR2(t))^2}} + \\
& \left. + \frac{(TR1(t) + TR2(t)) \sin\left(\hbar\sqrt{|Q_{22}(t)|^2 + (TR1(t) + TR2(t))^2}\right)}{2\sqrt{|Q_{22}(t)|^2 + (TR1(t) + TR2(t))^2}} \right] \quad (85)
\end{aligned}$$

$$U_{4,3}(t) = ie^{-i\hbar Q_{11}(t)} \left[\frac{(TR1(t) - TR2(t)) \sin\left(\hbar\sqrt{|Q_{22}(t)|^2 + (TR1(t) - TR2(t))^2}\right)}{2\sqrt{|Q_{22}(t)|^2 + (TR1(t) - TR2(t))^2}} + \right. \\ \left. - \frac{(TR1(t) + TR2(t)) \sin\left(\hbar\sqrt{|Q_{22}(t)|^2 + (TR1(t) + TR2(t))^2}\right)}{2\sqrt{|Q_{22}(t)|^2 + (TR1(t) + TR2(t))^2}} \right] \quad (86)$$

$$U_{4,4}(t) = \frac{1}{2}e^{-i\hbar Q_{11}(t)} \left[-iQ_{22}(t) \left[\frac{\sin\left(\hbar\sqrt{|Q_{22}(t)|^2 + (TR1(t) - TR2(t))^2}\right)}{\sqrt{|Q_{22}(t)|^2 + (TR1(t) - TR2(t))^2}} + \right. \right. \\ \left. \frac{\sin\left(\hbar\sqrt{|Q_{22}(t)|^2 + (TR1(t) + TR2(t))^2}\right)}{\sqrt{|Q_{22}(t)|^2 + (TR1(t) + TR2(t))^2}} \right] + \\ + \cos\left(\hbar\sqrt{|Q_{22}(t)|^2 + (TR1(t) - TR2(t))^2}\right) \\ + \cos\left(\hbar\sqrt{|Q_{22}(t)|^2 + (TR1(t) + TR2(t))^2}\right) \left. \right] \quad (87)$$

We set the quantum state to be $|\psi, t_0\rangle = |E_1\rangle$ at time t_0 so it is maximally entangled and its density matrix is $\rho(t_0) = |\psi, t_0\rangle \langle \psi, t_0| = |E_1\rangle \langle E_1| = \frac{1}{2} \begin{pmatrix} +1 & 0 & 0 & -1 \\ 0 & 0 & 0 & 0 \\ 0 & 0 & 0 & 0 \\ -1 & 0 & 0 & 1 \end{pmatrix}$.

Finally we obtain the following density matrix

$$\rho_{1,1}(t) = \frac{(TR1(t) - TR2(t))^2 \cos\left(2\hbar\sqrt{|Q_{22}(t)|^2 + (TR1(t) - TR2(t))^2}\right) + 2|Q_{22}(t)|^2 + (TR1(t) - TR2(t))^2}{4(|Q_{22}(t)|^2 + (TR1(t) - TR2(t))^2)} \quad (88)$$

$$\rho_{1,2}(t) = \frac{(TR1(t) - TR2(t)) \left[-i\sqrt{|Q_{22}(t)|^2 + (TR1(t) - TR2(t))^2} \sin\left(2\hbar\sqrt{|Q_{22}(t)|^2 + (TR1(t) - TR2(t))^2}\right) \right. \\ \left. + \frac{Q_{22}(t) \cos\left(2\hbar\sqrt{|Q_{22}(t)|^2 + (TR1(t) - TR2(t))^2}\right) - Q_{22}(t)}{4(|Q_{22}(t)|^2 + (TR1(t) - TR2(t))^2)} \right]}{4(|Q_{22}(t)|^2 + (TR1(t) - TR2(t))^2)} \quad (89)$$

$$\rho_{1,3}(t) = -(TR1(t) - TR2(t)) \frac{\left[-i\sqrt{|Q_{22}(t)|^2 + (TR1(t) - TR2(t))^2} \sin\left(2\hbar\sqrt{|Q_{22}(t)|^2 + (TR1(t) - TR2(t))^2}\right) \right. \\ \left. + \frac{Q_{22}(t) \cos\left(2\hbar\sqrt{|Q_{22}(t)|^2 + (TR1(t) - TR2(t))^2}\right) - Q_{22}(t)}{4(|Q_{22}(t)|^2 + (TR1(t) - TR2(t))^2)} \right]}{4(|Q_{22}(t)|^2 + (TR1(t) - TR2(t))^2)} +$$

$$+ \frac{Q_{22}(t) \cos \left(2\hbar\sqrt{|Q_{22}(t)|^2 + (TR1(t) - TR2(t))^2} \right) - Q_{22}(t)}{4(|Q_{22}(t)|^2 + (TR1(t) - TR2(t))^2)} \quad (90)$$

$$\rho_{1,4}(t) = - \frac{(TR1(t) - TR2(t))^2 \cos \left(2\hbar\sqrt{|Q_{22}(t)|^2 + (TR1(t) - TR2(t))^2} \right) + 2|Q_{22}(t)|^2 + (TR1(t) - TR2(t))^2}{4(|Q_{22}(t)|^2 + (TR1(t) - TR2(t))^2)} \quad (91)$$

$$\rho_{2,1}(t) = \frac{(TR1(t) - TR2(t)) \left(i\sqrt{|Q_{22}(t)|^2 + (TR1(t) - TR2(t))^2} \sin \left(2\hbar\sqrt{|Q_{22}(t)|^2 + (TR1(t) - TR2(t))^2} \right) \right)}{4(|Q_{22}(t)|^2 + (TR1(t) - TR2(t))^2)} +$$

$$+ \frac{Q_{22}(t) \cos \left(2\hbar\sqrt{|Q_{22}(t)|^2 + (TR1(t) - TR2(t))^2} \right) - Q_{22}(t)}{4(|Q_{22}(t)|^2 + (TR1(t) - TR2(t))^2)} \quad (92)$$

$$\rho_{2,2}(t) = \frac{(TR1(t) - TR2(t))^2 \sin^2 \left(\hbar\sqrt{|Q_{22}(t)|^2 + (TR1(t) - TR2(t))^2} \right)}{2(|Q_{22}(t)|^2 + (TR1(t) - TR2(t))^2)} \quad (93)$$

$$\rho_{2,3}(t) = - \frac{(TR1(t) - TR2(t))^2 \sin^2 \left(\hbar\sqrt{|Q_{22}(t)|^2 + (TR1(t) - TR2(t))^2} \right)}{2(|Q_{22}(t)|^2 + (TR1(t) - TR2(t))^2)} \quad (94)$$

$$\rho_{2,4}(t) = - \frac{(TR1(t) - TR2(t)) \left[i\sqrt{|Q_{22}(t)|^2 + (TR1(t) - TR2(t))^2} \sin \left(2\hbar\sqrt{|Q_{22}(t)|^2 + (TR1(t) - TR2(t))^2} \right) \right]}{4(|Q_{22}(t)|^2 + (TR1(t) - TR2(t))^2)} +$$

$$+ \frac{Q_{22}(t) \cos \left(2\hbar\sqrt{|Q_{22}(t)|^2 + (TR1(t) - TR2(t))^2} \right) - Q_{22}(t)}{4(|Q_{22}(t)|^2 + (TR1(t) - TR2(t))^2)} \quad (95)$$

$$\rho_{3,1}(t) = -(TR1(t) - TR2(t)) \frac{\left[i\sqrt{|Q_{22}(t)|^2 + (TR1(t) - TR2(t))^2} \sin \left(2\hbar\sqrt{|Q_{22}(t)|^2 + (TR1(t) - TR2(t))^2} \right) \right]}{4(|Q_{22}(t)|^2 + (TR1(t) - TR2(t))^2)} +$$

$$+ \frac{Q_{22}(t) \cos \left(2\hbar\sqrt{|Q_{22}(t)|^2 + (TR1(t) - TR2(t))^2} \right) - Q_{22}(t)}{4(|Q_{22}(t)|^2 + (TR1(t) - TR2(t))^2)} \quad (96)$$

$$\rho_{3,2}(t) = - \frac{(TR1(t) - TR2(t))^2 \sin^2 \left(\hbar \sqrt{|Q_{22}(t)|^2 + (TR1(t) - TR2(t))^2} \right)}{2 \left(|Q_{22}(t)|^2 + (TR1(t) - TR2(t))^2 \right)} \quad (97)$$

$$\rho_{3,3}(t) = \frac{(TR1(t) - TR2(t))^2 \sin^2 \left(\hbar \sqrt{|Q_{22}(t)|^2 + (TR1(t) - TR2(t))^2} \right)}{2 \left(|Q_{22}(t)|^2 + (TR1(t) - TR2(t))^2 \right)} \quad (98)$$

$$\begin{aligned} \rho_{3,4}(t) = & \frac{(TR1(t) - TR2(t)) \left(i \sqrt{|Q_{22}(t)|^2 + (TR1(t) - TR2(t))^2} \sin \left(2\hbar \sqrt{|Q_{22}(t)|^2 + (TR1(t) - TR2(t))^2} \right) \right)}{4 \left(|Q_{22}(t)|^2 + (TR1(t) - TR2(t))^2 \right)} + \\ & \frac{Q_{22}(t) \cos \left(2\hbar \sqrt{|Q_{22}(t)|^2 + (TR1(t) - TR2(t))^2} \right) - Q_{22}(t)}{4 \left(|Q_{22}(t)|^2 + (TR1(t) - TR2(t))^2 \right)} \end{aligned} \quad (99)$$

$$\rho_{4,1}(t) = - \frac{(TR1(t) - TR2(t))^2 \cos \left(2\hbar \sqrt{|Q_{22}(t)|^2 + (TR1(t) - TR2(t))^2} \right) + 2|Q_{22}(t)|^2 + (TR1(t) - TR2(t))^2}{4 \left(|Q_{22}(t)|^2 + (TR1(t) - TR2(t))^2 \right)} \quad (100)$$

$$\begin{aligned} \rho_{4,2}(t) = & -(TR1(t) - TR2(t)) \frac{\left[-i \sqrt{|Q_{22}(t)|^2 + (TR1(t) - TR2(t))^2} \sin \left(2\hbar \sqrt{|Q_{22}(t)|^2 + (TR1(t) - TR2(t))^2} \right) \right]}{4 \left(|Q_{22}(t)|^2 + (TR1(t) - TR2(t))^2 \right)} + \\ & + \frac{Q_{22}(t) \cos \left(2\hbar \sqrt{|Q_{22}(t)|^2 + (TR1(t) - TR2(t))^2} \right) - Q_{22}(t)}{4 \left(|Q_{22}(t)|^2 + (TR1(t) - TR2(t))^2 \right)} \end{aligned} \quad (101)$$

$$\begin{aligned} \rho_{4,3}(t) = & (TR1(t) - TR2(t)) \frac{\left[-i \sqrt{|Q_{22}(t)|^2 + (TR1(t) - TR2(t))^2} \sin \left(2\hbar \sqrt{|Q_{22}(t)|^2 + (TR1(t) - TR2(t))^2} \right) \right]}{4 \left(|Q_{22}(t)|^2 + (TR1(t) - TR2(t))^2 \right)} + \\ & \frac{Q_{22}(t) \cos \left(2\hbar \sqrt{|Q_{22}(t)|^2 + (TR1(t) - TR2(t))^2} \right) - Q_{22}(t)}{4 \left(|Q_{22}(t)|^2 + (TR1(t) - TR2(t))^2 \right)} \end{aligned} \quad (102)$$

$$\rho_{4,4}(t) = \frac{(TR1(t) - TR2(t))^2 \cos \left(2\hbar \sqrt{|Q_{22}(t)|^2 + (TR1(t) - TR2(t))^2} \right) + 2|Q_{22}(t)|^2 + (TR1(t) - TR2(t))^2}{4 \left(|Q_{22}(t)|^2 + (TR1(t) - TR2(t))^2 \right)} \quad (103)$$

It turns out that $\rho^n(t) = \rho(t)$ so one deals with a pure quantum state. Now we are obtaining reduced matrices describing the state of particle B from 2 particle density matrix.

$$\rho_B(t) = \begin{pmatrix} \rho_{11}(t) + \rho_{22}(t) & \rho_{13}(t) + \rho_{24}(t) \\ \rho_{31}(t) + \rho_{42}(t) & \rho_{33}(t) + \rho_{44}(t) \end{pmatrix} = \begin{pmatrix} \frac{1}{2} & \frac{Q_{22}(t)(TR1(t)-TR2(t)) \sin^2(\hbar\sqrt{|Q_{22}(t)|^2+(TR1(t)-TR2(t))^2})}{|Q_{22}(t)|^2+(TR1(t)-TR2(t))^2} \\ \frac{Q_{22}(t)(TR1(t)-TR2(t)) \sin^2(\hbar\sqrt{|Q_{22}(t)|^2+(TR1(t)-TR2(t))^2})}{|Q_{22}(t)|^2+(TR1(t)-TR2(t))^2} & \frac{1}{2} \end{pmatrix}. \quad (104)$$

Consequently we can compute entanglement entropy. At first we evaluate

$$\text{Log}(\rho_B(t)) = \begin{pmatrix} a & b \\ c & d \end{pmatrix}, \quad (105)$$

$$\begin{aligned} a &= \frac{1}{2} \left[\log \left[|Q_{22}(t)(TR1(t) - TR2(t)) \cos \left(2\hbar\sqrt{|Q_{22}(t)|^2 + (TR1(t) - TR2(t))^2} \right) + \right. \right. \\ &\quad \left. \left. + |Q_{22}(t)|^2 + Q_{22}(t)(TR2(t) - TR1(t)) + (TR1(t) - TR2(t))^2 \right] \right. \\ &\quad \left. - 2 \log \left[|Q_{22}(t)|^2 + (TR1(t) - TR2(t))^2 \right] \right] \\ &+ \log \left[\left[|Q_{22}(t)(TR2(t) - TR1(t)) \cos \left(2\hbar\sqrt{|Q_{22}(t)|^2 + (TR1(t) - TR2(t))^2} \right) + \right. \right. \\ &\quad \left. \left. |Q_{22}(t)|^2 + Q_{22}(t)(TR1(t) - TR2(t)) + (TR1(t) - TR2(t))^2 \right] - \log(4) \right] \\ b &= -\tanh^{-1} \left(\frac{Q_{22}(t)(TR1(t)-TR2(t)) \left(\cos \left(2\hbar\sqrt{|Q_{22}(t)|^2+(TR1(t)-TR2(t))^2} \right) - 1 \right)}{|Q_{22}(t)|^2+(TR1(t)-TR2(t))^2} \right) = c \\ d &= \frac{1}{2} \left[\log \left[|Q_{22}(t)(TR1(t) - TR2(t)) \cos \left(2\hbar\sqrt{|Q_{22}(t)|^2 + (TR1(t) - TR2(t))^2} \right) + \right. \right. \\ &\quad \left. \left. |Q_{22}(t)|^2 + Q_{22}(t)(TR2(t) - TR1(t)) + (TR1(t) - TR2(t))^2 \right] \right. \\ &\quad \left. - 2 \log \left[|Q_{22}(t)|^2 + (TR1(t) - TR2(t))^2 \right] \right] \\ &+ \log \left[\left[|Q_{22}(t)(TR2(t) - TR1(t)) \cos \left(2\hbar\sqrt{|Q_{22}(t)|^2 + (TR1(t) - TR2(t))^2} \right) + \right. \right. \\ &\quad \left. \left. |Q_{22}(t)|^2 + Q_{22}(t)(TR1(t) - TR2(t)) + (TR1(t) - TR2(t))^2 \right] - \log(4) \right] \end{aligned} \quad (106)$$

and we obtain the formula when we start from $TR1(t_0) = TR2(t_0)$ as

$$S_B(t) = \text{Tr}[\rho_B(t) \text{Log}[\rho_B(t)]] = \text{Tr} \left[\begin{pmatrix} \frac{1}{2} & \frac{Q_{22}(t)(TR1(t)-TR2(t)) \sin^2(\hbar\sqrt{|Q_{22}(t)|^2+(TR1(t)-TR2(t))^2})}{|Q_{22}(t)|^2+(TR1(t)-TR2(t))^2} \\ \frac{Q_{22}(t)(TR1(t)-TR2(t)) \sin^2(\hbar\sqrt{|Q_{22}(t)|^2+(TR1(t)-TR2(t))^2})}{|Q_{22}(t)|^2+(TR1(t)-TR2(t))^2} & \frac{1}{2} \end{pmatrix} \right] \times$$

$$\begin{aligned}
& \text{Log} \left[\left(\frac{Q_{22}(t)(TR1(t)-TR2(t)) \sin^2 \left(\frac{\hbar}{2} \sqrt{|Q_{22}(t)|^2 + (TR1(t)-TR2(t))^2} \right)}{|Q_{22}(t)|^2 + (TR1(t)-TR2(t))^2} \right)^{\frac{1}{2}} \frac{Q_{22}(t)(TR1(t)-TR2(t)) \sin^2 \left(\frac{\hbar}{2} \sqrt{|Q_{22}(t)|^2 + (TR1(t)-TR2(t))^2} \right)}{|Q_{22}(t)|^2 + (TR1(t)-TR2(t))^2} \right)^{\frac{1}{2}} \right] = \\
& = -\log(4) \frac{1}{2} + \frac{1}{2} \left[\log \left[Q_{22}(t)(TR1(t) - TR2(t)) \cos \left(2\hbar \sqrt{|Q_{22}(t)|^2 + (TR1(t) - TR2(t))^2} \right) + \right. \right. \\
& \quad \left. \left. + |Q_{22}(t)|^2 + Q_{22}(t)(TR2(t) - TR1(t)) + (TR1(t) - TR2(t))^2 \right] + \right. \\
& \quad \left. + \log \left[Q_{22}(t)(TR2(t) - TR1(t)) \cos \left(2\hbar \sqrt{|Q_{22}(t)|^2 + (TR1(t) - TR2(t))^2} \right) \right. \right. \\
& \quad \left. \left. + |Q_{22}(t)|^2 + Q_{22}(t)(TR1(t) - TR2(t)) + (TR1(t) - TR2(t))^2 \right] \right. \\
& \quad \left. - 2 \log \left[|Q_{22}(t)|^2 + (TR1(t) - TR2(t))^2 \right] \right. \\
& \quad \left. + \frac{4Q_{22}(t)(TR2(t) - TR1(t)) \sin^2 \left(\frac{\hbar}{2} \sqrt{|Q_{22}(t)|^2 + (TR1(t) - TR2(t))^2} \right)}{|Q_{22}(t)|^2 + (TR1(t) - TR2(t))^2} \right] \times \\
& \quad \times \tanh^{-1} \left(\frac{Q_{22}(t)(TR1(t) - TR2(t)) \left(\cos \left(2\hbar \sqrt{|Q_{22}(t)|^2 + (TR1(t) - TR2(t))^2} \right) - 1 \right)}{|Q_{22}(t)|^2 + (TR1(t) - TR2(t))^2} \right) \right] \\
& \hspace{15em} (107)
\end{aligned}$$

The results obtained allows for monitoring of entanglement entropy with time (Fig. 8).

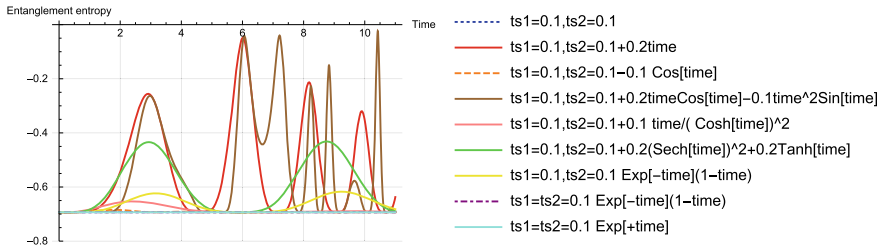


Fig. 8 Entanglement entropy with time for 2 interacting particles for different functions of hopping constant with time

8 Case of 2 Coupled Single Electron Lines

We follow the reasoning described in [3]. At first, we consider a physical system of an electron confined in a potential with two minima (position-dependent qubit with presence of electron at node 1 and 2) or three minima (position dependent qubit with presence of electron at nodes 1, 2 and 3), as depicted in Fig. 9a, which was also considered by Fujisawa [1] and Petta [2] and which forms a position-dependent qubit (or qudit). We can write the Hamiltonian in the second quantization as

$$\hat{H} = \sum_{i,j} t_{i \rightarrow j} \hat{a}_i^\dagger \hat{a}_j + \sum_i E_p(i) \hat{a}_i^\dagger \hat{a}_i + \sum_{i,j,k,l} \hat{a}_i^\dagger \hat{a}_j^\dagger \hat{a}_i \hat{a}_j V_{i,j}, \quad (108)$$

where \hat{a}_i^\dagger is a fermionic creator operator at i -th point in the space lattice and \hat{a}_j is fermionic annihilator operator at j -th point of the lattice. The hopping term $t_{i \rightarrow j}$ describes hopping from i -th to j -th lattice point and is a measure of kinetic energy. The potential $V_{i,j}$ represents particle-particle interaction and term $E_p(i)$ incorporates potential energy. In this approach we neglect the presence of a spin. It is convenient to write a system Hamiltonian of position based qubit in spectral form as

$$\begin{aligned} \hat{H}(t) &= E_{p1}(t) |1, 0\rangle \langle 1, 0| + E_{p2}(t) |0, 1\rangle \langle 0, 1| + \\ & t_{1 \rightarrow 2}(t) |0, 1\rangle \langle 1, 0| + t_{2 \rightarrow 1}(t) |1, 0\rangle \langle 0, 1| = \\ & \frac{1}{2}(\hat{\sigma}_0 + \hat{\sigma}_3)E_{p1}(t) + \frac{1}{2}(\hat{\sigma}_0 - \hat{\sigma}_3)E_{p2}(t) + \\ & \frac{1}{2}(\hat{\sigma}_1 - i\hat{\sigma}_2)t_{2 \rightarrow 1}(t) + \frac{1}{2}(i\hat{\sigma}_2 - \hat{\sigma}_1)t_{1 \rightarrow 2}(t) \end{aligned} \quad (109)$$

where Pauli matrices are $\hat{\sigma}_0, \dots, \hat{\sigma}_3$ while system quantum state is given as $|\psi(t)\rangle = \alpha(t) |1, 0\rangle + \beta(t) |0, 1\rangle$ with $|\alpha|^2 + |\beta|^2 = 1$ and is expressed in Wannier function eigenbases $|1, 0\rangle = w_L(x)$ and $|0, 1\rangle = w_R(x)$ which underlines the presence of electron on the left/right side as equivalent to picture from Schrödinger equation [4]. We obtain two energy eigenstates

$$\begin{aligned} |E_{1(2)}\rangle &= \left(\frac{(E_{p2} - E_{p1}) \pm \sqrt{4t_{1 \rightarrow 2}t_{2 \rightarrow 1} + |E_{p1} - E_{p2}|^2}}{2t_{1 \rightarrow 2}} \right) = \\ & \frac{(E_{p2} - E_{p1}) \pm \sqrt{4t_{1 \rightarrow 2}t_{2 \rightarrow 1} + |E_{p1} - E_{p2}|^2}}{2t_{1 \rightarrow 2}} |1, 0\rangle + |0, 1\rangle. \end{aligned}$$

and energy eigenvalues

$$E_{1(2)} = \frac{1}{2}(E_{p1} + E_{p2} \pm \sqrt{4t_{1 \rightarrow 2}t_{2 \rightarrow 1} + |E_{p1} - E_{p2}|^2}) =$$

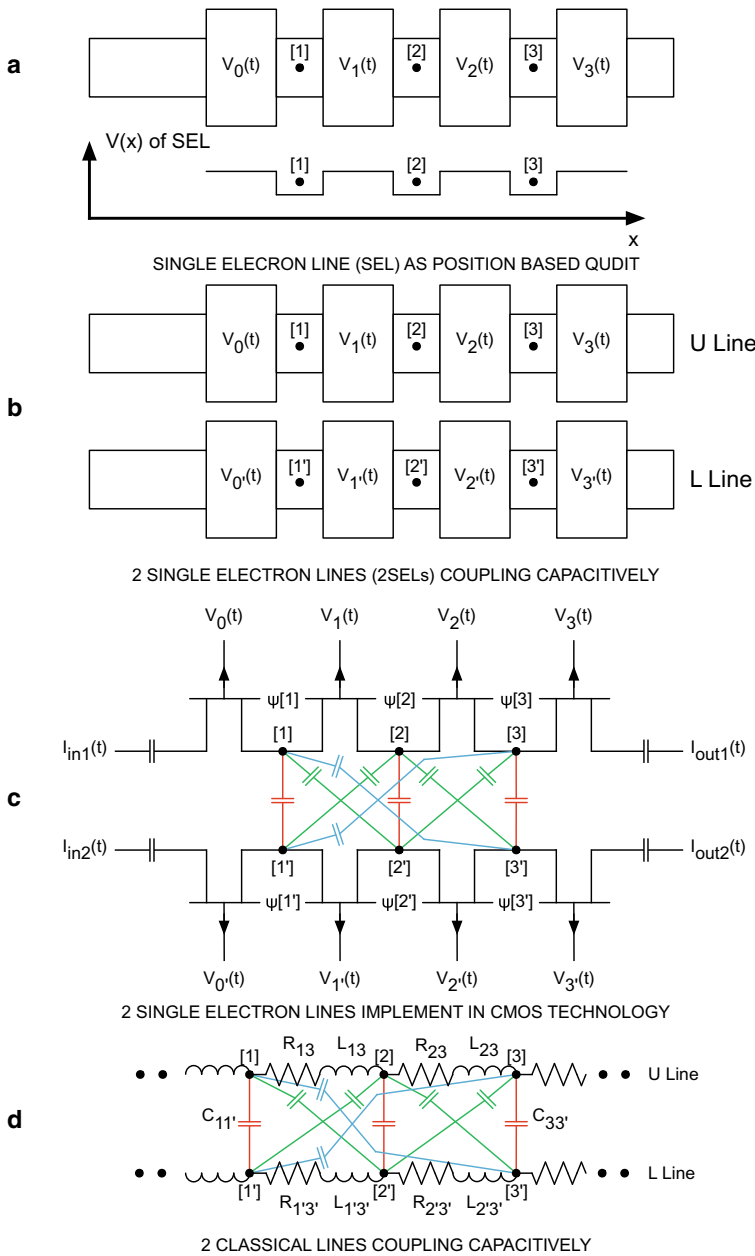


Fig. 9 Nanometer CMOS structure [4], effective potential and circuit representation of: **a** electrostatic position-dependent qubit [4] (the quantum dot dimensions are $80 \times 80 \text{ nm}^2$ in 22FDX FDSOI CMOS technology); **b, c** two electrostatic position-dependent qubits representing two inductively interacting lines (upper “U” and lower “L” quantum systems) in minimalistic way (more rigorously they shall be named as MOS transistor single-electron lines). Presented systems are subjected to the external voltage biasing that controls the local potential landscape in which electrons are confined. Classical limit is expressed by circuit D

$$\begin{aligned}
& \frac{1}{2}(E_{p1} + E_{p2} \pm 2|t_{1 \rightarrow 2}| \sqrt{1 + |\frac{E_{p1} - E_{p2}}{2t_{1 \rightarrow 2}t_{2 \rightarrow 1}}|^2}) \approx \\
& \frac{1}{2}(E_{p1} + E_{p2} \pm 2|t_{1 \rightarrow 2}|(1 + \frac{1}{2}|\frac{E_{p1} - E_{p2}}{2t_{1 \rightarrow 2}t_{2 \rightarrow 1}}|^2)) \approx \\
& \frac{1}{2}(E_{p1} + E_{p2}) \pm |t_{1 \rightarrow 2}|. \quad (110)
\end{aligned}$$

The last approximation is obtained in the limit of $t_{1 \rightarrow 2} \gg E_{p1}, E_{p2}$ (classical limit when system energy becomes big and $|t|$ has the interpretation of kinetic energy) what is the case depicted in the middle Fig. 3 when $|t| \rightarrow +\infty$. Since Schrodinger formalism can be also applied to the position based qubit that has discrete eigenenergy spectra, one expects that value E_p and t_s takes discrete values. It is even more pronounced when one is using formula being prescription for E_p and t_s parameters as

$$E_p(i) = \int_{-\infty}^{+\infty} dx \psi_i^*(x) \hat{H}_0 \psi_i(x), \quad (111)$$

where $\psi(x)_i$ is wavefunction of electron localized at i -th node (i -th quantum well) and \hat{H} is effective Hamiltonian. In similar fashion we can define hopping constant from node i -th to node j -th as energy participating in energy transport from one quantum well into the neighbouring quantum well so we define

$$t_{s,i \rightarrow j} = \int_{-\infty}^{+\infty} dx \psi_i^*(x) \hat{H}_0 \psi_j(x), \quad (112)$$

Another interesting fact is the transition from Schrodinger picture to the tight-binding picture that can be done by $|\psi\rangle = \int_{-\infty}^{\infty} \psi(x) dx |x\rangle \approx \sum_{k=-\infty}^{k=+\infty} \Delta x \psi(k) |k \Delta x\rangle$, where Δx is the distance between nodes. Having momentum operator defined as $\frac{\hbar}{\Delta x \sqrt{-1}}(-|k+1\rangle \langle k| + |k\rangle \langle k+1|) = \frac{\hbar}{\Delta x \sqrt{-1}} \frac{d}{dx} k$. We obtain the second derivative by Euler formula $(\frac{d^2}{dx^2})_k = \frac{1}{(\Delta x)^2} (|k+1\rangle \langle k| + |k\rangle \langle k+1| - 2|k\rangle \langle k|)$. Now we can recover the Schrodinger equation and we observe that $t_{s,i \rightarrow i+1} = \frac{\hbar^2}{2m \Delta x} w$, where w is positive and integer. Therefore $t_{s,i \rightarrow i+1}$ has the positive discrete values. We also observe that the potential in the Schrodinger equation can be connected with $E_p(i) - 2t_{s,i \rightarrow i+1} = V_p(i)$ at i -th node. Since kinetic energy is discrete and potential energy in Schrodinger equation is continuous one obtains discrete E_p . The eigenstate depends in the tight binding model depends on an external vector potential source acting on the qubit by means of $t_{1 \rightarrow 2} = |t_{1 \rightarrow 2}| e^{i\alpha} = t_{2 \rightarrow 1}^*$. Since every energy eigenstate is spanned by $|0, 1\rangle$ and $|1, 0\rangle$, we will obtain oscillations of occupancy between two wells [3–5]. It is worth-mentioning that the act of measurement will affect the qubit quantum state. Since we are dealing with a position-based qubit, we can make measurement of the electron position with the use an external single-electron device (SED) in close proximity to the qubit. This will require the use of projection operators that represent eigenenergy measurement as $|E_{0(1)}\rangle \langle E_{0(1)}|$ or, for

example, measurement of the electron position at left side so we use the projector $|1, 0\rangle \langle 0, 1|$. We can extend the model for the case of three (and more) coupled wells. In such a case, we obtain the system Hamiltonian for a position based qubit:

$$\hat{H} = \sum_s E_{ps} |s\rangle \langle s| + \sum_{l,s,s \neq l} t_{s \rightarrow l} |l\rangle \langle s|, \quad (113)$$

where $|1\rangle = |1, 0, 0\rangle$, $|2\rangle = |0, 1, 0\rangle$, $|3\rangle = |0, 0, 1\rangle$ and its Hamiltonian matrix

$$H(t) = \begin{pmatrix} E_{p1}(t) & t_{2 \rightarrow 1}(t) & t_{3 \rightarrow 1}(t) \\ t_{1 \rightarrow 2}(t) & E_{p2}(t) & t_{3 \rightarrow 2}(t) \\ t_{1 \rightarrow 3}(t) & t_{2 \rightarrow 3}(t) & E_{p3}(t) \end{pmatrix} \quad (114)$$

and quantum state $|\psi\rangle$ (with a normalization condition $|\alpha|^2 + |\beta|^2 + |\gamma|^2 = 1$) is given as

$$|\psi\rangle = \begin{pmatrix} \alpha(t) \\ \beta(t) \\ \gamma(t) \end{pmatrix} = \alpha(t) |1, 0, 0\rangle + \beta(t) |0, 1, 0\rangle + \gamma(t) |0, 0, 1\rangle. \quad (115)$$

Coefficients $\alpha(t)$, $\beta(t)$ and $\gamma(t)$ describe oscillations of occupancy of one electron at wells 1, 2 and 3. The problem of qubit equations of motion can be formulated by having $|\psi\rangle = c_1(0)e^{-\frac{i}{\hbar}tE_1} |E_1\rangle + c_2(0)e^{-\frac{i}{\hbar}tE_2} |E_2\rangle + c_3(0)e^{-\frac{i}{\hbar}tE_3} |E_3\rangle$, where $|c_1(0)|^2, |c_2(0)|^2$ and $|c_3(0)|^2$ are probabilities of occupancy of E_1, E_2 and E_3 energetic levels. Energy levels are roots of 3rd order polynomial

$$\begin{aligned} & (-E_{p1}E_{p2}E_{p3} + E_{p3}t_{12}^2 + E_{p1}t_{23}^2 + E_{p2}t_{13}^2 - 2t_{s12}t_{s13}t_{s23}) \\ & + (E_{p1}E_{p2} + E_{p1}E_{p3} + E_{p2}E_{p3} - t_{12}^2 - t_{23}^2 - t_{13}^2)E \\ & - (E_{p1} + E_{p2} + E_{p3})E^2 + E^3 = 0, \end{aligned}$$

where $|E_1\rangle, |E_2\rangle, |E_3\rangle$ are 3-dimensional Hamiltonian eigenvectors.

By introducing two electrostatically interacting qubits, we are dealing with the Hamiltonian of the upper and lower lines as well as with their Coulomb electrostatic interactions. We are obtaining the Hamiltonian in spectral representation acting on the product of Hilbert spaces in the form of $\hat{H} = \hat{H}_U \times I_L + I_U \times \hat{H}_L + \hat{H}_{U-L}$ where H_u and H_l are Hamiltonians of separated upper and lower qubits, H_{l-u} is a two-line Coulomb interaction and $I_{u(l)} = |1, 0, 0\rangle_{u(l)} \langle 1, 0, 0|_{u(l)} + |0, 1, 0\rangle_{u(l)} \langle 0, 1, 0|_{u(l)} + |0, 0, 1\rangle_{u(l)} \langle 0, 0, 1|_{u(l)}$. The electrostatic interaction is encoded in $E_c(1, 1') = E_c(2, 2') = E_c(3, 3') = \frac{e^2}{4\pi\epsilon_0\epsilon d} = q_1$ (red capacitors of Fig. 1) and $q_2 = E_c(2, 1') = E_c(2, 3') = E_c(1, 2') = E_c(3, 2') = \frac{e^2}{4\pi\epsilon_0\epsilon\sqrt{d^2+(a+b)^2}}$ and electrostatic energy of green capacitors of Fig. 1. is

$$E_c(1, 3') = E_c(3, 1') = q_2 = \frac{e^2}{4\pi\epsilon_0\epsilon\sqrt{d^2 + 4(a+b)^2}}, \quad (116)$$

where a, b and d are geometric parameters of the system, e is electron charge and ϵ is a relative dielectric constant of the material; ϵ_0 corresponds to the dielectric constant of vacuum. The very last Hamiltonian corresponds to the following quantum state $|\psi(t)\rangle$ ($|\gamma_1(t)|^2 + \dots + |\gamma_9(t)|^2 = 1$) given as

$$\begin{aligned} |\psi(t)\rangle = & \gamma_1(t) |1, 0, 0\rangle_u |1, 0, 0\rangle_l + \gamma_2(t) |1, 0, 0\rangle_u |0, 1, 0\rangle_l \\ & + \gamma_3(t) |1, 0, 0\rangle_u |0, 0, 1\rangle_l + \gamma_4(t) |0, 1, 0\rangle_u |1, 0, 0\rangle_l \\ & + \gamma_5(t) |0, 1, 0\rangle_u |0, 1, 0\rangle_l + \gamma_6(t) |0, 1, 0\rangle_u |0, 0, 1\rangle_l \\ & + \gamma_7(t) |0, 0, 1\rangle_u |0, 0, 1\rangle_l + \gamma_8(t) |0, 0, 1\rangle_u |0, 1, 0\rangle_l \\ & + \gamma_9(t) |0, 0, 1\rangle_u |0, 0, 1\rangle_l, \end{aligned} \quad (117)$$

where $|\gamma_1(t)|^2$ is the probability of finding two electrons at nodes 1 and 1' at time t (since γ_1 spans $|1, 0, 0\rangle_u |1, 0, 0\rangle_l$), etc. The Hamiltonian has nine eigenenergy solutions that are parametrized by geometric factors and hopping constants $t_{k,m}$ as well as energies $E_p(k)$ for the case of 'u' or 'l' system. Formally, we can treat $E_p(k) = t_{k \rightarrow k} \equiv t_{k,k} \equiv t_k \in \mathbf{R}$ as a hopping from k -th lattice point to the same lattice point k . We obtain the following Hamiltonian

$$\begin{aligned} \hat{H} = & \begin{pmatrix} \xi_{1,1'} & t_{1' \rightarrow 2'} & t_{1' \rightarrow 3'} & t_{1 \rightarrow 2} & 0 & 0 & t_{1 \rightarrow 3} & 0 & 0 \\ t_{2' \rightarrow 1'} & \xi_{1,2'} & t_{2' \rightarrow 3'} & 0 & t_{1 \rightarrow 2} & 0 & 0 & t_{1 \rightarrow 3} & 0 \\ t_{3' \rightarrow 1'} & t_{3' \rightarrow 2'} & \xi_{1,3'} & 0 & 0 & t_{1 \rightarrow 2} & 0 & 0 & t_{1 \rightarrow 3} \\ t_{2 \rightarrow 1} & 0 & 0 & \xi_{2,1'} & t_{1' \rightarrow 2'} & t_{1' \rightarrow 3'} & t_{2 \rightarrow 3} & 0 & 0 \\ 0 & t_{2 \rightarrow 1} & 0 & t_{2' \rightarrow 1'} & \xi_{2,2'} & t_{2' \rightarrow 3'} & 0 & t_{2 \rightarrow 3} & 0 \\ 0 & 0 & t_{2 \rightarrow 1} & t_{3' \rightarrow 1'} & t_{3' \rightarrow 2'} & \xi_{2,3'} & 0 & 0 & t_{2 \rightarrow 3} \\ t_{3 \rightarrow 1} & 0 & 0 & t_{3 \rightarrow 2} & 0 & 0 & \xi_{3,1'} & t_{1' \rightarrow 2'} & t_{1' \rightarrow 3'} \\ 0 & t_{3 \rightarrow 1} & 0 & 0 & t_{3 \rightarrow 2} & 0 & t_{2' \rightarrow 1'} & \xi_{3,2'} & t_{2' \rightarrow 3'} \\ 0 & 0 & t_{3 \rightarrow 1} & 0 & 0 & t_{3 \rightarrow 2} & t_{3' \rightarrow 1'} & t_{3' \rightarrow 2'} & \xi_{3,3'} \end{pmatrix} \\ = & \begin{pmatrix} H(1)_{1',3'} & H_{1,2} & H_{1,3} \\ H(1)_{2,1} & H(2)_{1',3'} & H_{2,3} \\ H_{3,1} & H_{3,2} & H(3)_{1,3'} \end{pmatrix} \end{aligned} \quad (118)$$

with diagonal elements ($[\xi_{1,1'}, \xi_{1,2'}, \xi_{1,3'}]$, $[\xi_{2,1'}, \xi_{2,2'}, \xi_{2,3'}]$, $[\xi_{3,1'}, \xi_{3,2'}, \xi_{3,3'}]$) set to ($[(E_{p1} + E_{p1'} + E_c(1, 1')), (E_{p1} + E_{p2'} + E_c(1, 2'))$, $(E_{p1} + E_{p3'} + E_c(1, 3'))]$, $[(E_{p1} + E_{p1'} + E_c(1, 1')), (E_{p2} + E_{p2'} + E_c(2, 2'))$, $(E_{p2} + E_{p3'} + E_c(2, 3'))]$, $[(E_{p3} + E_{p1'} + E_c(3, 1')), (E_{p3} + E_{p2'} + E_c(3, 2'))$, $(E_{p3} + E_{p3'} + E_c(3, 3'))]$). In the absence of magnetic field, we have $t_{k \rightarrow m} = t_{m \rightarrow k} = t_{k,l} = t_{m,k} \in \mathbf{R}$ and in the case of nonzero magnetic field $t_{k,m} = t_{m,k}^* \in \mathbf{C}$. It is straightforward to determine the matrix of two lines with N wells [=3 in this work] each following the math-

emational structure of two interacting lines with three wells in each line. Matrices $H_{1,2}, H_{2,3}, H_{1,3}$ are diagonal of size $N \times N$ with all the same terms on the diagonal. At the same time, matrices $H(1)_{1',N'}, \dots, H(N)_{1',N'}$ have only different diagonal terms corresponding to $((\xi_{1,N'}, \dots, \xi_{1,N'}), \dots, ((\xi_{N,N'}, \dots, \xi_{N,N'}))$ elements. In simplified considerations we can set $t_{1 \rightarrow N} = t_{N \rightarrow 1}$ and $t_{1' \rightarrow N'} = t_{N' \rightarrow 1'}$ to zero since a probability for the wavefunction transfer from 1st to N -th lattice point is generally proportional to $\approx \exp(-sN)$, where s is some constant. It shall be underlined that in the most general case of two capacitively coupled symmetric SELs with three wells each (being parallel to each other), we have six (all different $E_p(k)$ and $E_p(l')$) plus six (all different $t_{k \rightarrow s}, t_{k' \rightarrow s'}$) plus three geometric parameters (d, a and b) as well as a dielectric constant hidden in the effective charge of interacting electrons q . Therefore, the model Hamiltonian has 12+4 real-valued parameters (4 depends on the material and geometry of 2 SELs). They can be extracted from a particular transistor implementation of two SELs (Fig. 9c). There are two main physically important regimes when $t \ll E_p$ and when $t \gg E_p$. They correspond to the case of electron tunneling from one quantum well into another (electron is not in highly excited state) and the case when electron wavepacket can move freely between neighbouring wells (electron is in highly excited state).

9 Analytical and Numerical Modeling of Capacitively Coupled SELs

9.1 Analytical Results

The greatest simplification of matrix (8) is when we set all $t_{k' \rightarrow m'} = t_{o \rightarrow m} = |t|$, and all $E_p(k) = E_p(m') = E_p$ for $N = 3$. Let us first consider the case of two insulating lines (all wells on each line are completely decoupled so there is no electron tunneling between the barriers and the barrier energies are high) where there are trapped electrons so $|t| = 0$ (electrons are confined in quantum wells and cannot move towards neighbouring wells). In such a case, we deal with a diagonal matrix that has three different eigenvalues on its diagonal and has three different eigenenergy values

$$\hat{E} = \begin{cases} E_1 = q_1 = E_p + \frac{e^2}{4\pi\epsilon\epsilon_0 d}, \\ E_2 = q_2 = E_p + \frac{e^2}{4\pi\epsilon\epsilon_0 \sqrt{|d|^2 + (a+b)^2}}, \\ E_3 = q_3 = E_p + \frac{e^2}{4\pi\epsilon\epsilon_0 \sqrt{|d|^2 + 4(a+b)^2}}, \end{cases} \quad (119)$$

so $E_3 < E_2 < E_1$. In the limit of infinite distance between SELs, we have nine degenerate eigenenergies. They are set to E_{pk} which corresponds to six decoupled quantum systems (the first electron is delocalized into three upper wells, while the second electron is delocalized into three lowers wells).

Let us also consider the case of ideal metal where electrons are completely delocalized. In such a case, all $t_{k(k')} \gg E_{pl(s)}$ which brings Hamiltonian diagonal terms to be negligible in comparison with other terms. In such a case, we can set all diagonal terms to be zero which is an equivalent to the case of infinitely spaced SELs lines. It simply means that in the case of ideal metals, two lines are not 'seeing' each other.

Let us now turn to the case where processes associated with hopping between wells have similar values of energy to the energies denoted as $E_{pk(l')}$. In such a case, the Hamiltonian matrix can be parametrized only by three real value numbers due to symmetries depicted in Fig. 9b (we divide the matrix by a constant number $|t|$) so

$$\begin{cases} q_{11} = \frac{2E_p + \frac{e^2}{d}}{|t|}, \\ q_{12} = \frac{2E_p + \frac{e^2}{\sqrt{d^2 + (a+b)^2}}}{|t|}, \\ q_{13} = \frac{2E_p + \frac{e^2}{\sqrt{d^2 + 4(a+b)^2}}}{|t|}. \end{cases}$$

For a fixed $|t|$, we change the distance d and observe that q_{11} can be arbitrary large, while q_{12} and q_{13} have finite values for $d = 0$. Going into the limit of infinite distance d , we observe that all q_{11} , q_{12} and q_{13} approach a finite value $\frac{2E_p}{|t|}$. We obtain the simplified Hamiltonian matrix that is a Hermitian conjugate and has a property $H_{k,k} = H_{N-k+1, N-k+1}$. It is in the form

$$\hat{H} = \begin{pmatrix} q_{11} & 1 & 0 & 1 & 0 & 0 & 0 & 0 & 0 \\ 1 & q_{12} & 1 & 0 & 1 & 0 & 0 & 0 & 0 \\ 0 & 1 & q_{13} & 0 & 0 & 1 & 0 & 0 & 0 \\ 1 & 0 & 0 & q_{12} & 1 & 0 & 1 & 0 & 0 \\ 0 & 1 & 0 & 1 & q_{11} & 1 & 0 & 1 & 0 \\ 0 & 0 & 1 & 0 & 1 & q_{12} & 0 & 0 & 1 \\ 0 & 0 & 0 & 1 & 0 & 0 & q_{13} & 1 & 0 \\ 0 & 0 & 0 & 0 & 1 & 0 & 1 & q_{12} & 1 \\ 0 & 0 & 0 & 0 & 0 & 1 & 0 & 1 & q_{11} \end{pmatrix} \quad (120)$$

We can analytically find nine energy eigenvalues and they correspond to the entangled states. We have

$$\begin{cases} E_1 = q_{11}, \\ E_2 = q_{12}, \\ E_3 = \frac{1}{2}(q_{11} + q_{12} - \sqrt{8 + (q_{11} - q_{12})^2}), \\ E_4 = \frac{1}{2}(q_{11} + q_{12} + \sqrt{8 + (q_{11} - q_{12})^2}), \\ E_5 = \frac{1}{2}(q_{12} - q_{13} - \sqrt{8 + (q_{12} - q_{13})^2}), \\ E_6 = \frac{1}{2}(q_{12} - q_{13} + \sqrt{8 + (q_{12} - q_{13})^2}). \end{cases} \quad (121)$$

The last 3 energy eigenvalues are the most involving analytically and are the roots of a 3rd order polynomial

$$(2q_{1_1} + 6q_{1_3} - q_{1_1}q_{1_2}q_{1_3}) + (-8 + q_{1_1}q_{1_2} + q_{1_1}q_{1_3} + q_{1_2}q_{1_3})E_k - (q_{1_1} + q_{1_2} + q_{1_3})E_k^2 + E_k^3 = 0. \quad (122)$$

We omit writing direct and very lengthy formulas since the solutions of a 3rd-order polynomial are commonly known. The eigenvectors have the structure given in Appendix 1.

We can readily recognize that all nine energy eigenvectors are entangled. In particular first two eigenenergy states (given also in Formula 187) are linear combination of position dependent states,

$$\begin{aligned} |E_1\rangle &= |1, 0, 0\rangle_U |1, 0, 0\rangle_L - |0, 1, 0\rangle_U |0, 1, 0\rangle_L + \\ &\quad |0, 0, 1\rangle_U |0, 0, 1\rangle_L, \\ |E_2\rangle &= |1, 0, 0\rangle_U |0, 1, 0\rangle_L - |0, 1, 0\rangle_U |1, 0, 0\rangle_L \\ &\quad - |0, 1, 0\rangle_U |0, 0, 1\rangle_L + |0, 0, 1\rangle_U |0, 1, 0\rangle_L, \end{aligned} \quad (123)$$

so they have no equivalence in the classical picture of two charged balls in channels that are repelling each other.

9.2 Numerical Results for Case of Capacitively Coupled SETs

At first, we are analyzing available spectrum of eigenenergies as in the case of insulator-to-metal phase transition [6], which can be implemented in a tight-binding model by a systematic increase of the hopping term from small to large values, while at the same time keeping all other parameters constant, as depicted in Fig. 11. Described tight-binding model can mimic a metal ($t = 1$), semiconductor ($t = 0.1$) or insulator state ($t = 0.01$), as given in Fig. 10. We can recognize 2-SELs eigenenergy spectra dependence on distance between the two lines. Characteristic narrowing of bands is observed when one moves from large towards small distance d between SELs (what can be related to the ratio of W/U in the Hubbard model) and it is one of the signs of transition from metallic to insulator regime (Mott-insulator phase transition [6]). One of the plots referring to $t = 0.01$ describes Anderson localization of electrons and, in such a case, energy eigenspectra are determined by Formula (119) and hopping terms t can be completely neglected since electrons are localized in the quantum-well potential minima.

Bottom plots of Fig. 11. describe the ability of tunneling eigenenergy spectra with respect to quantum well lengths ($a + b$), E_p and t parameters. The last two parameters can be directly controlled by an applied voltage as earlier shown in Fig. 9, where eight voltage signals are used for controlling the effective tight-binding Hamiltonian. It is informative to notice that change of the quantum well length, expressed by $a + b$, does not affect the eigenenergy of 2-SELs significantly. The

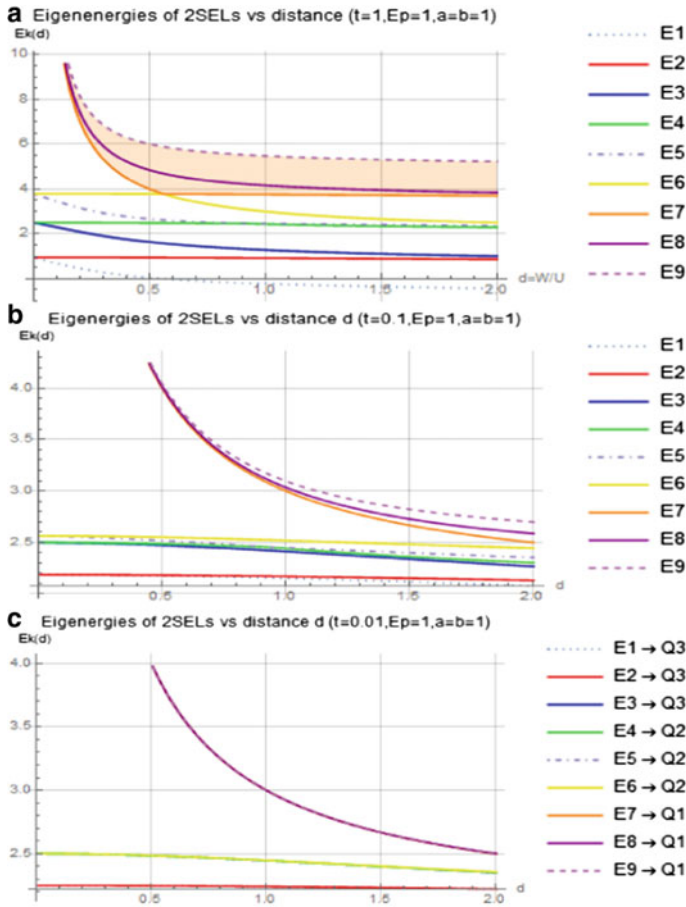


Fig. 10 Cases of: **a** metal ($t = 1, E_p = 1$); **b** semiconductor ($t = 0.1, E_p = 1$); and **c** insulator ($t = 0.01, E_p = 1$) state of 2-SELs given by eigenenergy spectra as function of distance d between two lines ($a = b = 1, e = 1$)

observed change affects the ratio of electrostatic to kinetic energy and thus is similar to the change in energy eigenspectra generated by different distances d . We can spot narrowing of the bands when moving from the situation of lower to higher electrostatic energy of interacting electron and again it is typical for metal-insulator phase transition. Change of ratio kinetic to electrostatic energy can be obtained by keeping quantum well size constant, constant distance between 2 SELs and by change of hopping constant t that is the measure of electron ability in conducting electric or heat current. Again one observes the narrowing of bands when we reduce t so the dominant energy of electron is due to the electron-electron interaction. The last plot of Fig. 11 describes our ability of tunneling eigenenergy spectra of system in linear way just by change of E_p parameter. In very real way we can

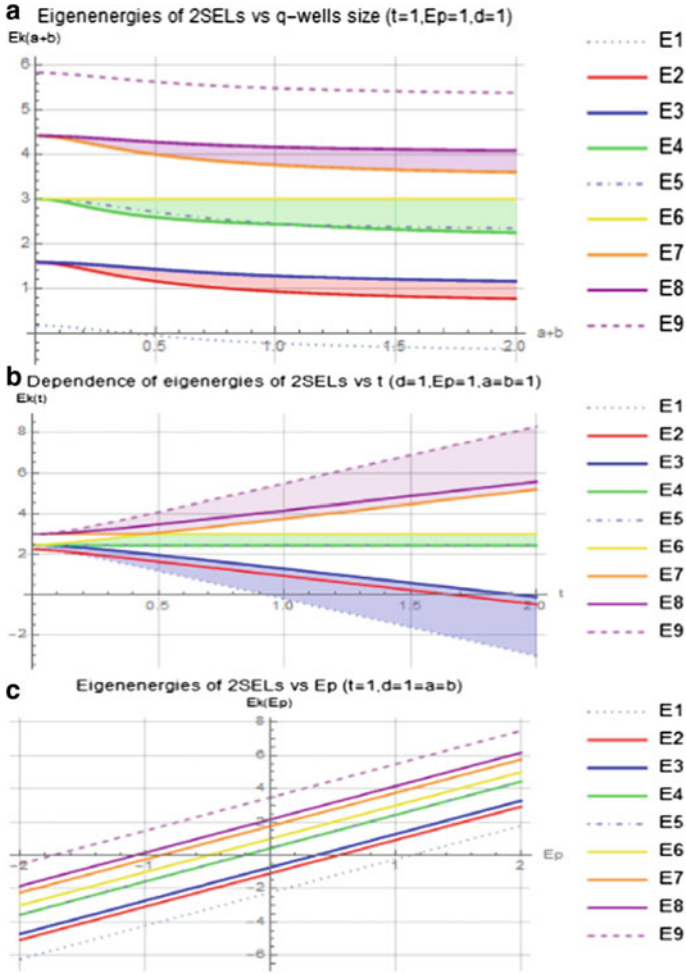


Fig. 11 Dependence of eigenenergy spectra versus **a** quantum well size $a + b$, **b** hopping term $|t|$, and **c** chemical potential E_p parameter

recognize the ability of tuning the chemical potential (equivalent to Fermi energy at temperatures $T = 0K$) by controlling voltages given in Fig.9. in our artificial lattice system. Due to controllability of energy eigenspectra by controlling voltages from Fig.9 one can recognize 2 SELs system as the first stage of implementation of programmable quantum matter. In general case considered 2-SELs Hamiltonian consists 12 different E_p parameters and 6 different t parameters that can be controlled electrostatically (18 parameters under electrostatic control) by 2-SELs controlling voltages $V_0(t), \dots, V_3(t), V_{0'}(t), \dots, V_{3'}(t)$ depicted in Fig. 1.

The numerical modeling of electron transport across coupled SELs is about solving a set of nine coupled recurrent equations of motion as it is in the case of

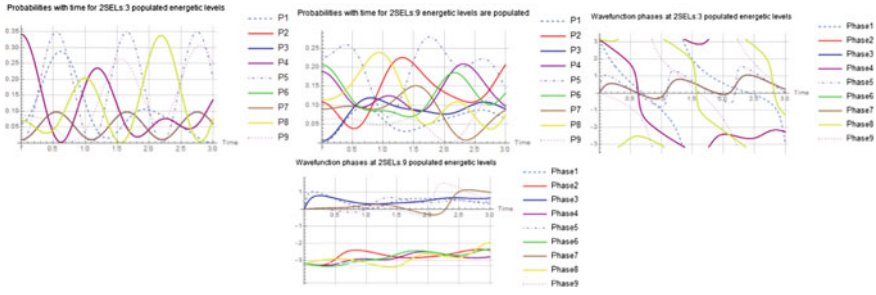


Fig. 12 Quantum state of two SELs over time: Upper (Lower) plots populate 3 (9) energy levels as given by Scenario I (Scenario II). The probabilities of finding both electrons simultaneously at the input $p_1(t) = |\gamma_1(t)|^2$ and output $p_9(t) = |\gamma_9(t)|^2$ is shown with time as well as evolution of phases $\phi_1(t), \dots, \phi_9(t)$ of $\gamma_1(t) = |\gamma_1(t)|e^{i\phi_1(t)}, \dots, \gamma_9(t) = |\gamma_9(t)|e^{i\phi_9(t)}$ corresponding to equation (117)

time-dependent 2 SELs Hamiltonian. In this work we consider time-independent Hamiltonian implying constant occupation of energetic levels. Therefore the quantum state can be written in the form $|\psi(t')\rangle = \alpha_1 e^{\frac{\hbar}{i} E_1 t'} |E_1\rangle + \dots + \alpha_9 e^{\frac{\hbar}{i} E_9 t'} |E_9\rangle$, so the probability of occupancy of energetic level E_1 is $|\alpha_1|^2 = |\langle E_1 | \psi(t) \rangle|^2 = p_{E1} = \text{constant}$, etc. Since we have obtained analytical form of all states $|E_k\rangle$ and eigenenergies E_k we have analytical form of quantum state dynamics $|\psi(t')\rangle$ with time. From obtained analytical solutions presented in Appendix 1 we recognize that every eigenenergy state is the linear combination of position-based states $|k\rangle \otimes |l'\rangle$ what will imply that quantum state can never be fully localized at two nodes k and l' as it is pointed by analytically obtained eigenstates of the 2-SELs Hamiltonian that are given in Appendix 1. In the conducted numerical simulations we visualize analytical solutions. We set $\hbar = 1$ and $\alpha_1 = \dots = \alpha_8 = \frac{1}{9}, \alpha_9 = \sqrt{1 - \frac{8}{81}}$ (Scenario I that has populated all 9 energetic levels) or $\alpha_1 = \alpha_2 = \frac{1}{2}, \alpha_9 = \frac{\sqrt{2}}{2}, \alpha_3 = \dots = \alpha_8$ (Scenario II that has populated 3 energetic levels) that will correspond to top or bottom plots of Fig. 12. We can recognize that probability of occupancy of $(1, 1')$ from Fig. 1. (when two electrons are at input of 2-SELs) is given by $|\langle (1, 0, 0) \otimes \langle 1, 0, 0 | \psi(t) \rangle|^2 = |\gamma_1(t)|^2 = p_1(t)$ (two electrons as SELs inputs) can be compared with occupancy of $(3, 3')$ given by $p_9(t) = |\gamma_9(t)|^2 = |\langle (0, 0, 1) \otimes \langle 0, 0, 1 | \psi(t) \rangle|^2$ (2 electrons at SELs outputs) as depicted in Fig. 12. It is relatively easy to identify probability of finding first electron at input as the sum of $p_1(t) + p_2(t) + p_3(t)$.

Various symmetries can be traced in the Scenario II (9 populated energy levels) given by Fig. 12. as between probability $p_2(t)$ and $p_8(t)$ or in the upper part of Fig. 12 in the Scenario I (3 populated energy levels) when $p_2(t) = p_8(t)$ or $\phi_2(t) = \text{phase}(\gamma_2(t)) = \phi_8(t)$. The same symmetry relations applies to the case of probability $p_4(t)$ and $p_6(t)$ as well as $\phi_4(\gamma_4(t))$ and $\phi_6(\gamma_6(t))$. These symmetries has its origin in the fact that 2 SELs system is symmetric along x axes what can be recognized in symmetries of simplified Hamiltonian matrix 120. It shall be underlined that in the

most general case when system matrix has no symmetries the energy eigenspectra might have less monotonic behaviour.

9.3 Act of Measurement and Dynamics of Quantum State

The quantum system dynamics over time is expressed by the equation of motion $\hat{H}(t') |\psi(t')\rangle = i\hbar \frac{d}{dt'} |\psi(t')\rangle$ that can be represented in discrete time step by relation

$$\frac{dt'}{i\hbar} \hat{H}(t') |\psi(t')\rangle + |\psi(t')\rangle = |\psi(t' + dt')\rangle. \quad (124)$$

It leads to the following equations of motion for quantum state expressed by Eq. (117) as follows

$$\begin{aligned} \vec{\gamma}(t' + dt') &= \left\{ \begin{array}{l} \gamma_1(t') + dt' \sum_{k=1}^9 \hat{H}_{1,k}(t') \gamma_k(t') = \\ f_1(\vec{\gamma}(t'), dt')[\hat{H}(t')], \\ \dots \\ \gamma_9(t') + dt' \sum_{k=1}^9 \hat{H}_{9,k}(t') \gamma_k(t') = \\ f_9(\vec{\gamma}(t'), dt')[\hat{H}(t')] \end{array} \right\} = \\ &= \vec{f}(\vec{\gamma}(t'), dt')[\hat{H}(t')] = \vec{f}(\vec{\gamma}(t'), dt')_{[\hat{H}(t')]} \end{aligned} \quad (125)$$

Symbol $[\cdot]$ denotes functional dependence of $\vec{f}(\vec{\gamma}(t'), dt')$ on Hamiltonian $\hat{H}(t')$. The measurement can be represented by projection operators $\hat{\Pi}(t')$ equivalent to the matrix that acts on the quantum state over time. The lack of measurement can simply mean that the state projects on itself so the projection is the identity operation ($\hat{\Pi}(t') = \hat{I}_{9 \times 9}$). Otherwise, the quantum state is projected on its subset and hence the projection operator can change in a non-continuous way over time. We can formally write the quantum state dynamics with respect to time during the occurrence of measurement process (interaction of external physical system with the considered quantum system) as

$$\vec{\gamma}(t' + dt') = \frac{\hat{\Pi}(t' + dt')(\vec{f}(\vec{\gamma}(t'), dt'))}{(\hat{\Pi}(t' + dt') \vec{f}(\vec{\gamma}(t'), dt'))^\dagger (\hat{\Pi}(t' + dt') \vec{f}(\vec{\gamma}(t'), dt'))}. \quad (126)$$

Let us refer to some example by assuming that a particle in the upper SELs was detected by the upper output detector (Fig. 9b). In such a case, the following projector $\hat{\Pi}(t, t + \Delta t)$ is different from the identity in time interval $(t, t + \Delta t)$ with $1_{1,t,t+\Delta t} = 1$ set to 1 in this time interval and 0 otherwise. The projector acts on the quantum state (diagonal matrix is given by diag symbol). It is given as

$$\begin{aligned}
\hat{\Pi}(t, t + \Delta t) &= (1 - 1_{t,t+\Delta t})(\hat{I}_U \times \hat{I}_L) + \\
&1_{t,t+\Delta t}(|0, 0, 1\rangle_U \langle 0, 0, 1|_U \times \hat{I}_L) = \\
&(1 - 1_{t,t+\Delta t})(\hat{I}_U \times \hat{I}_L) + \\
1_{t,t+\Delta t}(|0, 0, 1\rangle_U \langle 0, 0, 1|_U \times (|1, 0, 0\rangle_L \langle 1, 0, 0|_L + \\
&|0, 1, 0\rangle_L \langle 0, 1, 0|_L + |0, 0, 1\rangle_L \langle 0, 0, 1|_L)) = \\
&= (1 - 1_{t,t+\Delta t})\hat{I}_{9 \times 9} + 1_{t,t+\Delta t} \text{diag}(0, 0, 1) \times \hat{I}_{3 \times 3} \\
&= \text{diag}((1 - 1_{t,t+\Delta t}), (1 - 1_{t,t+\Delta t}), (1 - 1_{t,t+\Delta t}), \\
&(1 - 1_{t,t+\Delta t}), (1 - 1_{t,t+\Delta t}), (1 - 1_{t,t+\Delta t}), 1, 1, 1)
\end{aligned} \tag{127}$$

10 Correlations for the Case of 2 Electrostatically Interacting Qubits

We define correlation function as $C_c(a, b) = \frac{N_{+,+} + N_{-,-} - N_{+,-} - N_{-,+}}{N_{+,+} + N_{-,-} + N_{+,-} + N_{-,+}}$, where $N_{+,+}$ represents presence of 2 electrons at points 2 and 2', $N_{-,-}$ represents presence of electrons at points 1 and 1', $N_{+,-}$ is corresponding to presence of electrons at point 2 and 1' and $N_{-,+}$ is corresponding to presence of electrons at point 1 and 2'. It is convenient to introduce the operator

$$\begin{aligned}
N_{+,+} + N_{-,-} - N_{+,-} - N_{-,+} &= \langle \psi, t | \begin{pmatrix} 1 & 0 & 0 & 0 \\ 0 & -1 & 0 & 0 \\ 0 & 0 & -1 & 0 \\ 0 & 0 & 0 & 1 \end{pmatrix} | \psi, t \rangle \\
&= \langle \psi, t_0 | U(t, t_0)^{-1} \sigma_3 \times \sigma_3 U(t, t_0) | \psi, t_0 \rangle
\end{aligned} \tag{128}$$

Consequently we obtain

$$\begin{aligned}
|E_1\rangle_n &= \frac{1}{\sqrt{\left(8 \left(\frac{t_{sr1} - t_{sr2}}{\sqrt{(E_{c1} - E_{c2})^2 + 4(t_{sr1} - t_{sr2})^2 - E_{c1} + E_{c2}}}\right)\right)^2 + 2}} \\
&\begin{pmatrix} -1, \\ \frac{2(t_{sr1} - t_{sr2})}{\sqrt{(E_{c1} - E_{c2})^2 + 4(t_{sr1} - t_{sr2})^2 - E_{c1} + E_{c2}}}, \\ \frac{2(t_{sr1} - t_{sr2})}{\sqrt{(E_{c1} - E_{c2})^2 + 4(t_{sr1} - t_{sr2})^2 - E_{c1} + E_{c2}}}, \\ 1 \end{pmatrix} \\
&= \frac{1}{\sqrt{\left(8 \left(\frac{t_{sr1} - t_{sr2}}{\sqrt{(E_{c1} - E_{c2})^2 + 4(t_{sr1} - t_{sr2})^2 - E_{c1} + E_{c2}}}\right)\right)^2 + 2}} |E_1\rangle
\end{aligned}$$

$$\begin{aligned}
|E_1\rangle_n &= \frac{1}{\sqrt{\left(8\left(\frac{t_{sr1}-t_{sr2}}{\sqrt{(E_{c1}-E_{c2})^2+4(t_{sr1}-t_{sr2})^2-E_{c1}+E_{c2}}}\right)\right)^2+2}} \\
&\quad \left(\begin{array}{c} -1, \\ \frac{2(t_{sr1}-t_{sr2})}{\sqrt{(E_{c1}-E_{c2})^2+4(t_{sr1}-t_{sr2})^2-E_{c1}+E_{c2}}}, \\ \frac{2(t_{sr1}-t_{sr2})}{\sqrt{(E_{c1}-E_{c2})^2+4(t_{sr1}-t_{sr2})^2-E_{c1}+E_{c2}}} \\ 1 \end{array} \right) \\
&= \frac{1}{\sqrt{\left(8\left(\frac{t_{sr1}-t_{sr2}}{\sqrt{(E_{c1}-E_{c2})^2+4(t_{sr1}-t_{sr2})^2-E_{c1}+E_{c2}}}\right)\right)^2+2}} |E_1\rangle
\end{aligned}$$

$$\begin{aligned}
|E_2\rangle_n &= -\frac{1}{\sqrt{\left(8\left(\frac{t_{sr1}-t_{sr2}}{\sqrt{(E_{c1}-E_{c2})^2+4(t_{sr1}-t_{sr2})^2+E_{c1}-E_{c2}}}\right)\right)^2+2}} \\
&\quad \left(\begin{array}{c} -1 \\ \frac{2(t_{sr1}-t_{sr2})}{\sqrt{(E_{c1}-E_{c2})^2+4(t_{sr1}-t_{sr2})^2+E_{c1}-E_{c2}}} \\ -\frac{2(t_{sr1}-t_{sr2})}{\sqrt{(E_{c1}-E_{c2})^2+4(t_{sr1}-t_{sr2})^2+E_{c1}-E_{c2}}} \\ 1 \end{array} \right) \\
&= -\frac{1}{\sqrt{\left(8\left(\frac{t_{sr1}-t_{sr2}}{\sqrt{(E_{c1}-E_{c2})^2+4(t_{sr1}-t_{sr2})^2+E_{c1}-E_{c2}}}\right)\right)^2+2}} |E_2\rangle
\end{aligned}$$

$$\begin{aligned}
|E_3\rangle_n &= \frac{1}{\sqrt{\left(8\left(\frac{t_{sr1}+t_{sr2}}{\sqrt{(E_{c1}-E_{c2})^2+4(t_{sr1}+t_{sr2})^2-E_{c1}+E_{c2}}}\right)\right)^2+2}} \\
&\quad \left(\begin{array}{c} 1, \\ \frac{2(t_{sr1}+t_{sr2})}{\sqrt{(E_{c1}-E_{c2})^2+4(t_{sr1}+t_{sr2})^2-E_{c1}+E_{c2}}}, \\ -\frac{2(t_{sr1}+t_{sr2})}{\sqrt{(E_{c1}-E_{c2})^2+4(t_{sr1}+t_{sr2})^2-E_{c1}+E_{c2}}} \\ 1 \end{array} \right) \\
&= \frac{1}{\sqrt{\left(8\left(\frac{t_{sr1}+t_{sr2}}{\sqrt{(E_{c1}-E_{c2})^2+4(t_{sr1}+t_{sr2})^2-E_{c1}+E_{c2}}}\right)\right)^2+2}} |E_3\rangle
\end{aligned}$$

$$\begin{aligned}
 |E_4\rangle_n &= \frac{1}{\sqrt{\left(8\left(\frac{t_{sr1}+t_{sr2}}{\sqrt{(E_{c1}-E_{c2})^2+4(t_{sr1}+t_{sr2})^2-E_{c2}+E_{c1}}}\right)\right)^2+2}} \\
 &\quad \left(\begin{array}{c} 1, \\ \frac{2(t_{sr1}+t_{sr2})}{\sqrt{(E_{c1}-E_{c2})^2+4(t_{sr1}+t_{sr2})^2+E_{c1}-E_{c2}}}, \\ \frac{2(t_{sr1}+t_{sr2})}{\sqrt{(E_{c1}-E_{c2})^2+4(t_{sr1}+t_{sr2})^2+E_{c1}-E_{c2}}}, \\ 1 \end{array}\right) \\
 &= \frac{1}{\sqrt{\left(8\left(\frac{t_{sr1}+t_{sr2}}{\sqrt{(E_{c1}-E_{c2})^2+4(t_{sr1}+t_{sr2})^2-E_{c2}+E_{c1}}}\right)\right)^2+2}} |E_4\rangle.
 \end{aligned}$$

10.1 Correlation Function for Classical and Quantum Approaches for Single-Electron Lines

In this work, two capacitively coupled single-electron lines (SEL) are treated by the tight-binding model with the use of three nodes for each line to describe the electron occupancy. It should be highlighted that the most simplistic approach towards the two SELs can be attempted with the use of two nodes for each line. In such a case, it is possible to introduce a correlation function for both quantum and classical treatments of the system under consideration. Let us start from the quantum approach. The Hamiltonian of the system having flat bottoms of potentials can be written as

$$H = \begin{pmatrix} E_{c1} + 2E_p & e^{i\beta}t_{s2} & e^{i\alpha}t_{s1} & 0 \\ e^{-i\beta}t_{s2} & E_{c2} + 2E_p & 0 & e^{i\alpha}t_{s1} \\ e^{-i\alpha}t_{s1} & 0 & E_{c2} + 2E_p & e^{i\beta}t_{s2} \\ 0 & e^{-i\alpha}t_{s1} & e^{-i\beta}t_{s2} & E_{c1} + 2E_p \end{pmatrix}, \tag{129}$$

where $E_{c1} = \frac{q^2}{d}$ and $E_{c2} = \frac{q^2}{\sqrt{d^2+a^2}}$, so $E_{c1} - E_{c2} = \frac{q^2}{d} - \frac{q^2}{\sqrt{d^2+a^2}} > 0$. The hopping terms are parametrized by t_{s1} and t_{s2} . This last Hamiltonian refers to the quantum state describing the occupancy of four nodes at upper $U = (1, 2)$ or lower line $L = (1', 2')$ by two spatially separated electrons

$$|\psi\rangle = \gamma_1(t) |1\rangle |1'\rangle + \gamma_2(t) |1\rangle |2'\rangle + \gamma_3(t) |2\rangle |1'\rangle + \gamma_4(t) |2\rangle |2'\rangle. \tag{130}$$

Normalization condition requires $|\gamma_1|^2 + \dots + |\gamma_4|^2 = 1$. We have four eigenenergies

$$E_1 = \frac{1}{2}(E_{c1} + E_{c2} + 4E_p - \sqrt{(E_{c1} - E_{c2})^2 + 4(t_{s1} - t_{s2})^2}),$$

$$\begin{aligned}
E_2 &= \frac{1}{2}(E_{c1} + E_{c2} + 4E_p + \sqrt{(E_{c1} - E_{c2})^2 + 4(t_{s1} - t_{s2})^2}), \\
E_3 &= \frac{1}{2}(E_{c1} + E_{c2} + 4E_p - \sqrt{(E_{c1} - E_{c2})^2 + 4(t_{s1} + t_{s2})^2}), \\
E_4 &= \frac{1}{2}(E_{c1} + E_{c2} + 4E_p + \sqrt{(E_{c1} - E_{c2})^2 + 4(t_{s1} + t_{s2})^2}),
\end{aligned} \tag{131}$$

fulfilling $E_1 < E_2$, $E_3 < E_4$ as corresponding to four eigenenergy states

$$\begin{aligned}
|E_1\rangle &= \begin{pmatrix} -e^{i(\alpha+\beta)}, \\ \frac{2e^{i\alpha}(t_{s1}-t_{s2})}{\sqrt{(E_{c1}-E_{c2})^2+4(t_{s1}-t_{s2})^2}-E_{c1}+E_{c2}}}, \\ \frac{2e^{i\beta}(t_{s1}-t_{s2})}{\sqrt{(E_{c1}-E_{c2})^2+4(t_{s1}-t_{s2})^2}-E_{c1}+E_{c2}}}, \\ 1 \end{pmatrix}, \\
|E_2\rangle &= \begin{pmatrix} -e^{i(\alpha+\beta)}, \\ \frac{2e^{i\alpha}(t_{s1}-t_{s2})}{\sqrt{(E_{c1}-E_{c2})^2+4(t_{s1}-t_{s2})^2}+E_{c1}-E_{c2}}}, \\ \frac{2e^{i\beta}(t_{s1}-t_{s2})}{\sqrt{(E_{c1}-E_{c2})^2+4(t_{s1}-t_{s2})^2}+E_{c1}-E_{c2}}}, \\ 1 \end{pmatrix}, \\
|E_3\rangle &= \begin{pmatrix} e^{i(\alpha+\beta)}, \\ -\frac{2e^{i\alpha}(t_{s1}+t_{s2})}{\sqrt{(E_{c1}-E_{c2})^2+4(t_{s1}+t_{s2})^2}-E_{c2}+E_{c1}}}, \\ -\frac{2e^{i\beta}(t_{s1}+t_{s2})}{\sqrt{(E_{c1}-E_{c2})^2+4(t_{s1}+t_{s2})^2}-E_{c2}+E_{c1}}}, \\ 1 \end{pmatrix}, \\
|E_4\rangle &= \begin{pmatrix} e^{i(\alpha+\beta)}, \\ \frac{2e^{i\alpha}(t_{s1}+t_{s2})}{\sqrt{(E_{c1}-E_{c2})^2+4(t_{s1}+t_{s2})^2}+E_{c1}-E_{c2}}}, \\ \frac{2e^{i\beta}(t_{s1}+t_{s2})}{\sqrt{(E_{c1}-E_{c2})^2+4(t_{s1}+t_{s2})^2}+E_{c1}-E_{c2}}}, \\ 1 \end{pmatrix}.
\end{aligned} \tag{132}$$

with ground state

$$E_3 = E_g = \frac{1}{2}(E_{c1} + E_{c2} + 4E_p - \sqrt{(E_{c1} - E_{c2})^2 + 4(t_{s1} + t_{s2})^2}). \tag{133}$$

We observe that in the ground state, the probability of occurrence of two particles at the maximum distance $p_{1,2'} = p_{2,1'} = p_{\text{anticorr}}$ to the probability of two particles occurrence at the minimum distance $p_{1,1'} = p_{2,2'} = p_{\text{corr}}$ is given by the formula:

$$\frac{p_{\text{acorr}}}{p_{\text{corr}}} = \left[\frac{\sqrt{(E_{c1} - E_{c2})^2 + 4(t_{s1} + t_{s2})^2} - (E_{c1} - E_{c2})}{2(t_{s1} + t_{s2})} \right]^2 =$$

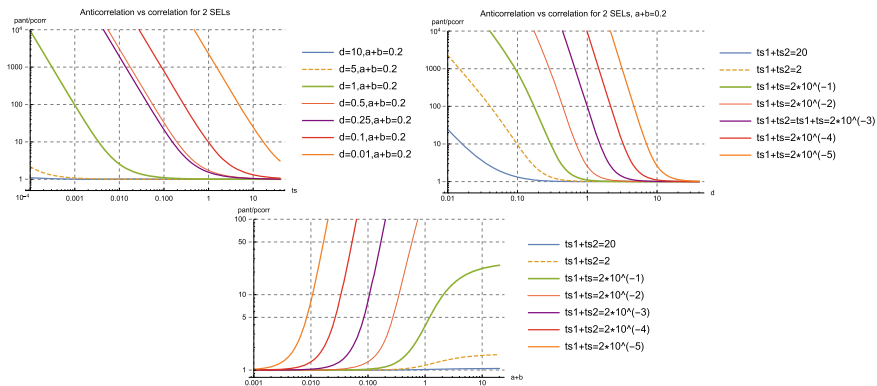


Fig. 13 The ratio of probabilities in 2 SELs ground state between correlated and anticorrelated quantum state components is very strongly depending on hopping constants by term $t_{s1} + t_{s2}$ and very strongly depends on size of quantum wells denoted by a and distance between two two neighbours a

$$\left[\frac{\sqrt{q^2(\sqrt{d^2 + (a+b)^2} - d)^2 + 4(t_{s1} + t_{s2})^2}}{2(t_{s1} + t_{s2})d\sqrt{d^2 + (a+b)^2}} - \frac{q^2(\sqrt{d^2 + (a+b)^2} - d)}{2(t_{s1} + t_{s2})d\sqrt{d^2 + (a+b)^2}} \right]^2 \quad (134)$$

It is worth mentioning that ground state of 2 coupled SELs brings electrons partly into anticorrelated position (2 electrons at maximum distance) and correlated positions (2 electrons at minimum distance) what simply means that anticorrelation is not greatly pronounced in quantum case at it is the case of classical picture. One can refer to the following dependence of ratio between probabilities for the state to be anticorrelated or correlated state as depicted by Fig. 13.

The quantum state in case of time-independent Hamiltonian can be expressed as

$$|\psi\rangle = \sqrt{p_{E1}} e^{\frac{\phi_{E10i}}{\hbar i}} e^{\frac{1}{\hbar i} E_1 t} |E_1\rangle + \sqrt{p_{E2}} e^{\frac{\phi_{E20i}}{\hbar i}} e^{\frac{1}{\hbar i} E_2 t} |E_2\rangle + \sqrt{p_{E3}} e^{\frac{\phi_{E30i}}{\hbar i}} e^{\frac{1}{\hbar i} E_3 t} |E_3\rangle + \sqrt{p_{E4}} e^{\frac{\phi_{E40i}}{\hbar i}} e^{\frac{1}{\hbar i} E_4 t} |E_4\rangle. \quad (135)$$

Having $E_{c1} = \frac{q^2}{d}$ and $E_{c2} = \frac{q^2}{\sqrt{d^2 + a^2}}$ so $E_{c1} - E_{c2} = \frac{q^2}{d} - \frac{q^2}{\sqrt{d^2 + a^2}} > 0$ and hopping terms t_{s1}, t_{s2} we obtain Hamiltonian and a correlation function C .

We refer to the physical situation depicted in Fig. 14 and utilize the correlation function C to capture as to what extent the two electrons are in a correlated state being both either on the left or on the right side that is corresponding to terms $N_{-,-}, N_{+,+}$, or in an anticorrelated state (expressed by terms $N_{+,-}$ and $N_{-,+}$). Such function is commonly used in spin systems and is a measure of non-classical correlations. Using a tight-binding model describing two electrostatically coupled SELs and using the same correlation function applicable in the test of Bell theory of entangled spins [7], we obtain the correlation function C given by formula:

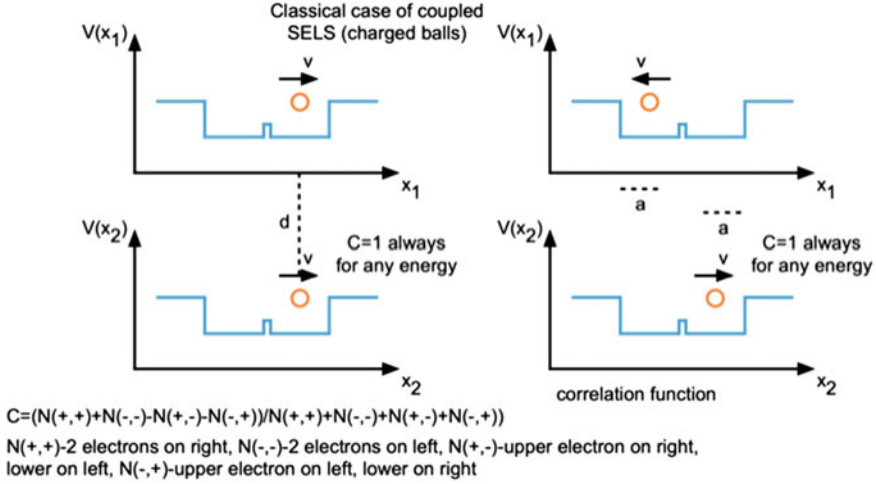


Fig. 14 Case of electrostatically coupled charged particles confined by local potentials and electrostatically interacting. Concept of correlation/anticorrelation in their positions

$$\begin{aligned}
 C &= \frac{N_{+,+} + N_{-,-} - N_{+,-} - N_{-,+}}{N_{+,+} + N_{-,-} + N_{+,-} + N_{-,+}} \\
 &= 4 \left[\frac{\sqrt{pE1}\sqrt{pE2}(t_{s1} - t_{s2}) \cos[-t\sqrt{(E_{c1} - E_{c2})^2 + 4(t_{s1} - t_{s2})^2} + \phi_{E10} - \phi_{E20}]}{\sqrt{(E_{c1} - E_{c2})^2 + 4(t_{s1} - t_{s2})^2}} \right. \\
 &\quad \left. + \frac{\sqrt{pE3}\sqrt{pE4}(t_{s1} + t_{s2}) \cos[-t\sqrt{(E_{c1} - E_{c2})^2 + 4(t_{s1} + t_{s2})^2} + \phi_{E30} - \phi_{E40}]}{\sqrt{(E_{c1} - E_{c2})^2 + 4(t_{s1} + t_{s2})^2}} \right] \\
 &\quad - (E_{c1} - E_{c2}) \left[\frac{pE1 - pE2}{\sqrt{(E_{c1} - E_{c2})^2 + 4(t_{s1} - t_{s2})^2}} \right. \\
 &\quad \left. + \frac{pE3 - pE4}{\sqrt{(E_{c1} - E_{c2})^2 + 4(t_{s1} + t_{s2})^2}} \right] \quad (136)
 \end{aligned}$$

Classical intuition points out that when the kinetic energy of electrons goes to zero they shall be anticorrelated due to the presence of the repulsive Coulomb force. On the other hand, when the kinetic energy is dominant, the Coulomb interaction does not matter so much and the correlation function shall be zero or positive. Four fundamental solutions for the correlation function corresponding to the occupancy of four eigenenergies are given by Fig. 15. Indeed, when only the ground state is occupied so $p_1 = 1$, then $C < 1$, as depicted in Fig. 16. It is remarkable to observe that $C = 0$ if $p_1 = p_3 = 0.5$. We also observe that if the two qubits are electrostatically decoupled then $C = 0$ does not need to be applied. However, for certain cases, the weaker the Coulomb interaction the sharper the peaks in the 2-SEL correlation function C , as depicted by Fig. 16 (Fig. 17).

Now we turn towards the classical description of the two coupled single-electron lines using Newtonian dynamics as we expect qualitative changes in the correlation

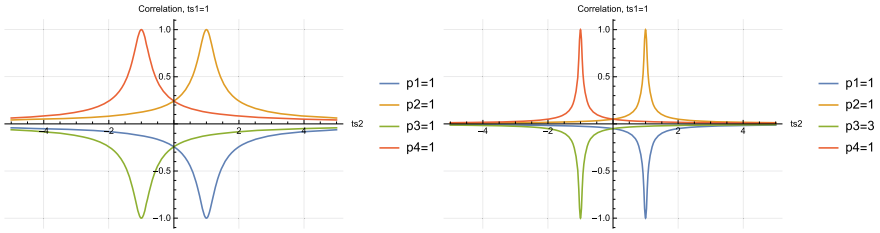


Fig. 15 Four main fundamental configurations named as anticorrelation and correlation for system of coupled SEL depicted in Fig. 14. The correlation function C that are grasped by Formula (136) corresponding to the full occupancy of one among four eigenenergies

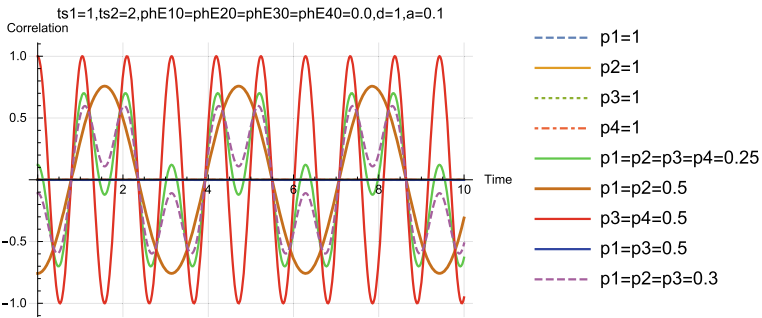


Fig. 16 Correlation function C with time for time-independent Hamiltonian corresponding to full and partial occupancy of 4 eigenenergies of 2-SEL system

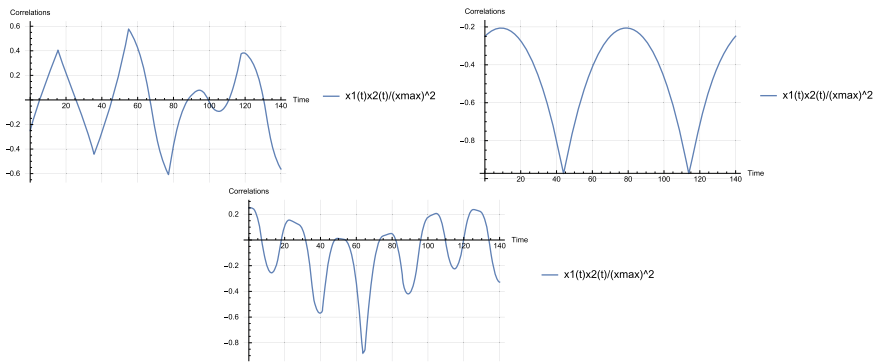


Fig. 17 Varying dependence of classical correlation function $[C = \frac{x_1(t)x_2(t)}{x_{max}^2}]$ over time. Upper case refers to 2-SELs with particles of significantly different speeds at anticorrelated positions at initial time; middle figure describes two perfectly anticorrelated particles (14); third case refers to the proceeding Fig. 18

function due to the unique differences between the quantum and classical pictures. The confinement potential is approximated as a step function and presence of Poynting vector is neglected in the space as Hamiltonian system is time-independent, and system Hamiltonian corresponds to the classical mechanical energy that is preserved if we omit radiation emission for two particles subjected to acceleration and deceleration during different moments of motion that can be periodic or aperiodic. We have the minimalistic classical Hamiltonian for 2SELS given as

$$\begin{aligned} \hat{H} = & \frac{1}{2m_1} p_1(t)^2 + \frac{1}{2m_2} p_2(t)^2 + \frac{q^2}{\sqrt{d^2 + (x_1(t) - x_2(t))^2}} \\ & + V_0 \Theta(x_1(t) - x_{\max 1}) + V_0 \Theta(-x_1(t) - x_{\max 1}) + \\ & V_0 \Theta(x_2(t) - x_{\max 2}) + V_0 \Theta(-x_2(t) - x_{\max 2}) \\ & + V_{b1} \Theta(x_1(t) - x_{b1}) + V_{b1} \Theta(-x_1(t) - x_{b1}) + \\ & V_{b2} \Theta(x_2(t) - x_{b2}) + V_{b2} \Theta(-x_2(t) - x_{b2}). \end{aligned} \quad (137)$$

We simplify the situation by having two symmetric masses $m_1 = m_2 = m$ and same charges q , and having $x_{\max 1} = x_{\max 2} = x_{\max}$. We set $x_{b1} = x_{b2} \rightarrow 0$. There are always two possible ground states of the classically interacting electrons in 2 SELs configuration corresponding to the same energy when charged particles of same charge are confined in local potential that corresponds to two positions of particle that are at maximum distance $x_2(t) = \mp x_{\min} = \text{constans}$, $\frac{dx_1}{dt}(t) = 0$, $\frac{d^2x_1}{dt^2}(t) = 0$, $x_2(t) = \pm x_{\min}$, $\frac{dx_1}{dt}(t) = 0$, $\frac{d^2x_1}{dt^2}(t) = 0$. Classical ground state is maximally anticorrelated. On the contrary the same situation in quantum picture has only one ground state and this state is not maximally anticorrelated and is partly correlated what is expressed by Formula 134. Moreover, in the classical picture of 2 SELs, one can observe the emergence of deterministic chaos that is heavily pronounced in the classical system, as depicted in Figs. 18 and 19. Now we are moving towards a description of classical 2-SEL system in case of perfect correlated or anticorrelated electrons. From the classical Hamiltonian we determine the equations of motion of the two electrons assuming the existence of the antisymmetric case $\pm x(t) = x_1(t) = -x_2(t)$ at all instances of motion for the system symmetric around $x = 0$. We assume that the distance between electrons $\sqrt{d^2 + x(t)^2} \approx d$. We have

$$mv^2(t) + \frac{q^2}{\sqrt{d^2 + x^2}} = E_c > 0, \quad \frac{d^2x}{dt} = \frac{xq^2}{(\sqrt{d^2 + x^2})^3}.$$

In simplified case $d \gg x$ and thus we can write

$$m \frac{d^2x(t)}{dt^2} = x \frac{q^2}{d^{\frac{3}{2}}}. \quad (138)$$

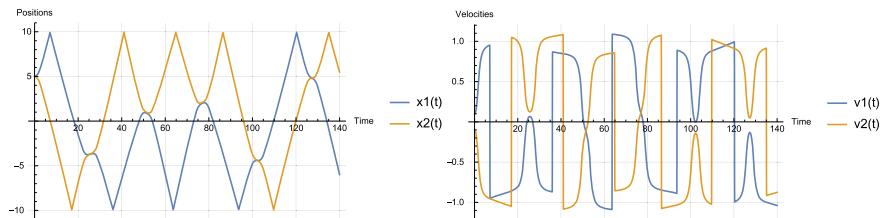


Fig. 18 Evolution of positions $x_i(t)$ and velocities $v_i(t)$ for the system of 2 electrostatically coupled SELs in classical picture

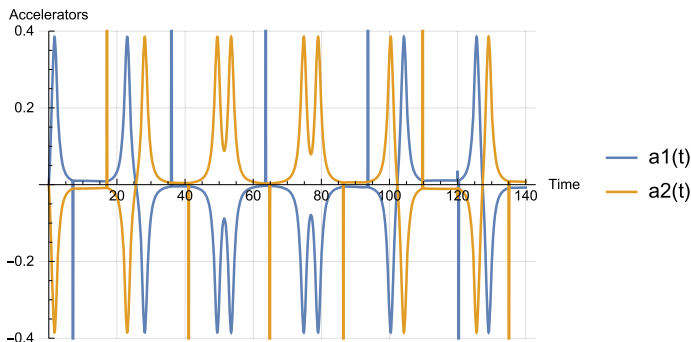


Fig. 19 Acceleration for the system of 2 coupled oscillators from Fig. 18 confined by local potential with coordinates $x_1, x_2 \in (-x_{\max}, x_{\max})$ with $x_{\max} = 10$

and it has solutions for each electron position

$$x(t) = \frac{\sqrt{m}v_0d^{3/4}}{q} \sinh\left(\frac{q}{\sqrt{m}d^{3/4}}t\right). \quad (139)$$

We notice that $x_{\max} = \frac{\sqrt{m}v_0d^{3/4}}{q} \sinh\left(\frac{q}{\sqrt{m}d^{3/4}}\frac{T}{4}\right)$ and the period of oscillations is

$$T = 4 \frac{\sqrt{m}d^{3/4}}{q} \operatorname{Ar}c_{\sinh}\left(\frac{qx_{\max}}{\sqrt{m}v_0d^{3/4}}\right) \quad (140)$$

if $x_1(t=0) = x_2(t=0) = 0$ and when $\frac{dx_1}{dt}(t=0) = -\frac{dx_2}{dt}(t=0) = v_0 \neq 0$, which is a definition of perfect anticorrelation. Collision with walls is occurring at $\frac{T}{4}$ time while the total size of classical well is $2x_{\max}$. We observe that $x_1(t) = \frac{\sqrt{m}v_0d^{3/4}}{q} \sinh\left(\frac{q}{\sqrt{m}d^{3/4}}t\right) = -x_2(t)$ for $t \in [0, \frac{T}{4}]$. Correlation function C is given analytically

$$C(t) = -\frac{1}{x_{\max}^2} \frac{mv_0^2d^{3/2}}{q^2} (\sinh\left(\frac{q}{\sqrt{m}d^{3/4}}t\right))^2 < 0 \quad (141)$$

and is negative for any energy E_c (function of q, d, v_0) of the system. Such situation occurs only in some subsets of the classical case since in the quantum case the sign of function C depends on the occupancy of the energetic levels. In the classical treatment of 2-SELs there exist the case of perfectly correlated electrons at any distance that is independent on the system energy if we are above the ground state.

It is possible to specify such situation when at $t = 0$ we have $x_1(t = 0) = x_2(t = 0) = 0$ and when $\frac{dx_1}{dt}(t = 0) = \frac{dx_2}{dt}(t = 0) = v_0$. In such a case, the Coulomb force will act perpendicular to the direction of motion and will play no role in the electron movement. Electron movement will be correlated and with constant speed over time, with periodic reflections from the potential walls. The correlation function will have the form

$$C(t) = \frac{1}{x_{max}^2} (v_0)^2 t^2 \quad (142)$$

within time $t \in [0, T/4]$. A perfect correlation of electrons in the classical situation can occur for any energy (if kinetic energy is larger than zero) of the system $E_c > 0$. It is one of the key differences from the quantum situation when the positive value of correlation function can occur only for certain system eigenenergies as given by Formula (136).

It should be underlined that the perfectly correlated electrons generate higher overall magnetic field energy as it is the case of two electric currents of the same sign (correlated electron movement in one direction) generated by each electron. In the case of anticorrelated electrons we are dealing with electric currents of opposite sign that are generating magnetic field in the opposite directions, thus decreasing the overall magnetic field. Therefore, thermal equilibrium of 2-SEL will favor anticorrelation of two electrons. It shall be underlined that, in accordance with the classical thermodynamics that applies to the case of two electrons treated classically, the movement of electron with certain acceleration will cause the occurrence of non-zero Poynting vector into the space and thus electron's energy will be emitted in the form of electromagnetic radiation. In such way one can introduce effective dissipative term to the movement of electrons and it will cause the system mechanical energy to eventually vanish. After sufficiently long time the electrons will stop their oscillatory movement and they will move into ground state that is perfectly anticorrelated and corresponds to the case when $x_2 = x_1 = \pm x_{max}$ and $\frac{d}{dt}x_1 = \frac{d}{dt}x_2$ and when $\frac{d^2}{dt^2}x_1 = 0 = \frac{d^2}{dt^2}x_2 = 0$. It is also worth mentioning that the ground state of two classical electrons in 2-SELs is different from the quantum ground state of 2-SELs.

A case described by two perfectly anticorrelated electrons at any distance in the classical treatment that is independent of the system energy. Such situation does not take place in the quantum case as treated by the tight-binding model given by Formula (136) that has discrete spectra of energies as specified by (131).

We can write the equations of motion of two electrons assuming the existence of antisymmetric case $x_1(t) = -x_2(t)$ at all instances of motion for the system symmetric around $x = 0$. From the equation

$$mv^2(t) + \frac{q^2}{\sqrt{d^2 + 4x(t)^2}} = E_c = \text{const} > 0,$$

we obtain the equation $\sqrt{\frac{q^4}{(E_c - mv^2(t))^2} - d^2} = 2x(t)$ and consequently we obtain the equation of motion

$$m \frac{dv}{dt} = \frac{1}{2} \sqrt{\frac{q^4}{(E_c - mv^2(t))^2} - d^2} \cdot q^2 (E_c - mv^2(t))^3 \frac{1}{q^6} = \frac{1}{2q^4} \sqrt{q^4 (E_c - mv^2(t))^4 - d^2 (E_c - mv^2(t))^6}. \quad (143)$$

Finally we obtain the equation

$$\frac{dv}{\sqrt{q^4 (E_c - mv^2(t))^4 - d^2 (E_c - mv^2(t))^6}} = dt \frac{1}{2mq^4} \quad (144)$$

We introduce a new variable $u = \frac{d}{q} (E_c - mv^2)$. We have $du = -2\frac{md}{q} v dv$. We also notice that $\sqrt{(\frac{E_c}{m} - \frac{q}{md}u)} = v$. The last expressions imply

$$dv = -\frac{q}{2md} \frac{du}{v} = -\frac{q}{2md} \frac{du}{\sqrt{(\frac{E_c}{m} - \frac{q}{md}u)}} = -\frac{\sqrt{q}}{2\sqrt{md}} \frac{du}{\sqrt{(\frac{E_c d}{q} - u)}}. \quad (145)$$

The last expression allows us to write integral

$$\begin{aligned} \int \frac{dv}{\sqrt{q^4 (E_c - mv^2)^4 - d^2 (E_c - mv^2)^6}} &= \frac{d^2}{q^4} \int \frac{du}{\sqrt{(\frac{E_c d}{q} - u)}} \frac{1}{u^2 \sqrt{1 - u^2}} \\ &= s_1 \int \frac{du}{\sqrt{(s - u)}} \frac{1}{u^2 \sqrt{1 - u^2}}. \end{aligned} \quad (146)$$

Setting $s_1 = \frac{d^2}{q^4}$ and $s = \frac{E_c d}{q}$ we obtain the integral $s_1 \int \frac{du}{\sqrt{(s - u)}} \frac{1}{u^2 \sqrt{1 - u^2}}$ that has a solution as three types of elliptic functions given in Appendix 2.

10.2 Classical Weak Measurement on 2-SEL System

Measurement on a given physical system is about introducing an interaction of it with an external physical system that acts as a probe. If this interaction is strong (weak) we are dealing with a strong (weak) measurement. We shall introduce an external charged particle at a certain distance that can move only in parallel to the

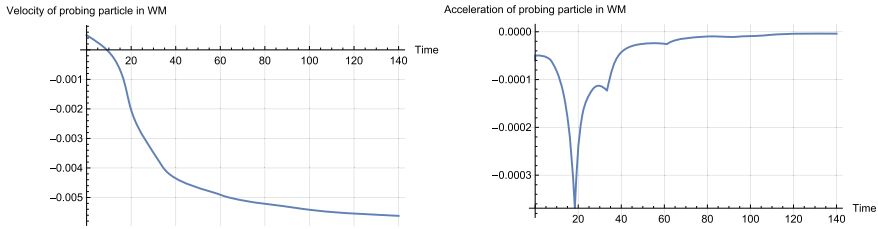


Fig. 20 Case of the classical measurement with electron used for probing of 2-SELs

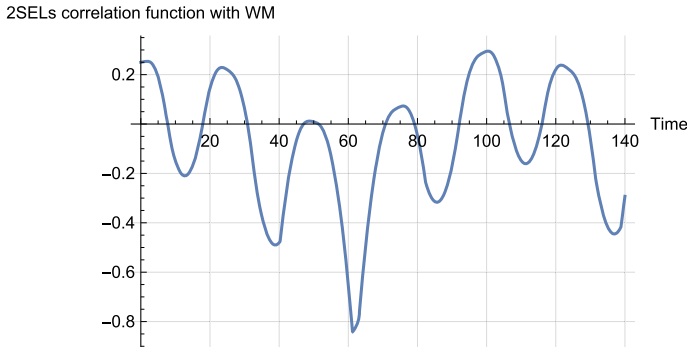


Fig. 21 Correlation function for 2-SELs under classical weak measurement from external probing charged particle. One shall refer to the bottom plot of Fig. 17 and to Fig. 22

system being probed and then we apply Newtonian equations of motion. For the sake of simplicity, we consider only interaction of the probe that is moving electron across one line with nearest charged particle, as depicted in Fig. 22. At a first level of approximation, the movement of external electron is the perturbation to the physical system of two electrons (2-SELs) (Figs. 20 and 21).

10.3 Weak Quantum Measurement on 2-SEL System

We consider an interaction of two single-electron lines (2-SEL) that incorporate qubits A and B with an external line along which there is a movement of position-based qubit C. The CMOS structures have the capability to impose a constrained ‘movement’ of a virtual qubit along single-electron lines. This way, the moving qubit becomes effectively a flying qubit, which is a term usually reserved for polarized photons participating in quantum information processing. At a very far distance, there is no interaction between the flying qubit and 2-SELs. In such a case one can have a tensor of two density matrices being a density matrix of 2-SELs denoted by ρ_{AB} and the external flying qubit. We have a three-body quantum density matrix given as

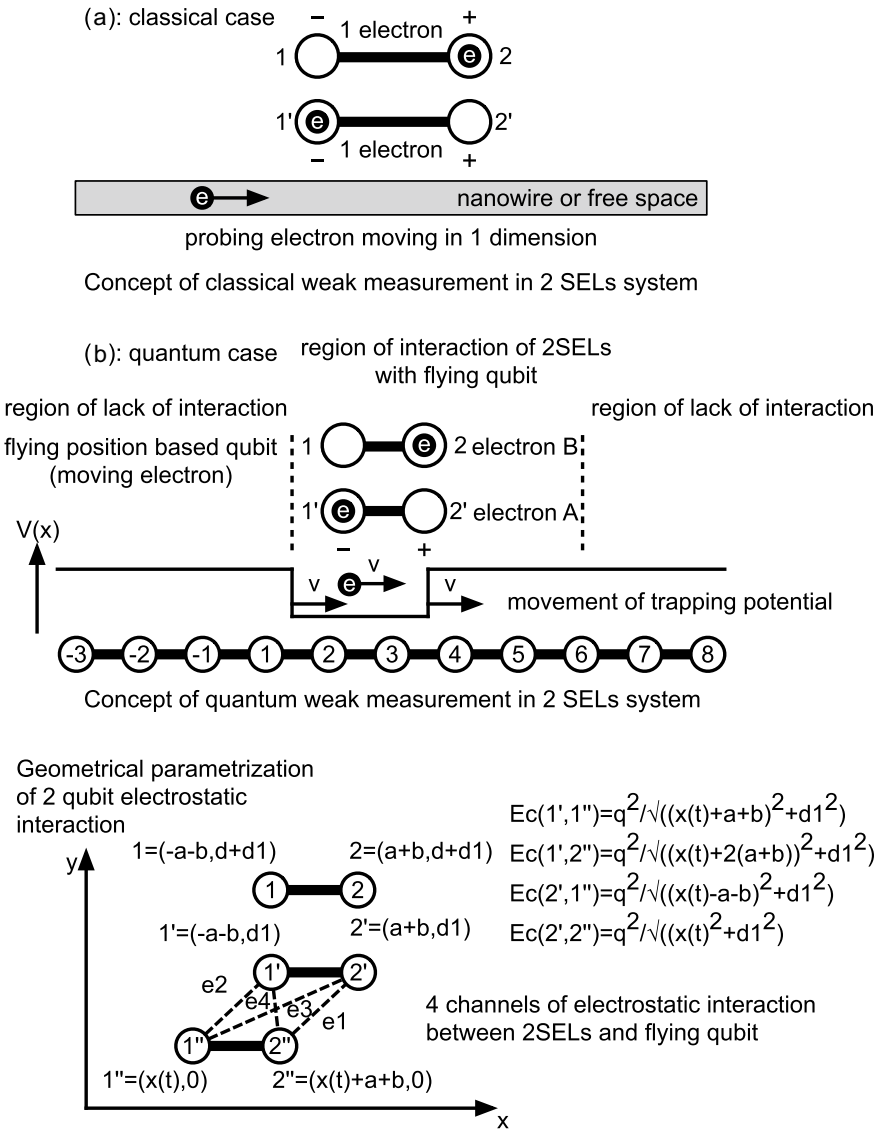


Fig. 22 Concept of classical and quantum weak measurements in a double single-electron line system. All simulations were conducted for the classical case

$$\hat{\rho}_{ABC} = \hat{\rho}_C \times \hat{\rho}_{AB} = \begin{pmatrix} \rho_C[1, 1] \hat{\rho}_{AB} & \rho_C[1, 2] \rho_{AB} \\ \rho_C[2, 1] \hat{\rho}_{AB} & \rho_C[2, 2] \rho_{AB} \end{pmatrix} = \begin{pmatrix} \hat{A}_1 & \hat{B}_1 \\ \hat{C}_1 & \hat{D}_1 \end{pmatrix}. \quad (147)$$

We immediately recognize that we can obtain the density matrix of particle C by tracing out the existence of density matrix AB

$$\hat{\rho}_C = \sum_{i_A=\{1,2\}, j_B=\{1',2'\}} \langle i_A, j_B | \hat{\rho}_{ABC} | i_A, j_B \rangle. \quad (148)$$

In similar way we obtain the density matrix for 2-SEL system

$$\hat{\rho}_{AB} = \sum_{k_C=\{1,2\}} \langle k_C | \hat{\rho}_{ABC} | k_C \rangle. \quad (149)$$

The last expressions can be expressed by formula

$$\hat{\rho}_C = \begin{pmatrix} Tr(\hat{A}_1) & Tr(\hat{B}_1) \\ Tr(\hat{C}_1) & Tr(\hat{D}_1) \end{pmatrix}, \hat{\rho}_{AB} = \hat{A}_1 + \hat{D}_1. \quad (150)$$

System of 2-SELS with the flying qubit can be regarded as non-dissipative system and thus one can write the following equations of motion

$$\rho(t) = e^{-\frac{1}{i\hbar} H_0 t} e^{\frac{1}{i\hbar} \int_0^t \hat{H}(t') dt'} \rho(t) e^{-\frac{1}{i\hbar} \int_0^t \hat{H}(t') dt'} e^{-\frac{1}{i\hbar} H_0 t}, \quad (151)$$

where H_0 is a time-independent Hamiltonian of isolated 2-SELS and isolated external qubit, while $H(t')$ stands for electrostatic interaction between the flying qubit and 2-SELS. We have the total system Hamiltonian having time-independent and time-dependent components

$$\hat{H}(t) = \hat{H}_0 + \hat{H}_1(t) = (\hat{I}_C \times \hat{H}_{AB} + \hat{H}_C \times \hat{I}_{AB})_0 + \hat{H}_{AC}(t) \times \hat{I}_B, \quad (152)$$

where \hat{I}_{AB} and \hat{I}_C are identity matrices acting on the 2-SELS and flying qubit, while \hat{H}_{AB} is 2-SEL Hamiltonian. \hat{H}_C is the flying qubit Hamiltonian and $\hat{H}_{AC}(t)$ is the interaction Hamiltonian between A line and flying qubit C (note: for the sake of simplicity we neglect the interaction between B line and C qubit). The detailed structure of those Hamiltonians are given in Appendix 3.

Defining 2-SEL correlation function previously defined by Formula (136), so $C = C_{AB}$, incorporated into three-body system takes form as $C_{AB,C} = \hat{I}_C \times \hat{C}_{AB}$ and, consequently, we obtain the following time dependence of correlation function given as

$$C(t) = Tr(C_{AB,C} \rho(t)). \quad (153)$$

Details of the calculations can be found in Appendix 3. Finally, we obtain the formula for correlation function of the 2-SEL system interacting weakly with the flying qubit in the form as

$$\begin{aligned}
C(t) = & \frac{(E_{c1} - E_{c2})^2 - 4 \cos \left(\frac{t \sqrt{(E_{c1} - E_{c2})^2 + 16}}{\hbar} \right)}{\left(\cos \left(\int_0^t dt' \frac{E_{c11''}(t') - E_{c1''2}(t')}{\hbar} \right) \right.} \\
& \left. + \cos \left(\int_0^t dt' \frac{E_{c2''1}(t') - E_{c2pp2}(t')}{\hbar} \right) - 2 \right) \frac{1}{(E_{c1} - E_{c2})^2 + 16}} \\
& + \frac{4 \cos \left(\int_0^t dt' \frac{E_{c11''}(t') - E_{c1''2}(t')}{\hbar} \right) + 4 \cos \left(\int_0^t dt' \frac{E_{c2''1}(t') - E_{c2''2}(t')}{\hbar} \right) + 8}{(E_{c1} - E_{c2})^2 + 16}
\end{aligned} \tag{154}$$

where

$$\begin{aligned}
E_{c11''}(t) &= \frac{q^2}{\sqrt{(x(t) + a + b)^2 + d_1^2}}, \\
E_{c12''}(t) &= \frac{q^2}{\sqrt{(x(t) + 2(a + b))^2 + d_1^2}}, \\
E_{c21''}(t) &= \frac{q^2}{\sqrt{(x(t) - (a + b))^2 + d_1^2}}, \\
E_{c22''}(t) &= \frac{q^2}{\sqrt{(x(t))^2 + d_1^2}}.
\end{aligned} \tag{155}$$

The movement of the flying qubit can be described, for example, by a constant velocity $v = v_0$, so $x(t) = x_0 + v_0 t$. In case of a time-dependent flying qubit, $x(t) = x(t_0) + \int_{t_0}^t v_f(t') dt'$, where $v_f(t)$ is an instantaneous speed of the flying qubit. The only assumption for this model is that particle at time $t = 0$ is at a far distance from 2-SELs.

11 Entangling Two Qubits by Means of RF Fields

We are placing electrostatic position-based qubit in external electromagnetic cavity. We assume that electromagnetic cavity maintains quantum coherence what is possible in case of cavities with small dissipation (high-quality factor) as it is the case of superconducting cavity. At the same time we are assuming quantum coherence of semiconductor position based qubit. What is more we assume coherent interaction of electromagnetic radiation with electron trapped in positron based qubit. Such system is depicted in Fig. 23. We expect that during this interaction it will be possible to entangle electromagnetic radiation with position based qubit. This entanglement will be essential in quantum information processing. Before moving to the detailed picture of qubit-radiation interaction let us review non-local realism in quantum mechanics.

11.1 Non-local Realism in Quantum Mechanical Picture

Quantum mechanics gives only probabilistic description of physical processes what does not support classical determinism but only stochastic determinism. Given particle can be localized in certain area of space as when it is in the potential minimum that is around certain point or can be distributed over big area as it is the case of conductive electron in metal. Once the measurement is conducted on the particle its position can be determined very exactly but at the prize that particle momentum is highly perturbed and essentially information about particle momentum is lost. In that way one cannot fully determine both position and momentum of the particle what is expressed in the non-commutation relation between momentum and position and it leads to the Heisenberg principle. The phenomena that one cannot determine position and momentum of the particle is commonly known from wave mechanics. Under the circumstance of particle being localized or delocalized the particles interact what affects the probability distribution. In very real sense quantum particle is like classical particle under very high noise so it is pointless to talk about the individual particle position but it makes sense to talk about probability of finding particle in given ensemble of particles. We use to say that canonical ensemble is attached to the individual behaviour of particle. Thus dealing with conglomerate of particles we are dealing with statistical ensemble [of single particle] attached to another statistical ensemble of environment in which the given particle is placed. Such reasoning indeed draws analogies of statistical mechanics with quantum mechanics. At some point one can say that there is no big difference between quantum mechanical or classical particle under the impact of external potential. Local principle holds for both classical and quantum pictures and two particles interact if they are close one to another. Coulomb electrostatic energy has the same formula both in classical and in quantum picture. However first main difference is the fact that quantum particle can be subjected to the self-interference as it is the case of two slit experiment when given wave (quantum particle) appears in certain regions with higher probability (higher wave intensity) and in other regions with lower probability. Self-interference requires that wavefunction of given particle is coherent what is strongly dependent on the environment. Self interference has classical counterpart in the theory of waves as given electromagnetic wave can interfere with itself. There is however the effect that has no classical counterpart in quantum picture and is named as entanglement that is the manifestation of non-local correlation. In classical physics it is however not surprising that when two particles are interacting the change of state of one particle brings the change of state of another particle. However the surprising aspect is when two particles being at very high distances are essentially no interacting and change of the state of one of particles is affecting the state of another particles in immediate way. Such event is called spooky action on the distance and is the example of non-local correlation that can only occur in quantum theory and is the manifestation of particle entanglement. In this work we will describe the entanglement between waveguide and position based qubits as well as entanglement between two far position based qubits mediated by waveguide. Most common picture of entanglement is illustrated by the Bell states.

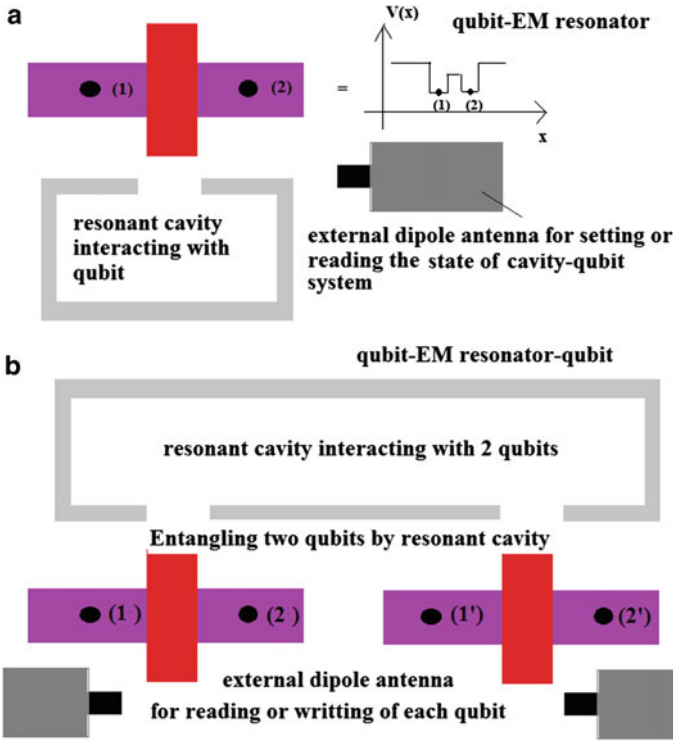


Fig. 23 Position based qubit in RF field (a) and position based qubits placed at high distance interlinked by waveguide (b)

11.2 Interaction of Radiation with Position Dependent Qubit

We are referring to the situation of placement of position based qubit in external radiofrequency field of electromagnetic cavity or waveguide as depicted in Fig. 23. Because of simplicity we are going to use Jaynes-Cumming Hamiltonian [8] that describes the interaction atom with cavity by means of electromagnetic field [more precise name can be tight-binding Jaynes-Cumming Hamiltonian or Hubbard Jaynes-Cumming Hamiltonian]. In the simplest approach the cavity Hamiltonian describing waveguide without dissipation is represented as

$$H_{\text{cavity}} = \hbar\omega_c \left(\frac{1}{2} + \hat{a}^\dagger \hat{a} \right) = E_{\phi_1} |E_{\phi_1}\rangle \langle E_{\phi_1}| + E_{\phi_2} |E_{\phi_2}\rangle \langle E_{\phi_2}|, \quad (156)$$

where \hat{a}^\dagger (\hat{a}) is the photon creation (annihilation) operator and number of photons in cavity is given as $n = \hat{a}^\dagger \hat{a}$. At the same we can represent the two level qubit system

$$H_{\text{qubit}} = E_g |g\rangle \langle g| + E_e |e\rangle \langle e|. \quad (157)$$

The interaction Hamiltonian is of the following form

$$H_{\text{qubit-cavity}} = g(\hat{a}^\dagger \sigma_- + \hat{a} \sigma_+), \quad (158)$$

where $\sigma_- = \sigma_1 - i\sigma_2$, $\sigma_+ = \sigma_1 + i\sigma_2$. The qubit-cavity interaction has the electric-dipole nature so quasicallyssically we can write

$$H_{\text{qubit-cavity}} = \hat{d} \cdot \hat{E} = g(\sigma_- + \sigma_+)(\hat{a} + \hat{a}^\dagger) \approx g(\hat{a}^\dagger \sigma_- + \hat{a} \sigma_+). \quad (159)$$

Here we have neglected the terms $g(\sigma_- \hat{a} + \sigma_+ \hat{a}^\dagger)$ and our approach is known as rotating phase. Constant g is depending on the distance between waveguide and position-dependent qubit as depicted Fig. 2. During photon emission from qubit the energy level is lowered and reversely during photon absorption the energy level of qubit is raised what is seen in the term $\hat{a} \sigma_+$. The system Hamiltonian is given as $H = H_{\text{cavity}} + H_{\text{qubit}} + H_{\text{qubit-cavity}}$. It is not hard to construct the Hilbert space for Jaynes-Cumming Hamiltonian. Essentially we are considering the tensor product of qubit space and cavity space.

$$|\psi\rangle = \gamma_1 |\phi_1\rangle |0\rangle + \gamma_2 |\phi_1\rangle |1\rangle + \gamma_3 |\phi_2\rangle |0\rangle + \gamma_4 |\phi_2\rangle |1\rangle = \begin{pmatrix} \gamma_1 \\ \gamma_2 \\ \gamma_3 \\ \gamma_4 \end{pmatrix},$$

$$1 = \langle \psi | \psi \rangle = |\gamma_1|^2 + \dots + |\gamma_4|^2. \quad (160)$$

Here $|0\rangle = |g\rangle$ and $|1\rangle = |e\rangle$ stands for E_g and E_e energetic state of position based qubit, while $|\phi_1\rangle$ and $|\phi_2\rangle$ stands for cavity with 1 and 2 photons. We have the following matrices $H_{\text{qubit}} + H_{\text{cavity}}$, $H_{\text{qubit-cavity}}$

$$H_{\text{qubit}} + H_{\text{cavity}} =$$

$$= \begin{pmatrix} E_g + E_{ph1} & 0 & 0 & 0 \\ 0 & E_e + E_{ph1} & 0 & 0 \\ 0 & 0 & E_g + E_{ph2} & 0 \\ 0 & 0 & 0 & E_e + E_{ph2} \end{pmatrix}$$

$$= E_g |E_g\rangle \langle E_g| + E_e |E_e\rangle \langle E_e| + E_{\phi_{1(2)}} |E_{\phi_{1(2)}}\rangle \langle E_{\phi_{1(2)}}|. \quad (161)$$

$$H_{\text{qubit-cavity}} = \begin{pmatrix} 0 & 0 & 0 & 0 \\ 0 & 0 & g_1 & 0 \\ 0 & g_1 & 0 & 0 \\ 0 & 0 & 0 & 0 \end{pmatrix} = g_1 (|E_{\phi_1}, E_e\rangle \langle E_{\phi_2}, E_g| + |E_{\phi_2}, E_g\rangle \langle E_{\phi_1}, E_e|),$$

$$(162)$$

what implies

$$H_{\text{qubit}} + H_{\text{cavity}} + H_{\text{qubit-cavity}} = \begin{pmatrix} E_g + E_{ph1} & 0 & 0 & 0 \\ 0 & E_e + E_{ph1} & g_1 & 0 \\ 0 & g_1 & E_g + E_{ph2} & 0 \\ 0 & 0 & 0 & E_e + E_{ph2} \end{pmatrix}. \quad (163)$$

The last Hamiltonian gives the eigenstates

$$|E_1\rangle = \begin{pmatrix} 1 \\ 0 \\ 0 \\ 0 \end{pmatrix}, \quad |E_2\rangle = \begin{pmatrix} 0 \\ 0 \\ 0 \\ 1 \end{pmatrix},$$

$$|E_3\rangle = \begin{pmatrix} 0 \\ \frac{(E_e - E_g) - (E_{ph2} - E_{ph1}) - \sqrt{((E_e - E_g) - (E_{ph2} - E_{ph1}))^2 + 4|g_1|^2}}{2g_1} \\ 1 \\ 0 \end{pmatrix} =,$$

$$\frac{(E_e - E_g) - (E_{ph2} - E_{ph1}) - \sqrt{((E_e - E_g) - (E_{ph2} - E_{ph1}))^2 + 4|g_1|^2}}{2g_1}$$

$$|\phi_1\rangle = |E_e\rangle + |\phi_2\rangle = |E_g\rangle,$$

$$|E_4\rangle = \begin{pmatrix} 0 \\ \frac{(E_e - E_g) - (E_{ph2} - E_{ph1}) + \sqrt{((E_e - E_g) - (E_{ph2} - E_{ph1}))^2 + 4|g_1|^2}}{2g_1} \\ 1 \\ 0 \end{pmatrix}, \quad (164)$$

and one obtains eigenenergies of the form

$$E_1 = E_g + E_{ph1},$$

$$E_2 = E_e + E_{ph2},$$

$$E_3 = \frac{1}{2}(E_g + E_e + E_{ph1} + E_{ph2}$$

$$- \sqrt{((E_e - E_g) - (E_{ph2} - E_{ph1}))^2 + 4|g_1|^2},$$

$$E_4 = \frac{1}{2}(E_g + E_e + E_{ph1} + E_{ph2}$$

$$+ \sqrt{((E_e - E_g) - (E_{ph2} - E_{ph1}))^2 + 4|g_1|^2}, \quad (165)$$

We recognize that state corresponding to eigenenergies E_3 and E_4 are entangled states of matter and radiation while states corresponding to eigenenergies E_1 and E_2 are non-entangled states of matter and radiation. In particular if state E_3 is subjected to the measurement of number of photons and value 1 was encountered than it implies that position based qubit is in the excited state corresponding to the energy E_e .

Otherwise if the number of photon is encountered to be 2 than the state of qubit is encountered to be E_g .

11.3 Case of 2 Qubits Interaction via Waveguide on the Distance and Teleportation on the Distance

We have the following Hamiltonian for 2 qubits interacting with waveguide in the case when qubit 1 is relatively far from qubit 2. If waveguide has L length and c is speed of signal propagation along waveguide we have $\Delta t = L/c$ and Hamiltonian is of the form:

$$\begin{aligned}
 H = & (E_{\phi_1}|\phi_1 \rangle \langle \phi_1| + E_{\phi_2}|\phi_2 \rangle \langle \phi_2|)I_{\text{qubit1}}I_{\text{qubit2}} + \\
 & + I_{\text{cavity}}(E_{g1}|g1 \rangle \langle g1| + E_{e1}|e1 \rangle \langle e1|)I_{\text{qubit2}} + \\
 & + I_{\text{cavity}}(E_{g1}|g1 \rangle \langle g1| + E_{e1}|e1 \rangle \langle e1|)I_{\text{qubit2}} + \\
 & + I_{\text{cavity}}I_{\text{qubit1}}(E_{g2}|g2 \rangle \langle g2| + E_{e2}|e2 \rangle \langle e2|) + \\
 & + g_1 f_1(t)[(|\phi_1 \rangle \langle \phi_2|)(|e1 \rangle \langle g1|) + \\
 & + (|\phi_2 \rangle \langle \phi_1|)(|g1 \rangle \langle e1|)]I_{\text{qubit2}} + \\
 & + g_2 f_1(t + \Delta t)[(|\phi_1 \rangle \langle \phi_2|)I_{\text{qubit1}}(|e2 \rangle \langle g2|) + \\
 & + (|\phi_2 \rangle \langle \phi_1|)I_{\text{qubit1}}(|g2 \rangle \langle e2|)].
 \end{aligned} \tag{166}$$

It is formally 3 interacting body system (qubit1)-(waveguide)-(qubit2) in which qubit 1 cannot directly interact with qubit 2 and the quantum state has the form

$$\begin{aligned}
 |\psi(t) \rangle = & \alpha_1(t)|\phi_1 \rangle |g1 \rangle |g2 \rangle + \alpha_2(t)|\phi_1 \rangle |g1 \rangle |e2 \rangle + \\
 & + \alpha_3(t)|\phi_1 \rangle |e1 \rangle |g2 \rangle + \alpha_4(t)|\phi_1 \rangle |e1 \rangle |e2 \rangle + \\
 & + \alpha_5(t)|\phi_2 \rangle |g1 \rangle |g2 \rangle + \alpha_6(t)|\phi_2 \rangle |g1 \rangle |e2 \rangle + \\
 & + \alpha_7(t)|\phi_2 \rangle |e1 \rangle |g2 \rangle + \alpha_8(t)|\phi_2 \rangle |e1 \rangle |e2 \rangle,
 \end{aligned} \tag{167}$$

The normalization condition is fulfilled $|\alpha_1(t)|^2 + \dots + |\alpha_8(t)|^2 = 1$. The system matrix is of the structure given below

$$H = \begin{pmatrix} E_{g1} + E_{g2} + E_{\phi_1} & 0 & 0 & 0 & 0 & 0 & 0 & 0 & 0 \\ 0 & E_{g1} + E_{e2} + E_{\phi_1} & 0 & 0 & f_1(t)e^{-id_2t}g_2 & 0 & 0 & 0 & 0 \\ 0 & 0 & E_{e1} + E_{g2} + E_{\phi_1} & 0 & f_1(t)g_1e^{-id_1t} & 0 & 0 & 0 & 0 \\ 0 & 0 & 0 & E_{e1} + E_{e2} + E_{\phi_1} & 0 & 0 & g_1 f_1(t)e^{-id_1t} & g_2 f_1(t)e^{-id_2t} & 0 \\ 0 & f_1(t)e^{id_2t}g_2 & f_1(t)e^{id_1t}g_1 & 0 & E_{g1} + E_{g2} + E_{\phi_2} & 0 & 0 & 0 & 0 \\ 0 & 0 & 0 & g_1 f_1(t)e^{id_1t} & 0 & E_{g1} + E_{g2} + E_{\phi_2} & 0 & 0 & 0 \\ 0 & 0 & 0 & f_1(t)e^{id_2t}g_2 & 0 & 0 & E_{e1} + E_{e2} + E_{\phi_2} & 0 & 0 \\ 0 & 0 & 0 & 0 & 0 & 0 & 0 & E_{e1} + E_{g2} + E_{\phi_2} & 0 \\ 0 & 0 & 0 & 0 & 0 & 0 & 0 & 0 & E_{e1} + E_{e2} + E_{\phi_2} \end{pmatrix} \tag{168}$$

This matrix can be simplified. We can preassume that $g_1 f_1(t) = gf(t)e^{id_1(t)}$ and $g_2 f_2(t) = gf(t)e^{id_2(t)}$ and we can divide all matrix by this value. Second simpli-

fication is by $E_g = E_{g1} = E_{g2} = E_{\phi1} = E_{\phi2} - E_{\phi1} = E_{e1} - E_{g1} = E_{e2} - E_{g2}$. In such case we obtain

$$\hat{H} = \begin{pmatrix} 3E_g & 0 & 0 & 0 & 0 & 0 & 0 & 0 \\ 0 & 4E_g & 0 & 0 & g_2e^{-id_2(t)} & 0 & 0 & 0 \\ 0 & 0 & 4E_g & 0 & g_1e^{-id_1(t)} & 0 & 0 & 0 \\ 0 & 0 & 0 & 5E_g & 0 & g_1e^{-id_1t} & g_2e^{-id_2(t)} & 0 \\ 0 & g_2e^{id_2(t)} & g_1e^{id_1(t)} & 0 & 4E_g & 0 & 0 & 0 \\ 0 & 0 & 0 & g_1e^{id_1(t)} & 0 & 5E_g & 0 & 0 \\ 0 & 0 & 0 & g_2e^{id_2(t)} & 0 & 0 & 5E_g & 0 \\ 0 & 0 & 0 & 0 & 0 & 0 & 0 & 6E_g \end{pmatrix}. \quad (169)$$

It shall be underlined that is g_1 and g_2 are proportional to the electric field in the resonator cavity so they are depending on frequency of oscillations and amplitude of electric field in resonator cavity. If we are dealing with 2 or more qubits we assume that they are at coupled to EM field in different way and that they catch oscillating EM field at different phase what is expressed by phase factors $e^{id_1(t)}$, $e^{id_2(t)}$. The last Hamiltonian matrix has the following energy eigenvalues $3E_g, 4E_g, 5E_g, 6E_g, 4E_g - \sqrt{g_1^2 + g_2^2}, 5E_g - \sqrt{g_1^2 + g_2^2}, 4E_g + \sqrt{g_1^2 + g_2^2}, 5E_g + \sqrt{g_1^2 + g_2^2}$. In general case g_1 is depending on how waveguide with hole is close to the position dependent qubit. Otherwise position dependent qubit must be placed in resonant cavity. We assume $E_p = E_{p1} = E_{p2} = E_{p1'} = E_{p2'}$ and we have found the following eigenstates

$$|E_1 \rangle = \begin{pmatrix} 1 \\ 0 \\ 0 \\ 0 \\ 0 \\ 0 \\ 0 \\ 0 \end{pmatrix} = |\phi_1 \rangle |g_1 \rangle |g_2 \rangle = \frac{1}{2} |\phi_1 \rangle (|x_1 \rangle - |x_2 \rangle)(|x_{1'} \rangle - |x_{2'} \rangle), \quad (170)$$

$$|E_2 \rangle = \begin{pmatrix} 0 \\ -(g_1/g_2)e^{i(-d_2+d_1)} \\ +1 \\ 0 \\ 0 \\ 0 \\ 0 \\ 0 \end{pmatrix} = -\left(\frac{g_1}{g_2}e^{i(-d_2+d_1)}\right)|\phi_1 \rangle |g_1 \rangle |e_2 \rangle + |\phi_1 \rangle |e_1 \rangle |g_2 \rangle$$

$$\begin{aligned}
 |E_3\rangle &= \begin{pmatrix} 0 \\ 0 \\ 0 \\ 0 \\ -\frac{g_2}{g_1}e^{i(-d_2+d_1)} \\ 1 \\ 0 \end{pmatrix} \\
 &= -\frac{g_2}{g_1}e^{i(-d_2+d_1)}|\phi_2\rangle + |g_1\rangle + |e_2\rangle + |\phi_2\rangle + |e_1\rangle + |g_2\rangle, \quad (171)
 \end{aligned}$$

$$|E_4\rangle = \begin{pmatrix} 0 \\ 0 \\ 0 \\ 0 \\ 0 \\ 0 \\ 0 \\ 1 \end{pmatrix} = +|\phi_2\rangle + |e_1\rangle + |e_2\rangle, \quad (172)$$

$$\begin{aligned}
 |E_5\rangle &= \begin{pmatrix} 0 \\ -\frac{g_2e^{id_2}}{\sqrt{g_1^2+g_2^2}} \\ -\frac{g_1e^{id_1}}{\sqrt{g_1^2+g_2^2}} \\ 0 \\ 1 \\ 0 \\ 0 \\ 0 \end{pmatrix} = \\
 &= -\frac{g_2e^{id_2}}{\sqrt{g_1^2+g_2^2}}|\phi_1\rangle + |g_1\rangle + |e_2\rangle - \frac{g_1e^{id_1}}{\sqrt{g_1^2+g_2^2}}|\phi_1\rangle + |e_1\rangle + |g_2\rangle + \frac{1}{\sqrt{2}}|\phi_1\rangle + |e_1\rangle + |e_2\rangle, \quad (173)
 \end{aligned}$$

$$|E_6\rangle = \begin{pmatrix} 0 \\ 0 \\ 0 \\ -\frac{e^{2id_2}\sqrt{g_1^2+g_2^2}}{g_2} \\ 0 \\ 1 \\ 1 \\ 0 \end{pmatrix}$$

$$\begin{aligned}
&= -\frac{e^{2id_2}\sqrt{g_1^2+g_2^2}}{g_2}|\phi_1 > |e_1 > |e_2 > +|\phi_2 > |e_1 > |g_2 > +|\phi_2 > |g_1 > |e_2 >, \\
|E_7 > &= \begin{pmatrix} 0 \\ e^{-id_2}\frac{g_2}{\sqrt{g_1^2+g_2^2}} \\ e^{-id_1}\frac{g_1}{\sqrt{g_1^2+g_2^2}} \\ 0 \\ 1 \\ 0 \\ 0 \\ 0 \end{pmatrix} = \\
&= e^{-id_2}\frac{g_2}{\sqrt{g_1^2+g_2^2}}(|\phi_1 > |e_1 > |g_2 > +e^{-id_1}\frac{g_1}{\sqrt{g_1^2+g_2^2}}(|\phi_1 > |g_1 > |e_2 > +|\phi_2 > |g_1 > |g_2 >, \\
|E_8 > &= \begin{pmatrix} 0 \\ 0 \\ 0 \\ e^{-i(2d_1+d_2)}\frac{\sqrt{g_1^2+g_2^2}}{g_2} \\ 0 \\ e^{-id_2+id_1}\frac{g_1}{g_2} \\ 1 \\ 0 \end{pmatrix} \\
&= e^{-i(2d_1+d_2)}\frac{\sqrt{g_1^2+g_2^2}}{g_2}|\phi_1 > |e_1 > |e_2 > +e^{-id_2+id_1}\frac{g_1}{g_2}|\phi_2 > |e_1 > |g_2 > +|\phi_2 > |g_1 > |e_2 >, \tag{174}
\end{aligned}$$

6 eigenstates among 8 Eigenstates (except E1 and E8) are entangled in energy bases.

It is noticeable to underline that all 8 energy eigenstates are entangled in position based representation especially when all E_p values corresponding to nodes in 2 different qubits are different.

12 Analytic Extensions of Topology of Chain of Coupled Quantum Dots

Since we have electrostatic control of interaction between quantum dots we can turn on coupling between two chains of quantum dots as it is depicted in Fig. 24, where Coulomb electrostatic interaction occurs between m and n' node of two separated chain and is given by $E_c(m, n') = f(m, n') = \frac{q^2}{d_{m,n'}}$. The quantum state of right-system is given as

$$\begin{aligned}
|\psi\rangle &= \gamma_{1,1'}(t)|1\rangle|1'\rangle + \gamma_{1,2'}(t)|1\rangle|2'\rangle + \gamma_{1,3'}(t)|1\rangle|3'\rangle + \gamma_{1,4'}(t)|1\rangle|4'\rangle + \gamma_{2,1'}(t)|2\rangle|1'\rangle + \gamma_{2,2'}(t)|2\rangle|2'\rangle + \\
&+ \gamma_{2,3'}(t)|2\rangle|3'\rangle + \gamma_{2,4'}(t)|2\rangle|4'\rangle + \gamma_{3,1'}(t)|3\rangle|1'\rangle + \gamma_{3,2'}(t)|3\rangle|2'\rangle + \gamma_{3,3'}(t)|3\rangle|3'\rangle + \gamma_{3,4'}(t)|3\rangle|4'\rangle. \tag{175}
\end{aligned}$$

where $\sum_{k,l'} |\gamma_{k,l'}|^2 = 1$. After extension by 2 elements the quantum state of left system is given as

$$\begin{aligned}
 |\psi\rangle = & \gamma_{1,1'}(t) |1\rangle |1'\rangle + \gamma_{1,2'}(t) |1\rangle |2'\rangle + \gamma_{1,3'}(t) |1\rangle |3'\rangle + \gamma_{1,4'}(t) |1\rangle |4'\rangle + \gamma_{2,1'}(t) |2\rangle |1'\rangle + \gamma_{2,2'}(t) |2\rangle |2'\rangle + \\
 & + \gamma_{2,3'}(t) |2\rangle |3'\rangle + \gamma_{2,4'}(t) |2\rangle |4'\rangle + \gamma_{3,1'}(t) |3\rangle |1'\rangle + \gamma_{3,2'}(t) |3\rangle |2'\rangle + \gamma_{3,3'}(t) |3\rangle |3'\rangle + \gamma_{3,4'}(t) |3\rangle |4'\rangle. \\
 & + \gamma_{1,5'}(t) |1\rangle |5'\rangle + \gamma_{2,5'}(t) |2\rangle |5'\rangle + \gamma_{3,5'}(t) |3\rangle |5'\rangle + \gamma_{1,6'}(t) |1\rangle |6'\rangle + \gamma_{2,6'}(t) |2\rangle |6'\rangle + \gamma_{3,6'}(t) |3\rangle |6'\rangle.
 \end{aligned} \tag{176}$$

where again $\sum_{s,w'} |\gamma_{s,w'}|^2 = 1$. The Hamiltonian of the system before extension is

$$\hat{H} = \begin{pmatrix} H_1 & H_2 \\ H_3 & H_4 \end{pmatrix} \tag{177}$$

and after extension into system depicted in Fig. 24 (left side) is

$$\hat{H}(t)_{ext} = \begin{pmatrix} H_1 & H_2 & H_{e1} \\ H_3 & H_4 & H_{e2} \\ H_{e5} & H_{e4} & H_{e3} \end{pmatrix} \tag{178}$$

with matrix subcomponents $\hat{H}_1(t) =$

$$\begin{pmatrix} E_{p1} + E_{p1'} + \frac{g^2}{d_{1,1'}} & t_{s1',2'} & 0 & 0 & t_{s12} & 0 \\ t_{s2',1'} & E_{p1} + E_{p2'} + \frac{g^2}{d_{1,2'}} & t_{s2',3'} & 0 & 0 & t_{s12} \\ 0 & t_{s3',2'} & E_{p1} + E_{p3'} + \frac{g^2}{d_{1,3'}} & t_{s3',4'} & 0 & 0 \\ 0 & 0 & t_{s4',3'} & E_{p1} + E_{p4'} + \frac{g^2}{d_{1,4'}} & t_{s1',2'} & 0 \\ t_{s2,1} & 0 & 0 & 0 & E_{p2} + E_{p1'} + \frac{g^2}{d_{1',2}} & t_{2',3'} \\ 0 & t_{s2,1} & 0 & 0 & t_{s2',1'} & E_{p2} + E_{p2'} + \frac{g^2}{d_{s,2'}} \end{pmatrix}.$$

$$\hat{H}_2 = \begin{pmatrix} 0 & 0 & 0 & 0 & 0 & 0 \\ 0 & 0 & 0 & 0 & 0 & 0 \\ t_{s1,2} & 0 & 0 & 0 & 0 & 0 \\ 0 & t_{s1,2} & 0 & 0 & 0 & 0 \\ 0 & 0 & t_{s2,3} & 0 & 0 & 0 \\ t_{s2',3'} & 0 & 0 & t_{s2,3} & 0 & 0 \end{pmatrix}, \hat{H}_3 = \begin{pmatrix} 0 & 0 & t_{s2,1} & 0 & 0 & t_{s3',2'} \\ 0 & 0 & 0 & t_{s2,1} & 0 & 0 \\ 0 & 0 & 0 & 0 & t_{s3,2} & 0 \\ 0 & 0 & 0 & 0 & 0 & t_{s3,2} \\ 0 & 0 & 0 & 0 & 0 & 0 \\ 0 & 0 & 0 & 0 & 0 & 0 \end{pmatrix},$$

$$\hat{H}_4(t) =$$

$$\begin{pmatrix} E_{p2}(t) + E_{p3'}(t) + \frac{g^2}{d_{2,3'}} & t_{s3',4'}(t) & 0 & 0 & 0 & 0 \\ t_{s4',3'}(t) & E_{p2}(t) + E_{p4'}(t) + \frac{g^2}{d_{2,3'}} & 0 & 0 & 0 & 0 \\ 0 & 0 & E_{p3}(t) + E_{p1'}(t) + \frac{g^2}{d_{2,3'}} & t_{s1',2'}(t) & 0 & 0 \\ 0 & 0 & t_{s2',1'}(t) & E_{p3}(t) + E_{p2'}(t) + \frac{g^2}{d_{3,2'}} & t_{s2',3'}(t) & 0 \\ 0 & 0 & 0 & t_{3',2'}(t) & E_{p3}(t) + E_{p3'}(t) + \frac{g^2}{d_{3,3'}} & t_{s3',4'}(t) \\ 0 & 0 & 0 & 0 & t_{s4',3'}(t) & E_{p3}(t) + E_{p4'}(t) + \frac{g^2}{d_{3,4'}} \end{pmatrix}.$$

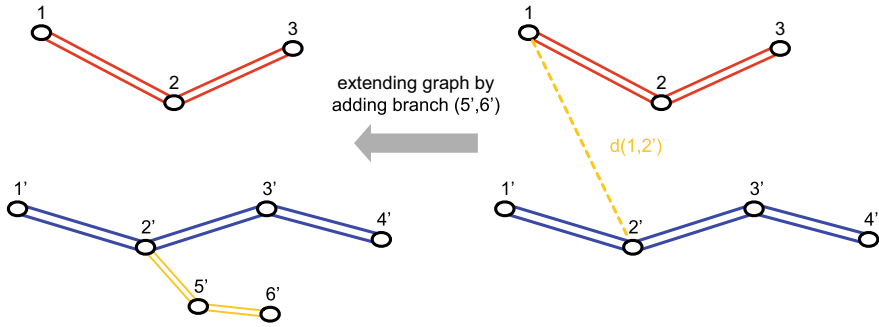


Fig. 24 Example of arbitrary extension of network of electrostatically coupled quantum dots with reference to technological scheme depicted in Fig. 2

We can determine inductive step of quantum dot graph extension by adding matrices $\hat{H}_{e1}, \dots, \hat{H}_{e5}$ to the Formula 178 in the form as given

$$\hat{H}_{e1} = \begin{pmatrix} 0 & 0 & 0 & 0 & 0 & 0 \\ t_{s2',5'} & 0 & 0 & 0 & 0 & 0 \\ 0 & 0 & 0 & 0 & 0 & 0 \\ 0 & 0 & 0 & 0 & 0 & 0 \\ 0 & 0 & 0 & 0 & 0 & 0 \\ 0 & t_{s2',5'} & 0 & 0 & 0 & 0 \end{pmatrix}, \hat{H}_{e5}, \hat{H}_{e2} = \begin{pmatrix} 0 & 0 & 0 & 0 & 0 & 0 \\ 0 & 0 & 0 & 0 & 0 & 0 \\ 0 & 0 & 0 & 0 & 0 & 0 \\ 0 & 0 & t_{s2',5'} & 0 & 0 & 0 \\ 0 & 0 & 0 & 0 & 0 & 0 \\ 0 & 0 & 0 & 0 & 0 & 0 \end{pmatrix} = \hat{H}_{e4}^\dagger, \quad (179)$$

$$\hat{H}_{e3} = \begin{pmatrix} E_{p1} + E_{p5'} + \frac{q^2}{d_{1,5'}^2} & t_{s1,2} & 0 & t_{s5',6'} & 0 & 0 \\ t_{s2,1} & E_{p2} + E_{p5'} + \frac{q^2}{d_{2,5'}^2} & t_{s2,3} & 0 & t_{s5',6'} & 0 \\ 0 & t_{s3,2} & E_{p3} + E_{p5'} + \frac{q^2}{d_{3,5'}^2} & 0 & 0 & t_{s5',6'} \\ t_{s6',5'} & 0 & 0 & E_{p1} + E_{p6'} + \frac{q^2}{d_{1,6'}^2} & t_{s1,2} & 0 \\ 0 & t_{s6',5'} & 0 & t_{s2,1} & E_{p2} + E_{p6'} + \frac{q^2}{d_{2,6'}^2} & t_{s2,3} \\ 0 & 0 & t_{s6',5'} & 0 & t_{s3,2} & E_{p3} + E_{p6'} + \frac{q^2}{d_{3,6'}^2} \end{pmatrix}$$

Similarly to before having the knowledge of quantum state at t_0 we can evaluate the state at time t by computing $\exp(\int_{t_0}^t \frac{1}{\hbar i} \hat{H}_{\text{ext}}(t) dt') |\psi, t_0\rangle = |\psi, t\rangle$ what bases on the same method already presented before in Eq. (8). We can also perform the procedure of heating up or cooling down of the quantum state in the way as it was described before.

13 Electrostatic Interaction of Josephson Junction Qubit with Semiconductor Electrostatic Qubit

The state of Josephson junction is well described by Bogoliubov-de Gennes (BdGe) equation [9] pointing the correlation between electron and holes as

$$\begin{pmatrix} H_0 & \Delta(x) \\ \Delta(x)^* & -H_0^\dagger \end{pmatrix} \begin{pmatrix} u_n(x) \\ v_n(x) \end{pmatrix} = E_n \begin{pmatrix} u_n(x) \\ v_n(x) \end{pmatrix}, \tag{180}$$

where $H_0 = -\frac{\hbar^2}{2m} \frac{d^2}{dx^2}$ is free electron Hamiltonian with self-consistency relation $\Delta(x) = \sum_n (1 - 2f(E_n))u_n(x)v_n(x)^*$, where $\Delta(x)$ is the superconducting order parameter and $f(E_n) = \frac{1}{1+e^{-\frac{E_n}{k_B T}}}$ is Fermi-Dirac distribution function and $u_n(x)$ and $v_n(x)$ are electron and hole wavefunctions. In case of bulk superconductor with constant superconducting order parameter we obtain $E_n = \pm\sqrt{|H_0|^2 + |\Delta|^2}$. In later considerations we are going to omit the self-consistency relation assuming the dependence of superconducting order parameter as step-like function. It shall be underlined that BdGe equation is mean field equation that is derived basing on BCS theory of superconductivity. It is thus naturally valid for the case of many particles. Semiconductor single electron line with 2 nodes can be regarded as electrostatic position dependent qubit and can be described by $H_{semi} = t_{s1,2} |1\rangle \langle 2| + t_{s2,1} |2\rangle \langle 1| + E_{p1} |1\rangle \langle 1| + E_{p2} |2\rangle \langle 2|$, Figs.7, 8 and 9.

We refer to the physical situation depicted in Fig. 25 that has some level of similarity to the situation depicted in Figs.7, 8 and 9. We can express coupling of 2 systems assuming 4 nodes for electron or hole and 2 nodes for electron confined in semiconductor so we have eigenvector having 16 components ($|0\rangle_e |1\rangle_s$, $|0\rangle_e |2\rangle_s$, $|1\rangle_e |1\rangle_s$, $|1\rangle_e |2\rangle_s$, $|2\rangle_e |1\rangle_s$, $|2\rangle_e |2\rangle_s$, $|3\rangle_e |1\rangle_s$, $|2\rangle_e |2\rangle_s$, $(|0\rangle_h |1\rangle_s, |0\rangle_h |2\rangle_s, |1\rangle_h |1\rangle_s, |1\rangle_h |2\rangle_s, |2\rangle_h |1\rangle_s, |2\rangle_h |2\rangle_s, |3\rangle_h |1\rangle_s, |2\rangle_h |2\rangle_s$) where s refers to semi-

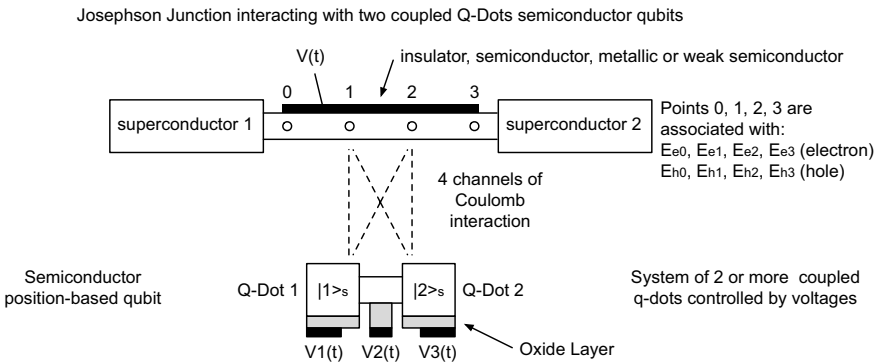


Fig. 25 Superconducting Josephson junction interacting with semiconductor position based qubit in minimalistic tight-binding approach, where tight-binding BdGe equation describing Josephson junction is coupled electrostatically to tight-binding model of semiconductor position based qubit

conductor qubit whose quantum state is superposition of $|1\rangle_s$ and $|2\rangle_s$ and states $|0\rangle_e, \dots, |3\rangle_e, |0\rangle_h, \dots, |3\rangle_h$ characterizes the state of electron and hole respectively in ABS [Andreev Bound State when electron moving in normal (non-superconducting) region between superconductors is reflected as hole when it comes into superconduction area and when hole moving in normal region is reflected as electron when it meets superconductor etc. ...] of Josephson junction. This time the quantum state of the system can be written as

$$|\psi, t\rangle = \gamma_1(t)|0\rangle_e|1\rangle_s + \gamma_2(t)|0\rangle_e|2\rangle_s + \gamma_3(t)|1\rangle_e|1\rangle_s + \gamma_4(t)|1\rangle_e|2\rangle_s + \gamma_5(t)|2\rangle_e|1\rangle_s + \gamma_6(t)|2\rangle_e|2\rangle_s + \gamma_7(t)|2\rangle_e|1\rangle_s + \gamma_8(t)|2\rangle_e|2\rangle_s + \gamma_9(t)|0\rangle_h|1\rangle_s + \gamma_{10}(t)|0\rangle_h|2\rangle_s + \gamma_{11}(t)|1\rangle_h|1\rangle_s + \gamma_{12}(t)|1\rangle_h|2\rangle_s + \gamma_{13}(t)|2\rangle_h|1\rangle_s + \gamma_{14}(t)|2\rangle_h|2\rangle_s + \gamma_{15}(t)|2\rangle_e|1\rangle_s + \gamma_{16}(t)|2\rangle_h|2\rangle_s. \quad (181)$$

Normalization condition implies $|\gamma_1(t)|^2 + |\gamma_2(t)|^2 + \dots + |\gamma_{16}(t)|^2 = 1$ at any instance of time t . Such system has 16 eigenenergies. The probability of find electron at node 1 under any presence of electron in semiconductor qubit at node 1 or 2 is obtained by applying projection of $\langle 1|_e \langle 1|_s + \langle 1|_e \langle 2|_s$ so $|\langle 1|_e \langle 1|_s + \langle 1|_e \langle 2|_s | \psi, t \rangle|^2$ is probability of finding electron at node 1 in Josephson junction. We obtain the following structures of matrices corresponding to H_0 part of BdGe equation in the form as

$$\hat{H}_{0[e]} = \begin{pmatrix} E_{p1} + E_{e0} & t_s & t_{e(1,0)} & 0 & t_{e(2,0)} & 0 & t_{e(3,0)} & 0 \\ t_s^* & E_{p2} + E_{e0} & 0 & t_{e(1,0)} & 0 & t_{e(2,0)} & 0 & t_{e(3,0)} \\ t_{e(1,0)}^* & 0 & E_{p1} + \frac{q^2}{a} + E_{e1} & t_s & t_{e(2,1)} & 0 & t_{e(3,1)} & 0 \\ 0 & t_{e(1,0)}^* & t_s^* & E_{p2} + E_{e1} + \frac{q^2}{b} & 0 & t_{e(2,1)} & 0 & t_{e(3,1)} \\ t_{e(2,0)}^* & 0 & t_{e(2,1)}^* & 0 & E_{p1} + E_{e2} + \frac{q^2}{b} & t_s & t_{e(3,2)} & 0 \\ 0 & t_{e(2,0)}^* & 0 & t_{e(2,1)}^* & t_s^* & E_{p2} + E_{e2} + \frac{q^2}{a} & 0 & t_{e(3,2)} \\ t_{e(3,0)}^* & 0 & t_{e(3,1)}^* & 0 & t_{e(3,2)}^* & 0 & E_{p1} + E_{3e} & t_s \\ 0 & t_{e(3,0)}^* & 0 & t_{e(3,1)}^* & 0 & t_{e(3,2)}^* & t_s^* & E_{p2} + E_{3e} \end{pmatrix} \quad (182)$$

Parameters E_{p1}, E_{p2}, t_s correspond to semiconductor position based qubit and distance between semiconductor qubit and Josephson junction is given by a and b . Other parameters $E_{e0}, E_{e1}, E_{e2}, E_{e3}, E_{h0}, E_{h1}, E_{h2}, E_{h3}$ describes localization energy of electron and hole at nodes 0, 1, 2 and 3 of Josephson junction. In analogical way we can write

$$\hat{H}_{0[h]} = \begin{pmatrix} E_{p1} + E_{h0} & t_s & t_{h(1,0)} & 0 & t_{h(2,0)} & 0 & t_{h(3,0)} & 0 \\ t_s^* & E_{p2} + E_{h0} & 0 & t_{h(1,0)} & 0 & t_{h(2,0)} & 0 & t_{h(3,0)} \\ t_{h(1,0)}^* & 0 & E_{p1} - \frac{q^2}{a} + E_{h1} & t_s & t_{h(2,1)} & 0 & t_{h(3,1)} & 0 \\ 0 & t_{h(1,0)}^* & t_s^* & E_{p2} + E_{h1} - \frac{q^2}{b} & 0 & t_{h(2,1)} & 0 & t_{h(3,1)} \\ t_{h(2,0)}^* & 0 & t_{h(2,1)}^* & 0 & E_{p1} + E_{h2} - \frac{q^2}{b} & t_s & t_{h(3,2)} & 0 \\ 0 & t_{h(2,0)}^* & 0 & t_{h(2,1)}^* & t_s^* & E_{p2} + E_{h2} - \frac{q^2}{a} & 0 & t_{h(3,2)} \\ t_{h(3,0)}^* & 0 & t_{h(3,1)}^* & 0 & t_{h(3,2)}^* & 0 & E_{p1} + E_{3h} & t_s \\ 0 & t_{h(3,0)}^* & 0 & t_{h(3,1)}^* & 0 & t_{h(3,2)}^* & t_s^* & E_{p2} + E_{3h} \end{pmatrix} \quad (183)$$

and two other matrices $\hat{\Delta}_1 = \text{diag}(\Delta(0), \Delta(0), \Delta(1), \Delta(1), \Delta(2), \Delta(2), \Delta(3), \Delta(3))$, $\hat{\Delta}_2 = \hat{\Delta}_1^\dagger$. Finally we obtain the following structure of tight-binding Bogoliubov-de Gennes equations including the interaction of semiconductor qubit with Josephson junction described in the minimalistic way in the form

$$\hat{H}_{\text{eff}} = \begin{pmatrix} \hat{H}_{0[e]} & \hat{\Delta}_1 \\ \hat{\Delta}_2 & \hat{H}_{0[h]} \end{pmatrix}. \quad (184)$$

Similarly as before, having knowledge of quantum state at t_0 we can evaluate the state at time t by computing $\exp(\int_{t_0}^t \frac{1}{\hbar i} \hat{H}_{\text{ext}}(t) dt') |\psi, t_0\rangle = |\psi, t\rangle$ which bases on the same method already presented before in Eq. (8). We can also perform the procedure of heating up or cooling down of the quantum state in the way as it was described before or we can regulate the population of pointed energetic level(s).

In most minimalistic tight-binding model of Josephson junction Sc-I-Sc (Superconductor-Insulator-Superconductor) we set $\Delta(1) = \Delta(2) = 0$ what corresponds to the simplest form of Andreev Bound State in Tunneling Josephson junction. However in weak-links and in the Field Induced Josephson junctions [10] all diagonal elements are non-zero and $|\Delta|$ has maximum at $\Delta(0)$ and $\Delta(3)$ that can be considered as superconducting state of bulk superconductors. Quite naturally, Field Induced Josephson junction [9] can have special profile of dependence of superconducting order parameter $\Delta(x)$ on position x with presence of built-in magnetic fields in area of junction. It will also have special complex-valued hopping constants for electron and hole in area of superconductor that will incorporate the profile of magnetic field present across Josephson junction. Specified Hamiltonian describing electrostatic interface between superconducting Josephson junction and semiconductor position-based qubit has the following parameters describing the state of position based semiconductor qubit $E_{p1}, E_{p2}, t_s = t_{sr} + it_{is}$ (4 real valued time dependent functions), and parameters describing the state of Josephson junction $E_{e0}, E_{e1}, E_{e2}, E_{e3}, E_{h0}, E_{h1}, E_{h2}, E_{h3}, \Delta(0), \Delta(1), \Delta(2), \Delta(3), t_{e(1,0)}, t_{e(2,1)}, t_{e(2,3)}, t_{e(3,0)}, t_{h(1,0)}, t_{h(2,1)}, t_{h(2,3)}, t_{h(3,0)}$ as well as geometrical parameters describing electrostatic interaction between semiconductor JJ and semiconductor qubit by a and b . It is worth mentioning that electrostatic interaction taken into account is only between nodes 1-1s, 1-2s, 2-1s, 2-2s what means 4 channels for Coulomb interaction and simplifies the model greatly so one can find analytical solutions as well. The assumption with four channels of electrostatic interaction is physically justifiable if one assumes that $\Delta(0) \neq 0, \Delta(3) \neq 0$ and $(\Delta(1), \Delta(2)) \rightarrow 0$. Therefore formally we have omitted the following channels of electrostatic interaction 0-1s, 3-1s, 0-2s, 3-2s. It is commonly known that superconducting state especially with strong superconductivity as in case of bulk superconductor is not supporting and shielding itself from the external and internal electrostatic field of certain strength as it naturally protects its ground superconducting macroscopic state. Having established the mathematical structure describing the electrostatic interaction between semiconductor position-based qubit and Josephson junction we can move into first analytical and numerical calculations. First simplification is that $\Delta(1) = \Delta(2) = 0$

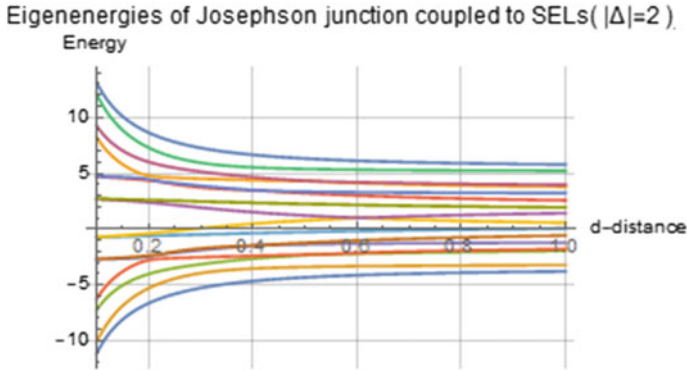


Fig. 26 Eigenenergies of semiconductor qubit coupled to Josephson junction in dependence on distance in tight-binding minimalistic approach

and $\Delta = \Delta(0) = \Delta(3) \in R$ so it means that there is no net electric current flowing via Josephson junction since the electric current flow imposes the condition of phase difference among superconducting order parameter $\Delta(0)$ and $\Delta(3)$ and in such case superconducting order parameter is complex valued scalar. Also it implies that there is no magnetic field in our system since magnetic field brings phase imprint between $\Delta(0)$ and $\Delta(3)$. Second simplification is that $E_{p1} = E_{p2} = E_p, t_s \in R$. Third simplification is that $E_{e0} = E_{e1} = E_{e2} = E_{e3} = -E_{h0} = -E_{h1} = -E_{h2} = -E_{h3} = V$ so it implies electron-hole symmetry in area of ABS that is the middle of Josephson junction. In such way all hole eigenenergies are corresponding to electron eigenenergies with $-$ sign. Last assumption is that electron or hole hopping in the area of ABS in between nearest neighbours is such that $t_{e(k,k+1)} \neq 0$ and $t_{h(k,k+1)} \neq 0$ and is 0 otherwise. One can name such feature of transport in Josephson junction as diffusive and not ballistic what brings the mathematical simplifications. Having established such facts we can move into analytical and numerical calculations. The Hamiltonian of physical system has such structure that allows analytic determination of all eigenenergies since Hamiltonian matrix has many symmetries. In particular we can obtain the spectrum of eigenenergies in dependence on the distance a as depicted in Fig. 26 and spectrum of eigenenergies in dependence of superconducting order parameter as given in Fig. 27. One can recognize certain similarities with Fig. 6. It simply means that increase of superconducting order parameter strength brings similar effect as increase of distance between interaction of semiconductor position based qubit and Josephson junction.

One of the most interesting feature is tuning the landscape of eigenenergies by applying small voltage (below the size $2e\Delta$) to non-superconducting region of Josephson junction. In such case one obtains the features as described in Fig. 28. In the described considerations the spin degree-of-freedom was omitted in case of Josephson junction as well as in case of semiconductor position based qubit. However they could be easily included but it would increase the size of matrix describing

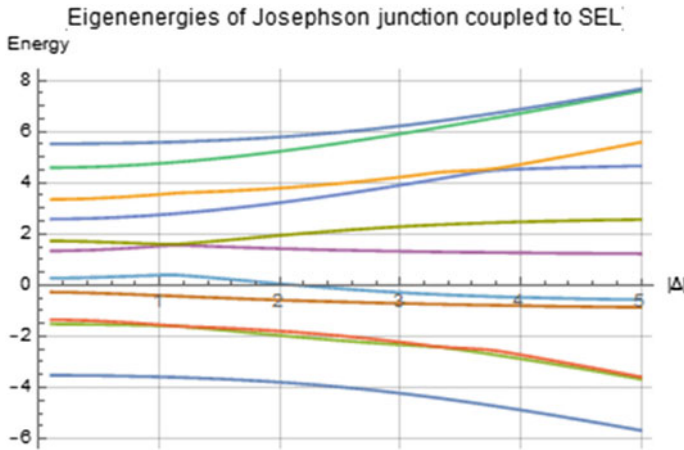


Fig. 27 Eigenenergies of semiconductor qubit coupled to Josephson junction in dependence on superconducting order parameter in minimalistic approach

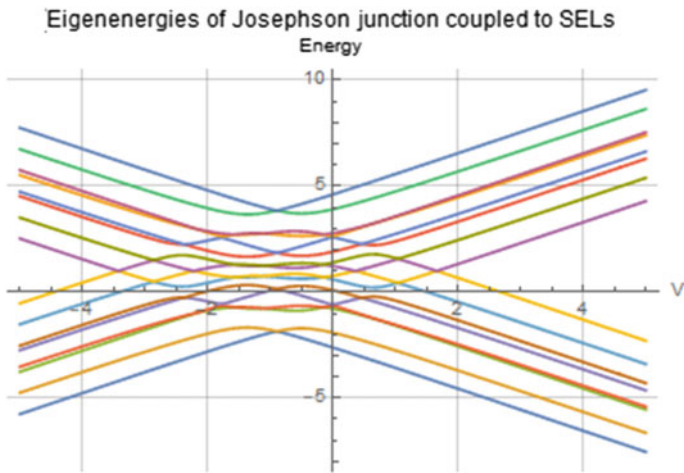


Fig. 28 Tuning the spectrum of eigenenergies in electrostatic qubit interacting with Josephson junction while we are changing the chemical potential of insulator region in Josephson junction at all nodes 0, 1, 2 and 3 in the same time

interaction between superconductor Josephson junction and semiconductor electrostatic qubit from 16 by 16 to the size $8 * 4 = 32$ so one obtains matrix 32 by 32. Adding strong spin-orbit interaction to the Hamiltonian of Josephson junction under the presence of magnetic field allows to describe topological Josephson junction. In such way we can obtain the effective 32 by 32 Hamiltonian for interaction between semiconductor position based qubit and topological Josephson junction in minimalistic way. It shall be also underlined that so far we have used BdGe formalism that is

suitable for mean field theory domain. However, in our case we have considered very special interactions between individual (electrons, holes) present in area of Josephson junction and specific individual electron present in area of semiconductor qubit. Usage of BdGe formalism is therefore first level of possible approximation and further more detailed study can be attempted in determination of microscopic processes present interacting Josephson junction with semiconductor qubit in more detailed way. It is sufficient to mention that in our case superconductors shall have relatively small size so we are dealing with relatively small number of electrons and holes in non-superconducting area. More detailed considerations are however beyond the scope of this work and requires Density Functional Theory (DFT) methods, etc.

14 Conclusions

The obtained results have meaning in the development of single-electron electrostatic quantum neural networks, quantum gates, such as CNOT, SWAP, Toffoli and Fredkin gates as well as any other types of quantum gates with N inputs and M outputs. Single-electron semiconductor devices can be attractive from point of view of power consumption and they can approach similar performance as Rapid Single Quantum Flux superconducting circuits [4] having much smaller dimensions than superconducting circuits. In conducted computations the spin degree-of-freedom was neglected. However it can be added in straightforward way doubling the size of Hilbert space. The obtained results allow us to obtain the entanglement of qubit A (for example) using bipartite Von Neumann entropy $S(t)_A$ of qubit A in two electrostatically interacting qubits with time as given by formula

$$S(t) = -Tr[\rho_A^{\hat{}}(t)(\log(\hat{\rho}_A(t)))], \quad (185)$$

where $Tr[.]$ is matrix trace operator and ρ_A is the reduced density matrix of A qubit after presence of B qubit was traced out. The obtained results can be mapped to Schrödinger formalism [11] in order to obtain higher accuracy and resolution in the description of quantum state dynamics. One can use the results in the determination of quantum transport in the single electron devices or arbitrary topology, which can be helpful in optimization of device functionality and sequence of controlling sequences shaping the electron confinement potential. Topological phase transitions as described by [12–14] are expected to take place in arrays of coupled electrostatic qubits due to the similarity of tight-binding applied in semiconductor coupled quantum well model to Josephson model in Cooper pair box superconducting qubits. All results are straightforward to be generalized for electrons and holes confined in net of coupled quantum dots (which changes only sign of electrostatic energy so $q^2 \rightarrow -q^2$) under the assumption that recombination processes do not occur. What is more the interaction between electrostatic position based qubit and Josephson junction was formulated and solved in tight-binding model. In a quite straightforward way one obtains the electrostatically coupled networks of graphs interacting

with single Josephson junction in analytical way. It will be important in the development of interface between semiconductor CMOS quantum computer and already developed superconducting computer.

Acknowledgements This work was supported by Science Foundation Ireland under Grant 14/RP/I2921. We would like to thank to professor Andrew Mitchell (UCD) for his long discussions on methodology of approach and to Erik Staszewski (erik.staszewski@ucd.ie) and to David Watté (david.watte@ucdconnect.ie) for his assistance in graphical design of figures.

Appendix 1

The simplified Hamiltonian, given by Eq. (120) for two electrostatically interacting single-electron lines (Fig. 9) has eigenvalues pointed by Formulas ((10)), ((11)) and has following eigenvectors

$$\hat{H} = \begin{pmatrix} q_{1_1} & 1 & 0 & 1 & 0 & 0 & 0 & 0 & 0 \\ 1 & q_{1_2} & 1 & 0 & 1 & 0 & 0 & 0 & 0 \\ 0 & 1 & q_{1_3} & 0 & 0 & 1 & 0 & 0 & 0 \\ 1 & 0 & 0 & q_{1_2} & 1 & 0 & 1 & 0 & 0 \\ 0 & 1 & 0 & 1 & q_{1_1} & 1 & 0 & 1 & 0 \\ 0 & 0 & 1 & 0 & 1 & q_{1_2} & 0 & 0 & 1 \\ 0 & 0 & 0 & 1 & 0 & 0 & q_{1_3} & 1 & 0 \\ 0 & 0 & 0 & 0 & 1 & 0 & 1 & q_{1_2} & 1 \\ 0 & 0 & 0 & 0 & 0 & 1 & 0 & 1 & q_{1_1} \end{pmatrix}, \quad (186)$$

$$|E_1\rangle = \begin{pmatrix} 1, \\ 0, \\ 0, \\ 0, \\ -1, \\ 0, \\ 0, \\ 0, \\ 0, \\ 1 \end{pmatrix}, |E_2\rangle = \begin{pmatrix} 0, \\ 1, \\ 0, \\ -1, \\ 0, \\ -1, \\ 0, \\ 1, \\ 0, \\ 0 \end{pmatrix},$$

$$|E_{3(4)}\rangle = \begin{pmatrix} -1, \\ \frac{1}{4}(q_{1_1} - q_{1_2} \pm \sqrt{8 + (q_{1_1} - q_{1_2})^2}), \\ 0, \\ \frac{1}{4}(q_{1_1} - q_{1_2} \pm \sqrt{8 + (q_{1_1} - q_{1_2})^2}), \\ 0, \\ -\frac{1}{4}(q_{1_1} - q_{1_2} \pm \sqrt{8 + (q_{1_1} - q_{1_2})^2}), \\ 0, \\ -\frac{1}{4}(q_{1_1} - q_{1_2} \pm \sqrt{8 + (q_{1_1} - q_{1_2})^2}), \\ 1 \end{pmatrix}, \quad (187)$$

$$|E_{5(6)}\rangle = \begin{pmatrix} -1, \\ \frac{1}{4}(q_{1_2} - q_{1_3} \pm \sqrt{8 + (q_{1_2} - q_{1_3})^2}), \\ 0, \\ \frac{1}{4}(q_{1_2} - q_{1_3} \pm \sqrt{8 + (q_{1_2} - q_{1_3})^2}), \\ 0, \\ -\frac{1}{4}(q_{1_2} - q_{1_3} \pm \sqrt{8 + (q_{1_2} - q_{1_3})^2}), \\ 0, \\ -\frac{1}{4}(q_{1_2} - q_{1_3} \pm \sqrt{8 + (q_{1_2} - q_{1_3})^2}), \\ 1 \end{pmatrix}, \quad (188)$$

$$|E_{k=(7\dots 9)}\rangle = \begin{pmatrix} 1, \\ (E_{k=(7\dots 9)} - q_{1_1})/2, \\ \frac{(-E_{k=(7\dots 9)} + q_{1_1})(-2 + E_{k=(7\dots 9)}^2 + q_{1_1}q_{1_2} - E_{k=(7\dots 9)}(q_{1_1} + q_{1_2}))}{2(-3E_{k=(7\dots 9)} + q_{1_1} + 2q_{1_3})}, \\ (E_{k=(7\dots 9)} - q_{1_1})/2, \\ 2, \\ (E_{k=(7\dots 9)} - q_{1_1})/2, \\ 2, \\ \frac{(-E_{k=(7\dots 9)} + q_{1_1})(-2 + E_{k=(7\dots 9)}^2 + q_{1_1}q_{1_2} - E_{k=(7\dots 9)}(q_{1_1} + q_{1_2}))}{2(-3E_{k=(7\dots 9)} + q_{1_1} + 2q_{1_3})} \end{pmatrix}. \quad (189)$$

It is important to recognize that in the case of electrons partly or wholly localized at the nodes of 2-SEL system, such that all hopping constants $t_{s1,kl}$ and $t_{s2,r'u'}$ are zero, we have no quantum entanglement between 2-SELs if it populates one energetic level and its Hamiltonian becomes diagonal. It brings the following energy eigenstates:

$$|E_1\rangle = \begin{pmatrix} 1 \\ 0 \\ 0 \\ 0 \\ 0 \\ 0 \\ 0 \\ 0 \\ 0 \end{pmatrix}, \dots |E_9\rangle = \begin{pmatrix} 0 \\ 0 \\ 0 \\ 0 \\ 0 \\ 0 \\ 0 \\ 0 \\ 1 \end{pmatrix}, \quad (190)$$

and Hamiltonian of system simulating two electrostatically charged insulators has the following structure

$$\hat{H} = \begin{pmatrix} q_{1_1} & 0 & 0 & 0 & 0 & 0 & 0 & 0 & 0 \\ 0 & q_{1_2} & 0 & 0 & 0 & 0 & 0 & 0 & 0 \\ 0 & 0 & q_{1_3} & 0 & 0 & 0 & 0 & 0 & 0 \\ 0 & 0 & 0 & q_{1_2} & 0 & 0 & 0 & 0 & 0 \\ 0 & 0 & 0 & 0 & q_{1_1} & 0 & 0 & 0 & 0 \\ 0 & 0 & 0 & 0 & 0 & q_{1_2} & 0 & 0 & 0 \\ 0 & 0 & 0 & 0 & 0 & 0 & q_{1_3} & 0 & 0 \\ 0 & 0 & 0 & 0 & 0 & 0 & 0 & q_{1_2} & 0 \\ 0 & 0 & 0 & 0 & 0 & 0 & 0 & 0 & q_{1_1} \end{pmatrix}, \quad (191)$$

what brings following eigenenergy values

$$\begin{aligned} E_1 = q_{1_1}, E_2 = q_{1_2}, E_3 = q_{1_3}, E_4 = q_{1_2}, E_5 = q_{1_1}, \\ E_6 = q_{1_2}, E_7 = q_{1_3}, E_8 = q_{1_2}, E_9 = q_{1_1}. \end{aligned} \quad (192)$$

Appendix 2: Details of Analytical Solution for Case of Coupled SELs

We continue derivation of the equation of motion imposed by classical picture of 2-SELs and from Hamiltonian 137 we obtain the following expression for velocity of interacting particles with positions $x_1(t) = -x_2(t)$ and velocity vs time as

$$\int \frac{dv}{\sqrt{q^4(E_c - mv^2)^4 - d^2(E_c - mv^2)^6}} = \frac{d^2}{q^4} \int \frac{du}{\sqrt{(\frac{E_c d}{q} - u) u^2 \sqrt{1-u^2}}} = s_1 \int \frac{du}{\sqrt{(s-u) u^2 \sqrt{1-u^2}}}. \quad (193)$$

Setting $s_1 = \frac{d^2}{q^4}$ and $s = \frac{E_c d}{q}$, we obtain the integral $s_1 \int \frac{du}{\sqrt{(s-u)} u^2 \sqrt{1-u^2}}$ that has the solution as

$$\begin{aligned}
s_1 \int \frac{du}{\sqrt{(s-u)} u^2 \sqrt{1-u^2}} &= \frac{s_1}{s\sqrt{1-u^2}} \left[\frac{(u^2-1)\sqrt{s-u}}{u} + \right. \\
&+ \frac{i(s-1)\sqrt{s-u}\sqrt{\frac{u-1}{s-1}} \left(\text{EllipticE} \left(i \sinh^{-1} \left(\sqrt{\frac{u-s}{s+1}} \right), \frac{s+1}{s-1} \right) - \text{EllipticF} \left(i \sinh^{-1} \left(\sqrt{\frac{u-s}{s+1}} \right), \frac{s+1}{s-1} \right) \right)}{\sqrt{\frac{u-s}{u+1}}} + \\
&+ \frac{is\sqrt{s-u}\sqrt{\frac{u-1}{s-1}} \text{EllipticF} \left(i \sinh^{-1} \left(\sqrt{\frac{u-s}{s+1}} \right), \frac{s+1}{s-1} \right)}{\sqrt{\frac{u-s}{u+1}}} \\
&- \frac{(\sqrt{s-1} + \sqrt{s+1})(\sqrt{s-1} - \sqrt{s-u})^2 \sqrt{\frac{\sqrt{s-1}(\sqrt{s+1}-\sqrt{s-u})}{(\sqrt{s-1}+\sqrt{s+1})(\sqrt{s-1}-\sqrt{s-u})}} \sqrt{\frac{\sqrt{s-1}(\sqrt{s-u}+\sqrt{s+1})}{(\sqrt{s-1}-\sqrt{s+1})(\sqrt{s-u}-\sqrt{s-1})}}}{\sqrt{s}(\sqrt{s-\sqrt{s-1}\sqrt{s+1}-1})} \times \\
&\times \sqrt{\frac{\sqrt{s-1}\sqrt{s-u}-\sqrt{s+1}\sqrt{s-u}+s-\sqrt{s-1}\sqrt{s+1}-1}{(\sqrt{s-1}+\sqrt{s+1})(\sqrt{s-1}-\sqrt{s-u})}} \times \\
&\times \left[(\sqrt{s-1} + \sqrt{s}) \text{EllipticF} \left(\sin^{-1} \left(\sqrt{\frac{(\sqrt{s-1}-\sqrt{s+1})(\sqrt{s-1}+\sqrt{s-u})}{(\sqrt{s-1}+\sqrt{s+1})(\sqrt{s-1}-\sqrt{s-u})}} \right), \frac{(\sqrt{s-1}+\sqrt{s+1})^2}{(\sqrt{s-1}-\sqrt{s+1})^2} \right) \right. \\
&- 2\sqrt{s-1} \times \\
&\times \text{EllipticPi} \left[\frac{(\sqrt{s-1}-\sqrt{s})(\sqrt{s-1}+\sqrt{s+1})}{(\sqrt{s-1}+\sqrt{s})(\sqrt{s-1}-\sqrt{s+1})}, \sin^{-1} \left(\sqrt{\frac{(\sqrt{s-1}-\sqrt{s+1})(\sqrt{s-1}+\sqrt{s-u})}{(\sqrt{s-1}+\sqrt{s+1})(\sqrt{s-1}-\sqrt{s-u})}} \right), \right. \\
&\left. \frac{(\sqrt{s-1}+\sqrt{s+1})^2}{(\sqrt{s-1}-\sqrt{s+1})^2} \right] \\
&- \frac{(\sqrt{s-1} + \sqrt{s+1})(\sqrt{s-1} - \sqrt{s-u})^2 \sqrt{\frac{\sqrt{s-1}(\sqrt{s+1}-\sqrt{s-u})}{(\sqrt{s-1}+\sqrt{s+1})(\sqrt{s-1}-\sqrt{s-u})}} \sqrt{\frac{\sqrt{s-1}(\sqrt{s-u}+\sqrt{s+1})}{(\sqrt{s-1}-\sqrt{s+1})(\sqrt{s-u}-\sqrt{s-1})}}}{\sqrt{s}(-s+\sqrt{s-1}\sqrt{s+1}+1)} \times \\
&\times \sqrt{\frac{\sqrt{s-1}\sqrt{s-u}-\sqrt{s+1}\sqrt{s-u}+s-\sqrt{s-1}\sqrt{s+1}-1}{(\sqrt{s-1}+\sqrt{s+1})(\sqrt{s-1}-\sqrt{s-u})}} \times \\
&\times \left[(\sqrt{s-1} - \sqrt{s}) \text{EllipticF} \left(\sin^{-1} \left(\sqrt{\frac{(\sqrt{s-1}-\sqrt{s+1})(\sqrt{s-1}+\sqrt{s-u})}{(\sqrt{s-1}+\sqrt{s+1})(\sqrt{s-1}-\sqrt{s-u})}} \right), \frac{(\sqrt{s-1}+\sqrt{s+1})^2}{(\sqrt{s-1}-\sqrt{s+1})^2} \right) \right. \\
&- 2\sqrt{s-1} \text{EllipticPi} \left[\frac{(\sqrt{s-1}+\sqrt{s})(\sqrt{s-1}+\sqrt{s+1})}{(\sqrt{s-1}-\sqrt{s})(\sqrt{s-1}-\sqrt{s+1})}, \right. \\
&\left. \sin^{-1} \left(\sqrt{\frac{(\sqrt{s-1}-\sqrt{s+1})(\sqrt{s-u}+\sqrt{s-1})}{(\sqrt{s-1}+\sqrt{s+1})(\sqrt{s-1}-\sqrt{s-u})}} \right), \frac{(\sqrt{s-1}+\sqrt{s+1})^2}{(\sqrt{s-1}-\sqrt{s+1})^2} \right] \Big]. \tag{194}
\end{aligned}$$

where $\text{EllipticF}[\cdot, \cdot]$ is the elliptic integral of the first kind, $\text{EllipticE}[\cdot, \cdot]$ is the elliptic integral of the second kind and $\text{EllipticPi}[\cdot, \cdot]$ is the complete elliptic integral of the third kind as in accordance with nomenclature used by Mathematica symbolic software [15].

Appendix 3: Details of Anticorrelation Function Calculation for the Case of Weak Measurement Performed on the 2-SELS

We refer to the Hamiltonian of 2-SEL system coupled to flying qubit given by Eq. (152) and we recognize that the time-dependent Hamiltonian $\hat{H}_{AC}(t)$ and evolution operator based on it is as follows

$$e^{\frac{1}{\hbar i} \int_0^{t'} (\hat{H}_{AC}(t') \times \hat{I}_B) dt'} = \quad (195)$$

$$\begin{pmatrix} e^{\frac{1}{\hbar} \int_0^{t'} E_{s1'2'} dt'} & 0 & 0 & 0 & 0 & 0 & 0 & 0 \\ 0 & e^{\frac{1}{\hbar} \int_0^{t'} E_{s1'1'} dt'} & 0 & 0 & 0 & 0 & 0 & 0 \\ 0 & 0 & e^{\frac{1}{\hbar} \int_0^{t'} E_{s2'1'} dt'} & 0 & 0 & 0 & 0 & 0 \\ 0 & 0 & 0 & e^{\frac{1}{\hbar} \int_0^{t'} E_{s2'1'} dt'} & 0 & 0 & 0 & 0 \\ 0 & 0 & 0 & 0 & e^{\frac{1}{\hbar} \int_0^{t'} E_{s1'2'} dt'} & 0 & 0 & 0 \\ 0 & 0 & 0 & 0 & 0 & e^{\frac{1}{\hbar} \int_0^{t'} E_{s1'2'} dt'} & 0 & 0 \\ 0 & 0 & 0 & 0 & 0 & 0 & e^{\frac{1}{\hbar} \int_0^{t'} E_{s2'2'} dt'} & 0 \\ 0 & 0 & 0 & 0 & 0 & 0 & 0 & e^{\frac{1}{\hbar} \int_0^{t'} E_{s2'2'} dt'} \end{pmatrix}$$

Now we are defining the correlation function for 2-SELs in case of the system interaction with the external flying qubit given by the matrix

$$C_{AB,C} = \hat{I}_C \times \hat{C}_{AB} = \begin{pmatrix} 1 & 0 \\ 0 & 1 \end{pmatrix} \times \begin{pmatrix} 1 & 0 & 0 & 0 \\ 0 & -1 & 0 & 0 \\ 0 & 0 & -1 & 0 \\ 0 & 0 & 0 & 1 \end{pmatrix} = \begin{pmatrix} +1 & 0 & 0 & 0 & 0 & 0 & 0 & 0 \\ 0 & -1 & 0 & 0 & 0 & 0 & 0 & 0 \\ 0 & 0 & -1 & 0 & 0 & 0 & 0 & 0 \\ 0 & 0 & 0 & +1 & 0 & 0 & 0 & 0 \\ 0 & 0 & 0 & 0 & +1 & 0 & 0 & 0 \\ 0 & 0 & 0 & 0 & 0 & -1 & 0 & 0 \\ 0 & 0 & 0 & 0 & 0 & 0 & -1 & 0 \\ 0 & 0 & 0 & 0 & 0 & 0 & 0 & +1 \end{pmatrix}. \quad (196)$$

Now we construct Hamiltonian for non-interacting C and AB physical systems given as

$$\begin{aligned} \hat{H} &= \hat{I}_C \times \hat{H}_{AB} + \hat{H}_C \times \hat{I}_{AB} = \\ &= \begin{pmatrix} \hat{H}_{AB} & \hat{0}_{4 \times 4} \\ \hat{0}_{4 \times 4} & \hat{H}_{AB} \end{pmatrix} + \begin{pmatrix} \hat{H}_C[1,1] & 0 & 0 & 0 & \hat{H}_C[1,2] & 0 & 0 & 0 \\ 0 & \hat{H}_C[1,1] & 0 & 0 & 0 & \hat{H}_C[1,2] & 0 & 0 \\ 0 & 0 & \hat{H}_C[1,1] & 0 & 0 & 0 & \hat{H}_C[1,2] & 0 \\ 0 & 0 & 0 & \hat{H}_C[1,1] & 0 & 0 & 0 & \hat{H}_C[1,2] \\ \hat{H}_C[2,1] & 0 & 0 & 0 & \hat{H}_C[2,2] & 0 & 0 & 0 \\ 0 & \hat{H}_C[2,1] & 0 & 0 & 0 & \hat{H}_C[2,2] & 0 & 0 \\ 0 & 0 & \hat{H}_C[2,1] & 0 & 0 & 0 & \hat{H}_C[2,2] & 0 \\ 0 & 0 & 0 & \hat{H}_C[2,1] & 0 & 0 & 0 & \hat{H}_C[2,2] \end{pmatrix} = \\ &= \begin{pmatrix} E_{p1} + E_{p1'} + E_{c1} & t_{s1'2'} & t_{s12} & 0 & 0 & 0 & 0 & 0 \\ t_{s1'2'}^* & E_{p1} + E_{p2'} + E_{c2} & 0 & t_{s12} & 0 & 0 & 0 & 0 \\ t_{s12}^* & 0 & E_{p2} + E_{p1'} + E_{c2} & t_{s1'2'} & 0 & 0 & 0 & 0 \\ 0 & t_{s12}^* & t_{s1'2'}^* & E_{p2} + E_{p2'} + E_{c1} & 0 & 0 & 0 & 0 \\ 0 & 0 & 0 & 0 & E_{p1} + E_{p1'} + E_{c1} & t_{s1'2'} & t_{s12} & 0 \\ 0 & 0 & 0 & 0 & t_{s1'2'}^* & E_{p1} + E_{p2'} + E_{c2} & 0 & t_{s12} \\ 0 & 0 & 0 & 0 & 0 & t_{s12}^* & E_{p2} + E_{p1'} + E_{c2} & t_{s1'2'} \\ 0 & 0 & 0 & 0 & 0 & t_{s12} & t_{s1'2'}^* & E_{p2} + E_{p2'} + E_{c1} \end{pmatrix} + \\ &+ \begin{pmatrix} E_{p1''} & 0 & 0 & 0 & t_{s1'2''} & 0 & 0 & 0 \\ 0 & E_{p1''} & 0 & 0 & 0 & t_{s1'2''} & 0 & 0 \\ 0 & 0 & E_{p1''} & 0 & 0 & 0 & t_{s1'2''} & 0 \\ 0 & 0 & 0 & E_{p1''} & 0 & 0 & 0 & t_{s1'2''} \\ t_{s1'2''}^* & 0 & 0 & 0 & E_{p2''} & 0 & 0 & 0 \\ 0 & t_{s1'2''}^* & 0 & 0 & 0 & E_{p2''} & 0 & 0 \\ 0 & 0 & t_{s1'2''}^* & 0 & 0 & 0 & E_{p2''} & 0 \\ 0 & 0 & 0 & 0 & 0 & 0 & 0 & E_{p2''} \end{pmatrix} = \\ &= \begin{pmatrix} E_{p1} + E_{p1'} + E_{c1} & t_{s1'2'} & t_{s12} & 0 & t_{s1'2''} & 0 & 0 & 0 \\ t_{s1'2'}^* & E_{p1} + E_{p2'} + E_{c2} & 0 & t_{s12} & 0 & t_{s1'2''} & 0 & 0 \\ t_{s12}^* & 0 & E_{p2} + E_{p1'} + E_{c2} & t_{s1'2'} & 0 & 0 & t_{s1'2''} & 0 \\ 0 & t_{s12}^* & t_{s1'2'}^* & E_{p2} + E_{p2'} + E_{c1} & 0 & 0 & 0 & t_{s1'2''} \\ t_{s1'2''}^* & 0 & 0 & 0 & E_{p1} + E_{p1'} + E_{c1} & t_{s1'2'} & t_{s12} & 0 \\ 0 & t_{s1'2''}^* & 0 & 0 & t_{s1'2'}^* & E_{p1} + E_{p2'} + E_{c2} & 0 & t_{s12} \\ 0 & 0 & t_{s1'2''}^* & 0 & 0 & 0 & E_{p2} + E_{p1'} + E_{c2} & t_{s1'2''} \\ 0 & 0 & 0 & 0 & 0 & t_{s12} & t_{s1'2'}^* & E_{p2} + E_{p2'} + E_{c1} \end{pmatrix} + \\ &+ \text{diag}(E_{p1''}, E_{p1''}, E_{p1''}, E_{p1''}, E_{p2''}, E_{p2''}, E_{p2''}, E_{p2''}). \end{aligned}$$

We recognize that diagonal elements of $\hat{I}_C \times \hat{H}_{AB} + \hat{H}_C \times \hat{I}_{AB}$ are

$$(E_{p1} + E_{p1'} + E_{c1} + E_{p1''}, E_{p1} + E_{p2'} + E_{c2} + E_{p1''}, E_{p2} + E_{p1'} + E_{c2} + E_{p1''}, E_{p2} + E_{p2'} + E_{c1} + E_{p1''}, \\ E_{p1} + E_{p1'} + E_{c1} + E_{p2''}, E_{p1} + E_{p2'} + E_{c2} + E_{p2''}, E_{p2} + E_{p1'} + E_{c2} + E_{p2''}, E_{p2} + E_{p2'} + E_{c1} + E_{p2''}).$$

Now we consider the interaction between qubits C and A denoted by H_{CA} and it will be incorporated into global Hamiltonian $\hat{H}_{CA} \times \hat{I}_B$ that has the following diagonal matrix representation

$$\hat{H}_{CA} = \begin{pmatrix} E_{c1''1}(t) & 0 & 0 & 0 \\ 0 & E_{c1''2}(t) & 0 & 0 \\ 0 & 0 & E_{c2''1}(t) & 0 \\ 0 & 0 & 0 & E_{c2''2}(t) \end{pmatrix} \quad (197)$$

and consequently

$$\hat{H}_{CA} \times \hat{I}_B = \begin{pmatrix} E_{c1''1}(t) & 0 & 0 & 0 & 0 & 0 & 0 & 0 \\ 0 & E_{c1''1}(t) & 0 & 0 & 0 & 0 & 0 & 0 \\ 0 & 0 & E_{c1''2}(t) & 0 & 0 & 0 & 0 & 0 \\ 0 & 0 & 0 & E_{c1''2}(t) & 0 & 0 & 0 & 0 \\ 0 & 0 & 0 & 0 & E_{c2''1}(t) & 0 & 0 & 0 \\ 0 & 0 & 0 & 0 & 0 & E_{c2''1}(t) & 0 & 0 \\ 0 & 0 & 0 & 0 & 0 & 0 & E_{c2''2}(t) & 0 \\ 0 & 0 & 0 & 0 & 0 & 0 & 0 & E_{c2''2}(t) \end{pmatrix}. \quad (198)$$

We have the total Hamiltonian for the flying qubit interacting with 2-SELs given as

$$\hat{H} = \hat{I}_C \times \hat{H}_{AB} + \hat{H}_C \times \hat{I}_{AB} + \hat{H}(t)_{CA} \times \hat{I}_B. \quad (199)$$

We recognize that the diagonal terms of total matrix are given as a following sequence

$$(E_{p1} + E_{p1'} + E_{c1} + E_{p1''} + E_{c1''1}(t), E_{p1} + E_{p2'} + E_{c2} + E_{p1''} + E_{c1''1}(t), E_{p2} + E_{p1'} + E_{c2} \\ + E_{p1''} + E_{c1''2}(t), E_{p2} + E_{p2'} + E_{c1} + E_{p1''} + E_{c1''2}(t), \\ E_{p1} + E_{p1'} + E_{c1} + E_{p2''} + E_{c2''1}(t), E_{p1} + E_{p2'} + E_{c2} + E_{p2''} \\ + E_{c2''1}(t), E_{p2} + E_{p1'} + E_{c2} + E_{p2''} + E_{c2''2}(t), E_{p2} \\ + E_{p2'} + E_{c1} + E_{p2''} + E_{c2''2}(t)). \quad (200)$$

Setting $E_{p1} = E_{p1'} = E_{p1''} = E_{p2} = E_{p2'} = E_{p2''} = E_p$, we obtain diagonal terms as

$$(E_{c1} + 3E_p + E_{c1''1}(t), E_{c2} + 3E_p + E_{c1''1}(t), E_{c2} + 3E_p + E_{c1''2}(t), 3E_p + E_{c1} + E_{c1''2}(t), \\ E_{c1} + 3E_p + E_{c2''1}(t), 3E_p + E_{c2} + E_{c2''1}(t), 3E_p + E_{c2} + E_{c2''2}(t), 3E_p + E_{c1} + E_{c2''2}(t)). \quad (201)$$

Subtracting element $3E_p + E_{c1}$ we obtain

$$\begin{aligned} & E_{c1'1}(t), E_{c2} - E_{c1} + E_{c1'1}(t), E_{c2} - E_{c1} + E_{c1'2}(t), E_{c1'2}(t), \\ & E_{c2'1}(t), E_{c2} - E_{c1} + E_{c2'1}(t), E_{c2} - E_{c1} + E_{c2'2}(t), E_{c2'2}(t). \end{aligned} \quad (202)$$

Now we are constructing the density matrix for the case of non-interacting qubit C with 2-SELs denoted as AB system. We assume that qubit C is in the ground state and that symmetric 2-SELs line is populated at energy E_1 or E_2 . In such a case, the density matrices are as follows

$$\hat{\rho}_C = \begin{pmatrix} +\frac{1}{2} & -\frac{1}{2} \\ -\frac{1}{2} & +\frac{1}{2} \end{pmatrix}, \hat{\rho}_{AB} = \begin{pmatrix} +\frac{1}{2} & 0 & 0 & -\frac{1}{2} \\ 0 & 0 & 0 & 0 \\ 0 & 0 & 0 & 0 \\ -\frac{1}{2} & 0 & 0 & +\frac{1}{2} \end{pmatrix} \quad (203)$$

Therefore, the density matrix of non-interacting qubit C with 2-SELs line denoted as AB system is given as

$$\hat{\rho}_{ABC} = \begin{pmatrix} +\frac{1}{2} & -\frac{1}{2} \\ -\frac{1}{2} & +\frac{1}{2} \end{pmatrix} \times \begin{pmatrix} +\frac{1}{2} & 0 & 0 & -\frac{1}{2} \\ 0 & 0 & 0 & 0 \\ 0 & 0 & 0 & 0 \\ -\frac{1}{2} & 0 & 0 & +\frac{1}{2} \end{pmatrix} = \begin{pmatrix} +\frac{1}{4} & 0 & 0 & -\frac{1}{4} & -\frac{1}{4} & 0 & 0 & +\frac{1}{4} \\ 0 & 0 & 0 & 0 & 0 & 0 & 0 & 0 \\ 0 & 0 & 0 & 0 & 0 & 0 & 0 & 0 \\ -\frac{1}{4} & 0 & 0 & +\frac{1}{4} & +\frac{1}{4} & 0 & 0 & -\frac{1}{4} \\ -\frac{1}{4} & 0 & 0 & +\frac{1}{4} & +\frac{1}{4} & 0 & 0 & -\frac{1}{4} \\ 0 & 0 & 0 & 0 & 0 & 0 & 0 & 0 \\ 0 & 0 & 0 & 0 & 0 & 0 & 0 & 0 \\ +\frac{1}{4} & 0 & 0 & -\frac{1}{4} & -\frac{1}{4} & 0 & 0 & +\frac{1}{4} \end{pmatrix}. \quad (204)$$

The density matrix follows the equation of motion

$$\rho(t) = e^{\frac{1}{i\hbar} \int_0^t H(t') dt'} \begin{pmatrix} +\frac{1}{4} & 0 & 0 & -\frac{1}{4} & -\frac{1}{4} & 0 & 0 & +\frac{1}{4} \\ 0 & 0 & 0 & 0 & 0 & 0 & 0 & 0 \\ 0 & 0 & 0 & 0 & 0 & 0 & 0 & 0 \\ -\frac{1}{4} & 0 & 0 & +\frac{1}{4} & +\frac{1}{4} & 0 & 0 & -\frac{1}{4} \\ -\frac{1}{4} & 0 & 0 & +\frac{1}{4} & +\frac{1}{4} & 0 & 0 & -\frac{1}{4} \\ 0 & 0 & 0 & 0 & 0 & 0 & 0 & 0 \\ 0 & 0 & 0 & 0 & 0 & 0 & 0 & 0 \\ +\frac{1}{4} & 0 & 0 & -\frac{1}{4} & -\frac{1}{4} & 0 & 0 & +\frac{1}{4} \end{pmatrix} e^{-\frac{1}{i\hbar} \int_0^t H(t') dt'}. \quad (205)$$

Since the structure of the Hamiltonian matrix $\hat{H}(t) = \hat{I}_C \times \hat{H}_{AB} + \hat{H}_C \times \hat{I}_{AB} + \hat{H}_{CA}(t) \times \hat{I}_B$ describing the interaction of three electrons confined to the flying position-based qubit C and 2-SEL system is known at all instances of time in the analytical way as well as the operators $e^{\pm \frac{1}{i\hbar} \int_0^t H(t') dt'}$ are known in the analytical way, the structure of the density matrix is known in the analytical way. This implies our full knowledge of the qubit C state and 2-SELs system at any instance of time thanks

to the Formula (149). Such reasoning opens the perspective of analytical approach towards quantum N -body electron (hole) system confined to the three disconnected graphs of quantum dots of any topology in the 3D space subjected to the steering mechanism from voltage polarization applied to CMOS gates, as depicted in Fig. 2. It is thus the subject of the future more detailed studies with use of both analytical and numerical tools. It also opens the perspective on new experiments and new technological novelties in the area of cryogenic CMOS single-electron device electronics [16] that have both importance in the implementation of quantum computer as well as in the development of classical single electron electronics.

References

1. Fujisawa T, Hayashi T, Cheong HD, Jeong YH, Hirayama Y (2004) Rotation and phase-shift operations for a charge qubit in a double quantum dot. *Phys E Low-dimensional Syst Nanostruct* 21(2–4):10461052
2. Petersson KD, Petta JR, Lu H, Gossard AC (2010) Quantum coherence in a one-electron semiconductor charge qubit. *Phys Rev Lett* 105:246804
3. Pomorski K, Giounanlis P, Blokhina E, Leipold D, Bogdan R, Staszewski (2019) Analytic view on coupled single-electron lines, semiconductor science and technology, <http://www.iopscience.iop.org/10.1088/1361-6641/ab4f40>
4. Pomorski K, Giounanlis P, Blokhina E, Leipold D, Peczkowski P, Bogdan R, Staszewski (2019) From two types of electrostatic position-dependent semiconductor qubits to quantum universal gates and hybrid semiconductor-superconducting quantum computer. In: *Proceedings SPIE 11054, superconductivity and particle accelerators 2018*, 110540M
5. Giounanlis P, Blokhina E, Pomorski K, Leipold DR, Staszewski RB (2019) Modeling of semiconductor electrostatic qubits realized through coupled quantum dots, *IEEE Access*. <https://doi.org/10.1109/ACCESS.2019.2909489>
6. Spalek J (2015) *Wstęp do fizyki materii skondensowanej*, PWN
7. Wikipedia: Bell theorem
8. Jaynes ET, Cummings FW (1963) Comparison of quantum and semiclassical radiation theories with application to the beam maser. *Proc IEEE* 51(1):89–109. <https://doi.org/10.1109/PROC.1963.1664>
9. Pomorski K, Prokopow P (2012) Possible existence of field-induced Josephson junctions, vol 249, No 9. *Physica Status Solidi B*
10. Leipold D Controlled rabi oscillations as foundation for entangled quantum aperture logic, Seminar at UC Berkley Quantum Labs, 25th July 2018
11. Xu HQ Method of calculations for electron transport in multiterminal quantum systems based on real-space lattice models. *Phys Rev B* 66:165305
12. Choi MS, Yi J, Choi MY, Choi J, Lee SI (1998) Quantum phase transitions in Josephson-junction chains. *Phys Rev B* 57:R716R719
13. Sachdev S (2011) *Quantum phase transitions*. Cambridge University Press
14. Maile D, Andergassen S, Belzig W (2018) Quantum phase transition with dissipative frustration. *Phys Rev B* 97
15. Wolfram Mathematica. <http://www.wolfram.com/mathematica/>
16. Pomorski K, Akaike H, Fujimaki A, Rusek K (2019) Relaxation method in description of ram memory cell in rsfq computer. *COMPEL* 38(1):395414

Morphology and Physico-mechanical Properties of Antifriction Epoxy Nanocomposites



V. Havrylova, S. Zhylytsova, Ye. Mamunya, N. Babkina, and V. Tkach

Abstract The article presents the study results of the properties of the antifriction epoxy polymer coating. To improve the adhesion and cohesion properties of the coating, the nanodisperse organosilicon modifier synthesized in situ by the sol–gel method was introduced into a matrix based on anhydride cured epoxy resin. Molybdenum disulfide was added to improve the mechanical and antifriction properties.

Keywords Epoxy-silica nanocomposite · Scanning electron microscopy · Thermomechanical analysis · Dynamic mechanical analysis · Coating for friction pairs · Sol–gel method · Molybdenum disulfide

1 Introduction

The formation of a nanostructured state is one of the most effective ways to achieve a high level of physical–mechanical, tribotechnical, anticorrosive properties of materials. Nanomaterials have a large proportion of near-surface atoms with their unsaturated bonds, the interaction of electrons with a free surface, as well as an increased volume fraction of interfaces, which are characterized by a non-equilibrium state, which causes elastic deformation of the material at the interfaces.

The high level of the surface energy of nanoparticles introduced to modify materials and coatings has a significant effect on the processes of cohesive and adhesive interactions of nanoparticles with the matrix phase. The introduction of nanoparticles

V. Havrylova (✉) · V. Tkach

V. Bakul Institute for Superhard Materials, National Academy of Sciences of Ukraine, 2 Avtozavodska Str., Kyiv 04074, Ukraine
e-mail: vsgavrilova@gmail.com

S. Zhylytsova

Vasyl' Stus Donetsk National University, 21 600-Richchia Str., Vinnytsia 21021, Ukraine

Ye. Mamunya · N. Babkina

Institute of Macromolecular Chemistry of National Academy of Sciences of Ukraine, 48 Kharkivske Shosse, Kyiv 02160, Ukraine

changes the conditions of thermal and electrophysical processes during the formation of the structure of the material, contributing to its dispersion and improvement of performance. In addition, a decrease in the size of particles to the nanoscale makes it possible to significantly reduce the degree of filling of modified materials [1–3].

Organic–inorganic nanocomposites can synergistically combine the properties of interacting components. The inorganic component possesses high chemical resistance, thermal stability, abrasion resistance; the organic one improves flexibility, ductility, strength, etc. By mixing these components, it is possible to create hybrids with much better properties than individual constituents, which significantly expands the possibilities of the application of the obtained materials [4]. Such hybrid organic–inorganic nanocomposites are three-phase systems including phases of organic and inorganic components and a phase that is the product of their interaction [5].

Epoxy-inorganic composites are often used as protective coatings for different surfaces [6]. At the same time, the purposeful introduction of a certain amount of filler, usually used in the preparation of materials, for example, with antifriction properties, will make it possible to synthesize a coating with both a high degree of interfacial interaction and the desired set of tribotechnical parameters. Such nanocoatings can become promising materials due to the synergistic combination of all the components that form this system. This work aimed to obtain, using the sol–gel method, epoxy-inorganic nanostructured coatings with improved mechanical and antifriction properties due to the introduction of molybdenum disulfide.

2 Experimental Technique

The polymeric matrix was formed of an epoxy resin (hydrogenated analog of DGEBA), an anhydride hardener (isomethyltetrahydrophthalic anhydride), and a tertiary amine as an accelerator. The curing of the polymer (sample 1) was carried out in a stepwise mode, by heating it from 120 to 180 °C. The inorganic component consisted of silica particles formed in situ by the sol–gel method based on organosilicon precursors. The content of the siloxane component was 1 wt.% (sample 2) and 3 wt.% (sample 3). Molybdenum disulfide (30 wt.%, sample 4) was additionally introduced into the liquid composition of sample 3 to provide the required complex physical and mechanical properties. The composites were cured in the same way as sample 1.

The structure and elemental composition of the samples were studied using an EVO 50XVP scanning electron microscope (Carl Zeiss, Germany).

Composites were studied by thermomechanical analysis [7] (TMA) with a TMA Q400EM analyzer (TA Instruments, United States). The TMA curves were obtained in the regime of the indenter penetration into the composite sample, which is identical to its deformation. The sample was placed onto a quartz base plate and pressured by a quartz indenter with a tip 0.85 mm in diameter. The effort applied to the indenter was 0.28 N, which provides constant compressive stress of 0.5 MPa on the sample.

The samples were cut from composite plates in the form of squares with a side size of 6 mm; the thickness of the samples was 0.3–0.4 mm.

The samples were heated at a constant rate of 5 °C/min. The TMA curves were recorded in the temperature range 25–160 °C.

The TMA curves were used to determine the glass transition and high elasticity temperatures T_g and T_e . We also calculated the relative deformation L , %:

$$L = \frac{\Delta l}{l_0} \cdot 100,$$

where Δl is the deformation of the sample under load, μm ; l_0 is the initial sample thickness, μm .

Previously, to eliminate the thermal history and internal stresses, the samples were heated in an oven at 150 °C for 3 h with slow cooling.

The calculation of the effective molecular weight between crosslinks in the polymer network M_c , g/mol, was carried out according to the formula

$$M_c = \frac{3R\rho T_e}{E_e},$$

where R is the universal gas constant, J/(mol·K); ρ —density of the sample, g/cm³; T_e —high elasticity temperature, K; E_e —equilibrium modulus, MPa.

Viscoelastic properties were determined by dynamic mechanical analysis (DMA) on Q800 dynamic analyzer (TA Instruments, USA) with a heating rate of 3 °C·min⁻¹ in the temperature range from 20 to 200 °C. The measurement of the viscoelastic characteristics such as the tangent of mechanical loss ($\tan \delta$) and the dynamic storage modulus (E') was carried out in the tensile strain mode at a frequency of 10 Hz. The glass transition temperature was defined as the temperature of the $\tan \delta$ maximum. The value of the storage modulus in the glassy state at $T = 25$ °C ($E'_{T=25}$ °C) and in the region of the high elasticity at $T = 150$ °C ($E'_{T=150}$ °C) was determined from the temperature dependences of E' .

Tensile strength σ_t of the adhesive joints of D16 aluminum alloy with the composite was determined on aluminum samples according to GOST 14760-69. Before joining, the surface was treated with corundum on a grinding plate to roughen the surface and remove the oxide film, after which it was degreased with acetone. The thickness of the adhesive layer was 60–80 μm . The measurement error did not exceed 10%.

Ultimate mechanical properties under uniaxial tension (fracture stress σ_f and deformation at break ε_b) were determined on a Polyany-type dynamometer at a strain rate of 3.8×10^{-5} m/s. The elastic modulus E was calculated from the slope of the initial straight-line part of the stress (σ)–strain (ε) curve. The measurement error did not exceed 10%.

3 Results and Its Discussion

It is known that the sol–gel method, depending on the synthesis conditions and system components, makes it possible to obtain nanocomposites with a uniform distribution of particles in a polymer matrix [8], which provides high homogeneity of such systems and reproducibility of material properties. These structural features are due to the high content of surface groups on the filler particles, which can have an affinity for the polymer component because of functionalization or the use of precursors containing organic fragments that are incapable of hydrolysis.

The data obtained by scanning electron microscopy indicate a significant change in the structure of the polymer upon the introduction of silica particles and an antifriction filler—molybdenum disulfide (Fig. 1). Figure 1a shows a homogeneous single-phase structure of the initial epoxy polymer. The introduction of silica particles causes the formation of regions with a pronounced layer morphology (see Fig. 1b), and the introduction of molybdenum disulfide leads to a further decrease in the grain size of the epoxy matrix and the formation of a heterophase layer structure with a uniform distribution of phases (see Fig. 1c, d), which can greatly improve the mechanical properties of the composite.

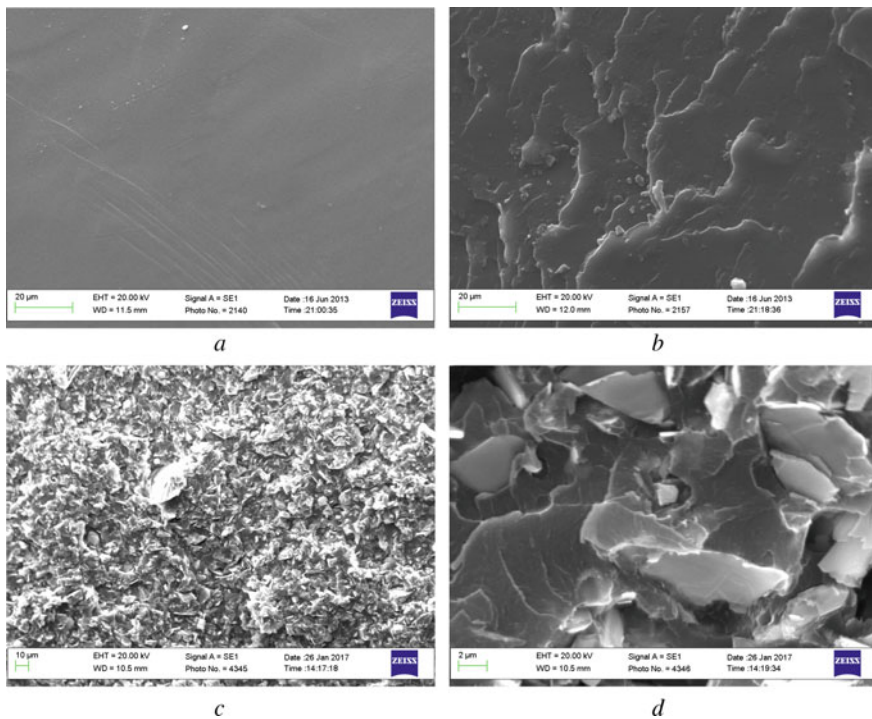


Fig. 1 Transformation of the structure of epoxy polymer (a), with the introduction of 3 wt.% silica particles (b), followed by the addition of molybdenum disulfide (c, d) according to SEM data

Primary SiO₂ nanoparticles in the grains of the epoxy matrix form aggregates with a size of 0.5–2.0 μm (Fig. 2). The ratio of elements in different parts of the structure of sample 2 is given in Table 1. They indicate that the light formations in the figure are agglomerates of silica particles.

Continuity of grain boundaries is important to ensure a reproducible set of material properties. It is known that if the boundaries between grains are continuous, in other words, the structure is denser, then the composite has the best physical and mechanical characteristics. The effect of molybdenum disulfide antifriction filler on the structure of epoxy-silica nanocomposite is analyzed. According to the SEM data (see Fig. 1c, d), the sample contains finer grains compared to the system without a filler. Analysis of micrographs (see Fig. 1b, c) indicates that the samples with the addition of silica particles and antifriction filler have a dense structure.

Such changes in the morphology of composites significantly affect their properties. The characteristics of composite samples with a silica particles content of 1 and 3 wt.%, as well as systems with the addition of MoS₂ (Fig. 3 and Table 2), were determined by thermomechanical analysis.

In the glassy state, samples of polymer (1) and composites (2, 3) do not exhibit thermal expansion under an applied load (Fig. 3). The TMA curve of sample 4, which contains an antifriction filler, molybdenum disulfide (see Fig. 3b), differs in shape from those described above and demonstrates the presence of thermal expansion during the action of the stress of 0.5 MPa.

Fig. 2 The structure of a composite based on the epoxy polymer with additives of 1 wt. % silica particles according to SEM data

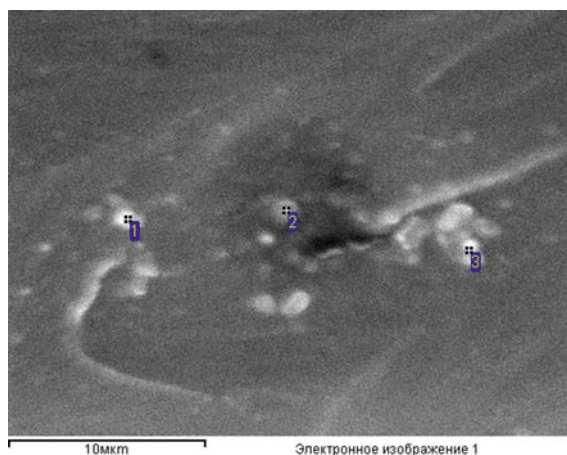


Table 1 The content of elements in different parts of the structure of the composite containing 1 wt.% silica particles

Site	Content of elements, % (by mass)		
	C	O	Si
1	77.24	21.87	0.89
2	81.83	17.09	1.08
3	83.12	15.65	1.23

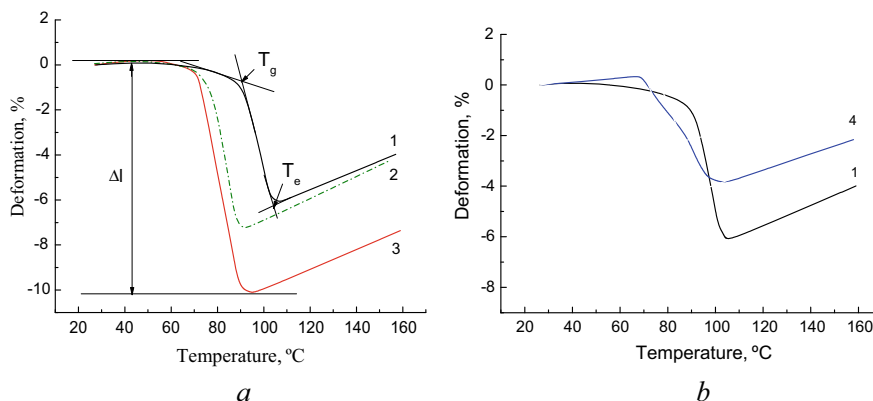


Fig. 3 TMA curves of samples 1–3 (a) and 1, 4 (b). Curve numbers correspond to sample numbers

Table 2 Characteristics of composite samples obtained from thermomechanical analysis data

Sample	T_g (°C)	T_e (°C)	$T_e - T_g$ (°C)	L_e (%)	ρ (g/cm ³)	M_c (g/mol)	$n_c \cdot 10^4$ (mol/cm ³)
1	90	103	13	6.0	1.15	1340	8.6
2	75	89	14	7.4	1.16	1600	7.3
3	71	90	19	10.2	1.18	2250	5.2
4	70	98	28	4.1	1.51	1180	12.8

The presence of SiO₂ particles formed by the sol–gel method in the epoxy matrix leads to a shift of the curves toward lower temperatures as compared to the epoxy polymer—the values of T_g and T_e decrease (Table 2), and the effect becomes more pronounced with an increase in the amount of silica particles. The glass transition temperature decreases from 90 °C for the epoxy polymer to 75 and 71 °C for samples 2 and 3 with the content of SiO₂ 1 and 3 wt.%, respectively. In this case, the values of the highly elastic deformation L_e increase from 6.0% for the unmodified epoxy polymer to 7.4 and 10.2% for samples 2 and 3, respectively. This indicates a decrease in the degree of crosslinking of the epoxy matrix in the presence of silica particles, which leads to its plasticization (that indicates a decrease of T_e) and a relative decrease in the physico-mechanical characteristics of the composite. This is indicated by an increase in the values of the effective molecular weight M_c between crosslinks of samples 2 and 3 in comparison with the unmodified epoxy polymer, sample 1 (see Table 2). It is seen that in the presence of 1 and 3 wt.% silica particles in the polymer matrix of the composite, the crosslink density decreases by ~20 and 70%, respectively.

It is known that the introduction of mineral fillers into polymers can significantly change the mechanical characteristics of materials [9]. To improve the operational properties of the obtained samples of the epoxy-silica nanocomposite, additives of molybdenum disulfide were introduced into the uncured composition. The obtained composite has low values of highly elastic deformation ($L_e = 4.1\%$), however, the

T_e-T_g difference is quite large (28 °C), which indicates a wide glass transition temperature range. An increase in the interval of transition from a glassy state to a highly elastic state indicates an increase in the heterogeneity of the composite in terms of molecular mobility. In this case, the crosslinking density of sample 4 is almost 1.5 times higher than that of the composite containing 3 wt.% silica particles without the addition of MoS₂ (sample 3) (see Table 2).

The mechanical characteristics of the composite with the addition of molybdenum disulfide are much higher than those for composites that do not contain an antifriction filler (samples 2, 3) (see Table 2). These data once again emphasize the role played by silica particles in providing the necessary physico-mechanical characteristics of the composite.

It is known that DMA is one of the effective methods for finding correlations between the structure and viscoelastic properties of polymers [10, 11]. The temperature dependences of the viscoelastic functions of the initial epoxy polymer (sample 1) and composites (samples 2–4) demonstrate the presence of a clear relaxation glass transition, which manifests itself as maximum $\tan \delta$ (Fig. 4) and a sharp decrease in E' (Fig. 5). The parameters of the viscoelastic characteristics of the studied samples are presented in Table 3.

It can be seen from Figs. 4 and 5 that for epoxy composites (curves 2–4) the glass transition region is shifted toward lower temperatures as compared to the initial polymer (curve 1), which is consistent with the results obtained by the TMA method. The presence of silica particles decreases the T_g by 15 °C at a content of 1 wt.% SiO₂ and by 19 °C at a content of 3 wt.% SiO₂ (Table 3). It may indicate a decrease in the degree of crosslinking of the epoxy matrix of the composite in the presence of silica particles. It should be noted that the values of T_g determined by the DMA method are 25 °C higher than from the TMA data (compare Tables 2 and 3). This can be explained by the fact that the TMA curves show the beginning of the glass transition process, while the DMA method reflects the losses in the entire glass transition area.

A decrease in the degree of crosslinking in epoxy-silica composites (samples 2 and 3) is also evidenced by a decrease in the values of $E'_{T=150\text{ °C}}$ (Table 3) since it

Fig. 4 Temperature dependences of mechanical losses ($\tan \delta$) of samples 1–4. Curve numbers correspond to sample numbers

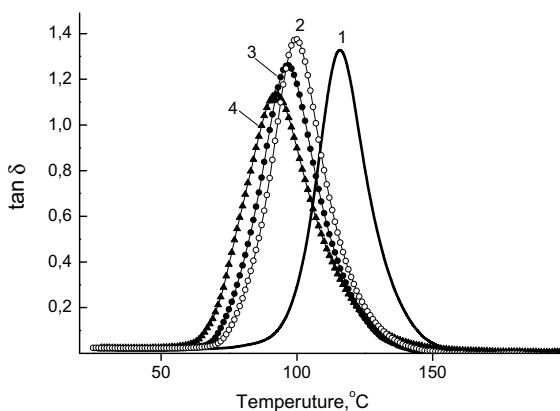


Fig. 5 Temperature dependences of the storage modulus (E') of samples 1–4. Curve numbers correspond to sample numbers

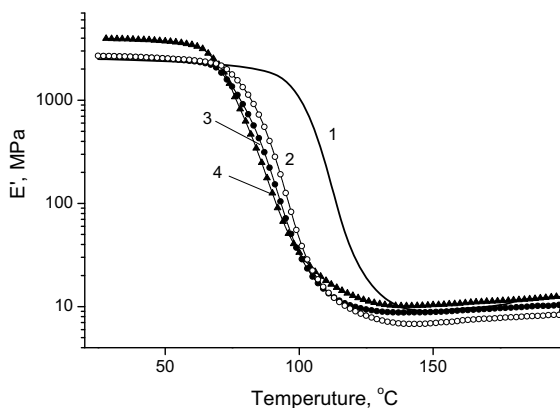


Table 3 Parameters of the viscoelastic characteristics of epoxy samples

Sample	T_g (°C)	$\tan \delta_{\max}$	$E'_{T=25\text{ °C}}$ (MPa)	$E'_{T=150\text{ °C}}$ (MPa)
1	115	1.33	2500	9.1
2	100	1.36	2690	6.9
3	96	1.24	2670	8.8
4	92	1.13	3960	10.4

is known that the value of the storage modulus in the region of the high elasticity directly correlates with the crosslink density for crosslinked polymers [10], which are epoxies. At the same time, the presence of 3 wt.% SiO_2 does not weaken the intermolecular interaction in the epoxy composite, which is indicated by the stability of the E' values in the glassy state (Fig. 5) for samples 2 and 3 (curves 2, 3) and the initial polymer (curve 1). It can be seen from Table 3 that the values of $E'_{T=25\text{ °C}}$ for composites with 1 and 3 wt.% SiO_2 (samples 2 and 3) are even slightly higher than the corresponding value for the initial polymer (sample 1).

It is shown that the addition of the antifriction filler MoS_2 (sample 4) together with the silica particles lowers the T_g of the epoxy composite insignificantly and leads to a decrease in the intensity of the glass transition (see Fig. 4). A decrease in $\tan \delta_{\max}$ for filled composites can be associated with a decrease in the polymer content in their composition. However, the additional introduction of MoS_2 by 1.5 times increases the value of E' of the composite at $T = 25\text{ °C}$ and significantly increases the value of the storage modulus even in the high elasticity region at $T = 150\text{ °C}$ (see Table 3) that may indicate an improvement of the physical interactions in the system. Thus, in the case of joint introduction of silica particles and molybdenum disulfide, the epoxy composite material acquires better physical and mechanical properties.

The revealed structural features also affect the deformation strength characteristics of the synthesized composites. It was found that the presence in the polymer matrix of SiO_2 particles synthesized by the sol–gel method, despite the plasticization effect,

Table 4 Influence of SiO₂ content on deformation strength characteristics and tensile strength of the adhesive joints of D16 aluminum alloy by the composites

Sample	E (GPa)	σ_f (MPa)	ε_b (%)	σ_t (MPa)
1	1.32	66	9.5	35
2	1.54	75	8.5	47
3	1.40	65	7.1	31

has a positive effect on the elastic modulus of composites in comparison with the unmodified epoxy polymer with a simultaneous tendency toward a decrease in the relative elongation of the sample (Table 4). For composites with a SiO₂ content of 1 wt.%, Young's modulus increases by 17% compared to the unmodified polymer, while the tensile strength increases by 14%. With an increase in the content of SiO₂ to 3 wt.%, there is a tendency to a decrease in the cohesive strength of the composite— σ_f decreases almost to the level of an unmodified epoxy polymer, at the same time, the elastic modulus, despite a certain decrease, is higher than for sample 1.

In addition to changing the cohesive strength of composites, an improvement in the adhesion characteristics of the material is also observed when the polymer matrix contains 1 wt.% SiO₂. It is shown that in the presence of silica particles containing a high amount of silanol groups on the surface, the tensile strength of the adhesive joints of D16 aluminum alloy by the composite increases by 35% with the cohesive failure mode. The authors of [12] observed a positive effect of the silica filler on the adhesive properties of composite coatings, explaining this by the formation of covalent Si–O–Al bonds between the surface of the aluminum substrate and the Si–OH groups of the organosilicon filler.

An increase in the content of silica particles to 3 wt.% results in a decrease in the strength of the adhesive joints of D16 aluminum alloy by the composites, which can be explained by a decrease in the cohesive strength of the sample due to the plasticization effect. At the same time, this effect of lowering the glass transition temperature usually helps to reduce brittleness, which is one of the disadvantages of highly crosslinked epoxy resins. Therefore, the observed plasticization effect in the presence of SiO₂ particles synthesized by the sol–gel method can positively affect the operational properties of the obtained composites, especially because of improved adhesion to metal surfaces and considering the possibility of modifying the system with molybdenum disulfide. Such a combination of components can provide a sufficient level of antifriction characteristics of a polymer nanocomposite coating, which can be promising for use in friction pairs.

4 Conclusions

The sol–gel method was used to obtain anhydride cured epoxy-silica nanocomposite with MoS₂ as an antifriction additive.

The data obtained by scanning electron microscopy indicate a homogeneous single-phase structure of the initial polymer. The introduction of the silica particles causes the formation of regions with a pronounced layered morphology, and the addition of MoS₂ leads to a decrease in the grain size of the matrix and the formation of a heterophase layered structure with a uniform distribution of phases. This significantly improves the mechanical properties of the nanocomposite.

The results of TMA and DMA methods indicate that the incorporation of 1–3 wt.% of silica particles leads to plasticization of the composite, which is expressed in a decrease in the glass transition temperature and a decrease in the effective crosslink density of the epoxy-anhydride matrix. At the same time, there is an increase in the tensile strength of the adhesive joints of the composite with D16 aluminum alloy by 35%, the tensile strength by 14%, and Young's modulus by 17%.

When MoS₂ is added to the specified composition with 3 wt.% of silica particles, the value of the highly elastic deformation of the composite decreases, the storage modulus increases, and the mechanical loss tangent decreases.

The developed antifriction nanocomposite is a promising coating for friction pairs.

References

1. Gao F (2012) *Advances in polymer nanocomposites: types and applications*. Woodhead Publishing, Cambridge, UK, p 651
2. Hassan T, Salam A, Khan A, Khan S, Khanzada H, Wasim M, Khan M, Kim I (2021) Functional nanocomposites and their potential applications: a review. *J Polym Res* 28(2). <https://doi.org/10.1007/s10965-021-02408-1>
3. Zou H, Wu S, Shen J (2008) Polymer/silica nanocomposites: preparation, characterization, properties, and applications. *Chem Rev* 108(9):3893–3957. <https://doi.org/10.1021/cr068035q>
4. Sanchez C, Julián B, Belleville P, Popall M (2005) Applications of hybrid organic–inorganic nanocomposites. *J Mat Chem* 15(35–36):3559. <https://doi.org/10.1039/B509097K>
5. Idumah C, Obele C (2021) Understanding interfacial influence on properties of polymer nanocomposites. *Surf Interf* 22:100879. <https://doi.org/10.1016/j.surfin.2020.100879>
6. Idumah C, Obele C, Emmanuel E, Hassan A (2020) Recently emerging nanotechnological advancements in polymer nanocomposite coatings for anti-corrosion, anti-fouling and self-healing. *Surf Interf* 21:100734. <https://doi.org/10.1016/j.surfin.2020.100734>
7. Teitelbaum BJ (1979) *Thermomechanical analysis of polymers*. Nauka, Moscow, p 236 [in Russian]
8. Rahman I, Padavettan V (2012) Synthesis of silica nanoparticles by sol-gel: size-dependent properties, surface modification, and applications in silica-polymer nanocomposites—a review. *J Nanomater* 2012:1–15. <https://doi.org/10.1155/2012/132424>
9. Lipatov YS (1995) *Polymer reinforcement*. Chemtec, Toronto, p 406
10. Nielsen LE, Landel RF (1994) *Mechanical properties of polymers and composites*, vol I. Dekker, New York, p 255
11. Menard K (2008) *Dynamic mechanical analysis*, p 218. <https://doi.org/10.1201/9781420053135>
12. Zheludkevich M, Salvado I, Ferreira M (2005) Sol-gel coatings for corrosion protection of metals. *J Mat Chem* 15(48):5099. <https://doi.org/10.1039/B419153F>

Advanced Carbon Nanomaterials and Their Composites for Removal of U(VI) Compounds from Aqueous Solutions (Review)



Yuliya Dzyazko, Olga Perlova, and Ivan Martovyi

Abstract This chapter is devoted to advanced carbon nanomaterials, such as graphene, nanotubes, and nanoribbons produced from them, for U(VI) removal from aqueous media. It is noted that the adsorption capacity of these materials is up to 100 mg dm^{-3} . Special approaches, such as oxidation and grafting organic fragments allow us to increase the capacity in several times. Carbon adsorbents possess high selectivity toward U(VI) compounds; they are not sensitive to ionic strength of a solution. This is due to U(VI) complexation with surface functional groups. However, adsorption is strongly affected by the solution pH: the highest removal degree is reached at $\text{pH} > 4\text{--}5$ due to the features of U(VI) speciation. In all cases, the rate-determining stage of adsorption is chemical reaction of pseudo-second order. It is stressed that the carbon nanomaterials are finely dispersive, this makes impossible their usage as a filler of ion exchange columns. In order to overcome this disadvantage, they are inserted into supports, such as inorganic ion-exchangers, synthetic or biopolymers, and even microorganisms. It is possible to obtain large granules by this manner. The carbon additions change morphology of a support providing high specific surface area, which is necessary for providing high adsorption capacity.

Keywords Carbon nanomaterials · Nanocomposites · Graphene · Nanotubes · Uranium(VI) · Adsorption

Y. Dzyazko

VI Vernadskii Institute of General and Inorganic Chemistry of the National Academy of Science of Ukraine, Kyiv, Ukraine

O. Perlova · I. Martovyi (✉)

Odessa II Mechnikov National University, Odessa, Ukraine

e-mail: ism_odesa@ukr.net

O. Perlova

e-mail: olga_perlova@onu.edu.ua

1 Introduction

Uranium content is about 3 ppb in the East crust [1] and ocean water [2]. This element is unevenly distributed in rocks. It is concentrated mainly in minerals, which contain a high amount of silicon, such as uraninite, carnotite, and torbernite. Some water sources contain heightened amount of uranium due to both its leaching from rocks and anthropogenic effect (working of nuclear power plants, mines, and mineral processing plants) [1]. Uranium also occurs in environment due to testing nuclear weapon, combustion of coal, and so on.

Since uranium is not only radioactive but also toxic, the maximal allowable concentration (MAC) of its soluble compounds is 15 ppb; smaller MAC values are also suggested [3]. Uranium and decay products attack all types of living cells causing organ pathologies, especially kidneys are poisoned. When uranium is accumulated in human organism, a risk of radiation sickness is enhanced. Thus, it is necessary to avoid the appearance of uranium in water sources, especially in drinking water. Among different methods, sorption technique is wide spread to remove small amounts of uranium from aqueous media.

Among a huge variety of inorganic and organic adsorbents of natural and synthetic origin, carbon materials are widely used for uranium removal, since they can be produced from cheap and available feedstock [4–6]. Moreover, activated carbon, particularly biochar, possesses considerable adsorption capacity, and resistance against acids and alkali. These materials can be easily utilized by means of combustion.

Recently, advanced carbon nanomaterials are in a focus of attention. Nanotubes, CNTs (single walled, SWCNTs, and multiwalled, MWCNTs) [7], and oxidized graphene (GO) [8] as well as graphene-like carbon nanomaterials occupy special position (Fig. 1). This is due to their hardness, ductility, light weight, and fast ion transport. Highly developed surface is attributed to them, this enhances adsorption. Both carbon nanotubes and GO can be easily modified. Moreover, GO initially contains considerable amount of $-\text{COOH}$ groups, which are able to exchange cation. The disadvantage of carbon nanomaterials is their fine dispersion. Thus, it is difficult to separate solid and liquid, especially in the case of purification of a large volume of water.

In order to overcome this disadvantage, carbon nanomaterials are included into composites, the base of which forms large granules. Earlier we applied this approach

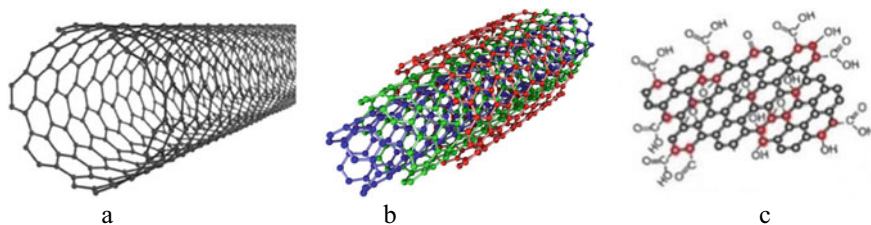


Fig. 1 Schematic images of SWCNT (a) MWCNT (b) and GO (c)

to partially unzipped MWCNTs and GO—they were inserted to hydrated zirconium dioxide (HZD) [9–11] and zirconium hydrophosphate (ZHP) [9, 10]. It should be mentioned that HZD and ZHP were also used as modifiers of ion exchange resins [12–15]: selectivity of composites towards U(VI) compounds is considered from the point of view of a change of porous structure of the polymer support [12, 15]. Moreover, formation of surface complexes of U(VI) is also taken into account similarly to d-metal ions like Ni^{2+} [16]. Hydrated oxides of multivalent metals are also applied to preparation of inorganic composites for U(VI) sorption [17–19] and also to modifying polymer and ceramic membranes of wide functional purpose [20–22].

Adsorption of uranium compounds strongly depends on their speciation in solutions, acidic-basic properties of polymer or inorganic support of carbon nanomaterials, and chemical composition of the surface of carbon nanomaterials. In this review, the effect of these factors on sorption is considered briefly.

2 U(VI) Speciation

The content of one or other form of U(VI) is affected by the solution composition. As an example, Fig. 2 illustrates the simplified diagrams for nitrate and sulfate solutions [17], which were calculated based on [23]. More complex diagrams are given in [24]. Regarding nitrate solutions, they contain mainly cations in acidic media. When $\text{pH} > 3$, UO_2^{2+} ions are transformed into $\text{UO}_2(\text{OH})^+$ species. Colloidal $\text{UO}_2(\text{OH})_2$ particles dominate in alkaline region. In the case of sulfate solutions, cationic, neutral, and anionic forms co-exist in acidic media; insoluble $\text{UO}_2(\text{OH})_2$ compound is formed in alkaline liquid.

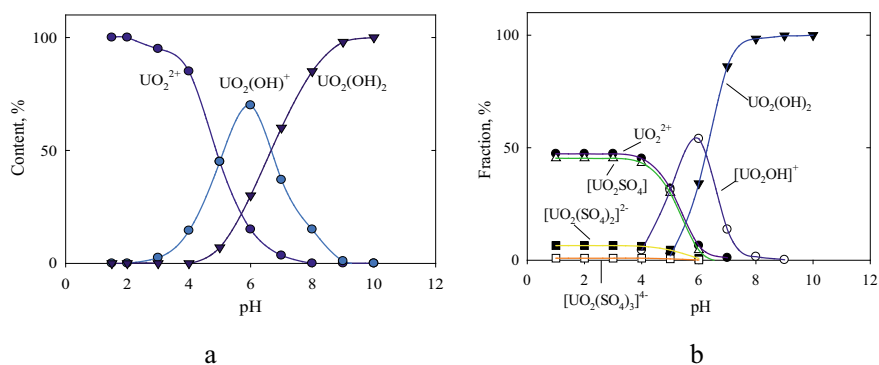


Fig. 2 U(VI) speciation in nitrate (a) and sulfate (b) solutions. Reproduced from [14] according to the permission of Springer Publisher

Speciation of U(VI) compounds strongly affects sorption behavior of carbon nano-materials and their composites. Besides U(VI) speciation, surface of carbon nano-materials plays a key role for adsorption. This information is summarized in a review [25].

3 Carbon Nanotubes

Nanotubes are related to an allotrope modification of carbon. They are empty cylinder, a diameter of which is within the interval of several angstroms to several tens nanometers. Their length is from micron to several centimeters. The cylinder walls are rolled graphene planes. CNTs are intertwined forming large bundles due to strong Van der Waals interactions (Fig. 3a, [26]).

The adsorption properties of non-modified CNTs are affected by their kinds (for instance, a number of walls), purity, pores, surface area, etc. CNTs contain different adsorption centers: inner and outside surface, grooves, interstitial channels, and contacts of nanotubes in bundles. As shown in the example of gas adsorption, the outer surface is occupied before the filling internal surface [27]. The information about the removal of toxic metal ions from water with participation of CNTs is summarized in [28, 29], the data about MWCNTs in nuclear waste management are given in [30].

Pristine MWCNTs contain phenolic, lactonic, and carboxyl groups, and their total amount is 0.8 mmol g^{-1} [31]. The presence of oxygen-containing functional groups on the surface of purchased CNTs is reported also in [32]. However, adsorption behavior of pristine nanotubes is different. The equilibrium time of U(VI) adsorption is reached during $\approx 2 \text{ min}$ [32] and 1 h [31] under similar conditions. This is caused by different content of functional groups, with which U(VI) forms surface complexes [33]. As a result, kinetic curves are approximated by the model of chemical reaction of pseudo-secondorder.

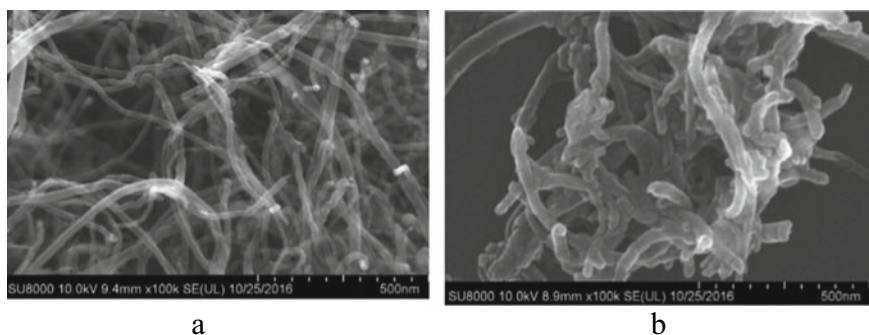


Fig. 3 SEM images of pristine MWCNTs (a) and MWCNTs (b) modified with amidoxime. Reproduced from [26] according to the permission of Elsevier Publisher

In order to enhance adsorption ability of CNTs, they are additionally oxidized with nitric acid [33–35] or plasma [36].

Different modifiers can be attached to the outer CNTs surface to provide adsorption ability towards toxic metal ions, particularly U(VI) compounds. For instance, MWCNTs modified with amidoxime were obtained by irradiation of the nanotubes followed by acrylonitrile grafting and its conversion into the adsorptive active component [26]. In general, modifying causes merging CNTs (see Fig. 3b). The models of Langmuir and chemical reaction of pseudo-second order were applied to U(VI) adsorption. The maximal capacity, which is realized at pH 3–5 (optimal conditions), is 68 mg g^{-1} . The equilibrium is reached during 60 min. It means, the adsorption rate is comparable with that for ion exchange resins and their composites [12–14], but slower comparing with ion exchange fibers [37]. In the last case, the equilibrium time is about several minutes.

SWCNTs surface can be treated with nitric acid, $-\text{COOH}$ groups are formed under these conditions [33]. Further, the nanotubes were modified with poly(amic-acid) by means of polymerization in-situ. The resulting material contained amide and carboxyl groups. Before the modifying with polymer, adsorption capacity toward U(VI) was 65 mg g^{-1} , the capacity was higher in three times after modifying. It remained practically the same after five cycles of adsorption–desorption. Adsorption of U(VI) in a presence of alkaline metal ions, hardness ions and also Mn^{2+} , Sr^{2+} , Ni^{2+} , Zn^{2+} , Sm^{2+} was investigated. The degree of U(VI) removal was 80% in the case of the modified SWCNHs. At the same time, no selectivity has been found for SWCNTs containing only $-\text{COOH}$ groups. It was suggested the complex formation between UO_2^{2+} on the one hand, amide and carboxyl groups on the other hand. The mechanism of U(VI) sorption on oxidized MWCNTs combines cation exchange and outer-sphere surface complexation in acidic media, precipitation occurs in neutral solutions [35]. Formation of complexes with amide groups is slower comparing with $-\text{COOH}$ groups [36]. The reaction rate is comparable with that for aminogroups [38]. As opposed to [33], the materials [36, 38] show faster adsorption rate, when the equilibrium time is 1 h and higher. The equilibrium time is about 5 min. The potential of zero charge (PZC) has been estimated as 4.4 (pristine MWCNTs) and 5 (oxidized MWCNTs).

Chitosan molecules were used for MWCNTs modifying by means of low temperature plasma method, which allows us a possibility to graft them to the surface [39]. As found, sorption of U(VI) on obtained materials is affected by the solution pH, but it is not influenced by ionic strength. Adsorption is accompanied by the formation of inner-sphere surface complexes: this mechanism dominates over ion exchange or outer-sphere complexation.

Functionalization of MWCNTs with fragments containing carbonyl, amino, and amidogroups was considered in [40]. Depending on the solution composition, the modified material shows maximal capacity at pH 7, or plateau in neutral and weakly alkaline media, where colloidal particles are formed. The equilibrium time is very short (5–10 min); this is comparable with the data of [37] for ion exchange fibers. The kinetic data are approximated by the model of chemical reaction of pseudo-second order: it means high rate of the complex formation.

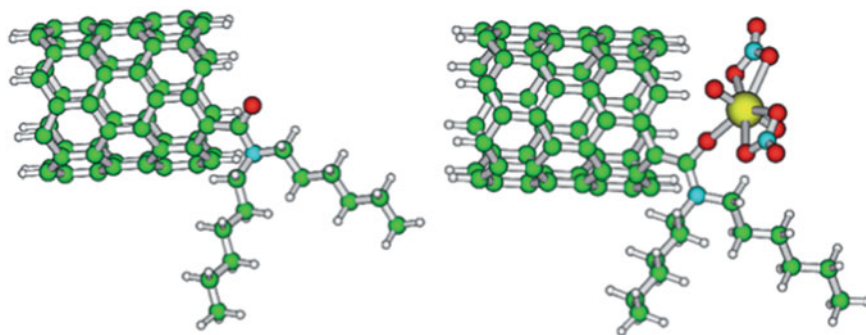


Fig. 4 Structure of UO_2^{2+} species adsorbed on MWCNTs modified with N,N-dihexyl amide [41]. Reproduced according to the permission of RSC Publisher

MWCNTs functionalized with N,N-dihexyl amide are considered in [41]. The capacity of 32 mg g^{-1} toward U(VI) has been found. The adsorbent possesses higher selectivity toward Th^{4+} comparing with U(VI). The structure of adsorbed UO_2^{2+} species has been proposed (Fig. 4).

Adsorption characteristics of MWCNTs are improved after impregnation with [2-(5-Bromo-2-pyridylazo)-5-(diethylamino)phenol] [42] or functionalization with dihydroimidazole [43]. Electronic and band structure of SWCNT with U atom at the outer surface were calculated by means of the density functional theory [44].

Since CNTs are finely dispersed, they cannot be related to perspective adsorbents. However, they can be used as an active component for composite preparation. This will be considered further.

4 Composites with CNTs

The composites including CNTs and magnetic nanoparticles are in a focus of attention, since magnets provide separation of finely dispersed carbon nanomaterials from liquid. The polyphosphazene-based composite containing CNTs and Fe_3O_4 nanoparticles (Fig. 5) was obtained and applied to U(VI) removal from aqueous solutions [45]. In this case, adsorption capacity is much higher comparing with that for pure CNTs. The maximal value, which was estimated from the Langmuir isotherm, reaches 606 mg g^{-1} . The capacity of 20 mg g^{-1} has been found for CNTs. As opposed to CNTs, pH 5 corresponds to maximal adsorption.

When the initial concentration of U(VI) is 100 mg dm^{-3} , no sufficient effect of NaCl on adsorption has been found (the concentration of this electrolyte was $0.1\text{--}0.5 \text{ mol dm}^{-3}$). If the solution contains ions of d- and f-metals. U(VI) compounds are sorbed preferably. Adsorption on the composite is expectedly faster comparing with CNTs. The adsorbent can be regenerated with HNO_3 solutions. In order to reach the desorption degree of 90% and higher, the solution concentration has to be

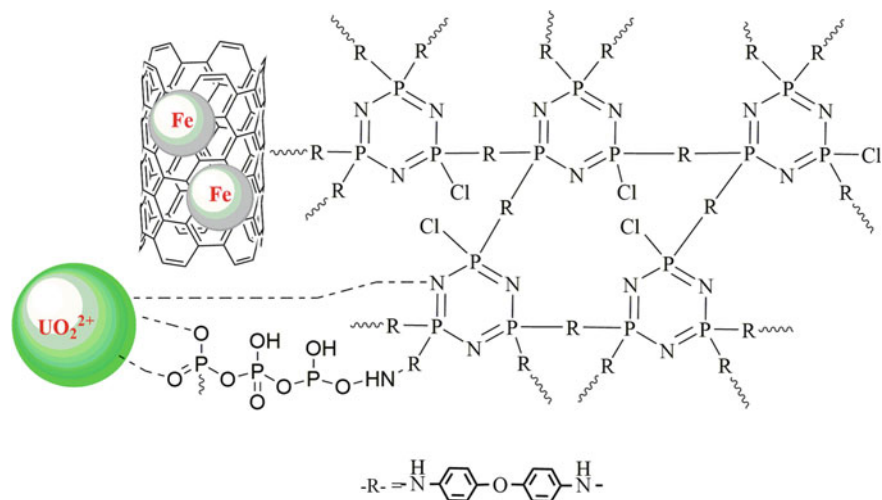


Fig. 5 Interaction of uranyl-ions with polyphosphazene, to which CNTs containing magnetic nanoparticles are incorporated [45]. Reproduced according to the permission of ACS Publisher

0.3–0.5 mol dm⁻³. From cycle to cycle of adsorption–desorption, the capacity of the composite decreased: its loss was ≈12%. Moreover, magnetic nanoparticles are dissolved during the treatment with acid. Their positive effect is providing convenient separation of solid and liquid.

The adsorbent of similar composition was obtained in [46]. However, aminogroups were inserted into polyphosphazene. The pH of PZC is 3.5, the maximal adsorption capacity is at pH 4–5. The capacity obtained from the Langmuir isotherm is 250 mg g⁻¹. This is lower comparing with the value of [45], In the case of [45, 46], the time of equilibrium state is 80 min, U(VI) complexation with phosphate [45] and aminogroups [46] is suggested.

Magnetic composite based on MWCNTs were synthesized [47]. Preliminarily the carbon nanomaterial was oxidized with H₂SO₄ and modified with polyethylenimine. Magnetic nanoparticles (up to 20 nm) are seen in TEM image as dark spots (Fig. 6).

As opposed to [45], the maximal adsorption capacity (450 mg g⁻¹) is achieved at pH 6 [47]. At pH 2–3, the capacity is up to 50 mg g⁻¹, further fast growth is observed. After pH 6, the capacity decreases down to 350 mg g⁻¹. The pH of PZC is 6.2, and the equilibrium state is reached during 15 min. Increasing the temperature from 20 to 40 °C depresses adsorption evidently due to enhancement of U(VI) hydrolysis and transformation of ions into insoluble colloidal particles. The composite is more easily regenerated than that described in [45]: the concentration of nitric acid is only 0.01 mol dm⁻³.

The rod-like dual-shell composite consisting of polypyrrole, cobalt ferrite and MWCNTs has been reported in [48]. The material was synthesized with a hydrothermal method. In fact, MWCNTs are encapsulated into the polymer shell, there are magnetic nanoparticles on its surface. As found, the highest adsorption

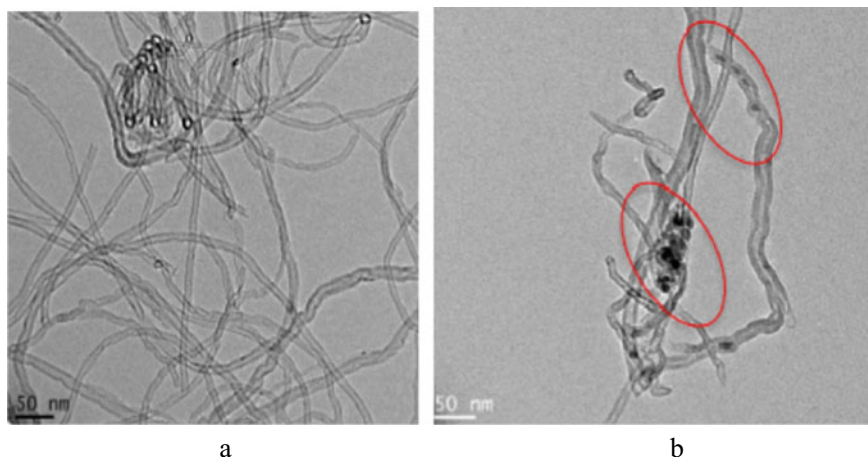


Fig. 6 TEM images of pristine MWCNTs (**a**) and composite based on MWCNTs modified with polyethyleneimine containing magnetic nanoparticles (**b**) [47]. Reproduced according to the permission of Elsevier Publisher

capacity is realized at pH 7 ($\approx 150 \text{ mg g}^{-1}$). It is suggested that U(VI) ions are attracted by π -electrons densities of the graphene structure. Other way is the $\text{UO}_2^{2+} \rightarrow \text{H}^+$ exchange, since MWCNTs are weak acceptors of protons. Electrostatic attraction of U(VI) and CoFe_2O_4 is also suggested. At last, surface complexation of U(VI) with nitrogen of polypyrrole is considered.

The composites of CNTs with polyvinylalcohol [49] and $\text{Cu}_2\text{O}-\text{CuO}$ [50] are reported. They are used both for U(VI) removal from water [49] and its analytical determination [50].

5 Unzipped CNTs

Among advance carbon nanomaterials, unzipped CNTs occupy special position. Graphene nanoribbons are graphene sheets with a width of tens nanometers [51] (Fig. 7). Their length corresponds to that for nanotubes. The nanoribbons can be related to the quasi one-dimensional CNTs, they derive functional properties from both CNTs and graphene. Chemical and electrochemical synthesis methods provide oxygen-containing functional groups on the surface of nanoribbons [52]. Three-dimensional aerogel consisting of graphene nanoribbons for uranium (VI) removal from water is reported in [53].

The nanoribbons were used for U(VI) adsorption [51]. As opposed to MWCNTs, which demonstrate considerable adsorption capacity only at the pH interval of 6–10 (maximal capacity is 90 mg g^{-1}), nanoribbons show wider pH diapason, where their adsorption ability is sufficient. For different samples, the capacity reaches 5–40

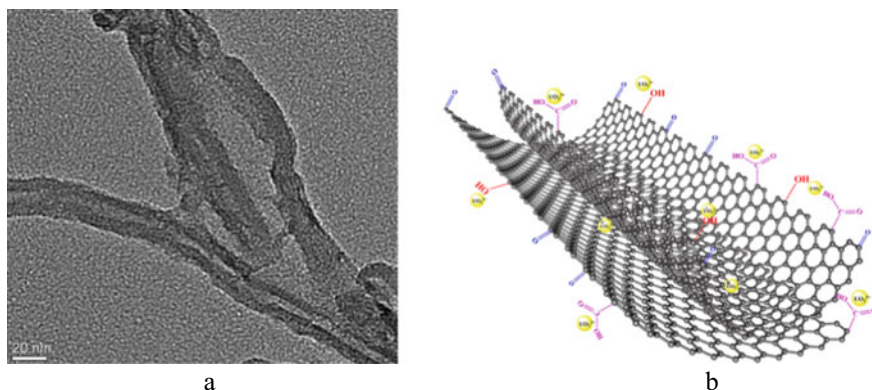


Fig. 7 TEM image (a) and scheme of unzipped nanotubes, which contain functional groups (b) [51]. These groups provide U(VI) adsorption. Reproduced according to the permission of Elsevier Publisher

(pH 2), 30–95 (pH 3), and 45–130 (pH 4) mg g^{-1} , when the initial concentration is 60 mg dm^{-3} . This value depends on the amount of functional groups. Further, no sufficient change of the capacity is observed. Based on isotherms, the maximal capacity is 430 mg g^{-1} .

The HZD- and ZHP-based composites containing partially unzipped MWCNTs were obtained in [9, 10]. Increase of their content in the composites results in a decrease of granule size. The optimal amount of the modifier is 2%; rather large granules (0.3–0.35 mm) are formed under these conditions. The carbon additions expand the pH interval, where adsorption capacity is sufficient. The unzipped MWCNTs increase sorption capacity of HZD at pH 3–4. Regarding ZHP, the addition is effective at pH 5–7. As found, the isotherms are modeled by Dubinin-Radushkevich equation indicating micropores, a size of which is comparable with uranyl ions. Different amount of carbon additions was inserted into inorganic matrixes. The ZHP-based composite removes U(VI) from aqueous media completely, when water contains hardness ions. In this case, the model of chemical reaction of the first order can be applied. When one-component solution is investigated, the model of pseudo-second order is the most suitable. The regeneration degree reaches 92%, when HNO_3 solution is used.

6 Oxidized Graphene

The possibility to use GO for U(VI) removal from water is intensively investigated. GO is attractive due to its thermal and radiation stability, a large content of functional groups, which are able to ion exchange. Highly developed porosity and large specific surface area are also attributed to GO, it should be noted that the value of

specific surface area, which is determined with a method of adsorption–desorption of nitrogen, is from 560 [54] to 900 [55] m^2g^{-1} , even lower values were obtained for partially unzipped MWCNTs ($230 \text{ m}^2\text{g}^{-1}$). This is much lower than the theoretical magnitude for the isolated graphene flakes ($\approx 2600 \text{ m}^2\text{g}^{-1}$ [56]). This discrepancy is due to overlapping, curling, and agglomeration of the flakes. As a result, a part of the surface is unavailable for N_2 molecules. The method of standard contact porosimetry gives $2000\text{--}2400 \text{ m}^2\text{g}^{-1}$, when water is used as a working liquid [57]. Disjoining pressure provides the liquid penetration between graphene flakes. For comparison, the values of 550 and $325 \text{ m}^2\text{g}^{-1}$ were obtained for SWCNTs and MWCNTs, respectively. The developed surface as well as functional groups provide excellent adsorption performance of GO.

Three methods of GO preparation from commercial exfoliated graphite were performed: chemical oxidation (Hummers method), electrolysis, and ball milling [58] (the techniques of preparation of GO-like materials from the feedstock of biological origin are given in [59]). Analysis of XRD patterns allows us to conclude that chemical treatment provides the most complete exfoliation and isolation of GO flakes. The peak at 10.2° corresponds to the interlayer distance of 0.87 nm. In the case of GO obtained by ball milling or electrolysis, the reflex at 22.5° indicates the distance of 0.4 nm. The compactness of structure decreases within the order: pristine carbon material > sample obtained by ball milling > sample obtained electrochemically > sample obtained by chemical oxidation (Fig. 8). Disordering structure is confirmed by Raman spectroscopy. XPS spectroscopy shows carbonyl, carboxyl and C – O groups for the chemically oxidized sample. Only C – O groups have been found for other GO samples.

For three samples, the equilibrium state for U(VI) adsorption is reached after 120 min. However, the highest adsorption capacity (about 250 mg g^{-1}) has been found for the sample obtained by chemical oxidation. Other samples show lower values ($\approx 70\text{--}80 \text{ mg g}^{-1}$). Slightly smaller value ($\approx 50 \text{ mg g}^{-1}$) has been found for reduced GO (rGO) [60], similar magnitude has been reported for sulfonated GO [61]. However, the value of 300 mg g^{-1} was suggested for GO obtained with Hummers method, the capacity for rGO is about 50 mg g^{-1} . Much lower capacity is attributed to GO doped with Fe and Ni (25 mg g^{-1}) [62]. All the data [58–63] were calculated from the Langmuir isotherms.

As found, adsorption curves for GO samples obtained with different methods obey the model of pseudo-second order [58]. The constant rate of the chemically obtained sample is lower in ten times comparing with other materials. It means, high oxidation degree, which is achieved by chemical oxidation, provides considerable U(VI) adsorption. However, adsorption is slower comparing with other samples due to the interaction of ions with the surface oxygen-containing groups. Unfortunately, no data about specific surface area are given in [58].

In order to improve adsorption properties of GO, it is modified with functional groups similarly to CNTs. For instance, aminogroups were grafted to the GO surface [64]. The adsorption capacity of GO and GO-NH₂ was found to be 97 and 215 mg g^{-1} , respectively, under ambient temperature. Functionalized adsorbent shows higher capacity than the pristine sample at pH 4.5–6.5. No sufficient improvement of

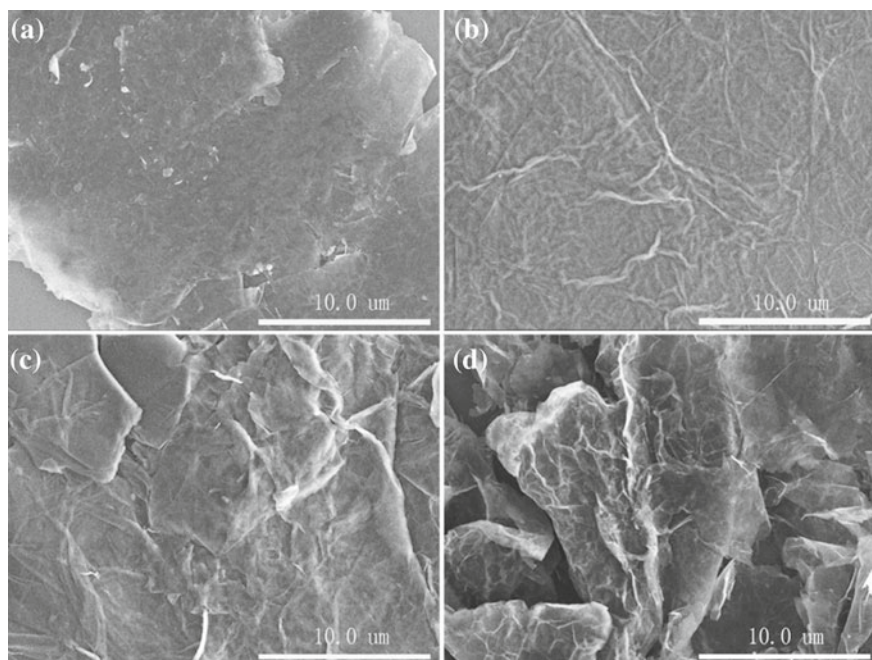


Fig. 8 SEM images of the pristine carbon material (evidently exfoliated graphite) (a) and samples obtained by ball milling (b), electrochemical (c) and chemical (d) oxidation [58]. Reproduced according to the permission of Springer Publisher

adsorption is observed outside this pH interval. The rate constant of adsorption is lower in ≈ 10 times for the modified GO. Functionalized adsorbent can be regenerated with a 0.5 M HCl solution. The loss of capacity is 10% after 3 cycles of adsorption–desorption. No effect of ionic strength (NaCl) on adsorption has been found.

More complex modifier, such as diethylenetriaminepentaacetic phenylenediamine, has been proposed in order to increase the GO capacity [65]. In this case, adsorption capacity of GO reaches about 500 mg g^{-1} . At the same time, the constant of adsorption rate is two orders less.

It is noted that π -conjugation system makes difficult the techniques for GO modifying [66]. A novel strategy has been proposed through post-decoration with amidoxime functionalized diaminomaleonitrile. This approach allows one to activate the inert sites in GO flakes. Adsorption capacity toward U(VI) reaches 935 mg g^{-1} , no sufficient change of this value is observed at pH 6–10. Unexpected result has been obtained: the time of the adsorption equilibrium is one third of that for GO. Preferable adsorption of U(VI) is realized, when the solution contains alkaline, alkaline earth, and d-metal ions.

Amidoxime-functionalized β -cyclodextrin/GO aerogel was synthesized in [67] using hydrothermal procedure (Fig. 9). The resulting material possesses higher

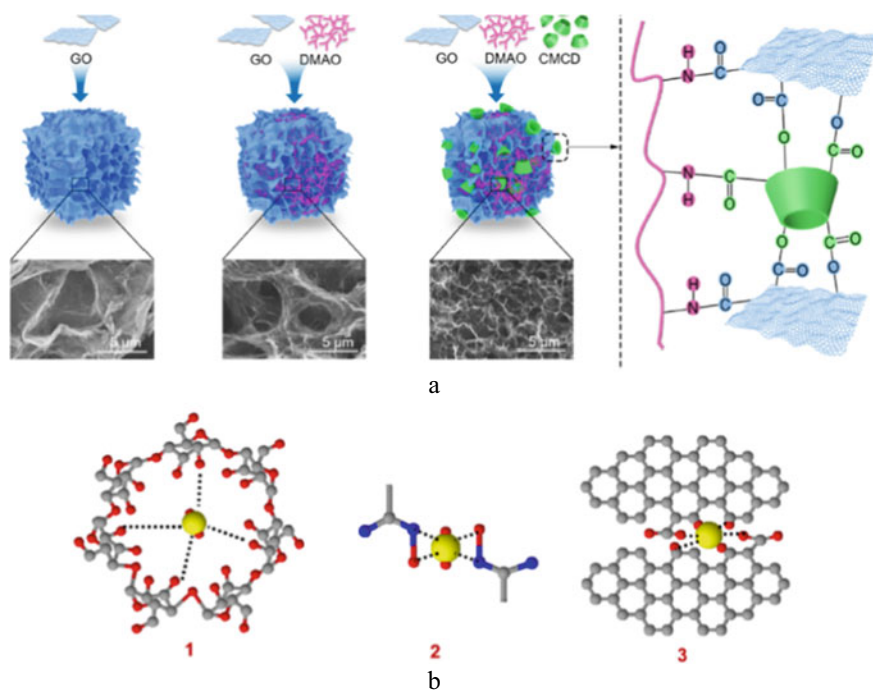


Fig. 9 Change of GO morphology during GO modifying and scheme of the resulting aerogel (a), mechanism of U(VI) adsorption [67]. Here, DMAO—amidoxime-functionalized diaminomaleonitrile, CMCD—carboxymethyl- β -cyclodextrin. Reproduced according to the permission of ACS Publisher

porosity caused by the cross-linkage of GO flakes. At the same time, β -cyclodextrin increases the interlayer spacing avoiding overlapping by $\pi - \pi$ stacking interactions. This also leads to loosening GO structure.

U(VI) adsorption reaches equilibrium after 60 min, the maximal adsorption capacity evaluated from Langmuir isotherms is 650 mg g^{-1} . The aerogel shows excellent adsorption performance in a presence of competitive cations, anions, and organic substances (oil). The capacity reaches 19.7 mg g^{-1} after 21 days of the aerogel exposition in 50 dm^3 of natural seawater. Cyclodextrine-modified GO was also used for the removal of both U(VI) and humic acids from water [68].

Aside from surface modifying, other approach was used—GO aerogel was impregnated with Tri-*n*-butyl phosphate (TBP)/*n*-dodecan [69]. Higher adsorption capacity (316 mg g^{-1}) has been reported comparing with [58–63]. The disadvantage of the impregnation technique is a leakage of solvent.

Besides U(VI), adsorption of compounds containing uranium of other valency, for instance, UC2, is considered [70].

It should be stressed that despite excellent adsorption performance, practical application of GO (except probably aerogel) is limited due to its fine dispersion. In order

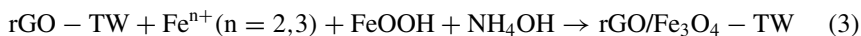
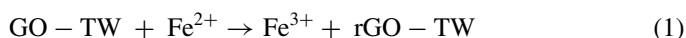
to overcome this difficultness, GO-containing composites are synthesized. This will be considered further.

7 Composites Containing GO

Last ten years, GO is in a focus of attention as a material for composite preparation. This addition provides high specific surface area of the support and, as a result, considerable adsorption capacity. The support forms large granules. It means, the composite can be used as a filler of ion exchange columns. It should be stressed that carbon additions lead to a decrease of granule size, when inorganic matrix is used [9, 71]. It means large content of GO is undesirable from the technological point of view.

As shown in the example of HZD, GO makes its structure less compact at nano- and microlevel, since GO flakes cover HZD particles [72] preventing their cross-linkage, deteriorating mechanical properties of granules and decreasing their size. GO possesses superhydrophilic properties similarly to ion exchange polymers, i.e., its porosity in water is higher than that in octane (ideally wetting liquid) [57]. Similar property is attributed to the HZD-GO composite [72]. Since GO contains only cation exchange groups, it enhances adsorption of cations on composites and depresses anion exchange.

In order to facilitate separation of solid from liquid, magnetic GO-containing composites were synthesized [73–76]. For instance, tea wastes (TW) were used as a support of rGO [76]. Following reaction occurred during the composite preparation:



The maximal value of adsorption capacity is realized at pH 5, the equilibrium time is about 60 min. Adsorption capacity, which was estimated from the Langmuir isotherms, is ≈ 90 (TW), 80 (GO), and 110 (GO-TW) mg g^{-1} . In other words, synergetic effect is observed. Reduction of GO causes a decrease of the capacity down to 100 mg g^{-1} . Despite lower capacity comparing with GO (see above) the composite is attractive, since it requires not so much GO, the support is low cost and cheap. At last, the adsorbent can be easily removed from liquid. Similar capacity magnitude has been obtained for the composite based on MnO_2 containing Fe_3O_4 and rGO ($\approx 90 \text{ mg g}^{-1}$ under ambient temperature) [73]. In this case, the equilibrium is achieved after 6 h. As opposite to the materials containing rGO, the capacity of GO-containing adsorbent based on ferberite (FeWO_4) is much higher (455 mg g^{-1}) [74].

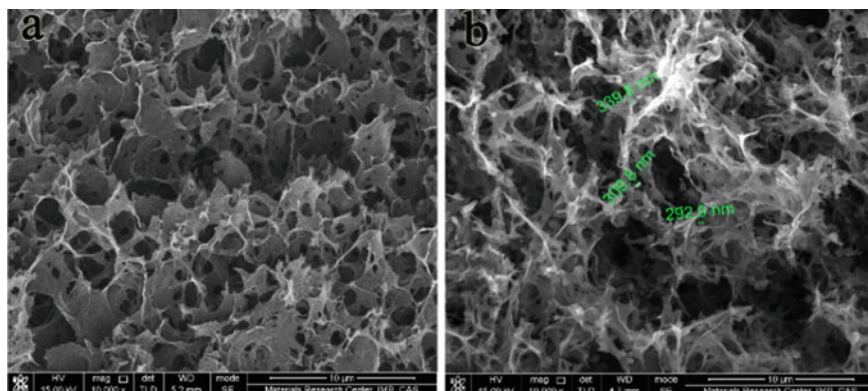


Fig. 10 SEM images of GO and the composite including Change of GO morphology during GO modifying and scheme of the resulting aerogel (a), amidoximated polyacrylonitrile [77]. Reproduced according to the permission of Elsevier Publisher

Synthetic polymers are also used as a support. For instance, the composite based on amidoximated polyacrylonitrile containing GO was obtained [77]. As shown in Fig. 10, GO flakes are transformed into dendrites after modifying. The maximal capacity of the composite towards U(VI) is about 200 mg g^{-1} .

Besides synthetic inorganic compounds and organic polymers, such natural materials as clay mineral [78], biopolymers [79–81] and even microorganisms [82] are considered as a support of graphene. The composites of graphene with these materials are effective adsorbents of U(VI) compounds.

8 Conclusions

This chapter is devoted to advanced carbon nanomaterials, such as graphene, nanotubes, and nanoribbons produced from them, for U(VI) removal from aqueous media. It is noted that the adsorption capacity of these materials is up to 100 mg dm^{-3} . Special approaches, such as oxidation and grafting organic fragments allow us to increase the capacity in several times. Carbon adsorbents possess high selectivity toward U(VI) compounds; they are not sensitive to ionic strength of a solution. This is due to U(VI) complexation with surface functional groups. However, adsorption is strongly affected by the solution pH: the highest removal degree is reached at $\text{pH} > 4\text{--}5$ due to the features of U(VI) speciation. In all cases, the rate-determining stage of adsorption is chemical reaction of pseudo-second order. It is stressed that the carbon nanomaterials are finely dispersive, this makes impossible their usage as a filler of ion exchange columns. In order to overcome this disadvantage, they are inserted into supports, such as inorganic ion-exchangers, synthetic or biopolymers and even microorganisms. It is possible to obtain large granules by this manner. The

carbon additions change morphology of a support providing high specific surface area, which is necessary for providing high adsorption capacity.

Further development of sorbents containing advanced carbon nanomaterials, which are selective toward U(VI) compounds, is a choice of suitable support. The support should possess a complex of needed functional properties: high adsorption capacity, selectivity, chemical stability as well as ability to form large durable granules. The synergetic effect is expected, when carbon nanomaterials would be inserted into such support.

References

1. Harmsen K, Haan FAM (1980) Occurrence and behaviour of uranium and thorium in soil and water. *Water Res* 14(1):40–62
2. Ku TL, Mathieu GG, Knauss KG (1977) Uranium in open ocean: concentration and isotopic composition. *Deep Sea Res* 24(11):1005–1017
3. Brine W (2010) The toxicity of depleted uranium. *Int J Environ Res Public Health* 7:303–313
4. Liao J, Ding L, Zhang Y et al (2022) Efficient removal of uranium from wastewater using pig manure biochar: understanding adsorption and binding mechanisms. *J Hazard Mater* 423(B):127190
5. Ahmed W, Mehmood S, Qaswar M et al (2022) Oxidized biochar obtained from rice straw as adsorbent to remove uranium(VI) from aqueous solutions. *J Environ Chem Eng* 9(2):105104
6. Guilhen SN, Rovani S, Araujo LG (2021) Uranium removal from aqueous solution using macauba endocarp-derived biochar: effect of physical activation. *Environ Pollut* 272:116022
7. Thostenson ET, Ren Z, Chou TW (2001) Advances in the science and technology of carbon nanotubes and their composites: a review. *Compos Sci Technol* 61(13):1899–1912
8. Chen D, Feng H, Li J (2012) Graphene Oxide: preparation, functionalization, and electrochemical applications. *Chem Rev* 112(11):6027–6053
9. Perlova OV, Dzyazko YS, Palchik AV et al (2020) Composites based on zirconium dioxide and zirconium hydrophosphate containing graphene-like additions for removal of U(VI) compounds from water. *Appl Nanosci* 10:4591–4602
10. Perlova OV, Ivanova IS, Dzyazko YS et al (2021) Sorption of U(VI) compounds on inorganic composites containing partially unzipped multiwalled carbon nanotubes. *Him Fiz Tehnol Poverhni* 12(1):16–31
11. Myronchuk VG, Zmievskii YG, Dzyazko YS et al (2019) Electrolytic whey demineralization involving polymer-inorganic membranes, anion exchange resin and graphene-containing composite. *Acta Periodica Technologica* 50:163–171
12. Dzyazko YS, Perlova OV, Perlova NA et al (2017) Composite cation-exchange resins containing zirconium hydrophosphate for purification of water from U(VI) cations. *Desalin Water Treat* 69:142–152
13. Perlova NA, Dzyazko YS, Perlova OV et al (2017) Formation of zirconium hydrophosphate nanoparticles and their effect on sorption of uranyl cations. *Nanoscale Res Lett* 12:209
14. Perlova OV, Dzyazko YS, Halutska IY et al (2018) Anion exchange resin modified with nanoparticles of hydrated zirconium dioxide for sorption of soluble U(VI) compounds. *Springer Proc Phys* 210:3–15
15. Dzyazko YS, Volfkovich YM, Perlova OV et al (2019) Effect of porosity on ion transport through polymers and polymer-based composites containing inorganic nanoparticles (review). *Springer Proc Phys* 222:235–253
16. Dzyazko YS, Trachevskii VV, Rozhdestvenskaya LM et al (2013) Interaction of sorbed Ni(II) ions with amorphous zirconium hydrogen phosphate. *Russ J Phys Chem* 87(5):840–845

17. Perlova OV, Dzyazko YS, Palchik AV et al (2021) Hydrated titanium dioxide modified with potassium cobalt hexacyanoferrate(II) for sorption of cationic and anionic complexes of uranium(VI). *Appl Nanosci.* <https://doi.org/10.1007/s13204-021-01721-x>
18. Yaroshenko NA, Sazonova VF, Perlova OV et al (2012) Sorption of uranium compounds by zirconium-silica nanosorbents. *Russ J Appl Chem* 85(6):849–855
19. Perlova OV, Sazonova VF, Yaroshenko NA et al (2014) Kinetics of sorption of uranium(VI) compounds with zirconium-silica nanosorbents. *Russ J Phys Chem A* 88(6):1012–1016
20. Dzyazko YS, Rozhdestvenska LM, Vasilyuk SL et al (2017) Composite membranes containing nanoparticles of inorganic ion exchangers for electro dialytic desalination of glycerol. *Nanoscale Res Lett* 12(1):438
21. Dzyazko Y, Rozhdestveskaya L, Zmievskaia Y et al (2019) Composite inorganic anion exchange membrane for electro dialytic desalination of milky whey. *Mater Today Proc* 6(2):250–259
22. Myronchuk VG, Dzyazko YS, Zmievskaia YG et al (2016) Organic-inorganic membranes for filtration of corn distillery. *Acta Periodica Technologica* 47:153–165
23. Nazarenko VA, Antonovich VP, Nevskaya EM (1979) Hydrolysis of metal ions in diluted solutions. Atomizdat, Moscow [in Russian]
24. Gapel G, Cormelis R, Caruso JA et al (2005) Handbook of elemental speciation II. Species in the environment, food, medicine and occupational health. Wiley, Chichester
25. Guo H, Mei P, Xiao J et al (2021) Carbon materials for extraction of uranium from seawater. *Chemosphere* 278:130411
26. Wu J, Tian K, Wang J (2018) Adsorption of uranium(VI) by amidoxime modified multiwalled carbon nanotubes. *Progr Nucl Energy* 106:79–86
27. Fujiwara A, Ishii K, Suematsu H et al (2001) Gas adsorption in the inside and outside of single-walled carbon nanotubes. *Chem Phys Lett* 336(3):205–211
28. Ouni L, Ramazani A, Fardood ST (2019) An overview of carbon nanotubes role in heavy metals removal from wastewater. *Front Chem Sci Eng* 13:274–295
29. Yu J-G, Zhao X-H, Yu L-Y et al (2014) Removal, recovery and enrichment of metals from aqueous solutions using carbon nanotubes. *J Radioanal Nucl Chem* 299:1155–1163
30. Sengupta A, Gupta NK (2017) MWCNTs based sorbents for nuclear waste management: a review. *J Environ Chem Eng* 5:5099–5114
31. Fafous II, Dawoud JN (2012) Uranium(VI) sorption by multiwalled carbon nanotubes from aqueous solution. *Appl Surf Sci* 259:433–440
32. Yu J, Wang J (2016) Removal of uranium from aqueous solution by carbon nanotubes. *Health Phys* 111:367–373
33. Jin T, Huang B, Huang J et al (2021) A novel poly (amic-acid) modified single-walled carbon nanohorns adsorbent for efficient removal of uranium(VI) from aqueous solutions and DFT study. *Colloids Surf A Physicochem Eng Aspects* 631:127747
34. Wang M, Qiu J, Tao X et al (2011) Effect of pH and ionic strength on U(IV) sorption to oxidized multiwalled carbon nanotubes. *J Radioanal Nucl Chem* 288:895–901
35. Sun Y, Yang S, Sheng G et al (2012) The removal of U(VI) from aqueous solution by oxidized multiwalled carbon nanotubes. *J Environ Radioact* 105:40–47
36. Song M, Wang Q, Meng Y (2012) Removal of UO_2^{2+} from aqueous solution by plasma functionalized MWCNTs. *J Radioanal Nucl Chem* 293:899–906
37. Sazonova VF, Perlova OV, Polikarpov AP (2017) Sorption of uranium(VI) compounds on fibrous anion exchanger surface from aqueous solutions. *Colloid J* 79:270–277
38. Alijani H, Beyki MH, Mirzababaei SN (2015) Adsorption of UO_2^{2+} ions from aqueous solution using amine functionalized MWCNT: kinetic, thermodynamic and isotherm study. *J Radioanal Nucl Chem* 306:165–173
39. Chen J-H, Lu D-Q, Chen B, OuYang P-K (2013) Removal of U(VI) from aqueous solutions by using MWCNTs and chitosan modified MWCNTs. *J Radioanal Nucl Chem* 295:2233–2241
40. Singh Deb AK, Pahan S, Dasgupta K et al (2018) Carbon nanotubes functionalized with novel functional group- amido-amine for sorption of actinides. *J Hazard Mater* 345:63–75
41. Sengupta A, Jayabun S, Boda A, Ali SM (2016) An amide functionalized task specific carbon nanotube for the sorption of tetra and hexa valent actinides: experimental and theoretical insight. *RSC Adv* 6:39553

42. Khamirchi R, Hosseini-Bandegharai A, Alahabadi A et al (2018) Adsorption property of Br-PADAP-impregnated multiwall carbon nanotubes towards uranium and its performance in the selective separation and determination of uranium in different environmental samples. *Ecotoxicol Environ Saf* 150:136–143
43. Tian K, Wu J, Wang J (2018) Adsorptive extraction of uranium(VI) from seawater using dihydroimidazole functionalized multiwalled carbon nanotubes. *Radiochim Acta* 106:719–731
44. Xie J-C, Tang Y-J, Zhang H (2011) A DFT study on the interaction between europium, uranium and SWCNT. *Cent Eur J Phys* 9:716–721
45. Liu Y, Zhao Z, Yuan D et al (2018) Fast and high amount of U(VI) uptake by functional magnetic CNT with phosphate group. *Ind Eng Chem Res* 57(43):14551–14560
46. Liu Y, Zhao Z, Yuan D et al (2019) Introduction of amino groups into polyphosphazene framework supported on CNT and coated Fe₃O₄ nanoparticles for enhanced selective U(VI) adsorption. *Appl Surf Sci* 466:893–902
47. Aljarrah MT, Al-harashsheh MS, Alrebaki MA et al (2020) Concentrative isolation of uranium traces in aqueous solutions via resurfaced-magnetic carbon nanotube suspension. *J Environ Manag* 271:110970
48. Liu Q, Zhu J, Tan L et al (2016) Polypyrrole/cobalt ferrite/multiwalled carbon nanotubes as an adsorbent for the removal of uranium ions from aqueous solutions. *Dalton Trans* 45(22):9166–9173
49. Abdeen Z, Akl ZF (2015) Uranium(VI) adsorption from aqueous solutions using poly (vinyl alcohol)/ carbon nanotube composites. *RSC Adv* 5(91):74220–74229
50. Aydin F, Yilmaz E, Olmez E (2020) Cu₂O-CuO ball like/multiwalled carbon nanotube hybrid for fast and effective ultrasound-assisted solid phase extraction of uranium at ultra-trace level prior to ICP-MS detection. *Talanta* 207:120295
51. Wang Y, Liu Y, Hu X et al (2021) Rational structure design for enhanced uranium(VI) capture and beyond: from carbon nanotubes to graphene oxide nanoribbons. *J Mol Liq* 323:114639
52. Danilov MO, Rusetskii IA, Slobodyanyuk IA et al (2016) Synthesis, properties, and application of graphene-based materials obtained from carbon nanotubes and acetylene black. *Ukr J Phys* 7(1):3–11
53. Li Y, He H, Liu Z et al (2021) A facile method for preparing three dimensional graphene nanoribbons aerogel for uranium(VI) and thorium(IV) adsorption. *J Radioanal Nucl Chem* 328:289–298
54. Seresht RJ, Jahanshahi M, Rashidi A et al (2013) Synthesize and characterization of graphene nanosheets with high surface area and nano-porous structure. *Appl Surf Sci* 276:672–681
55. McAllister MJ, Li JL, Adamson DH et al (2007) Single sheet functionalized graphene by oxidation and thermal expansion of graphite. *Chem Mater* 19(18):4396–4404
56. Dreyer DR, Park S, Bielawski CW et al (2010) The chemistry of graphene oxide. *Chem Soc Rev* 39(1):228–240
57. Volfkovich YM, Rychagov AY, Sosenkin VE et al (2014) Measuring the specific surface area of carbon nanomaterials by different methods. *Russ J Electrochem* 50(11):1099–1101
58. Wang Z, Wang Y, Liao J et al (2016) Improving the adsorption ability of graphene sheets to uranium through chemical oxidation, electrolysis and ball-milling. *J Radioanal Nucl Chem* 308:1095–1102
59. Dzyazko YS, Ogenko VM (2021) Polysaccharides: an efficient tool for fabrication of carbon nanomaterials. In: Inamuddin, Ahamed MI, Boddula R, Altalhi T (eds) *Polysaccharides: properties and applications*. Wiley, Hoboken, pp 337–366
60. He Y-R, Li S-C, Li X-L et al (2018) Graphene (rGO) hydrogel: a promising material for facile removal of uranium from aqueous solution. *Chem Eng J* 338:333–340
61. Zhang Z, Huang J, Dong Z et al (2019) Ultralight sulfonated graphene aerogel for efficient adsorption of uranium from aqueous solutions. *J Radioanal Nucl Chem* 321:1045–1055
62. Rohith S, Kishore Ramanan K, Santosh N et al (2020) Fe-Ni-doped graphene oxide for uranium removal-kinetics and equilibrium studies. *Water Air Soil Pollut* 231:444
63. Li Z, Chen F, Yuan L et al (2012) Uranium(VI) adsorption on graphene oxide nanosheets from aqueous solutions. *Chem Eng J* 210:539–546

64. Liu S, Li S, Zhang H et al (2016) Removal of uranium(VI) from aqueous solution using graphene oxide and its amine-functionalized composite. *J Radioanal Nucl Chem* 309:607–614
65. Liu S, Ouyang J, Luo J et al (2018) Removal of uranium(VI) from aqueous solution using graphene oxide functionalized with diethylenetriaminepentaacetic phenylenediamine. *J Nucl Sci Technol* 55(7):781–791
66. Yang P, Zhang H, Liu Q et al (2019) Nano-sized architectural design of multi-activity graphene oxide (GO) by chemical post-decoration for efficient uranium(VI) extraction. *J Hazard Mater* 375:320–329
67. Li N, Yang L, Wang D et al (2021) High-capacity amidoxime-functionalized β -cyclodextrin/graphene aerogel for selective uranium capture. *Environ Sci Technol* 55:9181–9188
68. Song WC, Shao DD, Lu SS et al (2014) Simultaneous removal of uranium and humic acid by cyclodextrin modified graphene oxide nanosheets. *Sci China Chem* 57(9):1291–1299
69. Chen M, Li Z, Li J et al (2017) The extraction of uranium using graphene aerogel loading organic solution. *Talanta* 166:284–291
70. Han J, Dai X, Cheng C et al (2013) Strong adsorption between uranium dicarbide and graphene surface induced by f electrons. *J Phys Chem C* 117(50):26849–26857
71. Dzyazko YS, Ogenko VM, Shteinberg LY et al (2019) Composite adsorbents including oxidized graphene: effect of composition on mechanical durability and adsorption of pesticides. *Him Fiz Tehnol Poverhni* 10(4):432–445
72. Dzyazko YS, Ogenko VM, Volkovich YM et al (2018) Composite consisting of hydrated zirconium dioxide and graphene oxide for removal of organic and inorganic components from water. *Him Fiz Tehnol Poverhni* 9(4):417–431
73. Tan L, Wang J, Liu Q et al (2015) Synthesis of manganese dioxide/iron oxide/graphene magnetic nanocomposite for enhanced uranium(VI) removal. *New J Chem* 39(2):868–876
74. El-Maghrabi HH, Abdelmaged SM, Nada AA et al (2017) Magnetic graphene based nanocomposite for uranium scavenging. *J Hazard Mater* 322:370–379
75. Amini A, Khajeh M, Oveisi AR et al (2021) A porous multifunctional and magnetic layered graphene oxide/3D mesoporous MOF nanocomposite for rapid adsorption of uranium(VI) from aqueous solutions. *J Ind Eng Chem* 93:322–332
76. Yang A, Zhu Y, Li P, Huang CP (2019) Preparation of a magnetic reduced-graphene oxide/tea waste composite for high-efficiency sorption of uranium. *Scientific Rep* 9:6471
77. Bai J, Chu J, Yin X et al (2020) Synthesis of amidoximated polyacrylonitrile nanoparticle/graphene composite hydrogel for selective uranium sorption from saline lake brine. *Chem Eng J* 391:123553
78. Cheng H, Zeng K, Yu J (2013) Adsorption of uranium from aqueous solution by graphene oxide nanosheets supported on sepiolite. *J Radioanal Nucl Chem* 298:599–603
79. Yang A, Wu J, Huang CP (2018) Graphene oxide-cellulose composite for the adsorption of uranium(VI) from dilute aqueous solutions. *J Hazard Toxic Radioact Waste* 22(2):04017029
80. Qian Y, Yuan Y, Wang H et al (2018) Highly efficient uranium adsorption by salicylal-doxime/polydopamine graphene oxide nanocomposites. *J Mater Chem A* 6:24676
81. Li S, Yang P, Liu X et al (2019) Graphene oxide based dopamine mussel-like crosslinked polyethylene imine nanocomposite coating with enhanced hexavalent uranium adsorption. *J Mater Chem A* 7:16902
82. Zhao C, Liu J, Deng Y et al (2019) Uranium(VI) adsorption from aqueous solutions by microorganism-graphene oxide composites via an immobilization approach. *J Cleaner Prod* 236:117624

The Effect of Ultra-fine Alloying Elements on High-Temperature Strength and Fracture Toughness of Ti–Si–X and Ti–Cr–X Composites



Bogdan Vasylyv, Z. A. Duriagina, V. V. Kulyk, V. I. Vavruk, P. Ya. Lyutyty, T. M. Kovbasiuk, I. A. Lemishka, V. V. Vira, and M. Ya. Holovchuk

Abstract In contrast to conventional titanium alloys, an operating temperature of which is limited by 300–500 °C, advanced Ti-based composites possess high fracture toughness and strength under bend and tensile loading in the temperature range of 20–650 °C. Owing to their high strength-to-weight ratio, these composites are promising for applications in components of modern engines (aircraft, rocket, and internal combustion ones) as well as other power equipment (compressors, gas turbines, fuel cells, etc.). However, there is a need to increase their operating temperature range up to 700–800 °C. In this work, mechanical behavior of Ti–Si–X composites (X = Al and/or Zr, Sn, C) has been studied. The content of alloying elements varied in a wide range (2–5 wt% Al, 2–5 wt% Zr, 1–5 wt% C). For comparison, mechanical behavior of Ti–Cr–X composite (X = Al and/or C) has been studied. The composites were

B. Vasylyv (✉)

Department of Hydrogen Technologies and Alternative Energy Materials, Karpenko Physico-Mechanical Institute of the NAS of Ukraine, 5 Naukova Str., Lviv 79060, Ukraine
e-mail: mechengin1111@gmail.com

Z. A. Duriagina · V. V. Kulyk · V. I. Vavruk · P. Ya. Lyutyty · T. M. Kovbasiuk · I. A. Lemishka
Department of Materials Science and Engineering, Lviv Polytechnic National University, 12 S. Bandera Str., Lviv 79000, Ukraine
e-mail: zduriagina@ukr.net

V. V. Kulyk
e-mail: kulykvolodymyrvolodymyrovych@gmail.com

V. I. Vavruk
e-mail: vavruk.valentyna@gmail.com

P. Ya. Lyutyty
e-mail: pavlo_lyutyty@ukr.net

T. M. Kovbasiuk
e-mail: felcproject@gmail.com

I. A. Lemishka
e-mail: mzihor@ukr.net

Z. A. Duriagina
Department of Materials Engineering, The John Paul II Catholic University of Lublin, 14 Raclawickie Al., 20-950 Lublin, Poland

© The Author(s), under exclusive license to Springer Nature Switzerland AG 2023
O. Fesenko and L. Yatsenko (eds.), *Nanomaterials and Nanocomposites, Nanostructure Surfaces, and Their Applications*, Springer Proceedings in Physics 279,
https://doi.org/10.1007/978-3-031-18096-5_10

manufactured with electron arc melting. As-cast and thermomechanically deformed series were examined. Beam specimens were cut of blanks, grinded, and polished to reach a good surface quality. Strength tests of specimen series were performed under three-point bending in a temperature range of 20–1000 °C. Single-edge notch beam (SENB) tests under three-point bending of specimen series were carried out in a temperature range of 20–900 °C for estimating fracture toughness of materials. Based on the constructed dependences of fracture toughness and strength on testing temperature for the specimen series as well as the microstructure and failure micromechanism analyses, the role of ultrafine alloying elements in achieving good high-temperature strength and fracture toughness of the studied composites was substantiated.

1 Introduction

Nowadays, to ensure required operating life of parts and products in hard operating conditions, there is a need to use high-strength and oxidation-resistant materials like advanced ceramic materials (silicon carbide, silicon nitride, alumina, zirconia, etc.) and various composites. Owing to their high-temperature strength and chemical inertness, these materials can be operated under high pressure or vacuum, high temperature, radiation, corrosion, etc. [1–10].

In contrast to conventional titanium alloys, an operating temperature of which is limited by 300–500 °C, advanced Ti-based composites possess high fracture toughness and strength under bend and tensile loading in the temperature range of 20–650 °C. Owing to their high strength-to-weight ratio, these composites are promising for applications in components of modern engines (aircraft, rocket, and internal combustion ones) as well as other power equipment (compressors, gas turbines, fuel cells, etc.) [11–23]. However, there is a need to increase their operating temperature range up to 700–800 °C. Under such conditions, these materials must meet the requirements on high strength and crack growth resistance as well as corrosion resistance [11, 24–26]. This should be taken into account while developing new materials and improving microstructure and mechanical properties of already existing ceramics and composites [27–34]. The substantiation of chemical composition and processing and treatment modes are crucial issues in improving the phase

V. V. Vira

Department of Strength of Materials and Structural Mechanics, Lviv Polytechnic National University, 12 S. Bandera Str., Lviv 79000, Ukraine
e-mail: viravolodymyr@gmail.com

M. Ya. Holovchuk

Department of Corrosion and Corrosion Protection, Karpenko Physico-Mechanical Institute of the NAS of Ukraine, 5 Naukova Str., Lviv 79060, Ukraine
e-mail: golovchuk86@gmail.com

compositions, microstructure, and mechanical properties of the developed materials [35–44].

Depending on the chemical composition, Ti and Cr-based composites may comprise some amount of high-temperature phases, namely, silicides, aluminides, MAX phases, etc. [45–57]. In particular, MAX phases are formed as quite distinct regions along the boundaries of titanium or chromium grains in Ti and Cr based composites [53, 58, 59]. It was shown in a number of works that MAX phases are of great practical interest in terms of creating materials for use in mechanical engineering, aerospace and nuclear industries [2, 59, 60]. MAX phases are ternary layered compounds corresponding to the conditional formula $M_{n+1}AX_n$ ($n = 1, 2, 3 \dots$), where M is a transition metal of the *d*-group (Sc, Ti, V, Cr, Zr, Nb, Mo, Hf, Ta), A is an element of the *p*-group (Si, Ge, Al, Ga, S, P, Sn, As, Cd, I, Tl, Pb), and X is carbon or nitrogen [61].

Among a variety of MAX phases, Ti_3SiC_2 MAX phase is not an ideal self-healing material. Its self-healing performance can be improved somewhat by partially replacing Si with Al due to the faster diffusion and oxidation of Al and a good oxidation resistance of Al_2O_3 . By partially replacing the A atoms of Ti_3SiC_2 with Al, $Ti_3Si_{1-x}Al_xC_2$ solid solutions are formed [18, 58, 62] that improves oxidation resistance of the material. Besides, in Ti_2AlC MAX phase, the oxidation temperature of Al could be lowered to 900 °C by partially replacing Al with Sn [18, 55, 58, 63]. At temperatures below 600 °C, SnO_2 can be already formed in $Ti_2Al_{1-x}Sn_xC$. This may serve as an attractive crack filling potential for $Ti_2Al_{1-x}Sn_xC$ at lower temperatures. However, no significant increase in the mechanical strength was found in such a composite due to the poor mechanical strength of the SnO_2 and the poor bond strength [58, 63].

It is known that MAX phases belong to the hexagonal crystal system. Similarly to other materials belonging to the hexagonal crystal system [57, 58, 61, 62], there exists a possibility to fabricate textured bulk MAX phases. Pressure-assisted sintering, e.g., HP and SPS, are the most widely used techniques to prepare textured bulk MAX phases. As a result, the material consists of plate-like grains preferentially oriented under external conditions (e.g., a magnetic field or a uniaxial pressure). In contrast to the mentioned fabrication techniques, spark plasma sintering or direct hot pressing of MAX phases does not allow formation of highly textured microstructures, but may result in formation comparatively distinct MAX phase regions along the boundaries of titanium grains in Ti and Cr-based composites [13, 58, 59, 64–67].

It is also known that textured bulk MAX phases have anisotropic properties due to the lamellar crystal structure [58, 61]. This is a reason of high mechanical strength and crack growth resistance of these materials along specific directions and make them applicable to more harsh service environments.

Strength and wear resistance tests of ceramic and composite materials are widely used to estimate the bearing capacity of the corresponding products [68–70]. However, to prevent the degradation of microstructure of materials in environmentally assisted harsh conditions [71, 72], there is a need to obtain material resistive to microstructural changes in such conditions [6, 73–78]. Microhardness and fracture toughness serve as characteristics of material for estimating its resistance to the

nucleation and growth of microcracks. For this purpose, the indentation test as one of the simplest known mechanical method is used [68, 79, 80]. Based on the indentation technique, a variety of loading schemes and formulas for calculating fracture toughness of materials were proposed [70–72, 79, 81, 82]. Thus, to develop a new ceramic or composite material with required physical and mechanical properties, it should be studied in terms of strength and crack growth resistance and their relations to the chemical and phase compositions.

The work is aimed at evaluating the effect of ultrafine alloying elements on phase composition, high-temperature strength, fracture toughness, and fracture micromechanisms of Ti–Si–X and Ti–Cr–X composites.

2 Materials and Methods

In this work, titanium-based composites of various systems have been studied. The composites were prepared from raw materials by arc melting in an argon atmosphere on a water-cooled copper hearth [59, 64]. The purity of the elements was as follows: Ti > 99.6 at%; Cr > 99.99 at%; and Si, C, Al, Sn, Zr > 99.99 at%. After melting, ingots were annealed at 1400 °C for 5 min. In some cases (composites 2 and 3, Table 1), ingots were rolled at a temperature of 1050 °C with applying the thermo-mechanical deformation of about 40%.

Beam specimens $5.0 \times 7.5 \times 50$ mm in size were machined from ingots or blanks, grinded, and polished (Table 1).

Strength tests of beam specimens were performed under three-point bending in a temperature range of 20–1000 °C. The fracture stresses (σ_f) were calculated using the “stress–flexure” diagrams at $P = P_{\max}$ by the equation [25, 32, 36, 76]

$$\sigma_f = \frac{1.5 \cdot P_{\max} \cdot L}{b \cdot t^2} \quad (1)$$

where P_{\max} is the maximum load (N); L is the span between two supporting rollers (mm); b and t are the specimen width and thickness (mm).

To characterize crack growth resistance of materials [83–86], along with microhardnes [87, 88], a fracture toughness characteristic, namely, the critical stress intensity factor (SIF) K_{Ic} is often used. One of the simplest methods of estimation of the fracture toughness is an indentation method implementing a variety of formulas

Table 1 Types of the investigated composited and their marking

Composite marking	System
1	Ti–Si–Al–Sn–C
2	Ti–Si–Al–Zr–C
3	Ti–Si–Al–Zr–C
4	Ti–Cr–Al–C

for calculating the SIF [89–98]. For a lot of materials, the K_{Ic} values calculated by some of these formulas are consistent with those obtained by conventional methods of fracture mechanics [79, 98, 99]. Among the last ones, a single-edge notch beam (SENB) test [100–102] is widely used to estimate fracture toughness of ceramic and composite materials. This method was thoroughly described in [99].

In our work, fracture toughness tests of specimen series were performed under three-point bending in a temperature range of 20–900 °C using the mentioned SENB test method. For estimating the critical SIF of materials corresponding formulas [100–102] were used.

At least three specimens were used for each test temperature of corresponding test methods.

A scanning electron microscope (SEM) Carl Zeiss EVO-40XVP equipped with an INCA Energy 350 system was used for the study of microstructure and fracture surface morphology of specimens and an energy-dispersive X-ray (EDX) microanalysis of chemical composition of the materials both in secondary electron (SE) and back-scattered electron (BSE) imaging modes.

X-ray powder diffraction data was obtained by using a X-ray diffractometer (Aeris, Malvern Panalytical) with Cu $K\alpha$ radiation operated at a voltage of 40 kV and a current of 15 mA. The angular range was 20°–90° and a step was 0.0217°. The X-ray diffraction (XRD) phase analysis was performed using Highscore software and referenced with the International Center for Diffraction Data (ICDD). All procedures including indexing, structure solutions, and refinement of profile and structural parameters were performed with the WinCSD [103] program package.

3 Results and Discussion

The microstructure and mechanical behavior of the titanium-based composites of Ti–Si–X and Ti–Cr–X systems in a wide temperature range have been studied.

3.1 XRD Analysis of the Studied Composites

Ti–Si–Al–Sn–C composite (1). The XRD patterns of the composites under study (Fig. 1) show in detail the peculiarities of their phase balances. The XRD pattern of composite 1 (Ti–Si–Al–Sn–C system) contains only peaks of the α -Ti and $TiC_{0.67}$ phases (Fig. 1a). The α -Ti phase percentage was found to be about 90 wt%, whereas the $TiC_{0.67}$ phase percentage was about 10 wt%. The morphology of these phases was investigated in details using the microstructure images made at various magnifications. At a low magnification, one can see quite homogeneous microstructure of the Ti–Si–Al–Sn–C composite (Fig. 2a). At a higher magnification, we can observe distinct microstructural components of this composite (Fig. 2b). According to a

general EDX analysis (spectrum 1 in Fig. 2b and Table 2), this material contains 87.41 wt% Ti, 6.09 wt% Al, 3.15 wt% Si, and 3.35 wt% Sn. The results of EDX analysis showed some difference in chemical composition of the Ti–Si–Al–Sn–C composite material as compared to the results of XRD analysis. According to EDX analysis (Fig. 2b and Table 2), this material is a metal-matrix composite of Ti–Si–Al–Sn–C system with high titanium content. It possibly comprises the titanium matrix phase, Ti_5Si_3 phase, Ti_3SiC_2 MAX phase, and titanium carbide phase.

The titanium phase (α -Ti of about 87 wt% Ti, spectrum 2 in Fig. 2b and Table 2) with some amounts of aluminum (6.26 wt%), silicon (2.39 wt%), and tin (3.88 wt%) is a matrix phase. The total amount of the α -Ti phase estimated optically using the microstructure image (Fig. 2b) is about 66–70 vol%.

The Ti_5Si_3 phase with small amounts of aluminum (4.35 wt%) and tin (2.2 wt%) looks like thin elongated curved areas of light-gray color about 25 μm in length (spectrum 3 in Fig. 2b). These areas are located at the boundaries of titanium lamella

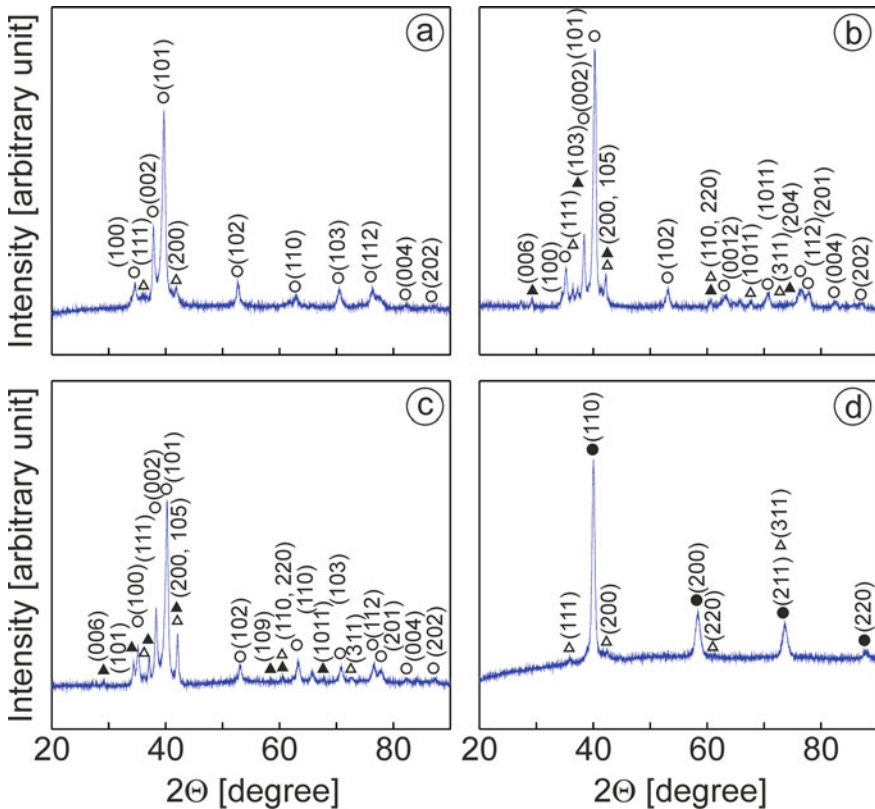


Fig. 1 XRD patterns of the investigated composites **a** 1, **b** 2, **c** 3, and **d** 4 (Table 1) showing peaks for the α -Ti (light circles), Ti(Cr) (dark circles), $TiC_{0.67}$ (light triangles) and Ti_3SiC_2 phases (dark triangles) and corresponding Miller indices (in parentheses)

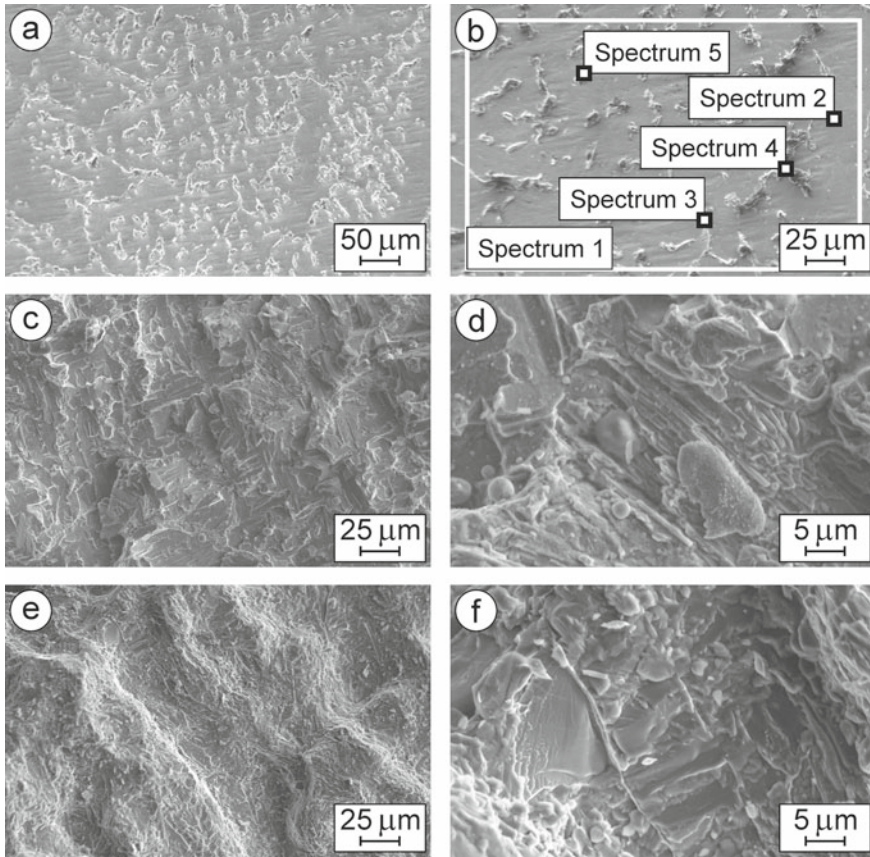


Fig. 2 SEM **a, b** microstructures (SE images) with marked zones of **b** general (spectrum 1) and local (spectra 2, 3, 4, and 5) EDX analyses, and **c–f** fractography (SE images) of specimens of composite 1 after fracture toughness tests at **c, d** 20 °C and **e, f** 650 °C (Table 1)

Table 2 The data of the EDX spectra 1–5 marked in Fig. 2 for a specimen of composite 1 (Table 1)

Chemical element and X-ray series	Spectra									
	1		2		3		4		5	
	wt%	at%	wt%	at%	wt%	at%	wt%	at%	wt%	at%
C K	–	–	–	–	–	–	14.88	38.85	24.62	54.32
Al K	6.09	10.31	6.26	10.66	4.35	6.98	3.25	3.77	2.74	2.69
Si K	3.15	5.12	2.39	3.92	12.44	19.14	9.87	11.04	9.68	9.13
Ti K	87.41	83.28	87.47	83.92	81.01	73.08	69.95	45.80	59.80	33.08
Fe K	–	–	–	–	–	–	–	–	0.21	0.10
Cd L	–	–	–	–	–	–	–	–	1.31	0.31
Sn L	3.35	1.29	3.88	1.50	2.20	0.80	2.05	0.54	1.64	0.37

packets. The total area occupied by them (Fig. 2b) is about 11–12 vol%. The Ti_5Si_3 phase was not detected by XRD analysis because of its small content.

The Ti_3SiC_2 MAX phase with small amounts of aluminum (3.25 wt%) and tin (2.05 wt%) looks like thick elongated areas of dark-gray color about 15 μm in size (spectrum 4 in Fig. 2b). These areas are located at the boundaries of titanium lamella packets similar to the Ti_5Si_3 phase. The total amount of the MAX phase (Fig. 2b) is about 14–15 vol%. Both the Ti_5Si_3 phase and the Ti_3SiC_2 MAX phase were not detected by XRD analysis because of their small content.

The titanium carbide phase ($\text{TiC}_{0.67}$, spectrum 5 in Fig. 2b) is in the form of distinct round-shaped particles of dark-gray color about 3 μm in size. The particles are distributed uniformly both in the matrix the α -Ti phase and at the boundaries of titanium lamella packets. The total area occupied by them (Fig. 2b) is about 5–7 vol%. Besides, small amounts of the Ti_5Si_3 phase and the Ti_3SiC_2 MAX phase are probably neighboring these carbide phase particles since some amount of silicon (9.68 wt%), along with small amounts of aluminum (2.74 wt%), iron (0.21 wt%), cadmium (1.31 wt%), and tin (1.64 wt%), were also detected in these areas.

Ti–Si–Al–Zr–C composite (2). The XRD pattern of composite 2 (Ti–Si–Al–Zr–C system) contains peaks of the α -Ti, $\text{TiC}_{0.67}$, and Ti_3SiC_2 MAX phases (Fig. 1b). Its phase composition was found to be as follows: α -Ti phase (about 70 wt%), $\text{TiC}_{0.67}$ phase (about 12 wt%), and Ti_3SiC_2 MAX phase (about 18 wt%). The microstructure image of the Ti–Si–Al–Zr–C composite made at a low magnification showed its homogeneous microstructure (Fig. 3a). The microstructure image of a higher magnification presents uniformly distributed areas of arbitrary shapes differing in colors (Fig. 3b). A general EDX analysis (spectrum 1 in Fig. 3b and Table 3) showed 76.79 wt% Ti, 6.77 wt% C, 3.88 wt% Al, 5.75 wt% Si, and 6.81 wt% Zr in this material. Thus, this material is a metal-matrix composite of Ti–Si–Al–Zr–C system possibly comprising the titanium matrix phase, (Ti, Zr) $_5\text{Si}_3$ phase, Ti_3SiC_2 MAX phase, and titanium carbide phase.

The α -Ti phase (89.65 wt% Ti, spectrum 2 in Fig. 3b and Table 3) with some amounts of aluminum (5.14 wt%), silicon (1.1 wt%), and zirconium (4.11 wt%) is a matrix phase. The total amount of the α -Ti phase (Fig. 3b) is about 52–55 vol%.

The (Ti, Zr) $_5\text{Si}_3$ phase looks like round-shaped particles of dark-gray color about 5 μm in size (spectrum 3 in Fig. 3b). These areas are adjacent to the titanium lamella packets. The total area occupied by them (Fig. 3b) is about 4–6 vol%. Besides, small amounts of the Ti_3SiC_2 MAX phase and the $\text{TiC}_{0.67}$ phase are probably neighboring these particles since some amount of carbon (6.97 wt%), along with a small amount of aluminum (1.46 wt%), was also detected in these areas. However, the (Ti, Zr) $_5\text{Si}_3$ phase was not revealed by XRD analysis because of its small percentage.

The titanium carbide phase $\text{TiC}_{0.67}$ with small amount of the Ti_3SiC_2 MAX phase and also small amounts of aluminum (5.09 wt%) and zirconium (2.69 wt%) looks like textured bulk MAX phase regions about 35–60 μm in size consisting of thin lamellae (spectrum 4 in Fig. 3b). These regions are uniformly distributed in the titanium matrix. The total amount of these regions (Fig. 3b) is about 35–45 vol%.

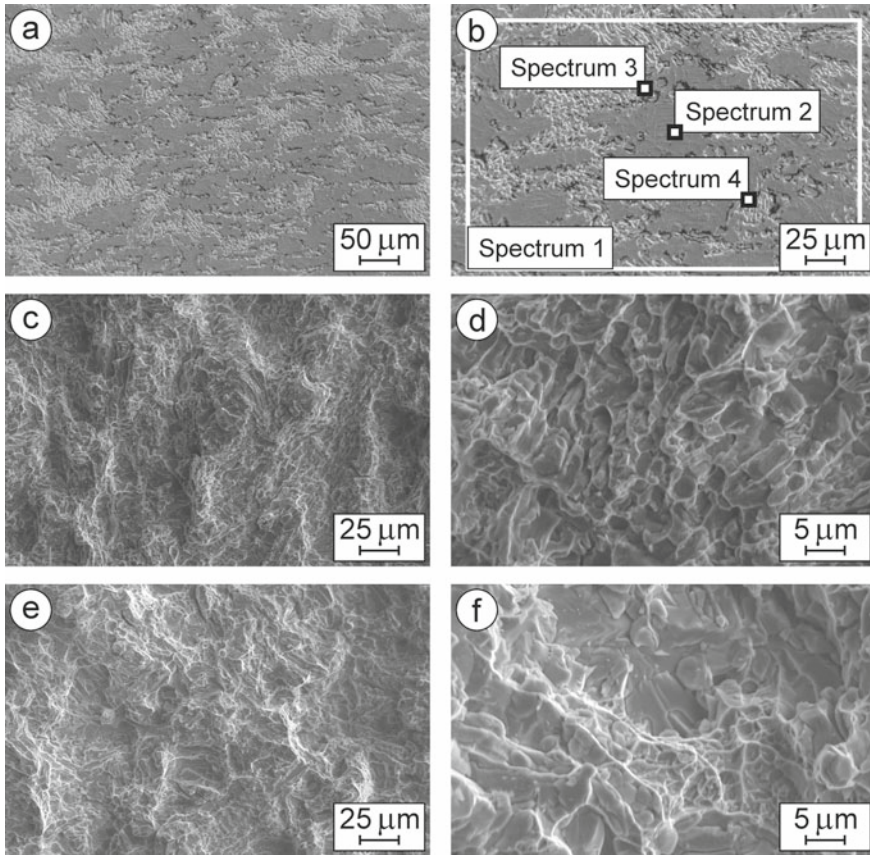


Fig. 3 SEM **a, b** microstructures (SE images) with marked zones of **b** general (spectrum 1) and local (spectra 2, 3, and 4) EDX analyses, and **c–f** fractography (SE images) of specimens of composite 2 after fracture toughness tests at **c, d** 20 °C and **e, f** 700 °C (Table 1)

Table 3 The data of the EDX spectra 1–4 marked in Fig. 3 for a specimen of composite 2 (Table 1)

Chemical element and X-ray series	Spectra							
	1		2		3		4	
	wt%	at%	wt%	at%	wt%	at%	wt%	at%
C K	6.77	21.75	–	–	6.97	21.55	7.30	22.94
Al K	3.88	5.56	5.14	8.88	1.46	2.01	3.07	4.29
Si K	5.75	7.91	1.10	1.82	19.69	26.04	10.62	14.26
Ti K	76.79	61.90	89.65	87.20	57.46	44.53	69.10	54.41
Zr L	6.81	2.88	4.11	2.10	14.42	5.87	9.91	4.10

Ti–Si–Al–Zr–C composite (3). The XRD pattern of composite 3 (Ti–Si–Al–Zr–C system) is similar to that of composite 2 and contains peaks of the α -Ti, TiC_{0.67}, and Ti₃SiC₂ MAX phases (Fig. 1c). Its phase composition is as follows: α -Ti phase (about 75 wt%), TiC_{0.67} phase (about 17 wt%), and Ti₃SiC₂ MAX phase (about 8 wt%). The microstructure image of the Ti–Si–Al–Zr–C composite made at a low magnification showed a quite homogeneous microstructure with some resemblance to the microstructure of composite 2 (Fig. 4a). The microstructure image of a higher magnification presents randomly distributed areas of arbitrary shapes (Fig. 4b). As a result of a general EDX analysis (spectrum 1 in Fig. 4b and Table 4), 83.1 wt% Ti, 5.07 wt% Al, 5.94 wt% Si, and 5.89 wt% Zr were found in this material. Unexpectedly, no signs of carbon were detected. Like composite 2, this material is a metal-matrix composite of Ti–Si–Al–Zr–C system possibly comprising the α -Ti matrix phase, (Ti, Zr)₅Si₃ phase, Ti₃SiC₂ MAX phase (only according to XRD analysis), and titanium carbide phase.

The α -Ti matrix phase (89 wt% Ti, spectrum 2 in Fig. 4b and Table 4) with some amounts of aluminum (5.99 wt%), silicon (1.07 wt%), and zirconium (3.94 wt%) is presented in an amount of about 56–60 vol%.

The (Ti, Zr)₅Si₃ phase with a small amount of aluminum (2.07 wt%) looks like particles of arbitrary shapes about 5–25 μ m in size united in colonies or distributed randomly (spectrum 3 in Fig. 4b). They occupy the total area of about 26–30 vol% (Fig. 4b). For an unknown reason, this phase was not detected by XRD analysis.

The TiC_{0.67} phase with a small amount of the Ti₃SiC₂ MAX phase and some amounts of aluminum (5.09 wt%) and zirconium (2.69 wt%) looks like particles of arbitrary shapes about 1–5 μ m in size distributed randomly in titanium matrix (spectrum 4 in Fig. 4b). The total amount of these particles (Fig. 4b) is about 14–18 vol%.

Ti–Cr–Al–C composite (4). The XRD pattern of composite 4 (Ti–Cr–Al–C system) contains peaks of the Ti(Cr) and TiC_{0.67} phases (Fig. 1b). Its phase composition was found to be as follows: Ti(Cr) phase (about 78 wt%) and TiC_{0.67} phase (about 22 wt%). At a low magnification, distinctly grained microstructure of the Ti–Cr–Al–C composite can be observed (Fig. 5a). The microstructure image of a higher magnification presents grains of a matrix phase with uniformly distributed tiny particles inside and the fringe-like grain boundary regions. The fringes consist of needle-shaped particles differing in colors (Fig. 5b). A general EDX analysis (spectrum 1 in Fig. 5b and Table 5) showed 54.4 wt% Ti, 37.34 wt% Cr, 5.12 wt% C, and 3.14 wt% Al in this material. The material presenting a metal-matrix composite of Ti–Cr–Al–C system possibly comprises the Ti(Cr) matrix phase, Al₂O₃ phase, and titanium/chromium carbide phase.

The Ti(Cr) matrix phase comprises titanium (57.3 wt%, spectrum 2 in Fig. 5b and Table 5) and chromium (39.2 wt%) with some amount of aluminum (3.5 wt%). The total amount of the Ti(Cr) phase (Fig. 5b) is about 66–72 vol%.

The titanium/chromium carbide phase and the Al₂O₃ phase (spectrum 3 in Fig. 5b) containing in total 49.17 wt% Ti, 25.14 wt% Cr, 14.3 wt% C, 8.08 wt% O, and 3.31

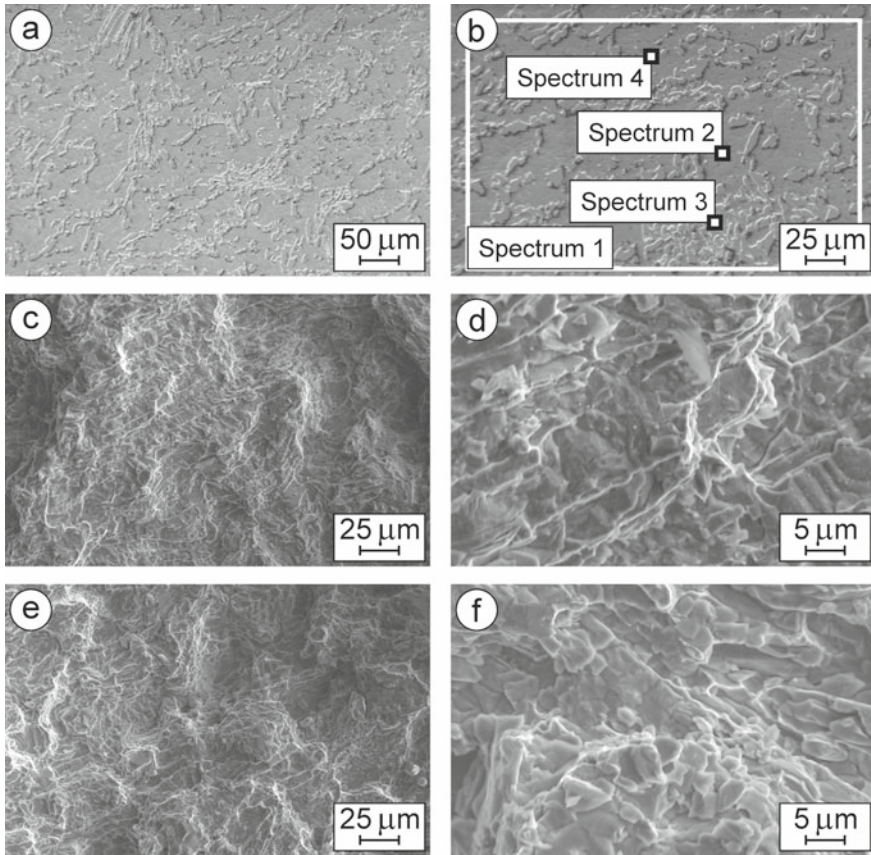


Fig. 4 SEM **a, b** microstructures (SE images) with marked zones of **b** general (spectrum 1) and local (spectra 2, 3, and 4) EDX analyses, and **c–f** fractography (SE images) of specimens of composite 3 after fracture toughness tests at **c, d** 20 °C and **e, f** 700 °C (Table 1)

Table 4 The data of the EDX spectra 1–4 marked in Fig. 4 for a specimen of composite 3 (Table 1)

Chemical element and X-ray series	Spectra							
	1		2		3		4	
	wt%	at%	wt%	at%	wt%	at%	wt%	at%
C K	–	–	–	–	–	–	11.22	32.70
Al K	5.07	8.55	5.99	10.27	2.07	3.32	5.09	6.61
Si K	5.94	9.61	1.07	1.76	20.85	32.09	0.88	1.09
Ti K	83.10	78.90	89.00	85.97	65.45	59.08	80.12	58.57
Zr L	5.89	2.94	3.94	2.00	11.63	5.51	2.69	1.03

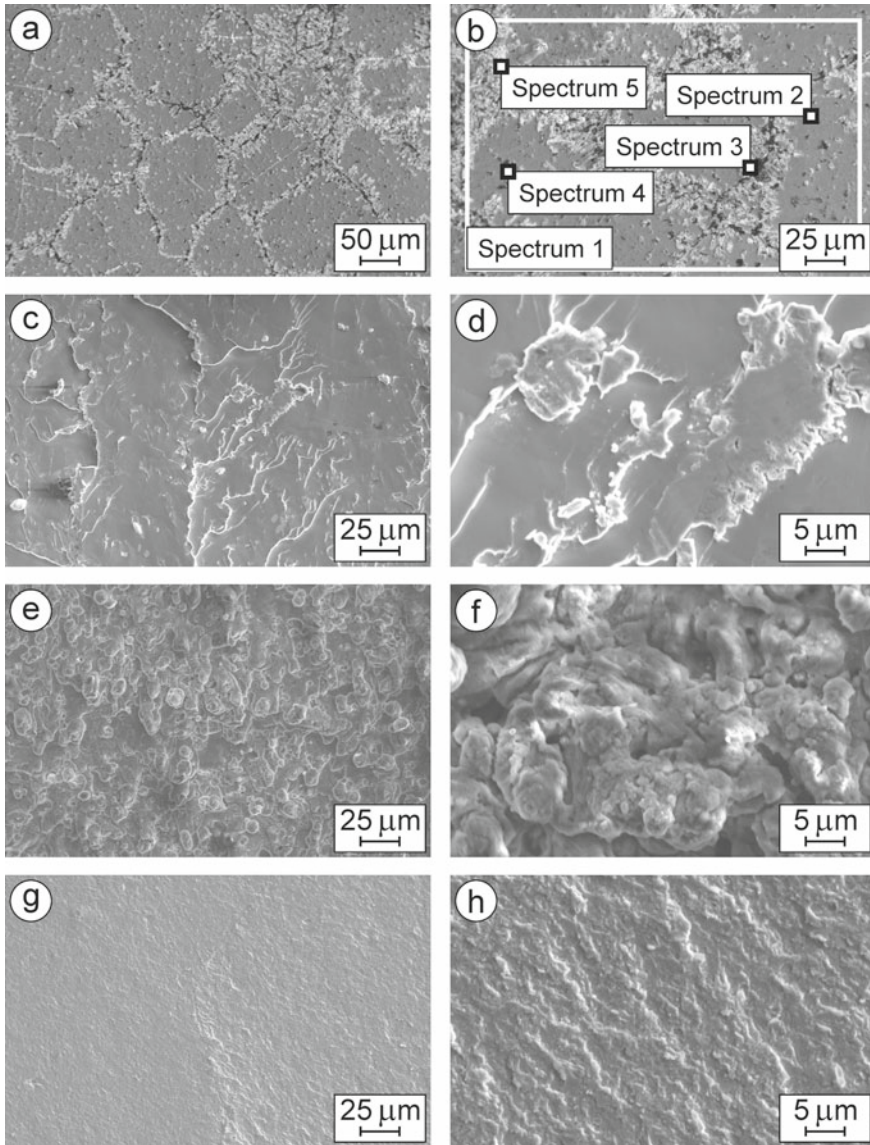


Fig. 5 SEM **a, b** microstructures (SE images) with marked zones of **b** general (spectrum 1) and local (spectra 2, 3, 4, and 5) EDX analyses, and **c–h** fractography (SE images) of specimens of composite 4 after fracture toughness tests at **c, d** 20 °C, **e, f** 700 °C, and **g, h** 800 °C (Table 1)

Table 5 The data of the EDX spectra 1–5 marked in Fig. 5 for a specimen of composite 4 (Table 1)

Chemical element and X-ray series	Spectra									
	1		2		3		4		5	
	wt%	at%	wt%	at%	wt%	at%	wt%	at%	wt%	at%
C K	5.12	17.78	–	–	14.30	35.77	11.99	35.30	6.29	19.95
O K	–	–	–	–	8.08	15.17	–	–	3.86	9.20
Al K	3.14	4.85	3.50	6.23	3.31	3.69	2.98	3.91	2.74	3.87
Ti K	54.40	47.40	57.30	57.52	49.17	30.84	50.98	37.63	50.29	40.00
Cr K	37.34	29.97	39.20	36.25	25.14	14.53	34.05	23.16	36.82	26.98

wt% Al were detected at the grain boundaries in the areas of black color. The total amount of these areas (Fig. 5b) was about 4–6 vol%.

A local EDX analysis of a round-shaped particle of dark-gray color about 1 μm in size (spectrum 4 in Fig. 5b and Table 5) showed 50.98 wt% Ti, 34.05 wt% Cr, 11.99 wt% C, and 2.98 wt% Al. This particle probably was the titanium carbide phase $\text{TiC}_{0.67}$ identified by XRD analysis, whereas some amounts of chromium and aluminum were detected by EDX analysis in the surrounding Ti(Cr) matrix phase. The total amount of these carbide particles was about 10–12 vol%.

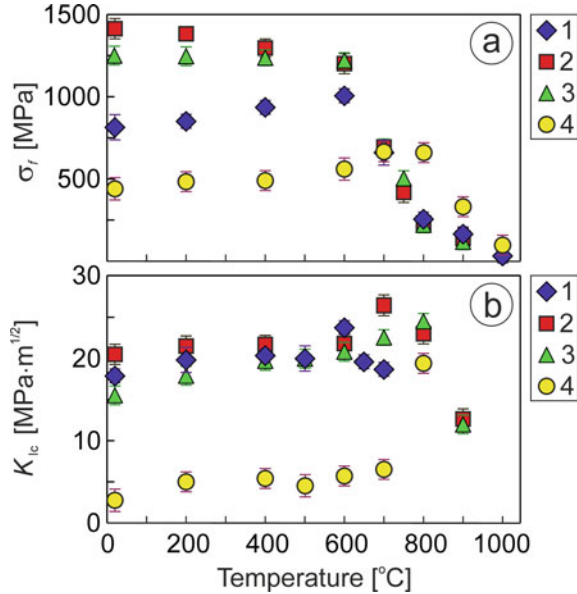
The thin needle-shaped particles of light-gray color about 15 μm in length (spectrum 5 in Fig. 5b) forming the fringe-like grain boundary regions and containing 50.29 wt% Ti, 36.82 wt% Cr, 6.29 wt% C, 3.86 wt% O, and 2.74 wt% Al present a mixture of the $\text{TiC}_{0.67}$ and Al_2O_3 phases that surrounds the Ti(Cr) phase grains. Their total amount is about 14–16 vol%. However, the Al_2O_3 phase was not detected by XRD analysis because of its small percentage.

In general, the subsequence of phases formation in the studied composites may be as follows: in the beginning of the solidification process, titanium carbides and titanium/zirconium silicides and MAX-phase were formed; then, the recrystallization of titanium/chromium grains occurred.

3.2 Mechanical Behavior of the Studied Composites and Microstructure Related Fracture Mechanisms

The studied composites exhibited distinct temperature dependences of both strength and fracture toughness (Fig. 6). In particular, the composites 1 (Ti–Si–Al–Sn–C system), 2 (Ti–Si–Al–Zr–C system), and 3 (Ti–Si–Al–Zr–C system) showed high and invariant values of fracture toughness (Fig. 6b) in a temperature range of 20–500 °C. In this range, fracture toughness of these composites is about 20 $\text{MPa}\cdot\text{m}^{1/2}$. In contrast, the monotonously changing temperature dependences of strength (increasing for composite 1 and decreasing for composites 2 and 3, Fig. 6a) were revealed.

Fig. 6 Temperature dependences of **a** strength and **b** fracture toughness of the studied composites (Table 1)



A specimen of composite 1 undergone to the fracture toughness test at 20 °C exhibited a distinct fracture surface (Fig. 2c, d) corresponding to a mixed fracture along the boundaries of titanium lamella packets and transgranular fracture across titanium grains in the case when a cleavage plane coincides with the direction of crack propagation. This fracture micromechanism is related to the comparatively high fracture toughness (Fig. 6b). Strength of this composite increased from about 760 MPa at 20 °C to 1000 MPa at 500 °C.

Fracture surface of a specimen of composite 2 tested at 20 °C (Fig. 3c, d) corresponds to a fracture along the boundaries of titanium lamella packets. No transgranular fracture across titanium grains occurred. Therefore, a coarse relief of fracture surface was formed that was a reason of high fracture toughness of the composite (Fig. 6b).

Similarly to this material, fracture surface of a specimen of composite 3 tested at 20 °C (Fig. 4c, d) exhibited a coarse relief corresponding to high fracture toughness of the composite (Fig. 6b).

Strength of composites 2 and 3 decreased from 1400 and 1250 MPa at 20 °C to 1230 MPa and 1240 MPa at 500 °C, respectively. Nevertheless, such a level of strength is high enough and meets the requirements to materials of this system.

A testing temperature in a range of 600–850 °C is critical for these three composites since for each composite a maximum of fracture toughness appeared on the corresponding dependence is shifted toward a certain temperature. Its location is related to the microstructural peculiarities of a composite, its chemical and phase compositions, as well as dominant fracture micromechanism.

For composite 1, a temperature above 600 °C is critical since it corresponds to the maximum of fracture toughness (Fig. 6b). A specimen undergone to the fracture toughness test at 650 °C exhibited blunted edges of titanium lamella packets (Fig. 2e), microregions of transverse fracture of thin Ti_3SiC_2 MAX phase lamellae (Fig. 2f), and signs of quazi brittle failure of the Ti_5Si_3 phase grains on fracture surface (Fig. 2f). The fracture toughness is as high as in the case of testing at 20 °C (Fig. 6b). Obviously, a transition from quazi brittle (at 600 °C) to high-temperature ductile fracture (at 650 °C) occurred that was followed by some lowering of fracture toughness (from $24 \text{ MPa}\cdot\text{m}^{1/2}$ at 600 °C to $19 \text{ MPa}\cdot\text{m}^{1/2}$ at 650 °C, Fig. 6b). Probably, tin also contributes to the transition process. Strength of this composite decreased from about 1000 MPa at 600 °C to 650 MPa at 700 °C (Fig. 6a).

A temperature corresponding to the maximum of fracture toughness for composite 2 is about 700 °C (Fig. 6b). Such a shift by 100 °C compared to composite 1 is important in terms of high-temperature mechanical stability of the studied composites. Fracture surface of a specimen of composite 2 tested at 700 °C (Fig. 3e, f) exhibited a coarse relief with signs of plastic elongation of titanium grains corresponding to the highest fracture toughness of the composite among the tested ones (Fig. 6b). No transgranular fracture across titanium grains occurred and no signs of debonding between Ti_5Si_3 phase grains or Ti_3SiC_2 MAX phase lamellae and titanium matrix were detected (Fig. 3f).

For composite 3, in contrast to composite 2, a temperature corresponding to the maximum of fracture toughness is about 800 °C (Fig. 6b). However, the shift by 200 °C compared to composite 1 is rather related to a difference in phase compositions of these materials. On fracture surface of a specimen of composite 3 tested at 700 °C (Fig. 4e, f), a coarse relief of fracture along titanium lamella packets with an average size smaller than in composite 2, with signs of plastic elongation of titanium grains, was observed. Such fracture surface morphology is consistent with slightly lower fracture toughness of composite 3 than composite 2 (Fig. 6b). Similarly to composite 2, no transgranular fracture across titanium grains was found and no signs of debonding between the $(\text{Ti}, \text{Zr})_5\text{Si}_3$ or $\text{TiC}_{0.67}$ or Ti_3SiC_2 MAX phase components and the α -Ti matrix phase were detected (Fig. 4f).

In contrast to mechanical behavior of above-mentioned materials, composite 4 showed invariant values of both strength (Fig. 6a) and fracture toughness (Fig. 6b) in a temperature range of 20–600 °C. Strength of this composite is about 500 MPa in this temperature range with a trend to increasing, whereas fracture toughness is about $5 \text{ MPa}\cdot\text{m}^{1/2}$. Increased strength (up to 650 MPa at 700 and 800 °C, Fig. 6a) and fracture toughness of the composite (steep increase up to $19 \text{ MPa}\cdot\text{m}^{1/2}$ at 800 °C, Fig. 6b) are the evidences of a change in the fracture micromechanism. Fracture surface of a specimen of composite 4 undergone to the fracture toughness test at 20 °C showed signs of transgranular cleavage fracture with separation of fringe-like grain boundary regions and the titanium carbide phase $\text{TiC}_{0.67}$ particles in places where the advancing crack crossed them (Fig. 5c, d). A different pattern of fracture surface was observed in a specimen of composite 4 after the fracture toughness test at 700 °C (Fig. 5e, f). Because of intense plasticization of the Ti(Cr) matrix phase at this temperature, multiple microregions of ductile metal surrounding each of titanium

carbide particles that are embodied into a Ti(Cr) matrix grains (Fig. 5e) with visible shear bands (Fig. 5f) as signs of plastic deformation of the matrix phase during crack growth can be seen. Such fracture micromechanism is related to temperature-assisted relaxation of stress in the crack tip vicinity that corresponds to some increase in fracture toughness of the material at 700 °C (Fig. 6b). Finally, a phenomenon of substantial increase in both strength (Fig. 6a) and fracture toughness of the composite (Fig. 6b) at 800 °C may be explained in terms of phase transformations due to high-temperature diffusion of some elements, in particular, aluminum and silicon [18, 58, 62]. This, in turn, causes a change in the fracture micromechanism [59, 76]. In this composite, high-temperature fracture occurred at 800 °C (Fig. 5g, h) with a steep increase in fracture toughness, due to diffusion of some elements and pore coalescence at the boundaries of the Ti(Cr) phase grains (Fig. 5h). No $\text{TiC}_{0.67}$ particles serve as stress concentrators, even in the places where the advancing crack crossed them (Fig. 5g). Thus, this temperature promotes quasi ductile character of crack growth resulted in striations (Fig. 5h) similar to fatigue crack growth in high-strength ductile materials at ambient temperature [59].

Thus, based on results of the strength test and fracture toughness tests along with analysis of microstructure peculiarities and fracture micromechanisms revealed in the whole temperature range investigated, the general tendencies in temperature dependent mechanical behavior of titanium-based composites have been substantiated. The Ti–Si–X composites can serve as high-temperature structural materials at an operating temperature up to 750 °C, whereas the Ti–Cr–X composite exhibits high-temperature stability at a higher temperature by about 50 °C.

4 Conclusions

In this work, mechanical behavior of the Ti–Si–X and Ti–Cr–X composites have been studied in a temperature range of 20–900 °C.

1. The microstructure peculiarities and phase composition of the studied composites were substantiated.
2. It was shown that strength and fracture toughness parameters are suitable for the characterization of mechanical behavior of the composites in the investigated temperature range.
3. The phenomenon of increased strength and fracture toughness of Ti–Cr–Al–C composite was revealed and explained in terms of the morphology of microstructural components and dominant fracture micromechanisms.

Acknowledgements The authors are deeply grateful to the staff of the Scientific Equipment Collective Use Center “Laboratory of Advanced Technologies, Creation and Physicochemical Analysis of a New Substances and Functional Materials” at Lviv Polytechnic National University (<https://lpnu.ua/ckkno>) for their kind help in performing X-ray diffraction studies.

References

1. Li D, Dong Y, Zhang Z et al (2021) An as-cast Ti-V-Cr-Al light-weight medium entropy alloy with outstanding tensile properties. *J Alloy Compd* 877:160199. <https://doi.org/10.1016/j.jalcom.2021.160199>
2. Prikhna TA, Ostash OP, Kuprin AS et al (2021) A new MAX phases-based electroconductive coating for high-temperature oxidizing environment. *Compos Struct* 277:114649. <https://doi.org/10.1016/j.compstruct.2021.114649>
3. Liu Z, Yang J, Qian Y et al (2020) In-situ reaction synthesis and mechanical properties of quaternary MAX phase $(\text{Cr}_{2/3}\text{Ti}_{1/3})_3\text{AlC}_2$. *Ceram Int* 46(14):22854–22860. <https://doi.org/10.1016/j.ceramint.2020.06.055>
4. Shabri HA, Othman MHD, Mohamed MA et al (2021) Recent progress in metal-ceramic anode of solid oxide fuel cell for direct hydrocarbon fuel utilization: a review. *Fuel Process Technol* 212:106626. <https://doi.org/10.1016/j.fuproc.2020.106626>
5. Serbenyuk TB, Prikhna TO, Sverdun VB et al (2018) Effect of the additive of Y_2O_3 on the structure formation and properties of composite materials based on AlN-SiC . *J Superhard Mater* 40(1):8–15. <https://doi.org/10.3103/S1063457618010021>
6. Dobrzański LA, Dobrzański LB, Dobrzańska-Danikiewicz AD (2020) Additive and hybrid technologies for products manufacturing using powders of metals, their alloys and ceramics. *Arch Mater Sci Eng* 102(2):59–85. <https://doi.org/10.5604/01.3001.0014.1525>
7. Posuvailo VM, Kulyk VV, Duriagina ZA et al (2020) The effect of electrolyte composition on the plasma electrolyte oxidation and phase composition of oxide ceramic coatings formed on 2024 aluminium alloy. *Arch Mater Sci Eng* 105(2):49–55. <https://doi.org/10.5604/01.3001.0014.5761>
8. Cherepova TS, Dmytrieva HP, Dukhota OI et al (2016) Properties of nickel powder alloys hardened with titanium carbide. *Mater Sci* 52(2):173–179. <https://doi.org/10.1007/s11003-016-9940-2>
9. Bocanegra-Bernal MH, Díaz de la Torre S (2002) Phase transitions in zirconium dioxide and related materials for high performance engineering ceramics. *J Mater Sci* 37:4947–4971. <https://doi.org/10.1023/A:1021099308957>
10. Ropyak LY, Makoviichuk MV, Shatskyi IP et al (2020) Stressed state of laminated interference-absorption filter under local loading. *Funct Mater* 27(3):638–642. <https://doi.org/10.15407/fm27.03.638>
11. Budzianowski WM, Milewski J (2011) Solid-oxide fuel cells in power generation applications: a review. *Recent Patents Eng* 5(3):1650–2189. <https://doi.org/10.2174/187221211797636926>
12. Komatsu Y, Sciazko A, Shikazono N (2021) Isostatic pressing of screen printed nickel-gadolinium doped ceria anodes on electrolyte-supported solid oxide fuel cells. *J Power Sources* 485:229317. <https://doi.org/10.1016/j.jpowsour.2020.229317>
13. Kashkarov EB, Pushilina NS, Syrtanov MS et al (2021) Pre-ceramic paper-derived $\text{SiC}_f/\text{Ti}_3\text{Al}(\text{Si})\text{C}_2$ and $\text{SiC}_f/\text{Ti}_3\text{SiC}_2$ MAX-phase based laminates fabricated using spark plasma sintering. *Scripta Mater* 194:113696. <https://doi.org/10.1016/j.scriptamat.2020.113696>
14. Tabares E, Cifuentes SC, Jiménez-Morales A et al (2021) Injection moulding of porous MAX phase Ti_3SiC_2 without using space-holder. *Powder Technol* 380:96–105. <https://doi.org/10.1016/j.powtec.2020.11.022>
15. Perevislov SN, Sokolova TV, Stolyarova VL (2021) The Ti_3SiC_2 max phases as promising materials for high temperature applications: formation under various synthesis conditions. *Mater Chem Phys* 267:124625. <https://doi.org/10.1016/j.matchemphys.2021.124625>
16. Silvestroni L, Melandri C, Gonzalez-Julian J (2021) Exploring processing, reactivity and performance of novel MAX phase/ultra-high temperature ceramic composites: the case study of Ti_3SiC_2 . *J Eur Ceram Soc* 41(12):6064–6069. <https://doi.org/10.1016/j.jeurceramsoc.2021.05.029>

17. Tan Y, Xia Y, Teng Z et al (2021) Synthesis and enhanced mechanical properties of compositionally complex MAX phases. *J Eur Ceram Soc* 41(8):4658–4665. <https://doi.org/10.1016/j.jeurceramsoc.2021.03.027>
18. Yu W, Pi X, Chen W et al (2021) Effects of A-site atoms in Ti_2AlC and Ti_3SiC_2 MAX phases reinforced Mg composites: interfacial structure and mechanical properties. *Mater Sci Eng A* 826:141961. <https://doi.org/10.1016/j.msea.2021.141961>
19. Yu D, Tan Y (2021) Oxidation behaviors of compositionally complex MAX phases in air. *Ceram Int* 47(21):30188–30193. <https://doi.org/10.1016/j.ceramint.2021.07.198>
20. Du P, Zhu B, Yang X et al (2021) Toxic elements-free low-cost Ti-Fe-Si metallic glass biomaterial developed by mechanical alloying. *J Alloy Compd* 886:161290. <https://doi.org/10.1016/j.jallcom.2021.161290>
21. Wejrzanowski T, Haj Ibrahim S, Cwieka K et al (2018) Multi-modal porous microstructure for high temperature fuel cell application. *J Power Sources* 373:85–94. <https://doi.org/10.1016/j.jpowsour.2017.11.009>
22. Podhurska V, Vasylyv B (2012) Influence of NiO reduction on microstructure and properties of porous Ni–ZrO₂ substrates. In: Proceedings of the 3rd international conference on oxide materials for electronic engineering (OMEE-2012), Lviv, Ukraine, pp 293–294. <https://doi.org/10.1109/OMEE.2012.6464761>
23. Danilenko I, Lasko G, Brykhanova I et al (2017) The peculiarities of structure formation and properties of zirconia-based nanocomposites with addition of Al₂O₃ and NiO. *Nanoscale Res Lett* 12:125. <https://doi.org/10.1186/s11671-017-1901-7>
24. Dobrzański LA, Dobrzański LB, Dobrzańska-Danikiewicz AD (2020) Manufacturing technologies thick-layer coatings on various substrates and manufacturing gradient materials using powders of metals, their alloys and ceramics. *J Achieve. Mater Manuf Eng* 99(1):14–41. <https://doi.org/10.5604/01.3001.0014.1598>
25. Vasylyv BD, Podhurska VY, Ostash OP et al (2018) Effect of a hydrogen sulfide-containing atmosphere on the physical and mechanical properties of solid oxide fuel cell materials. Nanochemistry, biotechnology, nanomaterials, and their applications. *Springer Proc Phys* 214:475–485. https://doi.org/10.1007/978-3-319-92567-7_30
26. Kulyk VV, Vasylyv BD, Duriagina ZA et al (2021) The effect of water vapor containing hydrogenous atmospheres on the microstructure and tendency to brittle fracture of anode materials of YSZ–NiO(Ni) system. *Arch Mater Sci Eng* 108(2):49–67. <https://doi.org/10.5604/01.3001.0015.0254>
27. Milewski J, Lewandowski J, Miller A (2008) Reducing CO₂ emissions from a coal fired power plant by using a molten carbonate fuel cell. *Proc ASME Turbo Expo* 2:389–395. <https://doi.org/10.1115/GT2008-50100>
28. Milewski J, Lewandowski J (2009) Solid oxide fuel cell fuelled by biogases. *Arch Thermodyn* 30(4):3–12. https://www.imp.gda.pl/fileadmin/doc/imp_publishing/wimp/archives%20of%20thermodynamics/C_09_4.pdf
29. Dobrzański LA, Dobrzański LB, Dobrzańska-Danikiewicz AD (2020) Overview of conventional technologies using the powders of metals, their alloys and ceramics in Industry 4.0 stage. *J Achieve Mater Manuf Eng* 98(2):56–85. <https://doi.org/10.5604/01.3001.0014.1481>
30. Savka SS, Popovych DI, Serednytski AS (2017) Molecular dynamics simulations of the formation processes of zinc oxide nanoclusters in oxygen environment. Nanophysics, nanomaterials, interface studies, and applications. *Springer Proc Phys* 195:145–156. https://doi.org/10.1007/978-3-319-56422-7_11
31. Milewski J, Kupecki J, Szczęśniak A et al (2021) Hydrogen production in solid oxide electrolyzers coupled with nuclear reactors. *Int J Hydrog Energy* 46(72):35765–35776. <https://doi.org/10.1016/j.ijhydene.2020.11.217>
32. Vasylyv B, Podhurska V, Ostash O (2017) Preconditioning of the YSZ–NiO fuel cell anode in hydrogenous atmospheres containing water vapor. *Nanoscale Res Lett* 12:265. <https://doi.org/10.1186/s11671-017-2038-4>
33. Witz G, Shklover V, Steurer W et al (2007) Phase evolution in yttria-stabilized zirconia thermal barrier coatings studied by Rietveld refinement of X-ray powder diffraction patterns. *J Am Ceram Soc* 90(9):2935–2940. <https://doi.org/10.1111/j.1551-2916.2007.01785.x>

34. Clarke DR, Levi CG (2003) Material design for the next generation thermal barrier coatings. *Annu Rev Mater Res* 33:383–417. <https://doi.org/10.1146/annurev.matsci.33.011403.113718>
35. Smyrnova-Zamkova MY, Ruban OK, Bykov OI et al (2018) Physico-chemical properties of fine-grained powder in $\text{Al}_2\text{O}_3\text{-ZrO}_2\text{-Y}_2\text{O}_3\text{-CeO}_2$ system produced by combined method. *Comp Theory Practice* 18(4):234–240. https://kompozyty.ptmk.net/pliczki/pliki/1290_2018_t04_maria-y-smyrnova-zamkova-.pdf
36. Vasylyv B, Milewski J, Podhurska V et al (2022) Study of the degradation of a fine-grained YSZ–NiO anode material during reduction in hydrogen and reoxidation in air. *Appl Nanosci* 12:965–975. <https://doi.org/10.1007/s13204-021-01768-w>
37. Smyrnova-Zamkova MY, Red'ko VP, Ruban OK et al (2017) The properties of nanocrystalline powder of 90% $\text{Al}_2\text{O}_3\text{-10% ZrO}_2$ (wt%) obtained via the hydrothermal synthesis/mechanical mixing. *Nanosistemi Nanomater Nanotechnol* 15(2):309–317. <https://doi.org/10.15407/nnn.15.02.0309>
38. Sukhova OV (2009) Influence of mechanisms of structure formation of interfaces in composites on their properties. *Metallofiz Noveishie Tekhnol* 31(7):1001–1012
39. Dudnik OV, Marek IO, Ruban OK et al (2020) Effect of heat treatment on the structure and phase composition of the nanosized powder based on a ZrO_2 solid solution. *Powder Metall Met Ceram* 59(1–2):1–8. <https://doi.org/10.1007/s11106-020-00132-x>
40. Efremenko VG, Chabak YG, Shimizu K et al (2017) Structure refinement of high-Cr cast iron by plasma surface melting and post-heat treatment. *Mater Des* 126:278–290. <https://doi.org/10.1016/j.matdes.2017.04.022>
41. Zhou XW, Shen YF, Jin HM (2011) Effect of deposition mechanism and microstructure of nano-ceria oxide addition on Ni-P coating by pulse electrodeposition. *Adv Mater Res* 326:151–156. <https://doi.org/10.4028/www.scientific.net/AMR.326.151>
42. Shevchenko AV, Lashneva VV, Ruban AK et al (2016) Synthesis and study of high-purity nanocrystalline powder of a solid solution of CeO_2 and Y_2O_3 in zirconium dioxide. *Powder Metall Met Ceram* 54(9–10):548–553. <https://doi.org/10.1007/s11106-016-9748-5>
43. Kujawa M, Suwak R, Dobrzański LA et al (2021) Thermal characterization of halloysite materials for porous ceramic preforms. *Arch Mater Sci Eng* 107(1):5–15. <https://doi.org/10.5604/01.3001.0014.8189>
44. Marek IO, Ruban OK, Redko VP et al (2019) Physicochemical properties of hydrothermal nanocrystalline $\text{ZrO}_2\text{-Y}_2\text{O}_3\text{-CeO}_2$ powders. *Powder Metall Met Ceram* 58(3–4):125–132. <https://doi.org/10.1007/s11106-019-00055-2>
45. Crossman FW, Yue AS (1971) Unidirectionally solidified Ti-TiB and Ti-Ti₅Si₃ eutectic composites. *Met Trans* 2:1545–1555
46. Zhao H, Hu L, Li C et al (2021) Influence of metallic Cr addition on the phase structure and mechanical properties of plasma-sprayed Ti-Si-C coatings. *Ceram Int* 47(12):17570–17579. <https://doi.org/10.1016/j.ceramint.2021.03.075>
47. Cao Z, Zhou P, Xiao X et al (2021) Investigation on Ti-Zr-Cr-Fe-V based alloys for metal hydride hydrogen compressor at moderate working temperatures. *Int J Hydrog Energy* 46(41):21580–21589. <https://doi.org/10.1016/j.ijhydene.2021.03.247>
48. Chiu WT, Wakabayashi K, Umise A et al (2021) Enhancement of mechanical properties and shape memory effect of Ti-Cr-based alloys via Au and Cu modifications. *J Mech Behavior Biomed Mater* 123:104707. <https://doi.org/10.1016/j.jmbbm.2021.104707>
49. Liu J, Xu J, Sleiman S et al (2021) Microstructure and hydrogen storage properties of Ti-V-Cr based BCC-type high entropy alloys. *Int J Hydrog Energy* 46(56):28709–28718. <https://doi.org/10.1016/j.ijhydene.2021.06.137>
50. Zhou J, Xu Y, Zhang Z et al (2020) Interdiffusion and atomic mobility in the bcc Ti-rich Ti-Cr-Mn system. *Calphad* 68:101747. <https://doi.org/10.1016/j.calphad.2020.101747>
51. Hong SH, Park SW, Park CH et al (2021) Relationship between phase stability and mechanical properties on near/metastable b-type Ti-Cr-(Mn) cast alloys *J Alloy Compd* 821:153516. <https://doi.org/10.1016/j.jallcom.2019.153516>
52. Kehal A, Saoula N, Abaidia SEH et al (2021) Effect of Ar/N₂ flow ratio on the microstructure and mechanical properties of Ti-Cr-N coatings deposited by DC magnetron sputtering on

- AIISI D2 tool steels. *Surf Coat Technol* 421:127444. <https://doi.org/10.1016/j.surfcoat.2021.127444>
53. Ivasyshyn A, Ostash O, Prikhna T et al (2016) Oxidation resistance of materials based on Ti_3AlC_2 nanolaminate at 600 °C in air. *Nanoscale Res Lett* 11:358. <https://doi.org/10.1186/s11671-016-1571-x>
 54. Chiu WT, Ishigaki T, Nohira N et al (2021) Effect of Cr additions on the phase constituent, mechanical properties, and shape memory effect of near-eutectoid Ti-4Au towards the biomaterial applications. *J Alloy Compd* 867:159037. <https://doi.org/10.1016/j.jallcom.2021.159037>
 55. Chiu WT, Wakabayashi K, Umise A et al (2021) Enhancement of the shape memory effect by the introductions of Cr and Sn into the β -Ti alloy towards the biomedical applications. *J Alloy Compd* 875:160088. <https://doi.org/10.1016/j.jallcom.2021.160088>
 56. Zhao X, Sokol M, Barsoum MW et al (2021) Effect of grain orientation on the compressive response of highly oriented MAX phase Ti_3SiC_2 . *Mater Sci Eng A* 809:140869. <https://doi.org/10.1016/j.msea.2021.140869>
 57. Prikhna T, Ostash O, Basyuk T et al (2015) Thermal stability and mechanical characteristics of densified Ti_3AlC_2 -based material. *Solid State Phenom* 230:140–143. <https://doi.org/10.4028/www.scientific.net/SSP.230.140>
 58. Zhang Z, Duan X, Jia D et al (2021) On the formation mechanisms and properties of MAX phases: a review. *J Eur Ceram Soc* 41(7):3851–3878. <https://doi.org/10.1016/j.jeurceramsoc.2021.02.002>
 59. Ostash OP, Ivasyshyn AD, Vasylyv BD et al (2006) High-temperature and cyclic corrosion crack resistance of alloys of the Ti–Si–Al–Zr system. *Mater Sci* 42(3):330–343. <https://doi.org/10.1007/s11003-006-0087-4>
 60. Frommeyer G, Rosenkranz R, Ludecke C (1990) Microstructure and properties of the refractory intermetallic Ti_5Si_3 compound and the unidirectionally solidified eutectic Ti– Ti_5Si_3 alloy. *Metallkunde* 81:307–313
 61. Barsoum M (2000) The $M_{n+1}AX_n$ phases: a new class of solids. *Prog Solid State Chem* 28(2000):201–281. [https://doi.org/10.1016/S0079-6786\(00\)00006-6](https://doi.org/10.1016/S0079-6786(00)00006-6)
 62. Liu R, Tane M, Kimizuka H et al (2021) Elastic isotropy originating from heterogeneous interlayer elastic deformation in a Ti_3SiC_2 MAX phase with a nanolayered crystal structure. *J Eur Ceram Soc* 41(4):2278–2289. <https://doi.org/10.1016/j.jeurceramsoc.2020.11.026>
 63. Park MS, Chiu WT, Nohira N et al (2021) Effects of Cr and Sn additives on the martensitic transformation and deformation behavior of Ti–Cr–Sn biomedical shape memory alloys. *Mater Sci Eng A* 822:141668. <https://doi.org/10.1016/j.msea.2021.141668>
 64. Mazur VI, Taran YN, Kapustnikova SV et al (1994) Titanium matrix composites. US Patent, No. 5366570, 22.11.1994
 65. Vasylyv B, Ivasyshyn A, Ostash O et al (2004) High-temperature fatigue crack growth resistance of thermo-mechanically and heat treated cast Ti–Si–Al–Zr composites. *Metallic materials with high structural efficiency*. Kluwer Academic Publishers, The Netherlands, pp 235–240
 66. Vasylyv BD, Ivasyshyn AD, Ostash OP et al (2002) Kinetics of corrosion-fatigue cracks in Ti–Si cermet composite. *Mater Sci* 38(2):220–224. <https://doi.org/10.1023/A:1020990103898>
 67. Ostash OP, Ivasyshyn AD, Vasylyv BD et al (2002) Influence of the structure and asymmetry of loading cycles on the cyclic crack resistance of Ti–Si composites. *Mater Sci* 38(1):55–61. <https://doi.org/10.1023/A:1020120714703>
 68. Jeong K-W, Han J-S, Yang G-U et al (2021) Influence of preaging temperature on the indentation strength of 3Y–TZP aged in ambient atmosphere. *Materials* 14:2767. <https://doi.org/10.3390/ma14112767>
 69. Gaddam A, Brazete DS, Neto AS et al (2021) Three-dimensional printing of zirconia scaffolds for load bearing applications: study of the optimal fabrication conditions. *J Am Ceram Soc* 104(9):4368–4380. <https://doi.org/10.1111/jace.17874>

70. Ji SH, Kim DS, Park MS et al (2021) Sintering process optimization for 3YSZ ceramic 3D-printed objects manufactured by stereolithography. *Nanomaterials* 11:192. <https://doi.org/10.3390/nano11010192>
71. Tao S, Yang J, Zhai M et al (2020) Thermal stability of YSZ thick thermal barrier coatings deposited by suspension and atmospheric plasma spraying. *Curr Comput-Aided Drug Des* 10(11):984. <https://doi.org/10.3390/cryst10110984>
72. Rudolph M, Galetz MC, Schütze M (2021) Mechanical stability diagrams for thermal barrier coating systems. *J Therm Spray Technol* 30:694–707. <https://doi.org/10.1007/s11666-021-01163-5>
73. Andreiko IM, Kulyk VV, Ostash OP (2012) Resistance of steels of railroad wheels to corrosion-fatigue fracture. *Mater Sci* 47(5):608–612. <https://doi.org/10.1007/s11003-012-9434-9>
74. Sciazko A, Shimura T, Komatsu Y et al (2021) Ni-GDC and Ni-YSZ electrodes operated in solid oxide electrolysis and fuel cell modes. *J Therm Sci Technol* 16(1):JTST0013. <https://doi.org/10.1299/jtst.2021jtst0013>
75. Nykyforchyn H, Krechkovska H, Student O et al (2019) Feature of stress corrosion cracking of degraded gas pipeline steels. *Procedia Struct Integrity* 16:153–160. <https://doi.org/10.1016/j.prostr.2019.07.035>
76. Romaniv OM, Vasylyv BD (1998) Some features of formation of the structural strength of ceramic materials. *Mater Sci* 34(2):149–161. <https://doi.org/10.1007/BF02355530>
77. Efremenko VG, Chabak YG, Lekatou A et al (2016) High-temperature oxidation and decarburization of 14.55 wt pct Cr-cast iron in dry air atmosphere. *Metall Mater Trans A* 47A(2):1529–1543. <https://doi.org/10.1007/s11661-016-3336-7>
78. Buchanec S, Sciazko A, Mozdziejz M et al (2019) A novel approach to the optimization of a solid oxide fuel cell anode using evolutionary algorithms. *IEEE Access* 7:34361–34372. <https://doi.org/10.1109/ACCESS.2019.2904327>
79. Romaniv OM, Zalite IV, Simin’kovych VM et al (1996) Effect of the concentration of zirconium dioxide on the fracture resistance of Al₂O₃-ZrO₂ ceramics. *Mater Sci* 31(5):588–594. <https://doi.org/10.1007/BF00558793>
80. Khajavi P, Hendriksen PV, Chevalier J et al (2020) Improving the fracture toughness of stabilized zirconia-based solid oxide cells fuel electrode supports: effects of type and concentration of stabilizer(s). *J Eur Ceram Soc* 40(15):5670–5682. <https://doi.org/10.1016/j.jeurceramsoc.2020.05.042>
81. Ivasyshyn AD, Vasylyv BD (2001) Effect of the size and form of specimens on the diagram of growth rates of fatigue cracks. *Mater Sci* 37(6):1002–1004. <https://doi.org/10.1023/A:1015669913601>
82. Vasylyv BD (2002) Initiation of a crack from the edge of a notch with oblique front in specimens of brittle materials. *Mater Sci* 38(5):724–728. <https://doi.org/10.1023/A:1024222709514>
83. Cook RF, Pharr GM (1990) Direct observation and analysis of indentation cracking in glasses and ceramics. *J Am Ceram Soc* 73(4):787–817. <https://doi.org/10.1111/j.1151-2916.1990.tb05119.x>
84. Ostash OP, Kulyk VV, Lenkovskiy TM et al (2018) Relationships between the fatigue crack growth resistance characteristics of a steel and the tread surface damage of railway wheel. *Arch Mater Sci Eng* 90(2):49–55. <https://doi.org/10.5604/01.3001.0012.0662>
85. Nastic A, Merati A, Bielawski M et al (2015) Instrumented and Vickers indentation for the characterization of stiffness, hardness and toughness of zirconia toughened Al₂O₃ and SiC armor. *J Mater Sci Technol* 31(8):773–783. <https://doi.org/10.1016/j.jmst.2015.06.005>
86. Duriagina Z, Kulyk V, Kovbasiuk T et al (2021) Synthesis of functional surface layers on stainless steels by laser alloying. *Metals* 11(3):434. <https://doi.org/10.3390/met11030434>
87. ASTM E 384-11 (2011) Standard test method for Knoop and Vickers hardness of materials, ASTM International. <https://doi.org/10.1520/E0384-11>
88. ASTM C 1327-03 (2003) Standard test method for Vickers indentation hardness of advanced ceramics, ASTM International. <https://doi.org/10.1520/C1327-03>

89. Lawn BR, Swain MV (1975) Microfracture beneath point indentations in brittle solids. *J Mater Sci* 10(1):113–122. <https://doi.org/10.1007/BF00541038>
90. Gogotsi GA, Dub SN, Lomonova EE et al (1995) Vickers and Knoop indentation behaviour of cubic and partially stabilized zirconia crystals. *J Eur Ceram Soc* 15(5):405–413. [https://doi.org/10.1016/0955-2219\(95\)91431-M](https://doi.org/10.1016/0955-2219(95)91431-M)
91. Evans AG, Charles EA (1976) Fracture toughness determinations by indentation. *J Am Ceram Soc* 59(7–8):371–372. <https://doi.org/10.1111/j.1151-2916.1976.tb10991.x>
92. Grigoriev ON, Vinokurov VB, Mosina TV et al (2017) Kinetics of shrinkage, structurization, and the mechanical characteristics of zirconium boride sintered in the presence of activating additives. *Powder Metall Met Ceram* 55(11–12):676–688. <https://doi.org/10.1007/s11106-017-9855-y>
93. Anstis GR, Chantikul P, Lawn BR et al (1981) A critical evaluation of indentation techniques for measuring fracture toughness: I, Direct crack measurement. *J Am Ceram Soc* 64(9):533–538. <https://doi.org/10.1111/j.1151-2916.1981.tb10320.x>
94. Danilenko I, Glazunov F, Konstantinova T et al (2014) Effect of Ni/NiO particles on structure and crack propagation in zirconia based composites. *Adv Mater Lett* 5(8):465–471. <https://doi.org/10.5185/amlett.2014.amwc1040II>
95. Lawn BR, Evans AG, Marshall DB (1980) Elastic/plastic indentation damage in ceramics: the median/radial crack system. *J Am Ceram Soc* 63(9–10):574–581. <https://doi.org/10.1111/j.1151-2916.1980.tb10768.x>
96. Smyrnova-Zamkova MY, Ruban OK, Bykov OI et al (2021) The influence of the ZrO₂ solid solution amount on the physicochemical properties of Al₂O₃–ZrO₂–Y₂O₃–CeO₂ powders. *Powder Metall Met Ceram* 60(3–4):129–141. <https://doi.org/10.1007/s11106-021-00222-4>
97. Lankford J (1982) Indentation microfracture in the Palmqvist crack regime: implications for fracture toughness evaluation by the indentation method. *J Mater Sci Lett* 1(11):493–495. <https://doi.org/10.1007/BF00721938>
98. Vasylyv B, Kulyk V, Duriagina Z et al (2020) Estimation of the effect of redox treatment on microstructure and tendency to brittle fracture of anode materials of YSZ–NiO(Ni) system. *Eastern-Eur J Enterprise Technol* 108/6(12):67–77. <https://doi.org/10.15587/1729-4061.2020.218291>
99. Kulyk VV, Duriagina ZA, Vasylyv BD et al (2021) Effects of yttria content and sintering temperature on the microstructure and tendency to brittle fracture of yttria-stabilized zirconia. *Arch Mater Sci Eng* 109(2):65–79. <https://doi.org/10.5604/01.3001.0015.2625>
100. ASTM E 399-20a (2020) Standard test method for linear-elastic plane-strain fracture toughness of metallic materials, ASTM International. <https://doi.org/10.1520/E0399-20A>
101. ASTM C 1421-18 (2018) Standard test methods for determination of fracture toughness of advanced ceramics at ambient temperature, ASTM International. <https://doi.org/10.1520/C1421-18>
102. Kübler J (2002) Fracture toughness of ceramics using the SEVNB method: From a preliminary study to a standard test method. In: Salem J et al (eds) *Fracture resistance testing of monolithic and composite brittle materials*. ASTM International, pp 93–106. <https://doi.org/10.1520/STP10473S>
103. Akselrud LY, Grin (2014) WinCSD: software package for crystallographic calculations (Version 4). *J Appl Crystallogr* 47:803–805. <https://doi.org/10.1107/S1600576714001058>

The Study of Properties of Mechanochemical and Ultrasonic Treated BaO/ZrO₂ Composites



Olena Sachuk, Valery Zazhigalov, Piotr Dulian, Dorota Rutkowska-Zbik, Olena Kiziun, Michael Kurmach, Ludmyla Kotynska, Volodymyr Starchevskyy, and Sergey Shcherbakov

Abstract Nanosized BaO/ZrO₂ = 1:1 compositions were successfully synthesized by mechanochemical (MChT for 4 h) and ultrasonic (UST for 1 and 2 h) treatment methods from oxides taken in molecular ratio 1:1. XRD and TEM results showed that obtained samples consist the particles about 15 nm after MChT and 1 h UST and 35 nm after 2 h UST. The isotropic destruction of zirconia, mesoporous powder formation and particle agglomeration with irregular shape occur. The photocatalytic properties of barium/zirconium oxide mixtures were examined in the water solution of prometryn degradation reaction. The activity of studied samples was increased after their MChT and USD activation.

Keywords Barium · Zirconium oxide · Mechanochemistry · Ultrasonic treatment · Nanoparticle · Photocatalyst

O. Sachuk (✉) · V. Zazhigalov · O. Kiziun · L. Kotynska
Institute for Sorption and Problems of Endoecology, National Academy of Sciences of Ukraine,
13, General Naumov Str, Kyiv 03164, Ukraine
e-mail: Slena951@ukr.net

P. Dulian
Faculty of Chemical Engineering and Technology, Cracow University of Technology, 24,
Warszawska Str, 31-155 Cracow, Poland

D. Rutkowska-Zbik
Jerzy Haber Institute of Catalysis & Surface Chemistry, Polish Academy of Sciences, 8,
Niezapominajek Str, 30-239 Cracow, Poland

M. Kurmach
L. V. Pisarzhevskii Institute of Physical Chemistry, National Academy of Sciences of Ukraine, 31,
Pr. Nauki, Kyiv 03028, Ukraine

V. Starchevskyy
National University «Lviv Polytechnic». 12, S. Bandery Str, Lviv 79013, Ukraine

S. Shcherbakov
M.G. Kholodny Institute of Botany, National Academy of Science of Ukraine, 2,
Tereshchenkivska Str, Kyiv 01004, Ukraine

1 Introduction

Among the various nanomaterials, nanodimensional baria and zirconia composites have attracted much interest since these materials are refractory ones, having high strength, fracture toughness, and surface area for effective immobilization of biomolecules with desired orientation [1], possess excellent chemical resistance, low thermal conductivity [2, 3], electrical, and surface charge properties [4]. Such properties make it highly useful in the field of structural, mechanical and high temperature applications [5–7]. A number of synthesis methods including solid phase synthesis [2], chemical vapour deposition (CVD) [8], sol–gel process [9], sintering, and coprecipitation [10] were used for Ba/Zr-containing nanomaterials preparation. It should be noted that the most of them require the improvement of the systems interfacial characteristics. Mechano- and sonochemistry are an alternative to traditional methods of large amount modern materials preparation and can be attributed to simple and environmentally friendly activation methods of solids. They allow the synthesis of nanosized powders and coatings, permit to obtain highly active fertilizers and solid solutions with an abnormal content of components and intermetallic compounds from a mixture of metal powders [11–15]. The prospect of both these methods for synthesis of nanosized barium titanate, molybdates of zinc and vanadium was shown in some publications [12, 16–22]. Also, it was found that the mechano- and sonochemistry can be effectively used in the preparation (manufacture) of highly active catalysts of the hydrocarbons oxidation reactions [20, 23–29].

The purpose of this study is the investigating of influence of mechanochemical and ultrasonic treatment of binary oxide barium/zirconium mixture on the structural, crystal, and photocatalytic properties of this system.

2 Experimental

Stoichiometric mixture of BaO and ZrO₂ in the molecular ratio 1:1 was subjected to intense mechanical treatment in Fritsch high-energetic planetary ball mill (Pulversitte-6). Zirconia vessel (250 mL) and balls ($\varnothing = 10$ mm) were used for the treatment of 10 g of the oxides mixture. The duration of the treatment was 4 h in air at 550 rpm, and balls-to-powder weight ratio (BPR) was 10:1.

The ultrasonic treatment of baria-zirconia aqueous solution (10 g of powder and 80 mL water) was conducted in stainless steel reactor and activated for 1 and 2 h using UZDN-2 T dispergator, which supplied a continuous 40 kHz ultrasonic wave under heating at 80 °C. After sonification the obtained precipitates were dried at 120 °C in air atmosphere for 2 h.

The activated powders were characterized by different techniques which are given below. In order to determine the crystallographic phase the prepared samples were

characterized by X-ray diffraction (XRD) in a Bruker D8 Advance X-ray diffractometer at 40 kV and 30 mA in the 2Θ range of $10\text{--}80^\circ$ (2Θ step: 0.05°) using nickel-filtered $\text{Cu K}\alpha_1$ radiation. Identification of phases was carried out by comparison the samples diffraction patterns obtained from XRD with standard JCPDS database. The Fourier transform infrared (FTIR) spectra were recorded using an Excalibur 300 Series Digilab spectrometer equipped by DTGS detector at room temperature with 100 scans at 2 cm^{-1} resolution. A sample disks were prepared by mixing 1wt% of sample with potassium bromide.

Thermal analysis of all powders was performed using a furnace derivatograph (Derivatograph-Q) upon to 850°C in air using 200 mg of powders at a heating rate of $10^\circ\text{C}/\text{min}$.

N_2 adsorption–desorption isotherms were registered at 77 K using Autosorb automated gas sorption system (Quantachrome). Prior to measurement, each sample was degassed for 20 h at 150°C . The specific surface area (S_{BET}) was calculated according to the standard BET method. Pore size distribution over the mesopore range was generated by the Barrett-Joyner-Halenda (BJH) analysis of the desorption branches, and the values of the average pore size were calculated.

The structural properties and particle size of the synthesized mixed oxide powders were examined by transmission electron microscopy TEM using a JEM-1230 instrument (300 kV). Each powder was homogeneously dispersed in water/ethanol solution by sonification for 3 min.

In order to estimate the photocatalytic performance of the synthesized materials the photodegradation of triazine herbicide “Gezagard” was realized where prometryn (PROM) was an active substance. The initial concentration of the solution was 1.38×10^{-6} mol/L. The dosage of the baria-zirconia powders was 0.150 mg for 300 ml of PROM solution with the pH value of 7.3. Before switching on irradiation, the herbicide solution was continuously stirred in the dark for 60 min to ensure adsorption–desorption equilibrium. Photodegradation tests were performed in a photoreactor with a UV radiation source (mercury lamp (Optima) with 125 W power) for 5 h. The destruction of the prometryn was monitored at 221 nm in the Shimadzu UV-2450 spectrophotometer. The photocatalytic transformation rate constants were calculated from the slope of the curve $\ln(C_0/C_t)$ vs. irradiation time assuming the first order kinetics, where C is prometryn concentration (C_0 —at the beginning of the experiment, C_t — during the experiment).

3 Results and Discussion

Figure 1 depicts the XRD patterns of oxide $\text{BaO}/\text{ZrO}_2 = 1:1$ mixtures before (Fig. 1a) and after mechanical (Fig. 1b) and ultrasonic synthesis (Fig. 1c, d). The diffractograms of all samples clearly exhibit the presence of two crystalline phases. The main crystalline phase is monoclinic zirconium oxide ($m\text{-ZrO}_2$). The peaks of this phase with 2Θ values of 24.2 , 28.2 , 31.4 and 34.3° reveal the presence of (110), (11–1), (111) and (002) crystalline planes, respectively and well correspond to the

standard JCPDS file No: 83–0944. The second phase shows the presence of tetragonal lattice structure of barium oxide BaO (JCPDS file No: 89–8425). No peaks corresponding to any impure phase is found in the XRD patterns. The reflection peak of *m*-ZrO₂ from (110) crystalline plane has maximal intensity for all BaO/ZrO₂ = 1:1 compositions. However, after treatment some differences in the diffractograms of compositions without any phase changes were observed. As can be seen from Fig. 1b, c, d the redistribution of reflex intensities in zirconium dioxide without change of major reflex occurs. The considerable increase of reflexes intensity and narrowing of all diffraction lines after MChT was observed (Fig. 1b). It is known that the samples suffer a coalescence process under heating conditions and as a result the increase of reflex intensity and crystal size occur. However, in our case the increase of reflex intensity accompanied by a decrease of average particle sizes, calculations of which were made using Scherrer equation and are given in Table 1. Such behavior could be attributed to the acceleration of isotropic effect which is due to dislocation of planes in oxides and their destruction appeared in milling process and also good crystallinity of the formed particles.

When the ultrasonic reaction time prolongs up to 2 h (Fig. 1d) the decrease in peaks intensity (Fig. 1 and Table 1) and increase of crystallite size occur. The last

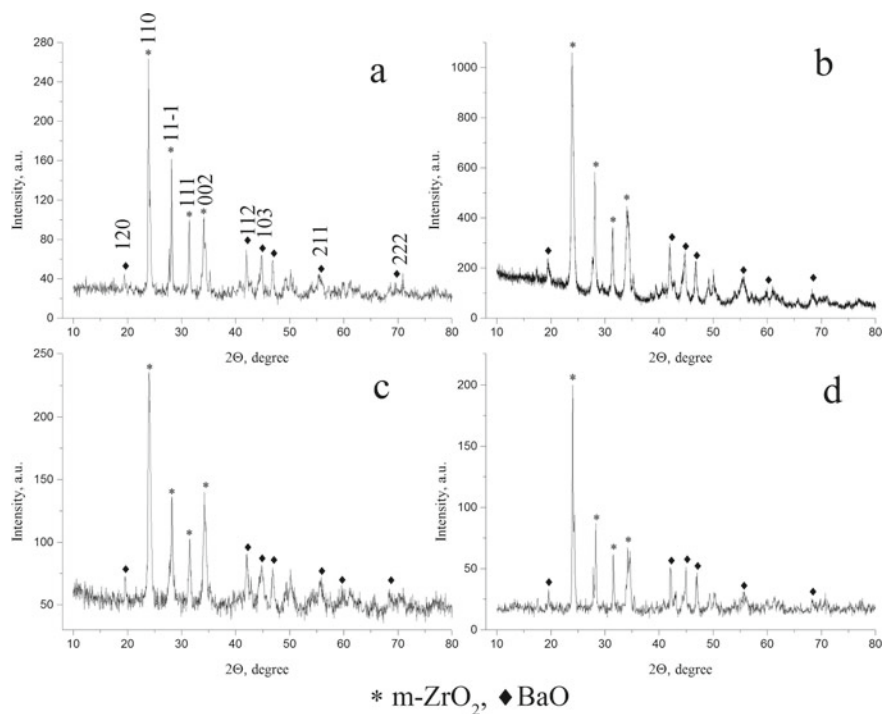


Fig. 1 XRD patterns of BaO/ZrO₂ = 1:1 mixtures: a–initial, b–after 4 h of MChT, c and d–after 1 and 2 h of UST respectively

Table 1 Some properties of BaO/ZrO₂ = 1:1 compositions

Parameter	Initial	MChT	UST 1 h	UST 2 h
*L [nm]	31	16	15	37
S _{BET} [m ² /g]	9	12	8	9
V _s × 10 ⁻² [cm ³ /g]	7.71	9.86	11.40	10.24
Kd*10 ⁻² [s ⁻¹]	0.7	1.4	1.1	1.3

*L—average crystallite size, determined from the maximum intensive reflex, S—specific surface area (BET) of the sample, V_s—total pore volume, Kd—degradation constant rate of prometryn solution

case can be explained through the different mechanisms of solids transformation: (1) the presence of crystal structure defects could create a charge imbalance, which can be compensated by the creation of oxygen vacancies. This in turn prompts a larger oxygen ion motion and thus bigger particle size; (2) longer times of ultrasonic treatment, which provide crystallite growth by diffusion, related to increases of the probability of collisions between particles due to the pressure system, *i.e.*, crystallization rate of the solid phases. As a result, a greater movement of atoms is attained, which facilitates the rapid arrangement of the crystalline structure and subsequent coalescence of the chemical species to form particle agglomeration. This phenomenon was confirmed by TEM method and surface area analysis.

The data presented on Fig. 2 show the morphology and size distribution of particles of BaO/ZrO₂ samples as bar charts alongside the TEM micrographs. As can be seen from the TEM images of the inactivated sample (Fig. 2a) and the samples after modification (Fig. 2b, c, d) of oxide composition, the presence of monoclinic zirconia and baria almost spherical morphology with some rectangular-shaped particles with a slightly agglomerated surface is observed. Individual particles are well resolved and their spherical morphology is evident from the figures.

The particles size distribution shows that more than 90% of the particles in samples after mechanical milling (Fig. 2b') and UST for 1 h (Fig. 2c') are the order 15–20 nm. However, a fraction of particles in the initial sample (Fig. 2a') and after its longer sonoactivation (2 h) (Fig. 2d') are found to have size above 30 nm. TEM results are in good agreement with XRD data. The structural properties of obtained samples were also studied by analysis based on FTIR method.

In order to ascertain the molecular nature of the synthesized material the FTIR spectra of the BaO/ZrO₂ compositions were taken (as shown in Fig. 3). Absorption bands in all IR-spectra of samples centered at 3460 and 1639 cm⁻¹ are the characteristic of surface-adsorbed water and hydroxyl groups, respectively.

FTIR spectra of initial sample (Fig. 3a) and treated oxide mixtures (Fig. 3b, c, d) show some changes in the absorption band position and their intensity. The weak vibration frequency at 1619 cm⁻¹ which is possibly characteristic of Ba–O stretching mode was observed in the spectra of all studied samples. The absorption peaks found in region 1390–1524 cm⁻¹ spectra of all powders could be due to a formation of BaCO₃ impurity after CO₂ absorption by BaO from atmosphere [30]. It should be noted that in XRD diffractograms the reflection peaks of BaCO₃ are

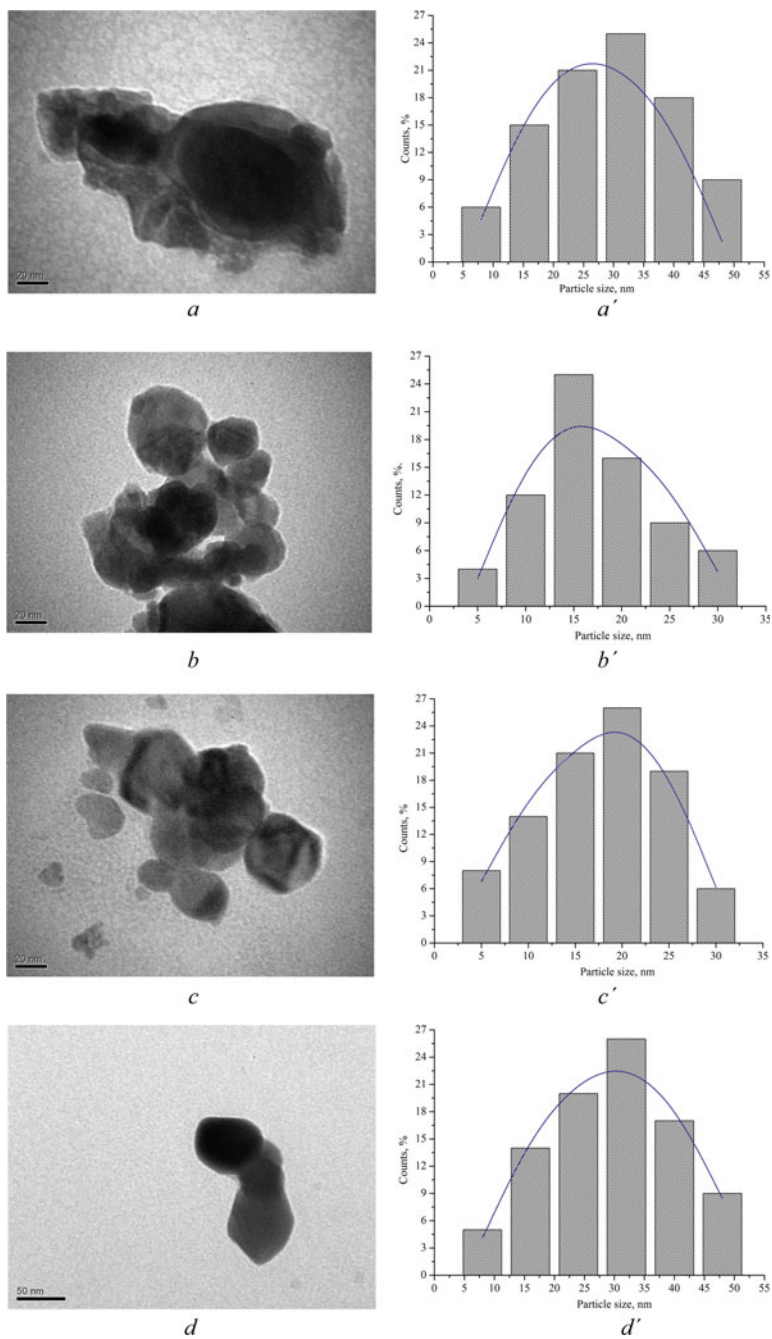


Fig. 2 TEM images of BaO/ZrO₂ powders and particle size distribution ('): a–initial, b–after MCHT, c–after sonication for 1 h and d–2 h

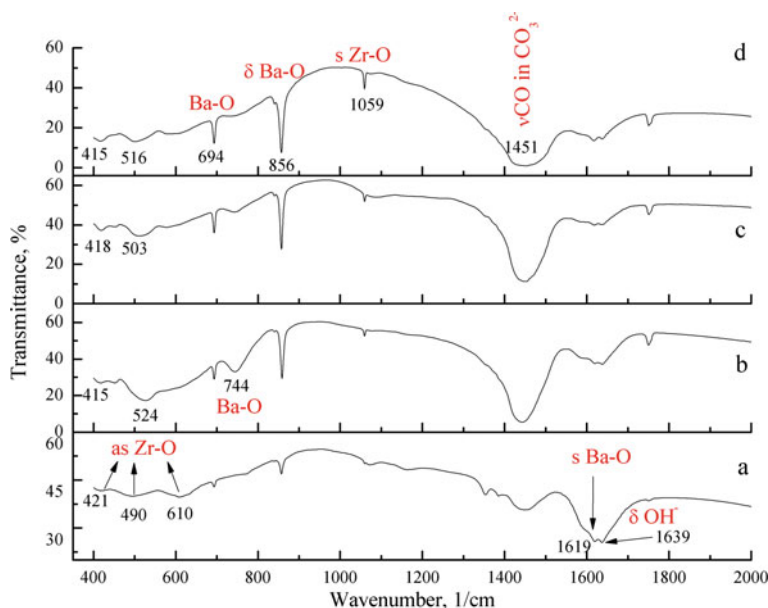
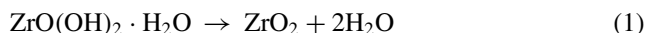


Fig. 3 FTIR spectra of BaO/ZrO₂ samples: a–initial, b–after MChT, c and d–after UST for 1 h and 2 h respectively

not detected. The peak with low intensity observed at 1059 cm⁻¹ corresponds to the symmetric vibrations of Zr-O bond and becomes more intensive after sonochemical treatment for 2 h. Similar changes apply to the absorption band at 856 cm⁻¹ which is attributed to the bonding vibrations of Ba-O. It can be related to an increase in the amount (per unit volume) of the functional group associated with the molecular bond in oxides. Curves of activated samples are characterized by appeared broad peak at wavenumbers 744 cm⁻¹ (more clearly visible in the spectrum of mechanochemical treated composition (Fig. 3b)) and increased intensity of absorption band at 694 cm⁻¹ that could be due to Ba-O bonding vibrations [31]. The obtained data suggest that after treatment the positions of number of peaks centered at 420, 495, and 610 cm⁻¹ corresponding to asymmetric vibration of Zr-O bond are somewhat changed. As can be seen from Fig. 3b, c, d the first two absorption bands are shifted up to 415–418 cm⁻¹ and 503–524 cm⁻¹, respectively, while the last one is almost disappeared. No other bands related with any other functional group were detected in the FTIR spectra.

The thermogravimetric analysis is used to describe the phase transformations and crystallization processes in the BaO/ZrO₂ compositions (figure is not given). The thermal analysis curves for all synthesized powders showed that water removal occurs in three steps: (i) the large peaks in the DTA-curves of sono- and mechanochemical treated samples were observed at 70–77 °C which is at lower temperature in comparison to initial mixture, where this index was above 90 °C. It was related to the removal of the physically adsorbed water; (ii) the second stage proceeds in higher temperature

range of 220–270 °C in DTA curves, which is caused by a loss of part of the crystal water. The third endothermic peak in DTA curves takes place in region 380–445 °C. Simultaneously this process can be assigned to both decomposition of BaCO₃ into BaO [32] that is in agreement with FTIR data and the loss of chemically coordinated (chemisorbed) water molecules present in hydrous zirconia [33] according to Eq. (1):



The total weight loss at heating of the samples up to 500 °C is equal about 1.5% while at heating up to 850 °C this indicator is equal to 5%. The process of crystallization of hydrous ZrO₂ appeared at 480 °C what is in good agreement with the data obtained for ZrO₂ synthesized by precipitation method [33]. There are no peaks which correspond to phase transforms in ZrO₂ were observed. This confirms the fact that monoclinic phase of zirconia is thermal stable and transforms reversibly to the tetragonal phase when heated to about 1170 °C [2, 34].

Nitrogen adsorption–desorption isotherms of the sample after mechanical milling are shown in Fig. 4. The adsorption–desorption curves of the sample belong to the typical IUPAC IV-type with hysteresis loop at P/P₀ = 0.45 to 0.98 in contrast to isotherms of inactivated and sonotreated samples (isotherms are not given) which belong to non-porous powders with II-type of isotherms.

It was found that nitrogen sorption isotherms of the milled sample have the H3-type hysteresis loop, which is a characteristic for pores consisting of plane-parallel particles and have a mesoporous structure. The pores size distribution curve of the mechanically activated BaO/ZrO₂ mixture is shown in the inset of Fig. 4. It can see

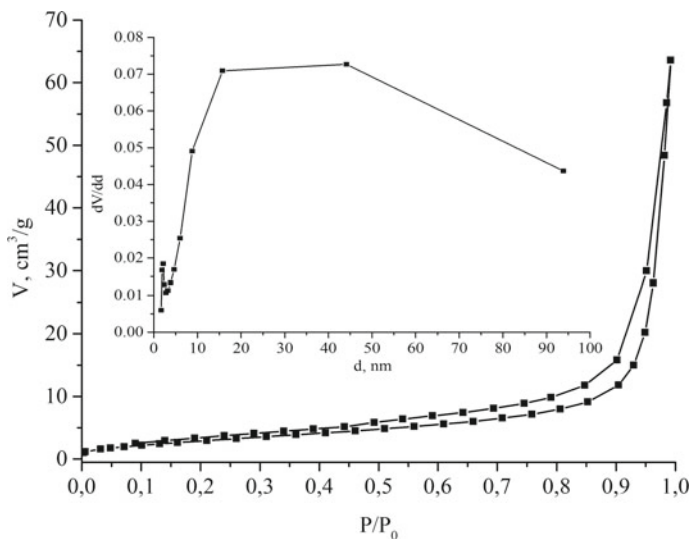


Fig. 4 Nitrogen adsorption–desorption isotherm curves and the corresponding BJH plot of pore-size distribution (inset) of BaO/ZrO₂ sample after 4 h MChT

that the sample reveals a broad distribution of the pores dimension in the mesoporous region (44 nm). The textural parameters including surface area and pore volume is inserted in Table 1.

A huge amount of various pesticides (predominantly herbicides), as a result of human economic activity, enter into the environment and not only slowly decompose in natural conditions, but also have cumulative properties. Nowadays, seeking novel strategies and methods to treat such chemicals in a way that does not have a negative impact on the environment into which it is disposed, has become crucial over the past years. Modern traditional methods, which have employed potent catalysts, showed successful degradation of the pesticides under various conditions as presented in [35]. But in most cases the destruction (oxidation) by ozone [36] and hydrogen peroxide [37], or the adsorption on porous solids, such as activated carbon, zeolites and clays was occurred. In our work the photocatalytic degradation as promising method for remove the toxic substances on example of water solution prometryn was conducted.

The plots showing prometryn degradation by BaO/ZrO₂ powders are presented in Fig. 5. It was found that activated samples (Fig. 5b) showed the higher activity in herbicide degradation process compared to initial sample that was evidenced by the calculations of degradation constant rate (Table 1). Also, some changes in UV-vis spectra of treated samples were noticed, namely, the blue shift from 221 nm up to 213 nm and decrease in intensity of the absorption maximum.

From above presented data, it can be assumed that the dissolved organic carbon (DOC), SO₄²⁻, NO₃⁻, NH₄⁺ were formed in triazine herbicide mineralization process. Also, the increasing of samples photocatalytic activity can be due to smaller particles formed after treatment that it was evidenced in [38].

So, it was found that mixed baria-zirconia compositions can be used as promising photocatalysts for herbicide remove.

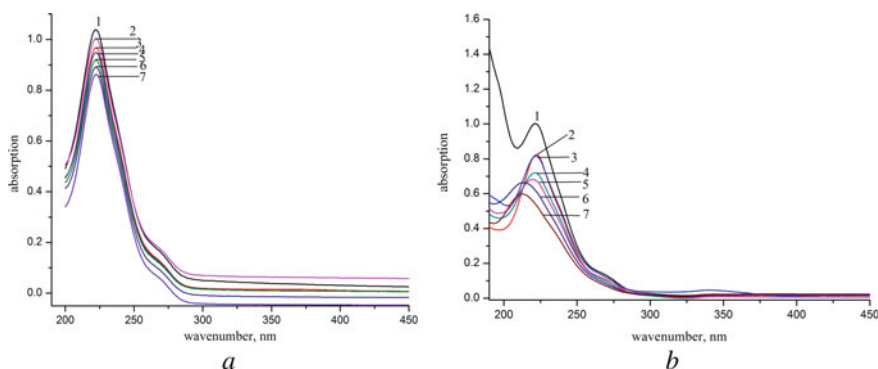


Fig. 5 Electron absorption spectra of water prometryn solution—1, after its dark sorption for 1 h—2 in the presence of inactivated BaO/ZrO₂ sample—*a* and after its MCHT—*b*, after irradiation for 1 h—3, 2 h—4, 3 h—5, 4 h—6, 5 h—7

4 Conclusion

This study demonstrates the significant changes in physical and chemical properties of BaO/ZrO₂ compositions after their mechanochemical and ultrasonic treatment. The decrease in particle size, mesoporous structure formation in the samples and increase of photocatalytic activity in prometryn degradation process were observed.

Acknowledgements This work was supported by NASU Programs: Fundamental Research “New Functional Substances and Materials for Chemical Engineering” (projects 07-17/18, 13-(19-21)) and Program for Young Scientists Discovery Project “Synthesis of selective catalysts for obtaining of pure hydrogen from ethanol at low temperatures” (project 22/02-(2020-21(2))).

References

1. Solanki PR, Kaushik A, Agrawal VV, Malhotra BD (2011) Nanostructured metal oxide-based biosensors. *NPG Asia Mater* 3:17–24
2. Jayakumar S, Ananthapadmanabhan PV, Perumal K, Thiagarajan TK, Mishra SC, Su LT, Tok AIY, Guo J (2011) Characterization of nano-crystalline ZrO₂ synthesized via reactive plasma processing. *Mater Sci Eng B* 176:894–899
3. Lin C, Wang S, Chen G, Wang K, Cheng Z, Lu X, Li C (2016) Thermodynamic evaluation of the BaO-ZrO₂-YO_{1.5} system. *Ceram Int* 42:13738–13747
4. Kumar S, Kumar S, Tiwari S, Srivastava S, Srivastava M, Yadav BK, Kumar S, Tran TT, Dewan AK, Mulchandani A, Sharma JG, Maji S, Malhotra BD (2015) Biofunctionalized nanostructured zirconia for biomedical application: a smart approach for oral cancer detection. *Adv Sci* 2(8):1500048
5. Bazeeraa AZ, Amrin MI (2017) Synthesis and characterization of barium oxide nanoparticles. *IOSR Journal of Applied Physics*. 1:76–80
6. Li W, Liu X, Huang A, Chu PK (2007) Structure and properties of zirconia (ZrO₂) films fabricated by plasma-assisted cathodic arc deposition. *J Phys D Appl Phys* 40:2293–2299
7. Berto da Silveira C, Denofre de Campos S, de Campos EA, Novaes de Oliveira AP (2002) Crystallization mechanism and kinetics of BaO-Li₂O-ZrO₂-SiO₂ glasses. *Mater Res* 5:21–26
8. Park JH, Hong KS, Cho WJ, Chung J-H (2003) Study on ZrO₂:Er thin films fabricated by metal-organic chemical vapor deposition. *Jpn J Appl Phys* 42:2839
9. Li W, Liu X, Huang A, Chu PK (2007) Structure and properties of zirconia (ZrO₂) films fabricated by plasma-assisted cathodic arc deposition. *J Phys D Appl Phys* 40. <https://doi.org/10.1088/0022-3727/40/8/S08>
10. Maschio S, Bachiorrini A, Lucchini E, Brückner S (2004) Synthesis and sintering of chemically derived BaO-ZrO₂ solid solutions. *J Eur Ceram Soc* 24:2241–2246
11. Balaz P (2008) Mechanochemistry in nanoscience and minerals engineering. Springer-Verlag, Berlin
12. Zazhigalov VA, Wieczorek-Ciurova K (2014) Mechanochemiczna aktywacja katalizatorów wanadowych. Politechnika Krakowska, Krakow
13. Avvakumov EG, Senna M, Kosova NV (2001) Soft mechanochemical synthesis: a basis for new chemical technologies. Kluwer Academic Publishers, New York, Boston, London, Moscow
14. Mason TJ, Lorimer J (2003) Applied sonochemistry: uses of power ultrasound in chemistry and processing. Wiley-VCH Verlag GmbH & Co., KGaA
15. Bergman L (1957) Ultrasound and its application in science and technology, 2nd edn. Izd-vo Inostr. Lit., Moscow

16. Zazhigalov VA, Sidorchuk VV, Khalameida SV, Kuznetsova LS (2008) Mechanochemical synthesis of BaTiO₃ from barium titanate oxalate. *Inorg Mater* 44:641–645
17. Gorelov BM, Kotenok EV, Makhno SN, Sydorochuk VV, Khalameida SV, Zazhigalov VA (2011) Structure and optical and dielectric properties of barium titanate nanoparticles obtained by the mechanochemical method. *Tech Phys* 56:83–91
18. Zazhigalov VA, Sachuk EV, Kopachevskaya NS, Bacherikova IV, Wiczorec-Ciurowa K, Shcherbakov SN (2016) Mechanochemical synthesis of nanodispersed compounds in the ZnO-MoO₃ system. *Theoret Exp Chem* 52:97–103
19. Sachuk O, Kopachevskaya N, Kuznetsova L, Zazhigalov V, Starchevskyy V (2017) Influence of ultrasonic treatment at properties of ZnO-MoO₃ oxide system. *Chem Chem Technology* 11:152–157
20. Zazhigalov VA, Wiczorec-Ciurowa K, Sachuk EV, Diyuk EA, Bacherikova IV (2018) Mechanochemical synthesis of nanodispersed molybdenum oxide catalysts. *Theoret Exp Chem* 54:225–234
21. Zazhigalov VA, Haber J, Stoch J, Kharlamov AI, Bacherikova IV, Bogutskaya LV (1997) Alternative methods to prepare and modify vanadium-phosphorus catalysts for selective oxidation of hydrocarbons. *Stud Surf Sci Catal* 110:337–346
22. Zazhigalov VA, Khalameida SV, Litvin NS, Bacherikova IV, Stoch J, Depero LE (2008) Effect of the mechanochemical treatment of a V₂O₅/MoO₃ oxide mixture on its properties. *Kinet Catal* 49:692–701
23. Zazhigalov VA, Haber J, Stoch J, Bogutskaya LV, Bacherikova IV (1996) Mechanochemistry as activation method of the V-P-O catalysts for n-butane partial oxidation. *Appl Catal A* 135:155–161
24. Zazhigalov VA, Haber J, Stoch J, Bogutskaya LV, Bacherikova IV (1996) Mechanochemistry in preparation and modification of vanadium catalysts. *Stud Surf Sci Catal* 101:1039–1047
25. Zazhigalov VA, Sachuk OV, Diyuk OA, Starchevskyy VL, Kuznetsova LS, Kurmach MM, Scherban ND (2019) Investigation of properties of the sonomodified ZnO-CeO₂ system. *Molec Cryst Liqid Cryst* 672:115–122
26. Zazhigalov VA, Sachuk OV, Diyuk OA, Starchevskyy VL, Kolotilov SV, Sawlowicz Z, Shcherbakov SM, Zakutevskyy OI (2018) The ultrasonic treatment as a promising method of nanosized oxide CeO₂-MoO₃ composites preparation. *Nanochemistry Biotechnol Nanomaterials Appl* 214:297–309
27. Zazhigalov VA, Diyuk OA, Sachuk OV, Diyuk NV, Starchevskyy VL, Sawlowicz Z, Bacherikova IV, Shcherbakov SM (2019) The effect of mechanochemical and ultrasonic treatments on the properties of composition CeO₂-MoO₃=1:1. *Nanochemistry Biotechnol Nanomaterials Appl* 221:109–123
28. Zazhigalov VA, Sachuk EV, Diyuk EA, Bacherikova IV, Scherban ND, Kurmach MM, Melnyk AK (2019) Mechanochemical preparation of nanodispersed Mo₃@CeO₂ composite and its catalytic properties in oxidation of ethanol. *Theoret Exp Chem* 55:215–221
29. Zazhigalov VO, Sachuk OV, Diyuk OA, Kopachevskaya NS, Starchevskyy VL, Kurmach MM (2019) The effect of ultrasonic treatment on the physico-chemical properties of ZnO/MoO₃ system. *Nanochemistry Biotechnol Nanomaterials Appl* 221:153–165
30. Thananathanachon T (2016) Synthesis and characterization of a perovskite barium zirconate (BaZrO₃): an experiment for an advanced inorganic chemistry laboratory. *J Chem Educ* 93(6):1120–1123
31. Mevada KC, Patel VD, Patel KR (2012) FT-IR, XRD and thermal studies of gel-grown barium tartrate crystals. *Arch Phy Res* 3:258–263
32. Arvanitidis I, Sichen Du, Seetharaman S (1996) A study of the thermal decomposition of BaCO₃. *Metall Mater Trans B* 27:409–416
33. Manivasakan P, Rajendran V (2011) Synthesis of monoclinic and cubic ZrO₂ nanoparticles from zircon. *J Am Ceram Soc* 94:1410–1420
34. Rauta PR, Manivasakan P, Rajendran V, Sahu BB, Panda BK, Mohapatra P (2012) Phase transformation of ZrO₂ nanoparticles produced from zircon. *Phase Transitions* 85:13–26

35. Kanan S, Moyet MA, Arthur RB, Patterson HH (2019) Recent advances on TiO₂-based photocatalysts toward the degradation of pesticides and major organic pollutants from water bodies. *Catal Rev* 62:1–65
36. Evgenidou E, Bizani E, Christophoridis C, Fytianos K (2007) Heterogeneous photocatalytic degradation of prometryn in aqueous solutions under UV–Vis irradiation. *Chemosphere* 68:1877–1882
37. Evgenidou E, Fytianos K (2002) Photodegradation of triazine herbicides in aqueous solutions and natural waters. *J Agric Food Chem* 50:6423–6427
38. Hafizah N, Sopyan I (2009) Nanosized TiO₂ photocatalyst powder via sol-gel method: effect of hydrolysis degree on powder properties. *Int J Photoenergy* 2009:1–8. <https://doi.org/10.1155/2009/962783>

State of the Art of Microplastic and Nanoplastic Pollution: Origin and Removal Methods



Svitlana Kyrii, Tetiana Dontsova, Olga Karaschuk, and Olena Yanushevska

Abstract Microplastic and nanoplastic are still an invisible problem on a global scale. Recognized as a contaminant only in 2004, microplastic and nanoplastic can have both instantaneous and long-term effects on living organisms at all levels—from molecular and genetic to population. This study examines the primary sources of microplastics and nanoplastics, their environmental hazards to the environment and humans. The factors influencing the degradation of plastic in natural conditions, methods of qualitative and quantitative detection of micro and nanoplastics, and methods of their removal from water are considered.

1 Introduction

Some characteristics of plastic, namely, its lightness, long service life, low cost, and durability, have prompted mankind to its mass production and usage. The industrial production of plastics has been actively growing every year since the twentieth century [1]. As for 2020, world plastic production amounted to 367 million tons (Fig. 1). The largest producers are the countries of Asia (50.1%), Europe (18.5%), the countries of the North American Free Trade Agreement (17.7%), the countries of the Middle East, Africa (7.71%), Latin America (4%), and Eastern European countries (2.6%). The production result of a large quantity of plastic is the formation of a considerable amount of waste in the form of micro-and nanoplastics, which have a significant negative impact on the ecology of our planet [2].

S. Kyrii (✉) · T. Dontsova · O. Karaschuk · O. Yanushevska
National Technical University of Ukraine “Igor Sikorsky Kyiv Polytechnic Institute”, Peremohy
av. 37, Kyiv 03056, Ukraine
e-mail: kysvit@gmail.com

T. Dontsova
e-mail: dontsova@ua.fm

O. Yanushevska
e-mail: l_rrr@ukr.net

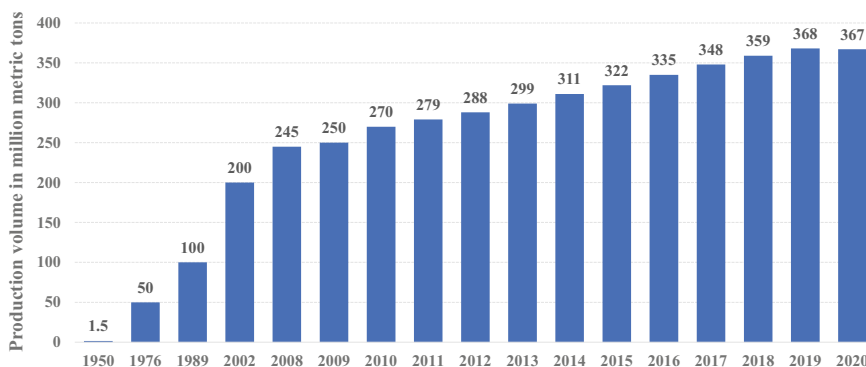


Fig. 1 World production of plastic from 1950 to 2020 [4]

Unfortunately, microplastic (MP) and nanoplastic (NP) cannot always be properly considered, so it is difficult to estimate the extent of contamination by them. For example, scientists have recently found that there may be from 12 to 21 million tons of MP and NP in the Atlantic Ocean, which is ten times more than previously estimated [3].

Microplastics are particles of fragmented synthetic polymers up to 5 mm in diameter and are resistant to biodegradation [2]. The first mention of the microplastics' harmful effects on biota in the literature dates to the 1970s. Initially, these works did not arouse widespread interest. However, over time, more and more work has begun to appear on marine animals suffering from large amounts of debris in the ocean. Some studies have confirmed that various marine mammals, zooplankton, seabirds, and turtles, and even some species of animals living in the depths of the sea consume plastic bags and lids [2]. Moreover, MP and NP can be spread over long distances due to their small size and lightweight. For example, micro and nanoplastic have been found even in Arctic glaciers [5], not to mention soils, oceans [6], and freshwater [7]. American scientists carried out demonstrative research of 159 water samples from various parts of the earth. They found that 83% of the samples contained plastic [8]. That is, MP and NP pollution are present in almost every country on our planet.

Another serious concern is the adsorbent properties of MP and NP, i.e., the ability to adsorb the contaminants in which it is found. Substances that can be adsorbed include heavy metals, polycyclic aromatic hydrocarbons, various pharmaceuticals, and drugs. Special additives used in the manufacture of plastics and articles thereof can also be toxic and get directly into the body of marine life. As a result, MP and NP can cause chronic toxicity due to its accumulation in the body [2]. As a result, micro and nanoplastic can cause chronic toxicity due to its accumulation in the body [2].

Fish and seafood are one of the primary sources of protein. Through the food chain, a person consumes all the plastic that enters the fish's body and cannot digest it in the stomach. Scientists estimate that a person consumes about 5 g of MP and NP per week, which is more than a teaspoon. It can enter the human body in three

main ways: with food, water, and air. These micro and nanoparticles affect the human body at all levels, from molecular to population. Once in the body, MP and NP have a complex effect and can cause various human diseases, including dysfunctions of the reproductive system. Through the digestive system, entering the bloodstream, toxic MP and NP are distributed throughout the body and can accumulate in the kidneys, liver, and other organs. Various mechanical damage and inflammatory processes can occur when MP and NP enter the lungs. The accumulation of plastic in the organs and cells of the body can lead to carcinogenic effects and cause various mutations and tumors [9].

MP and NP have been in the human digestive system for the longest time, which is why it is most affected. Swallowing such particles, even in small quantities can cause inflammation of the gastrointestinal tract and its irritation. The greatest danger is posed by particles whose size does not exceed 150 microns. Such particles are not able to be absorbed and excreted by the human body. In 2018, Australian scientists conducted a study and found that Antarctic krill can fragment pieces of polyethylene with a size of 31.5 nm into particles of 1 nm or less [10]. Thus, plastic decomposition into smaller particles continues in the middle of the body and is dangerous for its functioning.

Microplastic and nanoplastic are still an invisible problem on a global scale. Huge volumes of plastic production and extremely high prevalence of MP and NP as pollutants in soils, surface waters, oceans, and air increasingly exacerbate the environmental problem of its accumulation. Recognized as a contaminant only in 2004, MP and NP can have both instantaneous and long-term effects on living organisms at all levels—from molecular and genetic to population. MP and NP long decomposition time and durability due to the polymer structure and easy transportation in aqueous media make microplastics a hazardous problem.

The variety of shapes, small size, lightness, and low density of MP and NP contribute to its comprehensive transportation and easy distribution over long distances on land and in water systems. While large plastic particles are effectively removed during wastewater treatment, MP and NP often bypass treatment plants by entering and accumulating in the aquatic environment. In addition, MP and NP can have both instantaneous and long-term effects on living organisms, and their long decomposition time and easy transport in aquatic environments make it a hazardous problem. Establishing the sources of MP and NP origin and finding methods for their removal from water is a critical task.

2 Ecological Dangers of Microplastic and Nanoplastic

One of the negative dangers of MP and NP is that colored plastic particles of different sizes are perceived as nutrients by birds and fishes. Once in the digestive system, plastic cannot decompose by the enzymatic system of living organisms. Moreover, once in the stomach and other organs, MP and NP particles can lead to poisoning and death caused by starvation [2, 9].

Scientists have identified three main types of factors that can potentially adversely affect humans: chemicals that are part of the materials themselves, the physical effects of particles, and biofilm formed on the surface of particles due to the activity of microorganisms and bacteria. The following chemicals can cause the toxic properties of plastics [2]:

- Residual monomers, toxic additives, and softeners used in the manufacture of plastics can leach and be absorbed by marine animals.
- Intermediate products of chemical degradation. For example, the thermal decomposition of polystyrene may produce toxic styrene and other aromatic compounds. Styrene is a carcinogen, the accumulation of which can lead to malignant tumors.
- Persistent organic pollutants that are difficult to biodegrade and have pronounced toxic properties. These include various pesticides and technical products. In the context of MP and NP can be an example of polychlorobiphenyl used as a plasticizer.

Many chemical additives added to plastics during production can be released into the atmosphere, especially during degradation. The chemicals can then be reabsorbed by other plastic particles or lipids and enter the food chain by secondary means. The content of impurities varies depending on the type and purpose of the polymer [9].

In addition, some monomers used in plastic production are characterized by a tendency to desorption. A well-known example is bisphenol A, which is widely used to produce epoxy resins or polycarbonate and the inner coating of containers. A well-known example is bisphenol A, which is widely used to produce epoxy resins or polycarbonate and the inner coating of containers. The behavior of bisphenol resembles synthetic estrogens and is absorbed by the body [9].

Physically, MP and NP particles can enter the organs of the human body and cause mechanical damage, causing inflammation and various diseases. The shape, size, color, and chemical properties determine the toxicity of plastic micro and nanoparticles.

In water supply systems, the danger of MP and NP is the growth and reproduction of microorganisms in drinking water pipes and other surfaces and the formation of biofilms directly in the water we consume. Biofilms exfoliation from the walls of the pipes can lead to the consumption of opportunistic pathogens by humans [11].

Of particular importance are microorganisms that can cause intestinal disorders and multiply more actively after entering the human body. However, the risks associated with the presence of the biofilm are much lower than the toxicity of the substance that makes up the MP/NP and its ability to move pathogens [11].

3 Sources of Origin of Microplastic and Nanoplastic in Water Bodies

Both colored and transparent particles of MP and NP can be found in the environment. Colored particles usually come from plastic, which has a long service life, and transparent particles come from disposable plastic products, such as bottles, pots, and bags [12].

Also a variety of granules that are added in the manufacture of car tires, cosmetics, toothpaste, scrubs and shower gels, sequins, sequins on clothing and fishing lures, the so-called primary MP and NP are the source of pollutants that enter the waters of oceans. They are intentionally created by manufacturers and added to consumer goods to improve their consumer properties. In addition, much of the MP/NP enters the sewer with each wash of synthetic fabrics, from which hundreds of thousands of micro and nanofibers peel off. Another source of clogging is large plastic products, which under the action of mechanical, biological effects of the environment, radiation, and time, are destroyed into smaller particles and pollute the environment (so-called secondary MP and NP) [2]. For example, when bottles, disposable plastic utensils, are thrown away, they gradually disintegrate into smaller particles under the action of sunlight and water while maintaining their molecular structure. It happens due to the careless attitude of people who clutter the water with household waste, fishing equipment, and food packages.

According to morphological analysis, there are six primary forms in which MP and NP can be found: fibers, films, plates, foam, and spherical pieces [13]. The most common form in which plastic particles are found is fibers. The average size of the fibers found in water is 0.09–27.06 mm, and the average concentration is 0.02–25.8 fibers/liter. The most common form in which plastic particles are found is fibers. The average size of the fibers found in water is 0.09–27.06 mm, and the average concentration is 0.02–25.8 fibers/liter [14]. Particular attention should be paid to countries with a highly developed textile industry (India, Bangladesh, Vietnam, etc.). Foam particles are formed in water due to the decay of large products of which they are composed, and synthetic bags and food packaging serve as a source of MP and NP in the form of films. Spherical particles can be isolated from the resin contained in transport systems and various abrasive materials [1, 12].

The main sources of harmful substances in plastic which enter the human body are finishing and building materials (wallpaper, waterproofing, household items, insulation materials, etc.), furniture, appliances and plastic windows. The most quantity of plastic enters the human body from utensils [15].

Plastic containers in which food is often stored and heated in microwave ovens are becoming increasingly popular. During the heating and in contact with water that poisons and toxic substances are formed and released. All plastic products change over time and release decomposition products.

MP and NP were also found in bottled water. The State University of New York researched bottled water for its safety for the consumer. It was found that an average of 325 MP and NP particles enter the human body for every liter of bottled water. The

following types of plastic were found in the bottled water samples in the following percentage: 54% was polypropylene; 16% nylon; 10% polyethylene; 6% a mixture of polyethylene terephthalate and polyester; 3% fell on other inclusions. The same group of scientists found that tap water contains two times fewer plastic impurities [16].

4 Plastic Degradation under Natural Conditions

Degradation is a change in the chemical structure of a polymer by reducing its molecular weight. A significant degree of material degradation affects plastics' mechanical and physical properties, violating their integrity, shape, and characteristics.

Depending on the agents that have a destructive effect on the polymer, there are different types of plastic degradation. A significant role in the plastic decomposition duration is played place where the destruction of debris occurs near the shoreline or in the ocean [1].

The first type of degradation is biodegradation. It occurs under the action of microorganisms, both in surface waters and in its strata, and takes very long periods. Thus, a product made of different types of plastic can decompose from 400 to 700 years, and our usual plastic bags can be disposed of from 100 years and more [1].

The following destructive factors are thermal oxidation (oxidative decomposition) and photodegradation (destruction under sunlight). These processes most often occur with MP and NP in the coastal zone. When the plastic is heated to 40 °C, its disintegration begins according to the exponential law. Its fragility causes debris to turn into powdery micro- and nanoparticles easily consumed by zooplankton and other small marine animals or are subject to further biodegradation. Another cause of polymer degradation is hydrolysis, i.e., reaction with water [1].

All the above processes lead to the particles and fragments formation of MP and NP of different sizes and shapes, which harm marine nature and biota in general. Plastic that has undergone repeated decomposition and degradation becomes brittle, even powdery. Further decomposition of plastic leads to the MP and NP formation, which can further decompose and turn into CO₂ due to the activity of microorganisms [1].

5 Methods of Qualitative and Quantitative Detection and Chemical Characteristics of Microplastic and Nanoplastic

In order to detect MP and NP particles and measure their number, such methods as microscopy, IR spectroscopy with Fourier transform, Raman spectroscopy, mass spectroscopy, and chromatography are used [17].

Microscopic methods make it possible to classify plastic based on its physical characteristics using microscopes or stereoscopes. Such detection methods are the most common and easy to perform, but are pretty subjective, time-consuming, and depend on the human factor. Microscopic methods can help classify plastic particles by color, size, and shape and determine their origin. To simplify the detection process, scientists can use dyes that simplify the task. For example, Nile Red is a solvatochromic dye, making it possible to classify MP and NP into chemical groups using special software based on fluorescent shift [18].

IR Fourier and Raman spectroscopy are methods of chemical analysis that are among the most accurate and provide complete information about the presence of plastic in aqueous samples. Both types of spectroscopies are quite accurate and complement each other. As a result, they form a spectrum based on the interaction of light with molecules: the Fourier IR forms an infrared spectrum resulting from a change in the dipole moment, and Raman spectroscopy creates spectra based on the polarization of chemical bonds. These methods of spectroscopy allow us to get an idea about the structure and characteristics of the material. Raman microscopy allows the characterization of MP and less than 20 μm or NP, but the signals obtained may be weaker due to the high time of spectrum detection and various obstacles, depending on the characteristics of the material, such as color, decomposition, and fouling by microorganisms [19–21].

The method of pyrolysis gas chromatography and mass spectroscopy for MP and NP involves thermal decomposition under inert conditions. The resulting gas is captured by the cryogenic method, followed by separation on a chromatographic column. This method can characterize the MP and NP, but it does not contain the required information about the particles' mass, shape, and size. Due to this, the application of this method is limited [22].

6 Removal Methods of Microplastic and Nanoplastics from Water

In general, the development of MP and NP removal technologies is at an early stage, and there is no reliable method that could be used on an industrial scale. Currently, standard treatment methods are used; however, they cannot purify the MP and NP to the required degree.

6.1 Adsorption

Adsorption methods for removing various contaminants are widely used in different treatment systems due to a wide range of sorption materials [23, 24]. One of the innovative and promising methods of extracting MP and NP from water is the use of adsorbent materials. The latter is a physicochemical process that occurs due to Van der Waals forces or ion exchange and provides binding of the adsorbate on the adsorbent's surface. A group of Swiss scientists evaluated the possibility of removing nanoplastics from drinking water with granular activated carbon. It is established that the adsorption of MP and NP occurs in model water due to electrostatic interaction between positively charged MP/NP and negatively charged activated carbon. In the study of natural water of Geneva Lake, it was found that the ability to remove MP and NP is three times higher than model water due to the presence of dissolved organic matter. Thus, the studies indicate some prospects for MP and NP removal by sorption methods and activated carbon in particular [25].

Other scientists have developed a three-dimensional adsorbent based on graphene oxide to remove MP and NP from polystyrene. A strong π - π bond inside the benzene part of polystyrene and carbon atoms plays a vital role in this adsorbent to separate the MP and NP from the water. In addition, it is necessary to make sure that this adsorbent can be used repeatedly and to avoid secondary contamination of the environment [12].

In general, adsorption is a time-consuming process, and it is quite challenging to implement from a commercial point of view. The materials used for it can be secondary contaminants, requiring additional costs for regeneration or disposal. So, this method can be used before more advantageous methods, such as nanofiltration, reverse osmosis, or aggressive oxidation processes.

6.2 Magnetic Extraction

Magnetic extraction involves using nanoparticles of Fe [26] and an external magnetic field that attracts microparticles of plastic to iron. The iron nanoparticles usage is due to their low price and ferromagnetic properties. By this technology, almost 92% of granular beads made of polyethylene and polystyrene can be removed with a size range from 10 to 20 μm [12]. The problem with this method is that iron nanoparticles are not subject to biodegradation and lead to secondary pollution.

6.3 Chemical Coagulation

One of the alternative methods of removing MP and NP from natural waters is the usage of chemical coagulants. Iron and aluminum salts are usually used for this purpose. In addition, to reduce the coagulation process cost, treated industrial waste

is used as coagulation reagents [27, 28]. Such parameters as pollutants concentration, pH of the treated water, surface charge, etc., influenced the coagulation process. MP and NP particles have a negative surface charge and can be removed by chemical coagulation. Studies conducted by Finnish scientists indicate the high efficiency of the coagulation methods usage (up to 99.4%) for the removal of microplastics. The process can be optimized by choosing the appropriate coagulant and pH [29].

6.4 Photocatalytic Degradation of the Micro and Nanoplastics

The development of photocatalytic processes using renewable energy sources, such as solar energy, is becoming an increasingly attractive option from an economic, energy, and environmental point of view. Photocatalytic processes are used to decompose a wide range of organic contaminants, including pharmaceuticals and drugs [30], organic dyes [31, 32], and micro and nanoplastics [33–35]. In particular, a group of scientists studied the photocatalytic degradation of polystyrene and polyethylene plastic particles under the influence of ultraviolet radiation. TiO₂ nanoparticles were used as a catalyst, which showed complete plastics mineralization of 98.4% [36]. Thus, photocatalytic degradation is a promising alternative to minimize MP and NP contamination and reduce hazard by-products.

6.5 Membrane Technologies for Micro and Nanoplastics Water Purification

Membrane technologies are promising technological means for solving the water purification problem from an extensive range of pollutants [37–40]. Micro-, ultra-, nanofiltration, and reverse osmosis systems are used for water purification.

Microfiltration (MF) is a barometric process used to separate suspended and colloidal particles from 0.1 to 10 μm in size from water, including plastic particles. Recently, the direction of using ceramic microfiltration membranes has been successfully developed. They usually consist of a porous substrate (mainly based on aluminum oxides) and a non-porous selective surface layer. Such membranes have many advantages: resistance to chemically aggressive environments; high mechanical stability; ease of regeneration, high operating temperature (1000 °C and above), etc. The process of MP removing by a microfiltration membrane is somewhat similar to removing by an ultrafiltration membrane.

The ultrafiltration process is characteristic of the separation of systems where the mass of the dissolved component significantly exceeds the mass of the solvent. The ultrafiltration filter will retain almost all particles that exceed the size of 0.01 μm. The advantage of this method is its prevalence not only in the industrial but also in the

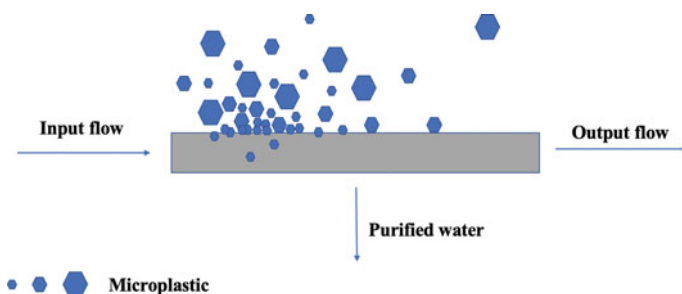


Fig. 2 Scheme of ultrafiltration microplastics extraction

domestic sector, as very often, such ultrafiltration modules are easily installed under the sink. The conditional scheme of microplastic removal is presented in Fig. 2.

The ultrafiltration process requires low energy consumption, is characterized by compact equipment and separation efficiency. This process is effective for removing a wide range of contaminants, in addition to microplastics-macromolecules, organic matter, turbidity, and more. However, water purification from MP by this method is poorly understood.

Nanofiltration membranes have a pore size of 1–3 nm and can retain electrolytes such as NaCl and organic compounds, including plastic. Reverse osmosis technology involves the use of non-porous and nanofiltration membranes operating under high pressure [41].

Membrane bioreactors (MBR) are systems in which a process stimulated by natural catalysts (enzymes and bacteria) takes place. At present, the use of MBR is considered to be an advanced, effective technology for industrial and municipal wastewater treatment. When MP and NP are removed with the help of MBR, a biodegradation process takes place, which simplifies the process. In comparison with other advanced cleaning technologies, this method provides the ability to remove MP and NP up to 99% [42].

7 Conclusions

Huge volumes of plastic production and extremely high prevalence of MP and NP as pollutants in soils, surface waters, oceans, and air increasingly exacerbate the environmental problem of its accumulation. MP and NP long decomposition time and durability due to the polymer structure and easy transportation in aqueous media make microplastics a hazardous problem. While large plastic particles are effectively removed during wastewater treatment, MP and NP often bypass treatment plants by entering and accumulating in the aquatic environment.

It is established that the main sources of micro- and nanoplastics in water are cosmetics (toothpaste, shower gel, etc.), building materials, synthetic clothing, which

separates plastic particles during washing, plastic utensils, decomposition products of large pieces of plastic, and more.

The main methods and their advantages and disadvantages for the quantitative and qualitative detection of micro- and nanoplastics, particularly microscopic methods, IR spectroscopy with Fourier transform, Raman spectroscopy, mass spectroscopy, and chromatography, are considered.

The main effective methods of removing micro- and nanoplastics from water include adsorption, magnetic extraction, chemical coagulation, photocatalytic degradation and membrane methods are considered. It is established that membranes are considered the most promising technological means to solve the problem of water purification from an extensive range of pollutants.

Acknowledgements The authors thank students of National Technical University of Ukraine «Igor Sikorsky Kyiv Polytechnic Institute» for actively participating in the discussion on the study topic.

References

1. Kleshchenkov AV, Filatova TB (2019) Microplastic is a problem of planetary scale. *Научный альманах стран Причерноморья*. Том 18(2):66–78
2. Poerio T, Piacentini E, Mazzei R (2019) Membrane processes for microplastic removal. *Mol* 24(22):1–15
3. Pabortsava K, Lampitt R (2020) High concentrations of plastic hidden beneath the surface of the Atlantic ocean. *Nat Commun* 11(4073):1–11
4. Tiseo I (2021) Annual production of plastics worldwide from 1950 to 2020. *Stat*. Retrieved from <https://www.statista.com/statistics/282732/global-production-of-plastics-since-1950>
5. Peeken I, Primpk S, Beyer B et al (2018) Arctic sea ice is an important temporal sink and means of transport for microplastic. *Nat Commun* 9(1506):1–12
6. Guo J, Huang X, Xiang L et al (2020) Source, migration and toxicology of microplastics in soil. *Environ Int* 137:1–13. <https://doi.org/10.1016/j.envint.2019.105263>
7. Wang S, Chen H, Zhou X et al (2020) Microplastic abundance, distribution and composition in the mid-west Pacific Ocean. *Environ Pollut* 246:1–8. <https://doi.org/10.1016/j.envpol.2020.114125>
8. Browne MA, Dissanayake A, Galloway TS et al (2018) Ingested microscopic plastic translocates to the circulatory system of the mussel, *mytilus edulis* (L). *Environ Sci Technol* 42:5026–5031. <https://doi.org/10.1021/es800249a>
9. Smirnova G, Shabanovich E, Kovsh D et al (2020) The problem of microplastics in the hydrosphere and aspects of the impact on human health. Modern issues of radiation and environmental medicine, radiation diagnostics and therapy: collection of materials of the republican scientific and practical conference with international participation, pp 328–333. [in Russian]
10. Dawson AL, Kawaguchi S, King CK et al (2018) Turning microplastics into nanoplastics through digestive fragmentation by antarctic krill. *Nat Commun* 9:1–8. <https://doi.org/10.1038/s41467-018-03465-9>
11. Elena G, Asa M, Rehab E (2021) Understanding biofilm formation in ecotoxicological assays with natural and anthropogenic particulates. *Front Microbiol* 12:1663. <https://doi.org/10.3389/fmicb.2021.632947>
12. Dey TK, Uddin ME, Jamal M (2021) Detection and removal of microplastics in wastewater: evolution and impact. *Environ Sci Pollut Res* 28(7)

13. Microplastics in drinking-water. Geneva: World Health Organization; 2019. Licence: CC BY-NC-SA 3.0 IGO
14. Napper IE, Thompson RC (2016) Release of synthetic microplastic plastic fibres from domestic washing machines: effects of fabric type and washing conditions. *Mar Pollut Bull* 112:39–45. <https://doi.org/10.1016/j.marpolbul.2016.09.025>
15. Dolina L, Savina O, Dolina D (2019) Water purification from plastic. *Science and progress in transport*. *Bull Dnipropetrovsk. National University of Railway Transport*, 2(80):27–40. [in Russian]
16. Mason ShA, Welch VG, Neratko J (2018) Synthetic polymer contamination in bottled water. *Front Chem* 6(407):1–11. <https://doi.org/10.3389/fchem.2018.00407>
17. Liu W, Zhang J, Liu H et al (2021) A review of the removal of microplastics in global wastewater treatment plants: characteristics and mechanisms. *Environ Intern* 28(7):1–14
18. Br N, Claveau-Mallet D, Hernandez LM et al (2019) Separation and analysis of microplastics and nanoplastics in complex environmental samples. *Acc Chem Res* 52(4):858–866. <https://doi.org/10.1021/acs.accounts.8b00602>
19. K ppler A, Windrich F, L der M et al (2015) Identification of microplastics by FTIR and Raman microscopy: a novel silicon filter substrate opens the important spectral range below 1300 cm⁻¹ for FTIR transmission measurements. *Anal Bioanal Chem* 407:6791–6801. <https://doi.org/10.1007/s00216-015-8850-8>
20. Zhao S, Danley M, Ward JE et al (2017) An approach for extraction, characterization and quantitation of microplastic in natural marine snow using Raman microscopy. *Anal Methods* 9:1470–1478. <https://doi.org/10.1039/C6AY02302A>
21. Chen Y, Wen D, Pei J et al (2020) Identification and quantification of microplastics using fourier-transform infrared spectroscopy: current status and future prospects. *Curr Opin Environ Sci Health* 18:14–19. <https://doi.org/10.1016/j.coesh.2020.05.004>
22. Li C, Gao Y, He S et al (2021) Quantification of nanoplastic uptake in cucumber plants by pyrolysis gas chromatography/mass spectrometry. *Environ Sci Technol Lett* 8(8):633–638. <https://doi.org/10.1021/acs.estlett.1c00369>
23. Ali I, Gupta V (2016) Advances in water treatment by adsorption technology. *Nat Protoc* 1:2661–2667. <https://doi.org/10.1038/nprot.2006.370>
24. Kyrii SO, Kosogina IV, Astrelin IV et al (2018) Investigation of the activated carbon modified by wastes of alumina production. *Voprosy khimii I khimicheskoi tekhnologii* 2:70–78
25. Arenas LR, Gentile St R, St Z et al (2021) Nanoplastics adsorption and removal efficiency by granular activated carbon used in drinking water treatment process. *Sci Total Environ* 791:1–12. <https://doi.org/10.1016/j.scitotenv.2021.148175>
26. Makarchuk O, Dontsova T, Perekos A (2017). Magnetic Nanocomposite Sorbents on Mineral Base. In: Fesenko O, Yatsenko L (eds) *Nanophysics, nanomaterials, interface studies, and applications*. NANO 2016. Springer proceedings in physics, vol 195. Springer, Cham. https://doi.org/10.1007/978-3-319-56422-7_54
27. Kyrii S, Dontsova T, Kosogina I et al (2020) Local wastewater treatment by effective coagulants based on wastes. *J Ecol Eng* 21(5):34–41. <https://doi.org/10.12911/22998993/122184>
28. Astrelin I, Kosogina I, Kyrii S (2020) Utilization processing of waste of alumina production into water treatment reagents. In: *Resource-saving technologies of raw-material base development in mineral mining and processing*, pp 371–391. <https://doi.org/10.31713/m924>
29. Rajala K, Gr nfors O, Hesampour M et al (2020) Removal of microplastics from secondary wastewater treatment plant effluent by coagulation/flocculation with iron, aluminum and polyamine-based chemicals. *Water Res* 183:1–26. <https://doi.org/10.1016/j.watres.2020.116045>
30. Kutuzova A, Dontsova T, Kwapinski W (2021) Application of TiO₂-based photocatalysts to antibiotics degradation: cases of sulfamethoxazole trimethoprim and ciprofloxacin. *Catal* 11(6):728. <https://doi.org/10.3390/catal11060728>
31. Kyrii S, Dontsova T, Kosogina I et al (2021) Effect of yttrium and niobium oxide modifiers on physicochemical and photocatalytic properties of titanium (IV) oxide. *East Eur J Enterp Technol* 4(6(112)):67–74

32. Dontsova TA, Kutuzova AS, Bila KO et al (2020) Enhanced photocatalytic activity of TiO₂/SnO₂ binary nanocomposites. *J Nanomater* 2020:1–13. <https://doi.org/10.1155/2020/8349480>
33. Uheida A, Mejía HG, Abdel-Rehim M et al (2021) Visible light photocatalytic degradation of polypropylene microplastics in a continuous water flow system. *J Hazard Mater* 406:124299. <https://doi.org/10.1016/j.jhazmat.2020.124299>
34. Ouyang Z, Yang Y, Zhangl C et al (2021) Recent advances in photocatalytic degradation of plastics and plastic-derived chemicals. *J Mater Chem A* 9:13402–13441. <https://doi.org/10.1039/D0TA12465F>
35. Bratovic A (2019) Degradation of micro- and nano-plastics by photocatalytic methods. *J Nanosci Nanotechnol Appl* 3:1–8. <https://doi.org/10.18875/2577-7920.3.304>
36. Nabi I, Bacha AU, Li K et al (2020) Complete photocatalytic mineralization of microplastic on TiO₂ nanoparticle film. *iSci* 23(7):101326. <https://doi.org/10.1016/j.isci.2020.101326>
37. Trus I, Radovenchyk I, Halysh V et al (2019) Innovative approach in creation of integrated technology of desalination of mineralized water. *J Ecol Eng* 20(8):107–113. <https://doi.org/10.12911/22998993/110767>
38. Litynska M, Antoniuk R, Tolstopalova N et al (2019) Ferric oxyhydroxide as fouling prevention reagent for low-pressure membranes. *J Ecol Eng* 20(3):77–84. <https://doi.org/10.12911/22998993/99736>
39. Trus I, Gomelya M (2021) Effectiveness nanofiltration during water purification from heavy metal ions. *J Chem Technol Metall* 56(3):615–620
40. Serhienko A, Dontsova T, Yanushevska O et al (2020) Ceramic membranes: new trends and prospects (short review). *Water Water Purif Technol Sci Tech News* 27(2):4–31
41. Poerio T, Piacentini E, Mazzei R (2019) Membrane processes for microplastic removal. *Mol* 24(22):4148. <https://doi.org/10.3390/molecules24224148>
42. Bayo J, López-Castellanos J, Olmos S (2020) Membrane bioreactor and rapid sand filtration for the removal of microplastics in an urban wastewater treatment plant. *Mar Pollut Bull* 156:111211. <https://doi.org/10.1016/j.marpolbul.2020.111211>

Nanostructured Iron-Based Sorption Materials for Drinking Water and Wastewater Treatment



Marta Litynska, Tetiana Dontsova, and Anna Gusak

Abstract The paper analyzed the usage and efficiency of different types (zero valent iron, oxides, hydroxides, oxyhydroxides, composites, etc.) of nanostructured iron-containing sorption materials in water treatment. It was noted that iron-based adsorbents are effective in removal wide range of pollutants (various organic compounds, arsenites, arsenates, phosphates, heavy metal ions, etc.). Nanoparticles of zero valent iron are one of the most popular iron-based nanomaterials for water treatment. There a lot of approaches to obtain these nanoparticles, including top-down (processing micro- or millimeter-sized iron) and bottom-up (using iron-containing compounds as starting materials) synthetic methods. Iron-based nanostructured materials are often used in the form of different doped oxides or nanocomposites with organic or inorganic substances. In the paper various methods of synthesis and application of nanostructured iron-based sorption materials are observed.

1 General

1.1 Introduction

Fresh water is very insignificant (about 3%) share of the total water on Earth, but parts of underground and surface water are extremely small (about 29% and less than 1%) [1]. Population growth leads to significant increasing of water demand and water crisis becomes real problem. Pure water is extremely important for efficient agriculture, energy production, chemical technologies, recreation, manufacturing, and

M. Litynska (✉) · T. Dontsova · A. Gusak
Igor Sikorsky Kyiv Polytechnic Institute, Kyiv, Ukraine
e-mail: m.litynska-2017@kpi.ua

T. Dontsova
e-mail: dontsova@ua.fm

A. Gusak
e-mail: maril91@ukr.net

many other various industries [2]. Evidently, water resources are extremely significantly affected by climate change, population density, and industry. Water demand may further escalate due to increasing of water consumption, extensive agriculture and non-ecological productions. Reckless water consumption has long resulted in water scarcity, while polluted water bodies and aquifers caused by agricultural and industrial activities dampens the sources of safe fresh water [2–6]. According to [6], in North China human induced excessive and non-rational water consumption is responsible for the substantially decreasing of rivers flow over the past 80 years. Although the capacity of wastewater treatment plants was increased, current water quality does not meet the national water requirements, because of the significant content of nitrogen compounds and high level of chemical oxygen demand. Wastewater and feedlots discharge are the main sources of these pollutants. A balance between the demand and resource of water is very important for economy of each country [2, 3]. The same problems are characteristic for Ukrainian rivers [7, 8]. Climate changes and different anthropogenic factors lead to the progress of overgrowth and «algal blooms» of Dnipro River. According to [8], during the period from 2010 to 2017, the area of overgrown Dnipro River (around Kyiv) increased more than 2 times and reached to 7.5% of the total water surface. From 2005 to 2017 the percentage of overgrowth of the water surface in the bays and straits of Dnipro River significantly increased to 14.5%, which is about 5 times more than in 2005 [8]. Phosphate contamination is one of the most significant reasons of algal blooms in Dnipro River.

But anthropogenic factors are not the only reasons of insufficient water quality in water bodies and aquifers. Leaching of toxic components (especially arsenic or heavy metal compounds) from minerals, rocks and soils, volcanic activity, biomass decomposition also pollute natural water.

Arsenic compounds, metal ions and fluoride-ions are common pollutants, which often intake to natural water, especially groundwater, due to leaching from different minerals or sediments. Arsenic compounds are often observed in natural surface water or groundwater and even in drinking water. Every year a lot of people are affected by toxic action of arsenic compounds [9]. Heavy metals are toxic, persistent and bio-accumulative, they quickly precipitate in natural water environment and tend to accumulate in sediments [10–12]. Sediments are the source of secondary contamination of water by heavy metals.

Natural organic matter is other commonly observed pollutant of surface water. Such waters often contain a lot of humic compounds, fulvic complexes, microbial polysaccharides, etc. [13]. Bacterial cells and algae produce extracellular and cellular organic compounds, including high-MW (>100 kDa) polysaccharides, peptides, proteins, etc. [14]. Presence of humic and fulvic compounds are the result of biomass decay [15]. During disinfection processes high content of natural organic matter can cause formation of toxic disinfection by-products. According to [16], aromatic disinfection by-products are significant intermediate products of dissolved organic matter during chlorination and chloramination processes. High molecular weight natural organic matter could convert to aromatic disinfection by-products via direct or indirect pathways and these compounds, especially heterocyclic, possess higher toxicity than a lot of other disinfection by-products [16].

Nowadays in the field of water treatment, there are different, competing and effective ways to remove toxic compounds. These methods include coagulation, electrocoagulation, ion exchange, nanofiltration, reverse osmosis, chemical precipitation, and also adsorption [17].

Adsorption is one of the most effective and popular methods of water treatment, because it allows the use of reusable adsorbents. Further to it, adsorbents can be made of recyclable, environmentally safe materials, while the efficiency of the method is not disimproved [18].

Iron-based sorption materials are effective sorbents for arsenic compounds removal, remediation of As-polluted soils, phosphate and humate removal in drinking water and wastewater treatment [19–21]. Low arsenic bioaccessibility by fixation in nanostructured iron-based materials is one of the significant advantages of this sorbents [22]. Thus, synthesis and application of novel nanostructured iron-based sorbents and nanocomposites are the areas of current interest due to the high toxicity of arsenic compounds and the widespread occurrence of these pollutants in natural water.

1.2 Types of Iron-Based Materials for Water Treatment

Iron-based sorption materials can be natural or artificial. Among examples of natural adsorbents there are iron-containing minerals, including hematite, magnetite, goethite, etc. But adsorbents with same chemical composition also can be synthesized. Nowadays there are a lot of effective iron-based materials for drinking water and wastewater treatment (Fig. 1).

At present, pollutants removal using natural materials or different industrial by-products has provided significant prospects for both economic and environmental positive developments in wastewater treatment procedures. The high cost of some adsorbents and significant regeneration time prevents to use these adsorbents in large scale systems. Scientists develop new adsorbents, which are both highly efficient and low-cost in the pollutant removal processes [23, 24].

Natural iron-based materials are relatively cheap, they include wustite (FeO), magnetite (FeO-Fe₂O₃), hematite (α -Fe₂O₃), maghemite (γ -Fe₂O₃), goethite (α -FeO(OH)), akaganeite (β -FeO(OH) with chloride-ions in structure), lepidocrocite (γ -FeO(OH)), ferroxhyte (δ -FeO(OH)), ferrihydrite (hydrrous ferric oxides), limonite (FeO(OH)·nH₂O), etc. All of these minerals can be used as adsorbents, but as usual adsorption capacity of natural materials is significantly lower, than adsorption capacity of artificial substances with similar chemical composition.

As part of focus on low-cost adsorbents, scientists research an eco-reagent that can be used as a basis for the production of adsorbents that can remove dissolved organic matter, different dyes and arsenic compounds—red mud [24–28]. It consists of iron hydroxide and is extracted as a waste product of the alumina production or some other ores processing. Adsorption of arsenic by red mud is a reaction that is based on hydrogen-ion concentration. An acidic solution with a pH range of 1.1–3.2

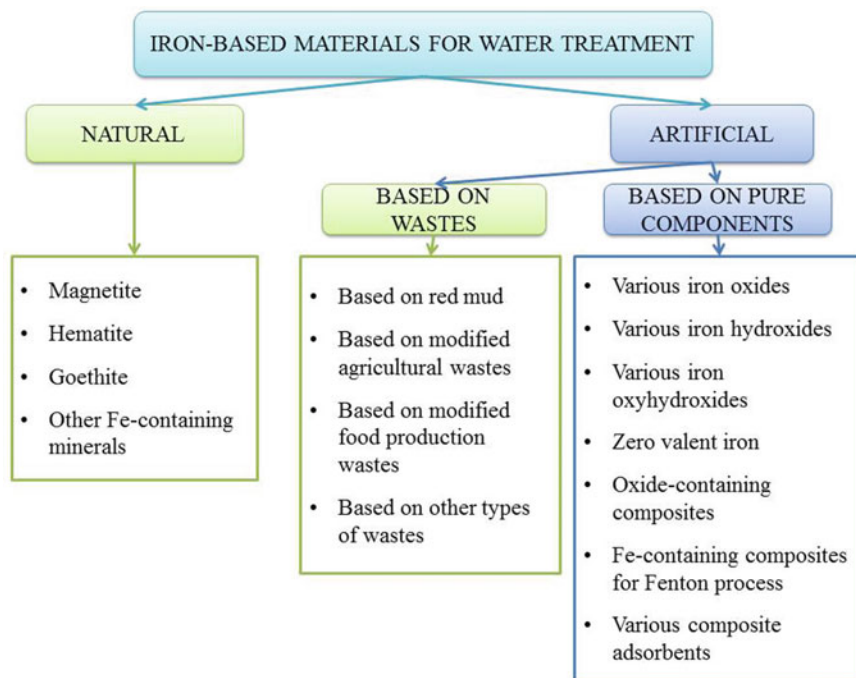


Fig. 1 Types of iron-based materials for water treatment

is effectual for extracting As(V), whereas an alkaline condition (pH 9.5) is preferable for removal As(III) [24, 28]. In the opinion of authors [25], activated carbon F300 modified by acidified red mud products can remove 98% humates with the initial humates concentration 4 g/L. In these sorption materials there are not only iron compounds, but also aluminum and titanium substances [26]. That's why adsorbents based on red mud are so effective.

Natural clay minerals modified by magnetic iron oxide combine advantages of natural and artificial adsorbents. They are relatively cheap, easily utilized, effective, and easy separate from treated water [28–32]. According to [33], modification by iron oxide nanoparticles significantly increases clinoptilolite efficiency in removal of methylene blue dye from aqueous solutions. Clinoptilolite without modification can remove only 26.8% of dye at pH = 3 and 48% at pH = 9, but modified clinoptilolite remove 96.4–98.6% and is effective at all pH range [33]. But modified clays often have lower adsorption capacity, than pure synthetic iron oxides.

Magnetite nanoparticles can be synthesized by different methods: constrained environment procedure, polyol method, hydrothermal technique, sonochemical procedure, electrochemical method, coprecipitation, etc. [34]. In accord with the first method it is possible to obtain magnetite nanoparticles with size 1–50 nm, second and fourth methods—about 10 nm, fifth approach—20–30 nm. Constrained environment

procedure is based on microemulsion structure, which involves magnetite nanoparticles synthesis mostly as a reverse emulsion corresponding to a water-in-oil suspension. In polyol method polyol has many functions: a solvent, reducing agent of the iron precursor, a stabilizer of nuclei growth step, aggregation preventer and the protective hydrophilic capping of nanoparticles surface. Hydrothermal technique is based on the ability of water to hydrolyze metal salts and dehydrate product under specific conditions of pressure and temperature. During sonochemical procedure acoustic cavitations are created into a liquid media. It leads to significant local increasing of pressure and temperature, which provoke chemicals to react in the gas state. In electrochemical method the first electrode gets oxidized into an aquatic solution of compound of metal, which is then reduced onto the cathode in presence of stabilizers. Co-precipitation is based on the partial oxidation of Fe^{2+} salts or on a maturing of stoichiometric mixture of Fe^{3+} and Fe^{2+} salts [34].

Maghemite nanoparticles synthesis in some moments is very similar to magnetite obtaining due to chemical composition and magnetic properties. This material can be synthesized by several methods: sol-gel, chemical precipitation, thermal-deposition, hydrothermal chemical, microemulsion, flame spray pyrolysis [35]. Thermal-deposition is the most popular method of maghemite nanoparticles synthesis due to it is simple and soft synthesis conditions. This approach is based on thermal decomposition of precursors. Ferric (III) acetylacetonate, iron nitrosophenyl hydroxylamine or iron pentacarbonyl are the most usable precursors. Dissolving of precursors in octyl ether and oleic or lauric acid and oxidation, leads to formation of iron oxide nanoparticles with size distribution in the range 4–16 nm [35]. According to [36], the first stage is to obtain prismatic shaped lepidocrocite nanoparticles. This material is prepared by precipitation and oxidation of FeCl_2 at room temperature [36, 37]. For transformation of lepidocrocite to maghemite, lepidocrocite powder is heated in a furnace under air at heating rates of 0.1–10 °C/min [36].

Hydrothermal synthesis is the main method of hematite production. In the opinion of authors [38], irregular hematite nanoparticles are synthesized using a water solution of ferric precursor and sodium acetate and hydrothermal heating at the temperature 180 °C during 12 h. But without usage of sodium acetate hematite ellipsoid 3D superstructures are obtaining. And in case of addition of urea and glycine hematite nanoplates are formed [38]. Thus, surfactants have very significant influence on the structure and morphology of hematite nanoparticles. The authors of the following work [39] produce iron oxide nanoparticles from laterite rock samples. After washing, drying, powdering, and sieving laterite is mixed with HCl solution and distilled water and refluxed for a digestion of laterite. The next stages are: centrifugation of the mixture, mixing with urea, heating at 90 °C under reflux conditions during 10 h, centrifugation of precipitate, calcination at 650 °C for 2 h. In this case the average hematite nanoparticle diameter is 35 nm and the purity is over 98% [39].

Most of the procedures for synthesis of nanocrystalline iron oxides require drastic conditions and complex mixtures of reagents, but in [40] authors produce nanocrystalline goethite-like hydrous ferric oxide nanoparticles by simple precipitation method using FeCl_3 , ammonia and HNO_3 . According to [41], goethite is

synthesized from $\text{Fe}(\text{NO}_3)_3$ solution with rapidly addition of KOH solution, dilution of precipitate by distilled water and heating in a closed polyethylene flask at the temperature $70\text{ }^\circ\text{C}$ for 60 h. Nanoparticle aggregation is one of the main problems in synthesis $\text{FeO}(\text{OH})$ nanomaterials. In [42] authors obtain 8–17 nm goethite nanoparticles (Fig. 2) by controlled synthesis at room atmosphere. They use secretory compounds from *Chlorella vulgaris* cells for prevention of nanoparticle aggregation.

Nanostructured $\beta\text{-FeO}(\text{OH})$ is other popular component of nanocomposite materials for water treatment [43]. But this iron-based compound also can be used as a seed in synthesis $\varepsilon\text{-Fe}_2\text{O}_3$ [44]. During calcination $\beta\text{-FeO}(\text{OH})$ is transformed to $\gamma\text{-Fe}_2\text{O}_3$, which is transformed in $\varepsilon\text{-Fe}_2\text{O}_3$.

In this case calcination temperature has a very significant influence on nanoparticles structure. Cubic rectangular-shaped $\varepsilon\text{-Fe}_2\text{O}_3$ nanocrystals are formed at low calcination temperature ($800\text{ }^\circ\text{C}$) and elongated rod-shaped $\varepsilon\text{-Fe}_2\text{O}_3$ nanocrystals are synthesized at high temperature ($1000\text{ }^\circ\text{C}$) [44]. According to [45], the most popular method of $\varepsilon\text{-Fe}_2\text{O}_3$ synthesis is based on the thermal annealing of maghemite nanoparticles. In this case $\varepsilon\text{-Fe}_2\text{O}_3$ forms as an intermediate phase between the maghemite and hematite ($\gamma \rightarrow \varepsilon \rightarrow \alpha$ pathway). But authors [45] demonstrate, that the reverse $\varepsilon \rightarrow \alpha$ transformation is possible at the temperature higher $600\text{ }^\circ\text{C}$.

Nanoparticles of zero valent iron (nZVI) are one of the most popular iron-based nanomaterials for water treatment. There a lot of approaches to obtain these nanoparticles, including top-down (processing micro- or millimeter-sized iron) and bottom-up (using iron-containing compounds as starting materials) synthetic methods (Fig. 3) [46].

Synthesis pathways have very big influence on structure and application of zero valent iron nanoparticles (Fig. 4). That's why this type of iron-based nanomaterials is very popular in water treatment not only as single component, but also as part of different nanocomposites. Zero valent iron nanoparticles are often used with carbon materials or other porous or nonporous supports [47]. Significant advantage is that nZVI and its nanocomposites can be used also as catalyst in Fenton processes for organic compounds decomposition [46].

Summarizing the above, it should be noted that iron-based nanostructured materials is often used in the form of different doped oxides or nanocomposites with organic or inorganic substances [48–52].

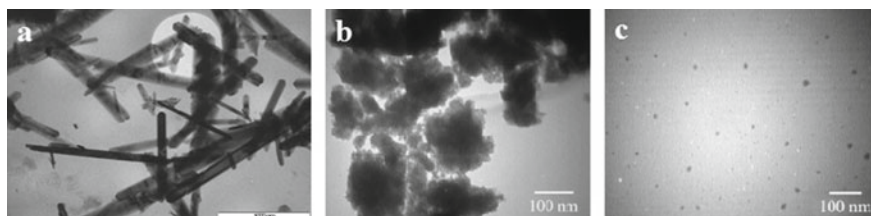


Fig. 2 Influence of synthesis conditions on goethite structure: **a**–nanocrystalline goethite-like hydrous ferric oxide [41], **b**–uncontrolled synthesis [42], **c**–controlled synthesis [42]

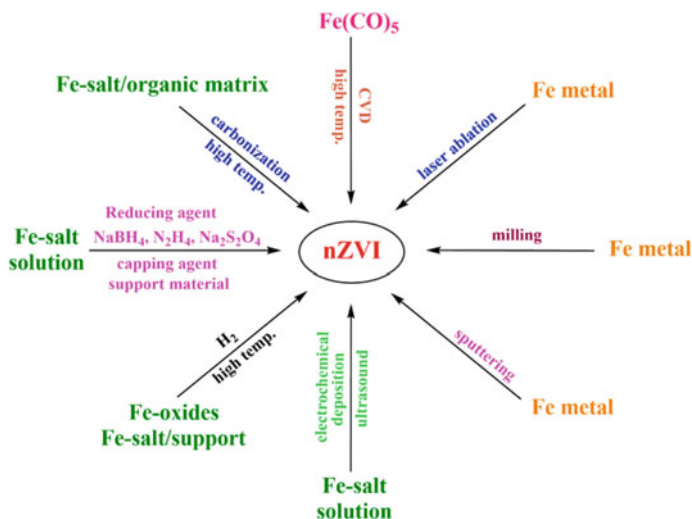


Fig. 3 Synthetic methods of zero valent iron nanoparticles [46]

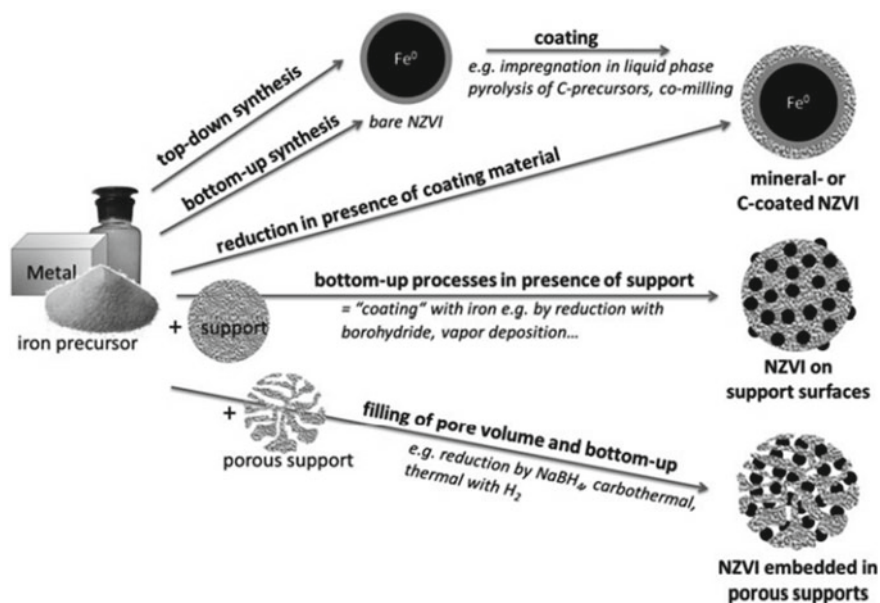


Fig. 4 Synthesis pathways of zero valent iron nanoparticles [47]

2 Usage and Perspectives of Iron-Based Sorption Materials in Water Treatment

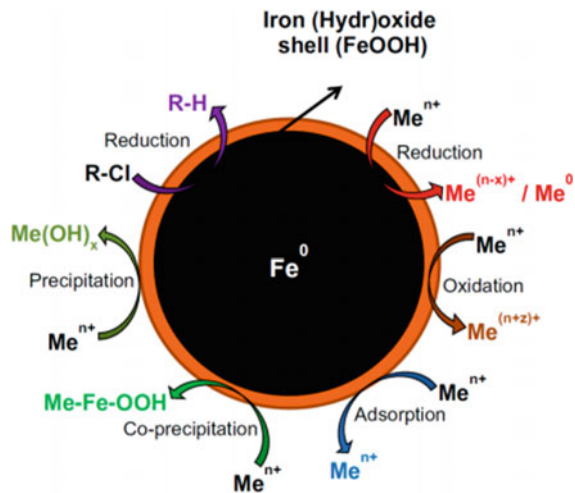
2.1 Application and Perspectives of Zero Valent Iron Nanoparticles

Zero valent iron nanoparticles and their composites have extremely wide usage for ecological purposes, including removal from water antibiotics, dyes, halogenated organic compounds, heavy metal ions, arsenates, arsenites, nitrates, etc. Also nZVI can be used for remediation of polluted soils, neutralization of contaminated sediments in water bodies and treatment of polluted groundwater in wells [47]. Figure 5 demonstrates various mechanisms for the removal of organic and inorganic pollutants from water by nZVI.

According to review data which represented in [47], bare nZVI can remove 8173 mg U(VI)/g, 102 mg As(III)/g, 118 mg As(V)/g; nZVI on Mg(OH)₂ support can remove 1986,6 mg Pb(II)/g.

Other important factor is toxic action of nZVI due to interaction with cell membrane and provoking of oxidation stress [48]. It is positive in context of disinfection, but negative for organisms, which can consume residual nZVI with drinking water.

Fig. 5 Mechanisms of pollutants removal by ZVI nanoparticles [47, 53]



2.2 Application and Perspectives of Oxide and Oxyhydroxide Iron-Based Sorption Materials

Oxide and oxyhydroxide iron-based nanomaterials are also often used for drinking water and wastewater treatment and soil remediation.

In consonance with works [9, 20, 54, 55], nanostructured iron oxyhydroxide obtained by homogeneous precipitation from iron(III) chloride solution demonstrated high efficiency in removal of As(III) and As(V) (about 70 mg/g) and humates (more than 98% removal). This adsorbent is suitable for hybrid adsorption-membrane filtration treatment method due to its particle size and filtration properties [54]. In accord with [56], ultrafine amorphous goethite nanoparticles (size about 5 nm) decorated graphitic carbon nitride demonstrate high efficiency in Fenton-like and photocatalytic processes. So, this adsorbent can be very effective in removal antibiotics from water.

The authors of the following work [19] give information that goethite nanospheres are significantly more effective in soil remediation, than zero valent iron nanoparticles. At the dose of 0.2% goethite nanospheres immobilize 82.5% of arsenic, while ZVI nanoparticles achieve notable results at the dose of 2% (89.5% decrease in As) [19].

Also as nZVI, other iron-based materials can be used for treated contaminated water in wells. In accord with [57], humic acid-coated goethite nanoparticles are proposed as an effective reagent for the in situ nanoremediation of contaminated aquifers (2 m radius of influence).

In the opinion of authors [58–61], iron oxide nanoparticles and their composites show high efficiency in removal organic pollutants and heavy metals. Chitosan-coated magnetite nanoparticles have a maximum adsorption capacity of 243.9 mg/g in case of removal of Evans Blue dye. Other anionic dyes (Cy5.5, Acid Green 25, Acid Yellow 25 and Acid Red 1) are also effectively removed by this composite [59].

In work [60] authors cited that Fe_3O_4 -silica can remove 97.34 and 90% for Pb(II) and Hg(II), respectively; extran- Fe_3O_4 nanoparticles can absorb about 90.5% of As(III); δ - FeOOH -coated γ - Fe_2O_3 has adsorption capacity be 25.8 mg Cr(VI)/g; amino-modified Fe_3O_4 has maximum adsorption capacity 12.43 mg Cu(II)/g and ions and 11.24 mg Cr(VI)/g.

Magnetic iron oxide also can be toward adsorbent and photocatalyst (Fig. 6).

According to [49], the nanomaterials of ortho-hexagonal Fe_2O_3 , Co- Fe_2O_3 , and Ni- Fe_2O_3 are very effective in Pb(II) adsorption (93.9, 136.0, and 97.5 mg/g, respectively).

It should be noted that in no case all oxide and oxyhydroxide iron-based nanostructure materials demonstrate high adsorption properties due to significant specific area.



Fig. 6 Mechanisms of pollutants removal by magnetic iron oxide [51]

3 Conclusions

Therefore, adsorption is one of the most effective and popular methods of water treatment, because it allows the use of reusable adsorbents. Further to it, adsorbents can be made of recyclable, environmentally safe materials. The high cost of some adsorbents and significant regeneration time prevents to use these adsorbents in large scale systems, but iron-based materials are relatively cheap due to low-cost of their precursors. There are different types of iron-containing adsorbents, but zero valent iron nanoparticles are one of the most popular and effective. But in some cases (arsenic immobilization in contaminated soils) oxyhydroxide adsorbents is more effective than zero valent iron nanoparticles. Iron-based nanostructure materials can effectively remove such dangerous pollutants as heavy metals, arsenic compounds, halogenated organics, antibiotics, etc. Consequently, low-cost adsorbents are interesting for many researchers, who are working to improve sorption activity and expand these material applications in the removal of pollutants.

Acknowledgements The authors thank colleagues and students Chemical Technological Faculty of National Technical University of Ukraine «Igor Sikorsky Kyiv Polytechnic Institute» for actively participating in the discussion on the study topic.

References

1. Velmurugan A, Swarnam P, Subramani T et al (2020) Water demand and salinity. In: Desalination - challenges and opportunities.
2. Zuraini A, Jaharudin P, Noorhaslinda KAR et al (2019) Factors affecting water demand: macro evidence in Malaysia. *J Ekonomi Malays* 53(1):17–25
3. Dounghanee P (2016) The nexus of agricultural water use and economic development level. *Kasetsart J Soc Sci* 37(1):38–45

4. Shah SH, Narain V (2019) Re-framing India's "water crisis": an institutions and entitlements perspective. *Geoforum* 101:76–79
5. Amiraslani F, Dragovich D (2021) Portraying the water crisis in Iranian newspapers: an approach using structure query language (SQL). *Water* 13(6):838
6. Dai D, Xu X, Sun M et al (2020) Decrease of both river flow and quality aggravates water crisis in north china: a typical example of the upper yongding river watershed *Environ Monit Assess* 192(7)
7. Kulishenko O, Klymenko N (2021) Cycles of solar activity as basis for forecasting the Dnieper water. *Water Water Purif Technol Sci Tech News* 30(2):3–17
8. Tomchenko O, Panchenko R, Mazurkevich L (2020) Change monitoring of the Dnipro river within Kyiv using satellite information. *Water Water Purif Technol Sci Tech News* 27(2):97–107
9. Litynska M, Dontsova T (2020) Suspension sorbents for removal of arsenic compounds and humates from water. *Water Water Purif Technol Sci Tech News* 28(3):14–25
10. Luo P, Xu C, Kang S et al (2021) Heavy metals in water and surface sediments of the fenghe river basin, china: assessment and source analysis. *Water Sci Technol* 1–19
11. Kumar V, Sharma A, Kumar R et al (2018) Assessment of heavy-metal pollution in three different Indian water bodies by combination of multivariate analysis and water pollution indices. *Hum Ecol Risk Assess Int J* 26(1):1–16
12. Joseph L, Jun BM, Flora JR et al (2019) Removal of heavy metals from water sources in the developing world using low-cost materials: a review. *Chemosphere* 229:142–159
13. Rosario-Ortiz FL, Snyder SA, Suffet IH (2007) Characterization of dissolved organic matter in drinking water sources impacted by multiple tributaries. *Water Res* 41(18):4115–4128
14. Pivokonsky M, Safarikova J, Baresova M et al (2014) A comparison of the character of algal extracellular versus cellular organic matter produced by cyanobacterium, diatom and green alga. *Water Res* 51:37–46
15. Kleber M, Eusterhues K, Keiluweit M et al (2015) Chapter one - mineral–organic associations: formation, properties, and relevance in soil environments. In Sparks DL (ed) vol 130. Academic Press, pp 1–140
16. Liu X, Chen L, Yang M et al (2020) The occurrence, characteristics, transformation and control of aromatic disinfection by-products: a review. *Water Res* 184:116076
17. Khan NA, Khan SU, Ahmed S et al (2020) Recent trends in disposal and treatment technologies of emerging-pollutants-a critical review. *TrAC Trends Anal Chem* 122:115744
18. Dotto GL, McKay G (2020) Current scenario and challenges in adsorption for water treatment. *J Environ Chem Eng* 8(4):103988
19. Baragaño D, Alonso J, Gallego JR et al (2020) Zero valent iron and goethite nanoparticles as new promising remediation techniques for As-polluted soils. *Chemosphere* 238:124624
20. Litynska M, Dontsova T, Yanushevska O et al (2021) Development of iron-containing sorption materials for water treatment from arsenic compounds. *East Eur J Enterp Technol* 10(110):35–42
21. Moreira RFP, Vandresen S, Luiz DB et al (2017) Adsorption of arsenate, phosphate and humic acids onto acicular goethite nanoparticles recovered from acid mine drainage. *J Environ Chem Eng* 5(1):652–659
22. Ciminelli VST, Antônio DC, Caldeira CL et al (2018) Low arsenic bioaccessibility by fixation in nanostructured iron (Hydr)oxides: quantitative identification of As-bearing phases. *J Hazard Mater* 353:261–270
23. Choong TSY, Robiaha Y, Koaya FLG et al (2019) Arsenic toxicity, health hazards and removal techniques from water: an overview. *Desalination* 217:139–166
24. Hao L, Liu M, Wang N et al (2018) A critical review on arsenic removal from water using iron-based adsorbents. *RSC Adv* 8(69):39545–39560
25. Kyrii SO, Kosogina IV, Astrelin IM et al (2018) Investigation of the activated carbon modified by wastes of alumina production. *Voprosy khimii I khimicheskoi tekhnologii* 2:70–78
26. Kyrii S, Dontsova T, Kosogina I et al (2020) Local wastewater treatment by effective coagulants based on wastes. *J Ecol Eng* 21(5):34–41

27. Astrelin I, Kosogina I, Kyrii S (2020) Utilization processing of waste of alumina production into water treatment reagents. In: Resource-saving technologies of raw-material base development in mineral mining and processing. Multi-authored monograph. Petroșani, Romania: Universitas Publishing, p 21
28. Yang JS, Lee JY, Park YT et al (2016) Adsorption of As(III), As(V), Cd(II), Cu(II), and Pb(II) from aqueous solutions by natural muscovite. *Sep Sci Technol* 45:814–823
29. Makarchuk O, Dontsova T, Perekos A (2017) Magnetic nanocomposite sorbents on mineral base. *Springer Proc Phys* 195:705–719
30. Fadillah G, Yudha SP, Sagadevan S et al (2020) Magnetic iron oxide/clay nanocomposites for adsorption and catalytic oxidation in water treatment applications. *Open Chem* 18(1):1148–1166
31. Mykhailenko NO, Makarchuk OV, Dontsova TA et al (2015) Purification of aqueous media by magnetically operated saponite sorbents. *East Eur J Enterp Technol* 10(76):13–20
32. Dontsova TA, Nahirniak SV, Astrelin IM (2019) Metaloxide nanomaterials and nanocomposites of ecological purpose. *J Nanomater* 2019:5942194
33. Badeenezhad A, Azhdarpoor A, Bahrami S et al (2019) Removal of methylene blue dye from aqueous solutions by natural clinoptilolite and clinoptilolite modified by iron oxide nanoparticles. *Mol Simul* 45(7):564–571
34. Wallyn J, Anton N, Vandamme TF (2019) Synthesis, principles, and properties of magnetite nanoparticles for in vivo imaging applications—a review. *Pharm* 11:601
35. Kour S, Sharma RK, Jasrotia R et al (2019) A brief review on the synthesis of maghemite (γ - Fe_2O_3) for medical diagnostic and solar energy applications. In: *Advances in basic Science (ICABS 2019)*. AIP Conf Proc, vol 2142, no 1, pp 1–7
36. Trushkina Y, Tai CW, Salazar-Alvarez G (2019) Fabrication of maghemite nanoparticles with high surface area. *Nanomaterials* 9(7):1004
37. Kozin PA, Salazar-Alvarez G, Boily JF (2014) Oriented aggregation of lepidocrocite and impact on surface charge development. *Langmuir ACS J Surf Colloids* 30:9017–9021
38. Tadic M, Trpkov D, Kopanja L et al (2019) Hydrothermal synthesis of hematite (α - Fe_2O_3) nanoparticle forms: synthesis conditions, structure, particle shape analysis, cytotoxicity and magnetic properties. *J Alloy Compd* 792:599–609
39. Dissanayake DMSN, Mantilaka MMMGPG, Palihawadana TC et al (2019) Facile and low-cost synthesis of pure hematite (α - Fe_2O_3) nanoparticles from naturally occurring laterites and their superior adsorption capability towards acid-dyes. *RSC Adv* 9(37):21249–21257
40. Lunin AV, Kolychev EL, Mochalova EN et al (2019) Synthesis of highly-specific stable nanocrystalline goethite-like hydrous ferric oxide nanoparticles for biomedical applications by simple precipitation method. *J Colloid Interface Sci* 541:143–149
41. Adebayo GB, Adekola FA, Adegoke HI et al (2020) Synthesis and characterisation of goethite, activated carbon and their composite. *J Chem Technol Metall* 55(5):1068–1077
42. Ghanbariasad A, Taghizadeh SM, Show PL et al (2019) Controlled synthesis of iron oxyhydroxide (FeOOH) nanoparticles using secretory compounds from *Chlorella vulgaris* microalgae. *Bioengineered* 10(1):390–396
43. Akhrame MO, Fagbayigbo BO, Perea O et al (2021) Beta- FeOOH nanoparticles: a promising nano-based material for water treatment and remediation. *J Nanopart Res* 23(1)
44. Tokoro H, Fukui J, Watanabe K et al (2020) Crystal growth control of rod-shaped ϵ - Fe_2O_3 nanocrystals. *RSC Adv* 10(65):39611–39616
45. Tadic M, Milosevic I, Kralj S et al (2020) Surface-induced reversal of a phase transformation for the synthesis of ϵ - Fe_2O_3 nanoparticles with high coercivity. *Acta Mater* 188:16–22
46. Pasinszki T, Krebsz M (2020) Synthesis and application of zero-valent iron nanoparticles in water treatment, environmental remediation, catalysis, and their biological effects. *Nanomaterials* 10(5):917
47. Phenrat T, Lowry G (2019) Nanoscale zerovalent iron particles for environmental restoration. In: *From fundamental science to field scale engineering applications*, 1st edn. Springer
48. Zhuang Y, Wang X, Zhang L et al (2019) Fe-Chelated polymer templated graphene aerogel with enhanced Fenton-like efficiency for water treatment. *Environ Sci Nano* 6(11):3232–3241

49. Chen W, Lu Z, Xiao B et al (2019) Enhanced removal of lead ions from aqueous solution by iron oxide nanomaterials with cobalt and nickel doping. *J Clean Prod* 211:1250–1258
50. Spivakov AA, Lin CR, Jhang CJ et al (2019) Synthesis and characterization of carbon-coated wustite nanoparticles. *Mater Lett* 249:147–150
51. Leonel AG, Mansur AA, Mansur HS (2021) Advanced functional nanostructures based on magnetic iron oxide nanomaterials for water remediation: a review. *Water Res* 190:116693
52. Otero-González L, Mikhailovsky SV, Václavíková M et al (2020) Novel nanostructured iron oxide cryogels for arsenic (As(III)) removal. *J Hazard Mater* 381:120996
53. O'Carroll D, Sleep B, Krol M et al (2013) Nanoscale zero valent iron and bimetallic particles for contaminated site remediation. *Adv Water Resour* 51:104–122
54. Litynska M, Antoniuk R, Tolstopalova N et al (2019) Ferric oxyhydroxide as fouling prevention reagent for low-pressure membranes. *J Ecol Eng* 20(3):77–84
55. Litynska M, Tolstopalova N, Astrelin I et al (2019) Influence of foreign ions on the adsorption of arsenate on iron(III) oxides and hydroxides. *Voprosy khimii i khimicheskoi tekhnologii* 3:22–29
56. Zhao H, Tian C, Mei J et al (2020) Synergistic effect and mechanism of catalytic degradation toward antibiotic contaminants by amorphous goethite nanoparticles decorated graphitic carbon nitride. *Chem Eng J* 390:124551
57. Velimirovic M, Bianco C, Ferrantello N et al (2020) A large-scale 3d study on transport of humic acid-coated goethite nanoparticles for aquifer remediation. *Water* 12(4):1207
58. Pan Z, Zhu X, Satpathy A et al (2019) Cr(VI) adsorption on engineered iron oxide nanoparticles: exploring complexation processes and water chemistry. *Environ Sci Technol* 53(20):11913–11921
59. Lee SY, Shim HE, Yang JE et al (2019) Continuous flow removal of anionic dyes in water by chitosan-functionalized iron oxide nanoparticles incorporated in a dextran gel column. *Nanomaterials* 9(8):1164
60. Bhatia R, Singh R (2019) A review on nanotechnological application of magnetic iron oxides for heavy metal removal. *J Water Process Eng* 31:100845
61. Singh S, Barick KC, Bahadur D (2013) Functional oxide nanomaterials and nanocomposites for the removal of heavy metals and dyes. *Nanomaterials Nanotechnol* 3:20

Tunneling of the Dirac Quasiparticles Through the Fermi Velocity Barriers Based on the Gapped Graphene



A. M. Korol, N. V. Medvid, A. I. Sokolenko, and O. Shevchenko

Abstract The transmission of ultrarelativistic quasi-electrons through barrier structures based on the gapped graphene is studied. The transmission coefficient is calculated within the continuum model using the solution of the Dirac-type equation for two types of structures in which the barriers are created due to the fact that the Fermi velocity acquires different values in the barrier and out-of-barrier regions. In one structure, the barrier has a step-like shape, the other is a single barrier resonance tunneling structure. The results of a detailed analysis of the transmission spectra depending on the parameters of the problem: the energy of the quasiparticles, the angle of their incidence on the barrier, the size of the energy gap, and the thickness of the barrier, are presented.

Keywords Gapped graphene · Transmission coefficient · Velocity barriers

1 Introduction

As known [1], graphene has a number of unique properties, which is why a large number of works are devoted to its study. Among these properties, we will name only some: a linear dispersion relation for the quasiparticles, unusual quantum Hall effect, the property of chirality, the Klein tunneling, high mobility, ballistic transport, etc. In addition, the use of graphene promises to be very promising in modern nanoelectronics. Charge carriers in graphene are fermions with a pseudospin equal to 0.5, and they obey an equation similar to Dirac relativistic equation. The key parameter that characterizes the dispersion relation of the Dirac quasiparticles is the Fermi velocity. Therefore, it is clear that significant efforts have been made to be able to control this value and also to use this control in practice [2–13]. For this purpose, a number of

A. M. Korol (✉) · N. V. Medvid · A. I. Sokolenko · O. Shevchenko
National University for Food Technologies, Volodymyrska Str., 68, Kyiv, Ukraine
e-mail: korolam@ukr.net

A. M. Korol
Laboratory On Quantum Theory in Linköping, International Society for Independent Research (ISIR), Box 8017, 58080 Linköping, Sweden

© The Author(s), under exclusive license to Springer Nature Switzerland AG 2023
O. Fesenko and L. Yatsenko (eds.), *Nanomaterials and Nanocomposites, Nanostructure Surfaces, and Their Applications*, Springer Proceedings in Physics 279,
https://doi.org/10.1007/978-3-031-18096-5_14

different methods were proposed and experimentally tested. Many articles have been published examining the effect of Fermi velocity on the characteristics of various graphene structures. The Fermi velocity can take different values in different parts of the given structures, i.e., be a spatially dependent quantity. In particular, in [2–12], the influence of the Fermi velocity on such structures as one- and two-barrier resonance-tunneling structures, as well as on different superlattices was analyzed. Both electrostatic and magnetic barriers were taken into account. Despite the good prospects for the use of graphene in practice, it has some drawbacks. From the point of view of the use of graphene as an element of transistor circuits, one of such defects is the Klein paradox, according to which graphene has a high transmission coefficient T for carriers the angle of incidence of which on the barrier θ is normal or close to normal (and $T = 1$ for $\theta = 0$). To correct this defect, various approaches have been proposed, one of which is the use of graphene with an energy gap (the gapped graphene). Motivated by the above, in this paper, we analyze the tunneling process in structures, part of which is the gapped graphene and show in which cases the effect of the energy gap on the transmission coefficient is significant. We must note here that the obtained expression for the transmission rates accounts for the π phase change of the transmitted wave function. It is known that taking into account this change leads to significant changes in the transmission spectra [14, 15], in particular, it manifests the phenomenon of the supertunneling [13]. We analyze the tunneling process in two structures: one with the step-like Fermi velocity barrier and another containing the single barrier with a finite width. The barrier region of these structures consists of the gapped graphene.

2 Model and Formulae

Assume that there is the single rectangular one-dimensional Fermi velocity barrier with the width d , the interfaces coordinates being $x_l = 0$ and $x_r = d$ for the left and the right interfaces, respectively. This barrier (of a rectangular shape) is created due to the fact that the Fermi velocity has different values in the barrier and out-of-barrier regions of the given structure; that is, we believe that both out-of-barrier regions consist of the massless graphene, and the barrier area is represented by the gapped graphene. The low-energy fermion excitations in the considered structure based on the gapped graphene can be described by the following Hamiltonian (see, e.g., [1]):

$$H = -iv_F \left(\sigma_x \frac{\partial}{\partial x} + \sigma_y \frac{\partial}{\partial y} \right) + \Delta \sigma_z \quad (1)$$

where Δ is half of the width of the energy gap, $\Delta = mv_F^2$, m quasielectron mass, v_F the Fermi velocity, σ_x and σ_y are the Pauli matrices, and σ_0 the unit matrix, and we put $\hbar = 1$.

In the case when the Fermi velocity varies in space, this Hamiltonian is not the hermitian one [16, 17]. Assume that the Fermi velocity depends on the coordinate x (only). As usual in the relevant cases, it is assumed also that the barrier width is much larger than the near-interface regions associated with the gradual change in the Fermi velocity. Then in accordance with the considerations made in [16, 17], we may present the Hamiltonian of the problem as follows:

$$H = -i\sqrt{v_F(x)}\left[\sigma_x \frac{\partial}{\partial x} \sqrt{v_F(x)} + \sqrt{v_F(x)}\sigma_y \frac{\partial}{\partial y}\right] + \Delta\sigma_z \quad (2)$$

and now it has the hermitian form [16, 17]. We must keep in mind that the derivative acts on the product $\sqrt{v_F(x)}\psi = \phi$ where ψ are the spinorial eigenfunctions. If the electron wave moves along the axis Ox from the left to the right, then for the wave functions in the left and in the right out-of-barrier regions it is possible to write, respectively [13, 15]:

$$\begin{aligned} \psi_l(x, y) &= \frac{1}{\sqrt{2}} \begin{pmatrix} 1 \\ e^{i\theta} \end{pmatrix} e^{i(k_x x + k_y y)} + \frac{r}{\sqrt{2}} \begin{pmatrix} 1 \\ e^{i(\pi - \theta)} \end{pmatrix} e^{i(-k_x x + k_y y)} \\ \psi_r(x, y) &= \frac{t}{\sqrt{2}} \begin{pmatrix} 1 \\ e^{i\theta} \end{pmatrix} e^{i(k_x x + k_y y)} \end{aligned}$$

for the barrier region

$$\begin{aligned} \psi_b(x, y) &= \frac{a}{\sqrt{2}} \begin{pmatrix} \gamma \\ \delta e^{i(\varphi + \pi)} \end{pmatrix} e^{i(q_x x + k_y y)} + \frac{b}{\sqrt{2}} \begin{pmatrix} \gamma \\ \delta e^{-i\varphi} \end{pmatrix} e^{-i(q_x x + k_y y)} \\ \gamma &= \sqrt{1 + \Delta} / \sqrt{\Delta^2 + v_{F2}^2 q_x^2}, \\ \delta &= \sqrt{1 - \Delta} / \sqrt{\Delta^2 + v_{F2}^2 q_x^2} \\ k_x &= \frac{E \cos \theta}{v_{F1}}, \quad q_x = \sqrt{\frac{E^2 - \Delta^2}{v_{F2}^2} - k_y^2}, \quad \theta = \arctan\left(\frac{k_y}{k_x}\right), \end{aligned} \quad (3)$$

and we assume that energy $E > 0$.

Using the following boundary conditions ([16, 17])

$$\begin{aligned} \sqrt{v_{F1}}\psi_l(x = 0^-) &= \sqrt{v_{F2}}\psi_b(x = 0^+) \\ \sqrt{v_{F2}}\psi_b(x = d^-) &= \sqrt{v_{F1}}\psi_r(x = d^+) \end{aligned} \quad (4)$$

one can find the coefficient t in expressions for the wave functions, and hence, the transmission coefficient $T = |t|^2$:

$$T(E, \varphi) = \rho \cos^2 \theta \cos^2 \varphi^2 / \left\{ \rho \cos^2 \theta \cos^2 \varphi^2 \cos(q_x d)^2 + \sin(q_x d)^2 [1 - \rho \sin(\theta) \sin(\varphi)]^2 \right\},$$

$$\rho = \frac{\varepsilon K}{\sqrt{\Delta^2 + (\varepsilon K)^2}}, K = \sqrt{k_x^2 + k_y^2}, \varepsilon = v_{F2} / v_{F1}, \tag{5}$$

v_{F2}, v_{F1} , being the Fermi velocity in the barrier and in the out-of-barrier regions, respectively. Using a similar approach, we can also derive the expression for the transfer coefficient T for a structure with a step-like barrier. The difference is that this structure consists of only two parts, the right of which is a semi-infinite Fermi velocity barrier and the left one is the pristine graphene. As in the above case of the single barrier with a finite width, the dispersion relation is expressed by formulas (3) in the out-of-barrier and in the barrier regions, respectively.

3 Results and Discussions

Figure 1 shows the dependence of the transmission coefficient T on an angle of incidence of quasielectrons on the barrier in a step-like structure. The Fermi velocity in the right part of the structure differs from the velocity in the left part so that the right part is a barrier for quasielectrons.

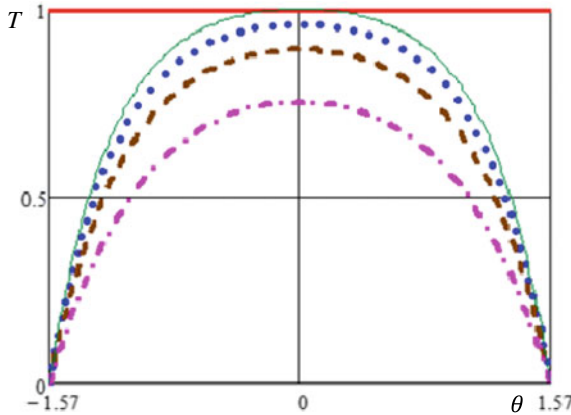


Fig. 1 Dependence of the transmission coefficient T on the incidence angle θ for the step-like structure. The values of the parameters for Fig. 1 are as follows: $E = 0.5, d = 1, \varepsilon = 0.3$ for all curves except for thick solid (red online) one for which $\varepsilon = 1; \Delta = 0$ for thick and thin solid (green) lines and $\Delta = 0.2, 0.3, 0.4$ for the dotted (blue), dashed (brown), and dashed-dotted (magenta) lines, respectively; the quantity θ is given in radians for all figures

Characterizing the presented in Fig. 1 dependence, we note the following: 1. Graph $T(E)$ has a pronounced angular dependence, and the barrier is the most transparent for the normal incidence of particles ($\theta = 0$) and its vicinity. 2. There is a marked decrease in T for all angles of incidence and its value increases with increasing energy gap Δ . 3. The Klein paradox disappears, i.e., the transmission for a normal incidence is not perfect. 4. The values of T significantly depend on the parameter ε . Note also that for many parameter values, the formation of the dependence $T(E)$ is influenced by the so-called critical angle. It is understood as such an angle that for all incidence angles greater than the critical one transmission rates falls sharply. The value of the critical angle can be derived using the Snell law and it is equal to

$$\theta_c = \arcsin\left(\sqrt{(E^2 - \Delta^2)} / E\varepsilon\right) \tag{6}$$

A horizontal solid (red) line, the value of T is the maximum ($T = 1$) for any angle of incidence. It refers to values: $\Delta = 0, \varepsilon = 1$, that is, to absence of the barrier.

It is seen that this dependence is not monotonic; its important feature is the presence of a maximum for a certain value of ε . Before reaching this maximum value of ε , the function $T(E)$ increases quite smoothly, and then falls sharply. At rather big values of Δ , the specified maximum does not take place any more. But note that such Δ values are already close to those that can be obtained in practice.

Regarding the dependence of T on energy of incident quasielectrons E , it should be noted that this dependence for the step-like barrier is monotonic, namely the value of T increases with increasing E . (Naturally, exceptions are small values of energy which are comparable to Δ). Obviously, the growth rate depends on the values of all parameters of the problem.

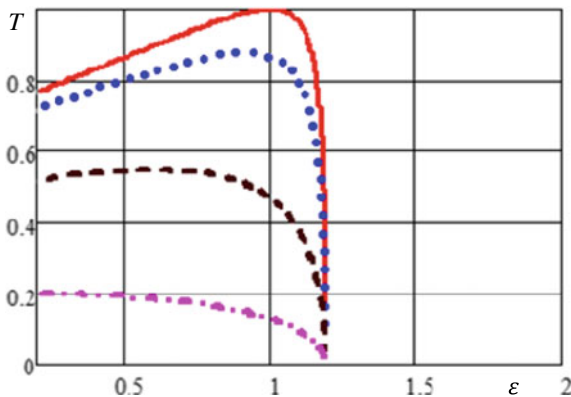


Fig. 2 Dependence of the transmission coefficient T on the parameter ε for the step-like structure. The values of the parameters for Fig. 2 are as follows: $E = 0.5, d = 1, \theta = 1$ for all curves, $\Delta = 0, 0.2, 0.4, 0.49$ for the solid (red), dotted (blue), dashed (brown), and dashed-dotted (magenta) lines, respectively

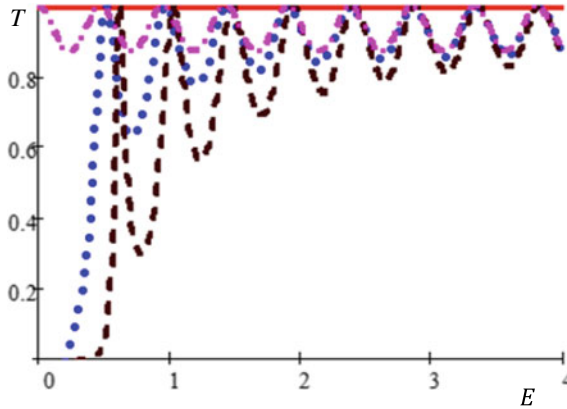


Fig. 3 Dependence of the transmission coefficient T on the quasiparticle energy E for the single barrier structure. The values of the parameters are as follows: $\theta = 0.5$, $d = 2$ for all lines; $\Delta = 0$, $\varepsilon = 1$ for the solid (red) line; $\Delta = 0$, $\varepsilon = 0.3$ for the dashed-dotted (magenta) curve; $\varepsilon = 0.3$, $\Delta = 0.2$, 0.4 for the dotted (blue) and dashed (brown) curves, respectively

The dependence of T on Δ for a given structure is also monotonic: The value of T decreases with increasing Δ ; here, it should be borne in mind that there may be different slopes of function $T(\Delta)$ for different delta values depending on the values of the problem parameters.

Figure 3 shows the dependence of T on the quasiparticles energy E for a structure with a single barrier of finite thickness d . This dependence is radically different from the similar one for a step-shaped barrier. Here, it is primarily characterized by the presence of numerous peaks with a maximum value of $T = 1$. These maxima are related to the presence in the expression for the transmission coefficient of the term $\sin(qd)$, which is zeroed under the condition $qd = n\pi$, as a result of which T becomes equal to 1. Thus, these maxima are Fabry–Perot-type resonances.

Their position on the energy axis is determined by the following formula.

$$d\sqrt{\frac{E^2 - \Delta^2}{\varepsilon^2} - k_y^2} = n\pi, \quad (7)$$

where $n = 1, 2, 3 \dots$

It follows from this formula that a smaller value of ε corresponds to a larger number of oscillations in a given range of Δ values. According to it, increasing the thickness of the barrier d facilitates the formation of Fabry–Perot resonances.

In particular, it follows from this formula that the energy position of the Fabry–Perot resonance data depends on the magnitude of Δ , which is confirmed by Fig. 3. The horizontal line with the value of $T = 1$ in Fig. 3 corresponds to the case of massless graphene and the value of $\varepsilon = 1$, i.e., the actual absence of the Fermi velocity barrier. If the barrier is present ($\varepsilon \neq 0$) but $\Delta = 0$, the dependence

$T(E)$ is an oscillating curve with the same amplitude of oscillations along the energy axis.

The fact that the presence of even a very small energy gap leads to noticeable changes in the spectrum of $T(E)$ is noteworthy (compare the dotted and dashed curves with the dashed-dotted one). It is seen in Fig. 3 that there is a wide transmission gap in the spectrum for small energy values. Its origin is due to the fact that the electron wave becomes evanescent at energies close to zero. The transmission gap width is very sensitive to changes in ε , and it increases rapidly with increasing ε (see Fig. 4). Also the transmission gap widens with increasing of the energy gap Δ or of the barrier thickness d . The number of Fabry–Perot-type resonances increases sharply with increasing in ε as well as in the barrier thickness. It is also seen that the difference in the effect of the Δ on T depends significantly on the value of ε . At the same time, the maxima associated with Fabry–Perot resonances remain equal to one; their position on the energy axis changes and the displacement increases with increasing Δ (according to formula (7)).

The plot of the $T(E)$ dependence for big values of beta is given by Fig. 4. We see that the oscillation period is much larger in comparison with that of Fig. 3.

Figure 5 provides the $T(\theta)$ dependence for the single barrier structure. The solid line refers to the case of $\varepsilon = 1, \Delta = 0$. Comparing Figs. 1 and 5 (which have the same values of the parameters), it is obvious that the effect of delta on T is much stronger for the single barrier structure than for the step-like one.

Figure 6 elucidates the T vs Δ dependence. One of the main conclusions that can be made on the basis of the dependence $T(\Delta)$ in Fig. 6 is that the transmission coefficient significantly depends on the size of the energy gap, namely that the presence of the gap can lead to a significant reduction of T and the decrease in T with increasing Δ may be quite sharp. The monotonic decreasing of T with increasing Δ takes place at the value of $\varepsilon > 1$ (for most values of the problem parameters).

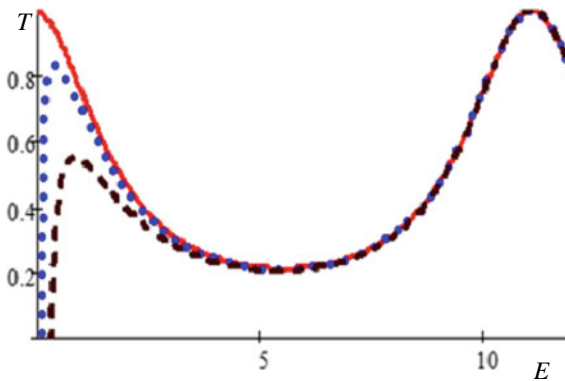


Fig. 4 Dependence of the transmission coefficient T on the quasiparticle energy E for the single barrier structure. The values of the parameters are as follows: $\theta = 0.5, d = 2, \varepsilon = 2$ for all lines; $\Delta = 0$ for the solid (red) line; $\Delta = 0.2, 0.4$ for the dotted (blue) and dashed (brown) curves, respectively

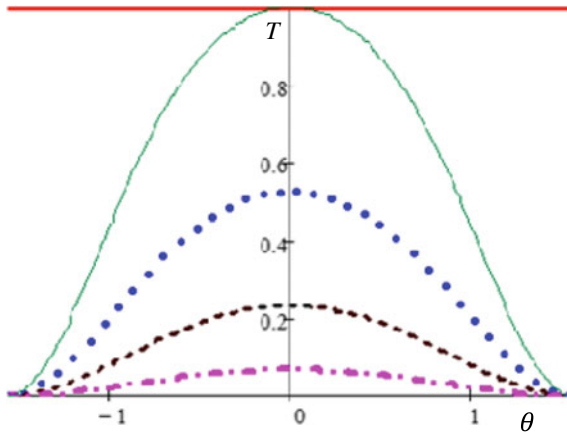


Fig. 5 Dependence of the transmission coefficient T on the incidence angle θ for the single barrier structure. The values of the parameters for Fig. 5 are as follows: $E = 0.5$, $d = 1$, $\varepsilon = 0.3$ for all curves except for thick solid (red online) one for which $\varepsilon = 1$; $\Delta = 0$ for thick and thin solid (green) lines and $\Delta = 0.2, 0.3, 0.4$ for the dotted (blue), dashed (brown), and dashed-dotted (magenta) lines, respectively

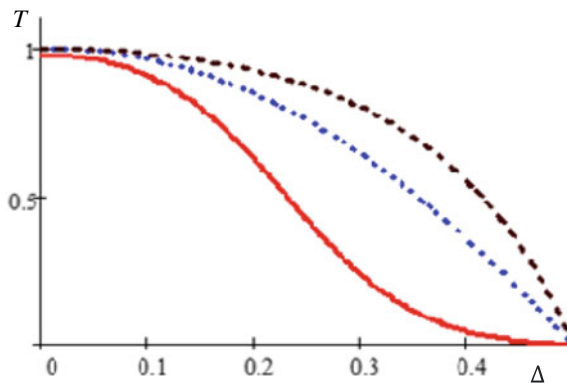


Fig. 6 Dependence of the transmission coefficient T on the energy Δ for the single barrier structure. The values of the parameters are as follows: $E = 0.5$, $\theta = 0.3$, $d = 1$ for all lines; $\varepsilon = 0.2, 1, 1.5$ for the dotted (blue) and dashed (brown) curves, respectively

It is also important that the dependence of $T(\Delta)$ can be oscillating one. This possibility follows from the formula for T (5) and is confirmed by Fig. 7. The maximum value of $T(\Delta) = 1$ corresponds to the resonances of the Fabry–Perot type. It follows from this formula that a smaller value of ε corresponds to a larger number of oscillations in a given range of Δ values.

In case of a normal incidence of massless particles on the barrier, the Klein tunneling is observed, for which $T = 1$ in the entire energy range. It is known that it also occurs in the presence of velocity barriers ($T = 1$, $\theta = 0$, $\varepsilon \neq 1$) [2–12].

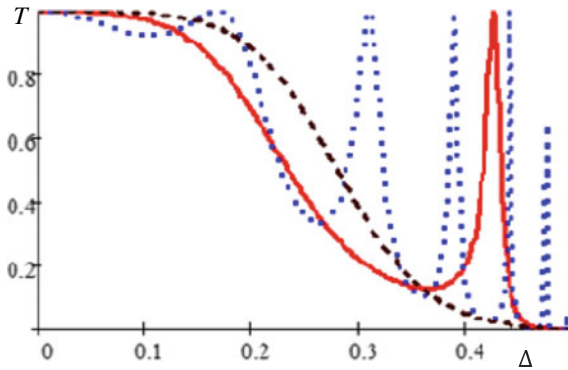


Fig. 7 Dependence of the transmission coefficient T on the energy gap Δ for the single barrier structure. The values of the parameters are as follows: $E = 0.5, \theta = 0, d = 12$ for all lines; $\varepsilon = 0.3, 1, 2$ for the dotted (blue), dashed (brown), and solid (red) curves, respectively

In case of massive particles ($\Delta \neq 0$), the Klein tunneling is suppressed, and the value of T decreases with increasing Δ .

Figure 8 represents the dependence of $T(\varepsilon)$. It has a pronounced oscillating character for small values of ε ($\varepsilon < 1$ for most values of other parameters), and the “period” of oscillations increases with increasing ε . The maximum values of T are equal to one and correspond to the Fabry–Perot-type resonances. The values of T decrease sharply in the intervals of energies between the peaks. There is also a significant difference in the magnitude of T for different Δ values.

Figure 9 illustrates the dependence of T on the barrier thickness d for different Δ and ε values. The horizontal line with $T = 1$ refers to the case: $\Delta = 0, \varepsilon = 1$. For nonzero Δ values, it is possible to observe two types of the function $T(d)$. For small values of ε , this function is an oscillating curve, and for sufficiently large values of ε ,

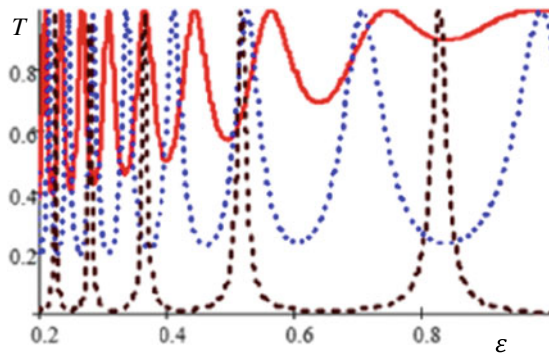


Fig. 8 Dependence of the transmission coefficient T on ε for the single barrier structure. The values of the parameters are as follows: $E = 0.5, \theta = 1, d = 12$ for all lines; $\Delta = 0, 0.2, 0.4$ for the solid (red), dotted (blue), and dashed (brown) curves, respectively

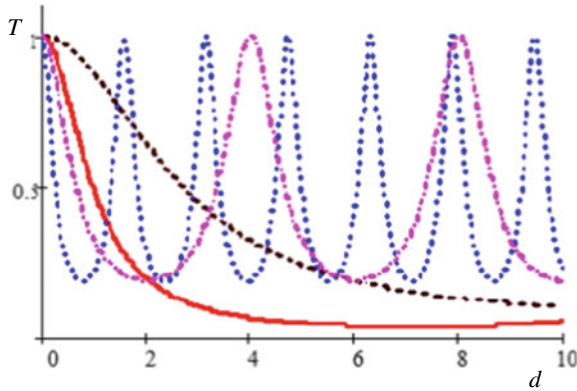


Fig. 9 Dependence of the transmission coefficient T on the barrier thickness d for different Δ and ε values for the single barrier structure. The values of the parameters are as follows: $E = 0.5$, $\theta = 0.4$, $\Delta = 0.3$, for all lines; $\varepsilon = 1, 0.2, 0.5, 2$ for the solid (red), dotted (blue), dashed-dotted (magenta), and dashed (brown) curves, respectively

the function $T(d)$ is represented by a descending curve—as in the case of conventional tunneling (see the dashed-dotted, dotted and the dashed, and solid lines, respectively, in Fig. 9). More massive particles give values of T significantly smaller than less massive ones. The number of oscillations in a given range of barrier thicknesses is noticeably smaller for more massive particles (compare the dashed-dotted and the dotted curves).

4 Conclusions

The two graphene-based structures are explored in this text: one with the step-like Fermi velocity barrier and another containing the single Fermi velocity barrier of a finite width. All out-of-barrier regions consist of the massless graphene, and the barrier area is represented by the gapped graphene. Some features of the transmission spectra (dependences of the transmission rates T on the parameter values) are common for both considered structures, namely: 1) magnitude of T is rapidly reduced with increasing in the energy gap (Δ) value (or the quasiparticle mass m); 2) spectra are highly anisotropic; that is, values of T markedly depend on the angle of incidence of the quasiparticle on the barrier θ ; 3) function $T(\theta)$ oscillates with the parameter values, in particular with the $\varepsilon = v_{F2}/v_{F1}$ value; and 4) the Klein tunneling is suppressed for the case of $m \neq 0$ ($\Delta \neq 0$). For the step-like barrier, the function $T(E)$ (E quasiparticle energy) is the monotonic and increasing with E one; there are no resonant energies. The function $T(\varepsilon)$ can reveal the pronounced maximum, and this function drops sharply to zero after reaching the maximum. For the rectangular barrier structure with a finite barrier width, a lot of maxima can be observed

in the $T(E)$ dependence as well as in the $T(\varepsilon)$ function—these are the Fabry–Perot-type resonances. The spectra $T(d)$ (d being the barrier width) is characterized by the following features. For nonzero Δ values, it is possible to observe two types of the function $T(d)$. For small values of ε , this function is an oscillating curve, and for sufficiently large values of ε , the function $T(d)$ is represented by a descending curve—as in the case of the conventional tunneling. More massive particles give values of T significantly smaller than less massive ones. The results of this work can be used in graphene-based nanoelectronics.

References

1. Neto AHC, Guinea F, Peres NMR, Novoselov KS, Geim AK (2009) The electronic properties of graphene. *Rev Mod Phys* 81:109
2. Liu L, Li Y-X, Liu J (2012) Transport properties of Dirac electrons in graphene based double velocity-barrier structures in electric and magnetic fields. *Phys Letters A* 376:3342–3350
3. Wang Y, Liu Y, Wang B (2013) Resonant tunneling and enhanced goos-hänchen shift in graphene double velocity barrier structure. *Phys E* 53:186–192
4. Sun L, Fang C, Liang T (2013) Novel transport properties in monolayer graphene with velocity modulation. *Chin Phys Lett* 30:047201
5. Raoux A, Polini M, Asgari R, Hamilton AR, Fasio R, Macdonald AH (2010) Velocity-modulation control of electron-wave propagation in graphene. *Phys Rev B* 81:073407
6. Concha A, Tešanović Z (2010) Effect of a velocity barrier on the ballistic transport of Dirac fermions. *Phys Rev B* 82:033413
7. Yuan JH, Zhang JJ, Zeng QJ, Zhang JP, Cheng Z (2011) Tunneling of Dirac fermions in graphene through a velocity barrier with modulated by magnetic fields. *Phys B* 406:4214–4220
8. Krstajic PM, Vasilopoulos P (2011) Ballistic transport through graphene nanostructures of velocity and potential barriers. *J Phys Condens Matter* 23(13):135302
9. Urban DF, Bercioux D, Wimmer M, Hausler W (2011) Barrier transmission of Dirac-like pseudospin-one particles. *Phys Rev B* 84:115136
10. Korol AM, Medvid NV, Sokolenko AI (2018) Transmission of the relativistic fermions with the pseudospin equal to one through the quasi-periodic barriers. *Phys Status Solidi B* 255(9):1800046
11. Korol AM, Medvid NV (2019) Influence of the fermi velocity on the transport properties of the 3D topological insulators. *Low Temp Phys* 45(10):1117
12. Korol AM (2019) Tunneling conductance of the s-wave and d-wave pairing superconductive graphene-normal graphene junction. *Low Temp Phys* 45(5):576
13. Korol AM (2021) Supertunneling effect in graphene. *Low Temp Phys* 47(2):133
14. Setare MR, Jahani D (2010) Electronic transmission through p-n and n-p-n junctions of graphene. *J Phys Condens Matter* 22:245503
15. Setare MR, Jahani D (2010) Klein tunneling of massive Dirac fermions in single-layer graphene. *Phys B* 405:1433
16. Takahashi R, Murakami S (2011) Gapless interface states between topological insulators with opposite Dirac velocities. *Phys Rev Lett* 107:166805
17. Sen D, Deb O (2012) Junction between surfaces of two topological insulators. *Phys Rev B* 85:245402

Electron Interaction-Driven Peculiarities of Strongly Correlated System Thermopower



Oleksandr Kramar, Yuriy Dovhopyatyy, and Yuriy Skorenkyy

Abstract In the present work, we make use of the theoretical model of electron subsystem for strongly correlated compound with a peculiar density of electronic states (DOS). The energy spectrum has been calculated within the unperturbative approach. The chemical potential and Seebeck coefficient have been calculated numerically for a number of realistic DOS forms for non-integer band fillings. Distinct types of Seebeck coefficient temperature behavior have been attributed to different electron interaction regimes to be realized in some regions of electron band filling and strongly influenced by the DOS form.

Keywords Strongly correlated electrons · Quasiparticle energy spectrum · Phase transitions · Thermopower

1 Introduction

Peculiar thermoelectric properties of narrow-band materials with strong electron correlations [1, 2] suggest their use for energy harvesting and other high-demand technologies. In particular, studies of the layered cobaltites [3, 4] and weakly electron-doped titanates [5] reveal thermopower values much larger than those typical for semiconductors. Interpreting these peculiarities requires a detailed characterization of band structure and electron correlations in these perspective materials. Recently, some progress has been achieved [6–8] in understanding of the temperature dependence of electron contribution to thermopower S in materials with narrow energy bands. In particular, it has been shown that for intermediate correlation strength, the optimal approach is the modification of the so-called Kelvin formula [8]. At the same time, in paper [9] within DMFT approach it has been proven for single-band Hubbard model that thermopower has non-monotonic temperature dependence and tends asymptotically to values predicted by the Mott-Heikes formula. Worthwhile to note, orbital degeneracy of energy levels is to be taken into account in studies

O. Kramar · Y. Dovhopyatyy · Y. Skorenkyy (✉)
Ternopil Ivan Puluž National Technical University, Ternopil, Ukraine
e-mail: skorenkyy.tntu@gmail.com

© The Author(s), under exclusive license to Springer Nature Switzerland AG 2023
O. Fesenko and L. Yatsenko (eds.), *Nanomaterials and Nanocomposites, Nanostructure Surfaces, and Their Applications*, Springer Proceedings in Physics 279,
https://doi.org/10.1007/978-3-031-18096-5_15

of the thermoelectric properties of strongly correlated electron systems [10, 11]. In paper [12], the thermopower has been shown to be strongly enhanced by the spin and orbital degrees of freedom; however, the effect on resistivity was significantly weaker. Later, the authors of paper [13] have proven that the Hund coupling, the crystal field splitting, and the Coulomb interaction cause the non-monotonic $S(T)$ behavior. It has been found as well that the sign of thermopower may change with temperature and electron density changes.

Temperature dependence of thermopower is determined primarily by the corresponding dependence of the chemical potential (see paper [14] in this respect). In previous papers [15, 16], we have shown that the temperature behavior of chemical potential and its changes with model parameters variations depends crucially on the form of the unperturbed electronic density of states (DOS) and the orbital degeneracy of the conduction band. Peculiarities of the translational processes in electronic subsystem and, specifically, role of the correlated hopping of electrons [17–19] for the thermoelectric properties of materials have been studied in detail in papers [20, 21] for specific cases of the model. The question arises of the aggregate effect of translational processes, DOS form, and variations of the model energy parameters on the thermopower behavior within the generalized Hubbard model.

In the present work, we make use of the theoretical model of electron subsystem for strongly correlated compound with a peculiar density of electronic states (DOS). The energy spectrum is calculated within the unperturbative approach [22]. The chemical potential and Seebeck coefficient are calculated numerically for non-integer band fillings.

2 Thermoelectric Properties of Narrow-Band Materials: General Principles

In a weak external electrical field \vec{E} at small temperature gradient ∇T , the current density $\langle \vec{j}_1 \rangle$ and the energy flux $\langle \vec{j}_2 \rangle$ are determined by formula

$$\langle \vec{j}_k \rangle = |e|^k \left(|e| L_{k1} \vec{E} - L_{k2} T^{-1} \nabla T \right), \quad (1)$$

where e is electron charge, L_{kn} are kinetic coefficients which satisfy Onsager relation $L_{kn} = L_{nk}$ in the absence of the magnetic field. From the Ohm's law $\langle \vec{j}_1 \rangle = \sigma \vec{E}$, it follows that $\sigma \equiv L_{11}$. At nonzero ∇T , the heat transport is balanced with electrical field \vec{E} ; therefore, at $\langle j_1 \rangle = 0$ one has for the thermopower value

$$S = \frac{L_{12}}{|e| T L_{11}} \quad (2)$$

Sign of S determines whether electrons or holes are the majority carriers. Using Sommerfeld expansion at condition $E_F > k_B T$, we obtain the following expression:

$$S = -\frac{\pi^2 k_B^2 T}{3|e|} \left[\frac{d \ln \sigma(E)}{dE} \right]_{E=E_F}, \quad (3)$$

where $E = E_F$ is the Fermi energy and k_B is the Boltzmann constant. The above equation is known as Mott equation. For the case of free electrons, using the Drude formula.

$$\sigma(E) = e^2 n(E) \tau(E) / m^*, \quad (4)$$

where m^* is the effective mass of a carrier, τ is the relaxation time, and $n(E)$ is the electron concentration in k -space under the surface of a constant $E = E_F$ (the $dn(E)/dE$ derivative equals the density of electron states $N(E)$), we have

$$S = -\frac{\pi^2 k_B}{3e} k_B T \left[\frac{N(E)}{n(E)} + \frac{1}{\tau(E)} \frac{\partial \tau(E)}{\partial E} \right]_{E=E_F}, \quad (5)$$

The above equation contains the electron concentration-dependent term as well as the relaxation-controlled term. The former, with $n(E)$ in the denominator, can be estimated as

$$S \sim -\frac{\pi^2 k_B}{3} \frac{k_B T}{ne E_F} \approx -0.9 \cdot 10^2 \frac{k_B T}{E_F} \frac{\mu V}{K}, \quad (6)$$

which estimate is in agreement with experimental observations (n at $k_B T / E_F \sim 10$). At the same time, S for semiconductors does not contain a small parameter $k_B T / E_F$ and appears to be much larger. $\tau(E)$ dependencies differ for various scattering mechanisms. At high temperatures, one has

$$\tau(E) \sim E^{3/2}, \quad n(E) \sim E^{3/2}, \quad \sigma(E) \sim E^3, \quad (7)$$

while, at low temperatures, when impurity scattering dominates and the mean electron's free path is constant, one obtains

$$\tau(E) \sim E^{-1/2}, \quad \sigma(E) \sim E. \quad (8)$$

This approach produces physically sound results for Na and K within the free electron model, values of S and the Hall coefficient being negative. However, these simple dependencies do not agree with experimental data for a majority of compounds. It is generally agreed that for a consistent analysis of thermopower peculiarities in narrow-band materials we have to consider a model, which takes into account the peculiar

properties of their electronic subsystems, namely strong electron interactions and orbital degeneracy of energy levels.

3 Effective Model Hamiltonians

Following papers [17, 19], we chose the initial form of Hamiltonian for non-degenerate band in Hubbard $X_i^{k\ell}$ -operators [23] representation as

$$H = H_0 + H_1 + H'_1 + H_2, \quad (9)$$

where

$$H_0 = (E_d - \mu) \sum_i (X_i^\uparrow + X_i^\downarrow + 2X_i^2) + U \sum_i X_i^2, \quad (10)$$

$$H_1 = \sum_{ij\sigma'} t_{ij}(n) X_i^{\sigma 0} X_j^{0\sigma} + \sum_{ij\sigma'} \tilde{t}_{ij}(n) X_i^{2\sigma} X_j^{\sigma 2}, \quad (11)$$

$$H'_1 = \sum_{ij} t'_{ij}(n) (X_i^{\downarrow 0} X_j^{\uparrow 2} - X_i^{\uparrow 0} X_j^{\downarrow 2} + h.g.), \quad (12)$$

$$H_2 = \sum_{ij\sigma\sigma'} \frac{V(\mathbf{ij})}{2} (X_i^\sigma + 2X_i^2) (X_j^{\sigma'} + 2X_j^2) - \sum_{ij\sigma} \frac{J(\mathbf{ij})}{2} ((X_i^\sigma + X_i^2)(X_j^\sigma + X_j^2) + X_i^{\sigma\bar{\sigma}} X_j^{\bar{\sigma}\sigma}) \quad (13)$$

$n_{i\sigma} = a_{i\sigma}^+ a_{i\sigma}$, $n_i = n_{i\uparrow} + n_{i\downarrow}$, μ stands for chemical potential, $t_{ij}(n) = t(ij) + n \sum_{k \neq i} \langle ik_r^{\frac{1}{r}} jk \rangle$ is an effective hopping parameter between the nearest neighbor sites, $t(ij)$ is a band hopping integral for electron transition from site j to site i , $T_1(ij) = \sum_{k \neq i} \langle ik_r^{\frac{1}{r}} jk \rangle$ and $T(ij)$ are the correlates hopping integrals, U is Hubbard on-site repulsion energy, and J is inter-site exchange interaction energy. The model Hamiltonian (9) takes into account principally important interactions in a narrow conduction band though ignores the orbital degeneracy effects. The above Hamiltonian has specific structure caused by the existence of three different types of electron hoppings, namely the band hopping and two types of the correlated hopping, which causes the electron-hole asymmetry in real materials [19, 22]. The configurational representation brings more benefits by emphasizing the non-equivalence of single-subband processes, grouped in H_1 and the hybridization of the Hubbard “ s -0”- and “ $\uparrow\downarrow$ - s ” subbands, described by H'_1 . Notations $t(n) = t(1 - \tau_1 n)$, $\tilde{t}(n) = t(1 - \tau_1 n - 2\tau_2)$, and $t'(n) = t(1 - \tau_1 n - \tau_2)$ for electron transport within the lower subband, the upper subband, and across subbands,

respectively, allow to write down the model Hamiltonian in a compact form and also distinguish between these non-equivalent transports.

Extension of the effective Hamiltonian method for model (9) leads to the effective Hamiltonian which can differ substantially from that of the Hubbard model. Let us apply a canonical transformation to exclude hybridization processes described by H'_1

$$\tilde{H} = e^S H e^{-S}, \tag{14}$$

where S is chosen in the following form

$$S = \sum_{ij} L(ij) \left((X_i^{\uparrow 0} X_j^{\downarrow 2} - X_i^{\downarrow 0} X_j^{\uparrow 2}) - h.c. \right). \tag{15}$$

If we restrict ourselves to quantities of the second order in effective Hamiltonian (14), taking H_0 to be a zeroth-order quantity, S , H_1 and H'_1 to be first-order and H_2 to be second-order ones, then we have

$$H = H_0 + H_1 + H'_1 + H_2 + [SH_0] + [SH_1] + [SH'_1] + \frac{1}{2}[S[SH_0]] \tag{16}$$

($[AB] = AB - BA$). When pair creation and annihilation of holes and doublons are forbidden in the first order in $t'_{ij}(n)/U$

$$H'_1 + [SH_0] = 0, \tag{17}$$

then

$$L(ij) = t'_{ij}(n) / U. \tag{18}$$

Therefore, in the considered model the quantity $t'_{ij}(n)/U$ is a small parameter, and not $t(ij)/U$ as in the Hubbard model which extends the domain of validity for the chosen approach.

Commutator $[SH_1]$ components have the following operator structure:

$$\frac{t_{ij}(n)t'_{jk}(n)}{U} \sum_{ijk} (X_i^{\bar{\sigma}} X_j^{\sigma 2} X_k^{\bar{\sigma} 0} + h.c.), \tag{19}$$

where sites j and k are the nearest neighbors to i . Expression (20) also describes pair creation and annihilation of holes and doublons (similar to H'_1), but not in the nearest neighboring sites. Finally, the effective Hamiltonian of the model with initial form (9) can be represented as

$$\begin{aligned}
H = & -\mu \sum_i \left(X_i^\uparrow + X_i^\downarrow + 2X_i^2 \right) + U \sum_i X_i^2 \\
& + \sum_{ij\sigma} t_{ij}(n) X_i^{\sigma 0} X_j^{0\sigma} + \sum_{ij\sigma} \tilde{t}_{ij}(n) X_i^{2\sigma} X_j^{\sigma 2} \\
& - \sum_{ij\sigma} \frac{J(ij)}{2} \left((X_i^\sigma + X_i^2)(X_j^\sigma + X_j^2) + X_i^{\sigma\bar{\sigma}} X_j^{\bar{\sigma}\sigma} \right) \\
& - \sum_{ij\sigma} \frac{t'_{ij}(n)t'_{ij}(n)}{U} \left(X_i^\sigma X_j^{\bar{\sigma}} - X_i^{\sigma\bar{\sigma}} X_j^{\bar{\sigma}\sigma} - X_i^0 X_j^2 \right) \\
& - \sum_{ijk\sigma} \frac{t'_{ij}(n)t'_{jk}(n)}{U} \left(X_i^{\sigma 0} X_j^{\bar{\sigma}} X_k^{0\sigma} - X_i^{\sigma 0} X_j^{\bar{\sigma}\sigma} X_k^{0\bar{\sigma}} \right) \\
& - \sum_{ijk\sigma} \frac{t'_{ij}(n)t'_{jk}(n)}{U} \left(X_i^{2\sigma} X_j^{\bar{\sigma}\bar{\sigma}} X_k^{\bar{\sigma}2} - X_i^{2\sigma} X_j^{\bar{\sigma}} X_k^{\sigma 2} \right), \tag{20}
\end{aligned}$$

Exclusion of the pair creation and annihilation processes has led to three terms in the Hamiltonian, the first of which corresponds to the indirect exchange interaction, and other two describe electron hoppings. The exchange mechanism is induced by virtual transitions of $|i\sigma\rangle$ -states to $|j\uparrow\downarrow\rangle$ -states and stabilizes antiparallel orientation of $|i\sigma\rangle$ and $|j\bar{\sigma}\rangle$.

In analogy to the above consideration of the non-degenerated band, we can transform the model for the doubly degenerated one. The initial Hamiltonian for the doubly degenerated model [24–26] of e_g -band in the limiting case of strong Hund's rule coupling in the formalism of X_i^{kl} -operators reads as

$$\begin{aligned}
H = & H_\alpha + H_\beta + H_{\alpha\beta} \\
& + (U - J_H) \sum_i X_i^{\sigma\sigma} - \mu \sum_{i\sigma} \left(X_i^{\gamma\uparrow} + X_i^{\gamma\downarrow} + 2X_i^{\uparrow\uparrow} + 2X_i^{\downarrow\downarrow} \right), \tag{21}
\end{aligned}$$

where

$$\begin{aligned}
H_\alpha + H_\beta = & \sum_{ij\sigma} t_{ij}(n) X_i^{\gamma\sigma,0} X_j^{0,\gamma\sigma} + \sum_{ij\sigma} \tilde{t}_{ij}(n) X_i^{\sigma\sigma,\gamma\sigma} X_j^{\gamma\sigma,\sigma\sigma}, \tag{22} \\
H_{\alpha\beta} = & \sum_{ij} \left(t'_{ij}(n) (X_i^{\beta\uparrow,0} X_j^{\alpha\uparrow,\uparrow\uparrow} - X_i^{\uparrow\uparrow,\beta\uparrow} X_j^{0,\alpha\uparrow} \right. \\
& \left. + X_i^{\alpha\downarrow,0} X_j^{\beta\downarrow,\downarrow\downarrow} - X_i^{\beta\downarrow,0} X_j^{\alpha\downarrow,\downarrow\downarrow} \right) + h.c.), \tag{23}
\end{aligned}$$

$H_\alpha + H_\beta$ describe the system at fixed number of holes and Hund's doublons (at a constant temperature), $H_{\alpha\beta}$ describes the processes of pair creation and annihilation of holes and doublons in the nearest neighboring sites. Let us exclude hybridization by the canonical transformation (14), with

$$S = \sum_{ij} \left(L(ij) \left(X_i^{\beta\uparrow} X_j^{\alpha\uparrow, \uparrow\uparrow} - X_i^{\uparrow\uparrow, \beta\uparrow} X_j^{0, \alpha\uparrow} + X_i^{\alpha\downarrow, 0} X_j^{\beta\downarrow, \downarrow\downarrow} - X_i^{\beta\downarrow, 0} X_j^{\alpha\downarrow, \downarrow\downarrow} \right) - h.c. \right), \quad (24)$$

where $L(ij)$ is determined by the condition

$$[SH_0] + H_{\alpha\beta} = 0. \quad (25)$$

Again, in second order in the hopping integral, we obtain the effective Hamiltonian

$$\begin{aligned} H = & H_0 + \sum_{ij\sigma} t_{ij}(n) X_i^{\gamma\sigma, 0} X_j^{0, \gamma\sigma} + \sum_{ij\sigma} \tilde{t}_{ij}(n) X_i^{\sigma\sigma, \gamma\sigma} X_j^{\gamma\sigma, \sigma\sigma} \\ & - \sum_{ij\gamma\sigma} \frac{t'_{ij}(n) t'_{ji}(n)}{U - J_H} \left(X_i^{\gamma\sigma} X_j^{\bar{\gamma}\sigma} + X_i^{\gamma\sigma, \bar{\gamma}\sigma} X_j^{\bar{\gamma}\sigma, \gamma\sigma} \right) \\ & - \sum_{ij\gamma\sigma} \frac{t'_{ij}(n) t'_{jk}(n)}{U - J_H} \left(X_i^{\gamma\sigma, 0} X_j^{\bar{\gamma}\sigma} X_k^{0, \gamma\sigma} - X_i^{\gamma\sigma, 0} X_j^{\bar{\gamma}\sigma, \gamma\sigma} X_k^{\bar{\gamma}\sigma} \right. \\ & \left. + X_i^{\sigma\sigma, \gamma\sigma} X_j^{\bar{\gamma}\sigma} X_k^{\gamma\sigma, \sigma\sigma} - X_i^{\sigma\sigma, \bar{\gamma}\sigma} X_j^{\gamma\sigma, \bar{\gamma}\sigma} X_k^{\gamma\sigma, \sigma\sigma} \right). \quad (26) \end{aligned}$$

The two last terms correspond to the indirect exchange interaction (kinetic superexchange) and indirect hopping of electrons, respectively. The main difference from the non-degenerated model is the ferromagnetic nature of the indirect exchange through the excited Hund's states. Virtual hopping processes are specified by terms of the effective Hamiltonian

$$\frac{t^2}{U - J_H} \sum_{ijk} X_k^{\alpha\uparrow, 0} X_j^{\beta\uparrow} X_i^{0, \alpha\uparrow}, \quad (27)$$

$$\frac{t^2}{U - J_H} \sum_{ijk} X_k^{\beta\uparrow, 0} X_j^{\alpha\uparrow, \beta\uparrow} X_i^{0, \alpha\uparrow}, \quad (28)$$

$$\frac{t^2}{U - J_H} \sum_{ijk} X_k^{\uparrow\uparrow, \alpha\uparrow} X_j^{\beta\uparrow} X_i^{\alpha\uparrow, \uparrow\uparrow}, \quad (29)$$

$$\frac{t^2}{U - J_H} \sum_{ijk} X_k^{\uparrow\uparrow, \beta\uparrow} X_j^{\alpha\uparrow, \beta\uparrow} X_i^{\alpha\uparrow, \uparrow\uparrow}, \quad (30)$$

which differ by the orbital distribution of electrons on the sites mediating the hopping. One can see that for the realization of the virtual processes termed superhopping, one needs real holes at electron concentrations $n < 1$ or Hund's doublons at $n > 1$. At $n = 1$, the concentration of these states is proportional to $\exp(-U/kT)$. This justifies the tendency to neglect the superhopping for the typical Mott–Hubbard ferromagnets but

for the compounds with large range of the electron concentrations the superhopping may play the role in the magnetic ordering stabilization which, in its turn, modifies the energy spectrum considerably.

4 Single Electron Green Function and the Energy Spectrum

Having the adequate model of the electron subsystem in the second quantization representation formulated, we can use the effective Hamiltonian (20) for a non-degenerated Mott–Hubbard electron system with two different electron hopping parameters, namely $t_{ij}(n)$ for holes and $\tilde{t}_{ij}(n)$ for doubly occupied states.

Let us consider the Green function $G_{pp'}(E) = \left\langle\left\langle X_p^{0\sigma} \middle| X_{p'}^{0\sigma} \right\rangle\right\rangle$ and write down the equation of motion for the case $n < 1$, when one can neglect the processes with doubly occupied states

$$\begin{aligned} (E + \mu + zJn_\sigma - z\tilde{J}n_\sigma)G_{pp'}(E) &= \frac{\delta_{pp'}}{2\pi} \langle X_p^\sigma + X_p^0 \rangle \\ &+ \left[\left\langle\left\langle X_p^{0\sigma}, \sum_{ij\sigma'} t_{ij}(n) X_i^{\sigma'0} X_j^{0\sigma'} \right\rangle\right\rangle \middle| X_{p'}^{0\sigma} \right]. \end{aligned} \quad (31)$$

Here, the exchange interaction is taken into account in the mean-field approximation, and z stands for the number of the nearest neighboring sites. Following papers [17, 19], we use the projection procedure as

$$\left[X_p^{0\sigma}, \sum_{ij\sigma'} t_{ij}(n) X_i^{\sigma'0} X_j^{0\sigma'} \right] = \sum_j \varepsilon^\sigma(\text{pj}) X_j^{0\sigma}, \quad (32)$$

where $\varepsilon^\sigma(\text{pj})$ is a non-operator expression. Anticommutation of (32) with $X_k^{\sigma 0}$ yields

$$\begin{aligned} \varepsilon^\sigma(\text{pk})(X_k^\sigma + X_k^0) &= t(n)(X_p^\sigma + X_p^0)(X_k^\sigma + X_k^0) + t(n)X_k^{\sigma\bar{\sigma}} X_p^{\bar{\sigma}\sigma} \\ &- \left[\delta_{\text{pk}} t(n) \sum_j X_k^{\bar{\sigma}0} X_j^{0\bar{\sigma}} \right] \end{aligned} \quad (33)$$

With the above expression for $\varepsilon^\sigma(\text{pj})$, we have from the Eq. (31)

$$\begin{aligned} (E + \mu + zJn_\sigma - z\tilde{J}n_\sigma)G_{pp'}(E) &= \frac{\delta_{pp'}}{2\pi} \langle X_p^\sigma + X_p^0 \rangle \\ &+ \sum_{j \neq p} \varepsilon^\sigma(\text{pj}) \left\langle\left\langle X_k^{0\sigma} \middle| X_{p'}^{0\sigma} \right\rangle\right\rangle + \varepsilon_p^\sigma \left\langle\left\langle X_p^{0\sigma} \middle| X_{p'}^{0\sigma} \right\rangle\right\rangle. \end{aligned} \quad (34)$$

Non-operator character of $\varepsilon^\sigma(\text{pj})$ and ε_p^σ is postulated in the following way. The expressions which contain quasi-Fermi operators are calculated self-consistently from the corresponding Green functions; for the quasi-Bose operator expressions, the variant of the approximate second quantization is applied. In papers [19, 22], a relation between Hubbard operators and configuration creation and annihilation operators was given as

$$X_i^{\text{kl}} = \alpha_{\text{ik}}^{+\alpha_{\text{il}}}, \quad (35)$$

α_{ik}^+ , α_{il} are operators of $|k\rangle$ -state creation and $|l\rangle$ -state annihilation, correspondingly, at a lattice site i (the Shubin–Wonsowsky operators). By substituting quasi-Bose combinations of Hubbard operators with the averages of Shubin–Wonsowsky operators (see [17] for details), we assure the non-operator character of the projection coefficients $\varepsilon^\sigma(\text{pj})$ and ε_p^σ

$$\alpha_{i\uparrow}^{+\alpha_{i\uparrow}} = \left(\frac{n - 2d + m}{2} \right)^{\frac{1}{2}}, \quad (36)$$

$$\alpha_{i\downarrow}^{+\alpha_{i\downarrow}} = \left(\frac{n - 2d - m}{2} \right)^{\frac{1}{2}}, \quad (37)$$

$$\alpha_{i\downarrow}^{+\alpha_{i\downarrow}} = \left(\frac{n - 2d - m}{2} \right)^{\frac{1}{2}}, \quad (38)$$

$$\alpha_{i0}^{+\alpha_{i0}} = (c)^{\frac{1}{2}}, \quad \alpha_{i2}^{+\alpha_{i2}} = (d)^{\frac{1}{2}},$$

Here, n , m stand for electron concentration and the system magnetization, respectively. Let us introduce notations

$$\varepsilon^\sigma(\text{pj}) = \alpha_\sigma t_{\text{pj}}(n), \quad \varepsilon_p^\sigma = \beta_\sigma(\text{pi}), \quad (39)$$

After the Fourier transformation, from (34) we have the expression for Green function

$$G_k^\sigma(E) = \frac{1}{2\pi} \frac{1 - n_{\bar{\sigma}}}{E - E_k^\sigma}, \quad (40)$$

where the quasiparticle energy spectrum

$$E_k^\sigma = -\mu + \alpha_\sigma t_k(n) + \beta_\sigma - z\text{Jn}_\sigma + z\tilde{J}n_\sigma \quad (41)$$

contains the correlation narrowing factor

$$\alpha_\sigma = 1 - n_{\bar{\sigma}} + \frac{n_{\bar{\sigma}}n_\sigma}{1 - n_{\bar{\sigma}}} = \frac{2 - n + \eta_\sigma m}{2} + \frac{n^2 - m^2}{2(2 - n + \eta_\sigma m)} \quad (42)$$

and the correlation shift of the band center

$$\beta_\sigma = -\frac{1}{1-n_\sigma} \sum_k t_k(n) \langle X_i^{\bar{\sigma}0} X_j^{0\bar{\sigma}} \rangle_k. \quad (43)$$

In the above formulae, n_σ is the concentration of electrons with spin σ .

Note that in distinction from the projection method of paper [17] where the quasi-classical approximation has been used for the calculation of band center shifts, in the present work, we use self-consistent approach [27] for such calculations. The resultant expressions for β_σ are determined by the form of the quasiparticle density of states.

Likewise, for the case $n > 1$ we consider the doublon Green function $\tilde{G}_{pp'}^\sigma(E) = \langle\langle X_p^{\sigma 2} | X_{p'}^{2\sigma} \rangle\rangle$ and write down the corresponding equation of motion

$$\begin{aligned} (E + \mu - U + zJn_\sigma - z\tilde{J}n_\sigma) \tilde{G}_{pp'}^\sigma(E) &= \frac{\delta_{pp'}}{2\pi} \langle X_p^\sigma + X_p^2 \rangle \\ &+ \left[\left\langle \left[X_p^{\sigma 2}, \sum_{ij\sigma'} \tilde{t}_{ij}(n) X_i^{2\sigma'} X_j^{\sigma'2} \right] | X_{p'}^{\sigma 0} \right\rangle \right]. \end{aligned} \quad (44)$$

In accordance with the projection procedure

$$\tilde{t}_{ij}(n) X_i^{2\sigma'} \left[X_p^{\sigma 2}, \sum_{ij\sigma'} \tilde{t}_{ij}(n) X_i^{2\sigma'} X_j^{\sigma'2} \right] = \sum_j \tilde{\varepsilon}^\sigma(pj) X_j^{\sigma 2} X_j^{\sigma'2}, \quad (45)$$

where $\tilde{\varepsilon}^\sigma(pj)$ is a non-operator expression. By anticommuting the above expression with $X_k^{2\sigma}$, we have

$$\begin{aligned} \tilde{\varepsilon}^\sigma(pk) (X_k^\sigma + X_k^2) &= \tilde{t}(n) (X_p^\sigma + X_p^2) (X_k^\sigma + X_k^2) + \tilde{t}(n) X_k^{\sigma\bar{\sigma}} X_p^{\bar{\sigma}\sigma} \\ &+ \delta_{pk} \tilde{t}(n) \sum_j X_k^{2\sigma} X_j^{\sigma 2}, \end{aligned} \quad (46)$$

After this substitution, the equation for Green function is

$$\begin{aligned} (E + \mu - U + zJn_\sigma - z\tilde{J}n_\sigma) \tilde{G}_{pp'}^\sigma(E) &= \frac{\delta_{pp'}}{2\pi} \langle X_p^\sigma + X_p^2 \rangle \\ &+ \sum_{j \neq p} \tilde{\varepsilon}^\sigma(pj) \langle\langle X_k^{\sigma 2} | X_{p'}^{2\sigma} \rangle\rangle + \tilde{\varepsilon}_p^\sigma \langle\langle X_p^{\sigma 2} | X_{p'}^{2\sigma} \rangle\rangle, \end{aligned} \quad (47)$$

After the Fourier transformation, we obtain for Green function

$$\tilde{G}_k^\sigma(E) = \frac{1}{2\pi} \frac{n_\sigma}{E - \tilde{E}_k^\sigma}, \quad (48)$$

where the spectrum of the upper quasiparticle subband is

$$\tilde{E}_k^\sigma = -\mu + U + \tilde{\alpha}_\sigma \tilde{t}_k(n) + \tilde{\beta}_\sigma - z\mathcal{J}n_\sigma + z\tilde{J}n_\sigma, \quad (49)$$

with correlation band narrowing

$$\tilde{\alpha}_\sigma = \frac{n + \eta_\sigma m}{2} + \frac{n^2 - m^2}{2(n + \eta_\sigma m)} \quad (50)$$

and the subband shift

$$\tilde{\beta}_\sigma = -\frac{1}{n_\sigma} \sum_k \tilde{t}_k(n) \langle X_i^{2\sigma} X_j^{2\sigma} \rangle_k. \quad (51)$$

Important peculiarities of the obtained spectra for the lower and the upper subbands are the correlation narrowing of the subband widths, the latter being non-equivalent due to the correlated hopping of electrons. Note also that the correlation narrowing increases with the subband filling.

Now, let us consider a Mott–Hubbard ferromagnet with the doubly degenerated band for electron concentrations $n < 1$. Equation of motion for Green function

$$G_{pl}^{\gamma\sigma}(E) = \left\langle \left\langle X_p^{0,\gamma\sigma} \left| X_l^{\gamma\sigma,0} \right. \right\rangle \right\rangle_E, \quad (52)$$

can be written as

$$\begin{aligned} (E + \mu)G_{pl}^{\gamma\sigma}(E) &= \frac{\langle X_p^{\gamma\sigma} + X_p^0 \rangle}{2\pi} \delta_{pl} \\ &+ \sum_j t(pj) \left[\left\langle \left\langle \left((X_p^{\gamma\sigma} + X_p^0) X_j^{0,\gamma\sigma} + X_p^{\gamma\bar{\sigma},\gamma\sigma} X_j^{0,\gamma\bar{\sigma}} \right) \left| X_l^{\gamma\sigma,0} \right. \right\rangle \right\rangle_E \right. \\ &\left. + \left\langle \left\langle \left(X_p^{\bar{\gamma}\sigma,\gamma\sigma} X_j^{0,\gamma\sigma} + X_p^{\bar{\gamma}\bar{\sigma},\gamma\sigma} X_j^{0,\bar{\gamma}\bar{\sigma}} \left| X_l^{\gamma\sigma,0} \right. \right) \right\rangle \right\rangle_E \right]. \end{aligned} \quad (53)$$

Let us restrict ourselves to the case of equivalent α and β orbitals. Following the approach utilized above for the non-degenerated case, we obtain for $n < 1$

$$G_k^{\gamma\sigma}(E) = \frac{1}{2\pi} \cdot \frac{1 - n + n_\sigma}{E - E_k^{\gamma\sigma}}, \quad (54)$$

where the quasiparticle spectrum of the lower subband is

$$E_k^{\gamma\sigma} = -\mu + \alpha_{\gamma\sigma} t_k(n) + \beta_{\gamma\sigma}. \quad (55)$$

There is a formal distinction between the band narrowing factor (42) and that for the orbitally degenerated case

$$\alpha_\sigma = 1 - n + n_\sigma + \frac{2n_{\bar{\sigma}}n_\sigma + n_\sigma n_\sigma}{1 - n + n_{\bar{\sigma}}}, \quad (56)$$

and, worth noting, the correlation subband center shift contains three correlation functions which are distinct in a general case, when the orbitals are non-equivalent

$$\beta_{\gamma\sigma} = -\frac{1}{1 - n + n_\sigma} \sum_k t_k(n) \left(\left\langle X_i^{\gamma\bar{\sigma},0} X_j^{0,\gamma\bar{\sigma}} \right\rangle_k + \left\langle X_i^{\bar{\gamma}\bar{\sigma},0} X_j^{0,\bar{\gamma}\bar{\sigma}} \right\rangle_k \right. \\ \left. + \left\langle X_i^{\bar{\gamma}\sigma,0} X_j^{0,\bar{\gamma}\sigma} \right\rangle_k \right). \quad (57)$$

Likewise, the corresponding Green function for the case $n > 1$ is obtained in the following form:

$$\tilde{G}_k^{\gamma\sigma}(E) = \frac{1}{2\pi} \cdot \frac{n_\sigma + n_{\sigma\sigma}}{E - \tilde{E}_k^{\gamma\sigma}}, \quad (58)$$

where the quasiparticle spectrum for the upper subband is

$$\tilde{E}_k^{\gamma\sigma} = -\mu + U - 3J' + \tilde{\alpha}_{\gamma\sigma} t_k(n) + \tilde{\beta}_{\gamma\sigma}. \quad (59)$$

Procedure we have applied for the non-degenerate model yields also the correlation band narrowing factor

$$\tilde{\alpha}_{\gamma\sigma} = n_\sigma + n_{\sigma\sigma} + \frac{n_\sigma^2}{n_\sigma + n_{\sigma\sigma}}, \quad (60)$$

and the correlation shift of the upper subband center

$$\tilde{\beta}_{\gamma\sigma} = \frac{1}{n_\sigma + n_{\sigma\sigma}} \sum_k t_k(n) \left\langle X_i^{\sigma\sigma,\bar{\gamma}\sigma} X_j^{\bar{\gamma}\sigma,\sigma\sigma} \right\rangle_k. \quad (61)$$

Comparing the obtained formulae (56) and (60) for the band narrowing factors, one finds that in the degenerated model the electron–hole asymmetry of cases $n < 1$ and $n > 1$ exists even in the absence of the correlated hopping of electrons (when $t(n) = \tilde{t}(n) = t$). This is a consequence of the physical non-equivalence of hole and Hund’s doublon states and taking the correlated hopping into account is but an additional factor to enhance this effect.

5 Results and Discussion

Above results for Green functions and energy spectra enable us to apply methods developed for calculation of the thermopower via electronic conductance tensor components

$$\sigma_{\mu\nu}(\omega) = \frac{i}{V} \lim_{\varepsilon \rightarrow 0^+} \int_0^\infty \langle [J_\mu(t), P_\nu] \rangle \exp(-i\omega t - \varepsilon t) dt, \quad (62)$$

which are expressed through polarization vector components

$$P_\nu = e \sum_{i\gamma\sigma} R_i^\nu n_{i\gamma\sigma}, \quad (63)$$

and components of current

$$J_\mu = i [P_\mu, H], \quad (64)$$

In the considered case, these vectors can be rewritten as

$$P_\nu = e \sum_{i\gamma\sigma} (X_i^{\gamma\sigma} + X_i^{\sigma\sigma}) R_i^\nu, \quad (65)$$

$$\begin{aligned} J_\mu &= ie \sum_{\text{pls}} \sum_{\substack{ij\sigma \\ \gamma\gamma'}} \left(t_{ij}^{\gamma\gamma'}(n) [X_p^{ls} + X_p^{ss}, X_i^{\gamma\sigma,0} X_j^{0,\gamma'\sigma}] \right. \\ &\quad \left. + \tilde{t}_{ij}^{\gamma\bar{\gamma}}(n) [X_p^{ls} + X_p^{ss}, X_i^{\sigma\sigma,\gamma'\sigma} X_j^{\gamma'\sigma,\sigma\sigma}] \right) \\ R_p^\mu &= ie (R_i^\mu - R_j^\mu) \sum_{ij\gamma\gamma'\sigma} \left(t_{ij}^{\gamma\gamma'}(n) X_i^{\gamma\sigma,0} X_j^{0,\gamma'\sigma} + \tilde{t}_{ij}^{\gamma\bar{\gamma}}(n) X_i^{\sigma\sigma,\gamma'\sigma} X_j^{\gamma'\sigma,\sigma\sigma} \right) \end{aligned} \quad (66)$$

For xx -component of the electronic conductance tensor (62), we have

$$\sigma_{xx} = \sigma + \tilde{\sigma}, \quad (67)$$

where

$$\sigma = -\frac{e^2 \tau z}{2Na} \sum_{\substack{ij\sigma \\ \gamma\gamma'}} t_{ij}^{\gamma\gamma'}(n) \langle X_i^{\gamma\sigma,0} X_j^{0,\gamma'\sigma} \rangle, \quad (68)$$

$$\tilde{\sigma} = -\frac{e^2\tau z}{2Na} \sum_{\substack{ij\sigma \\ \gamma\gamma'}} \tilde{t}_{ij}^{\gamma\gamma'}(n) \langle X_i^{\sigma\sigma,\gamma\sigma} X_j^{\gamma'\sigma,\sigma\sigma} \rangle. \quad (69)$$

The correlation functions in the right hand side of these expressions are related to the correlation shifts of the subbands centers, introduced in the previous section. Therefore, one can simplify the calculation by using these relations as

$$\sigma = -\frac{e^2\tau z}{6Na} \sum_{\gamma\sigma} \beta_{\gamma\sigma} (1 - n + n_\sigma), \quad (70)$$

$$\tilde{\sigma} = -\frac{e^2\tau z}{2Na} \sum_{\gamma\sigma} \tilde{\beta}_{\gamma\sigma} (n_{\sigma\sigma} + n_\sigma). \quad (71)$$

The spin-dependent shift is a function of temperature:

$$\begin{aligned} \beta_{\gamma\sigma} = & -\frac{1}{w(n)} \cdot \frac{1 - n + n_{\bar{\sigma}}}{1 - n + n_\sigma} \int_{-w(n)}^{w(n)} \frac{tdt}{\exp\left(\frac{E_{\gamma\bar{\sigma}}(t)}{\Theta}\right) + 1} \\ & - \frac{1}{2w(n)} \int_{-w(n)}^{w(n)} \frac{tdt}{\exp\left(\frac{E_{\gamma\sigma}(t)}{\Theta}\right) + 1}. \end{aligned} \quad (72)$$

Making use of the Sommerfeld expansion similar to that of [28, 29], we obtain

$$\begin{aligned} \beta_{\gamma\sigma} = & -\frac{2}{1 - n + n_\sigma} \left(\frac{1 - n + n_{\bar{\sigma}}}{2w(n)} \int_{-w(n)}^{w(n)} tdt + \frac{\pi^2}{6} \cdot \frac{1 - n + n_{\bar{\sigma}}}{\alpha_{\gamma\bar{\sigma}}^2} \cdot \frac{\Theta^2}{2w(n)} \right) \\ & - \frac{1}{1 - n + n_\sigma} \left(\frac{1 - n + n_\sigma}{2w(n)} \int_{-w(n)}^{w(n)} tdt + \frac{\pi^2}{6} \cdot \frac{1 - n + n_\sigma}{\alpha_{\gamma\sigma}^2} \cdot \frac{\Theta^2}{2w(n)} \right) \\ = & \frac{2w(n)(1 - n)n_{\bar{\sigma}}}{(1 - n + n_\sigma)(1 - n + n_{\bar{\sigma}})} - \frac{\pi^2}{6} \cdot \frac{1 - n + n_{\bar{\sigma}}}{1 - n + n_\sigma} \cdot \frac{\Theta^2}{w(n)\alpha_{\gamma\bar{\sigma}}^2} \\ & + \frac{w(n)(1 - n)n_\sigma}{(1 - n + n_\sigma)^2} - \frac{\pi^2}{12} \cdot \frac{\Theta^2}{w(n)\alpha_{\gamma\sigma}^2}. \end{aligned} \quad (73)$$

In a similar way for the case of $n > 1$, we find

$$\tilde{\beta}_{\gamma\sigma} = \frac{2\tilde{w}(n)n_\sigma n_{\sigma\sigma}}{(n_\sigma + n_{\sigma\sigma})^2} - \frac{\pi^2}{12} \cdot \frac{\Theta^2}{\tilde{w}(n)\tilde{\alpha}_{\gamma\sigma}^2}. \quad (74)$$

Comparison of energy spectra (41) and (55) allows us to conclude that for electron concentration $n < 1$, the non-degenerate model reproduces well all the features characteristic for the doubly degenerated one; therefore, the mechanisms governing the temperature and concentration dependences of thermopower may be studied with use of Hamiltonian (20). This simplification allows both to avoid computation resource-expensive calculations of extra components is band center shifts and to include the description of the band narrowing, associated with the correlated hopping of electrons. Moreover, within the present approach there exist reliable results for the chemical potential temperature behavior [15] which are in accordance with theoretical calculations and experimental data [14]. For $n > 1$, however, the results from models (20) and (26) may be quite different and will be studied elsewhere.

In a wide interval of the temperature and the carrier concentration values, the dependence of S on the temperature is determined by the corresponding dependence of the chemical potential. Character of the $S(T)$ dependence can be reproduced in the following way. Let us neglect both the diffusion component and the phonon drag thermopower to write down Kelvin formula (according to the terminology of Shastry [6, 7]) for the low-temperature estimate of the thermopower

$$S = \frac{1}{e} \frac{d\mu}{dT}. \quad (75)$$

For calculation of thermopower, the Heikes–Mott formula (3) can also be used in the form

$$S = -\frac{\pi^2 k_B^2 T}{3e\sigma(\varepsilon)} \left(\frac{d\sigma}{d\varepsilon} \right)_{\varepsilon=E_F}. \quad (76)$$

For the frequency dependence of the conductivity, we use the result of [15]

$$\sigma = \frac{e^2 z}{a} n \frac{(1-n)\omega(n)}{2-n} \frac{\tau}{1 + \varepsilon^2 \tau^2}. \quad (77)$$

Then,

$$S = \frac{\pi^2 k_B^2 T}{3e} \frac{2E_F \tau^2}{1 + E_F^2 \tau^2}. \quad (78)$$

At low temperatures, normalizing the energy values by the half bandwidth, the above formula can be rewritten as

$$S = \frac{\pi^2}{3} \frac{\theta}{\omega(n)} \frac{2 \left(\frac{\mu}{\omega(n)} \right) (\tau \omega(n))^2}{1 + \left(\frac{\mu}{\omega(n)} \right)^2 (\tau \omega(n))^2}. \quad (79)$$

The formulae (78) and (79) as well as the results of numerical calculations for the chemical potential and correlation shifts of subband centers allow us analyzing the concentration dependence of thermopower. In a wide interval of temperature and carrier concentration values, the dependence of the thermopower on temperature can be determined by the corresponding dependence of the chemical potential, which is calculated numerically with use of the obtained analytical expressions for Green functions and quasiparticle energy spectra. Distinctions of semi-elliptical DOS and model rectangular DOS application appear to be visible only for very low temperatures, where phase transitions may take place [22]. Different concentration dependence is quite prominent; for concentrations up to 0.67, the value of thermopower is negative and decreasing with the concentration increase, and for larger band fillings, the positive values of the thermopower increase very fast with the electron concentration close to 1, which may be attributed to the non-monotonic behavior of conductance investigated in [15] for the non-degenerated model and in [19] for the degenerated one.

In Figs. 1 and 2, the temperature dependence of the thermopower is studied with use of the model DOS which is characterized by the asymmetry of electron density distribution [30] for almost empty and almost half-filled non-degenerated band, respectively. Qualitatively, our results reproduce corresponding results for the doping-dependent temperature behavior of thermopower obtained in [10]; however, in the present approach, the electron–hole asymmetry has a natural explanation. The rate and slope of the thermopower value change with increasing temperature in accordance with the corresponding result of [31], and the more subtle tuning of the model is available, when the DOS asymmetry parameter is varied in interval 0.3–0.5. The same thermopower increase is observed, when standard DOS for sc or bcc lattices are used (see Fig. 3); however, these functions do not to reproduce saturation-like $S(T)$ behavior within physically achievable temperature range.

Fig. 1 Temperature dependence of the thermopower at $n = 0.1$. The uppermost (black) curve corresponds to rectangular DOS, other curves correspond to DOS with asymmetry parameter (up-to-down, $a = 0.3$ for blue, $a = 0.5$ for green, and $a = 0.9$ for red curve)

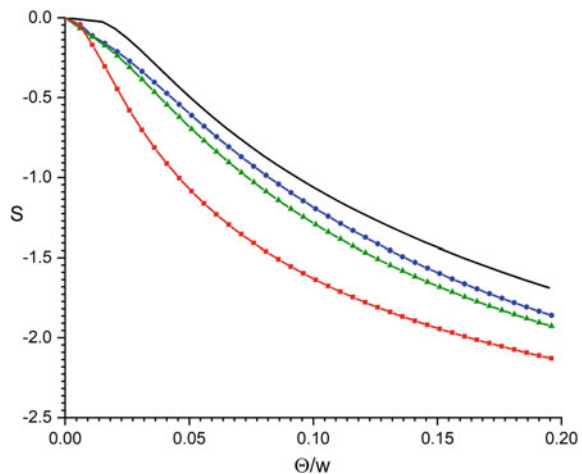


Fig. 2 Temperature dependence of the thermopower at $n = 0.8$. The lowermost (black) curve corresponds to rectangular DOS, other curves correspond to DOS with asymmetry parameter ($a = 0.3$ for the middle red one and $a = 0.9$ for the upper blue curve)

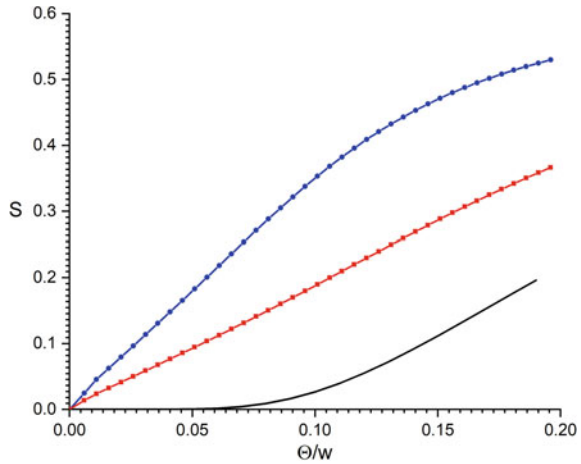
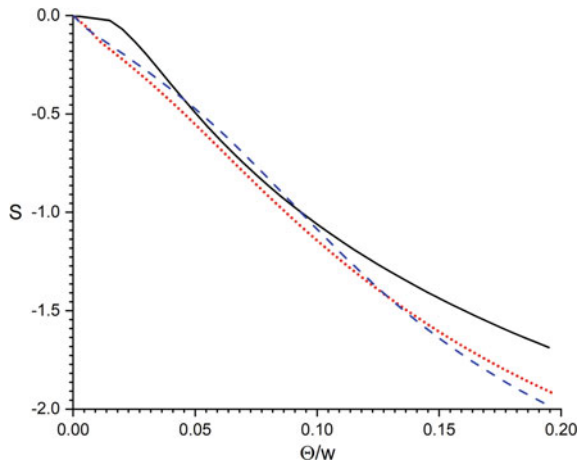


Fig. 3 Temperature dependence of the thermopower at $n = 0.1$. Solid curve corresponds to rectangular DOS, dotted red curve is for sc lattice, and dashed blue curve is for bcc lattice



6 Conclusions

Thermoelectric properties of narrow-band transition metal compounds may offer new solutions to the energy harvesting needs and theoretical modeling of the thermoelectric response allows better design of these materials. Use of generic models such as the Hubbard model and its generalization allows us to single out the essential mechanisms behind concentration and temperature dependencies to find optimal doping and temperature regimes for such materials. For low electron concentrations, we may use the non-degenerate model for calculation of the temperature dependences of the thermopower at condition that the model DOS is chosen appropriately to reproduce the characteristic features of the compound.

Distinct types of Seebeck coefficient temperature behavior have been observed for the model of electron subsystem with strong correlations. These distinctions can be attributed to different electron interaction regimes to be realized in some regions of electron band filling. Differences in $S(T)$ dependences are governed by the same mechanisms as the conductance and reflects the changes of single electron energy spectrum.







References

1. Urban JJ, Menon AK, Tian Zh, Jain A, Hippalgaonkar K (2019) New horizons in thermoelectric materials: correlated electrons, organic transport, machine learning, and more. *J Appl Phys* 125:180902. <https://doi.org/10.1063/1.5092525>
2. Matsuno J, Fujioka J, Okuda T, Ueno K, Mizokawa T, Katsufuji T (2018) Strongly correlated oxides for energy harvesting. *Sci Technol Adv Mater* 19:899–908. <https://doi.org/10.1080/14686996.2018.1529524>
3. Terasaki I, Sasago Y, Uchinokura K (1997) Large thermoelectric power in NaCo_2O_4 single crystals. *Phys Rev B* 56:R12685
4. Wang Y, Rogado N, Cava R et al (2003) Spin entropy as the likely source of enhanced thermopower in $\text{Na}_x\text{Co}_2\text{O}_4$. *Nat* 423:425. <https://doi.org/10.1038/nature01639>
5. Okuda T, Nakanishi K, Miyasaka S, Tokura Y (2001) Large thermoelectric response of metallic perovskites: $\text{Sr}_{1-x}\text{La}_x\text{TiO}_3$. *Phys Rev B* 63:113104. <https://doi.org/10.1103/PhysRevB.63.113104>
6. Shastry BS (2013) Thermopower in correlated systems. In: Zlatić V, Hewson A (eds) *New materials for thermoelectric applications: theory and experiment*. NATO Science for Peace and Security Series B: Physics and Biophysics. Springer, Dordrecht, pp 25–29. https://doi.org/10.1007/978-94-007-4984-9_2
7. Shastry BS (2006) Sum rule for thermal conductivity and dynamical thermal transport coefficients in condensed matter. *Phys Rev B* 73:085117. <https://doi.org/10.1103/PhysRevB.73.085117>
8. Peterson M, Shastry BS, Haerter J (2007) Thermoelectric effects in a strongly correlated model for Na_xCoO_2 . *Phys Rev B* 76:165118. <https://doi.org/10.1103/PhysRevB.76.165118>
9. Matsuo M, Okamoto S, Koshibae W, Mori M, Maekawa S (2011) Nonmonotonic temperature dependence of thermopower in strongly correlated electron systems. *Phys Rev B* 84:153107. <https://doi.org/10.1103/PhysRevB.84.153107>
10. Pálsson G, Kotliar G (1998) Thermoelectric response near the density driven Mott transition. *Phys Rev Lett* 80:4775. <https://doi.org/10.1103/PhysRevLett.80.4775>
11. Oudovenko VS, Kotliar G (2002) Thermoelectric properties of the degenerate Hubbard model. *Phys Rev B* 65:075102. <https://doi.org/10.1103/PhysRevB.65.075102>
12. Koshibae W, Maekawa S (2001) Effects of spin and orbital degeneracy on the thermopower of strongly correlated systems. *Phys Rev Lett* 87:236603. <https://doi.org/10.1103/PhysRevLett.87.236603>
13. Sekino M, Okamoto S, Koshibae W, Mori M, Maekawa S (2014) Temperature dependence of thermopower in strongly correlated multiorbital systems. *JPS Conf Proc* 3:017014. <https://doi.org/10.7566/JPSCP.3.017014>
14. Ishida Y, Ohta H, Fujimori A, Hosono H (2007) Temperature dependence of the chemical potential in Na_xCoO_2 : implications for the large thermoelectric power. *J Phys Soc Jpn* 76:103709. <https://doi.org/10.1143/JPSJ.76.103709>
15. Didukh L, Kramar O, Skorenkyy Yu, Dovhopyaty Yu. (2005) Magnetic field dependence of conductivity and effective mass of carriers in a model of Mott-Hubbard material. *Condens Matter Phys* 8(4):825. <https://doi.org/10.5488/CMP.8.4.825>

16. Skorenkyy Y, Kramar O, Dovhopyaty Y (2020) Electron-hole asymmetry in electron systems with orbital degeneracy and correlated hopping. *Condens Matter Phys* 23(4):43714. <https://doi.org/10.5488/CMP.23.43714>
17. Didukh L (2000) A modified form of the polar model of crystals. *Acta Phys Pol B* 31(12):3097–3133
18. Gorski G., Mizia J. (2004) Magnetic ordering of itinerant systems: the role of kinetic interactions. *Physica B* 344:231–242. [https://doi.org/10.1016/S0921-4526\(02\)01458-8](https://doi.org/10.1016/S0921-4526(02)01458-8)
19. Didukh L., Skorenkyy Yu., Kramar O (2008) Electron correlations in narrow energy bands: modified polar model approach. *Condens Matter Phys* 11:443–454. <https://doi.org/10.5488/CMP.11.3.443>
20. Shvaika AM (2014) Effect of correlated hopping on thermoelectric properties: exact solutions for the Falicov-Kimball model. *Condens Matter Phys* 17(4):43704. <https://doi.org/10.5488/CMP.17.43704>
21. Dobushovskiy DA, Shvaika AM (2020) Thermoelectric properties of Mott insulator with correlated hopping at microdoping. *Condens Matter Phys* 23(1):13703. <https://doi.org/10.5488/CMP.23.13703>
22. Skorenkyy Y, Didukh L, Kramar O, Dovhopyaty Y (2007) Mott transition, ferromagnetism and conductivity in the generalized Hubbard model. *Acta Phys Pol A* 111:635. <https://doi.org/10.12693/APhysPolA.111.635>
23. Hubbard J (1965) Electron correlation in narrow energy bands – IV. The atomic representation. *Proc Roy Soc A* 285:542. <https://doi.org/10.1098/rspa.1965.0124>
24. Didukh L, Skorenkyy Yu, Dovhopyaty Yu, Hankevych V (2000) Metal-insulator transition in a doubly orbitally degenerate model with correlated hopping. *Phys Rev B* 61:7893. <https://doi.org/10.1103/PhysRevB.61.7893>
25. Didukh L, Skorenkyy Yu, Hankevych V, Kramar O (2001) Ground state ferromagnetism in a doubly orbitally degenerate model. *Phys Rev B* 64:144428. <https://doi.org/10.1103/PhysRevB.64.144428>
26. Didukh L, Hankevych V, Kramar O, Skorenkyy Yu (2002) Itinerant ferromagnetism of systems with orbital degeneracy. *J Phys Condens Matter* 14:827. <https://doi.org/10.1088/0953-8984/14/4/315>
27. Kramar O, Skorenkyy Yu, Dovhopyaty Yu (2019) Effective masses of carriers in the degenerate conduction band: interplay of density of electronic states peculiarities and magnetization. *J Nano Electron Phys* 11(5):05030. [https://doi.org/10.21272/jnep.11\(5\).05030](https://doi.org/10.21272/jnep.11(5).05030)
28. Didukh L, Kramar O (2002) Metallic ferromagnetism in a generalized Hubbard model. *FizikaNizkikhTemperatur (Kharkov)* 28:42. <https://doi.org/10.1063/1.1449182>
29. Didukh L, Kramar O (2005) Metallic ferromagnetism in the systems with strongly correlated electrons. *Condens Matter Phys* 8:547. <https://doi.org/10.5488/CMP.8.3.547>
30. Vollhardt D, Blümer N, Held K, Kollar M, Schlipf J, Ulmke M, Wahle J (1999) Metallic ferromagnetism: progress in our understanding of an old strong-coupling problem. In: Kramer B (ed) *Advances in solid state physics*, vol 38. Springer, Berlin-Heidelberg, p 383. <https://doi.org/10.1007/BFb0107631>
31. Singh S, Pandey SK (2017) Understanding the thermoelectric properties of LaCoO₃ compound. *Phil Mag* 97(6):451. <https://doi.org/10.1080/14786435.2016.1263404>

Ultrasonic Synthesis and Characterization of Zinc Pyrovanadate Nanostructures



O. A. Diyuk , Valery Zazhigalov , N. D. Shcherban , N. V. Diyuk ,
V. V. Permyakov , S. M. Shcherbakov, L. S. Kuznetsova ,
and M. M. Tsyba

Abstract The unique low temperature synthesis of zinc pyrovanadate from oxides was proposed. $Zn_3V_2O_7(OH)_2 \cdot 2(H_2O)$ was synthesized by ultrasonic (US) method using ZnO and V_2O_5 as raw materials. It was established using SEM and TEM methods that $Zn_3V_2O_7(OH)_2 \cdot 2(H_2O)$ has the structure of nanosheets. The DTA method and XRD analysis showed the formation of the $Zn_3V_2O_8$ phase after the removal of crystallization water from $Zn_3V_2O_7(OH)_2 \cdot 2(H_2O)$. Ultrasonic treatment of oxides as initial reagents allows obtaining $Zn_3V_2O_8$ with the specific surface area of $14 \text{ m}^2/\text{g}$. For comparison, $Zn_3V_2O_8$ was synthesized by solid-state (SS) synthesis from oxides. The properties of zinc pyrovanadate obtained by US synthesis and conventional SS synthesis were compared. The advantages of US method over conventional SS synthesis were noted.

O. A. Diyuk (✉) · V. Zazhigalov · L. S. Kuznetsova · M. M. Tsyba
Institute for Sorption and Problems of Endoecology, National Academy of Sciences of Ukraine,
General Naumov Street, 13, Kyiv 03164, Ukraine
e-mail: diyukhelen@ukr.net

V. Zazhigalov
e-mail: zazhigal@ispe.kiev.ua

N. D. Shcherban
L.V. Pisarzhevsky Institute of Physical Chemistry, National Academy of Sciences of Ukraine, 31
Pr. Nauky, Kyiv 03028, Ukraine
e-mail: nataliyalisenko@ukr.net

N. V. Diyuk
Taras Shevchenko National University of Kyiv, 60 Volodymyrska Street, Kyiv 01033, Ukraine
e-mail: nvdiyuk@gmail.com

V. V. Permyakov
Institute of Geological Sciences, National Academy of Sciences of Ukraine, 55-B O.Gonchar Str.,
Kyiv 01054, Ukraine

S. M. Shcherbakov
M.G. Kholodny Institute of Botany, National Academy of Sciences of Ukraine, Tereshchenkivska
Str., 2, Kyiv 01004, Ukraine
e-mail: sbarba@ukr.net

Keywords Zinc pyrovanadate · $\text{Zn}_3\text{V}_2\text{O}_8$ · Ultrasonic synthesis · Nanostructures

1 Introduction

Vanadium compounds are widely used in chemical industry as catalysts for the production of maleic acid, sulfuric acid, purification of industrial gases from NO_x [1, 2]. Moreover, vanadium compounds seem to be promising as novel potential drugs in the treatment of diabetes, atherosclerosis, and cancer [3, 4].

In the past few decades, $\text{Zn}_3\text{V}_2\text{O}_8$ has attracted significant attention due to its unique properties and perspective for wide applications in industry, ecology, and medicine.

$\text{Zn}_3\text{V}_2\text{O}_7(\text{OH})_2 \cdot 2(\text{H}_2\text{O})$ and $\text{Zn}_3\text{V}_2\text{O}_8$ are considered to be perspective for the creation of photoluminescence materials and can be used as a phosphor for white light emitting diodes [5]. $\text{Zn}_3\text{V}_2\text{O}_8$ with nanosheet structure demonstrates high performance as an anode material for lithium-ion batteries with good rate capacity, high cycling stability, and excellent discharge capacity as reported in [6]. Moreover, the zinc pyrovanadate nanowires show significantly improved electrochemical performance as an intercalation cathode for an aqueous zinc-ion battery [7]. It can be used for effective catalytic delignification and fractionation of lignocellulosic biomass [8], selective oxidation of sugars to carboxylic acids [9], and as photocatalysts [10–12]. It can be also applied as material for the sensing electrode to detect acetone (to 100 ppm) [13] and as material for an ethanol gas sensor [14].

However, $\text{Zn}_3\text{V}_2\text{O}_8$ is usually obtained from soluble salts by a co-precipitation method [6, 11, 12, 15, 16] or from oxides by solid-state synthesis [10, 11, 17–20]. Both of these methods are not eco-friendly and require a long time. Usually for the obtaining $\text{Zn}_3\text{V}_2\text{O}_7(\text{OH})_2 \cdot 2(\text{H}_2\text{O})$ with subsequent formation of $\text{Zn}_3\text{V}_2\text{O}_8$, typical synthesis from soluble salts is applied. The salts, $\text{Zn}(\text{NO}_3)_2 \cdot 6\text{H}_2\text{O}$ and NH_4VO_3 , are used more often for the synthesis of $\text{Zn}_3\text{V}_2\text{O}_7(\text{OH})_2 \cdot 2(\text{H}_2\text{O})$ [13, 15, 16, 21, 22]. ZnCl_2 or ZnSO_4 is used less often [6, 12, 23] but for all the experiments the molar ratio of $\text{Zn}/\text{V} = 3:2$ was used. However, using highly diluted solutions due to the low solubility of NH_4VO_3 should be noted. In addition, after the synthesis, the product must be washed several times to remove by-products. The superiority of this synthesis is possible formation of 2D nanosheets [6, 15] or 3D microspheres [11, 15] or even nanobelts [11, 16] structures of $\text{Zn}_3\text{V}_2\text{O}_7(\text{OH})_2 \cdot 2(\text{H}_2\text{O})$. The most of these references mention the use of an autoclave for the successful synthesis [6, 11, 16, 21, 23, 24]. An alternative is a solid-state method of syntheses leading to the direct formation of $\text{Zn}_3\text{V}_2\text{O}_8$. However, this method results in the formation of $\text{Zn}_3\text{V}_2\text{O}_8$ with the grain shape possessing low S_{BET} of ca. $0.5 \text{ m}^2/\text{g}$ [5]. Only conventional SS synthesis as the way to the formation of $\text{Zn}_3\text{V}_2\text{O}_8$ from oxides was described in scientific literature. Although the SS synthesis can lead to the complete transformation of starting reagents without any pollution by by-products, it is impossible to obtain nanostructures by this method.

Therefore, the first method requires a lot of water for washing while the second one demands high temperature and doesn't lead to the formation of nanostructures. The possibility of the formation of zinc pyrovanadate from oxides under ultrasonic treatment has been studied in the current work. In addition, zinc pyrovanadate was synthesized by conventional solid-state method for comparison.

2 Experimental

The samples preparation

Ultrasonic synthesis was carried out according to the procedure described in the literature [25] with some modifications. ZnO 2.86 g and V₂O₅ 2.14 g powders (3:1 molar ratio) were mixed together, transferred into a beaker and de-ionized water (80 ml) was added. The weight ratio of initial oxides/water is 1/16. Ultrasonic treatment (UST) of the oxides mixture was carried out for 40 min at room temperature using an UZDN-A ultrasonic dispersant operating in an acoustic cavitations mode at a frequency of 22 kHz. A yellow suspension was obtained. The resulting product was filtered off, dried in air at 100 °C, and labeled as ZnVO_US_100. The sample ZnVO_US_100 was calcined at 500 °C in an alumina crucible in air for 4 h and labeled as ZnVO_US_500.

Additionally, Zn₃V₂O₈ was synthesized by a conventional solid-state method according to the procedure used in [10] with some modifications. ZnO 2.86 g and V₂O₅ 2.14 g powders (3:1 molar ratio of oxides) were grinded using an agate mortar for 3 min, then transferred in an alumina crucible and calcined at 600 °C in air for 5 h. Afterward, the sample was cooled and grinded again using an agate mortar for 3 min. Finally, the sample was calcined at 750 °C in air for 6 h and labeled as ZnVO_SS.

Characterization of the samples

To analyze the samples composition and morphology, a scanning electron microscope (SEM JSM6490 LV, JEOL, Japan) with an integrated system for electron microprobe analysis INCA Energy based on energy-dispersive and wavelength-dispersive spectrometers (EDS + WDS, OXFORD, UK) with HKL Channel system was used.

Transmission electron microscopy (TEM) JEM-1200 EX (JEOL, Japan) was applied to study the materials morphology.

Nitrogen ad(de)sorption isotherms at -196 °C were obtained on a Quantachrome NOVA-220e Gas Sorption Analyzer. Specific surface area S_{BET} was estimated using the BET equation.

Thermogravimetric analysis (DTA/TG) was carried out on a Derivatograph-Q apparatus with a heating rate of 10 °C/min under air atmosphere from room temperature to 700 °C. The sample mass was 200 mg.

3 Results and Discussion

XRD

Figure 1a shows the X-ray diffraction (XRD) patterns of the initial oxides mixture: ZnO (JCPDS card no. 00-080-0075) and V_2O_5 (JCPDS card no. 00-041-1426).

In XRD pattern of ZnVO_US_100 (Fig. 1b), all the reflexes can be attributed to hexagonal structure $Zn_3V_2O_7(OH)_2 \cdot 2(H_2O)$ (JCPDS card no. 00-087-0417) indicating high sample purity and crystallinity. ZnVO_US_500 has the diffraction signals corresponded to $Zn_3V_2O_8$ (JCPDS card no. 00-034-0378) (Fig. 1c). Any peaks from others phases were not detected in the XRD patterns both for ZnVO_US_100 and

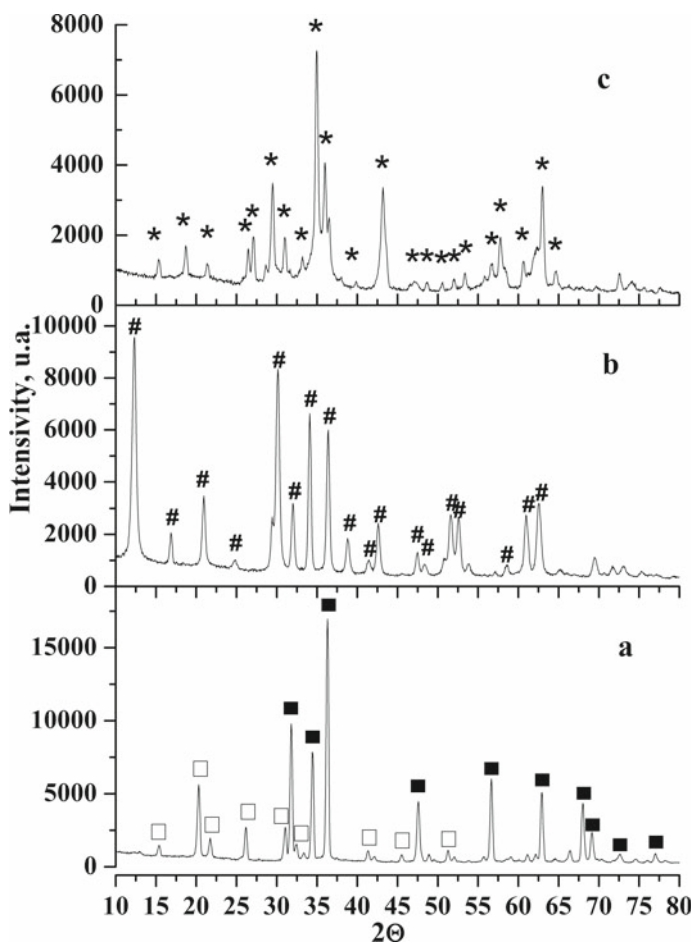
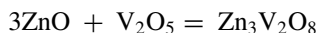
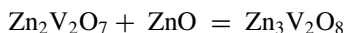
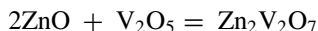


Fig. 1 XRD patterns of **a** the initial mixture ZnO and V_2O_5 , **b** $Zn_3V_2O_7(OH)_2 \cdot 2(H_2O)$, and **c** $Zn_3V_2O_8$ where ■—ZnO, □— V_2O_5 , #— $Zn_3V_2O_7(OH)_2 \cdot 2(H_2O)$, and *— $Zn_3V_2O_8$

ZnVO_US_500 testifying the high purity of $\text{Zn}_3\text{V}_2\text{O}_7(\text{OH})_2 \cdot 2(\text{H}_2\text{O})$ and $\text{Zn}_3\text{V}_2\text{O}_8$ synthesized by ultrasonic treatment.

Figure 2 shows the XRD pattern of ZnVO_SS. The most intensive peaks at 2Θ —15.4; 18.7; 21.4; 26.5; 27.1; 29.1; 31.0; 34.9; 36.0; 41.1; and 62.9 correspond to $\text{Zn}_3\text{V}_2\text{O}_8$ as a main product. Moreover, the impurity phases of $\text{Zn}_2\text{V}_2\text{O}_7$ (JCPDS card no. 00-070-1532) (2Θ —16.7; 25.8; 28.64; 33.6; 40.6; and 42.2) and ZnO (2Θ —31.7) were registered. It should be noted not long synthesis time (11 h) in our case compared to the conventional synthesis in other references [17–19]. Based on the XRD data, the following reactions can be assumed:



The synthesis of pyrovanadates by SS method usually is long-term and requires high temperatures. Therefore, the authors [11] synthesized vanadates by SS method during 1 week at $T = 797^\circ\text{C}$ (XRD pattern was not shown; also there is no information about the impurities). In [10], synthesis was carried out during 60 h, and authors failed to synthesize pure $\text{Zn}_3\text{V}_2\text{O}_8$ phase. The XRD patterns of their final product except $\text{Zn}_3\text{V}_2\text{O}_8$ also have several peaks corresponded to a little amount of impurity phase (the impurity phase was not identified). Kurzawa et al. [20] investigated V_2O_5 – ZnO system and corresponding phase diagram. It was pointed out that the molar ZnO to

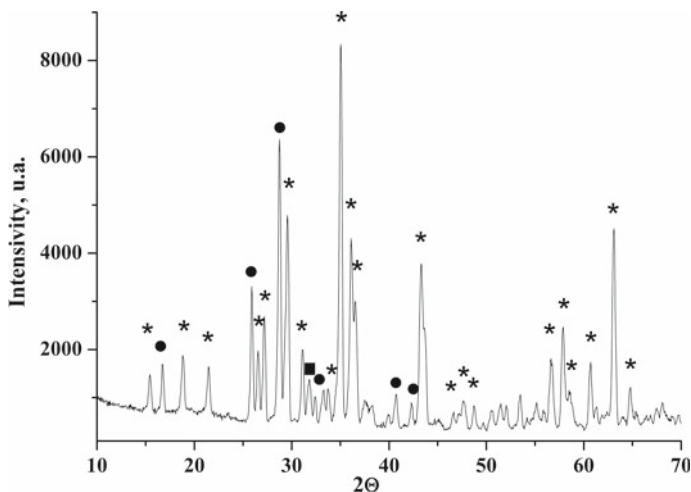
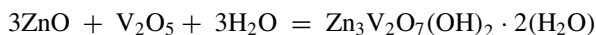


Fig. 2 XRD patterns of $\text{Zn}_3\text{V}_2\text{O}_8$ synthesized by solid-state synthesis from ZnO and V_2O_5 : *— $\text{Zn}_3\text{V}_2\text{O}_8$, ●— $\text{Zn}_2\text{V}_2\text{O}_7$, ■— ZnO

V_2O_5 ratio of 3:1 led to the formation of both $Zn_3V_2O_8$ as $Zn_2V_2O_7$ phases. It should be noted that the traditional solid-state synthesis of salts from oxides often leads to the formation of the main product with some amount of impurity phases [6, 25]. Comparison of the X-ray diffraction patterns of the product obtained as a result of ultrasonic and solvothermal synthesis allows to make an assumption about the key role of water in the formation of zinc pyrovanadate salt from oxides. And the key product is exactly zinc pyrovanadate crystal hydrate:



The absence of any impurity phases in the X-ray diffraction patterns of both ZnVO_US_100 and ZnVO_US_500 (Fig. 1b, c) also makes it possible to assume the formation of pure $Zn_3V_2O_7(OH)_2$ phase with the subsequent transformation into pure $Zn_3V_2O_8$ phase.

SEM

SEM image of ZnVO_US_100 is shown in Fig. 3. Morphology of ZnVO_US_100 has a typical overall view for $Zn_3V_2O_7(OH)_2 \cdot 2(H_2O)$ obtained by a conventional coprecipitate method [6, 9, 26]. Uniform size distribution of the particles in the sample is observed. The sample consists of nanoparticles in the form of nanosheets, each of which has a flat size of 0.1–1 μm and a thickness of 10–40 nm. The data of energy-dispersive X-ray spectroscopy (determined at four different points) demonstrate the uniform elements distribution in the sample (Table 1). The data of SEM and EDX are in a good agreement with the XRD data (Fig. 1a) and confirm complete oxides conversion to $Zn_3V_2O_7(OH)_2 \cdot 2(H_2O)$.

TEM

The TEM images of the initial oxides V_2O_5 and ZnO used for the preparation of zinc vanadate by both ultrasonic and solid-state methods are presented in Fig. 4a, b,

Fig. 3 SEM image of $Zn_3V_2O_7(OH)_2 \cdot 2(H_2O)$

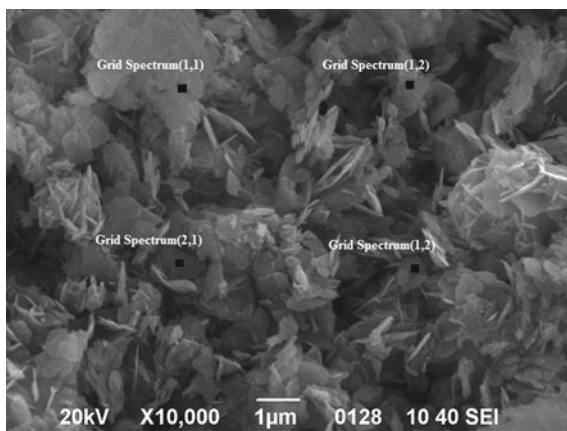


Table 1 The results of energy-dispersive X-ray spectroscopy for ZnVO_US_100^a

Spectrum	V	Zn	O
Grid Spectrum(1,1)	14.83	24.05	61.12
Grid Spectrum(2,1)	14.21	25.13	60.66
Grid Spectrum(1,2)	14.84	24.04	61.13
Grid Spectrum(2,2)	15.12	23.55	61.34
Mean	14.75	24.19	61.06
Std. deviation	0.38	0.67	0.29

^a (All results in atomic %)

respectively. Typical particle of $\text{Zn}_3\text{V}_2\text{O}_7(\text{OH})_2 \cdot 2(\text{H}_2\text{O})$ is displayed in TEM image Fig. 5a, b. TEM images of $\text{Zn}_3\text{V}_2\text{O}_7(\text{OH})_2 \cdot 2(\text{H}_2\text{O})$ don't contain the particles of the initials oxides (Fig. 4a, b) instead, the particles with sheet-like structure gathered in agglomerates can be observed. The size of the particle plane ranges from several nm to $1 \mu\text{m}$. The light color of the $\text{Zn}_3\text{V}_2\text{O}_7(\text{OH})_2 \cdot 2(\text{H}_2\text{O})$ particles indicate their small thickness. This is in a good agreement with the literature data about the sheet-like particles of $\text{Zn}_3\text{V}_2\text{O}_7(\text{OH})_2 \cdot 2(\text{H}_2\text{O})$ obtained by a co-precipitation method [6, 11]. In addition, some amount of particles with hexagonal structure is present in TEM images. As known, $\text{Zn}_3\text{V}_2\text{O}_7(\text{OH})_2 \cdot 2(\text{H}_2\text{O})$ crystallizes in the hexagonal space group P-6 [6, 11, 24].

Specific surface area

The data of nitrogen ad(de)sorption (Fig. 6) show that the sample $\text{Zn}_3\text{V}_2\text{O}_7$ obtained by a solid-state reaction is characterized by the low specific surface area (S_{BET} within $1 \text{ m}^2\text{g}^{-1}$) while the sample obtained by an US method have higher specific surface area (S_{BET} ca. $14 \text{ m}^2\text{g}^{-1}$), and ad(de)sorption isotherm has hysteresis in a wide area of relative nitrogen pressure indicating the presence of mesopores with different sizes.

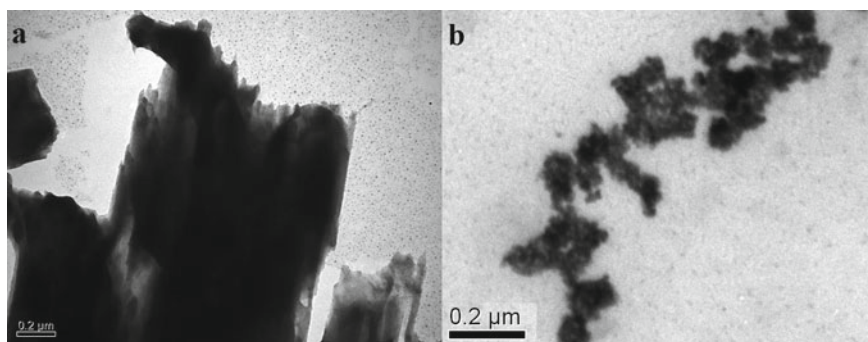


Fig. 4 TEM images of the initial oxides **a** V_2O_5 and **b** ZnO

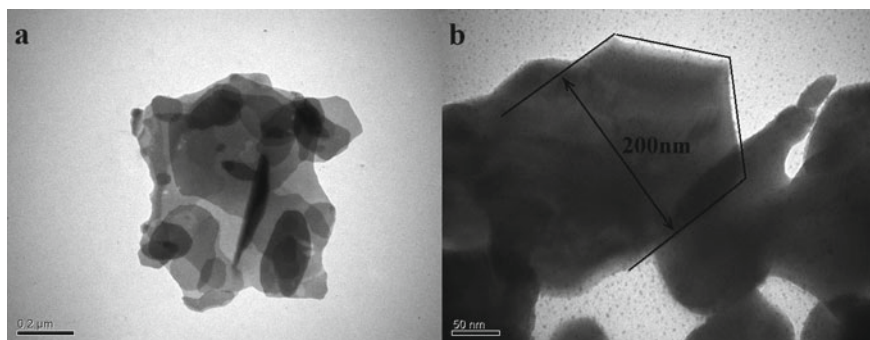


Fig. 5 TEM images of ZnVO_US_100

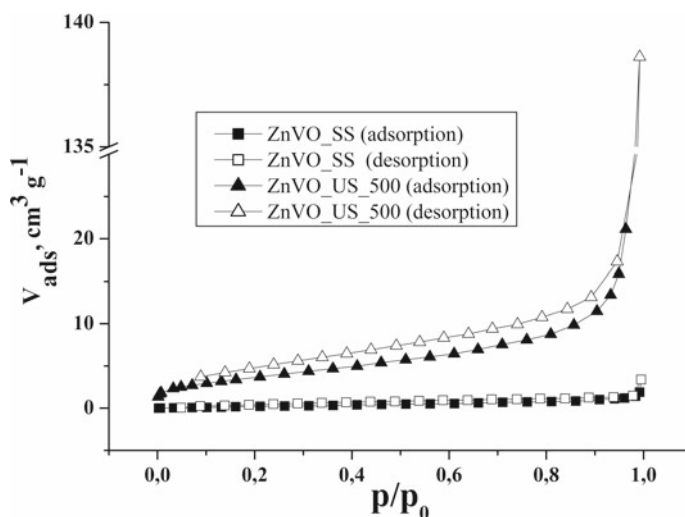


Fig. 6 Nitrogen ad(de)sorption isotherms (77 K) for $\text{Zn}_3\text{V}_2\text{O}_8$ synthesized by the solid-state method and $\text{Zn}_3\text{V}_2\text{O}_8$ synthesized by the ultrasonic method

DTA

The thermal stability of $\text{Zn}_3\text{V}_2\text{O}_7(\text{OH})_2 \cdot 2(\text{H}_2\text{O})$ was studied using DTA in air (Fig. 7). The TG curve has total weight loss of about 12.73% in an interval from 60 to 350 °C. The DTA curve has two endothermic peaks at 164 °C and 267 °C, being agreed well with weight loss on the TG curve. The removal of water of crystallization and coordinated water corresponds to the weight loss of 11.27%: $\text{Zn}_3\text{V}_2\text{O}_7(\text{OH})_2 \cdot 2(\text{H}_2\text{O}) = \text{Zn}_3\text{V}_2\text{O}_8 + 3\text{H}_2\text{O}$. Other 1.46% of weight loss can be explained by losing water adsorbed in the pore or on the surface. Published TG and DTA data for $\text{Zn}_3\text{V}_2\text{O}_7(\text{OH})_2 \cdot 2(\text{H}_2\text{O})$ are contradictory. The maximum of the first endothermic peak is located at 163 °C well corresponding to [11]. Next endothermic peak is

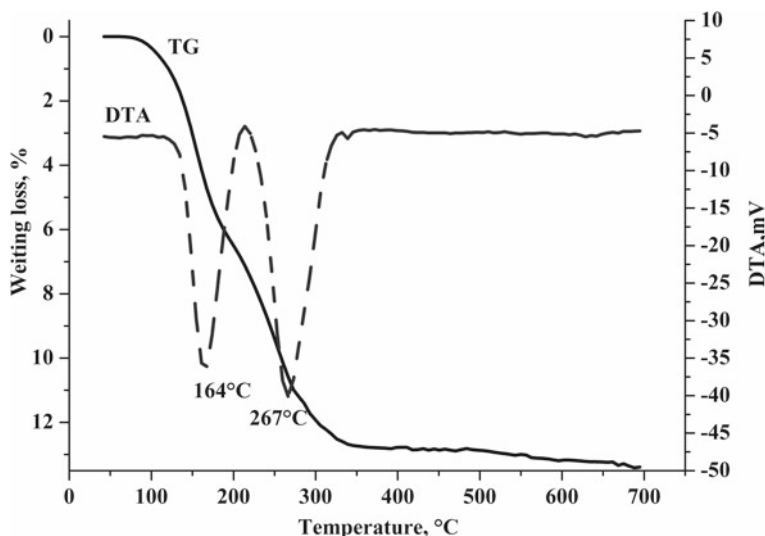


Fig. 7 TG and DTA analysis of $\text{Zn}_3\text{V}_2\text{O}_7(\text{OH})_2 \cdot 2(\text{H}_2\text{O})$

located at 267 °C being more similar to the data described in [27]. Moreover, DTA curves presented in [11, 27] have exothermic peak at 452 °C and 550 °C, respectively. However, in our case, no exothermic peak in DTA curves was observed as well as in [15]. Such differences in the location of the maxima of endothermic peaks can be explained by the differences in the synthesis or TG and DTA analysis conditions.

Additionally, TG and DTA of the initial mixture of oxides were carried out, but no thermodynamic effects and weight loss were observed.

4 Conclusions

In summary, a facile, eco-friendly method of synthesis of $\text{Zn}_3\text{V}_2\text{O}_7(\text{OH})_2 \cdot 2(\text{H}_2\text{O})$ followed by the formation of pure $\text{Zn}_3\text{V}_2\text{O}_8$ phase was proposed. This approach in contrast to conventional co-precipitation synthesis doesn't require a lot of water for washing from polluting ions. The advantages of the US synthesis compared to the conventional SS synthesis are lower duration and temperature, as well as the formation of pure $\text{Zn}_3\text{V}_2\text{O}_7(\text{OH})_2 \cdot 2(\text{H}_2\text{O})$ phase further transformed into pure $\text{Zn}_3\text{V}_2\text{O}_8$ phase. Moreover, US synthesis allows obtain samples with nanosheet structures and high S_{BET} . Thus, the ultrasonic method is much more environmentally friendly than other traditional methods of synthesis.

Acknowledgements This work was financially supported by NASU Program "New functional substances and materials of chemical production" (project 13-21).

References

1. Putluru SSR, Schill L, Godiksen A, Poreddy R, Mossin S, Jensen AD, Fehrmann R (2016) Promoted V_2O_5/TiO_2 catalysts for selective catalytic reduction of NO with NH_3 at low temperatures. *Appl Catal B* 183:282–290. <https://doi.org/10.1016/j.apcatb.2015.10.044>
2. Zazhigalov VA, Diyuk EA, Sidorchuk VV (2014) Development of VPO catalysts supported on mesoporous modified material based on an aerosol gel. *Kinet Catal* 55(3):399–408. <https://doi.org/10.1134/S002315840904017X>
3. Pessoa JC, Etcheverry S (2015) Vanadium compounds in medicine. *Coordination Chem Rev* 301–302:24–48. <https://doi.org/10.1016/j.ccr.2014.12.002>
4. Semiz S (2022) Vanadium as potential therapeutic agent for COVID-19: A focus on its antiviral, antiinflammatory, and antihyperglycemic effects. *J Trace Elem Med Biol* 69:126887. <https://doi.org/10.1016/j.jtemb.2021.126887>
5. Qian T, Fan B, Wang H, Zhu S (2019) Structure and luminescence properties of $Zn_3V_2O_8$ yellow phosphor for white light emitting diodes. *Chem Phys Lett* 715:34–39. <https://doi.org/10.1016/j.cplett.2018.11.022>
6. Gan L, Deng D, Zhang Y, Li G, Wang X, Jiang L, Wang C (2014) $Zn_3V_2O_8$ hexagon nanosheets: a high-performance anode material for lithium-ion batteries. *J Mater Chem A* 2:2461–2466. <https://doi.org/10.1039/C3TA14242F>
7. Xia C, Guo J, Lei Y, Liang H, Zhao C, Alshareef H (2017) Rechargeable aqueous Zinc-Ion battery based on porous framework Zinc pyrovanadate intercalation cathode. *Adv Mater* 1705580. <https://doi.org/10.1002/adma.201705580>
8. Khallouk K, Solhy A, Kherbeche A, Dubreucq E, Kouisni L, Barakat A (2020) Effective catalytic delignification and fractionation of lignocellulosic biomass in water over $Zn_3V_2O_8$ mixed oxide. *ACS Omega* 5(1):304–316. <https://doi.org/10.1021/acsomega.9b02159>
9. Khallouk K, Solhy A, Idrissi N, Flaud V, Kherbeche A, Barakat A (2020) Microwave-assisted selective oxidation of sugars to carboxylic acids derivatives in water over zinc-vanadium mixed oxide. *Chem Eng J* 385:123914. <https://doi.org/10.1016/j.cej.2019.123914>
10. Wang D, Tang J, Zou Z, Ye J (2005) Photophysical and photocatalytic properties of a new series of visible-light-driven photocatalysts $M_3V_2O_8$ ($M = Mg, Ni, Zn$). *Chem Mater* 17:5177–5182. <https://doi.org/10.1021/cm051016x>
11. Shi R, Wang Y, Zhou F, Zhu Y (2011) $Zn_3V_2O_7(OH)_2(H_2O)_2$ and $Zn_3V_2O_8$ nanostructures: controlled fabrication and photocatalytic performance. *J Mater Chem* 21:6313–6320. <https://doi.org/10.1039/C0JM04451B>
12. Mondal C, Ganguly M, Sinha AK, Pal J, Sahoo R, Pal T (2013) Robust cubooctahedron $Zn_3V_2O_8$ in gram quantity: a material for photocatalytic dye degradation in water. *Cryst Eng Comm* 15:6745–6751. <https://doi.org/10.1039/C3CE40852C>
13. Liu F, Guan Y, Sun R, Liang X, Sun P, Liu F, Lu G (2015) Mixed potential type acetone sensor using stabilized zirconia and $M_3V_2O_8$ ($M: Zn, Co$ and Ni) sensing electrode. *Sens Actuat B* 221:673–680. <https://doi.org/10.1016/j.snb.2015.07.023>
14. Hua K, Cui M, Luo Z, Fang D, Bao R, Qi Q, Yi J, Sun B, Chen C (2019) Fabrication of Zinc pyrovanadate ($Zn_3(OH)_2V_2O_7 \cdot 2H_2O$) nanosheet spheres as an ethanol gas sensor. *J Alloy Compd* 801:581–588. <https://doi.org/10.1016/j.jallcom.2019.06.015>
15. Zhang SY, Xiao X, Lu M, Li ZQ (2013) $Zn_3V_2O_7(OH)_2 \cdot 2H_2O$ and $Zn_3(VO_4)_2$ 3D microspheres as anode materials for lithium-ion batteries. *J Mater Sci* 48:3679–3685. <https://doi.org/10.1007/s10853-013-7164-5>
16. Zhang S, Lei N, Ma W, Zhang Z, Sun Z, Wang Y (2014) Fabrication of ultralong $Zn_3V_2O_7(OH)_2 \cdot 2H_2O$ nanobelts and its application in lithium-ion batteries. *Mat Lett* 129:91–94. <https://doi.org/10.1016/j.matlet.2014.05.047>
17. Gopal R, Calvo C (1971) Crystal structure of α - $Zn_3(VO_4)_2$. *Can J Chem* 49:3056–3059. <https://doi.org/10.1139/v71-510>
18. Clark GM, Pick AN (1975) DTA study of the reactions of V_2O_5 with metal (II) oxides. *J Therm Anal* 7:289–300. <https://doi.org/10.1007/BF01911939>

19. Nord AG, Stefanidis T (1985) Crystal chemistry of $a-(Zn, M)_2V_2O_7$ solid solutions correlation between preference for five-coordination and extension of solid solubility. *Mat Res Bull* 20:845–851. [https://doi.org/10.1016/0025-5408\(85\)90064-9](https://doi.org/10.1016/0025-5408(85)90064-9)
20. Kurzawa M, Rychlowska-Himmel I, Bosacka M, Blonska-Tabero A (2001) Reinvestigation of phase equilibria in the V_2O_5 –ZnO system. *J Therm Anal Calorim* 64:1113–1119. <https://doi.org/10.1023/A:1011524424682>
21. Yang G, Li S, Wu M, Wang C (2016) Zinc pyrovanadate nanosheet of atomic thickness: excellent li-storage properties and investigation of electrochemical mechanism. *J Mater Chem A* 4:10974–10985. <https://doi.org/10.1039/C6TA02782B>
22. Mazloom F, Masjedi-Arani M, Salavati-Niasari M (2017) Rapid and solvent-free solid-state synthesis and characterization of $Zn_3V_2O_8$ nanostructures and their phenol red aqueous solution photodegradation. *Solid State Sci* 70:101–109. <https://doi.org/10.1016/j.solidstatesciences.2017.06.013>
23. Low WH, Khiew PS, Lim SS, Siong CW, Chia CH, Ezeigwe ER (2019) Facile synthesis of graphene- $Zn_3V_2O_8$ nanocomposite as a high performance electrode material for symmetric supercapacitor. *J Alloy Compd* 784:847–858. <https://doi.org/10.1016/j.jallcom.2019.01.137>
24. Bayat A, Mahjoub AR, Amini MM (2018) Optical and magnetic properties of zinc vanadates: synthetic design of colloidal $Zn_3V_2O_7(OH)_2(H_2O)_2$, ZnV_2O_4 and $Zn_3V_2O_8$ nanostructures. *J Mater Sci: Mater Electron* 29:2915–2926. <https://doi.org/10.1007/s10854-017-8222-6>
25. Diyuk OA, Zazhigalov VA, Shcherban ND, Permyakov VV, Diyuk NV, Shcherbakov SM, Sachukl OV, Dulian P (2021) Kinetics of $ZnMoO_4 \cdot 0.8H_2O$ and α - $ZnMoO_4$ formation at ultrasonic treatment of ZnO and MoO_3 mixture. In: Fesenko O, Yatsenko L (eds) *Nanocomposites, nanostructures, and their applications*. Springer Proceedings in Physics book series, vol 263, 87–101. https://doi.org/10.1007/978-3-030-74741-1_6
26. Luo J, Ning X, Zhan L, Zhou X (2021) Facile construction of a fascinating Z-scheme $AgI/Zn_3V_2O_8$ photocatalyst for the photocatalytic degradation of tetracycline under visible light irradiation. *Sep Purif Technol* 255:117691. <https://doi.org/10.1016/j.seppur.2020.117691>
27. Hoyos DA, Echavarria A, Saldarriaga C (2001) Synthesis and structure of a porous zinc vanadate, $Zn_3(VO_4)_2 \cdot 3H_2O$. *J Mater Sci* 36:5515–5518. <https://doi.org/10.1023/A:1012418706071>

Electrical Characteristics of Nanosized ZnO Films, Obtained Using Polyvinyl Alcohol, in Different Atmospheres



A. P. Chebanenko, L. M. Filevska , V. S. Grinevych ,
and V. A. Smyntyna 

Abstract The work studied the effect of various media (water vapor, ammonia, and isopropanol in air) on the electrical characteristics of ZnO thin films. In all cases, changes in the electrical characteristics of the films were observed, but the nature of these changes was different. In the presence of ammonia vapor at room temperature, the film current almost doubled. Moreover, the adsorption process is more inertial than the desorption one. The same films at room temperature do not react to propanol vapors in the ambient air. At a temperature of 373 K, the sensitivity to propanol increases considerably. Films are sensitive to moisture at room temperature. However, in comparison with the reaction to ammonia, the reaction to water vapor is more inertial and the sensitivity is lower. The difference in the values and temperatures of the sensitivity of zinc oxide films to different adsorbates allows us to consider them as sensitive elements for multisensors.

Keywords Zinc oxide thin films · Electrical characteristics of thin films · Ammonia sensitivity · Sensitivity to propanol · Sensitive to moisture

1 Introduction

Nanosized films are actively used as transparent electrodes for solar cells, LEDs and other optoelectronic devices, and sensitive elements of gas sensors.

Zinc oxide nanosized films, in particular, are actively used in electronics as transparent electrodes for solar cells [1], light-emitting diodes [2], lasers, photodetectors, and other optoelectronic devices [3]. Recently, such films are actively used also as sensitive elements for sensors of various gases [4–6]. All of these and many other applications of zinc oxide are possible due to its physical properties. Zinc oxide is a

A. P. Chebanenko · L. M. Filevska (✉) · V. S. Grinevych · V. A. Smyntyna
Odesa I.I. Mechnikov National University, Dvoryanska Str., 2, Odesa 65082, Ukraine
e-mail: lfilevska@gmail.com

A. P. Chebanenko
e-mail: chebanenko@onu.edu.ua

wide-gap semiconductor (3.3–3.4 eV [6]) of the n-type. The advantage is the direct band gap transition of its energy structure, a fairly high value of the binding energy of excitons [6], and broad optical absorption band. Its insolubility, chemical stability, and good catalytic activity are also important for applications in catalysis and gas sensors.

Nanoscale forms of this material are actively used due to the enhancement of interesting existing features and to the acquisition of new ones. In the nanoscale form, its catalytic and sensory properties are intensified, which leads to a decrease in the working temperature of such processes. Various types of zinc oxide nanoforms can be obtained by both physical and chemical methods, among which there are enough simple and cheap ones [3, 7–10]. The sol–gel method was chosen for producing thin zinc oxide films as a simple and cheap method, allowing the introduction of various additives in the production process, for an example, to change the structure, doping, and, consequently, to improve its functional characteristics.

In this work, the effect of various media (water vapor, ammonia, and isopropanol in air) on the electrical characteristics of such films was studied. The ammonia vapors impact control is important in monitoring human health, the food industry, food trade, and agriculture. The usage of isopropanol widespread for cleaning beginning from electronics up to the service industry also requires the control of its vapors in such workplaces. Taking into account the effect of moisture on the components of electronic elements based on zinc oxide is also useful in industries and everyday life.

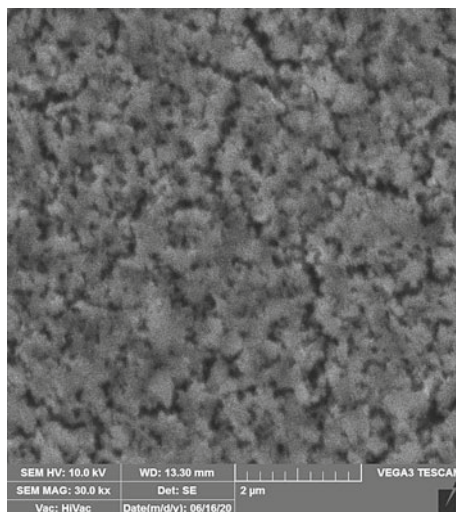
2 Methods

The investigated zinc oxide films were obtained from aqueous solutions of zinc acetate with the addition of polyvinyl alcohol as a structuring additive. The initial solutions were applied to the prepared glass substrates. The resulting preparatives were annealed in a muffle furnace. The method for producing films is described in detail in [10].

The films had a porous nanoscale structure, which was confirmed by SEM studies and is shown in Fig. 1. In addition to porosity, a certain fractality of the film structure is noticeable. Zinc oxide films obtained from zinc acetate by the sol–gel method by the authors of [11] In general, the structure looks like being composed of nanosized agglomerates up to 50–100 nm in diameter. Such a developed porous structure with a large surface area is preferable for adsorption-sensitive sensor elements. It provides good contact with the detected substances, and, therefore, a noticeable response when interacting with them.

The electrical characteristics: current–voltage characteristics (CVC), dark current temperature dependence (DCTD), and the conductivity kinetics of the films were measured in an atmosphere of dry air and in atmospheres containing water vapor, ammonia, and isopropyl alcohol. The atmosphere under study was formed in the measuring chamber by introducing a portion of the detected gas into the atmosphere of specially dried air.

Fig. 1 SEM image of the studied zinc oxide film



3 Results and Discussion

Investigations of the current–voltage characteristics were carried out to elucidate the dominant mechanism of conduction in zinc oxide films in air and with the addition of water or ammonia vapors to the research chamber.

Figure 2 shows the current–voltage characteristics of a zinc oxide film, which were measured in an air atmosphere at temperatures of 290 K (curve 1) and 420 K (curve 2) and in the presence of water vapor at a temperature of 290 K (curve 3). In an air atmosphere at temperatures of 290 K (curve 1), the CV characteristic of the studied zinc oxide film has an exponential dependence. This dependence is typical for the barrier mechanism of current flow. The CV characteristic in an air atmosphere at a temperature of 420 K shows the current flow values higher almost on the order of magnitude (at the same voltage values), and in addition, the degree of its superlinearity is less than at room temperature. This behavior indicates an increase in the concentration of electrons in the conduction band of the ZnO film with increasing temperature. Therefore, the effect of intercrystalline barriers on the current flow with increasing temperature is less pronounced.

It can be seen that in an atmosphere containing water vapor (Fig. 2, curve 3), the electrical conductivity shows higher values in comparison with the electrical conductivity in dry air. Similar results obtained on zinc oxide films are known in the literature [12] and are explained by the dissociative adsorption of water on the surface of the ZnO film. Water is absorbed on zinc oxide in both molecular and dissociative form. Dissociative adsorption on nanosized forms of ZnO mainly occurs on oxygen vacancies, which adsorb and neutralize hydroxyl groups OH^- [13].

In an atmosphere with ammonia vapor, the electrical conductivity of the studied zinc oxide films also differed from this indicator in dry air. Figure 3 shows the CV

Fig. 2 CVC of ZnO film in air atmosphere at 290 K (1) and 420 K (2) and in the presence of water vapor at 290 K (3)

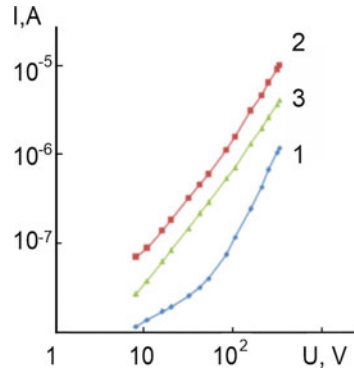
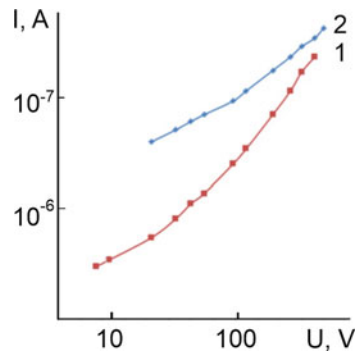


Fig. 3 CVC of ZnO film in air atmosphere (1) and with ammonia vapor (2) at 290 K



characteristic of a zinc oxide film in dry air (curve 1) and in air with ammonia vapor (curve 2). The exponential character of the dependence, as well as its straightening in the coordinates. $\ln I \sim U^{1/4}$, indicates the above-barrier Schottky emission through thin intercrystalline barriers [14] as the dominant mechanism of current transfer in the film.

In ammonia vapor, the CVC of the ZnO film (curve 2 in Fig. 3) is almost an order of magnitude higher than in air. This is especially noticeable in the region of low voltages.

In works [12, 15] it was shown that the stable configuration of NH_3 during adsorption on the surface of zinc oxide is the binding of the nitrogen atom (N) with the surface zinc atom (Zn). In this case, even at ambient temperature (~ 300 K) [15], charge transfer to the ZnO surface is observed. Molecular chemisorption of NH_3 occurs on the ZnO surface, in which ammonia molecules become donors of charge carriers. As a result, the equilibrium surface bending of the energy bands decreases and the conductivity of thin zinc oxide films increases.

The temperature dependences of the current of zinc oxide films were studied in dry air, in atmospheres with water vapor, ammonia, and isopropyl alcohol in the temperature range 290–723 K.

Fig. 4 Current temperature dependences in ZnO film in air atmosphere (1–2–3) and in the presence of water vapor (4–5–6). ($V = 200$ B)

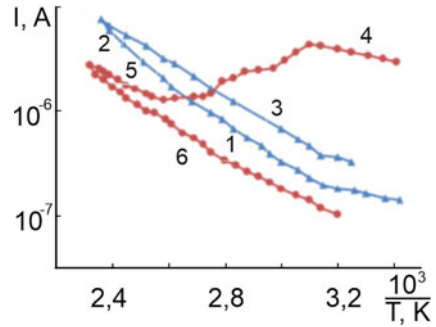


Figure 4 shows the DCTD of ZnO films in dry air (1–2–3) and in the presence of water vapor (4–5–6). Electrical conductivity was measured both when the sample was heated (Sections 1–2) and when it was cooled (Section 3).

In the atmosphere of dry air, the conductivity grows exponentially with temperature increasing wherein the dependence shows several sections with different activation energies. The minimal growth in conductivity is observed in the temperature range 290–320 K with conductivity activation energy of about 0.1 eV. These values correspond to the shallow donors’ contribution to the conductivity, often caused by surface defects. The conduction activation energies in other areas (E_1 , E_2 , and E_3) are presented in Table 1. Their numerical values (0.35–0.5) eV being close to each other are less than half the band gap of zinc oxide. In such cases, electrical conductivity is controlled by intercrystalline potential barriers, and its mechanism can be explained by the semiconductor model with large-scale potential relief fluctuations described in [16].

The current temperature dependence measured in the presence of water vapor has some specific features. So, on DCTD, when the film is heated, there are Sects. 4 and 5, in which the electrical conductivity increases with temperature. Between them there is a section of abnormal temperature dependence 322–395 K, where the electrical conductivity decreases with temperature growth. A similar dependence was observed on thin films of ZnO [17] and SnO₂ [18] in a humid environment. This anomaly can be explained by desorption of physically adsorbed water and hydroxyl groups present on the surface of oxides in a humid atmosphere. In this case, on the surface of the ZnO film, the number of adsorption centers for oxygen increases, which, being adsorbed, captures electrons from the conduction band, thereby leading to a reduction in current flow. A further rise in temperature stimulates desorption of oxygen, and, as a consequence, an increase in conductivity. The possibility of using

Table 1 Conduction activation energies (eV) calculated from the current temperature dependences in the ZnO film

E_1	E_2	E_3	E_4	E_5	E_6
0.37	0.5	0.35	0.1	0.3	0.3–0.35

zinc oxide films as adsorption-sensitive elements of gas sensors, can be clarified by conductivity kinetic studies during the periodic filling the measuring chamber with dry air and gas for detection.

Figure 5 shows the relaxation of the current in the ZnO film with periodic admission of water vapor and dry air into the chamber. The studies were carried out at a constant voltage of 200 V. As it can be seen, the resistance of the film decreases by more than five times when water vapor is let into the atmosphere of the chamber. When dry air is let in, the resistance value is restored to its initial value. Both processes are quite inertial and last 6–8 min. Using the classic sensitivity formula

$$S = \frac{R_o - R}{R_o} \quad (1)$$

(where R_o is the film resistance in air; R is the film resistance in water vapor), the sensitivity of the zinc oxide film to water vapor was calculated.

Similar measurements of current relaxation and sensitivity calculations were performed for other voltages in the range (50–320) V. The dependence of the sensitivity of the ZnO film to water vapor on the applied voltage is shown in Fig. 6. It can be seen that with an increase of the applied voltage, the sensitivity increases, reaches a maximum at a voltage of 200 V and is 0.37 in relative units.

The relaxation of the current with periodic admission of ammonia vapor or dry air into the measuring chamber is shown in Fig. 7. In the presence of ammonia vapor, the current in the ZnO film almost doubles. The adsorption of ammonia is a

Fig. 5 Relaxation of current in ZnO film at periodic inflow into the chamber of water vapor or dry air ($V = 200$ B) at $T = 293$ K

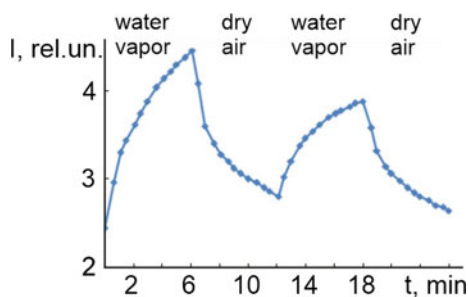


Fig. 6 Dependence of ZnO film sensitivity versus voltage to water vapor

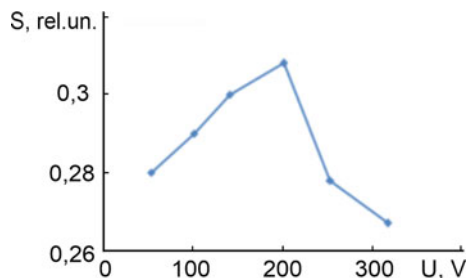


Fig. 7 Relaxation of current in the ZnO film with periodic inflow of ammonia vapor or dry air ($V = 175$ V) at $T = 293$ K into the chamber

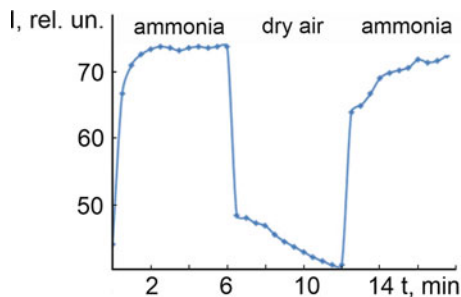
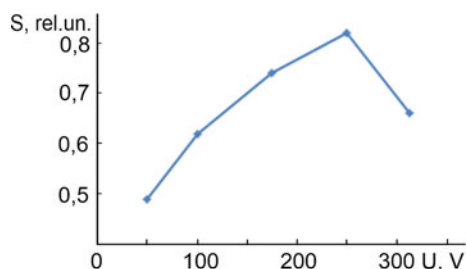


Fig. 8 Dependence of the sensitivity of the ZnO film to ammonia vapor on the applied voltage

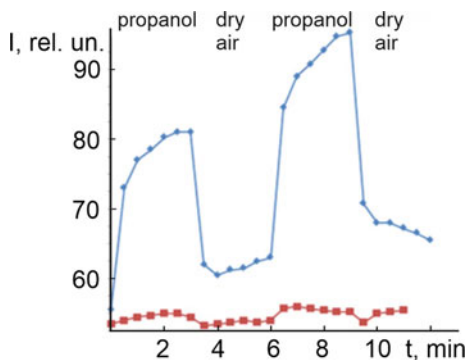


fairly fast-response process. The current reaches 90% of its stationary value (t_{resp} —response time) in about 48 s. After admitting dry air into the chamber, the current decreases almost to its initial value. This process, which actually reflects the ammonia desorption is more inertial than the adsorption process. The recovery time (t_{rel} is the time during which the current falls by 90% of its stationary value) is about 180 s.

From the relaxation curves measured at different values of the applied voltage, the sensitivity of the ZnO film to ammonia vapor was calculated. The dependence of the sensitivity on the applied voltage is shown in Fig. 8. It can be seen that the value of the sensitivity reaches its maximum at a voltage of 250 V and is 0.82 in relative units.

The isopropyl alcohol vapor influence on the conductivity of the studied zinc oxide films was additionally studied. Figure 9 shows the current relaxation measurements in the ZnO film with periodic filling of isopropyl alcohol vapors and dry air into the measuring chamber. As it can be seen, at room temperature (Fig. 9, curve 1), the change in the electrical conductivity of the film in the presence of isopropanol vapor is very small. However, when the ZnO film is heated, its sensitivity to isopropanol vapor increases and already at a temperature of about 363 K; it reaches 0.41 relative units (Fig. 9, curve 2). This indicator is comparable to the sensitivity of the studied ZnO films to water and ammonia vapors. The change in electrical conductivity upon contact of the films with ammonia, as well as the reverse process, occurs rather quickly; the response time can be considered equal to 60–70 s. However, the kinetic dependences show that the current does not reach its initial value during the observation time (180 s for each process). This indicates the formation of stronger chemical

Fig. 9 Relaxation of current in ZnO film when vapor of propanol or dry air is let into the chamber ($V = 200$ B). Red markers— $T = 293$ K and blue— $T = 393$ K



bonds between the isopropanol molecule and the surface at an elevated temperature (393 K) compared to the interaction at room temperature.

The result obtained is probably due to the more complex structure of the isopropyl alcohol (C_3H_7OH) molecule as compared to the H_2O and NH_3 molecules and requires further study. It may be interesting for the application of the same film in the joint control of several pollutants. In this case, local heating of a part of the sensitive element for isopropanol detection can be used.

4 Conclusion

In the studies carried out in all cases, changes in the electrical characteristics of the studied films were observed, but the nature of these changes differs and depends on the nature of the interaction of the adsorbate with the previously adsorbed oxygen.

In the presence of ammonia vapor at room temperature, the current in the film has almost doubled. Moreover, the adsorption process is quite inertial in contrast to the desorption process. The films' sensitivity was at the level of 0.82 relative units.

These same films at room temperature do not react to propanol vapors in the ambient air. However, as the temperature of the layers increases, their electrical conductivity increases. At a temperature of 373 K, the sensitivity to propanol S is 0.41 relative units.

The films have also been noticed to be sensitive to moisture at room temperature. However, compared to the reaction to ammonia, the reaction to water vapor was more inertial and the sensitivity was at the level of 0.37 relative units.

The difference in the values and temperature of the sensitivity of zinc oxide films to different adsorbates allows considering them as a sensitive elements of the multisensors.

References

1. He S, Zou X, Sun Z, Teng G (2013) Influence of precursor solution's concentration on double-layer ZnO structure and solar cell's performance. *Mater Lett* 91:258–260. <https://doi.org/10.1016/j.matlet.2012.09.112>
2. Rahman F (2019) Zinc oxide light-emitting diodes: a review. *Opt Eng* 58(1):010901. <https://doi.org/10.1117/1.OE.58.1.010901>
3. Kołodziejczak-Radzimska A, Jesionowski T (2014) Zinc oxide—from synthesis to application: a review. *Materials (Basel)* 7(4):2833–2881. <https://doi.org/10.3390/ma7042833>
4. Sun Y-F, Liu S-B, Meng F-L, Liu J-Y, Jin Z, Kong L-T, Liu J (2012) Metal oxide nanostructures and their gas sensing properties: a review. *Sensors* 12:2610–2631
5. Carpenter MA, Mathur S, Kolmakov A (2013) *Metal oxide nanomaterials for chemical sensors*. Springer Science & Business Media, New York
6. Jagadish C, Pearson SJ (eds) (2006) *Zinc oxide bulk, thin films and nanostructures*. Elsevier, Amsterdam
7. Sadraei R (2016) A simple method for preparation of nano-sized ZnO. *Res Rev: J Chem (RRJCHEM)* 5(2):45–49
8. Rawat A, Soni U, Malik RS, Pandey SC (2018) Facile synthesis of UV blocking nano-sized Zinc Oxide and Polymethyl-methacrylate polymer nanocomposite coating material. *Nano-Struct Nano-Obj* 16:371–380. <https://doi.org/10.1016/j.nanoso.2018.09.002>
9. Maroufa S, Beniaiche A, Guessas H, Azizi A (2017) Morphological, structural and optical properties of ZnO thin films deposited by dip coating method. *Mater Res* 20(1):88–95. <https://doi.org/10.1590/1980-5373-MR-2015-0751>
10. Chebanenko AP, Filevska LM, Grinevych VS, Bulyga YI, Brytavskiy IV, Smytyna VA (2021) The conductivity mechanisms of ZnO thin films structured using polyvinyl alcohol. In: Fesenko O, Yatsenko L (eds) *Nanomaterials and nanocomposites, nanostructure surfaces, and their applications*. NANO 2020. Springer Proceedings in Physics, vol 263. Springer, Cham. https://doi.org/10.1007/978-3-030-74741-1_27
11. Krasteva LK, Dimitrov DT, Papazova KI, Nikolaev NK, Peshkova TV, Moshnikov VA, Gracheva IE, Karpova SS, Kaneva NV (2013) Synthesis and characterization of nanostructured zinc oxide layers for sensor applications. *Semiconductor* 47(4):586–591
12. Kovalenko MV (2017) *Electronic energy structure, optical-spectral and sensory properties of ZnO-based nanostructures*. Ph.D. thesis, Lviv (in Ukrainian)
13. Noei H, Qiu H, Wang Y, Löffler E, Wöll C, Muhler M (2008) The identification of hydroxyl groups on ZnO nanoparticles by infrared spectroscopy. *Phys Chem Chem Phys* 10:7092–7097
14. Pikus GE (1972) *Fundamentals of the theory of semiconductor devices*, Nauka (in Russian)
15. Nancy AA, Rai PK, Jeyaprakash BG (2018) Understanding ammonia adsorption and charge transfer process on ZnO using experimental and DFT approach. *Mater Chem Phys* 214:540–547. <https://doi.org/10.1016/j.matchemphys.2018.04.101>
16. Bonch-Bruevich VL, Zvyagin IP, Kuiper R, Mironov AG, Enderline R, Esser B (1981) *Electronic theory of disordered semiconductors*. Nauka (in Russian)
17. Nakagawa M, Mitsudo H (1986) Anomalous temperature dependence of the electrical conductivity of zinc oxide thin films. *Surf Sci* 175:157–176
18. Harrison PG, Willett MI (1989) Tin oxide surfaces: electrical properties of tin oxide gel: nature of the surface species controlling the electrical conductance in air as a function of temperature. *J. Chem Soc Faraday Trans 1* 85(8):1921–1932

Estimation of the Role of Nanosized Stabilizing Powders in Gaining High-Level Crack Growth Resistance of Partially Stabilized Zirconia



V. V. Kulyk , Bogdan Vasylyv , Z. A. Duriagina , V. I. Vavrukh ,
P. Ya. Lyutyy , T. M. Kovbasiuk , T. L. Tepla , and M. Ya. Holovchuk 

Abstract Nowadays, zirconium oxide (ZrO_2) is widely used for applications in high temperature structural materials. These materials may have applications such as cracking furnaces, catalytic cracking units, fired heaters, hydrogen reformers, utility boilers, ammonia reformers, air heaters, etc. Zirconium oxide (zirconia) is often more useful in its phase stabilized state. In particular, products made of yttria-stabilized

V. V. Kulyk (✉) · Z. A. Duriagina · V. I. Vavrukh · P. Ya. Lyutyy · T. M. Kovbasiuk · T. L. Tepla
Department of Materials Science and Engineering, Lviv Polytechnic National University, 12 S.
Bandera Str., Lviv 79013, Ukraine
e-mail: kulykvolodymyrvolodymyrovych@gmail.com

Z. A. Duriagina
e-mail: zduriagina@ukr.net

V. I. Vavrukh
e-mail: vavrukh.valentyna@gmail.com

P. Ya. Lyutyy
e-mail: pavlo_lyutyy@ukr.net

T. M. Kovbasiuk
e-mail: felcproject@gmail.com

T. L. Tepla
e-mail: tetiana.l.tepla@lpnu.ua

B. Vasylyv
Department of Hydrogen Technologies and Alternative Energy Materials, Karpenko
Physico-Mechanical Institute of the NAS of Ukraine, 5 Naukova Str., Lviv 79060, Ukraine
e-mail: mechengin1111@gmail.com

Z. A. Duriagina
Department of Materials Engineering, The John Paul II Catholic University of Lublin, 14
Raclawickie Al, 20-950 Lublin, Poland

M. Ya. Holovchuk
Department of Corrosion and Corrosion Protection, Karpenko Physico-Mechanical Institute of the
NAS of Ukraine, 5 Naukova Str., Lviv 79060, Ukraine
e-mail: golovchuk86@gmail.com

zirconia ceramics are characterized by improved strength and crack growth resistance. In this work, ZrO_2 ceramics partially stabilized with 3, 4, and 5 mol% Y_2O_3 (hereinafter: 3YSZ, 4YSZ, and 5YSZ) have been studied. Three sintering temperatures were used to prepare beam specimens of each series: 1450 °C, 1500 °C, and 1550 °C. Vickers microhardness test and single-edge notch beam test were performed and fracture toughness of the material was estimated. It is known that in the case when the sufficient amount of the metastable tetragonal phase is present, an applied stress, magnified by the stress concentration in the crack tip vicinity, can cause the tetragonal phase to convert to monoclinic. This phase transformation associated with the volume expansion causes then put the crack into compression stress at the crack tip, retarding crack growth, and enhancing the fracture toughness. In the case of materials studied in this work, a distinct transformation toughening effect was found for 5YSZ ceramics. Based on the microstructure and fracture surface analyses it was found that nanosized stabilizing powders play a crucial role in gaining high-level crack growth resistance of partially stabilized zirconia.

Keywords YSZ ceramics · Microhardness · Fracture toughness · Microstructure · Fracture micromechanism

1 Introduction

Advanced ceramic materials (zirconia, aluminum oxide, sintered silicon carbide, or other ceramics) are widely used for manufacturing various products to ensure a long life cycle in extreme operating conditions such as high temperature, high pressure, abrasion, corrosion, [1–6]. Depending on the qualities required, ceramic products manufactured of yttria-stabilized zirconia (YSZ) are to be wear and corrosion resistant and possess high strength and crack growth resistance [7, 8]. In particular, the optimization the microstructure and operating modes of ceramic electrodes to increase the energy efficiency of high-temperature fuel cells is an urgent task [7, 9–13]. This promotes the deployment of renewables to meet global climate objectives [14, 15].

To improve the lifetime of products made of YSZ ceramics, there is a need to take into account the above-mentioned extremal conditions [14–22]. From this point of view, the substantiation of chemical composition and manufacturing modes are the crucial issues of the formation of resulting phase compositions and mechanical properties of the produced materials [23–32].

In the work [33], the correlations between chemical compositions, in particular, content of Y_2O_3 and Fe_2O_3 additives, and the microstructure, mechanical properties, and translucency of YSZ ceramics were evaluated. Specimens of zirconia with 3 mol% or 5 mol% Y_2O_3 were sintered at 1475, 1500, 1550, and 1600 °C for 2 h. The microstructure, phase composition, and a set of physical properties were analyzed. In 3YSZ ceramics, only tetragonal ZrO_2 was revealed, while in 5YSZ ceramics the cubic ZrO_2 phase was detected after sintering at 1600 °C. In this sintering mode, an

increase in grain size from 0.8 μm to 2.3 μm with an increase in the Y_2O_3 content from 3 to 5% was found. Besides, the effect of the Y_2O_3 content on strength of the material was revealed. However, the increase in Fe_2O_3 percentage did not cause changes in the microstructure and mechanical properties.

The authors of the work [34] studied ceramics aimed at applications in chemical industry. Series of ceramic specimens were sintered at 1000 °C for 10 h from YSZ powder. For comparison, series of specimens were also sintered from pure zirconium dioxide powder. Phase transformations due to doping were discussed, which allowed understanding the microstructure formation of zirconia with and without doping. Similarly, in the work [35], the authors used detonation synthesis of 2YSZ powder to obtain corresponding ceramics. Although no correlation between mechanical properties and grain size was found, an unusual combination of both very high fracture toughness and strength was revealed. In addition, it was found that during bending of the specimens the broad transformation zone containing shear bands and secondary microcracks was formed on their tensile side. Such fracture character is assumed to be related to the high fracture toughness.

In the works [36, 37], the phase evolution in plasma-sprayed YSZ coatings during annealing was studied. It was revealed using XRD analysis and neutron scattering studies that the tetragonal ZrO_2 phase decomposes into monoclinic and cubic phases with decreasing yttria amount in the tetragonal phase. The authors of the works [38, 39] studied EB-PVD and plasma-sprayed coatings using XRD analysis. They revealed that the tetragonal ZrO_2 phase transforms into a tetragonal phase with low yttria content and a cubic or tetragonal phase with high yttria content in the temperature range of 1300–1400 °C. The authors of the work [40] studied EB-PVD coatings heat-treated at temperatures in the range of 1100–1500 °C. A transmission electron microscopy (TEM) along with XRD analysis was used for studying phase transformations in material. The authors revealed that the tetragonal ZrO_2 phase decomposes into a tetragonal phase with low Y_2O_3 percentage and both tetragonal and cubic phases with high Y_2O_3 percentage. They detected alternation of layers with low and high Y_2O_3 percentage in TEM images. Finally, using computer simulations, it was found that a cubic-like structure of the domain boundaries contains a relatively large number of yttrium ions [41, 42].

In the work [43], zirconia stabilized with 3 mol% Y_2O_3 as a material of monolithic restorations in dentistry was studied. It also contained 0.25% Al_2O_3 additive. It was found that low-temperature degradation could occur when the t- ZrO_2 phase is transformed to m- ZrO_2 phase during aging at temperatures in a range of 100–300 °C. This transformation is accelerated when material is exposed to a humid environment. As a result, the degradation of its mechanical properties occurs. Based on the determined biaxial strength of indented specimens, the effect of pretreatment temperature was estimated and the durability of restorations was evaluated. It was experimentally confirmed that in the case of t-m phase transformation less than 52% the level of retaining residual compressive stresses on the surface is insufficient to affect substantially microstructure and cause degradation. The authors of the work [44] calculated the lattice distortion after t-m phase transformation. The

Kikuchi-band-based method was implemented, and the results of XRD analysis were compared with the BSD results.

Traditionally, the bearing capacity of ceramic products, in particular, ball valves, valve plates, mechanical seals, bearings, molds, friction slices, thermocouple tubes, nozzles, etc. is estimated using strength and wear resistance characteristics of corresponding materials [43, 45–47]. However, it is necessary to obtain material with an appropriate microstructure resistive to the degradation in operation conditions [48–55] to avoid the operating environment effects [56–58]. Therefore, more structurally sensitive methods should be developed for estimating load-bearing capacity of ceramic materials and products. The indentation test is known to be the simplest mechanical method [43, 59–61]. Besides, fracture toughness tests with a variety of loading schemes and specimen shapes are used [33, 45, 56, 57, 59, 60, 62, 63] to evaluate crack growth resistance of materials. Therefore, the correlation between the microstructure and crack growth resistance parameters of YSZ ceramics, sintered in different modes, need to be investigated to find out an appropriate way of formation of ceramic material with improved crack growth resistance.

The work is aimed at evaluating the effect of sintering temperature on the phase composition and microstructure as well as estimating the role of nanosized stabilizing yttria powders in gaining high-level crack growth resistance of partially stabilized zirconia.

2 Materials and Methods

In this work, we have studied yttria-stabilized zirconia (YSZ) ceramics sintered from commercial starting powders. Powders preparation technique and their morphology were thoroughly described in the work [64]. Initial particle sizes of the starting powders were as follows: 100–150 nm (ZrO_2 powder) and 10–30 nm (Y_2O_3 powder). Series of beam specimens of YSZ ceramics stabilized with 3, 4, and 5 mol% Y_2O_3 (hereinafter: 3YSZ, 4YSZ, and 5YSZ) approximately $4.2 \times 4.2 \times 50$ mm in size were sintered in a furnace for 2 h. Argon was used as an inert sintering atmosphere. Three sintering temperatures (1450 °C, 1500 °C, and 1550 °C) were used. Thus, nine variants of material were obtained (Table 1). For marking each variant, corresponding chemical composition and sintering temperature were indicated, e.g., 3YSZ–1450. After sintering, the side surfaces of specimens were polished to reach a required surface quality.

Vickers microhardness of the material variants was measured using a NOVOTEST TC-MKB1 microhardness tester according to the relevant standards [65, 66]. We used the following set of indentation loads: 0.49 N, 0.98 N, 1.96 N, 2.94 N, 4.91 N, and 9.81 N. This set was used for determining appropriate loading which allows obtaining invariant values of microhardness. At least 10 indentations for each level of the indentation load were made to determine microhardness of each material variant.

Table 1 Chemical composition, sintering modes, and mean values of Vickers microhardness and SENB fracture toughness of variants of the investigated material

Variant	Content of Y ₂ O ₃ , mol%	Sintering mode		Parameter			
		Temperature, °C	Time, h	H, GPa		K _{Ic} , MPa·m ^{1/2}	
				Mean value	Deviation	Mean value	Deviation
3YSZ–1450	3	1450	2	9.52	± 0.51	5.57	± 0.28
3YSZ–1500	3	1500	2	10.72	± 0.60	6.04	± 0.45
3YSZ–1550	3	1550	2	11.35	± 0.32	7.56	± 0.27
4YSZ–1450	4	1450	2	10.78	± 0.92	5.51	± 0.35
4YSZ–1500	4	1500	2	11.66	± 0.35	6.70	± 0.31
4YSZ–1550	4	1550	2	10.60	± 0.30	6.35	± 0.38
5YSZ–1450	5	1450	2	12.50	± 0.54	10.93	± 1.74
5YSZ–1500	5	1500	2	11.74	± 0.79	9.37	± 1.49
5YSZ–1550	5	1550	2	12.01	± 0.96	9.89	± 1.47

Along with microhardness, fracture toughness of material was estimated due to calculating the critical stress intensity factor (SIF) K_{Ic} . This characteristic made it possible to characterize the propensity of material to brittle fracture due to the nucleation and propagation of cracks [67–72]. There exists a wide range of methods for estimating the fracture toughness of materials. Among them, a method based on indentation with Vickers pyramid is quite simple. In the works [73–88] implementing this method, the formulas for calculating the K_{Ic} values contain both physical and mechanical parameters, as well as empirical co-efficients. Due to the comparison of the K_{Ic} values calculated by these formulas with those obtained by conventional methods of fracture mechanics it was recently concluded [89] that the formula presented by the authors of the work [83] fits the best for the characterization of ZrO₂–Y₂O₃ ceramics.

In our work, we used a conventional method of fracture mechanics for estimating fracture toughness of materials, namely, a single-edge notch beam (SENB) test [90–92]. An edge notch less than 0.1 mm in width was machined in a beam specimen. The three-point bending SENB tests were carried out on the MTS Criterion E43.104 test machine at 20 °C in air. The distance between supporting roller of the loading unit was 14 mm. For calculating the critical SIF K_{Ic} of material we used corresponding formulas [90–92]. The average K_{Ic} value was computed for each set of five specimens of the investigated material variants.

The material microstructure and morphology of the fracture surfaces of tested specimens were investigated using a Carl Zeiss EVO-40XVP scanning electron microscope (SEM). The chemical homogeneity of materials was evaluated with an energy-dispersive X-ray (EDX) microanalysis using an INCA Energy 350 system. A DRON-3.0 diffractometer was used to perform X-ray diffraction (XRD) studies.

3 Results and Discussion

The obtained XRD patterns of the material of variants tested (Table 1) exhibit, in general, the phase balance for 3YSZ, 4YSZ, and 5YSZ ceramics. The XRD patterns of the selected material variants (Fig. 1, variants 3YSZ–1450, 3YSZ–1550, 4YSZ–1500, and 5YSZ–1450) show in detail the peculiarities of the phase balance of the studied compositions.

The XRD pattern of 3YSZ ceramics of variant 3YSZ–1450 contains peaks of the t-ZrO₂, c-ZrO₂, and m-ZrO₂ phases (Fig. 1a). The peaks of the t-ZrO₂ phase are high corresponding to the amount of this phase of about 59 wt% (Table 2). The peaks of both the m-ZrO₂ and c-ZrO₂ phases are also quite high, and the amounts of these phases are 21 wt% and 20 wt%, respectively. The XRD pattern of variant 3YSZ–1550 (Fig. 1b) contains higher peaks of both the t-ZrO₂ and m-ZrO₂ phases and much lower peaks of the c-ZrO₂ phase as compared to the XRD pattern of variant 3YSZ–1450 (Fig. 1a).

The material of variant 4YSZ–1500 is characterized by peaks of the t-ZrO₂, m-ZrO₂, and c-ZrO₂ phases (Fig. 1c) of almost the same heights as for variant 3YSZ–1450 (Fig. 1a).

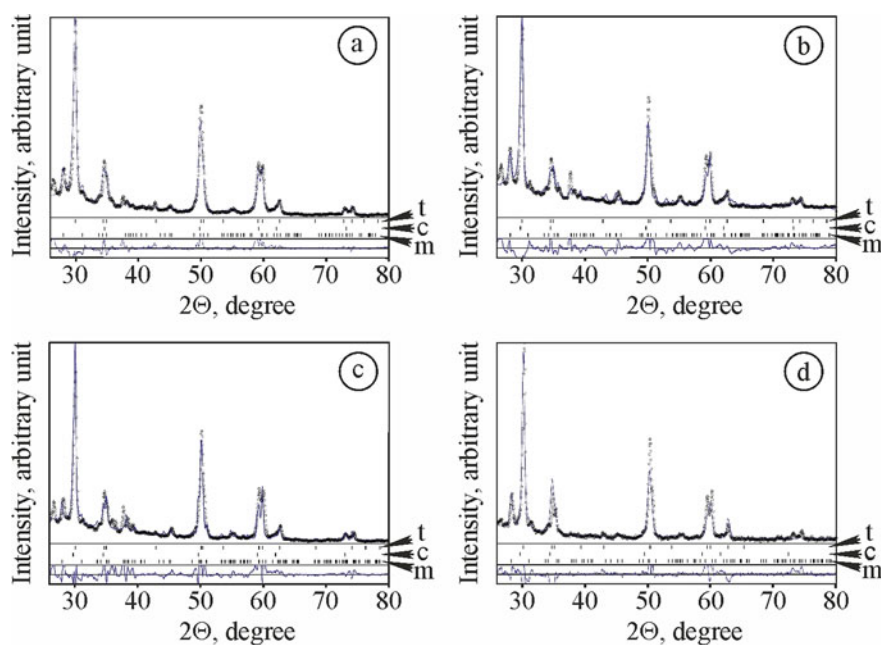


Fig. 1 XRD patterns of the investigated materials of variants **a** 3YSZ-1450, **b** 3YSZ-1550, **c** 4YSZ-1500, and **d** 5YSZ-1450 depending on the sintering temperature (Table 1). Phase marking: t—tetragonal, m—monoclinic, c—cubic

Table 2 The phase balance of variants of the investigated material

Variant	Mean value of corresponding phase, wt%		
	t-ZrO ₂	m-ZrO ₂	c-ZrO ₂
3YSZ–1450	59	21	20
3YSZ–1500	61	21	18
3YSZ–1550	66	32	2
4YSZ–1450	69	20	11
4YSZ–1500	60	23	17
4YSZ–1550	72	26	2
5YSZ–1450	73	22	5
5YSZ–1500	66	29	5
5YSZ–1550	57	25	18

The XRD pattern of variant 5YSZ–1450 (Fig. 1d) exhibits a behavior that is different from that of variant 4YSZ–1500 and simultaneously is similar to that of variant 3YSZ–1550 (Fig. 1a, b, respectively). This variant is intermediate in terms of peaks height of the m-ZrO₂ phase, whereas quite low peaks of the c-ZrO₂ phase and the highest peaks of the t-ZrO₂ phase are observed for it.

The general tendencies of changes in 3YSZ, 4YSZ, and 5YSZ ceramics phase compositions (Table 2) can be described as follows: (1) with increasing sintering temperature the percentage of the tetragonal phase increases when the content of the stabilizing Y₂O₃ additive is quite low (3YSZ ceramics); (2) the sintering temperature of 1500 °C is transitional in terms of phase composition of 4YSZ ceramics since a minimum of the tetragonal phase and a maximum of the cubic phase are reached; (3) when the content of the stabilizing Y₂O₃ additive is quite high (5YSZ ceramics), the cubic phase is probably the balance because the amount of cubic phase is quite low, especially in variants 5YSZ–1450 and 5YSZ–1500; (4) the maximum t-ZrO₂ phase percentage is reached in variant 5YSZ–1450; (5) with increasing sintering temperature the percentage of the tetragonal phase decreases when the content of the stabilizing Y₂O₃ additive is quite high (5YSZ ceramics).

In the work [89], a dependence of the microhardness of yttria-stabilized zirconia (ZrO₂–8 mol% Y₂O₃) on the indentation load known as the indentation size effect [93–95] was revealed. For this material, the average values of microhardness decreased with increasing indentation load from 0.49–9.81 N. Besides, a tendency was observed with the yield of microhardness values on the plateau at indentation loads in a range of 4.91–9.81 N. It was concluded that the values of fracture toughness and microhardness obtained in this range of indentation loads are invariant.

In our work, the invariant values of the material microhardness were obtained under the indentation load of 9.81 N for studying the evolution of changes in microhardness of the studied ceramic variants with a change in the sintering temperature from 1450 to 1550 °C (Table 1). It was revealed in general that the increase of sintering temperature from 1450 to 1550 °C leads to improvement of mechanical properties

of 3YSZ ceramics. In particular, an increase in microhardness (on average, by 19%, Table 1) was observed for this material.

The 4YSZ ceramics sintered at 1500 °C has the highest microhardness compared to variants 4YSZ–1450 and 4YSZ–1550. According to [96], microhardness of m-ZrO₂ is lower than t-ZrO₂. During indentation, the metastable tetragonal to monoclinic phase transition (t-m) occurs with the formation of m-ZrO₂ which causes lowering of microhardness [96]. In variant 4YSZ–1500 having the lowest percentage of the t-ZrO₂ phase compared to other 4YSZ variants (Table 2), a smaller amount of the m-ZrO₂ phase is formed in the process of the t-m transformation of ZrO₂. Besides, variant 4YSZ–1500 has the highest percentage of the c-ZrO₂ phase compared to other 4YSZ variants (Table 2). This also contributes to the microhardness level of variant 4YSZ–1500.

The ambiguous change in microhardness depending on the sintering temperature was revealed for 5YSZ ceramics. Material of variant 5YSZ–1450 contains the highest percentage of the t-ZrO₂ phase compared to other 5YSZ variants (Table 2) has the highest microhardness (Table 1). However, with lowering the t-ZrO₂ and simultaneous increasing the m-ZrO₂ phase percentages microhardness of material decreases (variant 5YSZ–1500). The increase of sintering temperature up to 1550 °C leads to intensive grain growth in 5YSZ ceramics. This, in turn, leads to the suppression of the process of the t-m transformation of ZrO₂ [96] in the case when an average grain size of the t-ZrO₂ phase is larger than the admissible one. It seems that the last is about 500 nm for ceramics of this type. Therefore, for material 5YSZ–1550 with an average grain size of the t-ZrO₂ phase exceeding 500 nm (Fig. 2), the formation of m-ZrO₂ is suppressed, and this is probably a reason for higher microhardness of material 5YSZ–1550 compared to 5YSZ–1500. A high content of the cubic phase also contributes to the microhardness level of variant 5YSZ–1550.

One of the simplest methods used in a number of works [68, 69, 82, 97] for estimating the fracture toughness of different ceramic materials is the Vickers indentation method.

Another approach to assessing fracture toughness of ceramics is a conventional method of fracture mechanics based on pre-cracked specimens [13, 98, 99]. Such a simplified method, namely, the three-point bending SENB test method was used in our work. As a result, an increase in fracture toughness (on average, by 35%) was observed for the selected material variants similarly to the trend in microhardness (Table 1).

A common result of the two above-mentioned processes, namely, suppression of the t-m transformation of ZrO₂ with the sintering temperature increase and the stress-induced formation of m-ZrO₂, is displayed in both microhardness and fracture toughness (Table 2). For 5YSZ ceramics sintered at 1500 °C, minimum values of fracture toughness were obtained, whereas for 4YSZ ceramics an opposite trend was observed and for 3YSZ ceramics a gradual increase in fracture toughness with increasing sintering temperature from 1450 °C to 1550 °C was revealed (Table 2). Therefore, the sintering temperature of 1500 °C is critical in the microstructure formation process.

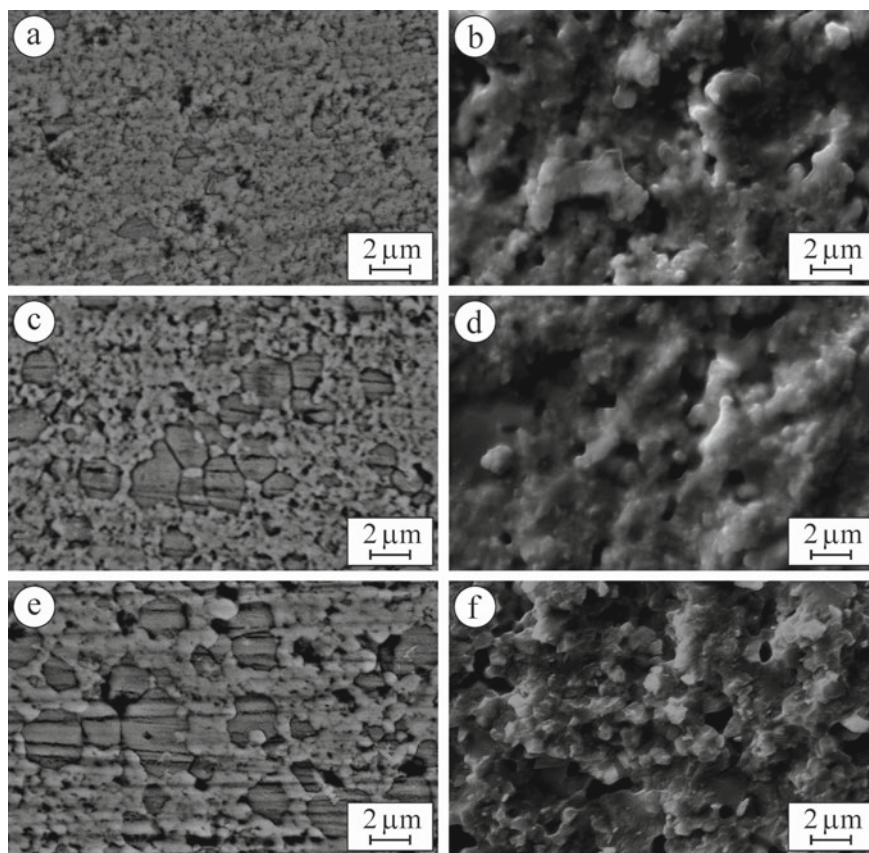


Fig. 2 SEM **a, c, e** microstructures (BSD images) and **b, d, f** fractography (SE images) of specimens of 3YSZ ceramics sintered at **a, b** 1450 °C, **c, d** 1500 °C, and **e, f** 1550 °C

Some regularities of increasing fracture toughness of 3YSZ, 4YSZ, and 5YSZ ceramics related to their phase compositions may be derived in terms microstructure formation similarly to other ceramics containing yttria admixtures [100]. Comparing to material variants 3YSZ–1500 and, especially, 3YSZ–1450, where no clear contours of the available phases can be recognized (Fig. 2a, c) and also slight signs of recrystallized particles can be found (Fig. 2b, d), variant 3YSZ–1550 are characterized by the distinct microstructure (Fig. 2e) and morphology of the fracture surface (Fig. 2f).

In the case of 3YSZ ceramics, the maximum fracture toughness was found for variant 3YSZ–1550 having the maximum content of the $t\text{-ZrO}_2$ phase. SEM microstructure of such material (Fig. 2e) presents the matrix ($t\text{-ZrO}_2$ phase) composed of nanoagglomerates with blurred contours of about 200–250 nm in size. Coarse agglomerates of another phase/phases consisting of particles of 2–3 μm in size are uniformly distributed in the $t\text{-ZrO}_2$ matrix. Based on the EDX analysis of 3YSZ,

4YSZ, and 5YSZ specimens, an increased yttrium concentration was found in these agglomerates. According to the literature data [38, 39], these coarse agglomerates are probably the $m\text{-ZrO}_2$ phase inclusions surrounded by cubic phase particles with high yttria content and tetragonal phase particles with low yttria content. Despite blurred contours of tetragonal phase particles (Fig. 2e), their average size can be estimated on fracture surface of a corresponding specimen (Fig. 2c, e). Here, an intergranular fracture micromechanism can be recognized and the average size of the particles is estimated to be about 500 nm. In contrast to this, signs of incomplete recrystallization in material of variants 3YSZ–1450 and 3YSZ–1500 can be observed at a higher magnification (Fig. 3a, b).

The microstructure and fracture surface morphology images (Fig. 4a, b, respectively) of a specimen of variant 4YSZ–1450 exhibit signs of an early stage of microstructure formation, namely, the $t\text{-ZrO}_2$ phase matrix of nanoagglomerates with blurred contours of about 150–200 nm in size as well as coarser agglomerates of another phase/phases (probably, the same as for variant 3YSZ–1550) consisting of particles of 1–2 μm in size distributed in the $t\text{-ZrO}_2$ matrix. The evolution of microstructure, in particular, growth of the $m\text{-ZrO}_2$ phase agglomerates, may be observed with increasing sintering temperature to 1500 °C (Fig. 4c, d) and 1550 °C (Fig. 4e, f). In the case of 4YSZ ceramics, the maximum fracture toughness was found for variant 4YSZ–1500 that corresponds to the higher percentage of the $c\text{-ZrO}_2$ phase

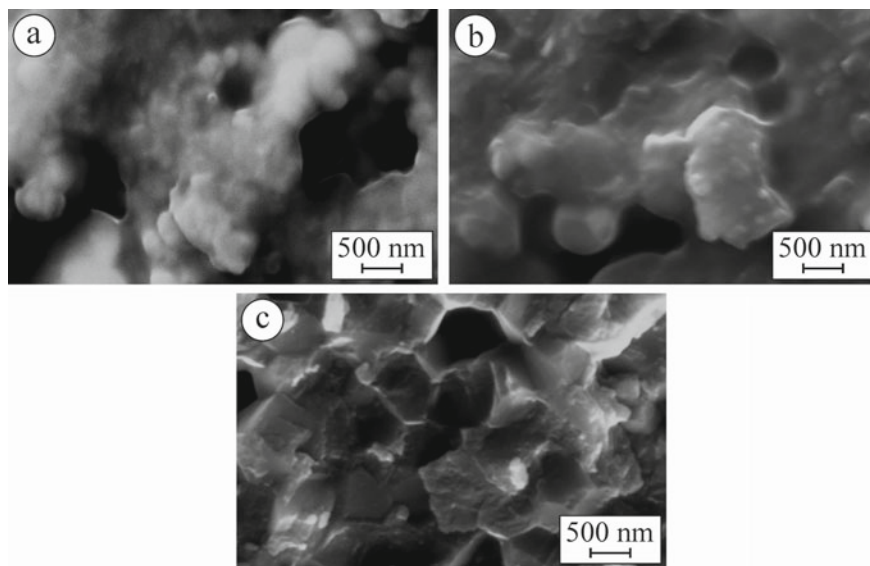


Fig. 3 SEM fractography (SE images) of specimens of 3YSZ ceramics sintered at **a** 1450 °C, **b** 1500 °C, and **c** 1550 °C

compared to variants 4YSZ–1500 and 4YSZ–1550 (Fig. 1b) and the higher microhardness (Table 1). At a higher magnification, blurred contours of nanoparticles can be observed on fracture surface of specimens of both variants 4YSZ–1450 and 4YSZ–1550 (Fig. 5a, c). Only material of variant 4YSZ–1500 exhibits quite distinct microstructure (Fig. 5b).

A fine-grained microstructure of the t-ZrO₂ phase matrix in 5YSZ ceramics was formed at a sintering temperature of 1450 °C (Fig. 6a). Fracture surface morphology of such a specimen (Figs. 6b and 7a) evidences the prospect of such a chemical composition and a sintering mode in gaining high crack growth resistance of YSZ ceramics [64].

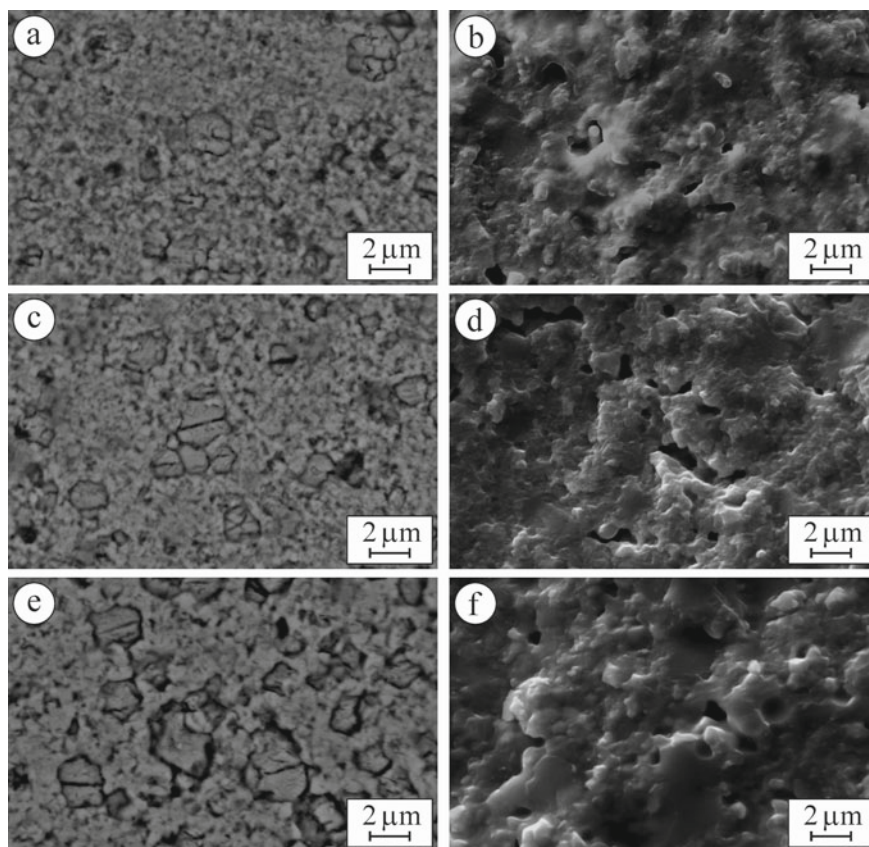


Fig. 4 SEM **a, c, e** microstructures (BSD images) and **b, d, f** fractography (SE images) of specimens of 4YSZ ceramics sintered at **a, b** 1450 °C, **c, d** 1500 °C, and **e, f** 1550 °C

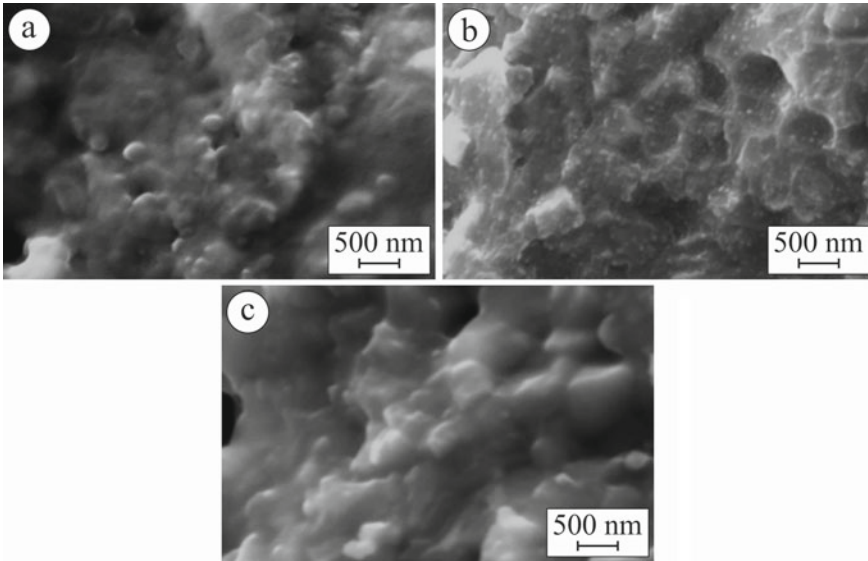


Fig. 5 SEM fractography (SE images) of specimens of 4YSZ ceramics sintered at **a** 1450 °C, **b** 1500 °C, and **c** 1550 °C

The relief fracture surface corresponding to nano/microcracking along the boundaries of t-ZrO₂ nanograins united into agglomerates of about 2–5 μm in size (Fig. 6b) is related to the highest fracture toughness as compared to other variants of material (Fig. 3). This also correlates with the highest percentage of the t-ZrO₂ phase (Fig. 1c). As mentioned above, for 5YSZ ceramics sintered at 1500 °C, fracture toughness related to the corresponding morphology of fracture surface (Fig. 7b) was determined to be lower compared to that of variant 5YSZ–1450. However, for variant 5YSZ–1550 an opposite trend was observed with a gradual increase in fracture toughness while increasing sintering temperature from 1500 to 1550 °C (Fig. 3). Such mechanical behavior with corresponding morphology of fracture surface (Fig. 7c) is a result of a steep increase in the c-ZrO₂ phase percentage (Fig. 1c).

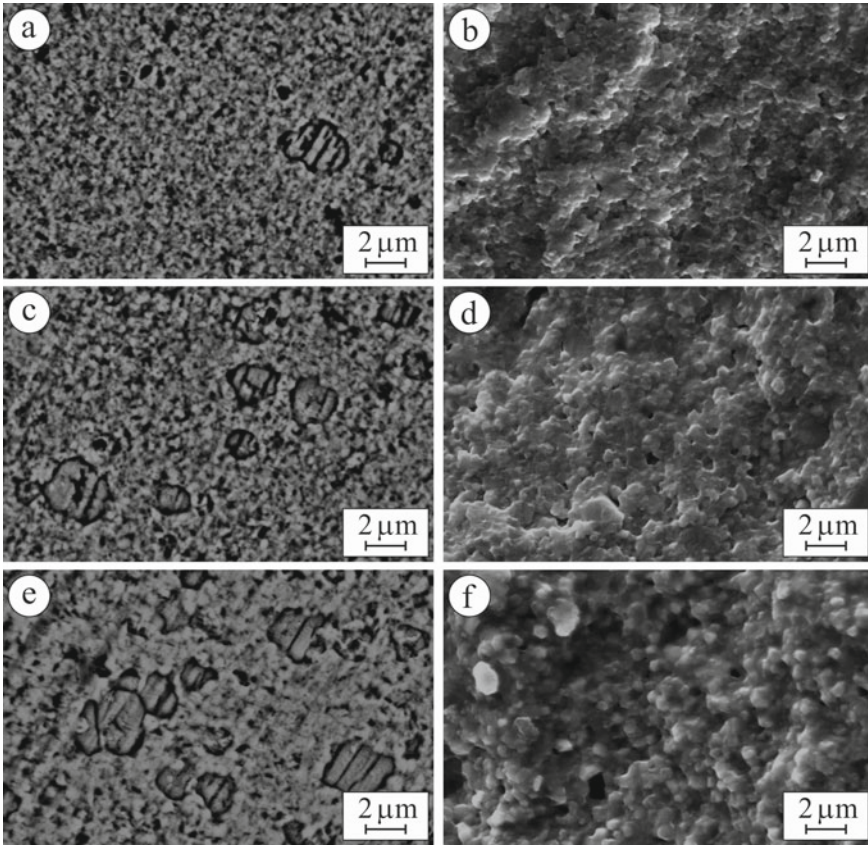


Fig. 6 SEM **a, c, e** microstructures (BSD images) and **b, d, f** fractography (SE images) of specimens of 5YSZ ceramics sintered at **a, b** 1450 °C, **c, d** 1500 °C, and **e, f** 1550 °C

Therefore, two ways may be appropriate to reach high crack growth resistance of YSZ ceramics: (1) increasing the t-ZrO₂ phase percentage due to implementing 5YSZ–1450 mode; (2) increasing the c-ZrO₂ phase percentage due to implementing 5YSZ–1550 mode. It also can be concluded that the data of fracture toughness of the studied materials are fully consistent with observed fracture patterns.

Thus, based on results of mechanical tests performed in this work, it can be concluded that 5YSZ ceramics sintered at a temperature of 1450 °C is the best variant of material among the studied ones.

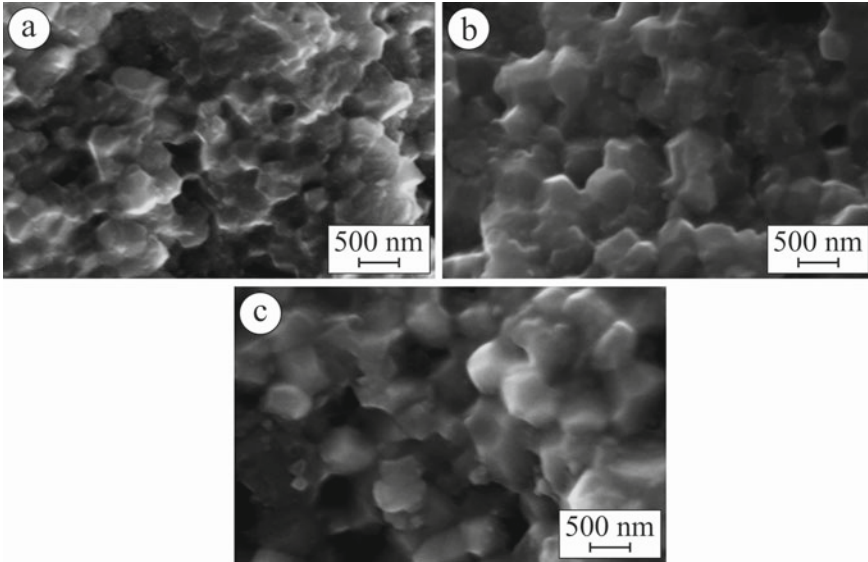


Fig. 7 SEM fractography (SE images) of specimens of 5YSZ ceramics sintered at **a** 1450 °C, **b** 1500 °C, and **c** 1550 °C

4 Conclusions

In this study, the microstructure, phase composition, and mechanical properties of 3YSZ, 4YSZ, and 5YSZ ceramics have been investigated.

1. It was shown that in a sintering temperature range of 1450–1550 °C microstructural changes occurring in the YSZ ceramics due to phase transformations in the presence of a stabilizing additive can be effectively characterized in terms of fracture toughness.
2. For the YSZ ceramics sintered at 1450 °C, 1500 °C, and 1550 °C, the formation of cubic, tetragonal, and monoclinic phases of zirconia was substantiated and microstructural peculiarities of the material variants were explained.
3. Dominant fracture micromechanisms in specimens of the studied YSZ ceramics were found. The highest level of fracture toughness revealed for 5YSZ ceramics sintered at 1450 °C was substantiated using fracture surface morphology patterns.

References

1. Dobrzański LA, Dobrzański LB, Dobrzańska-Danikiewicz AD (2020) Manufacturing technologies thick-layer coatings on various substrates and manufacturing gradient materials using powders of metals, their alloys and ceramics. *J Achievements in Mater and Manuf Eng* 99(1):14–41. <https://doi.org/10.5604/01.3001.0014.1598>
2. Ye K, Blikharskyy Z, Vira V et al (2021) Nanostructural changes in a Ni/NiO cermet during high-temperature reduction and reoxidation. *Nanomaterials and Nanocomposites, Nanostructure Surfaces, and Their Applications*. Springer Proc Phys 246:219–229. https://doi.org/10.1007/978-3-030-51905-6_17
3. Ropyak LY, Makoviichuk MV, Shatskyi IP et al (2020) Stressed state of laminated interference-absorption filter under local loading. *Funct Mater* 27(3):638–642. <https://doi.org/10.15407/fm27.03.638>
4. Posuvailo VM, Kulyk VV, Duriagina ZA et al (2020) The effect of electrolyte composition on the plasma electrolyte oxidation and phase composition of oxide ceramic coatings formed on 2024 aluminium alloy. *Arch Mater Sci Eng* 105(2):49–55. <https://doi.org/10.5604/01.3001.0014.5761>
5. Cherepova TS, Dmytrieva HP, Dukhota OI et al (2016) Properties of nickel powder alloys hardened with titanium carbide. *Mater Sci* 52(2):173–179. <https://doi.org/10.1007/s11003-016-9940-2>
6. Bocanegra-Bernal MH, Díaz de la Torre S (2002) Phase transitions in zirconium dioxide and related materials for high performance engineering ceramics. *J Mater Sci* 37:4947–4971. <https://doi.org/10.1023/A:1021099308957>
7. Budzianowski WM, Milewski J (2011) Solid-oxide fuel cells in power generation applications: A review. *Recent Patents Eng* 5(3):165–189. <https://doi.org/10.2174/187221211797636926>
8. Vasylyv BD, Podhurska VY, Ostash OP et al (2018) Effect of a hydrogen sulfide-containing atmosphere on the physical and mechanical properties of solid oxide fuel cell materials. *Nanochemistry, biotechnology, nanomaterials, and their applications*. Springer Proc Phys 214:475–485. https://doi.org/10.1007/978-3-319-92567-7_30
9. Komatsu Y, Sciazko A, Shikazono N (2021) Isostatic pressing of screen printed nickel-gadolinium doped ceria anodes on electrolyte-supported solid oxide fuel cells. *J Power Sources* 485:229317. <https://doi.org/10.1016/j.jpowsour.2020.229317>
10. Vasylyv BD (2010) Improvement of the electric conductivity of the material of anode in a fuel cell by the cyclic redox thermal treatment. *Mater Sci* 46(2):260–264. <https://doi.org/10.1007/s11003-010-9282-4>
11. Wejrzanowski T, Haj Ibrahim S, Cwieka K et al (2018) Multi-modal porous microstructure for high temperature fuel cell application. *J Power Sources* 373:85–94. <https://doi.org/10.1016/j.jpowsour.2017.11.009>
12. Danilenko I, Lasko G, Brykhanova I et al (2017) The peculiarities of structure formation and properties of zirconia-based nanocomposites with addition of Al₂O₃ and NiO. *Nanoscale Res Lett* 12:125. <https://doi.org/10.1186/s11671-017-1901-7>
13. Podhurska V, Vasylyv B (2012) Influence of NiO reduction on microstructure and properties of porous Ni–ZrO₂ substrates. In: *Proceedings of the 3rd international conference on oxide materials for electronic engineering (OMEE-2012)*, Lviv, Ukraine, pp 293–294. <https://doi.org/10.1109/OMEE.2012.6464761>
14. Milewski J, Lewandowski J, Miller A (2008) Reducing CO₂ emissions from a coal fired power plant by using a molten carbonate fuel cell. *Proceedings of the ASME Turbo Expo 2008: Power for Land, Sea, and Air*, pp 389–395. <https://doi.org/10.1115/GT2008-50100>
15. Milewski J, Lewandowski J (2009) Solid oxide fuel cell fuelled by biogases. *Arch Thermodyn* 30(4):3–12. https://www.imp.gda.pl/fileadmin/doc/imp_publishing/wimp/archives%20of%20thermodynamics/C_09_4.pdf

16. Savka SS, Popovych DI, Serednytski AS (2017) Molecular dynamics simulations of the formation processes of zinc oxide nanoclusters in oxygen environment. *Nanophysics, Nanomaterials, Interface Studies, and Applications*. Springer Proc Phys 195:145–156. https://doi.org/10.1007/978-3-319-56422-7_11
17. Dobrzański LA, Dobrzański LB, Dobrzańska-Danikiewicz AD (2020) Overview of conventional technologies using the powders of metals, their alloys and ceramics in Industry 4.0 stage. *J Achievements Mater Manuf Eng* 98(2):56–85. <https://doi.org/10.5604/01.3001.0014.1481>
18. Milewski J, Kupecki J, Szczeńsiak A et al (2021) Hydrogen production in solid oxide electrolyzers coupled with nuclear reactors. *Int J Hydrogen Energy* 46(72):35765–35776. <https://doi.org/10.1016/j.ijhydene.2020.11.217>
19. Andrzejczuk M, Vasylyev O, Brodnikovskiy I et al (2014) Microstructural changes in NiO–ScSZ composite following reduction processes in pure and diluted hydrogen. *Mater Charact* 87:159–165. <https://doi.org/10.1016/j.matchar.2013.11.011>
20. Clarke DR, Levi CG (2003) Material design for the next generation thermal barrier coatings. *Annu Rev Mater Res* 33:383–417. <https://doi.org/10.1146/annurev.matsci.33.011403.113718>
21. Vasylyv B, Podhurska V, Ostash O (2017) Preconditioning of the YSZ–NiO fuel cell anode in hydrogenous atmospheres containing water vapor. *Nanoscale Res Lett* 12:265. <https://doi.org/10.1186/s11671-017-2038-4>
22. Witz G, Shklover V, Steurer W et al (2007) Phase evolution in yttria-stabilized zirconia thermal barrier coatings studied by Rietveld refinement of X-ray powder diffraction patterns. *J Am Ceram Soc* 90(9):2935–2940. <https://doi.org/10.1111/j.1551-2916.2007.01785.x>
23. Smyrnova-Zamkova MY, Ruban OK, Bykov OI et al (2018) Physico-chemical properties of fine-grained powder in $\text{Al}_2\text{O}_3\text{--ZrO}_2\text{--Y}_2\text{O}_3\text{--CeO}_2$ system produced by combined method. *Comp Theory Practice* 18(4):234–240. https://kompozyty.ptmk.net/pliczki/pliki/1290_2018_t04_maria-y-smyrnova-zamkova-.pdf
24. Zhou XW, Shen YF, Jin HM (2011) Effect of deposition mechanism and microstructure of nano-ceria oxide addition on Ni-P coating by pulse electrodeposition. *Adv Mater Res* 326:151–156. <https://doi.org/10.4028/www.scientific.net/AMR.326.151>
25. Smyrnova-Zamkova MY, Red'ko VP, Ruban OK et al (2017) The properties of nanocrystalline powder of 90% $\text{Al}_2\text{O}_3\text{--}10\%\text{ZrO}_2$ (wt.%) obtained via the hydrothermal synthesis/mechanical mixing. *Nanosistemi Nanomater Nanotechnol* 15(2):309–317. <https://doi.org/10.15407/nnn.15.02.0309>
26. Vasylyv B, Milewski J, Podhurska V et al (2021) Study of the degradation of a fine-grained YSZ–NiO anode material during reduction in hydrogen and reoxidation in air. *Appl Nanosci*. <https://doi.org/10.1007/s13204-021-01768-w>
27. Shevchenko AV, Lashneva VV, Ruban AK et al (2016) Synthesis and study of high-purity nanocrystalline powder of a solid solution of CeO_2 and Y_2O_3 in zirconium dioxide. *Powder Metall Met Ceram* 54(9–10):548–553. <https://doi.org/10.1007/s11106-016-9748-5>
28. Sukhova OV (2009) Influence of mechanisms of structure formation of interfaces in composites on their properties. *Metallfiz Noveishie Tekhnol* 31(7):1001–1012
29. Efremenko VG, Chabak YG, Shimizu K et al (2017) Structure refinement of high-Cr cast iron by plasma surface melting and post-heat treatment. *Mater Des* 126:278–290. <https://doi.org/10.1016/j.matdes.2017.04.022>
30. Dudnik OV, Marek IO, Ruban OK et al (2020) Effect of heat treatment on the structure and phase composition of the nanosized powder based on a ZrO_2 solid solution. *Powder Metall Met Ceram* 59(1–2):1–8. <https://doi.org/10.1007/s11106-020-00132-x>
31. Kujawa M, Suwak R, Dobrzański LA et al (2021) Thermal characterization of halloysite materials for porous ceramic preforms. *Arch Mater Sci Eng* 107(1):5–15. <https://doi.org/10.5604/01.3001.0014.8189>
32. Marek IO, Ruban OK, Redko VP et al (2019) Physicochemical properties of hydrothermal nanocrystalline $\text{ZrO}_2\text{--Y}_2\text{O}_3\text{--CeO}_2$ powders. *Powder Metall Met Ceram* 58(3–4):125–132. <https://doi.org/10.1007/s11106-019-00055-2>

33. Alves MFRP, Ribeiro S, Suzuki PA et al (2021) Effect of Fe_2O_3 addition and sintering temperature on mechanical properties and translucence of zirconia dental ceramics with different Y_2O_3 content. *Mater Res* 24(2):e20200402. <https://doi.org/10.1590/1980-5373-MR-2020-0402>
34. Kumar A, Kumar P, Dhaliwal AS (2021) Structural studies of zirconia and yttria doped zirconia for analysing it phase stabilization criteria. *IOP Conf. Series: Mater Sci Eng* 1033:012052. <https://doi.org/10.1088/1757-899X/1033/1/012052>
35. Kern F, Gommeringer A (2020) Mechanical properties of 2Y-TZP fabricated from detonation synthesized powder. *Ceram* 3(4):440–452. <https://doi.org/10.3390/ceramics3040037>
36. Miller RA, Smialek JL, Garlick RG (1981) Phase stability in plasma sprayed, partially stabilized zirconia–yttria. In: Heuer AH, Hobbs LW (eds) *Advances in ceramics*, vol. 3, science and technology of Zirconia I. Am Ceram Soc, Columbus, pp 241–253
37. Ilavsky J, Stalick JK, Wallace J (2001) Thermal spray yttria-stabilized zirconia phase changes during annealing. *J Therm Spray Technol* 10(3):497–501. <https://doi.org/10.1361/105996301770349277>
38. Schulz U (2000) Phase transformation in EB-PVD yttria partially stabilized zirconia thermal barrier coatings during annealing. *J Am Ceram Soc* 83(4):904–910. <https://doi.org/10.1111/j.1151-2916.2000.tb01292.x>
39. Brandon JR, Taylor R (1991) Phase stability of zirconia-based thermal barrier coatings Part I, Zirconia-yttria alloys. *Surf Coat Technol* 46:75–90. [https://doi.org/10.1016/0257-8972\(91\)90151-L](https://doi.org/10.1016/0257-8972(91)90151-L)
40. Azzopardi A, Mevrel R, Saint-Ramond B et al (2004) Influence of aging on structure and thermal conductivity of Y-PSZ and Y-FSZ EB-PVD coatings. *Surf Coat Technol* 177–178:131–139. <https://doi.org/10.1016/j.surfcoat.2003.08.073>
41. Katamura J, Sakuma T (1998) Computer simulation of the microstructural evolution during the diffusionless cubic-to-tetragonal transition in the system $\text{ZrO}_2\text{-Y}_2\text{O}_3$. *Acta Mater* 46(5):1569–1575. [https://doi.org/10.1016/S1359-6454\(97\)00356-X](https://doi.org/10.1016/S1359-6454(97)00356-X)
42. Scott HG (1975) Phase relationships in the zirconia–yttria system. *J Mater Sci* 10:1527–1535. <https://doi.org/10.1007/BF01031853>
43. Jeong K-W, Han J-S, Yang G-U et al (2021) Influence of preaging temperature on the indentation strength of 3Y-TZP aged in ambient atmosphere. *Materials* 14:2767. <https://doi.org/10.3390/ma14112767>
44. Tsai Y-Y, Lee T-M, Kuo J-C (2021) Hydrothermal-aging-induced lattice distortion in yttria-stabilized zirconia using EBSD technique. *Micron* 145:103053. <https://doi.org/10.1016/j.micron.2021.103053>
45. Ji SH, Kim DS, Park MS et al (2021) Sintering process optimization for 3YSZ ceramic 3D-printed objects manufactured by stereolithography. *Nanomaterials* 11:192. <https://doi.org/10.3390/nano11010192>
46. Gaddam A, Brazete DS, Neto AS et al (2021) Three-dimensional printing of zirconia scaffolds for load bearing applications: study of the optimal fabrication conditions. *J Am Ceram Soc* 104(9):4368–4380. <https://doi.org/10.1111/jace.17874>
47. Podhurs'ka VY, Vasylyv BD, Ostash OP et al (2014) Structural transformations in the NiO-containing anode of ceramic fuel cells in the course of its reduction and oxidation. *Mater Sci* 49(6):805–811. <https://doi.org/10.1007/s11003-014-9677-8>
48. Dobrzański LA, Dobrzański LB, Dobrzańska-Danikiewicz AD (2020) Additive and hybrid technologies for products manufacturing using powders of metals, their alloys and ceramics. *Arch Mater Sci Eng* 102(2):59–85. <https://doi.org/10.5604/01.3001.0014.1525>
49. Andreiko IM, Kulyk VV, Ostash OP (2012) Resistance of steels of railroad wheels to corrosion-fatigue fracture. *Mater Sci* 47(5):608–612. <https://doi.org/10.1007/s11003-012-9434-9>
50. Sciazko A, Shimura T, Komatsu Y et al (2021) Ni-GDC and Ni-YSZ electrodes operated in solid oxide electrolysis and fuel cell modes. *J Therm Sci Technol* 16(1):JTST0013. <https://doi.org/10.1299/jtst.2021jtst0013>

51. Efremenko VG, Chabak YG, Lekatou A et al (2016) High-temperature oxidation and decarburization of 14.55 wt pct Cr-cast iron in dry air atmosphere. *Metall Mater Trans A* 47A(2):1529–1543. <https://doi.org/10.1007/s11661-016-3336-7>
52. Nykyforchyn H, Krechkovska H, Student O et al (2019) Feature of stress corrosion cracking of degraded gas pipeline steels. *Procedia Struct Integrity* 16:153–160. <https://doi.org/10.1016/j.prostr.2019.07.035>
53. Romaniv OM, Vasylyv BD (1998) Some features of formation of the structural strength of ceramic materials. *Mater Sci* 34(2):149–161. <https://doi.org/10.1007/BF02355530>
54. Włodarczyk-Fligier A, Polok-Rubiniec M, Konieczny J (2020) Thermal analysis of matrix composite reinforced with Al₂O₃ particles. *J Achievements in Mater and Manuf Eng* 100(1):5–11. <https://doi.org/10.5604/01.3001.0014.1957>
55. Buchaniec S, Sciazko A, Mozdierz M et al (2019) A novel approach to the optimization of a solid oxide fuel cell anode using evolutionary algorithms. *IEEE Access* 7:34361–34372. <https://doi.org/10.1109/ACCESS.2019.2904327>
56. Tao S, Yang J, Zhai M et al (2020) Thermal stability of YSZ thick thermal barrier coatings deposited by suspension and atmospheric plasma spraying. *Curr Comput-Aided Drug Des* 10(11):984. <https://doi.org/10.3390/cryst10110984>
57. Rudolph M, Galetz MC, Schütze M (2021) Mechanical stability diagrams for thermal barrier coating systems. *J Therm Spray Technol* 30:694–707. <https://doi.org/10.1007/s11666-021-01163-5>
58. Fan Z, Sun X, Zhuo X et al (2021) Femtosecond laser polishing yttria-stabilized zirconia coatings for improving molten salts corrosion resistance. *Cor Sci* 184:109367. <https://doi.org/10.1016/j.corsci.2021.109367>
59. Romaniv OM, Zalite IV, Simin'kovych VM, et al (1996) Effect of the concentration of zirconium dioxide on the fracture resistance of Al₂O₃-ZrO₂ ceramics. *Mater Sci* 31(5):588–594. <https://doi.org/10.1007/BF00558793>
60. Buyakov AS, Mirovoy YA, Smolin AY et al (2021) Increasing fracture toughness of zirconia-based composites as a synergistic effect of the introducing different inclusions. *Ceram Int* 47(8):10582–10589. <https://doi.org/10.1016/j.ceramint.2020.12.170>
61. Khajavi P, Hndriksen PV, Chevalier J et al (2020) Improving the fracture toughness of stabilized zirconia-based solid oxide cells fuel electrode supports: Effects of type and concentration of stabilizer(s). *J Eur Ceram Soc* 40(15):5670–5682. <https://doi.org/10.1016/j.jeurceramsoc.2020.05.042>
62. Ivashyshyn AD, Vasylyv BD (2001) Effect of the size and form of specimens on the diagram of growth rates of fatigue cracks. *Mater Sci* 37(6):1002–1004. <https://doi.org/10.1023/A:1015669913601>
63. Vasylyv BD (2002) Initiation of a crack from the edge of a notch with oblique front in specimens of brittle materials. *Mater Sci* 38(5):724–728. <https://doi.org/10.1023/A:1024222709514>
64. Kulyk VV, Duriagina ZA, Vasylyv BD et al (2021) Effects of yttria content and sintering temperature on the microstructure and tendency to brittle fracture of yttria-stabilized zirconia. *Arch Mater Sci Eng* 109(2):65–79. <https://doi.org/10.5604/01.3001.0015.2625>
65. ASTM E 384-11 (2011) Standard test method for Knoop and Vickers hardness of materials. ASTM International. <https://doi.org/10.1520/E0384-11>
66. ASTM C 1327-03 (2003) Standard test method for Vickers indentation hardness of advanced ceramics. ASTM International. <https://doi.org/10.1520/C1327-03>
67. Ostash OP, Kulyk VV, Lenkovskiy TM et al (2018) Relationships between the fatigue crack growth resistance characteristics of a steel and the tread surface damage of railway wheel. *Arch Mater Sci Eng* 90(2):49–55. <https://doi.org/10.5604/01.3001.0012.0662>
68. Cook RF, Pharr GM (1990) Direct observation and analysis of indentation cracking in glasses and ceramics. *J Am Ceram Soc* 73(4):787–817. <https://doi.org/10.1111/j.1151-2916.1990.tb05119.x>
69. Nastic A, Merati A, Bielawski M et al (2015) Instrumented and Vickers indentation for the characterization of stiffness, hardness and toughness of zirconia toughened Al₂O₃ and SiC armor. *J Mater Sci Technol* 31(8):773–783. <https://doi.org/10.1016/j.jmst.2015.06.005>

70. Adams JW, Ruh R, Mazdiyasi KS (1997) Young's modulus, flexural strength, and fracture of yttria-stabilized zirconia versus temperature. *J Am Ceram Soc* 80(4):903–908. <https://doi.org/10.1111/j.1151-2916.1997.tb02920.x>
71. Shabri HA, Othman MHD, Mohamed MA et al (2021) Recent progress in metal-ceramic anode of solid oxide fuel cell for direct hydrocarbon fuel utilization: A review. *Fuel Process Technol* 212:106626. <https://doi.org/10.1016/j.fuproc.2020.106626>
72. Lawn BR (1993) Fracture of brittle solids, 2nd edn, Cambridge. <https://doi.org/10.1017/CBO9780511623127>
73. Lawn BR, Swain MV (1975) Microfracture beneath point indentations in brittle solids. *J Mater Sci* 10(1):113–122. <https://doi.org/10.1007/BF00541038>
74. Lawn BR, Fuller ER (1975) Equilibrium penny-like cracks in indentation fracture. *J Mater Sci* 10(12):2016–2024. <https://doi.org/10.1007/BF00557479>
75. Evans AG, Charles EA (1976) Fracture toughness determinations by indentation. *J Am Ceram Soc* 59(7–8):371–372. <https://doi.org/10.1111/j.1151-2916.1976.tb10991.x>
76. Tanaka K (1987) Elastic/plastic indentation hardness and indentation fracture toughness: The inclusion core model. *J Mater Sci* 22(4):1501–1508. <https://doi.org/10.1007/BF01233154>
77. Niihara K, Morena R, Hasselman DPH (1982) Evaluation of K_{Ic} of brittle solids by the indentation method with low crack-to-indent ratios. *J Mater Sci Lett* 1(1):13–16. <https://doi.org/10.1007/BF00724706>
78. Niihara K (1983) A fracture mechanics analysis of indentation-induced Palmqvist crack in ceramics. *J Mater Sci Lett* 2(5):221–223. <https://doi.org/10.1007/BF00725625>
79. Danilenko I, Glazunov F, Konstantinova T et al (2014) Effect of Ni/NiO particles on structure and crack propagation in zirconia based composites. *Adv Mater Lett* 5(8):465–471. <https://doi.org/10.5185/amlett.2014.amwc1040II>
80. Grigoriev ON, Vinokurov VB, Mosina TV et al (2017) Kinetics of shrinkage, structurization, and the mechanical characteristics of zirconium boride sintered in the presence of activating additives. *Powder Metall Met Ceram* 55(11–12):676–688. <https://doi.org/10.1007/s11106-017-9855-y>
81. Gogotsi GA, Dub SN, Lomonova EE et al (1995) Vickers and Knoop indentation behaviour of cubic and partially stabilized zirconia crystals. *J Eur Ceram Soc* 15(5):405–413. [https://doi.org/10.1016/0955-2219\(95\)91431-M](https://doi.org/10.1016/0955-2219(95)91431-M)
82. Aswad MA (2014) Comparison of the fracture toughness of high temperature ceramic measured by digital image correlation and indentation method. *J University of Babylon* 22(4):927–937. <https://www.iasj.net/iasj?func=article&aid=99010>
83. Anstis GR, Chantikul P, Lawn BR et al (1981) A critical evaluation of indentation techniques for measuring fracture toughness: I, Direct crack measurement. *J Am Ceram Soc* 64(9):533–538. <https://doi.org/10.1111/j.1151-2916.1981.tb10320.x>
84. Lawn BR, Evans AG, Marshall DB (1980) Elastic/plastic indentation damage in ceramics: The median/radial crack system. *J Am Ceram Soc* 63(9–10):574–581. <https://doi.org/10.1111/j.1151-2916.1980.tb10768.x>
85. Blendell JE (1979) The origins of internal stresses in polycrystalline alumina and their effects on mechanical properties. Cambridge
86. Vasylyv BD (2009) A procedure for the investigation of mechanical and physical properties of ceramics under the conditions of biaxial bending of a disk specimen according to the ring–ring scheme. *Mater Sci* 45(4):571–575. <https://doi.org/10.1007/s11003-010-9215-2>
87. Lankford J (1982) Indentation microfracture in the Palmqvist crack regime: implications for fracture toughness evaluation by the indentation method. *J Mater Sci Lett* 1(11):493–495. <https://doi.org/10.1007/BF00721938>
88. Smyrnova-Zamkova MY, Ruban OK, Bykov OI et al (2021) The influence of the ZrO₂ solid solution amount on the physicochemical properties of Al₂O₃–ZrO₂–Y₂O₃–CeO₂ powders. *Powder Metall Met Ceram* 60(3–4):129–141. <https://doi.org/10.1007/s11106-021-00222-4>
89. Vasylyv B, Kulyk V, Duriagina Z et al (2020) Estimation of the effect of redox treatment on microstructure and tendency to brittle fracture of anode materials of YSZ–NiO(Ni) system. *Eastern-European J Enterprise Technol* 108/6(12):67–77. <https://doi.org/10.15587/1729-4061.2020.218291>

90. ASTM E 399-20a (2020) Standard test method for linear-elastic plane-strain fracture toughness of metallic materials. ASTM International. <https://doi.org/10.1520/E0399-20A>
91. ASTM C 1421-18 (2018) Standard test methods for determination of fracture toughness of advanced ceramics at ambient temperature. ASTM International. <https://doi.org/10.1520/C1421-18>
92. Kübier J (2002) Fracture toughness of ceramics using the SEVNB method: From a preliminary study to a standard test method. In: Salem J (eds) Fracture resistance testing of monolithic and composite brittle materials. ASTM International, 93–106. <https://doi.org/10.1520/STP10473S>
93. Peng Z, Gong J, Miao H (2004) On the description of indentation size effect in hardness testing for ceramics: analysis of the nanoindentation data. *J Eur Ceram Soc* 24(8):2193–2201. [https://doi.org/10.1016/S0955-2219\(03\)00641-1](https://doi.org/10.1016/S0955-2219(03)00641-1)
94. Spiridonova IM, Sukhovaya EV, Pilyaeva SB et al (2002) The use of composite coatings during metallurgical equipment parts repair. *Metallurgicheskaya i Gornorudnaya Promyshlennost* 3:58–61
95. Ropyak LY, Shatskyi IP, Makoviichuk MV (2017) Influence of the oxide-layer thickness on the ceramic-aluminium coating resistance to indentation. *Metallofiz Noveishie Tekhnol* 39(4):517–524. <https://doi.org/10.15407/mfint.39.04.0517>
96. Rodaev VV, Zhigachev AO, Tyurin AI et al (2021) An engineering zirconia ceramic made of baddeleyite. *Materials* 14(16):4676. <https://doi.org/10.3390/ma14164676>
97. Duriagina Z, Kulyk V, Kovbasiuk T et al (2021) Synthesis of functional surface layers on stainless steels by laser alloying. *Metals* 11(3):434. <https://doi.org/10.3390/met11030434>
98. Kulyk VV, Vasylyv BD, Duriagina ZA et al (2021) The effect of water vapor containing hydrogenous atmospheres on the microstructure and tendency to brittle fracture of anode materials of YSZ–NiO(Ni) system. *Arch Mater Sci Eng* 108(2):49–67. <https://doi.org/10.5604/01.3001.0015.0254>
99. Ostash OP, Vasylyv BD, Podhurs'ka VY et al (2011) Optimization of the properties of 10Sc1CeSZ–NiO composite by the redox treatment. *Mater Sci* 46(5):653–658. <https://doi.org/10.1007/s11003-011-9337-1>
100. Serbenyuk TB, Prikhna TO, Sverdun VB et al (2018) Effect of the additive of Y₂O₃ on the structure formation and properties of composite materials based on AlN–SiC. *J Superhard Materials* 40(1):8–15. <https://doi.org/10.3103/S1063457618010021>

The Effect of Sintering Temperature on Crack Growth Resistance Characteristics of Fine-Grained Partially Stabilized Zirconia Determined by Various Test Methods



V. V. Kulyk , Z. A. Duriagina , Bogdan Vasyliv , V. I. Vavrukh ,
T. M. Kovbasiuk , P. Ya. Lyutyty , and T. L. Tepla 

Abstract Zirconium oxide (zirconia) is widely used as a structural material in various applications. However, upon heating, zirconia undergoes disruptive phase changes. By adding small percentages of yttria, these phase changes are eliminated, and the resulting yttria-stabilized zirconia material has superior thermal, mechanical, and electrical properties. The transformation toughening mechanisms allow getting higher strength and crack growth resistance of such ceramics. In this work, yttria-stabilized zirconia ceramics sintered at various temperatures have been studied. The series of beam specimens of ZrO_2 ceramics partially stabilized with 3, 4, and 5 mol% Y_2O_3 were prepared using a conventional sintering technique. Three sintering temperatures were used for each series: 1450 °C, 1500 °C, and 1550 °C.

V. V. Kulyk (✉) · Z. A. Duriagina · V. I. Vavrukh · T. M. Kovbasiuk · P. Ya. Lyutyty · T. L. Tepla
Department of Materials Science and Engineering, Lviv Polytechnic National University,
12 S. Bandera Str., Lviv 79013, Ukraine
e-mail: kulykvolodymyrvolodymyrovych@gmail.com

Z. A. Duriagina
e-mail: zduriagina@ukr.net

V. I. Vavrukh
e-mail: vavrukh.valentyna@gmail.com

T. M. Kovbasiuk
e-mail: felcproject@gmail.com

P. Ya. Lyutyty
e-mail: pavlo_lyutyty@ukr.net

T. L. Tepla
e-mail: tetiana.l.tepla@lpnu.ua

Z. A. Duriagina
The John Paul II Catholic University of Lublin, 14 Raclawickie Al., 20-950 Lublin, Poland

B. Vasyliv
Department of Hydrogen Technologies and Alternative Energy Materials, Karpenko
Physico-Mechanical Institute of the NAS of Ukraine, 5 Naukova Str., Lviv 79060, Ukraine
e-mail: mechengin1111@gmail.com

Two different mechanical tests were performed: single-edge notch beam test under three-point bending and fracture toughness test by indentation method. In both cases, fracture toughness was calculated using obtained experimental data. Based on the constructed dependences of fracture toughness on sintering temperature for the specimen series, it was revealed that both the yttria percentage and sintering temperature affect the mechanical behavior of the ceramics. The maximum transformation toughening effect was revealed for ZrO_2 -5 mol% Y_2O_3 ceramics. Based on the studies of fracture surface images and X-ray diffraction analysis, it was concluded that transformation toughening of such ceramics is accompanied by distinct changes in the fracture surface morphology.

Keywords YSZ ceramics · Fracture toughness · Microhardness · Fracture micromechanism

1 Introduction

Nowadays, various precision products are often manufactured of advanced ceramic materials (alumina, zirconia, silicon carbide, silicon nitride, etc.). These materials ensure required operating life of corresponding parts and products in hard operating conditions, namely high pressure or vacuum, high temperature, corrosion, radiation, etc. [1–8].

There may be a set of requirements which ceramic products manufactured of yttria-stabilized zirconia (YSZ) have to meet. Among them, the requirements on high strength and crack growth resistance, as well as corrosion and wear resistance, play a crucial role [9–11]. In particular, the required high-temperature strength and microstructural stability of ceramic and cermet components of high-temperature fuel cells in reducing and oxidizing atmospheres must be provided due to the microstructural optimization of materials and search for optimal treatment modes to increase the energy efficiency of the cells [11–16]. To meet global climate objectives, in particular, to reduce carbon dioxide emission [17, 18] and solve related issues of the deployment of renewables, there exists a need in ceramic materials reliable in hard operating conditions. Such conditions must be taken into account while developing new materials and improving microstructure of already existing YSZ ceramics [17–25]. The substantiation of chemical composition and processing and treatment modes seems to be first base points in improving the phase compositions, microstructure, and mechanical properties of the developed materials [26–35].

It was shown in a number of works that YSZ ceramics may be used in chemical industry and dentistry as a bulk material [36–40] or as coatings obtained with different techniques [41–47].

To estimate the bearing capacity of ceramic products, strength and wear resistance tests of the material are performed [39, 48–50]. However, to slow down the environmentally assisted microstructural changes in material [51–53], it is required to obtain material resistive to the degradation in such conditions [3, 54–60]. Microhardness

and fracture toughness as indicators of resistance of material to the nucleation and growth of microcracks may serve for this purpose. Researchers use the indentation test as it is one of the simplest known mechanical method [39, 61–63]. To evaluate crack growth resistance of materials, fracture toughness tests [38, 49, 51, 53, 61, 63–65] implementing a lot of loading schemes are used. Thus, to develop an appropriate processing and treatment modes of formation of ceramic microstructure having high crack growth resistance in operating conditions, YSZ ceramics sintered in different modes should be studied in terms of crack growth resistance and its relation to the phase balance and microstructural changes.

The work is aimed at evaluating the effect of sintering temperature on the phase composition and mechanical properties of fine-grained YSZ ceramics stabilized by the various amount of yttria.

2 Materials and Methods

In this work, yttria-stabilized zirconia (YSZ) ceramics sintered from commercial starting powders have been studied. The ZrO_2 powder was stabilized with 3, 4, and 5 mol% Y_2O_3 (hereinafter: 3YSZ, 4YSZ, and 5YSZ). The technique of powders preparation was described in the work [66]. Initial particle sizes of ZrO_2 powder were about 100–150 nm, and Y_2O_3 powder was about 10–30 nm. Beam specimens $4.2 \times 4.2 \times 50$ mm in size were sintered in an electric resistance furnace for 2 h in argon. Various specimen series (nine variants) were obtained at sintering temperatures of 1450 °C, 1500 °C, and 1550 °C (Table 1). Each variant was marked in a fashion indicating corresponding chemical composition and sintering temperature, e.g., 4YSZ–1500.

Microhardness of the materials was measured with a NOVOTEST TC-MKB1 microhardness tester. The relevant standards [67, 68] regulate the microhardness

Table 1 Chemical composition and sintering modes of variants of the investigated material

Variant	Content of Y_2O_3 , mol%	Sintering mode	
		Temperature, °C	Time, h
3YSZ–1450	3	1450	2
3YSZ–1500	3	1500	2
3YSZ–1550	3	1550	2
4YSZ–1450	4	1450	2
4YSZ–1500	4	1500	2
4YSZ–1550	4	1550	2
5YSZ–1450	5	1450	2
5YSZ–1500	5	1500	2
5YSZ–1550	5	1550	2

measurement conditions. Vickers microhardness [in GPa] is calculated by the formula [68]:

$$H = 0.0018544 \left(\frac{P}{d^2} \right) \quad (1)$$

where P is the indentation load [N] and d is the average length of the diagonals of the indentation imprint [mm].

An optical microscope Neophot-21 was used for estimating the imprint and crack geometry.

To characterize crack growth resistance of material [69–73], fracture toughness tests were performed with calculating the critical stress intensity factor (SIF) K_{Ic} . An indentation method of determining the fracture toughness implementing a variety of formulas for calculating the K_{Ic} values [74–89] is widely used for this purpose. Recently, the K_{Ic} values calculated by these formulas were compared with those obtained by conventional methods of fracture mechanics [90]. The following formula derived in the work [83] was found to fit the best for the characterization of ZrO_2 – Y_2O_3 ceramics:

$$K_{Ic} = 0.016 \left(\frac{E}{H} \right)^{1/2} \left(\frac{P}{c^{3/2}} \right) \quad (2)$$

where E is Young's modulus [GPa], H is microhardness [GPa], P is the indentation load [N], and c is the radial crack length [m].

Therefore, we used this formula to estimate the fracture toughness of the materials under study.

For comparison, a single-edge notch beam (SENB) test [91–93] was performed to estimate fracture toughness of material. This technique was thoroughly described in the work [66]. Corresponding formulas presented in [91–93] were used for calculating the critical SIF K_{Ic} of material.

A scanning electron microscope (SEM) Carl Zeiss EVO-40XVP was used for the investigation of the fracture surface morphology in specimens after mechanical tests. Chemical composition of the material specimens in local areas was determined with an energy-dispersive X-ray (EDX) microanalysis using an INCA Energy 350 system. For performing X-ray diffraction (XRD) analysis, a DRON-3.0 diffractometer was used.

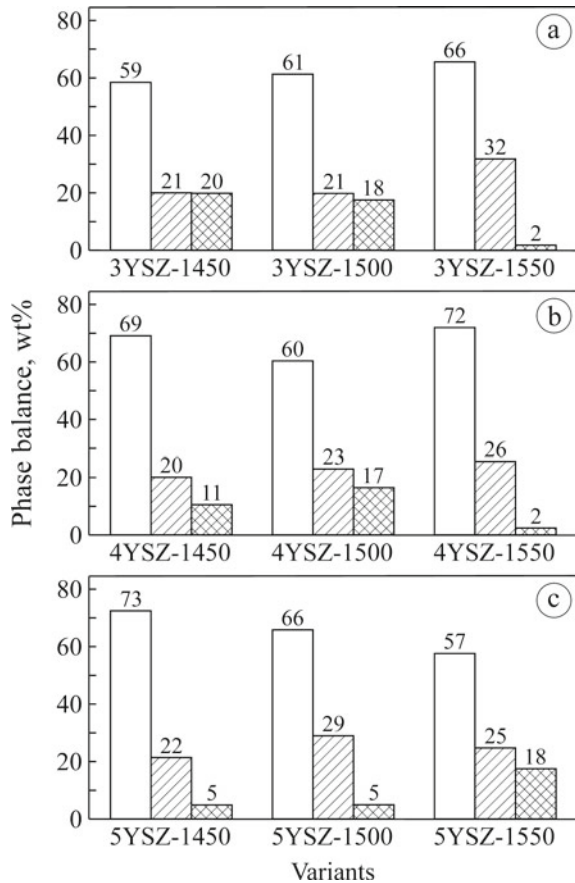
3 Results and Discussion

According to the obtained XRD patterns of the materials under study, general trends in the phase balance for 3YSZ, 4YSZ, and 5YSZ ceramics have been found (Fig. 1). A change in the phase composition of 3YSZ ceramics while increasing the sintering temperature from 1450 to 1550 °C was revealed to be ambiguous. In particular, for

this material sintered at a temperature of 1550 °C, a maximum percentage of t-ZrO₂ (about 66 wt%) along with a steep increase in m-ZrO₂ and a steep decrease in c-ZrO₂ weight fractions (to 32 wt% and 2 wt%, respectively) was found (Fig. 1a).

Thus, in 3YSZ ceramics, the sintering temperature of 1550 °C allows providing a relatively high percentage of the t-ZrO₂ phase, while the m-ZrO₂ phase weight fraction increases steeply comparing to variants 3YSZ–1450 and 3YSZ–1500. In contrast to this, the c-ZrO₂ phase weight fraction decreases steeply in 3YSZ–1550 ceramics comparing to these two variants. In 4YSZ ceramics, non-monotonous changes in the t-ZrO₂ and c-ZrO₂ phase percentages with a change in the sintering temperature from 1450 to 1550 °C were revealed (Fig. 1b). A minimum of the tetragonal phase and a maximum of the cubic phase were found for variant 4YSZ–1500. At 1550 °C, the t-ZrO₂ and m-ZrO₂ phase percentages reach their maxima, whereas the c-ZrO₂ phase percentage reaches its minimum. At this sintering temperature, a percentage of t-ZrO₂ is about 72 wt%. The highest content of t-ZrO₂ (about 73 wt%) was revealed for 5YSZ–1450 ceramics (Fig. 1c). Besides, a gradual lowering

Fig. 1 Zirconia phase balances of the investigated materials of variants **a** 3YSZ–1450, 3YSZ–1500, 3YSZ–1550, **b** 4YSZ–1450, 4YSZ–1500, 4YSZ–1550, and **c** 5YSZ–1450, 5YSZ–1500, 5YSZ–1550 (see Table 1). White bars–tetragonal phase; hatched bars–monoclinic phase; crosshatched bars–cubic phase; the numbers above the bars indicate the weight percentage of corresponding phases



of a $t\text{-ZrO}_2$ phase percentage was observed for 5YSZ ceramics with a change in the sintering temperature from 1450 to 1550 °C (Fig. 1c).

For the sintering temperature of 1550 °C, a steep decrease in $m\text{-ZrO}_2$ and a steep increase in $c\text{-ZrO}_2$ weight fractions (to 25 wt% and 18 wt%, respectively) were found, whereas a $t\text{-ZrO}_2$ phase, percentage was about 57 wt%.

In general, the phase balance in the ceramics under study reflects the competing effect of two factors, namely the sintering temperature of the ceramics and the content of the stabilizing Y_2O_3 additive. Therefore, the 5YSZ ceramics sintered at a temperature of 1450 °C contains a relatively high amount of metastable tetragonal phase.

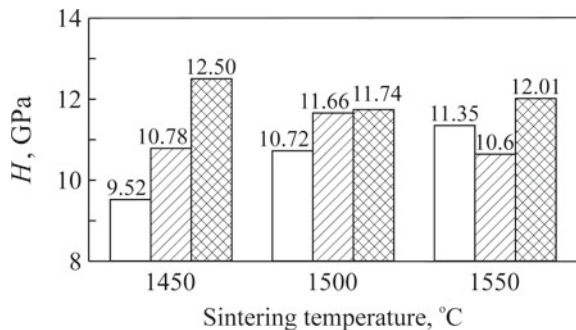
During microhardness measurements, the yield of average microhardness values on the plateau at indentation loads above 4.91 N was found for all the material variants. Such a dependence of the microhardness of 8YSZ ceramics on the indentation load known as the indentation size effect [94–96] was revealed by authors of the work [90].

The invariant values of the material microhardness obtained under the indentation load of 9.81 N were taken to construct histograms for investigating the changes in microhardness of the studied ceramics (Fig. 2). In general, microhardness of 3YSZ ceramics increased with increasing sintering temperature from 1450 to 1550 °C.

Comparing to 4YSZ–1450 and 4YSZ–1550 ceramics, variant 4YSZ–1500 shows higher microhardness that is probably related to the low percentage of the $t\text{-ZrO}_2$ phase in it and, as a consequence, formation of a smaller amount of the $m\text{-ZrO}_2$ phase during the $t\text{-m}$ transformation of ZrO_2 . This, in turn, does not lead to the lowering of microhardness similarly to the results of the work [97] since microhardness of $m\text{-ZrO}_2$ is lower than $t\text{-ZrO}_2$. In addition, variant 4YSZ–1500 has the high percentage of the $c\text{-ZrO}_2$ phase (Fig. 1b) which is harder than the $m\text{-ZrO}_2$.

The 5YSZ ceramics exhibit an ambiguous dependence of microhardness on the sintering temperature. The highest microhardness of material of variant 5YSZ–1450 (Fig. 2) can be related to the highest percentage of the $t\text{-ZrO}_2$ phase (Fig. 1c). With increasing a sintering temperature up to 1550 °C, two competing processes occur in 5YSZ ceramics: (i) lowering the $t\text{-ZrO}_2$ and simultaneous increasing the $m\text{-ZrO}_2$ phase and $c\text{-ZrO}_2$ phase percentages; (ii) intensive grain growth. The suppression of

Fig. 2 Changes in microhardness of 3YSZ (white bars), 4YSZ (hatched bars), and 5YSZ ceramics (crosshatched bars) depending on the sintering temperature. The numbers above the bars indicate the average values of microhardness



the m-ZrO₂ formation due to grain growth [97] and a high content of the cubic phase are probably reasons for higher microhardness of 5YSZ–1550 ceramics compared to 5YSZ–1500.

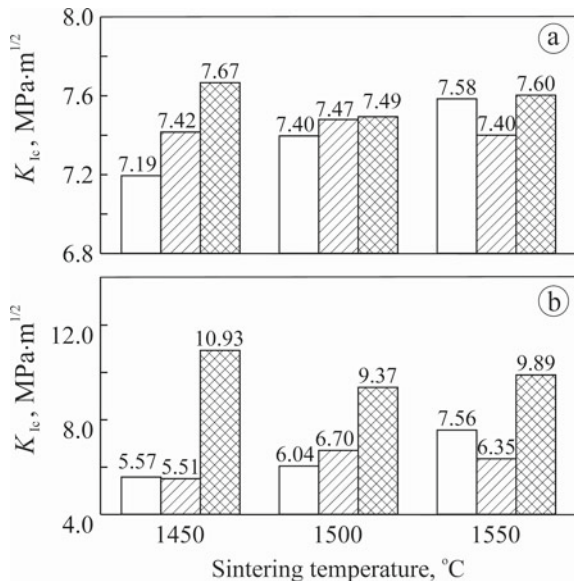
The authors of a number of works [69, 71, 81, 98] used the formula (2) for assessing the fracture toughness of different ceramic materials by the Vickers indentation method. It provided the values close to those obtained by conventional methods on pre-cracked specimens [15, 99, 100]. The values of fracture toughness of the material variants under study were also calculated by this formula according to an approach proposed in the work [90] using the selected set of indentation load *P* and the corresponding values of microhardness *H*.

Average values of fracture toughness of the material variants under study (Fig. 3a) exhibit the trend similar to that in microhardness (Fig. 2). Besides, the fracture toughness dependences based on the SENB test method (Fig. 3b) also show the similar tendency in fracture toughness.

It was found that in terms of both microhardness and fracture toughness, the sintering temperature of 1500 °C is critical affecting the process of microstructure formation (Figs. 2 and 3). For ceramics with a high percentage of yttria (5YSZ), such a sintering temperature does not provide relatively high level of fracture toughness. In contrast, this temperature is optimal for 4YSZ ceramics. With increasing sintering temperature from 1450 to 1550 °C, 3YSZ ceramics exhibit an increase in fracture toughness (Fig. 3).

It was found that increased fracture toughness of 3YSZ, 4YSZ, and 5YSZ ceramics is related to corresponding fracture micromechanisms, similarly to other ceramics containing some amount of YSZ [2].

Fig. 3 Changes in fracture toughness of 3YSZ (white bars), 4YSZ (hatched bars), and 5YSZ ceramics (crosshatched bars) depending on the sintering temperature: **a** Vickers indentation method under the indentation load of 9.81 N; **b** SENB method under three-point bending. The numbers above the bars indicate the average values of fracture toughness



The distinct morphology of the specimen fracture surface was revealed for 3YSZ–1550 ceramics (Fig. 4a, b), 4YSZ–1500 ceramics (Fig. 4c, d), and 5YSZ–1450 ceramics (Fig. 4e, f).

Other ceramics under study did not exhibit clear contours of microstructural components on fracture surfaces. An intergranular fracture micromechanism in a specimen of 3YSZ–1550 ceramics may be recognized at a high magnification (Fig. 4b). The average size of the particles is about 500–600 nm. For 4YSZ ceramics of variant 4YSZ–1500 having the relatively high percentage of the c-ZrO₂ phase (Fig. 1b) and exhibiting both the relatively high microhardness (Fig. 2) and fracture toughness (Fig. 3), clear contours of nanoparticles of about 500 nm in size may be observed at a high magnification on fracture surface of a specimen (Fig. 4d). The dominant fracture micromechanism is similar to that peculiar for 3YSZ–1550 ceramics.

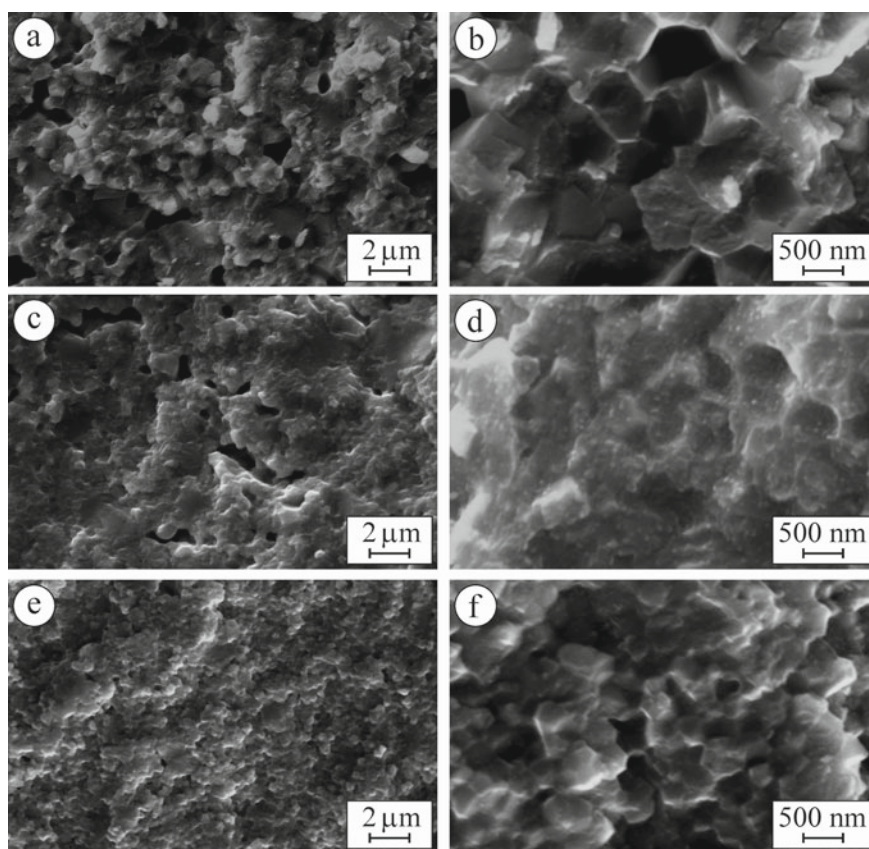


Fig. 4 SEM fractography (SE images) of specimens of **a, b** 3YSZ–1550, **c, d** 4YSZ–1500, and **e, f** 5YSZ–1450 ceramics at **a, c, e** low and **b, d, f** high magnifications

Variant 5YSZ–1450 exhibits a distinct fine-grained fracture surface (Fig. 4f) corresponding to a mixed fracture along the boundaries of t-ZrO₂ nanograins united into agglomerates. The average grain size is about 200–250 nm, whereas the agglomerates are 2–5 μm in size (Fig. 4f). This fracture micromechanism is related to the highest microhardness (Fig. 2) and fracture toughness (Fig. 3). It can be stated that such a chemical composition and a sintering mode are optimal for the formation of a promising microstructure of YSZ ceramics [66] providing its high crack growth resistance.

Thus, based on results of the microhardness test and fracture toughness tests using both the SENB and Vickers indentation methods, it can be concluded that the best variant of material is that of 5YSZ ceramics sintered at a temperature of 1450 °C (variant 5YSZ–1450).

4 Conclusions

In this work, the phase composition and mechanical properties of 3YSZ, 4YSZ, and 5YSZ ceramics have been studied.

1. It was shown that microhardness and fracture toughness parameters are suitable for the characterization of mechanical behavior of the YSZ ceramics depending on a percentage of a stabilizing additive and sintering temperature.
2. The dependences of the tetragonal, monoclinic, and cubic phase percentages of zirconia on the sintering temperature were found to have non-monotonous character. The correlations between microhardness, fracture toughness, and the tetragonal phase percentage for the YSZ ceramics were revealed.
3. It was found that 5YSZ ceramics sintered at 1450 °C has the highest microhardness and fracture toughness which is related to a high percentage of the tetragonal phase.

References

1. Shabri HA, Othman MHD, Mohamed MA et al (2021) Recent progress in metal-ceramic anode of solid oxide fuel cell for direct hydrocarbon fuel utilization: A review. *Fuel Process Technol* 212:106626. <https://doi.org/10.1016/j.fuproc.2020.106626>
2. Serbenyuk TB, Prikhna TO, Sverdun VB et al (2018) Effect of the additive of Y₂O₃ on the structure formation and properties of composite materials based on AlN–SiC. *J Superhard Materials* 40(1):8–15. <https://doi.org/10.3103/S1063457618010021>
3. Dobrzański LA, Dobrzański LB, Dobrzańska-Danikiewicz AD (2020) Additive and hybrid technologies for products manufacturing using powders of metals, their alloys and ceramics. *Arch Mater Sci Eng* 102(2):59–85. <https://doi.org/10.5604/01.3001.0014.1525>
4. Posuvailo VM, Kulyk VV, Duriagina ZA et al (2020) The effect of electrolyte composition on the plasma electrolyte oxidation and phase composition of oxide ceramic coatings formed on

- 2024 aluminium alloy. *Arch Mater Sci Eng* 105(2):49–55. <https://doi.org/10.5604/01.3001.0014.5761>
5. Cherepova TS, Dmytrieva HP, Dukhota OI et al (2016) Properties of nickel powder alloys hardened with titanium carbide. *Mater Sci* 52(2):173–179. <https://doi.org/10.1007/s11003-016-9940-2>
 6. Bocanegra-Bernal MH, Díaz de la Torre S (2002) Phase transitions in zirconium dioxide and related materials for high performance engineering ceramics. *J Mater Sci* 37:4947–4971. <https://doi.org/10.1023/A:1021099308957>
 7. Ropyak LY, Makoviichuk MV, Shatskyi IP et al (2020) Stressed state of laminated interference-absorption filter under local loading. *Funct Mater* 27(3):638–642. <https://doi.org/10.15407/fm27.03.638>
 8. Ye K, Blikharskyy Z, Vira V et al (2021) Nanostructural changes in a Ni/NiO cermet during high-temperature reduction and reoxidation. *Nanomaterials and nanocomposites, nanostructure surfaces, and their applications*. Springer Proc Phys 246:219–229. https://doi.org/10.1007/978-3-030-51905-6_17
 9. Dobrzański LA, Dobrzański LB, Dobrzańska-Danikiewicz AD (2020) Manufacturing technologies thick-layer coatings on various substrates and manufacturing gradient materials using powders of metals, their alloys and ceramics. *J Achieve Mater and Manuf Eng* 99(1):14–41. <https://doi.org/10.5604/01.3001.0014.1598>
 10. Vasylyv BD, Podhurska VY, Ostash OP et al (2018) Effect of a hydrogen sulfide-containing atmosphere on the physical and mechanical properties of solid oxide fuel cell materials. *Nanochemistry, biotechnology, nanomaterials, and their applications*. Springer Proc Phys 214:475–485. https://doi.org/10.1007/978-3-319-92567-7_30
 11. Budzianowski WM, Milewski J (2011) Solid-oxide fuel cells in power generation applications: A review. *Recent Patents Eng* 5(3):165–189. <https://doi.org/10.2174/187221211797636926>
 12. Komatsu Y, Sciazko A, Shikazono N (2021) Isostatic pressing of screen printed nickel-gadolinium doped ceria anodes on electrolyte-supported solid oxide fuel cells. *J Power Sources* 485:229317. <https://doi.org/10.1016/j.jpowsour.2020.229317>
 13. Vasylyv BD (2010) Improvement of the electric conductivity of the material of anode in a fuel cell by the cyclic redox thermal treatment. *Mater Sci* 46(2):260–264. <https://doi.org/10.1007/s11003-010-9282-4>
 14. Wejrzanowski T, Haj Ibrahim S, Cwieka K et al (2018) Multi-modal porous microstructure for high temperature fuel cell application. *J Power Sources* 373:85–94. <https://doi.org/10.1016/j.jpowsour.2017.11.009>
 15. Podhurska V, Vasylyv B (2012) Influence of NiO reduction on microstructure and properties of porous Ni–ZrO₂ substrates. In: *Proceedings of the 3rd international conference on oxide materials for electronic engineering (OMEE-2012)*, Lviv, Ukraine, pp 293–294. <https://doi.org/10.1109/OMEE.2012.6464761>
 16. Danilenko I, Lasko G, Brykhanova I et al (2017) The peculiarities of structure formation and properties of zirconia-based nanocomposites with addition of Al₂O₃ and NiO. *Nanoscale Res Lett* 12:125. <https://doi.org/10.1186/s11671-017-1901-7>
 17. Milewski J, Lewandowski J, Miller A (2008) Reducing CO₂ emissions from a coal fired power plant by using a molten carbonate fuel cell. *Proceedings of the ASME Turbo Expo* 2:389–395. <https://doi.org/10.1115/GT2008-50100>
 18. Milewski J, Lewandowski J (2009) Solid oxide fuel cell fuelled by biogases. *Arch Thermo* 30(4):3–12. https://www.imp.gda.pl/fileadmin/doc/imp_publishing/wimp/archives%20of%20thermodynamics/C_09_4.pdf
 19. Dobrzański LA, Dobrzański LB, Dobrzańska-Danikiewicz AD (2020) Overview of conventional technologies using the powders of metals, their alloys and ceramics in Industry 4.0 stage. *J Achievements in Mater and Manuf Eng* 98(2):56–85. <https://doi.org/10.5604/01.3001.0014.1481>
 20. Savka SS, Popovych DI, Serednytski AS (2017) Molecular dynamics simulations of the formation processes of zinc oxide nanoclusters in oxygen environment. *Nanophysics, Nanomaterials, Interface Studies, and Applications*. Springer Proc Phys 195:145–156. https://doi.org/10.1007/978-3-319-56422-7_11

21. Milewski J, Kupecki J, Szczęśniak A et al (2021) Hydrogen production in solid oxide electrolyzers coupled with nuclear reactors. *Int J Hydrogen Energy* 46(72):35765–35776. <https://doi.org/10.1016/j.ijhydene.2020.11.217>
22. Vasylyv B, Podhurska V, Ostash O (2017) Preconditioning of the YSZ–NiO fuel cell anode in hydrogenous atmospheres containing water vapor. *Nanoscale Res Lett* 12:265. <https://doi.org/10.1186/s11671-017-2038-4>
23. Witz G, Shklover V, Steurer W et al (2007) Phase evolution in yttria-stabilized zirconia thermal barrier coatings studied by Rietveld refinement of X-ray powder diffraction patterns. *J Am Ceram Soc* 90(9):2935–2940. <https://doi.org/10.1111/j.1551-2916.2007.01785.x>
24. Andrzejczuk M, Vasylyev O, Brodnikovskiy I et al (2014) Microstructural changes in NiO–ScSZ composite following reduction processes in pure and diluted hydrogen. *Mater Charact* 87:159–165. <https://doi.org/10.1016/j.matchar.2013.11.011>
25. Clarke DR, Levi CG (2003) Material design for the next generation thermal barrier coatings. *Annu Rev Mater Res* 33:383–417. <https://doi.org/10.1146/annurev.matsci.33.011403.113718>
26. Smyrnova-Zamkova MY, Ruban OK, Bykov OI et al (2018) Physico-chemical properties of fine-grained powder in $\text{Al}_2\text{O}_3\text{--ZrO}_2\text{--Y}_2\text{O}_3\text{--CeO}_2$ system produced by combined method. *Comp Theory Practice* 18(4):234–240. https://kompozyty.ptmk.net/pliczki/pliki/1290_2018_t04_maria-y-smyrnova-zamkova-.pdf
27. Vasylyv B, Milewski J, Podhurska V et al (2021) Study of the degradation of a fine-grained YSZ–NiO anode material during reduction in hydrogen and reoxidation in air. *Appl Nanosci*. <https://doi.org/10.1007/s13204-021-01768-w>
28. Smyrnova-Zamkova MY, Red'ko VP, Ruban OK et al (2017) The properties of nanocrystalline powder of 90% $\text{Al}_2\text{O}_3\text{--}10\%$ ZrO_2 (wt.%) obtained via the hydrothermal synthesis/mechanical mixing. *Nanosistemi Nanomater Nanotechnol* 15(2):309–317. <https://doi.org/10.15407/mnn.15.02.0309>
29. Sukhova OV (2009) Influence of mechanisms of structure formation of interfaces in composites on their properties. *Metallofiz Noveishie Tekhnol* 31(7):1001–1012
30. Dudnik OV, Marek IO, Ruban OK et al (2020) Effect of heat treatment on the structure and phase composition of the nanosized powder based on a ZrO_2 solid solution. *Powder Metall Met Ceram* 59(1–2):1–8. <https://doi.org/10.1007/s11106-020-00132-x>
31. Efremenko VG, Chabak YG, Shimizu K et al (2017) Structure refinement of high-Cr cast iron by plasma surface melting and post-heat treatment. *Mater Des* 126:278–290. <https://doi.org/10.1016/j.matdes.2017.04.022>
32. Zhou XW, Shen YF, Jin HM (2011) Effect of deposition mechanism and microstructure of nano-ceria oxide addition on Ni-P coating by pulse electrodeposition. *Adv Mater Res* 326:151–156. <https://doi.org/10.4028/www.scientific.net/AMR.326.151>
33. Shevchenko AV, Lashneva VV, Ruban AK et al (2016) Synthesis and study of high-purity nanocrystalline powder of a solid solution of CeO_2 and Y_2O_3 in zirconium dioxide. *Powder Metall Met Ceram* 54(9–10):548–553. <https://doi.org/10.1007/s11106-016-9748-5>
34. Kujawa M, Suwak R, Dobrzański LA et al (2021) Thermal characterization of halloysite materials for porous ceramic preforms. *Arch Mater Sci Eng* 107(1):5–15. <https://doi.org/10.5604/01.30014.8189>
35. Marek IO, Ruban OK, Redko VP et al (2019) Physicochemical properties of hydrothermal nanocrystalline $\text{ZrO}_2\text{--Y}_2\text{O}_3\text{--CeO}_2$ powders. *Powder Metall Met Ceram* 58(3–4):125–132. <https://doi.org/10.1007/s11106-019-00055-2>
36. Kumar A, Kumar P, Dhaliwal AS (2021) Structural studies of zirconia and yttria doped zirconia for analysing its phase stabilization criteria. *IOP Conf. Series: Mater Sci Eng* 1033:012052. <https://doi.org/10.1088/1757-899X/1033/1/012052>
37. Kern F, Gommeringer A (2020) Mechanical properties of 2Y–TZP fabricated from detonation synthesized powder. *Ceram* 3(4):440–452. <https://doi.org/10.3390/ceramics3040037>
38. Alves MFRP, Ribeiro S, Suzuki PA et al (2021) Effect of Fe_2O_3 addition and sintering temperature on mechanical properties and translucence of zirconia dental ceramics with different Y_2O_3 content. *Mater Res* 24(2):e20200402. <https://doi.org/10.1590/1980-5373-MR-2020-0402>

39. Jeong K-W, Han J-S, Yang G-U et al (2021) Influence of preaging temperature on the indentation strength of 3Y-TZP aged in ambient atmosphere. *Materials* 14:2767. <https://doi.org/10.3390/ma14112767>
40. Tsai Y-Y, Lee T-M, Kuo J-C (2021) Hydrothermal-aging-induced lattice distortion in yttria-stabilized zirconia using EBSD technique. *Micron* 145:103053. <https://doi.org/10.1016/j.micron.2021.103053>
41. Brandon JR, Taylor R (1991) Phase stability of zirconia-based thermal barrier coatings Part I, Zirconia-yttria alloys. *Surf Coat Technol* 46:75–90. [https://doi.org/10.1016/0257-8972\(91\)90151-L](https://doi.org/10.1016/0257-8972(91)90151-L)
42. Schulz U (2000) Phase transformation in EB-PVD yttria partially stabilized zirconia thermal barrier coatings during annealing. *J Am Ceram Soc* 83(4):904–910. <https://doi.org/10.1111/j.1151-2916.2000.tb01292.x>
43. Azzopardi A, Mevrel R, Saint-Ramond B et al (2004) Influence of aging on structure and thermal conductivity of Y-PSZ and Y-FSZ EB-PVD coatings. *Surf Coat Technol* 177–178:131–139. <https://doi.org/10.1016/j.surfcoat.2003.08.073>
44. Miller RA, Smialek JL, Garlick RG (1981) Phase stability in plasma sprayed, partially stabilized zirconia–yttria. In: Heuer AH, Hobbs LW (eds) *Advances in Ceramics*. Vol. 3, Science and Technology of Zirconia I. Am Ceram Soc, Columbus, pp. 241–253
45. Ilavsky J, Stalick JK, Wallace J (2001) Thermal spray yttria-stabilized zirconia phase changes during annealing. *J Therm Spray Technol* 10(3):497–501. <https://doi.org/10.1361/105996301770349277>
46. Scott HG (1975) Phase relationships in the zirconia–yttria system. *J Mater Sci* 10:1527–1535. <https://doi.org/10.1007/BF01031853>
47. Katamura J, Sakuma T (1998) Computer simulation of the microstructural evolution during the diffusionless cubic-to-tetragonal transition in the system ZrO_2 – Y_2O_3 . *Acta Mater* 46(5):1569–1575. [https://doi.org/10.1016/S1359-6454\(97\)00356-X](https://doi.org/10.1016/S1359-6454(97)00356-X)
48. Gaddam A, Brazete DS, Neto AS et al (2021) Three-dimensional printing of zirconia scaffolds for load bearing applications: study of the optimal fabrication conditions. *J Am Ceram Soc* 104(9):4368–4380. <https://doi.org/10.1111/jace.17874>
49. Ji SH, Kim DS, Park MS et al (2021) Sintering process optimization for 3YSZ ceramic 3D-printed objects manufactured by stereolithography. *Nanomaterials* 11:192. <https://doi.org/10.3390/nano11010192>
50. Podhurs'ka VY, Vasylyv BD, Ostash OP, et al (2014) Structural transformations in the NiO-containing anode of ceramic fuel cells in the course of its reduction and oxidation. *Mater Sci* 49(6):805–811. <https://doi.org/10.1007/s11003-014-9677-8>
51. Tao S, Yang J, Zhai M et al (2020) Thermal stability of YSZ thick thermal barrier coatings deposited by suspension and atmospheric plasma spraying. *Curr Comput-Aided Drug Des* 10(11):984. <https://doi.org/10.3390/cryst10110984>
52. Fan Z, Sun X, Zhuo X et al (2021) Femtosecond laser polishing yttria-stabilized zirconia coatings for improving molten salts corrosion resistance. *Cor Sci* 184:109367. <https://doi.org/10.1016/j.corsci.2021.109367>
53. Rudolphi M, Galetz MC, Schütze M (2021) Mechanical stability diagrams for thermal barrier coating systems. *J Therm Spray Technol* 30:694–707. <https://doi.org/10.1007/s11666-021-01163-5>
54. Ostash OP, Andreiko IM, Kulyk VV et al (2013) Influence of braking on the microstructure and mechanical behavior of steels of railroad wheel. *Mater Sci* 48(5):569–574. <https://doi.org/10.1007/s11003-013-9539-9>
55. Sciazko A, Shimura T, Komatsu Y et al (2021) Ni-GDC and Ni-YSZ electrodes operated in solid oxide electrolysis and fuel cell modes. *J Therm Sci Technol* 16(1):JTST0013. <https://doi.org/10.1299/jtst.2021jtst0013>
56. Nykyforchyn H, Krechkovska H, Student O et al (2019) Feature of stress corrosion cracking of degraded gas pipeline steels. *Procedia Struct Integrity* 16:153–160. <https://doi.org/10.1016/j.prostr.2019.07.035>





57. Romaniv OM, Vasylyv BD (1998) Some features of formation of the structural strength of ceramic materials. *Mater Sci* 34(2):149–161. <https://doi.org/10.1007/BF02355530>
58. Efremenko VG, Chabak YG, Lekatou A et al (2016) High-temperature oxidation and decarburization of 14.55 wt pct Cr-cast iron in dry air atmosphere. *Metall Mater Trans A* 47A(2):1529–1543. <https://doi.org/10.1007/s11661-016-3336-7>
59. Buchanec S, Sciazko A, Mozdziej M et al (2019) A novel approach to the optimization of a solid oxide fuel cell anode using evolutionary algorithms. *IEEE Access* 7:34361–34372. <https://doi.org/10.1109/ACCESS.2019.2904327>
60. Włodarczyk-Fligier A, Polok-Rubiniec M, Konieczny J (2020) Thermal analysis of matrix composite reinforced with Al₂O₃ particles. *J Achievements in Mater and Manuf Eng* 100(1):5–11. <https://doi.org/10.5604/01.3001.0014.1957>
61. Romaniv OM, Zalite IV, Simin'kovych VM, et al (1996) Effect of the concentration of zirconium dioxide on the fracture resistance of Al₂O₃-ZrO₂ ceramics. *Mater Sci* 31(5):588–594. <https://doi.org/10.1007/BF00558793>
62. Khajavi P, Hndriksen PV, Chevalier J et al (2020) Improving the fracture toughness of stabilized zirconia-based solid oxide cells fuel electrode supports: Effects of type and concentration of stabilizer(s). *J Eur Ceram Soc* 40(15):5670–5682. <https://doi.org/10.1016/j.jeurceramsoc.2020.05.042>
63. Buyakov AS, Mirovoy YA, Smolin AY et al (2021) Increasing fracture toughness of zirconia-based composites as a synergistic effect of the introducing different inclusions. *Ceram Int* 47(8):10582–10589. <https://doi.org/10.1016/j.ceramint.2020.12.170>
64. Ivasyshyn AD, Vasylyv BD (2001) Effect of the size and form of specimens on the diagram of growth rates of fatigue cracks. *Mater Sci* 37(6):1002–1004. <https://doi.org/10.1023/A:1015669913601>
65. Vasylyv BD (2002) Initiation of a crack from the edge of a notch with oblique front in specimens of brittle materials. *Mater Sci* 38(5):724–728. <https://doi.org/10.1023/A:1024222709514>
66. Kulyk VV, Duriagina ZA, Vasylyv BD et al (2021) Effects of yttria content and sintering temperature on the microstructure and tendency to brittle fracture of yttria-stabilized zirconia. *Arch Mater Sci Eng* 109(2):65–79. <https://doi.org/10.5604/01.3001.0015.2625>
67. ASTM E 384-11 (2011) Standard test method for Knoop and Vickers hardness of materials. ASTM International. <https://doi.org/10.1520/E0384-11>
68. ASTM C 1327-03 (2003) Standard test method for Vickers indentation hardness of advanced ceramics. ASTM International. <https://doi.org/10.1520/C1327-03>
69. Cook RF, Pharr GM (1990) Direct observation and analysis of indentation cracking in glasses and ceramics. *J Am Ceram Soc* 73(4):787–817. <https://doi.org/10.1111/j.1151-2916.1990.tb05119.x>
70. Ostash OP, Kulyk VV, Poznyakov VD et al (2017) Fatigue crack growth resistance of welded joints simulating the weld-repaired railway wheels metal. *Arch Mater Sci Eng* 86(2):49–55. <https://doi.org/10.5604/01.3001.0010.4885>
71. Nastic A, Merati A, Bielawski M et al (2015) Instrumented and Vickers indentation for the characterization of stiffness, hardness and toughness of zirconia toughened Al₂O₃ and SiC armor. *J Mater Sci Technol* 31(8):773–783. <https://doi.org/10.1016/j.jmst.2015.06.005>
72. Lawn BR (1993) Fracture of brittle solids, 2nd edn, Cambridge. <https://doi.org/10.1017/CBO9780511623127>
73. Adams JW, Ruh R, Mazdiyasi KS (1997) Young's modulus, flexural strength, and fracture of yttria-stabilized zirconia versus temperature. *J Am Ceram Soc* 80(4):903–908. <https://doi.org/10.1111/j.1151-2916.1997.tb02920.x>
74. Lawn BR, Swain MV (1975) Microfracture beneath point indentations in brittle solids. *J Mater Sci* 10(1):113–122. <https://doi.org/10.1007/BF00541038>
75. Lawn BR, Fuller ER (1975) Equilibrium penny-like cracks in indentation fracture. *J Mater Sci* 10(12):2016–2024. <https://doi.org/10.1007/BF00557479>
76. Niihara K, Morena R, Hasselman DPH (1982) Evaluation of K_{IC} of brittle solids by the indentation method with low crack-to-indent ratios. *J Mater Sci Lett* 1(1):13–16. <https://doi.org/10.1007/BF00724706>

77. Tanaka K (1987) Elastic/plastic indentation hardness and indentation fracture toughness: The inclusion core model. *J Mater Sci* 22(4):1501–1508. <https://doi.org/10.1007/BF01233154>
78. Evans AG, Charles EA (1976) Fracture toughness determinations by indentation. *J Am Ceram Soc* 59(7–8):371–372. <https://doi.org/10.1111/j.1151-2916.1976.tb10991.x>
79. Gogotsi GA, Dub SN, Lomonova EE et al (1995) Vickers and Knoop indentation behaviour of cubic and partially stabilized zirconia crystals. *J Eur Ceram Soc* 15(5):405–413. [https://doi.org/10.1016/0955-2219\(95\)91431-M](https://doi.org/10.1016/0955-2219(95)91431-M)
80. Niihara K (1983) A fracture mechanics analysis of indentation-induced Palmqvist crack in ceramics. *J Mater Sci Lett* 2(5):221–223. <https://doi.org/10.1007/BF00725625>
81. Aswad MA (2014) Comparison of the fracture toughness of high temperature ceramic measured by digital image correlation and indentation method. *J Univ Babylon* 22(4):927–937. <https://www.iasj.net/iasj?func=article&aId=99010>
82. Grigoriev ON, Vinokurov VB, Mosina TV et al (2017) Kinetics of shrinkage, structurization, and the mechanical characteristics of zirconium boride sintered in the presence of activating additives. *Powder Metall Met Ceram* 55(11–12):676–688. <https://doi.org/10.1007/s1106-017-9855-y>
83. Anstis GR, Chantikul P, Lawn BR et al (1981) A critical evaluation of indentation techniques for measuring fracture toughness: I, Direct crack measurement. *J Am Ceram Soc* 64(9):533–538. <https://doi.org/10.1111/j.1151-2916.1981.tb10320.x>
84. Danilenko I, Glazunov F, Konstantinova T et al (2014) Effect of Ni/NiO particles on structure and crack propagation in zirconia based composites. *Adv Mater Lett* 5(8):465–471. <https://doi.org/10.5185/amlett.2014.amwc1040II>
85. Blendell JE (1979) The origins of internal stresses in polycrystalline alumina and their effects on mechanical properties. Cambridge
86. Lawn BR, Evans AG, Marshall DB (1980) Elastic/plastic indentation damage in ceramics: The median/radial crack system. *J Am Ceram Soc* 63(9–10):574–581. <https://doi.org/10.1111/j.1151-2916.1980.tb10768.x>
87. Vasylyv BD (2009) A procedure for the investigation of mechanical and physical properties of ceramics under the conditions of biaxial bending of a disk specimen according to the ring–ring scheme. *Mater Sci* 45(4):571–575. <https://doi.org/10.1007/s11003-010-9215-2>
88. Smyrnova-Zamkova MY, Ruban OK, Bykov OI et al (2021) The influence of the ZrO₂ solid solution amount on the physicochemical properties of Al₂O₃–ZrO₂–Y₂O₃–CeO₂ powders. *Powder Metall Met Ceram* 60(3–4):129–141. <https://doi.org/10.1007/s1106-021-00222-4>
89. Lankford J (1982) Indentation microfracture in the Palmqvist crack regime: implications for fracture toughness evaluation by the indentation method. *J Mater Sci Lett* 1(11):493–495. <https://doi.org/10.1007/BF00721938>
90. Vasylyv B, Kulyk V, Duriagina Z et al (2020) Estimation of the effect of redox treatment on microstructure and tendency to brittle fracture of anode materials of YSZ–NiO(Ni) system. *Eastern-European J Enter Tech* 108/6(12):67–77. <https://doi.org/10.15587/1729-4061.2020.218291>
91. ASTM E 399-20a (2020) Standard test method for linear-elastic plane-strain fracture toughness of metallic materials. ASTM International. <https://doi.org/10.1520/E0399-20A>
92. ASTM C 1421-18 (2018) Standard test methods for determination of fracture toughness of advanced ceramics at ambient temperature. ASTM Inter. <https://doi.org/10.1520/C1421-18>
93. Kübler J (2002) Fracture toughness of ceramics using the SEVNB method: From a preliminary study to a standard test method. In: Salem J (ed) Fracture resistance testing of monolithic and composite brittle materials. ASTM International, 93–106. <https://doi.org/10.1520/STP10473S>
94. Peng Z, Gong J, Miao H (2004) On the description of indentation size effect in hardness testing for ceramics: analysis of the nanoindentation data. *J Eur Ceram Soc* 24(8):2193–2201. [https://doi.org/10.1016/S0955-2219\(03\)00641-1](https://doi.org/10.1016/S0955-2219(03)00641-1)
95. Ropyak LY, Shatskyi IP, Makoviichuk MV (2017) Influence of the oxide-layer thickness on the ceramic-aluminium coating resistance to indentation. *Metallofiz Noveishie Tekhnol* 39(4):517–524. <https://doi.org/10.15407/mfint.39.04.0517>

96. Spiridonova IM, Sukhovaya EV, Pilyaeva SB et al (2002) The use of composite coatings during metallurgical equipment parts repair. *Metallurgicheskaya i Gornorudnaya Promyshlennost* 3:58–61
97. Rodaev VV, Zhigachev AO, Tyurin AI et al (2021) An engineering zirconia ceramic made of baddeleyite. *Materials* 14(16):4676. <https://doi.org/10.3390/ma14164676>
98. Duriagina Z, Kulyk V, Kovbasiuk T et al (2021) Synthesis of functional surface layers on stainless steels by laser alloying. *Metals* 11(3):434. <https://doi.org/10.3390/met11030434>
99. Kulyk VV, Vasyliv BD, Duriagina ZA et al (2021) The effect of water vapor containing hydrogenous atmospheres on the microstructure and tendency to brittle fracture of anode materials of YSZ–NiO(Ni) system. *Arch Mater Sci Eng* 108(2):49–67. <https://doi.org/10.5604/01.3001.0015.0254>
100. Ostash OP, Vasyliv BD, Podhurs'ka VY, et al (2011) Optimization of the properties of 10Sc1CeSZ–NiO composite by the redox treatment. *Mater Sci* 46(5):653–658. <https://doi.org/10.1007/s11003-011-9337-1>

Conductivity of Polymer Composites with Nanocarbon Filler



Iryna V. Ovsiienko , Lyudmila L. Vovchenko , Lyudmila Yu. Matzui ,
Tatiana L. Tsaregradskaya , Tetiana A. Len , Galyna V. Saenko ,
and Vladyslav M. Heraskevych

Abstract The results of resistivity investigations of polymer composites based on thermoexfoliated graphite and reinforced by carbon fibers with different polymers are presented. For preparation of composites, three polymers (polyvinyl acetate, phenol–formaldehyde resin, and silicon-organic binder) have been chosen. The concentration of nanocarbon filler ranged from 0.04 to 1 mass parts. The electrical resistance of obtained polymer-nanocarbon specimens perpendicular and parallel to the compression axis at room temperature and perpendicular to the compression axis in the temperature interval from 77 to 293 K has been measured by a four-probe compensation method. It is shown that resistivity concentration dependence has a percolation character both for specimens based on thermoexfoliated graphite and on the thermoexfoliated graphite and reinforced with carbon fiber. The type of polymer does not significantly affect the character of the concentration dependence of resistivity perpendicular to the compression axis. Differences in concentration dependences of anisotropy parameter for polymer composites with different polymers are revealed. It was found that the main factor that determines the value of electrical resistivity in polymer composites with carbon filler is the content of carbon filler in these composites.

Keywords Thermoexfoliated graphite · Polymer composite · Concentration · Carbon fiber · Electrical resistance · Anisotropy

1 Introduction

The use of different types of polymer matrices at the creation of composite materials makes it possible to significantly expand the temperature range of use of these materials in different operating conditions and to obtain materials with a wide range of

I. V. Ovsiienko (✉) · L. L. Vovchenko · L. Yu. Matzui · T. L. Tsaregradskaya · T. A. Len · G. V. Saenko · V. M. Heraskevych
Department of Physics, Taras Shevchenko National University of Kyiv, Volodymyrska 64/13, Kyiv 01601, Ukraine
e-mail: okalenyk@ukr.net

physical and chemical characteristics. One of the most common organic substances used to make polymer composites is polyvinyl acetate and phenol–formaldehyde resin [1, 2]. The use of these polymers in the creation of composites based on TEG makes it possible to obtain polymer composites with electrophysical, thermal, and mechanical properties, which can be changed in a fairly wide range by varying the type and concentration of organic binder [3–6]. It was found that compositions with polyvinyl acetate are stable up to 120 °C, and composites with phenol–formaldehyde resin are stable up to a higher temperature of 200 °C [7, 8]. Therefore, by changing the type of organic binder, it is possible to significantly expand the interval of thermal stability of composites. In [9], the effect of silicon-organic binder on the electrical, thermal, and mechanical properties of composite materials based on TEG with organic fillers has been studied. In work, it is shown that choice of silicon-organic binder as an organic filler makes it possible to expand the temperature range of use of composites based on TEG and organic binder up to 400 °C. At the same time, composites with silicon-organic binder in contrast to composites with phenol–formaldehyde resin have the worst mechanical characteristics: They are very plastic; after removal of mechanical stress, their form is not restored. There is no stabilization of mechanical characteristics of these polymer composites under cyclic loading. The properties of composites with silicon-organic binder deteriorate significantly with increasing temperature.

One of the promising materials that can be used as a filler in the composite material is thermally expanded graphite (TEG). Thermoexpanded graphite and composite materials based on it have an exceptional ability to compress without the use of additional binders and high temperatures.

Another promising direction is the creation of composite materials with carbon filler and reinforced with carbon and cellulose fibers or carbon nanotubes [10–12]. In [13], it is shown that the properties of composites reinforced with carbon fiber significantly depend on the interaction at the fiber-matrix boundary. The better the adhesion between the carbon fiber and the carbon filler and the more heat-resistant are fiber-reinforced composites. The correct choice of source components in the creation of polymer composites (fiber type, matrix), as well as the use of organic binder, makes it possible to significantly improve the mechanical properties of composites with carbon fiber. The addition of a small amount of carbon fiber (up to 10% of the mass) to the composites with phenol–formaldehyde resin significantly improves the mechanical properties of the composites. These composites are more elastic, and they have increased values of the ultimate mechanical load and elongation at which fracture begins. Such composites are thermally stable; their mechanical characteristics are rapidly stabilized under cyclic loading.

The aim of this work is to identify the effect of modification of TEG by organic substances on the electrophysical characteristics of polymer composites. For this purpose, measurements of electrical resistance at room temperature along the compression axis and perpendicular to the compression axis and temperature dependences of electrical resistance perpendicular to the compression axis have been performed, and the anisotropy parameter has been determined for composites with

different concentrations of polymers and reinforced and not reinforced with carbon fibers.

2 Experimental

2.1 Preparation of Polymer Composites Based on Thermoexfoliated Graphite

In the work, polymer composites based on thermoexfoliated graphite (TEG) with different polymers have been investigated. Also, fiber-reinforced polymer composites have been studied. The TEG has been produced by thermal shock from natural monocrystalline dispersive graphite (crystallite size $L \sim 1 \mu\text{m}$, interplanar spacing $d_{002} = 0.335 \text{ nm}$), which was pre-intercalated with sulfuric acid by the dichromatic method to the first stage [14]. Carbon non-graphitized polyacrylonitrile fiber (PAN fiber) has been used to reinforce the polymer composites. PAN fiber is an elongated filamentous structure with a diameter of $11 \mu\text{m}$. According to X-ray investigations, crystallite size L for TEG is $\sim 100 \text{ nm}$, and for PAN, fiber is $\sim 0.1 \text{ nm}$. Interplanar spacing d_{002} is 0.336 nm for TEG, and d_{002} is 0.341 nm for PAN fiber, correspondingly. The structure of TEG is described in detail in [15].

Three types of polymers have been used for making of composite specimens. These polymers are polyvinyl acetate (PVA), phenol–formaldehyde resin (PF), and silicon-organic binder (SOB). The properties of polymers are significantly different due to the different structure of complex polymer molecules. PVA is a rigid polymer with molecular formula $(\text{C}_4\text{H}_6\text{O}_2)_n$, whose molecules contain strongly polar groups $(\text{C}(\text{O})\text{CH}_3\text{—OH})$. PVA is an inert, non-toxic, and odorless polymer with a density of $(1180\text{—}1190) \text{ kg/m}^3$.

PF is a rubber-like polymer that is an oligomeric product of polycondensation of phenols with formaldehyde. During polycondensation of the resin, complex macromolecules are formed, which are oligomers of predominantly linear structure. PF is a solid brittle structure of yellow–brown color with a density of 1200 kg/m^3 and a molecular mass of $450\text{—}900$. PF is soluble in acetone, ethyl alcohol, and other polar solvents.

SOB is a solution of polymethylphenyl-siloxane resin in toluene obtained by hydrolytic condensation. The qualitative composition of the binder can be expressed by the formula: $\{[(\text{C}_6\text{H}_5)\text{SiO}_{1.5}][(\text{CH}_3)\text{SiO}]_{0.7}\}_n$. SOB is light yellow liquid, without mechanical inclusions with a density of 976 kg/m^3 .

The main stages of preparation of composites with different polymers are presented in Table 1.

Table 1 Main stages of preparation of composites with different polymers

Polymer	Main stages of preparation
PVA	<ol style="list-style-type: none"> 1. Preparation of a water solution of PVA (1:1) 2. Preparation of a suspension of TEG in a water solution of PVA 3. Primary drying at the temperature ~50–60 °C for 50 h 4. Final drying at 100–110 °C until complete evaporation of water 5. Pression of specimen at maximum load (10–100 MPa)
PF	<ol style="list-style-type: none"> 1. Preparation of a solution of PF in acetone in a ratio 1:1 or 1:3 2. Preparation of a suspension of TEG in solution of PF in acetone 3. Primary drying at the temperature ~20 °C for 50–75 h. with periodic stirring 4. Final drying at 100–110 °C until complete evaporation of acetone 5. Pressing of specimen at maximum load (10–100 MPa)
SOB	<ol style="list-style-type: none"> 1. Preparation of a solution of SOB in toluene in the ratio from 15:1 to 1:4 2. Preparation of a suspension of TEG in solution of SOB in toluene 3. Primary drying at the temperature ~20 °C for 100 h 4. Final drying at 200–250 °C until complete evaporation of toluene (~50 min.). 5. Pression of specimen at maximum load (10–100 MPa)

2.2 Parameters of Polymer Composites' Bulk Specimens

For investigations of resistivity, the bulk specimens of polymer composites with different mass concentration of nanocarbon filler have been prepared by cool pressing in rectangular mold and in round molds with a diameter of 10 and 13 mm. Bulk specimens of polymer composites reinforced with carbon fiber have been obtained in two types: with the fiber oriented along the mold, respectively, perpendicular to the compression axis, and with the non-oriented fiber.

The volume fraction of filler φ_v in the polymer composite has been calculated by the formula:

$$\varphi_v = \left(1 + \frac{C_p d_f}{C_f d_p} \right)^{-1}, \quad (1)$$

where C_p and C_f are the mass fractions of polymer and filler, respectively, and d_p and d_f their densities.

The porosity P of the obtained polymer composites specimens has been determined according to the formula:

$$P = 1 - \frac{d_{CM}}{d_{0CM}}, \quad (2)$$

where d_{CM} is the experimental density of obtained bulk specimen of polymer composite, d_{0CM} is the calculated density of ideal non-porous specimen of identical composition. This density can be calculated as

$$d_{0CM} = \frac{d_f d_p}{C_f d_p + C_p d_f}. \quad (3)$$

Table 2 presents the composition, experimentally determined, and calculated according to (1–3) parameters of bulk specimens of composites based on TEG with different polymers.

As it follows from the Table, there have been produced three series of specimens with different polymers. Each series contains two types of specimens with TEG as filler as well as with TEG, reinforced by CF. Moreover, carbon fiber-reinforced specimens with SOB polymer are of two types: with oriented and non-oriented fiber. As can be seen from the Table, an important feature of the obtained bulk polymer composites is the fact that at different concentrations of polymer in the specimens, the values of their densities and porosities are close.

For room temperature, measurements of electrical resistance ρ_c along compression axis specimens of cylindrical form with height $h = (5-10) \cdot 10^{-3}$ m and diameter $D = (1.0-1.4) \cdot 10^{-2}$ m have been pressed. To study the electrical resistance ρ_a perpendicular to the axis of compression, the specimens in the form of a rectangular parallelepiped have been cut from the cylindrical specimens. The electrical resistance perpendicular and parallel to the compression axis at room temperature has been measured by a four-probe compensation method. Resistivity has been calculated by formula:

$$\rho_{a,c} = \frac{RS}{l}, \quad R = R_{et} \frac{U_x}{U_{et}}, \quad (4)$$

where U_x is the voltage drop on the specimen, U_{et} is the voltage drop on the standard resistance, R_{et} is the reference resistance 0.01Ω , S is the cross-sectional area of the specimen, l is the specimen length. The resistivity measurement error did not exceed 0.5%.

The electrical resistance measuring method in the bulk pressed specimens of polymer composites is described in detail in [16].

3 Results and Discussion

3.1 Resistivity of Polymer Composites Based on Thermoexfoliated Graphite

Figure 1 presents the mass concentration dependences of resistivity perpendicular (ρ_a) and parallel (ρ_c) to the compression axis at room temperature for composites based on TEG with different polymers.

As can be seen from the Figure, all specimens TEG modified with organic substances in the range of the studied concentrations are conductors. The character

Table 2 Composition, mass (C_f), and volume (φ_V) fractions of TEG, porosity (P), experimental (d_{CM}), and calculated ideal (d_{0CM}) densities of composites based on TEG with different polymers

C_f , fr	φ_V , fr	d_{0CM} , kg/m ³	d_{CM} , kg/m ³	P
<i>TEG</i>				
1	1	2.24	1.44	0.357
<i>TEG + PVA</i>				
0.05	0.027	1.219	0.91	0.253
0.12	0.068	1.261	0.96	0.231
0.21	0.124	1.32	1.013	0.233
0.48	0.329	1.535	1.13	0.264
0.76	0.627	1.849	1.35	0.270
<i>TEG + CF (2.5% mass) + PVA</i>				
0.05	0.027	1.219	0.86	0.295
0.12	0.068	1.261	0.98	0.223
0.21	0.124	1.32	1.015	0.231
0.48	0.329	1.535	1.22	0.205
0.76	0.627	1.849	1.52	0.178
<i>TEG + PF</i>				
0.267	0.163	1.37	0.91	0.336
0.422	0.281	1.492	1.11	0.256
0.593	0.407	1.656	1.22	0.263
<i>TEG + CF (2.5% mass) + PF</i>				
0.267	0.163	1.37	0.97	0.292
0.422	0.281	1.492	1.15	0.229
0.593	0.407	1.656	1.16	0.299
<i>TEG + SOB</i>				
0.04	0.018	0.999	0.81	0.189
0.065	0.029	1.013	0.832	0.179
0.094	0.043	1.031	0.858	0.168
0.143	0.068	1.062	0.91	0.143
0.25	0.127	1.136	0.97	0.146
0.455	0.267	1.313	1.09	0.170
0.629	0.425	1.513	1.234	0.184
0.735	0.547	1.668	1.298	0.222
<i>TEG + CF non-orient. (10% mass) + SOB</i>				
0.143	0.068	1.062	0.89	0.162
0.455	0.267	1.313	1.103	0.16
0.735	0.547	1.668	1.43	0.143

(continued)

Table 2 (continued)

C_f , fr	φ_V , fr	d_{OCM} , kg/m ³	d_{CM} , kg/m ³	P
<i>TEG + CF orient. (10% mass) + SOB</i>				
0.143	0.068	1.062	0.91	0.143
0.455	0.267	1.313	1.113	0.152
0.735	0.547	1.668	1.49	0.107

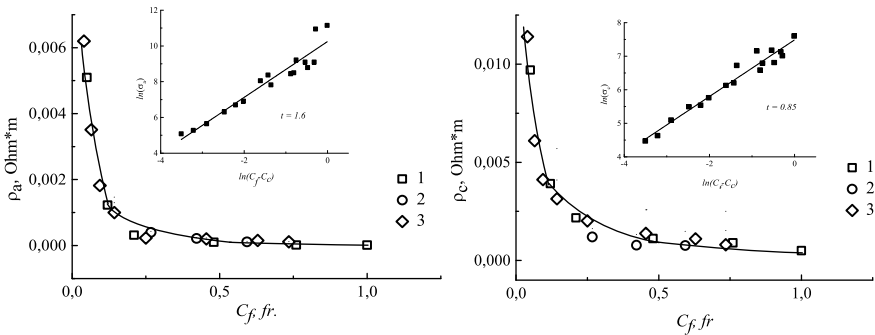


Fig. 1 Dependences of resistivity ρ_a perpendicular to the compression axis (a) and resistivity ρ_c parallel to the compression axis (b) on mass fraction of filler C_f at room temperature for composites based on TEG with different polymers: 1—TEG + PVA, 2—TEG + PF, 3—TEG + SOB. Insets: dependences $\ln(\sigma_a) = f(\ln(C_f - C_c))$ (a) $\ln(\sigma_c) = f(\ln(C_f - C_c))$ (b)

of mass concentration dependences of resistivity perpendicular and parallel to the compression axis at room temperature is similar. Resistivity decreases sharply (up to 6 times) with increasing mass fraction of TEG in the composite to ~0.15. With a further increase in the mass concentration of TEG in composites, the resistivity continues to decrease for both ρ_a and ρ_c . But the resistivity dependence on temperature is very weak at when the mass fraction of filler is more than 0.5.

As it is followed from figure, the percolation dependence of resistivity on TEG mass concentration is observed, and the type of polymer does not significantly affect the value of resistivity. For all specimens of polymer composites, regardless of the type of polymer, the electrical conductivity both in the direction perpendicular and parallel to the compression axis is described by the dependence of the type:

$$\sigma(C) = \sigma_0(C_f - C_c)^{-t}, \tag{5}$$

where σ_0 is the electrical conductivity of filler, C_f and C_c are the arbitrary and critical, i.e., at which there is a sharp increase in electrical conductivity, filler’s concentrations, $\sigma(C)$ is conductivity at arbitrary filler mass concentration, t is the critical index.

The dependences $\ln(\sigma_a) = f(\ln(C_f - C_c))$ and $\ln(\sigma_c) = f(\ln(C_f - C_c))$ are presented in the Fig. 1 (insets). As follows from figures, both dependences are close to linear. The value of the critical indices t equals to 1.6 for conductivity perpendicular

to the compression axis, and t is 0.85 for conductivity parallel to the compression axis.

3.2 Resistivity of Polymer Composites Based on Thermoexfoliated Graphite and Reinforced by Carbon Fibers

Figure 2 presents the experimental dependences of resistivity perpendicular (a) and parallel (b) to the compression axis on mass concentration of filler for polymer composites based on TEG and reinforced by carbon fiber. The mass concentration of the filler takes into account both TEG and carbon fiber.

As can be seen from the figure, in the dependences of resistivity on mass concentration of filler for polymer composites reinforced with carbon fibers, there are a number of significant differences compared to similar composites not reinforced with carbon fiber. In concentration dependence of resistivity $\rho_a(C_f)$, as well as for non-reinforced composites, the influence of the type of polymer on the character of dependence $\rho_a(C_f)$ is practically absent. However, the decrease in resistivity ρ_a with increasing filler content is slower. The range of filler concentrations for which there is a pronounced decrease in the value of resistivity ρ_a is greater. The calculated value of the critical index t is 1.5 for these polymer composites (inset, Fig. 2a).

As it is followed from Fig. 2b, the dependence $\rho_c(C_f)$ has the form of atypical for the dependences of polymer composite resistivity on the content of conductive filler. For specimens of fiber-reinforced composites with the lowest content of filler at which the study was conducted, the resistivity is almost twice less than for similar non-reinforced specimens. But with increasing filler content, the reduction in resistivity

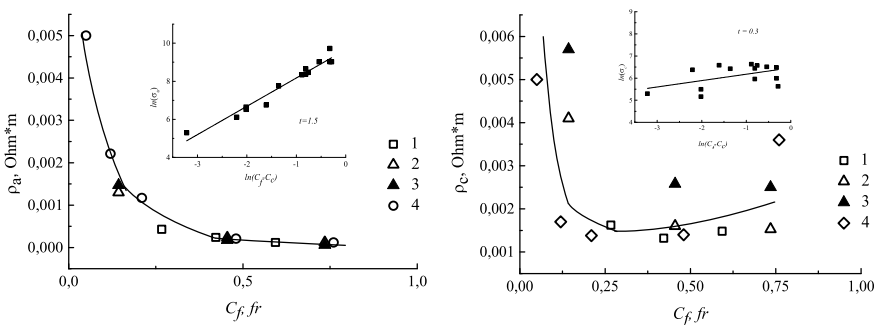


Fig. 2 Dependences of resistivity ρ_a perpendicular to the compression axis (a) and resistivity ρ_c parallel to the compression axis (b) on mass fraction of filler C_f for polymer composites based on TEG reinforced by carbon fibers: 1—TEG + CF + PF, 2—TEG + CFno + SOB, 3—TEG + CFo + SOB, 4—TEG + CF + PVA. Insets: dependences $\ln(\sigma_a) = f(\ln(C_f - C_c))$ (a) $\ln(\sigma_c) = f(\ln(C_f - C_c))$ (b)

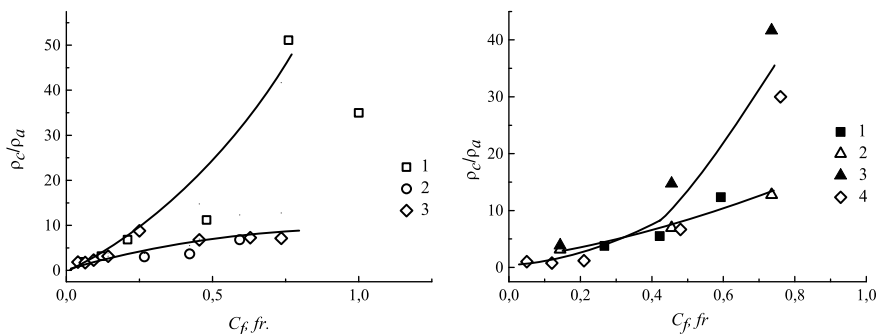


Fig. 3 Dependence $\rho_c/\rho_a(C_f)$ for polymer composites based on TEG (a) with PVA (1), PF (2), SOB (3) and for polymer composites based on TEG and reinforced by carbon fibers (b) with PF (1), SOB, CF is not oriented (2) and oriented (3), PVA (4)

ρ_c is not as significant as for non-reinforced specimens. In addition, as can be seen from the Figs. 1 and 2, the dependence $\rho_c(C_f)$ is the only one where the value of the resistivity increases with increasing filler content. Moreover, an increase in the value of resistivity ρ_c is observed both for specimens of polymer composites with oriented fibers and for specimens with fibers oriented in an arbitrary manner, as well as for specimens with non-oriented fibers based on PVA.

Thus, in contrast to the specimens of polymer composites based on TEG and not reinforced with carbon fibers for reinforced specimens, both the types of polymer and the orientation of the carbon fibers in the composite affect on the character of the concentration dependence of resistivity parallel to the compression axis. The value of the critical index t determined from the dependence $\ln(\sigma_c) = f(\ln(C_f - C_c))$ is 0.3 (insert).

Figure 3 presents the mass concentration dependences of anisotropy parameter ρ_c/ρ_a for both types of polymer composites with TEG and with TEG reinforced by carbon fibers.

As it is seen from figures, anisotropy parameters ρ_c/ρ_a increase for both types of polymer composites. For specimens of polymer composites based on TEG with PF and SOB, anisotropy parameters increase gradually, and the maximal value of ρ_c/ρ_a equals to ~ 7 . Exceptions are polymer composites with PVA. For such composite at a filler content of 0.76, the value of the anisotropy parameter reaches 50. For pure pressed TEG, this parameter decreases to 35. The similar situation is observed for polymer composites reinforced by carbon fibers. For reinforced by randomly-oriented carbon fibers composites with PF and SOB, anisotropy parameter is slightly larger ~ 13 . And if for composites with oriented fibers, a large value of the anisotropy parameter is expected, then for composites with non-oriented carbon fibers based on PVA, the sharply increasing dependence $\rho_c/\rho_a(C_f)$ is unusual. But this dependence $\rho_c/\rho_a(C_f)$ correlates with analogous dependence for polymer composite with PVA based only on TEG.

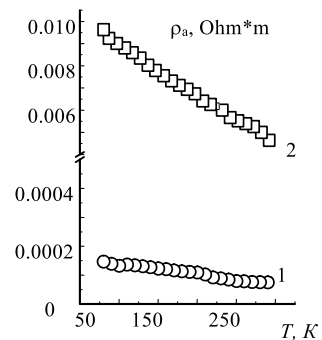
Thus, for polymer composites with PVA independently on presents of carbon fibers, resistivity perpendicular and parallel to the compression axis is essentially differ.

3.3 Temperature Dependence of Resistivity

The measurements of temperature dependence of resistivity ρ_a perpendicular to pressing axis in the temperature interval from 77 K up to 293 K have been carried out for bulk specimens of polymer composites based on TEG with SOB. The Fig. 4 presents the results of these investigations: dependences $\rho_a(T)$ for specimens with mass content of TEG 0.25 and 0.04.

As can be seen from the figure with increasing temperature, the electrical resistance of polymer composites decreases regardless of the concentration of TEG in composite. This dependence is typical for graphite materials with an imperfect structure. The ratio ρ_{a77}/ρ_{a293} for composite with TEGs mass content 0.04 is 2.16, and for composite with TEGs, mass content 0.25 is 1.89, respectively. These values ρ_{a77}/ρ_{a293} are higher than for a pure compacted TEG, for which this ratio is ~ 1.5 . Thus, the character of the temperature dependence of the electrical resistance $\rho_a(T)$ for polymer composites with a concentration of TEG above the flow threshold, i.e., when an infinite cluster of TEG particles has formed in composite, is determined by the character of the temperature dependence of resistivity in pure TEG. With increasing concentration of TEG in polymer composite, the course of resistivity temperature dependence for composite approaches the course of resistivity temperature dependence for pure bulk TEG. If the concentration of TEG in polymer composite is less than the threshold concentration, then a significant contribution to the mechanisms of the temperature dependence of the electrical resistance is made by the processes associated with changes in the contacts region of individual particles of TEG.

Fig. 4 Temperature dependence of resistivity ρ_a perpendicular to pressing axis for polymer composites with SOB and TEG. The mass content of TEG is 0.25 (1) and 0.04 (2)



3.4 Discussion

Analysis of the data of dependence of electrical resistance both parallel and perpendicular to the axis of compression on the content of TEG in polymer composites and comparison of these data with data on electrical resistance in non-polymer composites based on modified by metal TEG [16] allow to conclude about the differences in the factors that determine the nature of the electrical resistance in composites with organic and inorganic modifiers.

In non-polymeric composites based on metal-modified TEG, the main parameter that determines the value of resistivity is the density, or in other words, the porosity of the composite, and other parameters, in particular, the concentration of the modifier, have less effect on the resistivity.

TEG, modified by metals, can be considered as shown in [16] as a graphite matrix, which contains metal particles. The concentration of metal up to 50% by mass, which corresponds to ~17% atomic, is small to create a continuous cluster of metal particles required to significantly reduce the electrical resistance. The electrical resistance of the system TEG and metal is determined by the sum of two contributions: the electrical resistance of the metal particles and the TEG particles and the contact electrical resistance between the metal particles and the TEG particles. The contact resistance between the TEG particles due to the peculiarities of the particles surface morphology is negligible. If the introduction of metal particles into the graphite matrix leads to only a slight decrease in the total electrical resistance, the contact resistance, which depends on the pressure on the contact area between the particles, i.e., determined by the density of the material, can change the total system's resistance in great interval. At low density of composite, the contact resistance is high, which results into a significant increase in the total resistance of the composite. With increasing density of the material, the contact resistance decreases, which leads to a decrease in the electrical resistance of the composite as a whole. The decrease in resistance with increasing density of the composite is almost the same for all types and concentrations of the metal-modifier.

In contrast, in polymer composites based on TEG, the main parameter that determines the value of resistivity is the mass (or volume) fraction of TEG in the composite. If the concentration C_f of TEG is greater than the critical concentration C_c , then the system TEG—polymer is an infinite cluster of TEGs particles with blocked nodes of the polymer modifier. With a further increase in the mass fraction of TEG, the number of “dead ends” in an infinite cluster of TEG decreases, which leads to a slight decrease in electrical resistance. In this case, the material of the polymer, as in the case of modification of TEG by metals, is not significant.

It should be noted that when modifying TRG with organic substances, the contact resistance between the particles of TRG and the polymer also contributes to the total electrical resistance. However, since its value in the studied specimens of polymer composites is close to the value of the resistance of TEG particles, in contrast to composites TEG with metal, in these composites, the density does not have a significant effect on the value of electrical resistance.

Let us consider the features of structure change of based on TEG composites in the pressing process. The bulk pressed TEG with a density (0.2–0.3) g/cm³ is completely isotropic materials with a chaotic arrangement of TEGs particles. As the compression pressure increases, the TEGs particles are oriented in the same way, and a layered structure with the orientation of the layers perpendicular to the axis of compression begins to form. This results into significant decrease in the electrical resistance perpendicular to the axis of compression and an increase in electrical resistance along the axis of compression. This process occurs for pressed specimens with a density up to (0.7–0.8) g/cm³. With further increase in density of the pressed specimens, the electrical resistance ρ_a continues to slowly decrease, and ρ_c increases slightly, which is due to the formation of a more ordered layered structure. The fact that in pressed specimen with density of ~0.8 g/cm³, a layered structure is formed is also evidenced by the value of the anisotropy parameter ρ_c/ρ_a —22 given in [16], which increases only slightly with increasing specimens density to 1.33 g/cm³.

It is in this interval of polymer composites densities that electrical resistance studies have been conducted in the presented work. Obtaining of polymer composites specimens by pressing has its own peculiarities. Modification of TEG with polymer binders leads to the fact that the formation of a layered structure in bulk specimens with increasing compression pressure is significantly slowed down. That is, with increasing pressure during the process of compaction of polymer composite with a given content of filler, it is impossible to obtain a bulk specimen with a higher density or with a greater layered ordering. This is reflected in the values of electrical resistance and anisotropy parameter. According to Fig. 3, only for PVA at a high content of TEG in specimen formation of a layered structure occurs. The value of the anisotropy parameter ρ_c/ρ_a for composite with PVA at the mass content of TEG ~0.75 even exceeds the value of this parameter for pure TRG. For reinforced with carbon fiber specimens of polymer composites, the increase of pressure in compacting process causes the fibers to be oriented so that the fibers axis is perpendicular to the compression axis. In this case, some disorientation of the fibers in the plane perpendicular to the axis of compression will be maintained. That is why the value of anisotropy parameter for specimens of polymer composites reinforced of randomly placed carbon fibers does not reach large values (~12). Exceptions as for the case of polymer composites with TEG are composites with PVA. For them, the value of the anisotropy parameter reaches 30. If the specimens of polymer composites were initially reinforced with oriented fiber, then for them, a significantly larger difference between the values of resistance perpendicular and parallel to the compression axis is observed.

4 Conclusion

Thus, the carried out investigations of electrical resistance in bulk specimens of polymer composites based on TEG have shown that all pressed specimens of polymer composites based of TEG and TEG with carbon fiber with a content of filler mass

fraction from 0.04 to 0.76 are conductors regardless of which polymer was used for their preparation. The resistivity concentration dependence has a percolation character both for specimens on the basis of TEG and on the basis of TEG and reinforced with carbon fiber. The type of polymer also does not significantly affect the course of the concentration dependence of resistivity perpendicular to the compression axis. The concentration dependence of resistivity parallel to the axis of pressing is more sensitive to the polymer material. This causes different concentration dependences of the anisotropy parameter ρ_c/ρ_a for composites with different polymers. For polymer composites with phenol-formaldehyde resin and silicon-organic binder, anisotropy parameter ρ_c/ρ_a is ~ 10 , that is, three times less than in pure TEG of similar density. For polymer composites based on polyvinyl acetate with mass contents of TEG ~ 0.75 , the anisotropy parameter ρ_c/ρ_a reaches 50, which is close to the anisotropy parameter value in pure pressed TEG.

The main factor that determines the value of electrical resistivity in polymer composites with carbon filler is the content of carbon filler in these composites. This situation is different from that observed in TEG-metal systems, where the main parameter determining electrical resistivity is the density or porosity of the composite.

The character of temperature dependence of resistivity in polymer composites based on TEG is determined mainly by the mechanisms of temperature dependence in TEG. The greater is the concentration of modifier the more similar are the temperature dependences of resistivities in polymer composites based on TEG and pure pressed TEG.

References

1. Santi R, Cigada A, Del Curto B, Farè S (2019) *J Appl Biomat Fund Mat* 17(1):1–7. <https://doi.org/10.1177/2280800019831224>
2. Frollini E, Castellan A (2012) *Wiley encyclopedia of composites*. <https://doi.org/10.1002/9781118097298.weoc167>
3. Li C, Hou T, She X, Wei X, She F, Gao W, Kong L (2015) *Polymer degradation and stability* 119:178–189. <https://doi.org/10.1016/j.polymdegradstab.2015.05.0>
4. Hossain J, Alam MS, Paul SC, Islam S (2018) *Industrial Chem* 4(1). <https://doi.org/10.4172/2469-9764.1000127>
5. S. Stawarz , M. Stawarz, W. Kucharczyk , W. Żurowski, A. Różycka. (2019). *Adv Sci Tech Res J* 13(4):223–229. <https://doi.org/10.12913/22998624/113089>
6. Kaith BS, Chauhan A (2008) *E-J Chem* 5(s1):1015–1020. <https://doi.org/10.1155/2008/328426>
7. Yan D, Li X, Jiang Y, Zhang H-B, Jia B-B, Ma H-L, Yu Z-Z (2014) *Materials Lett* 118:212–216. <https://doi.org/10.1016/j.matlet.2013.12.080>
8. Salh S, Raswl DA (2018) *Open access J Phys* 2(2):5–10
9. da Rocha RM, Cairo C, Mario LA (2006) *Materials science and engineering A* 437(2):268–273. <https://doi.org/10.1016/j.msea.2006.08.102>
10. Hajeeassa KS, Hussein MA, Anwar Y, Tashkandi NY, Al-amshany Z (2018) *Nanobiomedicine* 5: 1–12. <https://doi.org/10.1177/1849543518794818>
11. Athijayamani A, Chrispin Das M, Sekar S, Ramanathan K (2017). *BioRes* 12(1):1960–1967
12. Igarashi A, Terasawa T, Kanie M, Yamanobe T, Komoto T (2005) *A morphological. Comp Polym J* 37:522–528. <https://doi.org/10.1295/polymj.37.522>

13. Pattanashetty BB, Bheemappa S, Rajashekaraiiah H (2017) *Int J Eng Tech* 13: 24–38. <https://doi.org/10.18052/www.scipress.com/IJET.13.24>
14. Matzui L, Ovsiienko I, Vovchenko L, Brusilovets A, Tsurul M (2001) *Functional Mat* 8(2):345–350 (in Ukraine)
15. Perets YS, Ovsiienko IV, Vovchenko LL, Yu L, Matzui OA, Brusilovetz, Pundyk IP (2012) *Ukr J Phys* 57(2):219–223
16. Ovsiienko IV, Vovchenko LI, Yu L, Matzui TI, Tsaregradskaya G, Saenko V, Marinin OD, Len TA (2020) *Nanomaterials and nanocomposites, nanostructure surfaces, and their applications*. Springer Proc Phys 263:179–191. https://doi.org/10.1007/978-3-030-74741-1_12

Properties of Spectral Parameters of Multicascade Nanostructure Being a Model of Quantum Cascade Detector



J. Seti , E. Vereshko , O. Voitsekhivska , and M. Tkach 

Abstract Within the approximation of effective mass and model of rectangular potential barriers, the theory of electron states in a multicascade nanostructure of closed type and, for comparison, in a structure with a periodic potential of the Kronig-Penny type is developed. The properties of spectral parameters, wave functions, and probabilities of an electron location in different cascades are studied for the both models. It is shown that, in contrast to the Kronig-Penny model, the properties of electron states in closed single- and multicascade structures differ significantly.

Keywords Electron · Spectrum · Quantum cascade detector

1 Introduction

The rapid development of nanotechnology has significantly intensified the study of nanostructures, in general, and multilayer structural nanoelements of the modern devices, such as quantum cascade lasers (QCLs) and quantum cascade detectors (QCDs) [1–4], in particular. QCL and QCD are unipolar devices, and the design of the band structure of which is selected in such a way that the transitions between electronic levels of dimensional quantization are accompanied by radiation or detection of electromagnetic waves. The range of operating wavelengths of these devices is determined by the depths of quantum wells in their cascades and covers the actual infrared (IR) region.

The first QCL [5] which operated in the middle IR range was produced in 1994 by a scientific group led by Capasso. Since then, a phase of intensive QCL research has begun, which has resulted in lasers [6–10] functioning in middle- and far-IR range being based at different heterojunctions of semiconductor materials (InGaAs/InAlAs, GaAs/AlGaAs, InGaAs/AlAs, InGaAs/AlSb, and others).

J. Seti (✉) · E. Vereshko · O. Voitsekhivska · M. Tkach
Department of Theoretical Physics and Computer Simulation, Yuriy Fedkovych Chernivtsi National University, 2, Kotsyubinsky Str., Chernivtsi 58012, Ukraine
e-mail: j.seti@chnu.edu.ua

Later, in 2004, the QCD [11], which combined the ideas of the operation of quantum well IR photodetectors [12, 13] and QCL [5], was created for the first time. The first and many modern QCDs [14–17] are based at the structures GaAs/AlGaAs, InGaAs/AlInAs, and others, with small depths of quantum wells, which limit their operation interval to medium- and far-IR. One of the approaches to reach the wavelengths of near-IR range is to use the materials with a wider band gap and respectively, deeper potential wells as the structural elements of QCD. For example: GaN/AlGaIn, GaN/InGaIn [18–22], InGaAs/AlAsSb [23], ZnCdSe/ZnCdMgSe [24], ZnO/ZnMgO [25].

A wide range of operating wavelengths (from IR to terahertz) and temperatures (from cryogenic to room), small dark currents, high-speed efficiency, and other important characteristics make QCD and QCL very perspective for practical applications [22, 26]. This explains the permanent efforts of researchers, applied for the improvement of operating parameters of such nanodevices for more than 20 years.

It is well known that typical structural elements of QCD and QCL consist of several dozens (10–50) of the same cascades. Their identity is ensured by precise technologies of molecular beam epitaxy or organometallic vapor-phase epitaxy, which makes their production and research both complicated and expensive. Therefore, for the purposeful improvement of their characteristics, a consistent theory of physical processes in the structural elements is needed. Such theory, unfortunately, is far from complete.

In the majority of theoretical papers, assuming the properties of electron states in all cascades as the same, a simplified model of a separate region of a cascade (active region, extractor, injector), single- or double-cascade structure [27–36] is often used. In such model, the energy spectra of quasiparticles, the intensities of photon- and phonon-accompanied quantum transitions, the influence of dissipative subsystems (phonons, impurities, imperfect heterointerfaces), electric and magnetic fields, etc., were studied by various theoretical methods. The results obtained in these papers allow us to understand the basic physical processes in multilayer nanostructures of separate cascades or their components. However, according to the principles of quantum mechanics, these results cannot be generalized for the case of many interacting cascades, which are the elements of real QCD.

In the proposed paper, we develop the theory and investigate the properties of electron states in multicascade nanostructures with potential profile of closed-type and Kronig-Penny potential. The expediency of studying the closed model is due to its compliance with multicascade structural elements of experimental QCDs, and the Kronig-Penny model is unique as a limit case of the structure with an infinite number of cascades.

2 Theory of Electron States in a Multicascade Nanostructure in a Closed and Kronig-Penny Models

A multilayer nanostructure consisting of N identical three-well cascades (Fig. 1), being the model of a typical structural element of QCD, is considered. The properties of such an N -cascade structure are studied in two models: the closed-type model [32, 36], in which the multilayer structure is placed into a bulk medium-barrier (C -model) and in the model with Kronig-Penny-type potential [37, 38], which satisfies the known conditions of the Born-Karman periodicity (KP-model). Under such conditions, considering the insignificant difference between the values of lattice constants in wells and barriers, the electron states in both models for nanostructures are obtained in the approximation of the effective mass and rectangular potential profiles. Next, we present the main stages of the solution of the formulated problem simultaneously in both models, logically using the indices C and KP.

In a Cartesian coordinate system with z -axis perpendicular to the planes of nanostructure interfaces, the effective mass and potential energy of an electron in C - and KP-models are periodic functions of z -coordinate with a period equal to the length (d) of a separate cascade:

$$m_{C,KP}(z) = \begin{cases} m_b, & U_{C,KP}(z) = \begin{cases} U, & z_{i,j-1} < z < z_{i,j}, j = \begin{cases} j = 2, 4, 6 \\ j = 1, 3, 5 \end{cases} \\ 0, & \end{cases} \end{cases} \quad i = 1, 2, \dots, N. \quad (1)$$

Here, i is the number of cascade, j is the number of the layer in i -th cascade, $z_{i,j} = z_{1,j} + (i - 1)d$ are the coordinates of the heterointerfaces in i -th cascade, $d = z_{1,6}$ is the length of separate cascade, N is the number of cascades, U is the height of potential barriers, m_w, m_b and E_{gw}, E_{gb} are the effective masses and energy gaps in the respective bulk crystals.

In C -model, in external semi-infinite media, the effective mass and potential energy are determined by the respective physical parameters of the barrier $m_C(z < 0) = m_C(z > z_{N,6}) = m_b, U_C(z < 0) = U_C(z > z_{N,6}) = U$. In the infinite KP-model,

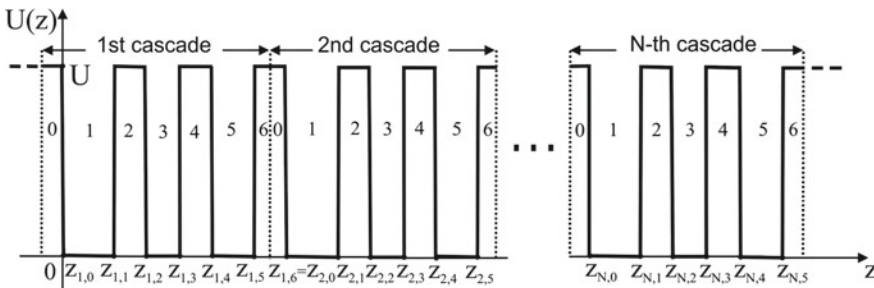


Fig. 1 Potential profile of N -cascade nanostructure. The dashed lines indicate the potential of the external semi-infinite barrier-medium in C -model

they satisfy additional periodicity conditions: $m_{\text{KP}}(z + L) = m_{\text{KP}}(z)$, $U_{\text{KP}}(z + L) = U_{\text{KP}}(z)$ (with the period $L = Nd$ equal to the size of the N-cascade structure).

Assuming the electron movement as one-dimensional, its wave functions and energy spectrum are determined by the solutions of Schrödinger equation

$$H_{C,\text{KP}}\Psi^{C,\text{KP}}(z) = E\Psi^{C,\text{KP}}(z) \quad (2)$$

with Hamiltonian

$$H_{C,\text{KP}} = -\frac{\hbar^2}{2} \frac{d}{dz} \frac{1}{m_{C,\text{KP}}(z)} \frac{d}{dz} + U_{C,\text{KP}}(z). \quad (3)$$

Equations (2) have the exact solutions, written in a compact form

$$\Psi^{C,\text{KP}}(z) = \begin{cases} A_0^C e^{\chi z} + B_0^C e^{-\chi z}, & z < 0 \\ A_{i,j}^{C,\text{KP}} e^{\chi(z-z_{i,j})} + B_{i,j}^{C,\text{KP}} e^{-\chi(z-z_{i,j})}, & j = 2, 4, 6, \quad z_{i,j-1} < z < z_{i,j} \\ A_{i,j}^{C,\text{KP}} \cos(k(z-z_{i,j})) + B_{i,j}^{C,\text{KP}} \sin(k(z-z_{i,j})), & z_{i,j-1} < z < z_{i,j}, \quad j = 1, 3, 5 \\ A_{N+1}^C e^{\chi(z-L)} + B_{N+1}^C e^{-\chi(z-L)}, & z > L \end{cases} \quad (4)$$

where

$$k = \sqrt{\frac{2m_w E}{\hbar^2}}; \quad \chi = \sqrt{\frac{2m_b(U-E)}{\hbar^2}}; \quad i = 1, 2, \dots, N$$

According to quantum mechanics [37, 38], the conditions of continuity of wave functions and their densities of probability currents

$$\begin{cases} \Psi^{C,\text{KP}}(z_{i,j} - 0) = \Psi^{C,\text{KP}}(z_{i,j} + 0), \quad i = 1, \dots, N, \quad j = 1, \dots, 6 \\ \left. \frac{1}{m_{C,\text{KP}}(z)} \frac{d\Psi^{C,\text{KP}}(z)}{dz} \right|_{z=z_{i,j}-0} = \left. \frac{1}{m_{C,\text{KP}}(z)} \frac{d\Psi^{C,\text{KP}}(z)}{dz} \right|_{z=z_{i,j}+0} \end{cases} \quad (5)$$

should be fulfilled at all heterointerfaces of the structure together with the normality condition for the wave functions in C- and KP-models, respectively

$$\int_{-\infty}^{\infty} |\Psi_n^C(z)|^2 dz = 1, \quad (6)$$

$$\int_0^L |\Psi_n^{KP}(z)|^2 dz = 1 \quad (7)$$

According to the physical considerations in C -structure, the wave functions at $z \rightarrow \pm\infty$ are finite that uniquely fixes two coefficients $B_0^C = A_{N+1}^C = 0$. Then, from fitting conditions (5), we get a system of $2(6N + 1)$ linear equations with respect to A_0^C , B_{N+1}^C , $A_{i,j}^C$, and $B_{i,j}^C$ ($i = 1, \dots, N; j = 1, \dots, 6$), from which, together with the normality condition (6), all coefficients for the wave functions are obtained. Using the same system of linear homogeneous equations, provided that its determinant is equal to zero, a dispersion equation for the electron energy E_n^C ($n = 1, 2, \dots$) is found.

In KP- model, taking into account the Born-Karman condition with the period $L = Nd$

$$\Psi^{\text{KP}}(z + L) = \Psi^{\text{KP}}(z) \quad (8)$$

and using the Bloch's theorem, the wave function is written in the form

$$\Psi^{\text{KP}}(z + d) = e^{iKd} \Psi^{\text{KP}}(z), \quad K = \frac{2\pi}{L}g, \quad g = 0, 1, \dots, N - 1. \quad (9)$$

Taking into account (9), the fitting conditions (5) are written only for the functions of an arbitrary i -th cascade, from which a system of 12 linear equations is obtained. In its turn, it gives the dispersion equations for electron energies E_n^{KP} ($n = 1, 2, \dots$). From the same system of equations, together with the normality condition (7), all coefficients $A_{i,j}^{\text{KP}}$, $B_{i,j}^{\text{KP}}$ ($i = 1, \dots, N; j = 1, \dots, 6$) and the wave functions in KP- model are obtained.

3 Properties of Electron States in Multicascade Nanostructure in C - and KP-Models

The theory developed in the previous section allows us to investigate the properties of spectral parameters in multicascade C - and KP-structure. These models are studied based on a three-well cascade with GaAs wells and $\text{Al}_{0.33}\text{Ga}_{0.67}\text{As}$ barriers with physical parameters: $m_w = 0.067 m_e$, $m_b = 0.095 m_e$, $U = 276$ meV. The geometrical sizes of potential wells ($a_1 = 6.8$ nm, $a_2 = 2.4$ nm, $a_3 = 3.7$ nm) and barriers ($b_1 = b_2 = b_3 = 3$ nm) of the separate cascade are chosen such that the electron energy levels satisfactorily simulate a typical energy scheme of experimental QCD [3] cascade with two operating levels. Transitions between these levels are accompanied by absorption of electromagnetic wave. The levels of such "phonon ladder" provide relaxation of electron energy during phonon-assisted tunneling between neighbor cascades of the structure.

As a result, the calculations show that in the separate three-well cascade of C - and KP-structure, there are four electron states with the following energies:

$$E_{n=1}^C = 53.2 \text{ meV}, E_{n=2}^C = 106.2 \text{ meV}, E_{n=3}^C = 159.8 \text{ meV}, E_{n=4}^C = 212.0 \text{ meV};$$

$$E_{n=1}^{KP} = 52.8 \text{ meV}, E_{n=1}^{KP} = 107.1 \text{ meV}, E_{n=1}^{KP} = 157.8 \text{ meV}, E_{n=1}^{KP} = 218.9 \text{ meV}.$$

The energy values of E_n^C and E_n^{KP} differ by no more than 1% for $n = 1, 2, 3$ and 3% for $n = 4$.

Figure 2 shows the distributions of probability densities ($|\tilde{\Psi}_n^{KP}|^2$, $|\tilde{\Psi}_n^C|^2$) of the electron in separate cascade and its energies in the respective states. For clarity, the starting points of $|\tilde{\Psi}_n^{KP}|^2$ and $|\tilde{\Psi}_n^C|^2$ are shifted to the positions of the corresponding energy levels. Figure proves that in such scale, the difference between $|\tilde{\Psi}_n^{KP}|^2$ and $|\tilde{\Psi}_n^C|^2$ is almost not visible. In both models, the electron in the ground state ($n = 1$) and highest excited state ($n = 4$) is located in the first (active) potential well. The strong overlap of the wave functions of these states provides an intensive quantum transition between them, accompanied by the absorption of electromagnetic field in IR range ($E_{n=4}^{C,KP} - E_{n=1}^{C,KP}$). In the excited states $n = 2$ and $n = 3$, the electron is localized in the third and second potential wells of the extractor, respectively. These states simulate a “phonon ladder” along which the electron performs the radiation-free quantum transitions accompanied by the creation of optical phonons and tunnels between the active regions of multicascade structure.

Now let us study the behavior of electron states in the structures with many cascades. In Fig. 3, the energy spectrum as function of number (N) of cascades is shown. It is clear that increasing N in both models leads to the formation of quasidiscrete bands in the vicinity of the energies (E_n^{KP} , E_n^C , $n = 1, 2, 3, 4$) of the corresponding single-cascade structure. Thus, for the convenience of further analysis, we use double energy numbering: E_{ns}^{KP} , E_{ns}^C , where n index indicates the number of the band, and s index is the number of the level in the n -th band. At $N = 1$, each band degenerates into the energy level of the single-cascade structure $E_{n,s=1}^{KP} \equiv E_n^{KP}$, $E_{n,s=1}^C \equiv E_n^C$, $n = 1, 2, 3, 4$.

Also, Fig. 3 proves that in both models, the number of levels (p_n^{KP} , p_n^C) in all energy bands of N -cascade structure is the same: $p_1^{KP} = p_2^{KP} = p_3^{KP} = p_4^{KP}$, $p_1^C = p_2^C = p_3^C = p_4^C$. In C -model, the values p_n^C are equal to the number of

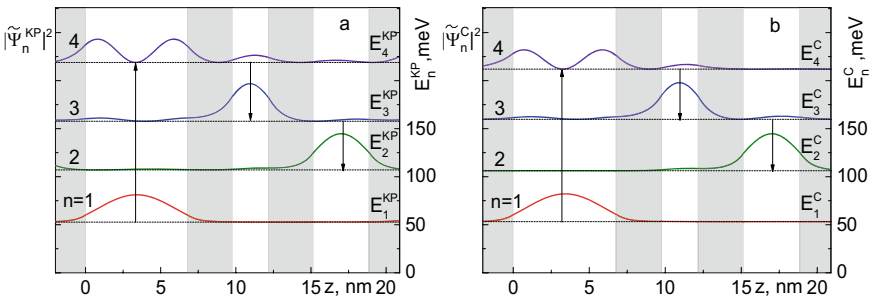


Fig. 2 Distributions of probability densities ($|\tilde{\Psi}_n^{KP}|^2$, $|\tilde{\Psi}_n^C|^2$) and energies (E_n^{KP} , E_n^C) of electron states ($n = 1, 2, 3, 4$) in three-well cascade in KP- (a) and C-model (b)

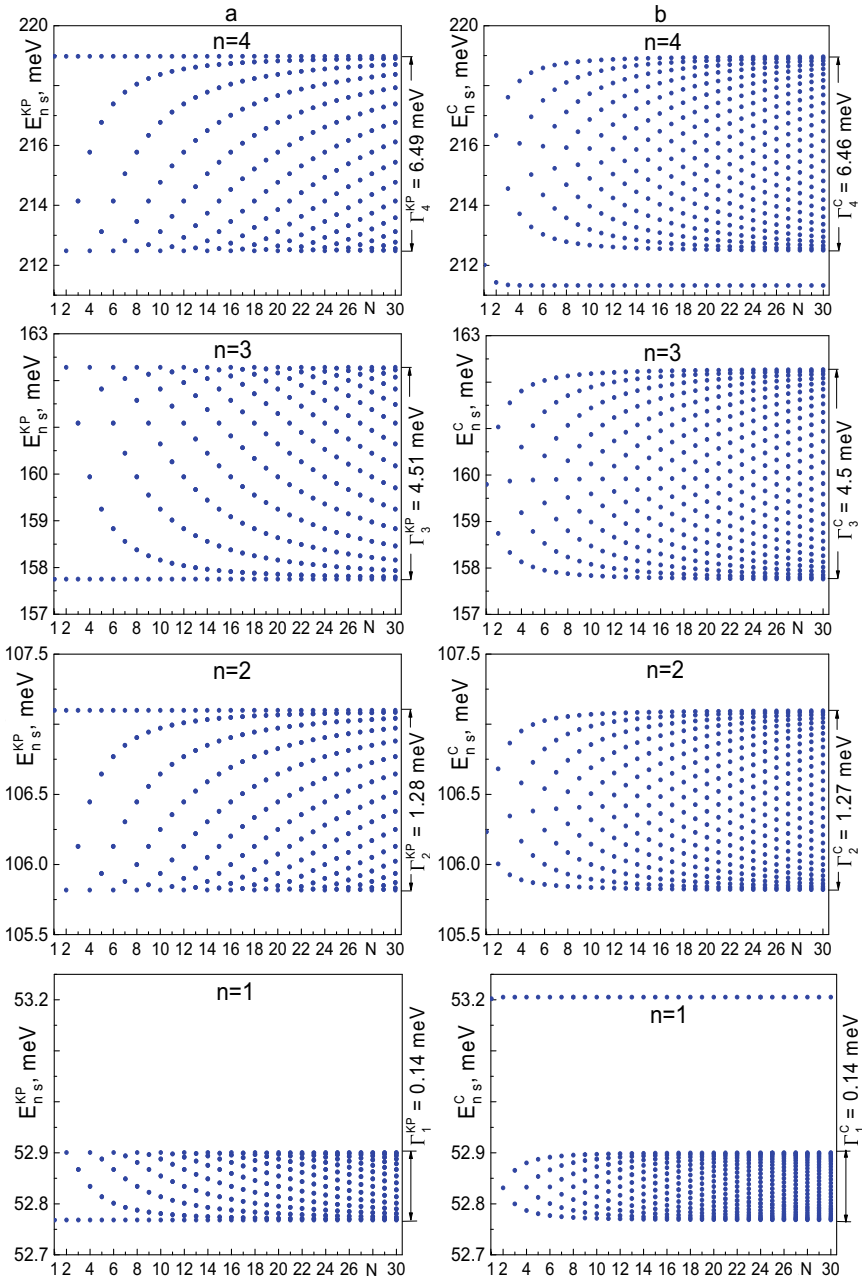


Fig. 3 Electron energy spectrum (E_{ns}^{KP} , E_{ns}^C) as function of the number of cascades (N) in KP- (a) and C-model (b)

cascades ($p_n^C = N$) increasing for bigger N . The number of levels (p_n^{KP}) in the bands of KP-model depends on N parity, so that $p_n^{KP} = p_n^{KP(\text{odd})} = (N+1)/2$ for odd N and $p_n^{KP} = p_n^{KP(\text{even})} = N/2$ for even N . In the limit case $N \rightarrow \infty$, according to the physical considerations, continuous energy bands are formed in both structures.

From Fig. 3b, it is also seen that in C -model, in the high-energy vicinity of the first ($n = 1$) band and low-energy vicinity of the fourth ($n = 4$) band, one can see a single level with the energies $E_{n=1,s=N}^C$ and $E_{n=4,s=1}^C$, respectively. In KP-model (Fig. 3a), such separate levels are absent for the reasons that will be discussed below.

The band widths (Γ_n^{KP} , Γ_n^C) in C - and KP-models have the same dependences on the band number, increasing at bigger n , and different dependences on the number of cascades N . In particular, in the C -model, at bigger N , Γ_n^C widths increase and quickly reach saturation. In KP-model, Γ_n^{KP} depends on N parity so that in structures with even ($N = 2, 4, 6, \dots$) number of cascades, $\Gamma_n^{KP(\text{even})}$ is the same and equal to the widths of the bands $\Gamma_n^{KP(N=2)}$ in two-cascade structure. For the odd number ($N = 1, 3, 5, \dots$), $\Gamma_n^{KP(\text{odd})}$ increases, asymptotically approaching $\Gamma_n^{KP(\text{even})}$. From the values Γ_n^{KP} and Γ_n^C at $N = 30$, Fig. 3, it is seen that the difference between the widths of the bands in both models does not exceed 1% for the typical number of cascades for experimental QCD.

Figure 4 shows the distributions of probability densities ($|\tilde{\Psi}_{ns}^C|^2$) of electron states in two-, three-, four- and five-cascade C -structures. In the same figure, to illustrate the differences between C - and KP-models, the probability densities ($|\Psi_{ns}^{KP}|^2$) in two-cascade structure are presented.

We should note that, as it was already mentioned, in the studied KP-model of multicascade nanostructure, the probability densities ($|\Psi_{ns}^{KP}(z)|^2$) are periodic functions with a period equal to the size (d) of separate cascade (see, for example, Fig. 4a). Since, the probabilities of electron location in the states ln , $s >$ in different cascades ($i = 1, \dots, N$) are the same and equal to $W_{ns}^{KP}(i) = \int_{z_{i,0}}^{z_{i,6}} |\Psi_{ns}^{KP}(z)|^2 dz = 1/N$.

In contrast to KP-, in C -model (Fig. 4), the probability densities $|\Psi_{ns}^C|^2$ for all states ln , $s >$ are aperiodic, and the probabilities ($W_{ns}^C(i) = \int_{z_{i,0}}^{z_{i,6}} |\Psi_{ns}^C(z)|^2 dz$) of electron location in different cascades are different (Table 1). If the number of cascades becomes bigger, the heterogeneity of distribution $|\Psi_{ns}^C(z)|^2$ becomes stronger (Fig. 4d). It leads to a formal two types of cascades: those with a high probability of electron localization (numbers are highlighted in bold in the Table 1) and cascades with low probability. It is worth to note that as calculations show (the results of which are not presented due to cumbersomeness), at $N > 5$, the number of cascades with low localization probabilities increases at bigger N . Therefore, in multicascade QCD elements in C -model, the properties of electron states in different cascades can differ essentially. Unbalancing the interaction between the cascades, it will negatively affect the operation of the device.

Analysis of the Table 1 also shows that independently of the number of cascades (N), and there are two states ($ln = 1, s = N >$ and $ln = 4, s = 1 >$), in which the electron is localized only in the first ($i = 1$) cascade and almost does not penetrate into all other cascades of the structure. From physical considerations, it is obvious that these states are observed due to the finite sizes of the multicascade structure

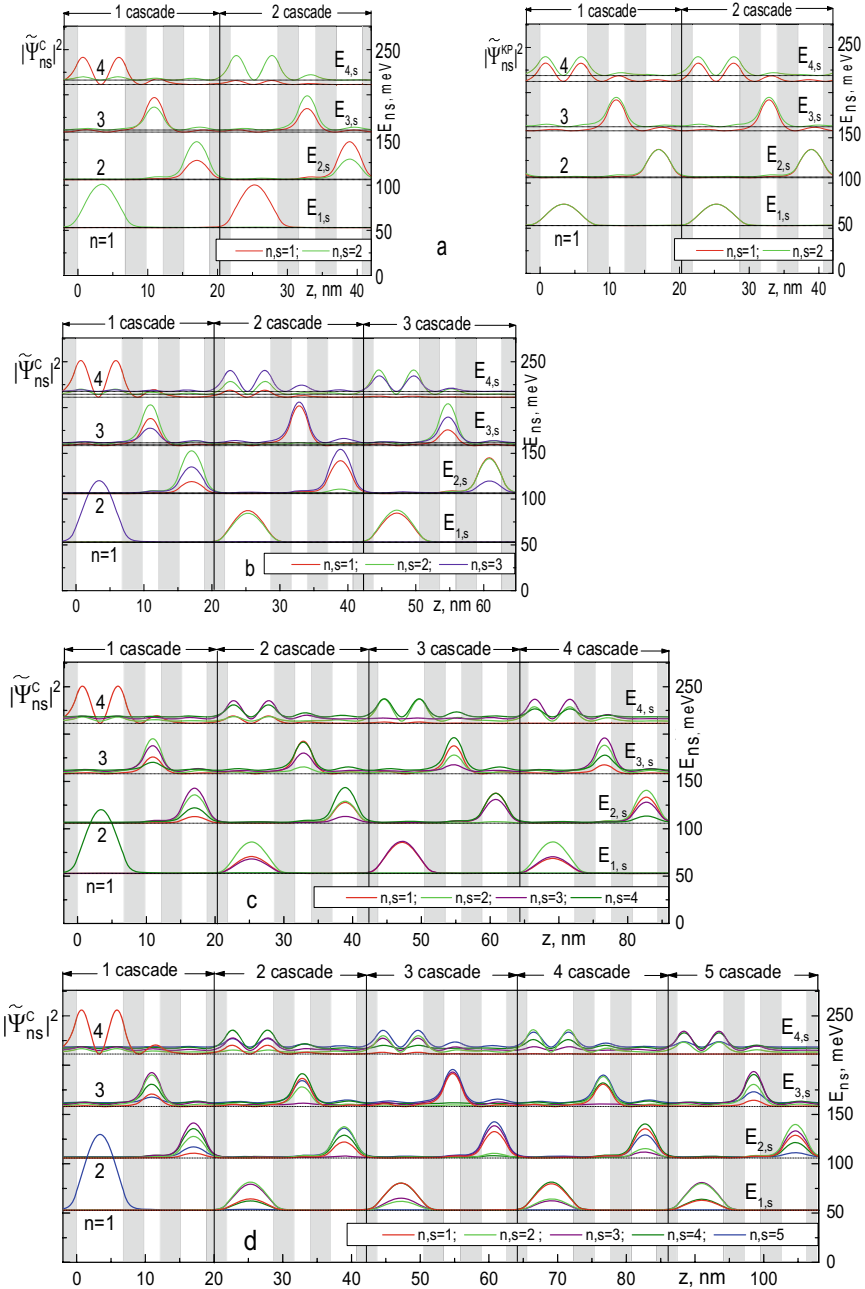


Fig. 4 Distributions of probability densities normalized with respect to the energies in two-well (a), three-well (b), four-well (c), and five-well structure (d)

Table 1 Energies (E_{ns}^C) and the probabilities of electron location ($W_{ns}^C(i)$) in the cascades (i) of two-, three-, four- and five-cascade C -structure. The highest probabilities of electron localization in cascades are highlighted in bold

n	s	$N = 2$					$N = 3$					$N = 4$					$N = 5$					
		E_{ns}^C , meV		$W_{ns}^C(i)$		$W_{ns}^C(i)$	E_{ns}^C , meV		$W_{ns}^C(i)$		$W_{ns}^C(i)$	E_{ns}^C , meV		$W_{ns}^C(i)$		$W_{ns}^C(i)$	E_{ns}^C , meV		$W_{ns}^C(i)$		$W_{ns}^C(i)$	
		$i = 1$	$i = 2$	$i = 1$	$i = 2$		$i = 1$	$i = 2$	$i = 1$	$i = 2$		$i = 1$	$i = 2$	$i = 1$	$i = 2$		$i = 1$	$i = 2$	$i = 1$	$i = 2$		$i = 1$
4	5																218.42	0.02	0.19	0.36	0.31	0.10
	4						218.15	0.03	0.32	0.45	0.19	216.95	0.06	0.36	0.20	0.30	216.95	0.06	0.24	0.23	0.08	0.36
	3						216.06	0.09	0.41	0.04	0.45	215.02	0.08	0.24	0.23	0.08	215.02	0.08	0.30	0.40	0.18	0.18
	2						213.71	0.09	0.11	0.48	0.31	213.27	0.07	0.04	0.30	0.40	213.27	0.07	0.15	0.03	5 × 10⁻³	8 × 10⁻⁴
	1						211.32	0.77	0.15	0.03	4 × 10⁻³	211.32	0.76	0.15	0.03	5 × 10⁻³	211.32	0.76	0.15	0.03	5 × 10⁻³	8 × 10⁻⁴
3	5																161.94	0.06	0.22	0.33	0.27	0.10
	4						161.80	0.10	0.34	0.38	0.17	161.06	0.20	0.29	9 × 10⁻³	0.21	161.06	0.20	0.29	9 × 10⁻³	0.21	0.28
	3						160.60	0.32	0.20	0.09	0.39	159.89	0.32	0.01	0.32	0.01	159.89	0.32	0.01	0.32	0.01	0.33
	2						159.19	0.39	0.08	0.20	0.33	158.78	0.29	0.19	9 × 10⁻³	0.28	158.78	0.29	0.19	9 × 10⁻³	0.28	0.22
	1						158.74	0.58	0.42	0.20	0.48	158.33	0.32	0.48	0.20	0.22	158.33	0.32	0.48	0.20	0.22	0.06
2	5																106.99	0.09	0.28	0.34	0.22	0.04
	4						106.95	0.16	0.41	0.35	0.08	106.72	0.28	0.22	0.32	0.02	106.72	0.28	0.22	0.32	0.22	0.15
	3						106.58	0.39	0.08	0.27	0.24	106.38	0.33	0.02	0.31	0.06	106.38	0.33	0.02	0.31	0.06	0.25
	2						106.68	0.64	0.36	0.51	0.07	106.34	0.51	0.07	0.31	0.05	106.34	0.51	0.07	0.31	0.05	0.32
	1						106.00	0.33	0.66	0.40	0.44	105.92	0.14	0.40	0.26	0.29	105.87	0.04	0.16	0.26	0.29	0.23
1	5																53.20	0.99	8 × 10⁻³	7 × 10⁻⁵	6 × 10⁻⁷	5 × 10⁻⁹
	4						53.20	0.99	8 × 10⁻³	7 × 10⁻⁵	6 × 10⁻⁷	52.88	3 × 10⁻³	0.13	0.35	0.37	52.88	3 × 10⁻³	0.13	0.35	0.37	0.14
	3						52.88	5 × 10⁻³	0.23	0.50	0.26	52.85	7 × 10⁻³	0.34	0.16	0.12	52.85	7 × 10⁻³	0.34	0.16	0.12	0.36
	2						53.20	0.99	8 × 10⁻³	0.47	0.51	52.86	0.01	0.49	0.12	0.15	52.81	8 × 10⁻³	0.37	0.12	0.15	0.35
	1						52.83	0.02	0.98	0.47	0.47	52.78	5 × 10⁻³	0.27	0.36	0.34	52.78	5 × 10⁻³	0.27	0.36	0.34	0.13

in C -model. Therefore, one can expect that “near-surface” localized states of such nature can be manifested in real nanoheterostructures.

To detect the influence of geometric configurations of cascades on the spectral characteristics of multicascade structures, the energies and bandwidths as functions of the sizes of layers were calculated. The results obtained in both models revealed to be close to each other. Thus, to illustrate their main properties, the dependences of the energies (E_{ns}^C) and widths (Γ_n^C) of the bands in ten-cascade ($N = 10$) C -structure on the sizes of potential wells (a_1, a_2, a_3) and potential barriers (b_1, b_2, b_3) are presented in Figs. 5 and 6, respectively. For the sake of simplicity, we temporarily omit s index in the notation of energies.

If the width of one of the potential wells ($a_i, i = 1, 2, 3$) increases, at the fixed size of the other two wells, the energies E_n^C demonstrate a non-linear descending character with anticrossings (Fig. 5). In the vicinity of anticrossing of n -th and $n + 1$ bands, their widths (Γ_n^C and Γ_{n+1}^C) increase. In the other intervals of the widths, they only decrease. The widths of anticrossings are determined by the thicknesses of the potential barriers and decrease at bigger b_i .

The increase of one of the barriers ($b_i, i = 1, 2, 3$) in the intervals of small thicknesses ($0 < b_i < 3$ nm) and fixed size of the other two leads to the high- or low-energy energy shift of E_n^C , depending on the state number (n). For the strong barriers ($b_i > 3$ nm), the energies change weakly (Fig. 6). The widths of bands (Γ_n^C) decrease at bigger b_i , except the vicinity of $b_2 \approx 1.5$, where anticrossing occurs between E_3^C and E_4^C . In limit case $b_i \rightarrow \infty$, according to the physical considerations, the energy bands degenerate into discrete levels of the three-well structure.

4 Main Results and Conclusion

In the approximation of position-dependent effective mass and rectangular potentials, the theory is developed, and a comparative analysis of the properties of electron states in the multicascade nanostructure in C -model with infinite external barriers and in KP-model with a periodic potential is performed.

The spectral parameters are studied as functions of the number of cascades (N). It is shown that in the both models, if N becomes bigger, the quasidiscrete energy bands are formed. The number of levels in each band in C -model is equal to the number of cascades, while and in KP-model, it depends on the parity of N , being equal to $(N + 1)/2$ for odd N and $N/2$ for even. The bands widths in C -structure increase with increasing N and asymptotically approach the widths of corresponding bands in KP-structure.

It is shown that in the realistic C -structure, the probabilities of electron location in different cascades differ significantly. Since, in multicascade structures, there are regions of one or more cascades with negligibly small probabilities of electron location. In contrast, in KP-model, the periodicity of the wave function leads to the same probabilities for all states, being equal to $1/N$ of the values of the electron location in different cascades of the structure.

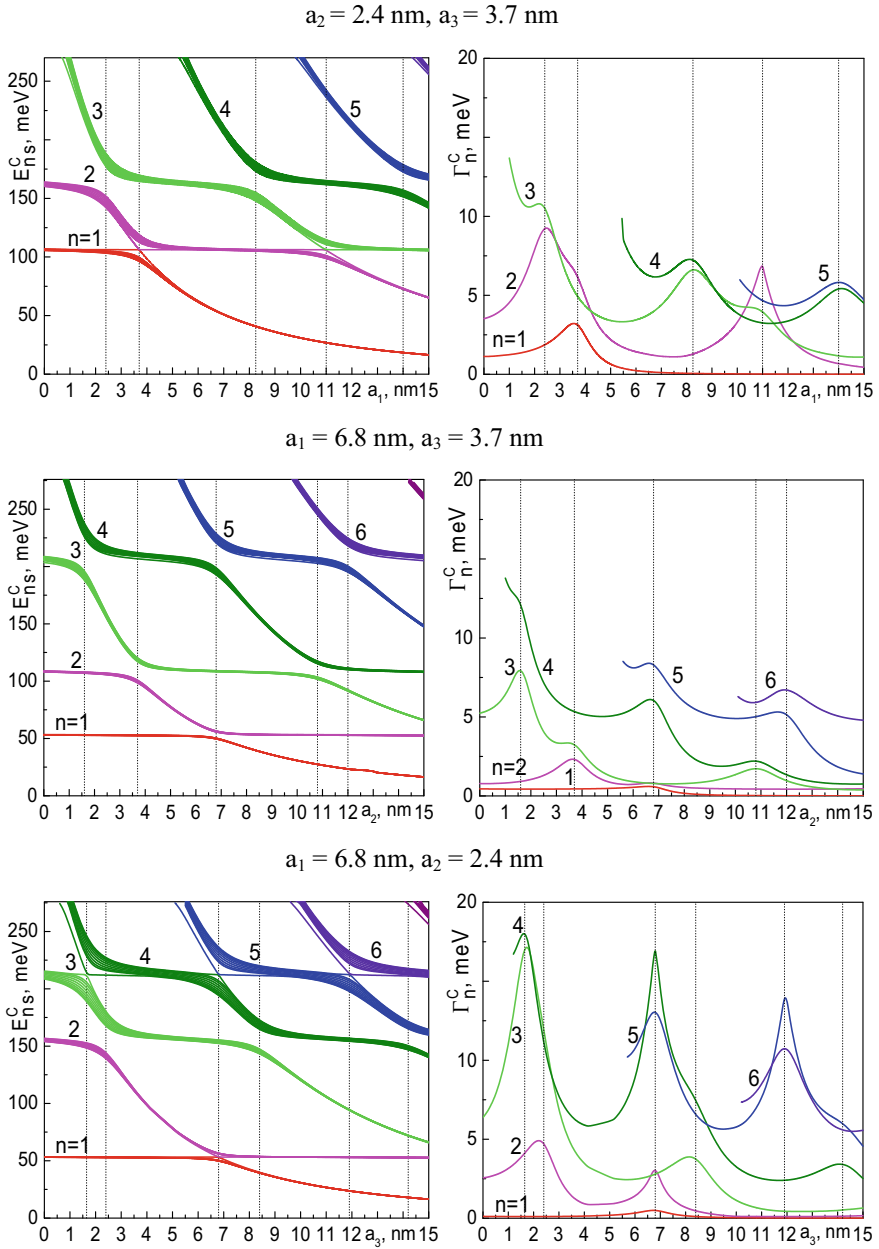


Fig. 5 Bands energies (E_{ns}^C) and widths (Γ_n^C) as functions of the wells widths (a_1, a_2, a_3) in C-structure with ten cascades at fixed barrier thickness $b_1 = b_2 = b_3 = 3 \text{ nm}$

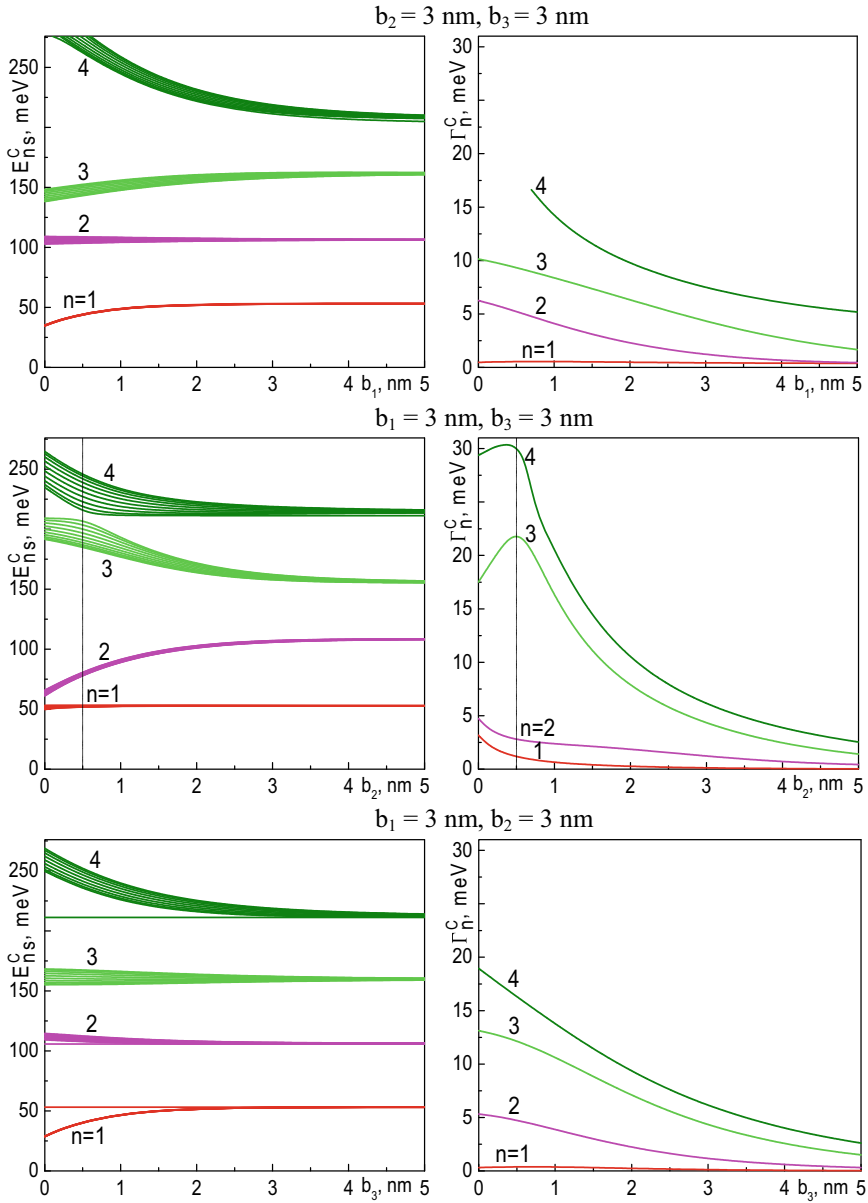


Fig. 6 Bands energies (E_{ns}^C) and widths (Γ_n^C) as functions of the barrier thicknesses (b_1, b_2, b_3) in C-structure with ten cascades at fixed wells widths $a_1 = 6.8$ nm, $a_2 = 2.4$ nm, $a_3 = 3.7$ nm

It is revealed that the dependences of bands energies on the geometric parameters of potential wells and barriers of the multicascade structure are similar to the corresponding dependences of the discrete levels in the separate cascade. If the well widths increase, the band energies decrease manifesting anticrossing effect. The increasing barrier thicknesses has little effect on the energy spectrum.

References

1. Belkin MA, Capasso F (2015) New frontiers in quantum cascade lasers: high performance room temperature terahertz sources. *Phys Scr* 90:118002. <https://doi.org/10.1088/0031-8949/90/11/118002>
2. Matsuoka Y, Semtsiv MP, Masselink WT (2020) Quantum cascade lasers. *Mid-infrared Optoelectronics; Woodhead Publishing Series in Electronic and Optical Materials* 131–179. <https://doi.org/10.1016/B978-0-08-102709-7.00004-8>
3. Giorgetta FR, Baumann E, Graf M, et al (2009) Quantum cascade detectors. *IEEE J Quantum Elect* 45:1039. <https://doi.org/10.1109/JQE.2009.2017929>
4. Schwarz B, Wang CA, Missaggia L et al (2017) Watt-level continuous-wave emission from a bifunctional quantum cascade laser/detector. *ACS Photonics* 4:1225. <https://doi.org/10.1021/acsp Photonics.7b00133>
5. Faist J, Capasso F, Sivco DL, Sirtori C, Hutchinson AL, Cho AY (1994) Quantum cascade laser. *Science* 264:553. <https://doi.org/10.1126/science.264.5158.553>
6. Kumar S, Williams BS, Hu Q, Reno JL (2006) 1.9THz quantum-cascade lasers with one-well injector. *Appl Phys Lett* 88:121123. <https://doi.org/10.1063/1.2189671>
7. Castellano F, Bismuto A, Amanti MI, Terazzi R, Beck M et al (2011) Loss mechanisms of quantum cascade lasers operating close to optical phonon frequencies. *J Appl Phys* 109:102407. <https://doi.org/10.1063/1.3576153>
8. Katz S, Vizbaras A, Meyer R, Amann M-C (2011) *J Appl Phys* 109:081101. <https://doi.org/10.1063/1.3566072>
9. Heydari D, Bai Y, Bandyopadhyay N, Slivken S, Razeghi M (2015) High brightness angled cavity quantum cascade lasers. *Appl Phys Lett* 106:091105. <https://doi.org/10.1063/1.4914477>
10. Dunn A, Poyser C, Dean P, et al (2020) High-speed modulation of a terahertz quantum cascade laser by coherent acoustic phonon pulses. *Nat Comm* 11. <https://doi.org/10.1038/s41467-020-14662-w>
11. Gendron L, Carras M, Huynh A, Ortiz V, Koeniguer C, Berger V (2004) Quantum cascade photodetector. *Appl Phys Lett* 85:2824. <https://doi.org/10.1063/1.1781731>
12. Levine BF (1993) Quantum-well infrared photodetectors. *J Appl Phys* 74:R1. <https://doi.org/10.1063/1.354252>
13. Schneider H, Liu HC (2007) *Quantum well infrared photodetectors: physics and applications*. Springer. <https://doi.org/10.1007/978-3-540-36324-8>
14. Gendron L, Koeniguer C, Berger V, Marcadet X (2005) High resistance narrow band quantum cascade photodetectors. *Appl Phys Lett* 86:121116. <https://doi.org/10.1063/1.1884257>
15. Giorgetta FR, Baumann E, Graf M, et al (2007) 16.5 μm quantum cascade detector using miniband transport. *Appl Phys Lett* 90:231111. <https://doi.org/10.1063/1.2743955>
16. Reininger P, Schwarz B, Detz H et al (2014) Diagonal-transition quantum cascade detector. *Appl Phys Lett* 105:091108. <https://doi.org/10.1063/1.4894767>
17. Liu J, Zhou Y, Zhai S, Liu F, Liu S, Zhang J, Zhuo N, Wang L, Wang Z (2018) High-frequency very long wave infrared quantum cascade detectors. *Semicond Sci Technol* 33:125016. <https://doi.org/10.1088/1361-6641/aaebd4>
18. Vardi A, Bahir G, Guillot F, Bougerol C, Monroy E, Schacham SE, Tchernycheva M, Julien FH (2008) Near infrared quantum cascade detector in GaN/AlGaIn/AlN heterostructures. *Appl Phys Lett* 92:011112. <https://doi.org/10.1063/1.2830704>

19. Vardi A, Kheirodin N, Nevou L, Machhadani H, Vivien L, Crozat P, Tchernycheva M, Colombelli R, Julien FH, Guillot F, et al (2008) High-speed operation of GaN/AlGaIn quantum cascade detectors at $\lambda \approx 1.55 \mu\text{m}$. *Appl Phys Lett* 93:193509. <https://doi.org/10.1063/1.3021376>
20. Sakr S, Crozat P, Gacemi D, Kotsar Y, Pesach A, Quach P, Isac N, Tchernycheva M, Vivien L, Bahir G, et al (2013) GaN/AlGaIn waveguide quantum cascade photodetectors at $\lambda \approx 1.55 \mu\text{m}$ with enhanced responsivity and ~ 40 GHz frequency bandwidth, *Appl Phys Lett* 102:011135. <https://doi.org/10.1063/1.4775374>
21. Paiella R, Capasso F, Gmachl C, Sivco DL, Baillargeon JN, Hutchinson AL, Cho AY, Liu HC (2000) Self-mode-locking of quantum cascade lasers with giant ultrafast optical nonlinearities. *Science* 290:1739. <https://doi.org/10.1126/science.290.5497.1739>
22. Beeler M, Trichas E, Monroy E (2013) III-nitride semiconductors for intersubband optoelectronics: a review. *Semicond Sci Technol* 28:074022. <https://doi.org/10.1088/0268-1242/28/7/074022>
23. Giorgetta FR, Baumann E, Hofstetter D, Manz C, Yang Q, Kohler K, Graf M (2007) InGaAs/AlAsSb quantum cascade detectors operating in the near infrared. *Appl Phys Lett* 91:111115. <https://doi.org/10.1063/1.2784289>
24. Jollivet A, Hinkov B, Pirota S, Hoang H, Derelle S, Jaeck J, Tchernycheva M, Colombelli R, Bousseksou A, Hugues M et al (2018) Short infrared wavelength quantum cascade detectors based on m-plane ZnO/ZnMgO quantum wells. *Appl Phys Lett* 113:251104. <https://doi.org/10.1063/1.5058120>
25. Lei W, Jagadish C (2008) Lasers and photodetectors for mid-infrared 2–3 μm applications. *J Appl Phys* 104:091101. <https://doi.org/10.1063/1.3002408>
26. Koeniguer C, Dubois G, Gomez A, Berger V (2006) Electronic transport in quantum cascade structures at equilibrium. *Phys Rev B* 74:235325. <https://doi.org/10.1103/PhysRevB.74.235325>
27. Terazzi R, Faist J (2010) A density matrix model of transport and radiation in quantum cascade lasers. *New J Phys* 12:033045. <https://doi.org/10.1088/1367-2630/12/3/033045>
28. Jirauschek C, Kubis T (2014) *Appl Phys Rev* 1:011307. <https://doi.org/10.1063/1.4863665>
29. Zegrya GG, Tkach NV, Boiko IV et al (2013) Quasi-stationary electron states in a multilayered structure in longitudinal electric and transverse magnetic fields. *Phys Solid State* 55:218. <https://doi.org/10.1134/S106378341310034X>
30. Botez D, Chang C-C, Mawst LJ (2016) Temperature sensitivity of the electro-optical characteristics for mid-infrared ($\lambda = 3\text{--}16 \mu\text{m}$)-emitting quantum cascade lasers. *J Phys D: Appl Phys* 49:043001. <https://doi.org/10.1088/0022-3727/49/4/043001>
31. He J, Wang P, Chen H, Guo X, Guo L, Yang Y (2017) Study on temperature effect on properties of ZnO/MgZnO based quantum cascade detector in mid-infrared region. *Appl Phys Express* 10:011101. <https://doi.org/10.7567/APEX.10.011101>
32. Tkach M, Seti J, Voitsekhivska O (2017) Spectrum of electron in quantum well within the linearly-dependent effective mass model with the exact solution. *Superlattices and Microstruct* 109:905. <https://doi.org/10.1016/j.spmi.2017.06.013>
33. Saha S, Kumar J (2017) Role of interface roughness scattering, temperature, and structural parameters on the performance characteristics of III-nitride quantum cascade detectors. *J Appl Phys* 121:053104. <https://doi.org/10.1063/1.4975481>
34. Li Z, Wang P, He J, Chen H, Cheng J (2017) Effect of polarization on the performance of ZnO/MgZnO quantum cascade detector. *Superlattices Microstruct*. <https://doi.org/10.1016/j.spmi.2017.07.046>
35. Rojas-Briseño JG, Del Rio-De Santiago A, Mora-Ramos ME, Martínez-Orozco JC (2020) Nonlinear intersubband absorption coefficient in an $\text{Al}_x\text{Ga}_{1-x}\text{As}/\text{GaAs}$ quantum cascade laser-like profile. *Optik* 201:163431. <https://doi.org/10.1016/j.ijleo.2019.163431>
36. Seti J, Voitsekhivska O, Vereshko E et al (2021) Effect of interface phonons on the functioning of quantum cascade detectors operating in the far infrared range. *Appl Nanosci*. <https://doi.org/10.1007/s13204-021-01708-8>

37. Davies JH (1998) *The physics of low-dimensional semiconductors: an introduction*. Cambridge University Press. <https://doi.org/10.1017/CBO9780511819070>
38. Harrison P, Valavanis A (2016) *Quantum wells, wires and dots: theoretical and computational physics of semiconductor nanostructures*, 4th edn. Wiley. <https://doi.org/10.1002/9781118923337>

Theory of Double Injection in Core-shell Nanowire Radial $p-i-n$ Diodes



Vitalii L. Borblik 

Abstract This paper presents analytical theory of forward current–voltage characteristic for core–shell–shell radial diode with the core of n -type and external shell of p -type ($n-i-p$ diode). Results are compared with those for diode with opposite sequence of the layers (core of p -type and external shell of n -type, i.e., $p-i-n$ diode) and also with those for planar $p-i-n$ diode with analogous parameters. It is shown that in both radial diodes, spatial distribution of current carriers injected into the i -layer possesses (at equal electron and hole mobilities) by its own specific asymmetry connected with cylindrical geometry of the structure. And asymmetry of the distribution component due to inequality of the mobilities proves to be the same type in $n-i-p$ diode while of the opposite type in $p-i-n$ diode. The current density as a function of radial thickness of the i -layer demonstrates maximums at the thicknesses close to ambipolar diffusion length, and these maximums are the most high in radial $p-i-n$ diode.

Keywords Core-shell nanowire · Radial $p-i-n$ diode · Spatial concentration distribution · Current-voltage characteristics · Ambipolar diffusion length

1 Introduction

Core–shell nanowires take a great attention as building blocks for nanoelectronics. Many of novel devices use nanowire radial $p-i-n$ structures: for photovoltaic applications [1, 2], as photodetectors [3], for harvesting different kind of energy [4], for creation of light emitting diodes [5], etc. As a rule study of properties of such the devices include also investigation of their dark current–voltage characteristics.

As it is known the double injection in planar $p-i-n$ diodes is characterized by certain spatial distribution of current carriers injected into the i -layer. At equal electron and hole mobilities, this distribution is completely symmetric relative to middle of the i -layer but at their inequality, the distribution acquires asymmetric component which

V. L. Borblik (✉)

V. Lashkarev Institute of Semiconductor Physics, Kyiv, Ukraine
e-mail: borblik@isp.kiev.ua

© The Author(s), under exclusive license to Springer Nature Switzerland AG 2023
O. Fesenko and L. Yatsenko (eds.), *Nanomaterials and Nanocomposites, Nanostructure Surfaces, and Their Applications*, Springer Proceedings in Physics 279,
https://doi.org/10.1007/978-3-031-18096-5_22

377

raises carrier concentration at the edge of the i -layer adjoining to p -region and lowers it at the edge of the i -layer adjoining to n -region [6].

Cylindrical geometry of a radial p - i - n diode, as it turned out [7], results in its own specific asymmetry of the concentration distribution which superimposes to asymmetry connected with mobilities inequality. As a result, in p - i - n diode with p -type core and n -type external shell, two asymmetric components prove to be of opposite type and compensate partially each other [7].

It is of interest to consider the case of a radial p - i - n diode with opposite sequence of the layers, i.e., with the core of n -type and external shell of p -type (n - i - p diode). In planar geometry, sequence of the layers, of course, has not any role.

2 Spatial Distribution of the Carrier Concentration in the i -Layer

Schematic view of the structure under consideration is shown in Fig. 1, where i -layer is located between r_1 and r_2 , r_n and r_p are the depletion region boundaries.

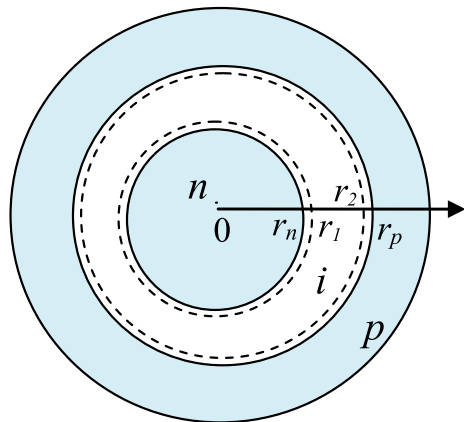
Basic equations of the task are continuity equations

$$\operatorname{div} I_n = R, \tag{1}$$

$$\operatorname{div} I_p = -R, \tag{2}$$

where $R = \frac{n}{\tau} = \frac{p}{\tau}$ describes recombination (τ is a lifetime of the non-equilibrium carriers, the high injection level is supposed, i.e., $n(r) = p(r)$), and partial electron and hole currents are

Fig. 1 Schematic view of the radial n - i - p structure



$$I_n = q(D_n \text{grad}(n) + \mu_n n(r) E(r)), \quad (3)$$

$$I_p = q(-D_p \text{grad}(p) + \mu_p p(r) E(r)), \quad (4)$$

where q is electron charge, D_n , D_p , μ_n , and μ_p are electron and hole diffusion coefficients and mobilities, $E(r)$ is radial electric field.

As well as in Ref. [7], we follow here to approach used in paper [8] under consideration of planar *p-i-n* diode. It consists in assumption that at the borders of the highly doped *p*- and *n*-regions, the current is carried only by holes and electrons, respectively. Thus,

$$I_p(r_1) = 0, \quad (5)$$

$$I_n(r_1) = -I, \quad (6)$$

$$I_p(r_2) = -I, \quad (7)$$

$$I_n(r_2) = 0 \quad (8)$$

where minus at current density I is connected with reverse of the applied voltage.

Then according to (5),

$$I_p(r_1) = q\mu_p \left(-\theta \frac{dp}{dr} \Big|_{r=r_1} + p(r_1) E(r_1) \right) = 0$$

where $\theta = kT/q$ (k is the Boltzmann constant, T is temperature), whence

$$E(r_1) = \frac{\theta}{p(r_1)} \frac{dp}{dr} \Big|_{r=r_1}. \quad (9)$$

and according to (8),

$$I_n(r_2) = q\mu_n \left(\theta \frac{dn}{dr} \Big|_{r=r_2} + n(r_2) E(r_2) \right) = 0$$

whence it follows that

$$E(r_2) = -\frac{\theta}{n(r_2)} \frac{dn}{dr} \Big|_{r=r_2}. \quad (10)$$

Next, according to (6) with using (9),

$$I_n(r_1) = q\mu_n \left(\theta \frac{dp}{dr} \Big|_{r=r_1} + n(r_1)E(r_1) \right) = 2q\mu_n\theta \frac{dn}{dr} \Big|_{r=r_1} = -I,$$

whence

$$\frac{dn}{dr} \Big|_{r=r_1} = -\frac{I}{2q\mu_n\theta}, \quad (11)$$

and according to (7) with using (10),

$$I_p(r_2) = q\mu_p \left(-\theta \frac{dp}{dr} \Big|_{r=r_2} + p(r_2)E(r_2) \right) = -2q\mu_p\theta \frac{dn}{dr} \Big|_{r=r_2} = -I,$$

whence it follows that

$$\frac{dn}{dr} \Big|_{r=r_2} = \frac{I}{2q\mu_p\theta}. \quad (12)$$

Expressions (11) and (12) will be used as the boundary conditions for solution of ambipolar diffusion equation

$$\operatorname{div}[\operatorname{grad}(n)] = \frac{n(r)}{D_{\text{amb}}\tau}$$

which follows from Eqs. (1–2), and under conditions of cylindrical geometry, takes the form

$$\frac{1}{r} \frac{d}{dr} \left(r \frac{dn}{dr} \right) = \frac{n(r)}{D_{\text{amb}}\tau} \quad (13)$$

where $D_{\text{amb}} = (\mu_p D_n + \mu_n D_p) / (\mu_n + \mu_p)$.

Solution of Eq. (13) is

$$n(r) = C_1 I_0(r/L_{\text{amb}}) + C_2 K_0(r/L_{\text{amb}}) \quad (14)$$

where $L_{\text{amb}} = \sqrt{D_{\text{amb}}\tau}$, I_0 , and K_0 are modified Bessel functions of 1st and 2nd kind, respectively. Introducing new variable $x = r/L_{\text{amb}}$, we obtain for derivative of (14)

$$\frac{dn}{dx} = C_1 I_1(x) - C_2 K_1(x). \quad (15)$$

Using now Eqs. (11) and (12),

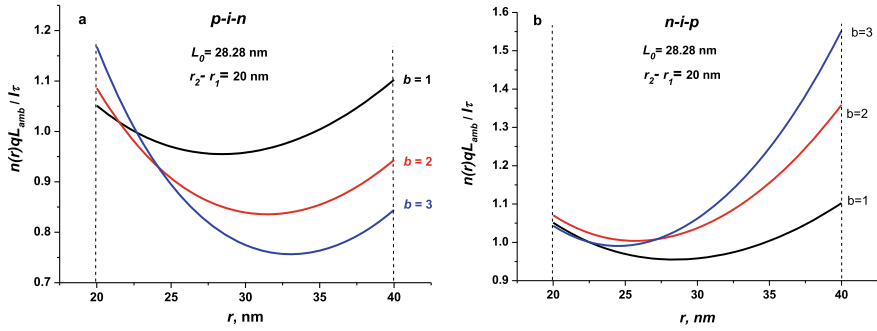


Fig. 2 Dimensionless factor of spatial distribution of carrier concentration in the i -layer of radial p - i - n structure [7] (a) and radial n - i - p structure (b)

$$\left. \frac{dn}{dx} \right|_{x=x_1} = C_1 I_1(x_1) - C_2 K_1(x_1) = -\frac{I L_{amb}}{2q\mu_n\theta}, \quad (16)$$

$$\left. \frac{dn}{dx} \right|_{x=x_2} = C_1 I_1(x_2) - C_2 K_1(x_2) = \frac{I L_{amb}}{2q\mu_p\theta} \quad (17)$$

we obtain finally the carrier distribution

$$n(x) = \frac{I\tau}{qL_{amb}(1+b)\Delta} \left\{ \begin{array}{l} [bK_1(x_1) + K_1(x_2)]I_0(x) \\ + [bI_1(x_1) + I_1(x_2)]K_0(x) \end{array} \right\} \quad (18)$$

where $b = \mu_n / \mu_p$ is mobility ratio, $\Delta = I_1(x_2)K_1(x_1) - I_1(x_1)K_1(x_2)$.

At $b = 1$, this distribution does not differ from that for radial diode with p - i - n structure, i.e., possesses by the same own specific asymmetry (see Fig. 2a). But the asymmetry of the component which is due to $b \neq 1$ proves here to be of the same type, i.e., both asymmetric components are adding (Fig. 2b) enhancing significantly common asymmetry of the concentration distribution.

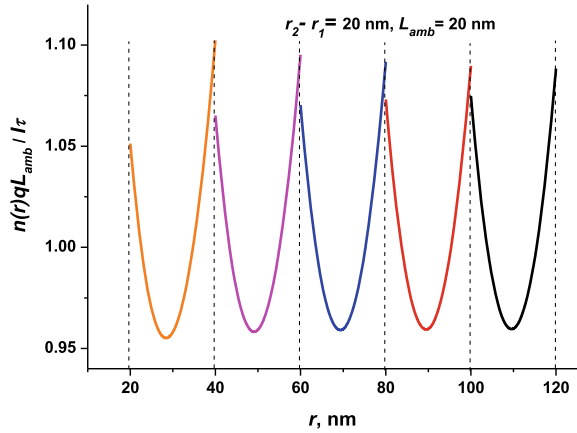
It should be noted that the own specific distribution asymmetry connected with cylindrical geometry of the structure is enhancing when the i -layer is closer and closer to the nanowire center (Fig. 3).

3 The Forward Current–Voltage Characteristic

Under conditions of Boltzmann statistics, we have at left edge of the i -layer

$$\frac{p(r_1)}{n_i} = \frac{n(r_1)}{n_i} = e^{-\frac{qU_l}{kT}} \quad (19)$$

Fig. 3 Spatial distribution of non-equilibrium carriers in the *i*-layer at different its positions relative to the nanowire center



and at the right one—

$$\frac{n(r_2)}{n_i} = \frac{p(r_2)}{n_i} = e^{-\frac{qU_r}{kT}} \tag{20}$$

where

$$\begin{aligned} n(r_1) &= \frac{I\tau}{qL_{amb}(1+b)\Delta} \left\{ [bK_1(x_1) + K_1(x_2)]I_0(r_1) \right. \\ &\quad \left. + [bI_1(x_1) + I_1(x_2)]K_0(r_1) \right\} \\ &\equiv \frac{I\tau}{qL_{amb}(1+b)\Delta} \{ \}_1, \\ n(r_2) &= \frac{I\tau}{qL_{amb}(1+b)\Delta} \left\{ [bK_1(x_1) + K_1(x_2)]I_0(r_2) \right. \\ &\quad \left. + [bI_1(x_1) + I_1(x_2)]K_0(r_2) \right\} \\ &\equiv \frac{I\tau}{qL_{amb}(1+b)\Delta} \{ \}_2. \end{aligned}$$

Multiplying (19) and (20), one can obtain an expression for the current–voltage characteristic in the form

$$I = \frac{qL_{amb}n_i}{\tau} \frac{(1+b)\Delta}{\sqrt{\{ \}_1 \{ \}_2}} e^{-\frac{q(U_l+U_r)}{2kT}}. \tag{21}$$

Under introducing the whole voltage $U = U_l + U_m + U_r$ where U_m is a voltage drop across the *i*-layer, the current–voltage characteristic takes the form

$$I = \frac{qL_{amb}n_i}{\tau} \frac{(1+b)\Delta}{\sqrt{\{ \}_1 \{ \}_2}} e^{\frac{qU_m}{2kT}} e^{-\frac{qU}{2kT}} \equiv \frac{qL_{amb}n_i}{\tau} F(r_1, r_2) e^{-\frac{qU}{2kT}} \tag{22}$$

where dependence of the current–voltage characteristics on position and thickness of the *i*-layer is described by factor $F(r_1, r_2)$. A voltage drop across the *i*-layer is given by $U_m = \int_{r_1}^{r_2} E(r)dr$, where radial electric field $E(r)$ is determined from Eqs. (3) and (4) after their summation

$$E(r) = \frac{I}{q(1+b)\mu_p n(r)} - \frac{(b-1)\theta}{(b+1)n(r)} \frac{dn}{dr}. \tag{23}$$

Figure 4 presents dependence of the current density determined by factor $F(r_1, r_2)/\sqrt{1+b}$ (when accounting its dependence on mobility ratio) on radial extent of the *i*-layer at given L_{amb} in comparison with analogous results for radial *p-i-n* structure [7] and for planar *p-i-n* diode with the same parameters. It is seen from this figure that both in planar and in radial *p-i-n* and *n-i-p* diodes, these dependences demonstrate maximums at *i*-layer thicknesses close to ambipolar diffusion length falling both at small thicknesses (case of “short” diode) and at large thicknesses (case of “long” diode). But value of the current density in maximum proves to be higher in radial *p-i-n* structure and lower in radial *n-i-p* structure than in analogous planar *p-i-n* diode.

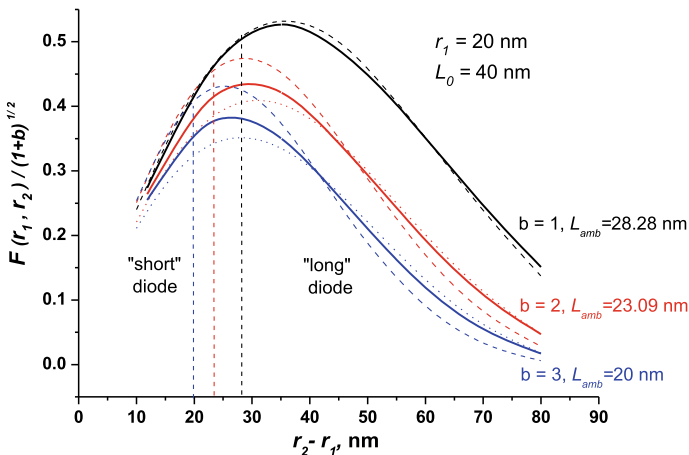


Fig. 4 Dependences of the current density on radial extent of the *i*-layer at given $L_{amb} = L_0/\sqrt{1+b}$ for radial *n-i-p* structure (dot lines), for radial *p-i-n* structure [7] (dash lines) and for planar *p-i-n* diode (calculated on the base of corresponding formulas of Ref. [8]) with the same parameters (solid lines)

4 Conclusion

Thus from the point of view of obtaining maximal current density, just radial *p-i-n* structure is most preferential. But, for example, maximum of recombination radiation proves to be closer to external nanowire surface in the *n-i-p* structure.

Acknowledgements This work was supported by the National Academy of Sciences of Ukraine.

References

1. Yoo J, Dayeh SA, Tang W, Picraux ST (2013) Epitaxial growth of radial Si p-i-n junctions for photovoltaic applications. *Appl Phys Lett* 102:093113. <https://doi.org/10.1063/1.4794541>
2. Zhang Y, Sanchez AM, Aagesen M, Huo S, Fonseka HA, Gott JA, Kim D, Yu X, Chen X, Xu J, Li T, Zeng H, Boras G, Liu H (2019) Growth and fabrication of high-quality single nanowire devices with radial p-i-n junctions. *Small* 15:1803684. <https://doi.org/10.1002/sml.201803684>
3. Soci C, Zhang A, Bao X-Y, Kim H, Lo Y, Wang D (2010) Nanowire Photodetectors. *J Nanosci Nanotechnol* 10:1430–1449. <https://doi.org/10.1166/jnn.2010.2157>
4. Goktas NI, Wilson P, Ghukasyan A, Wagner D, McNamee S, LaPierre RR (2018) Nanowires for energy: a review. *Appl Phys Rev* 5:041305. <https://doi.org/10.1063/1.5054842>
5. Svensson CPT, Mårtensson T, Trägårdh J, Larsson C, Rask M, Hessman D, Samuelson L, Ohlsson J (2008) Monolithic GaAs/InGaP nanowire light emitting diodes on silicon. *Nanotechnology* 19:305201. <https://doi.org/10.1088/0957-4484/19/30/305201>
6. Herlet A (1968) The forward characteristic of silicon power rectifiers at high current densities. *Solid-State Electron* 11:717–742. [https://doi.org/10.1016/0038-1101\(68\)90053-1](https://doi.org/10.1016/0038-1101(68)90053-1)
7. Borblik VL (2021) Analytic theory for current-voltage characteristic of a nanowire radial p-i-n diode. *Semicond Phys Quantum Electron Optoelectron* 24(4):419–424. <https://doi.org/10.15407/spqeo24.04.419>
8. Benda H, Spence E (1967) Reverse recovery processes in silicon power rectifiers. *Proc IEEE* 55:1331–1354. <https://doi.org/10.1109/PROC.1967.6093>

Selection of Optimal Technological Parameters for Obtaining Encapsulated Organic-Mineral Fertilizers with Nanoporous Structure



S. V. Vakal, V. S. Vakal, A. E. Artyukhov, V. Y. Shkola, and A. O. Yanovska

Abstract The work is devoted to improving the technology of obtaining organo-mineral fertilizers by modifying the composition of the organic shell, which allows the formation of its developed nanoporous structure. Perspective directions of the “green” transition of agriculture in the concept of sustainable innovative outpacing are substantiated. The relevance of using granular products with a porous structure in chemical production and the agricultural industry is given. A review of methods for obtaining granules with a nanoporous structure is also carried out. The necessity of creating a new type of fertilizers, combining nutrients included in the composition of mineral fertilizers and organic elements, has been substantiated. The technological bases of encapsulation of mineral fertilizers with an organic shell are presented. A new composition of the shell for encapsulation has been proposed, in which biochar is used as an additional pore-forming agent. The results of studying the structure of granules of organo-mineral fertilizers with biochar in the shell are presented.

Keywords Nanoporous structure · Organic-mineral fertilizers · Granulation · Concept of green innovative outpacing/proactivity

1 Introduction

Tackling climate risks, resulting from anthropogenic pressures on ecosystems, involves global reductions in greenhouse gas emissions in all sectors of the economy and a “green” transition of national economies to climate neutrality and sustainable development [1–3] in accordance with the documents “The European Green Deal” [4] and “Fit for 55”: delivering the EU’s 2030 Climate Target on the way to

S. V. Vakal · V. S. Vakal

Scientific-Research Institute of Mineral Fertilizers and Pigments of the Sumy State University, 12, Kharkovskaya Str, Sumy 40012, Ukraine

A. E. Artyukhov · V. Y. Shkola · A. O. Yanovska (✉)

Sumy State University, Rymskogo-Korsakova Str., 2, Sumy 40007, Ukraine

e-mail: a.yanovska@teset.sumdu.edu.ua

© The Author(s), under exclusive license to Springer Nature Switzerland AG 2023

385

O. Fesenko and L. Yatsenko (eds.), *Nanomaterials and Nanocomposites, Nanostructure Surfaces, and Their Applications*, Springer Proceedings in Physics 279,

https://doi.org/10.1007/978-3-031-18096-5_23

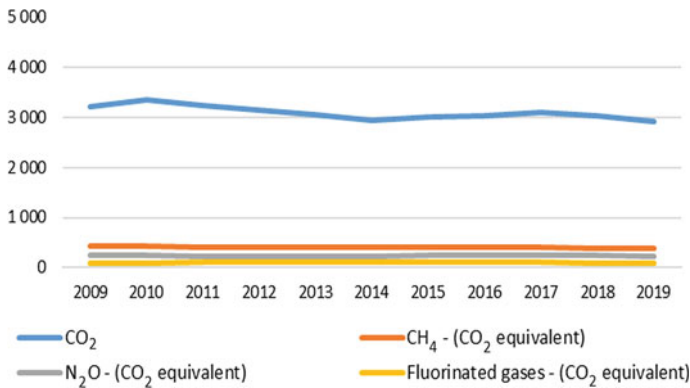


Fig. 1 Dynamics of greenhouse gas emissions in the EU, thousand kt (developed by authors based on data [7])

climate neutrality [5], adopted by the European Commission in response to climate and environmental-related challenges [6].

According to the European Environment Agency [7], the largest polluter in terms of anthropogenic N₂O greenhouse gas emissions in the EU is the agricultural sector, which accounted for 74.59% of nitrogen oxide emissions (or 174,965.9 kt CO₂ eq.) in 2019. The overall dynamics of greenhouse gas formation in the EU countries is shown in Fig. 1. In Ukraine, according to the annual inventory submissions 2021 [8, 9], the volume of nitrogen oxide emissions in the agricultural sector was 111.3 kt in 2019, 78% of which are direct and indirect emissions from agricultural land (as a result of the use of organic and mineral fertilizers).

The dynamics of fertilizer use in the agricultural sector of Ukraine for the period 2000–2020 indicates an increase in consumption of mineral fertilizers by almost 886% (from 0.28 million tons in 2000 to 2.78 million tons in 2020) while reduction of organic fertilizers by 60.6% compared to 2000 (from 29 million tons to 11.4 million tons). Meanwhile, the share of agricultural lands treated with mineral fertilizers increased only by 252.7% and in 2020 amounted to 39.5%, and the share of agricultural lands treated with organic fertilizers increased by 41.2% and in 2020 amounted to 2.4% [10]. These data indicate that while maintaining current trends, the volume of greenhouse gases in agriculture will increase, and hence, the “green” transition to organic production will take place at an extremely slow pace, even if it is focused on achievement of the climate neutrality goals by 2060 or even by 2070, as defined in [11, 12].

The need to accelerate the “green” transition of Ukraine to climate neutrality through the introduction of environmental innovations is identified in the National Economic Strategy for the period up to 2030 [11]. Moreover, the trigger for a “green” transition in Europe is the ever-growing hybrid threats from the Russian Federation, which intensify migration processes, including due to climate change, and affect the food, energy, environmental, and national security of European countries. In this regard, according to the concept of sustainable innovative outpacing, one of means of

accelerating the “green” transition in agriculture is to use new generation fertilizers that are environmentally safe at all stages of their ecological and economic cycle, including the stages of life cycle and customization one [13–15], and based on an innovative approaches to the technologies of the fertilizer production and the use of only clean energy sources in the production process [16–19].

Obtaining granules with a nanoporous structure is a prerequisite for the implementation of some processes in chemical technology and ensuring the necessary characteristics of a granulated product at the stage of its economic use. For example, for blasting operations in the mining industry using ANFO, a prerequisite is the use of ammonium nitrate with a developed network of nanopores (porous ammonium nitrate, PAN) [20–22] simultaneously with the development of the technological foundations of the process [23, 24] and the determination of the laws of hydrodynamics [25] and heat and mass transfer processes [26–28]. The porosity of adsorbents and catalysts is also a prerequisite for successfully implementing processes in chemical technology [29, 30].

It is necessary to highlight the direction of obtaining granules with a porous structure for further use as fertilizers. This is especially important when it is required to ensure a time-controlled dissolution of granules in the soil. Moreover, in the case of using multilayer fertilizers, the structure of each layer should ensure the release of components (nutrients) according to a given law.

Obtaining a porous structure of granules is possible both with special processing and simultaneously with the formation of granules:

1. Introduction of pore-forming and modifying additives in the process of granule formation.
2. Introduction of pore-forming and modifying additives in the process of additional processing of already formed granules.
3. Moistening and heat treatment of the formed granules with pore formation due to moisture removal, incl. with components to the humidifier (except for pore-forming and modifying), which can be further used as nutrients.

Research into the needs of the fertilizer market has shown that the most promising direction for increasing the efficiency of nitrogen granules is their encapsulation with phosphate-containing shells. Considering the highest nitrogen losses from urea granules in the soil, it is adopted as the core of the encapsulated granule. The well-known property of phosphates to dissolve more slowly in comparison with nitrogen fertilizers predetermined to take them as the basis of the shell. At the same time, changes in climatic conditions for growing agricultural plants and a decrease in the humus content in the soil require different solutions to increase it. One of the alternatives to compensate for the lack of organic matter is the use of sodium and potassium humates. Considering the removal of significant amounts of nutrients with the harvest, including calcium, we have developed a technical solution for the production and use of calcium humate, which was tested in the conditions of vegetation and small-scale experiments and confirmed its effectiveness.

The basic scheme for obtaining organo-mineral fertilizers can be presented as shown in Fig. 2.

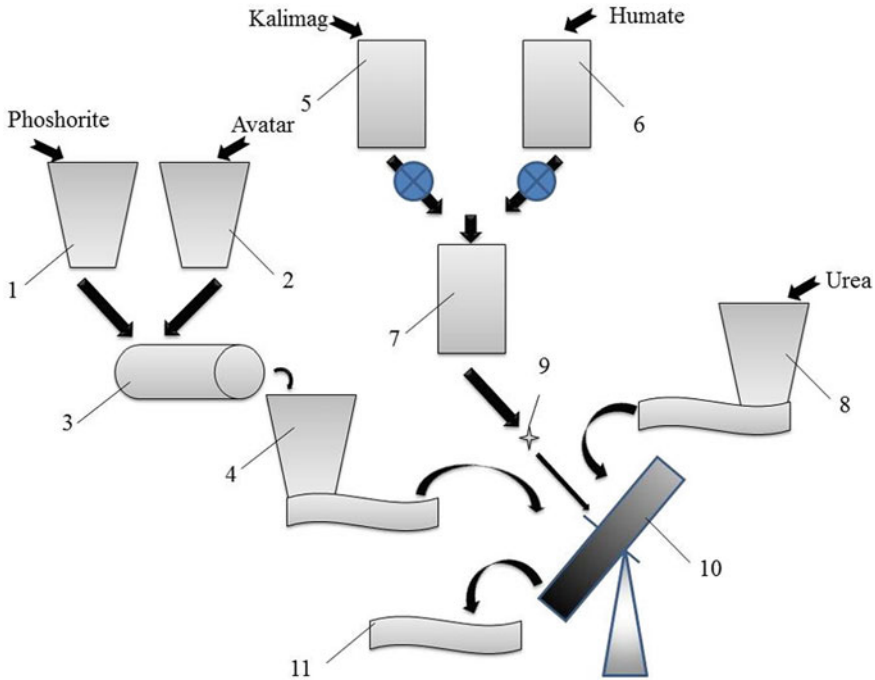


Fig. 2 Model installation for encapsulating fertilizers [13]: 1—phosphorite bunker; 2—microelements bunker; 3—mixer; 4—dispenser; 5—potassium-magnesium solution tank; 6—humate solution tank; 7—potassium-magnesium and humate mixing tank; 8—urea granule feed unit; 9—nozzle; 10—disc granulator; 11—tray for granulated product

Obtaining a nanoporous structure of the granule shell is one of the ways to ensure a given rate of dissolution of fertilizer with soil moisture. The amount of moisture that can penetrate into the membrane and stay there to ensure the transfer of nutrients to the kidney depends on the pores' structure, size, and volume. Thus, in this work, two problems are simultaneously solved: the proposal of a new shell composition for encapsulation and the study of the properties of the nanoporous structure of granules of organic-mineral fertilizers.

2 Technological, Constructive, and Optimization Calculation

The developed technical solution for obtaining encapsulated organo-mineral fertilizers consists of forming a phosphate-containing shell on a granule (prill) of carbamide in a pelletizing granulator. The process is carried out by the method of agglomeration of fine powders by wetting them with a plasticizer, which is used as

one of the types of mineral or organic fertilizers. Common shells for encapsulation of nitrogen fertilizers are sulfur, polymer, and suspension coatings. The main substance of the shell is sulfur and polymeric materials applied to the granules in the form of solutions or suspensions. The introduction of polymer components into the shell composition reduces the overall nutritional value of the fertilizer. It requires special conditions to apply a uniform thickness of a thin solid coating, which significantly increases the cost of fertilizers.

To increase the nutritional value of the encapsulated fertilizer, shells based on suspensions of ammophos or powdered ammoniated superphosphate and phosphorite concentrates have recently been used. Aqueous solutions of other fertilizers are used as a plasticizer to form the shell based on powdered phosphates. However, the use of solutions of inorganic fertilizers in the composition of such a shell does not allow to create its stable porous structure, which when dissolving the shell increases its pore size and increases the rate of dissolution of the nitrogen core of the granule.

The shells of encapsulated fertilizers formed on the core of nitrogen, phosphorus, or potassium fertilizers are known. They include an inorganic substance in the form of a natural phosphorus-glaucinite concentrate as the base of the shell, and a binder in the form of aqueous solutions of potassium or nitrogen fertilizers, or combinations thereof. The disadvantage of such granule structure forming is the use of aqueous solutions of nitrogen and potassium fertilizers as a plasticizer, which leads to the rapid dissolution of these fertilizers in the soil and does not allow the creation of a porous shell structure for the entire period of dissolution of the granule core.

The prototype is the shells of nitrogen fertilizers, which include powdered ammoniated superphosphate moistened with calcium humate as a plasticizer, which is formed by agglomeration, followed by rolling and drying of the encapsulated product. Shell formation is carried out at a ratio of inorganic coating substance and calcium humate 1 (0.0012 ÷ 0.01).

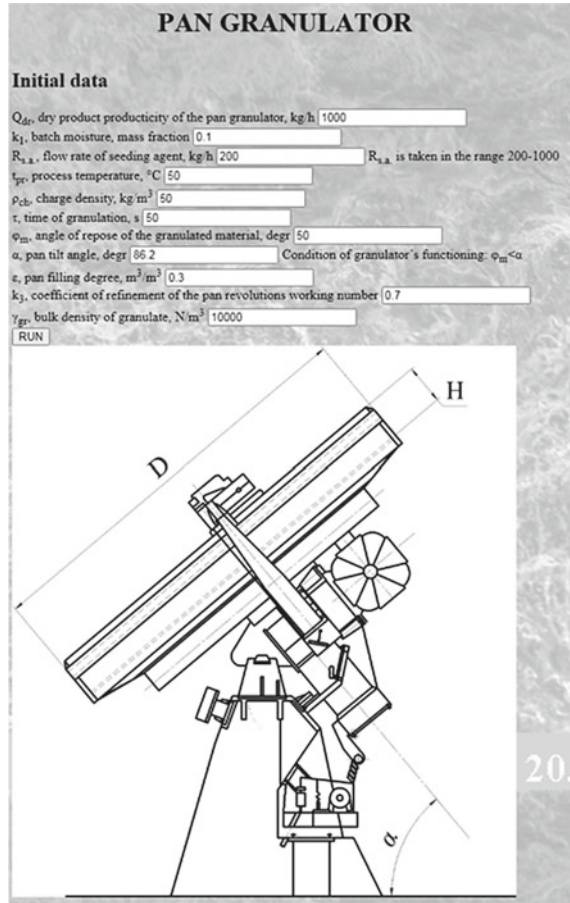
The disadvantage of these shells of nitrogen fertilizer granules is the use of powdered ammoniated superphosphate, which requires pre-acid decomposition of phosphorite and low pH of the fertilizer as a whole, which affects the degree of crop yield.

The new model is based on the task of creating a microporous coating of nitrogen fertilizer granules, which effectively acts to increase crop yields on all types of soils.

The problem is solved by using phosphate-glaucinite concentrate with the addition of biochar in the amount of 5–10% by weight of phosphate-glaucinite concentrate and an aqueous solution of calcium humate. The ratio of a mixture of phosphate-glaucinite concentrate with biochar and calcium humate is 1: (0.09–0.11).

The physical model of encapsulation can be represented as follows. A fraction (2–4) mm of carbamide granules, powdered phosphate-glaucinite concentrate with a particle size of fewer than 200 microns, and an aqueous solution of calcium humate containing up to 85% water are preliminarily prepared by sieving. Urea granules are encapsulated in a disc granulator (Fig. 3) on the pellet surface while simultaneously dosing urea granules, powdered phosphate-glaucinite concentrate into the granulator, and wetting the surface of the granules, and powder with a plasticizer in the form of an aqueous calcium humate solution.

Fig. 3 Design scheme of the granulator and initial data for calculating the encapsulation process



When the granulator plate rotates, the moistened carbamide granules move (roll) along the trajectory of an irregular spiral, and as they increase in size, approach the plate side, and are discharged from it. The process of granule growth occurs due to the adhesion of moist small particles of phosphate-glaucanite concentrate. In the process of pellet rolling, these particles are compacted on the surface of the granule, then after the next cycle of irrigation and rolling of the granule, additional adhesion occurs, followed by compaction of other particles, and so on until the required thickness of the granule shell is reached. At a certain, given diameter, it rolls over the side of the plate. Further, the encapsulated granule is sent for drying, followed by the separation of the commercial fraction.

Implementing the encapsulation process on a pan granulator has its advantages. After reaching the required size, the granules are removed from the apparatus, and visual control of the granule growth process allows you to quickly track changes in the technological parameters of encapsulation.

To obtain encapsulated organo-mineral fertilizers when conducting laboratory studies, carbamide granules of fraction 2–4 mm were used, with 46.1% nitrogen, phosphate-glaucinite concentrate with a total content of P_2O_5 14%, and a particle size of no more than 200 microns, potassium and calcium humates with a mass moisture content of 85 and 87%, and the mass fraction of potassium and calcium humates (in terms of dry matter) 18 and 16%, respectively. At the same time, the humate solution has a $pH = 10.8$, which allows us to consider it as a blocker of heavy elements in the soil. Biochar powder was prepared by sieving to a fraction of fewer than 200 microns, with a carbon content of 93%. The production of potassium and calcium humates was carried out on a model homogenizer.

The general technique of the experiment is described in [15].

The choice of a plasticizer in the form of potassium and calcium humates is due to the positive results of agrochemical tests, which showed an additional increase in yield compared to a plasticizer based on potassium (an aqueous solution of potassium mag). In the first series of experiments, the dependence of the strength of the applied coating on the amount of plasticizer-calcium humate was determined (Table 1).

As follows from the experimental data obtained, the dependence of the strength of the granules on the moisture content of the granulated phosphate-containing mixture is extreme depends on the rheological properties of the phosphate-containing additive, and the optimal amount of moisture is 12.5%, which correlates with the data of other researchers—8–15%. When the moisture content of the phosphate-containing charge is less than 10%, not all of the charge is uniformly moistened and cannot be involved in the agglomeration process. In this case, the rolling process is disrupted, and the strength of the phosphate-containing shell is low, with low adhesion of the shell to the carbamide granule. When the moisture content of the charge is more than 15%, the phosphate-containing charge is granulated to a moisture content of 12.5%. Then, the over moistening of the charge follows with the formation of stuck together granules and ultimately, the disruption of the agglomeration process. Additional studies on introducing a carbon-containing nanoporous additive—biochar into the shell composition—showed an insignificant change in the moisture content of the charge while maintaining the trend of optimal moisture content. It was interesting to determine the maximum amount of biochar that can be introduced into the composition of the phosphate-containing shell. In experiment 1, biochar was not introduced into the composition of the shell (comparison experiment). In experiments 2–5, it

Table 1 Results of the study of the consumption of the plasticizer on the properties of the granule

Indicator	Experience number				
	1	2	3	4	5
Plasticizer consumption, %	8	10	12.5	15	20
Granule strength, kgf/granule	0.7	1.32	1.5	1.05	0.95
Moisture content of finished granules	0.1	0.25	0.7	0.65	0.53

Table 2 Results of experimental studies

Indicator	Experience number				
	1	2	3	4	5
Biochar content in the shell, %	–	5	10	10	15
Plasticizer consumption, %	25	25	25	30	25
Strength of granules, kgf/granule	1.5	1.26	1.085	1.035	0.97
Moisture content of finished granules	0.12	0.19	0.15	0.095	0.32

was introduced in various quantities with its preliminary mixing with phosphate-glaucanite concentrate. The results of experimental studies are presented in Table 2.

As follows from the presented experimental results, for a given phosphate-containing mixture, the maximum content of biochar based on the strength characteristics of the shell is not more than 10%. At the same time, according to other researchers' data, its effect on increasing fertilizer efficiency begins to show itself even when it is present in 1%. Thus, an increase in the content of biochar with nano-sized pores will make it possible to more efficiently use the nutrient elements of the granule and accordingly, increase the yield of agricultural crops. This statement was confirmed during test vegetation experiments and showed an increase in yield compared to the sample without nanoporous additives by 23%.

3 Phase Composition and Crystal Structure of Granules of Organic-Mineral Fertilizers

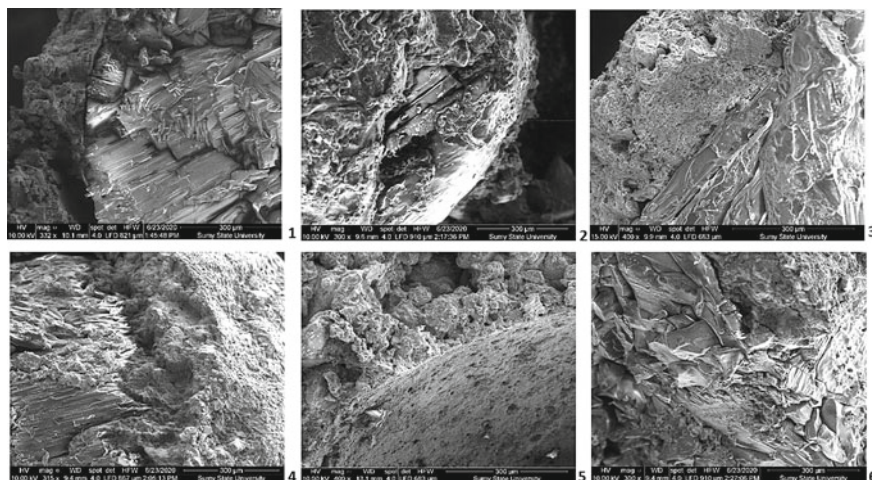
The main characteristics of samples of organic-mineral fertilizers are presented in Table 3.

Samples 5 and 6 contained biochar in various compositions. According to the results of the experiments, a composition with 10% biochar addition into a phosphate shell with calcium humate as a plastiziser was more successful for obtaining the nanoporous shell. The cross-section analysis of obtained samples showed that with the addition of biochar into phosphate coating of the granule, the attachment between granule of carbamide and phosphate shell increased, and the interface between layers became more uniform structure (Fig. 4). The addition of biochar slightly decreases the density of the granules but makes such fertilizers more appropriate for agricultural application.

The nanoporous structure of biochar is presented in the Fig. 5a. A micrograph of biochar microstructure is shown in the Fig. 5b, c.

Table 3 Composition of produced samples of fertilizers based on carbamide in phosphate shell [15]

No. of sample	Composition, %			Plasticizer	The density of granules, MPa
	P ₂ O ₅ , %	N, %	K ₂ O, %		
Sample 1	7.20	23.80	0.31	Calcium humate	2.10
Sample 2	7.13	23.60	0.21	Potassium humate	2.07
Sample 3	7.84	21.80	0.42	Potassium-magnesium	2.09
Sample 4 with "Avatar"	7.40	22.80	0.21	Calcium humate	1.71
Sample 5 with the addition of biochar to the shell	8.90	25.60	2.20	Potassium humate	1.06
Sample 6 with 10% of biochar	8.10	25.90	0.39	Calcium humate	1.00

**Fig. 4** SEM images of granules cross section containing carbamide in phosphate shell with various plastisizers 1—calcium humate, 2—potassium humate, 3—potassium-magnesium, 4—calcium humate with complex Avatar, 5—potassium humate with biochar addition to the shell, 6—calcium humate with addition of 10% biochar into phosphate shell

4 Conclusions

The research results have shown that the improvement of the composition of the organic shell in the process of encapsulating the mineral fertilizer makes it possible to create a developed nanoporous structure of this shell. The introduction of biochar into the shell leads to the formation of an ordered structure of organic-mineral fertilizer and the creation of conditions for a controlled process of its solubility in soil.

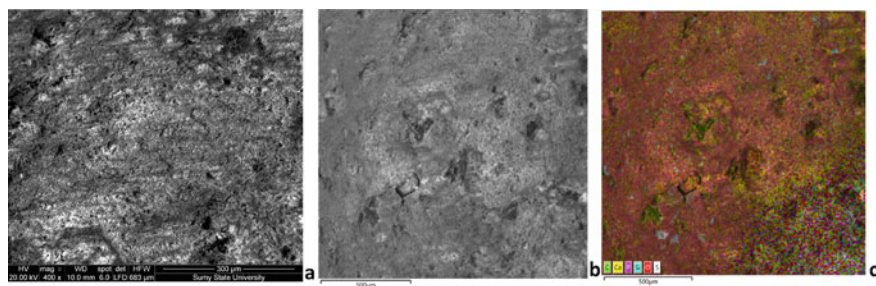


Fig. 5 SEM image of biochar morphology (a) and biochar microstructure (b) with elemental analysis (c) with an increase in $\times 5000$

The introduction of a new type of fertilizer will increase the security of producers and consumers, improve national security, global competitiveness, inclusive, and “green” economic growth, and accelerate the achievement of the Sustainable Development Goals and climate neutrality.

The research results obtained allow in future to assess the competitiveness of a new type of fertilizer in the context of the concept of sustainable innovative outpacing.

Acknowledgements This research work had been supported by the Ministry of Science and Education of Ukraine under the project No 0120U102003 “process of formation of the novel ecologically safe fertilizers with prolonged action based on the phosphorite deposits raw materials”.

References

1. Wang C (2015) Explaining connotation of regional green transition. In: Proceedings of the 2015 International conference on industrial technology and management science (ITMS 2015), 34, 1203–1205
2. Sutherland LA, Darnhofer I, Wilson GA, Zagata L (2015) Transition pathways towards sustainability in agriculture: case studies from Europe. CABI Publishing
3. Shen J, Zhu Q, Jiao X, Ying H, Wang H, Wen X, Xu W, Li T, Cong W, Liu X, Hou Y, Cui Z, Oenema O, Davies WJ, Zhang F (2020) Agriculture green development: a model for China and the world. *Front Agri Sci Eng* 7(1):5–13
4. European Commission (2021) The European Green Deal
5. European Commission (2021) Communication from the commission to the European Parliament, the Council, the European economic and social committee and the committee of the regions ‘Fit for 55’: delivering the EU’s 2030 Climate Target on the way to climate neutrality. COM/2021/550 final
6. World Economic Forum (2021) The Global Risks Report 2021
7. European Environment Agency (2021) EEA greenhouse gases—data viewer. Data viewer on greenhouse gas emissions and removals, sent by countries to UNFCCC and the EU Greenhouse Gas Monitoring Mechanism (EU Member States)
8. UNFCCC (2021). National Inventory Submissions 2021

9. UNFCCC (2021) Ukraine. 2021 Common Reporting Format (CRF)
10. State Statistics Service of Ukraine (2021) Application of mineral and organic fertilizers (1919–2020)
11. Resolution of the Cabinet of Ministers of Ukraine (2021) On approval of the National Economic Strategy for the period up to 2030” from 03.03.2021 No. 179
12. Ministry of Environmental Protection and Natural Resources of Ukraine (2021) Draft Concept of “green” energy transition of Ukraine until 2050
13. Artyukhov A, Vakal S, Shkola V, Vakal V, Yanovska A (2021) Obtaining of the novel organo-mineral fertilizers in pan granulators: technological fundamentals. In: Ivanov V, Pavlenko I, Liaposhchenko O, Machado J, Edl M (eds) *Advances in design, simulation and manufacturing IV. DSMIE 2021. Lecture Notes in Mechanical Engineering*, 207–217
14. Shkola V, Prokopenko O, Stoyka A, Nersesov V, Sapiński A (2021) Green project assessment within the advanced innovative development concept. *Estudios de Economía Aplicada* 39(5)
15. Vakal S, Yanovska A, Vakal V, Artyukhov A, Shkola V, Yarova T, Dmitrikov V, Krmela J, Malovanyy M (2021) Minimization of soil pollution as a result of the use of encapsulated mineral fertilizers. *J Ecol Eng* 22(1):221–230
16. Kotenko O, Domashenko M, Shkola V (2019) Production costs decreasing by introduction of energy-efficient technologies within the enterprise’s counter-crisis management strategy. *Inter J Ecol Econ Statis* 40(3):88–97
17. Kurbatova T, Skibina T (2019) Renewable energy policy in Ukraine’s household sector: measures, outcomes, and challenges. In: *IEEE International Conference on Modern Electrical and Energy Systems*, 234–237
18. Kurbatova T, Sotnyk I, Kubatko O, Baranchenko Y, Arakpogun E, Roubik H (2020) State support policy for renewable energy development in emerging economies: the case of Ukraine. *Inter J Global Environ Issues* 19(1–3):26–52
19. Trypolska G, Kravda O, Kurbatova T, Andrushchenko O, Suleymanov C, Brydun Y (2021) Impact of new renewable energy capacities on employment in Ukraine in 2021–2030. *Inter J Energy Econ Policy* 11(6):98–105
20. Artyukhov A, Artyukhova N, Krmela J, Krmelová V (2020) Granulation machines with highly turbulized flows: creation of software complex for technological design. In: *IOP Conference Series: Materials Science and Engineering* 776(1):Article no. 012018
21. Artyukhov A, Artyukhova N, Krmela J, Krmelová V (2020) Complex designing of granulation units with application of computer and software modeling: case “Vortex granulator”. *Mat Sci Eng* 776(1):Article no. 012016
22. Artyukhov A, Artyukhova N (2018) Utilization of dust and ammonia from exhaust gases: new solutions for dryers with different types of fluidized bed. *J Environ Health Sci Eng* 16(2):193–204
23. Artyukhov AE, Artyukhova NO (2019) Technology and the main technological equipment of the process to obtain N_4HNO_3 with Nanoporous Structure. *Springer Proc Phys* 221:585–594
24. Artyukhov AE, Ivaniia AV (2017) Obtaining porous ammonium nitrate in multistage and multifunctional vortex granulators. *Naukovyi Visnyk Natsionalnoho Hirnychoho Universytetu* 6:68–75
25. Ivaniia AV, Artyukhov AY, Olkhoviy AI (2019) Hydrodynamic and thermodynamic conditions for obtaining a nanoporous structure of ammonium nitrate granules in vortex granulators. *Springer Proc Phys* 221:257–268
26. Artyukhov AE, Krmela J, Gavrylenko OM (2019) Evaluation of the impact made by the hydrodynamic regime of the granulation equipment operation on the nanoporous structure of N_4HNO_3 granules. *J Nano Elect Phys* 11(3):03033
27. Yukhymenko M, Ostroha R, Artyukhov A (2016) Hydrodynamic and kinetic processes of the mineral fertilizer granules encapsulating in the multistage device with suspended layer. *Eastern-European J Enter Technol* 6(6–84):22–28
28. Ostroha R, Yuhymenko M, Yakushko S, Artyukhov A (2017) Investigation of the kinetic laws affecting the organic suspension granulation in the fluidized bed. *Eastern-European J Enterprise Technol* 4(1):4–10

29. Chuah CY, Li W, Yanqin Yang Y, Bae T-H (2020) Evaluation of porous adsorbents for CO₂ capture under humid conditions: the importance of recyclability. *Chem Eng J Adv* 3:100021
30. Broom D (2021) Characterizing adsorbents for gas separations Measurement needs and laboratory techniques (white paper). Hiden Isochema

Nanostructure Surfaces

Dispersion Kinetics of Thin Double Hafnium-Copper Films Deposited onto Oxide Materials and Annealed in Vacuum



T. V. Stetsyuk, I. I. Gab, O. M. Fesenko, and D. B. Shakhnin

Abstract Dispersion kinetics research of two-layer hafnium-copper coatings (films) onto oxide materials (leucosapphire, alumina, and zirconia ceramics) during annealing in vacuum at 900–1100 °C at different annealing time in the range of 2–20 min are describe. According to the research results, the kinetic curves of film dispersion are built. Based on these graphs, the parameters of the joining of metallized non-oxide materials by soldering were selected.

Keywords Dispersion · Kinetics · Two-layer hafnium-copper coatings · Oxide materials · Annealing · Vacuum · Temperature

1 Introduction

Joining ceramic materials with each other and with metals is carried out by two main methods:

- (1) brazing with molten metallic solders [1–3];
- (2) solid-phase pressure welding [4–6].

Since ceramic materials, particularly oxide ones, are usually poorly wetted by molten metals, metal coatings are often used applied in various ways (electron-beam sputtering, magnetron sputtering, chemical deposition, etc.). Adhesive-active metals such as titanium, chromium, niobium, and others are the most commonly used to make such coatings. Then, thus, metallized ceramic parts are brazed in vacuum or

T. V. Stetsyuk (✉) · I. I. Gab
Frantsevich Institute for Problems of Materials Science of National Academy Sciences of Ukraine, 3, Krzhynzhanskyi St, Kyiv 03142, Ukraine
e-mail: tvst@ukr.net

O. M. Fesenko
Institute of Physics of National Academy Sciences of Ukraine, 46, Nauky Ave, Kyiv 03680, Ukraine

D. B. Shakhnin
University “Ukraine”, 23 Lvivska St, Kyiv 03115, Ukraine

an inert medium (argon, helium, etc.) by molten metallic solders on the basis of tin, silver, copper, nickel, etc. In this case, the thickness of the solder seam is from 50 to 100 μm up to several millimeters. Sometimes, multilayer metal coatings are used, but the thickness of the layers and brazed seams remains high [7–9].

At the same time, there is information that the reduction in the thickness of the brazed seam leads to a significant increase in the strength of the brazed joint [10–12]. Obtaining brazed or welded joints of metallized ceramics is possible through reducing the thickness of both the metallization coating on the ceramics and the brazing layer by itself. This can be achieved if the soldering metal or alloy is also applied in the form of a rather thin film, the thickness of which does not exceed several μm . In addition, a thin soldering seam allows you to obtain precision welded or brazed ceramic and ceramic–metal units which can be used in microelectronics, radio engineering, microwave engineering, etc.

This objective can be achieved by application onto the ceramic surfaces of double metal films, one of which is 100–200 nm thick and consists of an adhesion-active metal such as Ti, Cr, and Hf, and the other is slightly thicker (2–3 μm) and serves as a solder, e.g., Cu, Ag, Ni, etc., which will ensure joining of metallized ceramic materials during brazing or welding with fine (2–4 μm thickness) solder seam.

The structure of such two- or multiphase coatings, determination of the optimal ratio of the thickness of each layer, processes of interaction at the phases interface, and behavior of these double films, during annealing of them, is also an important area of research.

The study of dispersion kinetics two-layer hafnium-copper coatings (films) on oxide materials during annealing in vacuum and the creation of brazed and welded oxide ceramics joints based on them with super-thin brazed seam, the thickness of which does not exceed 3 μm , is the main task of the present work.

2 Materials and Experimental Methods

In this paper, an electron-beam method for sputtering of metal (Hf, Cu) thin films was used.

The thickness of the deposited films was measured by two methods:

- (1) the metal of the given weight (calculated for films of the required thickness) is completely evaporated; then, the thickness of the film can be easily calculated according to the law of Lambert [13, 14];
- (2) with the help of a special quartz sensor located in the vacuum sputtering chamber near the sample on which the film is deposited.

Solid non-metallic substrates were made of leucosapphire, alumina, and zirconia ceramics as small thin plates $4 \times 3 \times 2$ mm in size. One of the flat surfaces of each specimen was well polished to a roughness $R_z = 0.03\text{--}0.05$ μm . After polishing, all specimens were thoroughly defatted and burned in air at 1100 $^\circ\text{C}$ for 1 h.

As a metal deposited directly onto non-metallic surfaces, hafnium was used. Metallized samples were then coated by copper films serving as a solder when joining the samples.

The quality of all applied thin films was controlled using a XJL-17 metallographic microscope.

The specimens with deposited onto them metal films were annealed in a vacuum chamber for various periods of time (from 5 up to 20 min) and at different temperatures (from 900 to 1100 °C) in the vacuum no worse than 2×10^{-3} Pa.

Annealed specimens were investigated using SEM and ASM microscopy with microphotographs storing. Using these microphotographs, the areas of metal islets on the surface of non-metallic samples were determined by the planimetric method [10]. The experimental data obtained were processed in the form of graphs showing the dependence of the surface area of the samples covered with metal thin films on the annealing parameters (temperature, time).

3 Results and Discussion

The double hafnium-copper film on substrates of leucosapphire, alumina, and zirconia ceramics consisted of a hafnium metallization layer 150 nm thick, on which a copper layer 1.5 μm thick was deposited.

The original hafnium-copper films on all three oxides were continuous and remained almost unchanged after 5 min of annealing at 900 °C. After 10 min of exposure at this temperature, noticeable changes occurred in the film, which intensified after 20 min of annealing (Fig. 1). As a result of annealing of films at 1000 °C, noticeable changes in their morphology were found after 5 min; after 10 min, these changes intensified; and after 20 min of annealing, there were noticeable signs of dispersion (Fig. 2) although the integrity of the films was still quite significant since they are still covering more than 80% of the substrates surface area. Of course, a further annealing temperature rise had, as in previous cases, accelerated the films dispersing process. So, after 5 min of annealing at 1050 °C, significant changes in the films' morphology were revealed, intensifying after 10 min; and after 20 min of annealing, the film began to crack. (Fig. 3). An increase in the annealing temperature up to 1100 °C led to the films integrity violation by swelling and cracking after only 5 min. This is very clearly shown by the images of the hafnium-copper double film onto leucosapphire (Fig. 4a) and zirconia ceramics (Fig. 4b) at high magnification under an atomic force microscope. After 20 min of annealing at 1100 °C, the films were not only dispersed, but also, apparently, copper began to interact with hafnium metallization of oxides (Fig. 5).

In Fig. 6, kinetic curves of dispersion of copper films on oxides metallized with hafnium nanofilms and annealed in vacuum at temperatures of 900–1100 °C at different exposition times.

Using a double hafnium-copper film, joint of zirconia ceramics was obtained by soldering at a temperature of 1100 °C under low load up to 2 MPa (Fig. 7). The

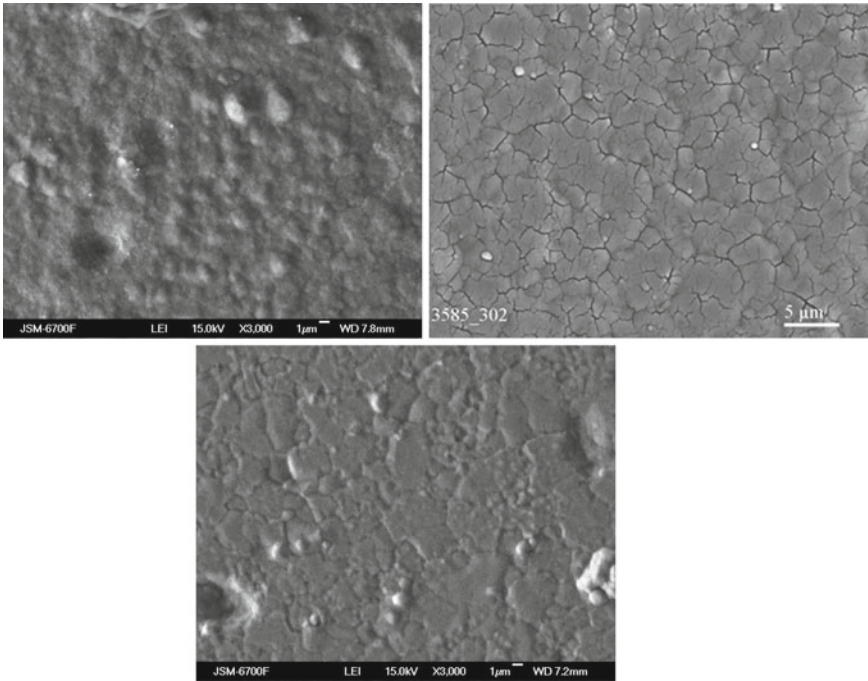


Fig. 1 SEM image ($\times 3000$) double hafnium-copper film deposited onto oxide materials and further annealed at 900 °C during 20 min in vacuum: **a** alumina ceramics; **b** leucosapphire; **c** zirconia ceramics

thickness of the soldered seam was about 2 μm , and the shear strength of the joint reached 130 MPa.

4 Conclusions

The kinetics of decomposition during vacuum annealing of double hafnium-copper films deposited on leucosapphire, alumina, and zirconia ceramics was studied. Annealing was performed in vacuum not worse than 2×10^{-3} Pa at temperatures up to 1100 °C with different exposition times at each temperature (from 5 up to 20 min). The behavior of the films on all three oxides during annealing was almost identical. It was found that the first slight changes in the films appear after 10 min of annealing at 900 °C. Further increase in the annealing temperature intensifies the process of changing the morphology of the films, especially with increasing annealing time. In particular, after 20 min at 1000 °C, noticeable signs of dispersion were already found, and after 20 min of annealing at 1050 °C, the film began to crack. At 1100 °C,

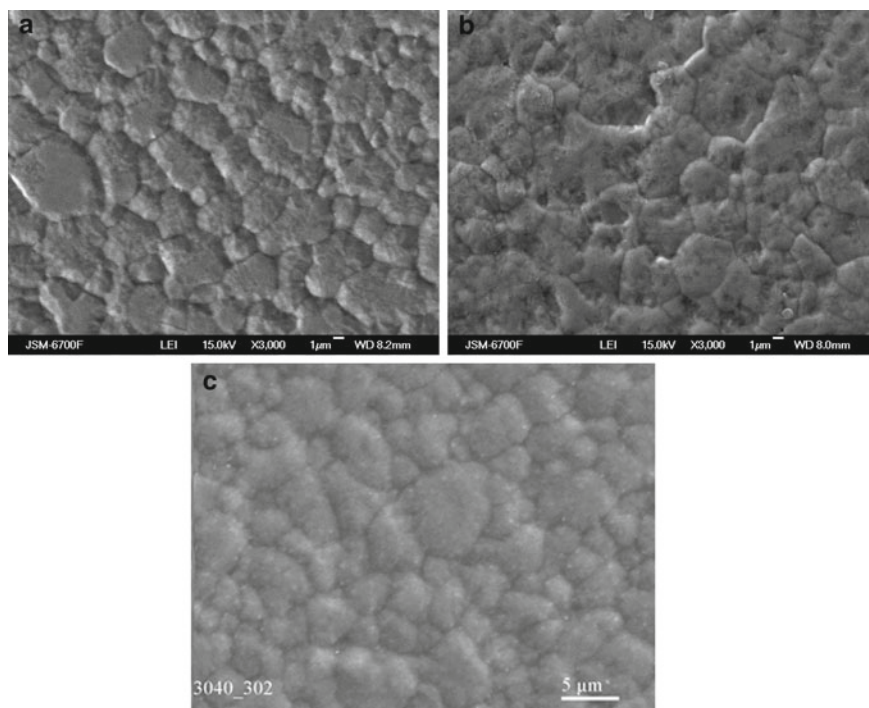


Fig. 2 SEM image ($\times 3000$) double hafnium-copper film deposited onto oxide materials and further annealed at 1000 °C during 20 min in vacuum: **a** alumina ceramics; **b** leucosapphire; **c** zirconia ceramics

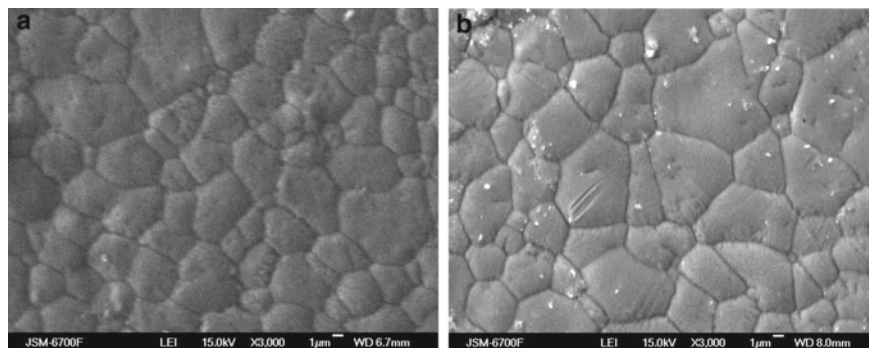


Fig. 3 SEM image ($\times 3000$) double hafnium-copper film deposited onto oxide materials and further annealed at 1050 °C during 20 min in vacuum: **a** alumina ceramics; **b** leucosapphire; **c** zirconia ceramics

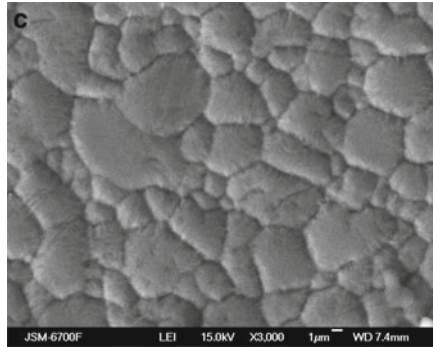
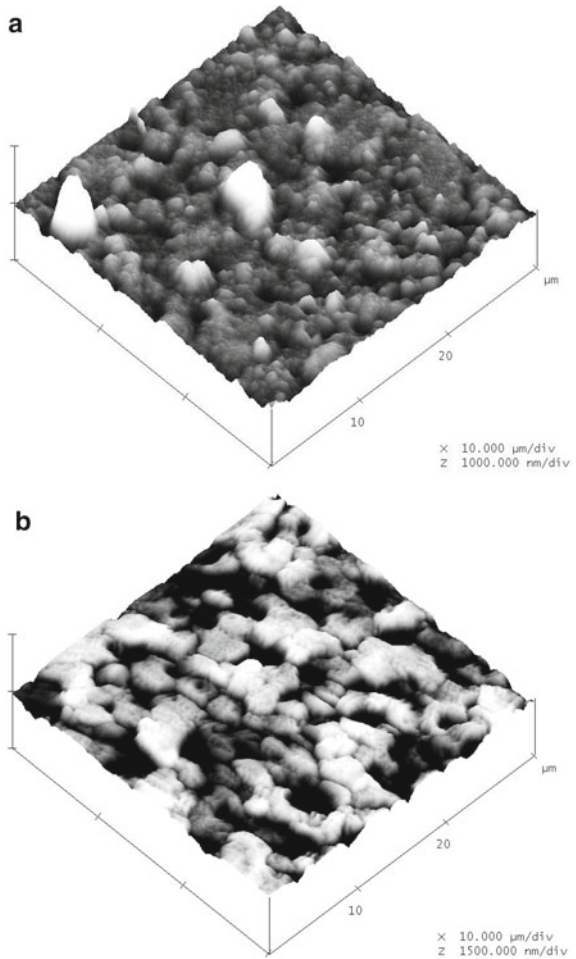


Fig. 3 (continued)

Fig. 4 Three-dimensional AFM image thin double hafnium-copper film deposited onto oxide materials and further annealed at 1100 °C during 5 min in vacuum: **a** leucosapphire; **b** zirconia ceramics



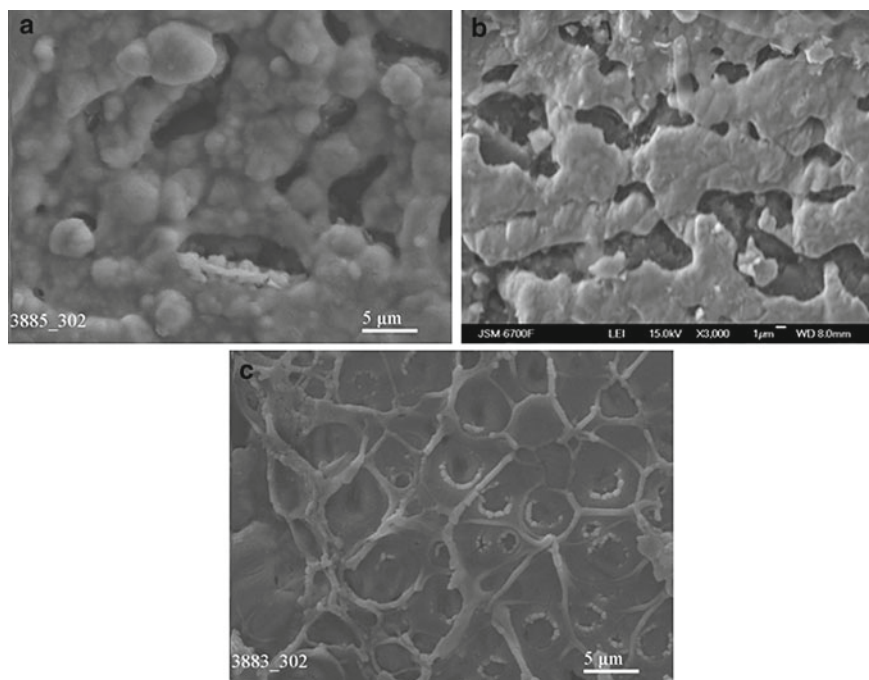


Fig. 5 SEM image ($\times 3000$) double hafnium-copper film deposited onto oxide materials and further annealed at $1100\text{ }^{\circ}\text{C}$ during 20 min in vacuum: **a** alumina ceramics; **b** leucosapphire; **c** zirconia ceramics

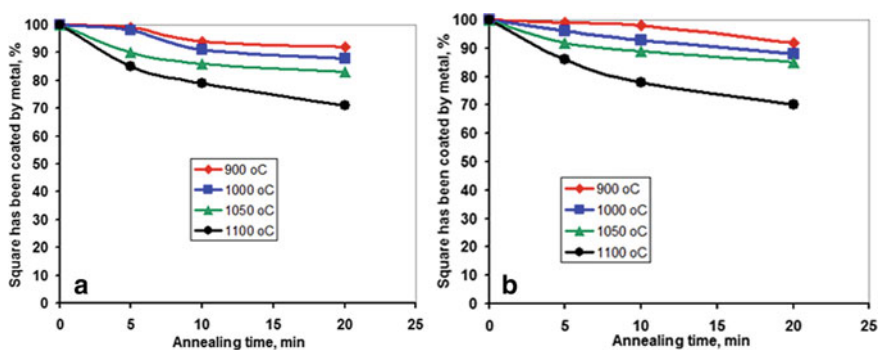


Fig. 6 Dependence of oxide materials surface area covered with a double hafnium-copper film on the annealing time at different temperatures (900–1100 °C): **a** alumina ceramics; **b** leucosapphire; **c** zirconia ceramics

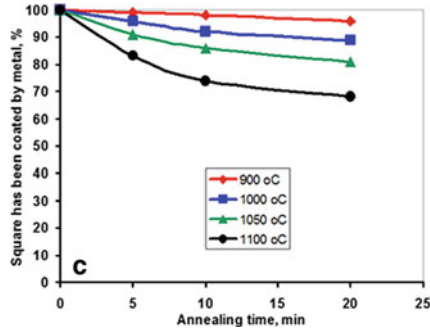
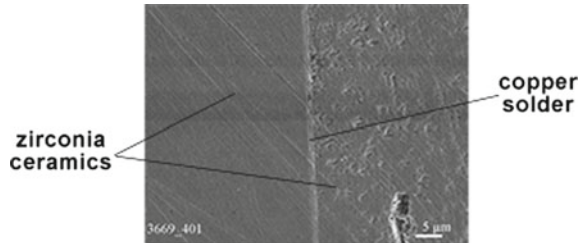


Fig. 6 (continued)

Fig. 7 The soldered joint of zirconia ceramics through a double hafnium-copper film with ultrathin seam, $\times 2000$



the film disperses significantly, and, after a 5-min exposure, the interaction of copper with hafnium metallization of oxides occurs.

According to the research results, the kinetic curves of film dispersion are built, using which it is possible to select the optimal parameters (temperature, time) of the processes of metallized ceramics joining. Based on these graphs, the parameters of the joining of metallized zirconia ceramics by soldering were selected, according to which the joints themselves were made with an ultrathin seam about $2 \mu\text{m}$ thick, the shear strength of which reached 140 MPa.

References

1. Yevdokimov VR, Kashtanov SL, Lado LN, Shubin SN (1995) Diffuzionnaya svarka okhvatyvayushchego soyedineniya alyumooksidnoy keramiki s korrozionnostoykoy stal'yu. *J Svarochnoye proizvodstvo* 8:2 (in Russian)
2. Request 60–239373, C04B 37/02, B23K 20/00, 28 Nov. 1985
3. Request 380163, C04B 37/02, B23K 3/00, 04 Apr. 1991
4. Yu N (1999). High strength ceramics brazed joints: scientific and technological bases. *J Industrial Ceramic* 19(3):162
5. Andreyev AA, Kostyuk GI, Minayev NA (2012) Effektivnyye nanostrukturnyye mnogoslownyye pokrytiya dlya rezhushchikh instrumentov i detaley meditsinskogo naznacheniya, rabotayushchikh v dinamicheskom rezhime. *J Aviatsionno-kosmicheskaya tekhnika i tekhnologiya* 2(89):28 (in Russian)

6. Zaytsev SV, Gerasimenko YuV, Lobanov MV, Khoviv AM (2014) Issledovaniye morfologii poverkhnosti oksidiro-vannykh plenok sistem Ti-Nb. *J Kondensirovannyye sredy i mezhfaznyye granitsy* 16(2):153 (in Russian)
7. Lobanova TA, Volkhonskiy AO, Blinkov IV (2013) *J Innovatsionnyye tekhnologii polucheniya iznoso-toykich i triboadaptiruyemykh pokrytiy v industrii nanosistem* 1(10):76 (in Russian)
8. Velikodnyy DV, Protsenko CI, Protsenko IYe, (2008) Tenzoeffekt v dvukhsloynnykh plenkakh Cu/Cr i Fe/Cr. *J Fizicheskaya inzheneriya poverkhnosti*. 6(1–2):37 (in Russian)
9. Naveed M, Obrosof A, Weib S (2015) Investigation of the wear resistance properties of Cr/CrN multilayer coatings against sand erosion. *Hindawi Publ. Corp. Conf. Papers in Sci. Volume. Article ID 873543*. <https://doi.org/10.1155/2015/873543>
10. Naydich Y, Gab II, Kostyuk BD, Stetsyuk TV, Kurkova DI, Dukarov SV (2007) Investigation of the ceramic materials connection processes (soldering) using metal nanofilms. *J Rep Natl Acad Sci Ukr* 35:97 (in Ukrainian)
11. Naydich YuV, Gab II, Kostyuk BD, Stetsyuk TV, Kurkova DI, Dukarov SV (2006) Issledovaniye struktury, morfologii i smachiva-niya metallami metallicheskich nanoplenok, nanesennykh na poverkhnost' oksida alyuminiya s tsel'yu polucheniya svarnykh i payanykh soyedineniy materialov na yego osnove. *J Tekhnika mashinostroyeniya* 1:28 (in Russian)
12. Yakovich VM, Komarovskaya VM (2016) *Mnogosloynnyye pokrytiya. Inzhenerno-pedagogicheskoye obrazovaniye v XXI veke: materialy XII Respublikanskoy nauchno-prakticheskoy konferentsii molodykh uchenykh i studentov BNTU, Minsk, pp 215–218* (in Russian)
13. Metfessel S (1963) *Tonkie plenki, sh szgotovlenie I izmerenie*. Gosenergoizdat, Moscow-Leningrad (in Russian)
14. Khaas G, Tun PE (1968) *Thin film physics*. Mir, Moskow (in Russian)

Structure-Properties Relationships of Nanocomposites Based on Polyethylene Oxide and Anisometric Nanoparticles



E. A. Lysenkov, Valeriy Klepko, and M. M. Lazarenko

Abstract The electrical properties of systems based on polyethylene oxide (PEO), carbon nanotubes (CNTs), and organoclays were studied using the methods of X-ray diffraction analysis, optical microscopy, and impedance spectroscopy. It is established that the introduction of nanofillers into the PEO matrix leads to a significant reduction in its degree of crystallinity. For systems filled with CNTs, a percolation transition is observed, which was analyzed in the framework of the scaling approach. It was found that the structure of composites that contain organoclays significantly depends on their type. For systems containing montmorillonite, the process of intercalation is observed, and for systems filled with laponite, there is exfoliation of organoclay. It is shown that when organomodified laponite (OLP) is introduced into the system, the percolation threshold is shifted to the region of lower CNT concentrations. At the same time, loosening of aggregates from CNT is observed. Modeling of impedance spectra for systems based on PEO by the method of equivalent circuits is carried out. It is established that the introduction of OLP more than 0.4% into the system leads to a significant reduction in electrical conductivity. This effect is explained by the fact that the OLP plates form their own network and prevent the formation of direct contacts between nanotubes.

Keywords Polymer nanocomposites · Carbon nanotubes · Organoclay · Percolation · Electrical conductivity

E. A. Lysenkov (✉)

Petro Mohyla Black Sea National University, Mykolaiv, Ukraine

e-mail: ea.lysenkov@ukr.net

V. Klepko

Institute of Macromolecular Chemistry NAS of Ukraine, Kyiv, Ukraine

e-mail: klepko_vv@ukr.net

M. M. Lazarenko

Taras Shevchenko National University of Kyiv, Kyiv, Ukraine

e-mail: maxs@univ.kiev.ua

1 Introduction

Polymer composites, which contain nanosized fillers (nanocomposites) are the objects of intensive research due to their excellent properties compared to conventional mixtures. Various combinations of polymers and nanofillers have been developed to study their potential to improve the physical properties of the polymers with minimal addition of nanofillers [1–4]. Many authors have shown that the introduction of a small amount of filler (approximately < 1 wt%) in the polymer matrix leads to a rapid increase in the functional characteristics of such composites. Today, there are many types of nanofillers, but the most suitable materials to increase the efficiency of the polymers are carbon nanotubes (CNTs) [5–7] and organoclay [8].

At present, extensive studies have been conducted on nanocomposites containing CNTs, which have been reported to achieve unique mechanical and electrical properties of such materials. The phenomenon of percolation is most pronounced in polymer-CNT systems. Upon reaching the percolation threshold, the electrical conductivity of such systems can increase by more than 10 orders of magnitude. The structure of such a composite changes significantly and percolation clusters of CNTs are formed, which penetrate the entire volume of the material [9].

Like CNTs, organically modified clays are excellent candidates for the fabrication of highly efficient polymer nanocomposites [10]. Montmorillonite (MMT) and its synthetic analog laponite (LP) consist of thin individual layers, several nanometers thick. Unmodified clays have hydrophilic characteristics and require organic modifications to show affinity for hydrophobic polymers.

The peculiarity of the use of organoclay as fillers is the variety of structures that they form in the polymer matrix. For example, depending on the method of preparation of the nanocomposite, the organic clay may be either in the intercalated state or in the exfoliated state. Da Silva et al. investigated bionanocomposites made of polyhydroxybutyrate (PHB), polyethylene glycol (PEG) as plasticizer, and as fillers, the clays: Cloisite 20A organoclay montmorillonite and organophilic vermiculite at concentrations of 1 and 3% by weight. [11]. According to the type of clay used, the systems possibly present partially intercalated or exfoliated structures. Regarding the FTIR, the results indicated that the addition of different clays to PHB/PEG blend did not promote significant changes in the chemistry of the polymer matrix.

The authors of the paper [12] studied the phenomena of intercalation-exfoliation in PEO-organoclay systems. From XRD analyses, it could be said that the increase in the exfoliation degree with the increase in the clay content makes diffusion of PEO chains into interlayer regions easier. In addition, the increased PEO diffusion forces the spherical micelles into lateral bilayer adsorption, which leads to more exfoliation because of the higher clay content.

However, when filling the polymer matrix with nanoparticles, there is a serious problem associated with the aggregation of filler particles. The formation of aggregates of both carbon nanotubes and organoclay particles leads to a deprivation of the properties of the material. One of the ways to overcome aggregation and increase

the properties of polymer nanocomposites is to use a combined filler CNTs and organoclay.

Loginov et al. investigated the effect of laponite on the properties of the water-CNT system and found that in this hybrid system, hydrophilic plates of laponite cover CNT and form a hydrophilic charged shell on their surface [13].

Yaroshchuk et al. proposed a simple and effective approach to improve the distribution of CNTs in E7 liquid crystals [14]. This approach consists in the introduction of nanosized laponite into the E7-CNTs system, which shows a high affinity for nanotubes. Organomodified plates surround the CNTs and prevent the formation of their aggregates. At the same time, laponite nanoparticles do not interfere with the orientational ordering of CNTs in liquid crystal matrices. This approach allows to replace the direct organomodification of CNTs, which is associated with the deterioration of their structure and unique properties. Increasing the degree of CNTs distribution leads to a significant improvement in the dielectric and electro-optical characteristics of the studied suspensions.

Much of the research effort concerning layered materials is directed toward their use as building blocks for the development of hybrid nanostructures with well-defined dimensions and behavior. Chalmpes et al. reported the fabrication through layer-by-layer deposition and intercalation chemistry of a new type of clay-based hybrid film, where functionalized carbon nanotubes are sandwiched between nanometer-sized smectite clay platelets [15]. Smectite clay nanoplatelets act as a structure-directing interface and reaction media for grafting functionalized carbon nanotubes in a bidimensional array, allowing for a controllable layer-by-layer growth at a nanoscale.

The hybrid fillers of 1D multiwalled carbon nanotubes and 2D montmorillonite have led to excellent physical and chemical properties in high performance elastomer nanocomposites. In the study [16], the hybridization of polydiallyldimethylammonium chloride (PDDA) functionalized MWNTs (P-MWNTs) and hydroxyl-functionalized MMT (H-MMT) was prepared by the electrostatic interaction between the positive charge on the MWNTs and the negative charge on the MMT using a simple solution mixing process. The nanocomposites with the hybrid nanofillers exhibited outstanding mechanical properties including modulus, tensile strength, and elongation at break, due to the enhanced interfacial bonding with the elastomer matrix. Furthermore, the hybrid nanofillers in the polymer matrix showed superior thermal and electrical properties and gas barrier performance at low loadings.

The effects of organically modified clay (OMC) incorporation on the microstructure and the electrical and mechanical properties of polypropylene (PP)/polyethylene (PE) blends filled with carbon nanotubes (CNTs) were investigated in paper [17]. All blends were prepared by melt mixing in a batch mixer. The microstructures were characterized by scanning electron microscopy. In the OMC:CNTs filled blends, the CNTs were found to selectively localize within the PE phase, while the clay particles were observed in the PP phase. The electrical resistivity of OMC:CNTs filled blends did not show any significant change as a result of the clay addition since it was localized in the CNTs free phase. On the other hand, the addition of clay degraded

the blends mechanical properties due to the poor adhesion between the OMC and the PP matrix.

Khajehpour et al. investigated the effect of clay addition on the broadband dielectric properties of multiwalled carbon nanotube/polyvinylidene fluoride (MWCNT/PVDF) composites, that is, frequency range of 10^1 – 10^6 Hz [18]. The dielectric spectroscopy showed that introducing clay into the MWCNTs/PVDF nanocomposites at a critical MWCNTs concentration improved dielectric properties tremendously. It was interestingly observed that the incorporation of a specific amount of clay, that is, 1.0 wt%, into the (MWCNTs/PVDF) nanocomposite at a critical MWCNTs loading, that is, 0.5 wt% MWCNTs, resulted in a huge increase in the dielectric permittivity (670% at 100 Hz) and a considerable reduction in the dissipation factor (68% at 100 Hz).

Lysenkov et al. investigated the effect of laponite on the percolation behavior of the polypropylene glycol (PPG)-CNTs system [19]. It is shown that the introduction of organomodified laponite leads to a significant effect on the percolation behavior of the PPG-CNTs system. With the addition of 0.1% laponite, the percolation threshold decreased from 0.45 to 0.2%, and the overall electrical conductivity of the system increased. This effect was explained by the increase in the size of CNTs units due to the better spatial distribution of nanotubes. It has been established that laponite particles cover nanotubes only partially, leaving the possibility of CNTs to form direct contacts. However, as the value of the laponite/CNT ratio increases, the laponite plates completely cover the nanotube, which leads to a significant reduction in the electrical conductivity of the system. Therefore, to achieve a percolation threshold of 0.2%, the optimal ratio of CNTs/laponite (C_{NT}/C_L) should be 2. However, the features of the influence of organomodified laponite on the percolation behavior of the polymer-CNTs system with a fixed value of the ratio of laponite/CNTs remain unexplored. The aim of this work was to study the features of the structure, properties, and percolation behavior of polymer nanocomposites based on polyethylene oxide filled with anisometric nanofillers of different nature.

2 The Experimental Part

Model systems based on polyethylene oxide, carbon tubes, and organoclay were used for the study.

Polyethylene oxide (PEO 1000), $\text{HO}[-\text{CH}_2-\text{CH}_2-\text{O}]_n\text{H}$ ($n \approx 22$) with molecular weight $M_w = 1000$, manufactured by Aldrich. At $T = 298$ K, PEO-1000 is a solid with a density $\rho = 1225$ kg/m³ and a viscosity $\eta \approx 120$ MPa s. The melting point is 308 K.

Multiwalled CNTs manufactured by Spetsmash Ltd. (Ukraine) are made of ethylene by chemical vapor deposition (CVD) using a FeAlMo catalyst. The content of mineral impurities was not more than 0.1%. Specific surface is 190 m²/g, outer diameter is 20 nm, length is equal $(5 \div 10)$ μm , and aspect ratio $L/d \approx 250 \pm 170$. The density of CNTs is equal to the density of pure graphite and is $\rho = 2045$ kg/m³.

Montmorillonite (MMT) and artificially synthesized laponite (Laponite-RD) manufactured by Southern Clay Products were used as a layered nanofiller. Transition of MMT and LP into organoform was performed according to the following method. To facilitate the conversion of the clay to the organoform, the clay was pre-converted to the sodium form by treating the aqueous dispersion of the mineral (0.1 mol/l) with a solution of sodium chloride five times. The mineral was then separated from the treatment solution by centrifugation, followed by washing with sodium chloride until a negative reaction to the silver chlorine ion.

To obtain organomodified laponite (OLP) and organomodified montmorillonite (OMMT), the sodium clay thus obtained was treated with a stoichiometric amount of organic salt, in particular cetyltrimethylammonium bromide (CTAB, $C_{16}H_{33}-N(CH_3)_3Br$) manufactured by Fluka, at a temperature of 360 K for 24 h. The loose precipitate of cetyltrimethylammonium clay was concentrated in a centrifuge and subjected to freeze-drying to maintain its high dispersion and ability to disperse in organic media.

PEO was dehydrated by heating in vacuum for 4 h at 350–370 K and a residual pressure of 300 Pa. The samples were made by ultrasonic mixing in a polymer melt at a temperature of 353 K using an ultrasonicator UZD-650. The content of fillers varied within $(0.1 \div 2)$ wt%. The volume fraction of nanofillers in the composites was calculated as

$$\varphi = \left(1 + (C_p \cdot \rho_f) / (C_f \cdot \rho_p)\right)^{-1},$$

where C_f and C_p are the weight contents of the nanofiller and polymer, respectively.

To establish the effect of the filler on the structure of the polymer matrix in the region of small (up to 4 nm) spatial orders, the method of wide-angle X-ray scattering (WAXS) was used. Used $Cu K_\alpha$ radiation with a wavelength $\lambda = 0.154$ nm.

Curves of small-angle X-ray scattering (SAXS) were obtained in a vacuum chamber of the Kratki type, in the radiation of a copper anode, monochromatic full internal reflection, and a nickel filter [20]. The survey was performed in the mode of multiple step-by-step scanning of the scintillation detector in the range of scattering angles from 0.03 to 4.0°, which corresponds to the values of the wave vector, q , from 0.022 to 2.86 nm⁻¹ ($q = 4\pi \sin\theta/\lambda$, θ is a half the scattering angle, and λ is the wavelength of X-rays). This provides the ability to study microheterogeneous formations (areas with greater or lesser density than in the matrix or micropores) with characteristic dimensions (defined as $2\pi/q$) from 2 to 280 nm. Processing of SAXS curves was performed using the program FFSAXS.

Micrographs of systems based on PEO and anisometric nanoparticles were obtained using a digital optical microscope SIGETA MB-303 (Ukraine), which is equipped with a digital video camera SIGETA DCM-800 (Ukraine). For research, materials in the molten state were placed between two plane-parallel glass plates, and the gap between which was 80 μm. To obtain information about the fractality of the structure of clusters with CNTs, the obtained micrographs were processed using the program ImageJ v1.41.

The study of electrical properties was performed using the method of impedance spectroscopy, implemented on the basis of impedance meter E7-20. The sample was placed between the electrodes of the cell, while measuring its real (Z') and imaginary (Z'') part of the impedance. From the dependences of the complex impedance, the electrical conductivity at direct current was determined as $\sigma_{dc} = \frac{d}{SR_{dc}}$, where S is the area of the sample; d is the thickness of the sample. Measurements were performed at room temperature in the frequency range 25 Hz–1 MHz. The constant gap between the electrodes was 0.11 mm. Simulation of impedance spectra by the method of equivalent circuits was performed using EIS spectrum analyzer.

3 Results and Their Discussion

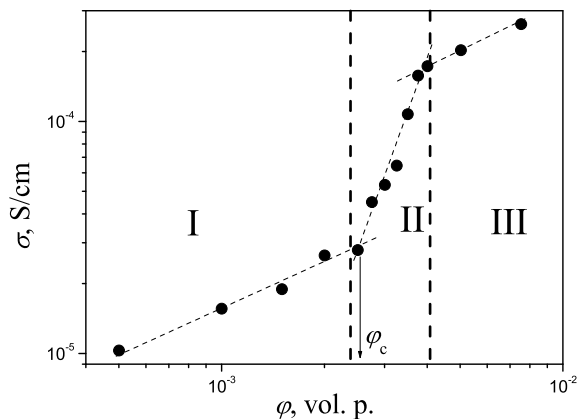
To study the effect of nanoparticles on the polymer matrix, it is necessary to use model systems that can provide a wide range of experimental conditions for preparation and research, as well as variation of their own characteristics. One such compound that meets these requirements is polyethylene oxide. The main advantages of such polymer matrix are the ability to significantly vary the degree of crystallinity within a single homologous series; it has a high (relative to dielectrics) intrinsic conductivity, which changes significantly with the change in molecular weight of oligomers; can be in different phase and aggregate states; used as a reactive oligomer for the synthesis of various matrix polymers, such as polyetherurethanes; has a low melt viscosity, which makes it possible to prepare nanocomposites based on them by ultrasonic dispersion; they are sufficiently transparent, which makes them an acceptable environment for the study of the structural organization of the introduced dispersed particles by optical microscopy.

3.1 *Structure and Properties of Nanocomposites Based on Polyethylene Oxide and Carbon Nanotubes*

Figure 1 shows the dependence of electrical conductivity on the filler content for the system PEO-CNTs. It shows that the dependence $\sigma(\varphi)$ is characterized by nonlinear behavior. This nonlinear behavior of the dependence $\sigma(\varphi)$ can be explained in the framework of the percolation theory [21].

In the region of low concentrations of filler (region I), there is a gradual increase in electrical conductivity. Until the system reaches a critical concentration of filler (percolation threshold) (from 0 to 2.2×10^{-3} vol. p.) in the volume of the matrix, there are isolated CNTs or their small clusters. Increasing the concentration of the filler leads to the growth and merging of individual clusters. When the critical concentration is reached (approximately $(2.3 \div 2.5) \times 10^{-3}$ vol. p.), a cluster is formed, which penetrates the entire volume of the system, which leads to an abrupt increase in its

Fig. 1 Dependence of electrical conductivity on the filler content for the PEO-CNTs system at $T = 293$ K



electrical conductivity. A rapid increase in electrical conductivity is observed in the region of concentrations $(2.5 \div 4) \times 10^{-3}$ vol. p., which is, in essence, the region of percolation transition (region II). At higher concentrations of CNTs $(4 \div 8) \times 10^{-3}$ vol. p., there is an increase in the percolation cluster, and then an increase in the number of continuous clusters, which leads to a smoother increase in electrical conductivity (region III).

Such ideas are confirmed by optical microscopy. Figure 2 shows photomicrographs for the PEO-CNTs system, which represent the typical structures observed in certain concentration regions of CNTs, shown in Fig. 1. Figure 2a shows that when a content of CNT is equal 0.0015 vol. p. (region to the percolation threshold), nanotubes form single clusters that do not connect with each other. At the same time, there is a tendency to the formation of large aggregates. When the content of CNTs is equal 0.003 vol. p., which lies in the region of the percolation transition, a continuous percolation cluster is formed (Fig. 2b). With a further increase in the content of CNTs, clusters of nanotubes begin to grow and condense, forming more and more continuous conductive channels (percolation network). It should be noted that since the optical axis of the microscope coincides with the geometric axis of the dielectric cell, the structures of clusters with CNTs in the photomicrographs shown in Fig. 2 are not an exact representation of the clusters connecting the opposite electrodes. However, as shown by the authors [22], who studied the electrical conductivity of liquid crystal-CNTs systems parallel and perpendicular to the suspension layer, at a sample thickness of more than 50 μm , the electrical conductivity of such systems does not depend on the direction of measurement. Since the thickness of the samples we studied was around 100 μm , we can assume that the picture of the distribution of clusters with CNTs in the plane perpendicular to the presented microphotographs will be similar.

The X-ray diffraction technique allows to study the morphological features of nanocomposites based on polyethylene oxide and CNTs at the level of microphase formations, at the supramolecular level of the structure. Figure 3 shows wide-angle diffraction patterns for PEO-1000 and nanocomposite based on it. The figure shows

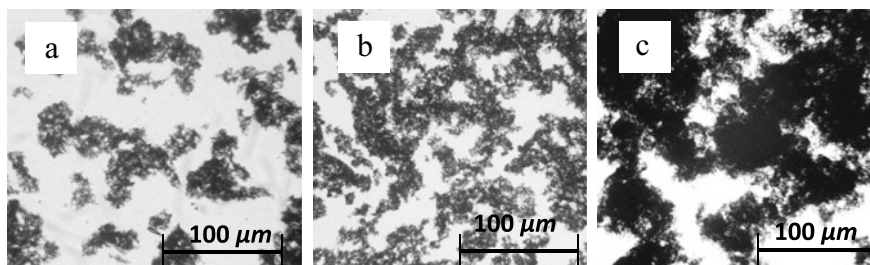


Fig. 2 Microphotographs of the system based on PEO and CNTs at $T = 293$ K. The content of nanotubes: **a** 0.0015 vol. p.; **b** 0.003 vol. p.; **c** 0.0045 vol. p

that the introduction of CNTs changes the diffraction curves, which indicates the effect of nanotubes on the structure of PEO-1000.

Determination of the relative degree of crystallinity (χ_{cr}) for systems based on PEO and CNT was performed using the Matthews method. This method is based on the comparison of the area of diffraction maxima characterizing the crystal structure of an amorphous-crystalline polymer (Q_{cr}) with the total area of the diffraction curve in the selected information angular interval ($2\theta_1 \div 2\theta_2$), which includes the main diffraction pattern for the whole series of polymers:

$$\chi_{kp} = \frac{Q_{kp}}{(Q_{kp} + Q_{am})} \quad (1)$$

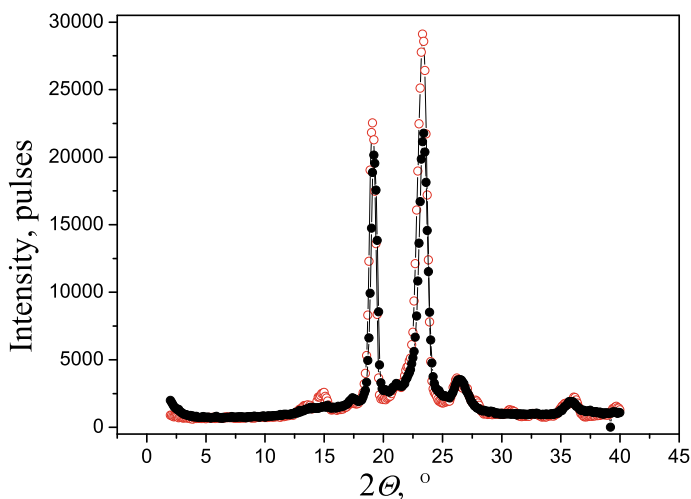


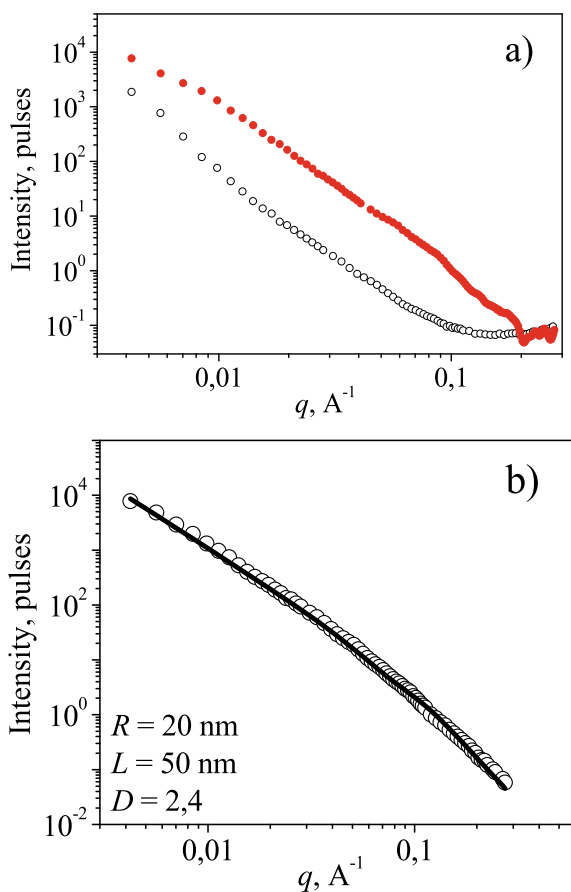
Fig. 3 Curves of wide-angle X-ray scattering. Empty circles correspond to unfilled PEO-1000, painted circles correspond to PEO-1000 filled with 1.5% CNTs

According to the calculations, the relative degree of crystallinity decreases from 82% for pure PEO-1000 to 65.2% for filled. This fact is a consequence of steric interference created by the developed surface of the nanofiller, reducing the flexibility of polymer chains.

Figure 4a shows the SAXS curves of pure PEO and PEO-CNT nanocomposite. It is seen that with the addition of filler to PEO, the scattering curve of the latter changes significantly. This type of small-angle X-ray scattering profile is similar to that observed for small-angle neutron scattering data [23], which shows a good correspondence of experimental curves with model ones calculated using two sets of cross-sectional radii of flexible polydisperse cylinders—14–16 nm and 130 nm, respectively.

The scattering intensity of the nanocomposite is more than an order of magnitude higher than the scattering intensity of the unfilled PEO-1000. This makes it possible to obtain the scattering profile of CNTs, subtracting from the scattering of the nanocomposite scattering of the polymer matrix. The resulting scattering profile

Fig. 4 **a** Curves of small-angle scattering of X-rays. Empty circles correspond to unfilled PEO-1000, painted circles correspond to PEO-1000 filled with 1.5% CNT; **b** curve of small-angle X-ray scattering of CNTs described using the model of flexible rods. Empty circles indicate experimental data, and a solid line corresponds to a model



of CNTs, which are dispersed in the PEO matrix, is shown in Fig. 4b. The parameters of CNTs in the polymer matrix are significantly different from the parameters of the tubes in the free state. The persistent length is halved, and the fractal dimension is increased.

The scattering intensity of the nanocomposite is more than an order of magnitude higher than the scattering intensity of the unfilled PEO-1000. This makes it possible to obtain the scattering profile of CNTs, subtracting from the scattering of the nanocomposite scattering of the polymer matrix. The resulting scattering profile of CNTs, which are dispersed in the PEO matrix, is shown in Fig. 4b. The parameters of CNTs in the polymer matrix are significantly different from the parameters of the tubes in the free state. The persistent length is halved and the fractal dimension is increased.

A decrease in the persistent length of the flexible nanotube indicates an increase in the flexibility of the CNT. This fact can be explained by the destruction of CNTs under the action of ultrasonic waves during dispersion. Therefore, the flexibility of CNTs dispersed in the polymer matrix can increase due to two processes: fracture of long nanotubes, which leads to the formation of CNTs fragments, and the length of which is approximately equal to the persistent length or the destruction of CNTs beams [24].

The next step in the study was to use a scaling approach to analyze the percolation dependences for a system based on polyethylene oxide filled with CNTs. According to the percolation theory, in a filled system after the percolation threshold, the relationship between the electrical conductivity and the content of the conductive nanofiller is described by the following scaling law [25]:

$$\sigma \propto (\varphi - \varphi_c)^t \quad \text{for } \varphi > \varphi_c, \quad (2)$$

where σ is the electrical conductivity of the system, φ is the fraction of the conductive nanofiller, φ_c is the critical fraction of the nanofiller at the percolation transition (percolation threshold), t is the exponent, the critical conductivity index, which mainly depends on the system dimension and does not depend on the particle structure clusters and their interaction (for a three-dimensional system, the theoretical value of t is in the range from 1.6 to 2 [26]).

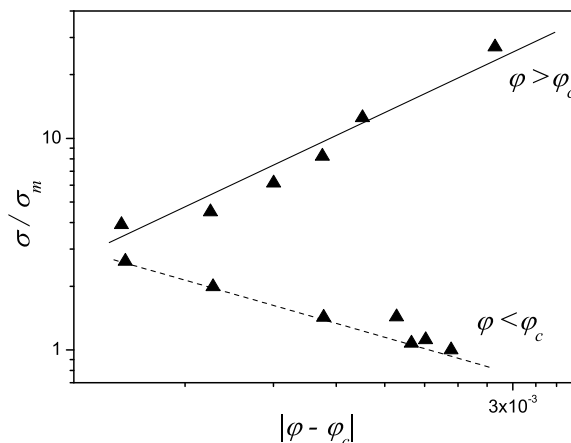
On the other hand, the electrical conductivity of systems to the percolation threshold can be described by another scaling law, which is written as:

$$\sigma \propto (\varphi_c - \varphi)^{-s} \quad \text{for } \varphi < \varphi_c, \quad (3)$$

where s is the critical index (the theoretical value $s \approx 0,73$ for a three-dimensional system [26]).

Applying the method of least squares and Eqs. (2) and (3) to describe the experimental data (Fig. 1) determined the values of the percolation threshold and critical exponents that characterize the structural organization of the nanofiller in the composite and the structure of the clusters. The results of approximation of experimental data in a wide range of nanotube concentrations are presented in Fig. 5.

Fig. 5 Dependences of electrical conductivity on the content of CNTs in the coordinates of Eqs. (2) and (3) for polyethylene oxide-based systems



Although the scaling laws (2) and (3) stipulate that the dependences $\log(\sigma)$ from $\log|\varphi - \varphi_c|$ must be strictly linear, but Fig. 5 shows that the constructed experimental results have some deviations from linearity. Such deviations lead to significant errors in determining the parameters of the Eqs. (2) and (3) [27].

Using the method of intersection of the two tangents, determined the value of the percolation threshold for the PEO-CNTs system, which is 0.0024 vol. p. It should be noted that the obtained value $\varphi_c = 0.0024$ vol. p. is quite low compared to other PEO-carbon filler systems. For example, the value of the percolation threshold for the PEO-carbon black system is 0.01 vol. p. [28], and for the PEO-PVC-graphite system is 0.075 vol. p. [29]. As can be seen, systems containing an isometric filler are characterized by a higher value of the percolation threshold compared to systems containing an anisometric filler. Therefore, the value obtained for PEO-CNTs systems is typical for strongly anisometric nanoparticles in dispersed media with low viscosity [30, 31]. In particular, directly, for the PEO-CNTs system, depending on the method of preparation, the value of the percolation threshold can vary from 0.005 vol. p. [32] to 0.00015 vol. p. [33].

The calculated value of the critical conductivity exponent t is 1.55 ± 0.18 . It is seen that the values of t are much lower than the universal value of $t = 2$, theoretically calculated by statistically distributed spherical particles in a three-dimensional system. Such values of t are very close to the value of the critical exponent obtained for the two-dimensional system $t = 1, 3$. Similar low values of t were obtained experimentally for different types of polymer-CNTs systems, for example, polyepoxide-CNTs ($t = 1, 2$) [34] and polyvinyl alcohol-CNTs ($t = 1, 36$) [35]. Also, the obtained values of t correlate well with some theoretically calculated values. Fogel et al. suggested that the deviation of the value of the critical exponent t from the universal one is a consequence of the large anisometry of the shape of the electrically conductive filler [36]. After performing numerical calculations, they found that for CNTs with an aspect ratio greater than 500, the value of t varied in the range 1.2–1.4.

For PEO-CNT system, using Eq. (3), the value of the critical exponent s , which is 0.43 ± 0.02 , was calculated. This value is much lower than the theoretical one (for a three-dimensional system, the universal value $s \approx 0.73$) [26]. In percolation theory, s is related to the size of the conductive zones consisting of CNTs that form clusters. According to [21], s characterizes the average number of CNTs in any cluster. The values of the critical exponent s differ from the universal one. A significant difference (toward higher values) from the universal value of s was observed by Panda et al. [37] for systems based on PVDF filled with Ni particles of different sizes and prepared by different methods, the value of the critical index s varied between $1.09 \div 1.73$. However, in the PVDF-steel fiber system, the obtained value of the critical exponent was $s = 0.36$, which was less than universal. The authors explained this difference by the significant anisotropy of the filler [38]. In addition, a decrease in the critical exponent s that observed in epoxy-CNTs systems are explained by the process of aggregation of nanotubes and the formation of a heterogeneous nature of the distribution of the filler during the curing process [39].

3.2 Structure and Properties of Nanocomposites Based on Polyethylene Oxide and Organoclay

In the introduction, it was discussed that by changing the nature of the distribution of nanosized organ clay in the polymer matrix (intercalation, exfoliation), it is possible to influence the functional characteristics of nanofilled systems. Therefore, the study of the structural organization of the clay in the polymer system is very important, because the structure determines the properties of nanocomposites. However, despite the relevance of these studies, today, little studied are the different types of structural organization of nanoclay in polymer matrices.

Figure 6 shows WAXS for systems based on PEO and layered silicates of different nature, and Table 1 gives the positions of the diffraction peaks and the values of their half-widths. It is seen that all the studied systems are partially crystalline. For nanocomposites based on PEO-1000 and OMMT, at scattering angles of $\sim 5^\circ$, diffraction reflexes are observed, which are responsible for the interplanar distance of OMMT (Fig. 6a.) The intensity of these reflexes increases with increasing content of OMMT in the system. On X-ray patterns for nanocomposites based on OLP (Fig. 6b), such reflexes are not observed, which may be evidence of complete destruction of OLP tactoids during ultrasonic treatment.

For a more detailed understanding of the processes occurring in the polymer-layered filler system, nanocomposites were investigated by the method of small-angle X-ray scattering. The resulting WAXS and SAXS curves for nanocomposites based on PEO-1000 and 5% of filler are presented in Fig. 7.

Figure 7a shows that the X-ray scattering curve of PEO-OMMT has 2 diffraction reflexes that correspond to the interplanar distances (d) of OMMT. The first reflex ($d = 3.7$ nm) indicates the intercalation of PEO in the interlayer space OMMT, and

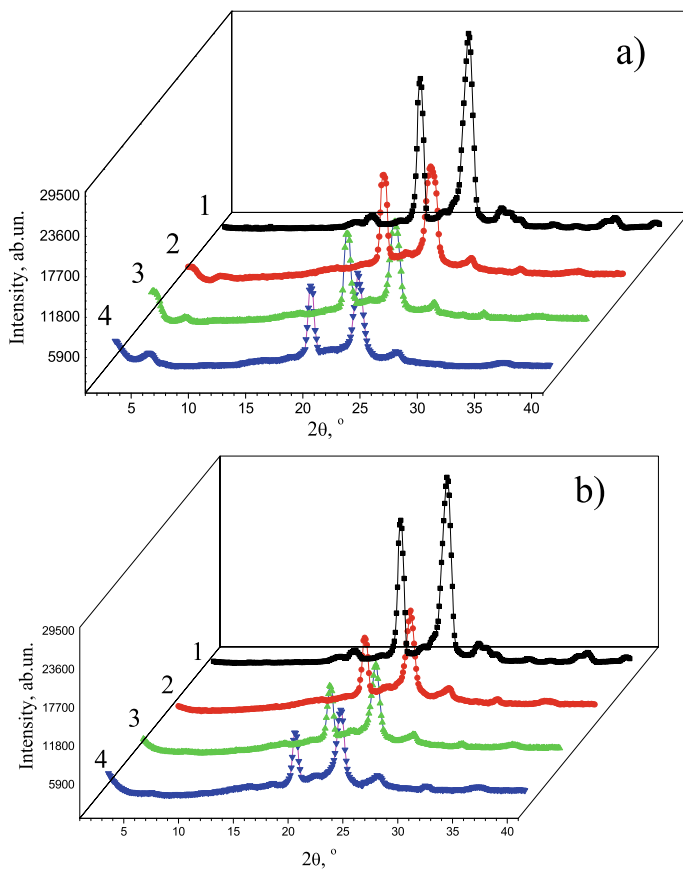
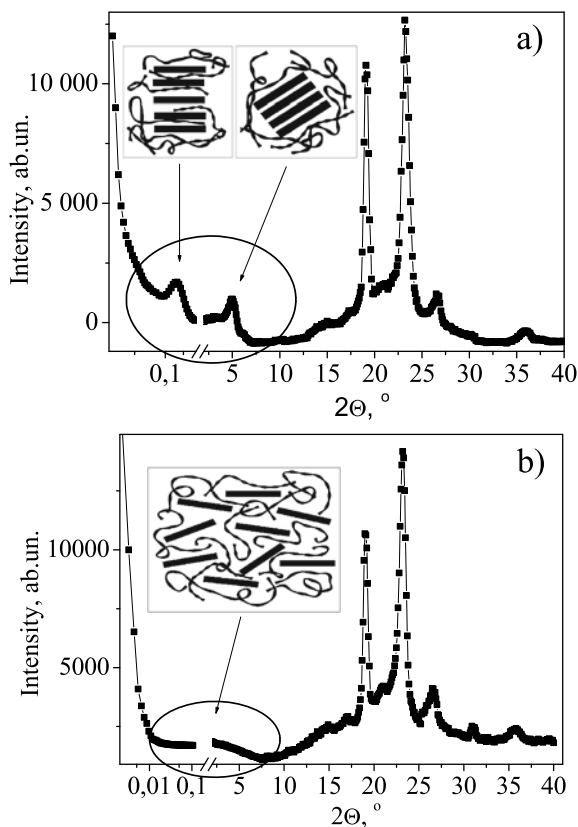


Fig. 6 Wide-angle diffraction patterns of nanocomposites based on PEO-1000, filled with: **a** OMMT, **b** OLP. Filler content: 1–0, 2–1, 3–3, 4–5%. For greater clarity, the curves are offset along the x -axis

Table 1 Structural characteristics of nanocomposites based on PEO-1000

Sample	$\theta_m, ^\circ$ $\pm 0.1^\circ$	$\beta, ^\circ$ $\pm 0.05^\circ$	$L, \text{ nm}$ $\pm 0.05 \text{ nm}$	$\chi_{\text{cryst}}, \%$
PEO	23.3	0.75	11.80	78.3
PEO-1% OMMT	23.3	0.90	10.00	52.0
PEO-3% OMMT	23.3	0.75	11.55	49.8
PEO-5% OMMT	23.3	0.75	12.55	46.3
PEO-1% OLP	23.2	0.70	13.30	48.7
PEO-3% OLP	23.2	0.70	13.45	45.0
PEO-5% OLP	23.2	0.70	13.95	41.2

Fig. 7 Resulting diffraction patterns of nanocomposites based on PEO-1000, filled with 5% OMMT (a), OLP (b)



the second ($d = 1.9$ nm) is really responsible for the intact tactoids OMMT [40]. In Fig. 7b, diffraction reflexes which are responsible for the interplanar distance of the OLP are absent, which is indisputable evidence of complete exfoliation [40].

Thus, according to the data of WAXS and SAXS in systems containing OMMT, there are partial processes of intercalation, and in systems with OLP take place a full exfoliation. This discrepancy may be due to the shape of the layered filler. Since the OMM consists of long plates up to 200 nm long, more energy must be applied to delaminate them than to the separation of OLP disks up to 25 nm in diameter.

Since nanocomposites based on PEO-1000 and layered silicate fillers have a partially crystalline structure, the effective size of the crystallites can be calculated using Scherrer equation (4):

$$L = \frac{k\lambda}{\beta \cos \theta_m}, \quad (4)$$

where β is the angular expansion of the diffraction maximum (in radians), which is usually defined as the width of the maximum at half its height (“half-width” of the

maximum) after subtracting the background scattering; k is a coefficient depending on the shape of the crystallite (if the shape is not known, then $k = 0.9$); θ_m is the angular position of the diffraction maximum. The half-width of the most intense maximum was used to calculate the effective crystallite size for each nanocomposite.

Table 1 gives the values of half-widths, positions of maxima and calculated by Eq. (4) the size of the crystallites for systems based on PEO-1000. To calculate the effective crystallite size for each nanocomposite, the half-width of the most intense maximum was used.

Table 1 also gives that the angular position of the crystal maxima of PEO-1000 is practically unchanged. Their half-width, in the case of filling OMMT (Fig. 6a), first increases with increasing nanofiller content, which corresponds to a decrease in the effective size of the crystallites, and then decreases to the previous value (Table 1). This fact is evidence of the additional disorder of the partially crystalline material of the polymer matrix under the influence of the surface of the nanofiller due to the limitation of the conformational set of fragments of polymer chains. In contrast to OMMT, the introduction of OLP in the entire concentration range leads to a decrease in half-width and to an increase in the effective size of the crystallites (Fig. 6b).

To determine the influence of the structural organization of nanoclays in the polyethylene oxide matrix on the electrical properties of nanocomposites, the impedance formalism $Z''(Z')$ was used. Figure 8 shows the dependences of $Z''(Z')$ for pure PEO-1000 and nanocomposites filled with layered silicates of different nature.

The isotherms of the dependences $Z''(Z')$ in the classical variant are semicircles with deviations in the low-frequency region. These deviations are the result of surface polarization effects, which become more obvious with increasing temperature and, consequently, with increasing segmental mobility in the polymer system. At frequencies lower than the frequency corresponding to the minimum Z'' (in the case of implicit minima, the approximation $Z'' \rightarrow Z_0$ is performed), the surface processes dominate over the bulk ones, and the values of Z' of these minima correspond to the bulk resistance of the material R_{dc} . From the dependences of the complex electrical resistance, the conductivity at direct current was determined as $\sigma_{dc} = \frac{d}{SR_{dc}}$, where S is the area of the sample, d is the thickness of the sample. Figure 9 shows the concentration dependences of σ_{dc} of the investigated polymer nanocomposites in semi-logarithmic coordinates.

Figure 9 shows that in the case of filling with different organoclays, the nature of the concentration dependence of electrical conductivity differs significantly. The graph for the electrical conductivity of a system filled with OMMT is linear in semi-logarithmic coordinates. The monotonic increase in electrical conductivity with increasing content of OMMT is explained by a decrease in the degree of crystallinity of the polymer matrix. At the same time, the fraction of the amorphous phase of PEO increases, in which charge transfer is mainly realized.

The dependence of electrical conductivity on the content of OLP is extreme. The electrical conductivity first increases, reaching a maximum at 3% of OLP content, and then gradually decreases. This behavior of the conductivity graph is a consequence of the presence of two processes in the system: reducing the crystallinity of the polymer

Fig. 8 Z'' - Z' dependence for nanocomposites based on PEO-1000, filled with OMMT (a), OLP (b)

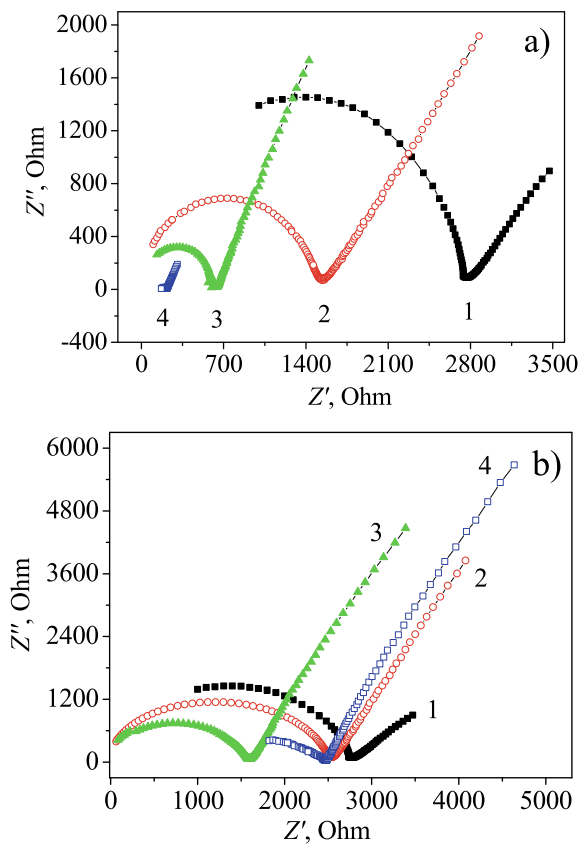
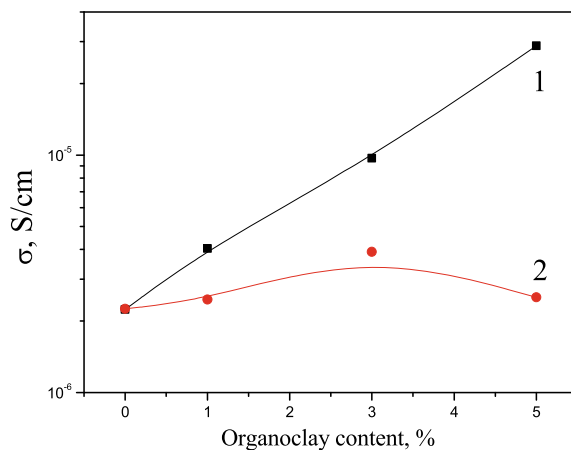


Fig. 9 Dependence of electrical conductivity on the content of OMMT (1) and OLP (2) for systems based on polyethylene oxide



matrix, which increases the electrical conductivity, and the formation of a network of laponite nanoplates, which destroys the paths of charge transfer.

3.3 Synergetic Effects of Combined CNTs/Organoclay Filler in Nanocomposites Based on Polyethylene Oxide

The formation of aggregates with CNTs leads to the devaluation of the functional properties of the material due to a significant reduction in the interaction surface between the polymer and the filler. To overcome the aggregation, various modifiers are introduced into the composition of the polymer-CNTs type system, for example, oxide nanoparticles [41], organoclays [42], carbon black [43], etc. The introduction of layered silicates into the polymer-CNTs system significantly changes its percolation behavior [41, 43, 44]. For example, for the polyepoxide-CNTs system, the value of the percolation threshold decreased in 2.5 times with the introduction of montmorillonite [42]. The authors of [44–46] showed that the optimal ratio of CNT:MMT to improve the properties of the nanocomposite is 1:1.

It is seen from the introduction that the value of the percolation threshold and the overall conductivity of nanofilled systems can be influenced by the introduction of additional inorganic filler. In this paper, we consider the effect of additives of layered silicates on the percolation behavior of systems based on polyethylene oxide and CNTs.

To establish the effect of layered silicates on the microstructure and electrical properties of filled systems, studies of the system based on PEO-1000 and CNTs with the addition of organomodified montmorillonite (OMMT), which is able to intercalate in the matrix and organomodified laponite (OLP), which is completely exfoliated, are conducted. Layered silicates were added to the system before dispersion. The content of silicates ranged from 0.0005 vol. p. up to 0.001 vol. p.

To analyze the morphological features of the clusters, the microstructure was studied using the method of optical microscopy. Figure 10 shows microphotographs for PEO-CNTs systems filled with OMMT at the content of CNTs in the region of the percolation threshold (0.0025 vol. p.). Figure 10 also shows that the introduction of the system of PEO-CNTs particles OMMT significantly changes its microstructure. Visually, the destruction of large units of CNTs and the formation of a more branched network of nanotubes. It was shown that with the introduction of even 0.5% of OMMT, CNTs are distributed more evenly.

To establish the effect of OMMT on the electrical properties of the PEO-CNTs system, conduct a study of electrical conductivity in two different states of the polymer matrix: in the partially crystalline state ($T = 290$ K) and melt ($T = 340$ K). Figure 11 shows the results of electrical conductivity studies for systems based on PEO-1000. Figure 11 presents that for both states of the polymer matrix, there is a similar trend in the filling of CNTs and OMMT. Thus, when introduced into the composition of PEO-1000 OMMT, the electrical conductivity increases only a few

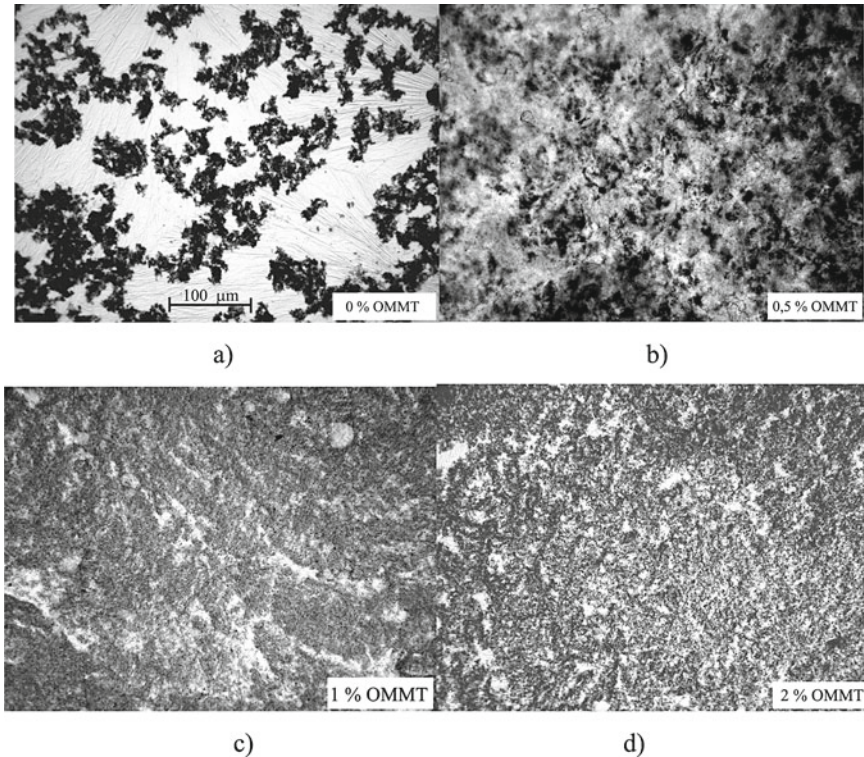
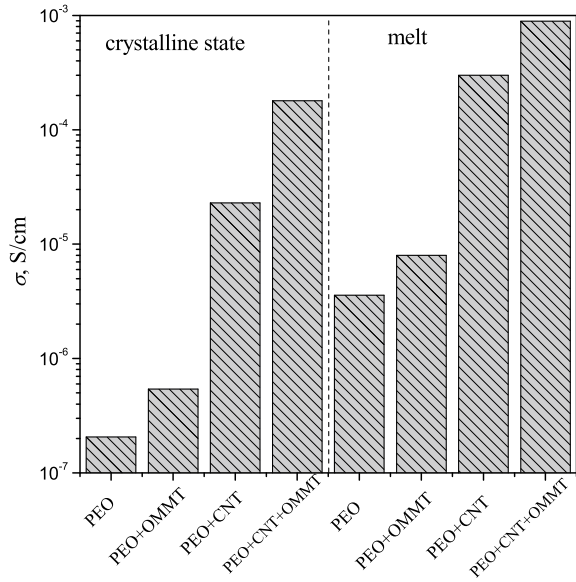


Fig. 10 Microphotographs of PEO-1000 systems filled with CNTs ($C_{\text{CNT}} = 0.0025$ vol. p.) and OMMT ($C_{\text{OMMT}} = 0\text{--}2\%$)

times. With the introduction of 0.0025 vol. p. CNTs into PEO, electrical conductivity increases by one and a half to two orders of magnitude, which is associated with the percolation transition. When entering the system PEO-CNTs-OMMT, the electrical conductivity increases by an order of magnitude in the crystalline state and by half an order of magnitude in the melt PEO-1000. This behavior can be explained by the fact that OMMT particles destroy aggregates with CNTs, which leads to better contact between individual nanotubes [46, 47].

The effect of OMMT is more pronounced for PEO-1000 in the crystalline state due to additional amorphization of the matrix through the introduction of additional filler. As Fig. 11 shows, the electrical conductivity of PEO-1000 in the melt (amorphous state) is an order of magnitude higher than in the crystalline state. However, the impact of OMMT was much smaller than expected. Perhaps, this effect occurs due to the fact that the tactoids of OMMT cannot exfoliate in this mode of ultrasonic treatment of the system PEO-CNTs-OMMT, and there are only processes of partial interaction.

Fig. 11 Electrical conductivity of systems based on PEO-1000 in the crystalline state and the melt filled with 0.0025 vol. p. CNTs and/or 0.5% OMMT



The introduction of the modifier into the polymer-CNTs system significantly affects its microstructure. To establish the effect of the modifier on the fractal dimension of nanotube aggregates, studies of the PEO-CNTs system filled with 0.1% of laponite (LP) and organomodified laponite (OLP) were performed.

From the microscopic images, it is possible to estimate the fractal dimension d_f , which reflects the morphology of clusters with CNTs in two-dimensional projection. The fractal dimension d_f was calculated by counting the number of cells required to cover the perimeter of the aggregates N from the cell size L [48]:

$$N \propto L^{d_f}. \tag{5}$$

To assess the fractal dimension, all images were translated into binary (black and white) format. The method of calculating of d_f given in [49]. The value of d_f is between 1 (the case of linear aggregates) and 2 (the case of dense aggregates). To move to the fractal dimension of three-dimensional aggregates, you can use the following Eq. [48]:

$$d_f^3 = d_f^2 + 1, \tag{6}$$

where d_f^3 is the fractal dimension of three-dimensional aggregates, d_f^2 is the fractal dimension of two-dimensional aggregates.

Table 2 gives that the introduction of the modifier significantly changes the fractal dimension of the PEO-CNTs system. According to X-ray diffraction analysis, LP particles are in the form of tactoids (bundles of plates), and OLP exfoliates, evenly

distributed in the form of plates. Table 2 also gives that the introduction of OLP leads to a greater increase in d_f of the system than the introduction of LP. This effect is explained by the different size of the interaction surface between the plates of laponite and CNTs. Thus, the introduction of only 0.1% of OLP contributes to significant loosening of units with CNTs, which probably affects the electrical properties of the PEO-CNTs system [19].

Therefore, to achieve a percolation threshold of 0.001 vol. p., the optimal ratio of CNTs/laponite (C_{NT}/C_L) should be 2. However, the features of the influence of organomodified laponite on the percolation behavior of the polymer-CNTs system with a fixed value of the ratio of laponite/CNTs remain unexplored. Therefore, the next task was to study the electrical properties and percolation behavior of model systems based on PEO-1000, carbon nanotubes, and laponite, with a fixed value $C_{NT}/C_L = 2$.

Figure 12 presents the experimental results of the dependence of electrical conductivity on the filler content for nanocomposites PEO-CNTs-OLP. Figure 12 shows that the concentration dependence of electrical conductivity is nonlinear. Dependence can be divided into two regions: I–region (from 0 vol. p. to 0.0032 vol. p. of CNTs), where the electrical conductivity of the nanocomposite exhibits a typical percolation behavior; II–region (from 0.0032 vol. p. to 0.005 vol. p. of CNTs), where there is a decrease in electrical conductivity due to the significant influence of laponite particles.

Table 2 Value of the fractal dimension for PEO-CNT systems, filled with laponite

The content of CNTs, vol. p	Without OLP	With OLP	The content of CNTs, vol. p	Without OLP	With OLP
0.001	1.55	1.66	0.002	1.79	1.73
0.0015	1.69	1.89	0.0025	1.83	1.84

Fig. 12 Dependence of electrical conductivity on the content of CNTs for the system PEO-CNTs-OLP. The ratio $C_{NT}/C_L = 2$

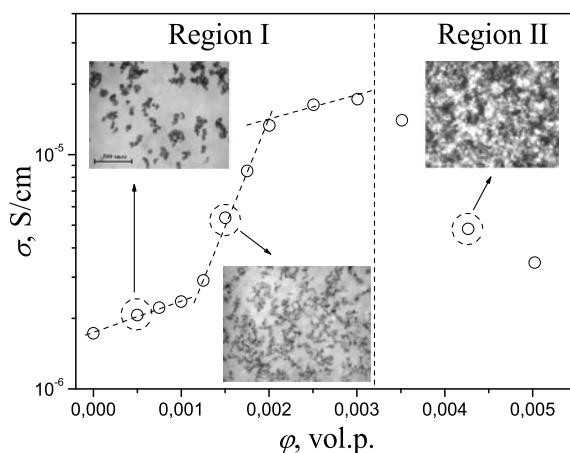


Figure 13 shows the dependence of electrical conductivity on the filler content for the studied systems PEO-CNTs and PEO-CNTs-OLP. The step-like change in electrical conductivity associated with the phenomenon of percolation is observed in the concentration range of 0.001–0.004 vol. p. For the PEO-CNTs system, at a content of 0.004 vol. p. of nanotubes, the electrical conductivity of the systems is more than an order of magnitude higher than the electrical conductivity to the percolation threshold, and for the PEO-CNTs-OLP system, at a content of 0.002 vol. p. is almost an order of magnitude higher.

Applying the approximation of Eqs. (2) and (3) to describe the experimental data (Fig. 13) determined the values of the percolation threshold and critical exponents t and s , which characterize the structural organization of the nanofiller in the composite and the structure of the clusters. The results of the approximation are shown in Fig. 14a. The values of the percolation threshold and critical exponents for the system based on PEO are given in Table 3.

Fig. 13 Dependence of the reduced electrical conductivity on the content of CNTs for systems: 1—PEO-CNTs; 2—PEO-CNTs-OLP (concentration region I)

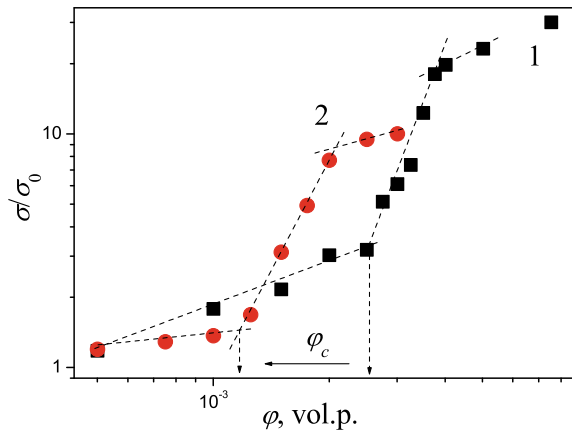


Fig. 14 Dependence of the electrical conductivity of the PEG-CNTs system (1) and PEG-CNTs-OLP (2) on $(\varphi - \varphi_c)$ in logarithmic coordinates. Solid and dotted lines are approximation of Eqs. (2) and (3), respectively

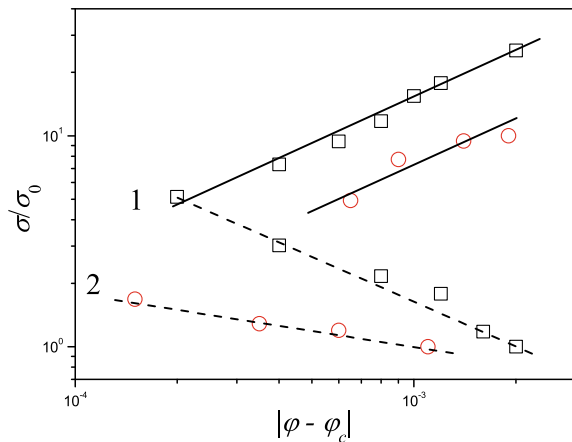


Table 3 Parameters of Eqs. (2) and (3)

	$p_c, \%$	t	s
PEO-CNTs	0.0025 vol. p	1.17	0.65
PEO-CNTs-OLP	0.0011 vol. p	1.09	0.21

In this case, the low value of the critical exponent t does not indicate a decrease in the dimension of the system, and, apparently, due to the processes of aggregation of CNTs after preparation of these systems, as well as the influence of laponite particles. In our opinion, the formation of an electrically conductive network, due to the strong attraction between individual CNTs, is not a statistical percolation process, which assumes a uniform distribution of nanofiller particles.

The critical exponent s in Eq. (3) is related to the size of the conductive zones and characterizes the average number of CNTs in any cluster [50]. This exponent for the PEO-CNTs system was much higher than for the PEO-CNTs-OLP system (Table 3).

The analysis of the values of the critical exponent s for PEO-based systems shows that the clusters in the system filled with laponite contain significantly fewer nanotubes than in the system without the addition of OLP. This is explained by the fact that the introduction of OLP particles leads to loosening of clusters with CNTs and prevents their further aggregation (see microphotographs in Fig. 10).

Table 3 gives that with the introduction of laponite in the PEO-CNTs system, the value of the percolation threshold decreases more than twice from 0.0025 vol. p. up to 0.0011 vol. p. This effect is associated with a change in the degree of distribution of the tubes over the volume of the polymer matrix. When introduced into the material, OLP nanoparticles begin to interact with the surface of nanotubes and are attracted to it. As a result, the surface of the nanotubes is partially covered with laponite plates, as schematically shown in Fig. 15a. It should be noted that at this degree of coverage, there is a probability for the formation of direct contacts between CNTs [19].

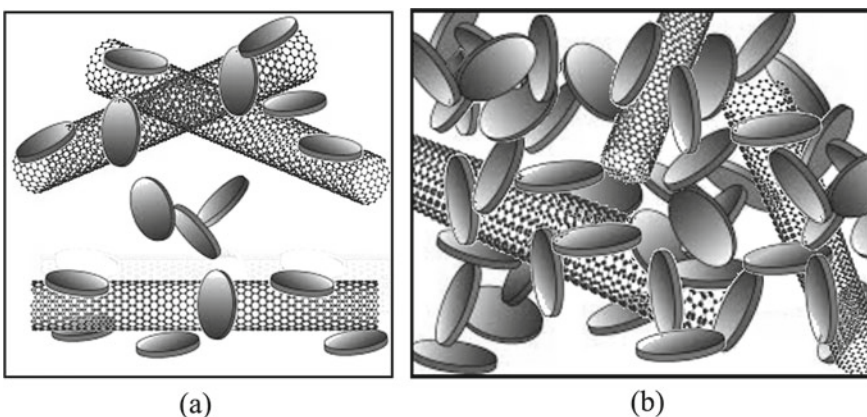


Fig. 15 Schematic representation of the structure of CNTs-OLP in the system based on PEO at low (a) and high (b) laponite content

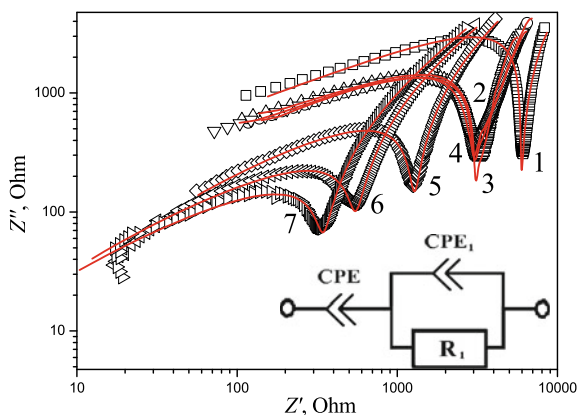
For a more detailed analysis of the experimental results of electrical conductivity, impedance spectra for the PEO-CNTs-OLP system were modeled by the method of equivalent circuits, which allows to quickly and easily get a complete picture of the features of charge transfer processes [51]. The impedance of the polymer material is often simulated using a resistor and a capacitor connected in parallel. However, for nanofilled systems, such an equivalent scheme is incorrect [52]. To compensate for the inhomogeneities in the system caused by the fractal structure of the studied samples, the constant phase element (CPE) is introduced into the equivalent circuit [53].

Figure 16 shows Nyquist plots (dependences of Z' on Z'') for PEO-CNTs-OLP systems with nanotube content from 0 to 0.0025 vol. p. Figure 16 also shows that all impedance spectra have a similar appearance: there are two incomplete semicircles separated by a minimum. To model the impedance spectra, we used the equivalent circuit shown in Fig. 16. In this, circuit R is the total volume resistance of the nanocomposite material, and CPE is a constant phase element, which is a generalized and universal tool for modeling the impedance of a wide class of electrochemical systems.

The proposed circuit showed full compliance with the experimental results (Fig. 16). It should be noted that for unfilled PEO, as a result of fitting, the elements of the CPE were converted into capacitive elements (capacitors). An equivalent circuit can be used to judge the processes of charge transfer in this system. In the equivalent circuit shown in Fig. 16, the series-connected elements CPE₁ and R_1 are responsible for the movement of charges in the volume of the material, and the element CPE is responsible for contact phenomena. In this case, contact phenomena can occur both in contact between individual nanotubes or their aggregates (electron tunneling) and in the interaction between the electrode and the nanocomposite. Therefore, the introduction of OLIP particles into the composition of PEO-CNTs in small quantities does not affect the processes of charge transfer in the system.

With the introduction of a relatively high content of laponite in PEO-CNTs systems, the electrical conductivity is significantly reduced (region II, Fig. 12). At

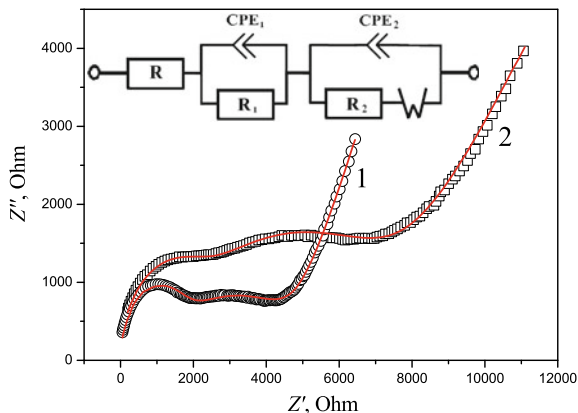
Fig. 16 Impedance spectra (Nyquist plots) for the system PEO-CNTs-OLP. CNTs content: 1—0 vol. p.; 2—0.0005 vol. p.; 3—0.00075 vol. p.; 4—0.001 vol. p.; 5—0.0015 vol. p.; 6—0.002 vol. p.; 7—0.0025 vol. p. Solid lines correspond to modeling using the equivalent circuit



the content 0.005 vol. p. of CNTs, the electrical conductivity is reduced almost to the level of unfilled PEO, i.e., the effect of CNTs is leveled. Microphotographs in Fig. 10 show that the distribution of CNTs in the system remains fairly uniform, and the photograph does not show large aggregates of nanotubes. It is most likely that the phenomenon of reduced electrical conductivity is due to the fact that due to the obstacles created by the nanoplates of the OLP, CNTs cannot contact each other. This makes it impossible to form a conducting cluster. This effect of reducing the electrical conductivity was observed for the system PEO-CNTs-OLP at different ratios C_{NT}/C_L , which was 1, 0.4, and 0.2. This effect was explained by the formation around the CNTs of a dense layer of OLP plates, which prevented the formation of direct contacts between nanotubes. However, in our case, $C_{NT}/C_L = 2$ in the entire concentration range of the filler. Therefore, the effect of reducing the electrical conductivity of the system at high filler content can be explained by assuming that laponite nanoplates form a three-dimensional network that permeates the entire volume of the material. Given that the ratio C_{NT}/C_L is constant, when the content of CNT is 0.005 vol. p., the content of OLP is 0.5%. According to [54], a typical liquid-gel transition is observed in this concentration region in the PEO-laponite-NaCl system. It should be noted that during visual observation, the PEO-CNTs-OLP system with a high content of filler after dispersion of all components had the form of a gel-like substance. Thus, in the process of forming the PEO-CNTs-OLP system, laponite plates interact with each other and with polymer molecules, forming a three-dimensional quasi-network. The OLP particles prevent individual nanotubes from forming their own percolation network. As a result, nanotubes, remaining isolated from each other (Fig. 15b), cannot form direct contacts with each other, which leads to a significant reduction in the electrical conductivity of the system.

Figure 17 presents Nyquist plots for PEO-CNT-OLP systems with a high content of nanotubes. It shows that the impedance spectra have a similar appearance, and there are three incomplete semicircles separated by minima. This type of impedance spectra differs significantly from those shown in Fig. 16 spectra for a system with a low content of OLP. To model the impedance spectra, we used the equivalent circuit shown in Fig. 17. This equivalent circuit contains all the elements of the circuit shown in Fig. 16, but with the addition of another block, which is associated with the contribution of interfacial conductivity. With a high CNT content, the nanotubes come into direct contact with the electrode, in fact, increasing its interaction surface with the ion-conducting polymer matrix. In the case when the measuring electrodes are not completely blocked, a current can flow through the electrode-ion-conducting nanocomposite boundary by charging the double layer. Thus, on the equivalent circuit (Fig. 17) together with the active resistance of the bulk material (circuit in Fig. 16), there will be a parallel connection of the resistor R_2 , which corresponds to the active resistance of the layer at the electrode boundary, and the element CPE_2 , which characterizes electric capacity of a double electric layer. If the kinetics of charge transfer is also controlled by the process of ion diffusion to the electrode-ion-conducting nanocomposite interface, then in series with the resistance R_2 , the equivalent circuit also contains the so-called Warburg impedance Z_W . The impedance of the element W is determined by the following empirical equation [51]:

Fig. 17 Impedance spectra (Nyquist plots) for the system PEO-CNTs-OLP. CNTs content: 1—0.0042 vol. p.; 2—0.005 vol. p



$$Z_W = \lambda(j\omega)^{-1/2}, \quad (7)$$

where λ is the coefficient (Warburg coefficient); n is the exponential index that characterizes the phase deviation.

As a result of fitting, the proposed circuit showed good compliance with the experimental results (Fig. 17). Thus, the impedance spectra and the equivalent circuit in Fig. 17 show that in a system with a high content of laponite significantly increases the contribution of the interfacial layers to the total impedance. Laponite particles interact with PEO molecules to form an interfacial layer whose electrical conductivity is much higher than the bulk electrical conductivity of the polymer. As the OLP plates cover the surface of the CNT, the surface area of the interfacial layer increases. Accordingly, a high concentration of charges (protons) is concentrated at the polymer-nanotube interface, which cannot pass to the electrode connected to the nanotubes. The analysis of the impedance spectrum and the values of the parameters of the elements of the equivalent circuit also shows that the direct contacts between the nanotubes are almost absent, as evidenced by the high value of the contact resistance R , which is about $10^{-12} \Omega$.

4 Conclusions

It can be concluded that the introduction of anisometric nanofillers significantly affects the structure and properties of polymeric nanocomposites based on polyethylene oxide. As a result of the study using the methods of wide-angle and low-angle X-ray scattering, it was shown that the studied CNTs are multilayer, the radii of the tubes vary between 15 and 25 nm and they aggregate, depending on the conditions in dense or looser plait. The introduction of nanotubes in PEO leads to a decrease in

its degree of crystallinity. When dispersing of CNTs in a polymer matrix, their flexibility increases. This effect is due to the destruction of nanotube beams by ultrasonic waves.

It is shown that the structure and electrical properties of PEO-based nanocomposites significantly depend on the nature and content of the layered silicate filler. It is established that in systems filled with OMMT, partial intercalation processes take place, while in systems filled by OLP, complete exfoliation is observed. From the data of X-ray diffraction analysis, it can be seen that the introduction of OLP leads to greater amorphization of the system than the introduction of OMMT. The presence of OLP in the system, in contrast to OMMT, promotes the formation of larger crystallites. Based on electrical studies, it is shown that by varying the content and nature of the silicate filler in PEO-based polymer nanocomposites, relaxation processes and conductivity can be significantly influenced.

As a result of the conducted researches, it was established that the introduction of organomodified laponite into the PEO-CNTs system can significantly affect its percolation characteristics. It is established that with the introduction of laponite into the PEO-CNTs system, the value of the percolation threshold shifts to the range of lower concentrations from 0.5 to 0.22%. This effect is associated with a change in the degree of distribution of the tubes over the volume of the polymer matrix. When introduced into the material, OLP nanoparticles begin to interact with the surface of nanotubes and are attracted to it. As a result, the surface of the nanotubes is partially covered with laponite plates. At this degree of coverage, there is a probability for the formation of direct contacts between CNTs. It was found that the introduction of small amounts of OLP particles into the composition of PEO-CNTs does not affect the processes of charge transfer in the system. It is shown that when a relatively high content of laponite is introduced into the PEO-CNTs system, the electrical conductivity decreases significantly, and when the CNTs content is 1%, the electrical conductivity decreases almost to the level of unfilled PEO. The effect of reducing the electrical conductivity of the system at high filler content can be explained by assuming that laponite nanoplates form a three-dimensional network that permeates the entire volume of the material, i.e., the system turns into a gel. As a result of engagement between polymer molecules and laponite plates, nanotubes, while remaining isolated from each other, cannot form direct contacts with each other, which leads to a significant reduction in the electrical conductivity of the system.

References

1. Fu S, Sun Z, Huang P, Li Y, Hu N (2019) Some basic aspects of polymer nanocomposites: a critical review. *Nano Mater Sci* 1(1):2
2. Lysenkov EA, Klepko VV, Lysenkova IP (2020) Features of structural organization of nanodiamonds in the polyethylene glycol matrix. *J Nano Electron Phys* 12(4):04006
3. Lysenkov EA, Lysenkova IP (2020) Influence of nanodiamonds on the structure and thermophysical properties of polyethylene glycol-based systems. *Func Mater* 27(4):774









4. Shameem MM, Sasikanth SM, Annamalai R, Raman RG (2021) A brief review on polymer nanocomposites and its applications. *Mater Today Proc* 45(2):2536
5. Ghoshal S (2017) Polymer/carbon nanotubes (CNT) nanocomposites processing using additive manufacturing (three-dimensional printing) technique: an overview. *Fibers* 5(4):40
6. Lysenkov EA, Klepko VV, Yakovlev YV (2016) Specifics of percolation behavior in the polyether-carbon nanotube systems doped with LiClO₄. *Surf Eng Appl Electrochem* 52(2):186
7. Lysenkov EA, Klepko VV (2015) Characteristic features of the thermophysical properties of a system based on polyethylene oxide and carbon nanotubes. *J Engin Phys Thermophys* 88(4):1008
8. Guo F, Aryana S, Han Y, Jiao Y (2018) A review of the synthesis and applications of polymer-nanoclay composites. *Appl Sci* 8:1696
9. Lysenkov EA, Klepko VV, Lysenkova IP (2017) Features of microstructure and percolation behavior of polypropylene glycol, filled by multiwalled carbon nanotubes. *J Nano Electron Phys* 9(5):05021
10. Cancan B, Yangchuan K, Xu H, Liang X, Yi Z, Shichao L, Yuan L (2020) Preparation and properties of amphiphilic hydrophobically associative polymer/montmorillonite nanocomposites. *R Soc Open Sci* 7(5):200199
11. Da Silva JRM, Damasceno CI, Da Silva NJE, Soares AT, Renata B (2016) Characterization of bionanocomposites PHB, PEG and organophilic clay. *Mater Sci Forum* 869:303
12. Gurses A, Ejder-Korucu M, Dogar C (2012) Preparation of PEO/clay nanocomposites using organoclay produced via micellar adsorption of CTAB. *Sci World J* 2012:270452. <https://doi.org/10.1100/2012/270452>
13. Loginov M, Lebovka N, Vorobiev E (2012) Laponite assisted dispersion of carbon nanotubes in water. *J Colloid Interface Sci* 365:127
14. Yaroshchuk O, Tomylko S, Kovalchuk O, Lebovka N (2014) Liquid crystal suspensions of carbon nanotubes assisted by organically modified laponite nanoplatelets. *Carbon* 68:389
15. Chalmes N, Kouloumpis A, Zygouri P, Karouta N, Spyrou K, Stathi P, Tsoufis T, Georgakilas V, Gournis D, Rudolf P (2019) Layer-by-layer assembly of clay-carbon nanotube hybrid superstructures. *ACS Omega* 4(19):18100
16. Song SH (2018) The effect of clay/multiwall carbon nanotube hybrid fillers on the properties of elastomer nanocomposites. *Hindawi Int J Polym Sci* 2018:5295973
17. Al-Saleh MH (2015) Effect of clay addition on the properties of carbon nanotubes-filled immiscible polyethylene/polypropylene blends. *J Macromol Sci Part B Phys* 54(10):1259
18. Khajehpour M, Arjmand M, Sundararaj U (2014) Dielectric properties of multiwalled carbon nanotube/clay/polyvinylidene fluoride nanocomposites: effect of clay incorporation. *Polym Compos* 37:161
19. Lysenkov EA, Lebovka NI, Yakovlev YV, Klepko VV, Pivovarova NS (2012) Percolation behaviour of polypropylene glycol filled with multiwalled carbon nanotubes and laponite. *Compos Sci Technol* 72:1191
20. Lysenkov EA, Leonova NG, Zhiltsova SV (2019) Effect of the silicon-containing phase on the hierarchy of the structure of epoxy-silica nanocomposites. *Theor Exper Chem* 55(4):250
21. Stauffer D, Aharony A (1994) Introduction to percolation theory. Taylor and Francis, London, p 318
22. Tomylko S, Koval'chuk A, Yaroshchuk O, Lebovka N (2017) Structural evolution and dielectric properties of suspensions of carbon nanotubes in nematic liquid crystals. *Phys Chem Chem Phys* 19(25):16456
23. Sen D, Dasgupta K, Bahadur J et al (2008) Morphology of carbon nanotubes prepared via chemical vapour deposition technique using acetylene: a small angle neutron scattering investigation. *J Phys* 71(5):971
24. Sato H, Sano M (2008) Characteristics of ultrasonic dispersion of carbon nanotubes aided by antifoam. *Col Surf A Physicochem Eng Aspects* 322:103
25. Efron AL, Shklovskii BI (1973) Critical behaviour of conductivity and dielectric constant near the metal-non-metal transition threshold. *Phys Stat Sol B* 76:475

26. Mitescu CD, Musolf MJ (1983) Critical exponent for 3-D percolation conductivity. *J Physique* 44:L-679
27. Lysenkov EA, Klepko VV (2016) Analysis of percolation behavior of electrical conductivity of the systems based on polyethers and carbon nanotubes. *J Nano Electron Phys* 8(1):01017
28. Elimat ZM, Al-Hussami SA, Zihlif AM (2012) Effect of carbon black on the thermoelectrical properties of poly(ethylene-oxide) composites. *J Compos Mater* 47(28):3525
29. Hajar MDS, Supri AG, Hanif MPM, Yazid MIM (2017) Effect of graphite loading on the electrical and mechanical properties of poly (ethylene oxide)/poly (vinyl chloride) polymer films. *IOP Conf Ser J Phys* 908:012020
30. Bauhofer W, Kovacs JZ (2009) A review and analysis of electrical percolation in carbon nanotube polymer composites. *Compos Sci Technol* 69:1486
31. Lysenkov EA, Klepko VV (2016) Features of percolation transition in nanocomposites based on polyethers and carbon nanotubes. *J Phys Stud* 20(3):3702
32. Yadav RM, Dobal PS (2012) Structural and electrical characterization of bamboo-shaped C-N nanotubes–poly ethylene oxide (PEO) composite films. *J Nanopart Res* 14:1155
33. Chatterjee T, Yurekli K, Hadjiev VG, Krishnamoorti R (2005) Single-walled carbon nanotube dispersions in poly(ethylene oxide). *Adv Fund Mater* 75:1832
34. Sandler JKW, Kirk JE, Kinloch IA, Shaffer MSP, Windle AH (2003) Ultralow electrical percolation threshold in carbonnanotube epoxy composites. *Polymer* 44:5893
35. Kilbride BE, Coleman JN, Fraysse J, Fournet P, Cadek M, Drury A, Hutzler S, Roth S, Blau WJ (2002) Experimental observation of scaling laws for alternating current and direct current conductivity in polymercarbon nanotube composite thin films. *J Appl Phys* 92(7):4024
36. Foygel M, Morris RD, Anez D, French S, Sobolev VL (2005) Theoretical and computational studies of carbon nanotube composites and suspensions: electrical and thermal conductivity. *Phys Rev B* 71(10):104201
37. Panda M, Thakur AK, Srinivas V (2010) Thermal effects on the percolation behavior of polyvinylidene fluoride/nickel composites. *J Appl Polym Sci* 117:3023
38. Li YJ, Xu M, Feng JQ, Dang Z-M (2006) Dielectric behavior of a metal-polymer composite with low percolation threshold. *Appl Phys Lett* 89:072902
39. Chang J, Liang G, Gu A, Cai S, Yuan L (2012) The production of carbon nanotube/epoxy composites with a very high dielectric constant and low dielectric loss by microwave curing. *Carbon* 50(2):689
40. Paul DR, Robeson LM (2008) Polymer nanotechnology: nanocomposites. *Polymer* 49:3187
41. Ciselli P, Zhang R, Wang Z (2009) Oriented UHMW-PE/CNT composite tapes by a solution casting-drawing process using mixed-solvents. *Eur Polym J* 45:2741
42. Kotaki JM, Wang K, Toh ML, Chen L, Wong SY, He CB (2006) Electrically conductive epoxy/clay/vapor grown carbon fiber hybrids. *Macromolecules* 39(3):908
43. Feller JF, Bruzaud S, Grohens Y (2004) Influence of clay nanofiller incorporation on electrical and rheological properties of conductive polymer composite (CPC). *Mater Lett* 58:739
44. Levchenko V, Ye M, Boiteux G (2011) Influence of organo-clay on electrical and mechanical properties of PP/MWCNT/OC nanocomposites. *Eur Polym J* 147:1351
45. Etika KC, Liu L, Hess LA, Grunlan JC (2009) The influence of synergistic stabilization of carbon black and clay on the electrical and mechanical properties of epoxy composites. *Carbon* 47:3128
46. Lysenkov E, Melnyk I, Bulavin L, Klepko V, Lebovka N (2015) Structure of polyglycols doped by nanoparticles with anisotropic shape. In: Bulavin L, Lebovka N (eds) *Physics of liquid matter: modern problems, springer proceedings in physics*. Springer International Publishing, Switzerland, pp 165–198
47. Lebovka NI, Lysenkov EA, Goncharuk AI, Gomza YuP, Klepko VV, Boiko YuP (2011) Phase behaviour, microstructure, and percolation of poly (ethylene glycol) filled by multiwalled carbon nanotubes and organophilic montmorillonite. *J Compos Mater* 45(24):2555
48. Feder J (2013) *Fractals*. Springer Science & Business Media, 284 p
49. Deriabina O, Lebovka N, Bulavin L, Goncharuk A (2014) Regulation of dispersion of carbon nanotubes in mixture of good and bad solvents. *Phys E* 59:150

50. Sahimi M (1994) Applications of percolation theory. Taylor and Francis, Boca Raton, Fla, USA, p 276
51. Macdonald J (1987) Impedance spectroscopy. Wiley, New York, p 346
52. Lysenkov EA, Klepko VV (2011) Influence of anisometric fillers on electrical properties of polypropylene glycol-based nanocomposites. Ukr J Phys 56(5):484
53. Kochowski S, Nitsch K (2002) Description of the frequency behaviour of metal-SiO₂-GaAs structure characteristics by electrical equivalent circuit with constant phase element. Thin Solid Films 415:133
54. Sun W, Yang Y, Wang T, Huang H, Liu X, Tong Z (2012) Effect of adsorbed poly(ethylene glycol) on the gelation evolution of laponite suspensions: aging time-polymer concentration superposition. J Colloid Interface Sci 376(1):76

Gas-Phase and Plasma-Chemical Bromination: Key Techniques to Prepare Heteroatom-Functionalized Carbon Surfaces



V. E. Diyuk , L. M. Grishchenko , A. V. Vakaliuk , G. G. Tsapyuk ,
O. V. Mischanchuk , O. Yu. Boldyrieva , R. Mariychuk ,
and V. V. Lisnyak 

Abstract Nanoporous activated carbons (NACs), multiwalled carbon nanotubes (MWCNTs), carbon black (CB), and activated carbon fibers (ACFs) were directly brominated in gas phase with bromine vapor in the temperature range of 30–800 °C and plasma-chemically brominated using a 27.12 MHz atmospheric inductively coupled bromine plasma at 22 °C. Isothermal bromination in the temperature range of 200–500 °C leads to chemisorption of bromine in the amount of 0.5–2.5 mmol g⁻¹. The largest amounts of grafted bromine were found on materials with developed microporosity: NACs and ACFs. However, the surface reactivity per 1 m² was significantly higher for CB and MWCNTs. The diffusion of bromine in a carbon porous structure determines the bromination rate and completeness of the bromination process at any temperature. The bromination reaction is completed within 1–2.5 h, depending on the porous structure of the CM. Amination of brominated CMs with diethylamine leads to partial substitution of bromine for amino groups in the amount of 0.30–1.55 mmol g⁻¹. Bromination of ACFs with bromine plasma at 22 °C leads to chemisorption of up to 1 mmol g⁻¹ of bromine. During short-term (5–30 min) treatment with bromine plasma, significant amounts of physisorbed and intercalated bromine are formed on the ACF surface. Increasing the bromination time to 60 min leads to the maximum amount of chemisorbed bromine (up to 1.04 mmol g⁻¹). About 60–70% of the grafted bromine can be replaced by thermally stable acid SO₃H groups. It is shown that 100% conversion of 2-propanol to propene on the obtained acid catalysts is observed at 190–205 °C.

V. E. Diyuk (✉) · L. M. Grishchenko · A. V. Vakaliuk · G. G. Tsapyuk · O. Yu. Boldyrieva · V. V. Lisnyak

Taras Shevchenko National University of Kyiv, Kyiv 01601, Ukraine

e-mail: vdiyuk@gmail.com

O. V. Mischanchuk

Chuiko Institute of Surface Chemistry of the NAS of Ukraine, Kyiv 03164, Ukraine

R. Mariychuk

Faculty of Humanities and Natural Sciences, University of Prešov, Prešov 08001, Slovakia

Keywords Carbon materials · Gas-phase bromination · Plasma-chemical bromination · Bromination kinetics · Surface amination · Surface sulfonation

1 Introduction

Carbon nanomaterials and porous carbon materials have a developed surface. They are sorbents in the processes of separation and purification of gas and liquid mixtures [1], for gas storage [2], in catalysis as carriers [3], or directly, as catalysts [4–6], and as electrode materials in energy generation and storage processes [7].

The functional properties of carbon materials are related to specific interactions between the carbon surface and the gas or liquid phase. Therefore, together with the porous structure, the properties of carbon materials will be significantly affected by their functional cover. One can optimize carbon materials for specific applications by creating a specially selected layer with surface functional groups. The simplest method of forming a layer of functional groups is through the use of oxidation [8–11]. Because of the significant affinity of carbon for oxygen, the surface of any carbon material is covered with various O-containing groups. Among these groups, the most common are carboxyl (Cx), phenolic (Ph), quinone (Qu), and carbonyl (Cb) groups [8–11]. Nearest-neighboring oxygen-containing groups can interact, with each other, to form more complex sites, such as surface anhydride (A) and lactone (L) groups [12–18]. However, oxidation adversely affects the porous structure and specific surface area of CMs [19], and the oxygen-containing groups can exhibit weak acidic properties only and cannot give significant basicity to the carbon surface [20].

The modification of the surface by heteroatoms changes its acid-base and hydrophilic-hydrophobic properties in a wide range and significantly expands the use of modified carbon materials [21–24]. The main obstacle to obtaining CMs modified by heteroatoms is the low chemical activity of the carbon matrix, which mainly contains carbon atoms in the sp^2 -hybridized state in the composition of condensed aromatic rings [25, 26]. The basal surface of such graphene layers is chemically inert. A small number of defects and surface groups, mostly localized at the edges of graphene layers, are few active sites available in the carbon matrix. The solution to this problem is the selection of adequate methods of chemical modification, which will provide sites for the covalent attaching of a significant number of chemical groups to the active sites of the surface.

Pre-bromination can be used to increase the concentration of surface-attached groups. Bromination is one of the most well-known and effective ways of carbon surface functionalization, and it gives high yields [27–29]. Many bromination methods are currently known [30, 31]. The simplest method of bromination is treatment with molecular bromine in the liquid phase [32, 33] or in the gas phase [34–37]. But, the treatment with molecular bromine, including bromination in solutions containing bromine, is accompanied by significant oxidation of the carbon surface and bulk [38]. Other bromination methods are the bromination of oxidized carbon

nanomaterials, such as graphene oxide and graphite oxides, with $\text{H}_2\text{O}_2/\text{HBr}$ solutions [39] or using bromine or hydrobromic acid under reflux conditions or in an autoclave at elevated temperatures and pressures [40], and also by using the reduction of few-layer graphene sheets with a sodium-naphthalide solution and then brominated them by the direct method [41]. The bromination can be used to purify and open carbon nanotubes [42]. Besides, chemical bromination of carbon nanotubes catalyzed by the Lewis acid is also reported [43]. Alternative methods of bromination of CMs include electrothermal [44], hydrothermal [45], plasma-chemical [46–50], photochemical [51–53], and microwave processing [54] methods. Bromination is a simple method for determining multiple bonds in organic compounds [55] and can be used to quantify the active centers of CMs. Chemisorbed bromine atoms have been shown to react readily with nucleophilic substituents. Using brominated precursors opens the way to preparing various CMs with covalently attached scaffolds and dyes or with grafted functional groups [56, 57].

It should be noted that brominated carbons can be used to purify gases and contaminated water from mercury by the adsorption method [58–62]. The use of brominated carbons also improves the capacity of electrochemical energy storage devices [63–65]. Bromine-containing carbon materials can be used in catalysis, particularly as active additives in the oxidation of alkyl and aromatic hydrocarbons, cumene, oil diesel fraction, and low-density polyethylene [66–68]. By using the bromination reaction, one can perform further functionalization; for example, bromine attached to the carbon surface can be replaced by diethylamine residues or other amino groups [69, 70].

Therefore, it is crucial to develop a convenient and efficient method of bromination of CMs to achieve significant yields of attached bromine. One way to solve the problem is to use bromine vapor, which can be activated by high temperature or high-frequency plasma discharge. Kinetic studies conducted in a wide range of temperatures can provide valuable information about the mechanism of bromination to determine its optimal conditions. It is important to study the reactivity of the attached bromine for further modification to obtain carbon surfaces functionalized with N- or S-heteroatoms.

2 Experimental

2.1 Materials and Reagents

As the initial CMs, we used three types of nanoporous activated carbons (NACs), labeled as NAC1, NAC2, and NAC3, multiwalled carbon nanotubes (MWCNTs), carbon black (CB), and activated carbon fibers (ACF). The NAC1 was an activated carbon obtained from peach stones; The NAC2 was a spherical nitrogen-containing NAC obtained by standard method for carbonization and vapor activation of vinyl pyridine rubber; The NAC3 was obtained from the same raw material as NAC2.

But, at the carbonization stage, the level of carbon burnoff was kept above 80%. The MWCNTs (JSC ALIT, Kyiv, Ukraine, 95%) were prepared by a chemical vapor deposition method with a metal Ni/Mg catalyst. For purification, crude MWCNTs were treated with a mixture of hydrochloric and nitric acids [71]. The CB sample (K354 trademark, 98%) was obtained as soot by impingement of small natural gas diffusion flames in a burning camera on a channel iron. The ash content in the CB samples is about 0.05 mass%. The CB was used as is without any additional treatment. The ACF is carbon fiber made from polyacrylonitrile, which is carbonized and simultaneously activated in an atmosphere of water vapor at 1000 °C.

All chemicals used in this study were p.a. grade from Merck, Fluka, Fischer, and Sigma Aldrich, and they were used as received without further purification. All solutions were prepared with deionized water of resistivity not less than 18.2 M Ω cm⁻¹. The pure argon gas (99.999%) used in the bromination and thermal desorption experiments was supplied in gas cylinders by Linde Gas Ukraine.

2.2 Functionalization

Bromination of CMs by bromine vapors

Bromination of CMs with bromine vapors was performed under gravimetric control with a thermogravimetric analyzer. It was based on the McBain spring microbalances and operated under a dynamic gas atmosphere. The studied sample (50 mg) was placed in a quartz basket and transferred within it into a quartz reactor. The reactor was placed in a temperature-controlled furnace regulated by a programmer-controller TRP-09TP (LLC Byte, Zhytomyr, Ukraine). The basket with the sample was hung to a ferrite rod through two quartz hooks. The ferrite rod was suspended on a tungsten spring placed inside an upper vessel. The rod was moved in the tube connecting the vessel and the reactor and positioned inside a gap of an induction coil imposed externally and mounted stationary. The change in the weight of the sample caused a change in the length of the spring. The spring tension–compression moved the position of the ferrite rod in the inductor coil. The electromagnetic response of the inductor in the electrical circuit with the microcontrollers was recorded automatically on a laptop. This signal was linearly proportional to the weight of the sample at the respective temperature of the sample. This construction ensured the registration of the effects of weight change at the level of 4×10^{-5} g. The upper vessel, where the tungsten spring was located, was carefully thermostated with a water condenser jacket operated by a circulating thermostat (Carl Roth, E5s model). At experiments, an argon flow (40 ml min⁻¹) was passed through the upper vessel to the quartz reactor to protect against bromine vapors. The flow of argon (40–50 ml min⁻¹) was saturated with bromine vapor (bromine concentration about 1×10^{-3} mol L⁻¹) to prepare an Ar-Br₂ gas mixture, which was fed, by gas controllers, to the reactor directly, with no contact with the ferrite rod and tungsten spring.

The bromination reaction was investigated under non-isothermal and isothermal conditions. In non-isothermal experiments, three different heating rates were used, namely, 3, 5, and 10 °C min⁻¹. From the beginning of the non-isothermal experiment, the Ar-Br₂ gas mixture was introduced into the interaction with the sample of certain CM. In the course of the experiment, these samples were heated from 30 to 800 °C at a selected heating rate. Isothermal bromination was performed at 200, 300, 400, and 500 °C. During these studies, two types of experiments were performed. In the first experiments, typically, the sample was heated in argon flow to a given temperature. At this temperature, the sample was kept (in the reactor) up to a constant weight. After that, the Ar-Br₂ gas mixture was fed into the system. The weight change under the constant temperature was recorded until the growth of the weight of the sample ceased under the Ar-Br₂ gas mixture flow. The experiments of the second type were used to study the thermal stability of the attached bromine. In the typical experiment, pure argon gas was fed into the system, and then the bromine desorption under isothermal conditions was investigated by weight loss recording. Additionally, the samples of the brominated CMs were obtained for further studies without the bromine desorption stage. These samples were rapidly cooled in the reaction mixture of Ar-Br₂ and thoroughly vacuumed at 100 °C to remove physisorbed bromine. The resulting samples were designated as the CM-Br-T, where T is the bromination temperature.

Plasma-chemical bromination of ACF

Before modification, the ACF samples (2 g) were dried in air at 120 °C for 2 h. The dried ACF samples were vacuum evacuated in the installation directly before the plasma bromination. Plasma-chemical bromination of the ACF surface was performed with bromine vapor at pressure 0.1 mmHg at 22 °C under high-frequency inductive plasma discharge at a frequency of 27.12 MHz. The duration of plasma treatment varied from 5 to 30 min. The samples were designated as the ACF-Br-*t*, where *t* is the bromine plasma treatment time.

Amination of brominated carbon materials

A sample of brominated CM (1 g) was transferred in an autoclave screwcap tube, and then a 20 ml solution of 20 wt% Et₂NH in ethanol was added. The closed and filled autoclave screwcap tube was placed in a stainless steel autoclave. The stainless steel autoclave was heated up to 110 °C and then was kept at this temperature for 12 h. After barothermal treatment, the sample was washed on a filter with distilled water and then with dilute H₂SO₄ solution to remove the adsorbed amine. As a result of the acid treatment, the amino groups form salts, so the samples were further washed with an aqueous solution of 10 wt% of Na₂CO₃ and water to neutral pH. Next, the aminated samples were dried in air at 120 °C. Aminated CMs were designated as the CM-Br-T-N, where *T* is the bromination temperature.

Sulfonation of brominated carbon materials

Samples of the unmodified ACF and the brominated ACF-Br-*t* were placed in screwcap test tubes, poured with a concentrated solution of sodium mercaptoacetate

(MA), and kept immersed for the period of 15 h in the closed test tubes thermostated at 120 °C [72]. The prepared samples were boiled with 15 wt% of HCl to hydrolyze the S-containing surface groups. After the boiling, the samples were treated with 30 wt% of H₂O₂ to oxidize HS-containing surface groups, washed with water, and dried at 120 °C. The obtained samples were designated as the ACF-S and ACF-Br-*t*-S, respectively.

2.3 Methods

For analysis, to quantify the bromine content, the samples of brominated CMs were dissolved in a melt of NaOH–NaNO₂ (molar ratio 3:1). The dissolution was done at a temperature of about 500 °C. After cooling, the resulting melt was dissolved in water and acidified, and then the content of bromide ions was determined by an inverse titration by the Volgard method. Scanning electron microscopy (SEM) studies and energy-dispersive X-ray spectroscopy (EDS) measurements were performed on a Zeiss EVO-50 SEM microscope equipped with an INCA Energy 350 spectrometer [73, 74].

Before the studies, the samples were dried at 120 °C and vacuumed for 5 h. FTIR-ATR spectra of the samples were obtained on Shimadzu IRAffinity-1S and IRPrestige 21 Fourier spectrometers. Recording and search match procedures for the spectra lines were performed using a standard software package LabSolutions IR from Shimadzu. For the studies, the samples were thoroughly dried and ground into powder. The spectra were recorded in the wavelength range 650–4000 cm⁻¹, with a step of 0.5 cm⁻¹, in the mode of accumulation of 1025 and 3000 scans by the method of disturbed total internal reflection (ATR) using the Horizontal ATR Basics ATR-8000A, which was equipped with prisms based on zinc selenide and metallic germanium.

Nitrogen adsorption-desorption isotherms were measured up to 1 atm at –196 °C on a Micromeritics ASAP 2010 unit. All samples were outgassed at 150 °C under vacuum for 24 h before measurement. The specific surface area (S_{BET}) was calculated using the Brunauer–Emmett–Teller (BET) method. The total pore volume (V_{tot}) was estimated at a relative pressure of $p/p_0 = 0.99$. For the pore size distribution (PSD) calculations, the adsorption branches of isotherms were analyzed with the SAIEUS program (<http://www.nldft.com>) using the kernel carbon–N₂ model for porous carbons having a heterogeneous surface [75]. This model was derived from the 2D non-local density functional theory (NLDFT). The micropore surface area (S_{micro}) and micropore volume (V_{micro}) were found from the PSD data. The mesopore surface area (S_{meso}) and mesopore volume (V_{meso}) were found as $S_{\text{meso}} = S_{\text{BET}} - S_{\text{micro}}$ and $V_{\text{meso}} = V_{\text{tot}} - V_{\text{micro}}$. The parameters of the Dubinin–Radushkevich (DR) equation: the limiting micropore volume (V_{DR}), and the characteristic adsorption energy (E_{DR}) were found as in [76].

Thermogravimetric analysis (TGA) was used to study the thermal stability of the prepared and pristine samples. The samples were heated from 30 to 800 °C at a rate of 10 °C min⁻¹ in an argon flow of 50 ml min⁻¹. Thermal desorption with IR spectrometric registration of gaseous products (TPD IR) was used in combination with the TGA method to determine the concentration of oxygen-containing surface groups (C_{FG}). As a result of heating, the thermal decomposition of oxygen-containing groups causes the release of CO₂ and CO gases. The flow of argon was diluted and directed the decomposition products into the gas cuvette of the IR spectrometer, where the concentrations of carbon oxides ($C(\text{CO}_2)$ and $C(\text{CO})$) were measured with the gas standards of known concentrations [77]. The temperature profiles of ($C(\text{CO}_2)$ and $C(\text{CO})$) were decomposed into components using Gaussian functions, and the concentration C_{FG} was determined according to [78].

The thermoprogrammed desorption mass spectroscopy (TPD MS) method was used to determine the surface functional groups. In a typical experiment, the sample was heated in a vacuum (10⁻⁴ Pa) at a rate of 10 °C min⁻¹ from 30 to 800 °C. All volatile products of desorption or the products of the thermal decomposition of functional groups were analyzed by the MS method. Mass spectra were recorded in a cyclic mode, which allowed for obtaining a set of mass spectra for the gas phase at different temperatures on the sample. After that, the dependence of the signal intensity in the mass spectrum on the temperature of the sample (thermodesorption profile) was plotted for each value of m/z . A unipolar quadrupole mass spectrometer MX 7304 A (Selmi, Sumy, Ukraine) was used, and the mass spectrum was obtained by electronic ionization at 70 eV [79]. The Boehm titration method was used to determine the concentration of different O-containing surface groups that can participate in cation exchange processes [80]. The functional O-containing surface groups are acidic; they can be neutralized with solutions of bases of different strengths. The Cx groups are the most acidic; they react with NaHCO₃. Under the action of a stronger Na₂CO₃ base, the L and A cycles are opened, and proton replacement in the Ph groups takes place in water solutions of a strong NaOH base. The study was performed as follows. The dried sample (0.1 g) was immersed in a 10 ml solution of 0.05 M NaHCO₃, 0.05 M Na₂CO₃, or 0.05 M NaOH and then shaken for 24 h to achieve adsorption equilibrium. The carbon solids were separated from the solution. After that, a 2 ml aliquot was taken to be titrated with 0.1 M HCl solution to determine the volume of the base that reacted with the surface functional groups. At the same time, we conducted a comparison experiment.

X-ray photoelectron spectroscopy was used to determine the chemical state of bromine in the surface layer with a thickness of 30–40 Å. The XP spectra were obtained by means of a VG Scientific ESCALAB-210 electron spectrometer, employing Mg K α X-rays.

3 Results and Discussion

3.1 Characterization of Pristine Carbon Materials

Figure 1a–f shows SEM micrographs of the unmodified CMs.

All NAC samples are granular materials with a granule size of 1–3 mm. Spherical granules of the NAC2 and NAC3 samples have approximately the same size. The size of the initial NAC2 spheres practically does not decrease during prolonged activation, forming the NAC3 sample. The structure of the NAC1 sample derived from the fruit

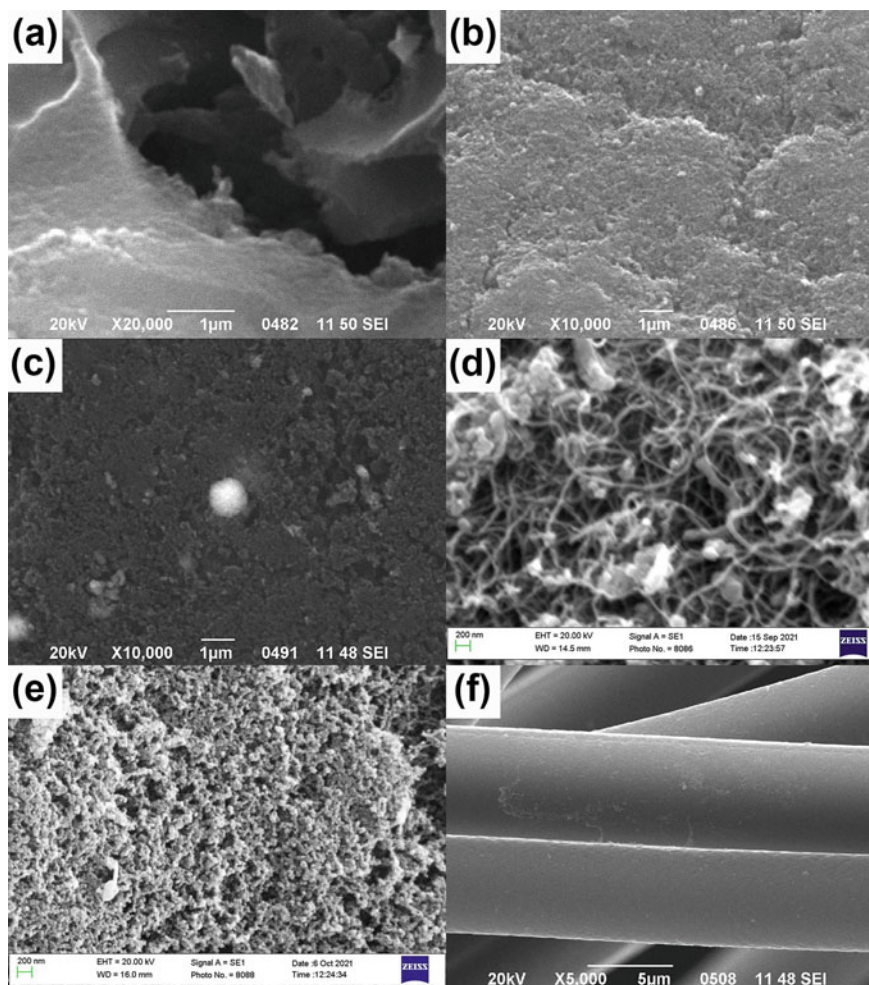


Fig. 1 SEM micrographs of **a** NAC1, **b** NAC2, **c** NAC3, **d** MWCNTs, **e** CB, and **f** ACF samples

Table 1 Texture parameters and EDX analysis results

Sample	Specific surface area, m^2g^{-1}			Specific volume, cm^3g^{-1}				E_{DR} , kJ mol^{-1}	EDX, at%	
	S_{BET}	S_{micro}	S_{meso}	V_{tot}	V_{micro}	V_{meso}	V_{DR}		C	O
NAC1	951	926	25	0.45	0.37	0.08	0.40	6.9	95.9	4.1
NAC2*	1300	1165	135	1.09	0.59	0.50	0.46	8.4	95.4	3.5
NAC3	2500	1695	805	3.06	0.67	2.39	0.76	5.9	97.3	2.7
MWCNTs	150	21	129	0.51	0.04	0.47	0.05	6.0	94.5	5.5
CB	110	103	7	0.08	0.04	0.04	0.05	4.2	95.3	4.7
ACF*	680	675	5	0.34	0.33	0.01	0.34	4.7	94.2	5.0

* NAC2 and ACF contain 1.1 and 0.9 at% of N, respectively

seeds retains large transport channels of 1–3 μm wide (Fig. 1a). These channels are remnants of the structure of the initial raw material. Their size significantly exceeds the dimensions of micropores and mesopores. The surface of NAC2 and NAC3 granules is smoother and contains small channels, the size of which does not exceed 0.3–0.5 μm (Fig. 1b, c). The original sample of MWCNTs consists of nanotubes with an outer diameter of 20–100 nm and a length exceeding a few microns (Fig. 1d). The MWCNTs are distorted and branched, which indicates a significant number of defects on their surface. The CB (Fig. 1e) consists of predominantly rounded aggregates 50–100 nm in size. The carbon fibers in the ACF sample are composed of individual strands 5–7 μm thick (Fig. 1f). Their surface looks rather smooth and does not contain large channels. According to the EDX analysis data, the initial CMs belong to non-oxidized materials, and the oxygen content does not exceed 5.0 at % (Table 1).

The isotherms of nitrogen adsorption registered for the studied sorbents are markedly different from each other (Fig. 2a). Both MWCNTs and CB samples are characterized by the lowest nitrogen adsorption (at low p/p_0 values) because of the low microporosity of these materials, as can be seen from Table 1. All other samples $p/p_0 < 0.1$ contain a range of significant adsorption because of a noticeable contribution of micropores to the porous structure of these samples. As the specific surface area S_{BET} increases, the studied CMs can be arranged in ascending order as follows: $\text{CB} < \text{MWCNTs} < \text{ACF} < \text{NAC1} < \text{NAC2} < \text{NAC3}$ (Table 1). The hysteresis loops are observed when scanning the adsorption and desorption branches of the nitrogen physisorption isotherms for all studied sorbents. These observations clearly reveal pronounced mesoporosity. However, the fraction of the surface area that accounts for the mesopores is very different for the studied sorbents. The CB, ACF, and NAC1 are mainly microporous sorbents, and the contribution of the mesopore surface area S_{meso} to the specific surface area S_{BET} is 1–7%. Despite a large number of micropores (90%) for the NAC2 sample, its porous structure contains mesopores. The volume of mesopores V_{meso} is 46% of the total pore volume V_{tot} . For the NAC3 sample, the contribution of mesopores to the specific surface area S_{BET} is about 30%, and this material is a micro-mesoporous sorbent. The MWCNTs have a

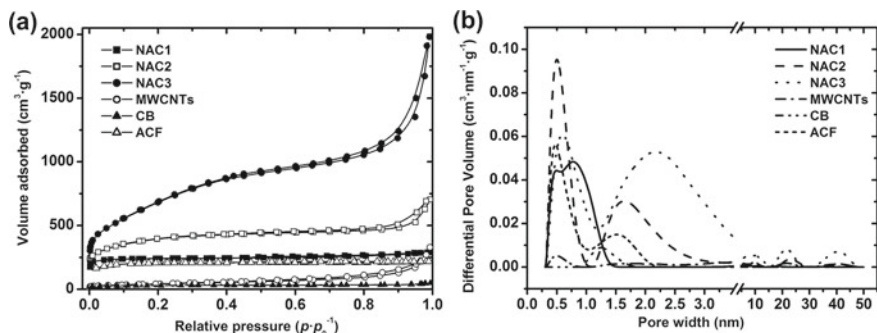


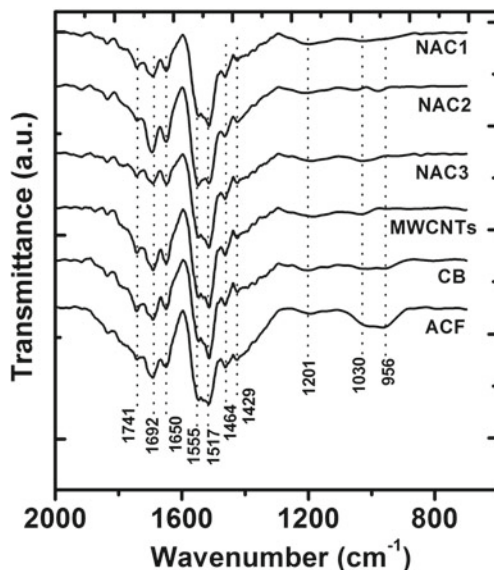
Fig. 2 **a** Nitrogen adsorption/desorption isotherms and **b** differential pore volume against pore width for the pristine CMs

mesoporous structure. The contribution of micropores to the structural and sorption parameters of MWCNTs does not exceed 14%. According to the ratio of micropores to mesopores, the studied sorbents can be arranged in descending order as follows: ACF > NAC1 > CB > NAC2 > NAC3 > MWCNTs.

The total pore volume for the studied samples is very dissimilar; the pore size distribution (PSD) curves confirm different porous structures of CMs (Fig. 2b). In the series CB < ACF < NAC1 < MWCNTs < NAC2 < NAC3, the total pore volume significantly increases. This increase for various CMs is due to the increasing contribution of micropores or mesopores. From the PSD dependences (Fig. 2b), one can conclude that the ACF, NAC1, and CB sorbents are almost microporous solids with small micropores having a width of about 0.48 and 1.52, 1.25, and 0.50 and 0.78 nm, correspondingly. The larger micropores with sizes of about 0.50 and 1.66 nm are found in the nanoporous NAC2 sorbent. Fine micropores of 0.60 nm wide, larger pores of 2.16 nm wide, and a noticeable number of mesopores within the range of 3–25 nm are found for the sample of NAC3 sorbent. An insignificant contribution from the pores of 0.50 and 1.64 nm in size is registered for the MWCNTs. However, the largest contribution to the total pore volume is made by mesopores of 3.59, 5.73, 9.66, 21.8, and 40.6 nm in size. The Dubinin-Radushkevich adsorption energy E_{DR} , describing adsorption in micropores, reaches the values typical for CMs (Table 1). The smallest E_{DR} values are found for the CMs with the highest matrix ordering, like the CB and ACFs. Consequently, the initial CMs selected for research have different structural and sorption parameters; in other words, the selected sorbents ranged from almost microporous to mesoporous solids. On the other hand, for the MWCNTs and CB, and partly for the ACF, the contribution of the external (or easily accessible) surface is significant compared to the samples of NACs.

FTIR ATR spectra of the CMs are presented in Fig. 3. The most intense absorption bands at 1555 and 1517 cm⁻¹, and the shoulder at 1464 cm⁻¹, belong to skeletal vibrations of aromatic and/or conjugated C=C bonds of the carbon matrix. The shape of these bands is not very different for all CMs, which means that the structure of the conjugated aromatic component of the carbon matrix of these CMs is practically

Fig. 3 Comparison of the FTIR ATR spectra of the pristine CMs



the same. All studied CMs belong to sp^2 -carbon materials formed as a result of high-temperature treatment and contain graphene-like regions [81–84].

The absorption bands at 1741, 1692, and 1650 cm^{-1} are assigned to the stretching vibrations of the C=O bonds in the A and L groups, Cx groups, and Qu groups, correspondingly. The highest intensity of these bands is observed for the samples of MWCNTs, ACF, CB, and NAC2, which is consistent with the preparation methods used to obtain them. The absorption bands of low intensity, which are assigned to the stretching vibration of C=O bonds, are characteristic for the sample of NAC3. The low intensity of the aforementioned bands is associated with prolonged carbonization and removal of the most reactive part of the carbon matrix during the preparation of NAC3.

The absorption band of low intensity at 1429 cm^{-1} can be associated with the deformation vibrations of the C–H bonds in the C=CH groups or with the deformation vibrations of the OH bonds in the Ph groups. Low-intensity absorption bands at 1201 cm^{-1} are associated with C–OH vibrations of the Ph groups. As can be seen, the Ph groups are presented, in a significant amount, on the surface of all samples. The bands at 1030 and 963 cm^{-1} may relate to the absorption of the C–O–C groups of surface anhydrides and lactones, the OH groups of acidic nature, or the CH groups in the aromatic component of the matrix. For all samples, the bands related to the absorption of oxygen-containing groups have a low intensity, which is consistent with the data of EDX analysis (Table 1) and confirms the low oxygen content in the unmodified (pristine) CMs.

Figure 4 shows the typical temperature dependencies of the weight change and the release of the main decomposition products of surface groups (CO and CO₂) for the initial CM. The first effect of weight loss in the temperature range of 30–180 °C

relates to the thermal desorption of physisorbed water. The weight loss at higher temperatures (m_{FG}) corresponds to the decomposition of oxygen-containing surface groups (Table 2). Regardless of the nature of the CM, a relatively small total weight loss (2–6%) is observed in the temperature range of 170–850 °C, which is explained by the insignificant concentration of surface oxygen-containing groups. This result agrees with the EDX and FTIR ATR data and confirms the low surface oxidation state of the unmodified CMs. The course of the temperature dependences for the release of carbon oxides differs little for different types of CMs (see Fig. 4a, b). The main release of CO₂ occurs at a temperature range of 200–400 °C, which corresponds to the thermal decomposition of Cx surface groups. The A and L groups are present in small amounts for the NAC2, MWCNTs, and ACF. The minor evolution of CO₂ and CO in the temperature range of 400–600 °C is clear evidence of their presence. Intensive release of CO occurs at temperatures above 600 °C, which is associated with the thermal decomposition of Ph and Qu groups [85].

The temperature ranges for the release of carbon oxides are consistent with the corresponding weight loss effects on the differential thermogravimetric (DTG) curves. A common feature for all studied samples is the presence of mainly high-temperature oxygen-containing groups on their surface. The most intense weight loss in the temperature range of 600–850 °C confirms the presence of Ph and Qu

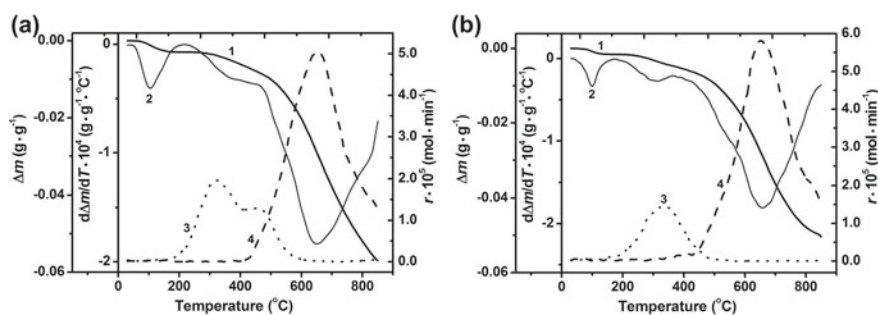


Fig. 4 TGA/EGA for **a** MWCNTs and **b** CB. TGA: TG (1) and DTG (2) curves, EGA: CO₂ (3) and CO (4) profiles

Table 2 Surface chemistry of the initial CMs

Sample	TGA	TPD/Boehm titration, C_{FG} , mmol g ⁻¹			$C(\text{CO})/C(\text{CO}_2)$
	Δm_{FG} , g g ⁻¹	Cx	A-L	Ph	
NAC1	0.0504	0.09/0.08	0.04/~0	0.86/0.74	6.7
NAC2	0.0449	0.25/0.22	0.16/0.10	0.55/0.47	1.5
NAC3	0.0227	0.07/0.07	0.03/~0	0.44/0.35	4.7
MWCNTs	0.0570	0.25/0.18	0.17/0.13	0.98/0.92	2.6
CB	0.0504	0.21/0.17	0.05/~0	1.23/1.06	5.1
ACF	0.0410	0.20/0.18	0.12/~0	0.61/0.52	2.5

groups. Typically, the ratio between different types of oxygen-containing groups for different CMs varies within wide ranges. As seen from the $C(\text{CO})/C(\text{CO}_2)$ ratio presented in Table 2, the thermal stability of the surface layer of NAC1 and CB is high. These samples contain high-temperature oxygen-containing groups, mainly Ph and Qu groups. Both Ph and Qu groups decompose with the release of CO at high temperatures. For the NAC2 and MWCNTs samples, the $C(\text{CO})/C(\text{CO}_2)$ ratio is much lower. These observations indicate a higher concentration of CO₂-bearing sites on the carbon surface, causing lower thermal stability of the surface layer for these CMs. The surface concentrations of the groups determined by the Boehm method showed a similar result. However, one should note that for the investigated CMs, about 75–90% of all oxygen-containing groups are reactive in solution.

3.2 Non-isothermal Bromination of Carbon Materials

The non-isothermal bromination of CMs was investigated at various heating rates, in the range from 3 to 10 °C min⁻¹. It was found that for all CMs (Fig. 5a), with an increase in the heating rate, the effects of weight gain decrease, which is explained by the slow diffusion of bromine vapors in the microporous structures. Therefore, the comparison of the efficiency of the bromination of various CMs was carried out at the minimal heating rate (3 °C min⁻¹), at which the effect of bromine diffusion on the total bromination rate is negligible (Fig. 5b). The temperature function of weight change as a result of bromination $\Delta m(\text{Br})$ (Fig. 5) was found from the difference between the total weight change during bromination and the decrease in the weight of a sample as a result of the processes of the thermal decomposition of functional surface groups Δm_{FG} (see Table 2).

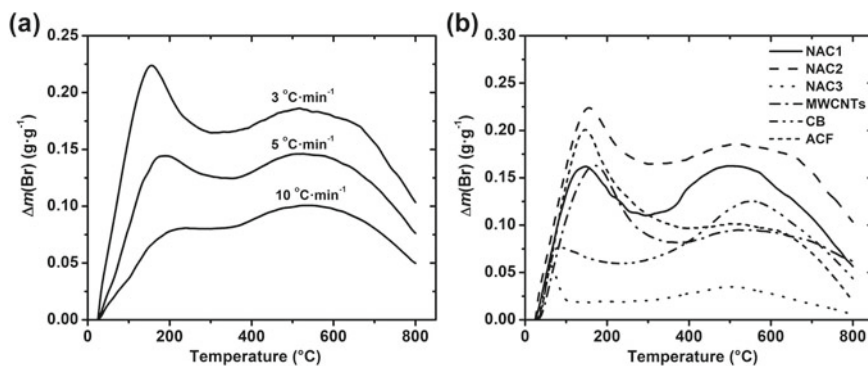


Fig. 5 Kinetic curves of the non-isothermal bromination of CMs: **a** non-isothermal bromination of NAC2 at heating rates from 3 to 10 °C min⁻¹ and **b** non-isothermal bromination of CMs at the heating rate of 3 °C min⁻¹

As can be seen, the temperature profiles of $\Delta m(\text{Br})$ changes for different CMs are similar in shape and show two effects of weight gain. The first effect in the temperature range of 30–350 °C is due to the formation of weakly adsorbed forms of bromine. At 400–700 °C, the formation of strongly adsorbed (chemisorbed) forms of bromine takes place. The parameters of the aforementioned bromination processes, which are the temperatures at the maximal weight gain (T_{m1} and T_{m2}) and the weight gain assigned to the attached bromine (Δm_1 and Δm_2), and the total bromine concentrations per gram and per square meter of the specific surface area ($C(\text{Br})$ and $C_{\text{Surf}}(\text{Br})$) of the resulting brominated CMs are given in Table 3. The temperature of the first maximum naturally increases in going from the sample of MWCNTs to CB, ACF, and further to the samples of NACs, which is explained by the size of their particles. Notably, the smallest sizes have the MWCNTs with a cross-section of 20–100 nm and a length of a few μm (see Fig. 1). The CB aggregates and the individual ACF filaments are 5–10 μm in size, and the NAC granules are 0.5–2 mm in size. The smaller the particle, the faster the diffusion of bromine vapors inside them, filling all the pores with adsorbed bromine, and so, the less T_{m1} will be. Clearly, in the framework of a more rigorous approach and predicting the value of T_{m1} for different CMs, in addition to the particle size of the material, one should also take into account the width, length/width ratio, and mean length of the pores.

The first effect is characterized by a sharper change in $\Delta m(\text{Br})$, which is consistent with the features of the process of physisorption of bromine on the surface of CMs and intercalation inside the inner volume. The magnitude of the first maximum depends much more on the nature of the carbon material than the second one. As seen from Fig. 5b, the first maximum is the largest for the NACs samples with a developed porous structure. For the samples of CB and MWCNTs, the porosity of which is considerably less developed, the first maximum is small. Figure 6 shows the positive correlations between the mass of physisorbed (intercalated) bromine (Δm_1) and the structural parameters of CMs, which are the S_{BET} and V_{micro} . The found correlation dependencies indicate the improvement of bromine adsorption with the increase in the contribution of micropores to the porous volume of CMs. The NAC3 sample is

Table 3 Parameters of the non-isothermal bromination of CMs, which were determined at the heating rate of 3 °C min⁻¹, and the total bromine concentrations in the resulting brominated CMs

Sample	The parameters of non-isothermal bromination				Total bromine concentration	
	T_{m1} , °C	Δm_1 , g g ⁻¹	T_{m2} , °C	Δm_2 , g g ⁻¹	$C(\text{Br})$, mmol g ⁻¹	$C_{\text{Surf}}(\text{Br})$, $\mu\text{mol m}^{-2}$
NAC1	150	0.161	510	0.162	2.03	2.13
NAC2	158	0.224	518	0.186	2.33	1.79
NAC3	170	0.163	551	0.095	1.19	0.48
MWCNTs	62	0.061	505	0.036	0.45	3.00
CB	85	0.078	552	0.126	1.58	14.32
ACF	147	0.202	520	0.101	1.26	1.86

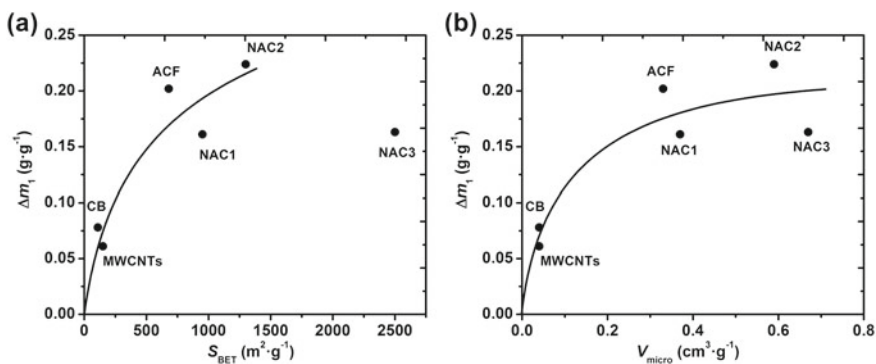


Fig. 6 a, b Positive correlations between the weight gain (Δm_1), which was found from the results of the chemical analysis of the non-isothermally brominated CMs, and the textural parameters (S_{BET} and V_{micro}) of unmodified CMs

somewhat fallen out of the positive correlations. This observation can be explained by the prolonged activation of source material at the preparation of NAC3 with water vapor and a decrease in the number of adsorption sites on the resulting carbon surface.

The second effect of weight gain for all CMs has a plateau in the temperature range of 505–551 °C. With the relatively high temperatures of T_{m2} , this effect is unambiguously attributed to the process of bromine chemisorption. Additional studies have shown (see Sect. 3.4) that in the above temperature range, the thermal desorption of adsorbed forms of bromine occurs exclusively in the form of HBr. These results also confirm the conclusion about the chemisorption of bromine in this range. The moderately narrow range of T_{m2} values can be explained by the fundamentally identical nature of active sites for different CMs. As noted earlier, the active centers of the bromination of CMs are double HC=CH bonds, which are located at the edges of the graphene layers of the carbon matrix. The chemisorbed bromine weight (Δm_2) has a complex dependence on the type of CM. Table 3 gives the highest values of the amount of chemisorbed bromine $C(\text{Br}) = 2.03\text{--}2.33 \text{ mmol g}^{-1}$ are characteristic of the NAC1 and NAC2 sorbents; those are the materials with a very developed surface. Compared to the NAC1 and NAC2 sorbents, the amount of chemisorbed bromine for the NAC3 sorbent is 2 times less, despite the highest S_{BET} of the NAC3 sorbent. This observation agrees with the decomposition of some active sites upon prolonged activation of the NAC3 sorbent with water vapor.

However, the lowest concentrations of chemisorbed bromine per unit area ($C_{\text{Surf}}(\text{Br})$) are found for the sorbents with developed porous structures, such as NACs. This result is quite natural because the physical activation of CMs by water vapor or other oxidants at high temperatures removes the most reactive part of the carbon matrix. The most chemically active surface is found for the CB sorbent, which has 5–10 times more active sites per 1 m² than other studied CMs. The most significant feature of the soot structure is a large number of graphenic layers stacked in

packages. The edges of such aggregates contain numerous HC=CH bonds, giving active sites for bromination reactions.

3.3 Isothermal Bromination of Carbon Materials

The kinetics regularities of bromination under isothermal conditions were additionally investigated, taking into account the complexity of the kinetic description of the non-isothermal dependences of bromination. For this study, 50–60 mg of a given sample was placed into the open quartz basket and heated from room temperature up to 200 °C at a heating rate of 3 °C min⁻¹ under an argon flow rate of 80 mL min⁻¹. The temperature range of 200–500 °C, in which bromine chemisorption was observed, was chosen to treat the CM sample with bromine vapor. Figure 7 shows typical TG profiles recorded under isothermal conditions to measure the weight gain (m) upon bromination time. Here, the empty basket served as a reference.

In the investigated temperature range, the kinetic curves of isothermal bromination, regardless of the temperature and nature of CMs, are saturation curves. For most CMs, the bromination process prolongs about 2–2.5 h until a constant sample weight ($m(\text{Br})$) is reached. The initial area of weight gain lasts about 20 min. During this time, there is a significant increase in weight, which is up to 80% of ($m(\text{Br})$). Bromination of MWCNTs is faster, and a constant mass of samples is achieved in 50–60 min after the beginning of bromination. This fact can be explained by the rapid diffusion of bromine to the active sites due to the small size of individual MWCNTs' particles and the presence of a significant number of mesopores.

Kinetic analysis of the obtained bromination data under isothermal conditions was performed using the Eq. (1)

$$r = dm/dt = kC_{\text{Br}}(m(\text{Br}) - m), \quad (1)$$

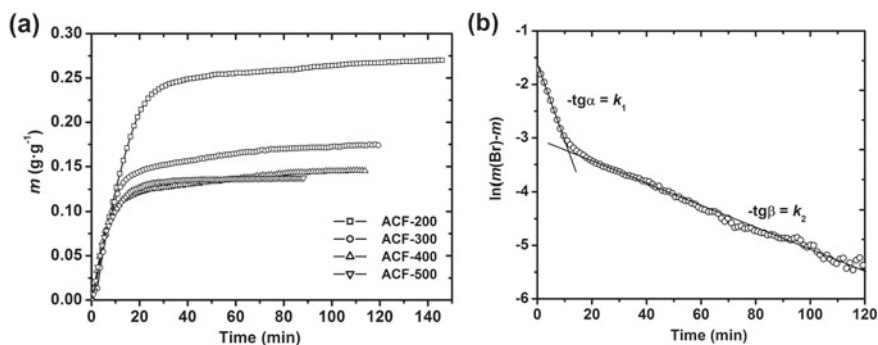


Fig. 7 **a** Isothermal TG profiles showing the bromination kinetic of the ACF sample held in bromine vapors at a selected temperature between 200 and 500 °C and **b** typical TG profile linearized in the semi-logarithmic coordinates

where m is the weight of chemisorbed bromine at the time τ , which varies from 0 to $m(\text{Br})$, k is the effective constant of the bromination rate, and C_{Br} is the concentration of bromine in the gas phase ($1.0 \times 10^{-3} \text{ mol L}^{-1}$). The concentration of bromine in the gas phase is excessive compared to the amount of bromine that reacts with the CMs, so the Eq. (1) can be simplified

$$r = dm/dt = k_{\text{Br}}(m(\text{Br})-m), \quad (2)$$

where $k_{\text{Br}} = kC_{\text{Br}}$.

The integration of Eq. (2) gives

$$\ln(m(\text{Br})-m) = \ln(m(\text{Br}))-k_{\text{Br}}t, \quad (3)$$

The value of $m(\text{Br})$, which is required for kinetic analysis, was first determined from the kinetic curves of Fig. 7a and then refined by the variation method. This procedure consisted in varying the $m(\text{Br})$ values in a small interval. It was performed in order to achieve the best linear dependence in the semi-logarithmic coordinates (Fig. 7b). As can be seen, a typical kinetic curve in the semi-logarithmic coordinates consists of two linear sections. The first linear section (up to 15 min) corresponds to the initial process when bromination is rapid. The most accessible active sites of the CMs surface are involved in bromination at this stage. The fraction of such centers is quite high and is 60–75% of all active sites. The second, much longer section corresponds to a slower bromination process, which lasts the next 100–120 min. During this time, there is a bromination of the active sites located in the longest micropores. The processes of “fast” and “slow” bromination often do not have a smooth transition, so they can be considered as the interaction of bromine with two types of surface, active sites, and the reactivity of which is different. The kinetic equation, which takes into account these two simultaneous parallel bromination processes, is as follows:

$$r = dm_{\text{Br}}/dt = k_1(m_1(\text{Br})-m) + k_2(m_2(\text{Br})-m), \quad (4)$$

where $m_1(\text{Br})$ and $m_2(\text{Br})$ are the weights of bromine that can be chemisorbed at the time periods, which are corresponded to the first (fast) and the second (slow) sections of the kinetic bromination curve, k_1 and k_2 are the respective effective rate constants of the bromine reaction with the aforementioned active sites of two types. The dependencies graphed in the semi-logarithmic coordinates were used to determine kinetic parameters for the bromination of CMs. The resulting values of constants are listed in Table 4.

The amount of bromine attached to the carbon surface at the first and second bromination stages differs significantly. Regardless of the nature of CMs, the $m_1(\text{Br})$ value is 3–5 times larger than that of $m_2(\text{Br})$. This experimental fact is consistent with the observation that the most active sites of CMs are available and react quickly with bromine vapor. It should be noted that the value of $m_2(\text{Br})$ has a weak dependence on the bromination temperature for a particular CM. The limiting stage in

Table 4 Kinetic parameters of the isothermal bromination of CMs

Sample	$m(\text{Br}), \text{g g}^{-1}$	$m_1(\text{Br}), \text{g g}^{-1}$	$k_1 \times 10^{-2}, \text{min}^{-1}$	$m_2(\text{Br}), \text{g g}^{-1}$	$k_2 \times 10^{-2}, \text{min}^{-1}$
NAC1-Br-200	0.198	0.159	2.42	0.039	2.08
NAC1-Br-300	0.179	0.138	2.83	0.041	2.30
NAC1-Br-400	0.175	0.138	3.19	0.037	2.66
NAC1-Br-500	0.171	0.136	3.41	0.035	2.99
NAC2-Br-200	0.256	0.199	4.12	0.067	2.44
NAC2-Br-300	0.196	0.132	4.58	0.064	2.49
NAC2-Br-400	0.196	0.141	4.86	0.055	3.20
NAC2-Br-500	0.184	0.130	5.67	0.054	3.27
NAC3-Br-200	0.192	0.099	5.29	0.053	2.10
NAC3-Br-300	0.123	0.075	8.01	0.048	2.23
NAC3-Br-400	0.115	0.071	9.97	0.044	3.45
NAC3-Br-500	0.098	0.057	11.0	0.041	3.89
MWCNTs-Br-200	0.041	0.024	19.4	0.017	2.51
MWCNTs-Br-300	0.037	0.021	22.7	0.016	2.88
MWCNTs-Br-400	0.036	0.018	31.6	0.018	3.12
MWCNTs-Br-500	0.036	0.019	38.6	0.017	3.29
CB-Br-200	0.142	0.102	4.11	0.040	0.94
CB-Br-300	0.139	0.100	5.01	0.039	1.09
CB-Br-400	0.137	0.093	6.96	0.044	1.24
CB-Br-500	0.136	0.094	8.05	0.042	1.51
ACF-Br-200	0.286	0.236	6.43	0.050	1.09
ACF-Br-300	0.179	0.131	8.74	0.048	1.23
ACF-Br-400	0.152	0.108	10.7	0.044	1.85
ACF-Br-500	0.138	0.061	13.5	0.041	2.06

the involvement of less accessible active sites in the bromination reaction should be the diffusion of bromine vapor in the porous system of sorbent. So, such a process is assumed to have low activation energy. These assumptions are consistent with the weak temperature dependence of k_2 . So, from the respective calculations, the almost constant value of $m_2(\text{Br})$ is found in the bromination temperature range of 300–500 °C. The effective constants k_1 and k_2 for the MWCNTs, CB, and ACF differ from 5 to 10 times. Presumably, this is because of the different accessibility of active sites on the outer and inner surfaces of these materials. For all samples of NACs, the difference between k_1 and k_2 does not exceed 2–3 times. This difference is observed because the contribution of the outer surface is small. All surface sites, which are active for the bromination at the second stage, are located inside the porous structure of these samples. Therefore, the effective constants k_1 for the MWCNTs, CB, and ACF have much higher numerical values as compared to those of the NACs. The

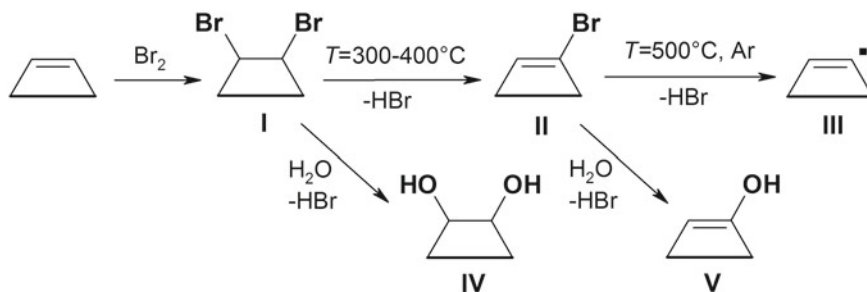


Fig. 8 Schematic diagram showing the chemical changes of the carbon surface after bromination, including hydrolysis of the attached bromine

numerical values of k_2 for all investigated CMs are quite close. This observation means that the bromination in the second stage involves less accessible active sites deep inside the porous system.

The obtained results of both liquid-phase and gas-phase bromination processes can be explained by the general scheme (Fig. 8).

The active sites of gas-phase bromination are the double C=C bonds of the carbon matrix. The initial addition of bromine to the active site gives the product (I), which contains two bromine atoms per the active site. The product (I), when heated, i.e., under the reaction conditions, can cleave the HBr molecule to form the product (II). If one looks at the preparation of the product (I), one can see that more of the product (II) is formed at a higher temperature. After completion of bromination during storage of samples, a part of the most chemically active bromine can be hydrolyzed to form Ph groups, shown as the products (IV) and (V) in Fig. 8.

For all CMs, the maximum amount of bromine grafted ($m(\text{Br})$) is observed at the lowest temperature (200 °C). When the temperature increases to 300 °C, the $m(\text{Br})$ value decreases markedly and becomes a constant number in the temperature range of 400–500 °C. This temperature dependence of $m(\text{Br})$ can be due to several reasons. Low temperatures increase the likelihood of the formation of the weakly bound forms of bromine, which include intercalated forms of bromine. An increase in the bromination temperature leads to the decomposition of the weakly bound forms of bromine and causes a decrease in the $m(\text{Br})$ value. Another reason for such dependence is the significant formation of the dibromo derivative, the product (I), at low temperatures (Fig. 8). When the bromination temperature rises to 400–500 °C, a parallel process of the desorption of HBr passes intensively, and the product (II) is formed. This product (II) contains twice less attached bromine per one active site.

Physical adsorption and the formation of the intercalation forms of bromine at temperatures of 300–500 °C are unlikely. The close values of $m(\text{Br})$ correspond to the formation of only the chemisorbed forms of bromine. There is a complete saturation of all surface sites with bromine forming the product (II). According to these data, it is possible to estimate accurately the surface concentration of active sites that can participate in electrophilic addition reactions. The absence of an increase in

the amount of attached bromine in the temperature range of 300–500 °C (Table 4) indicates that the surface oxygen-containing groups have practically no effect on the bromination process. In the studied temperature range, there is no thermal decomposition of Ph groups. One should note that their fraction reaches 57–87% of the total number of oxygen-containing groups. The formation of new active sites at the decomposition of Cb, A, and L groups occurs in minor quantities. This situation is due to the low concentration of unstable oxygen-containing groups compared to the amount of chemisorbed bromine. The effective attachment of bromine to CMs at the temperature range of 200–300 °C indicates a predominantly ionic mechanism of bromination without the formation of bromine radicals. Bromine radicals are likely to be formed at temperatures above 400 °C. But the radical formation does not lead to an increase in bromine chemisorption. This fact is consistent with the relatively low activity of bromine radicals, which complicates the reaction of substitution of surface hydrogen atoms for bromine. Therefore, it can be argued that gas-phase bromination provides quite significant amounts (up to 2.5 mmol g⁻¹) of chemisorbed bromine. This process has high selectivity toward certain active sites of the surface, which are the double CH=CH bonds.

From the temperature dependences of the effective constants k_1 and k_2 , the effective activation energies of bromination (E_{a1} and E_{a2}) were determined from the first and second sections of the kinetic curves, see Fig. 9a and b, respectively.

The obtained values of the effective activation energies are small; they vary from 3 to 8 kJ mol⁻¹. Such low values of E_{a1} and E_{a2} indicate a significant effect of diffusion on the total rate of the bromination reaction. The lowest values of E_{a1} and E_{a2} are obtained for the microporous NAC1 and NAC2 sorbents with large granule sizes. In general, the values of E_{a2} are lower than those of E_{a1} . This observation confirms the assumption that the effect of diffusion inhibition increases at the second bromination stage.

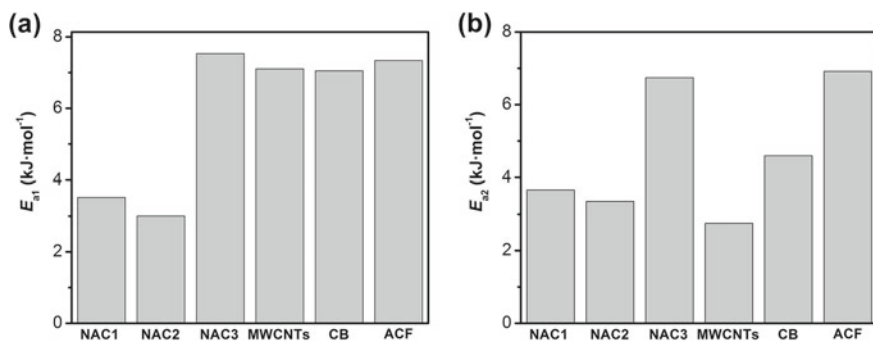


Fig. 9 Effective activation energies of bromination (E_{a1} and E_{a2}) calculated from **a** the first (starting) shorter and **b** the second longer sections of the kinetic curve

3.4 Thermal Stability and Surface Properties of Brominated Carbon Materials

After bromination under isothermal conditions, the thermal stability of the attached bromine was investigated. Figure 10 shows typical kinetic curves of bromine thermal desorption.

The desorption curves of the attached bromine are satisfactorily described by the equation of the first order, Eq. (5)

$$r = -\frac{dm_{\text{des}}}{d\tau} = k_{\text{des}}m_{\text{des}}, \quad (5)$$

or in the integral form, Eq. (6)

$$\ln \frac{\Delta m_{\text{des}}}{m_{\text{des}}} = k_{\text{des}}\tau, \quad (6)$$

where m_{des} is the current moment weight of the sample.

By Eq. (6), the bromine desorption rate constant (k_{des}) was determined, and the maximum desorbed bromine weight Δm_{des} was specified (Table 5). From the obtained data, the value of Δm_{des} is much higher for the samples brominated at 200 and 500 °C. The weight of thermostable bromine, which is the difference between the weight of the attached bromine ($m(\text{Br})$) (see Table 4), and the weight of desorbed bromine (Δm_{des}) takes positive values for all samples in the temperature range of 200–500 °C. This fact is a confirmation of the formation of chemisorbed bromine, which is thermally stable at the synthesis temperature.

Typical temperature dependence is observed in the study of bromine thermal desorption. The highest rate of desorption of bromine (the steepest initial site of weight loss) and the highest constants of the rate of desorption are found for a

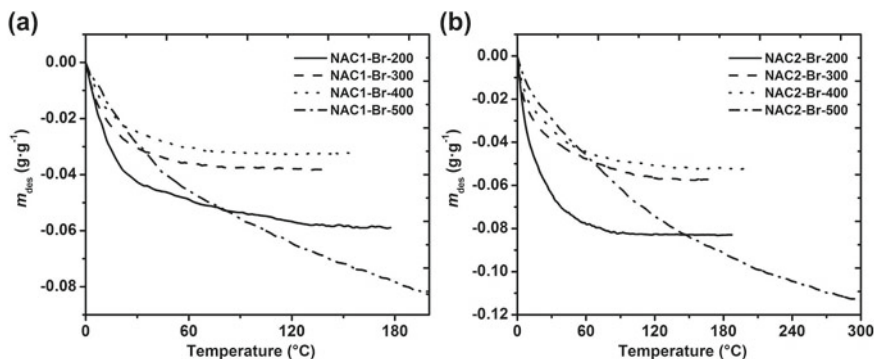


Fig. 10 a, b Typical kinetic profiles of the bromine thermal desorption between 200 and 500 °C in dynamic argon flow

Table 5 Kinetic parameters for the thermal desorption of chemisorbed bromine in argon flow determined at different temperatures

Sample	$\Delta m_{\text{des}}, \text{g g}^{-1}$	$k_{\text{des}} \times 10^2, \text{min}^{-1}$	$m(\text{Br}) - \Delta m_{\text{des}}, \text{g g}^{-1}$
NAC1-Br-200	0.0605	4.85	0.1375
NAC1-Br-300	0.0381	4.25	0.1409
NAC1-Br-400	0.0326	3.90	0.1424
NAC1-Br-500	0.1185	0.51	0.0525
NAC2-Br-200	0.0829	4.45	0.1731
NAC2-Br-300	0.0586	2.49	0.1374
NAC2-Br-400	0.0525	2.29	0.1435
NAC2-Br-500	0.1304	0.67	0.0536
NAC3-Br-200	0.0429	4.17	0.1491
NAC3-Br-300	0.0261	2.88	0.0969
NAC3-Br-400	0.0165	2.05	0.0985
NAC3-Br-500	0.0731	0.59	0.0249
MWCNTs-Br-200	0.0031	6.57	0.0379
MWCNTs-Br-300	0.0025	5.17	0.0345
MWCNTs-Br-400	0.0053	3.44	0.0307
MWCNTs-Br-500	0.0251	2.08	0.0109
CB-Br-200	0.0747	4.69	0.0673
CB-Br-300	0.0616	3.82	0.0774
CB-Br-400	0.0571	3.11	0.0799
CB-Br-500	0.1338	1.71	0.0022
ACF-Br-200	0.1247	3.75	0.1613
ACF-Br-300	0.0939	2.04	0.0851
ACF-Br-400	0.0708	1.95	0.0812
ACF-Br-500	0.1261	1.08	0.0119

temperature of 200 °C. The highest total weight loss Δm_{des} is registered after 1.5–2.5 h of the thermal desorption at this temperature. This weight loss reaches about 8.5 wt% and 7.1 wt% for the samples of the brominated NAC1 and NAC2, respectively. At higher temperatures (300 and 400 °C), the thermal desorption rate at the initial step and the value of Δm_{des} is significantly reduced. This observation confirms the formation of weak bonded (intercalated) bromine during bromination at low temperatures. At the highest temperature (500 °C), the initial rate of the thermal desorption of bromine is even lower. However, the weight loss curve does not reach a constant value for the amount of desorbed bromine. So, the value of Δm_{des} is large and is more than 8–10 wt%.

Such a temperature dependence of desorption indicates the existence of surface bromine forms of different thermal stability. In addition to weakly bound (intercalated) bromine, which can be easily desorbed, the formation of chemisorbed bromine

forms, type (I) and (II), is possible in the temperature range of 200–400 °C (see Fig. 8). As the temperature rises, the contribution of the product (I) will decrease, and the contribution of the product (II) should increase. This observation can explain the decrease in the Δm_{des} values with increasing temperature from 200 to 400 °C. For many brominated CMs, the values of $m(\text{Br}) - \Delta m_{\text{des}}$ are similar for temperatures of 200, 300, and 400 °C, while for the temperature of 500 °C, these values are much lower. This observation indicates a different mechanism of thermal desorption of the attached bromine at high temperatures at and above 500 °C. Very large Δm_{des} values and, as a consequence, small values of $m(\text{Br}) - \Delta m_{\text{des}}$ (for 500 °C) are explained by the possible desorption of any form of surface bromine. This desorption can take place by a radical mechanism with the formation of the product (III); for the mechanism, see Fig. 8.

Figure 11 shows almost all absorption bands characteristic of the initial (unmodified) CMs in the FTIR ATR spectra of the brominated CMs. In the spectra of the brominated CMs, absorption bands additionally appear between 550 and 750 cm^{-1} , which, in our opinion, corresponds to the vibrations of the C–Br bonds. A slight increase in the intensity of the absorption bands in the range from 900 to 1230 cm^{-1} is also observed. In particular, the intensity of the bands peaked at 1187, 1028, and 951 cm^{-1} increases. However, the intensity of the absorption bands ranged between 1600 and 1800 cm^{-1} for the brominated CMs is slightly reduced. This reduction will be clearly seen if one compares the spectral band intensity with that of the respective bands in the spectra of the pristine CMs. This experimental fact indicates the partial decomposition of C=O-bearing groups during bromination. Typically, these groups are mainly Cx groups and partially A-L groups. An increase in the surface concentration of Ph groups increases the intensity of absorption bands in the range of 900–1230 cm^{-1} . These groups are formed after bromination as a consequence of hydrolysis. The most chemically active bromine groups can hydrolyze. Typically in a hydrolysis reaction, the hydroxyl group (OH^-) replaces the Br groups. So, the Ph groups are formed (see Fig. 8).

The thermal stability of attached bromine was studied by the TG analysis in combination with the TPD MS method. Figure 12 shows typical TG/DTG curves and temperature profiles obtained from mass spectra for the brominated CMs. For the NAC2-Br-200 sample, two significant effects of weight loss (at 180–500 °C and above 500 °C) are observed, in addition to thermal desorption of physisorbed water (Fig. 12a). As can be seen, the effect of weight loss in the temperature range of 180–500 °C corresponds to the release of HBr^+ (m/z 80) peaked at 280 °C (Fig. 12b). Hydrogen bromide partially dissociates in the mass spectrometer chamber with the formation of Br^+ fragment ion (m/z 79). Therefore, this weight loss effect is associated with the thermal decomposition of the most active forms of bromine available on the sample surface. The formation of HBr is realized mainly because of the elimination process: the transformation of the product (I) into the product (II) (see Fig. 8). Both the temperature range and the position of the maximum of this effect depend on the bromination temperature. With increasing the bromination temperature, this effect shifts to the high-temperature region.

Fig. 11 FTIR ATR spectra of the brominated CMs: (1) NAC1-Br-400, (2) NAC2-Br-400, and (3) MWCNTs-Br-400

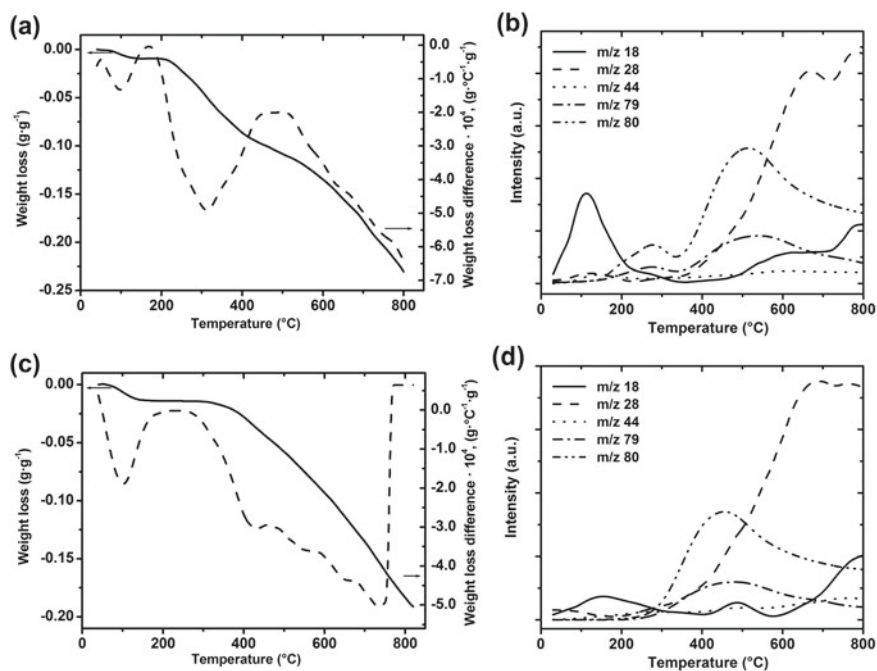
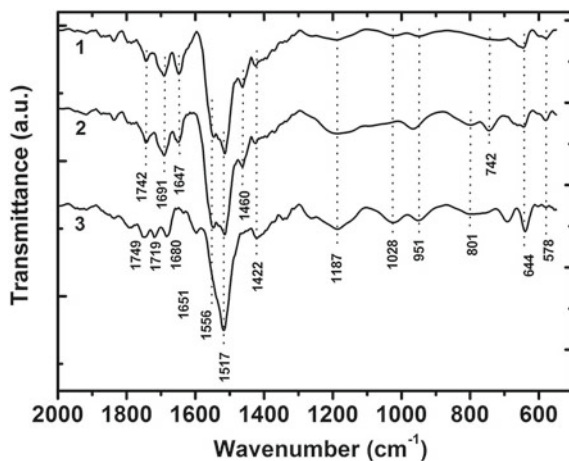


Fig. 12 a, c TG/DTG curves and b, d TPD MS profiles of the brominated CMs: a, b NAC2-Br-200 and c, d NAC2-Br-400

The effect of weight loss observed at above 500 °C is consistent with the thermal desorption of the product of the thermal decomposition of the most stable bromine forms, registered at 515 °C in the TPD MS spectra. The same is true for CO, which is the product of thermal decompositions of (i) Ph groups at 670 °C and (ii) more stable CO-bearing complexes at 780 °C. In this temperature range, the passage of these processes is evidenced by the intense profiles of HBr⁺ and CO⁺ (*m/z* 28), respectively (Fig. 12b). Cleavage of the second HBr molecule probably occurs due to a certain radical process.

For the sample of NAC2-Br-400, the thermal decomposition of the most active forms of the attached bromine is less intense and is shifted to the region of higher temperatures (Fig. 12c). The profile of HBr⁺ shows one broad effect with a maximum of about 455 °C (Fig. 12d). The temperature dependences of the mass change indicate significant thermal stability of the attached bromine-containing groups, which are present on the surface of the samples of CMs.

The intensive signal of HBr⁺ is observed at temperatures close to or greater than the bromination temperature. The main thermal desorption product for all samples is HBr. This fact unambiguously proves the chemisorption of bromine on the surface of CMs. The passage of bromine chemisorption is well consistent with the bromination scheme (Fig. 8). According to the obtained data, the surface of brominated CMs does not undergo significant oxidation. This observation is in contrast to the thermal behavior of the CMs brominated in solution [86]. Typically, CO₂-bearing sites are almost absent on the surface of the brominated CMs. The significant content of CO-bearing sites is caused by their high thermal stability. Typically, these sites do not undergo decomposition during bromination. A small part of CO-bearing sites may form because of hydrolysis of the most active chemisorbed bromine.

3.5 Bromination of ACF with Bromine Plasma

During plasma bromination of the ACF under a low-temperature gas discharge, we found that the concentration of attached bromine (*C*(Br)) strongly depends on the bromination time. When increasing the bromination time from 5 to 30 min, the bromine content increases rapidly. But further, it does not change considerably with a subsequent prolonging of the bromination time. The highest bromine content of up to 1.04 mmol g⁻¹ can be obtained by the plasma bromination for 60 min (Fig. 13), while further bromination time prolongation does not lead to an increase in the *C*(Br) value.

Compared to gas-phase bromination (see Fig. 7), plasma-chemical bromination occurs somewhat faster; however, it passes with lower bromination efficiency. Plasma-chemical bromination is more effective than bromination with liquid Br₂ or aqueous solutions of Br₂-KBr reagent [86].

Figure 14 shows the curve-fitted Br 3d core-level XP spectra of the ACF-Br-30 and ACF-Br-60 samples. The XPS spectra were fitted with several components, taking into account the possible formation of different surface forms of bromine [87–89].

Fig. 13 Bromine content against the time of the plasma-chemical bromination of ACF

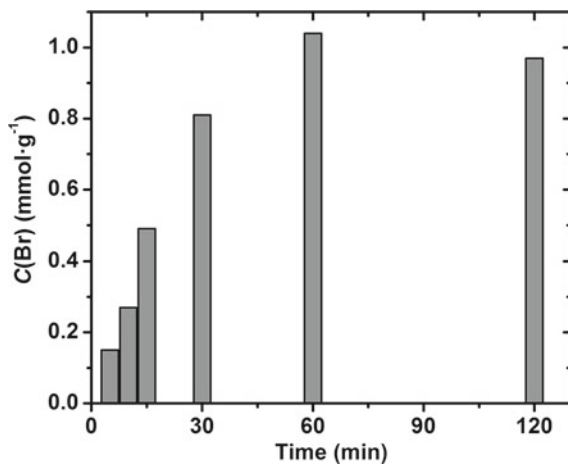
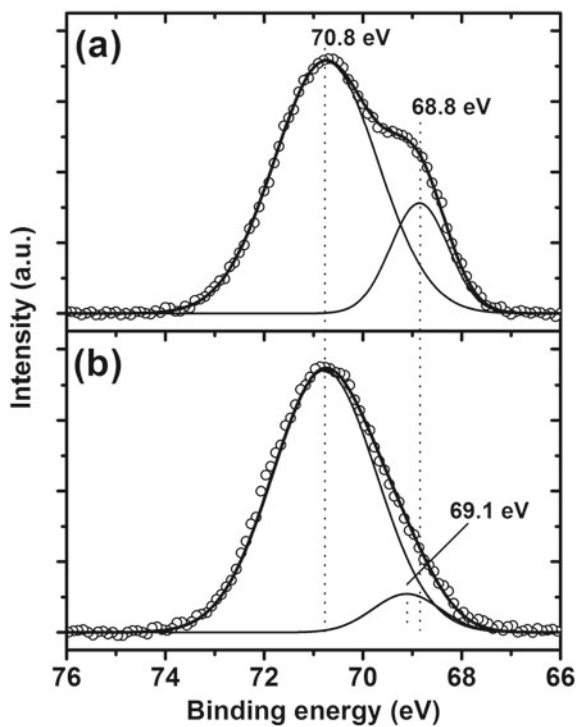


Fig. 14 Br 3d core-level curve-fitted XP spectra of **a** ACF-Br-30 and **b** ACF-Br-60



The resulting curve-fitted Br 3d core-level XP spectra of the ACF-Br-30 contain two components (Fig. 14a) with a binding energy of 70.8 and 68.8 eV. The component with the highest (80%) intensity and binding energy of 70.8 eV corresponds to bromine covalently bound to sp^2 - or sp^3 -hybridized carbon atom. The component with a binding energy of 68.8 eV corresponds to weakly bonded bromine. This bromine is physisorbed on the surface of the carbon matrix and can intercalate into the inner volume of the sample. Considerable broadening (half-width of about 3.5 eV) of the Br 3d core-level XPS spectra and the splitting of ~ 1.05 eV between the $3d_{5/2}$ and $3d_{3/2}$ components confirm the presence of several different forms of bromine in the sample of ACF-Br-30. The contribution of weakly bonded bromine forms is about 20% of the total contribution of all bromine forms into the total area of the signal under the fitted curve. Therefore, despite the relatively short bromination time, mainly chemisorbed forms of bromine are formed on the surface of the ACF-Br-30 sample. A component with a binding energy of 70.8 eV has especially prevailed in the Br 3d core-level curve-fitted XPS spectra of the ACF-Br-60 sample. This spectral feature means that the percentage of chemisorbed forms of bromine exceeds 90% for this sample. The binding energy of the second component is 69.1 eV, which is 0.3 eV more than the respective binding energy of the second component in the curve-fitted Br 3d core-level XPS spectra of the ACF-Br-30 sample. These results indicate an overall increase in the strength of C–Br bonds, which is expressed in an increase in the amount of chemisorbed bromine and the disappearance of weakly bound forms of bromine with increasing time of plasma-chemical bromination.

Thermal decomposition of Br-containing surface sites is of special interest in order to estimate the modification regularities. They were studied from the results of the TPD MS analysis on the example of the brominated ACFs. In their MS spectra, HBr^+ (m/z 80 and 82) and Br^+ (m/z 79 and 81) ions were registered. The results of bromination of the ACF samples with bromine vapor at heating and by bromine plasma are much different. Plasma-chemical bromination causes the formation of a lot of weakly bound forms of bromine. These forms are thermodecomposed at low temperatures (140–270 °C) and registered in the MS spectra in the form of Br^+ . Their thermal decomposition contrasts with that of chemisorbed bromine. In the case of chemisorbed bromine, thermal decomposition products are registered in the form of HBr^+ . As can be seen from the TPD MS data, the temperature profiles of HBr^+ and Br^+ for the plasma-brominated samples are significantly different (Fig. 15). These differences are both in the different shapes of the HBr^+ and Br^+ temperature profiles in the low-temperature region and in the different ratios of the integrated intensities of HBr^+ (I_{HBr^+}) and Br^+ (I_{Br^+}), which is clearly seen for the samples obtained by the bromination varying the bromination time (Tables 6 and 7).

As can be seen, the value of I_{HBr^+} increases while the value of I_{Br^+} decreases with the increasing time of plasma-chemical bromination. At any bromination time, the value of I_{HBr^+} is greater than that of I_{Br^+} by 2.3–8.6 times. Therefore, the main bromine-containing product of thermodesorption is HBr^+ , which confirms the formation of predominantly chemisorbed bromine. Temperature profiles of HBr^+ and Br^+ in the temperature range of 270–700 °C can be described as a set of three ($\beta_1(HBr^+)$, $\beta_2(HBr^+)$, and $\beta_3(HBr^+)$) and four ($\beta_1(Br^+)$, $\beta_2(Br^+)$, $\beta_3(Br^+)$, and $\beta_4(Br^+)$) components,

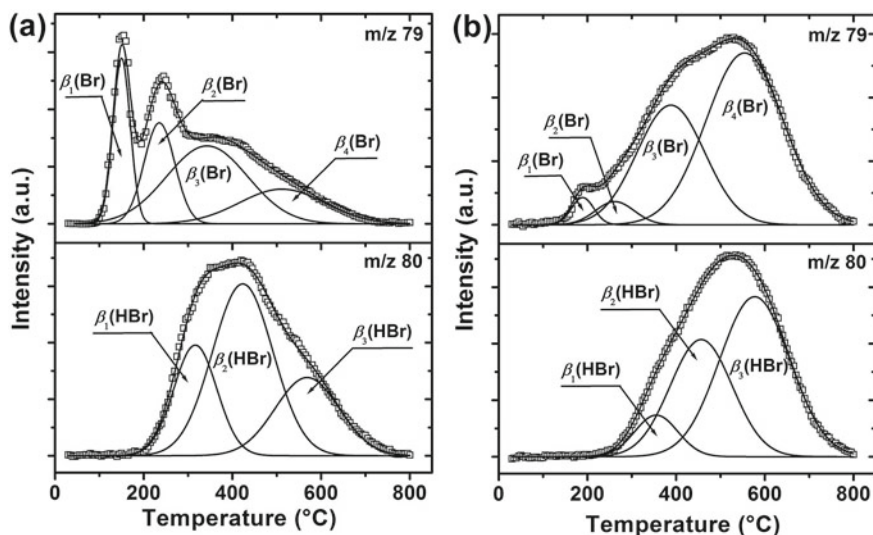


Fig. 15 Deconvolution of the TPD-MS profiles of Br^+ (m/z 79) and HBr^+ (m/z 80) ions for **a** ACF-Br-5 and **b** ACF-Br-60

Table 6 Analysis of TPD-MS profiles for m/z 79

Sample	$\beta_1(\text{Br})$		$\beta_2(\text{Br})$		$\beta_3(\text{Br})$		$\beta_4(\text{Br})$		I_{Br}
	$T_1, ^\circ\text{C}$	%	$T_2, ^\circ\text{C}$	%	$T_3, ^\circ\text{C}$	%	$T_4, ^\circ\text{C}$	%	
ACF-Br-5	147	18.8	239	20.4	343	41.5	513	19.3	30.1
ACF-Br-10	149	18.7	238	21.2	373	35.7	554	24.4	27.2
ACF-Br-15	161	15.3	243	18.3	365	32.8	547	33.6	18.1
ACF-Br-30	183	15.1	269	12.9	405	37.4	554	34.6	15.9
ACF-Br-60	190	2.7	263	3.9	394	35.3	552	58.1	10.5
ACF-Br-120	184	0.2	–	0.5	372	48.6	495	50.7	9.8

Table 7 Analysis of TPD-MS profiles for m/z 80

Sample	$C_{\text{Br}}, \text{mmol g}^{-1}$	$\beta_1(\text{HBr})$		$\beta_2(\text{HBr})$		$\beta_3(\text{HBr})$		I_{HBr}
		$T_1, ^\circ\text{C}$	%	$T_2, ^\circ\text{C}$	%	$T_3, ^\circ\text{C}$	%	
ACF-Br-5	0.15	314	23.6	422	51.6	566	24.8	69.9
ACF-Br-10	0.27	328	17.7	418	42.3	565	40.0	72.8
ACF-Br-15	0.49	323	15.5	429	39.4	561	45.1	81.9
ACF-Br-30	0.81	355	16.1	456	29.6	559	54.3	84.1
ACF-Br-60	1.04	358	8.9	455	36.3	574	56.1	89.5
ACF-Br-120	0.97	370	9.2	476	25.7	556	65.1	90.2

respectively. Each component (a surface bromine form) is characterized by the maximum temperature of desorption found from the intensity of the peaks in the TPD profiles, the temperatures $T_{\#}(\text{HBr})$ and $T_{\#}(\text{Br})$ are given in Tables 6 and 7.

As can be seen, the components $\beta_1(\text{Br})$ and $\beta_2(\text{Br})$ are isolated at moderate-high temperatures (below 270 °C) and have no analogs (by temperature) among the components $\beta_{\#}(\text{HBr})$. Therefore, one can assign the components $\beta_1(\text{Br})$ and $\beta_2(\text{Br})$ to the physisorbed and intercalated forms of bromine.

The other two components Br^+ ($\beta_3(\text{Br})$ and $\beta_4(\text{Br})$) are isolated at temperatures of 370 ± 20 °C and 530 ± 35 °C, respectively. In this temperature range, the release of all three forms of HBr^+ is observed. From the high temperatures of the maxima of the desorption peaks for these components, they should be attributed to chemisorbed forms of bromine. Components $\beta_3(\text{Br})$, $\beta_1(\text{HBr})$, and $\beta_2(\text{HBr})$ were identified as bromine chemisorbed in mesopores and micropores. The components $\beta_4(\text{Br})$ and $\beta_3(\text{HBr})$ correspond to bromine chemisorbed in narrow micropores. Since the intensities of $\beta_1(\text{HBr})$, $\beta_2(\text{HBr})$, and $\beta_3(\text{HBr})$ significantly exceed the intensities of $\beta_3(\text{Br})$ and $\beta_4(\text{Br})$, it can be argued that Br^+ in the temperature range of 300–800 °C is the product of dissociation of HBr^+ in the ionization chamber of the mass spectrometer.

For the ACF-Br-5 sample, the components $\beta_1(\text{Br})$ (21.2%) and $\beta_2(\text{Br})$ (26.1%), which are released at 152 °C and 234 °C, respectively, have a significant relative intensity (Fig. 15a). For this sample, the most contribution of Br^+ is observed. This contribution is from the physisorbed forms of bromine, which constitute 30.1% of all bromine-containing forms. However, a significant amount of chemisorbed bromine forms is presented on the surface of this sample. As the plasma-chemical bromination time increases, the content of weakly bound forms of bromine decreases. Besides, on the background of the bromination time increase, one can see a simultaneous increase in the content of chemisorbed bromine. Also, the thermal decomposition temperature range for all forms of the attached bromine is shifting to higher temperatures (Fig. 15b, c, see also Tables 6 and 7).

Thus, for the brominated samples of ACF, there is a gradual conversion of physisorbed bromine to chemisorbed bromine with increasing time of plasma-chemical bromination. Desorption of the chemisorbed forms of bromine occurs with the release of HBr at low temperatures due to the elimination reaction and at high temperatures because of radical reactions involving chemisorbed hydrogen.

3.6 Amination of Brominated Carbon Materials

If required to prepare heteroatom-functionalized carbon surfaces, the chemical properties of chemisorbed bromine are of considerable interest. The reactivity of chemisorbed bromine towards nucleophilic substitution was investigated using amination as a probe reaction. The CMs were brominated with bromine vapor at 200, 300, 400, or 500 °C. After that, the prepared brominated CMs were treated with an alcoholic solution of diethylamine. The heating of the resulting aminated CMs causes a significant weight loss effect, which is observed between 180 and

400 °C. However, the weight loss at high temperatures (above 400 °C) associated with bromine desorption, in the form of HBr, is largely reduced (Fig. 16a).

In the TPD MS spectra, there is a rather intense MS signal from the fragment m/z 30 ions in the same temperature range (Fig. 16b). This fragment ions could be assigned to the $\text{H}_2\text{C}=\text{NH}_2^+$ ions resulting from ionization and fragmentation of the products of thermal decomposition of amino groups. So, the effect of weight loss in the temperature range 180–400 °C is due to the thermal decomposition of attached amino groups; that is why the magnitude of this weight loss effect was used to determine the content of amino groups (C_N) in various aminated CMs (Table 8). As can be seen, the highest content of amino groups (1.21–1.55 mmol g^{-1}) was found for the nanoporous CMs with a large specific surface area (NAC1 and NAC2). The amount of attached amino groups is practically independent of the temperature of preliminary bromination, which is explained by the same number of active sites as the number of the edge $\text{C}=\text{C}$ bonds. Regardless of the nature of the studied CMs and the bromination temperature used, the maximum rate of thermal decomposition of attached amino groups is registered at $T_N = 300 \pm 15$ °C. This result confirms the chemisorption of diethylamine on the same surface sites that occupied the bromine groups.

Thermal desorption studies using the TPD MS method also confirm significant changes in the surface layer of aminated samples. Because of the symbatic temperature profiles for the $\text{H}_2\text{C}=\text{NH}_2^+$ ion and fragment ions (m/z 16 and 44), these fragments can be (in part) attributed to NH_2^+ and $\text{H}_3\text{C}-\text{HC}=\text{NH}_2^+$ ions, respectively (Fig. 16b). Additionally, other fragment ions (m/z 16 and 44) can be CH_4^+ and CO_2^+ . They are also formed because of the thermal decomposition of amino groups and oxygen-containing groups, respectively. The formation of a significant number of amino groups leads to an increase in the hydrophilicity of the surface layer. The aminated CMs have the highest hydrophilicity as compared with the brominated CMs. This statement is confirmed by the thermal desorption of water in a wide temperature range. At the same time, desorption of HBr^+ from all prepared aminated

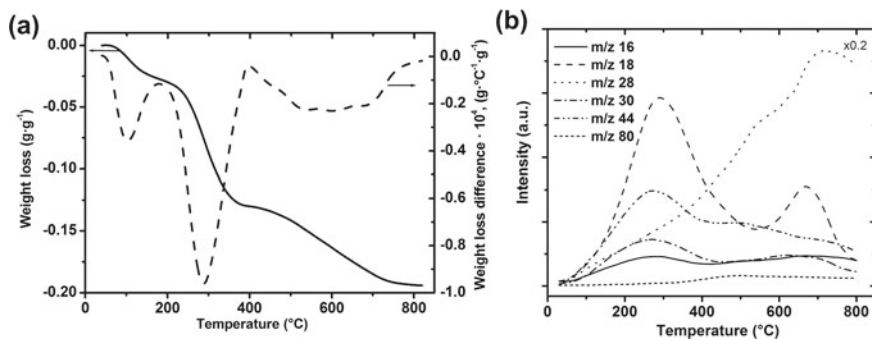


Fig. 16 Typical **a** TG/DTG curves and **b** TPD MS profiles of the aminated CMs, on the example of the NAC2-Br-400-N sample

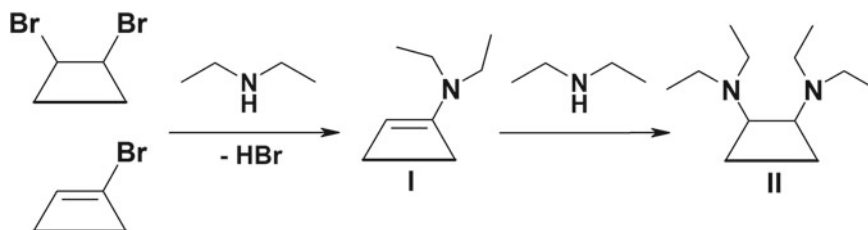
Table 8 Surface chemistry of the aminated CMs found from the chemical analysis and TG data

Sample	T_N , °C	$\Delta C(\text{Br})$, %	C_N , mmol g ⁻¹
NAC1-Br-200-N	304	78	1.34
NAC1-Br-300-N	297	71	1.26
NAC1-Br-400-N	311	66	1.21
NAC1-Br-500-N	307	65	1.15
NAC2-Br-200-N	293	79	1.55
NAC2-Br-300-N	296	69	1.48
NAC2-Br-400-N	301	69	1.46
NAC2-Br-500-N	298	62	1.37
MWCNTs-Br-200-N	306	80	0.33
MWCNTs-Br-300-N	310	78	0.36
MWCNTs-Br-400-N	314	77	0.34
MWCNTs-Br-500-N	306	75	0.30
CB-Br-200-N	290	75	1.04
CB-Br-300-N	296	70	0.98
CB-Br-400-N	298	65	0.95
CB-Br-500-N	302	66	0.94

CMs is not very intense. This observation is consistent with the removal of a significant part of surface bromine during amination. According to the results of chemical analysis, amination leads to the detachment of 62–80% of bromine groups ($\Delta C(\text{Br})$). However, the amount of attached amino groups is less than expected for the direct substitution of each bromine group by an amino group. The number of attached amino groups reaches only 65–85% of the presented bromine groups that can be replaced by amino groups. About 35–15% of the bromine groups are hydrolyzed, while Ph groups are formed on the freeing surface sites.

The chemical transformations during the amination of brominated CMs can be schematized as in (Fig. 17).

Amination of the brominated CMs leads to the removal of bromine from the carbon surface. This removal takes place through the elimination of HBr in the basic

**Fig. 17** Schematic diagram showing the carbon surface chemistry changes at the amination of the brominated CMs

amine medium. Alternatively, it can be passed due to the replacement of bromine by an amino group with the formation of the product (I). This product (I) becomes stable due to the restoration of the double C=C bonds involved in the conjugated system through formal double bonds with adjacent carbons. Further, the amination of the product (I) with the formation of product (II) becomes possible. But, only some of the active sites can give the product (II). This explanation is correct for the isolated C=C bonds since they are not from the conjugated system of C=C bonds within the carbon matrix. Thus, the brominated CMs readily react with diethylamine. By the proposed amination, one can replace bromine groups and functionalize the carbon surface layer with amino groups. According to chemical analysis, one can attach up to 1.45–1.65 mmol g⁻¹ of amino groups in such a way. The resulting sorbents have the basic properties of the surface layer. In contrast to the amination of the brominated CMs with diethylamine, the pristine CMs have low reactivity toward direct amination. Therefore, the direct amination gives an insignificant content of the amino groups of ~ 0.1 mmol g⁻¹ in the resulting aminated CMs.

3.7 Sulfonation of Brominated Carbon Materials

The samples of ACF-Br-30, ACF-Br-60, and ACF-Br-120 are characterized by a significant content of chemisorbed bromine. So, we selected them to functionalize their surface layer with acidic SO₃H groups. Treatment of these samples with a concentrated aqueous solution of sodium thioglycolate causes the practically complete removal of bromine from the surface layer. For comparison, a sample of the unmodified ACF was also sulfonated using the same procedure. As can be seen from Table 9, the specific surface area S_{BET} and the total pore volume V_{tot} of the resulting sulfonated ACFs are slightly reduced compared with those of the unmodified (pristine) ACFs.

The surface layer of the sulfonated samples was examined by FTIR ATR (Fig. 18). The spectra of the sulfonated samples obtained do not differ from the spectrum of the original ACF in the region of characteristic resonant absorption for aromatic and/or conjugated C=C bonds of the carbon matrix (in the range 1600–1450 cm⁻¹). In the range of 1840–1640 cm⁻¹, one can see a decrease in the intensity of the spectral bands; they correspond to the absorption of C=O bonds. This decrease is because of

Table 9 Textural parameters of the sulfonated ACFs

Sample	S_{BET} , m ² g ⁻¹	V_{tot} , cm ³ g ⁻¹
ACF	680	0.34
ACF-S	618	0.31
ACF-Br-30-S	544	0.28
ACF-Br-60-S	529	0.27
ACF-Br-120-S	535	0.27

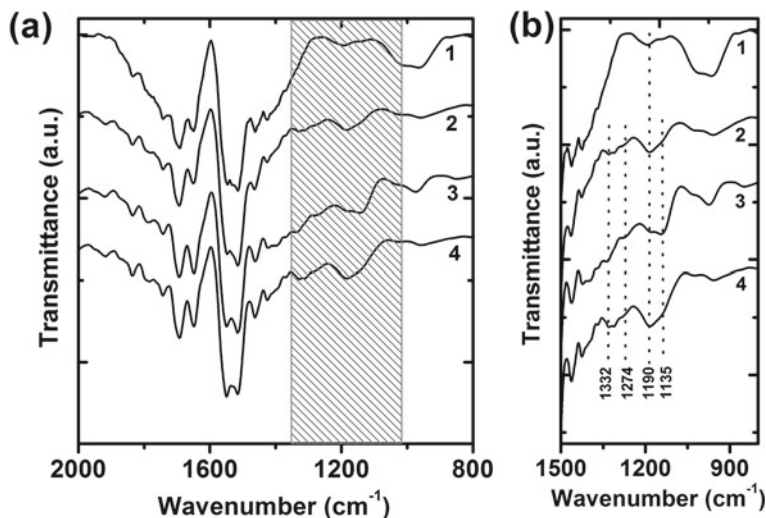


Fig. 18 FTIR ATR spectra of the initial ACF (1), ACF-Br-30-S (2), ACF-Br-60-S (3), and ACF-Br-120-S (4): **a** the characteristic part of spectra and **b** a magnified part of **a**

a fall in the concentration of Cx, A, and L groups. It takes place after bromination and following sulfonation of the carbon surface. The identification of sulfo groups attached to the surface of carbon materials presents significant difficulties due to the overlap of the absorption regions of the S=O and S–O bonds and the C–O bonds [90]. Given the lack of appreciable oxidation and the formation of additional C=O groups during sulfonation, the detected increase in the absorption intensity in the range of 1350–1000 cm^{-1} (indicated in Fig. 18a) for the sulfonated ACFs, as compared with the unmodified ACF, can be attributed to the absorption of sulfo groups.

A more detailed analysis of FTIR ATR spectra in the 1350–1000 cm^{-1} region revealed bands that can be attributed to the vibrations of the S=O and S–O bonds that are part of the sulfo groups (Fig. 18b). Compared with the initial ACF spectrum, the absorption bands at 1332 and 1274 cm^{-1} are found in the spectra of the sulfonated samples. These bands can be assigned to the asymmetric and symmetric vibrations of S=O bonds in the sulfo groups. A rather intense absorption band at 1190 cm^{-1} corresponds to the vibrations of S=O bonds in the SO_3^- anions. This fact confirms the formation of surface groups with high acidity on the ACF surface. The absorption band at 1135 cm^{-1} presumably corresponds to the vibrations of S–O bonds in the SO_3H groups.

Figure 19 shows typical TGA/EGA profiles for the sulfonated ACFs. The weight loss as a result of thermal desorption occurs in three temperature ranges. The first effect of weight loss at about 100 °C is small and is caused by the release of physisorbed water. The second effect with a sharp weight loss is observed in the temperature range of 200–500 °C. This effect is absent for the unmodified and brominated ACFs and is associated with the thermal decomposition of sulfo groups.

The third effect is observed at temperatures of 500–800 °C. It is registered for the sulfonated ACFs as well as for the unmodified ACF. This effect corresponds to the thermal decomposition of Ph groups. The total weight loss because of the decomposition of functional groups (Δm_{FG}) increases in the series of samples from the ACF-S to the ACF-Br-60-S, and it correlates with the sulfur content ($C(S)$) in the prepared sulfonated CMs (Table 10).

The DTG analysis revealed a weight loss step peaked at 268 °C and assigned to the decomposition of SO_3H groups. Between 150 °C and 500 °C, a weight loss observed by the thermal analysis is registered simultaneously with the detection of SO_2 (m/z 64) in the TPD MS experiments. This weight loss was attributed to the decomposition of most SO_3H groups, in agreement with the temperature range of their decomposition reported in [72]. This wide temperature range (in which SO_2^+ is detected) means the existence of a continuous spectrum of the surface forms presented by SO_3H groups. For the sulfonated ACFs, the MS peak of SO_2^+ has an asymmetric shape and can be divided into β_1 , β_2 , β_3 , and β_4 components (Table 10).

For each component, the peak maximum temperature (T_m) and the relative area under the peak (%) were found and listed in Table 10. From the tabulated data, one can see β_2 , β_3 , and β_4 components. They are assigned to the attached SO_3H groups

Fig. 19 Typical TGA/EGA for the sulfonated ACFs, on the example of the ACF-Br-60-S sample. TGA: TG (1) and DTG (2) curves, and EGA (3): SO_2 profile

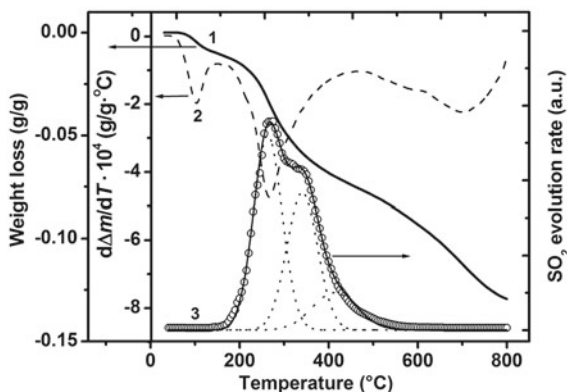


Table 10 Surface chemistry of the sulfonated ACFs from the chemical analysis, TGA, and TPD MS data

Sample	$C(S)$, mmol g^{-1}	$C(S)/C(Br)$	TGA Δm_{FG} , $g\ g^{-1}$	TPD MS profile of m/z 64 (SO_2^+)			
				Peak temperatures (T_m), °C/relative area, %			
				β_1	β_2	β_3	β_4
ACF-S	0.18	–	0.066	171/28.9	220/41.7	304/29.4	–
ACF-Br-30-S	0.51	0.63	0.107	–	248/58.2	331/33.9	401/7.9
ACF-Br-60-S	0.72	0.69	0.124	–	263/48.6	340/36.8	413/14.6
ACF-Br-120-S	0.65	0.67	0.116	–	267/44.2	357/40.7	431/15.1

that are differed by their binding energy with the carbon surface. As deduced from the spectra of the pre-brominated sulfonated ACFs, their surface layer decomposition caused the release of SO_2 gas, which thermal desorption profile could be modeled with three Gauss peaks centered at 258 ± 10 °C, 344 ± 13 °C, and 416 ± 15 °C, correspondingly. The significant difference in thermal decomposition temperatures is explained by the arrangement of the SO_3H groups in pores of different sizes and because of the effect of the nearest neighboring groups of different functions. By extending the bromination time, one can noticeably increase the thermal stability of the attached SO_3H groups. After prolonged bromination, the temperature range of SO_2 release and the relative area under the profile for the most high-temperature (β_3 and β_4) forms simultaneously increase. According to the TPD MS data for the vacuum thermolysis of the resulting samples, these effects can be explained by the involvement of small micropores in the bromination reactions because only the subsequent replacement of bromine groups by sulfo groups can be a reason for the observed changes.

Thus, thermal stability for each of the ACF-Br-30-S, ACF-Br-60-S, and ACF-Br-120-S samples considerably exceeds that found for the ACF-S sample obtained by omitting the bromination stage. For the ACF-S sample, the most stable (β_4) form is absent in the TPD MS profile. Nevertheless, the β_1 form is present. For this β_1 form, the peak temperature of SO_2 desorption is only 171 °C. We suggested that the β_1 corresponds to H_2SO_4 molecules forming a dense “hydrogen bond network” filling tight micropores. The sulfonation of the brominated ACF can be summarized by the following scheme (Fig. 20). The interaction of various forms of chemisorbed bromine with sodium thioglycolate leads to its addition with the elimination of hydrogen bromide causes the formation of product (I). As a result of the acidic hydrolysis of the product (I) and subsequent oxidation of the hydrolysis product, products (II) and (III) are formed, respectively. From the $C(\text{S})/C(\text{Br})$ ratio, only 60–70% of bromine can be substituted by sulfur-containing groups. The decrease in the yield of the final product (III) is because of the basic hydrolysis of bromine groups. This hydrolysis cleaves a part of added bromine in a sodium thioglycolate solution. In comparison with other methods used for bromination, implementing plasma-chemical bromination showed reasonable pros. One can mostly eliminate the effect of parallel oxidation by plasma-chemical bromination, resulting in a greater yield of the product (III).

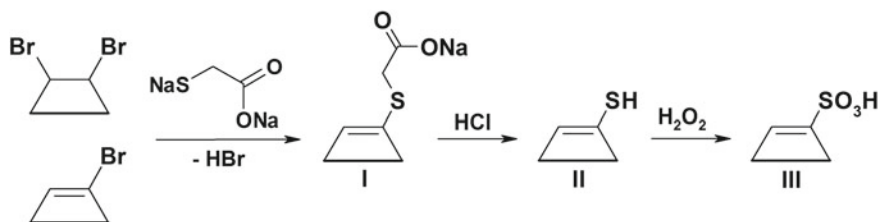
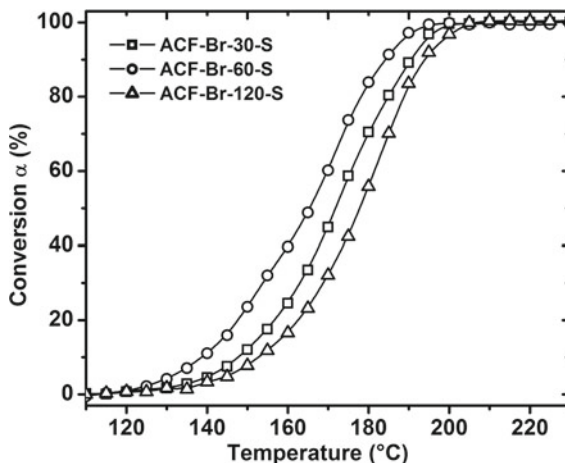


Fig. 20 Schematic diagram showing the chemical transformations during the staged sulfonation of the brominated carbon surface

Fig. 21 Temperature dependences of the conversion of 2-propanol to propene catalyzed by the sulfonated ACFs



The obtained data prove that pre-bromination is the best way to covalent attaching the sulfo group on the ACF surface. The use of the brominated ACF samples to modify the carbon surface with sulfo groups is more efficient and allows obtaining 0.51–0.72 mmol g⁻¹ of thermally stable S-containing groups. In the studies of the catalytic activity of the sulfonated ACFs in the dehydration reaction of 2-propanol, we found nearly 100% conversion of 2-propanol to propene over the ACF-Br-30-S, ACF-Br-60-S, and ACF-Br-120-S samples only. For the ACF-S sample, the maximum conversion of 2-propanol is 92% at 248 $^{\circ}\text{C}$, and with a further increase in temperature, the conversion degree only decreases. Therefore, the sample ACF-S contains thermally unstable acid centers that can be deactivated easily. For the samples of ACF-Br-30-S, ACF-Br-60-S, and ACF-Br-120-S, the 100% conversion of 2-propanol to propene is achieved at the temperatures of 195–206 $^{\circ}\text{C}$, and it is not strongly dependent on concentrations of sulfo groups (Fig. 21).

We explained this by unavailable (hidden) sulfo groups that do not participate in catalysis. Typically, the structurally restricted availability of some sulfo groups is due to their location in narrow and tight micropores. The most characteristic feature of the studied catalysts is their high thermal stability when operating in a reaction medium at 150–230 $^{\circ}\text{C}$ for several hours.

4 Concluding Remarks

In modifying CMs, which are different by chemical nature, only direct bromination with bromine vapor is effective. The optimal temperature range for the maximal chemisorption of bromine is found to be from 300 to 500 $^{\circ}\text{C}$. This range does not depend on the nature of CMs. At lower temperatures, the forming of physisorbed (intercalated) bromine is possible. But at higher temperatures, the processes of

bromine desorption predominate. The relatively low temperatures and the weak dependence of the maximum amount of attached bromine on temperature suggest that this reaction is selective. Kinetic studies showed two regimes of the isothermal bromination reaction. A fast process causes chemisorption of up to 80% bromine for about 20 min, while a slow process lasts until 1–2 h. Regardless of the many parameters, e.g., kinetic region, bromination temperature, and structural-sorption parameters of CMs, the bromination reaction is limited by diffusion. The limiting stage of kinetics is a transfer of the bromine molecule to the surface-active site. When studying the thermal desorption from the brominated CMs, a spectrum of forms of surface bromine with different decomposition and detachment temperatures, from 200 to 800 °C, was found. It is established that the thermal decomposition of any form of bromine occurs in the form of HBr, which proves its chemisorption. The highest content of attached bromine of about 2.5 mmol g⁻¹ is found for the brominated NACs. However, the reactivity per unit area was higher for CB, MWCNTs, and ACFs. The reactivity of CMs in the bromination reaction is determined by the number of active sites (HC=CH bonds) and depends significantly on the method used to prepare CMs. All studied CMs with a developed surface, which is due to activation by water vapor, have a lower reactive ability to bromine. Most attached bromine (up to 80%) is chemically active and can be substituted by amino groups. The aminated CMs are characterized by high thermal stability in the temperature range of 30–200 °C. The thermal decomposition peak of amino groups is recorded at 300 ± 15 °C. This decomposition temperature does not depend on the nature of CM and bromination temperature. This experimental fact proves the covalent fixation of amino groups on the surface. The obtained aminated CMs contain up to 1.55 mmol g⁻¹ amino groups. In fact, these sorbents have the potential to be used as selective sorbents or carriers.

Plasma bromination of ACFs at 22 °C causes adsorption of bromine, and up to 1 mmol g⁻¹ of bromine can be attached. During the short-term, from 5 to 30 min, plasma-chemical treatment, a significant amount of physisorbed bromine is formed on the ACF surface, and a lot of intercalated bromine is registered in the inner (free) volume. Increasing the time of plasma-chemical treatment to 60 min leads to the maximum amount of chemisorbed bromine (up to 1.04 mmol g⁻¹). About 60–80% of the attached bromine can be replaced by thermally stable acidic SO₃H groups. It was found that pre-bromination leads to surface modification with more SO₃H groups into the surface layer of ACFs than at the direct bromination. It is shown that 100% conversion of 2-propanol to propene on the obtained acid catalysts is observed at 190–200 °C.

Acknowledgments This work was funded by grants from the Ministry of Education and Science of Ukraine ([0111U006260], [0114U003554], and [0116U002558]). This work has been supported by the Ministry of Education and Science of Ukraine: Grant of the Ministry of Education and Science of Ukraine for perspective development of a scientific direction named “Mathematical sciences and natural sciences” at the Taras Shevchenko National University of Kyiv.

References

1. Tascón JMD (ed) (2012) *Novel Carbon Adsorbents*, 1st edn. Elsevier, Amsterdam
2. Kaneko K, Rodríguez-Reinoso F (eds) (2019) *Nanoporous Materials for Gas Storage*. Springer, Singapore
3. Hasse B, Gläsel J, Kern AM, Murzin DY, Etzold BJM (2015) Preparation of carbide-derived carbon supported platinum catalysts. *Catal Today* 249:30–37. <https://doi.org/10.1016/j.cattod.2014.10.049>
4. Yan P, Zhang X, Herold F, Li F et al (2020) Methanol oxidative dehydrogenation and dehydration on carbon nanotubes: active sites and basic reaction kinetics. *Catal Sci Technol* 10:4952–4959. <https://doi.org/10.1039/D0CY00619J>
5. Li F, Yan P, Herold F, Drochner A et al (2020) Oxygen assisted butanol conversion on bifunctional carbon nanotube catalysts: activity of oxygen functionalities. *Carbon* 170:580–588. <https://doi.org/10.1016/j.carbon.2020.08.053>
6. Sheng J, Yan B, Lu W-D et al (2021) Oxidative dehydrogenation of light alkanes to olefins on metal-free catalysts. *Chem Soc Rev* 50:1438–1468. <https://doi.org/10.1039/D0CS01174F>
7. Hulicova-Jurcakova D, Seredych M, Lu GQ, Bandosz TJ (2009) Combined effect of nitrogen- and oxygen-containing functional groups of microporous activated carbon on its electrochemical performance in supercapacitors. *Adv Funct Mater* 19:438–447. <https://doi.org/10.1002/adfm.200801236>
8. Jaramillo J, Modesto P, Gómez-Serrano AV (2010) Oxidation of activated carbon by dry and wet methods: surface chemistry and textural modifications. *Fuel Process Technol* 91:1768–1775. <https://doi.org/10.1016/j.fuproc.2010.07.018>
9. Marsh H, Rodríguez-Reinoso F (eds) (2006) *Activated carbon*. Elsevier, Amsterdam
10. Bansal RC, Goyal M (eds) (2005) *Activated carbon adsorption*. CRC Press, Boca Raton
11. Bandosz TJ (ed) (2006) *Activated carbon surfaces in environmental remediation*. Interface science and technology, vol 7. Academic Press, San Diego
12. Daud WMAW, Houshamnd AH (2010) Textural characteristics, surface chemistry and oxidation of activated carbon. *J Natural Gas Chem* 19:267–279. [https://doi.org/10.1016/S1003-9953\(09\)60066-9](https://doi.org/10.1016/S1003-9953(09)60066-9)
13. Shen W, Li Z, Yihong L (2008) Surface chemical functional groups modification of porous carbon. *Recent Patents Chem Eng* 1:27–40. <https://doi.org/10.2174/2211334710801010027>
14. Moreno-Castilla C, López-Ramón MV, Carrasco-Marín F (2000) Changes in surface chemistry of activated carbons by wet oxidation. *Carbon* 38:1995–2001. [https://doi.org/10.1016/S0008-6223\(00\)00048-8](https://doi.org/10.1016/S0008-6223(00)00048-8)
15. Wepasnick KA, Smith BA, Schrote KE, Wilson HK, Diegelmann SR, Fairbrother DH (2011) Surface and structural characterization of multi-walled carbon nanotubes following different oxidative treatments. *Carbon* 49:24–36. <https://doi.org/10.1016/j.carbon.2010.08.034>
16. Lisovskii A, Semiat R, Aharoni C (1997) Adsorption of sulfur dioxide by active carbon treated by nitric acid: I. Effect of the treatment on adsorption of SO₂ and extractability of the acid formed. *Carbon* 35:1639–1643. [https://doi.org/10.1016/S0008-6223\(97\)00129-2](https://doi.org/10.1016/S0008-6223(97)00129-2)
17. Pradhan BK, Sandle NK (1999) Effect of different oxidizing agent treatments on the surface properties of activated carbons. *Carbon* 37:1323–1332. [https://doi.org/10.1016/S0008-6223\(98\)00328-5](https://doi.org/10.1016/S0008-6223(98)00328-5)
18. Almarri M, Ma X, Song C (2009) Role of surface oxygen-containing functional groups in liquid-phase adsorption of nitrogen compounds on carbon-based adsorbents. *Energ Fuel* 23:3940–3947. <https://doi.org/10.1021/ef900051r>
19. Domingo-García M, López-Garzón FJ, Pérez-Mendoza M (2000) Effect of some oxidation treatments on the textural characteristics and surface chemical nature of an activated carbon. *J Colloid Interface Sci* 222:233–240. <https://doi.org/10.1006/jcis.1999.6619>
20. Montes-Morán MA, Suárez D, Menéndez JA, Fuente E (2004) On the nature of basic sites on carbon surfaces: an overview. *Carbon* 42:1219–1225. <https://doi.org/10.1016/j.carbon.2004.01.023>

21. Ma C, Lu T, Shao J, Huang J et al (2022) Separation and purification technology biomass derived nitrogen and sulfur co-doped porous carbons for efficient CO₂ adsorption. *Sep Purif Technol* 281:119899. <https://doi.org/10.1016/j.seppur.2021.119899>
22. Cruz-Silva E, Cullen DA, Gu L, Romo-Herrera JM et al (2008) Heterodoped nanotubes: theory, synthesis, and characterization of phosphorus–nitrogen doped multiwalled carbon nanotubes. *ACS Nano* 2:441–448. <https://doi.org/10.1021/nn700330w>
23. Saha D, Kienbaum MJ (2019) Role of oxygen, nitrogen and sulfur functionalities on the surface of nanoporous carbons in CO₂ adsorption: a critical review. *Microporous Mesoporous Mater* 287:29–55. <https://doi.org/10.1016/j.micromeso.2019.05.051>
24. Li OL, Qin L, Takeuchi N, Kim K, Ishizaki T (2019) Effect of hydrophilic/hydrophobic properties of carbon materials on plasma-sulfonation process and their catalytic activities in cellulose conversion. *Catal Today* 337:155–161. <https://doi.org/10.1016/j.cattod.2019.04.025>
25. Georgakilas V, Perman JA, Tucek J, Zboril R (2015) Broad family of carbon nanoallotropes: classification, chemistry, and applications of fullerenes, carbon dots, nanotubes, graphene, nanodiamonds, and combined superstructures. *Chem Rev* 115:4744–4822. <https://doi.org/10.1021/cr500304f>
26. Karlicky F, Datta KKR, Otyepka M, Zboril R (2013) Halogenated graphenes: rapidly growing family of graphene derivative. *ACS Nano* 7:6434–6464. <https://doi.org/10.1021/nn4024027>
27. Friedrich J, Wettmarshausen S, Hennecke M (2009) Haloform plasma modification of polyolefin surfaces. *Surf Coat Tech* 203:3647–3655. <https://doi.org/10.1016/j.surfcoat.2009.05.050>
28. Friedrich JF, Hidde G, Lippitz A, Unger WES (2014) Plasma bromination of graphene for covalent bonding of organic molecules. *Plasma Chem Plasma Process* 34:621–645. <https://doi.org/10.1007/s11090-013-9509-x>
29. Do Nascimento GM, Hou T, Kim YA et al (2008) Double-wall carbon nanotubes doped with different Br₂ doping levels: a resonance Raman study. *Nano Lett* 8:4168–4172. <https://doi.org/10.1021/nl801605u>
30. Zarska S, Kulawik D, Pavlyuk V et al (2021) A facile and efficient bromination of multi-walled carbon nanotubes. *Materials* 14:3161. <https://doi.org/10.3390/ma14123161>
31. Zarska S, Kulawik D, Drabowicz J, Ciesielski W (2017) A review of procedures of purification and chemical modification of carbon nanotubes with bromine. *Fuller Nanotub Carbon Nanostructures* 25:563–569. <https://doi.org/10.1080/1536383x.2017.1330266>
32. Jin Z-x, Xu GQ, Goh SH (2000) A preferentially ordered accumulation of bromine on multi-wall carbon nanotubes. *Carbon* 38:1135–1139. [https://doi.org/10.1016/s0008-6223\(99\)00237-7](https://doi.org/10.1016/s0008-6223(99)00237-7)
33. Grishchenko LM, Diyuk VE, Marychuk RT et al (2020) Surface reactivity of nanoporous carbons: preparation and physicochemical characterization of sulfonated activated carbon fibers. *Appl Nanosci* 10:2923–2939. <https://doi.org/10.1007/s13204-019-01069-3>
34. Grishchenko LM, Vakaliuk AV, Diyuk VE et al (2017) Functionalization of surface layer of nanoporous carbon fibers with bromine and amine functional groups. In: *Proceedings of 2017 IEEE 7th International Conference on Nanomaterials: Application & Properties, NAP 2017, vol 2017, pp 01PCSI19-1–01PCSI19-6*. <https://doi.org/10.1109/NAP.2017.8190155>
35. Diyuk VE, Zaderko AN, Veselovska KI, Lisnyak VV (2015) Functionalization of surface of carbon materials with bromine vapors at mediate high temperature: a thermogravimetric study. *J Thermal Anal Calorim* 120:1665–1678. <https://doi.org/10.1007/s10973-015-4495-2>
36. Bulusheva LG, Lobiak EV, Fedoseeva YuV, Mevellec J-Y, Makarova AA, Flahaut E, Okotrub AV (2020) Effect of ultrasound pretreatment on bromination of double-walled carbon nanotubes. *Synth Met* 259:116233. <https://doi.org/10.1016/j.synthmet.2019.116233>
37. Mazov I, Krasnikov D, Stadnichenko A, Kuznetsov V, Romanenko A, Anikeeva O, Tkachev E (2012) Direct vapor-phase bromination of multiwall carbon nanotubes. *J Nanotechnol* 2012:954084. <https://doi.org/10.1155/2012/954084>
38. Veselovska KI, Veselovskiy VL, Zaderko OM, Diyuk VE, Ishchenko OV (2015) Effect of the oxidation and thermal treatment on bromination of activated carbon. *J Superhard Mater* 37:39–43. <https://doi.org/10.3103/S1063457615010062>

39. Li Y, Chen H, Voo LY, Ji J et al (2012) Synthesis of partially hydrogenated graphene and brominated graphene. *J Mater Chem* 22:15021–15024. <https://doi.org/10.1039/C2JM32307A>
40. Jankovský O, Šimek P, Klimová K et al (2014) Towards graphene bromide: bromination of graphite oxide. *Nanoscale* 6:6065–6074. <https://doi.org/10.1039/C4NR01154F>
41. Au H, Rubio N, Shaffer M (2017) Brominated graphene as a versatile precursor for multifunctional grafting. *Chem Sci* 9:209–217. <https://doi.org/10.1039/c7sc03455e>
42. Chen YK, Green MLH, Griffin JL et al (1996) Purification and opening of carbon nanotubes via bromination. *Adv Mater* 8:1012–1015. <https://doi.org/10.1002/adma.19960081216>
43. Hanelt S, Friedrich JF, Orts-Gil G, Meyer-Plath A (2012) Study of Lewis acid catalyzed chemical bromination and bromoalkylation of multi-walled carbon nanotubes. *Carbon* 50:1373–1385. <https://doi.org/10.1016/j.carbon.2011.11.009>
44. Janas D, Boncel S, Koziol KKK (2014) Electrothermal halogenation of carbon nanotube films. *Carbon* 73:259–266. <https://doi.org/10.1016/j.carbon.2014.02.062>
45. Duesberg G, Graupner R, Downes P, Minett A, Ley L, Roth S, Nicoloso N (2004) Hydrothermal functionalisation of single-walled carbon nanotubes. *Synth Met* 142:263–266. <https://doi.org/10.1016/j.synthmet.2003.09.009>
46. Bezugla TM, Grishchenko LM, Vakaliuk AV, Diyuk VE, Mischanchuk OV, Lisnyak VV (2018) Covalent bonding of sulfogroups to activated carbon fibers: the role of bromine plasma pretreatment. *Molec Cryst Liquid Cryst* 661:58–67. <https://doi.org/10.1080/15421406.2018.1460240>
47. Abdelkader VK, Domingo-García M, Melguizo M, López-Garzón R, Javier López-Garzón F, Pérez-Mendoza M (2015) Covalent bromination of multi-walled carbon nanotubes by iodine bromide and cold plasma treatments. *Carbon* 93:276–285. <https://doi.org/10.1016/j.carbon.2015.05.070>
48. Lippitz A, Friedrich JF, Unger WES (2013) Plasma bromination of HOPG surfaces: a NEXAFS and synchrotron XPS study. *Surface Sci* 611:L1–L7. <https://doi.org/10.1016/j.susc.2013.01.020>
49. Multian VV, Kinzerskyi FE, Vakaliuk AV et al (2017) Surface response of brominated carbon media on laser and thermal excitation: optical and thermal analysis study. *Nanoscale Res Lett* 12:146. <https://doi.org/10.1186/s11671-017-1873-7>
50. Moradi L, Etesami I (2016) New route for bromination of multiwalled carbon nanotubes under mild and efficient conditions. *Fuller Nanotub Carbon Nanostructures* 24:213–218. <https://doi.org/10.1080/1536383X.2015.1136820>
51. Gopalakrishnan K, Subrahmanyam KS, Kumar Prashant, Govindaraj A, Rao CNR. Reversible chemical storage of halogens in few-layer graphene. *RSC Adv* 2:1605–1608. <https://doi.org/10.1039/C1RA00403D>
52. Hines D, Rummeli MH, Adebimpe D, Akins DL (2014) High-yield photolytic generation of brominated single-walled carbon nanotubes and their application for gas sensing. *Chem Commun* 50:11568–11571. <https://doi.org/10.1039/C4CC03702B>
53. Oliveira L, Lu F, Andrews L, Takacs G, Mehan M, Debies T (2013) UV photo-chlorination and -bromination of single-walled carbon nanotubes. *J Mater Res* 29:239–246. <https://doi.org/10.1557/jmr.2013.382>
54. Colomer J-F, Marega R, Traboulsi H, Meneghetti M, Tendeloo GV, Bonifazi D (2009) Microwave-assisted bromination of double-walled carbon nanotubes. *Chem Mater* 21:4747–4749. <https://doi.org/10.1021/cm902029m>
55. Morrison RT, Boyd RN, Bhattacharjee KS (2010) *Organic chemistry*, 7th edn. Pearson Education, New Delhi
56. Salavagione HJ, Martínez G, Ellis G (2011) Recent advances in the covalent modification of graphene with polymers. *Macromol Rapid Commun* 32:1771–1789. <https://doi.org/10.1002/marc.201100527>
57. Krishtab M, Armini S, Meersschant J, De Gendt S, Ameloot R (2021) Cyclic plasma halogenation of amorphous carbon for defect-free area-selective atomic layer deposition of titanium oxide. *ACS Appl Mater Interfaces* 13:32381–32392. <https://doi.org/10.1021/acsami.1c04405>

58. Yao Y, Velpari V, Economy J (2013) In search of brominated activated carbon fibers for elemental mercury removal from power plant effluents. *J Mater Chem A* 39:12103–12108
59. Wilcox J, Sasmaz E, Kirchofer A, Lee SS (2011) Heterogeneous mercury reaction chemistry on activated carbon. *J Air Waste Manage Assoc* 61:418–426
60. Hower JC, Senior CL, Suuburg EM, Hurt RH, Wilcox J, Olson ES (2010) Mercury capture by native fly ash carbons in coal-fired power plants. *Prog Energy Combust Sci* 36:510–529
61. Rupp E, Wilcox J (2014) Mercury chemistry of brominated activated carbons—packed-bed breakthrough experiments. *Fuel* 117A:351–353
62. Huggins FE, Yap N, Huffman GP, Senior CL (2003) XAFS characterization of mercury captured from combustion gases on sorbents at low temperatures. *Fuel Proc Technol* 82:167–196
63. Barpanda P, Amatucci G (2008) Structure and electrochemistry of carbon-bromine nanocomposite electrodes for electrochemical energy storage. *MRS Proc* 1127:1127-T01-11. <https://doi.org/10.1557/PROC-1127-T01-11>
64. Barpanda P, Fanchini G, Amatucci GG (2011) Structure, surface morphology and electrochemical properties of brominated activated carbons. *Carbon* 49:2538–2548. <https://doi.org/10.1016/j.carbon.2011.02.028>
65. Jabeen M, Ishaq M, Song W, Xu L, Deng Q (2017) Synthesis of Ni/Co/Al-layered triple hydroxide@brominated graphene hybrid on nickel foam as electrode material for high-performance supercapacitors. *RSC Adv* 7:46553–46565. <https://doi.org/10.1039/C7RA08744F>
66. Zeynalov EB, Friedrich J, Meyer-Plath A, Hidde G et al (2013) Plasma-chemically brominated single-walled carbon nanotubes as novel catalysts for oil hydrocarbons aerobic oxidation. *Appl Catal A Gen* 454:115–118. <https://doi.org/10.1016/j.apcata.2013.01.003>
67. Zeynalov E, Wagner M, Friedrich J, Magerramova M et al (2017) The peculiar behavior of functionalized carbon nanotubes in hydrocarbons and polymeric oxidation environments. *J Adhesion Sci Technol* 31:988–1006. <https://doi.org/10.1080/01694243.2016.1239304>
68. Zeynalov E, Friedrich J, Wagner M, Hidde G (2015) Effect of Br-grafted multi-walled carbon nanotubes on the model oxidative environment. *Chem Chem Technol* 9:51–54. <https://doi.org/10.23939/chcht09.01.051>
69. Diyuk VE, Zaderko AN, Grischenko LM, Tsapyuk GG, Vakaliuk AV, Lisnyak VV, Mariychuk R (2020) CO₂ adsorption on pristine, oxidized, and diethylamine-functionalized activated carbon sorbents. *E3S Web Conf* 154:07001. <https://doi.org/10.1051/e3sconf/202015407001>
70. Grishchenko LM, Tsapyuk GG, Novichenko NS, Mischanchuk OV, Yatsymyrskiy AV, Boldyrieva OY, Diyuk VE (2020) Amination of brominated nanoporous activated carbon beads for the preparation of CO₂ adsorbents. *Molec Cryst Liquid Cryst* 699:20–33. <https://doi.org/10.1080/15421406.2020.1732535>
71. Zabuga VYA, Bochechka OO, Tsapyuk GG, Diyuk VE, Panova AM, Lisnyak VV (2018) On multiwalled carbon nanotubes oxidation: thermogravimetric, spectral and macrokinetic studies. *Mol Cryst Liquid Cryst* 661:81–90. <https://doi.org/10.1080/15421406.2018.1460257>
72. Grishchenko LM, Vakaliuk AV, Diyuk VE, Mischanchuk OV, Boldyrieva OY, Bezugla TM, Lisnyak VV (2018) From destructive CCl₄ adsorption to grafting SO₃H groups onto activated carbon fibers. *Molec Cryst Liquid Cryst* 673:1–15. <https://doi.org/10.1080/15421406.2019.1578488>
73. Khavryuchenko VD, Khavryuchenko OV, Shkilnyy AI et al (2009) Characterization by SEM, TEM and quantum-chemical simulations of the spherical carbon with nitrogen (SCN) active carbon produced by thermal decomposition of poly(vinylpyridine-divinylbenzene) copolymer. *Materials* 2:1239–1251. <https://doi.org/10.3390/ma2031239>
74. Veselovskiy VL, Ischenko EV, Gayday SV, Lisnyak VV (2012) A high efficient two phase CuO/Cu₂(OH)₃NO₃(Co²⁺/Fe³⁺) composite catalyst for CO-PROX reaction. *Catal Commun* 18:137–141. <https://doi.org/10.1016/j.catcom.2011.11.024>
75. Jagiello J, Olivier JP (2013) Carbon slit pore model incorporating surface energetical heterogeneity and geometrical corrugation. *Adsorption* 19:777–783. <https://doi.org/10.1007/s10450-013-9517-4>

76. Diyuk VE, Zaderko AN, Grishchenko LM, Afonin S, Mariychuk R, Boldyrieva OY, Skryshesky VA, Kaňuchová M, Lisnyak VV (2021) Surface chemistry of fluoroalkylated nanoporous activated carbons: XPS and ^{19}F NMR study. *Appl Nanosci*. <https://doi.org/10.1007/s13204-021-01717-7>
77. Uklein AV, Diyuk VE, Grishchenko LM et al (2016) Characterization of oxidized carbon materials with photoinduced absorption response. *Appl Phys B* 122:287. <https://doi.org/10.1007/s00340-016-6561-2>
78. Tsapyuk GG, Diyuk VE, Mariychuk R et al (2020) Effect of ultrasonic treatment on the thermal oxidation of detonation nanodiamonds. *Appl Nanosci* 10:4991–5001. <https://doi.org/10.1007/s13204-020-01277-2>
79. Ischenko EV, Matzui LY, Gayday SV, Vovchenko LL, Kartashova TV, Lisnyak VV (2010) Thermo-exfoliated graphite containing $\text{CuO}/\text{Cu}_2(\text{OH})_3\text{NO}_3:(\text{Co}^{2+}/\text{Fe}^{3+})$ composites: preparation, characterization and catalytic performance in CO conversion. *Materials* 3(1):572. <https://doi.org/10.3390/ma3010572>
80. Boehm HP (2002) Surface oxides on carbon and their analysis: a critical assessment. *Carbon* 40:145–149. [https://doi.org/10.1016/S0008-6223\(01\)00165-8](https://doi.org/10.1016/S0008-6223(01)00165-8)
81. Khavryuchenko VD, Tarasenko YA, Khavryuchenko OV et al (2010) Nanostructurization in the SKS active carbon, characterized by SEM, TEM, EDX and quantum-chemical simulations. *Int J Modern Phys B* 24:1449–1462. <https://doi.org/10.1142/S0217979210055627>
82. Khavryuchenko OV, Khavryuchenko VD, Lisnyak VV, Peshlherbe GH (2011) A density-functional theory investigation of the electronic structure of the active carbon graphite-like and amorphous domains. *Chem Phys Lett* 513:261–266. <https://doi.org/10.1016/j.cplett.2011.08.009>
83. Khavryuchenko VD, Khavryuchenko OV, Tarasenko YA, Lisnyak VV (2008) Computer simulation of N-doped polyaromatic hydrocarbons clusters. *Chem Phys* 352:231–234. <https://doi.org/10.1016/j.chemphys.2008.06.019>
84. Khavryuchenko VD, Khavryuchenko OV, Lisnyak VV (2010) High multiplicity states in disordered carbon systems: ab initio and semiempirical study. *Chem Phys* 368:83–86. <https://doi.org/10.1016/j.chemphys.2009.12.022>
85. Figueiredo JL, Pereira MFR, Freitas MMA, Orfao JJM (1999) Modification of the surface chemistry of activated carbons. *Carbon* 37:1379–1389. [https://doi.org/10.1016/S0008-6223\(98\)00333-9](https://doi.org/10.1016/S0008-6223(98)00333-9)
86. Diyuk VE, Zaderko AN, Grishchenko LM, Vakaliuk AV, Mariychuk R, Lisnyak VV (2021) Surface reactivity of carbon nanoporous materials studied with chemical bromination. *Springer Proc Phys* 264:171–205. https://doi.org/10.1007/978-3-030-74800-5_12
87. Papirer E, Lacroix R, Donnett JB, Nansé G, Fioux P (1994) XPS study of the halogenation of carbon black—part I. Bromination. *Carbon* 32:1341–1358. [https://doi.org/10.1016/0008-6223\(94\)90121-x](https://doi.org/10.1016/0008-6223(94)90121-x)
88. Zheng J, Liu HT, Wu B et al (2012) Production of graphite chloride and bromide using microwave sparks. *Sci Rep* 2:662. <https://doi.org/10.1038/srep0066210.1038/srep00662>
89. Sasmaz E, Kirchofer A, Jew AD et al (2012) Mercury chemistry on brominated activated carbon. *Fuel* 99:188–196. <https://doi.org/10.1016/j.fuel.2012.04.036>
90. Socrates G (2001) Infrared and Raman characteristic group frequencies: tables and charts, 3rd ed. Wiley (2001)

Theoretical Analysis of the Heating Process of the Material Surface by a Laser Pulse with Allow for the Accompanying Factors



L. V. Shmeleva, A. D. Suprun, and S. M. Naumenko

Abstract The paper considers the process of laser heating of different types of surfaces. The research can be useful in various areas of technological applications. The expressions obtained here for the temperature of the near-surface layer take into account a wide range of processes that accompany the interaction of laser radiation with substance. Temperature dependences direct at taking into account at most possible parameters of both the irradiated material and the characteristics of the radiation itself. Laser heating, especially in terms of accurate applications, is a complicated transcendental dependence due to the fact that the coefficients of total dissipative losses depend, in particular, on temperature. They take into account the effects of reflection and scattering and constantly change during the time of action of laser radiation. It is shown that all temperature solutions must be found allow for the given, according to the surface structure, expressions for the loss coefficients. Examples of determining the threshold characteristics of the radiation flux, which separate the destructive and non-destructive processing of the material, are given.

Keywords Loss factor · Temperature · Absorption and reflection coefficient · Laser heating

1 Introduction

Laser radiation makes it possible to obtain the limit values of many parameters, which is realized in the zone of influence [1]. Laser processing is applicable to almost all materials regardless of their hardness and viscosity (metals, hard alloys, ceramics, glass, plastics, rubber, semiconductor materials, precious stones, biological materials). Therefore, the use of laser technology is relevant in many areas: from medicine to the military industry [2–5]. The practical use of powerful lasers takes of high material and energy costs. Therefore, theoretical and numerical forecast of

L. V. Shmeleva (✉) · A. D. Suprun · S. M. Naumenko
Faculty of Physics, Taras Shevchenko National University of Kyiv, Volodymyrska Street, 64/13,
Kyiv 01601, Ukraine
e-mail: lshmel@univ.kiev.ua

the results of laser exposition to various types of materials surface does not lose its relevance [6].

The research is based, first of all, on the developments that allow to calculate the conditions that distinguish between different types of surface treatment [7], namely non-destructive treatment, destructive treatment with surface melting, and destructive treatment without melting. For frequent uses, it is interesting to process without melting the irradiated substance as more exact [8]. The solution of this problem presumes the study of the dynamics of baro- and thermocharacteristics of the surface, which is irradiated until the moment of destruction and tracking of these indicators in the process of destruction [9].

To model the entire irradiation process, a general algorithm for the interaction of radiation with solid has been developed [7–10]. An important fact is that the laser technology of the material processing process is associated with local heating that is with the transfer of energy from the electromagnetic pulse to the substance. When interacting with the surface of the radiation medium, it is partially reflected and partially penetrates into the material, absorbed in it, and quickly converted into heat. The whole process of the heating surface of the substance can be divided into several stages: heating the material without destruction; destruction of the material and the flying-off of the products formed (ablation); cooling after the end of the interaction.

Laser heating can be accompanied by changes in the optical and thermophysical properties of the material, its thermal expansion, as well as phase transitions [7] in the solid state and melting. In some cases, heating can activate diffusion processes in a solid and some chemical reactions on its surface and in the near-surface layer. The stage of heating materials with laser radiation is the main relative to the physical essence of technological operations that are carried out without destruction of the material (heat treatment, diffusion, etc.). For operations of laser processing of materials related to the destruction and removal of some of them, the heating stage is the initial, but important, because its analysis allows to determine the conditions of the beginning of the destruction. Modern research is aimed at achieving controlled heating of irradiated surfaces for the purpose of modify them [11–15]. Therefore, the study of temperature dynamics during laser irradiation of a material is an important part of a comprehensive study of the interaction of radiation with substance.

2 Basic Formulation of the Problem of Laser Heating of the Near-Surface Layer of the Substance

The problem of surface destruction without melting is considered. Until to the destruction, the irradiated material is a substance that exists in the solid state. With the arising of fracture on the surface of the material in the local area exposed to radiation, the substance is ablated. This new substance is formed as a result of a local phase transition. And we will also consider it a continuous plasma-gas medium. If each of the coexisting phases is in itself a continuous medium, then the system

of equations describing them will be common to both media [7]. Such a system is significantly heterogeneous due to the presence of bulk sources and effluents in the gas phase during the solid–gas phase transition. To take them into account, self-consistent (with solutions of the system of equations) functions were introduced: sources of mass runoff and mass density of force acting on the flow of gaseous phase from the radiation side [16]. This system was formulated for the coexistence of two phases: solid and plasma-gas, and the appropriate boundary conditions were obtained for it [7]. The result of the analysis of these boundary conditions was a system of two differential equations that describe the process of crater formation on the surface of a solid and track the dynamics of near-surface pressure that occurs on the surface under the action of radiation:

$$\frac{\partial \Sigma}{\partial \theta} = \Pi^\beta \sqrt{1 + \left(\frac{\partial \Sigma}{\partial x}\right)^2 + \left(\frac{\partial \Sigma}{\partial y}\right)^2}, \tag{1}$$

$$\frac{\partial \Pi}{\partial \theta} = (-1 + \Lambda e_q \vartheta_\tau) \Pi^{\beta+\eta} - \Pi^{\beta+1} + \frac{e_q \vartheta_\tau \Pi^\eta}{\sqrt{1 + \left(\frac{\partial \Sigma}{\partial x}\right)^2 + \left(\frac{\partial \Sigma}{\partial y}\right)^2}}. \tag{2}$$

Here, Π and Σ are, respectively, dimensionless surface pressure and the function of the crater formation, ϑ_τ is the stepwise Heaviside function: $\vartheta_\tau \equiv \vartheta(\tau - \theta)$. The parameter e_q determines the ratio of the flow incident on the surface of the substance q_s to the original flow q_{in} , i.e., in dimensionless units:

$$e_q \equiv q_s/q_{in} = f(x, y) \exp(-\Lambda M \Pi^{\eta+\beta} \Sigma) \tag{3}$$

In (3), function $f(x, y)$ determines the transverse shape of the stimulating impulse and adds to (1) an additional dependence on x, y , M is dimensionless parameter determined by equality $M = \frac{q_0 \gamma^2 L^2}{2\varphi_0^{3/2} \kappa^2 \rho_0 \alpha^{1/2}}$, Λ is parameter that determines the degree of interaction of the substance that evaporates with incident radiation: $\Lambda = \frac{bL\gamma^3 q_{in}}{2\kappa\alpha\varphi_0} h(\omega)$, where κ is polytropic index, $\alpha \equiv \kappa + 1$, $\gamma \equiv \kappa - 1$, $\beta \equiv \alpha/(2\kappa)$, $\eta \equiv 1/\kappa$, φ_0 is specific heat of the condensate-gas phase transition, ρ_0 is the density of the near-surface layer of solid, L is the coefficient of heat loss. $b \equiv \frac{2R_\Gamma m_a^2}{3\pi\sqrt{\pi}\gamma\mu_a d_a^2 k_b}$, R_Γ is gas constant, μ_a is gas molecular weight; d_a is molecule effective diameter; m_a is evaporated matter atom mass, and k_b is Boltzmann constant. The function $h(\omega)$ determines a constant (independent of pressure) part of the absorption coefficient but depends on the frequency characteristics of the gaseous medium.

On the other hand, before the beginning of destruction, when the gas phase is absent and the irradiated surface is stationary, we can use the general equation of thermal conductivity [7]:

$$\rho_0 C_v^{(0)} \frac{\partial T_0}{\partial t} = \text{div}(\lambda_0 \nabla T_0) - \text{div} \mathbf{q}_0 \tag{4}$$

Here, q_0 is the external energy flow in the volume of the solid phase; λ_0 is its thermal conductivity coefficient; T_0 is the temperature of the solid phase, which is a function of time and coordinates; $C_v^{(0)}$ is its mass specific heat (heat capacity per unit mass).

The solution of Eq. (4) must satisfy the boundary condition:

$$\lambda_{0s}(\mathbf{n} \cdot \text{grad } T_{0s}) = (1 - L)\lambda_s(\mathbf{n} \cdot \text{grad } T_s) \quad (5)$$

Here, the index “s” denotes the surface characteristics of the gas phase, the indices “0s” denote the solid-phase index, and \mathbf{n} denotes the normal to the surface. Equation (4) together with the boundary condition (5) makes it possible to trace the temperature changes of the volume of the material during laser heating, as well as the temperature dynamics on the surface (at the interface). At the moment, we are interested in the problem of laser surface heating for a one-dimensional case. It has the form [17]:

$$\rho C_v \frac{\partial T}{\partial t} = \lambda \frac{\partial^2 T}{\partial t^2} - \vartheta_\tau L \frac{\partial q}{\partial z} \quad (6)$$

With corresponding initial and boundary conditions:

$$T(0, z) = T_{\text{in}}, T(t, \infty) = T_{\text{in}} \frac{\partial T}{\partial z}(t, 0) = -\frac{L_d}{\lambda} \vartheta_\tau q_s \quad (7)$$

As already noted, the parameters with the index “0” determine the parameters of the solid irradiated phase. Since there are only them in Eq. (6), we discarded the index “0” to avoid the cumbersomeness of the records. In Eq. (6) and boundary conditions (7), $T = T(t, z)$ is the temperature of the material, τ is the time of action of the laser pulse on the surface, $\vartheta_\tau \equiv \vartheta(\tau - t)$ is the stepwise Heaviside function, which is equal to one when $t < \tau$ and is equal to zero when $t > \tau$ the action of radiation ceases, q_s is the flux density of radiation energy (hereinafter, flux) in the middle of the solid phase, q_{in} is the input value of flux, λ is the thermal conductivity of the material, ρ is its density, C_v is the mass specific heat, T_{in} is the initial temperature of the material, and L_d is the coefficient of optical losses.

In the study, we introduced two parameters of losses, because on the surface of the irradiated substance, there are losses not only thermal (loss factor L), but also optical (loss factor L_d). Both coefficients vary in the range from 0 to 1. The zero value of the coefficients means the complete absence of corresponding losses: The luminous flux, in this case, does not suffer losses when passing through the surface of the material. In other words, the surface of the substance is transparent to radiation. And the value of these coefficients, equal to 1, corresponds to the complete loss of flow at the boundary. In particular, the condition $L_d \rightarrow 1$ corresponds to the situation when metals and opaque materials are irradiated. It is clear that both of these coefficients should not really take extreme values. That is, the condition $0 < \{L_d, L\} < 1$ must always be satisfied for them. In [18], it was proved that with a high degree of accuracy, especially for metals, the relation: $L = 1 - L_d$.

3 Changes of the Temperature of the Surface Local Area Caused by Laser Influence

The absorption coefficient of many materials, particularly metals, in a good approximation can be considered infinitely large. But conditions can be realized under which the absorption coefficient in the volume is not only a finite value but also a function of the magnitude of the radiation flux q , i.e., $k = k(q)$. This is the case when it comes to irradiating semiconductors and dielectrics that are sufficiently transparent for a given frequency range with intense radiation in the visible and near ranges. Also, when metals are irradiated of intense radiation of the far ultraviolet and soft X-ray ranges. In this case, the dependence of the radiation flux q on the depth of its penetration z into the material is determined by Bouguer’s law.

As a result of the solution of the system (6), (7), it is possible to obtain a general solution of the temperature dynamics of the surface in the local region of laser heating. In the approximation of the unlimited absorption coefficient peculiar to metals, laser heating can be described by the dependence [17]:

$$T(t) = T_{in} + \frac{2q_s L_d}{\sqrt{\pi \lambda \rho C_v}} \sqrt{t} \tag{8}$$

That is, in this approximation, the temperature increases in proportion to the factor $q_s L_d \sqrt{t}$. When the surface layer of the irradiated material is almost transparent to radiation ($L_d \rightarrow 0$), the heating will be insignificant, and the material with high absorbency will heat up quickly. The nature of the coefficient L_d is tied to the optical characteristics of the radiation. And we assume that all optical losses are determined by the reflection coefficient and the processes of scattering of the radiation flux on the surface. If the surface is smooth, then scattering can be neglected. Then, L_d can be considered proportional only to the reflection coefficient R , and it, for one’s turn, varies depending on the temperature [19], i.e., $L_d(T) \sim R(T)$. The reflection coefficient R from the surfaces of conductive media, in particular from metal surfaces, for radiation in the optical and infrared ranges is determined mainly by the excitation of plasma oscillations. Given this, the dynamics of surface temperature T and the coefficient L_d are determined by a system of two equations [18]:

$$L_d(T) = R_{in} - \frac{\sqrt{\rho N_A} e}{\sigma_{el} \sqrt{\pi \mu m_e}} \ln\left(\frac{T}{T_{in}}\right) \tag{9}$$

$$\frac{T}{T_{in}} = 1 + L_d(T) \frac{2q_s \sqrt{t_0}}{T_{in} \sqrt{\pi \lambda \rho C_v}} \sqrt{t} \tag{10}$$

Here, the notation is introduced: t_0 is a parameter that normalizes the time to the dimensionless form: $t_0 = b\gamma^4 \varphi_0 / (\alpha^2 \kappa^{5/2} q_{in})$, R_{in} is the basic value of the reflection coefficient, t is the dimensionless time normalized to the value of t_0 , e is the charge of the electron, N_A is the Avogadro’s number, and σ_{el} is the electrical conductivity.

These two equations represent a single system, and only a general numerical solution can clarify the picture of the development of laser surface heating. For example, a numerical analysis of these two equations was performed for silver in [18]. In [19], on the example of gold, it was proved that taking into account the dependence of the reflection coefficient on the electron temperature significantly have an influence on the results of calculations of the energy absorbed by the material. It is well known that the reflection coefficient depends on the surface properties, temperature, and type of material. As a rule, smooth, polished surfaces have a higher reflectivity than rough, matte surfaces made of the same material.

While the surface is only heated, the scattering losses make a smaller contribution than the reflection losses. At this time, scattering is associated with stationary surface inhomogeneities (surface roughness). However, they should be allowing for, because they also depend on temperature and increase with increasing inhomogeneities. In addition, in some materials with lower reflection losses, the scattering losses may be of the order of optical.

During laser heating, the surface losses of scattering radiation can be considered in the model of hemispherical inhomogeneities of radius a , and they are determined by the following dimensionless factor [18]:

$$\sigma_r(a, T) = \frac{5\pi a^4 \omega^4}{12c^4} \left(1 + \frac{\pi^4}{400} \cdot \frac{e^4 N_A^2}{c^4 m_e^2} \cdot \frac{a^4 \rho^2}{\mu^2} \cdot \frac{1}{1 + (k_B T / \hbar \omega)^2} \right), \quad (11)$$

which can be directly used in the loss factor L_d . The definition (11) additionally includes the radiation frequency, the Planck constant, and the speed of light. As a result, we can write a new definition of the coefficient $L_d(T)$ [18]:

$$L_d(a, T) = R_{in} - \frac{e}{\sigma_{el}} \cdot \sqrt{\frac{\rho N_A}{\pi \mu m_e}} \cdot \ln\left(\frac{T}{T_0}\right) + \frac{5\pi a^4 \omega^4}{12c^4} \left(1 + \frac{\pi^4}{400} \cdot \frac{e^4 N_A^2}{c^4 m_e^2} \cdot \frac{a^4 \rho^2}{\mu^2} \cdot \frac{1}{1 + (k_B T / \hbar \omega)^2} \right). \quad (12)$$

As can be seen from the definition (11), besides to the temperature dependence T , the optical loss coefficient L_d has a perceptible dependence on the radius of inhomogeneity a . Thus, it is possible to estimate $L_d(a, T)$ for any rough surfaces of materials.

Often, at the expense of surface modification, try to get quicker heating of the surface under the action of radiation [11]. Sometimes, it is important to select a material that can heat up and at the same time, not collapse [20, 21]. Therefore, expedient to determine the critical parameters at which non-destructive processing of the material is finished, and the destruction of the material begins.

After analyzing the dependence (8), we can see that the maximum value of the surface temperature will be reached when the action of radiation ceases that is at $t = \tau$, where τ is the time of action of the laser pulse. Therefore:

$$T_{\max}(q_s) = T_{\text{in}} + \frac{2q_s L_d}{\sqrt{\pi \lambda} > C_v} \sqrt{\tau} \quad (13)$$

We assume that the maximum temperature $T_{\max}(q_s)$ at the moment finishing of the action of the radiation reaches the phase PVT-diagram of the phase interface. The critical surface temperature T_{cr} depends on the thermodynamic parameters. In particular, according to the relation: $Q = P/c$, where c is the speed of light, P is the electromagnetic pressure of radiation, P is proportional to the flux Q . Then from the condition $T_{\max}(q_s) = T_{\text{cr}}(Q)$, we can determine the threshold flux Q for no destruction. It is obvious that here $T_{\text{cr}}(Q)$ is the critical temperature, which depends on the intensity of the flow Q . Taking into account the relation (13), we obtain the threshold condition [17]:

$$Q^2 \tau = \frac{\pi \lambda Q C_v}{4L_d^2} (T_{\text{cr}}(Q) - T_{\text{in}}).$$

As long as the radiation flux satisfies the condition $q_s < Q$, the surface of the irradiated material is not destroyed. Thus, the threshold value of the flow Q at which the surface of the material begins to destroyed with the considered infinite value of the constant absorption coefficient has the form:

$$Q = \frac{\sqrt{\pi \lambda Q C_v}}{2L_d \sqrt{\tau}} (T_{\text{cr}}(Q) - T_{\text{in}}), \quad (14)$$

where L_d is denoted in (9) for smooth mirror surfaces, or expression (12) for rough surfaces, or surfaces with foreign hemispherical inclusions.

The above results are applicable to materials whose thickness is bigger than the depth of penetration of electromagnetic waves. For real conductors such as silver, copper, gold, and aluminum, this depth is very small. For example, for gold at a depth of 400–850 nm, the degree of transparency for wavelengths bigger than 500 nm varies from 20 to 10% [22].

4 Laser Heating of Films

It is known that thin layers of precious metals are often used for plasmon resonance sensors [23, 24]: silver, gold, etc. Various coverings for these materials are also being tested. If the radiation flux is directed into a thin layer (film) of material, then there is an additional need to take into account the thickness of the layer, or at least take into account the finiteness of the absorption coefficient. In this case, the change in the temperature of the surface layer during laser heating will be determined by the ratio [17]:

$$T_k(t) = T_{in} + \frac{q_s}{\lambda k_0} \left\{ \frac{\sqrt{\chi t}}{\sqrt{\pi}} + (1 - L_d) \left[\exp\left(\frac{\chi t}{4}\right) \operatorname{erfc}\left(\frac{\sqrt{\chi t}}{2}\right) - 1 \right] \right\}, \quad (15)$$

were $\chi \equiv 4k_0^2\lambda/(\rho C_v)$, and $T_k(t)$ is the temperature of laser heating at a finiteness of the absorption coefficient of radiation by the film. In this case, the use of the definitions of the parameter L_d from (9) or (12) makes the search for temperature $T_k(t)$ a transcendental problem, because in both cases, L_d is a function of temperature. But their use will allow you to more accurately determine of the laser heating magnitude of the film.

Let us analyze the dependence (15). To do this, we use the approximation of the maximum optical losses during the passage of the surface by radiation: $L_d \rightarrow 1$ (note that the condition $L_d \rightarrow 1$ is equivalent to the condition $k_0 \rightarrow \infty$). Then, the speed of heat loss $L = 1 - L_d$ is zero, the third term disappears, and (15) is automatically reduced to (8).

If we apply another limit case, assume that the surface completely transmits radiation ($L_d \rightarrow 0$), then (15) is reduced to the expression $T_k(t) = T_{in} + \frac{q_s}{\lambda k_0} \left\{ \frac{\sqrt{\chi t}}{\sqrt{\pi}} + \exp\left(\frac{\chi t}{4}\right) \operatorname{erfc}\left(\frac{\sqrt{\chi t}}{2}\right) - 1 \right\}$. Given the asymptotic approximation near zero $\exp\left(\frac{\chi t}{4}\right) \operatorname{erfc}\left(\frac{\sqrt{\chi t}}{2}\right) \rightarrow 1 - \frac{\sqrt{\chi t}}{\sqrt{\pi}}$. In this case, $T_k(t) = T_{in}$. Both extreme cases confirm the validity of the expression (15). For this case (15), the magnitude of the threshold radiation flux will be determined by the equality:

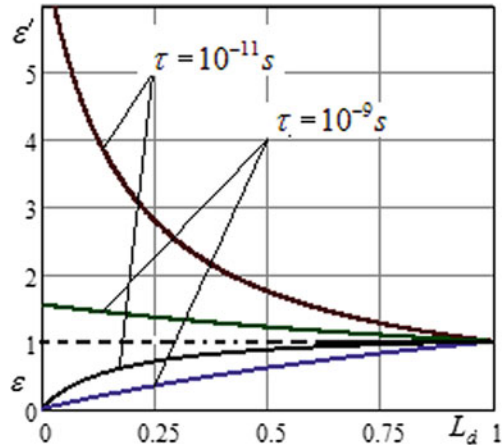
$$Q_k = \frac{\lambda k_0 \sqrt{\pi}}{\sqrt{\pi}(1 - L_d) \left[\exp\left(\frac{\chi t}{4}\right) \operatorname{erfc}\left(\frac{\sqrt{\chi t}}{2}\right) - 1 \right] + \sqrt{\chi t}} (T_{cr}(Q_k) - T_{in}), \quad (16)$$

The ratio of the flow thresholds for a constant coefficient Q_k to the flow threshold (14) at an infinite absorption coefficient (or $L_d \rightarrow 1$): $\varepsilon' \equiv Q_k/Q_\infty$ and to the flow threshold for a small absorption coefficient ($k_0 \rightarrow 0$) under the condition $L_d \rightarrow 0$: $\varepsilon \equiv Q_k/Q_0$ was analyzed earlier [17]. They were analyzed for arbitrary values of L_d with conservation the asymptotics of k_0 . The results of this analysis are reproduced in Fig. 1.

In Fig. 1, the two lower curves correspond to the relation ε , and the two upper curves correspond to the relation ε' . The graphs show their dependences on the coefficient of optical dissipative surface losses L_d for different durations of stimulating laser radiation. Estimates were performed for silicon parameters. The analysis of the results shows that both approximations (infinite and zero volumetric absorption coefficients) give errors with relatively to the case of taking into account the finite absorption coefficient (on the graph—corresponds to the dotted line $\varepsilon = 1$). These mistakes are the least only for materials with large of surface losses ($L_d \rightarrow 1$). As the coefficient of optical dissipative losses decreases, the mistakes in determining the threshold of thermal destruction in the approximation (16) increase.

This is evidence of that the use of the expression for the finite absorption coefficient (15) is more accurate when assessing laser heating. And taking into account the dependence of the coefficient L_d on temperature (9) for smooth mirror surfaces, or

Fig. 1 Dependence of the ratio of thresholds values ε' and ε on the coefficient of total optical dissipative losses



(12) for rough surfaces or surfaces with spherical foreign inclusions give accurate forecast of laser surface heating.

If the action of laser radiation is short-term or low-power and condition, (16) is not realized, then the destruction of the surface does not occur. When, at that, the action of the laser pulse stops, the material heated by the laser begins to refrigerate [25] according to the equation:

$$T_k(t) = T_{in} + \frac{q_s}{\lambda k_0} \frac{\sqrt{\chi t}}{\sqrt{\pi}} (\sqrt{t} - \sqrt{t - \tau}) + \frac{Lq_s}{\lambda k_0} \exp\left(\frac{\chi t}{4}\right) \left(\operatorname{erfc}\left(\frac{\sqrt{\chi t}}{2}\right) - \exp\left(-\frac{\chi \tau}{4}\right) \operatorname{erfc}\left(\frac{\sqrt{\chi(t - \tau)}}{2}\right) \right) \quad (17)$$

Equation (17) determines the dynamics of surface cooling after cessation of laser exposure. In the approximation of the infinite absorption coefficient, Eq. (17) is simplified to the form $T(t) = T_{in} + \frac{2q_s L_d}{\sqrt{\pi} \lambda \rho C_v} (\sqrt{t} - \sqrt{t - \tau})$ and of course, has a descending root dependence. Such temperature dynamics is physically logical, but when using accurate technologies, it is necessary to carry out a more detailed analysis of heating. Therefore, to calculate the temperature cooling of the surface, it is still necessary to take into account the specified form of the parameter $L = 1 - L_d$, where L_d should be represented by expressions (9), or (12).

5 Destruction of the Surface Without Melting, with Account for Temperature Effects

If condition (16) is realized, then the surface of the material begins to destruction. If the criterion of destruction without the formation of a liquid phase is realized [7],

then the system of differential equations (1), (2) requires some transformations. In these equations, the temperature is not explicit. There is pressure in it. Therefore, to improve the algorithm (1), (2), it will be appropriate to select the parameters L and L_d and replace the temperature in them with pressure, using the thermodynamic equation of state [18].

6 Conclusions

The process of laser surface heating is considered in the paper. To do this, on the basis of general basic presentations, a system of equations was formulated that characterizes the changes in the parameters of substance under the action of laser irradiation. One of the equations is the equation of thermal conductivity. It makes it possible to trace temperature changes during the preliminary (before the destruction) laser heating.

In this article, attention was giving to thermal effects, so the one-dimensional equation of thermal conductivity was considered. The solution to this equation is a bulky and complex expression. Therefore, it has been presented in several technological approximations. For series of technological applications, we have considered cases of materials with strong absorbency and for materials that almost do not absorb laser radiation. In particular, for films, the expression for the temperature with a finite absorption coefficient was obtained. The peculiarity of these solutions is that they include new, previously ignored, parameters L and L_d . Both parameters describe the losses during the passage of radiation the surface of the material. The first (L) describes heat loss, and the second (L_d) is optical.

These parameters are not constant values, as they depend on the reflection and scattering coefficients of radiation from the surface. And those, in turn, vary depending on the temperature. Therefore, all temperature solutions should be considered in combination with expression (9), if you want to investigate the effect of radiation on a smooth (mirror) surface, or with expression (12), if the surface being irradiated has irregularities or foreign inclusion. Examples of determining the thresholds at which the irradiated surface begins to destruction are given.

References

1. Afanasieva OV, Lalazarova NO, Fedorenko E.P. (2020) Laser surface treatment of materials. Monograph. Kharkiv, 100 p. ISBN 978-617-7859-35-1. (in Ukraine)
2. Goswami D (2019) Lasers and their applications. Indian Institute of Technology Kanpur, Kanpur, March India, Chapter 7, pp 79–95. https://www.iitk.ac.in/stc/Publications/DGoswami/linked_Chapter_07.pdf
3. Joe DJ et al (2017) Laser–material interactions for flexible applications. Adv Mater 29(26). <https://doi.org/10.1002/adma.201606586>

4. Zhang J et al (2018) Laser processing transparent materials with nanosecond, picosecond and femtosecond pulses for industrial applications. In: Laser applications in microelectronic and optoelectronic manufacturing (LAMOM) XXIII, vol 10519. International Society for Optics and Photonics, p 105190Y. <https://doi.org/10.1117/12.2291511>
5. Chowdhury IH, Xu X (2003) Heat transfer in femtosecond laser processing of metal. *Numer Heat Transf Part A Appl Int J Comput Methodol* 44(3):219–232. <https://doi.org/10.1080/716100504>
6. Cocean I et al (2019) Alpha keratin amino acids BEHAVIOR under high FLUENCE laser interaction. *Med Appl Appl Surface Sci* 488:418–426. ISSN 0169-4332. <https://doi.org/10.1016/j.apsusc.2019.05.207>
7. Shmeleva LV, Suprun AD, Yezhov SM, Datsyuk VV (2021) Specificity of boundary conditions for laser-stimulated destructive surface treatment without melting, vol 246. *Springer Proceedings in Physics*, pp 289–301. Chapter 23. https://link.springer.com/chapter/10.1007%2F978-3-030-51905-6_23
8. Çelik O et al (2021) Deconsolidation of thermoplastic prepreg tapes during rapid laser heating. *Compos Part A Appl Sci Manuf* 149:106575. <https://doi.org/10.1016/j.compositesa.2021.106575>
9. Shmeleva LV, Suprun AD, Yezhov SM (2019) Simulation of the formation of a surface nanocrater under the action of high-power pulsed radiation. Chapter 34 in “nanocomposites, nanostructures, and their applications”, vol 221. *Springer Proceedings in Physics*, pp 505–515. https://doi.org/10.1007/978%2D3%2D030%2D17759%2D1_34
10. Shmeleva LV, Suprun AD, Yezhov SM, Datsyuk VV (2021) Influence of changes in the phase state of the surface and external factors of laser irradiation on the nanocraters formation, vol 263. *Springer Proceedings in Physics*. Springer, Cham, pp 223–233. https://doi.org/10.1007/978-3-030-74741-1_15
11. Zaifuddin Q et al (2021) Enhancement of laser heating process by laser surface modification on Titanium alloy. *J Mech Eng Sci (JMES)* 15(3):8310–8318. <https://doi.org/10.15282/jmes.15.3.2021.09.0653>
12. Dutta J, Kundu B, Biswas R (2021) Analytical model for ultrashort pulse laser heating in a titanium nanofilm by implementing dual-phase-lag theory in mathematical analysis. *J Therm Anal Calorim*. <https://doi.org/10.1007/s10973-021-11044-2>
13. Yong J et al (2020) Designing “supermetallophobic” surfaces that greatly repel liquid metal by femtosecond laser processing: does the surface chemistry or microstructure play a crucial role? *Adv Mater Interfaces* 7:1901931. <https://doi.org/10.1002/admi.201901931>
14. E. Stratakis et al (2020) Laser engineering of biomimetic surfaces. *Mater Sci Eng R Rep* 141:100562. <https://doi.org/10.1016/j.mser.2020.100562>
15. Jalil SA, Lai B, ElKabbash M et al (2020) Spectral absorption control of femtosecond laser-treated metals and application in solar-thermal devices. *Light Sci Appl* 9:14. <https://doi.org/10.1038/s41377-020-0242-y>
16. Alekseev BV (1982) *Mathematical kinetics of reacting gases*. Nauka, Moscow. 419 p. (in Russian). https://scholar.google.com.ua/scholar?hl=ru&as_sdt=0%2C5&q=Alekseev+B.+V.+Mathematical+Kinetics+of+Reacting+Gases.+Nauka%2C+Moscow%2C+1982&btnG
17. Suprun AD, Shmeleva LV, Razumova MA (2011) The influence of bulk absorption of substance on the threshold of destruction by the intensive pulse of electromagnetic radiation. *Functional Mater* 18(2):237–243. <http://functmaterials.org.ua/contents/18-2/fm182-16.pdf>
18. Shmeleva LV, Suprun AD, Yezhov SM, Datsyuk VV (2021) Temperature dependence of the loss coefficients during the formation of surface laser-stimulated nanostructures. *Appl Nanosci*. <https://link.springer.com/article/10.1007%2Fs13204-021-01711-z>
19. Lizunov SA, Zhukov VP, Bulgakov AV, Bulgakova NM (2021) Numerical study of the dynamics of gold heating by ultrashort dichromatic pulses of laser radiation. *Siberian Phys J* 16(1):5–20. (in Russian). <https://doi.org/10.25205/2541-9447-2021-16-1-5-20>, <https://nguphys.elpub.ru/jour/article/view/144/122>
20. Luo C, Jiao T, Tang Y, Kong J (2018) Excellent electromagnetic wave absorption of iron-containing SiBCN ceramics at 1158 K high-temperature. *Adv Eng Mater* 20(6). <https://doi.org/10.1002/adem.201701168>

21. Yang Z, Bauereiß A, Markl M, Körner C (2021) Modeling laser beam absorption of metal alloys at high temperatures for selective laser melting. *Adv Eng Mater* 23:2100137. <https://doi.org/10.1002/adem.202100137>
22. Ushakov NM, Vasilkov MY, Fedorov FS (2017) Influence of a thin film of gold on the optical spectral characteristics of the porous membrane of anodic alumina. *Lett J Tech Phys* 43(14):26–33
23. Makarenko OV, Yampolskiy AL et al (2019) Mueller polarimetry of discontinuous gold films. *Semicond Phys Quantum Electron Optoelectron* 22(3):338–342. ISSN 1560-803. <https://doi.org/10.15407/spqeo22.03.338>
24. Poperenko LV, Yampolskiy AL, Makarenko OV, Zavalistyi OI (2019) Optimization of optical parameters of metal—dielectric heterostructures for plasmonics sensor formation. *Metallofizika i Noveishie Tekhnologii* 41(6):751–764. <https://doi.org/10.15407/mfint.41.06.0751>
25. Chepak-Gizbrekht M, Knyazeva A (2020) Temperature evolution in a two-layer material with the alteration of optical properties during laser processing. *AIP Conf Proc* 2310:020057. <https://doi.org/10.1063/5.0034175>

Dielectric Behavior of Solid Polymer Electrolyte Films Formed by Double Hydrophilic Block Copolymers



L. Kunitskaya, T. Zheltonozhskaya, S. Nesin, Valeriy Klepko,
and N. Minenko

Abstract Polymer electrolyte membranes (PEM) based on diblock copolymer poly(ethylene oxide)/polyacrylamide MePEO-*b*-PAAm (DBC), its partially hydrolyzed derivative MePEO-*b*-P(AAm-*co*-AAc) (DBC_{hydr}) and graft copolymer polyvinyl alcohol/polyacrylamide (PVA-*g*-PAAm), that form intramolecular poly-complexes, have been prepared by using solution casting technique. The ionic conductivity of PEM systems comprising mentioned copolymers in their pure form and in compositions with LiPF₆ were measured at the ambient temperature and humidity. It was noticed that introduction of additional ionic groups -COOH in polyacrylamide block of DBC affected positively the conductive characteristics of the polymer membranes. The ionic conductivity of the membranes filled with LiPF₆ increased with the growth of the Li-salt content. The reason for the application of DBCs and PVA-*g*-PAAm as possible ion-conducting membranes for Li-ion batteries, solar cells, and fuel cells are discussed.

Keywords Solid polymer electrolytes · Block copolymer · Ionic conductivity · Intramolecular polycomplexes

1 Introduction

Recently, much attention has been paid to the development of alternative energy sources, like dye sensitized solar cells (DSSC), solid proton exchange membrane fuel cells (PEMFC), rechargeable solid-state lithium batteries (LB), etc. [1–7]. All the above cells work on a common principle, i.e., mobility of ions between two electrodes through a suitable electrolyte. For these devices a non-corrosive, high conductive, electrochemically, and chemically stable, low cost electrolyte is very important. The solid solvent-free polymer electrolytes (SPEs) based on amorphous polymer materials could be the best for these purposes.

L. Kunitskaya (✉) · T. Zheltonozhskaya · S. Nesin · V. Klepko · N. Minenko
Institute of Macromolecular Chemistry of the NAS of Ukraine, 48 Kharkiv's'ke Shosse St,
Kyiv 02160, Ukraine
e-mail: Larisa_kunitskaya@ukr.net

Polyvinyl alcohol (PVA) and its derivatives are considered to be quite attractive materials for fuel cell membranes in terms of mechanical properties and high chemical stability [8–14]. PVA was examined as a proton exchange membrane in proton conductivity and methanol permeability experiments. The result indicated that PVA membranes employed in pre-evaporation process were much better methanol barriers than Nafion[®] due to their dense molecular packing structure caused by inter and intramolecular hydrogen bonding. A drawback of PVA membranes is the absence of negatively charged ions, and thus, it is a poor proton conductor when compared to the commercially available Nafion[®] membranes [14].

Currently, a wide range of polymer electrolytes and composite materials are offered to be perspective SPEs, but the most attractive and widely studied among them are polymer matrixes based on polyethylene oxide (PEO), which are now used in Li-batteries and solar cells due to good chain flexibility, superior electrochemical stability to lithium metal, low glass transition temperature, and excellent solubility to conductive lithium salts and good interface stability against Li anode [15–21]. In PEO, the repeating unit ($-\text{CH}_2-\text{CH}_2-\text{O}-$) presents a favorable arrangement for effective interaction of the free electron pair on the oxygen with the alkali metal cations. This occurs because the PEO chains are arranged in a helical conformation with a cavity that presents ideal distances for oxygen-cation interactions. However, high crystallinity of PEO leads to low ion conductivity and inferior Li^+ transference numbers (0.2–0.3) at room temperature, which affects the high rate capability of LBs. Numerous approaches have been carried out to improve electrochemical properties of PEO, such as blending [22, 23], copolymerization [24, 25], and crosslinking [26–28]. Among these strategies, preparing copolymers, especially graft and block copolymers, can decrease the crystallinity of a PEO-based solid electrolyte system effectively. The largest decrease in the crystallinity degree was observed in the triblock copolymers comprising central block PEO and two side amorphous blocks [29]. Another way to reduce PEO crystallization in PEO-based SPEs is to use intermolecular polycomplexes (InterPCs) which are formed due to cooperative hydrogen bonds between PEO and proton-donor polymers [30]. The amorphous structure of such InterPCs and their high ability to bind ions, organic compounds, and colloidal particles are well known [31]. Meanwhile, the tendency to decompose into individual components under the influence of external factors or strong competitors that destroy the system of hydrogen bonds, reduce the formation and operation of multicomponent solid electrolytes based on InterPCs. From this viewpoint, PEO-based intramolecular polycomplexes (IntraPCs) are more promising since they combine properties of both the block-type copolymers and InterPCs due to cooperative H-bonds systems between their components. They demonstrate higher stability in competitive processes which accompany the formation of multicomponent polymer electrolytes.

Previously, we have found that macromolecules of diblock copolymers formed by poly(ethylene glycol) monomethyl ether (MePEG) and polyacrylamide (PAAm) exist as intramolecular polycomplexes (IntraPC) due to the interaction of polymer components [32]. Careful study of the block structure of MePEO-*b*-PAAm diblock copolymers has shown that the formation of IntraPC leads to the destruction of the

crystal structure of PEO chains and, as a consequence, ensures the existence of a homogeneous amorphous structure. It was found that the grafted copolymers of polyvinyl alcohol and polyacrylamide PVA-*g*-PAAm also exist as IntraPCs, formed by hydrogen bonds of the base-graft type and stabilized by H-bonds of graft-graft [29].

The above facts have become decisive for the development and research the PEO- and PVA-containing IntraPCs in terms of their ionic conductivity in relation to their structure. In the present work, we investigated graft copolymer polyvinyl alcohol/polyacrylamide (PVA-*g*-PAAm), diblock copolymer polyethylene oxide/polyacrylamide MePEO-*b*-PAAm (DBC), and its partially hydrolyzed derivative polyethylene oxide/poly (acrylamide-*co*-acrylic acid) MePEO-*b*-P(AAm-*co*-AAc) (DBC_{hydr}) as possible ion-conducting membranes for LBs, DSSC, and PEFCs. We also determined the influence of LiPF₆ on the conductive characteristics of copolymer membranes and estimate the possibility of increasing conductivity by introducing additional ionic groups –COOH into PAAm chains.

2 Experimental

2.1 General Procedure for Block Copolymerization

In DBC syntheses, monomethyl ether of poly(ethylene glycol) (MePEG), cerium (IV) ammonium nitrate, and acrylamide (AAm) was used. Cerium (IV) ammonium nitrate and MePEG (Mn = 5 kDa) were purchased from Aldrich (USA) and used as received. AAm was purchased from Merck (Germany) and twice re-crystallized from chloroform before used. The reaction was carried out in deionized water by the radical block copolymerization with participation of MePEO radicals which were formed due to redox reaction between terminal hydroxyl groups and Ce^{IV} ions at $T = 20$ °C in argon atmosphere according to the technique describe in our previous papers [33]. The chemical structure of the copolymers and the number-average molecular weights of PAAm blocks were determined from ¹H NMR spectra, which were recorded in D₂O at $C = 1$ kg·m⁻³ and a room temperature using a Bruker ARX 400 spectrometer operating at 400 MHz. The chemical shifts (δ) were measured relatively to tetramethylsilane as a standard.

2.2 Partial Hydrolysis of Polyacrylamide Blocks

The partially hydrolyzed diblock copolymer (DBC_{hydr}) was obtained from DBC sample by the alkaline hydrolysis reaction of acrylamide units. DBC solution in the deionized water of $C_{\text{DBC}} = 10$ kg m⁻³ concentration was stirred in the presence of NaOH ($C_{\text{NaOH}} = 5$ mol·dm⁻³) at $T = 50$ °C for 20 min. The Na⁺-form of the

Table 1 Molecular parameters of the diblock copolymers

Copolymer	$M_{n\text{PEO}}$, kDa	$M_{n\text{PAAm}}$, kDa	$M_{n\text{DBC/DBC hydr}}$, kDa ^a	W_{PEO} , wt% ^b
DBC	5	241.08	246.08	0.202
DBC _{hydr}	5	196.48	247.71	0.201

^a The molecular weight of the copolymer was calculated by equation $M_{n\text{DBC}} = M_{n\text{PEO}} + M_{n\text{PAAm}}$

^b The weight fraction of PEO in the copolymer

modified diblock copolymer was transformed into H-form by treating with 0.5 N HCl to pH ~ 2. The gel-like DBC_{hydr} was re-precipitated by acetone, dissolved in water and freeze-dried. The hydrolysis degree of acrylamide units in the modified copolymer was determined by potentiometric titration and reached 18.5 mol%. The molecular characteristics both initial and modified diblock copolymers are presented in Table 1.

2.3 Potentiometric Titration Procedure

The potentiometric titration of aqueous solutions of the initial and modified copolymer ($C = 2 \text{ kg m}^{-3}$) was performed with 0.2 N NaOH in an argon atmosphere at $T = 25 \pm 0.1 \text{ }^\circ\text{C}$ using a 1–160 M ionomer (Belarus), calibrated with five standard buffer solutions.

The accuracy of pH measurements was 0.02 units. Potentiometric titration of a copolymer-free deionized water was carried out under the same experimental conditions. The hydroxyl-ion absorption value, $\sigma_{\text{OH}^-} = f(\text{pH})$, was calculated from the titration data using the Eq. (1)

$$\sigma_{\text{OH}^-} = \frac{C_0}{g} (1 - 10^{\text{pH} - \text{pH}_0}) \quad (1)$$

where σ_{OH^-} —the value of OH^- -ions absorption, C_0 is the titrant's concentration (mg-eq m^{-3}), g —copolymer content in 100 cm^3 of solution, and pH and pH_0 —the negative logarithms of the concentration of OH^- -ions in the copolymer solution and solvent, respectively. The limit value of the hydroxyl-ion absorption (σ_{lim}) corresponded to the quantity of carboxyl groups in the polymer sample, which was achieved at $\text{pH} = 8.5\text{--}9.0$. The hydrolysis degree was calculated according to the (2) relation

$$A = \frac{\sigma_{\text{lim}} \times 10^{-3}}{\frac{w'_{\text{PAAm}}}{71} + \sigma_{\text{lim}} \times 10^{-3}} \cdot 100\% \quad (2)$$

where w'_{PAAm} is the weight fraction of PAAm chains in the modified DBC_{hydr} sample.

2.4 General Procedure for Graft Copolymerization

The graft copolymer PVA-g-PAAm has been prepared by the radical graft polymerization of PAAm from the PVA chains using cerium (IV) ammonium nitrate according to the method described earlier [34]. The reaction mixture was stirred in deionized water and an inert atmosphere at 20 °C for 24 h. The synthesized sample was reprecipitated by acetone, then dissolved in the deionized water and freeze-dried. The molecular weight of PVA-g-PAAm, as well as the number and length of grafts, was found by viscosimetry, elemental analysis, and differential thermogravimetric analysis (DTGA). To determine the molecular weight of grafts, the method of selective oxidation of the main chain under the action of concentrated HNO₃ was used. As a result, PVA is oxidized to oxalic acid, and PAAm is hydrolyzed to polyacrylic acid (PAAc) without changing of the polymerization degree. The low molecular weight reaction products were separated by dialysis against deionized water for two weeks. The molecular weight of the formed PAAc was determined by viscosimetry in 0.2M NaCl solution at $T = 20$ °C and was calculated based on the value of the reduced viscosity by the Eq. (3)

$$[\eta] = 1.4 \times 10^{-5} \cdot M_v^{0.78} \quad (3)$$

The number of grafted chains N was calculated using (4) formula

$$N = n_{\text{PAAm}}/n_{\text{PVA}}, \quad (4)$$

where n_{PAAm} and n_{PVA} the moles number of respective polymer components equations. The molecular weight of PVA-g-PAAm was found in accordance to (5) relation

$$M_{\text{PVA-PAAm}} = M_{\text{PVA}} + N \cdot M_{\text{PAAm}} \quad (5)$$

The molecular characteristics of PVA-g-PAAm are presented in Table 2.

Table 2 Molecular parameters of the graft copolymer

Copolymer	$M_{w_{\text{PVA}}}$ (kDa)	$w_{\text{PAAm}},^a$ (wt%)	$w_{\text{H}_2\text{O}},^b$ (wt%)	$w_{\text{PVA}},^c$ (wt%)	$M_{w_{\text{PAAm}}},^d$ (kDa)	N
PVA-g-PAAm	90	85.9	13.4	0.69	366	31

^a The weight fraction of PAAm, determined by elemental analysis

^b The weight fraction of H₂O determined by DTGA

^c The weight fraction of PVA calculated by equation $W_{\text{PVA}} = 1 - W_{\text{PAAm}} - w_{\text{H}_2\text{O}}$

^d The weight of grafts

2.5 The Ionic Conductivity Measurement

In order to prepare polymer electrolyte film, initial and modified DBC samples were dissolved in deionized water and stirred carefully for 24 h to achieve a homogenous mixture. The solutions were cast on polystyrene Petri dishes with a diameter 25 mm and allowed them dried completely at room temperature until a film was obtained. The samples were stored in desiccator for further use.

The measurements of dielectric characteristics of the obtained films were performed in the frequency range 10^2 – 10^5 Hz using a dielectric spectroscope developed on the basis of the alternative current bridge of P5083 and a three-electrode cell. The sample temperature was controlled by a chromel-kopel thermocouple fed through a hole in the shielded electrode. After stabilization of the temperature (10–15 min), the values of the tangents of the loss angles ($\text{tg}\delta$) and capacitances of the capacitor (C) in the operating frequency range were recorded. The capacity of empty cell C_o was calculated by Eq. (6)

$$C_o = S\varepsilon_o/d, \quad (6)$$

where $\varepsilon_o = 8.85 \times 10^{-14}$ (electric constant), S —surface area of the film, and d —film thickness. The response of the material to the applied voltage (or current) was characterized with the tangent of the flow angles $\text{tg}\delta$, the real part of the complex permittivity ε' and the real part of the complex conductivity σ' at a frequency 1 kHz for all samples.

3 Results and Discussion

Polymer electrolyte membranes of DBC, DBC_{hydr}, and PVA-*g*-PAAm were prepared by using solution casting technique and their conductivity σ' was evaluated at the ambient temperature and humidity. As can be seen from the plots in Fig. 1a, even carefully dried films are able to conduct current. Obviously, it can be explained by a sufficiently high affinity of mentioned copolymers for water. Another reason is that PEO chains lose their ability of crystallizing because of the interaction with PAAm ones [35]. This increases the mobility of PEO chains and promotes the conductivity of DBC films. All dried samples demonstrate almost the same level of conductivity, which indicates the similar proton mobility. Thus, the σ' value for PVA-*g*-PAAm, DBC, and DBC_{hydr} at the frequency 1 kHz is equal to 1.48×10^{-10} , 1.51×10^{-10} , and 1.92×10^{-10} S cm⁻¹ correspondently (Fig. 1a).

As it was mentioned below, PEO-blocks have the same length both in DBC and DBC_{hydr} macromolecules and so, their contribution to the conductivity of these block copolymers should be the same. Nevertheless, the σ' value of hydrolyzed sample is slightly higher than that of DBC. In this case, it may be caused by the introduction of the additional ionogenic groups only. Thus, the appearance even a small number

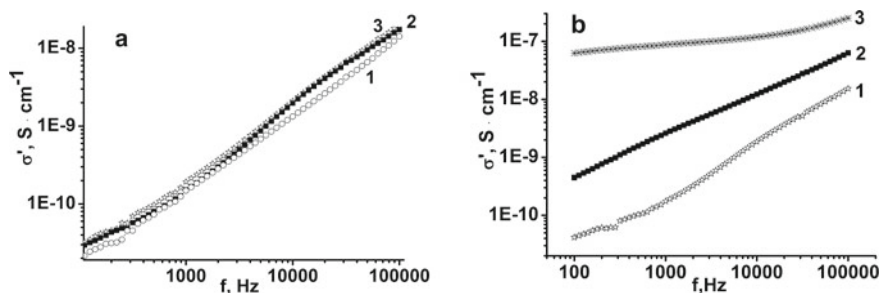


Fig. 1 Dependences of the conductivity versus frequency for SPE membranes of DBC—1, DBC_{hydr}—2, PVA-*g*-PAAm—3 for **a** dried samples and **b** kept in air for 100 h

Table 3 Conductivity of SPE membranes kept in air for 100 h frequency 1 kHz

Copolymer	ϵ'	σ' , S cm ⁻¹
DBC	5.37	1.75×10^{-10}
DBC _{hydr}	16.2	2.61×10^{-9}
PVA- <i>g</i> -PAAm	45.6	8.78×10^{-8}

of -COOH groups in PAAm chain leads to the growth of current conductivity of the host block copolymer.

It should pay attention to the increase in conductivity for all examined samples when keeping them in the air. Thus, 100 h of samples exposure at 25 °C and humidity ~ 70% leads to an increase in DBC_{hydr} and PVA-*g*-PAAm conductivity of almost 100 and 1000 times, respectively (Fig. 1b). It is known that PVA- and PEO-containing copolymers have a very high affinity for water. PAA_m is also highly hydrophilic and can adsorb up to four molecules of H₂O. A feature of low-temperature proton conductors is that the conductivity is usually carried out along the hydrogen bond system of structural water (crystal water, water of micropores, and water on the surface of the nanoparticles) [35]. Therefore, the value of their conductivity strongly depends on the content of bonded water and, ultimately, on ambient humidity. In addition, the adsorbed water can swell and stretch the polymer chains acting as a plasticizer which tend to enhance the segmental motion and increase ionic movement.

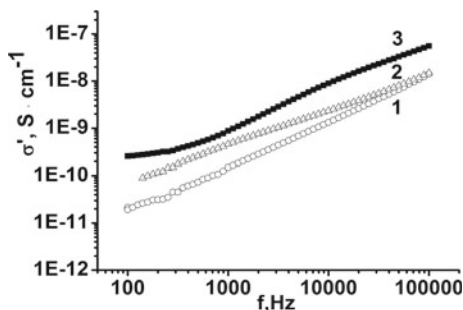
In the next experimental series, we examined the PVA-*g*-PAAm, DBC, and DBC_{hydr} films doped with LiPF₆. The electrolyte content in the initial compositions was varied relatively to DBCs or PVA-*g*-PAAm. The results are represented in Table 4 and Figs. 2, 3 and 4. It was noticed an increase in ionic conductivity of all examined films upon incorporation of LiPF₆. The results presented in Table 4 show a considerable rise of σ' values for PVA-*g*-PAAm and DBC_{hydr} membranes with the growth of lithium salt content. This effect is not surprising and could be interpreted by increase in the concentration of the charge carriers. However, the dopant's role in assisting ion conduction became insignificant at [PEO]/[LiPF₆] or [PVA]/[LiPF₆] molar ratio equal to 0.15. This might be due to a dual function of Li-salt, since it not only increases the concentration of ions in films. The Li-ions interact with oxygen

Table 4 Conductivity of the SPE membranes based on initial copolymers and that doped with LiPF₆ at frequency 1 kHz

Copolymer composition	[PEO(PVA)]/[LiPF ₆], base-mol mol ⁻¹	[DBC]/[LiPF ₆], base-mol mol ⁻¹	σ' , S cm ⁻¹
DBC	–	–	1.75×10^{-10}
DBC-LiPF ₆	0.15	4.75	1.95×10^{-5}
DBC-LiPF ₆	0.09	2.85	1.74×10^{-5}
DBC _{hydr}	–	–	2.61×10^{-9}
DBC _{hydr} -LiPF ₆	0.09	2.85	5.80×10^{-7}
DBC _{hydr} -LiPF ₆	0.06	1.02	4.69×10^{-6}
PVA-g-PAAm	–	–	4.61×10^{-10}
PVA-g-PAAm-LiPF ₆	0.09	–	3.47×10^{-6}
PVA-g-PAAm-LiPF ₆	0.06	–	2.46×10^{-5}

atoms of PEO and/or carbonyls of PAAm amide groups [36, 37]. This interaction competed with hydrogen bonding of PEO, PAAm, or PVA blocks and resulted in the plasticizing action of LiPF₆ additives on copolymer's film structure. A similar plasticizing action of Li-salts on bulk structure of neat PEO and PEO-containing block copolymers is well known from literature [38].

A comparison study on ionic conductivity between DBC, DBC_{hydr}, and PVA-g-PAAm films doped with the same amount of LiPF₆ reveals that ionic conductivity of compositions using DBC and PVA-g-PAAm is higher than that of DBC_{hydr} (Fig. 4). This unexpected effect contradicted the assumption that the polarity of –COOH group should cause an increase in the dissociation of the lithium salt due to the formation of a donor–acceptor bond between the carboxyl groups of the macromolecule and the metal cation and, thus, enhance the conductivity in general [1]. According to above considerations, the DBC_{hydr} membrane should have the highest conductivity

**Fig. 2** Dependences of the conductivity versus frequency of SPE membranes on the base of PVA-g-PAAm without dopant—1, doped with LiPF₆ at molar ratio [PVA]/[LiPF₆] = 0.09—2; doped with LiPF₆ at molar ratio [PVA]/[LiPF₆] = 0.06—3. *T* = 25 °C

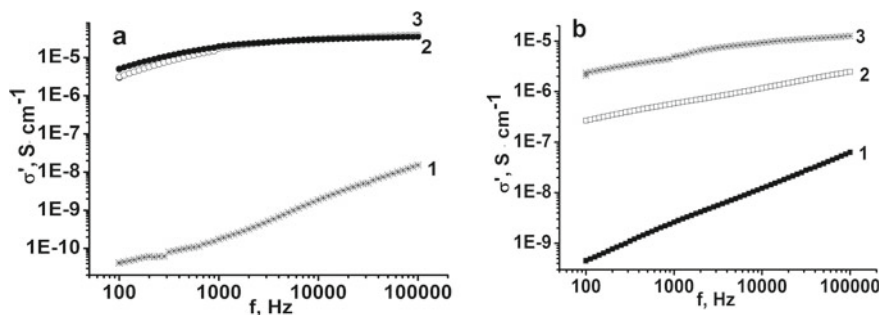


Fig. 3 Dependences of the conductivity versus frequency for SPE membranes of **a** DBC and **b** DBC_{hydr} without dopant—1, doped with LiPF₆ at molar ratio [PEO]/[LiPF₆] = 0.09—2, doped with LiPF₆ at molar ratio [PEO]/[LiPF₆] = 0.06—3

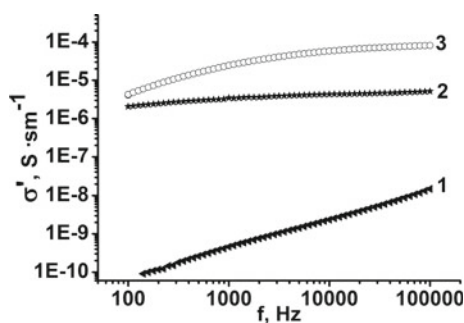


Fig. 4 Dependences of the conductivity versus frequency of SPE membranes on the base of DBC—1, DBC_{hydr}—2, and PVA-*g*-PAAM—3 doped with LiPF₆ at molar ratio [PEO]/[LiPF₆] = 0.09 and [PVA]/[LiPF₆] = 0.09

as in the case of non-doped sample. On the contrary, it occupies the lowest position after PVA-*g*-PAAM and DBC. This might be due to the peculiarity of complex formation of polymer components in DBC_{hydr} macromolecules. But this assumption requires additional, more thorough research to assess the features of DBC and DBC_{hydr} morphology and bulk structure so as their role in the creating the necessary conditions for the effective ions movement.

4 Conclusion

In the present study, ion conductive polymer membranes were readily prepared from water solutions of graft copolymer polyvinyl alcohol/polyacrylamide (PVA-*g*-PAAM), diblock copolymer polyethylene oxide/polyacrylamide MePEO-*b*-PAAM

(DBC) and, its partially hydrolyzed derivative polyethylene oxide/poly(acrylamide-*co*-acrylic acid) MePEO-*b*-P(AAm-*co*-AAc) (DBC_{hydr}), which form intramolecular polycomplexes (IntraPC). The ion conductivity of pure copolymers and their compositions with LiPF₆ was studied at room temperature. It was noticed the enhancement in ionic conductivity when introduction additional ionic groups –COOH in PAAm chains of DBC macromolecule. The addition of LiPF₆ into the polymer matrix increases the ion conductivity of polymer membranes on the base of DBC, DBC_{hydr}, and PVA-*g*-PAAm and allows to achieve ion conductivity at 1 kHz frequency up to 10⁻⁵ S cm⁻¹. The preliminary obtained results allow consider graft and block copolymers comprising interacting polymer components as potential matrix for SPE membranes and open new ways for their application in Li-batteries, solar, and fuel cells. They also demonstrate the possibility of using commercially available, non-toxic solid polymer electrolytes in electrochemical devices and implementation of their development at low cost and with high safety for the environment.

References

1. Satiabrata S (2013) Additives for solid polymer electrolytes: the layered nanoparticles. *Key Eng Mat* 571: 23–56. <https://doi.org/10.4028/www.scientific.net/KEM.571.27>
2. Ye YS, Rick J, Hwang BJ (2012) Water soluble polymers as proton exchange membranes for fuel cells. *Polymers* 4:913–963. <https://doi.org/10.3390/polym4020913>
3. Quartarone E, Angioni S, Mustarelli P (2017) Polymer and composite membranes for proton-conducting, high-temperature fuel cells: a critical review. *Materials* 10:687–704. <https://doi.org/10.3390/ma10070687>
4. Baroutaji A, Carton JG, Sajjia M, Olabi A-G (2016) Materials in PEM fuel cells. *Ref Mod Mat Sci Mat Eng*. <https://doi.org/10.1016/B978-0-12-803581-8.04006-6>
5. Gupta S, Singh PK, Bhattacharya B (2018) Low-viscosity ionic liquid-doped solid polymer electrolytes: electrical, dielectric, and ion transport studies. *High Perf Polym* 30(8):986–992. <https://doi.org/10.1177/0954008318778763>
6. Silvaa MM, Barrosa SC, Smitha MJ, MacCallumb JR (2006) Characterization of solid polymer electrolytes based on poly(trimethylenecarbonate) and lithium tetraborate. *Electrochim Acta* 49:1887–1891. <https://doi.org/10.1016/j.electacta.2003.12.017>
7. Agrawal RC, Pandey GP (2008) Solid polymer electrolytes: materials designing and all-solid-state battery applications: an overview. *J Phys D:Appl Phys* 41:223001. <http://iopscience.iop.org/0022-3727/41/22/223001>
8. Hwang BJ, Joseph J, Zeng YZ, Lin CW, Cheng MY (2011) Analysis of states of water in poly (vinyl alcohol) based DMFC membranes using FTIR and DSC. *J Membr Sci* 369:88–95. <https://doi.org/10.1016/j.memsci.2010.11.031>
9. Rhim JW, Park HB, Lee CS, Jun JH, Kim DS, Lee YM (2004) Crosslinked poly(vinyl alcohol) membranes containing sulfonic acid group: proton and methanol transport through membranes. *J Membr Sci* 238:143–151. <https://doi.org/10.3390/nano9030397>
10. Lin CW, Huang YF, Kannan AM (2007) Semi-interpenetrating network based on cross-linked poly(vinyl alcohol) and poly(styrene sulfonic acid-*co*-maleic anhydride) as proton exchange fuel cell membranes. *J Power Source* 164:449–456. <https://doi.org/10.1016/j.jpowsour.2006.10.081>
11. Lin CW, Huang YF, Kannan AM (2007) Cross-linked poly(vinyl alcohol) and poly(styrene sulfonic acid-*co*-maleic anhydride)-based semi-interpenetrating network as proton-conducting membranes for direct methanol fuel cells. *J Power Sources* 171:340–347. <https://doi.org/10.1016/j.jpowsour.2007.06.145>

12. Qiao J, Hamaya T, Okada T (2005) New highly proton-conducting membrane poly(vinylpyrrolidone)(PVP) modified poly(vinyl alcohol)-2-acrylamido-2-methyl-1-propanesulfonic acid (PVA-PAMPS) for low temperature direct methanol fuel cells (DMFCs). *Polymer* 46(24):10809–10816. <https://doi.org/10.1016/j.polymer.2005.09.007>
13. Borogula MS, Celik SU, Boz I, Bozkurt A (2013) Sulfonated poly(vinyl alcohol)/triazole blends as anhydrous proton conducting membranes for polymer electrolyte membrane fuel cells. *Mater Res* 28(11):1458–1465. <https://doi.org/10.1557/jmr.2013.111>
14. Pivovar BS, Wang Y, Cussler EL (1999) Pervaporation membranes in direct methanol fuel cells. *J Membr Sci* 154:155–162. [https://doi.org/10.1016/S0376-7388\(98\)00264-6](https://doi.org/10.1016/S0376-7388(98)00264-6)
15. Han HW, Liu W, Zhang J, Zhao XZ (2005) A hybride poly (ethylene oxide)poly(vinylidene fluoride)/TiO₂ nanoparticle solid-state redox electrolyte for dye-sensitized nanocrystalline solar cells. *Adv Fun Mat* 15:1940–1944. <https://doi.org/10.1002/adfm.200500159>
16. Wei D (2010) Dye sensitized solar cells. *Int J Mol Sci* 11:1103–1113. <https://doi.org/10.3390/ijms11031103>
17. Ye YS, Rick JB, Hwang J (2012) Water soluble polymers as proton exchange membranes for fuel cells. *Polymers* 4:913–963. <https://doi.org/10.3390/polym4020913>
18. Trigg EB, Gaines TW, Marochal M, Moed DE, Rannou P, Wagener KB, Stevens MJ, Karen I (2018) Self-assembled highly ordered acid layers in precisely sulfonated polyethylene produce efficient proton transport. *Nature Mat* 17:725–731. <https://doi.org/10.1038/s41563-018-0097-2>
19. AnM E, Jannasch P (2006) Solid electrolyte membranes from semi-interpenetrating polymer networks of PEG-grafted polymethacrylates and poly(methyl methacrylate). *Sol State Ion* 177:573–579. <https://doi.org/10.1016/j.ssi.2005.12.021>
20. Stephan AM (2006) Hybrid inorganic–organic polymer electrolytes. *Eur Pol J* 42:21–42. <https://doi.org/10.1016/j.polymer.2006.05.069>
21. Gretzel M (2009) Recent advances in sensitized mesoscopic solar cells. *Acc Chem Res* 42:1788–1798. <https://doi.org/10.1021/ar900141y>
22. Gray FM (1997) *Polymer electrolytes*. The royal society of chemistry monographs. Cambridge, London
23. Appetecchi GB, Scaccia S, Passerini S (2000) Invetigation on the stability of the lithium polymer electrolyte interface. *J Electrochem Soc* 147:4448–4452. <https://doi.org/10.1149/1.1394084>
24. Stergiopoulos T, Arabatzis IM, Katsaros G, Falaras P (2002) Binary polyethelene oxide/titania solid-state redox electrolite forhighly effecien nanocrystalline TiO₂ photoelectrochemical cells. *Nano Lett* 2:1259–1261. <https://doi.org/10.1021/nl02579u>
25. Nogueira AF, Durrant JR, DE Paoli M-A (2001) Dye-sensitized nanocrystalline solar cells employing a polymer electrolyte. *Adv Mater* 13:826–830. [https://doi.org/10.1002/1521-4095\(200106\)13:11<826::AID-ADMA826>3.0.CO;2-L](https://doi.org/10.1002/1521-4095(200106)13:11<826::AID-ADMA826>3.0.CO;2-L)
26. Ogata N (2002) Ion-conducting polymers. *Macromol Sci Part C Polym Rev* 42:399–438. <https://doi.org/10.1081/MC-120006454>
27. Uchiyama R, Kusagawa K, Hanai K, Imanishi N, Nirano A, Takeda Y (2009) Development of dry polymer electrolyte based on polyethelene oxide with co-bridging agent crosslinked by electron beam. *Sol State Ion* 180:205–216. <https://doi.org/10.1016/j.ssi.2008.11.015>
28. Kang M-S, Kim JH, Won J, Kang YS (2006) Dye-sensitized solar cells based on crosslinked poly(ethelene glycol) electrolytes. *J Photochem Photobiol A Chem* 183:15–36. <https://doi.org/10.1016/j.jphotochem.2006.02.013>
29. Zheltonozhskaya T, Permyakova N, Momot L. (2009) Intramolecular polycomplexes in block and graft copolymers. In: *Hydrogen-bonded interpolymer complexes: formation, structure and application*. Chapter 5. World Scientific Publ. Corp., New Jersey, London, Singapore, pp 85–154
30. Tsuchida E, Ohno H, Tsunemi K, Kobayashi N (1983) Lithium ionic conduction in poly (methacrylic acid)-poly(ethylene oxide) complex containing lithium perchlorate. *Solid State Ionics* 11:227–260. [https://doi.org/10.1016/0167-2738\(83\)90028-0](https://doi.org/10.1016/0167-2738(83)90028-0)
31. Jiang M, Li M, Xiang M, Zhou H (1999) Interpolymer complexation and miscibility enhancement by hydrogen bonding. *Adv Polym Sci* 146:121–217. https://doi.org/10.1007/3-540-49424-3_3

32. Zheltonozhskaya T, Shembel E, Fedorchuk S, Kunitskaya L, Maksyta I, Pemyakova N, Gomza Y (2012) Nanostructured triblock copolymers with chemically complementary components and their ionic conductivity. *J Res Upd Pol Sci* 1(2):1–12. <https://doi.org/10.6000/1929-5995.2012.01.02.4>
33. Kunitskaya L, Zheltonozhskaya T, Aleinichenko V, Berkova S (2011) Diblock copolymers containing polyacrilamide and monomethoxy-poly(ethylene) oxide: bulk structure and micellization. *Mater und Werkst* 42(2):109–113. <https://doi.org/10.1002/mawe.201100740>
34. Zheltonozhskaya T, Zagdanskaya N, Demchenko O, Momot L, Permyakova N, Syromyatnikov V, Kunitskaya L (2004) Graft copolymers with chemically complementary components as a special class of high-molecular-weight compounds. *Russ Chem Rev* 73:811–829. <https://doi.org/10.1070/RC2004v073n08ABEH000901>
35. Galperin D, Khalatur PG, Khokhlov AR (2009) Morphology of Nafion membranes: microscopic and mesoscopic modelling. In: Paddison SJ, Promislow KS (eds) *Device and materials modelling in PEM fuel cells*, vol 113. Springer, Heidelberg, pp 453–483. https://doi.org/10.1007/978-0-387-78691-9_17
36. Permyakova NM, Zheltonozhskaya TB, Shilov VV et al (2005) Structure of triblock-copolymers based on poly(ethylene oxide) and poly(acrylamide) with central blocks varying length. *Theor Exper Chem* 41:382–389. <https://doi.org/10.1007/s11237-006-0007-6>
37. Baron MH, Fillaux F (1985) Vibrational spectra and structure of N-methylacetamide in some solid complexes with neutral salts. *Can J Chem* 63:1473–1479. <https://doi.org/10.1080/15421400802463092>
38. Bruce PG (1995) *Solid state electrochemistry*. Cambridge University Press, Cambridge, 344 pp. <https://doi.org/10.1002/adma.19960080417>

Hybrid Magnetic Particles Based on Laponite RD[®]: Structure, Stability, and Electrosurface Properties



Maryna Manilo, Tetiana Borodinova, Valeriy Klepko, Serhii Cherepov, and Nikolai Lebovka

Abstract Hybrid magnetic particles based on Laponite[®] (Lap) (Rockwood Additives Ltd., UK) and nanomagnetic (NM) particles have been synthesized. The NM was synthesized using the Elmore method. For preparation of LapM hybrids, the Lap and NM were mixed in aqueous suspensions at pH 7.3 and $T = 298$ K. The concentration of NM particles at suspensions was fixed at 0.75 wt%, and concentration of Lap was varied in the range of 0.0375–1.5 wt% (the mass ratio $X_m = m_{\text{NM}}/m_{\text{Lap}}$ was varied within the range 20.0–0.5). The Lap, LapM, and NM particles were characterized using FTIR-spectroscopy, X-ray diffraction, magnetic susceptometry, transmission electron microscopy, measurements of particle size distribution function, and electrophoretic mobility. The observed variations in magnetic susceptibility χ , ζ -potential and overcharging were explained by the deep integration between Lap and NM particles, and interplaying between hydrophobic and electrostatic interactions in LapM hybrids.

Keywords Laponite[®] · Platelet · Magnetic hybrid nanoparticles · Electrosurface properties

M. Manilo (✉) · T. Borodinova · N. Lebovka
IBCC: F. D. Ovcharenko Institute of Biocolloidal Chemistry, National Academy of Sciences of Ukraine, 42, Vernadsky Av, Kyiv 03142, Ukraine
e-mail: manilomaryna@gmail.com

T. Borodinova
e-mail: borodinova.t@gmail.com

N. Lebovka
e-mail: lebovka@gmail.com

V. Klepko
Institute of Macromolecular Chemistry, NAS of Ukraine, 48, Kharkivske Road, Kyiv 02160, Ukraine
e-mail: klepko_vv@ukr.net

S. Cherepov
Institute of Magnetism NAS of Ukraine, NAS of Ukraine, 36-B, Vernadsky Av, Kyiv 03142, Ukraine
e-mail: cherepov@meta.ua

Abbreviations

AFM	Atomic force microscopy
FTIR	Fourier-transform infrared
Lap	Laponite [®]
LapM	Magnetically modified Lap
NM	Nanomagnetite
TEM	Transmission electron microscopy
XRD	X-Ray diffraction

1 Introduction

Nowadays, magnetic nanoparticles have attracted great attention in practical applications for preparation effective adsorbent for water purification [1], preparation of medical contrast agents [2] and for targeted therapies [3], etc. The magnetic nanoparticles can be effectively positioned, recovered, separated, and reutilized in external magnetic field. Recently, hybrid magnetic nanoparticles based on Laponite[®] (Lap) platelets were synthesized. The Lap was first synthesized in the 1960s [4–6]. It is synthetic material with 2:1 layered structure similar to the natural trioctahedral clay mineral hectorite [7]. In water, the Lap platelets exist as 1 nm thick disks with diameters of 25 nm and their faces carry a net negative surface charge. Lap includes different types of active sites such as the interlayer, surface, edge, and interparticle sites [7]. Nowadays, the Lap is widely used in many practical applications as the components of household items, agricultural, horticultural, and cosmetic products (toothpastes, skincare and sunscreen emulsions, cosmetics, shampoos, creams), etc. [8].

Magnetic modifications of Lap allow fine regulation of properties of Lap platelets, their dispersibility, surface charge, colloidal stability, and affinity toward biomolecules [9]. Moreover, magnetic LapM hybrids or LapM-based composite materials can be easily separated or manipulated in magnetic field. The LapM hybrids prepared using a co-precipitation route were used as a contrast agents for in vivo MRI detection of tumors [2]. The detailed analysis revealed that Fe₃O₄ is immobilized directly on Lap platelets.

The different strategies for preparation of LapM have been applied [10–14]. One-step co-precipitation method was used to synthesize LapM with different weight ratios $X = \text{Fe}_3\text{O}_4/\text{Lap}$ ($=0-2$) [10–12]. An increased aggregation of LapM particles in aqueous suspensions was revealed. The interactions in the mixtures of Lap with magnetic particles have been also studied [15–18].

LapM hybrids have been used for preparation of different types magneto-responsive hydrogels systems [19]. The magnetic hydrogels based on hydroxypropyl methylcellulose–polyacrylamide showed sensitivity to changes in both pH and

external magnetic field [3]. Different magnetic hydrogels were tested for adsorption capacity of bovine serum albumin (BSA). For example, improved adsorption capacity of BSA was observed for chitosan-based magnetic beads [20] and PVA-based hydrogels [21]. These magnetic hydrogels may be attractive for biomedical applications such as drug delivery and enzyme immobilization. In several works, the magnetic hydrogels with incorporated LapM hybrids have been tested as adsorbent for removal of contaminants and dyes from aqueous solutions [3, 22, 23]. For example, the magnetic hydrogels based on poly(vinyl alcohol) (PVA) have shown high efficiency for removal of Cd²⁺ [24], hydrogels based on PVA demonstrated high efficiency for removal of methylene blue dye [23], and hydrogels based on κ -carrageenan demonstrated the increased adsorption capacity of crystal violet dye [22].

This work is devoted to the detailed studies of colloidal stability and electrokinetic behavior of LapM hybrids in aqueous solutions. The NM was synthesized using the Elmore method and its concentration in suspensions was fixed at 0.75 wt%. Then, the Lap was added into the NM suspension and the NM and Lap ratio was varied within the range 0.5–20. Electrophoretic mobility and overcharging of Lap, NM, and hybrid nanoparticles (LapM) in wide range of pH values were studied. The properties of LapM hybrids were also characterized using the methods of FTIR-spectroscopy, transmission electron microscopy, X-ray diffraction, and dynamic light scattering.

2 Materials and Methods

2.1 Materials

In this work, the gel-forming grades of the Laponite RD[®] (Lap) (Rockwood Additives Ltd., UK) was used. This grade is the most popular and frequently used in different applications for rheology control in surface coatings, household products, and other industrial fields. Each layer of the ideal Lap platelet consists of a hexagonal network of basal oxygen atoms of the tetrahedral Si–O. Some of the magnesium atoms in the structure are substituted by lithium ions, and some spaces are empty, giving the empirical chemical formula Na_{+0.7}[(Si₈Mg_{5.5}Li_{0.3})O₂₀(OH)₄]_{-0.7}. The cation exchange capacity (CEC) of Lap is ≈ 0.75 meq/g [25] at pH ≥ 8.0 , the specific surface area (determined by N₂ adsorption) is ≈ 358.5 m²/g [26], and the density of Lap is $\rho = 2.53$ g/cm³ [27].

In all experimental procedures double distilled water, iron sulfate (FeSO₄ \times 7H₂O), iron chloride (FeCl₃ \times 6H₂O), 25% aqueous ammonia, sodium hydroxide, and hydrochloric acid (all chemical grade purity from Renal, Hungary) were used.

2.2 Synthesis Procedures

The synthesis of NM particles was done by precipitating iron salts, $\text{FeSO}_4 \times 7\text{H}_2\text{O}$ and $\text{FeCl}_3 \times 6\text{H}_2\text{O}$ with molar ratio of 1:2 in alkaline medium at ambient conditions under constant stirring (for the details, see [28]). The precipitate of magnetite particles was separated by using the permanent magnet and washed with distilled water until neutral pH was reached. The concentration of NM in a bulk suspension was 15.0 mg/cm^3 (1.5 wt%).

The LapM hybrids were prepared by mixing of NM and Lap aqueous suspension at pH 7.3 and $T = 298 \text{ K}$. NM suspension was sonicated at 50 W for 10 min (AOYUE 9050, China), mixed with aqueous suspension of Lap, and finally sonicated for 10 min. The concentration of suspension was selected to have the fixed concentration of NM in final suspension (0.75 wt%), and NM and Lap ratio ($X_m = m_{\text{NM}}/m_{\text{Lap}}$) was 0.5–20 (1.5–0.0375 wt% of Lap).

2.3 Instrumentation Methods

FTIR analyses were performed using IR Affinity-1S (Shimadzu, Japan) spectrometer in the spectral range of $400\text{--}4000 \text{ cm}^{-1}$. The powder samples of Lap, NM, and LapM were mixed with KBr powder in 5 wt%, and a pure KBr spectrum was used as reference. Pellets were prepared using the standard technique under a pressure of 15 ton/cm^2 with a barrel 16 mm in diameter.

The X-ray diffraction patterns of Lap, NM, and LapM samples were obtained with a wide angle X-ray diffraction (XRD) instrument DRON-2 (Bourestnik, Inc., St. Petersburg, Russia.) with CuK_α source of emission at the wavelength $\lambda = 0.15418 \text{ nm}$, Ni filter in 2θ range from 10 to 80° with a step of 0.05° . The classical Debye–Scherrer transmission geometry was used. The air scattering effects were corrected by subtraction of the scattering of empty chamber. The interlayer distance inside the Lap stacks, d , was calculated from Bragg formula $d = 0.5\lambda/\sin\vartheta$, where ϑ is a half of the diffraction angle. The International Centre of Diffraction Data (ICDD) were used for determination of diffraction reflection hkl indexes (Miller indexes).

For determination of the magnetic susceptibility, χ , the inductive-frequency magnetometry was used [29]. The measurements were done using the magnetic susceptometer constructed at the Institute of Magnetism of the National Academy of Sciences of Ukraine. In this method, the aqueous suspension of NM was placed inside the coil inductor and changes in the frequency of the generator in the oscillating circuit were measured. The data were presented ratio $\chi^* = \chi/\chi_{\text{NM}}$, where χ_{NM} is a magnetic susceptibility of pure NM particles.

Transmission electron microscopic (TEM) images were recorded using the instrument Selmi 125 K (100 kV, Ukraine). Aqueous suspensions of particles were sonicated during 2 min in ultrasonic bath at 35 kHz (Transsonic T 570 Elma, Germany). The drop of suspension was put on Lacey carbon and was dried at ambient conditions.

Zeta potentials and the particle size distributions were measured by a light scattering technique using a Zetasizer NS (Malvern Instruments, United Kingdom). Electrophoretic measurements were performed at room temperature ($T = 298$ K) in the range of external electric field gradients of 6–15 V/cm. The electrophoretic mobility was transformed into ζ -potential using the classical Smoluchowski equation with the software of the instrument. Such a procedure is widely accepted in the literature, and it can serve for comparison purposes, i.e., to follow the effect of different variables on the electrophoretic mobility and ζ -potential. Before measurements all samples were diluted in 60 times and sonicated during 10 min in ultrasonic bath at 35 kHz (Transsonic T 570 Elma, Germany). For pH measurements, the samples were held for 90 min to reach equilibrium pH. Ezodo PL-700PV (Taiwan) equipment was used for pH measurements.

2.4 Statistical Analysis

Data were represented as mean \pm standard deviation of 3–5 independent experiments. ANOVA was employed for statistical evaluation of data, and $p < 0.05$ was deemed to be significant.

3 Results and Discussion

Figure 1 shows examples of FTIR spectra for pristine Lap ($X = 0$), LapM ($X_m = 1$) and NM ($X \rightarrow \infty$) samples. The broad bands in the interval between 3000–3700 cm^{-1} , and bands near 1630 cm^{-1} correspond to the OH stretching vibrations of hydroxyl groups and adsorbed water on samples. These bands were observed for all samples. Particularly, for the pristine Lap, the bands in the interval 3600–3700 cm^{-1} correspond to the stretching vibrations of the “inner” hydroxyl groups Si–OH (3620 cm^{-1}) and Mg–OH (3676 cm^{-1}) bonded to octahedral cations [30].

The band with maximum at ≈ 650 cm^{-1} may be attributed to the O–Si–O bending vibration [31]. The broad band in the interval 900–1000 cm^{-1} with maximum at 970 cm^{-1} can be assigned to Si–OH and Al–OH stretching vibrations in different environments in layered silicates [32, 33]. The intensity of this band decreases for LapM sample and it completely disappears for NM sample. The bands at 3400 cm^{-1} , 1630 cm^{-1} , and ≈ 650 cm^{-1} can be attributed to the adsorbed water in all samples. The obtained data for pure NM were in correspondence with the data reported earlier [34–36]. For LapM and NM samples, the intense bands with maximums at 520 cm^{-1} correspond to the vibration mode in the bond Fe–OH. In magnetized samples, LapM the both bands corresponding to the pristine Lap at ≈ 970 cm^{-1} , ≈ 650 cm^{-1} , and pure NM at ≈ 520 cm^{-1} were observed. The noticeable suppression of the O–Si–O bending vibration (≈ 650 cm^{-1}) of pure Lap in LapM sample may reflect strong interactions between NM and Lap species in magnetized LapM sample.

Fig. 1 FTIR spectra (absorbance, A , versus wave number, ν) of pristine Lap ($X_m = 0$), LapM ($X_m = 1$), and NM ($X_m \rightarrow \infty$) samples

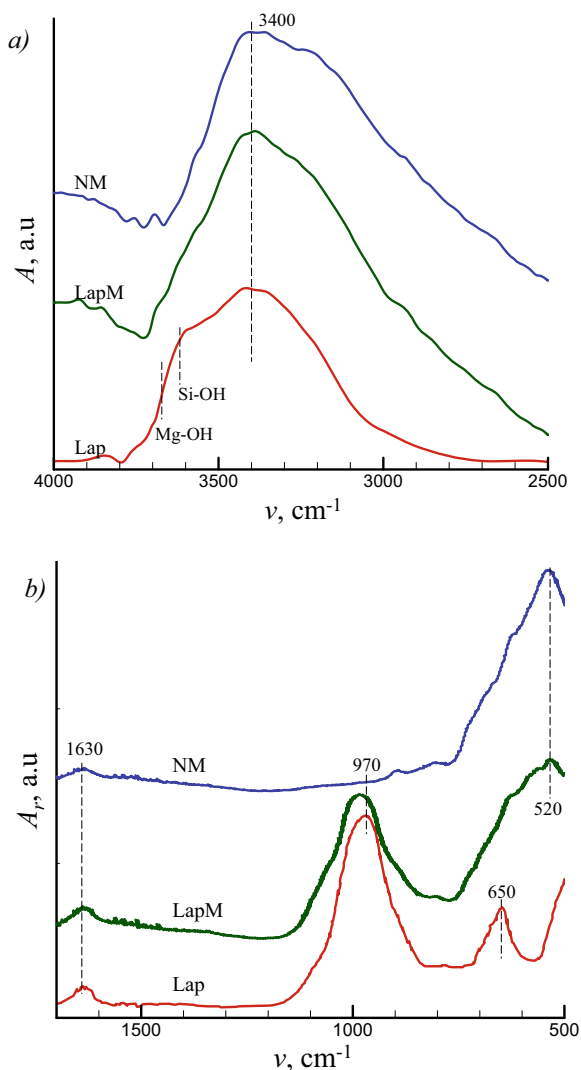
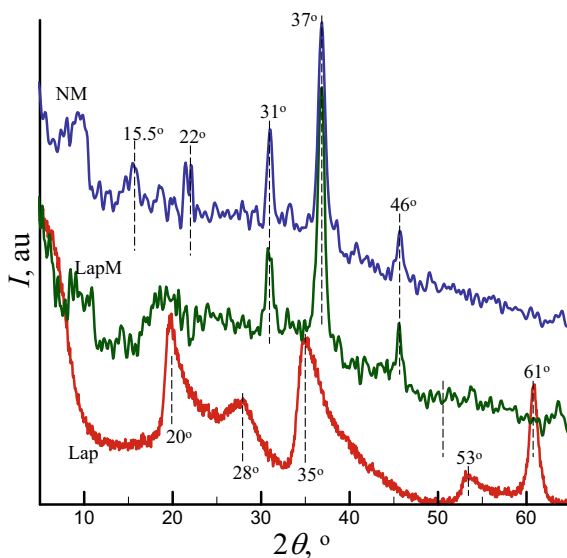


Figure 2 shows the XRD patterns for pristine Lap ($X_m = 0$), LapM ($X_m = 1$), and NM ($X_m \rightarrow \infty$) samples. Diffraction peaks of the pristine Lap powder were observed at $\approx 20^\circ$ (plane 110), 28° (005), 35° (200), 53° (300), 61° (060), and 72° [37, 38]. The position of peaks for NM may importantly depend upon pH of medium, temperature, and other details of synthesis [28, 39].

The most intensive diffraction peaks of the pure NM powder were observed at $\approx 31^\circ$ (220), 37° (311), and 46° (400). In the magnetized LapM, many diffraction peaks of pristine Lap disappeared, while the characteristic peaks related with NM

Fig. 2 XRD patterns for pristine Lap ($X_m = 0$), LapM ($X_m = 1$), and NM ($X_m \rightarrow \infty$) samples



appeared. It also may reflect strong interactions between NM and Lap species in magnetized LapM sample.

Figure 3 shows the relative magnetic susceptibility, χ^* , versus the ratio of NM and Lap ($X_m = m_{\text{NM}}/m_{\text{Lap}}$) in LapM samples. The observed function $\chi^*(X_m)$ was non-monotonic and rather surprising. The value of χ^* noticeably increased with increasing of X_m , gone through the maximum $\chi^* \approx 1.12$ at $X_m \approx 0.67$ and then decreased to the minimum $\chi^* \approx 0.76$ at $X_m \approx 1.5$. The further increase of X_m resulted in increase of χ^* to the value of $\chi^* = 1$ in the limit of $X_m \rightarrow \infty$.

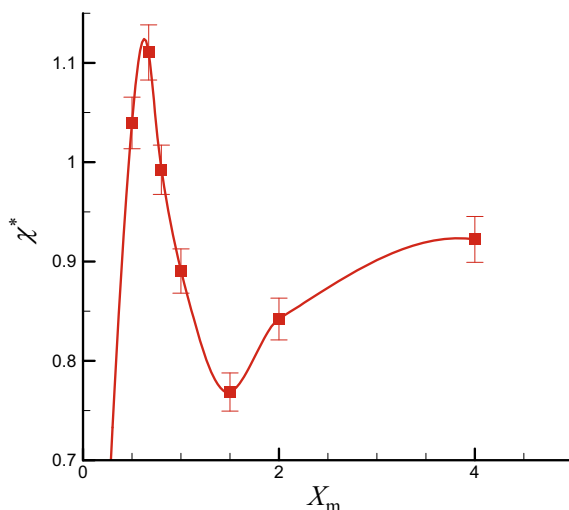
Such anomalous $\chi^*(X_m)$ behavior may reflect the following phenomena. The magnetic susceptibility of the studied systems reflects the magnetizing ability of NM particles in non-magnetic liquid (water). In general case, the value of magnetic susceptibility in colloidal suspensions can depends upon the size, particle shape, extend of their aggregation and self-assembly, structure and porosity of aggregates, viscosity of the medium, and temperature [40, 41].

Initial increase of χ^* at $X_m \leq 0.67$ (Fig. 3) surely reflects formation of magnetized LapM particles with deeply integrated Lap and NM particles. This integration is supported by the above discussed changes in IR spectra (Fig. 1) and XRD patterns (Fig. 2). Note that in our experimental conditions, the small values of X_m correspond to the high concentrations of Lap (e.g., at $X_m = 0.5$ the concentration of Lap is 1.5%) and large viscosity of suspension. The decrease in viscosity of suspension with increase of X_m can also results in increase of χ^* .

However, at higher values of X_m above 0.67, the more complex changes in structure of LapM may occur.

Figure 4 compares TEM images of LapM ($X_m = 1.5$) and NM ($X_m \rightarrow \infty$) particles. At $X_m = 1.5$, the large scale volumetric structures of integrated Lap and NM particles

Fig. 3 Relative magnetic susceptibility, χ^* , versus the ratio of NM and Lap, X_m (m_{NM}/m_{Lap}), in LapM samples. All suspensions were freshly prepared at pH 9.2 and $T = 293$ K. Symbols are experimental data, and solid lines are to guide the eye



were formed Fig. 4a). It can be speculated that such volumetric structures display a moderate magnetic properties as compared with the pure NM particles of sizes of 10–20 nm and higher magnetic susceptibility. The observed changes in magnetic susceptibility of LapM suspensions can be also related with aggregation of particles.

Figure 5 presents the normalized distribution functions $f^*(d)$ ($=f/f_{\max}$) of diameter of aggregates, d , at different values of X_m . The data were obtained at fixed value pH 5.5 ± 0.3 . At such value of pH, the electrostatic stabilization was insignificant and aggregation was observed at all values of X_m . Moreover, it increased with increasing of X_m .

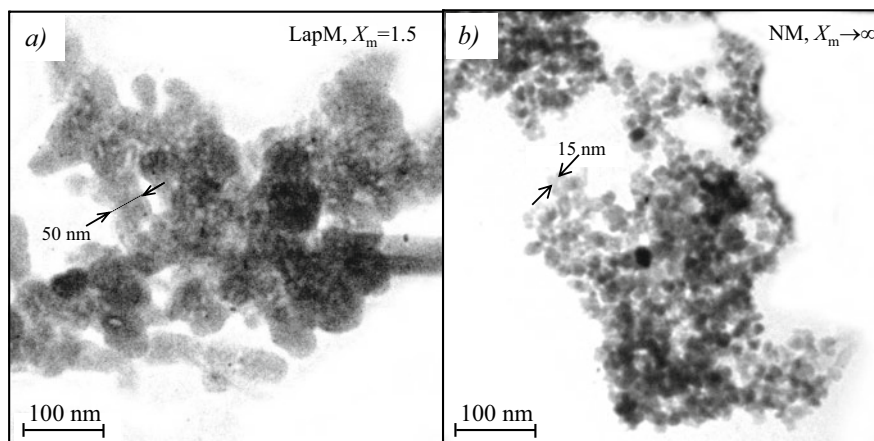


Fig. 4 Examples of TEM images of LapM ($X_m = 1.5$) and NM ($X_m \rightarrow \infty$) nanoparticles

Fig. 5 Normalized distribution functions of diameter of aggregates, $f^*(d)$ ($\equiv f/f_{\max}$), at different values of X_m . The data were obtained at pH 5.5 and $T = 298$ K. Symbols are experimental data, and solid lines are to guide the eye

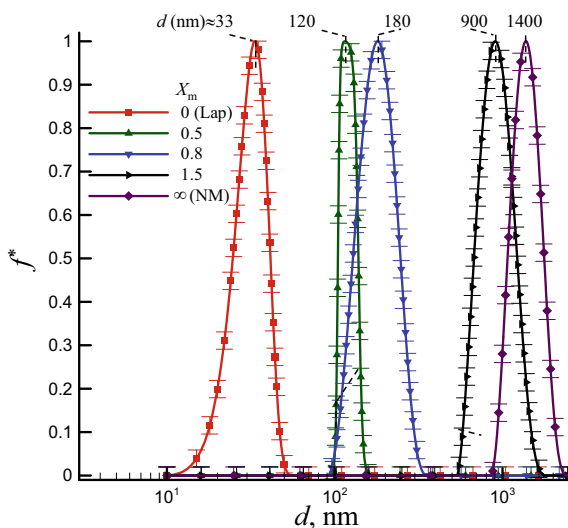


Figure 6 presents the size of aggregates, d_{\max} , (it corresponds to the maximum of functions $f^*(d)$) versus the value of X_m . The monotonically increasing function $d_{\max}(X_m)$ was observed. The size of aggregates of pure NM particles reached the value of $d_{\max} \approx 1400$ nm than considerably exceed the size of individual NM particle, $d \approx 15$ nm (Fig. 4b). Formation of this rather large aggregates reflects the high hydrophobic interaction between particles in the vicinity of isoelectric point of pure NM, pH 5.

Fig. 6 Size of aggregates, d_{\max} , versus the value of X_m . The data were obtained at pH 5.5 and $T = 298$ K. Symbols are experimental data, and solid lines are to guide the eye. The value of d_{\max} corresponds to the maximum of functions $f^*(d)$. Photos present the images of stable suspensions

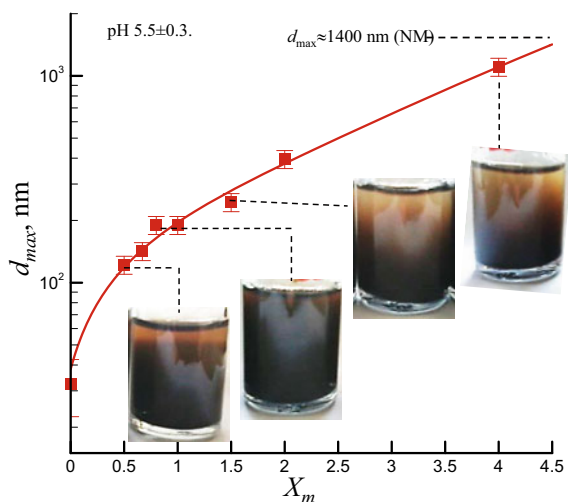


Fig. 7 ζ -potential versus pH of suspensions for pristine Lap ($X_m = 0$, 0.0375% Lap), LapM ($X_m = 1.5$), and NM ($X_m \rightarrow \infty$, 0.75 wt% NM) samples. Inset shows ζ -potential versus X_m dependence at fixed pH 4.3. The value $X_m \approx 7.7$ corresponds to the isoelectric point for hybrid particles. Symbols are experimental data, and solid lines are to guide the eye

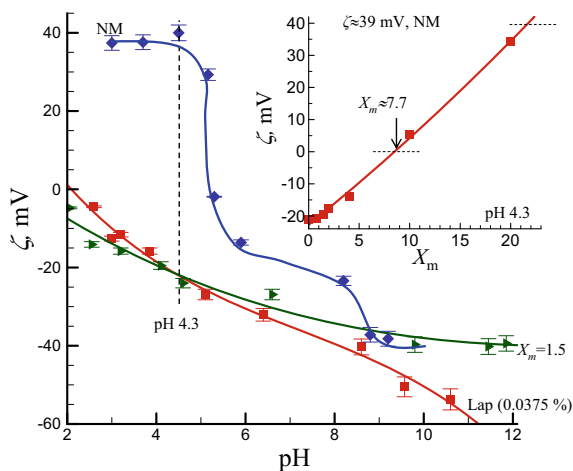


Figure 7 shows representative pH-dependence of ζ -potential of pristine Lap, LapM hybrids with $X_m = 1.5$ and NM particles. At acidic media at low pH values (<5), pristine Lap particles and LapM hybrids were negatively charged and have relatively small negative ζ -potentials (-20 mV or smaller). At these conditions, the pure NM particles were positively charged with rather large ζ -potential (≈ 39 mV). Inset to Fig. 7 shows ζ -potential versus X_m dependence at fixed pH 4.3. Value of ζ -potential continuously changed with X_m and isoelectric point was observed at $X_m \approx 7.7$.

Therefore, in acidic media, the stability of the hybrid particles can be finely regulated the changing of content Lap. The negatively charged Lap platelets serve as the stabilizing platforms for positively charged NM particles. The stability of suspension noticeably depends upon concentration of Lap. At large concentration of Lap ($X_m = 0.5$, $C_{\text{Lap}} = 1.5$ wt%), the formation of gel-like sediment was observed and in the interval $X_m = 0.67$ – 0.8 formation of the stable dark suspensions was observed. In an alkaline environment at elevated pH values (>10), all species Lap, LapM, and NM demonstrated rather large negative surface charges.

4 Conclusions

This work discusses properties of hybrid magnetic particles based on Lap platelets and nanomagnetic (NM) particles. The LapM hybrids were prepared by mixing of Lap and NM aqueous suspensions at different NM/Lap ratio, X_m . All particles were characterized using FTIR-spectroscopy, X-ray diffraction, magnetic susceptometry, transmission electron microscopy, measurements of particle size distribution function, and electrophoretic mobility. FTIR and XDR data revealed the deep integration of Lap and NM particles in LapM hybrids. The observed anomalous behavior of magnetic susceptibility can reflect existence of complex interactions between Lap

and NM particles in dependence on X_m . It was concluded that in the acidic media the stability of the hybrid particles can be finely regulated the changing of content Lap. The observed variations in magnetic susceptibility χ , ζ -potential and overcharging were also explained by the deep integration between Lap and NM particles, and interplaying between hydrophobic and electrostatic interactions in LapM hybrids. The obtained data evidenced that the structure and magnetic properties of LapM hybrids may be finely regulated by changing the concentration of Lap and NM particles in aqueous suspensions, the ratio X_m , and pH of medium.

Acknowledgements This work was supported by the funding of the National research foundation of Ukraine, Project #2020.02/0138 “Electrokinetic phenomena in natural nano/microfluidic and disperse systems: characterizing, treatment, modeling”, and by the funding from the National Academy of Sciences of Ukraine, Projects 7/9/3-f-4-1230-2020 #0120U100226 and #0120U102372/20-N.

References

1. Zeinali S, Tatian S (2019) Vanadium removal from fuel oil and waste water in power plant using humic acid coated magnetic nanoparticles. *Int J Nanosci Nanotechnol* 15(4):249–263
2. Ding L, Hu Y, Luo Y, Zhu J, Wu Y, Yu Z, Cao X, Peng C, Shi X, Guo R (2016) LAPONITE[®] - stabilized iron oxide nanoparticles for in vivo MR imaging of tumors. *Biomater Sci* 4:474–482. <https://doi.org/10.1039/C5BM00508F>
3. Mahdavinia GR, Ettehad S, Amini M, Sabzi M (2015) Synthesis and characterization of hydroxypropyl methylcellulose-g-poly(acrylamide)/LAPONITE RD nanocomposites as novel magnetic- and pH-sensitive carriers for controlled drug release. *RSC Adv* 5:44516–44523. <https://doi.org/10.1039/C5RA03731J>
4. Ghadiri M, Chrzanowski W, Rohanzadeh R (2015) Biomedical applications of cationic clay minerals. *RSC Adv* 5:29467–29481. <https://doi.org/10.1039/C4RA16945J>
5. Neumann BS (1965) Behaviour of a synthetic clay in pigment dispersions. *Rheol Acta* 4:250–255. <https://doi.org/10.1007/BF01973660>
6. Shafran K, Jeans C, Kemp SJ, Murphy K (2020) Dr Barbara S. Neumann: clay scientist and industrial pioneer; creator of Laponite[®]. *Clay Miner* 55:256–260. <https://doi.org/10.1180/clm.2020.35>
7. Zhang J, Zhou CH, Petit S, Zhang H (2019) Hectorite: synthesis, modification, assembly and applications. *Appl Clay Sci* 177:114–138. <https://doi.org/10.1016/j.clay.2019.05.001>
8. Gholamipour-Shirazi A, Carvalho MS, Huila MFG, Araki K, Dommersnes P, Fossum JO (2016) Transition from glass-to gel-like states in clay at a liquid interface. *Sci Rep* 6:37239. <https://doi.org/10.1038/srep37239>
9. Samoylenko O, Korotych O, Manilo M, Samchenko Y, Shlyakhovenko V, Lebovka N (2021) Chapter 15. Biomedical Applications of Laponite[®]-based Nanomaterials and Formulations. In: Bulavin L, Lebovka N (eds) *Soft matter systems for biomedical applications*. Springer Proceedings in Physics, pp 385–452
10. Goncharuk O, Samchenko Y, Kernosenko L, Korotych O, Poltoratska T, Pasmurtseva N, Oranska O, Sternik D, Mamyshev I (2020) Thermoresponsive hydrogels physically crosslinked with magnetically modified LAPONITE[®] nanoparticles. *Soft Matter* 16:5689–5701. <https://doi.org/10.1039/D0SM00929F>

11. Goncharuk O, Samchenko Y, Sternik D, Kernosenko L, Poltorats'ka T, Pasmurtseva N, Abramov M, Pakhlov E, Derylo-Marczewska A (2020b) Thermosensitive hydrogel nanocomposites with magnetic laponite nanoparticles. *Appl Nanosci* 1–11. <https://doi.org/10.1007/s13204-020-01388-w>
12. Lebovka NI, Samchenko YM, Kernosenko LO, Poltoratska TP, Pasmurtseva NO, Mamyshev IE, Gigiberiya VA (2020) Temperature sensitive hydrogels cross-linked by magnetic laponite RD: effects of particle magnetization. *Mater Adv* 1:2994–2999. <https://doi.org/10.1039/D0M00687D>
13. Mahdavinia GR, Mousanezhad S, Hosseinzadeh H, Darvishi F, Sabzi M (2016) Magnetic hydrogel beads based on PVA/sodium alginate/laponite RD and studying their BSA adsorption. *Carbohydr Polym* 147:379–391. <https://doi.org/10.1016/j.carbpol.2016.04.024>
14. Tzitzios V, Basina G, Bakandritsos A, Hadjipanayis CG, Mao H, Niarchos D, Hadjipanayis GC, Tucek J, Zboril R (2010) Immobilization of magnetic iron oxide nanoparticles on Laponite discs – an easy way to biocompatible ferrofluids and ferrogels. *J Mater Chem* 20:5418. <https://doi.org/10.1039/c0jm00061b>
15. Cousin F, Cabuil V, Grillo I, Levitz P (2008) Competition between entropy and electrostatic interactions in a binary colloidal mixture of spheres and platelets. *Langmuir* 24:11422–11430. <https://doi.org/10.1021/la8015595>
16. Cousin F, Cabuil V, Levitz P (2002) Magnetic colloidal particles as probes for the determination of the structure of laponite suspensions. *Langmuir* 18:1466–1473. <https://doi.org/10.1021/la010947u>
17. Galicia JA, Sandre O, Cousin F, Guemghar D, Ménager C, Cabuil V (2003) Designing magnetic composite materials using aqueous magnetic fluids. *J Phys Condens Matter* 15:S1379. <https://doi.org/10.1088/0953-8984/15/15/306>
18. de Paula FLO, da Silva GJ, Aquino R, Depeyrot J, Fossum JO, Knudsen KD, Helgesen G, Tourinho FA (2009) Gravitational and magnetic separation in self-assembled clay-ferrofluid nanocomposites. *Braz J Phys* 39:163–170. <https://doi.org/10.1590/S0103-9733200900200007>
19. Weeber R, Hermes M, Schmidt AM, Holm C (2018) Polymer architecture of magnetic gels: a review. *J Phys Condens Matter* 30:63002. <https://doi.org/10.1088/1361-648X/aaa344>
20. Mahdavinia GR, Soleymani M, Etemadi H, Sabzi M, Atlasi Z (2018) Model protein BSA adsorption onto novel magnetic chitosan/PVA/laponite RD hydrogel nanocomposite beads. *Int J Biol Macromol* 107:719–729. <https://doi.org/10.1016/j.ijbiomac.2017.09.042>
21. Soleymani M, Akbari A, Mahdavinia GR (2019) Magnetic PVA/laponite RD hydrogel nanocomposites for adsorption of model protein BSA. *Polym Bull* 76:2321–2340. <https://doi.org/10.1007/s00289-018-2480-1>
22. Mahdavinia GR, Rahmani Z, Mosallanezhad A, Karami S, Shahriari M (2016) Effect of magnetic laponite RD on swelling and dye adsorption behaviors of κ -carrageenan-based nanocomposite hydrogels. *Desalin Water Treat* 57:20582–20596. <https://doi.org/10.1080/19443994.2015.1111808>
23. Mahdavinia GR, Soleymani M, Sabzi M, Azimi H, Atlasi Z (2017) Novel magnetic polyvinyl alcohol/laponite RD nanocomposite hydrogels for efficient removal of methylene blue. *J Environ Chem Eng* 5:2617–2630. <https://doi.org/10.1016/j.jece.2017.05.017>
24. Mola-ali-abasiyan S, Mahdavinia GR (2018) Polyvinyl alcohol-based nanocomposite hydrogels containing magnetic laponite RD to remove cadmium. *Environ Sci Pollut Res* 25:14977–14988. <https://doi.org/10.1007/s11356-018-1485-5>
25. Thompson DW, Butterworth JT (1992) The nature of laponite and its aqueous dispersions. *J Colloid Interface Sci* 151:236–243. [https://doi.org/10.1016/0021-9797\(92\)90254-J](https://doi.org/10.1016/0021-9797(92)90254-J)
26. Fripiat JJ, Letellier M, Cases JM, Francois M, Delon JF, Rouquerol J (1982) Comportement microdynamique et thermodynamique de l'eau dans les suspensions argileuses. *Stud Surf Sci Catal* 10:449–477
27. Anonymous (2018) Technical Information B-RI 21 Laponite. Performance Additives. BYK
28. Mahadevan S, Gnanaprakash G, Philip J, Rao BPC, Jayakumar T (2007) X-ray diffraction-based characterization of magnetite nanoparticles in presence of goethite and correlation with magnetic properties. *Phys E* 39:20–25. <https://doi.org/10.1016/j.physe.2006.12.041>

29. Lugovskoy N, Berzhansky V, Semuk E, Shaposhnikov A (2019) Susceptibility and FMR in ferrite garnet epitaxial films for eddy current magneto-optical defectoscopy. *J Phys Conf Ser* 1389:12102
30. de Guimarães AMF, Ciminelli VST, Vasconcelos WL (2007) Surface modification of synthetic clay aimed at biomolecule adsorption: synthesis and characterization. *Mater Res* 10:37–41. <https://doi.org/10.1590/S1516-14392007000100009>
31. Pálková H, Madejová J, Zimowska M, Serwicka EM (2010) Laponite-derived porous clay heterostructures: II. FTIR study of the structure evolution. *Microporous Mesoporous Mater* 127:237–244. <https://doi.org/10.1016/j.micromeso.2009.07.012>
32. Balan E, Saitta AM, Mauri F, Lemaire C, Guyot F (2002) First-principles calculation of the infrared spectrum of lizardite. *Am Mineral* 87:1286–1290. <https://doi.org/10.2138/am-2002-1003>
33. Moenke HHW (1974) Vibrational spectra and the crystal-chemical classification of minerals. In: Farmer VS (ed) *The infrared spectra of minerals, VC*, mineralogical society monograph. Cambridge University Press, London (Mineralogical Society), pp 111–118
34. El-Mahdy GA, Atta AM, Al-Lohedan HA (2014) Synthesis and evaluation of poly (sodium 2-acrylamido-2-methylpropane sulfonate-co-styrene)/magnetite nanoparticle composites as corrosion inhibitors for steel. *Mol* 19:1713–1731. <https://doi.org/10.3390/molecules19021713>
35. Manuel J, Kim J-K, Ahn J-H, Cheruvally G, Chauhan GS, Choi J-W, Kim K-W (2008) Surface-modified maghemite as the cathode material for lithium batteries. *J Power Sources* 184:527–531. <https://doi.org/10.1016/j.jpowsour.2008.02.079>
36. Morales MP, Veintemillas-Verdaguer S, Montero MI, Serna CJ, Roig A, Casas L, Martinez B, Sandiumenge F (1999) Surface and internal spin canting in γ -Fe₂O₃ nanoparticles. *Chem Mater* 11:3058–3064. <https://doi.org/10.1021/cm991018f>
37. Iurascu B, Siminiceanu I, Vione D, Vicente MA, Gil A (2009) Phenol degradation in water through a heterogeneous photo-Fenton process catalyzed by Fe-treated laponite. *Water Res* 43:1313–1322. <https://doi.org/10.1016/j.watres.2008.12.032>
38. Le Luyer C, Lou L, Bovier C, Plenet JC, Dumas JG, Mugnier J (2001) A thick sol–gel inorganic layer for optical planar waveguide applications. *Opt Mater (Amst)* 18:211–217. [https://doi.org/10.1016/S0925-3467\(01\)00111-2](https://doi.org/10.1016/S0925-3467(01)00111-2)
39. Cabrera L, Gutierrez S, Menendez N, Morales MP, Herrasti P (2008) Magnetite nanoparticles: electrochemical synthesis and characterization. *Electrochim Acta* 53:3436–3441. <https://doi.org/10.1016/j.electacta.2007.12.006>
40. González-Martín R, Gutiérrez-Serpa A, Pino V (2021) The use of ferrofluids in analytical sample preparation: a review. *Sep* 8:47. <https://doi.org/10.3390/separations8040047>
41. Huke B, Lücke M (2004) Magnetic properties of colloidal suspensions of interacting magnetic particles. *Rep Prog Phys* 67:1731. <https://doi.org/10.1088/0034-4885/67/10/R01>

Technological Calculation of Granulation Equipment for the Production of Ammonium Nitrate with a Nanoporous Structure: Algorithm and Software Implementation



A. E. Artyukhov, I. I. Volk, J. Krmela, O. B. Shandyba, A. S. Chernenko, and D. Ospanov

Abstract The work is devoted to developing the optimal design for granulation equipment aimed to modify ordinary ammonium nitrate with the subsequent obtaining of nanoporous structure. We present the fundamental technological calculation of vortex-type granulation equipment with various configurations of a vortex fluidized bed (including a combined one). We introduce an algorithm for deriving the optimal design of a vortex granulator able to provide a developed nanoporous structure of ammonium nitrate granules and their specific properties. The need for an optimization calculation of granulation equipment using computer modeling was substantiated. We demonstrate computer modeling and automated computation in the general method of engineering calculation of granulation equipment. The electron microscopy results of porous ammonium nitrate samples are presented, and the pore structure features (size, configuration, specific porous volume, etc.) are analyzed.

Keywords Nanoporous structure · Ammonium nitrate · Granulation

A. E. Artyukhov (✉) · I. I. Volk
Sumy State University, Rymskogo-Korsakova Str., 2, Sumy 40007, Ukraine
e-mail: a.artyukhov@pohnp.sumdu.edu.ua

J. Krmela
Alexander Dubcek University of Trencin, I. Krasku, 491/30, 02001 Puchov, Slovak Republic

O. B. Shandyba
Sumy National Agrarian University, Herasya Kondratieva Str, Sumy 16040000, Ukraine

A. S. Chernenko
Odessa I.I. Mechnikov National University, Dvoryanskaya Str., 2, Odessa 65082, Ukraine

D. Ospanov
Saken Seifullin Kazakh Agrotechnical University, Zhenis Avenue, 62, Nur-Sultan 010011, Republic of Kazakhstan

1 Introduction

The technology for producing porous ammonium nitrate (PAN) involves various methods of its implementation.

PAN can be obtained using one of the following methods:

1. *PAN obtained through pore-forming substances and surfactants*

The essence of these methods lies in the fact that pore-forming substances evenly distributed in the melt volume or in ammonium nitrate solution evaporate during the subsequent crystallization and drying of the product, resulting in voids and capillaries forming in particles of the product, increasing its sorption properties.

Non-volatile pore-forming substances possessing sorption properties addition to the nitrate solution or melt results in the increase of nitrate granules porosity both due to the properties of the additive itself and due to the occurrence of artificial crystallization centers in the melt that change the crystal structure of granules.

According to [1], granular PAN is obtained by initially introducing the aqueous ferric sulfate solution into a concentrated melt with ferric sulfate content of 0.06–0.08% (mass) in terms of Fe. The obtained granules do not agglomerate, possess water-repellant properties, and have the durability of 760 g/granule.

However, ammonium nitrate granules obtained this way tend to have low durability and a high degree of caking, which forbids transporting the product without proper containers.

Increasing PAN quality, including the increase in durability and water repellency and reduction of caking, is done by introducing an additive containing ferric sulfate into the concentrated melt of ammonium nitrate and further adding the suspension consisting of pore-forming chalk and dispersant additives. The obtained granules are treated with a mixture of fatty acids and paraffin.

The method of obtaining a porous granular ammonium nitrate with the proposed sequence of additives introduction into the concentrated melt of ammonium nitrate provides an increase in durability and water repellency of the granules due to the presence of the Fe ion. Ferric sulfate with excess acidity partially interacts with the chalk to form calcium sulfate, which also helps to increase granules' durability. Carbon dioxide released as a result of the reaction increases the porosity of the granules of ammonium nitrate.

In addition, part of the ferric sulfate reacts with fatty acids, forming a film of iron salts of fatty acids on the surface of the granules, thus increasing the water repellency.

After introducing ferric sulfate and pore-forming (chalk and dispersant) additives, the process is carried out according to the common scheme, i.e., the melt is

granulated. The granules are treated with a mixture of fatty acids and paraffin in the amount of 0.3%.

Granular PAN shows little tendency to cake, which allows transporting the product in bulk.

The production of PAN is also carried out in a heat-insulated tank, where the first granulated ammonium nitrate is loaded. Then, liquid nitrogen is fed into the lower part of the tank. The evaporation of nitrogen is provoked by exposing it to low temperatures. The formed stream of nitrogen gas is directed to the granules of ammonium nitrate. It forms a fluidized bed, where heat is exchanged between low-temperature nitrogen gas and granular ammonium nitrate (having the temperature equal to ambient one) up until the latter cools down to negative temperatures. After completion of the processing in the fluidized bed, ammonium nitrate with increased porosity due to previous processes is unloaded from the tank into a sealed storage hopper without air access.

Pros of this methods group: good sorption capacity and porosity.

Cons of this methods group: the ability of crystals to cake and stick together, the long duration of the process.

2. *Obtaining PAN by heat treatment of its granules*

Thermal methods are based on ammonium nitrate crystal lattice properties to experience polymorphic transformations at certain temperatures, which occur with a change in the volume of the crystals. Under certain conditions, the granules increase slightly in volume and become less dense and more porous.

According to [2], granular ammonium nitrate is subjected to the different number of heating and cooling cycles. The process of obtaining granular porous ammonium nitrate is carried out as follows. The melt with the concentration of 99.7% NH_4NO_3 at a temperature of 178 °C is sprayed in the granulation tower, and the cooling process of the melt drop in the tower is regulated so that the granules come out at 100 ÷ 110 °C. Then, the granules are cooled in rotating drums or in a fluidized bed below 32 °C and reheated above 84 or 124 °C. The granules can be heated either in a paddle stirrer with a steam jacket or in a dryer by airstream at 140°C. The hot nitrate granules coming out of the dryer are again cooled by air to a temperature below 32 °C in the cooling drums and the heating–cooling cycle is repeated several times, after which the porous granules are obtained in bulk density 772 kg/m³ with sorption capacity of 10% and porosity of 21.8%.

For deeper impregnation of granules with liquid fuel, it is recommended to heat and cool the granules in a mixture with liquid fuel, bringing the mixture's temperature close to the temperature of allotropic transformations. Then, the mixture is cooled and the heating–cooling cycle is repeated.

The heat treatment method is sometimes combined with humidifying the granules with a solution or water and the addition of crushed substances that do not dissolve

in the melt. This allows obtaining a product with the specified quality indicators by varying heating and cooling temperature and the cyclicity of humidification of the granules with the solution.

In the process of heat treatment, nitrate granules become less durable. The decrease in the mechanical durability of the granules is directly dependent on the number of heat treatment cycles. In addition, the presence of certain impurities in the nitrate causes a significant impact. The granules of ammonium nitrate, which have no impurities, lose their durability first. In this case, 4–5 cycles of heat treatment are enough for the complete destruction of such nitrate granules. Weak granules of porous ammonium nitrate, passing through various transport and mixing devices, are partially destroyed, increasing the content of dust particles in the product, which complicates its further use.

To increase the durability of PAN granules, 0.3–0.4% ammonium sulfate is added to the solution during production. Next, calcium nitrate solution at the rate of 0.1–0.4% CaO is added to the previously formed melt. Thus, calcium sulfate is formed due to the joint presence of these components in melted ammonium nitrate, which has cementing effect and reduces the loss of durability of the granules during their subsequent heat treatment.

Pros of this methods group: good sorption capacity and porosity.

Cons of this methods group: loss of durability of the output product due to heat treatment.

3. *Obtaining porous ammonium nitrate by drying its granules or crystals*

This method is based on the fact that the pore formation process takes place in ammonium nitrate granules or crystals in the drying process. Moisture is removed in various ways: in the devices working at rarefaction, in rotating sequentially included drums, or in the suspended layer devices.

According to [3], obtaining a granular ammonium nitrate including granulation of a hot melt of ammonium nitrate in a rotating granulator by applying the melt to the surface of the cooled solids with the formation during its rotation of the finished product and its subsequent unloading at a temperature 4–25 °C below its point melting, characterized in that before granulation the flow of hot melt of ammonium nitrate is divided into two independent streams, in one of which the concentration of ammonium nitrate is adjusted to 0.2–0.5% H₂O, and in the second to 1–5% H₂O, after where the first stream is fed to the surface of the cooled solids and when the particles of solids and temperatures above 115–135 °C is treated with a secondary stream.

Work [3] discussed PAN obtaining method based on granulating hot melt of ammonium nitrate in rotating granulator through directing the melt on the surface of cool solids. Output product is formed during the granulator rotation and is unloaded at temperatures 4–25 °C below the melting point. This operation stands

out by separating the hot melt stream into two independent streams before granulation. The concentration of ammonium nitrate reaches 0.2–0.5% H₂O in one stream and 1–5% H₂O in other one. After reaching these concentrations, the first stream is directed on the surface of cool solids, and when solid particles reach a temperature of 115–135 °C and higher they are exposed to the second stream.

However, this method is characterized by the low productivity of the granulator and the insufficient durability of the obtained granules at high porosity. According to this method, the granulator performance depends on the amount of heat that can be received by the cooled solid (return) that came to the granulator. This, in turn, is determined by the temperature difference between the return particles and output product, along with the amount of return fed to the granulator.

Vacuum drying method for obtaining PAN is proposed in [4]. According to it, ammonium nitrate solution saturated at 90–100 °C is fed into the first vacuum camera from where at nearly 120 °C it is fed into the next camera under deeper vacuum and where at 50 °C the melt is dried to the moisture level approx. 0.07%. PAN granules have a density of 400–500 kg/m³.

It is recommended to mix granular or crystalline ammonium nitrate with about 10% water for a short time, sufficient to only wet the surface of the granules. A concentrated solution of ammonium nitrate can be used instead of water. The wet mixture is dried at the inlet air temperature 120 °C. To reduce the solubility of nitrate on the surface of the granules, a small fraction of dry granules is added to the moistened mixture and before drying. The bulk density of the obtained product is 730–770 kg/m³.

Pros of this methods group: good sorption capacity and porosity.

Cons of this methods group: relatively complex technological production line.

Other methods for obtaining PAS are also presented in the works [5–10].

The main indicator of PAN quality is the absorption and retention capacity in relation to diesel fuel. Each of the listed methods provides the required value of these indicators. At the same time, ecological indicators of production decrease (method 1), there is a loss in granules durability (method 2), and the production line becomes complicated (method 3).

To eliminate the shortcomings of PAN obtaining methods stated in the review, we propose a new organization of the process using equipment with vortex and highly turbulent flows [12–16]. The diagram of this method is presented in Fig. 1 based on the data of the author's materials [17–20].

The theoretical foundations of the granulation and dehydration processes during the PAN obtaining are based on fundamental works [21–25].

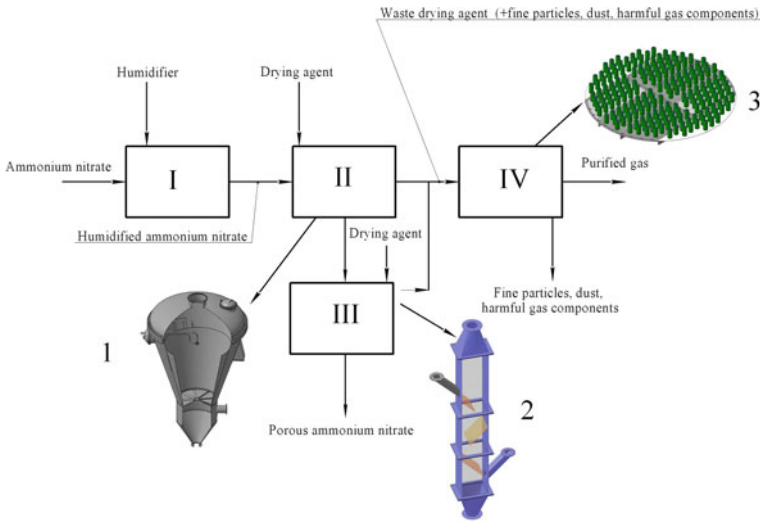


Fig. 1 Diagram of porous ammonium nitrate production according to the method [11]: I—humidification of ordinary ammonium nitrate; II—heat treatment and drying of ordinary ammonium nitrate after humidification; III—final drying of PAN; IV—cleaning of exhaust gases; 1—vortex granulator; 2—multistage gravitational shelf dryer; 3—contact tray with heat and mass transfer-separation elements

2 Technological, Constructive, and Optimization Calculation

For each element of the technological scheme, technological, and constructive calculations are performed through the following algorithm:

1. Technological calculation with pore formation process main parameters determination:
 - Vortex granulator: temperature, stream rates, humidifier properties, and seeding agent properties;
 - Multistage gravitational shelf dryer: temperature, stream rates, drying agent properties, and seeding agent properties;
 - Contact tray with heat and mass transfer-separation elements: temperature, stream rates, and exhaust gas properties.
2. Optimization calculation with the determination of the optimal technological parameters at each stage of the PAN production process and the optimal equipment design. It is performed on the design stage of the vortex granulator and multistage gravitational shelf dryer based on microscopic research on PAN granules obtained by different technological modes.
3. Final decision on the main technological parameters of the process and equipment design.

4. Constructive calculation determining the size of the apparatus and their design features:
 - Vortex granulator: working space dimensions;
 - Multistage gravitational shelf dryer: working space dimensions and shelf structure on each stage;
 - Contact tray with heat and mass transfer-separation elements: contact nozzles dimensions and plate surface dimensions.

As a result of the calculations, the final design of the equipment is formed. (Fig. 2).

3 Properties of Nanoporous Layers in Granules of PAN

As stated above, the optimization calculation of PAN with nanoporous structure obtaining process is one of the main stages in the design of the technological scheme. This stage is carried out considering the following characteristics of the work process:

1. Fractional composition of seeding agent.
2. Humidifier properties.
3. Unit performance.

The experimental batch of PAN is obtained based on previous research on the main equipment design for the selected parameters from items 1–3. Experimental PAN batch (showcase fraction) has to possess the following properties:

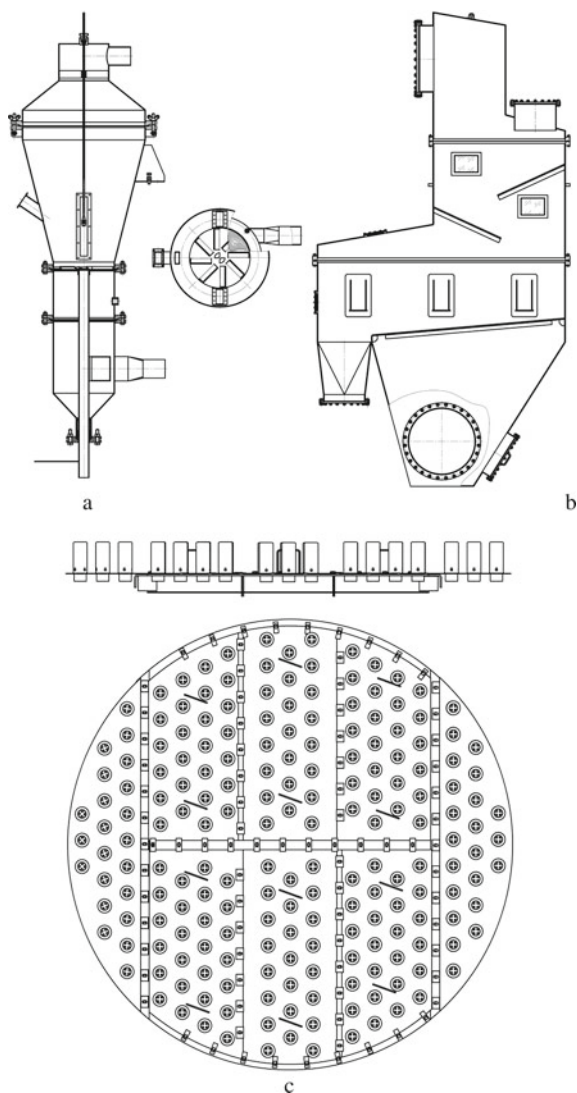
1. Uniform porous structure.
2. The minimal number of “mechanical” pores.
3. Nanopores are predominantly curvilinear and deep.
4. Integrity of the granule core.
5. Standard value of durability.
6. Standard value of the absorbency and retention capacity in relation to liquid fuels.

Figure 3 presents the examples of microscopy results of PAN granules nanoporous structure, obtained as a result of experimental studies at the optimization calculation stage. As shown in the figures, obtaining a developed nanoporous structure is possible after several stages of adjusting the optimal conditions for the pore formation process.

4 Conclusions

The design of PAN with a developed nanoporous structure production facility is carried out based on an optimization calculation considering the results of experimental research. This process is multistage and implementation gaps are identified at each stage. After the approval of optimal technological parameters for process implementation, a constructive calculation of the main unit equipment is performed.

Fig. 2 Main equipment of a granulation unit for PAN with nanoporous structure generation: 1—vortex granulator; 2—multistage gravitational shelf dryer; 3—contact tray with heat and mass transfer-separation elements



The apparatus's dimensions and design are selected to provide the necessary hydrodynamic and thermodynamic operating conditions of the facility at each stage of nanoporous structure formation.

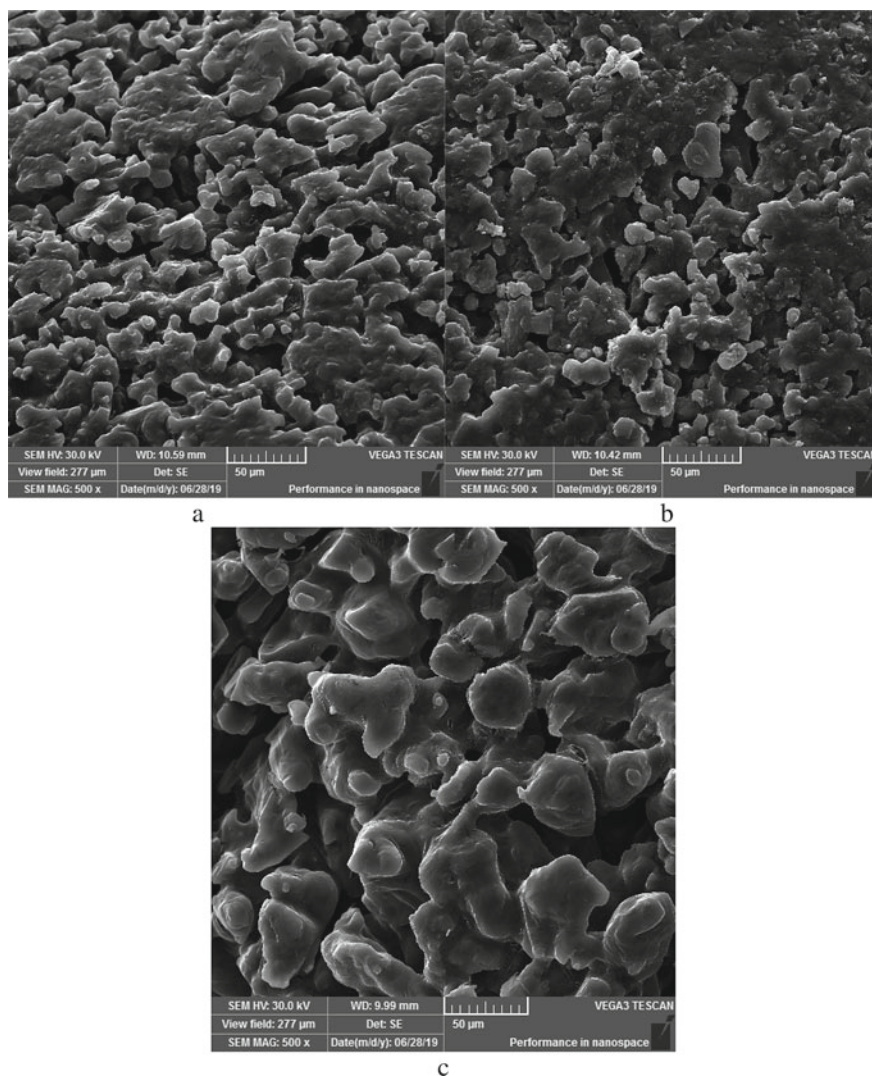


Fig. 3 Results of electron microscopy of PAN samples with nanoporous structure: **a**—non-porous areas with uneven humidification; **b**—non-porous areas with insufficient residence time at the granulation stage; **c**—developed nanoporous structure at the optimal implementation of the process

Acknowledgements This research work had been supported by the Ministry of Science and Education of Ukraine under the project “Development of a vortex granulator for obtaining granules of porous ammonium nitrate”, project No. 0121U109465.

References

1. Patent 2063929 RU (1996) Method for producing porous granular ammonium nitrate
2. Patent 2018503 RU (1994) Method for producing porous granular ammonium nitrate
3. Patent 9483 UA (1996) Method for producing porous granular ammonium nitrate
4. Patent 2021235 RU (1998) Method for producing porous granular ammonium nitrate
5. Janssen TJ (2011) Explosive materials: classification, composition and properties. Nova Science Publishers, Inc.
6. Erode GM (2013) Ammonium nitrate explosives for civil applications: slurries, emulsions and ammonium nitrate fuel oils. Wiley-VCH Verlag & Co, Weinheim
7. Kubota N (2015) Propellants and explosives: thermochemical aspects of combustion, 3rd edn. Wiley-VCH Verlag & Co, Weinheim
8. Zygmunt B, Buczkowski D (2007) Influence of ammonium nitrate prills' properties on detonation velocity of ANFO. *Propellants Explos Pyrotech* 32(5):41–414
9. Lipinska K et al (2005) Demilitarized propellants as ingredients in commercial explosives. In: European federation of explosives engineers. Brighton Conference Proceedings, Brighton, pp 493–498
10. Martin G, Barbour W (2003) Industrial nitrogen compounds and explosives, chemical manufacture and analysis. Watchmaker Publishing
11. Artyukhov AE, Ivaniia AV (2017) Obtaining porous ammonium nitrate in multistage and multifunctional vortex granulators. *Naukovyi Visnyk Natsionalnoho Hirnychoho Universytetu* 6:68–75
12. Artyukhov AE, Artyukhova NO (2019) Technology and the main technological equipment of the process to obtain N_4HNO_3 with nanoporous structure. *Springer Proc Phys* 221:585–594
13. Obodiak V, Artyukhova N, Artyukhov A (2020) Calculation of the residence time of dispersed phase in sectioned devices: theoretical basics and software implementation. In: *Advances in design, simulation and manufacturing II*. DSMIE 2019. Lecture notes in mechanical engineering. Springer, Cham, pp 813–820
14. Yukhymenko M, Ostroha R, Artyukhov A (2016) Hydrodynamic and kinetic processes of the mineral fertilizer granules encapsulating in the multistage device with suspended layer. *East Eur J Enterp Technol* 6(6–84):22–28
15. Artyukhov A, Gabrusenoks J (2018) Phase composition and nanoporous structure of core and surface in the modified granules of N_4HNO_3 . *Springer Proc Phys* 210:301–309
16. Ostroha R, Yuhymenko M, Yakushko S, Artyukhov A (2017) Investigation of the kinetic laws affecting the organic suspension granulation in the fluidized bed. *East Eur J Enterp Technol* 4(1):4–10
17. Artyukhov AE, Krmela J, Gavrylenko OM (2019) Evaluation of the impact made by the hydrodynamic regime of the granulation equipment operation on the nanoporous structure of N_4HNO_3 granules. *J Nano Electron Phys* 11(3):03033
18. Artyukhov A, Artyukhova N, Krmela J, Krmelová V (2020) Complex designing of granulation units with application of computer and software modeling: case “vortex granulator.” *IOP Conf Ser Mater Sci Eng* 776(1):012016
19. Ivaniia AV, Artyukhov AY, Olkhovik AI (2019) Hydrodynamic and thermodynamic conditions for obtaining a nanoporous structure of ammonium nitrate granules in vortex granulators. *Springer Proc Phys* 221:257–268
20. Artyukhov A, Artyukhova N, Ivaniia A, Galenin R (2017) Progressive equipment for generation of the porous ammonium nitrate with 3D nanostructure. In: *Proceedings of the 2017 IEEE 7th International conference on nanomaterials: applications and properties (NAP)*. IEEE, pp 03NE06-1-03NE06-4
21. Kudra T, Mujumdar AS (2002) *Advanced drying technologies*. Marcel Dekker, New York
22. Sinaiski EG (2010) *Hydromechanics: theory and fundamentals*. WILEY-VCH Verlag GmbH & Co. KGaA, Weinheim
23. Wan Daud WR (2008) Fluidized bed dryers – recent advances. *Adv Powder Technol* 19(5):403–418

24. Crowe C (2006) Multiphase flow handbook. Taylor & Francis Group, Boca Raton
25. Mujumdar AS (2006) Handbook of industrial drying. Taylor & Francis Group, Boca Raton

Glass Binding for Nanocomposite Materials for Thick-Film Hybrid Integrated Circuits



Ya. I. Lepikh, V. A. Borshchak, N. N. Sadova, and N. P. Zatovskaya

Abstract Modern multilevel hybrid integrated circuits (HIC) and microelectronic sensors are widely used as thick-film elements dispersed composites based on «glass–metal compounds», which are a multiphase heterogeneous system consisting of powder functional material, glass powders, and organic compounds and are formed by annealing. The composite formation is accompanied by complex physical and chemical processes between the conductive phase, on the one hand, and the glass component, on the other hand, and determine, under the selected annealing modes, the phase composition, microstructure, and electrophysical parameters of the obtained nanocomposites.

1 Introduction

Currently, composite materials are widely used, representing a multiphase heterogeneous system consisting of components with various physical and chemical properties. One of the main structural elements that determine the relationship between the structure and the nanocomposite electrophysical parameters is the glass component. In the process of nanocomposites annealing, glass powders melt and sinter into a glass matrix, which, on the one hand, ensures the adhesion of the composition to the lining, and on the other hand, creates a “rigid frame” that fixes the position of the conductive phase particles. Thus, the glasses perform two functions: they keep the particles of the functional material in contact and ensure the fixation of the composition on the substrate.

The most important characteristics when choosing a permanent glass binder are the temperature dependence of the glass viscosity, which determines the annealing mode of the composition, surface tension, with the effect of which the phenomena of wetting, adsorption, action of capillary forces, chemical activity, and coefficient of thermal expansion are associated. By ensuring the stability of the glass component

Ya. I. Lepikh (✉) · V. A. Borshchak · N. N. Sadova · N. P. Zatovskaya
Odesa I.I. Mechnikov National University, 2 Dvoryanska Str, Odesa 65082, Ukraine
e-mail: ndl_lepikh@onu.edu.ua

© The Author(s), under exclusive license to Springer Nature Switzerland AG 2023
O. Fesenko and L. Yatsenko (eds.), *Nanomaterials and Nanocomposites, Nanostructure Surfaces, and Their Applications*, Springer Proceedings in Physics 279,
https://doi.org/10.1007/978-3-031-18096-5_31

531

characteristics, it will be possible to solve the problems associated with negative processes occurring in glasses over time and causing HIC failure.

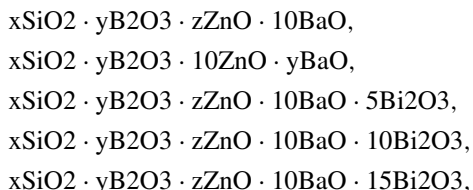
2 Research Methods

Experimental studies on the development of new glass compositions were carried out using the method of constructing diagrams of multicomponent systems based on a picture of sections by hyperplanes with a given percentage of one or more components of multidimensional figures depicting systems in multidimensional space. The method makes it possible to find out the influence of the components of the systems on the glasses properties. Glasses were obtained by melting the charge in a fiery gas furnace. The charge was made up of quartz sand, chemically pure barium carbonate, boric acid, and bismuth dioxide. Glass melting was carried out at temperatures of 900–1200 °C in porcelain crucibles with a sinter of 0.3 L. A neutral environment was maintained in the furnace during the entire cooking process. Samples were annealed in an electric muffle at a temperature of 300–350 °C for 1 h. Cooling was carried out inertially together with the furnace during the day. The glass crystallization ability was determined by the gradient method in the range of 400–800 °C with a two-hour exposure. The temperature in the gradient furnace was maintained automatically. When studying the crystallization ability, the temperature of the upper and lower crystallization boundaries was visually determined. The softening onset temperature was measured by immersing the tip of the rod into the glass under the load 100 g. The onset of softening was recorded by a dial indicator with a scale of 0.002 mm. The thermal expansion coefficient was measured by the dilatometric method in the temperature range 20–400 °C. The chemical stability of the experimental glasses was determined by the accelerated powder method with respect to the action of water, alkali, and acids. A weighed portion of the powder with a grain size of 0.25–0.5 mm in an amount of 2 g was kept in 100 ml of the solution at the boiling point for an hour. Chemical resistance was expressed by weight loss as a percentage of the original sample.

3 Results and Discussion

The glass component is a complex system, divided into two main parts: unchanged (main)—an alloy of siliceous, which in most glasses is 60% and variable—metal oxides, and besides their nature and ratio determine the main properties of glasses. Analysis of works in the field of a permanent binder application for nanocomposites showed that it is advisable to use borosilicate glasses as a glass component, which contain oxides of barium, zinc, and bismuth [1–4]. Bismuth oxide, according to literature data [1], promotes stabilization dielectric constant of pastes, does not affect the conductive part of the HIC elements and is introduced into the glass composition as

a neutral material in this respect. It also improves the wetting and adhesion of glass to the substrate, takes part in the structure creation as a glass former, and replaces toxic lead oxide. In this work, the $\text{SiO}_2\text{-B}_2\text{O}_3\text{-Bi}_2\text{O}_3\text{-BaO-ZnO}$ system was studied. The synthesis of glasses was carried out in the offensive crossings of the system:



where x varied from 35 to 60 ml. %, y —from 5 to 10 ml. %, and z —from 25 to 45 ml. %. Glasses of the first series ($\text{BaO} = \text{const} = 10\%$) were cooked in an electric furnace at a temperature of 1300°C without holding. Opaque milky glasses were obtained. Glasses of series 2 ($\text{ZnO} = \text{const} = 10\%$) were cooked at a temperature of 1430°C with exposure at a maximum temperature of 1.5 h. Transparent glasses were obtained (Fig. 1). As shown by experimental data, with an increase in temperature from 1300°C (the first series of glasses) to 1430°C , cooking properties are significantly improved. If in the first series were obtained opaque milky glasses, then with an increase in the melting temperature to 1430°C , the area of transparent glasses increases.

The research results showed that glasses containing boron oxide concentration from 5 to 15 mol% partially crystallize, forming a crystal crust (Fig. 2).

An increase in the concentration of B_2O_3 in the glass composition enhances the crystallization ability. The measured softening temperature of the studied glasses is within $440\text{--}635^\circ\text{C}$. To reduce the softening temperature of the research glasses, CdO was introduced into the above system, and BaO was replaced with MgO . Thus, the $\text{SiO}_2\text{-B}_2\text{O}_3\text{-Bi}_2\text{O}_3\text{-ZnO-CdO-MgO}$ system was obtained, a part of which,

Fig. 1 Skilting in the $\text{SiO}_2\text{-B}_2\text{O}_3\text{-Bi}_2\text{O}_3\text{-BaO-ZnO}$ ZnO systems at a brew glass 1430°C . (•—milky colored glasses, ○—glazed glass)

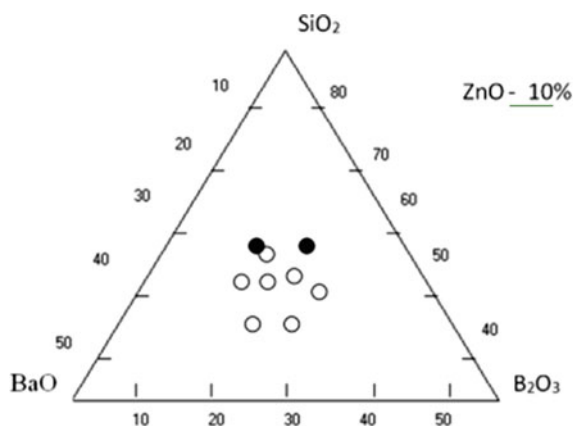
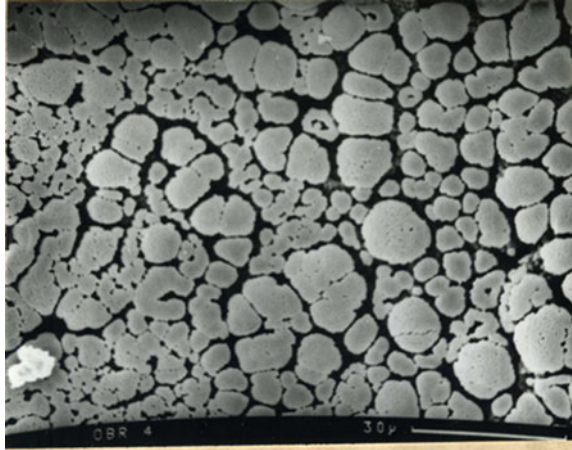


Fig. 2 Surface of a nanocomposite film in the presence of a crystal crust on the surface. Increase-500



namely $x\text{SiO}_2\text{-}y\text{B}_2\text{O}_3\text{-}30\text{Bi}_2\text{O}_3\text{-}z\text{ZnO}\text{-}10\text{CdO}\text{-}2.5\text{MgO}$, was studied. Experimental data have shown that glasses of this intersection are well boiled and clarify under experimental conditions, although on the surface of the molten glass they have an insignificant floating crust in the form of a gray bloom. The cooking temperature does not exceed 1000 °C. Cadmium oxide provides a beneficial effect on the improvement of glass formation processes (lowering the cooking temperature to 900 °C). It was established by preliminaries that in a given section the glasses are resistant to crystallization and remain transparent during heat treatment in the entire temperature range (Fig. 3).

Analysis and generalization of the results of studying of the $\text{SiO}_2\text{-B}_2\text{O}_3\text{-Bi}_2\text{O}_3\text{-ZnO-MgO-CdO}$ system glasses properties made it possible to suggest that an increase in the softening onset temperature and a decrease in LTEC of these glasses depend on

Fig. 3 Surface of a crystallization-resistant nanocomposite film. Increase-500



their chemical composition and are determined by the characteristics of the cations included in the glass structural network.

Thus, a high electronegativity, a high degree of a covalent bond, a small ionic radius, and a high valence of Si + 4 cations provide a denser packing in the glass structure and a high bond strength, and contributes to an increase in the softening temperature. Studies have shown that the tested glasses are resistant to water. The weight loss of the powder upon boiling for five hours in water ranged from 0.01 to 0.05%. The destructive effect of water increases with an increase in the content of boron oxide in their compositions and a decrease in zinc oxide. Zinc oxide is most effective in increasing the chemical resistance to water. It has been established that the water resistance of glasses mainly depends on boron and zinc and increases in inverse proportion to the increase in the content of B_2O_3 .

4 Conclusion

During the research, we found that the glass component of nanocomposites provides the distribution of particles of the functional material and adhesion to the substrate. In the process of the element annealing, it is not removed and remains in the finished product. When choosing a glass composition, it is necessary to take into account the dependence of its viscosity on temperature, substrate wetting, chemical activity, thermal expansion coefficient, and crystallization features. These properties of glass affect the modes of heat treatment of nanocomposites, the formation of mechanical bonds between the grains of the functional material and the resistivity of the film. The stability of the nanocomposite parameters largely depends on the composition of the glass component.

It was found that an increase in the softening temperature and a decrease in the LTEC of glasses depend on their chemical composition and are determined by the characteristics of the cations included in the structural glass network. It is shown that glasses containing boron oxide with concentration from 5 to 15 mol% partially crystallize, forming a crystal crust. An increase in the concentration of B_2O_3 in the glass composition enhances the crystallization ability.

It has been established that the water resistance of glasses mainly depends on boron and zinc and increases in inverse proportion to the increase in the content of B_2O_3 . Low-melting glass for thick-film nanocomposites does not contain toxic lead compounds.

References

1. Patent na vinakhid № 113565 A2017 10203, Legkoplavke sklo dla nanokompozitiv// Lepikh .I., Lavrenova T.I.// Opubl. Bul. № 3/2017 vid 10.02.2017. zajavl.08.11.2017. (Patent for the invention No. 113565 A2017 10203, Easymelt Glass for nanocomposites // Lepikh. Bul. No. 3/2017 dated February 10, 2017. declared 08.11.2017.)
2. Chamuylova V.N., Manchenko Z.F. Cintez i issledovanie vismutsodergashchikh legkoplavkikh stekol.–V kn.: Cteklo, sitaly i silikaty. Minck, izd. BPI. – 1978. 137 - №7. – c. 39–45. (Chamuylova V.N., Manchenko Z.F. Synthesis and study of bismuth-containing low-melting glasses.–In the book: Glass, glass-ceramics and silicates. Minsk, ed. BPI. - 1978. 137 - No. 7. - with. 39–45.)
3. Annealing temperature modes influence on properties of heterophase nanocomposites based on ceramics “glass - Ag-Pd” systems / Ya. I. Lepikh, T. I. Lavrenova T. N. Bugayova, N. P. atovskaya, P. O. Snigur // Functional Materials - 2014. - 21, № 3. - C. 297–301.
4. Aoki Ceiki, Bada Micyo. Steklo dla rezistora na osnove glazuri, sodergashchikh okis kadmjai //Yapon. Pat. Kl. CO3 c 3/30, CO3 c 3/14, №47–753/9, opubl. 8.05.80. (Aoki Tseiki, Bada Michio. Glass for a resistor based on glazes containing cadmium oxides //Jap. Pat. Cl. CO3 c 3/30, CO3 c 3/14, no. 47–753/9, publ. 05/8/80.)

Influence of Titanium Nitride Thin Films on the Electrical Properties of Isotype n -TiN/ n -Si Heterostructures



I. G. Orletskyi, M. I. Ilashchuk, I. P. Koziarskyi, M. M. Solovan,
D. P. Koziarskyi, E. V. Maistruk, and O. A. Parfenyuk

Abstract The conditions for the formation of the energy barrier in isotypic n -TiN/ n -Si heterojunctions by the reactive magnetron sputtering method of thin films of titanium nitride on n -Si crystalline substrates have been studied. Based on the analysis of C - V -characteristics, the role of states localized at the n -TiN/ n -Si boundary in the formation of the energy barrier is clarified and its parameters are determined. A model of the energy diagram of the n -TiN/ n -Si heterojunction, which well describes the experimental electrophysical phenomena, is proposed. The mechanisms of electron motion through the energy barrier of the heterojunction at forward and reverse biases are analyzed according to the temperature dependences of the I - V characteristics.

Keywords Energy diagram · Heterostructures · I - V -characteristics · TiN · Current transfer

1 Introduction

Thin films of titanium nitride (TiN) have physical properties that contribute to widespread use in the creation of electronic devices. They are used in photovoltaic devices as an electrode material for dye-sensitized solar cells [1], in ultrathin organic solar cells [2], as selective contacts of organic–inorganic hybrid solar cells [3], in plasmonic silicon solar cells [4]. The wide band gap $E_g \approx 3.4$ eV and low electrical resistivity $\rho \approx 0.4 \Omega \text{ cm}$ [5, 6] allow to produce photosensitive TiN/ p -CdTe heterojunctions [7], in which the low-impedance front layer TiN provides a high degree of transmission of light quanta into the absorber layer. The high electrical conductivity of TiN films contributes to the efficient removal of charge carriers into the external electrical circuit. A wide range of values of the energy parameter work function 3.5–4.4 eV [8–11] obtained under different conditions of TiN films is used

I. G. Orletskyi · M. I. Ilashchuk · I. P. Koziarskyi (✉) · M. M. Solovan · D. P. Koziarskyi · E. V. Maistruk · O. A. Parfenyuk
Department of Electronics and Power Engineering, Yuriy Fedkovych Chernivtsi National University, Chernivtsi 58002, Ukraine
e-mail: i.koziarskyi@chnu.edu.ua

in semiconductor structures to create ohmic contacts to n -CdS [8], n -Si [12] and the gate electrodes of MOS structures on silicon based [13].

In addition to ohmic contacts, thin TiN films are able to form with semiconductors heterojunctions with diode properties. This is manifested when they are applied on semiconductor materials Ge [14, 15] and Si [16–20], and to crystals of compounds $\text{Hg}_3\text{In}_2\text{Te}_6$ [21] and InSe [22]. When using substrates with a hole type of electrical conductivity, the energy parameters and electrical properties of anisotypic heterojunctions TiN/Ge, TiN/ p -Si, TiN/ p - $\text{Hg}_3\text{In}_2\text{Te}_6$, and TiN/ p -InSe agree satisfactorily with models that use fixed at the heteroboundaries (~ 3.69 – 3.75 eV) value of work function for TiN films. When using these models for isotypic heterojunctions, such as TiN/ n -Si, there are discrepancies with the experimental data. Based on the model with constant energy parameters, the TiN/ n -Si heterocontact should be ohmic with the formation of an electron-enriched region in n -Si. Experimental data indicates the diode characteristics of the TiN/ n -Si heterojunction [18]. It is known that in isotypic heterojunctions a significant role in the properties is played by energy states at the boundary of the heterojunction [23, 24]. In this paper, based on the study and analysis of the electrical properties of the isotypic TiN/ n -Si heterojunction, which is made by reactive magnetron sputtering, clarified the role of energy states at the interface of TiN and n -Si materials in the formation of an energy barrier, which able to rectify current.

2 Experiment Details

Substrates of n -type silicon crystals were used to fabricate the structures. At a temperature of 295 K, they had a resistivity $\rho = 3 \Omega \text{ cm}$ and a concentration of charge carriers $n = 2.6 \cdot 10^{15} \text{ cm}^{-3}$. Location of the Fermi level in the band gap of Si $E_C - E = 0.23 \text{ eV}$.

Thin TiN films were applied by reactive magnetron sputtering at constant voltage use a titanium target in a mixture of nitrogen and argon gases on polished crystalline silicon substrates measuring $5 \text{ mm} \times 5 \text{ mm} \times 0.3 \text{ mm}$ using a Leybold-Heraeus L560 universal vacuum unit. Short-term etching of the surface with argon ions was used to clean the target and substrates. In the spraying process, the partial pressures of the gases in the vacuum chamber were: for argon— 0.35 Pa , for nitrogen— 0.7 Pa . Magnetron power— 120 W . The duration of the spraying process at a substrate temperature of 573 K was about 15 min. In this spraying mode, the TiN film had n -type conductivity, the specific conductivity at $T = 295 \text{ K}$ was $\sigma = 0.17 \Omega^{-1} \text{ cm}^{-1}$, the electron concentration $n = 1.7 \cdot 10^{19} \text{ cm}^{-3}$.

Ohmic contacts to the thin film of TiN were made by thermal evaporation of indium at a substrate temperature of 423 K. For Si substrates, ohmic contacts were made by pre-doping with phosphorus to a depth of $\sim 1 \mu\text{m}$ to form a strongly doped n^+ -Si layer. After that, an adhesive layer of chromium, a copper film to ensure electrical conductivity ($\sim 3 \mu\text{m}$ thick) and a nickel layer for passivation against oxidation were applied by thermal evaporation.

I-V-characteristics of *n*-TiN/*n*-Si heterostructures were measured using a hardware-software complex based on the Arduino platform, Agilent 34410A digital multimeter, and Siglent SPD3303X programmable power supply, which were controlled by a personal computer using software created by the authors in Labiew. The measurements of capacitance-voltage (*C-V*) characteristics of structures under investigation were carried out by a LCR Meter BR2876.

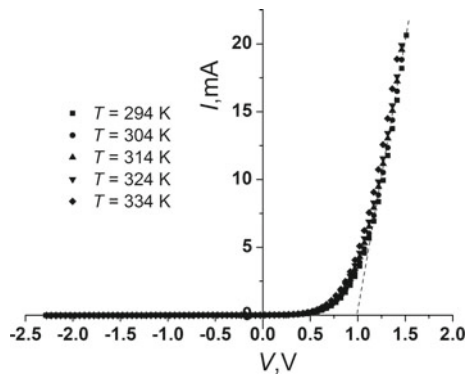
3 Results and Discussion

I-V-characteristics of isotypic *n*-TiN/*n*-Si heterojunctions in the temperature range $T = 294\text{--}334\text{ K}$ are shown in Fig. 1. The forward bias, at which an increase in current is observed, corresponds to a positive potential on the TiN film. At reverse voltages, a positive potential is applied to *n*-Si. The current rectification ratio (at $|V| = 1.5\text{ V}$ and $T = 294\text{ K}$) is $\sim 10^3$. A sharp increase in current at forward bias, by extrapolation of the rectilinear section of the *I-V*-characteristics is observed at a voltage of $V_0 \approx 1.0\text{ V}$.

As can be seen from Fig. 1, characteristic of currents measured in the area of forward biases, is their slight change with increasing temperature. This is usually observed in rectifier structures due to the temperature dependence of the height of the potential barrier due to the change with increasing temperature of the effective energy density in the allowed zones, the concentration of charge carriers and the band gap of the semiconductor. The value of the series resistance of the studied *n*-TiN/*n*-Si heterojunctions determined from the linear sections of the *I-V*-characteristics was $R_s = 23\ \Omega$, which corresponds to the resistance of the base material *n*-Si.

It should be noted that the surface energy levels at the interface of the structural components due to the misfit dislocations play a significant role in the formation of the profile of energy zones of isotypic heterojunctions, which in turn determine

Fig. 1 *I-V*-characteristic of the isotypic *n*-TiN/*n*-Si heterojunction at different temperatures



their main electrical and photoelectric properties. In the first approximation, their concentration $N_{ss} \sim x^{-2}$, where x is the distance between the misfit dislocations, which is determined by the following expression

$$x = a_{Si}a_{TiN} / (a_{Si} - a_{TiN}) \tag{1}$$

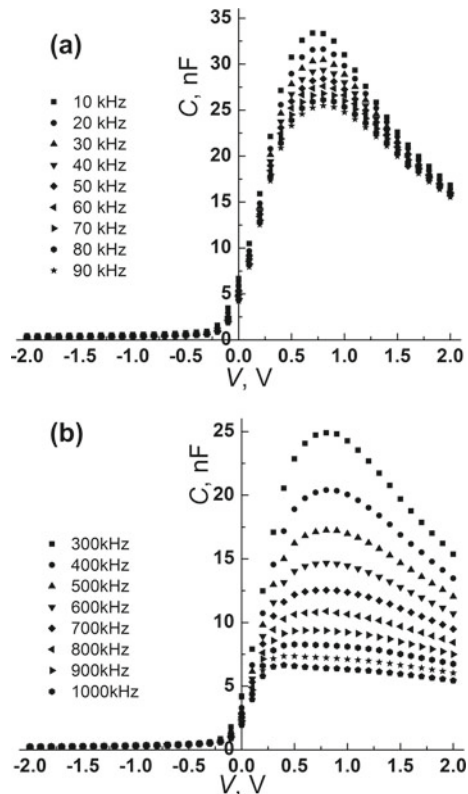
where a_{Si} , a_{TiN} are the lattice constants Si and TiN, respectively.

Using the values $a_{Si} = 5.43 \text{ \AA}$ and $a_{TiN} = 4.24 \text{ \AA}$ [20], we obtain $N_{ss} = 2.67 \cdot 10^{13} \text{ cm}^{-2}$. At this concentration, surface states, which are usually centers of capture or recombination, can significantly affect the profile of energy zones and the properties of heterojunctions [25].

To construct the energy diagram of n -TiN/ n -Si heterojunctions and determine their main parameters, a detailed analysis of C - V -characteristics measured at the low ($f = 10$ – 90 kHz) and high ($f = 300$ – 1000 kHz) frequencies of the excitation alternating signal was performed (Fig. 2).

In the region of reverse bias, the capacitance of the n -TiN/ n -Si heterojunction decreases with increasing external voltage, which is due to the expansion of the

Fig. 2 C - V -characteristics of n -TiN/ n -Si structures in the region of low $f = 10$ – 90 kHz **a** and high $f = 300$ – 1000 kHz **b** frequencies



space charge region in n -Si. At forward bias, the capacitance of the structure begins to increase sharply, which may explain the decrease in the thickness of the contact region depleted in the main charge carriers in n -Si. Characteristic of the dependences $C = f(V)$ in the region of forward biases is the decrease in the capacitance at $V > 0.8$ V with increasing voltage. The dependence of the capacitance on the frequency of the alternating signal is observed, which indicates a significant effect of the charge of the surface energy levels.

According to the theory of isotypic heterojunctions, this nature of the dependence $C = f(V)$ can be explained within the framework of the double-Schottky barrier model [25]. In this model, it has been suggested that defects, mainly misfit dislocations at the interface, create a large number of electrically active states. The presence of such states, which can be by nature both donors and acceptors, can significantly change the energy band diagram of the contact. In an isotypic n - n heterojunction, if the concentration of surface states at the interface is high enough, electrons are captured by these centers from the conduction band of both semiconductors, which leads to depletion of regions on both sides of the heterojunction. Based on the model in which the heterojunction is represented as two Schottky diodes turned on toward each other, the capacitances of the first and second barriers are expressed by the formulas.

$$C_1 = (q\varepsilon_1\varepsilon_0N_{D1}/2)^{1/2}(\phi_{k1} - V_1)^{-1/2} \quad (2)$$

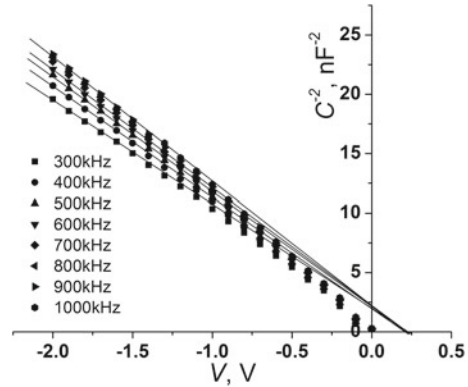
$$C_2 = (q\varepsilon_2\varepsilon_0N_{D2}/2)^{1/2}(\phi_{k2} + V_2)^{-1/2} \quad (3)$$

where ε_1 , ϕ_{k1} , N_{D1} and ε_2 , ϕ_{k2} , N_{D2} are the relative permittivity, the height of the potential barrier, the concentration of the alloying impurity of the first and second Schottky diodes, respectively; $\varepsilon_0 = 8.85 \cdot 10^{-12}$ F/m—permittivity of vacuum.

Analysis of the C - V -characteristics of the investigated n -TiN/ n -Si heterojunction was performed taking into account the significant effect on the value of the heterojunction capacitance of the phenomena of states recharging at the interface by the modulating alternating signal during measurement. At high frequencies, their charge is practically not modulated and the total capacity of the heterostructure is equal to the capacity of the depletion region of the heterojunction. That is why the analysis of C - V characteristics measured in the high frequency range was performed (Fig. 2b).

The dependence $C^{-2} = f(V)$ at reverse biases is characterized by linear sections with different angles α to the voltage axis and only at frequencies $f = 800$ – 1000 kHz its dependence on the frequency of the alternating signal is not observed. This indicates the practical absence of the influence of deep levels on the value of the capacitance of junction. Since, in this case, the positive potential is on n -Si, based on the double-Schottky barrier model used, it can be assumed that the measured capacitance is related to the space charge region in this semiconductor. The magnitude of the contact potential difference distributed in n -Si, determined by extrapolation of rectilinear sections of the dependences $C^{-2} = f(V)$ to the intersection with the voltage axis was $\varphi_{k2} = 0.25$ V (Fig. 3).

Fig. 3 C-V-characteristics of the *n*-TiN/*n*-Si heterojunction in the region of reverse biases (positive potential to *n*-Si)



Determined by a known method, using relation (2), based on the expression

$$\text{tg}\alpha = \frac{q}{2\varepsilon\varepsilon_0N_{D2}} \tag{4}$$

where $\varepsilon = 11.7$ is the permittivity of Si, the concentration of the donor impurity in the Si substrates was $N_{D2} = 2.8 \cdot 10^{15} \text{ cm}^{-3}$.

The size of the space charge region d_2 at $V = 0$, calculated by the known formula is $d_2 = 340 \text{ nm}$.

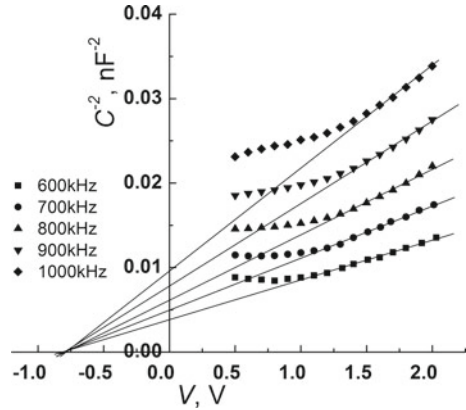
$$d_2 = \left(\frac{2\varepsilon\varepsilon_0}{qN_{D2}} \cdot \phi_k \right)^{1/2} \tag{5}$$

When the polarity of the external voltage changes (positive potential to *n*-TiN), the measured capacitance is the barrier capacitance of the film (Fig. 4). The height of the potential barrier determined by the above method was $q\phi_{kl} = 0.8 \text{ eV}$. Since the dependences $C^{-2} = f(V)$ show some change in the angle of inclination of the rectilinear sections, the values of $N_{D1} \approx 4.0 \cdot 10^{18} \text{ cm}^{-3}$ and $d_1 \approx 15 \text{ nm}$ were calculated on the basis of expressions (4) and (5).

The calculated concentrations of impurities, both in the base material and in the film, are in good agreement with those determined in the study of their electrical characteristics.

To construct the energy profile of the studied *n*-TiN/*n*-Si heterojunction (Fig. 5), taken into account the experimentally determined potential distribution in the contact region of both semiconductors, the values of electron affinities $\chi(\text{TiN}) \approx 3.91 \text{ eV}$ and $\chi(\text{Si}) = 4.05 \text{ eV}$ [26], the band gap $E_g(\text{TiN}) = 3.4 \text{ eV}$ [5] and $E_g(\text{Si}) = 1.12 \text{ eV}$ [27]. Location of the Fermi level in degenerate semiconductor TiN thin films produced by reactive magnetron sputtering, $\delta_1 \approx 0.05 \text{ eV}$ [18, 20]. For crystalline, Si $\delta_2 = 0.23 \text{ eV}$ was calculated according to the expression for the concentration of equilibrium charge carriers in nondegenerate semiconductors [28]:

Fig. 4 C-V-characteristics of the *n*-TiN/*n*-Si heterojunction in the region of forward biases (positive potential to *n*-TiN)

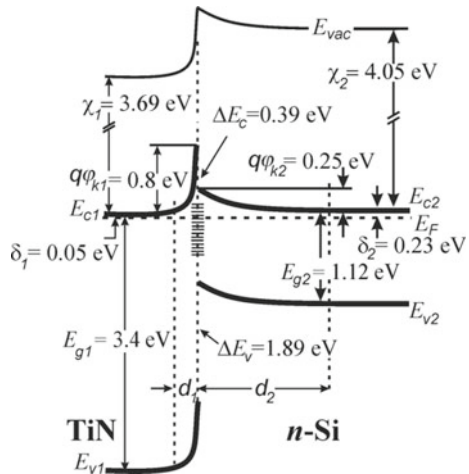


$$E_C - E_F = kT \cdot \ln \left(2 \cdot \left(\frac{2\pi m_n kT}{h^2} \right)^{3/2} \cdot \frac{1}{n} \right) \tag{6}$$

where m_n is the effective mass of electrons, E_F is the energy of the Fermi level in the band gap of the semiconductor. The electron concentration values were taken from the analysis of the C-V-characteristics of the heterojunction.

It should be noted that the analysis of the work function of semiconductors $A(n\text{-TiN}) = 3.96 \text{ eV}$ and $A(n\text{-Si}) = 4.28 \text{ eV}$ in the formation of the *n*-TiN/*n*-Si heterojunction shows that *n*-Si should be enriched in electrons. Such a structure should not have rectifying properties, which contradicts the experiment and confirms the validity of the applied model of isotypic heterojunction.

Fig. 5 Energy diagram of the isotype *n*-TiN/*n*-Si heterojunction taking into account the influence of a negative charge on the heterocontact interface ($d_1 = 15\text{--}35 \text{ nm}$, $d_2 \approx 250\text{--}270 \text{ nm}$)



The I - V -characteristics of the structure were plotted in the coordinates $\ln I = f(V)$ (Fig. 6) to determine the mechanism of the flow of forward currents. As can be seen from Fig. 6, the dependences $\ln I = f(V)$ are approximated by straight lines with constant temperature slope with diode coefficient $A \approx 5.4$ in a wide voltage range $3kT/q < V < 1.0$ V, which indicates the dominant tunneling mechanism of current transfer.

The energy diagram (Fig. 7), which corresponds to the forward bias of the barrier in n -Si, explains well the mechanism of carrier tunneling through the rectifying contact. The current in this case is formed by the electrons of the n -Si conduction band due to a significant gap in the edges of the valence bands. Bands in n -Si are straightened at low forward biases and then bent down.

Electrons are accumulated in the contact area. In this case, the height of the barrier in the titanium nitride film increases, since this barrier is turned on in the opposite direction. The total thickness of the barrier in the film at $V = 0$ V is $d_1 = 15$ nm due to the significant concentration of electrons. Tunneling at forward bias occurs at a

Fig. 6 Forward branches of the I - V -characteristics of the n -TiN/ n -Si heterojunction in semi-logarithmic coordinates at different temperatures T (positive potential applied to the TiN film)

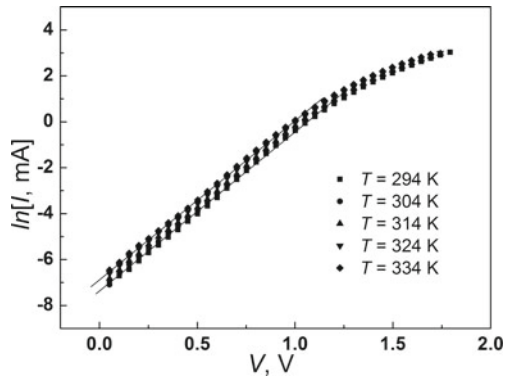


Fig. 7 Energy diagram of the isotype n -TiN/ n -Si heterojunction at forward bias (positive potential applied to the TiN film)

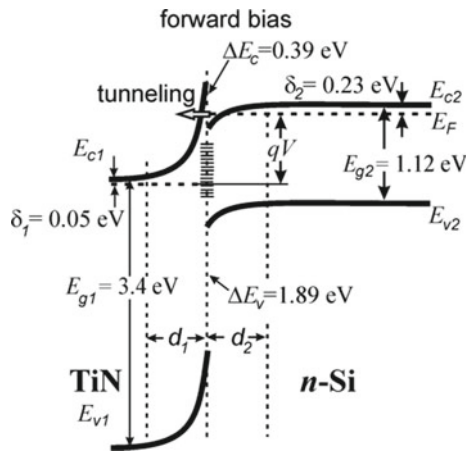
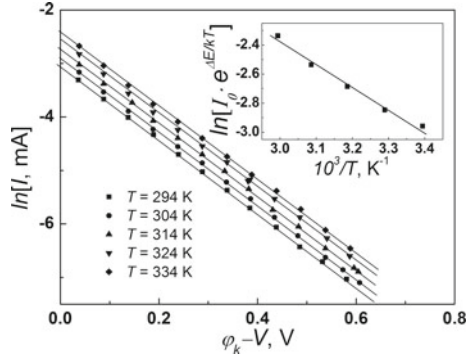


Fig. 8 Forward branches of the I - V -characteristics of n -TiN/ n -Si heterostructures in $\ln I = f(\varphi_k - V)$ coordinates, at different temperatures T (positive potential applied to the TiN film)



height $E_{C1} + qV$ relative to the base of the barrier. The barrier thickness for these electron energies is several nanometers, which significantly increases the probability of tunneling from the electron-enriched n -Si near-surface layer into the conduction band of the film.

Note that in the theory of isotype n - n -heterojunctions, the components of which are strongly doped semiconductors, tunneling is considered as the main mechanism of current transfer, due to the narrow barrier for electrons [29].

In this case, the forward current is described by the expression

$$I(V) = I_0 \exp(\Delta E / kT) \exp[-\alpha(\varphi_k - V)] \tag{7}$$

where ΔE is the temperature-related activation energy of the tunneling process; α is a coefficient that characterizes the probability of tunneling.

The straightness of the dependences $\ln I = f(\varphi_k - V)$ allows the use of analytical expression (7) to explain the experimental results (Fig. 8).

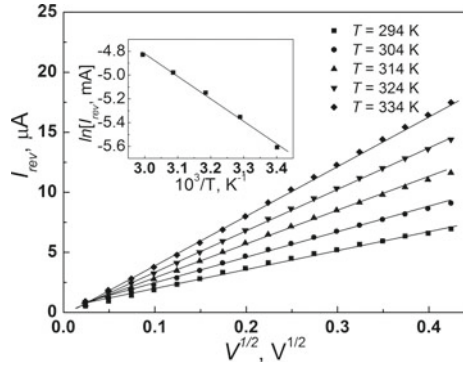
The height of the potential barrier for electrons from n -Si was determined taking into account the discontinuity of the conduction bands ($\varphi_k = \Delta E_C + \varphi_{k2}$). The activation energy of the electron tunneling process in this case was determined from the temperature dependence $I_0 \exp(\Delta E / kT) = f(10^3 / T)$ (Fig. 8, inset). Its value was $\Delta E = 0.18$ eV.

Reverse currents (positive potential applied to n -Si) are characterized by the manifestation of two current transfer mechanisms. In the voltage range $-0.5 < V < 0$ V, the reverse branches of the I - V -characteristic in the entire temperature range of studies are described by the power law $I \sim V^{1/2}$, which is typical for the generation mechanism of the reverse current formation (Fig. 9). The generation of charge carriers (in this case—electrons) occurs in the depleted region of n -Si. The reverse current is formed by electron movement to the bulk of the base region.

The depth of the donor energy level, from which the thermal generation of charge carriers occurs, was $\Delta E = 0.16$ eV. This ΔE is determined from the dependence $\ln I_{rev} = f(10^3 / T)$ (Fig. 9, inset), obtained at a constant voltage value.

With increasing reverse displacement $V < -0.8$ V I - V -characteristics of the studied n -TiN/ n -Si structures are characterized by the presence of linear sections.

Fig. 9 Reverse branches of the I - V -characteristic of the n -TiN/ n -Si heterostructure in the coordinates $I_{\text{rev}} = f(V^{1/2})$ at different temperatures (positive potential applied to the n -Si film)



The angle of inclination of the linear sections to the voltage axis does not depend on the temperature, which indicates the process of tunneling the charge carriers through the potential barrier. The tunneling mechanism in this case is illustrated in the energy diagram of the n -TiN/ n -Si contact (Fig. 10). The tunneling current at a reverse bias $V < -0.8$ V of the n -TiN/ n -Si heterostructure is described by the expression for forward tunneling currents (7) through the barrier in the TiN film with a height of ~ 0.8 eV. It should be noted that at negative voltages at the n -TiN/ n -Si heterojunction, most of the voltage V_2 is applied to the high-resistance n -Si depleted region, and a small part of the voltage V_1 is applied to the forward-biased barrier in n -TiN.

In expression (7), the value $\varphi_{kl} - V_1 \approx \varphi_{kl}$. In this case, tunneling phenomena are best described by the Simons' equation [30] for small values of external voltage ($qV \ll E_b$)

$$I_{\text{rev}} = \frac{q^2 \sqrt{2m\phi}}{4\pi^2 \hbar^2} \frac{V}{\Delta z} \exp\left(-2\sqrt{\frac{2m\phi}{\hbar^2}} \Delta z\right) \quad (8)$$

Fig. 10 Energy diagram of the isotype n -TiN/ n -Si heterojunction at reverse bias (positive potential applied to the n -Si crystal)

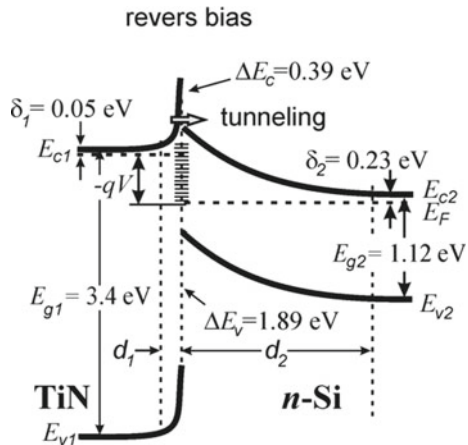
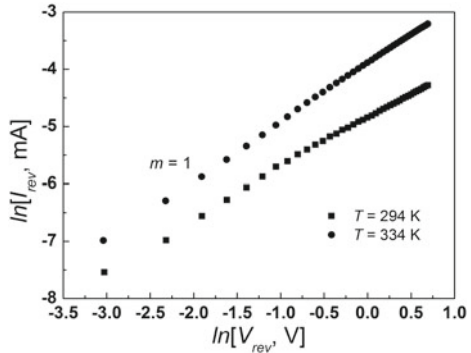


Fig. 11 The dependences $\ln I_{rev} = f(\ln V_{rev})$ for the n -TiN/ n -Si heterojunction at reverse bias



where $\Delta z = d_1$ is the barrier thickness, $\varphi = E_b = q\phi_{k1}$ is the barrier height.

According to (8), the reverse current I_{rev} is proportional to V_{rev} , and the dependence $\ln I_{rev} = f(\ln V_{rev})$ in this case will be linear with the tangent of the angle of inclination $m = 1$, which is confirmed in Fig. 11.

4 Conclusions

The isotype n -TiN/ n -Si heterojunctions with a current rectification ratio of $\sim 10^3$ are fabricated by the reactive magnetron sputtering method. The diode characteristics of the heterojunction are due to energy barriers with a height of ~ 0.8 eV in the TiN film and ~ 0.25 eV in the n -Si crystal. Barriers are formed with the participation of energy states at the interface. In the region of forward voltages of the TiN/ n -Si heterojunction at $3kT/q < V < 1.0$ V, the current flows by tunneling electrons from the states of the n -Si conduction band through the barrier into the conduction band of the TiN film. The accumulation of electrons occurs in the contact region from the n -Si side at forward bias. The reverse current at voltages $-0.5 \text{ V} < V < -3kT/q$ V is formed due to generation processes in the depleted region of n -Si with participation in the thermal generation of the donor energy level with a depth in the forbidden zone of silicon $\Delta E = 0.16$ eV. The reverse current flows by tunneling electrons from the states of the conduction band of the TiN film through a barrier with a height of ~ 0.8 eV into the conduction band of Si at biases $-2 \text{ V} < V < -0.5$ V.

The C - V -characteristics of the TiN/ n -Si heterojunction agree well with the double-Schottky barrier model and confirm the participation of negatively charged energy states at the TiN/ n -Si interface in the formation of the energy barrier.

References

1. Mohan T, Baiju KG, Murali B, Kumaresan D (2018) Titanium nitride blended graphene nanoplatelets as low-cost and efficient composite counter electrode for dye-sensitized solar cells. In: 2018 IEEE international conference on system, computation, automation and networking (ICSCAN), IEEE, Pondicherry, pp 1–5. <https://doi.org/10.1109/ICSCAN.2018.8541145>
2. Khezripour Z, Mahani FF, Mokhtari A (2018) Performance improvement of ultrathin organic solar cells utilizing light-trapping aluminum-titanium nitride nanosquare arrays. *Opt Mater* 84:651–657. <https://doi.org/10.1016/j.optmat.2018.07.073>
3. Lu Z, Liu X, Hou G, Chen J, Zhu T, Xu J, Chen K (2020) Doping-free titanium nitride carrier selective contacts for efficient organic-inorganic hybrid solar cells. *ACS Appl Energ Mater* 3:9208–9215. <https://doi.org/10.1021/acsaem.0c01517>
4. Khalifa AE, Swillam MA (2014) Plasmonic silicon solar cells using titanium nitride: a comparative study. *J Nanophoton* 8:084098. <https://doi.org/10.1117/1.JNP.8.084098>
5. Solovan MM, Brus VV, Maistruk EV, Maryanchuk PD (2014) Electrical and optical properties of TiN thin films. *Inorg Mater* 50:46–51. <https://doi.org/10.1134/S0020168514010178>
6. Jeon H, Lee J-W, Kim Y-D, Kim D-S, Yi K-S (2000) Study on the characteristics of TiN thin film deposited by the atomic layer chemical vapor deposition method. *J Vac Sci Technol A: Vac Surf Films* 18:1595–1598. <https://doi.org/10.1116/1.582391>
7. Solovan MM, Brus VV, Maryanchuk PD, Ilashchuk MI, Rappich J, Nickel N, Abashin SL (2014) Fabrication and characterization of anisotype heterojunctions n-TiN/p-CdTe. *Semicond Sci Technol* 29:015007. <https://doi.org/10.1088/0268-1242/29/1/015007>
8. Didden A, Battjes H, Machunze R, Dam B, van de Krol R (2011) Titanium nitride: a new Ohmic contact material for n-type CdS. *J Appl Phys* 110:033717. <https://doi.org/10.1063/1.3615946>
9. Matenoglou GM, Koutsokeras LE, Patsalas P (2009) Plasma energy and work function of conducting transition metal nitrides for electronic applications. *Appl Phys Lett* 94:152108. <https://doi.org/10.1063/1.3119694>
10. Ishii S, Shinde SL, Jevasuwan W, Fukata N, Nagao T (2016) Hot electron excitation from titanium nitride using visible light. *ACS Photonics* 3:1552–1557. <https://doi.org/10.1021/acsphotonics.6b00360>
11. Naldoni A, Guler U, Wang Z, Marelli M, Malara F, Meng X, Besteiro LV, Govorov AO, Kildishev AV, Boltasseva A, Shalaev VM (2017) Broadband hot-electron collection for solar water splitting with plasmonic titanium nitride. *Adv Opt Mater* 5:1601031. <https://doi.org/10.1002/adom.201601031>
12. Yang X, Liu W, De Bastiani M, Allen T, Kang J, Xu H, Aydin E, Xu L, Bi Q, Dang H, AlHabshi E, Kotsovos K, AlSaggaf A, Gereige I, Wan Y, Peng J, Samundsett C, Cuevas A, De Wolf S (2019) Dual-function electron-conductive, hole-blocking titanium nitride contacts for efficient silicon solar cells. *Joule* 3:1314–1327. <https://doi.org/10.1016/j.joule.2019.03.008>
13. Lima L, Diniz JA, Doi I, Fo JG (2012) Titanium nitride as electrode for MOS technology and Schottky diode: alternative extraction method of titanium nitride work function. *Microelectron Eng* 92:86–90. <https://doi.org/10.1016/j.mee.2011.04.059>
14. Shinde SL, Ishii S, Nagao T (2019) Sub-bandgap photodetection from titanium nitride/germanium heterostructure. *ACS Appl Mater Interfaces* 11:21965–21972. <https://doi.org/10.1021/acsaami.9b01372>
15. Wu HD, Huang W, Lu WF, Tang RF, Li C, Lai HK, Chen SY, Xue CL (2013) Ohmic contact to n-type Ge with compositional Ti nitride. *Appl Surf Sci* 284:877–880. <https://doi.org/10.1016/j.apsusc.2013.08.028>
16. Solovan MM, Brus VV, Maryanchuk PD (2013) Electrical and photoelectric properties of anisotype n-TiN/p-Si heterojunctions. *Semiconductors* 47:1174–1179. <https://doi.org/10.1134/S1063782613090248>

17. Gosciniak J, Atar FB, Corbett B, Rasras M (2019) CMOS-compatible titanium nitride for on-chip plasmonic schottky photodetectors. *ACS Omega* 4:17223–17229. <https://doi.org/10.1021/acsomega.9b01705>
18. Solovan MN, Brus VV, Maryanchuk PD (2014) Specific features of the recombination loss of the photocurrent in n-TiN/p-Si anisotype heterojunctions. *Semiconductors* 48:1504–1506. <https://doi.org/10.1134/S106378261411027X>
19. Gosciniak J, Atar FB, Corbett B, Rasras M (2019) Plasmonic Schottky photodetector with metal stripe embedded into semiconductor and with a CMOS-compatible titanium nitride. *Sci Rep* 9:6048. <https://doi.org/10.1038/s41598-019-42663-3>
20. Solovan MN, Brus VV, Maryanchuk PD (2014) Isotype surface-barrier n-TiN/n-Si heterostructure. *Semiconductors* 48:219–223. <https://doi.org/10.1134/S1063782614020274>
21. Solovan MN, Mostovyi AI, Brus VV, Mastruk EV, Maryanchuk PD (2016) Electrical and photoelectric properties of n-TiN/p-Hg₃In₂Te₆ heterostructures. *Semiconductors* 50:1020–1024. <https://doi.org/10.1134/S1063782616080236>
22. Orletsky IG, Ilashchuk MI, Brus VV, Marianchuk PD, Solovan MM, Kovalyuk ZD (2016) Electrical and photoelectric properties of the TiN/p-InSe Heterojunction. *Semiconductors* 50:334–338. <https://doi.org/10.1134/S1063782616030167>
23. Orlets'kyi IG, Ilashchuk MI, Mastruk EV, Parkhomenko HP, Maryanchuk PD (2021) Electrical properties and energy parameters of photosensitive n-Mn₂O₃/n-CdZnTe heterostructures. *Ukrainian J Phys* 66, 792. <https://doi.org/10.15407/ujpe66.9.792>
24. Koziarskyi IP, Mastruk EV, Orletsky IG, Ilashchuk MI, Koziarskyi DP, Marianchuk PD, Solovan MM, Ulyanytsky KS (2020) Influence of properties of hematite films on electrical characteristics of isotype heterojunctions Fe₂O₃/n-CdTe. *Semicond Sci Technol* 35:025018. <https://doi.org/10.1088/1361-6641/ab6107>
25. Sharma BL, Purohit RK (1974) *Semiconductor heterojunctions* (Pergamon Press, 1974) [ISBN:9781483280868]
26. Fahrenbruch AL, Bube RH (1983) *Fundamentals of Solar Cells* (Academic Press, 1983) [ISBN: 9780323145381]
27. *Handbook of photovoltaic science and engineering 2011* Edited by A.Luque and S. Hegedus. (2nd ed. John Wiley & Sons, Ltd.)
28. Sze SM, Kwok KN (2006) *Physics of semiconductor devices* (Wiley, 2006) [ISBN: 9780471143239]
29. A.G. Milnes, D.L. Feucht. *Heterojunctions and metal-semiconductor junctions* (Academic Press, 1972) [ISBN:0124980503].
30. Simmons JG (1963) Generalized Formula for the Electric Tunnel Effect between Similar Electrodes Separated by a Thin Insulating Film. *J Appl Phys* 34:1793–1803. <https://doi.org/10.1063/1.1702682>

Water-Soluble Polymers as Substances Modifying the Stability of Colloidal Systems, the Nanostructure of Adsorption Layers



Małgorzata Wiśniewska

Abstract The stabilizing and destabilizing properties of polymers soluble in the aqueous medium are used in numerous technological and ecological processes leading to maintaining a specific product form (no phase delamination) as well as separation of undesirable and toxic substances. Among the wide applications of macromolecular compounds, it is worth mentioning the paint, varnish, pharmaceutical, cosmetic, food, medicine, drinking water, and industrial wastewater treatment processes as well as agriculture. In the latter case, the use of polymeric flocculants counteracting water and wind erosion of soil by binding loose soil particles into larger aggregates contributes to the substrate consistency and durability increase. Taking the above into consideration, this paper characterizes various stability mechanisms of solid aqueous suspensions occurring in the presence of a polymer and also presents the results of research on the influence of the ionic polyacrylamide type on the structure of polymer adsorption layer formed at the chromium(III) oxide interface. The specific conformation of adsorbed macromolecules determines directly the mechanism of the Cr_2O_3 suspension stability which enables its effective separation from the liquid phase.

Keywords Water-soluble polymers · Steric stabilization · Bridging flocculation · Nanostructured polymeric layers · Colored solid removal

1 Introduction

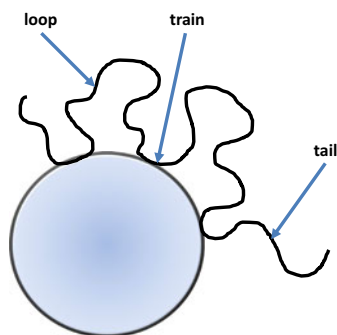
The possibility of influencing the stability of solid aqueous suspensions by the addition of a suitably selected polymer results primarily from the fact that, depending on the conditions in the system, macromolecules can assume specific conformations at

M. Wiśniewska (✉)

Faculty of Chemistry, Department of Radiochemistry and Environmental Chemistry, Institute of Chemical Sciences, Maria Curie-Skłodowska University in Lublin, Maria Curie-Skłodowska Sq. 3, 20-031 Lublin, Poland

e-mail: malgorzata.wisniewska@mail.umcs.pl

Fig. 1 Polymeric chain containing the train, loop, and tail structures adsorbed on the colloidal particle surface



the interface [1]. The polymer chains present in the solution under appropriate conditions tend to develop spatially, and by adsorbing on the solid surface, they assume a specific conformation with segments located in one of three types of structures, i.e., trains, loops, and tails (Fig. 1).

Even for small molecular weights, the degree of macromolecule straightening in a given solvent is comparable to the range of the attractive van der Waals forces acting between the colloidal particles (and in many cases in the range larger than attractive interactions which equal to 5–10 nm).

The polymer adsorption process at the solid–solution interface is complex, as the conformation of macromolecules depends on many factors [2–4]. They are related not only to the type of used polymer and adsorbent but also to the conditions under which the experiment is conducted (Table 1). The most important parameters influencing the polymer adsorption process on the solid surface include the molecular weight and the type of functional groups of the polymer, its degree of polydispersity; concentration and type of adsorbent surface groups, porosity and degree of contamination of the solid; pH and ionic strength of the solution, and temperature.

The way of polymer chains binding with active sites on the solid surface results in the specific structure of the formed adsorption layer which influences directly the stability of this type of colloidal systems.

Table 1 Parameters influencing the polymeric chains adsorption on the solid surface

Polymer	Adsorbent	Solution	Another
<ul style="list-style-type: none"> • Type (ionic, non-ionic) • Average molecular weight • Concentration • Polydispersity • Presence of inorganic impurities 	<ul style="list-style-type: none"> • Type and concentration of surface groups (pH_{pzc}, pH_{iep} values) • Specific surface area • Porosity • Presence of impurities 	<ul style="list-style-type: none"> • Type of supporting electrolyte • pH • Ionic strength • Presence of additional substances (i.e., surfactants, metal ions, drugs, pesticides) 	<ul style="list-style-type: none"> • Temperature • Magnetic field

2 Stabilization/Destabilization of Colloidal Systems in the Polymer Presence

The two main mechanisms of stabilization of colloidal suspensions by the adsorbed polymer chains are as follows: Steric stabilization and electrosteric stabilization presented schematically in Fig. 2 [5–8]. The steric stabilization results from the effective repulsion of particles whose surfaces are completely covered with an adsorbed polymer, usually of a small molecular weight. This is a result of chemical or physical adsorption of polymer chains on the surface of the stabilized particles. Due to the spatial hindrance created by the chains of bonded macromolecules, solid particles cannot get close to each other and remain dispersed in the system.

Combination of electrostatic and steric stabilization, the so-called electrosteric stabilization, is common in many biological systems. The source of electrostatic interactions is the charges accumulated on the particle surface as well as those distributed along the adsorbed polymer chains, resulting from the dissociation of their functional groups.

The mechanisms of steric and electrostatic stabilization play a key role in many technological processes, including: the production of paints, inks, adhesives; in photography and photocopying; in the production of various types of emulsions and suspensions for the pharmaceutical and food industry; in the production of detergents and other cleaning agents; in chemical washing processes and to ensure the biocompatibility of medical prostheses. These stabilization mechanisms play an important role in the biological dispersed systems stabilization. This is due to the two reasons: (a) the ionic strength of biological dispersions is relatively large; therefore, electrostatic stabilization is less effective in such cases; (b) predominantly, natural polymers are of ionic character, and their solutions (polyelectrolytes) are commonly found in nature.

Destabilization of colloidal particles is usually caused by adsorbed polymers of large molecular weight and is referred to as flocculation [9–12]. The two most important types of flocculation are as follows: bridging flocculation and surface charge neutralization flocculation (Fig. 3).

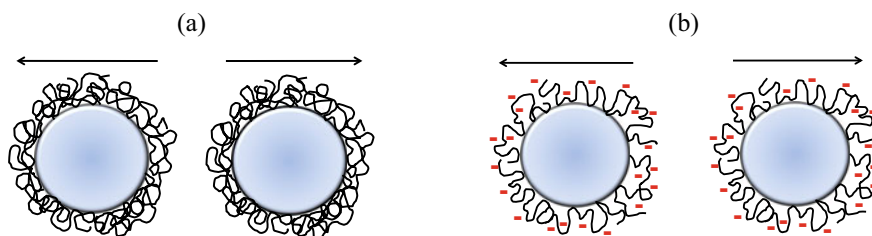


Fig. 2 Schematic representation of stabilization mechanisms: **a** steric and **b** electrosteric, caused by the adsorbed polymer macromolecules

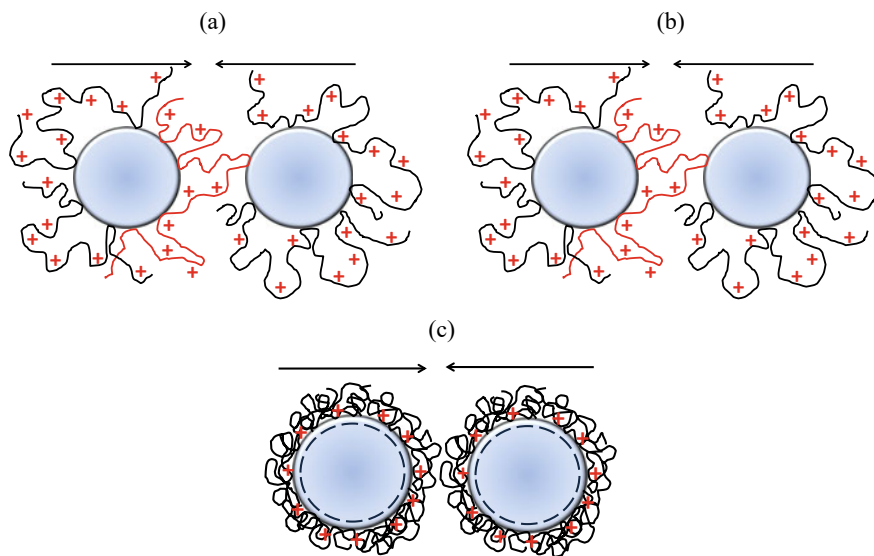


Fig. 3 Schematic representation of flocculation mechanisms: **a** intramolecular bridging, **b** intermolecular bridging, and **c** surface charge neutralization caused by the adsorbed polymer macromolecules

Bridging flocculation occurs in the case of polymer adsorption on the particles surfaces with the macromolecules conformation characterized by a significant share of their segments in the loop and tail structures. This type of flocculation can occur in two ways. The first one is bridging by adsorption of one macromolecule onto two or more particles in the system (intramolecular bridges formation, Fig. 3a). The second type is bridging as a result of the interactions of two polymer chains, which are adsorbed on the surfaces of different particles (intermolecular bridges formation, Fig. 3b).

The first of the above bridging ways occurs when there are met the following conditions: (a) the concentration of the polymer in the system is small; hence, the small coverage of the particle surface by macromolecules enables the adsorption of chains associated with the surface of adjacent particles; (b) adsorbed macromolecules have long chains branched or highly extended toward the solution, which allow them to be attached to the surface of more than one colloidal particle.

On the other hand, the second way takes place when: (a) the surface coverage of the particles by the adsorbed polymer chains is large, which limits the adsorption of subsequent macromolecules; (b) the attraction force between the two interacting polymer chains adsorbed on the surface of two different particles is greater than their repulsion due to the steric hindrance.

An important mechanism of destabilization of colloidal suspensions in the presence of a polymer is flocculation due to the neutralization of the surface charge of solid particles by the adsorbed macromolecules. In this case, the adsorbed polymer

chains are charged opposite to the surface charge of the adsorbent, thereby neutralizing it. As a result, significant weakening of electrostatic repulsion between the particles and an increased tendency toward their aggregation are observed (Fig. 3c). This destabilization mechanism usually takes place under the conditions of partial dissociation of the polymer ionic groups which interact directly with the solid surface, and the uncharged fragments of the adsorbed macromolecules are directed toward the liquid phase. At the same time, the polymer forms rather the thin adsorption film on the solid surface.

The following types of interactions are responsible for the polymer adsorption on the solid surface: (a) chemical (covalent) with the energy above 40 kJ/mol (e.g., for O–H bond: 500 kJ/mol); (b) physical (non-covalent) with the energy below 40 kJ/mol. Among the latter, there are as follows: (a) electrostatic interactions (approx. 25 kJ/mol); (b) hydrogen bonds (below 40 kJ/mol); (c) hydrophobic forces (interactions of hydrophobic groups caused by avoiding water molecules); (d) van der Waals forces (Keesom forces—between the permanent dipoles; Debye forces—the dipole-induced dipole interactions; London dispersion forces—between the electrically neutral molecules).

The changes in the colloidal system stability can be influenced by macromolecules that do not adsorb on the solid surface, but exist as a free chain in the solution (Fig. 4) [13, 14]. At a high concentration of the unadsorbed polymer, so-called depletion destabilization can occur. It takes place when colloidal particles dispersed in the polymer solution come closer to each other at a distance smaller than the macromolecule diameter. Then, the polymer chains are pushed from the space between the particles into the solution which ensures the energy minimum in the system. The emerging osmotic pressure acts on the particles on the outer sides, reducing the distance between them.

At very high polymer concentrations, depletion stabilization is observed. The polymer-depleted region between the particles is formed by the separation of the polymer macromolecules and the solvent molecules. In good quality solvents, this separation process is thermodynamically unfavorable, and under such conditions, depletion stability can occur.

The parameter related to the stability of a colloidal suspension is the zeta (ζ) potential, also known as the electrokinetic potential. This is the potential in the slipping plane which is an important element of the electrical double layer and separates the stiffly bound solution layer from its movable diffusion part. The suspension is assumed to be stable if the absolute value of the zeta potential exceeds 30 (Fig. 5) [15]. When the zeta potential is equal to zero, there occurs the so-called isoelectric point of a solid at which the colloidal suspension is extremely unstable.

However, the above rule is not true for the polymer containing solid suspensions in which flocculation can occur even at high values of the electrokinetic potential. This is due to the great complexity of the polymer adsorption process at the solid–liquid interface.

The determined zeta potential value of the particles dispersed in the liquid medium in the presence of a polymer is influenced by the following effects: (a) shift of the slipping plane caused by the adsorbed macromolecules; (b) blockade of active sites

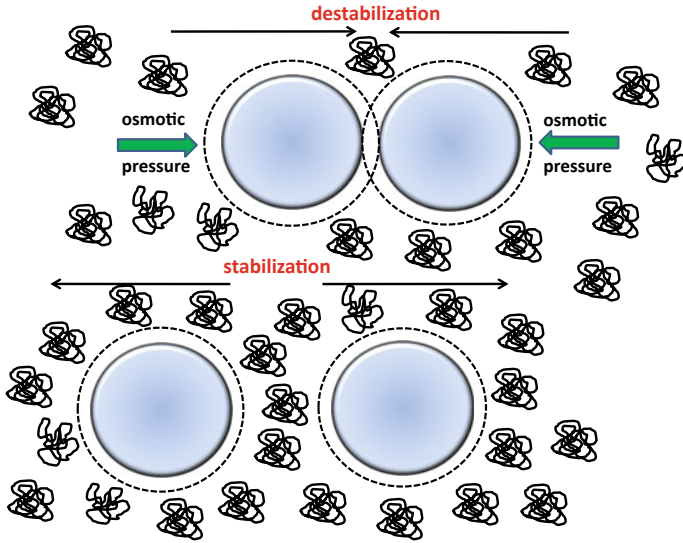
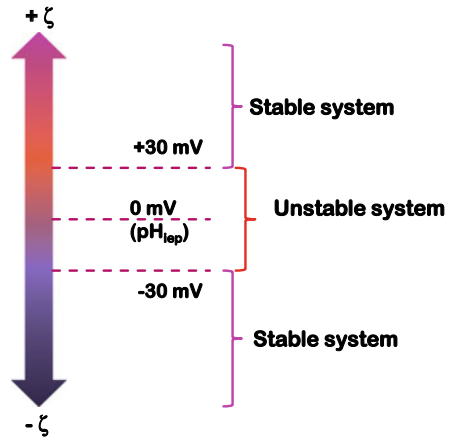


Fig. 4 Schematic representation of depletion stabilization–destabilization mechanisms caused by unadsorbed polymer macromolecules

Fig. 5 Schematic representation of the colloidal suspensions stability without a polymer based on the zeta potential absolute values



on the solid surface by the adsorbed polymer chains and counter-ions shifting from the surface layer; (c) presence of charged functional groups of the adsorbed polymer macromolecules in the slipping plane area [16].

The stability in the polymer presence has several significant advantages over the electrostatic stability of the dispersed solid particles. They are as follows: (a) small sensitivity to the presence of electrolytes; (b) comparable effectiveness in the aqueous and non-aqueous dispersion media; (c) similar effectiveness with small and large contents of colloidal particles; (d) flocculation reversibility [17–19].

3 Polymer-Solid Systems

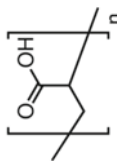
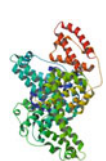
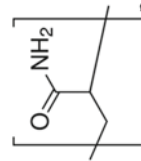
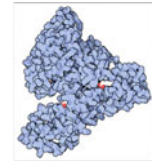
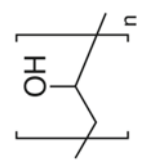

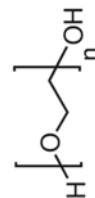
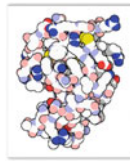
Technological development aimed at new solutions friendly for the natural environment leads to the development of more ecological and effective methods of harmful substances removal from aqueous solutions. This trend of research fits very well in the implementation of processes that use compounds of natural origin, e.g., proteins, polypeptides, as well as various types of sorbents obtained from waste materials. The use of such substances does not burden the natural environment as their complete microbial decomposition into simple compounds takes place. With this in mind, apart from the synthetic polymers, biopolymers were also used in the research. Among synthetic polymers, there were applied their following groups and their representatives: (a) linear polymers—poly(acrylic acid)—PAA [20], polyacrylamide—PAM [21], poly(vinyl alcohol)—PVA [22], poly(ethylene glycol)—PEG [23], poly(ethylene oxide)—PEO [24], polyvinylpyrrolidone—PVP [25]; (b) dendrimers—3rd generation anionic dendrimer—3G-TMP-COOH with trimethylpropane (TMP) core and 24 peripheral carboxyl groups [26]; (c) polyaminoacids—poly(L-aspartic acid)—ASP [27], poly(L-Lysine)—LYS [28] and their di- and triblock copolymers with poly(ethylene glycol)—PEG: ASP-PEG, LYS-PEG, ASP-PEG-ASP, LYS-PEG-LYS [29, 30]. Among the natural polymers, there were tested: (a) globular proteins—bovine serum albumin—BSA, human serum albumin—HSA, ovalbumin—OVA [31]; (b) enzymatic protein—lysozyme (LSZ) [32]; polysaccharide—exopolysaccharide synthesized by the bacteria *Sinorhizobium meliloti* (EPS) [33]. Their chemical formulae are presented in Table 2.

Proteins are macromolecular compounds composed of amino acids arranged in a strictly defined sequence linked together by covalent peptide bonds. These bonds are formed between the α -amino and α -carboxyl groups of two adjacent amino acids. In turn, polyaminoacid macromolecules are composed of only one type of amino acid linked by an amide bond (as opposed to the proteins which contain many different amino acids in their structure). Exopolysaccharides (EPSs) are macromolecular compounds synthesized by all soil bacteria of the *Rhizobiaceae* family. They are produced in large numbers for the external environment.

Polymers belonging to the group of dendrimers have a specific molecular structure. Their macromolecules contain a core, from which dendrons (like tree branches) diverge radially. The subsequently joined layers (called the generations) contribute to formation of more and more branched macromolecules. The dendrimer macromolecules provide also possibility of creating complexes with simple ions and other molecules that can be located in their interior or on the edges in the so-called peripheral units. The usage of such systems allows their application in the processes in which it is necessary to control the kinetics of various ions or more complex chemical substances release (for example, in the drug delivery systems) [34] (Fig. 6).

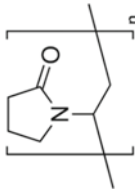
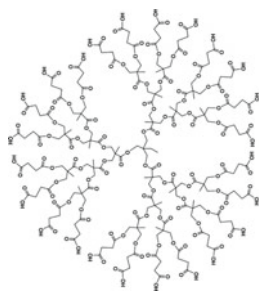
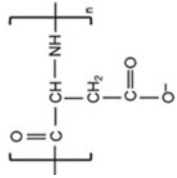
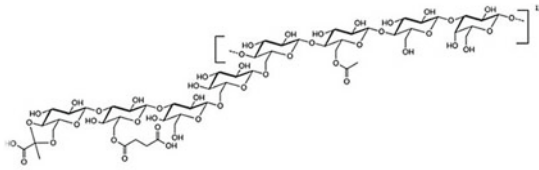
The solids examined in the previous papers are listed in Table 3. These were metal and semi-metal oxides [35], natural and synthetic minerals [36], activated carbons [37], and carbon-based composites [38].

Table 2 Chemical formulae of the examined synthetic and natural polymers. www.sigmaaldrich.com; www.alamanda-polymers.com

Synthetic polymers		Natural polymers	
PAA		BSA	
PAM		HSA	
PVA		OVA	
PEG		LYS	
PEO			

(continued)

Table 2 (continued)

Synthetic polymers		Natural polymers	
PVP			
3G-TMP-COOH			
ASP			

(continued)

Table 2 (continued)

Synthetic polymers	Natural polymers
LYS $\left[\begin{array}{c} \text{O} \\ \parallel \\ \text{C} - \text{CH} - \text{NH} \\ \\ (\text{CH}_2)_4 \\ \\ \text{H} - \text{N}^+ - \text{H} \\ \\ \text{H} \end{array} \right]_n$	
ASP-PEG $\left[\begin{array}{c} \text{O} \\ \parallel \\ \text{C} - \text{CH} - \text{NH} \\ \\ \text{CH}_2 \\ \\ \text{C} = \text{O} \\ \\ \text{O}^- \end{array} \right]_{50} \left[\begin{array}{c} \text{H} \\ \\ \text{N} \\ \\ \text{O} - \text{CH}_2 - \text{CH}_2 \end{array} \right]_{104}$	
LYS-PEG $\left[\begin{array}{c} \text{O} \\ \parallel \\ \text{C} - \text{CH} - \text{NH} \\ \\ (\text{CH}_2)_4 \\ \\ \text{H} - \text{N}^+ - \text{H} \\ \\ \text{H} \end{array} \right]_{25} \left[\begin{array}{c} \text{H} \\ \\ \text{N} \\ \\ \text{O} - \text{CH}_2 - \text{CH}_2 \end{array} \right]_{300}$	
ASP-PEG-ASP $\left[\begin{array}{c} \text{O} \\ \parallel \\ \text{C} - \text{CH} - \text{NH} \\ \\ \text{CH}_2 \\ \\ \text{C} = \text{O} \\ \\ \text{O}^- \end{array} \right]_{100} \left[\begin{array}{c} \text{H} \\ \\ \text{N} \\ \\ \text{O} - \text{CH}_2 - \text{CH}_2 \end{array} \right]_{25} \left[\begin{array}{c} \text{O} \\ \parallel \\ \text{C} - \text{CH} - \text{NH} \\ \\ \text{CH}_2 \\ \\ \text{C} = \text{O} \\ \\ \text{O}^- \end{array} \right]_{100}$	

(continued)

Table 2 (continued)

Synthetic polymers		Natural polymers
LYS-PEG-LYS $\left[\text{NH}-\underset{\text{(CH}_2\text{)}_4}{\text{CH}}-\overset{\text{O}}{\parallel}{\text{C}}-\underset{\text{Cl}^-}{\text{NH}_3^+} \right]_x \left[\text{CH}_2\text{CH}_2\text{O} \right]_n \left[\overset{\text{O}}{\parallel}{\text{C}}-\underset{\text{Cl}^-}{\text{NH}_3^+}-\underset{\text{(CH}_2\text{)}_4}{\text{CH}}-\text{NH} \right]_z$		

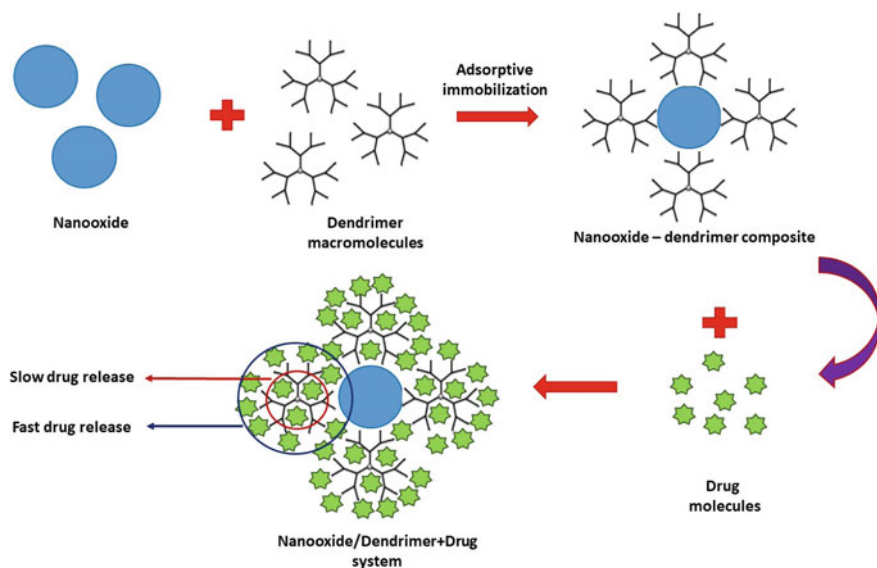


Fig. 6 Schematic representation of drug release from the nanooxide-dendrimer composite system

Table 3 Solids studied in the polymer presence with respect to their stability

Metal and semi-metal oxides	Minerals	Activated carbons	Carbon-based composites
<ul style="list-style-type: none"> • Aluminum(III) oxide • Chromium(III) oxide • Iron(III) oxide • Silicon(IV) oxide • Manganese(IV) oxide • Zirconium (IV) oxide • Double and triple oxides based on silica 	<ul style="list-style-type: none"> • Montmorillonite • Kaolinite • Gibbsite • Goethite • Natural and synthetic zeolites (sodalite, clinoptilolite, Na-A, Na-X, Na-P1) 	Obtained from precursors: <ul style="list-style-type: none"> • Peat • Cherry stones • Corn cobs • Peanut shells • Horsetail • Hay 	<ul style="list-style-type: none"> • Carbon-silica • Carbon-silica/Mn • Carbon-silica/Fe • Carbon-Na-X zeolite • Carbon-Na-P1 zeolite

The green chemistry research trend also includes the use of activated biocarbons and synthetic zeolites to remove polymer compounds from the aqueous phase in the surfactants and metal ions (including heavy metals) presence. Activated biocarbons were obtained from various types of waste materials such as peanut shells, cherry stones, corncobs, and peat as well as horsetail herb. On the other hand, zeolites of the Na-A, Na-X, and Na-P1 type were obtained from the troublesome wastes originating from the combustion of hard coal, i.e., fly ash.

Generally, studies with the use of the above-mentioned adsorbates and adsorbents included the following stages: (a) determination of the stability of solid aqueous

suspensions in the polymer presence—turbidimetric tests; (b) specification of the most probable structure of the polymer adsorption layer (adsorption and electrokinetic measurements); (c) explanation of the stability mechanism of solid particles dispersed in the aqueous polymer solution. They will be discussed in the next chapter with the Cr_2O_3 -ionic PAM suspension as an example.

4 Influence of Ionic Polyacrylamide Adsorption on the Stability Mechanism of the Aqueous Suspension of Chromium(III) Oxide

Chromium(III) oxide is insoluble in water and organic solvents. It is very resistant to light, weather conditions, high temperature, and corrosive gases (including SO_2 , H_2S). Due to its intense blue color, it is mainly used as a green dye in the paint, ceramic, cosmetic, and glass industries. In a small amount, Cr(III) is non-toxic and an essential trace element facilitating the glucose absorption into the blood cells. It maintains the proper concentration of glucose in the blood (affecting insulin) and is necessary for the metabolism of glucose, proteins, and lipids. Chromium(III) stimulates plant growth, but in excess, it can cause allergies.

However, its presence in surface waters is undesirable. Due to its intense green color, it confines the penetration of sunlight into deep layers of water decreasing the photosynthesis efficiency by aquatic plants and algae—oxygen deficit. As a result, the inhibition of life processes taking place in water ecosystems occurs.

The ionic polyacrylamide (PAM) used as an adsorbate dissolves well in water. It is non-toxic (as opposed to its monomer—acrylamide which is a strong neurotoxin). PAM is biodegradable and is used as a flocculant in drinking water treatment processes, as a dispersing agent, stabilizer and thickener in the cosmetic, dyeing, and paper industries. Polyacrylamide is applied for the intensification of oil extraction and as a fertilizer for soil erosion inhibition. Moreover, PAM hydrogels are used for the treatment of burns.

The objectives of the research were as follows: (a) determination of the influence of the ionic PAM presence on the stability of Cr_2O_3 aqueous suspension—turbidimetric tests; (b) determination of the effect of solution pH (3–10) on the ionic polyacrylamide (PAM) adsorption mechanism on the colloidal chromium(III) oxide surface—adsorption and electrokinetic studies (surface charge density and zeta potential measurements); (c) explanation of the stability mechanism of the aqueous suspension of chromium(III) oxide in the presence of ionic polyacrylamide [39, 40].

The schematic representation of the suspensions is given in Fig. 7.

A convenient parameter that enables estimation of the examined suspension stability is the TSI stability index (TSI—Turbiscan Stability Index). Its value is calculated by the appropriate computer software cooperating with the turbidimeter (Turbiscan Lab^{Expert}, Formulacion, France). Possible values of the TSI are in the

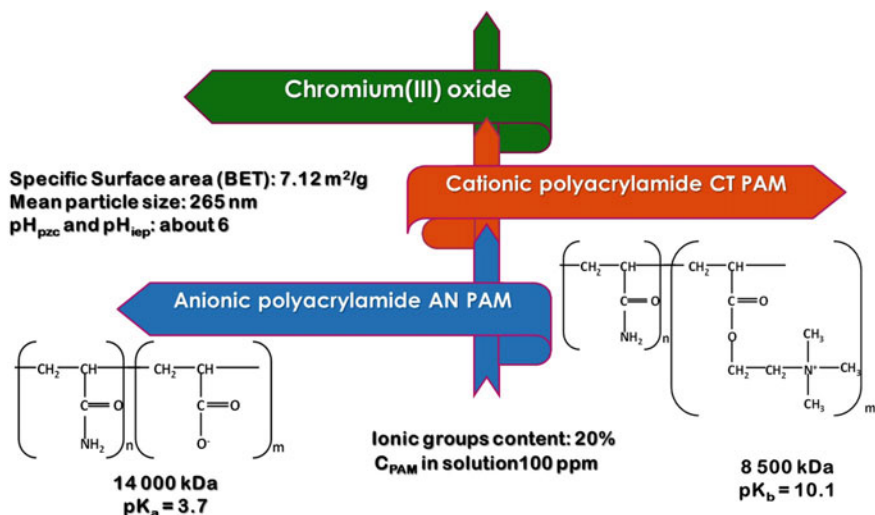


Fig. 7 Schematic representation of the Cr₂O₃ suspensions without and with cationic or anionic polyacrylamides (pzc—the point of zero charge, iep—the isoelectric point)

range 0–100. For the largely stable systems, the TSI takes values close to zero, and the increase in its value indicates a decrease in the suspension stability.

The analysis of the TSI values (Fig. 8a) shows that the chromium(III) oxide suspension without the polymer is quite stable at pH 3 (TSI = 12.8). On the other hand, at pH 6, it is significantly destabilized (TSI = 61), and at pH 9, it becomes an intermediate state between the two extreme tested pH values (TSI = 29.3). Moreover, the addition of cationic PAM has a greater effect on the stability of the solid suspension (especially at pH 3 and 6) compared to the anionic polymer.

Such behavior can be explained based on the analysis of adsorption and electrokinetic properties of the systems.

The adsorbed amount of ionic PAM depends evidently on the solution pH (Fig. 8(b)). In the case of AN PAM, a decrease in the polymer adsorption is observed

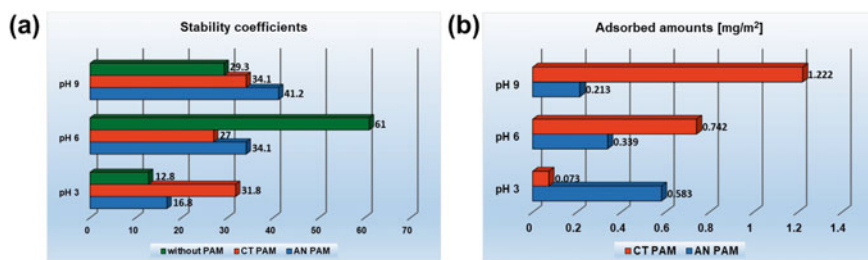


Fig. 8 Stability coefficients **a** and adsorbed amounts **b** obtained in the examined systems at pH 3, 6, and 9

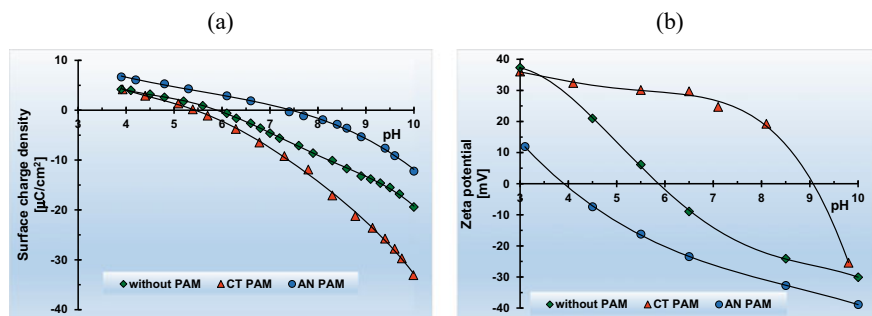


Fig. 9 Surface charge density **a** and zeta potential **b** of chromium(III) oxide particles without and covered with the PAM adsorption layers

with an increase of the solution pH, whereas for CT PAM, this tendency is reversed. This is due to both changes in the sign and density of the surface charge of the solid (pH_{pzc} is about 6) and the degree of ionization of the polymer functional groups.

The analysis of changes in the surface charge density of chromium(III) oxide particles caused by the polyacrylamide adsorption leads to the conclusion that the presence of CT PAM causes a decrease in the surface charge density of the solid compared to the system without the polymer (Fig. 9a). In turn, the addition of AN PAM results in the increase of the solid surface charge density. This is a result of the interactions of the ionic groups of macromolecules with the surface active sites, the presence of which in the by-surface layer of the solution results in the formation of additional charged adsorbent groups: negative ones (in the case of CT PAM) or positive ones (in the case of AN PAM).

The changes in the zeta potential of solid particles in the presence of PAM (Fig. 9b) are the result of three overlapping effects: (a) the presence of charges originating from the functional groups of the adsorbed polymeric chains; (b) the shift of the slipping plane by the macromolecules bound to the adsorbent surface; (c) the shift of counterions in the Stern layer due to the polymer adsorption. In the case of the studied systems, the greatest contribution seems to be the effect of the ionized functional groups of macromolecules presence in the area of the slipping plane associated with the segments located in the loop and tail structures of the adsorbed PAM chains.

Considering the above information, it can be concluded that the main reason for the drastic destabilization of the suspension in the polymer absence at pH 6 is the fact that this pH value corresponds to Cr_2O_3 pH_{iep} (the electrokinetic potential of the solid particles is zero). The zero charge of the diffusion layer means no electrostatic repulsive forces between the particles. This makes it much easier for them to collide with each other resulting in the system coagulation.

The greatest changes in the stability of the Cr_2O_3 aqueous suspension in the presence of ionic PAM (in relation to the system without the polymer) were observed for the cationic form of polyacrylamide at pH 3 and 6 (Fig. 10).

The deterioration of the stability of the cationic PAM containing system at pH 3 is mainly due to the formation of polymer bridges between the solid particles.

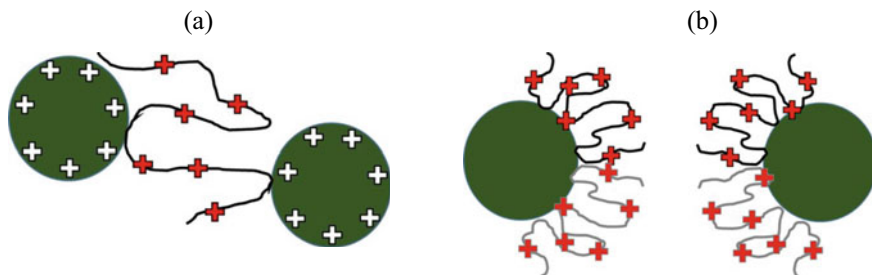


Fig. 10 Schematic presentation of the most probable mechanisms of chromium(III) oxide suspension stability in the PAM presence at **a** pH 3 and **b** pH 6

This is favored by: (a) the smallest PAM adsorption; (b) the stretched conformation of macromolecules; (c) the adsorbent-adsorbate repulsion. On the other hand, a significant increase in the stability of the system at pH 6 is a result of electrosteric interactions which are a consequence of: (a) larger CT PAM adsorption, (b) less stretched conformation of macromolecules, (c) the lack of adsorbent-adsorbate repulsion.

5 Conclusion

Constantly growing problems of natural environment protection due to larger and larger amounts of industrial wastes and communal sewages containing highly dispersed solids as well as significant amounts of organic substances promote search for effective methods of solid-phase separation with simultaneous removal of dissolved compounds from the aqueous medium. The use of water-soluble polymers seems to be an excellent solution to this problem. This is mainly due to the possibility of adopting many different conformations by the adsorbed polymer chains, depending on the parameters of the system related to the characteristics of adsorbate and adsorbent as well as the process conditions (solution composition, its pH and ionic strength, temperature). Controlling these parameters, it is possible to obtain an adsorptive polymer layer with a specific structure which affects directly the solid suspension stability and the possibility of its effective separation.

References

1. Napper DH (1983) Polymeric stabilization of colloidal dispersions, Academic Press. INC, London
2. Wiśniewska M (2011) A Review of temperature influence on adsorption mechanism and conformation of water soluble polymers on the solid surface. *J Dispers Sci Tech* 32:1605–1623

3. Wiśniewska M, Chibowski S (2005) Influences of temperature and purity of polyacrylic acid on its adsorption and surface structures at ZrO_2 -polymer solution interface. *Ads Sci Tech* 23:655–667
4. Wiśniewska M, Chibowski S, Urban T (2016) Adsorption properties of the nanozirconia/anionic polyacrylamide system—effects of surfactant presence, solution pH and polymer carboxyl groups content. *Appl Surf Sci* 370:351–356
5. Miller CA, Neogi P (1985) *Interfacial phenomena—equilibrium and dynamic effects*. Marcel Dekker Inc., New York
6. Farrokhpay S (2009) A review of polymeric dispersant stabilization of titania pigment. *Adv Colloid Interf Sci* 151:24–32
7. Heller W, Pugh TL (1960) “Steric” stabilization of colloidal solutions by adsorption of flexible macromolecules. *J Polym Sci* 47:203–217
8. Tadros T (2012) Electrostatic and Steric Stabilization of Colloidal Dispersions in “Electrical Phenomena at Interfaces and Biointerfaces: Fundamentals and Applications in Nano-, Bio-, and Environmental Sciences”, chapter 10, H Ohshima Ed., John Wiley & Sons, Inc.
9. Somasundaran P, Runkana V (2005) Investigation of the flocculation of colloidal suspensions by controlling adsorbed layer microstructure and population balance modelling. *Chem Eng Res Design* 83:905–914
10. Tripathy T, De BR (2006) Flocculation: a new way to treat the waste water. *J Phys Sci* 19:93–127
11. Brostow W, Lobland HE, Pal S, Singh RP (2009) Polymeric flocculants for wastewater and industrial effluent treatment. *J Mat Educ* 31:157–166
12. Guozhong C (2004) *Nanostructures and nanomaterials—synthesis*. Imperial College Press, London, Properties & Applications
13. Landman J, Schelling MPM, Tuinier R, Vis M (2021) Repulsive and attractive depletion forces mediated by nonadsorbing polyelectrolytes in the Donnan limit. *J Chem Phys* 154:164904
14. Shvets AA, Semenov AN (2013) Effective interactions between solid particles mediated by free polymer in solution. *J Chem Phys* 139:054905
15. Riddick TM (1968) *Control of colloid stability through zeta potential*. Livingston Pub. Co. edition, Wynnewood, PA
16. M’Pandou A, Siffert B (1987) Polyethyleneglycol adsorption at the TiO_2 - H_2O interface—distortion of ionic structure and shear plane position. *Colloids Surf A* 24:159–172
17. Chibowski S, Wiśniewska M, Urban T (2010) Influence of solution pH on stability of aluminum oxide suspension in presence of polyacrylic acid. *Adsorption* 16:321–332
18. Wiśniewska M, Chibowski S, Urban T (2012) Investigation of the stability of an alumina suspension in the presence of ionic polyacrylamide. *Thin Solid Films* 520:6158–6164
19. Wiśniewska M (2011) The temperature effect on electrokinetic properties of the silica—polyvinyl alcohol (PVA) system. *Colloid Polym Sci* 289:341–344
20. Wiśniewska M (2013) Possibilities of colloidal silica separation from water suspension in the polyethylene glycol (PEG) presence at different temperatures. *Sep Sci Tech* 48:1073–1080
21. Wiśniewska M, Chibowski S, Urban T (2011) The spectrophotometric investigation of nonionic polymer adsorption (polyethylene glycol (PEG), polyethylene oxide (PEO) and polyvinyl alcohol (PVA)) Influence on the alumina suspension stability—effects of polymer type, its molecular weight and solution pH. *J Macromol Sci Part A* 48:851–854
22. Perez Huertas S, Terpiłowski K, Wiśniewska M, Zarko VI (2017) Influence of polyvinylpyrrolidone adsorption on stability of silica aqueous suspension—effects of polymer concentration and solid content. *Physicochem Prob Min Process* 53:121–135
23. Wiśniewska M, Chibowski S, Urban T, Sternik D (2017) Studies of anionic dendrimer adsorption mechanism on the zirconium(IV) oxide surface—electrokinetic and thermal properties of nanosized composites. *J Molec Liq* 246:25–31
24. Ostolska I, Wiśniewska M (2014) Application of the zeta potential measurements to explanation of colloidal Cr_2O_3 stability mechanism in the presence of the ionic polyamino acids. *Colloid Polym Sci* 292:2453–2464
25. Ostolska I, Wiśniewska M (2014) Comparison of the influence of polyaspartic acid and polylysine functional groups on the mechanism of polymeric film formation at the Cr_2O_3 —aqueous solution interface. *Appl Surf Sci* 311:734–739

26. Ostolska I, Wiśniewska M (2015) Investigation of the colloidal Cr_2O_3 removal possibilities from aqueous solution using the ionic polyamino acid block copolymers. *J Hazard Mat* 290:69–77
27. Ostolska I, Wiśniewska M, Nosal-Wiercińska A, Szabelska A, Gołębiowska B (2016) Adsorption layer structure in the system of the ionic block polyamino acid copolymers/ SiO_2 particles. *Colloids Surf A* 488:138–144
28. Szewczuk-Karpisz K, Wiśniewska M (2015) Investigation of removal possibilities of chromium(III) oxide from water solution in the presence of albumins. *Int J Env Sci Tech* 12:2947–2956
29. Szewczuk-Karpisz K, Wiśniewska M, Myśliwiec D (2015) Lysozyme adsorption on the colloidal chromium(III) oxide surface: its impact on the system stability. *Appl Surf Sci* 347:491–498
30. Szewczuk-Karpisz K, Wiśniewska M, Pac-Sosińska M, Choma A, Komanińska I (2016) Stability mechanism of the silica suspension in the *Sinorhizobium meliloti* 1021 exopolysaccharide presence. *J Ind Eng Chem* 35:108–114
31. Svenson S, Tomalia DA (2005) Dendrimers in biomedical applications - reflections on the field. *Adv Drug Deliv Rev* 14:2106–2129
32. Wiśniewska M, Nosal-Wiercińska A, Dąbrowska I, Szewczuk-Karpisz K (2013) Effect of the solid pore size on the structure of polymer film at the metal oxide/polyacrylic acid solution interface—temperature impact. *Micropor Mesopor Mat* 175:92–98
33. Fijałkowska G, Wiśniewska M, Szewczuk-Karpisz K, Jędruchiewicz K, Oleszczuk P (2021) Comparison of lead(II) ions accumulation and bioavailability on the montmorillonite and kaolinite surfaces in the presence of polyacrylamide soil flocculant. *Chemosphere* 276:130088
34. Szewczuk-Karpisz K, Wiśniewska M, Nowicki P, Oleszczuk P (2020) Influence of protein internal stability on its removal mechanism from aqueous solutions using eco-friendly horsetail herb-based engineered biochar. *Chem Eng J* 388:124156
35. Szewczuk-Karpisz K, Wiśniewska M, Medykowska M, Galaburda MV, Bogatyrov VM, Oranska OI, Błażnio M, Oleszczuk P (2021) Simultaneous adsorption of Cu(II) ions and poly(acrylic acid) on the hybrid carbon-mineral nanocomposites with metallic elements. *J Hazard Mat* 412:125138
36. Wiśniewska M, Chibowski S, Urban (2015) Impact of polyacrylamide with different contents of carboxyl groups on the chromium (III) oxide adsorption properties in aqueous solution. *J Hazard Mat* 283:815–823
37. Wiśniewska M, Chibowski S, Urban T (2016) Synthetic polyacrylamide as a potential flocculent to remove commercial chromium(III) oxide from aqueous suspension. *Int J Env Sci Tech* 13:679–690

Kinetic Regularities of the Interphase Diffusion-Controlled Processes Within Thin Film Formation



Yu. P. Vyshnevska  and I. V. Brazhnyk 

Abstract The diffusion kinetic regularities of the metal ionization processes in regard to the anionic composition of the electrolyte have been investigated. Analytical relations for studying processes of anodic dissolution involving labile complexes with the anions of the medium that reflect the nature of limiting current, Tafel slopes, and orders of reaction have been obtained. The mechanism of phase layers formation in presence of organic ligands and corresponding theoretical model representing the polarization resistance evolution during the film growth process has been discussed. Established kinetic relations constitute a theoretical basis for the analysis of the dynamic electrochemical systems with phase layers formation as advanced surface engineering and functionalization technique.

1 Introduction

Theoretical basis and analytical representation of the regularities of the transition metals ionization processes remains an area of high interest as it plays an important role in many scientific fields and practical applications. Extensive studying of the electrochemical kinetics of the anodic dissolution processes has been performed in [1–5] that remain a solid theoretical foundation for modern research. At the same time, the emerging areas like thin-film deposition, surface engineering, and functionalization are constantly elevating the importance of theoretical representation of mixed-phase and interphase diffusion processes.

Yu. P. Vyshnevska (✉)

National Technical University of Ukraine, Igor Sikorsky Kyiv Polytechnic Institute, 37, Peremohy Ave, Kyiv 03056, Ukraine

e-mail: vishnevsk@ukr.net

I. V. Brazhnyk

Gimasi SA, Piazzale Roncà, 4, 6850 Mendrisio, Switzerland

© The Author(s), under exclusive license to Springer Nature Switzerland AG 2023

O. Fesenko and L. Yatsenko (eds.), *Nanomaterials and Nanocomposites, Nanostructure Surfaces, and Their Applications*, Springer Proceedings in Physics 279,

https://doi.org/10.1007/978-3-031-18096-5_34

In present work, the most essential kinetic and diffusion regularities of the underlying processes of metal ionization, the diffusion of the reaction components accompanied by the formation of the labile and inert complexes in the dynamic systems amid the formation of phase layers are being discussed.

2 Materials and Experimental Methods

Polarization measurements were carried out in potentiostatic and potentiodynamic regimes in a three-electrode cell with separated cathodic and anodic compartments at 25 °C temperature in 0.5 M H₂SO₄ and 0.5 M HCl solutions. Armco iron and steel 08 kp were used as the working electrodes, platinum—as the counter-electrode and an Ag|AgCl|KCl(sat.) electrode—as the reference one. In this paper, the potential values are given with respect to the normal hydrogen electrode potential.

Polarization resistance measurements were used for the investigation of the metal ionization kinetics. Measurements have been carried out using two identical cylindrical electrodes in two-electrodes configuration with total surface area of 8 cm² according to the standard procedure commonly used for corrosion monitoring. Readings are presented as raw data and then interpreted with improved theoretical models to exclude any potential influence of the compensation mechanisms implemented within instrument.

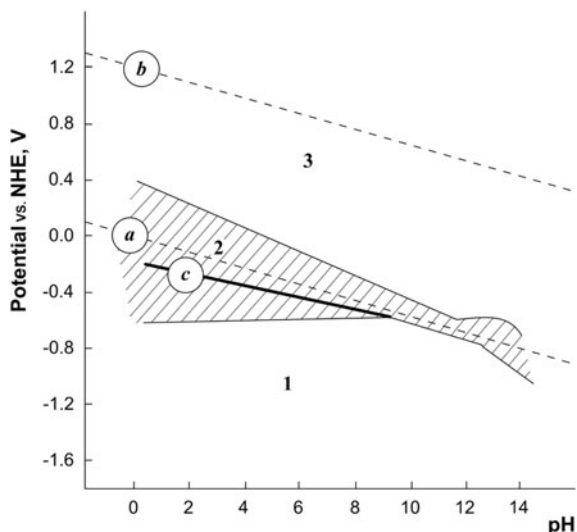
3 Results and Discussion

The electrochemical system may be defined using its thermodynamic, kinetic, and diffusion parameters. Surface effects involving metal ionization processes and subsequent formation of phase layers in neutral medium have been covered in [6] from the thermodynamic perspective. In this study, the thermodynamic states and transitions diagrams serve as a starting point while focusing predominantly on the investigation of kinetic and diffusion regularities of the metal ionization processes in regard to the anionic composition of the electrolyte as well as the complexation phenomena that may result in a drastic change in the electrochemical behavior of the system.

3.1 Diffusion Kinetic Regularities of the Metal Ionization Processes

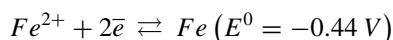
Figure 1 shows Pourbaix diagram for the Fe-H₂O system, where line *a* and *b* represent the relation of potential against pH for the hydrogen and oxygen electrode, respectively, while line *c*—relation of iron corrosion potential against pH. Area 1

Fig. 1 Pourbaix diagram of the Fe-H₂O system



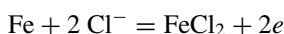
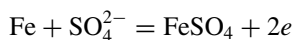
corresponds to immunity zone, area **2**—corrosion zone, and area **3**—passivation zone.

According to a Pourbaix diagram for the Fe-H₂O system [6–8], the metal potential in acidic medium is determined by an equilibrium:



This idealized model implies that the iron is present in the solution in the form of “free” Fe²⁺ cations. For the multicomponent Fe-H₂O-SO₄²⁻ or Fe-H₂O-Cl⁻ systems in a wide range of pH (pH 0–5), the metal ions do exist predominantly in a form of ion pairs Fe²⁺-SO₄²⁻ or Fe²⁺-Cl⁻, respectively. Such ion pairs may be treated as labile complexes and as will be shown play a crucial role in the metal ionization process.

Total reaction schema for sulfate and chloride anions may be presented as follows:



For the case of sulfate anions, the concentration of “free” Fe²⁺ cations may be calculated using complex instability constant:

$$K_H = 10^{-3} = \frac{[Fe^{2+}] \cdot [SO_4^{2-}]}{FeSO_4^{2-}} \quad (1)$$

Thus, only, $\approx 10^{-3}$ of total dissolved iron is present in a form of “free” Fe^{2+} cations. The calculated value may be used for the determination of the metal potential in presence of sulfate anions according to Nernst equation, as follows:

$$E = E^0 + \frac{b}{2} \lg 10^{-3} + \frac{b}{2} \lg [\text{FeSO}_4] - \frac{b}{2} \lg [\text{SO}_4^{2-}] \quad (2)$$

or in more convenient form:

$$E = \text{const} + \frac{b}{2} \lg [\text{FeSO}_4] - \frac{b}{2} \lg [\text{SO}_4^{2-}] \quad (3)$$

3.2 Limiting Current Nature and Theoretical Representation

The value of anodic current should be in agreement with a flow of the FeSO_4 as the reaction product from the metal surface. This assumption may be described using the equation of the Fick's First Law:

$$i = \frac{2 \cdot F \cdot D \cdot ([\text{FeSO}_4]_S - [\text{FeSO}_4]_0)}{\delta} \quad (4)$$

where $[\text{FeSO}_4]_S$ and $[\text{FeSO}_4]_0$ —concentration of the reaction product near the surface and within the bulk solution, respectively. For the studied systems with diluted solutions, the concentrations may be used instead of thermodynamic activity with sufficient accuracy.

For the pure sulfuric acid solution, (4) may be presented as:

$$i = \frac{2 \cdot F \cdot D \cdot [\text{FeSO}_4]_S}{\delta} \quad (5)$$

thus,

$$[\text{FeSO}_4]_S = \frac{i \cdot \delta}{2 \cdot F \cdot D} \quad (6)$$

Equation (6) for the surface concentration now may be used for substitution in (3) which gives:

$$E = \text{const}^* + \frac{b}{2} \lg i - \frac{b}{2} \lg [\text{SO}_4^{2-}]_S \quad (7)$$

For the relatively high concentration of sulfate anions in a solution and low anodic polarization currents, the value of surface concentration $[\text{SO}_4^{2-}]_S$ may be taken equal to bulk concentration $[\text{SO}_4^{2-}]_0$.

In the case of high polarization current density, the high concentration gradient of “free” sulfate anions will be established near the electrode/electrolyte interface. Thus, the surface concentration may be determined using relation $[SO_4^{2-}]_s = [SO_4^{2-}]_0 - i\delta/2FD$ which after substitution to (7) gives:

$$E_a = \text{const}^{**} + \frac{b}{2} \lg i - \frac{b}{2} \lg \left([SO_4^{2-}]_0 - \frac{i \cdot \delta}{2 \cdot F \cdot D} \right) \quad (8)$$

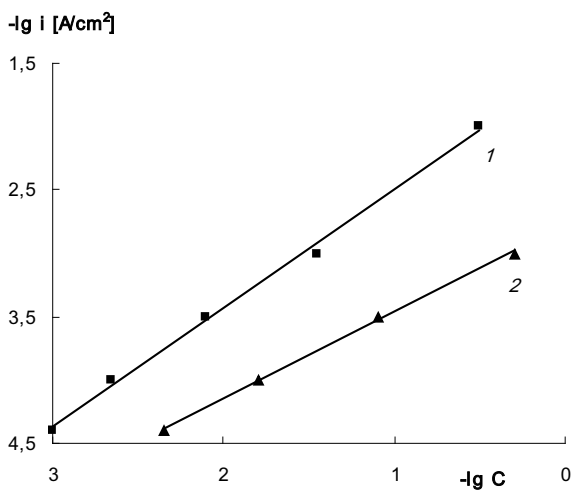
Analysis of Eq. (8) shows that for certain high current density values the under logarithmic component that represents the surface anion concentration may reach close-to-zero values that will be accompanied by a potential shift toward positive direction. Such conditions are established when the maximum delivery rate for the sulfate anions to the electrode surface has been reached that in current units may be presented as follows:

$$i_{\max} = \frac{2FD[SO_4^{2-}]_0}{\delta} \quad (9)$$

According to (9), i_{\max} is a limiting current of anodic dissolution of iron that is direct proportional to the sulfate anions concentration. Similar equations may be obtained for chloride anions while taking into account that the formation of such labile complex will require two Cl^- ions.

Analytically obtained relations are found to be in a good agreement with experimental data for systems with sulfate and chloride ions. Figure 2 represents dependence of current density against respected anion concentration in double logarithmic coordinates.

Fig. 2 Dependence of current density versus SO_4^{2-} (1) and Cl^- (2) anion concentration in double logarithmic coordinates



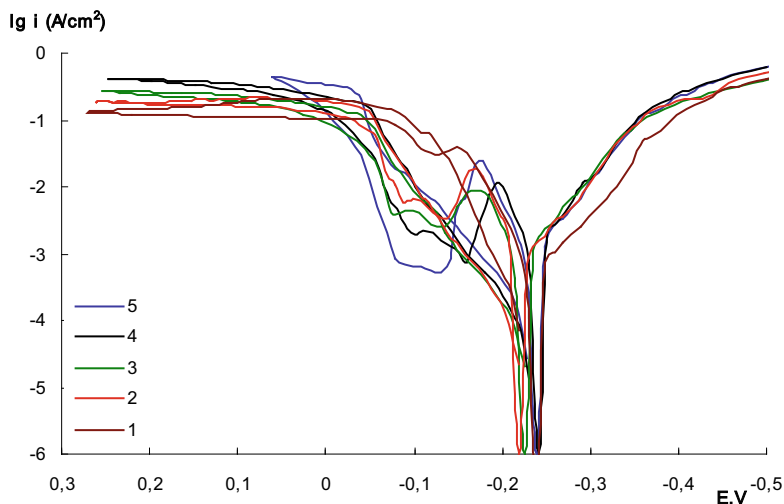


Fig. 3 Cathodic and anodic polarization curves for Armco iron in: 1—0.5 M H₂SO₄, 2—0.5 M H₂SO₄ + 0.5 M HCl (3:1), 3—0.5 M H₂SO₄ + 0.5 M HCl (1:1), 4—0.5 M H₂SO₄ + 0.5 M HCl (1:3), 5—0.5 M HCl

Analysis of polarization curves for sulfuric and hydrochloric acids solutions and their isomolar binary mixtures (Fig. 3) also shows marked correlation between diffusion coefficient of the respected anion and the value of limiting current density. Higher content of chloride ions that characterized by a higher value of diffusion coefficient expectedly produces higher value of limiting current density.

Thus, the experimental dependence of limiting anodic current value against the anion concentration has been obtained analytically that reaffirms proposed theoretical representation of direct participation of sulfate and chloride anions in the metal ionization process.

3.3 Tafel Slopes Theoretical Representation

Relation (8) may be interpreted as an equation of the polarization curve of the anodic process where the concentration of the SO₄²⁻ anions is taken into account. According to equation, the slope of the volt-ampere characteristic curve of the anodic process equals to 29 mV/decade (for $t = 25^{\circ}\text{C}$). Such slopes have been confirmed experimentally for the sulfuric acid solutions [5, 9].

Equation (8) also implies that the potential values and, thus, the shift of the polarization curve depend on the sulfate anions concentration. Increase in SO₄²⁻ concentration by 10 times leads to a potential shift of 29 mV toward negative direction.

For the investigation of the anion influence on the current value at constant potentials, (8) may be presented as:

$$\frac{b}{2} \lg i = E - E^0 - \frac{b}{2} \lg 10^{-3} - \frac{b}{2} \lg \frac{\delta}{2 \cdot F \cdot D} + \frac{b}{2} \lg [\text{SO}_4^{2-}] \quad (10)$$

or

$$\lg i = \text{const}^{**} + \frac{2 \cdot \eta}{b} + \lg [\text{SO}_4^{2-}] \quad (11)$$

where $\eta = E - E^0$ —overpotential of the anodic process, while $\text{const}^{**} = -\frac{b}{2} \lg 10^{-3} - \frac{b}{2} \lg \frac{\delta}{2 \cdot F \cdot D}$.

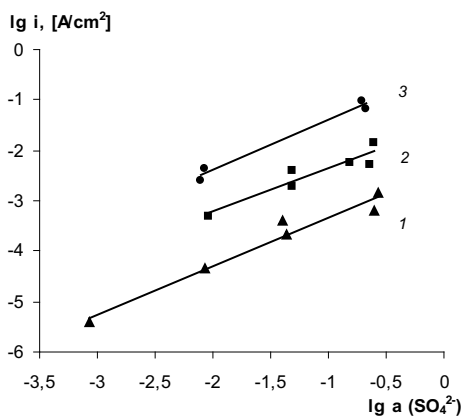
Here, overpotential is considered as difference between current potential value and standard electrode potential. Using a standard electrode potential as a defining point has advantage as the stationary (corrosion) potential may not always be presented in simple analytical form.

3.4 Order of Reaction

According to (11) during the anodic dissolution process in sulfuric acid solutions, the current value increases linearly with the concentration of the sulfate anions; thus, the reaction order for SO_4^{2-} is 1. Reaction order of 1 for such cases has been confirmed experimentally in [5, 9, 10]. It may be also demonstrated using the data presented in [11] processed in double logarithmic coordinates (Fig. 4).

According to $\text{Fe} + 2 \text{Cl}^- = \text{FeCl}_2 + 2e$, the order of reaction for chloride anions is 0.5 as one Fe^{2+} cation requires two Cl^- anions.

Fig. 4 Iron anodic dissolution rate at $E = -0.35 \text{ V}$ vs. thermodynamic activity of sulfate-ion in solution with different pH values: 1— 3 ± 0.1 ; 2— 4 ± 0.2 ; versus 3—5.0 (according to [11])



Equation (8) may also be transformed to the following expression that is commonly used for the electrochemical kinetics analysis:

$$i = \text{const}^{**} [\text{SO}_4^{2-}] \exp\left(\frac{2 \cdot R \cdot T \cdot \eta}{F}\right) \quad (12)$$

or

$$i = \text{const}^{**} [\text{SO}_4^{2-}]_s \exp\left(\frac{R \cdot T \cdot \eta}{0.5 \cdot F}\right) \quad (13)$$

Obtained Eq. (13) implies direct proportional relation between current density and the anions concentration that is found to be in a good agreement with experimental results. Important to notice that commonly adopted practice is to use similar equations assuming $\alpha = 0.5$ as a so-called dimensionless transfer coefficient suggesting that the anodic process is irreversible and take place in several single-electron electrochemical reactions. Thus, such coefficient serves mainly for the purpose to numerically equalize calculated values with experimental data, while in the proposed interpretation, the 0.5 coefficient value has been obtained analytically.

4 Mechanism and Regularities of the Phase Layers Formation

Discussed metal ionization schema and obtained kinetic regularities have been further expanded to cover multicomponent systems that contain ligands that are able to form inert complex compounds. This section highlights the preconditions, mechanism, and generic regularities of the phase layers formation in the presence of ligands of a different nature that constitute a theoretical basis for advanced metal protection, surface engineering, and functionalization techniques.

4.1 Phase Layers Formation Mechanism

The anionic composition of the electrolyte plays a critical role in metal ionization process. Introduction of organic or inorganic ligands that may form stable and slightly soluble complexes or complex salts into a system leads to a dramatic change in the electrode processes kinetics. Assuming the substantially higher stability constants when compared to labile complexes discussed earlier such an inert complex compounds via direct or possible intermediate complexation reaction would be the end product of the anodic dissolution process. Low solubility of such inert complex compounds prevents their extraction from the reaction zone with the diffusion flow caused by the concentration gradient. Accumulation of sufficiently stable and slightly

soluble complex compounds leads to a formation of phase layers on the metal surface that may slow down further ionization process.

4.2 Diffusion-Controlled Processes Within Thin Films

Kinetic regularities of the solid-state films growth on the metal surface have been extensively studied in [12]. Formation of dense and partially permeable films on metals may be analytically described using the following equation:

$$h^2 = k \cdot t = (2 \cdot D \cdot C) \cdot t, \quad (14)$$

where h —film height, D and C —diffusion coefficient and concentration of the reagents, t —time.

For the cases when deposition of inert complex compounds produce phase layers with low electrical conductivity and their resistance depends linearly from the layer thickness, the polarization resistance method may be used to study film growth process in a first approximation [13].

Due to a presence of growing film, the registered value of total polarization resistance value includes not only resistance of the charge transfer R_{ct} but also a diffusion resistance R_d . For the cases $R_d \gg R_{ct}$, the evolution of total polarization resistance reflects the dynamics of phase layer growth.

Figure 5 illustrates the evolution of total polarization resistance ($R_{total} = R_{ct} + R_d$) in time for two types of organic ligands amino acids (a) and guanidine derivatives (b).

The fact that rate-limiting step of the film growth process is diffusion within phase layers being formed and does not rely on the ligand delivery from the bulk solution may be demonstrated using the Fick's First Law for the case of methionine which show the slowest increase in total polarization resistance among other studied ligands. For ligand concentration 10^{-3} mol/l and the diffusion coefficient $\approx 10^{-5}$ cm²/sec and the diffusion layer thickness $\delta = 10^{-2}$ cm [14], the ligand flow toward 1 cm² of the electrode surface may be calculated as follows: $\Pi = D \cdot C / \delta = 10^{-9}$ mol/sec. Given such ligand delivery rate and the layer thickness of ≈ 10 nm that take into account geometrical parameters of the ligand molecule, the time required for complete layer formation is ≈ 10 s. This fact confirms that registered extended evolution of total polarization resistance in the studied systems does not caused by limited ligand delivery from the bulk solution.

Thus, obtained datasets for organic ligands of different nature sufficiently correlate with theoretical expectations and obey to parabolic law that may be described using the following equation:

$$R_{total} = R_{ct} + R_d = (2 \cdot D \cdot C)^{0.5} \cdot \rho \cdot t^{0.5}, \quad (15)$$

where ρ —effective specific resistance of the phase layer.

derivatives (b).

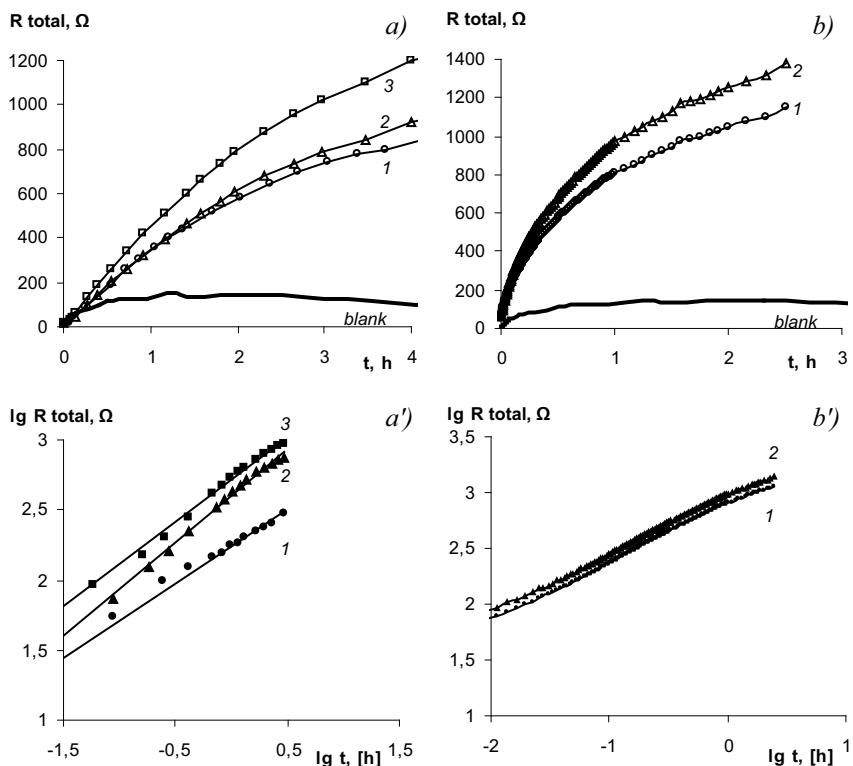


Fig. 5 Dependence of the total polarization resistance vs. exposure time in direct (a, b) and double logarithmic coordinates (a', b'). a), a'): 1–0.5 M H₂SO₄, 2–0.5 M H₂SO₄ + 5 g/l methionine, 3–0.5 M H₂SO₄ + 5 g/l cysteine, 4–0.5 M H₂SO₄ + 5 g/l acetylcysteine; b), b'): 1–0.5 M H₂SO₄, 2–0.5 M H₂SO₄ + 5 g/l polyhexamethyleneguanidine, 3–0.5 M H₂SO₄ + 5 g/l polyhexamethylene biguanidine

Analysis of the plot slopes in double logarithmic coordinates (5a' and 5b') allows one to determine the value of index in last equation. For the guanidine derivatives, the slopes value are found to be consistent across the range and equal to 0.51, which practically matches theoretical value of 0.5 for pure diffusion control of film growth. In the case of amino acids, (5a') the slopes tend to increase over time reaching the peak value of 0.48 after four hours of exposure that may be attributed to gradual changes in film structure and density.

4.3 Model Verification

According to (15), the value of total polarization resistance should depend linearly from the square root of ligand concentration. Taking into account the gradual changes in the system parameters during the film formation process, the datasets have been analyzed for 1000, 2000, 3000, and 8000 s of exposure time in the presence of different concentration of methionine (Fig. 6).

The experimental data are found to be in good agreement with theoretical expectations. Slopes tend to increase overtime for the systems with relatively porous films that may improve their density during formation. The slopes in double logarithmic coordinates $\lg R_{\text{total}} - \lg C$ allow one to determine the exact value of the index number A for the $(2 \cdot D \cdot C)^A$ component of Eq. (15) (Fig. 7). The slope values equal to 0.18, 0.31, 0.33, and 0.52 for 1000, 2000, 3000, and 8000 s, respectively.

Fig. 6 Dependence of the total polarization resistance vs. square root of the methionine concentration in 0.5 M H_2SO_4 at exposure time: 1–1000 s; 2–2000s; 3–3000 s; 4–8000 s

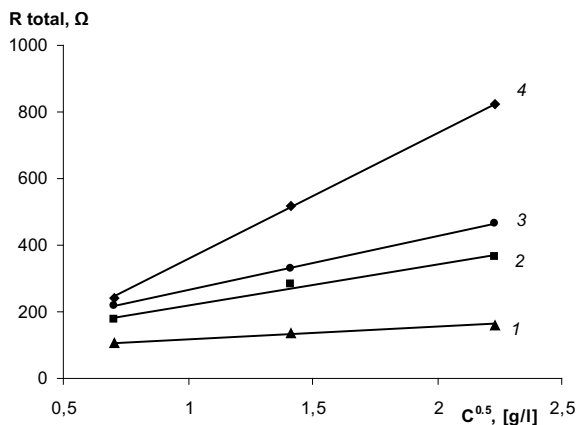


Fig. 7 Dependence of the total polarization resistance vs. methionine concentration in 0.5 M H_2SO_4 in double logarithmic coordinates at exposure time: 1–1000 s; 2–2000s; 3–3000 s; 4–8000 s

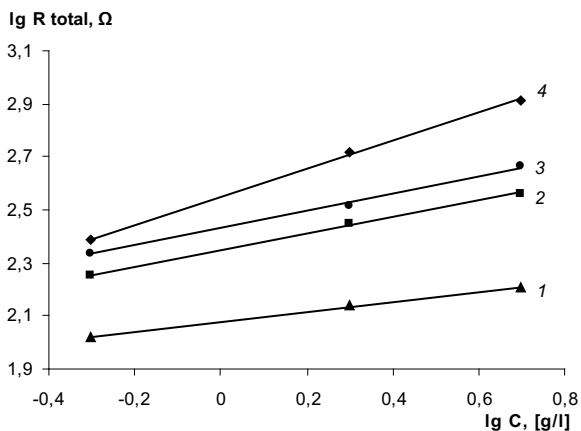


Fig. 8 Dependence of the total polarization resistance vs. methionine concentration in 0.5 M H₂SO₄ using the determined value of index number A at exposure time: 1–1000 s; 2–2000s; 3–3000 s; 4–8000 s

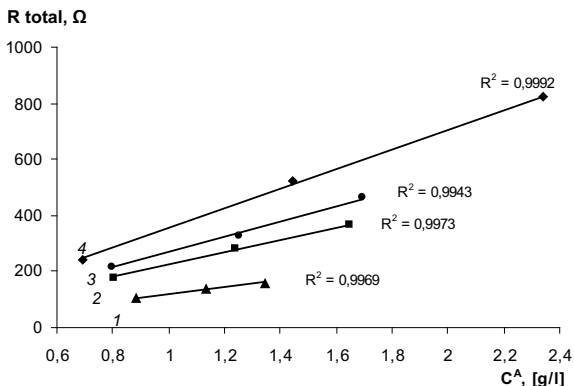


Figure 8 represents the plot based on adjusted data using the determined value of index number A. The value of standard deviation lay in range $0.99 < R^2 < 1$.

Equation (15) that has been initially derived from the equation for film growth with diffusion control has been verified against extensive set of ligands of different nature within practically justified concentration and time ranges that confirm its applicability for analysis of phase layers formation in such systems.

4.4 Applicability

One of the most significant practical consequences of the proposed mechanism and obtained theoretical representation of the phase layer formation processes in presence of ligands is that it allowed to uncover the nature of previously known equation that is widely used in corrosion science:

$$\lg \gamma = \text{const}_\gamma + \beta_\gamma \cdot \lg C, \quad (16)$$

where γ —inhibition coefficient, const_γ and β_γ —empirical constants.

The inhibition coefficient γ may be presented as v_0/v_i , where v_0 and v_i —corrosion rate in the solutions without and with inhibitors, respectively. Given the polarization resistance has the reverse value to the corrosion rate, the inhibition coefficient may be presented as

$$\gamma = v_0/v_i = R_i/R_0. \quad (17)$$

Thus,

$$R_i = \gamma \cdot R_0 \quad (18)$$

That after substitution to Eq. (15) gives

$$\gamma \cdot R_0 = (2 \cdot D \cdot C)^{0.5} \cdot \rho \cdot t^{0.5}$$

or

$$\gamma = [(2 \cdot D \cdot C)^{0.5} \cdot \rho \cdot t^{0.5}] / R_0 \quad (19)$$

Equation (19) now may be expressed in logarithmic form:

$$\lg \gamma = -\lg R_0 + 0.5 \lg(2 \cdot D \cdot t) + \lg \rho + 0.5 \lg C, \quad (20)$$

Which for any given exposure time ($t = \text{const}$) may be presented as follows:

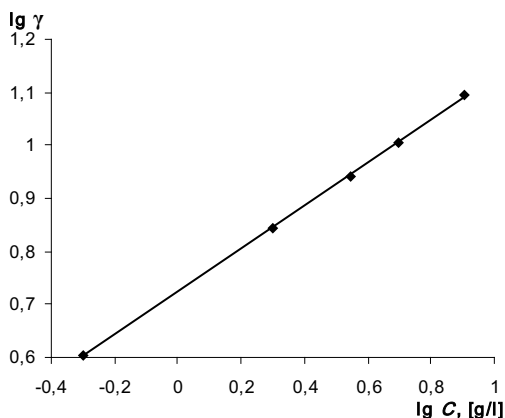
$$\lg \gamma = \text{const} + 0.5 \lg C \quad (21)$$

Experimental confirmation of such relation requires that the dependence of the inhibition coefficient against the ligand concentration in the coordinates $\lg \gamma - \lg C$ should be rendered as a straight line. Analysis has been carried out using the gravimetric measurements for different concentrations of methionine 0.5; 2; 3.5; 5; 8 g/l, and constant exposure time 168 h (Fig. 9).

Thus, the relation (21) analytically obtained from base Eq. (15) adequately represents the behavior of studied system that has been carried out using independent direct measurement method. Analysis of Eq. (20) shows that during the formation of phase layers the const_γ from the Eq. (16) corresponds to $-\lg R_0 + 0.5 \lg(2 \cdot D \cdot t) + \lg \rho$ [13], while the β_γ represents a slope in double logarithmic coordinates $\lg \gamma - \lg C$ that is found to be related to the structure of the formed film.

It may be concluded that obtained relations may be applied in a field of advanced surface engineering that rely on in situ synthesis and purposeful deposition of phase layers and improving the theoretical basis of the materials degradation prevention methods.

Fig.9 Dependence of the inhibition coefficient versus the methionine concentration in 0.5 M H_2SO_4 in double logarithmic coordinates



5 Conclusions

The diffusion kinetic regularities of the metal ionization processes in regard to the anionic composition of the electrolyte have been studied. Theoretical representation implying direct participation of the anions of electrolyte in the anodic dissolution process has been presented. Analytical relations for studying processes involving labile complexes with the metal cations that reflect the nature of limiting current of anodic dissolution, Tafel slopes, and orders of reaction have been obtained. The interpretation of so-called dimensionless transfer coefficient $\alpha = 0.5$ that is commonly used in the electrochemical kinetics analysis has been obtained analytically.

The mechanism of phase layers formation in presence of organic ligands in conjunction with the theoretical model representing the polarization resistance evolution during the film growth process has been discussed. Equation similar to $\lg \gamma = \text{const}_\gamma + \beta_\gamma \cdot \lg C$ that is commonly used in corrosion science has been obtained analytically from the relation for film growth with diffusion control. The nature of const_γ and β_γ , empiric values has been revealed, and the model applicability has been demonstrated for wide range of conditions.

Acknowledgements This chapter contains substantial amount of results obtained under supervision of Professor Dmytro Tkachenko. Over the years, he dedicated most of his energy to a great honor of finding and solving scientific challenges in the field of electrochemical kinetics of molten salts and corrosion science. His valuable contribution to a scientific knowledge puts him in a line with the most remarkable members of Kyiv Electrochemical School.

References

1. Hibert F, Miyoshi Y, Eichkorn G, Lorenz WJ (1971) Correlations between the kinetics of electrolytic dissolution and deposition of iron. *J Electrochem Soc* 118:1919–1926. <https://doi.org/10.1149/1.2407869>
2. Atkinson A, Marshall A (1978) Anodic dissolution of iron in acidic chloride solutions. *Corros Sci* 18:427–439. [https://doi.org/10.1016/S0010-938X\(78\)80038-9](https://doi.org/10.1016/S0010-938X(78)80038-9)
3. El Miligy AA, Geana D, Lorenz WJ (1975) A theoretical treatment of the kinetics of iron dissolution and passivation. *Electrochim Acta* 20:273–281. [https://doi.org/10.1016/0013-4686\(75\)90005-5](https://doi.org/10.1016/0013-4686(75)90005-5)
4. Bockris JO, Drazic D, Despic AR (1961) The electrode kinetics of the deposition and dissolution of iron. *Electrochim Acta* 4:325–361. [https://doi.org/10.1016/0013-4686\(62\)87007-8](https://doi.org/10.1016/0013-4686(62)87007-8)
5. Drazic DM (1989) Iron and its electrochemistry in an active state. *Mod Aspects Electrochem* 19:69–192
6. Ledovskykh VM, Vyshnevskaya YP, Brazhnyk IV, Levchenko SV (2021) Thermodynamic States and Transitions Diagrams in Surface Engineering for the Material Degradation Prevention. In: Fesenko O, Yatsenko L (eds) *Nanomaterials and nanocomposites, nanostructure surfaces, and their applications*. NANO 2020. Springer Proceedings in Physics, vol 263. Springer, Cham. https://doi.org/10.1007/978-3-030-74741-1_30
7. Pourbaix M (1974) *Atlas of electrochemical equilibria in aqueous solutions*. National Association of Corrosion Engineers, Houston, Texas, p 551

8. Pourbaix M, Pourbaix A (eds) (1982) Diagrams of chemical and electrochemical equilibria: their setting-up and applications, proceedings of a NATO advanced research workshop, CEBELCOR's reports techniques 142, RT 263, CEBELOR, Brussels
9. Vishnevskaya YP, Tkalenko DA, Byk MV et al (2007) To the Tafel slopes at the anodic dissolution of iron in sulfuric electrolytes. *Prot Met* 43:492–494. <https://doi.org/10.1134/S003317320705013X>
10. Tkalenko DA, Vishnevskaya YP, Byk MV (2008) The effect of anionic composition of electrolytes on the anodic dissolution of iron-family metals. *Prot Met* 44:415–417. <https://doi.org/10.1134/S0033173208040206>
11. Florianovich GM (1978) Mechanism of the active dissolution of metals of the iron group. *VINITI Series Corros Rust Protect* 6:136–179
12. Dybkov VI (2010) Reaction diffusion and solid state chemical kinetics. Trans Tech Publications Ltd, Zurich. <https://doi.org/10.4028/www.scientific.net/MSFo.67-68>
13. Tkalenko DA, Vyshnevs'ka YP, Herasymenko YS et al (2013) Changes in polarization resistance in the process of formation of protective phase layers with participation of organic ligands. *Mater Sci* 49:304–310. <https://doi.org/10.1007/s11003-013-9615-1>
14. Kublanovskii VS, Gorodyskii AV, Belinskii VN, Glushchak TS (1978) Changes of concentration in near-electrode layers in the process of electrolysis. *Naukova Dumka*, Kyiv

Ionic Conductivity in Single Crystals, Amorphous and Nanocrystalline $\text{Li}_2\text{Ge}_7\text{O}_{15}$ Doped with Cr, Mn, Cu, Al, Gd



M. Trubitsyn, M. Koptiev, and M. Volnianskii

Abstract Electrical conductivity σ was studied in single crystals, amorphous and nanocrystalline lithium heptagermanate $\text{Li}_2\text{Ge}_7\text{O}_{15}$ doped with Cr, Mn, Cu, Al, and Gd ions. The single crystals of $\text{Li}_2\text{Ge}_7\text{O}_{15}$ were grown by Czochralskii method; the glass was prepared by quenching the melt. Nanometer-sized crystals were obtained by controlled crystallization of the amorphous phase. Heterovalent doping strongly influences σ in $\text{Li}_2\text{Ge}_7\text{O}_{15}$ single crystals and makes it possible to control ionic transport in a broad range. The doping effects are discussed based on the models of the impurity ions in $\text{Li}_2\text{Ge}_7\text{O}_{15}$ crystal structure. In undoped amorphous and nanocrystalline $\text{Li}_2\text{Ge}_7\text{O}_{15}$, conductivity increases in about three and four orders of magnitude correspondingly as compared to a single crystal. Doping of $\text{Li}_2\text{Ge}_7\text{O}_{15}$ glass and nanocrystals with small amounts of the impurities has a less pronounced effect than for the single crystal. It is argued that electrical conductivity in various structural states of $\text{Li}_2\text{Ge}_7\text{O}_{15}$ is provided by mobile lithium ions which are weakly bound to the germanium-oxygen framework of the structure.

Keywords Ionic conduction · Single crystal · Nanocrystals · Glass · Doping · Lithium heptagermanate

1 Introduction

Rapid development of solid-state ionics is stimulated by wide applications of solid electrolytes in batteries, fuel cells, supercapacitors, gas sensors [1, 2]. The structure of the solids is one of the most important factors providing for fast ionic transport. Therefore, design of new superionic materials includes purposeful modification of the structure on atomic, nano- and micrometer scales, formation of the morphology in multiphase composites. Variation of chemical composition and introduction of impurities represents an effective way to enhance ionic conduction. The effect of

M. Trubitsyn (✉) · M. Koptiev · M. Volnianskii
Experimental Physics Department, Oles Honchar Dnipro National University, Gagarina Ave-72,
Dnipro 49045, Ukraine
e-mail: trubitsyn_m@ua.fm

doping with isovalent impurity often can be attributed to mechanical disturbance introduced due to mismatch of the radiuses of impurity and the host ions. Heterovalent doping in addition introduces certain electrical perturbation because of charge imbalance between impurity and substituted host. In the latter case, electroneutrality of the lattice can be kept by generation of additional charged defects which compensate charge misfit of the impurity. As a rule, charge compensation of the heterovalent dopant can be provided by the defects with relatively low activation energy of creation. Namely, such defects can be vacancies or interstitials of the host ions which are the typical intrinsic defects of the crystalline media. Often, the charge-compensating defects can be mobile enough to make a considerable contribution to charge transfer. In that case, the effect of heterovalent doping on conductivity is determined by mobile charge-compensating defects, and not by the impurity itself.

Lithium heptagermanate $\text{Li}_2\text{Ge}_7\text{O}_{15}$ is the representative of lithium-germanium oxides family ($\text{Li}_2\text{O-GeO}_2$) [3] which undergoes structural phase transition to polar state below $T_C = 283$ K [4, 5] and attracts attention owing to unusual features of so-called weak ferroelectricity [6]. The crystals of $\text{Li}_2\text{O-GeO}_2$ family have the lattices of framework type. The lattices skeletons are formed by covalent Ge-O polyhedrons. Li ions occupy the sites within structural cavities and being loosely bound to the structural frame, demonstrate high amplitudes of thermal vibrations around the regular positions. As first shown in [7], electrical conductivity σ of $\text{Li}_2\text{O-GeO}_2$ ceramics was dependent on the ratio between Li_2O and GeO_2 components in the chemical formulae and enhanced in the compounds with higher content of lithium oxide. Such correlation between σ value and the chemical composition gave suggestion on Li ions contribution to charge transfer in the crystals of lithium-germanium oxides. Subsequent studies of electrical properties [8–10] as well as ^7Li NMR spectra and spin–lattice relaxation [11] showed that electrical conductivity of $\text{Li}_2\text{Ge}_7\text{O}_{15}$ crystals was mainly determined by mobile lithium interstitials A_{Li} . Li ions transport is now considered as a main mechanism of charge transfer in the compounds of $\text{Li}_2\text{O-GeO}_2$ family.

Synthesis of confined systems and nanocomposites determines the modern trend in design of materials for solid-state ionic [2, 12, 13]. Compared to single crystals, strong increase of conductivity was found for amorphous and nanocrystalline $\text{Li}_2\text{O-}x\text{GeO}_2$ compounds ($x = 7, 11.5, 18$) [14–17]. In this paper, we study the influence of doping with Cr, Mn, Cu, Al, and Gd impurities on ionic conductivity in the single crystals, nanocrystalline and amorphous lithium heptagermanate.

2 The Technology and Experimental Details

The dopants were added in certain amounts to the chemicals, and the resulting mixture was synthesized and subsequently used for the crystal growing and the glass preparation. Nominally, pure and doped $\text{Li}_2\text{Ge}_7\text{O}_{15}$ single crystals were grown from the melt by Czochralskii method. The crystals were transparent and lightly colored depending on the dopant used. The lithium heptagermanate glasses were prepared

by quenching the melted charge. The glasses were transparent and did not contain visible inhomogeneities, turbidities, and inclusions. Nanocrystalline glass–ceramics and micrometer-sized polycrystalline samples were prepared by controlled glass devitrification as described in [14, 15].

Electrical properties were measured in AC field by a bridge method (AC bridge E7-10, LCR-Meter Keysight E4980AL). The samples were prepared as the plane parallel plates with dimensions of about $5 \times 5 \text{ mm}^2$ and widths near 1 mm. The main planes of the single crystalline samples were cut off perpendicular to the crystal axes. Pt electrodes were sputtered on the sample's main planes in an Ar atmosphere.

3 Ionic Conductivity in Pure and Doped $\text{Li}_2\text{Ge}_7\text{O}_{15}$ Single Crystals

3.1 Anisotropy of the Electrical Conductivity and the Crystal Structure

The measurements of electrical properties revealed strong anisotropy of conductivity in $\text{Li}_2\text{Ge}_7\text{O}_{15}$ single crystals [8]. Figure 1 shows the dependences $\sigma(1/T)$ measured in AC field along the crystal axes and plotted in a semi-logarithmic scale. Here, $b > c > a$ is in accord with the notations in [18–20].

One can see that in high temperature interval ($T > 500 \text{ K}$), conductivity becomes strongly anisotropic (Fig. 1). Along a axis σ is more than an order of magnitude higher than conductivity along c axis and two orders of magnitude higher as compared with σ measured along b axis. Above $\sim 500 \text{ K}$, the $\sigma(1/T)$ dependences for $E \parallel a$ and c axes in Arrhenius scale show nearly the same slope corresponding to activation energy value of about 1.04 eV. Such behavior testifies for the single mechanism of charge transfer. Naturally, that the observed anisotropy of σ is determined by the specific features of $\text{Li}_2\text{Ge}_7\text{O}_{15}$ crystal structure (Fig. 2).

Fig. 1 Temperature dependence of $\text{Li}_2\text{Ge}_7\text{O}_{15}$ single-crystal conductivity, measured along the crystal axes: $E \parallel a$ (1), b (2), and c (3) [8]. The experimental data are plotted in a semi-logarithmic scale as a product ($\sigma \times T$) vs reciprocal temperature. AC field frequency was $f = 1 \text{ kHz}$

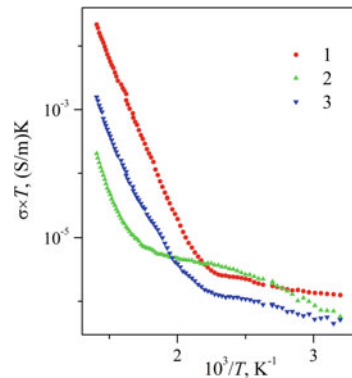
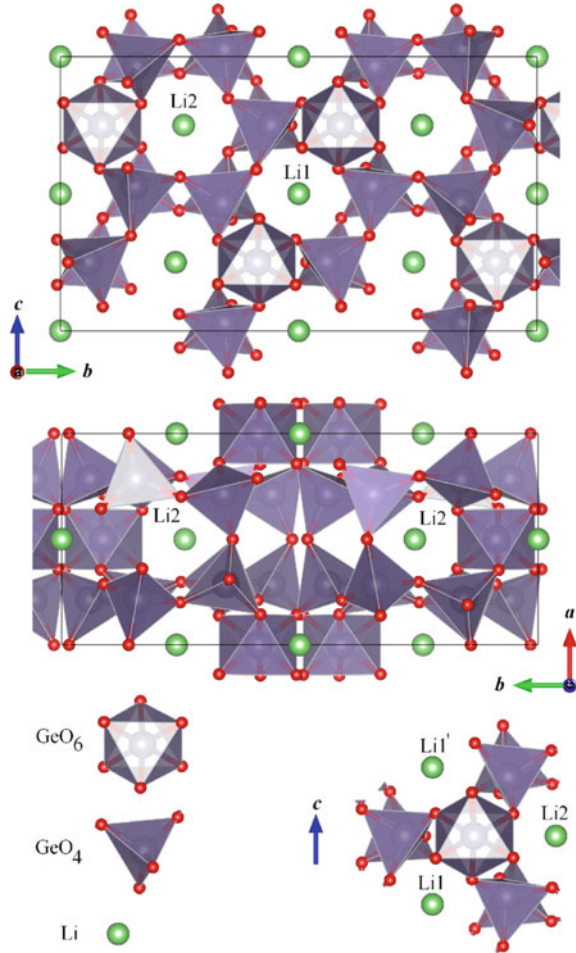


Fig. 2 Crystal structure of $\text{Li}_2\text{Ge}_7\text{O}_{15}$ in paraelectric phase: projection on (bc) and (ab) planes [19, 20]. At the bottom right—the structural unit consisting of a single $[\text{GeO}_6]$ octahedron linked to six $[\text{GeO}_4]$ tetrahedra and two structurally inequivalent Li1 and Li2 ions



According to X-ray and neutron diffraction studies [18–20] in the paraelectric phase ($T > T_C = 283$ K [4, 5]), the symmetry of $\text{Li}_2\text{Ge}_7\text{O}_{15}$ structure corresponds to orthorhombic D_{2h}^{14} space group, and the unit cell includes $Z = 4$ formula units. The frame of the crystal structure is formed by octahedral GeO_6 and tetrahedral GeO_4 anion complexes (Fig. 2). The germanium-oxygen groups are linked by oxygen ions in the common vertices of the polyhedrons.

The essential feature of $\text{Li}_2\text{Ge}_7\text{O}_{15}$ crystal structure is the presence of two types of the structural channels which pass through the germanium-oxygen lattice framework and directed along a and c axes. Lithium ions occupy two structurally inequivalent positions Li1 (point symmetry C_i) and Li2 (point symmetry C_2). Li1 is located in the sites within the structural channels directed along a axis. Li2 occupies the special positions at the intersection points of the structural channels directed along a and c axes (Fig. 2).

From the data shown in Figs. 1 and 2, one can see that the values of conductivity reflect the features of the crystal structure. Conductivity is highest in directions of \mathbf{a} and \mathbf{c} axes, i.e., along the structural channels in which Li ions are located. This fact testifies in favor of lithium charge transfer in $\text{Li}_2\text{Ge}_7\text{O}_{15}$ single crystals. There are two types of the structural channels along \mathbf{a} axis (Fig. 2). The defects from both lithium sublattices Li1, 2 can contribute to charge transfer that provides maximal conductivity in this direction. Along \mathbf{c} axis, there is only one type of the structural channels with Li2 sites and for $\mathbf{E} \parallel \mathbf{c}$ conductivity has an intermediate value. Absence of the channels in \mathbf{b} direction hinders Li ions migration and results in minimal values of σ (Fig. 1).

The question what defects in lithium sublattices (interstitials A_{Li} or vacancies V_{Li}) determine the ionic transport can be answered by studying influence of aliovalent doping on conductivity in $\text{Li}_2\text{Ge}_7\text{O}_{15}$ single crystals. The first results on this subject were reported in [21, 22].

3.2 Doping Effects on Conductivity in Single Crystals

Figure 3 shows the $\sigma(1/T)$ dependences measured in $\text{Li}_2\text{Ge}_7\text{O}_{15}$ single crystals doped with Cr, Mn, Cu, Al, and Gd ions. The data are presented for field orientation $\mathbf{E} \parallel \mathbf{a}$, at which the conductivity is maximal (Fig. 1). The activation energies estimated for $T > 500$ K are gathered in Table 1.

One can see that small amounts of the used dopants change conductivity value of about two orders of magnitude. Some dopants (Cr, Al) notably increase conductivity whereas another impurities (Mn, Gd) decrease σ . For all these dopants, activation energy has nearly the same value (Table 1). Somewhat different behavior of conductivity is observed for $\text{Li}_2\text{Ge}_7\text{O}_{15}:\text{Cu}$ crystal (curve 4 in Fig. 3)—at $T > 500$ K, the $\sigma(1/T)$ dependence has a greater slope in comparison with other dopants (Table 1).

Fig. 3 $\sigma(1/T)$ dependencies for $\text{Li}_2\text{Ge}_7\text{O}_{15}$: 1—pure single crystal and the single crystals doped with 2—Cr (0.1% wt), 3—Mn (0.03% wt) [21], 4—Cu (0.09% wt), 5—Al (0.15% wt), 6—Gd (0.03% wt). $\mathbf{E} \parallel \mathbf{a}$, $f = 1$ kHz

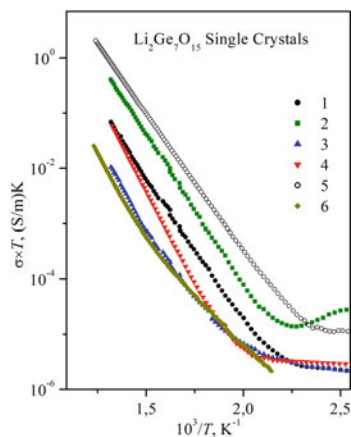


Table 1 Values of conductivity and activation energy determined from the data in Fig. 3 for pure and doped $\text{Li}_2\text{Ge}_7\text{O}_{15}$ single crystals

Pure and doped $\text{Li}_2\text{Ge}_7\text{O}_{15}$ crystals	Conductivity σ , S/m, ($T = 500$ K)	Activation energy, U_a , eV, $Ella$
Undoped crystal	3.9×10^{-8}	1.04
Cr (0.1% wt)	1.6×10^{-7}	1.08
Mn (0.03% wt)	1.3×10^{-8}	1.09
Cu (0.09% wt)	1.2×10^{-8}	1.27
Al (0.15% wt)	6.7×10^{-7}	1.00
Gd (0.03% wt)	1.3×10^{-8}	0.94

The information on the impurities charge state and location in the crystal structure can help to interpret the doping effects on σ .

$\text{Li}_2\text{Ge}_7\text{O}_{15}:\text{Cr}$. $\text{Li}_2\text{Ge}_7\text{O}_{15}$ crystals doped with chromium were studied, first, as the promising optical medium [23]. Somewhat later, the authors of [24] studied EPR spectra and proposed that chromium substituted for germanium hosts within oxygen octahedral groups $\text{Cr}^{3+} \rightarrow \text{Ge1}$ (Fig. 2). Such conclusion seems reasonable accounting ionic charges of chromium impurity ($r_{\text{Cr}^{3+}} = 0.615$ Å, Coordination Number = VI) and the host cations Ge^{4+} ($r_{\text{Ge}^{4+}} = 0.39$ Å (CN = IV), 0.53 Å (CN = VI)), Li^+ ($r_{\text{Li}^+} = 0.59$ Å (CN = IV), 0.76 Å (CN = VI)) [25]. Lowering the positional symmetry of the paramagnetic ions from C_2 to C_1 was attributed to formation of pair centers in accord with the scheme [24]: $\text{Cr}^{3+} - \text{A}_{\text{Li}^+}$, where lithium interstitials acted as local charge compensators of the excess charge introduced by the heterovalent substitution $\text{Cr}^{3+}(\text{Ge}^{4+})$. Afterward, this model was confirmed by studying luminescence [26–28] and EPR spectra [29, 30]. In accord with this model, locally broken C_2 axis generates two equivalent $\text{Cr}^{3+} - \text{A}_{\text{Li}^+}$ centers with oppositely directed dipole moments. Reorientations of $\text{Cr}^{3+} - \text{A}_{\text{Li}^+}$ pair centers between equivalent configurations were detected by dielectric measurements [31] and by motional broadening of EPR lines [32].

The available information shows that doping with Cr increases a number of lithium interstitials A_{Li} . These interstitials are excess as compared to the stoichiometry of the crystal and can move in an external electric field. Correspondingly, increase of conductivity in $\text{Li}_2\text{Ge}_7\text{O}_{15}:\text{Cr}$ (Fig. 3) can be attributed to A_{Li} moving along the structural channels.

$\text{Li}_2\text{Ge}_7\text{O}_{15}:\text{Mn}$. The study of EPR spectra in [33] and luminescence spectra in [27, 28] showed that in $\text{Li}_2\text{Ge}_7\text{O}_{15}$ crystal lattice manganese impurity exists in bivalent Mn^{2+} and tetravalent Mn^{4+} states. The ionic radii of the impurity ions ($r_{\text{Mn}^{2+}} = 0.67$ Å (CN = VI), $r_{\text{Mn}^{4+}} = 0.53$ Å (CN = VI)) [26] and the relative intensities of Mn^{2+} and Mn^{4+} EPR spectra [33] showed that bivalent manganese ions substitute for lithium in certain position $\text{Mn}^{2+} \rightarrow \text{Li2}$ (about 87% from the total impurity content); tetravalent manganese ions substitute for germanium hosts within octahedral groups $\text{Mn}^{4+} \rightarrow \text{Ge1}$ (about 13% from the total content).

Isovalent substitution $\text{Mn}^{4+}(\text{Ge}^{4+})$ does not introduce an electrical disbalance into the lattice and consequently does not require charge compensation. One can assume that the centers $\text{Mn}^{4+}(\text{Ge1})$ have no significant effect on conductivity. In contrast, the

heterovalent substitution $\text{Mn}^{2+}(\text{Li}^+)$ has to generate an additional negatively charged defect. In the crystals of lithium-germanium oxides, the defects in lithium sublattice are considered as the most probable. Thus, lithium vacancies V_{Li} can be proposed as the charge-compensating defects for $\text{Mn}^{2+}(\text{Li}_2)$. Since Mn^{2+} ions keep the positional symmetry (C_2) of the hosts [33], charge-compensating vacancies V_{Li} should be located far enough from the paramagnetic ions. The formation of the associated pair centers of the type $\text{Mn}^{2+}(\text{Li}_2) - V_{\text{Li}}$ is seemed unlikely. Really, motion of V_{Li} should be accompanied by overcoming the significant potential barrier separating the regular Li ions positions. Lithium interstitials A_{Li} can move along the structural channels much more freely since their migration occurs through quasiequilibrium interstitial positions with flatter relief. Thus, vacancies V_{Li} compensating the excess charge of $\text{Mn}^{2+}(\text{Li}_2)$ centers can be assumed as distant with respect to paramagnetic centers. The vacancies V_{Li} generated by Mn^{2+} impurity can act as the traps for lithium interstitials and effectively decrease their concentration. Consequently, doping with Mn lowers conductivity of $\text{Li}_2\text{Ge}_7\text{O}_{15}$: Mn single crystal (curve 3 in Fig. 3).

$\text{Li}_2\text{Ge}_7\text{O}_{15}$:Cu. Anisotropy and temperature changes of EPR spectra on passing through the ferroelectric phase transition were studied in $\text{Li}_2\text{Ge}_7\text{O}_{15}$:Cu crystal in [34, 35]. Two structurally inequivalent centers Cu1 and Cu2 were found, the local symmetry of which were the same as of the Li1 and Li2 regular sites correspondingly. This result as well as comparison of the radiuses of the paramagnetic probe ($r_{\text{Cu}^{2+}} = 0.57 \text{ \AA}$ (CN = IV), 0.73 \AA (CN = VI)) [26] and the host cations made it possible to argue the substitution by copper impurity for lithium hosts: $\text{Cu1} \rightarrow \text{Li1}$ and $\text{Cu2} \rightarrow \text{Li12}$ [34]. The distant V_{Li} vacancies were proposed as non-local charge compensators. In this case, one might expect that the effect of Cu doping on conductivity had to be similar as manganese doping influence (Fig. 3). Nevertheless, the experimental behavior of $\sigma(1/T)$ for $\text{Li}_2\text{Ge}_7\text{O}_{15}$:Cu crystal qualitatively differs from the conductivity dependences for the other doped crystals (Fig. 3). Really, doping with Cu notably decreases conductivity. In addition, in $\text{Li}_2\text{Ge}_7\text{O}_{15}$:Cu, the activation energy of σ noticeably exceeds the values of U_a for nominally pure and other doped crystals (Table 1). Presumably, Cu ions hinder motion of A_{Li} through the structural channels. Moreover, it is possible that the impurity ions themselves can contribute to the charge transport. More detailed studying of EPR spectra in a broad temperature range could elucidate the specific features of $\sigma(1/T)$ dependence in $\text{Li}_2\text{Ge}_7\text{O}_{15}$:Cu crystal (Fig. 3).

$\text{Li}_2\text{Ge}_7\text{O}_{15}$:Al. Figure 3 shows that doping with Al ions increases conductivity of the $\text{Li}_2\text{Ge}_7\text{O}_{15}$ single crystal, i.e., the effect is the same as for chromium dopant. Such behavior seems natural accounting trivalent stable oxidation state Al^{3+} and ionic radiuses $r_{\text{Al}^{3+}} = 0.39 \text{ \AA}$ for CN = IV and 0.53 \AA for CN = VI [25] which practically coincide with the radiuses of germanium hosts with the same coordination numbers. Substitution by Al^{3+} ions for Li^+ should introduce great electrical imbalance and can be considered as much less probable. In contrast to the chromium impurity, the heterovalent substitution $\text{Al}^{3+} \rightarrow \text{Ge}^{4+}$ can be proposed for all inequivalent germanium sites located within oxygen octahedron Ge1 and tetrahedral Ge2-7 (see Fig. 2 and the notations for atoms in [18–20]). The charge imbalance of the substitutional impurity $\text{Al}^{3+}(\text{Ge}^{4+})$ can be compensated by excess non-stoichiometric interstitials

A_{Li} which can move along the structural channels and contribute to conductivity. Up to now, there is no reliable evidences on the formation of associated pairs $Al^{3+}(Ge^{4+}) - A_{Li}$ as it was observed for $Li_2Ge_7O_{15}:Cr$ crystal. Possibly, such pairs are absent because of weak electrostatic interaction between doping ions $Al^{3+}(Ge^{4+})$ and charge-compensating interstitials A_{Li} . Besides, if aluminum ions can substitute for Ge hosts in various sites within oxygen polyhedrons, dielectric response from a few possible coupled pairs would be difficult to detect. In any case, careful study of dielectric spectra in $Li_2Ge_7O_{15}:Al$ crystal for different orientations of external field can help to clarify the model of aluminum centers in $Li_2Ge_7O_{15}$ crystal structure.

$Li_2Ge_7O_{15}:Gd$. Gadolinium ions have a stable state Gd^{3+} . However, in contrast to the other crystals with trivalent dopants (Cr^{3+} and Al^{3+}), conductivity of $Li_2Ge_7O_{15}:Gd$ crystal decreases notably (Fig. 3). Considering the ionic radiuses of the impurity $r_{Gd^{3+}} = 0.94 \text{ \AA}$ (CN = VI) and germanium host [25], incorporation of Gd^{3+} into oxygen octahedron seems low probable. As shown in [18–20], Li1, 2 ions are located within quite wide structural cavities (Fig. 2). Hence, substitution $Gd^{3+} \rightarrow Li^+$ can be supposed. Excess positive charge ($+2e$) introduced by the doping ion can be compensated by appearance of two lithium vacancies V_{Li} . As we discussed above, generation of the excess vacancies V_{Li} reduces the content of mobile interstitials V_{Li} that results in conductivity decrease. One can expect that studying EPR in $Li_2Ge_7O_{15}:Gd$ crystal should give more information on gadolinium ions position and the mechanisms of charge compensation in the lattice.

Summing up the results presented in Sect. 3.2, one can note that doping with the small amounts (0.01–0.1% wt) of heterovalent impurities changes ionic conductivity in $Li_2Ge_7O_{15}$ single crystals in a diapason of about two orders of magnitude (the data in Fig. 3 and Table 1). The effect is determined by the position of the impurity ions in the lattice and by the mechanism of the charge mismatch compensation. If the doping is accompanied by appearance of additional interstitials A_{Li} , the conductivity of the single crystals increases. In a case when impurity ions generate excess vacancies V_{Li} , doping significantly decreases conductivity. The noticeable effects of the dopants on conductivity testify that in the studied interval temperature increase of σ is determined by thermal activation of the charge carriers mobility.

4 Conductivity of Glassy and Nanocrystalline $Li_2Ge_7O_{15}$

4.1 Undoped Glass and Nanocrystals

As shown above, ionic conductivity in $Li_2Ge_7O_{15}$ single crystal occurs through A_{Li} movement along the channels of the framework type structure. It is of interest to clear up the role of long-range ordering and to find out how lithium conductivity can be modified in amorphous and nanocrystalline lithium heptagermanate. The first results on the devitrification of $Li_2O-xGeO_2$ glasses were published in [36–38]. In [14, 17], we reported fast quenching the $Li_2O-xGeO_2$ glasses ($x = 2.67, 7, 11.5$,

18) with the compositions varied around the stoichiometry of lithium heptagermanate ($x = 7$). It was shown that the glasses could be crystallized on heating or by isothermal treating [15]. Devitrification performed on heating was manifested by exothermic anomalies detected by differential scanning calorimetry (DSC) [39] (Fig. 4). The subtle anomaly at T_g corresponds to glass transition temperature and indicates softening the amorphous structure and start of the crystallization process. Two intense DSC peaks at T_1 and T_2 show that crystallization proceeds in stages through intermediate metastable state. The structure and morphology of the as-quenched glass and the states appeared on heating above T_1 and T_2 where characterized by X-ray phase analysis and atomic force microscopy (AFM) [17, 40]. It was shown that heating above T_1 transformed the glass into partially crystallized state consisted of nanometer-sized ordered nuclei (about 80% of the samples volume) surrounded by amorphous medium (~20% of the volume). Heating above T_2 finally transformed the samples into the polycrystalline state with micrometer-sized crystallites. Ordering processes occurred within the samples bulk and were slowed down near the samples surface [39]. Thus, the surface stabilized the disordered amorphous state of the structure. The dependencies of conductivity $\sigma(1/T)$ for $\text{Li}_2\text{Ge}_7\text{O}_{15}$ single crystal, glass, nano- and micrometer-structured states are shown in Fig. 5.

One can see (Fig. 5) that the lowest conductivity is observed for $\text{Li}_2\text{Ge}_7\text{O}_{15}$ single crystal. σ value for glass is found to be about three orders of magnitude higher. The highest conductivity is observed for nanometer-structured crystalline state for which σ is about four orders exceeds conductivity of single crystal. Thus, nanostructuring demonstrates its high efficiency for increasing ionic conductivity in the $\text{Li}_2\text{O-GeO}_2$ compounds.

In the next section, we discuss the doping effect on conductivity in amorphous and nanocrystalline lithium heptagermanate.

Fig. 4 DSC curve measured on heating $\text{Li}_2\text{Ge}_7\text{O}_{15}$ glass with the rate 10 K/min [39]

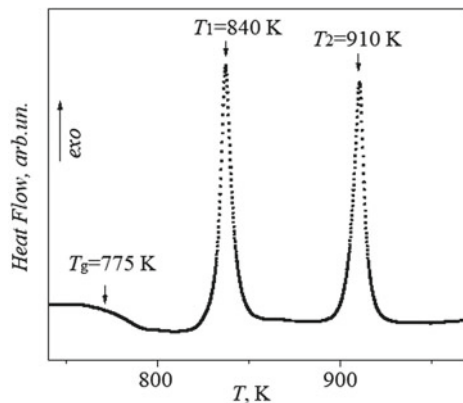
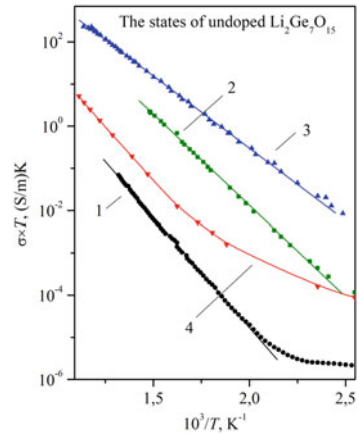


Fig. 5 $\sigma(1/T)$ dependences for undoped $\text{Li}_2\text{Ge}_7\text{O}_{15}$ single crystal (curve 1, $E \parallel a$), glass (2), nanocrystalline state (3) and micrometer-structured polycrystal (4). $f = 1$ kHz



4.2 Doping Effect on Conductivity in Glass and Nanocrystals

In Sect. 3.2, it has been shown that ionic conductivity in $\text{Li}_2\text{Ge}_7\text{O}_{15}$ single crystals can be considerably enhanced or lowered by introducing the small amounts of heterovalent dopants. It is of interest to explore doping effect on conductivity in glassy and nanocrystalline $\text{Li}_2\text{Ge}_7\text{O}_{15}$.

The experimental dependences of conductivity $\sigma(1/T)$ for doped $\text{Li}_2\text{Ge}_7\text{O}_{15}$ glasses and nanocrystals are plotted in Arrhenius scale in Fig. 6a, b. For comparison, the values of σ and activation energy are presented in Table 2.

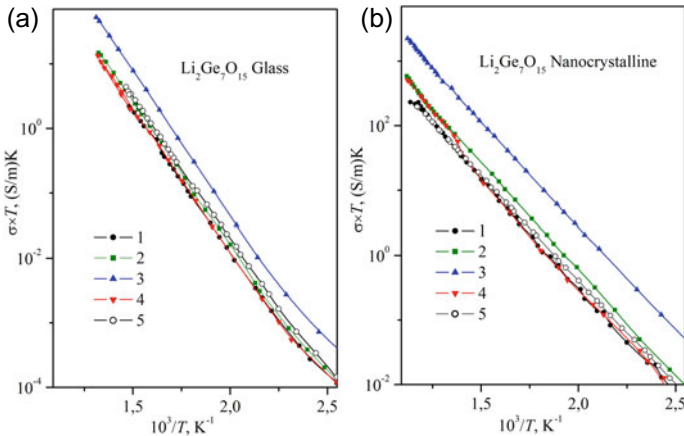


Fig. 6 $\sigma(1/T)$ dependences for the glass **a** and the nanocrystalline **b** $\text{Li}_2\text{Ge}_7\text{O}_{15}$: 1—the undoped samples and the samples doped with 2—Cr (0.06% wt), 3—Mn (0.06% wt), 4—Cu (0.09% wt), 5—Al (0.3% wt). $f = 1$ kHz

Table 2 Values of conductivity and activation energy for amorphous and nanocrystalline $\text{Li}_2\text{Ge}_7\text{O}_{15}$: Cr, Mn, Cu, Al (Fig. 6)

$\text{Li}_2\text{Ge}_7\text{O}_{15}$ dopants	Conductivity σ , S/m ($T = 500$ K)		Activation energy U_a , eV	
	Glass	Nanocrystalline	Glass	Nanocrystalline
Undoped	2.4×10^{-5}	4.8×10^{-4}	0.89	0.69
Cr (0.06% wt)	3.3×10^{-5}	1.2×10^{-3}	0.89	0.66
Mn (0.06% wt)	8.9×10^{-5}	5.3×10^{-3}	0.89	0.66
Cu (0.09% wt)	2.4×10^{-5}	5.4×10^{-4}	0.89	0.74
Al (0.3% wt)	4.1×10^{-5}	8.2×10^{-4}	0.89	0.65

One can see that the doping effects in the glass and the nanocrystals (Fig. 6) are quite different from the effects observed in the single crystals (Fig. 3). Indeed, all the dopants slightly increase conductivity of the glasses and the nanocrystalline samples. Such effect can be attributed to loosening the structure and weakening interatomic bonds by the dopants. The most pronounced increase of σ is observed for $\text{Li}_2\text{Ge}_7\text{O}_{15}$: Mn glass and nanocrystals whereas for the single crystal Mn impurity notably decreases conductivity (Fig. 3). The influence of other dopants is minor. The value of activation energy remains practically unchanged for all used impurities. The only exception is nanocrystalline $\text{Li}_2\text{Ge}_7\text{O}_{15}$:Cu for which the value of U_a is somewhat higher than for others, just as it is observed for the Cu-doped single crystals (Tables 1, 2).

So, the data in Fig. 6 give evidence that doping with small amounts of the impurities weakly affect conductivity of amorphous and nanocrystalline states. This result seems natural. Really, increase of conductivity in $\text{Li}_2\text{Ge}_7\text{O}_{15}$:Cr (Fig. 3) and the well-argued model of the $\text{Cr}^{3+}-\text{A}_{\text{Li}^+}$ pair centers make it possible to estimate equilibrium concentration of mobile interstitials A_{Li} in the single crystal as $10^{-5}-10^{-4}$. Introduction of small amounts of the dopants which generate the excess defects A_{Li} or V_{Li} in lithium sublattice can change drastically the concentration of lithium interstitials and significantly affects conductivity of the single crystals (Fig. 3).

In glass, the concepts of regular lattice sites and of interstitials lose their sense; the number of weakly bound ions sufficiently increases and σ grows in about three orders of magnitude as compared with single crystal (Fig. 5). On the other hand, the structural channels (Fig. 2), which make possible ion migration in the single crystal, are absent in the glass. Appearance of nanometer-sized nuclei with nearly ordered structure leads to a further increase in conductivity, which becomes four orders of magnitude higher relative to conductivity of the single crystal (Fig. 5). The number of weakly bound and mobile Li ions in nanocrystalline state can be estimated as comparable to the total number of lithium ions.

Nevertheless, it is assumed, that doping effect in amorphous and nanocrystalline $\text{Li}_2\text{Ge}_7\text{O}_{15}$ can be enhanced [41]. One can propose to use much more high concentrations of the heterovalent dopants which substitute for Ge hosts and introduce a negative charge imbalance. For the compositions with excess non-stoichiometric

portion of Li_2O , such additives can be expected to stabilize a great number of weakly bound lithium ions.

5 Conclusions

The doping effect on ionic conductivity was studied in single crystalline, amorphous, and nanometer-structured lithium heptagermanate $\text{Li}_2\text{Ge}_7\text{O}_{15}:\text{Cr}$, Mn , Cu , Al , and Gd . It was shown that the small amounts of the dopants significantly affected conductivity of $\text{Li}_2\text{Ge}_7\text{O}_{15}$ single crystals. The heterovalent dopants, that induced appearance of charge-compensating lithium vacancies V_{Li} , notably decreased conductivity. The impurities, generating excess lithium interstitials A_{Li} , significantly enhanced ionic conductivity. The obtained results confirmed that charge transfer in $\text{Li}_2\text{Ge}_7\text{O}_{15}$ crystal was determined by lithium interstitials moving through the structural channels. Thermal activation of the charge carrier's mobility caused temperature increase of conductivity.

In amorphous and nanocrystalline $\text{Li}_2\text{Ge}_7\text{O}_{15}$, the number of weakly bound lithium ions increased essentially. Relative to the single crystal, in these states, ionic conductivity became higher in three and four orders of magnitude correspondingly. Doping with small amounts of the impurities had minor effect on ionic transport in amorphous and nanocrystalline samples. It is expected that the impurity effect on conductivity can be enhanced by introducing the certain heterovalent dopants in much more high concentration.

References

1. Maier J (2004) Physical chemistry of ionic materials. Wiley, ISBN 0-470-87076-1. <https://doi.org/10.1002/0470020229>
2. Maier J (2005) Nanoionics: ion transport and electrochemical storage in confined systems. *J Nature Mater* 4(11):805–815. <https://doi.org/10.1038/nmat1513>
3. Murthy MK (1964) Studies in germanium oxide systems: I, Phase equilibria in the system $\text{Li}_2\text{O}-\text{GeO}_2$. *J Am Ceram Soc* 47(7):328–331. <https://doi.org/10.1111/j.1151-2916.1964.tb14433.x>
4. Haussuhl S, Wallrafen F, Recker K, Eckstein J (1980) Growth, elastic properties and phase transition of orthorhombic $\text{Li}_2\text{Ge}_7\text{O}_{15}$. *Z Kristallogr* 153:329–337. <https://doi.org/10.1524/zkri.1980.153.3-4.329>
5. Wada M, Sawada A, Ishibashi Y (1981) Ferroelectricity and soft mode in $\text{Li}_2\text{Ge}_7\text{O}_{15}$ crystals. *J Phys Soc Japan* 50(6):1811–1812. <https://doi.org/10.1143/JPSJ.50.1811>
6. Tagantsev AK (1993) Weak Ferroelectrics. In: Setter N, Colla EL (eds) *Ferroelectric Ceramics*. Monte Verità. Birkhäuser Basel, 147–161. https://doi.org/10.1007/978-3-0348-7551-6_5
7. Liebert BE, Huggins RA (1976) Ionic conductivity of Li_4GeO_4 , Li_2GeO_3 and $\text{Li}_2\text{Ge}_7\text{O}_{15}$. *Mat Res Bull* 11(5):533–538. [https://doi.org/10.1016/0025-5408\(76\)90235-X](https://doi.org/10.1016/0025-5408(76)90235-X)
8. Volnyanskii MD, Trubitsyn MP, Obaidat YAH (2008) Anisotropy of the electrical conductivity of lithium heptagermanate crystals. *Phys Solid State* 50(3):422–424. <https://doi.org/10.1134/S1063783408030049>

9. Volnyanskii MD, Plyaka SN, Trubitsyn MP, Obaidat YAH (2012) Ion conduction and space-charge polarization processes in $\text{Li}_2\text{Ge}_7\text{O}_{15}$ crystals. *Phys Solid State* 54(3):499–503. <https://doi.org/10.1134/S1063783412030353>
10. Volnyanskii M, Plyaka S, Trubitsyn M, Obaidat YAH (2014) Frequency dispersion of conductivity and complex impedance in $\text{Li}_2\text{Ge}_7\text{O}_{15}$ single crystal. *Ferroelectrics* 462(1):74–79. <https://doi.org/10.1080/00150193.2014.890880>
11. Vogel M, Petrov O, Trubitsyn M, Nesterov O, Volnyanskii M (2020) ^7Li NMR spectra and spin-lattice relaxation in lithium heptagermanate single crystal. *Ferroelectrics* 558(1):46–58. <https://doi.org/10.1080/00150193.2020.1735888>
12. Nanocomposites: Ionic Conducting Materials and Structural Spectroscopies. (2008) In: Knauth P, Schoonman J (ed), Springer, ISBN 978-0-387-33202-4.
13. Leon C, Habasaki J, Ngai KL (2017) Dynamics of glassy, crystalline and liquid ionic conductors: experiments, theories, simulations. *Topics in Applied Physics*, Springer, ISBN 978-3-319-42389-0. <https://doi.org/10.1007/978-3-319-42391-3>
14. Volnyanskii MD, Nesterov AA, Trubitsyn MP (2012) Thermal and electrical properties of glass-ceramics based on lithium heptagermanate. *Phys Solid State* 54(5):945–946. <https://doi.org/10.1134/S1063783412050459>
15. Nesterov OO, Trubitsyn MP, Volnyanskii DM (2015) Metastable State of the $\text{Li}_2\text{O}-11.5\text{GeO}_2$ GlassCeramics with a High Electrical Conductivity. *Phys Solid State* 57 (4): 683–688. <https://doi.org/10.1134/S1063783415040204>
16. Nesterov OO, Trubitsyn MP, Plyaka SM, Volnyanskii DM (2015) Complex impedance spectra of glass and glass ceramic $\text{Li}_2\text{O}-11.5\text{GeO}_2$. *Phys Solid State* 57(9): 1759–1763. <https://doi.org/10.1134/S1063783415090255>
17. Nesterov O, Trubitsyn M, Petrov O, Vogel M, Volnyanskii M, Koptiev M, Nedilko S, Rybak Y (2019) Electrical conductivity and ^7Li NMR spin-lattice relaxation in amorphous and nano- and microcrystalline $\text{Li}_2\text{O}-7\text{GeO}_2$. In book: Fesenko O, Yatsenko L (eds) *Nanocomposites, nanostructures, and their applications*. Springer Proceedings in Physics 221 (Chapter 6): 85–96. Publisher: Springer. ISBN 978-3-030-17759-1. https://link.springer.com/chapter/https://doi.org/10.1007/978-3-030-17759-1_6
18. Vollenke H, Wittman A, Nowotny H (1970) Die kristall-structure des lithiumheptagermanats $\text{Li}_2\text{Ge}_7\text{O}_{15}$. *Monatsh Chem* 101:46–45
19. Iwata Y, Shibuya I, Wada M, Sawada A, Ishibashi Y (1985) Neutron diffraction study of ferroelectric transition in $\text{Li}_2\text{Ge}_7\text{O}_{15}$. *Jpn J Appl Phys* 24 (2): 597–599. <https://iopscience.iop.org/article/https://doi.org/10.7567/JJAPS.24S2.597/pdf>
20. Iwata Y, Shibuya I, Wada M, Sawada A, Ishibashi Y (1987) Neutron diffraction study of structural phase transition in ferroelectric $\text{Li}_2\text{Ge}_7\text{O}_{15}$. *J Phys Soc Jpn* 56(7):2420–2427. <https://doi.org/10.1143/JPSJ.56.2420>
21. Trubitsyn MP, Volnyanskii MD, Obaidat YAH (2008) Ionic conduction in $\text{Li}_2\text{Ge}_7\text{O}_{15}$ crystals doped with Cr and Mn ions. *Phys Solid State* 50(7):1234–1237. <https://doi.org/10.1134/S106378340807007X>
22. Koptiev MM, Trubitsyn MP, Volnyanskii MD, Plyaka SM, Yu KA (2020) Electrical conductivity of $\text{Li}_2\text{Ge}_7\text{O}_{15}$ crystals doped with Al. *Mol Cryst Liq Cryst* 700(1):13–21. <https://doi.org/10.1080/15421406.2020.1732547>
23. Powell RC (1968) Energy transfer between chromium ions in nonequivalent sites in $\text{Li}_2\text{Ge}_7\text{O}_{15}$. *Phys Rev* 173(2):358–366. <https://doi.org/10.1103/PhysRev.173.358>
24. Galeev AA, Khasanova NM, Bykov AV, Vinokurov VM, Nizamutdinov NM, Bulka GR (1990) EPR of Cr^{3+} and Fe^{3+} ions in $\text{Li}_2\text{Ge}_7\text{O}_{15}$ single crystals. In: Morozov VP (ed) *Spectroscopy, crystal chemistry, and the real structure of minerals and their analogues* (Kazan University, Kazan): 77–92. [in Russian].
25. Shannon RD (1976) Revised effective ionic radii and systematic studies of interatomic distances in halides and chalcogenides. *Acta Crystallogr A* 32(5):751–767. <https://doi.org/10.1107/S0567739476001551>
26. Basun SA, Feofilov SP, Kaplyanskii AA (1993) Ferroelectric phase transition induced by pseudo-stark splitting in spectra of $\text{Li}_2\text{Ge}_7\text{O}_{15}:\text{Cr}^{3+}$ crystals. *Ferroelectrics* 143(1):163–170. <https://doi.org/10.1080/00150199308008325>

27. Kaplyanskii AA, Basun SA, Feofilov SP (1995) Ferroelectric transition induced dipole moments in probe ions in $\text{Li}_2\text{Ge}_7\text{O}_{15}$ crystals doped with Mn^{4+} and Cr^{3+} . *Ferroelectrics* 169(1):245–248. <https://doi.org/10.1080/00150199508217335>
28. Kaplyanskii AA, Basun SA, Feofilov SP (1995) New spectroscopic effects of ferroelectric phase transition in $\text{Li}_2\text{Ge}_7\text{O}_{15}$ crystals doped with $3d^3$ -Ions. *Radiat Eff Defects Solids* 135(1–4):69–72. <https://doi.org/10.1080/10420159508229808>
29. Trubitsyn MP, Volnyanski MD, Busoula IA (1998) EPR study of the ferroelectric phase transition in $\text{Li}_2\text{Ge}_7\text{O}_{15}:\text{Cr}^{3+}$. *Phys Solid State* 40(6): 1006–1008. <https://pdf.zlibcdn.com/dtoken/0c9f8b7f7a7ff511c0c90b922da36c75/1.1130476.pdf>
30. Trubitsyn MP, Volnyanskii MD, Yu KA (2004) The influence of chromium impurity centers on the critical properties of a weakly polar ferroelectric $\text{Li}_2\text{Ge}_7\text{O}_{15}$. *Phys Solid State* 46(9):1730–1736. <https://doi.org/10.1134/1.1799194>
31. Volnyanskii MD, Trubitsyn MP, Obaidat YAK (2007) Dielectric relaxation of Cr^{3+} - Li^+ pair centers in $\text{Li}_2\text{Ge}_7\text{O}_{15}$ crystals. *Phys Solid State* 49(8): 1453–1456. <https://doi.org/10.1134/S1063783407080082>
32. Volnyanskii MD, Trubitsyn MP, Obaidat YAK (2007) EPR and dielectric spectroscopy of reorienting Cr^{3+} - Li^+ pair centres in $\text{Li}_2\text{Ge}_7\text{O}_{15}$ crystal. *Condensed Matter Phys* 10(1) (49): 75–78. <https://doi.org/10.5488/CMP.10.1.75>
33. Trubitsyn MP, Volnyanskii MD, Yu KA (1991) EPR of Mn^{2+} ions in lithium heptagermanate crystal. *Kristallografiya* 36(6):1472–1476
34. Trubitsyn MP, Volnianskii MD, Yu KA (2005) EPR of LGO: Cu^{2+} crystals. *Ferroelectrics* 316:121–123. <https://doi.org/10.1080/00150190590963237>
35. Trubitsyn MP, Volnyanski MD, Dolinchuk AN (2008) EPR study of copper ions in $\text{Li}_2\text{Ge}_7\text{O}_{15}$ crystals. *Phys Solid State* 50(8):1373–1377. <https://doi.org/10.1134/S1063783408080076>
36. Pernice P, Aronne A, Marotta M (1992) The non-isothermal devitrification of lithium tetragermanate glass. *Mater Chem Phys* 30(3):195–198. [https://doi.org/10.1016/0254-0584\(92\)90223-u](https://doi.org/10.1016/0254-0584(92)90223-u)
37. Marotta A, Pernice P, Aronne A, Catauro M (1993) The non-isothermal devitrification of lithium germanate glasses. *J Thermal Anal* 40(1):181–188. <https://doi.org/10.1007/BF02546568>
38. Aronne A, Catauro M, Pernice P, Marotta A (1993) Gel synthesis and crystallization of $\text{Li}_2\text{O}-7\text{GeO}_2$ glass powders. *Thermochim Acta* 216:169–176
39. Nesterov OO, Trubitsyn MP, Nedilko SG, Volnianskii MD, Plyaka SM, Rybak Ya O (2018) Ionic conductivity in multiphase $\text{Li}_2\text{O}-7\text{GeO}_2$ compounds. *Acta Phys Polonica* 133(4):892–896. <https://doi.org/10.12693/APhysPolA.133.892>
40. Volnianskii MD, Nesterov OO, Trubitsyn MP (2014) Devitrification of the $\text{Li}_2\text{O}-x(\text{GeO}_2)$ Glass. *Ferroelectrics* 466(1):126–130. <https://doi.org/10.1080/00150193.2014.895173>
41. Knauth P (2009) Inorganic solid Li ion conductors: an overview. *Solid State Ionics* 180:911–916. <https://doi.org/10.1016/j.ssi.2009.03.022>

Granulation Unit for Modification and Obtaining of Ammonium Nitrate with Nanoporous Structure: Basics of Calculation and Design



N. O. Artyukhova, J. Krmela, A. E. Artyukhov, O. V. Savastru, I. I. Volk, N. S. Borozenets, and D. Ospanov

Abstract Current paper is devoted to the description of the algorithm for obtaining porous ammonium nitrate granules in granulation units using devices with different configurations of the fluidized bed. We present brief theoretical background for calculation of the granulation plant main equipment. We propose the design of individual units for sequential implementation of the main stages of ammonium nitrate modification to obtain a nanostructured porous surface layer. We carry out an assessment of ammonium nitrate nanoporous structure quality and show further ways of improving the technology. Current work also pays attention to methods for ensuring the necessary specific quality indicators of porous ammonium nitrate by choosing the optimal technological unit operation mode and the design characteristics of the main equipment.

Keywords Nanoporous structure · Ammonium nitrate · Granulation · Calculation

N. O. Artyukhova (✉) · A. E. Artyukhov · I. I. Volk
Sumy State University, Rymskogo-Korsakova Str., 2, Sumy 40007, Ukraine
e-mail: n.artyukhova@pohnp.sumdu.edu.ua

J. Krmela
Alexander Dubcek University of Trencin, I. Krasku, 491/30, 02001 Puchov, Slovak Republic

O. V. Savastru
Odessa I.I. Mechnikov National University, Dvoryanskaya Str., 2, Odessa 65082, Ukraine

N. S. Borozenets
Sumy National Agrarian University, Herasya Kondratieva Str., 160, Sumy 40000, Ukraine

D. Ospanov
Saken Seifullin Kazakh Agrotechnical University, Zhenis Avenue, 62, Nur-Sultan 010011, Republic of Kazakhstan

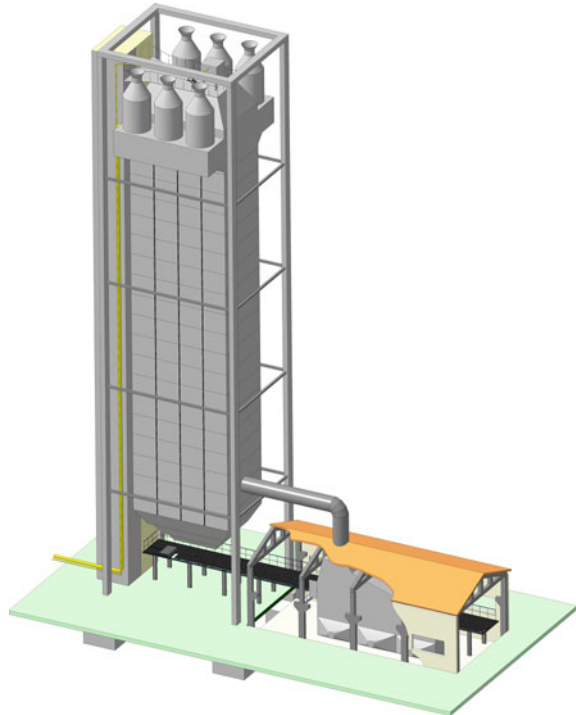
1 Introduction

Setting up the production of granular porous ammonium nitrate (PAN) of medium and small tonnage capacity is one of the important tasks to be solved by designers and technologists. Currently, the large-scale production of PAN is carried out in granulation towers (Fig. 1) [1–3]. For small-scale PAN production, the use of granulation towers is associated with a number of shortcomings:

1. Granulation tower has fixed productivity, and its reduction is associated with an increase in production costs. Readjustment of the granulation tower is possible without changing its design, which leads to ineffective use of its working capacity.
2. Changing humidifier composition (solution or melt) requires the production readjustment and recalculation of the unit's technological characteristics (with a change in sizes of auxiliary equipment).
3. Granulation Unit is Stationary, and Transportation is not Available.

Research and development of small-sized mobile units for PAN production are possible based on devices using other granulation and modification methods. At the same time, the use of granules as film applying centers with further removal of moisture and the formation of a developed nanopores network emerges as a promising direction. We propose to use the technology of granulation in a fluidized bed as a

Fig. 1 PAN production unit in granulation towers



shortcomings, e.g., the lack of granules classification process, uneven application of the melt film. In addition, the granulation unit is accompanied by grinding and scattering equipment, or it is used after the granulation tower for growing completion, leading to additional energy costs.

BATCH-FB (batch granulators) and CONTI FB (continuous devices) from Neuhaus Neotec Corporation, Heinen Drying[®], technology are distinguished among the industrial samples of vortex granulators with suspended layer [22] (Fig. 4).

The disadvantage of such devices is their batch operation (for BATCH-FB devices) along with the presence of rotating parts and Wurster system when supplying liquid to the suspended layer. Such devices are similar in principle to devices with gushing

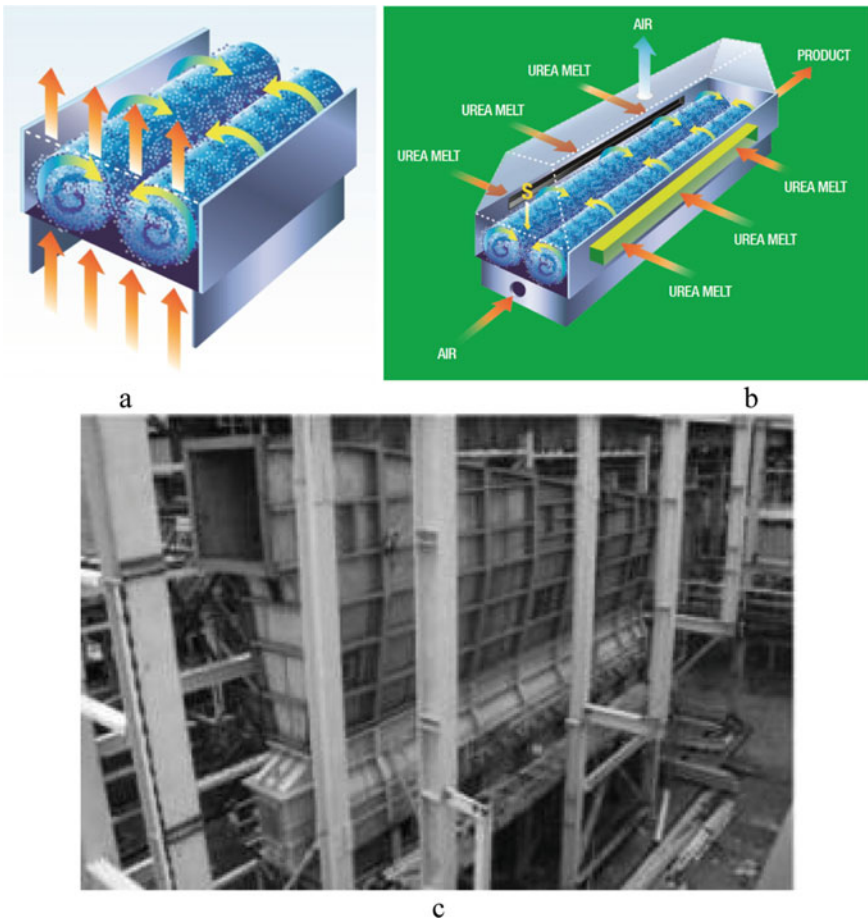


Fig. 3 Vortex[®] granulator: **a**—operation principle; **b**—stream motion; **c**—industrial setup

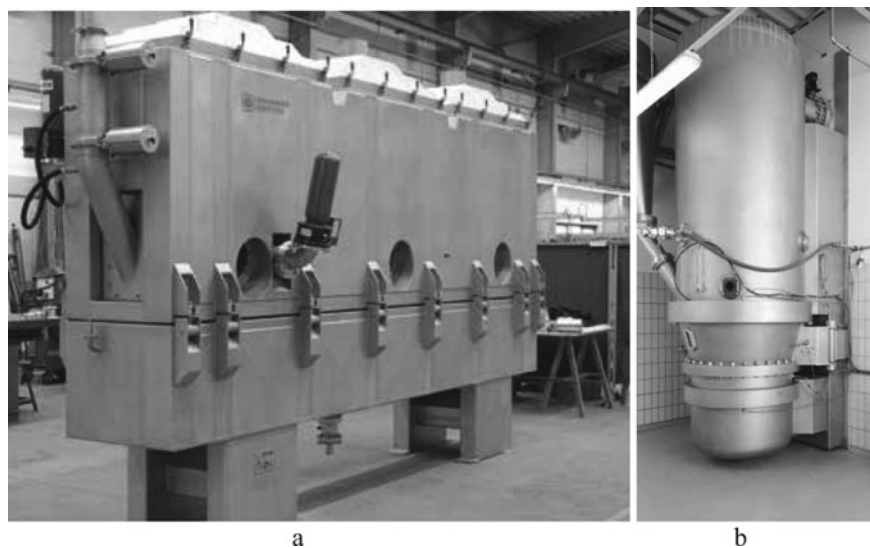


Fig. 4 Neuhaus Neotec vortex granulators: **a**—BATCH-FB; **b**—CONTI FB

stopped layer without directional movement of the liquefying agent. Discussed granulators do not allow the process of granules classification and internal circulation of the return in order to complete its growing to the showcase fraction.

The brochures of a number of suspended layer vortex granulators (Fig. 5) produced by Indian [23] and Chinese [24–27] companies state that the former “possess a specialized air distributor that ensures continuous movement of the material and solves potential problems with channel flow occurrence and “dead angle”. Other data on the mechanisms of gas flow vortex motion and the peculiarities of granulation are not provided by the manufacturers, but a comparative analysis of the design of Indian and Chinese devices with the CONTI FB device from Neuhaus Neotec allows to estimate a high probability of simple copying. The disadvantages of these devices are similar to the disadvantages of CONTI FB.

Another type of vortex granulation apparatus is the granulator by Changzhou Xiandao drying equipment [28], based on the Wurster scheme with a central swirling of the gas flow at the granulation solution introducing stage (Fig. 6). In contrast to the widespread technology of top-down spraying, this device utilizes a direct flow of the gas stream and granules due to the bottom-up spraying of liquid material.

At the initial forming stage, the granules carry out an orderly movement and form a stable vortex in the central tube.

Vortex flow eliminates the problem of possible stagnation. At the same time, the device is suitable for the production of small granules. It is possible since the droplet’s likelihood of agglomeration and deformation in the vortex flow increases with increasing granule size.

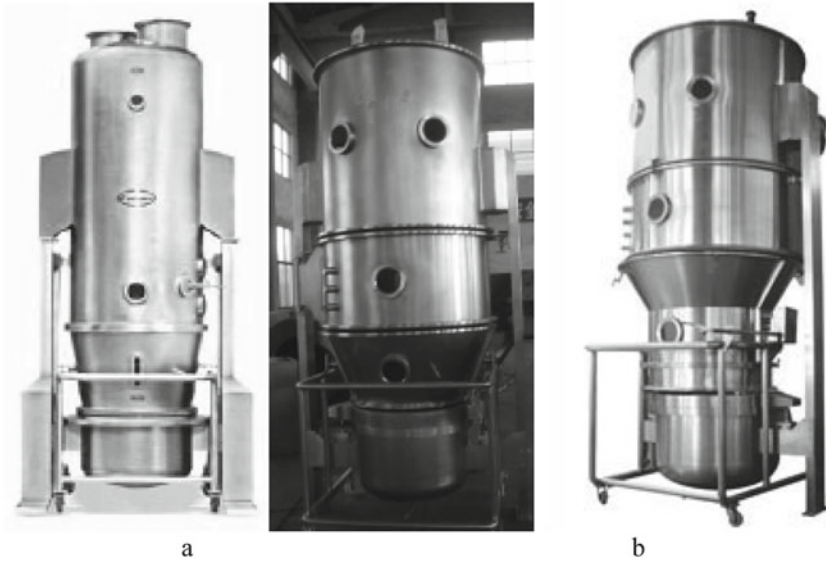
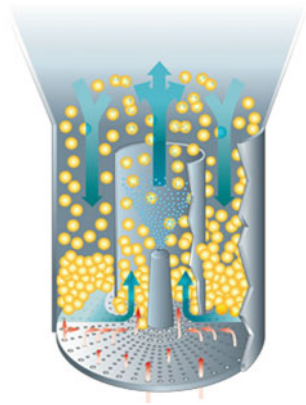


Fig. 5 Indian **a** and Chinese **b** analogs of CONTI FB (Neuhaus Neotec) device

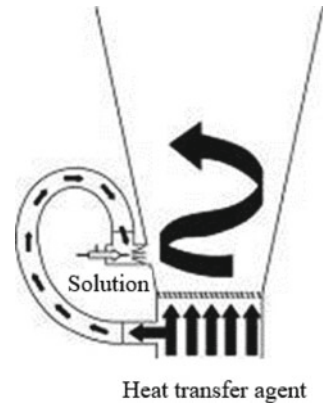
Fig. 6 Granulator with Wurster scheme and central gas flow swirling



Next to discuss are FlexStream™ devices [29], combining the tangential introduction of the solution and the use of vortex gas flow (Fig. 7). Such devices provide uniform growth of granules with low fragility. At the same time, extensive suspended layer humidification is possible during the implementation of granulation in such devices.

Other examples of vortex granulators that have not received widespread industrial use include an apparatus with a rotating weighted layer on a rotating disk [30], a multi-section box-type apparatus with a perforated gas distribution device [31], apparatus with a plate gas distribution device [32].

Fig. 7 FlexStream™ granulator



Some designs of vortex-type granulators have been developed in the CIS countries. Such developments include apparatus with a vortex layer of granules, a dryer-granulator of the vortex type with counter-streams, a granulator with separation of particles in the vortex layer. Rough classification and separation take place in these granulators as auxiliary processes.

Sumy State University scientists developed vortex granulators with height-varying cross-sectional area [33, 34] (Fig. 8). In addition to the actual granulation, such devices allow processes of granules classification by size, separation of small granules, and their use as an internal return. The theoretical foundations of the granules obtaining process in such granulators, the results of experimental research and computer modeling are covered in [12, 15]. A number of works [13, 14, 16, 34] are devoted to using vortex granulators and auxiliary equipment of granulation units to obtain PAN. The results of experimental and industrial implementation of granulators of such design proved their efficiency and viability. The latter suggests the possibility for such granulators to enter the market, provided a thorough theoretical description of the process and a reliable engineering calculation method.

3 Technological Process Calculation

The process of basic equipment calculation for the granulation unit includes the following main blocks, shown in Fig. 9.

According to the calculation results, the following characteristics of the unit and its individual components are obtained:

1. Deliverability
2. Temperature and humidity indicators of streams
3. Humidifier properties
4. Granules drying time
5. Necessary stay time of granules in device work area

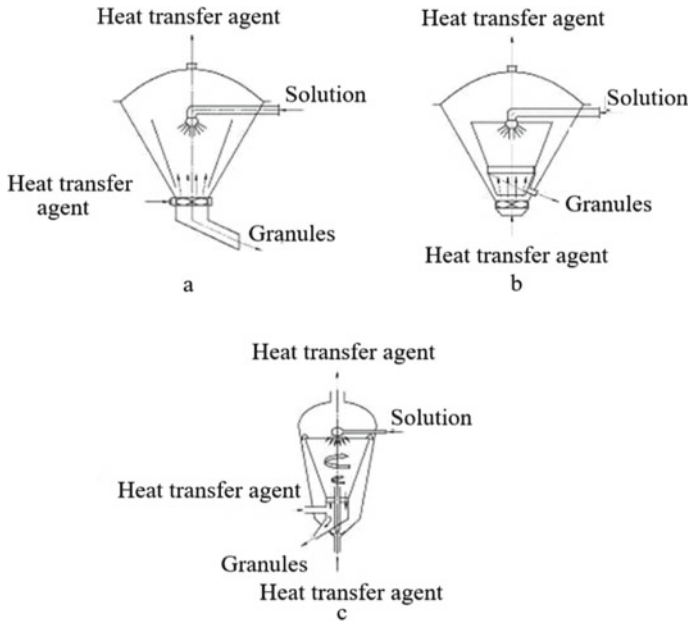


Fig. 8 Vortex granulators with height-varying cross-sectional area: **a**—with inner cone and lower granule outlet; **b**—with inner cone and side granule outlet; **c**—with internal return circulation

6. Granulator nodes size
7. Estimated stay time of granules in the apparatus considering its design.

The unit's model is designed, and its elements are arranged based on the calculation results. An example of vortex granulator arrangement as part of a granulation unit for the PAN with nanoporous structure production is shown in Fig. 10.

4 Nanoporous Layers Properties in PAN Granules

At the testing stage of the vortex granulator, the study of the nanoporous structure of PAN granules obtained in different versions of the process takes place. The testing stage precedes the constructive calculation and in fact is an optimization stage aimed at finding parameters for the implementation of the modification process. Obtained PAN samples can have different nanoporous structure, both satisfying and defective. This is exactly the aim of the optimization stage at the calculation of unit operating modes. The following are examples of the different structure of PAN granules depending on the obtaining parameters (Figs. 11–13). At the same time, not only the high-quality nanoporous structure is shown, but also the options that may arise if the modification technology is not followed.

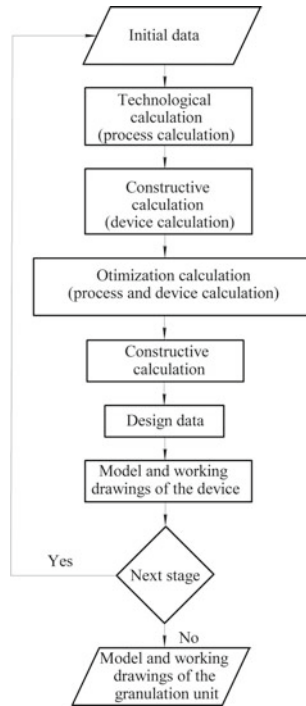


Fig. 9 Block diagram of the PAN obtaining process calculation and the main unit equipment

5 Conclusions

The choice of the vortex granulator optimal design and the technological mode of its operation is made based on the algorithm defined in this work. Particular attention should be paid to the granulator optimization calculation stage based on experimental studies of the nanoporous structure of PAN granules. Control mechanisms of the granule nanoporous structure are quite complex and depend on a set of parameters. Therefore, the search for a combination of these parameters that satisfy the conditions for obtaining a developed nanoporous structure is a promising task that requires further study.

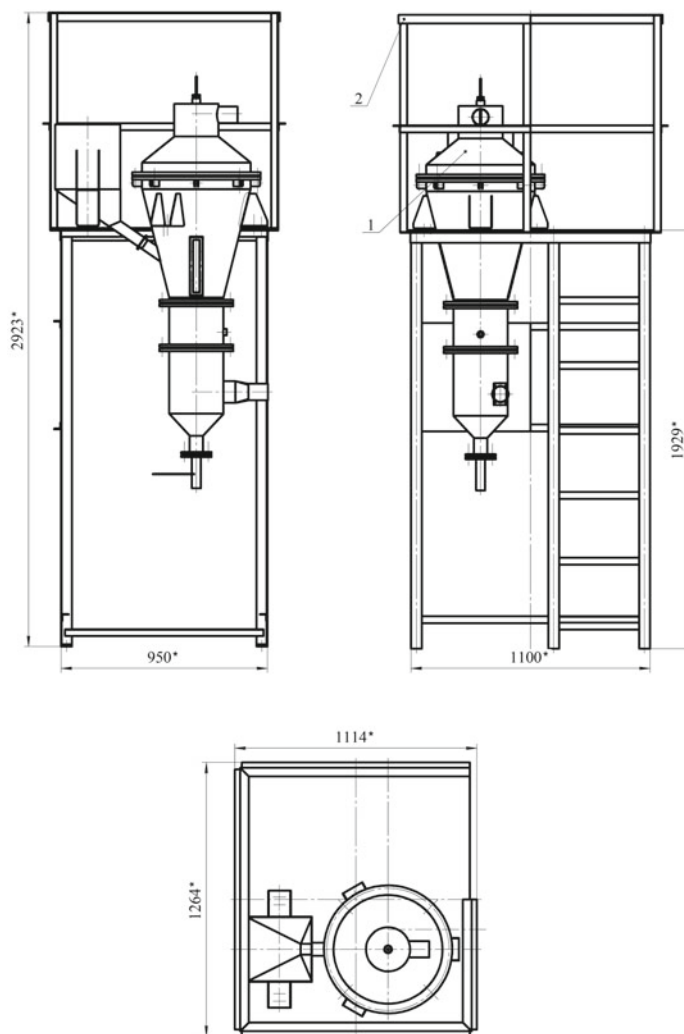


Fig. 10 Arrangement of vortex granulator as part of granulation unit for PAN with nanoporous structure production

Fig. 11 PAN granule structure at uneven solution film application

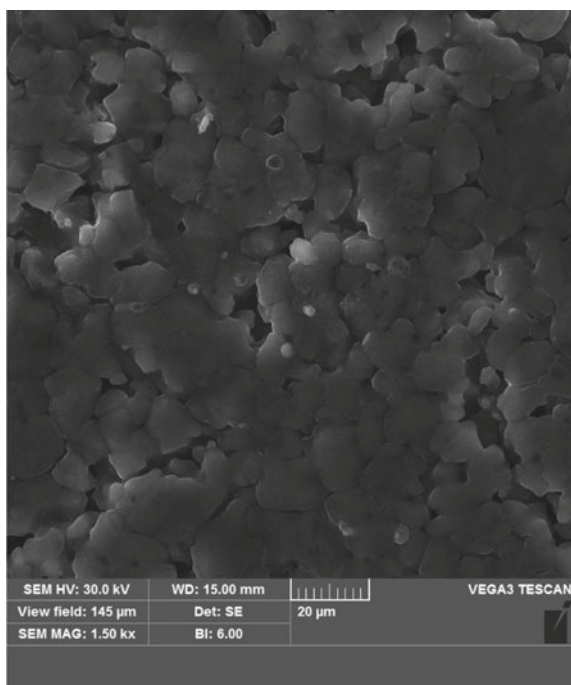


Fig. 12 PAN granule structure at suboptimal humidifier composition (both component and proportional)

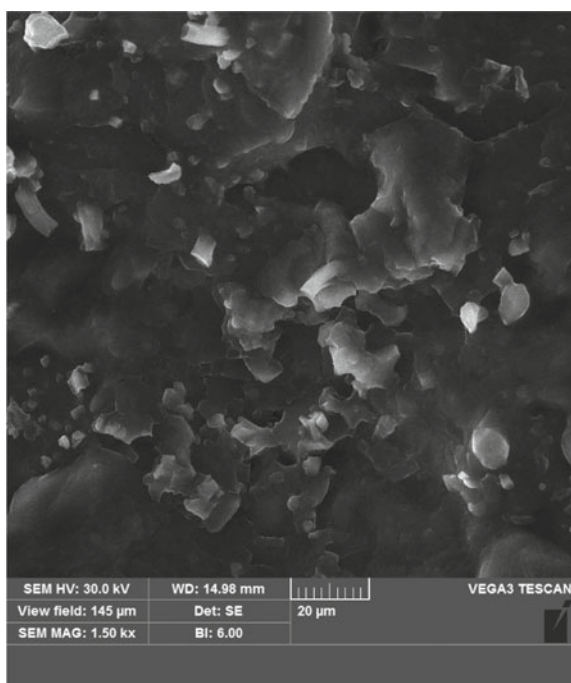
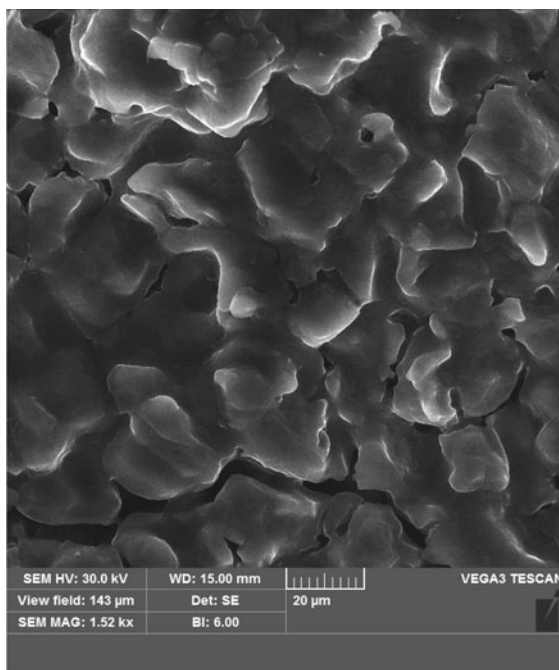


Fig. 13 PAN granule structure at insufficient stay time (drying time) of the granule in the granulator work area



Acknowledgements This research work had been supported by the Ministry of Science and Education of Ukraine under the project “Development of a vortex granulator for obtaining granules of porous ammonium nitrate”, project No. 0121U109465.

References

1. Erode GM (2013) Ammonium nitrate explosives for civil applications: slurries, emulsions and ammonium nitrate fuel oils. Wiley-VCH Verlag & Co, Weinheim
2. Janssen TJ (2011) Explosive materials: classification. Nova Science Publishers, Inc., Composition and Properties
3. Martin G, Barbour W (2003) Industrial nitrogen compounds and explosives. Watchmaker Publishing, Chemical Manufacture and Analysis
4. Stahl H (2004) Comparing different granulation techniques. *Pharmaceutical technology Europe*, pp 23–33
5. Ostroha R, Yukhymenko M, Yakushko S, Artyukhov A (2017) Investigation of the kinetic laws affecting the organic suspension granulation in the fluidized bed. *Eastern-European J Enterp Technol* 4(1):4–10
6. Muralidhar P, Bhargav E, Sowmya C (2016) Novel techniques of granulation: a review. *Int Res J Pharmacy* 7(10):8–13
7. Yukhymenko M, Ostroha R, Artyukhov A (2016) Hydrodynamic and kinetic processes of the mineral fertilizer granules encapsulating in the multistage device with suspended layer. *Eastern-European J Enterp Technol* 6(6–84):22–28

8. Litster J, Ennis B (2004) The science and engineering of granulation processes. Springer-Science+Business Media
9. Srinivasan S (2015) Granulation techniques and technologies: recent progresses. *Bioimpacts* 5(1):55–63
10. Solanki HK, Basuri T, Thakkar JH, Patel CA (2010) Recent advances in granulation technology. *Int J Pharm Sci Rev Res* 5(3):48–54
11. Saikh MA (2013) A technical note on granulation technology: a way to optimise granules. *Int J Pharm Sci Rev Res* 4:55–67
12. Obodiak V, Artyukhova N, Artyukhov A (2020) Calculation of the residence time of dispersed phase in sectioned devices: theoretical basics and software implementation. *Lecture Notes Mech Eng*, pp 813–820
13. Artyukhov A, Gabrusenoks J (2018) Phase composition and nanoporous structure of core and surface in the modified granules of N_4HNO_3 . *Springer Proc Phys* 210:301–309
14. Artyukhov AE, Krmela J, Gavrylenko OM (2019) Evaluation of the impact made by the hydrodynamic regime of the granulation equipment operation on the nanoporous structure of N_4HNO_3 granules. *J Nano Electron Phys* 11(3):03033
15. Artyukhov A, Artyukhova N, Krmela J, Krmelová V (2020) Complex designing of granulation units with application of computer and software modeling: case “Vortex granulator”. In: IOP conference series: materials science and engineering 776(1): 012016
16. Ivaniia AV, Artyukhov AY, Olkhovik AI (2019) Hydrodynamic and thermodynamic conditions for obtaining a nanoporous structure of ammonium nitrate granules in vortex granulators. *Springer Proc Phys* 221:257–268
17. Pat. № 1698393 EP, Int. Cl B01J2/16. Process and device for fluidized bed granulation / Bedetti Gianfranco, Burlando Carla; assignee Urea Casale S.A.—№ 05004654.9; filed 03.03.2005; issued 06.09.2006.
18. Zardi F, Gabbiandini S (2011) Vortex granulation: the new route to high-quality solid nitrogen fertilizers/Nitrogen & Syngas conference & exhibition, pp 15
19. Pat. № 2013/0316078 A1, US, Int. Cl C07C 273/02. Fluid bed granulation of urea and related apparatus / Gianfranco Benedetti; assignee Urea Casale S.A.—№ 13/984733; filed 09.12.2011; issued 28.11.2013.
20. Pat. № 7955566 B2, US, Int. Cl B01J8/18. Fluid bed granulator / Gianfranco Benedetti; assignee Urea Casale S.A.—№ 11/939915; filed 14.11.2007; issued 07.07.2011.
21. Pat. № 2006/094620 A1, WO, Int. Cl, B01J2/16. Process and device for fluidized bed granulation / Gianfranco Benedetti, Carla Burlando; assignee Urea Casale S.A.—№ PCT/EP2006/001502; filed 20.02.2006; issued 14.09.2006.
22. Vortex layer technology: implementation of ideas/«Neuhaus Neotec» GmbH, (2014)
23. Fluidized Bed Granulation/Umang Pharmatech Pvt. Ltd., (2014)
24. Huizhou Pingfang Trading Co. Ltd. [Electronic source]. Access mode: <http://pharmach.en.alibaba.com/>
25. Changzhou Fengqi Drying Equipment Co. Ltd. [Electronic source]. Access mode: <http://czfengqi.en.alibaba.com/>
26. Yixin Drying Equipment Co. Ltd. [Electronic source]. Access mode: <http://yixindrying.en.alibaba.com/>
27. Changzhou Xianfeng Drying Equipment Co. Ltd [Electronic source]. Access mode: <http://www.tradekey.com/company/Changzhou-Xianfeng-Drying-Equipment-Co-Ltd-5251482.html>
28. Changzhou Xiandao Drying Equipment Co. Ltd [Electronic source]. Access mode: <http://www.china-dryer.com/en/index.html>
29. Wong PM, Chan LW, Heng PWS (2013) Investigation on side-spray fluidized bed granulation with swirling airflow. *AAPS PharmSciTech* 14(1):211–221
30. Pat. № 1020040047753 A KR, Int. Cl B01J8/38 (2006/01). Device for treating powder particles by rotary flow / Wakamatsu Yoshihiro, Watano Satoru; assignee Nara Machinery Co Ltd.—№ 1020037016134; filed 10.12.2003; issued 05.06.2004.

31. Pat. № 5695701 US, Int. Cl B01J2/16. Apparatus and a process for the preparation of an agglomerated material/Christian Reedtz Funder, Jens Mourits Sorensen, Morten Mohr Hansen; assignee Niro Holding A/S—№ 564149; filed 15.11.1994; issued 09.12.1997.
32. Pat. № 8628276 US, Int. Cl B65G53/10, B01J8/00. Fluidizing apparatus with swirl-generating means/James Edward Delves, Neil Keith Young, David Oliver Drew; assignee Cameron International Corporation—№ 10/514960; filed 30.05.2003; issued 14.01.2014.
33. Artyukhov AE, Artyukhova NO (2019) Technology and the main technological equipment of the process to obtain N_4HNO_3 with nanoporous structure. Springer Proc Phys 221:585–594
34. Artyukhov A, Artyukhova N, Ivaniia A, Galenin R (2017) Progressive equipment for generation of the porous ammonium nitrate with 3D nanostructure. In: proceedings of the 2017 IEEE 7th international conference on nanomaterials: applications and properties, NAP 2017, 2017-January, 03NE06

Features Forming and Studying Quantum-Dimensional Structures on Surface Electrons Over Helium



V. A. Nikolaenko

Abstract The contemporary nanoelectronic widely uses a quantum-size structures (QSSs). Two-dimensional QSSs are formed in potential well near the smooth matter boundary. The substrate modulation using either linear or dot inhomogenaties reduces QSSs either to one-dimensional system or to zero-dimensional one which are described the Schrödinger's equation. In this work, some possibilities creating and study features of QSSs with surface electrons (SEs) over helium were considered. Examples of the electron systems are applied. One of them is the quasi-one-dimensional system at the relative large potential well, and other one is combination the surface electrons and the surface anions over helium layer. The substrate modulation was performed either the dielectric microcylinders or add the semi-spheres accordingly. The electrostatic model these objects in the uniform electric field confirms the forming quantum wires or quantum dots with SEs over inhomogeneities. The simplest electron transport method for the QSS-SEs features research was applied. The experiments carried out in the temperature interval 0.8–3 K at the electron density up to 10^9 cm^{-2} .

Keywords Quantum dot · Quantum wire · Liquid helium · Surface electrons · Anion

1 Introduction

The modern nanotechnology gives a new glance the some physical effects in the quantum-size structures (QSSs) with possibility the structures use in the nanoelectronic innovations [1]. The electrons form a two-dimensional (2D) structure in the potential well near the smooth surface boundary the different matters or the matter phases. Modulation the substrate surface properties either in one direction or in both directions lets designed artificial a quantum wires (QWs) or a quantum dots (QDs)

V. A. Nikolaenko (✉)

B.Verkin Institute for Low Temperature Physics and Engineering of NAS of Ukraine, Prospekt Nauky, 47, Kharkov 61103, Ukraine

e-mail: nikolaenko@ilt.kharkov.ua

accordingly. The energy spectrum of QW is quantized to across of the electron line and is continuous along line. The QD energy spectrum is quantized at all basis directions.

The surface electrons (SEs) relate to QSSs. The specific properties of two-dimensional surface electrons over helium were discovered at the theoretical analyze by Cole and Cohen [2] and by Shikin [3]. The Fermi energy of surface electrons, $E_F = \pi \hbar^2 n_s / (2m)$, (here, \hbar is the Plank's constant and n_s is the electron density) is small and not achieves 10 mK, so the SEs are a non-degenerated system at the practical temperature. The SE motion is quantized to the surface normal and is quasi-free along. The substrate modulation reduces the SEs to the one-dimensional (1D-SEs) system or to zero-dimensional (0D-SEs) one in view the helium specific. Modulation can easy perform introducing under liquid helium either the row of the dielectric microcylinders or periodically situated dielectric microspheres. Surface electrons serve as well as the object research as the model conducting solid-state matter. SEs can be too the basis the sensitive chips and the quantum bits the quantum computer using both the energy levels of electrons or the electron spins [4–6]. The carry of surface electrons is very sensitive to the electron system confinement, so simplest the electron transport method can apply to research the QSS-SEs system features including the quantum phenomena therein.

2 To Description of the Quantum-Size System

The quantum parameters of QSS are defined from solution the Schrödinger's equation, $\hat{H}\psi(\mathbf{r}) = E_n \psi(\mathbf{r})$, with the appropriate boundary potential, U . Here, $\hat{H} = (\hbar^2/2m)\Delta + U$ is the Hamilton's operator (where m is the electron mass, E_n is the electron energy spectrum, and $\psi(\mathbf{r})$ is the electron wave function). For 2D electron system with the rectangular potential well to normal direction, the electron energy spectrum is $(\pi^2 \hbar^2 n^2)/(2mL^2)$ (here, L is the electron localization size in potential well and $n = 1; 2; \dots$, accordingly). The quantum effects in QSSs are observed at next conditions: The energy interval in the electron spectrum must be more temperature, T , and the electron time relaxation or the electron mobility must be sufficient.

Relative to the surface electrons can note next. The surface electron over helium is localized in shallow potential well expressed as $\varphi(z) = Q_d^2 e^2/z$ (here, Q_d is the parameter characterized the polarization degree of dielectric, and z is the effective electron distance to the helium surface). The SE is distanced from the substrate because the weak helium polarization and that leads to the SE system near 2D ideal. The motion electron normal to substrate is quantized by a "soft" hydrogen-like spectrum. The SE motion along substrate is limited the electron scattering by both the helium atoms in gas at high temperature and the riplons (the helium surface quantum oscillations) at low T . The quantum parameters 2DSE can be estimated exactly enough using de Broglie relation, $p \cdot z \approx \hbar$, and the virial theorem consequence, $2p^2/2m = (Q_d^2 e^2)/z$ [7]. The quantum parameters of surface electron hereby are $E_l = Q_d^2 \cdot R/l^2$ and $z = (4\pi \cdot \varepsilon_0 / Q_d)(\hbar^2/m \cdot e^2)$ (here, R is Ridberg's constant, and ε_0

is the vacuum permittivity). Because the ^4He polarization parameter is 0.007, the values magnitude E_1 and z are 8 K and ~ 10 nm correspondingly. It is must note the row of cryogenic matters with a negative electron affinity, and smooth surface can serve by basis for SE too.

2.1 *The Quantum Expressions for the 1D-SE System and for the 0D-SE One*

1D-SE. The basic electron wave function of 1D-SE across to the conducting channel, y , is

$$\psi(y) = \pi^{-1/4} y_0^{-1/2} \exp\left(-\frac{y^2}{2y_0^2}\right) \quad (1)$$

The value y_0 is the electron localization size the magnitude which is approximately 50 nm. The energy spectrum 1D-SE in the substrate channel is

$$E_n = (n + 1/2) \cdot \hbar\omega + \hbar^2 \kappa^2 / 2m \quad (2)$$

Here, value, ω , is the frequency of the harmonic 1D-SE spectrum in potential well. Second expression is a continuous spectrum in the longitudinal direction of channel where k is the wave vector.

0D-SE. The SE wave function structured substrate is correspond expression (1) at the isotropy-parabolic potential well. The 0D-SE energy spectrum is

$$E_n = (n + 1/2) \cdot \hbar\omega \quad (3)$$

The energy spectrum scale of SE can achieve several hundred mK in magnitude at the large potential well.

3 **The Electrostatic Problem in the Uniform Electric Field for the Cylinder and for the Sphere**

As noted above, the reducing of SEs dimensionality is caused the substrate properties modulation to one or to two directions and that can be performed either the row dielectric cylinders or the set dielectric spheres, respectively. From the electrostatic model using Laplace equation in uniform field, E_\perp , the solution gives the parabolic potential near tops these inhomogeneities. The electric field distribution near the dielectric cylinder and the dielectric sphere correspondingly are considered beneath.

3.1 The Dielectric Cylinder in Uniform Electric Field—1D Model

The Laplace electrostatic expression in uniform electric field under the dielectric cylinder without charges is $\Delta\varphi = 0$ (Fig. 1).

(φ is potential, and Δ is Laplassian). The Fourier substitution, $\varphi = M(r)\cdot N(\alpha)$, leads to an equation with separable variables on r and on α .

$$\frac{r}{M} \frac{d}{dr} \left(r \cdot \frac{dM}{dr} \right) + \frac{1}{N} \frac{d^2 N}{d\alpha^2} = 0 \tag{4}$$

The boundary condition is

$$\varepsilon_i \left(\frac{\partial \varphi_i}{\partial r} \right)_{r=a} = \varepsilon_e \left(\frac{\partial \varphi_e}{\partial r} \right)_{r=a} \tag{5}$$

The electric potential, φ_i and electric field, E_i near border are accordingly

$$\varphi_i = -E_{\perp} \frac{2\varepsilon_i}{\varepsilon_i + \varepsilon_e} \cdot r \cdot \cos \alpha + \varphi_0 \tag{6}$$

$$E_i = -\frac{d\varphi_i}{dx} = E_{\perp} \frac{2\varepsilon_i}{\varepsilon_i + \varepsilon_e} \tag{7}$$

For SEs over the profiled substrate covered by thin dielectric film with the helium layer, the equation solution in uniform field, E_{\perp} , gives the parabolic view potential near tops of inhomogeneities. At values $\varepsilon_i > \varepsilon_e$ the electric field E_i twice more relative E_{\perp} .

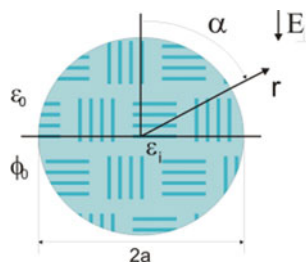


Fig. 1 Cross-section of the dielectric cylinder in uniform electric field, E . Here r and α are radial and angular coordinates, correspondently and $2a$ is cylinder diameter (others symbols are indicated in text)



Fig. 2 (left). Example of a separate sphere. (right). The set of spheres covered by the smooth plate with helium film or the massive helium layer

3.2 The Dielectric Sphere(s) in Uniform Electric Field—0D Model

The electrostatic model with use Laplace equation in the spherical coordinate system is (according to the algorithm in previous) (Fig. 2).

$$\frac{1}{M} \frac{d}{dr} \left(r^2 \cdot \frac{dM}{dr} \right) + \frac{1}{N \sin \alpha} \frac{d}{d\alpha} \left(\sin \alpha \frac{dN}{d\alpha} \right) = 0 \tag{8}$$

The boundary conditions of this problem are same as (6), and solutions for sphere are next

$$\varphi_i = -E_{\perp} \frac{3\varepsilon_i}{\varepsilon_i + \varepsilon_e} \cdot r \cdot \cos \alpha + \varphi_0 \tag{9}$$

$$E_i = E_{\perp} \frac{3\varepsilon_i}{\varepsilon_i + \varepsilon_e} \tag{10}$$

The electric field value in the dielectric sphere is $E_i = 3E_{\perp}$ at values, $\varepsilon_i > \varepsilon_e$.

So, takes a place concentration of the electric field over the inhomogeneities tops (dielectric cylinder or dielectric sphere, here). That is leading to the condition for forming either QW or QD with SEs over the helium layer correspondingly.

4 Some Experimental Investigation of the Low-Dimensional Systems with the SEs Over Helium

Here is considered researches the SEs low-dimensional systems of two types: quasi-one-dimensional system (Q1D) and quazi-zero-dimensional system (Q0D).

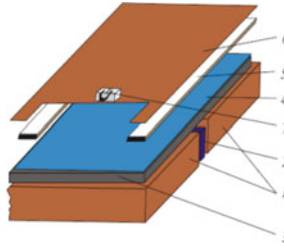


Fig. 3 Cell sketch for the SE conductivity measurement. Here, 1–2—the measurement electrodes, 3—dielectric substrate, 4—helium film, 5—guard electrode, 6—upper electrode, 7—heat filament

4.1 The Experimental Setup

The investigation QSSs can be performed either spectroscopy method or the low frequency the charge transport method. The last is simplest for the arranging and the experimental study the low-dimensional systems conductivity (semi-conductivity, in particular). The essence method is measure in current regime the signal via sample coupled capacitively with the measurement electrodes and the calculation on signal components either admittance (Re part, here) or impedance. The cell is shown in Fig. 3. The effective electron density, n , for SEs is determined by the capacity potential, V , as $C = ne/V$.

It can note the number of investigations SEs had been performed such method in the different variation, for example [8, 9].

4.2 The Experimental Results

According to the phase diagram “electron gas—Wigner crystal” the research was performed in the electron gas region at temperature higher the Fermi energy and at the electron densities far “quantum melting”. Some features as well the Q1D as the specific features Q0D electron systems over helium considered beneath. (The number of results was presented at International Conferences NANO 2019–NANO 2021).

Q1D. The Q1D-SEs over the curvature surface of helium in grooves of the profiled substrate proposed and realized in [10 and 11] accordingly and detailed in [12]. Here, the profiled substrate is a row the dielectric fibers. Need to note at high the SE surface density and the pressing electric field has a place the electrohydrodynamic instability with losing electrons (or its part). Stabilization SE in channels was performed by the negatively charged meander line [13]. Here, additional to outer field, the electron charge field on the fiber tops was used. The temperature range in experiments was from 1.5 to 0.9 K and the ^3He refrigerator used for lowering temperature. The measurement was performed by two-phase lock-in-analyzer working on

the signal frequency 20 kHz at 2–150 mV rms accordingly. The experimental procedure is next. At start, the non-thermalized electrons charged the substrate for creating the inner electric field. After that the slow electrons (at $T \sim 1.4$ K) form Q1D-SEs at corresponding outer field. The conductance of SE at changing T is measured. The researches features are demonstrated in Figs. 4–6. On Fig. 4 shown this dependence at small potential both inner and outer electric field. The temperature dependence carried out into both the scanning directions.

The more quality dependence takes a place at number scanning on T for both the charged stripes and the SEs with potential near 15 V (Fig. 5).

The differential of last dependence is shown on Fig. 6. Notice, the dependence diff σ versus T is like the electron density states, and the peaks distance accord the Q1D-SEs energy spectrum.

Q0D. The SEs conductivity with surface anion (SA) here has demonstrated. It is known that in dense helium gas or in presence of high field (outer or inner), the surface electron forms surface anion [9, 14]. Related to SE mobility, SA is essentially low caused the hydrodynamic it is moving. The disk-shaped SA formed threshold

Fig. 4 Temperature dependence σ versus T at small charges substrate and SEs (in begin of experiment)

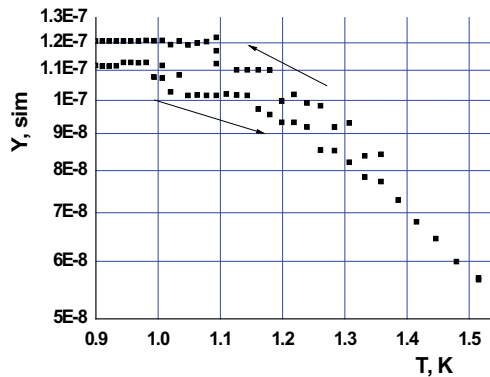


Fig. 5 Dependence σ versus T after some T -cycles at potential near 15 V for both the charged stripes and the SEs

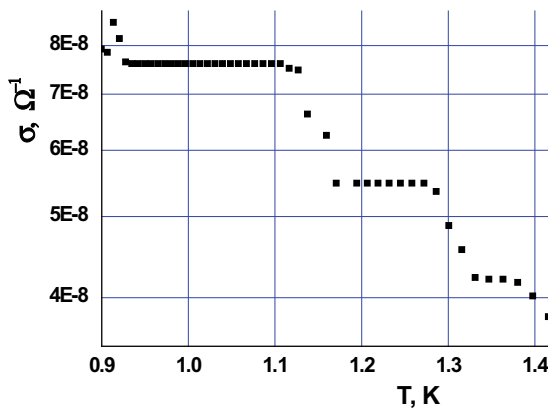
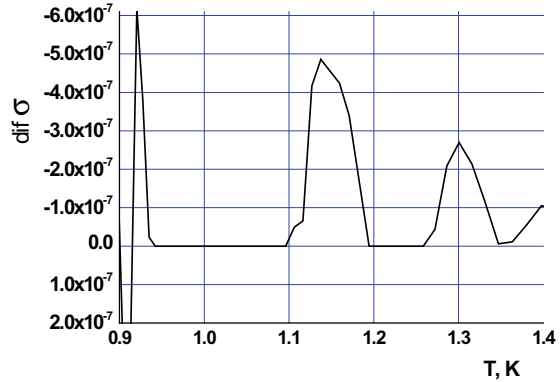


Fig. 6 Dependence $\text{dif } \sigma$ versus T (according to Fig. 4)



way in density gas was considered [15]. In Q1D-SEs system, SA experimentally studies in [16].

In this work, the inhomogeneities for SEs and SA were on polymer film as a lattice of near semi-spheres of $5 \times 5 \mu\text{m}$ in period. The film placed on row of a glass guide lights $220 \mu\text{m}$ in diameter. The substrate placed on two measurement electrodes $4 \times 8 \text{mm}^2$ in size is situated about 4 mm above the helium surface.

The electron conductivity σ was measured in the temperature range 1.7–3.0 K, where its value is limited by the interaction of electrons with the helium atoms in vapor. Under the monotonic increase in temperature (exponential increase in the density of a vapor phase), the conductivity of SE decreases as usually. However, at $T = 2.45 \text{ K}$, an abrupt increase of σ near 2.5 times is observed. Further increase in T leads to the slowly decrease in σ according to the gas density. And then to fall near two orders are caused full SE to SA transition. The fall in conductivity takes a place at the higher value T when the higher start the electron density: $\sim 4 \times 10^8 \text{ cm}^{-2}$ (Fig. 6) and $\sim 6 \times 10^8 \text{ cm}^{-2}$ (Fig. 7). The reverse dependence $\sigma(T)$ is characterized by low conductivity of the system up to same temperature 2.45 K and growth conductivity by approximately the order magnitude near initial value. Jump can be attributed to the topology consisting from “heavy” SAs is surrounded by “light” SEs (Fig. 8).

5 Conclusion

Study structural and phase transitions in a low-dimensional electron system chase as well the fundamental as the applied aims. The surface electron system over helium is good object and model for research where takes in view the helium-specific features. The simplest transport measurement method is acceptable here for study the transition features. The electrostatic model either the microcylinders or microspheres under the smooth dielectric plate and the helium surface demonstrates the substrate modulation

Fig. 7 Dependence conductivity of SEs, σ over helium from temperature, T (the gas scattering electron region) in presence of SAs at electron concentration $\sim 4 \times 10^8 \text{ cm}^{-2}$

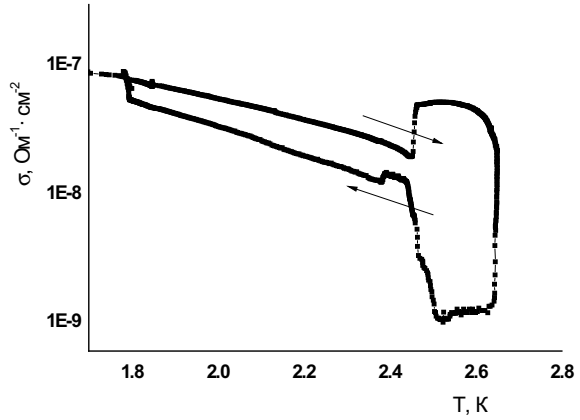
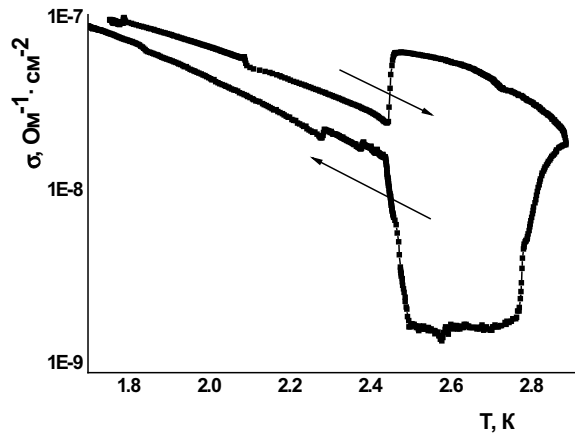


Fig. 8 Temperature dependence the SEs conductivity over helium (the electrons gas scattering region) in presence of SAs. The charge concentration is about $6 \times 10^8 \text{ cm}^{-2}$



with the possibility charging the structure tops. That leads either to 1D-SEs or to 0D-SEs systems over helium layer with the quantum parameters according by parabolic potential.

The experimental study is showed both the 1D-SEs conductivity is quantized and has a place the unusual 0D-SEs conductivity jump at SE-SA transition at the density helium gas. So, a new possibility creating low-dimensional structures with SEs over helium layer is appearing. The study features with surface electrons at considering conditions need be continued. Some other features of QSS-SE considered using the zone theory noted in work [17]. The theoretical consideration the experimental results can qualitatively add these investigations.

References

1. Alferov ZI (1998) The history and the future of semiconductor heterostructures. *Semicond Phys Technol* 32(1):3
2. Cole MW, Cohen MH (1969) Image-potential-induced surface bands in insulators. *Phys Rev Lett* 23:1238
3. Shikin VB (1948) About moving of the helium ions near boundary vapor-liquid. *JETPH* 58: 1748 (in Russian)
4. Platzman PM, Dykman MI (1999) Quantum computing with electrons floating on liquid helium. *Science* 284:1967–1969
5. Lyon SA (2006) Spin-based quantum computing using electrons on liquid helium. *Phys. Rev A*74: 052338
6. Nikolaenko VA, Pashchenko AG (2020) Longitudinal quantum oscillations of surface electrons over helium film on a structured substrate for quantum computer. *Int Res Practice Conference. Nanotechnology and Nanomaterials (NANO2020)*, P 507
7. Landau LD, Lifshitz EM (1965) *Theoretical Physics (Mechanics)*. Moscow: Nauka, P 35 (in Russian)
8. Sommer WT, Tanner DJ (1971) Mobility of electrons on the surface of liquid ^4He . *Phys Rev Lett* 27(30):1345–1349
9. Andrei EY (1984) Observation of the polaronic transition in a two-dimensional electron system. *Phys Rev Lett* 52(16):1449–1452
10. Kovdrya YZ, Monarkha YP (1986) 1D electron system over liquid helium. *Fiz Nizk Temp* 12:1011–1015
11. Kovdrya YZ, Nikolaenko VA (1992) Q1D electron system over liquid helium. *Fiz Nizk Temp* 18:1278–80
12. Sokolov SS, Hai Guo-Qiang, Nelson S (1995) Mobility of electrons in Q1D channel on the liquid helium surface. *PRB* 51:5977–5988
13. Marty D (1986) Stability of two-dimensional surface electrons on the profiled helium surface. *J Phys C* 19:6097
14. Monarkha YP (1975) Self-trapped electron surface states above a helium film. *Low Temp Phys* 1:524–534
15. Shikin VB (2004) Disk-shaped electron bubbles in gas helium. *JETP-Lett* 80(6):472–476
16. Nikolaenko VA, Smorodin AV, Sokolov SS (2011) Possible formation of autolocalized state of quasi-one-dimensional surface electrons in dense helium vapor. *Low Temp Phys* 37(2):119–126
17. Ginzburg VL, Monarha YP (1978) Surface electrons in helium over macroscopic structure. *Fiz Nizk Temp* 4:1236–1239

Porous Surface Structure and Physico-Chemical Properties of the Urea–Formaldehyde Polyfoam



S. Kurta, A. Nemish, S. Fedorchenko, O. Khatsevich, and V. Riy

Abstract A new method and laboratory installation for measuring gaseous formaldehyde emissions were proposed, by using the automatic formaldehyde analyzer MIS-98170, for urea–formaldehyde resins (UFR), thermal insulation foams based on them, during their manufacture and operation. In order to reduce the toxic characteristics of UFR and urea–formaldehyde polyfoam (UFF), foaming of the composition(UFF) was performed in a foam generator with compressed air. Research has shown that the addition to the UFR resin of 1% $\text{CO}(\text{NH}_2)_2$, reduced by 2 times the content of free formaldehyde in the resin, and reduce by 7.5 times the emission of free formaldehyde from urea–formaldehyde foams into the atmosphere, when drying in air. At the same time, the additional introduction of standard UFF foam composition, 1.5% CaCO_3 as a gas generator, reduces the linear and volumetric shrinkage of UFF polyfoam by 5–8 times and improves its thermal insulation properties.

Keywords Urea · Formaldehyde · Resins · Polyfoam · Toxic · Shrinkage

1 Introduction

Thermal insulation microporous foams based on various polymer compositions have been widely used for thermal insulation of buildings and equipment in various industries. However, the cost of raw materials for the production of most of them is quite high. In this regard, the production of foams based on cheap and available water-soluble polymers, such as urea–formaldehyde resins (UFC) [1], is relevant.

S. Kurta (✉) · A. Nemish · S. Fedorchenko · O. Khatsevich · V. Riy
Department of Chemistry, Vasyl Stefanyk Precarpathian National University, Halyska Street.
201/320, Ivano-Frankivsk, Ukraine
e-mail: sergiykurta@pnu.edu.ua

O. Khatsevich
e-mail: khatsevich.olga@meta.ua

V. Riy
e-mail: skylark.ua@ukr.net

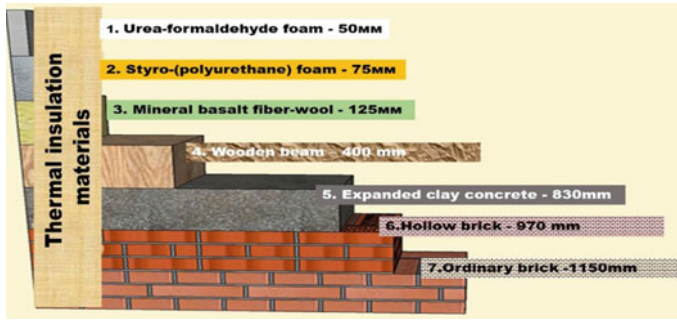


Fig. 1 Comparison of the thickness of different thermal insulation materials for the same thermal insulation efficiency: 1-urea–formaldehyde foam insulation, 2-expanded polystyrene, 3-mineral-basalt fiber-wool, 4-wooden beam, 5-expanded clay concrete, 6-hollow brick, 7-solid brick

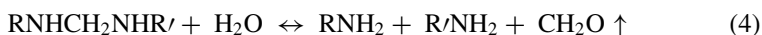
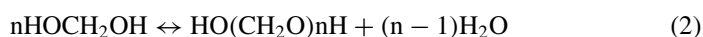
Urea–formaldehyde polyfoam (UFF)—occupy a special place among the cheapest gas-filled plastics for thermal and sound insulation. UFFoam does not have the ability to self-combustion, UFF stops burning after removing the flame source and it does not forms a polymer melt during combustion, which confirms high fire safety compared to common polystyrene and polyurethane foam [2]. Urea–formaldehyde foams are almost as good as polystyrene and polyurethane foams in terms of industrial use for thermal insulation. Their main advantages are good thermophysical characteristics, low cost and availability of raw materials and simple technology for forming foams. But UFFoams have a number of disadvantages, in particular, the significant release of toxic formaldehyde from UFFoams in their manufacture and foaming. In addition, UFFoams have a large shrinkage—15–20% reduction in linear and volumetric dimensions after forming, which leads to a decrease of the physical and mechanical characteristics of the material. UFFoams also have high water and moisture absorption, which also reduces the thermal insulation properties during long-term operation [3] (Fig. 1).

The aim of the work is to reduce the evaporation of free formaldehyde from urea–formaldehyde foam insulation by introducing special chemical acceptors, as well as reducing the shrinkage of the foam after drying, by introducing chemical foaming agents. Based on our goal, it was necessary to perform the following tasks: (1) to develop a method for determining the emission of gaseous formaldehyde from CF foam using an automatic formaldehyde analyzer MIS-98170 [4]; (2) test and select the best chemical formaldehyde acceptor to reduce the emission of gaseous formaldehyde from the foam during its preparation and operation; (3) to offer a chemical gasifier to reduce the linear and volumetric shrinkage of the foam insulation after its manufacture and use.

2 Experimental

For the production of foam insulation (UFF) use mainly urea–formaldehyde resin with a reduced content of free formaldehyde (0.1–0.15% (wt.)) [5]. However, when forming, approving and using such UFF, a large amount of gaseous formaldehyde diffuses into the air of the working area of such insulation, which can significantly exceed the maximum permissible concentration, for humans, in the air of the working area $\geq 0.5 \text{ mg/m}^3$ (0.4 ppm) [6]. Table 1 shows the characteristics of UFR brand KPS-G for the manufacture of foam type UFF [7].

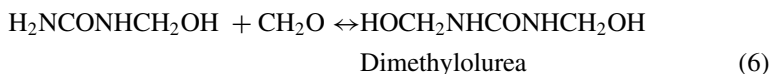
The chemical reactions (1, 2, 3 and 4) that lead to the diffusion of gaseous formaldehyde from the foam during the preparation, drying and operation of the foam are as follows:



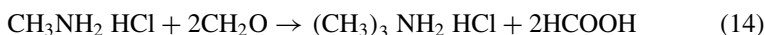
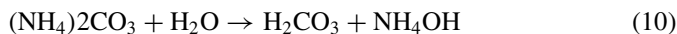
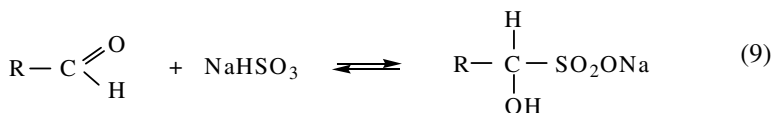
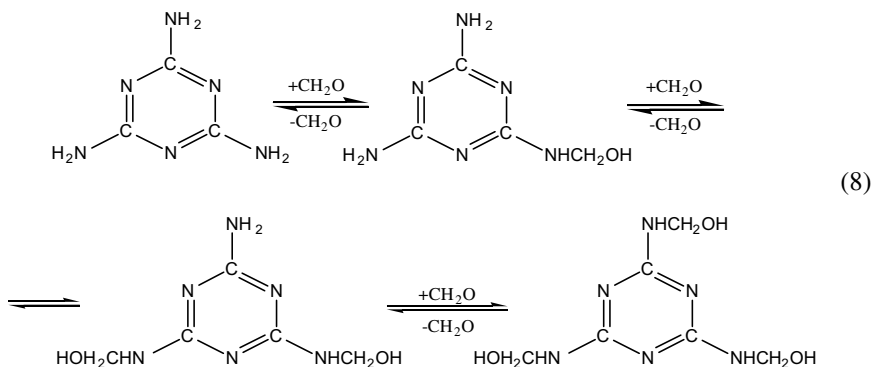
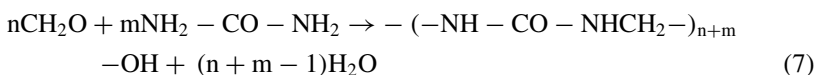
The chemistry of the process of neutralization of formaldehyde can take place by reactions (5 and 6), the addition of formaldehyde to urea, resulting in the formation of methylol derivatives of urea:

Table 1 Characteristics of urea–formaldehyde resin, brand KPS-G, for the manufacture of foam UFF

No.	Name of characteristics	Requirements of the technical standard	Mark KPS-G
1	Appearance	Homogeneous suspension	Corresponds to the standard
2	Mass fraction of non-volatile substances, at 105 °C 2 hours, %	51–56	52,58
3	Density of resin, g/cm ³	1,28±0,1	1,196
4	Concentration of hydrogen ions, pH	7,5-8,5	7,67
5	Miscibility with water at 20 °C	1:1	1:2
6	Gelatinization time at 100 °C, sec	60	82
7	Mass fraction of free formaldehyde, %	0,25	0,266



In this work, an attempt was made to reduce the toxicological properties of CFP by reducing the emission of free formaldehyde from foams, with the introduction of 5-various chemical acceptors of formaldehyde in urea-formaldehyde resin for foam [7]. The interaction of these 5-substances with formaldehyde can occur by the following reactions (7–14).



3 Results and Discussion

We have developed a method and designed a laboratory installation (Fig. 2), with using the formaldehyde analyzer MIS-98170, for to measure the amount of gaseous formaldehyde diffusing with UFR and UFF in the process of their manufacture and use.

Free formaldehyde, which diffuses from urea–formaldehyde foam, with air flow from the compressor, passes through the electrochemical sensor of the automatic formaldehyde analyzer MIS-98170, which is closed in a circle, Fig. 2, to stabilize the CH_2O concentration. This installation was used to determine the concentration of CH_2O in the air of the working area during the formation and operation of the UFF.

Studies have shown that the diffusion of gaseous formaldehyde with UFF can be effectively reduced by adding the above-mentioned chemical acceptors of formaldehyde to urea–formaldehyde resin at various technological stages of the foam production. As can be seen from Fig. 3, when introduced into the UFR resin 0.5–1.0% wt. % as an acceptor of urea ($\text{CO}(\text{NH}_2)_2$, immediately before mixing the components of the foam, the diffusion of formaldehyde gas decreased by 5–7 times, compared to UFF made without the addition of an acceptor at 20 °C for 4 h, and fell to almost zero after drying the foam for 24 h. In particular, it should be noted that when drying UFF at 35–40 °C diffusion of formaldehyde with foam increases slightly, but immediately drops to zero from the sample containing 1% of the acceptor $-\text{CO}(\text{NH}_2)_2$.

From Fig. 3, it is seen that in the manufacture, curing and drying of foam made from UFR resin without acceptors, the emission of free formaldehyde is so intense that significantly exceeds the recommended maximum allowable concentration of formaldehyde for a short period of time 2.00 mg/m^3 (ppm) (short-term exposure limit 15 min STEL OSHA). However, this value does not decrease throughout the manufacturing process of foam to the recommended limit value for indoor use (0.1 ppm)



Fig. 2 Laboratory unit for measuring the diffusion of free formaldehyde: 1-conical flask with a sample of UFR or UFF, 2-flow gas analyzer for formaldehyde MIS-98170, 3-air compressor for air supply with two tubes, 4-tube that blows air with CH_2O with flasks and feeds in MIS-98170; 5-tube that absorbs air together with CH_2O from MIS-98170 and feeds into the air compressor

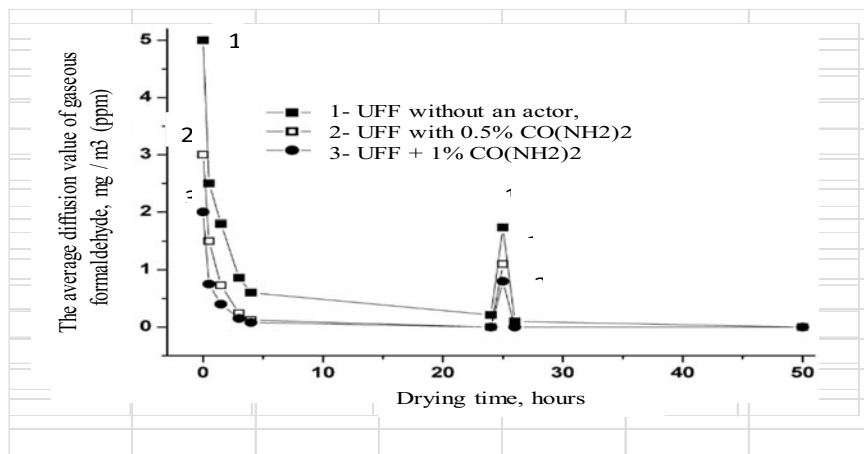
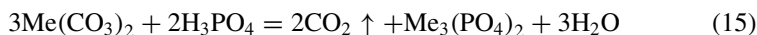


Fig. 3 The average value of the diffusion the gaseous formaldehyde into the air of the working area during the manufacture of foam from CFS (after drying in air at 20 °C): 1-without acceptor, 2-addition-0.5% CO (NH₂)₂, 3-addition 1% CO (NH₂)₂ and after heating to 40 oC, after 24 h

[7]. It was found that positive results in the neutralization of formaldehyde, also gives melamine in the amount of 0.1%. The peculiarity is that the effective action of melamine as an acceptor of formaldehyde is detected only when adding to the composition of the foam-forming composition with additional heating.

To reduce the emission of formaldehyde from the UFF, the introduction of an additional component—a gas-forming agent—CaCO₃, was also investigated. At the same time, a gaseous substance—CO₂, which was released due to a chemical reaction between the components of the foam—hardener—H₃PO₄ and CaCO₃, additionally acts as a foaming agent in the composition. This is a chemical reaction (16) with the release of carbon dioxide, which further foams the CFS, but chemically: 1.3% CO(NH₂)₂ urea was added to the urea–formaldehyde resin as an acceptor of formaldehyde and 1.5% chalk CaCO₃ as a gasifier (Fig. 4). As can be seen from Fig. 4, the emission of formaldehyde from the approved UFF obtained from resin without additives (histogram 1 Fig. 4) is reduced from 6.9 ppm to 2.5 ppm for CFP from resin with the addition of 1.3% CO(NH₂)₂ (histogram 0.2 Fig. 4)), further reduced to 1.25 ppm for UFF with the addition of 1% CO(NH₂)₂ and 1.5% CaCO₃ (histogram 3 Fig. 4). Therefore, we can conclude that from the foam made of UFF with the addition of urea and chalk, the emission of free formaldehyde into the atmosphere is reduced by 5.5 times according to the data in Fig. 4. Our results have been confirmed by other authors [10].



The next stage of our research was to improve the morphological properties of UFF, namely, to study the effect of additional chemical gas generators on reducing the shrinkage of urea–formaldehyde foam. From the literature [11, 12] and from

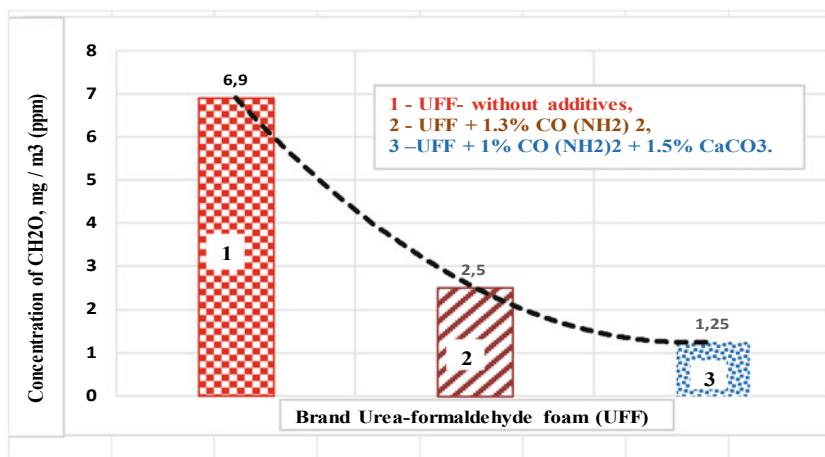


Fig. 4 Histogram of the dependence of diffusion of gaseous formaldehyde (CH₂O) from samples of urea–formaldehyde foam on the content of additives (acceptor –CO(NH₂)₂ and gasifier –CaCO₃): 1—CFP without additives; 2—CFP + 1.3% CO(NH₂)₂; 3—KFP + 1% CO(NH₂)₂ + 1.5% CaCO₃

practice it is well known that urea–formaldehyde foams have one serious drawback during their application and operation, namely, a very significant reduction in linear and volumetric dimensions after complete drying from water (up to 60% of the mass). The reduction in the linear size of the UFF of the foam can be 6–8%, and the volume shrinkage can reach 15–22%. This disadvantage leads to a reduction in the size of the manufactured thermal insulation material, which causes the formation of cracks, holes, and significantly impairs the thermal and sound insulation and physical and mechanical properties of the material. As a result, the foam forms gaps between the form and the formwork when filling, in the insulating layer of foam there are voids and dips. Heat and sound insulation properties of polyfoam deteriorate by 15–25%. In practice, this requires re-filling cracks and voids with a new portion of foam, which also does not guarantee the full density of the resulting material [12, 13]. It was impossible to correct this shortcoming in the approved and dried UFF of the foam by mechanical or any other method, because it depends on the internal porous structure of the foam.

UFF foam has open pores of different sizes (Fig. 5), which are formed during the curing of mechanically formed foam and drying of urea–formaldehyde foam. In the UFF, which made from UFR resins with additional components—formaldehyde acceptor 1.3% CO(NH₂)₂, find gas-forming 1.5% CaCO₃, we can see partially closed pores with much smaller pore size (Fig. 6).

We set a goal to reduce the linear and volumetric shrinkage of the UFF foam during manufacture and after drying to a minimum of 2–6%. Such values of shrinkage almost do not affect the thermal insulation and physical and mechanical properties and appearance of the foam, do not cause cracks and other structural defects. The raw material for UFF foam is a 50–65% dispersion of urea–formaldehyde resin in

Fig. 5 Photomicrograph of CFP made of no additional components (microscope MBS-10 (magnification $\times 400$))

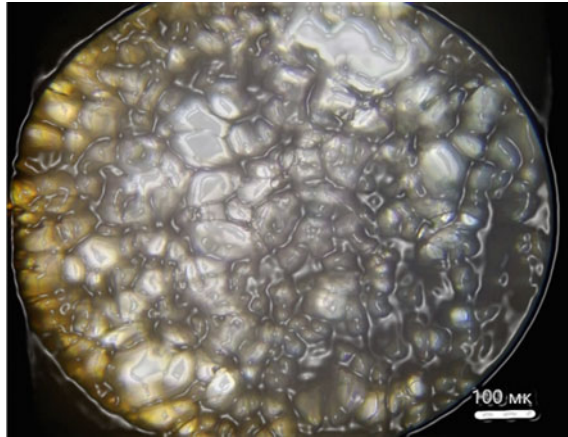
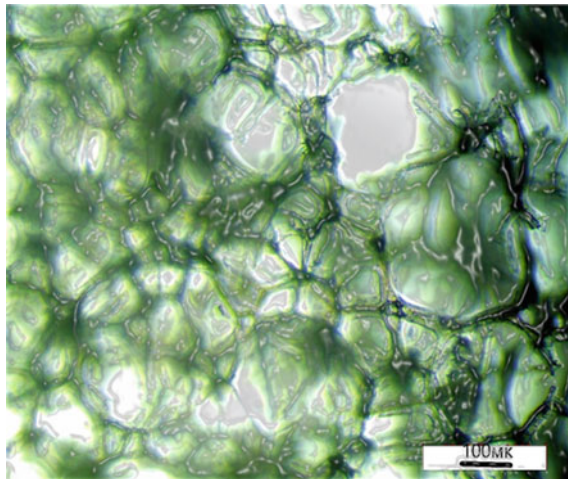


Fig. 6 Photomicrograph of CFP made with the addition of 1.3% $\text{CO}(\text{NH}_2)_2$ and foaming agent 1.5% CaCO_3 . (MBS-10 ($\times 400$))



water, which before mixing with the foaming agent and hardener is again diluted with water to 25–30% concentration [14]. Therefore, when drying the foam should evaporate up to 70–75% of water, which reduces the linear and volumetric dimensions of the mechanically formed foam and the finished foam—shrinkage by 8–20%. It was proposed to solve this problem by introducing into the composition of the foam composition of an additional foaming reactive reagent—gas-forming CaCO_3 .

As the main mechanical foaming agent in the composition for the foam used synthetic surfactants—alkyl- and aryl sulfonic acids (ROSO_2OH , where $\text{R} = (-\text{C}_n\text{H}_{2n+1})$ or C_6H_5-). To obtain foam, they are mixed with UFR in the amount of 1–3%, and then intensively mechanically foamed with air in a special installation, in a laboratory high-speed mixer (1500–10,000 rpm). To the formed foam is added

an acid hardener—concentrated-90% H_3PO_4 , which is a crosslinking reagent in the curing of urea–formaldehyde resin and forms solid urea–formaldehyde foams.

Figures 7 and 8 show the differential distribution of pores in UFF by size depending on the number and nature of the introduced additives from the photo in Figs. 5 and 6. As can be seen from the above histograms, in UFF made of UFR without additives, the average pore size is in the range of 60–80 μm (Fig. 7). Whereas for UFF, made of UFR with additional components—1.3% $\text{CO}(\text{NH}_2)_2$ and 1.5% CaCO_3 , the average pore size is 1.5–2 times smaller and corresponds to the range of 40–60 microns (Fig. 8).

Improvements in the morphological properties of UFF are confirmed by our other experimental data, namely, the additional use of the chemical gas-forming CaCO_3 , leads to an increase in the multiplicity of foam by 1.5–2 times (ratio of foam to volume of UFR solution) in the manufacture of foam. In Figs. 9 and 10 show the dependence of the volume of foam and density of urea–formaldehyde foams without additives UFF-1, and with additives UFF-2, UFF-3, on the nature and amount of additives— CaCO_3 and $\text{CO}(\text{NH}_2)_2$ —after manufacture and drying UFF for 48 h.

As can be seen from Fig. 9, after introduction into the UFR composition, for the manufacture of urea–formaldehyde foam UFF -2 additionally, as a formaldehyde acceptor of 1.3% (wt.) $\text{CO}(\text{NH}_2)_2$, the volume of foam increases from 160 $\text{cm}^3/30$ ml to 250 $\text{cm}^3/30$ ml (foam multiplicity for UFF-2 is 8) (foam multiplicity for UFF-1 is 5), multiplicity increases by 50–60%. After adding as a foaming agent 1.5% wt. CaCO_3 together with 1.3% (wt.) $\text{CO}(\text{NH}_2)_2$, the volume of foam, in the manufacture of UFF-3 increases from 160 $\text{cm}^3/30$ ml to 310 $\text{m}^3/30$ ml (foam multiplicity-10), the multiplicity increases 2 times. Thus, by adding to the UFR a composition of additional components— $\text{CO}(\text{NH}_2)_2$ (1.3% wt.) and CaCO_3 (1.5% wt.)—you can get almost 2 times more foam by volume. At the same time, it was determined that

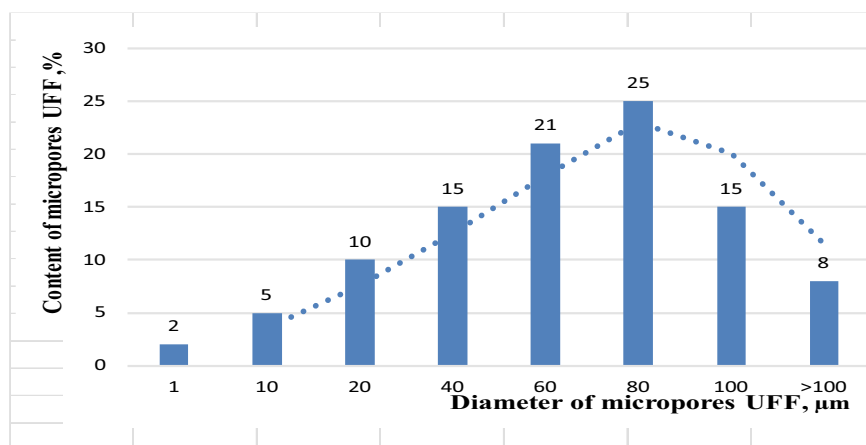


Fig. 7 Pore size distribution in UFF foam made of urea–formaldehyde resin (UFR) without additives

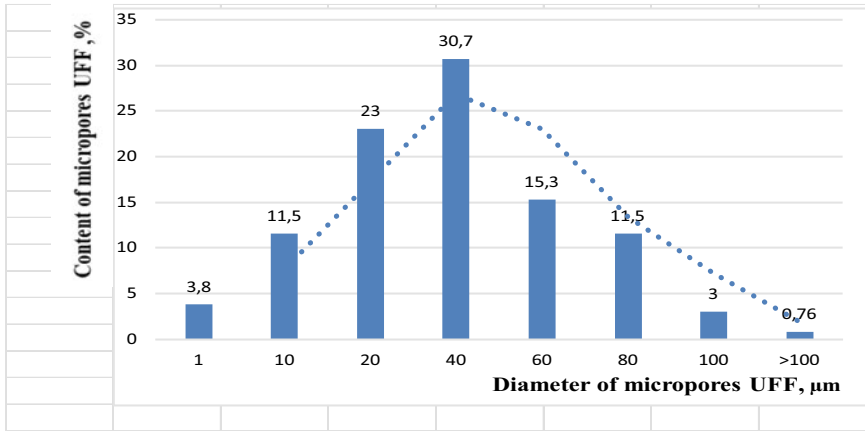


Fig. 8 Pore size distribution in UFF foam made of urea–formaldehyde resin (UFR), with additives—formaldehyde acceptor $\text{CO}(\text{NH}_2)_2$ (1.3% wt.) and gas-forming CaCO_3 (1.5% wt.)

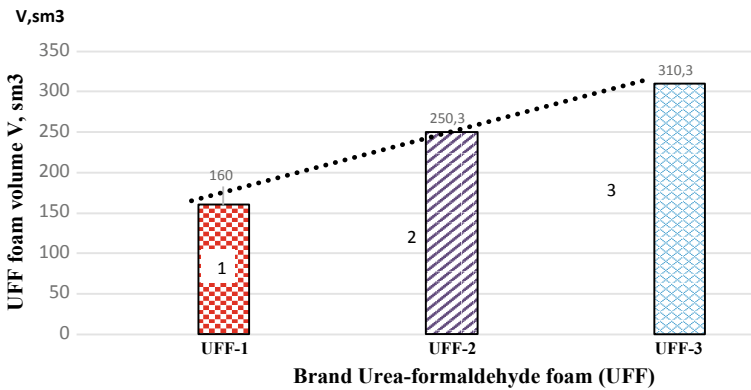


Fig. 9 Dependence volume of UFF foam from the composition and nature of additives: 1—UFF-1-foam made of UFR without additives; 2—UFF-2-foam made of UFR with the addition of $\text{CO}(\text{NH}_2)_2$; 3—UFF-3 foam made of CFS with the addition of $\text{CO}(\text{NH}_2)_2$ and CaCO_3

the introduction of the proposed components reduces the density of samples of UFF-2 and UFF-3 foam compared to the density of UFF-1 foam without additives (Fig. 10). As can be seen from the histograms, the density of UFF-2 foams with formaldehyde acceptor and UFF-3 with acceptor and gasifier is reduced from 10 kg/m^3 to 8.5 kg/m^3 and 6.5 kg/m^3 , respectively, while the density of the foam is reduced by 65%, which helps increase its sound and thermal insulation properties.

But most of all in the research to improve the physical and mechanical properties of urea–formaldehyde foams we were interested in reducing the shrinkage—the size of UFF after curing and drying. To do this, we measured the changes in linear dimensions and calculated the volumetric dimensions (% shrinkage) of the samples obtained UFF

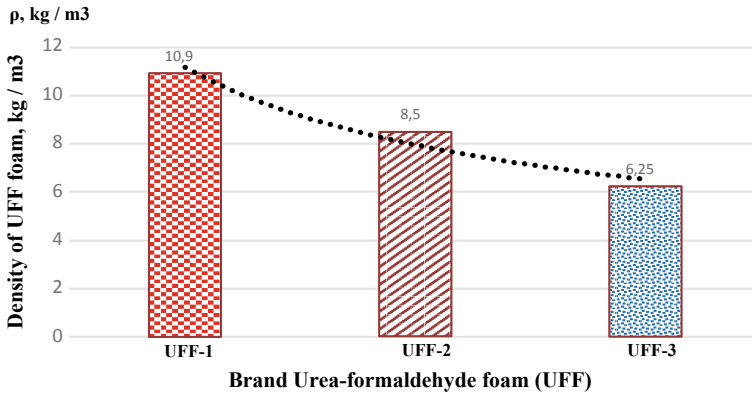


Fig. 10 Dependence density of UFF foam from the composition and nature of additives: 1—UFF-1—foam made of UFR without additives; 2—UFF-2—foam made of UFR with the addition of CO (NH₂)₂; 3—UFF-3—foam made of UFR with the addition of CO(NH₂)₂ and CaCO₃

foams with the addition of acceptor and gasifier. The results are presented in Figs. 11 and 12. As can be seen from the above histograms, compared to UFF foam made of UFR resin without additives, the shrinkage of which is 12.5%, after the introduction as a formaldehyde acceptor of 1.3% (wt.) CO(NH₂)₂, the linear shrinkage of the foam decreases to 8.5%, and falls to 1.6% with the introduction of 1.5% wt. CaCO₃ as an additional foaming agent. That is, shrinkage is reduced by 8 times, which significantly improves the physical properties and reduces the defects of the structure of the foam and, accordingly, increases its insulating properties. At the same time, the volume shrinkage, with the introduction of the above additives, also decreases 5 times—from 20% in UFR without additives, to 4% with the introduction of 1.3% acceptor and 1.5% gas generator (Fig. 12).

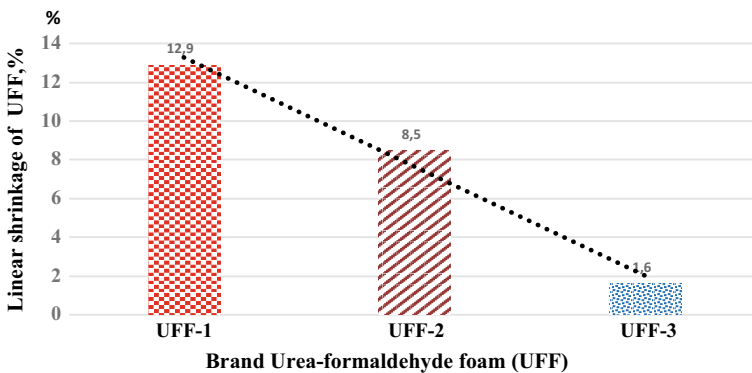


Fig. 11 Dependence of linear shrinkage of UFF from the composition and nature of additives: 1—UFF-1—foam made of UFR without additives; 2—UFF-2—foam made of UFR with the addition of CO (NH₂)₂; 3—UFF-3—foam made of UFR with the addition of CO(NH₂)₂ and CaCO₃

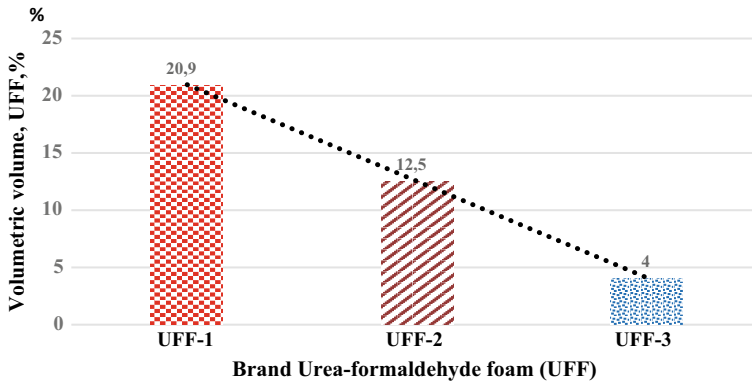


Fig. 12 Dependence of bulk shrinkage UFF from the composition and nature of additives: 1—UFF-1—foam made of UFR without additives; 2—UFF-2—foam made of UFR with the addition of $\text{CO}(\text{NH}_2)_2$; 3—UFF-3—foam made of UFR with the addition of $\text{CO}(\text{NH}_2)_2$ and CaCO_3

4 Conclusion

1. As a result of the research, a new method was proposed, as well as a new installation for measuring the emission of gaseous formaldehyde, using an automatic formaldehyde analyzer MIS-98170, for urea–formaldehyde resins UFR, thermal insulation foams and chipboard their manufacture and operation.
2. In order to reduce the toxic characteristics of UFR and foams, by foaming the UFR composition in the foam generator with compressed air, studies have shown that the addition to the UFR resin 1% $\text{CO}(\text{NH}_2)_2$, reduced by 2 times the content of free formaldehyde in resin, and greatly reduce by 7.5 times the evaporation of free formaldehyde from UFF into the atmosphere of the working area, when drying in air.
3. Additional introduction into the standard UFR composition for foam at the same time other components—1.3% $\text{CO}(\text{NH}_2)_2$ as an acceptor of formaldehyde and 1.5% CaCO_3 as a gasifier—reduces the linear and volume shrinkage of the foam in 5–8 times and improves its thermal insulation properties.

References

1. Виршпа З., Бжезинський Я. Аминопласти. – М.: Химия, 1973. – 344 с.
2. Курта С. А., Федорченко С. В., Хабер М. В. Модификация карбамидоформальдегидных смол на стадии поликонденсации// Вопросы химии и химической технологии. – 2002, №3. – С.73–76.
3. Ляшок Т. В., Федорченко С. В., Курта С. А. Аналіз та пошук акцепторів формальдегіду для отримання низькотоксичного карбамидоформальдегідного пінопласту //Матеріали XXI Міжнародної науково-практичної інтернет-конференції “Тенденції та перспективи розвитку науки і освіти в умовах глобалізації”, м. Переяслав-Хмельницький, 31 січня 2017 р. – С.668–672.
4. Ляшок Т. В., Федорченко С.В. Вдосконалення властивостей спієних амінопластів// Матеріали II Міжнародної науково-практичної конференції “Інноваційний розвиток науки нового тисячоліття”, м. Хмельницький, 22–23 грудня 2017 р. – С. 190–192.
5. Портативний газоаналізатор на формальдегід (CH₂O) <https://simvolt.ua/gazoanalizator-na-formaldegid-mic-98170.html/>
6. Хацевич О. М., Федорченко С.В., Ляшок Т.В., Курта С.А., Нетикша В. Синтез та властивості карбамідо-формальдегідного пінопласту типу “Екоізол”// Тези XX Міжнародної конференції студентів, аспірантів «Сучасні проблеми хімії» (XX ICSPHDS «Modern Chemistry Problems»), м. Київ, 15–17 травня 2019 р. – С. 195.
7. Неміш Андрій, Курта Сергій, Болахан Василь. Удосконалення технології синтезу та властивостей пінопласту”// Матеріали VI Міжнародної науково-практичної інтернет-конференції “Сучасні виклики і актуальні проблеми науки, освіти та виробництва, Київ, 1 липня 2020 р. – С.164–169 https://openscilab.org/wp-content/uploads/2020/07/suchasni-vikliki-i-aktualni-problemi-nauki-osviti-ta-virobnictva_2020_07_01_tezy.pdf
8. ГОСТ 14231–88. Смолы карбамидоформальдегидные. Технические условия. – М.: Изд-во стандартов, 1988. – 22 с. <https://docs.cntd.ru/document/1200020671>
9. Гранично допустимі концентрації хімічних і біологічних речовин в атмосферному повітрі населених місць. <https://zakon.rada.gov.ua/laws/show/z0156-20#Text>
10. Хабаров В.Б. Определение формальдегида, метанола и метилала в фанере, шпоне и карбамидоформальдегидной смоле методом газовой хроматографии с помощью нового устройства для парофазного анализа// Аналитика и контроль. – 2013. – Т.17, №2. – С. 196–203. https://journals.urfu.ru/index.php/analitik_a/article/view/764
11. Панкрушин А.А. Технологическая и экономическая целесообразность применения карбамидных пенопластов / А.А. Панкрушин // Строительные материалы. – 2004. – №5. – С. 10–12.
12. Берлин А.А. Химия и технология газонаполненных высокополимеров / А.А. Берлин, Ф.А. Шутов. – М.: Наука, 1980. – 503 с.
13. Bender J (1964) Handbook of foamed plastics. J Bender N.Y, pp 330
14. Дементьев, А.Г. Стрoение карбамидоформальдегидных пенопластов с взаимoпроникающими ячеистыми структурами/А.Г. Дементьев, Б.В. Левинский, О.Г. Тараканов // Пластические массы. – 1986. – №5. – С. 16–17.
15. Sedlak L (1974) Process for making insulating materials of low combustibility on the basis of foam like urea-formaldehyde resin/United States Patent №3986988. <https://patentimages.storage.googleapis.com/5f/d6/83/6397e560a2dd8f/US5160679.pdf>